

# Transactions of the ASME®

HEAT TRANSFER DIVISION  
Chairman, J. R. WELTY  
Secretary, O. A. PLUMB  
Technical Editor, R. VISKANTA  
Associate Technical Editors,  
R. O. BUCKIUS (1993)  
W. A. FIVELAND (1992)  
L. S. FLETCHER (1992)  
F. P. INCROPERA (1993)  
H. R. JACOBS (1992)  
J. H. KIM (1993)  
J. R. LLOYD (1992)  
D. M. McELIGOT (1992)  
R. J. SIMONEAU (1993)  
W. A. SIRIGNANO (1992)  
L. C. WITTE (1992)

BOARD ON COMMUNICATIONS  
Chairman and Vice President  
M. E. FRANKE

Members-at-Large  
W. BEGELL  
T. F. CONRY  
T. DEAR  
R. L. KASTOR  
J. KITTO  
R. MATES  
W. MORGAN  
E. M. PATTON  
R. E. REDER  
A. VAN DER SLUYS  
F. M. WHITE  
B. ZIELS

President, N. H. HURT, JR.  
Executive Director,  
D. L. BELDEN  
Treasurer,  
ROBERT A. BENNETT

PUBLISHING STAFF  
Mng. Dir., Publ.,  
CHARLES W. BEARDSLEY  
Managing Editor,  
CORNELIA MONAHAN  
Sr. Production Editor,  
VALERIE WINTERS  
Production Assistant,  
MARISOL ANDINO

Transactions of the ASME, Journal of Heat  
Transfer (ISSN 0022-1481) is published quarterly  
(Feb., May, Aug., Nov.) for \$160.00 per year by The  
American Society of Mechanical Engineers, 345 East  
47th Street, New York, NY 10017. Second class  
postage paid at New York, NY and additional  
mailing offices. POSTMASTER: Send address  
changes to Transactions of the ASME,  
Journal of Heat Transfer, c/o THE  
AMERICAN SOCIETY OF MECHANICAL ENGINEERS,  
22 Law Drive, Box 2300,  
Fairfield, NJ 07007-2300.

CHANGES OF ADDRESS must be received at Society  
headquarters seven weeks before they are to be  
effective. Please send old label and new address.

PRICES: To members, \$36.00, annually;  
to nonmembers, \$160.00.

Add \$15.00 for postage to countries outside the  
United States and Canada.

STATEMENT from By-Laws. The Society shall not be  
responsible for statements or opinions advanced in  
papers or printed in its publications (B7.1, para. 3).

COPYRIGHT © 1991 by The American Society of  
Mechanical Engineers. Reprints from this publication  
may be made on condition that full credit be given the  
TRANSACTIONS OF THE ASME,  
JOURNAL OF HEAT TRANSFER,  
and the author, and date of  
publication be stated.

INDEXED by Applied Mechanics Reviews  
and Engineering Information, Inc.  
Canadian Goods & Services Tax Registration #126148048

# Journal of Heat Transfer

Published Quarterly by The American Society of Mechanical Engineers

VOLUME 113 • NUMBER 4 • NOVEMBER 1991

## ANNOUNCEMENTS

- 1047 Change of address form for subscribers
- 1048 Author Index: Volume 113, 1991
- 1053 Call for nominations: The Nusselt-Reynolds Prize
- 1053 Call for papers: Xth National Heat Transfer Conference
- 1054 Announcement and call for papers: International Symposium on Heat Transfer in Turbomachinery
- 1055 Call for papers: 1992 Winter Annual Meeting
- 1057 Call for papers: Fourth Brazilian Thermal Science Meeting
- 1058 Announcement and call for papers: First International Conference on Aerospace Heat Exchanger Technology
- 1059 Information for Authors

## TECHNICAL PAPERS

- 788 Correlation of Thermal Conductivities of Unidirectional Fibrous Composites Using Local Fractal Techniques  
R. Pitchumani and S. C. Yao
- 797 Effect of Interfacial Roughness on Phonon Radiative Heat Conduction  
A. Majumdar
- 806 The Effect of Thermal Conductivity on the Singular Behavior of the Near-Tip Temperature Gradient  
D. Y. Tzou
- 814 Optimization of Radiating Fin Array Including Mutual Irradiations Between Radiator Elements  
B. T. F. Chung and B. X. Zhang
- 823 Numerical Predictions of Local Entropy Generation in an Impinging Jet  
M. K. Drost and M. D. White
- 830 Analysis of Matrix Heat Exchanger Performance  
G. Venkatarathnam and S. Sarangi
- 837 Simultaneously Developing, Laminar Flow, Forced Convection in the Entrance Region of Parallel Plates  
T. V. Nguyen and I. L. Maclaine-cross
- 843 Influence of High Mainstream Turbulence on Leading Edge Heat Transfer  
A. B. Mehendale, J. C. Han, and S. Ou
- 851 Local Heat/Mass Transfer Distributions on the Surface of a Wall-Mounted Cube  
M. K. Chyu and V. Natarajan
- 858 Surface Curvature Effect on Slot-Air-Jet Impingement Cooling Flow and Heat Transfer Process  
C. Gau and C. M. Chung
- 865 Heat Transfer in a Staggered Tube Array for a Gas-Solid Suspension Flow  
D. B. Murray and J. A. Fitzpatrick
- 874 Simultaneous Heat and Mass Transfer From a Two-Dimensional, Partially Liquid-Covered Surface  
Y.-X. Tao and M. Kaviany
- 883 The Aspect Ratio Effect on Natural Convection in an Enclosure With Protruding Heat Sources  
M. Keyhani, L. Chen, and D. R. Pitts
- 892 Natural Convection in a Square Cavity With Thin Porous Layers on Its Vertical Walls  
P. Le Breton, J. P. Caltagirone, and E. Arquis
- 899 On the Low Rayleigh Number Asymptote for Natural Convection Through an Isothermal, Parallel-Plate Channel  
L. Martin, G. D. Raithby, and M. M. Yovanovich
- 906 Three-Dimensional Laminar Natural Convection in an Inclined Air Slot With Hexagonal Honeycomb Core  
Y. Asako, H. Nakamura, Z. Chen, and M. Faghri
- 912 Natural Convection in Vertically Vented Enclosures  
D. M. Sefcik, B. W. Webb, and H. S. Heaton

- 919 Turbulent Natural Convection in a Horizontal Layer of Small-Prandtl-Number Fluid  
F. B. Cheung, S. W. Shiah, D. H. Cho, and L. Baker, Jr.
- 926 Simultaneous Hydrodynamic and Thermal Development in Mixed Convection in a Vertical Annulus With Fluid Property Variations  
W. Aung, H. W. Moghadam, and F. K. Tsou
- 932 A Study of Thermal Radiation Transfer in a Solar Thruster  
S. Venkateswaran, S. T. Thynell, and C. L. Merkle
- 939 Determination of Radiative Fluxes in an Absorbing, Emitting, and Scattering Vapor Formed by Laser Irradiation  
P. Erpelding, A. Minardi, and P. J. Bishop
- 946 Nongray Radiative Gas Analyses Using the *S-N* Discrete Ordinates Method  
T. K. Kim, J. A. Menart, and H. S. Lee
- 953 Optical Diagnostics and Radiative Properties of Simulated Soot Agglomerates  
J. C. Ko and K.-H. Shim
- 959 Combustion of a Fuel Droplet Surrounded by Oxidizer Droplets  
Tsung Leo Jiang and Huei-Huang Chiu
- 966 A Model for Correlating Flow Boiling Heat Transfer in Augmented Tubes and Compact Evaporators  
S. G. Kandlikar
- 973 Bubble Dynamics in Boiling Under High Heat Flux Pulse Heating  
A. Asai
- 980 Temperature Uniformity Across the Surface in Transition Boiling  
Y. Haramura
- 985 Vapor Dynamics of Heat Pipe Start-Up  
F. Issacci, I. Catton, and N. M. Ghoniem
- 995 Transient Multidimensional Analysis of Nonconventional Heat Pipes With Uniform and Nonuniform Heat Distributions  
Y. Cao and A. Faghri
- 1003 A Study of High-Temperature Heat Pipes With Multiple Heat Sources and Sinks: Part I—Experimental Methodology and Frozen Startup Profiles  
A. Faghri, M. Buchko, and Y. Cao
- 1010 A Study of High-Temperature Heat Pipes With Multiple Heat Sources and Sinks: Part II—Analysis of Continuum Transient and Steady-State Experimental Data With Numerical Predictions  
A. Faghri, M. Buchko, and Y. Cao

## TECHNICAL NOTES

- 1017 Numerical Analysis of Two-Dimensional Transient Freezing in a Spheroidal Capsule  
Y. Asako, H. Nakamura, S. Toyoda, and M. Faghri
- 1020 The Effect of the Thermal Boundary Condition on Heat Transfer From a Cylinder in Crossflow  
J. W. Baughn and N. Saniei
- 1023 An Experimental Study of Entrainment Effects on the Heat Transfer From a Flat Surface to a Heated Circular Impinging Jet  
J. W. Baughn, A. E. Hechanova, and Xiaojun Yan
- 1025 An Investigation of Ejection, Mixing, and Suction Mechanisms in an Open-Ended Horizontal Annulus  
J. Eftefagh and K. Vafai
- 1029 Was Lord Rayleigh Right?  
J. G. Georgiadis
- 1031 Natural Convection From a Horizontal Heated Copper-Graphite Composite Surface  
Wen-Jei Yang, H. Takizawa, and D. L. Vrable
- 1033 Natural Convection in a Vertical Enclosure Filled With Anisotropic Porous Media  
J. Ni and C. Beckermann
- 1037 Analysis of Heat Flux Measurement by Circular Foil Gages in a Mixed Convection/Radiation Environment  
C. H. Kuo and A. K. Kulkarni
- 1040 Evaluation of Direct-Exchange Areas for a Cylindrical Enclosure  
J. Sika
- 1044 Accelerating the Hemi-Cube Algorithm for Calculating Radiation Form Factors  
H. E. Rushmeier, D. R. Baum, and D. E. Hall

# Correlation of Thermal Conductivities of Unidirectional Fibrous Composites Using Local Fractal Techniques

R. Pitchumani  
Graduate Student.

S. C. Yao  
Professor.  
Fellow ASME

Department of Mechanical Engineering,  
Carnegie Mellon University,  
Pittsburgh, PA 15213

*The arrangement of fibers strongly influences heat conduction in a composite. Traditional approaches using unit cells to describe the fiber arrangements work well in the case of ordered arrays, but are not useful in the context of disordered arrays, which have been analyzed in the literature by statistical means. This work presents a unified treatment using the tool of local fractal dimensions (although, strictly speaking, a composite cross section may not be an exact fractal) to reduce the geometric complexity of the relative fiber arrangement in the composite. The local fractal dimensions of a fibrous composite cross section are the fractal dimensions that it exhibits over a certain small range of length scales. A generalized unit cell is constructed based on the fiber volume fraction and local fractal dimensions along directions parallel and transverse to the heat flow direction. The thermal model resulting from a simplified analysis of this unit cell is shown to be very effective in predicting the conductivities of composites with both ordered as well as disordered arrangement of fibers. For the case of square packing arrays, the theoretical result of the present analysis is identical to that of Springer and Tsai (1967).*

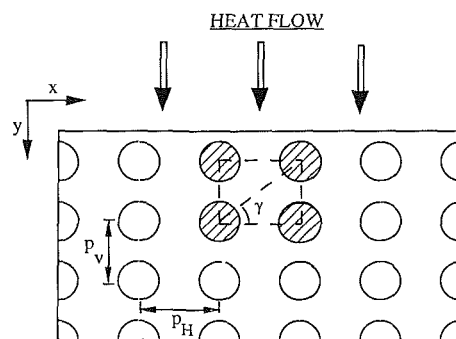
## 1 Introduction

With the increasing use of composites in various thermal environments, the thermal properties of unidirectional fibrous composites have been the focus of many investigations in the last few years. These studies have essentially been along two parallel, but related paths: One is a model-based approach, where the fiber arrangements are modeled by simplified geometric equivalents; the second is a statistical approach, which employs statistical techniques to determine upper and lower bounds on the effective properties. This paper deals with the problem of determining the effective transverse thermal conductivity of fibrous composites. The effective thermal conductivity is defined as the conductivity of an equivalent homogeneous medium, which exhibits the same steady-state thermal characteristics as the composite material.

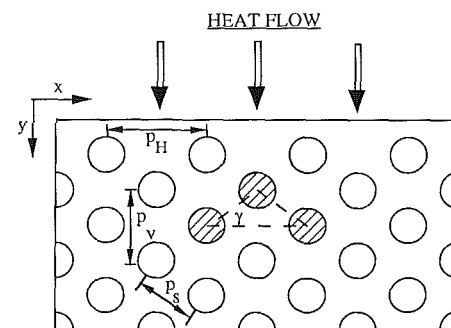
The model-based studies assume an ordered arrangement of fibers in the matrix with the fiber centers located at the vertices of either a rectangle (called rectangular arrays) or a triangle (called staggered arrays), as shown in Fig. 1. The effective thermal conductivities of these arrays can be obtained by analyzing representative rectangular or staggered unit cells, of which the composite cross section is assumed to be composed. Literature abounds with both analytical (Springer and Tsai, 1967; Behrens, 1968) and numerical (Han and Cosner, 1981; James and Keen, 1985; Muralidhar, 1990) results for the effective thermal conductivity of ordered arrays. However, with the exception of the work by Han and Cosner (1981), the other model-based studies are restricted mainly to the case of square packing arrays, for which  $\gamma$  equals 45 deg in Fig. 1.

Investigations found in the literature on disordered media (Hashin, 1970; Milton, 1982; Smith and Torquato, 1989) are aimed at determining upper and lower bounds on the effective thermal conductivities. The bounds are generally in terms of the fiber volume fraction ( $v$ ), the fiber-matrix conductivity ratio ( $\beta$ ), and a microstructural parameter  $\zeta_2$ , which is a multifold integral that depends upon the choice of the probability

distribution function for the composite (Smith and Torquato, 1989). Given only  $\beta$  and  $v$ , Hashin (1970) has obtained the best estimate of the bounds on the effective conductivity of transversely isotropic fiber-reinforced materials. Other re-



(a) Rectangular Array



(b) Staggered Array

Fig. 1 Schematic of ordered fiber arrangements: (a) rectangular array; (b) staggered array

Contributed by the Heat Transfer Division for publication in the JOURNAL OF HEAT TRANSFER. Manuscript received by the Heat Transfer Division December 7, 1990; revision received April 16, 1991. Keywords: Conduction, Materials Processing and Manufacturing Processes.

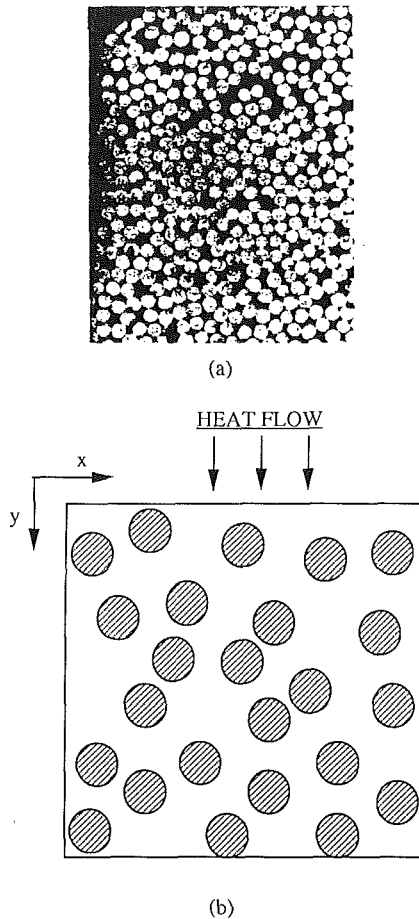


Fig. 2 (a) Photomicrograph of a section of a pultruded Carbon Fiber Reinforced Plastic rod (p. 23, Spencer, 1983); (b) schematic of a general composite cross section

search in the area of disordered arrays has been toward evaluating the microstructural parameter accurately, thereby narrowing the bounds. For example, Milton (1982) has derived fourth-order bounds, which improve significantly over the other bounds in the literature. An excellent summary of the work

in the area of composites appears in the review article by Hashin (1983).

Recently, statistical simulation techniques have been employed to relate the microstructural parameter,  $\zeta_2$ , to the fiber volume fraction  $v$  (Smith and Torquato, 1989). Kim and Torquato (1990) applied a Brownian motion simulation technique to determine the effective thermal conductivities of disordered media, and showed that the Milton bounds agree very closely with their simulation results.

In the composites found in practice, shown in Fig. 2, the fibers hardly assume an ordered arrangement. This is especially true of the products of continuous manufacturing systems such as pultrusion (Spencer, 1983). Even if an ordered arrangement is intended by design, the final product is likely to be perturbed to various degrees depending on the processing conditions. Therefore, in almost all practical situations, the ordered array simplification is inaccurate in describing such composites. The statistical simulation techniques, on the other hand, are computationally intensive and require several CPU hours on a supercomputer (Kim and Torquato, 1990).

The problem of determining the effective thermal conductivity can be decomposed into two steps:

- 1 "quantifying" the relative fiber arrangement by a characteristic measure;
- 2 relating the effective conductivity to the measure of the "relative fiber arrangement" obtained in step (1).

Traditionally, the effective conductivity ( $k_e$ ) has been expressed as a ratio with respect to the matrix conductivity ( $k_m$ ), and is of the form

$$\frac{k_e}{k_m} = f(\beta, v, \text{"relative fiber arrangement"}) \quad (1)$$

where  $k_e/k_m$  is the effective conductivity ratio,  $\beta$  is the fiber-matrix conductivity ratio, and  $v$  is the fiber volume fraction. In the literature, the "relative fiber arrangement" for ordered arrays has been quantified using a pitch to diameter ratio and/or a fiber packing angle  $\gamma$  (Han and Cosner, 1981) (see Fig. 1). These methods, however, suffer from many drawbacks. The pitch-to-diameter ratio ceases to be a unique quantity even in the case of some ordered arrangements, where several different pitches may exist (Fig. 1). In the realm of disordered media, the pitch-to-diameter ratio is not only non-unique, but also an inappropriate parameter to describe the geometry. The

## Nomenclature

$A$  = area of cross section,  $m^2$   
 $c$  = parameter defined in Eq. (14)  
 $d_f$  = fractal dimension of an object  
 $d_T$  = local fractal dimension of a composite cross section in the direction normal to heat flow  
 $d_p$  = local fractal dimension of a composite cross section in the direction of heat flow  
 $D$  = diameter of fibers, m  
 $E$  = Euclidean dimension of an object  
 $k_e$  = effective thermal conductivity of a composite,  $Wm^{-1}K^{-1}$   
 $k_f$  = conductivity of the fibers,  $Wm^{-1}K^{-1}$   
 $k_m$  = conductivity of the matrix,  $Wm^{-1}K^{-1}$

$k_R$  = conductivity of the rectangular unit cell (Fig. 8),  $Wm^{-1}K^{-1}$   
 $k_S$  = conductivity of the staggered unit cell (Fig. 8),  $Wm^{-1}K^{-1}$   
 $L$  = length scale, m  
 $L_T$  = length of the generalized unit cell normal to the heat flow direction, m  
 $L_o$  = scaling factor, m  
 $L_p$  = length of the generalized unit cell along the heat flow direction, m  
 $M(L)$  = measure of an object with a length scale  $L$   
 $p_H$  = horizontal pitch (Fig. 1), m  
 $p_s$  = slant distance between a fiber and its nearest neighbor in the adjacent staggered column, m  
 $p_V$  = vertical distance between two fibers, m

$p_\Delta$  = spacing between two adjacent fibers in an equilateral triangular arrangement of fibers, m  
 $q$  = total heat flow per unit length,  $Wm^{-1}$   
 $q_1, q_2, q_3$  = components of  $q$  (Fig. 5),  $Wm^{-1}$   
 $v$  = fiber volume fraction  
 $\bar{v}$  = parameter defined in Eq. (14)  
 $x, y$  = coordinate axes  
 $\beta$  = ratio of fiber conductivity to matrix conductivity the generalized unit cell, K  
 $\gamma$  = fiber packing angle  
 $\delta$  = parameter defined in Eq. (14)  
 $\zeta_2$  = a microstructural parameter used to describe disordered arrays

fiber packing angle, again, is not applicable to disordered arrays. Disordered “relative fiber arrangements” have been quantified in the literature by means of the microstructural parameter  $\zeta_2$  (Smith and Torquato, 1989).

From a practical point of view, it is desirable to have a universal means of quantifying the “relative fiber arrangements,” which will be applicable to ordered and disordered arrays alike. In response to this, Yao and Pitchumani (1990) introduced a new method, wherein the pattern of fiber arrangement in a cross section is characterized as a *local fractal object*, and described in terms of *local fractal dimensions*. Based on preliminary investigations, the approach was shown to correlate the thermal conductivities of ordered arrays very well. An empirical correlation was proposed that unified the analysis of all ordered configurations. It was argued that since the local fractal description characterizes the *geometric pattern* formed by the fibers, it is equally applicable to both ordered as well as disordered arrangements.

In this paper, we extend their ideas and present a more detailed analysis of the problem of heat conduction in fibrous composites using the tool of *local fractal dimensions*. Although the composite cross section may not be an exact fractal by nature, the *technique* of local fractal dimensions can be used to reduce the geometric complexity of the fiber arrangements in the cross section. We restrict our focus to the types of situations encountered in practice, where the thermal conductivity ratio,  $\beta$ , ranges between 0 and  $\infty$ , and the volume fraction  $v$  lies in the range 30 to 70 percent. The local fractal characterization of ordered (Fig. 1) and uniform-random (Fig. 2a) arrangements is presented.

A thermal model is then developed by analyzing a generalized unit cell, which is constructed in terms of the fiber volume fraction and the local fractal dimensions. An analytical expression for the effective composite conductivity, as a function of the fiber volume fraction, the fiber-matrix thermal conductivity ratio, and the local fractal dimensions, results from a simplified analysis of the generalized unit cell. The applicability of the model to ordered as well as disordered arrays is verified in this work. Before presenting the heat transfer analysis, the general background of fractal geometry and the essential concepts of the “local fractal” theory are briefly reviewed in the following section.

## 2 Fractal Geometry

Euclidean geometry describes regular objects like points, curves, surfaces, and cubes using integer dimensions 0, 1, 2, and 3, respectively. However, many of the objects in nature, such as the surfaces of mountains, coastlines, microstructure of metals, etc., are not Euclidean objects. Such objects are called fractals, and are described by a nonintegral dimension called the *fractal dimension* (Mandelbrot, 1983).

For example, if one were to measure the length of a coastline, the length would depend on the size of the measuring stick used. Decreasing the length of the measuring stick leads to a better resolution of the convolutions of the coastline, and as the length of the stick approaches zero, the coastline’s length tends to infinity. This is the fractal nature of the coastline. Since a coastline is so convoluted, it tends to fill space, and its fractal dimension lies somewhere between that of a line (which has a value 1) and a plane (which has a value 2).

The measure of a fractal object  $M(L)$  (namely length, area, or volume) is governed by a *scaling* relationship of the form

$$M(L) \sim L^{d_f} \quad (2)$$

where the “ $\sim$ ” should be read as “scales as,” and  $d_f$  is the fractal dimension of the object. As an illustration of the above relationship, consider the microstructure of a metal showing grains of various shapes and sizes. This is a fractal object in a two-dimensional plane. It is observed that the average area,  $M(L)$ , of the grains within squares of different sizes  $L$  by  $L$

(defined as the arithmetic mean of only those samples for which the center of the square falls on the grain) scales with the length,  $L$ , over a range of lengths, as per the above relationship (Kindo et al., 1989). The fractal dimension,  $d_f$ , calculated as the slope of a log–log plot of  $M(L)$  against  $L$ , lies in the range  $1 < d_f < 2$ . Alternatively, the microstructure can be described in terms of two *linear* fractal dimensions, each having a value between 0 and 1, along mutually perpendicular directions. The *linear* fractal dimensions are obtained from a scaling relationship as in Eq. (2), where  $M(L)$  denotes the average total length of the intercepts between a measuring line of size  $L$ , and the microstructure.

Associated with Eq. (2) is the property of self-similarity, which implies that the  $d_f$  calculated from the relationship in Eq. (2) remains constant over a range of length scales,  $L$ . Exact fractals like the Sierpiński gasket, Koch curve, etc., exhibit self-similarity over an infinite range of length scales (Mandelbrot, 1983). In actual applications, self-similarity in a global sense is seldom observed, and the “fractal” description is usually based on a *statistical self-similarity*, which the objects exhibit in some average sense, over a certain *local* range of the length scale  $L$ , which is of relevance to the problem (Voss, 1985; Pickover and Khorasani, 1985; Pickover, 1985). The fractal dimension calculated based on the *local, statistical* self-similarity is termed the *local fractal dimension* to distinguish from the term fractal dimension, which implies global self-similarity at all length scales. The fractal dimensions (local or global) of statistical fractals are usually estimated in the same manner as in the illustration of the microstructure, using a scaling relationship between  $M(L)$  and  $L$  of the form in Eq. (2) (Voss, 1985).

The concept of local, statistical self-similarity has been used in many applications ranging from characterization of the microstructure of materials (Kindo et al., 1989) to analysis of speech waveforms and signals (Pickover and Khorasani, 1985; Maragos and Sun, 1990). For example, in the area of speech recognition, it is found that important phonetic and prosodic information in a speech reside in the region of short time scales (Pickover and Khorasani, 1985; Pickover, 1985), and this information tends to be lost or smeared out over large time scales. While the term local fractal dimension is used by some investigators (Maragos and Sun, 1990), others refer to it simply as the fractal dimension (Kindo et al., 1990). We will adopt the term local fractal dimension in this paper.

In the field of heat transfer, Majumdar and Tien (1989) have successfully used fractal dimensions to model contact resistance between surfaces. The roughness of the contacting surfaces was modeled as a Koch curve, which is an exact fractal. In all these applications, the fractal dimensions have been an effective means of rendering complex geometry tractable. It is this capability of the technique that will be made use of in our analysis, even though the composite cross section may not be a fractal by nature. More details of fractal geometry appear in publications by Mandelbrot (1983), Stanley (1985), Stanley and Ostrowsky (1986), and Feder (1988).

## 3 Local Fractal Description of Composites

From the point of view of heat conduction, since each fiber influences only a small region around itself, it suffices to characterize the “relative fiber arrangement” in a local vicinity of the fiber. Furthermore, the use of a limited range of length scales is consistent with the analyses in the literature, such as the unit cell description for ordered arrays and the composite cylindrical assemblage (CCA) model (Hashin, 1970, 1983) for disordered arrays, which also consider only a small region around a fiber.

In the common fractal applications found in the literature (Pickover, 1985; Pickover and Khorasani, 1985; Maragos and Sun, 1990; Kindo et al., 1989), the ranges of length/time scales

are sufficiently large to justify the use of the term “fractal” in their description. In the characterization of the microstructure, the length scales range from  $4\ \mu\text{m}$  to  $40\ \mu\text{m}$ , and in the analysis of speech waveforms, the time scales are in the range 0.01 to 2 seconds.

A composite cross section, although it may not be an exact fractal by nature, exhibits statistical self-similarity over a small range of length scales around a fiber. It is observed that the average fiber area,  $M(L)$  (defined in a manner similar to the case of the microstructure described earlier), enclosed within squares of different sizes  $L$  by  $L$ , scales with  $L$  in accordance with Eq. (2) over a range of length scales spanning a few fiber diameters. Because of the small range of length scales, the use of the term “local fractal” seems appropriate, although the present range is much smaller than those in the conventional fractal applications.

The exponent  $d_f$  in Eq. (2) has been a very effective measure of the scaling phenomena in the applications mentioned above. Therefore, in applying the technique to our problem, we expect that the local fractal dimension could be a powerful means of quantifying the “relative fiber arrangements” in composites. Further, since heat conduction is a directional phenomenon, it is useful to represent the cross section in terms of two mutually perpendicular linear local fractal dimensions,  $d_p$  parallel with the direction of heat flow, and  $d_T$  transverse to the heat flow direction. The exact range of length scales over which to evaluate the local fractal dimensions is presented in the next section along with the procedure for the evaluation. Here we present some physical interpretations of  $d_p$  and  $d_T$ .

The local fractal dimensions  $d_p$  and  $d_T$  provide a measure of the extent of “connectedness” of the fibers in a particular direction. Certain functional dependencies of  $d_p$  and  $d_T$  are readily seen. Since  $d_p$  and  $d_T$  characterize an object in a two-dimensional plane, they are mutually independent.  $d_p$  and  $d_T$  are functions of the fiber arrangement and the fiber volume fraction. A closely packed array, resulting either from a high fiber volume fraction or a close fiber packing angle, corresponds to a high degree of “connectedness” of fibers. Consequently, its local fractal dimensions will be close to 1. Conversely, the farther away the fibers are relative to one another (small degree of “connectedness” of fibers), the smaller the value of the local fractal dimensions.

It is possible for two different fiber arrangements to have the same values of  $d_p$  and  $d_T$ . Physically, this means that in both the arrangements, on the average, each fiber has nearly the same effect on the neighboring fibers within its range of influence. Therefore, the two arrangements are likely to have nearly the same value of the effective conductivity. This fact was verified in our studies, the details of which are presented in section 6.

In view of the characterization of the “relative fiber arrangement” using  $d_p$  and  $d_T$ , Eq. (1) can be rewritten as follows:

$$\frac{k_e}{k_m} = f(\beta, \nu, d_p, d_T) \quad (3)$$

An expression for the above functional form will be derived using a heat conduction model in section 5 of the paper.

#### 4 Evaluation of $d_p$ and $d_T$

In order to be able to evaluate the local fractal dimensions,  $d_p$  and  $d_T$ , we need first to identify the appropriate range of length scales. Since we are interested in a region surrounding a fiber, the minimum length scale is clearly the fiber diameter,  $D$ . The maximum length scale is obtained by estimating the “range of influence” of a fiber for heat conduction.

Consider a fiber distribution wherein each fiber is equally separated from its closest neighbors. For a given fiber volume fraction,  $\nu$ , the equilateral triangular arrangement (staggered

array with a fiber packing angle of 30 or 60 deg), with an interfiber distance (pitch)  $p_\Delta$ , represents an equispaced distribution. (In terms of energies, hypothetically, if the fibers mutually repel one another, this represents minimum potential energy configuration.) If the “range of influence” of each fiber in the equispaced configuration is assumed to be independent of, and nonoverlapping with, the “ranges of influence” of the other fibers, the maximum such range is a concentric region of diameter  $p_\Delta$  around a fiber. Note that the square arrangement of fibers (rectangular array with a fiber packing angle of 45 deg) also represents an equispaced arrangement. Since the equilateral triangular pitch,  $p_\Delta$ , is greater than the square pitch for a given fiber volume fraction,  $p_\Delta$  is clearly a better estimate of the maximum length scale. This suggests that length scales in the range  $D \leq L \leq p_\Delta$ , where  $D$  is the fiber diameter and  $p_\Delta$  is the equilateral triangular pitch corresponding to the fiber volume fraction, may be used for the evaluation of the local fractal dimensions  $d_p$  and  $d_T$ .

The following procedure for the evaluation of  $d_p$  and  $d_T$  is a variation of the “sandbox method” of measuring fractal dimensions, proposed by Stanley et al. (1985):

(i) Discretize the composite cross section into a number of grid cells so as to ensure equiprobable samplings in the procedure described below. Typically, grid cells about one-tenth the fiber diameter in size provide a good resolution of the cross section.

(ii) By placing a line of length  $L$  parallel to the direction of heat flow on every grid cell, systematically scan the entire cross section. This is equivalent to a purely random sampling with every cell being an equally probable origin for the measurement. Each time the center of the line falls on a fibrous region, record the total length of the intercepts between the line and the fibers. The average of these intercepted total lengths is the mean length  $M(L)$ .

(iii) Repeat step (ii) above for several values of  $L$  in the range  $D \leq L \leq p_\Delta$ , and make a log-log plot of  $M(L)$  against  $L$ .

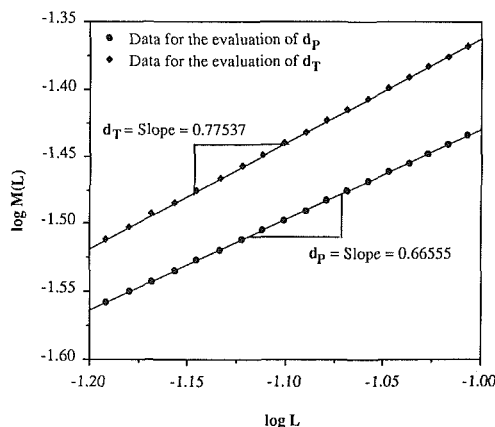
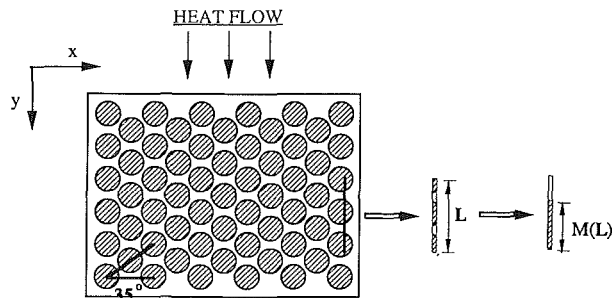


Fig. 3 Evaluation of the local fractal dimensions  $d_p$  and  $d_T$

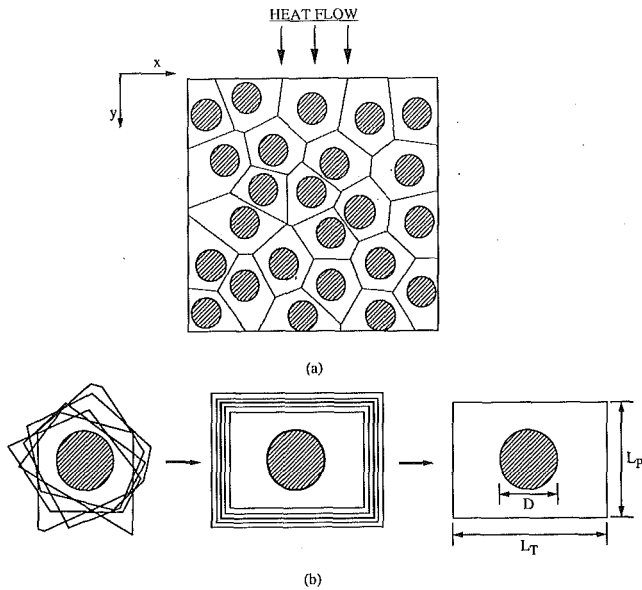


Fig. 4 (a) Wigner-Seitz cells around each fiber in a general composite cross section; (b) representation of the average of the Wigner-Seitz cells by a generalized, rectangular unit cell

The slope of the best line fit through the points in this plot gives the exponent in Eq. (2), which is the local fractal dimension  $d_p$ .

(iv) The procedure for calculating  $d_T$  is identical to the steps for calculating  $d_p$  with the difference that the lines parallel to the heat flow in step (ii) are replaced by lines transverse to the heat flow.

The procedure is illustrated in Fig. 3, which shows the cross section of a staggered array with a fiber packing angle of 35 deg and a fiber volume fraction of 60 percent. Heat flows along the  $y$  direction across the cross section. The cross section was discretized in both the  $x$  and the  $y$  directions to yield a resolution of 41 grid cells per unit cell width in the respective direction. In step (iii), 20 different scale lengths,  $L$ , were considered in the range  $D \leq L \leq p\Delta$ , for the evaluation of  $d_p$  and  $d_T$ . One representative line is seen on the cross section in the figure. The intercepts between the fibers and the line, and the consolidated fiber intercepts are shown alongside the cross section. The line is shown as a narrow rectangle for the purpose of illustration.

As mentioned earlier, the local fractal dimensions measure the extent of "connectedness" of the fibers in a particular direction. In Fig. 3, we see that the fibers are closer to one another in the direction transverse to the heat flow ( $x$  direction) than in the direction of heat flow. That is, the extent of "connectedness" is more in the transverse direction, and as a result  $d_T$  is greater than  $d_p$ .

## 5 Heat Conduction Model

Here we seek a simplified heat conduction model to relate the effective thermal conductivity ratio,  $k_e/k_m$ , to the parameters listed in Eq. (3). The model is based on the analysis of a generalized unit cell, which is constructed in terms of the fiber volume fraction and the local fractal dimensions.

**5.1 Generalized Unit Cell Geometry.** In the case of ordered (rectangular and staggered) fiber arrangements, representative unit cells can be used to study heat conduction (Springer and Tsai, 1967; Han and Cosner, 1981). Because of the relative simplicity of analysis associated with unit cells, we would like to extend the concept of a unit cell to disordered media as well. So, the problem is now reduced to that of determining the shape and size of a generic unit cell, a problem similar to that often encountered in solid-state physics and

crystallography. One commonly used solution is to find Wigner-Seitz cells (Kittel, 1986), which are, in general, polygonal cells of various sizes (Fig. 4a).

Figure 4(a) shows the Wigner-Seitz cells constructed around each fiber in a general fiber arrangement. Since the Wigner-Seitz cells are of different shapes and sizes, for the sake of simplicity, an average of these cells could be considered to represent a generalized unit cell. Figure 4(b) shows a schematic of the transformation, which is a two-step process. First, each of these Wigner-Seitz cells is represented ideally by an equivalent rectangular cell, which has approximately the same heat transfer behavior. Then all these rectangular cells are lumped into a single rectangular unit cell so as to preserve the heat transfer characteristics.

It is also evident from Fig. 4(a) that the size of the Wigner-Seitz cells depends upon the fiber volume fraction  $v$ , and the relative fiber arrangement, which, in our case, is quantified by  $d_p$  and  $d_T$ . Therefore, the generalized unit cell dimensions  $L_P$  and  $L_T$  (Fig. 4b), parallel and transverse to the direction of heat flow, respectively, can be expressed in terms of  $v$ ,  $d_p$  and  $d_T$ . It follows from the scaling relationship in Eq. (2), with  $M(L)$  denoting an average linear measure, that on the average, the characteristic fiber dimension along the heat flow direction, enclosed within the generalized unit cell length  $L_P$  (Fig. 4b), is proportional to  $L_P^{d_p}$ . Similarly, the characteristic fiber dimension transverse to the heat flow direction, enclosed within the generalized unit cell length  $L_T$  (Fig. 4b), is proportional to  $L_T^{d_T}$ . As seen in Fig. 4(b), since the fiber is circular in cross section, the characteristic fiber dimensions along  $L_T$  and  $L_P$  in the generalized unit cell both equal the fiber diameter,  $D$ . Thus the linear version of Eq. (2) applied to the generalized unit cell along  $L_T$  and  $L_P$  yields

$$D = L_o^{(1-d_T)} L_T^{d_T} \quad \text{or} \quad \left(\frac{D}{L_o}\right) = \left(\frac{L_T}{L_o}\right)^{d_T} \quad (4)$$

$$D = L_o^{(1-d_p)} L_P^{d_p} \quad \text{or} \quad \left(\frac{D}{L_o}\right) = \left(\frac{L_P}{L_o}\right)^{d_p} \quad (5)$$

where  $L_o$  is a scaling length introduced to invoke equality in the scaling relationship in Eq. (2). The second equation in Eqs. (4) and (5) is in the dimensionless form where all length variables have been nondimensionalized with respect to  $L_o$ . The scaling length,  $L_o$ , allows for enlargement or reduction of the size of the generalized unit cell and the enclosed fiber by a constant factor.

The ratio of the fiber area to the area of the generalized unit cell is the fiber volume fraction,  $v$ , and may be written as

$$v = \frac{\frac{\pi}{4} \left(\frac{D}{L_o}\right)^2}{\left(\frac{L_T}{L_o}\right) \left(\frac{L_P}{L_o}\right)} \quad (6)$$

Solving Eqs. (4), (5), and (6) for the three unknowns  $D/L_o$ ,  $L_T/L_o$ , and  $L_P/L_o$ , one obtains

$$\left(\frac{D}{L_o}\right) = \left(\frac{4v}{\pi}\right)^{\delta_1} \quad (7)$$

$$\left(\frac{L_T}{L_o}\right) = \left(\frac{4v}{\pi}\right)^{\delta_1/d_T} \quad (8)$$

$$\left(\frac{L_P}{L_o}\right) = \left(\frac{4v}{\pi}\right)^{\delta_1/d_p} \quad (9)$$

where

$$\delta_1 = \frac{-d_T d_p}{d_T - 2d_T d_p + d_p} \quad (10)$$

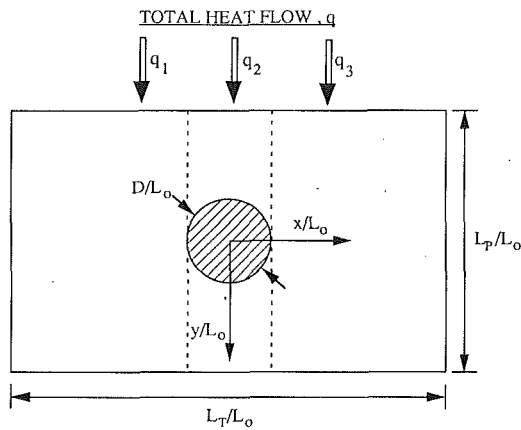


Fig. 5 Schematic of heat conduction through the generalized unit cell

**5.2 Thermal Analysis of the Generalized Unit Cell.** The generalized unit cell can now be analyzed for heat conduction. The underlying assumptions of our analysis are: (a) the fibers and the matrix forming the composite are individually homogeneous and isotropic materials, (b) the fibers and matrix are perfectly bonded so that contact resistance may be neglected (this assumption may be relaxed in a more accurate model), (c) the problem is two dimensional with no temperature gradient along the direction of the fibers, and (d) heat flows vertically (along the  $y$  direction in Fig. 5) through the generalized unit cell; transverse flow of heat (along the  $x$  direction in Fig. 5) is negligible.

The last assumption overestimates the thermal resistance, and consequently underestimates the thermal conductivity of the generalized unit cell. The assumption is made so as to obtain quick, approximate estimates of the effective thermal conductivity. As shown in the next section, an accurate analysis of the generalized unit cell yields better results.

The simplified model for heat conduction through the generalized unit cell parallels the circular filament model of Springer and Tsai (1967). Figure 5 shows a schematic of our thermal model. A net heat flow per unit length,  $q$ , in the  $y$  direction results due to a constant temperature difference between  $y/L_0 = \mp(L_P/L_0)/2$ , and can be decomposed into three independent components  $q_1$ ,  $q_2$ , and  $q_3$  (by virtue of assumption (d) above) such that

$$q = q_1 + q_2 + q_3. \quad (11)$$

We present here only the final expression for the effective thermal conductivity ratio  $k_e/k_m$ . The details of the derivation may be found from Springer and Tsai (1967). For the generalized unit cell geometry given by Eqs. (7)–(10), the following expression for  $k_e/k_m$  results:

$$\frac{k_e}{k_m} = \left[ 1 - \left( 1 + \frac{\pi}{2c} \right) \bar{v} \right] + \frac{2\bar{v}}{c\sqrt{1-c^2}} \tan^{-1} \sqrt{\frac{1+c}{1-c}} \quad c \geq -1 \quad (12)$$

$$= \left[ 1 - \left( 1 + \frac{\pi}{2c} \right) \bar{v} \right] + \frac{\bar{v}}{c\sqrt{c^2-1}} \ln(-c + \sqrt{c^2-1}) \quad c \leq -1 \quad (13)$$

where

$$c = \left( \frac{\beta-1}{\beta} \right) \left( \frac{4v}{\pi} \right)^{(1-\delta)/2}, \quad \bar{v} = \left( \frac{4v}{\pi} \right)^{(1+\delta)/2}, \quad \text{and } \delta = \frac{d_P - d_T}{d_P - 2d_P d_T + d_T}. \quad (14)$$

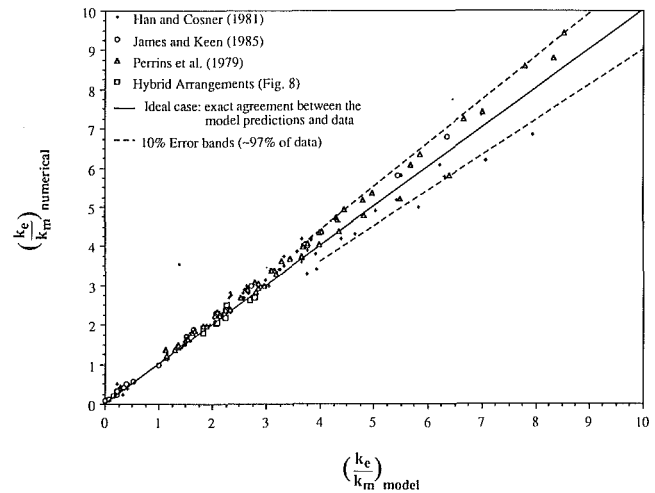


Fig. 6 Comparison of the model predictions,  $(k_e/k_m)_{\text{model}}$  (Eqs. (12), (13)), with the numerical results from the literature,  $(k_e/k_m)_{\text{numerical}}$

Table 1 The parameters and their values used in data comparisons

| Investigator          | $\beta$                       | Fiber Arrangement | $v$ (%) | $\gamma$                          |
|-----------------------|-------------------------------|-------------------|---------|-----------------------------------|
| Han and Cosner (1981) | 0.1, 1, 2, 10, 100 & $\infty$ | Rectangular       | 50      | 35°, 45°, 55°                     |
|                       |                               |                   | 60      | 45°, 50°                          |
|                       |                               | Staggered         | 50      | 25°, 30°, 35°, 45°, 55°, 60°, 65° |
|                       |                               |                   | 60      | 25°, 30°, 35°, 45°, 55°, 60°, 65° |
| James and Keen (1985) | 0.01, 0.1, 10 & 100           | Rectangular       | 30      | 45°                               |
|                       |                               |                   | 50      |                                   |
|                       |                               |                   | 70      |                                   |
| Perrins et al. (1979) | 10, 50 & $\infty$             | Rectangular       | 10 - 75 | 45°                               |
|                       |                               |                   | 70      |                                   |
|                       |                               | Staggered         | 10 - 70 | 30°                               |

## 6 Results and Discussion

**6.1 Ordered Arrays.** The local fractal dimensions  $d_P$  and  $d_T$  were evaluated in the present work using a computer program to execute the procedure outlined in section 4, in the range of length scales  $D \leq L \leq p_\Delta$ .

Springer and Tsai (1967) studied rectangular arrays with a fiber packing angle  $\gamma = 45$  deg (square packing arrays). Their results are a special case of the present model. In the case of square packing arrays,  $d_P = d_T$ , and  $\delta$ , from Eq. (14), becomes 0. The expression obtained from Eqs. (12)–(13) with  $\delta = 0$  becomes the same as the thermal conductivity equation resulting from the analysis of Springer and Tsai (1967).

The predictions of the proposed thermal model were compared with the numerical results of Han and Cosner (1981), James and Keen (1985), and Perrins et al. (1979). Table 1 details the parameters and their values used in the comparison. Figure 6 presents a comparison between the model predicted conductivity ratios (along the abscissa) and the published numerical data (along the ordinate). The solid line diagonal to the plot frame represents the case of perfect agreement between the data and the predictions of Eqs. (12)–(13), and the dashed lines indicate the 10 percent error bands. The error bands are not shown all the way down to the origin for the sake of clarity. There are about 235 different cases presented in the comparison. These include the various combinations of the parameters listed in Table 1, and the hybrid arrangements (denoted by squares in Fig. 6) discussed in section 6.2.

Not included in the comparison (Fig. 6) are the ordered



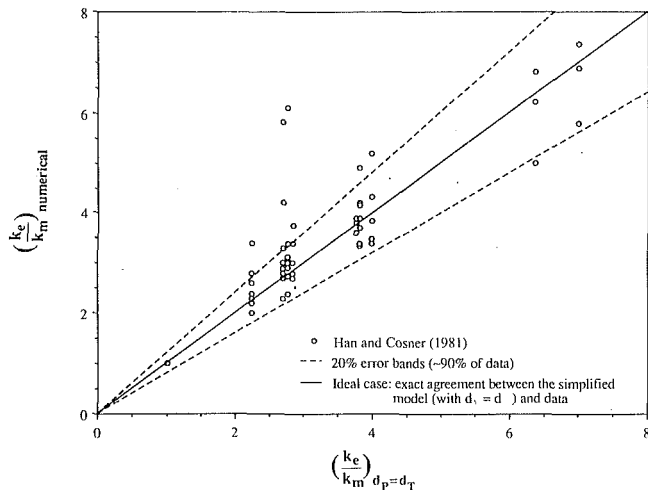


Fig. 7 Comparison of the simplified model predictions ( $d_p = d_T$ ) with the numerical results,  $(k_e/k_m)_{\text{numerical}}$ , corresponding to various fiber packing angles  $\gamma$  in Table 1, for  $v = 50, 60,$  and  $70$  percent, and  $\beta = 10, 100,$  and  $\infty$

arrangements with extremely small, and large fiber packing angles. In these cases, the equilateral triangular pitch,  $p_\Delta$ , is not representative of the interfiber spacings. Therefore, the range of length scales,  $D \leq L \leq p_\Delta$ , used in the present analysis for evaluating the local fractal dimensions, is not appropriate. Also not included in the comparison are the experimental data of Thornburg and Pears (1965). For the composites with a high value of  $\beta$  and fiber volume fraction near 65 percent, their data show a decrease in the value of the effective thermal conductivity ratio for an increase in the fiber volume fraction, which is not explainable physically. This behavior is also seen in the data comparison in Springer and Tsai (1967).

It is evident from Fig. 6 that overall, the present fractal-based model predictions and numerical data from other studies compare very well over a wide range of parameters. In about 97 percent of the cases, the thermal conductivities obtained using the model lie within 10 percent of the exact values. Also, in most of the cases, the model underpredicts the values of the effective thermal conductivity. This is expected since the cross-flow of heat was neglected in the analysis of the generalized unit cell. In the case of ordered arrays with extremely small, and larger fiber packing angles, for reasons mentioned above, the thermal conductivities predicted by the present model could be in error by as much as 20 percent. If the experimental data of Thornburg and Pears (1965) were included in the comparison, in about three cases corresponding to the high value of  $\beta$  ( $=667$ ), the model predictions and the data differ by a maximum of about 20 percent. In all the other cases, the agreement is within 10 percent.

As mentioned in section 3, generally there is no unique mapping between the fiber packing arrangement and the local fractal dimensions  $d_p$  and  $d_T$ . In our studies, we did not come across different arrangements having exactly the same values of  $d_p$  and  $d_T$ . An example of two arrangements having nearly the same  $d_p$  and  $d_T$  is that of a *rectangular* array with  $v = 60$  percent,  $\gamma = 50$  deg, and a *staggered* array with  $v = 60$  percent and  $\gamma = 65$  deg. For the rectangular arrangement, the values of  $d_p$  and  $d_T$  are 0.75 and 0.91, respectively, and for the staggered array, the corresponding values are 0.72 and 0.87. Numerical results of Han and Cosner (1981) show that the thermal conductivity ratios  $(k_e/k_m)$  of the rectangular and the staggered arrangement, for  $\beta = \infty$ , are 3.49 and 3.40, respectively. This supports our conjecture that arrangements having similar values of  $d_p$  and  $d_T$  have almost the same value of the effective thermal conductivity.

**Simplified Model With  $d_p = d_T$ .** It was stated earlier in connection with the evaluation of the local fractal dimensions

that as a simplification, or in the absence of information about the arrangement of fibers in the composite, the two fractal dimensions  $d_p$  and  $d_T$  may be assumed to be equal. This assumption, as explained above, leads to the results of Springer and Tsai (1967). The extent of validity of the approximation was assessed using the data of Han and Cosner (1981) for the different fiber packing angles  $\gamma$  given in Table 1,  $\beta = 10, 100,$  and  $\infty$ , and  $v = 50, 60,$  and  $70$  percent.

For every combination of the above  $\beta$  and  $v$ , the effective thermal conductivity ratio was evaluated using the model (Eqs. (12)–(13)), with the approximation  $d_p = d_T$ . These are plotted along the horizontal axis in Fig. 7 as  $(k_e/k_m)_{d_p=d_T}$ . The values of the conductivity ratios, from the numerical data of Han and Cosner (1981), are plotted along the vertical axis. The solid line in the figure represents the case of perfect agreement between the literature data and the model predictions with  $d_p = d_T$ . The lines seen to fan out from the origin form the 20 percent error band. The approximation yields conductivities that are accurate to within 20 percent of the exact values in nearly 90 percent of the cases, and to within 15 percent in about 82 percent of the cases. The points that lie outside the error bands are those for arrangements having relatively small fiber packing angles (less than  $\sim 35$  deg).

This suggests that the simplification, or equivalently the results of Springer and Tsai (1967) for square packing arrays ( $\gamma = 45$  deg), could be employed to obtain quick, rough estimates of the conductivity of composites with ordered fiber arrangements in general. For a more accurate result, however, an evaluation using the local fractal dimensions becomes necessary.

**6.2 Disordered Arrays.** In the composites produced by a manufacturing process such as pultrusion (Spencer, 1983), the fibers are dispersed in a uniform random manner within the matrix. Verification of the model for disordered arrays, however, is not as straightforward as that for ordered arrays since, unlike ordered arrays, they defy a systematic classification. Available data on disordered arrays are limited, and are restricted to purely random arrangements without fiber clusters, called uniform-random arrays. The information on uniform-random arrays is in the form of upper and lower bounds on the effective thermal conductivity. Unfortunately, the exact conductivity of a specific disordered fiber arrangement can be obtained only from a full numerical solution or experiments. Such data are not available in the literature.

**Hybrid Arrangements.** To alleviate the situation of lack of precise data on disordered arrays, a hybrid arrangement was constructed, for a preliminary examination, by combining rectangular and staggered unit cells. The resulting hybrid unit cell is shown in Fig. 8. The exact conductivity of the hybrid cell was calculated from the conductivities of the rectangular and staggered unit cells,  $k_R$  and  $k_S$ , respectively, using the formula given in the figure. The formula results from a simple conductivity analysis of the hybrid cell, assuming the constituent rectangular and staggered unit cells to be homogeneous media with conductivities  $k_R$  and  $k_S$ , respectively. The values of  $k_R$  and  $k_S$  were obtained using the data of Han and Cosner (1981) and James and Keen (1985). The local fractal dimensions  $d_p$  and  $d_T$  were evaluated using a computer program.

The exact conductivities are compared with the predictions of the model, shown as squares in Fig. 6, for  $\beta = 10, 100,$  and  $\infty$ , and the overall fiber volume fraction  $v = 40$  and 50 percent. It can be seen that the agreement is extremely good for the cases considered.

**Uniform-Random Arrangements.** Finally, we present a comparison of the model predictions with the upper and lower bounds on the thermal conductivities reported in the literature on disordered media. For uniform-random fiber arrangements, in the absence of any more information about the fiber ar-

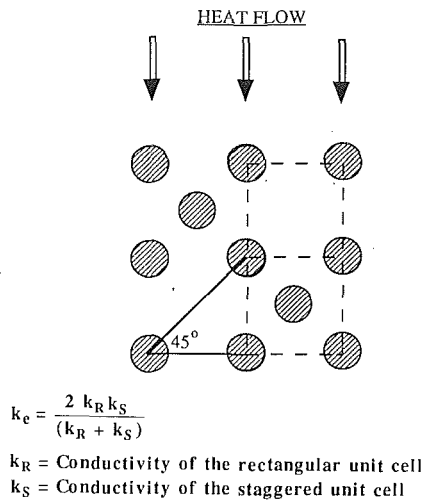


Fig. 8 Hybrid unit cell composed of rectangular and staggered unit cells

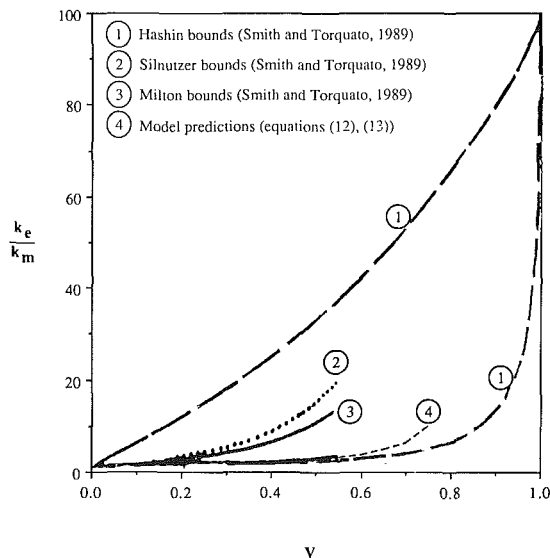


Fig. 9 Comparison of the model predictions in the case of uniform random arrays, for  $\beta = 100$ , with the upper and lower bounds found in the literature

rangements, the two local fractal dimensions  $d_p$  and  $d_T$  may be assumed to be equal since the arrangement is statistically identical both parallel and transverse to the heat flow. Figure 9 shows the results obtained from the model, with  $d_p = d_T$ , along with the upper and lower bounds of Hashin, Milton, and Silnutzer (Smith and Torquato, 1989) for  $\beta = 100$ , and varying fiber volume fraction. The figure was obtained by superposing the values of the thermal conductivity ratios from the present study on Fig. 11 of Smith and Torquato (1989), which shows the three bounds mentioned above.

The model, with  $d_p = d_T$ , yields conductivities that are very close to the lower bounds reported in the literature. Smith and Torquato (1989) reported that the lower bounds accurately estimate the effective properties in the absence of large fiber clusters (for  $\beta \geq 1$ ). It therefore follows from Fig. 9 that the present model, with the simplification  $d_p = d_T$ , can accurately predict the conductivities of composites having a uniform-random arrangement. It may be recalled that the present model (Eqs. (12)–(13)) under the condition  $d_p = d_T$ , also reduces to the result of Springer and Tsai (1967) for square packing arrays. Thus, it is interesting to note that their result, which was originally developed for square packing arrays, is also effective in predicting the conductivities of uniform random arrays.

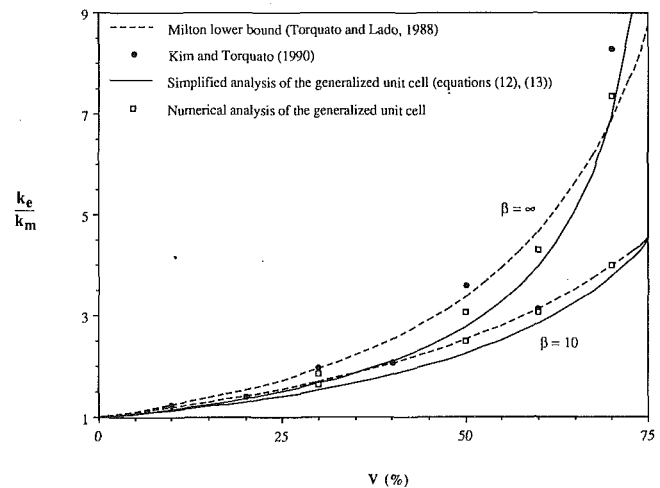


Fig. 10 Comparison among the model predictions, the Milton lower bounds, and the simulation results of Kim and Torquato (1990), for  $\beta = 10$  and  $\infty$ ; the squares are the results of a numerical analysis of the generalized unit cell

Figure 10 presents a comparison between the simplified model predictions, with  $d_p = d_T$ , and the Milton lower bounds (Torquato and Lado, 1988) for  $\beta = 10$  and  $\infty$ . Also shown in the figure are the numerical simulation results of Kim and Torquato (1990). The Milton lower bounds were obtained using the expression for the microstructural parameter,  $\zeta_2$ , given by Torquato and Lado (1988). Figure 10 shows an underprediction of the present model relative to the Milton bounds and the simulation data, by a maximum of about 10 percent.

The conductivity of the generalized unit cell was also evaluated numerically for fiber volume fractions of 30, 50, and 70 percent, and  $\beta = 10$  and  $\infty$ . The results are shown as unfilled squares in Fig. 10. It may be noted from Fig. 10 that the numerical results coincide with the Milton lower bound and the simulation data for  $\beta = 10$ , and are very close to the bound and the simulation data for  $\beta = \infty$ . This implies that accurate results can be obtained by a better heat transfer analysis of the generalized unit cell.

As seen in Fig. 10, improvements to the present model, either in the form of a refined shape of the generalized unit cell and/or a refined analysis of the generalized unit cell, will result in accurate predictions. In the present study, disordered arrays have been considered in the absence of the exact microstructural information (i.e., the approximation  $d_p = d_T$  has been used). The real value of the local fractal technique will be evident when micrographs of actual cross sections are analyzed as described in section 4, and the present (or better) model predictions compared with the exact (experimentally or numerically determined) conductivities. These issues will be addressed in a future work.

## 7 Conclusions

A unified approach using local fractal dimensions to characterize a fibrous composite cross section was developed. Local fractal dimensions, although a composite cross section may not be an exact fractal, prove to be a simple and effective way of reducing the geometric complexity of the fiber arrangements in a composite. For ordered as well as disordered arrays, the proposed method proves to be advantageous in terms of eliminating intensive numerical computations, which are otherwise involved with direct numerical simulations.

An approximate model based on a simplified theoretical analysis of a generalized unit cell was derived. Calculations based on the model compared very well with the data of other investigators over a wide range of parameters. The well-known result of Springer and Tsai (1967) for square packing arrays

( $\gamma = 45$  deg) is a special case of the present work, obtained by setting  $d_p = d_T$  in our analysis. It was shown in this study that the approximation  $d_p = d_T$  may also be used to obtain quick, approximate estimates of the thermal conductivities of composites. However, for an accurate prediction, an exact evaluation using the local fractal dimensions is necessary. It was also shown that refinements to the thermal model could lead to tremendous improvements in the accuracy of the predictions.

The validity of the model for disordered fiber arrangements was confirmed by means of data comparison with the upper and lower bounds in the literature, and by analyzing composite cross sections formed of combinations of rectangular and staggered unit cells.

## Acknowledgments

We gratefully acknowledge the support of the Alcoa Foundation and the Center for Engineered Materials of Carnegie Mellon University.

## References

- Behrens, E., 1968, "Thermal Conductivities of Composite Materials," *Journal of Composite Materials*, Vol. 2(1), pp. 2-17.
- Feder, J., 1988, *Fractals*, Plenum, New York.
- Han, L. S., and Cosner, A. A., 1981, "Effective Thermal Conductivities of Fibrous Composites," *ASME JOURNAL OF HEAT TRANSFER*, Vol. 103, pp. 387-392.
- Hashin, Z., 1970, "Theory of Composite Materials," in: *Mechanics of Composite Materials*, F. W. Wendt, H. Liebowitz, and N. Perrone, eds., Pergamon, New York, pp. 201-242.
- Hashin, Z., 1983, "Analysis of Composite Materials—A Survey," *ASME Journal of Applied Mechanics*, Vol. 50, pp. 481-505.
- James, B. W., and Keen, G. S., 1985, "A Nomogram for the Calculation of the Transverse Thermal Conductivity of Uniaxial Composite Lamina," *High Temperatures—High Pressures*, Vol. 17, pp. 477-480.
- Kim, I. C., and Torquato, S., 1990, "Determination of the Effective Conductivity of Heterogeneous Media by Brownian Motion Simulation," *Journal of Applied Physics*, Vol. 68, No. 8, pp. 3892-3903.
- Kindo, K., et al., 1989, "High Magnetic Field Effect in Martensitic Transformation," *Physica B*, Vol. 155, pp. 207-210.
- Kittel, C., 1986, *Introduction to Solid State Physics*, Wiley, New York.
- Majumdar, A., and Tien, C. L., 1989, "Fractal Network Model for Contact Conductance," presented at the Joint ASME/AIChE National Heat Transfer Conference, Philadelphia, PA.
- Mandelbrot, B. B., 1983, *The Fractal Geometry of Nature*, W. H. Freeman, New York.
- Maragos, P., and Sun, F.-K., 1990, "Measuring the Fractal Dimension of Signals: Morphological Covers and Iterative Optimization," Technical Report CICS-P-193, Center for Intelligent Control Systems, M.I.T., Cambridge, MA 02139.
- Milton, G. W., 1982, "Bounds on the Elastic and Transport Properties of Two-Component Composites," *Journal of the Mechanics and Physics of Solids*, Vol. 30, pp. 177-191.
- Muralidhar, K., 1990, "Equivalent Conductivity of Heterogeneous Medium," *International Journal of Heat and Mass Transfer*, Vol. 33, No. 8, pp. 1759-1765.
- Perrins, W. T., et al., 1979, "Transport Properties of Regular Arrays of Cylinders," *Proc. Royal Society of London, Series A*, Vol. 369, pp. 207-225.
- Pickover, C. A., 1985, "A Monte Carlo Approach for  $\epsilon$  Placement in Fractal-Dimension Calculations for Waveform Graphs," Research Report No. 11498, Computer Science Dept., IBM Thomas J. Watson Research Center, Yorktown Heights, NY 10598.
- Pickover, C. A., and Khorasani, A., 1985, "On the Fractal Structure of Speech Waveforms and Other Sampled Data," Research Report No. 11305, Computer Science Dept., IBM Thomas J. Watson Research Center, Yorktown Heights, NY 10598.
- Smith, P. A., and Torquato, S., 1989, "Computer Simulation Results for Bounds on the Effective Conductivity of Composite Media," *Journal of Applied Physics*, Vol. 65, No. 3, pp. 893-900.
- Spencer, R. A. P., 1983, "Developments in Pultrusion," in: *Developments in GRP Technology—1*, B. Harris, ed., Applied Science Publishers, London, pp. 1-36.
- Springer, G. S., and Tsai, S. W., "Thermal Conductivities of Unidirectional Materials," *Journal of Composite Materials*, Vol. 1, pp. 166-173.
- Stanley, H. E., 1985, "Fractal Concepts for Disordered Systems: The Interplay of Physics and Geometry," in: *Scaling Phenomena in Disordered Systems*, R. Pynn and A. Skjeltorp, eds., NATO ASI Series B, Plenum, New York, Vol. 133, pp. 49-69.
- Stanley, H. E., et al., 1985, "Applications of Scaling and Disorderly Growth Phenomena to Oil Recovery," in: *Scaling Phenomena in Disordered Systems*, R. Pynn and A. Skjeltorp, eds., NATO ASI Series B, Plenum, New York, Vol. 133, pp. 85-97.
- Stanley, H. E., and Ostrowsky, N., eds., 1986, *On Growth and Form. Fractal and Non-fractal Patterns in Physics*, NATO ASI series, Series E: Applied Sciences, No. 100. Martinus Nijhoff, Dordrecht, The Netherlands.
- Thornburg, J. D., and Pears, C. D., 1965, "Prediction of the Thermal Conductivity of Filled and Reinforced Plastics," ASME Paper No. 65-WA/HT-4.
- Torquato, S., and Lado, F., 1988, "Bounds on the Conductivity of a Random Array of Cylinders," *Proc. Royal Society of London, Series A*, Vol. 417, pp. 59-80.
- Voss, R. F., 1985, "Random Fractals: Characterization and Measurement," in: *Scaling Phenomena in Disordered Systems*, R. Pynn and A. Skjeltorp, eds., NATO ASI Series B, Plenum, New York, Vol. 133, pp. 1-11.
- Yao, S. C., and Pitchumani, R., 1990, "Fractal Based Correlation for the Evaluation of Thermal Conductivities of Fibrous Composites," *Transport Phenomena in Materials Processing*, ASME HTD-Vol. 146, pp. 55-60.

# Effect of Interfacial Roughness on Phonon Radiative Heat Conduction

A. Majumdar

Department of Mechanical and Aerospace  
Engineering,  
Arizona State University,  
Tempe, AZ 85287

The interface between a solid and a liquid or two dissimilar solids poses a resistance to heat transport by phonons, which are quanta of lattice vibrational energy. The classical theory explains that the resistance  $R$  arises due to a mismatch in acoustic impedances of the two media and predicts  $R$  to vary with temperature  $T$  as  $R \sim T^{-3}$ . Experiments with copper and liquid  $^3\text{He}$  have shown that first, although  $RT^3$  is a constant below 0.1 K, its value is much less than that predicted by the classical theory. Second, at higher temperatures the resistance behaves as  $R \sim T^{-n}$  where  $n > 3$ . This study explains these observations in the temperature range of 0.06 K–1 K and  $^3\text{He}$  pressure range from zero atmospheres in liquid state to solid state, by including the effects of surface roughness and phonon attenuation in solids by electrons or dislocations. Roughness measurements have shown that solid surfaces have a fractal structure and are characterized by a fractal dimension  $D$  lying between 2 and 3 for a surface. Using the fractal characteristics, the thermal boundary resistance is shown to follow the relation  $RT^3 \sim (1 + \eta T^\beta)^{-1}$  where  $\beta$  is a function of the dimension  $D$  and  $\eta$  is a scaling constant. The predictions are in excellent agreement with the experimental observations, indicating that, in addition to other surface effects, the fractal surface structure could have a strong influence on thermal boundary resistance.

## Introduction

Heat is transported in solids either by electrons or by lattice vibrations. In materials with high electrical conductivity, like metals, the contribution of electrons is dominant, whereas in dielectric nonmagnetic materials, vibrations of the crystal lattice provide the only method of heat conduction. The lattice vibrations behave as waves in a crystal and are characterized by a frequency and an amplitude. The energy of these waves is quantized and the quantum of a lattice vibration is called a phonon (Kittel, 1986). When phonons of a particular frequency are incident on a boundary between two different media, only a fraction of the energy gets transmitted, whereas the rest gets reflected. This is analogous to the reflection and transmission of energy, observed when electromagnetic waves are incident on an interface between two media having different refractive indices. In the case of phonons, the property responsible for the amount of transmitted energy is the ratio of the acoustic impedances of the two media. Since only a fraction of the incident phonon energy is transmitted, an interface effectively imposes a resistance, called a *thermal boundary resistance*. This resistance is most critical at cryogenic temperatures, specially near or below 1 K. It is a factor in the design of refrigeration systems, temperature sensors, superconducting integrated circuits, as well as solid–solid joints in space applications. It is therefore necessary to understand the role of interfaces and physical properties on thermal boundary resistance. In addition, the study of resistance to phonon transmission provides an ideal opportunity to understand the physics of heat conduction by phonons not only at surfaces but also in bulk media. In view of its engineering relevance and its fundamental nature, this paper makes an in-depth study of the phenomenon of boundary resistance to phonon radiative heat conduction.

Thermal boundary resistance between a solid and liquid helium was first observed by Kapitza (1941) and this phenomenon is now called Kapitza resistance. Subsequently, thermal resistance between two dissimilar solids has also been observed.

Khalatnikov (1952) developed the theory of acoustic mismatch to predict the boundary resistance between a solid and a liquid to be varying as  $T^{-3}$ . Little (1959) extended the acoustic mismatch theory (AMT) to predict the resistance between two dissimilar solids. Although the predictions of the AMT showed reasonably correct trends at temperatures below 1 K, experiments on solid–liquid interfaces indicated that the actual resistance was much less than the predictions, and usually showed trends different from the  $T^{-3}$  behavior. This is evident in Fig. 1, which shows some measurements of the thermal resistance between copper and liquid  $^3\text{He}$  at different pressures in the liquid (Anderson et al., 1964). The results are plotted as  $RT^3$  versus  $T$ . Since the AMT theory predicts a  $T^{-3}$  behavior, its predictions would be straight horizontal lines in Fig. 1. The

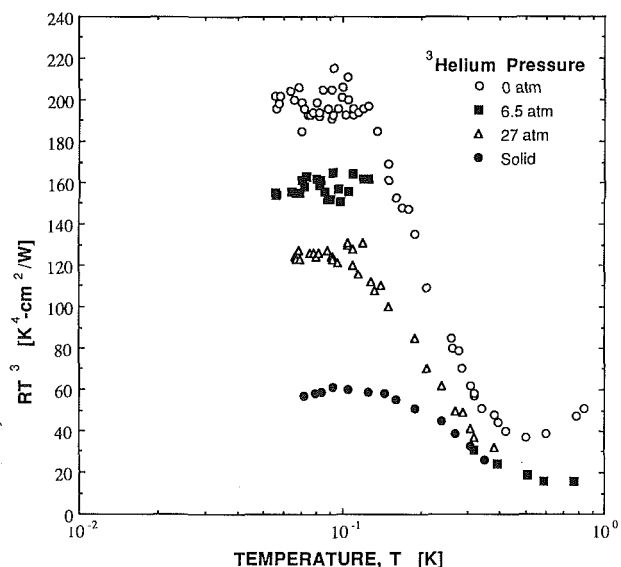


Fig. 1 Product of thermal boundary resistance and the third power of temperature plotted against temperature. Experimental data for an interface of copper and liquid  $^3\text{He}$  at different pressures of the liquid and of copper and solid  $^3\text{He}$  (Anderson et al., 1964).

Contributed by the Heat Transfer Division and presented at the ASME/JSME Thermal Engineering Joint Conference, Reno, Nevada, March 17–21, 1991. Manuscript received by the Heat Transfer Division December 17, 1990; revision received February 19, 1991. Keywords: Conduction, Cryogenics, Radiation.

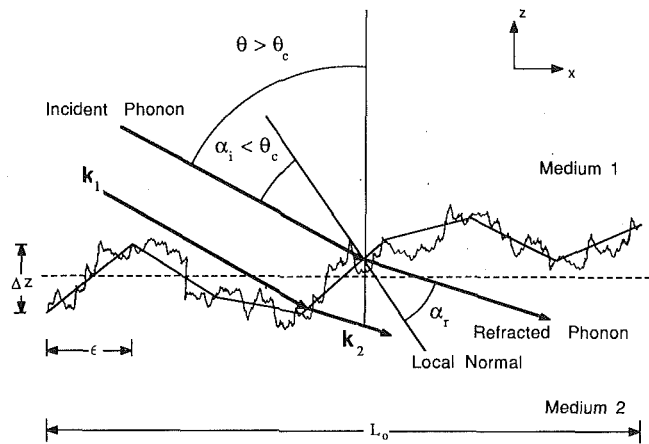


Fig. 2 Schematic diagram showing facets of a rough surface as well as local values of angles of incidence and refraction

experiments suggested that first, although  $RT^3$  is a constant below 0.1 K, its value is much less than that predicted by the AMT. For instance, the experiments show that for liquid  $^3\text{He}$  at a pressure of 0 atm and temperatures below 0.1 K,  $RT^3 \sim 200 \text{ K}^4\text{-cm}^2/\text{W}$ , whereas the AMT predicts it to be close to  $1500 \text{ K}^4\text{-cm}^2/\text{W}$ . Second, for  $T > 0.1 \text{ K}$  the resistance behaves as  $R \sim T^{-n}$ , where  $n > 3$ . Several explanations have been proposed for this anomalous behavior and are discussed in an excellent review by Swartz and Pohl (1989). Although it is not certain which effects are dominant, it is clear that surface roughness plays a vital role in reducing the thermal boundary resistance below the predictions of the AMT where such an effect is neglected.

Most of the previous works on roughness contribution have focused on scattering of phonons by Rayleigh surface waves (Shiren, 1981; Nakayama, 1985a, 1985b, 1986). When Rayleigh waves scatter phonons in both media, they assist in transmitting phonons that are incident at angles larger than the critical angle  $\theta_c$  for total internal reflection of phonons. The enhanced transmission reduces the thermal boundary resistance. Shiren (1981) showed that by using appropriate parameters for surface roughness, the theory of Rayleigh scattering agreed well with the experiments for temperatures above 0.2 K, but predicted vastly different trends for lower temperatures.

To explain the experimental results for the temperature range shown in Fig. 1, this study takes a different approach by considering the effect that although a phonon may be incident at angles greater than  $\theta_c$  formed by a flat surface, the local angle of incidence  $\alpha_i$  may be less than  $\theta_c$ , as shown in Fig. 2. This effectively exposes more surface area to the incident phonons and thus reduces the thermal resistance. Although such an effect has been suggested by Khalatnikov (1952) and Little (1959), no investigation has been made so far. The main difficulty lay in the inability to quantify the structure of surface roughness due to its disorder and multiscale nature. Recent measurements of surface roughness of deposited thin films and machined metals have shown that roughness follows a *fractal* structure (Majumdar and Tien, 1990a; Majumdar and Bhushan, 1990). This provides a simple scaling law for roughness at different length scales. The present study uses the fractal surface structure in a modified acoustic mismatch theory to predict the anomalous behavior of the thermal resistance observed in Fig. 1.

This paper first gives a brief background on the physics of phonons and the acoustic mismatch theory. It then shows experimental observations of the fractal roughness structure. The fractal structure is then used to modify the AMT to include

## Nomenclature

|  |   |  |
|--|---|--|
| $a$ = atomic spacing, m  | $\dot{q}$ = rate of energy flux transfer, $\text{Wm}^{-2}$                | $\sigma'$ = standard deviation of surface slopes   |
| $A$ = area, $\text{m}^2$   | $\dot{Q}$ = rate of energy transfer, W                                    | $\tau''$ = bidirectional transmissivity            |
| $c$ = speed of sound, $\text{ms}^{-1}$   | $R$ = thermal boundary resistance, $\text{m}^2 \text{KW}^{-1}$            | $\tau'$ = directional-hemispherical transmissivity |
| $C$ = constant defined in Eq. (16)   | $S$ = structure function defined in Eq. (16), $\text{m}^2$                | $\tau$ = transmissivity                            |
| $D$ = fractal dimension of a surface profile   | $T$ = temperature, K  | $\phi$ = azimuthal angle                           |
| $\mathcal{D}(\omega)$ = density of states, $\text{sm}^{-3}$                                    | $\mathcal{J}$ = rotation matrix defined in Eq. (A.7)                      | $\Phi$ = phase difference                          |
| $f(\omega)$ = factor representing increase in effective area                                   | $\mathbf{u}$ = displacement vector for atoms in a lattice wave, m         | $\omega$ = frequency of phonon, $\text{s}^{-1}$    |
| $G$ = scaling constant for a fractal surface, m  | $z(x)$ = height of a surface profile at a location $x$ , m                | $\Omega$ = solid angle, sr                         |
| $h_b$ = thermal boundary conductance, $\text{Wm}^{-2} \text{K}^{-1}$                           | $Z$ = acoustic impedance = $\rho c$ , $\text{kgm}^{-2} \text{s}^{-1}$     |  |
| $\hbar$ = Planck's constant divided by $2\pi$ , Js   | $\alpha$ = local angle of incidence or refraction                         |  |
| $I$ = phonon intensity, $\text{Wm}^{-2} - \text{sr}^{-1} \text{s}$                             | $\beta$ = exponent of temperature defined in Eq. (21)                     |  |
| $k_B$ = Boltzmann constant, $\text{JK}^{-1}$   | $\epsilon$ = energy of phonons, J   |  |
| $\mathbf{k}$ = wavevector, $\text{m}^{-1}$   | $\epsilon$ = horizontal distance between two points of a rough surface, m |  |
| $L$ = length, m  | $\theta$ = angle from normal to a flat surface                            |  |
| $l$ = mean free path of phonons, m   | $\lambda$ = wavelength of lattice wave, m                                 |  |
| $n$ = number of phonons  | $\xi$ = spatial frequency of roughness defined as reciprocal of           |  |
| $N$ = product of $\mathcal{D}(\omega)$ and equilibrium phonon distribution $\langle n \rangle$ |   |  |
| $p$ = probability density function for directions of facet normals                             |   |  |
| $P$ = power in surface spectrum, $\text{m}^3$  |   |  |

## Subscripts

|  |
|--|
| 1, 2 = referring to medium                         |
| 1 - 2 = transport from medium 1 to medium 2        |
| $c$ = critical                                     |
| $D$ = Debye cutoff                                 |
| $i$ = incidence                                    |
| $m$ = maximum                                      |
| $n$ = facet normal                                 |
| $o$ = nominally flat surface or incident intensity |
| $p$ = polarization of lattice waves                |
| $r$ = refraction                                   |
| $R$ = roughness                                    |

## Superscript

|   |
|---|
| $\bar{\quad}$ = normalized by probability distribution or effect of attenuation |
|---|

roughness effects. Finally, the results of this work are discussed.

### Physics of Phonons

Elastic vibrations of atoms propagate as waves in a crystal lattice (Ziman, 1960; Kittel, 1986). The displacements of atoms from their equilibrium positions can be written as

$$\mathbf{u} = \mathbf{u}_0 \exp(i(\mathbf{k} \cdot \mathbf{r} - \omega t)) \quad (1)$$

where  $\mathbf{u}_0$  is the amplitude of vibration,  $\mathbf{k}$  is the wavevector of propagation with  $|\mathbf{k}| = 2\pi/\lambda$ ,  $\lambda$  is the wavelength of oscillation,  $\mathbf{r}$  is the position vector of an atom in a lattice, and  $\omega$  is the frequency of vibration. The group velocity of such a wave is  $v_g = d\omega/dk$ . The wavelength of elastic vibrations is restricted to values of  $\lambda > 2a$  where  $a$  is the atomic spacing in a particular direction. The energy  $\mathcal{E}$  of the elastic mode of frequency  $\omega$  is equal to the sum of the kinetic and the potential energy and is quantized as

$$\mathcal{E} = \left(n + \frac{1}{2}\right) \hbar \omega \quad (2)$$

where  $\hbar$  is Planck's constant divided by  $2\pi$  and  $n$  is the number of phonons occupying the frequency mode  $\omega$ . The equilibrium distribution of phonons  $\langle n \rangle$  at any temperature follows the Bose-Einstein statistics and is given as

$$\langle n \rangle = \frac{1}{\exp\left(\frac{\hbar \omega}{k_B T}\right) - 1} \quad (3)$$

where  $k_B$  is the Boltzmann constant and  $T$  is the temperature. The total phonon energy in a solid is

$$Q = \sum_p \int \langle n \rangle \hbar \omega \mathcal{D}(\omega) d\omega \quad (4)$$

where  $\mathcal{D}(\omega)$  is the density of states and  $\mathcal{D}(\omega)d\omega$  is equal to the number of phonon modes in a frequency range  $\omega$  and  $\omega + d\omega$ . The summation in Eq. (4) is over the different polarizations of quantized lattice waves: two transverse and one longitudinal for solids and only longitudinal for liquids. It is common to invoke the Debye approximation here, that phonons behave as if the crystal lattice is a continuum for which  $\omega = ck$ , where  $c$  is the speed of sound in the solid. This approximation is valid for temperatures lower than 1/50th the Debye temperature, which is around 343 K for copper (Kittel, 1986). The density of states then reduces to

$$\mathcal{D}(\omega) = \frac{\omega^2}{2\pi^2 c^3}; \quad 0 < \omega < \omega_D \quad (5)$$

where  $\omega_D$  is the cutoff frequency for the Debye density of states. The Bose-Einstein statistics along with the Debye density of states make the physics of phonons analogous to that of photons. It is therefore common to call heat conduction by phonons a *radiation phenomenon*. At low temperatures when the integration over frequency extends from zero to infinity, one finds the flux of phonon energy per unit time and per unit area to follow the familiar Stefan-Boltzmann relation  $\dot{q} = \sigma T^4$ . For the acoustic case, the value of the Stefan-Boltzmann constant  $\sigma$  is (Swartz and Pohl, 1989)

$$\sigma = \frac{\pi^2 k_B^4}{120 \hbar^3} \sum_p \frac{1}{c_p^2} \quad (6)$$

Due to the similarity between phonons and photons with respect to their wave nature, it is natural to expect phenomena such as reflection, refraction, and diffraction to be common to both. This is explored further in the following discussion.

### Acoustic Mismatch Theory

Consider a flat interface separating two media, 1 and 2. The number of phonons of energy  $\hbar \omega$  incident upon a small area  $dA$  of the interface per unit time and at an angle of incidence of  $\theta$  from the surface normal in a solid angle  $d\Omega$  is equal to  $N_{1p}(\omega, T) c_{1p} \cos \theta d\Omega / 4\pi$  where  $d\Omega = \sin \theta d\theta d\phi$  and  $N_{1p}(\omega, T)$  is

$$N_{1p}(\omega, T) = \langle n \rangle \mathcal{D}(\omega) = \frac{\omega^2}{2\pi^2 c_{1p}^3 [\exp(\hbar \omega / k_B T) - 1]} \quad (7)$$

The total energy per unit time crossing the interface from medium 1 to medium 2 is then

$$\dot{Q}_{1-2}(T) = \sum_p \int_A \int_{\Omega=2\pi} \int_0^{\omega_D} \frac{N_{1p}}{4\pi} c_{1p} \cos \theta \hbar \omega \tau_{1-2} d\omega d\Omega dA \quad (8)$$

The quantity  $\tau_{1-2}$  is the transmissivity of acoustic waves across a flat interface and is given as (Rayleigh, 1894)

$$\tau_{1-2} = \frac{4Z_1 Z_2 \cos \theta \cos \theta_r}{(Z_2 \cos \theta + Z_1 \cos \theta_r)^2} \quad (9)$$

where  $Z = \rho c$  is the acoustic impedance of a material. The angles of incident  $\theta$  and refraction  $\theta_r$  satisfy Snell's law

$$\frac{\sin \theta}{\sin \theta_r} = \frac{c_1}{c_2} \quad (10)$$

From Eq. (9) it is clear that  $\tau_{1-2}(\theta, \theta_r) = \tau_{2-1}(\theta_r, \theta)$ . Note that the transmissivity depends on the polarization of a phonon through the speed of sound. From Eq. (10), the critical angle for total internal reflection can be found in the medium with lower speed of sound. If considered over all the azimuthal angles, one can define a critical cone. Any phonon incident from outside this cone will not be transmitted, thus resulting in a resistance to heat flow.

Since the acoustic mismatch theory considers a flat interface and the transmissivity to be independent of frequency, Eq. (8) can be simplified to

$$\begin{aligned} \frac{\dot{Q}_{1-2}(T)}{A} &= \sum_p c_{1p} \bar{\tau}_{1-2} \int_0^{\omega_D} N_{1p} \hbar \omega d\omega \\ &= \frac{\pi^2 k_B^4 T^4}{60 \hbar^3} \sum_p \frac{\bar{\tau}_{1-2}}{c_p^2} \end{aligned} \quad (11)$$

where

$$\bar{\tau}_{1-2} = \frac{1}{4\pi} \int_{\phi=0}^{2\pi} \int_{\theta=0}^{\pi/2} \tau_{1-2} \cos \theta \sin \theta d\theta d\phi \quad (12)$$

The thermal boundary conductance  $h_b$  is defined as

$$h_b = \frac{\dot{Q}_{1-2}(T_1) - \dot{Q}_{1-2}(T_2)}{A(T_1 - T_2)} \quad (13)$$

Note that one need not calculate  $\dot{Q}_{2-1}(T)$  if it is assumed that the transmissivities are independent of temperature (Swartz and Pohl, 1989). For small values of the ratio  $(T_1 - T_2)/T_1$ , one can differentiate Eq. (11) with respect to  $T$  to obtain the conductivity in a convenient form as

$$h_b = \frac{\pi^2 k_B^4 T^3}{15 \hbar^3} \sum_p \frac{\bar{\tau}_{1-2}}{c_p^2} \quad (14)$$

The thermal boundary resistance  $R$  is defined as  $R = 1/h_b$  and is therefore seen to follow the relation  $R \sim T^{-3}$ .

**Effect of Attenuation.** As observed in Fig. 1, the experiments show that below 0.1 K the value of  $RT^3$  is a constant. However, the value of the constant is much less than that

predicted by the acoustic mismatch theory, as expressed in Eq. (14). To explain such a discrepancy, Peterson and Anderson (1972, 1973) and Haug and Weiss (1972) proposed the following mechanism. Consider a phonon incident on an interface from outside the critical cone that undergoes total internal reflection. To satisfy the boundary conditions on the other side of the interface, there will be an evanescent wave, which will decay exponentially in the solid. If this exponentially decaying wave is scattered in the solid by electrons or surface dislocations, then energy will be transmitted across the interface. This effectively broadens the critical cone and thus reduces the boundary resistance. It is simple to implement this phenomenon in the AMT by assuming the velocity of sound to be complex as (Peterson and Anderson, 1973)

$$c' = \frac{c}{\left(1 + \frac{i\lambda}{4\pi l}\right)} \quad (15)$$

where  $\lambda$  is the wavelength of a phonon and  $l$  is the mean free path of attenuation of the evanescent wave. If the complex speed of sound is used in Eq. (1) for the wave equation, it is observed that the amplitude attenuates exponentially. If  $\lambda \sim l$ , as in the case for either scattering by electrons in a metal or by dislocations (Haug and Weiss, 1972), then it can be shown that  $R \sim T^{-3}$ . However, the value of  $RT^3$  can be less than that predicted by AMT by more than an order of magnitude. Therefore, the effect of attenuation is considerable and has to be accounted for in analyzing thermal boundary resistance. However, it does not explain the anomalous behavior in Fig. 1 where  $RT^3$  varies with temperature.

**Effect of Boundary Layers.** When a solid and liquid helium are in contact, the force of attraction due to van der Waals forces between the dissimilar atoms is very strong. Consequently, the first few monolayers of the helium are solid and the density falls off gradually away from the solid to the bulk value. The thickness of the dense layer of helium at the interface is about 30 Å (Franchetti, 1956). The effect of the dense boundary layer of helium on the transmission of phonons was considered by Challis et al. (1961) who found that long wavelengths are not affected by the layer. However, for phonons of wavelength less than four times the layer thickness, transmission is enhanced. At temperatures above 0.1 K, they found the relation  $R \sim T^{-4.2}$ . Therefore, this is one possible explanation for the anomalous behavior observed in Fig. 1. However, note that even for solid helium in Fig. 1, there is a drop in the value of  $RT^3$  as temperature increases. Hence there must be some other mechanism responsible for the anomalous behavior.

### Fractal Structure of Surface Roughness

Solid surfaces are known to be composed of several scales of roughness, ranging from nanometers (Avnir et al., 1984) to several kilometers, as that of the earth. Surface roughness appears random and disordered and is usually characterized by statistical parameters such as the standard deviations of the height, slope, and curvature (Nayak, 1971). However, it has been experimentally shown that due to the multiscale nature of roughness, these roughness parameters depend on either the length of the statistical sample or the resolution of the measuring instrument (Majumdar and Bhushan, 1990). Therefore, the parameters conventionally used are scale-dependent and do not uniquely characterize surface roughness.

An interesting feature of surface roughness observed by Mandelbrot (1982) is that upon magnification, the appearance of surfaces remains similar over several length scales. He concluded that for such surfaces, which are never smooth at any length scale, the dimension of the surface is not an integer value but is a fraction between 2 and 3. Consequently, the

profile or a vertical cut of a surface is of a dimension between 1 and 2. Such surfaces and profiles are called fractal (Mandelbrot, 1982). The theory of fractal geometry and the characterization of surface roughness is well-described elsewhere (Majumdar and Tien, 1990a; Majumdar and Bhushan, 1990; Majumdar, 1991; Mandelbrot, 1982; Voss, 1988). Here only a brief description of the characterization is provided.

If  $z(x)$  is a fractal roughness profile of dimension  $D$  lying between 1 and 2, then the statistics of the function is well represented by the structure function  $S(\epsilon)$  defined as the mean square increment of  $z(x)$ ,  $S(\epsilon) = \langle (z(x + \epsilon) - z(x))^2 \rangle$ . For a fractal surface, the structure function follows the relation (Majumdar and Bhushan, 1990)

$$S(\epsilon) = \frac{G^{2(D-1)}}{(2-D)} \sin\left(\frac{\pi(2D-3)}{2}\right) \Gamma(2D-3) \epsilon^{(4-2D)} \\ = CG^{2(D-1)} \epsilon^{(4-2D)} \quad (16)$$

When  $S(\epsilon)$  is plotted versus  $\epsilon$  on a log-log plot, the value of  $D$  can be obtained from the slope and that of  $G$  from the intercept. The value of  $D$  obtained represents the dimension of a surface profile, whereas the fractal dimension of a surface is equal to  $D + 1$ . It should be noted that the parameters  $D$  and  $G$ , which characterize the structure function, are independent of  $\epsilon$  and therefore scale-independent.

Figure 3(a) shows the structure function of a high- $T_c$  thin film superconductor surface (Majumdar et al., 1991). The  $\text{YBa}_2\text{Cu}_3\text{O}_{7-\delta}$  was sputter deposited on an MgO substrate and the film was superconducting in-situ with  $T_c = 60$  K. The roughness was measured by a scanning tunneling microscope (STM) over a region of  $1.5 \mu\text{m} \times 1.5 \mu\text{m}$  with a resolution of 6 nm. The measurement was composed of 256 profiles with each profile containing 256 digitized points. The structure function was found for each profile and then averaged over the 256 profiles for each value of  $\epsilon$ . Figure 3(b) shows the structure function of a single profile of a ground stainless steel surface. The roughness was measured by a diamond-stylus profilometer, which had a resolution of  $5 \mu\text{m}$  and a scan containing 1000 points. The data were analyzed in a manner similar to that employed in Fig. 3(a). Due to the power law behavior of  $S(\epsilon)$  in Figs. 3(a) and 3(b), it is concluded that both surfaces were fractal. The sputtered surface has  $D = 1.49$  and  $G = 3.34$  nm, whereas the stainless steel surface has  $D = 1.46$  and  $G = 0.548$  nm. The sputter-deposited surface was fractal possibly due to the nonequilibrium growth process associated in sputtering (Meakin, 1987; Medina et al., 1989). Microfracture in metals, involved in machining, is also known to produce fractal surfaces as experimentally shown by Mandelbrot et al. (1984).

### Phonon Transmission Across a Rough Interface

The following discussion assumes that interactions of phonons with Rayleigh waves and other surface excitations are negligible. It explores a new approach to study the influence of surface roughness and attenuation by electrons and dislocations on thermal boundary resistance.

**Exposed Surface Area.** Several studies have suggested that roughness exposes more area to incident phonons, thereby reducing the resistance to heat flow (Khalatnikov, 1951; Little, 1959; Challis et al., 1961). Little (1959) proposed that the increase in effective area could be included in the heat transport relation of Eq. (8) by assuming  $dA = dA_0 \omega^n$  where  $\omega$  is the frequency of the phonon and  $dA_0$  is the nominal area of the elemental region. Under this assumption it is observed that  $RT^3 \sim T^{-n}$ . Such a behavior, however, is not experimentally observed for temperatures below 0.2 K. As explained later, Little's proposition is valid in the limit of high frequencies. This is apparent because when  $\omega \rightarrow 0$  the surface should appear smooth and  $dA = dA_0$ . Consider now a region of nominal

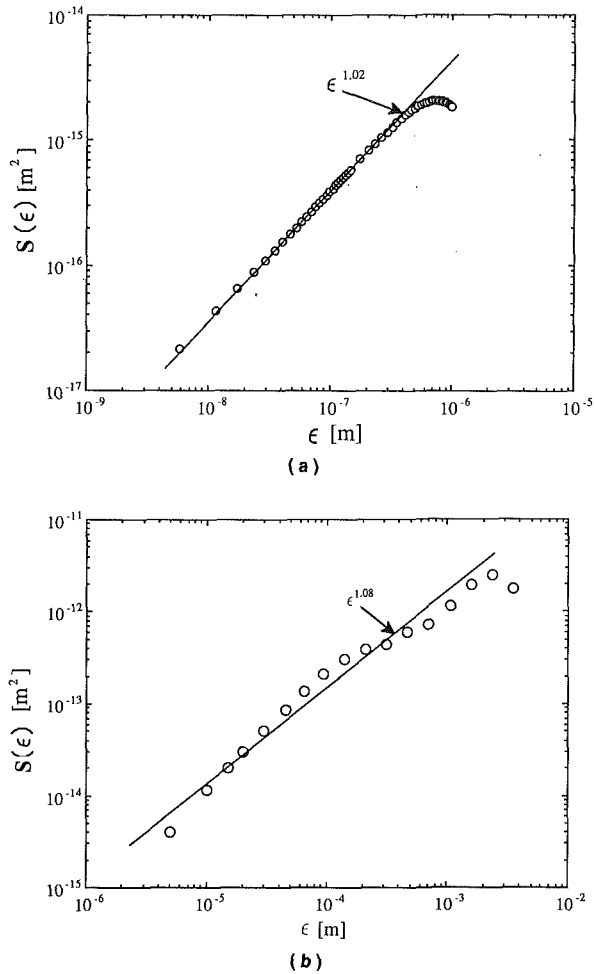


Fig. 3 Structure function of surface profiles for (a) high- $T_c$  thin film superconductor; (b) ground stainless steel

length  $L_0$  of fractal surface profile, shown in Fig. 2, whose structure function follows Eq. (16). If  $\epsilon$  is the length of a segment in the  $x$  direction then the nominal length is  $L_0 = N\epsilon$  where  $N$  is the number of segments. However the actual length  $L$  of the profile is equal to

$$L = N\sqrt{\epsilon^2 + (\Delta z)^2} = L_0\sqrt{1 + (\Delta z/\epsilon)^2} \quad (17)$$

From Eq. (16), it is known that  $\langle (\Delta z/\epsilon)^2 \rangle = C(G/\epsilon)^{2(D-1)}$  where  $C = \sin(\pi(2D-3)/2)\Gamma(2D-3)/(2-D)$ . Therefore the effective elemental area  $dA = L^2$  is

$$dA = dA_0 \left[ 1 + C \left( \frac{G}{\epsilon} \right)^{2(D-1)} \right] \quad (18)$$

It is clear from Eq. (18) that, in contrast with Little's (1959) proposition, for a large unit of measurement  $\epsilon$  the actual area tends to the nominal area, whereas for finer units of measurement, the actual area becomes larger.

Now consider a phonon of wavevector  $\mathbf{k}_1$  incident on a rough interface from medium 1 and refracted in medium 2 with wavevector  $\mathbf{k}_2$  as shown in Fig. 2. The rough surface can be divided into several facets with each facet behaving like a flat interface. The question that arises out of this procedure is: What is the size of a facet? Due to the wave nature of phonons, one can use Helmholtz-Kirchhoff diffraction theory to predict the scattering pattern of acoustic waves (Beckmann and Spizichino, 1963). The scattered amplitude at any angle can be obtained by adding the phases of waves emanating from every point on the surface (Majumdar and Tien, 1990b). If the surface is perfectly flat, then the phases would add up only

in directions where the angle of reflection equals the angle of incidence and where the angle of refraction satisfies Snell's law. When the surface is rough, however, the phases add up in other directions, thus giving rise to diffuse reflection and refraction. Since the effect of roughness on the phases contributes to the diffuse scattering of waves, the size of a facet should be decided by how much phase difference is produced by a facet on a rough surface. The phase difference  $\Phi$  between two parallel incident and refracted beams (see Fig. 2) is

$$\Phi = (\mathbf{k}_1 - \mathbf{k}_2) \cdot (\epsilon \hat{x} + \Delta z \hat{z}) \quad (19)$$

The first term in Eq. (19),  $\Phi_x = (\mathbf{k}_1 - \mathbf{k}_2) \cdot \epsilon \hat{x}$  is the  $x$  component of the phase difference between two parallel waves incident on a flat horizontal interface and does not contain any roughness effect. If one considers only this phase difference, then the surface would behave as a flat interface with angles of incidence and refraction satisfying Snell's law. The  $z$  component  $\Phi_z = (\mathbf{k}_1 - \mathbf{k}_2) \cdot \Delta z \hat{z}$  is purely due to roughness. Therefore a rough surface should be considered flat if  $|\Phi_z| \leq 1$ . The facet size is decided by invoking the equality in this relation. To simplify it further, if one assumes that both the incident and refracted beam are normal to the facet and that  $k_m$  is the larger of  $k_1$  and  $k_2$ , then  $k_m \Delta z = 1$  should decide the size of the facet. In particular, consider medium 1 to be copper and medium 2 to be liquid  $^3\text{He}$ . Since the speed of sound for the liquid is far less than that of the solid copper, the critical cone in the liquid helium would be extremely small with most phonons traveling nearly in the  $z$  direction. In addition, since  $|\mathbf{k}_2| \gg |\mathbf{k}_1|$  due to the difference in speeds of sound,  $(\mathbf{k}_1 - \mathbf{k}_2) \approx -\mathbf{k}_2$  which is in the  $z$  direction. Therefore, the phase difference follows as  $|\Phi| \approx k_2 \Delta z$ . From the statistics of the roughness it is known that  $\Delta z = G^{D-1} \epsilon^{2-D}$ . Using this in the flatness criterion, one gets the value of  $\epsilon$  for a facet as

$$\epsilon = \frac{1}{k_m^{1/(2-D)} G^{(D-1)/(2-D)}} \quad (20)$$

From Eq. (18) the effective area is obtained in terms of the frequency as

$$dA = dA_0 [1 + C(Gk_m)^\beta] = dA_0 [1 + C(G\omega/c)^\beta] \quad (21)$$

where  $\beta = 2(D-1)/(2-D)$ .

The question remains whether at the wavelength dominant in phonon energy, is a rough surface fractal? By invoking the Debye approximation, one gets the Planck distribution for phonons. The maximum of the Planck distribution occurs at a value of  $hc/(\lambda kT) = 4.965$  (Knuth, 1966). This yields the relation  $\lambda_{\text{dom}} T = 9.676 \times 10^{-12} c$  s-K where  $\lambda_{\text{dom}}$  is the wavelength dominant in phonon energy. The speeds of sound for transverse and longitudinal waves are  $2.50 \times 10^3$  m/s and  $4.91 \times 10^3$  m/s, respectively, for copper and  $0.194 \times 10^3$  m/s for longitudinal waves in liquid  $^3\text{He}$  at saturation vapor pressure (Swartz and Pohl, 1989). Therefore, the dominant wavelengths at  $T = 0.5$  K are 48 nm and 96 nm for transverse and longitudinal waves, respectively, in copper and 4 nm for liquid  $^3\text{He}$ . For the copper-liquid  $^3\text{He}$  interface the relevant wavelength for roughness interactions is 4 nm in liquid  $^3\text{He}$ . Assuming typical values of  $G = 1$  nm and  $D = 1.5$  for a polished surface (Majumdar and Tien, 1990a) and considering  $\Delta z/\lambda \sim 1$  for determining a facet, one gets  $\Delta z = 4$  nm for the roughness height and  $\epsilon = 16$  nm for the lateral size of the facet. Although roughness of a copper surface has not been measured at that scale, topography measurements of sputter-deposited high- $T_c$  thin film by STM do indicate the fractal structure at these scales as shown in Fig. 3(a). In addition, the roughness amplitude  $\Delta z = 4$  nm, which is of the order of the thickness of the solid-He boundary layer. Therefore, it should be noted that the effects of boundary layers and surface roughness overlap in length scales. However, since  $RT^3$  varied with temperature  $T$  even for a copper-solid He interface (see Fig. 1), the



influence of surface roughness is significant. Therefore this study neglects the effect of boundary layers.

**Transmissivity of a Rough Surface.** Analogous to the concept of bidirectional reflectivity of a rough surface (Siegel and Howell, 1982), the bidirectional transmissivity  $\tau''(\theta, \phi, \theta_r, \phi_r, \omega)$  can be defined as the contribution of the incident phonon energy flux to the transmitted intensity in the  $(\theta_r, \phi_r)$  direction

$$\tau''(\theta, \phi, \theta_r, \phi_r, \omega) = \frac{I(\theta_r, \phi_r, \omega)}{I_o(\theta, \phi, \omega) \cos \theta d\Omega} \quad (22)$$

Here  $I_o(\theta, \phi, \omega) \cos \theta d\Omega$  is the incident energy flux of phonons. To determine the bidirectional transmissivity one needs to first find the transmitted intensity  $I(\theta_r, \phi_r, \omega)$ .

Consider the coordinate system depicted in Fig. 4. Since the surface roughness is random in nature, the facets of the rough surface have normals randomly distributed in directions  $(\theta_n, \phi_n)$ . Let the number of facets of the exposed area with normals within  $\theta_n$  and  $\theta_n + d\theta_n$  and  $\phi_n$  and  $\phi_n + d\phi_n$  be equal to

$$p(\theta_n, \phi_n, \omega) d\theta_n d\phi_n \quad (23)$$

where  $p(\theta_n, \phi_n, \omega)$  is the probability density function for the facet normals (see Appendix 1 for details of the probability density function). The fraction of the exposed area with normals in the direction  $(\theta_n, \phi_n)$  and within  $d\theta_n d\phi_n$  is

$$p(\theta_n, \phi_n, \omega) d\theta_n d\phi_n f(\omega) dA_o \quad (24)$$

where  $f(\omega) = 1 + C(G\omega/c)^\beta$  and  $dA_o$  is the nominal area. The phonon energy  $dQ$  incident on these exposed areas is

$$dQ = I_o \cos \alpha_i d\Omega p(\theta_n, \phi_n, \omega) d\theta_n d\phi_n f(\omega) dA_o \quad (25)$$

where  $\alpha_i$  is the local angle between the incident direction  $(\theta, \phi)$  and the facet normal  $(\theta_n, \phi_n)$ . The transmitted energy  $dQ_t$  is related to the incident energy as  $dQ_t = \tau_{1-2}(\alpha_i, \alpha_r, Z_1, Z_2) dQ$  where  $\tau_{1-2}(\alpha_i, \alpha_r, Z_1, Z_2)$  is the transmissivity for a flat interface given in Eq. (9). The transmitted intensity  $I(\theta_r, \phi_r, \omega)$  is therefore

$$I(\theta_r, \phi_r, \omega) = \frac{\tau_{1-2} dQ}{dA_o \cos \theta_r d\Omega_r} = \frac{\tau_{1-2} I_o \cos \alpha_i d\Omega p(\theta_n, \phi_n, \omega) f(\omega) d\theta_n d\phi_n}{\cos \theta_r d\Omega_r} \quad (26)$$

When the facet normals have a wide angular spread, the surface will appear diffuse. The deviation of the bidirectional transmissivity from a purely diffuse or Lambert's cosine-law approximation is decided by the spread of the probability density function  $p(\theta_n, \phi_n, \omega)$  and is discussed in the appendix. The directional-hemispherical transmissivity  $\tau'(\theta, \phi, \omega)$ , defined as the fraction of the energy incident from the direction  $(\theta, \phi)$  that is transmitted into all solid angles, is related to the bidirectional transmissivity as

$$\tau'(\theta, \phi, \omega) = \int_{\Omega_r=0}^{2\pi} \tau''(\theta, \phi, \theta_r, \phi_r, \omega) \cos \theta_r d\Omega_r = \frac{f(\omega)}{\cos \theta} \int_{\phi_n=0}^{2\pi} \int_{\theta_n=0}^{\pi/2} \tau_{1-2} \cos \alpha_i p(\theta_n, \phi_n, \omega) d\theta_n d\phi_n \quad (27)$$

This can be written in a simpler form as  $\tau'(\theta, \phi, \omega) = f(\omega) \bar{\tau}'(\theta, \phi, \omega)$  where  $\bar{\tau}'(\theta, \phi, \omega)$  is the directional-hemispherical transmissivity weighted by the probability distribution of the facet normals.

**Heat Transport.** The total phonon energy crossing a rough interface can be found from Eq. (8) with  $\tau_{1-2}$  substituted by  $\tau'(\theta, \phi, \omega)$ . This can be written as

$$\frac{\dot{Q}_{1-2}(T)}{A_o} = \sum_p \int_{\phi=0}^{2\pi} \int_{\theta=0}^{\pi/2} \int_0^{\omega_D} \left( \frac{N_{1p}}{4\pi} c_{1p} \cos \theta h \omega \bar{\tau}'(\theta, \phi, \omega) f(\omega) d\omega \right) \sin \theta d\theta d\phi \quad (28)$$

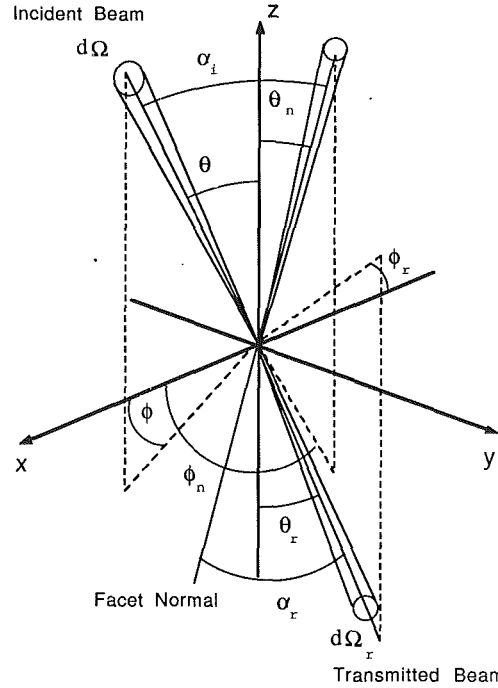


Fig. 4 Coordinate system for surface facets, incident and transmitted phonon beams

Before evaluating these integrals, it is necessary to determine the dependence of the directional-hemispherical transmissivity on the frequency  $\omega$ . The appendix contains the algorithm for numerically evaluating  $\bar{\tau}'(\theta, \phi, \omega)$ . If it is assumed that the probability distribution of surface heights is isotropic then it can be shown that the quantity  $\bar{\tau}'(\theta, \phi, \omega)$  is independent of the azimuthal angle  $\phi$  and can therefore be written as  $\bar{\tau}'(\theta, \omega)$  (see appendix). The frequency dependence of  $\bar{\tau}'(\theta, \omega)$  originates in the standard deviation  $\sigma'$  of the facet normals as given in Eq. (A.3). To check whether there is a strong frequency dependence, the quantity  $\bar{\tau}'(\theta, \omega)$  was evaluated for different values of  $\sigma'$ . The computations were performed for a transverse phonon of speed  $2.5 \times 10^5$  cm/s incident from copper and transmitted as a longitudinal phonon into liquid  $^4\text{He}$  with a speed of  $0.238 \times 10^5$  cm/s (Swartz and Pohl, 1989). The density of copper is  $8.96$  gm/cm $^3$  and that of liquid  $^4\text{He}$  is  $0.145$  gm/cm $^3$ . Figure 5 shows the effect of  $\sigma'$  on the directional-hemispherical transmissivity. The reason for choosing values of  $\sigma'$  only up to unity is that experimentally it has been found that values of  $G$  range from  $10^{-6}$  cm to  $10^{-9}$  cm (Majumdar and Tien, 1990a; Majumdar and Bhushan, 1990) which is of the order of or a fraction of a few unit cells. Therefore the quantity  $G/\epsilon$  will usually be less than unity.

From the results of Fig. 5 it can be safely assumed that  $\bar{\tau}'(\theta, \omega)$  is independent of the frequency, thus simplifying Eq. (28) to

$$\frac{\dot{Q}_{1-2}(T)}{A_o} = \frac{1}{4\pi^2} \sum_p \frac{\bar{\tau}}{c_{1p}^2} \int_0^{\omega_D} \frac{h\omega^3 f(\omega) d\omega}{\exp(h\omega/k_B T) - 1} \quad (29)$$

where  $\bar{\tau}$  is given as

$$\bar{\tau} = \int_{\theta=0}^{\pi/2} \bar{\tau}'(\theta) \cos \theta \sin \theta d\theta \quad (30)$$

Using the functional form of  $f(\omega)$  and assuming the temperature is low enough for  $h\omega_D/k_B T$  to tend to infinity, Eq. (29) can be solved to get

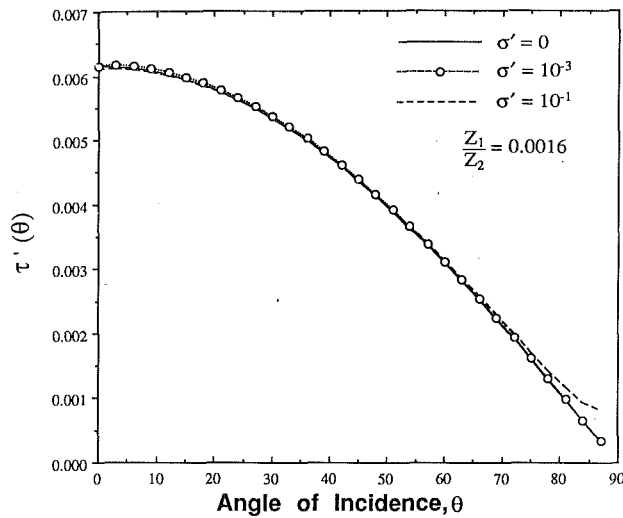


Fig. 5 Directional-hemispherical transmissivity plotted against angles of incidence for different values of the rms slope of surface facets

$$\frac{\dot{Q}_{1 \rightarrow 2}(T)}{A_o} = \sum_p \left[ \left( \frac{\bar{\tau}}{c_p^2} \right) \left( \frac{\pi^2 k_B^4 T^4}{60 h^3} \right) + \frac{C}{4\pi^2} \left( \frac{G}{c_p} \right)^\beta \frac{(k_B T)^{(4+\beta)}}{h^{(3+\beta)}} \Gamma(4+\beta) \zeta(\beta) \right] \quad (31)$$

where  $\Gamma$  is the gamma function and

$$\zeta(\beta) = \sum_{s=1}^{\infty} \frac{1}{s^{4+\beta}} \quad (32)$$

The first term in Eq. (31) represents phonon transmission for a flat surface where the  $T^4$  dependence of the heat flux is the blackbody radiation of phonons. The second term contains the effects of surface roughness and varies as  $T^{4+\beta}$ . If the surface is perfectly flat, that is when  $G = 0$ , then the second term vanishes.

## Results and Discussion

The thermal boundary resistance  $R$ , defined as  $R = A_o(d\dot{Q}/dT)^{-1}$ , can now be obtained from Eq. (31). To compare the results with the experimental data of Fig. 1, it is convenient to find an expression for  $RT^3$  as

$$RT^3 = \frac{\left( \frac{15h^3}{\pi^2 k_B^4} \right) \left[ \sum_p \bar{\tau}/c_p^2 \right]^{-1}}{\left[ 1 + \frac{15(4+\beta)\Gamma(4+\beta)\zeta(\beta)}{4\pi^4} \frac{\sum_p \bar{\tau} \left( \frac{T}{T_{Rp}} \right)^\beta}{\sum_p \bar{\tau}/c_p^2} \right]} \quad (33)$$

where  $T_{Rp} = hc_p/Gk_B$ . The numerator in Eq. (33) is the prediction for the AMT, whereas the denominator represents the effect of surface roughness. The influence of roughness is well quantified by the parameter  $T_R$ , which is an effective temperature representing the amplitude of roughness.

The effect of attenuation by electron or defect scattering can easily be incorporated in Eq. (33) through the value of  $\bar{\tau}$ . Peterson and Anderson (1973) used the complex speed of sound given in Eq. (15) to evaluate  $\bar{\tau}$  and  $RT^3$ . They concluded that the experimental results of  $RT^3$  at temperatures lower than 0.1 K agreed with the predictions when the phonon wavelength

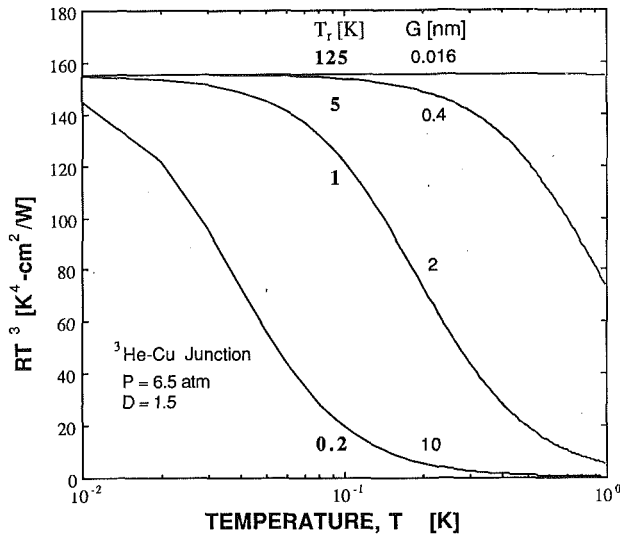
was nearly equal to the phonon mean free path,  $\lambda \approx l$ . This implies that the complex part of the speed of sound is independent of the frequency. This assumption was also made by Haug and Weiss (1972) for scattering by static dislocations. In order to include the effect of attenuation in the present study, Eq. (33) can be written as

$$RT^3 = \frac{\overline{RT^3}}{\left[ 1 + \frac{15(4+\beta)\Gamma(4+\beta)\zeta(\beta)}{4\pi^4} \frac{\sum_p \bar{\tau} \left( \frac{T}{T_{Rp}} \right)^\beta}{\sum_p \bar{\tau}/c_p^2} \right]} \quad (34)$$

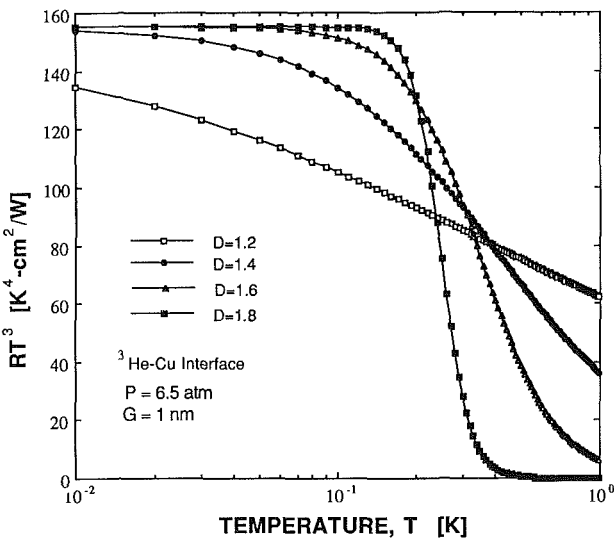
where  $\overline{RT^3}$  and  $\bar{\tau}$  are the predictions of Peterson and Anderson (1973) after including attenuation. Figures 6(a) and 6(b) show the results for an interface between copper and liquid  $^3\text{He}$  at a pressure of 6.5 atm. The denominator in Eq. (34) was computed for phonons in the liquid  $^3\text{He}$ , which contains only the longitudinal polarization. It can be observed that as the value of  $G$  decreases in Fig. 6(a), the surface becomes smoother, and therefore, the value of  $RT^3$  tends to be a constant. A decrease in  $G$  also increases the roughness temperature  $T_R$ . When the roughness temperature increases, the effect of roughness on phonon transmission is felt at a higher temperature. Figure 6(b) shows that as the surface fractal dimension is increased, the drop in the value of  $RT^3$  due to roughness becomes sharper. In the limiting case when  $D$  tends to unity, the exponent  $\beta$  becomes zero and therefore the roughness has no effect on the boundary resistance.

When these results are compared with Fig. 1, it is clear that the predictions show the correct trends. The experiments show that the drop in the resistance occurs at about 0.1 K for all the cases. This suggests that the value of  $T_R$  for all of them is nearly constant and does not depend on the pressure. Hence  $T_R$  is decided by the phonons in the copper. Figure 7 shows a comparison between the prediction of present theory with the experiments of Anderson et al. (1964). The results were obtained for  $D = 1.6$  and  $G = 3$  nm. It was encouraging to see that for the same values of  $D$  and  $G$  the predictions were in excellent agreement with the experimental data for the four different cases. These values of the roughness parameters are well within the range found by roughness measurements by STM and stylus profilometers. In spite of the agreement at temperatures below 0.7 K, the value of  $RT^3$  increases above this temperature. Little (1961) showed that microroughness interactions, that is when the roughness amplitude is comparable to phonon wavelength, actually increase boundary resistance. This may explain the experimental results above 0.7 K, since at higher temperatures the dominant phonon wavelength is smaller, thus leading to microroughness effects. This effect was not considered in this study since the assumption in defining a surface facet was  $|\Phi_z| \leq 1$  thereby considering interactions of large-wavelength phonons for which  $|\Phi_z| > 1$ .

This study combines the effects of attenuation (Peterson and Anderson, 1973) and roughness on thermal boundary resistance. The roughness effect is included only through the function  $f(\omega)$ , which represents the increase in exposed area for phonons of frequency  $\omega$ . The fractal characterization allows one to determine  $f(\omega)$  in Eq. (21) through the power-law behavior of the structure function. A more realistic model would need to include effects of shadowing due to surface roughness. In addition, to get a complete understanding of the dominant mechanisms involved in thermal boundary resistance, one needs to integrate the fractal roughness structure with other surface phenomena such as solid boundary layers, Rayleigh wave scattering, and the microroughness effects.



(a)



(b)

Fig. 6 Theoretical predictions showing the dependence of the product of thermal boundary resistance and the third power of temperature on temperature for (a) different values of roughness scaling constant  $G$  and (b) different values of fractal dimension  $D$

## Conclusions

The influence of surface roughness on heat conduction by phonons across an interface between two dissimilar media is analyzed in this study. Previous experiments have shown that at temperatures below 0.1 K, the resistance between copper and liquid  $^3\text{He}$  varies as  $T^{-3}$  but is much less than that predicted by the classical acoustic mismatch theory. At higher temperatures the resistance behaves as  $T^{-n}$  with  $n > 3$ . To explain the observations for 0.1 K, the present study included the effect of attenuation of phonons by electrons or surface dislocations in the copper. It is suggested that the behavior at higher temperatures is due to the influence of surface roughness. Roughness of solid surfaces is observed to follow a fractal structure. The fractal structure is characterized by two parameters: the fractal dimension  $D$ , which lies between 2 and 3 for a surface or 1 and 2 for a surface profile, and a scaling constant  $G$ , which has units of length. Using the fractal characterization, this study showed that the amount of surface exposed to incident phonons increased with the frequency of phonons. Due to the increase in surface area, the resistance to heat transport by phonons decreased for higher frequencies. The predictions

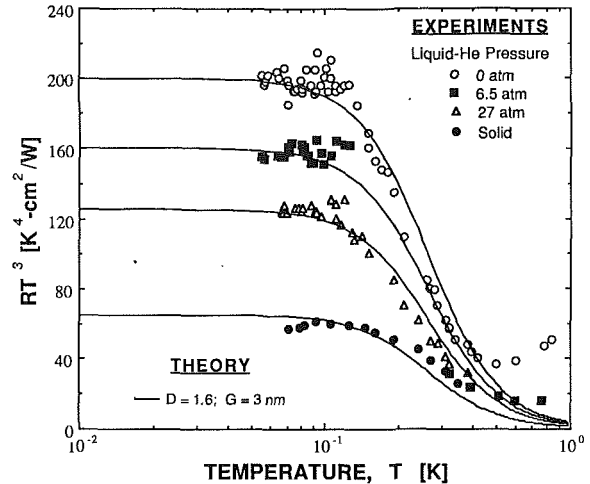


Fig. 7 Comparison between the theoretical predictions and experimental observations (Anderson et al., 1964) for the product of thermal boundary resistance and the third power of temperature as a function of temperature

of the present study are in excellent agreement with previous experimental observations for reasonable values of  $D$  and  $G$ .

## Acknowledgments

I would like to thank Professor R. O. Pohl and Dr. E. T. Swartz for their cooperation and encouragement. I am grateful to M. Williamson for helping me with graphics. This work was supported in part by NSF Grant No. CTS-9010311 and by the MAE Department of Arizona State University.

## References

- Anderson, A. C., Connolly, J. I., and Wheatley, J. C., 1964, "Thermal Boundary Resistance Between Solids and Helium Below 1 K," *Physical Review*, Vol. 135, pp. A910-A921.
- Avnir, D., Farin, D., and Pfeifer, P., 1984, "Molecular Fractal Surfaces," *Nature*, Vol. 308, pp. 261-263.
- Beckmann, P., and Spizzichino, A., 1963, *The Scattering of Electromagnetic Waves From Rough Surfaces*, McMillan, New York.
- Challis, L. J., Dransfeld, K., and Wilks, J., 1961, "Heat Transfer Between Solids and Liquid Helium II," *Proceedings of the Royal Society of London*, Vol. A 260, pp. 31-46.
- Franchetti, R., 1956, "On the Problem of the Static Helium Film," *Nuovo Cimento*, Vol. 4, p. 1504.
- Harrington, S., 1983, *Computer Graphics*, McGraw-Hill, New York.
- Haug, H., and Weiss, K., 1972, "A Modified Theory of the Kapitza Resistance," *Physics Letters*, Vol. 40A, pp. 19-21.
- Kapitza, P. L., 1941, "The Study of Heat Transfer in Helium II," *Journal of Physics (USSR)*, Vol. 4, p. 181; in: *Collected Papers of P. L. Kapitza*, D. ter Haar, ed., 1965, pp. 581-624.
- Khalatnikov, I. M., 1952, *Journal of Experimental and Theoretical Physics (USSR)*, Vol. 22, p. 687.
- Kittel, C., 1986, *Introduction of Solid State Physics*, 6th ed., Wiley, New York.
- Knuth, E. L., 1966, *Introduction to Statistical Thermodynamics*, McGraw-Hill, New York.
- Little, W. A., 1959, "The Transport of Heat Between Dissimilar Solids at Low Temperatures," *Canadian Journal of Physics*, Vol. 37, pp. 334-349.
- Little, W. A., 1961, "Unimportance of Surface Roughness Upon the Kapitza Resistance," *Physical Review*, Vol. 123, pp. 1909-1911.
- Majumdar, A., and Bhushan, B., 1990, "Role of Fractal Geometry in Roughness Characterization and Contact Mechanics of Surfaces," *ASME Journal of Tribology*, Vol. 112, pp. 205-216.
- Majumdar, A., and Tien, C. L., 1990a, "Fractal Characterization and Simulation of Rough Surfaces," *Wear*, Vol. 136, pp. 313-327.
- Majumdar, A., and Tien, C. L., 1990b, "Reflection of Radiation by Rough Fractal Surfaces," *Proceedings of the AIAA/ASME Thermophysics and Heat Transfer Conference*, Seattle, HTD-Vol. 137, pp. 27-35.
- Majumdar, A., 1991, "Role of Fractal Geometry in the Study of Thermal Phenomena," *Annual Review of Heat Transfer*, Vol. 4, in press.
- Majumdar, A., Whitfield, S., Thomson, R. E., Clarke, J., Chin, D., van Duzer, T., Flik, M. I., and Tien, C. L., 1991, "Surface Topography of High- $T_c$  Thin Film Superconductor Studied by Scanning Tunneling Microscopy," in preparation.

Mandelbrot, B. B., 1982, *The Fractal Geometry of Nature*, W. H. Freeman, New York.

Mandelbrot, B. B., Passoja, D. E., and Paullay, A. J., 1984, "Fractal Character of Fractured Surfaces of Metals," *Nature*, Vol. 308, pp. 1571-1572.

Meakin, P., 1987, "Fractal Scaling in Thin Film Condensation and Material Surfaces," *CRC Critical Reviews in Solid State and Materials Science*, Vol. 13, pp. 143-189.

Medina, E., Hwa, T., Kardar, M., and Zhang, Y. C., 1989, "Burger's Equation With Correlated Noise: Renormalization-Group Analysis and Applications to Directed Polymers and Interface Growth," *Physical Review A*, Vol. 39, pp. 3053-3075.

Nakayama, T., 1985a, "New Channels of Energy Transfer Across a Solid-Liquid He Interface," *Journal of Physics C: Solid State Physics*, Vol. 18, pp. L667-L671.

Nakayama, T., 1985b, "Diffuse Scattering of High-Frequency Phonons at Solid Surfaces," *Physical Review B*, Vol. 32, pp. 777-780.

Nakayama, T., 1986, "Scattering of High-Energy Phonons at Irregular Surfaces Without and With Liquid Helium," *Physical Review B*, Vol. 33, pp. 8664-8676.

Nayak, P. R., 1971, "Random Process Model of Rough Surface," *ASME Journal of Lubrication Technology*, Vol. 93, pp. 398-407.

Peterson, R. E., and Anderson, A. C., 1972, "The Transport of Heat Between Solids at Low Temperature," *Solid State Communications*, Vol. 10, pp. 891-894.

Peterson, R. E., and Anderson, A. C., 1973, "The Kapitza Thermal Boundary Resistance," *Journal of Low Temperature Physics*, Vol. 11, pp. 639-665.

Press, W. H., Flannery, B. P., Teukolsky, S. P., and Vetterling, W. T., 1988, *Numerical Recipes—The Art of Scientific Computing*, Cambridge Univ. Press, United Kingdom, pp. 420-429.

Rayleigh, Lord, 1894, *Theory of Sound*, Macmillan and Co., London.

Shiren, N. S., 1981, "Surface Roughness Contribution to Kapitza Resistance," *Physical Review Letters*, Vol. 47, pp. 1466-1469.

Siegel, R., and Howell, J. R., 1982, *Thermal Radiation Heat Transfer*, 2nd ed., Hemisphere Publishing Corp.

Swartz, E. T., and Pohl, R. O., 1989, "Thermal Boundary Resistance," *Reviews of Modern Physics*, Vol. 61, pp. 605-668.

Vicsek, T., 1986, "Formation of Solidification Patterns in Aggregation Models," in: L. Pietronero and E. Tosatti, eds., *Fractals in Physics*, pp. 247-250, Elsevier Science Publishing, New York.

Voss, R. F., 1988, "Fractals in Nature: From Characterization to Simulation," in: *The Science of Fractal Images*, H. O. Peitgen and D. Saupe, eds., pp. 21-70, Springer-Verlag, New York.

Ziman, J. M., 1960, *Electrons and Phonons*, Oxford University Press, London.

## APPENDIX

If the probability distribution of the surface heights is Gaussian, then the probability distribution for the surface tangents is also Gaussian with a zero mean (Beckmann and Spizzichino, 1963). Consider the chord joining two points on the surface separated by a distance  $\epsilon$  and with a height difference  $\Delta z$  as shown in Fig. 2. Such a chord defines a facet of a rough surface. The normal to this facet is inclined at an angle  $\theta_n$  from the vertical direction and  $\phi_n$  from the  $x$  axis. From the structure

$$\mathfrak{J} = \begin{pmatrix} \cos^2 \phi_n \cos \theta_n + \sin^2 \phi_n & \sin \phi_n \cos \phi_n (\cos \theta_n - 1) & -\sin \theta_n \cos \phi_n \\ \sin \phi_n \cos \phi_n (\cos \theta_n - 1) & \sin^2 \phi_n \cos \theta_n + \cos^2 \phi_n & -\sin \theta_n \sin \phi_n \\ \sin \theta_n \cos \phi_n & \sin \theta_n \sin \phi_n & \cos \theta_n \end{pmatrix} \quad (\text{A.7})$$

function of the fractal surface (Eq. (16)) it can be concluded that

$$\left\langle \left( \frac{z(x+\epsilon) - z(x)}{\epsilon} \right)^2 \right\rangle = \langle \tan^2 \theta_n \rangle = C \left( \frac{G}{\epsilon} \right)^{2(D-1)} \quad (\text{A.1})$$

Equation (A.1) shows that the variance of  $\tan \theta_n$  depends on the unit of measurement  $\epsilon$ , which in turn depends on the frequency of a phonon through Eq. (20). The probability distribution for  $\tan \theta_n$  can be written as

$$p(\tan \theta_n, \omega) = \frac{1}{\sqrt{2\pi\sigma'}} \exp\left(-\frac{\tan^2 \theta_n}{2\sigma'^2}\right) \quad (\text{A.2})$$

where

$$\sigma' = \sqrt{C} \left( \frac{G\omega}{c} \right)^{(D-1)/(2-D)} \quad (\text{A.3})$$

is the standard deviation of  $\tan \theta_n$ . Assuming that the surface is isotropic and that the distribution in the  $\phi_n$  direction is uniform, the probability density function is reduced to

$$p(\theta_n, \phi_n, \omega) = \frac{1}{\pi} \frac{1}{\sqrt{2\pi\sigma'} \cos^2 \theta_n} \exp\left(-\frac{\tan^2 \theta_n}{2\sigma'^2}\right) \quad (\text{A.4})$$

Equation (A.4) satisfies the relation

$$\int_{\phi_n=0}^{2\pi} \int_{\theta_n=0}^{\pi/2} p(\theta_n, \phi_n, \omega) d\theta_n d\phi_n = 1 \quad (\text{A.5})$$

For a wider angular spread of the distribution function, the surface will appear more diffuse. The spread of the distribution is quantified by the standard deviation of the facet slopes. As discussed earlier the maximum value of  $\sigma'$  is about unity. If  $p(\theta_n, \phi_n, \omega)$  is plotted against  $\theta_n$  for this value, the probability density remains uniform for  $\theta_n < 60$  deg from the surface normal and then falls rapidly to zero. Such a distribution will produce a uniform distribution of transmitted intensity for angles less than 60 deg and would therefore be close to Lambert's cosine law. As the value of  $\sigma'$  is reduced, both the distribution peak and the angle where the sharp fall occurs, shift toward  $\theta_n = 0$ , thus tending toward more specular behavior.

Equation (27) shows that the directional-hemispherical transmissivity  $\bar{\tau}'(\theta, \phi, \omega)$  for a rough surface is weighted by the probability density function as

$$\bar{\tau}'(\theta, \phi, \omega) = \frac{1}{\cos \theta} \int_{\phi_n=0}^{2\pi} \int_{\theta_n=0}^{\pi/2} \tau_{1-2}(\alpha_i, \alpha_r, Z_1, Z_1) \times \cos \alpha_i p(\theta_n, \phi_n, \omega) d\theta_n d\phi_n \quad (\text{A.6})$$

The main difficulty in evaluating the integrals in Eq. (A.6) lies in determining the angles  $\alpha_i$  and  $\alpha_r$ , which the incident and the transmitted beams make with the facet normal, respectively, and satisfy Snell's law. These angles are obtained by rotating the coordinate system  $(x, y, z)$  of Fig. 4 to  $(x', y', z')$  so as to align it with the facet normal. The coordinates of the incident beam are then found in the new coordinate system to give  $\alpha_i$ . Then Snell's law is used to determine  $\alpha_r$ . The transformation matrix used in rotating the coordinate system is (Harrington, 1983)

The evaluation of  $\bar{\tau}'(\theta, \phi, \omega)$  is done numerically due to the complexity involved in the probability density function and the determination of the  $\alpha_i$  and  $\alpha_r$ .

It should be noted that since the probability distribution is uniform in the azimuthal angle  $\phi_n$ , the quantity  $\bar{\tau}'(\theta, \phi, \omega)$  does not depend on  $\phi$  and can be written as  $\bar{\tau}'(\theta, \omega)$ . The frequency dependence originates through the standard deviation of the facet slopes as given in Eq. (A.3). One should note that if the surface is perfectly flat, that is when  $\sigma'$  is very small, then  $\alpha_i \rightarrow \theta$  and as expected,  $\bar{\tau}' \rightarrow \tau_{1-2}$ .

# The Effect of Thermal Conductivity on the Singular Behavior of the Near-Tip Temperature Gradient

D. Y. Tzou

Department of Mechanical Engineering,  
University of New Mexico,  
Albuquerque, NM 87131  
Mem. ASME

*The singular behavior of the temperature gradient in the vicinity of a macrocrack tip is studied in this work. The emphasis is placed on the effect of thermal conductivity on the power of singularity of the near-tip temperature gradient. Both the temperature dependency and the inhomogeneity of the thermal conductivity are investigated analytically. In the near-tip region, they are the sensitive factors influencing the singular behavior of the temperature gradient. The physical conditions under which their effect dominates over the geometric singularity at the crack tip are studied in detail. In some cases, their strong effects can even make the singularity of the temperature gradient diminished at the crack tip. Consequently, the thermal energy intensification disappears.*

## Introduction

According to the line crack model, the geometric curvature at the crack tip possesses a discontinuous jump. As a result, the temperature gradient develops a singularity when approaching the crack tip. For a Fourier solid, the temperature gradient is proportional to the heat flux vector. The intensity factor of the temperature gradient (IFTG) is thus a physical scale measuring the accumulation of thermal energy at the crack tip. This concept is useful in assessing the postdamage performance of thermal systems. The strategy of repairing a crack, for example, is to dissipate the intensified thermal energy accumulated at the crack tip. Under the same service conditions, therefore, the desirable patch configuration should be the one giving the smallest value of IFTG among the possible configurations. From a thermomechanical point of view, a smaller value of IFTG is equivalent to a smaller force driving the crack to grow. A damaged system with a lower value of IFTG at the crack tip, therefore, would perform more stably in operations. A detailed example illustrating this idea was recently given by Tzou (1991a). The IFTG was used as the physical index in determining the optimal stacking sequence of the material layers for composite laminates resisting an intensified thermal irradiation.

The IFTG is a direct result from the  $r$  dependency of the temperature gradient in the near-tip region. The value of  $r$  here stands for the radial distance measured from the crack tip. The design philosophy developed in this sense thus requires a detailed understanding on the thermal field around the crack tip. As illustrated in Fig. 1, the major difficulty for crack problems lies in the presence of mixed boundary conditions. At the same boundary of  $y=0$ , the boundary condition specified at the crack surface ( $x<0$ ) is different from that specified in the region ahead of the crack tip ( $x>0$ ). Analytically, the Muskhelishvili formulation employing the analytic complex functions (Sih, 1965), the dual integral equation approach (Tzou, 1985), and the Williams method of eigenfunction expansions (Tzou, 1990, 1991b) can properly handle this type of problem. The Williams method of eigenfunction expansions is especially efficient in determining the power of singularity of the temperature gradient.

The singular behavior of the temperature gradient also reflects the combined effects of geometric singularity and thermal properties of the solid medium. When the geometric singularity

dominates over the effect of thermal properties, the power of singularity of the temperature gradient is always one-half ( $1/2$ ). Typical examples are a crack in an isotropic solid and an interfacial crack between dissimilar materials (Tzou, 1991b). When the effect of thermal properties overcomes the geometric singularity, on the other hand, the power of singularity depends on the thermal properties. A typical example is a crack in an orthotropic medium (Tzou, 1991b). When the ratio of thermal conductivities in the principal directions ( $k_r/k_\theta$  in Fig. 1) exceeds a critical value of  $1/4$ , the power of singularity is  $A$ . For a highly directional medium with  $k_r/k_\theta < 1/4$ , singularity in the temperature gradient diminishes at the crack tip. The power of singularity in the latter case is thus zero. Diminution of singularity in the temperature gradient implies the absence of energy accumulation at the crack tip. Associated with the popular use of high-performance materials such as composites, this knowledge is desirable in preventing crack evolution in a thermal system with damage.

As a continuation, the present work further explores the effects of thermal conductivity on the singular behavior of the

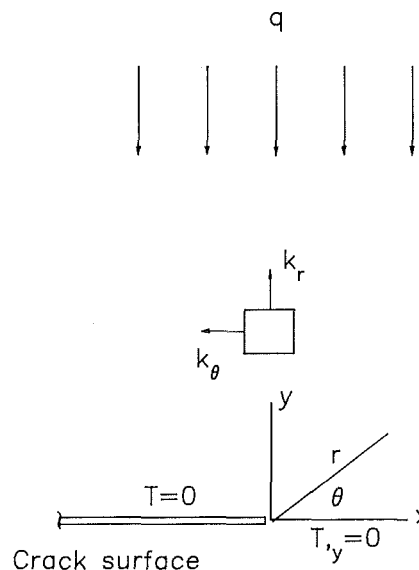


Fig. 1 Mixed boundary conditions specified along the crack line for  $x < 0$  and  $x > 0$  at  $y = 0$ ; physical interpretation for diminution of temperature gradient at the crack tip when  $k_r \gg k_\theta$ .

Contributed by the Heat Transfer Division for publication in the JOURNAL OF HEAT TRANSFER. Manuscript received by the Heat Transfer Division July 16, 1990; revision received May 17, 1991. Keywords: Conduction.

temperature gradient. The temperature dependency and inhomogeneity of thermal conductivity are the major factors under consideration. In particular, this work emphasizes the physical conditions in which thermal energy diminishes at the crack tip.

### Boundary Conditions at the Crack Surfaces

The boundary conditions imposed on the crack surfaces dominate the singular behavior of the temperature gradient in the near-tip region (Tzou, 1990, 1991a). A detailed understanding on the thermodynamic behavior of the gas arrested in the crack closure is therefore necessary. Initially, let us assume that the air in the closure is in equilibrium with the solid medium. Both are at a reference temperature of  $T_0$ . A thermal disturbance then propagates through the solid medium and disturbs the air arrested inside the closure. The thermodynamic state of the air consequently changes and evolves according to certain thermodynamic processes. Since the line-crack model assumes an infinitesimal space between the crack surfaces, we further assume that the thermodynamic states inside the closure are uniform. Thus, no spatial variation of temperature or pressure across the closure will be considered. The thermodynamic behavior of the gas is governed by the equation of state  $f(p, T, v) = 0$ , with  $p$ ,  $v$ , and  $T$  being the pressure, specific volume, and temperature of the gas. For illustration, let us first consider an ideal behavior for the gas:

$$pv = RT \quad \text{or} \quad f(p, v, T) = pv - RT \quad (1)$$

where  $R$  is the gas constant. From Eq. (1), the differential changes of  $p$ ,  $v$ , and  $T$  are related by

$$pdv + vdp = RdT. \quad (2)$$

The specific volume change  $dv$  in Eq. (2) is dominated by the crack opening due to thermomechanical deformations. The opening displacement, however, is usually very small due to rigidity of the solid medium confining the gas. For metals, the value of  $dv/v$  is on the order of  $10^{-8}$  to  $10^{-10}$ . The rate of change of pressure with temperature, according to Eq. (2), is then

$$dp/dT \approx R/v = R\rho \quad (3)$$

with  $\rho$  being the density of the gas. For ordinary gases, the value of  $dP/dT$  is on the order of  $10^{-5}$  to  $10^{-6}$  MPa/ $^{\circ}$ C. It depicts a pressure increase of one-hundredth (1/100) to one-thousandth (1/1000) of one atmospheric pressure under a temperature increase of  $100^{\circ}$ C. Such a minor increase in pressure supports the assumption of an isobaric process for the change of thermodynamic states of the gas in crack opening. According to Eq. (2), moreover, an isobaric process also results in an isothermal process because the density change of the gas

due to crack opening is very small. The Van Der Waals equation of state, i.e.,

$$p = RT/(v-b) - c/v^2, \quad (4)$$

is a more realistic model accounting for the finite volume and mutual interactions of gas molecules. For air, as an example, Eq. (4) yields a value of  $dp/dT = 2.7 \times 10^{-4}$  MPa/ $^{\circ}$ C. Again, this small change in pressure with temperature is negligible in practice. An isothermal process for the change of thermodynamic states in the aerial closure, therefore, is a reliable approximation. Applications of this process to heat conduction problems with cracks or voids are popular in the related field of research (Loeb, 1954; Sih, 1965; Kassir, 1971; Tzou, 1990, 1991a, 1991b). Other types of boundary conditions assuming crack surfaces being insulated (Florence and Goodier, 1960, 1963; Tzou and Chen, 1990) or exchanging thermal energy with the air in cavities by natural convection (Tzou, 1991c) have also been employed. At least as a first-order approximation, these simplified models are sufficient for most engineering purposes. As an overall evaluation to these approximations, however, the temperature change across the aerial closure of cracks or voids must be sufficiently smooth. Should a dramatic temperature increase across the crack surfaces result, such as LOCA (loss of coolant accident) in nuclear reactors, not only the compressibility and irreversibility of the gas must be taken into account, but also the effects of heat convection and radiation in the aerial closure ought to be incorporated as an entirety.

### Effect of Thermal Conductivity

Based on the previous discussions, we assume a constant temperature at the crack surfaces. For both cases with temperature- and space-varying thermal conductivities, the power of singularity of the temperature gradient at the crack tip is the major concern of this work. While the transient effect only influences the magnitude of the IFTG, the power of singularity is depicted by the steady-state solutions (Sih, 1965; Tzou, 1985). With emphasis on the diminution or amplification of the thermal energy toward the crack tip, therefore, a steady-state analysis is sufficient.

**(a) Temperature-Dependent Thermal Conductivity.** When the thermal conductivity is a function of temperature, the energy equation,

$$\nabla \cdot [k(\mathbf{r}, T) \nabla T] = 0, \quad (5)$$

becomes nonlinear. The use of a polar coordinate system centered at the crack tip is more convenient to describe the state of the affairs in the near-tip region (Tzou, 1990, 1991a, 1991b, for example). The operator  $\nabla$  in Eq. (5) is therefore  $\nabla \equiv [\partial/$

### Nomenclature

|   |   |  |
|---|---|--|
| $a$ = half length of crack, m   |   |  |
| $A, B$ = material parameter modeling the thermal conductivity                       | $k_R$ = ratio of the thermal conductivity = $k_r/k_\theta$              | $X_{,i}$ = partial differentiations of $X$ with respect to the coordinates $i$ , $i=r, \theta, x$ , or $y$ |
| $A_{ij}$ = determinants resulting from the finite difference scheme for eigenvalues | $m$ = positive integers   | $x, y$ = physical coordinates, m   |
| $C_{ij}$ = amplitudes of the eigenfunctions, $i, j=0, 1, 2, \dots$                  | $n$ = material parameter modeling the thermal conductivity              | $\beta_m$ = a function of the eigenvalues, Eq. (29)  |
| $F$ = eigenfunctions of the near-tip temperature                                    | $p$ = power of singularity of the temperature gradient at the crack tip | $\Delta X$ = incremental quantities of $X$   |
| $F_j$ = nodal values of $F(\theta)$ at the $j$ th node                              | $q$ = remote heat flux vector   | $\theta$ = polar angles measured from the leading edge of the crack, deg                                   |
| $k$ = thermal conductivity, W/mK  | $r$ = radial distance measured from crack tip, m                        | $\lambda_m$ = eigenvalues, $r$ dependency of the near-tip temperature gradient                             |
| $k_r, k_\theta$ = components of the orthotropic thermal conductivity, W/mK          | $T$ = temperature, K  | $\nabla^2$ = Laplacian operator  |
|   | $V$ = pseudo-temperature in the Kirchhoff transformation                |  |

$\partial r, \partial/(r\partial\theta)$ . For crack surfaces kept at a constant temperature, Eq. (5) is to be solved for the temperature distribution  $T$ . The boundary conditions at the crack surfaces are

$$T=0 \quad \text{at} \quad \theta=\pi \quad (6)$$

$$T_{,\theta}=0 \quad \text{at} \quad \theta=0. \quad (7)$$

Without loss in generality, we assume a zero temperature at the crack surface. As illustrated in Fig. 1, the boundary condition (7) results from symmetry of the problem. It is independent of the gaseous behavior in the crack enclosure. In general, the solution for temperature in Eq. (5) varies in space. Consequently, the temperature-dependent thermal conductivity would become nonhomogeneous in an implicit sense. For illustration, let us consider a simple form for the functional relationship.

$$k(T)=AT^n. \quad (8)$$

The coefficient  $A$  and the exponent  $n$  are the behavioral parameters of the material. From the second law of thermodynamics, obviously, the coefficient  $A$  must be positive definite. In practice, the power law shown by Eq. (8) may result from the piecewise curve fitting for the variation of thermal conductivity in a particular range of temperature.

Under certain conditions, Eq. (5) can be linearized by applying the Kirchhoff transformation (Ames, 1965). Defining a pseudotemperature  $V$  as

$$V=\int k(T)dT, \quad (9)$$

substitution of Eq. (8) into Eq. (9) gives the explicit relationship between  $V$  and  $T$ :

$$V=\left(\frac{A}{n+1}\right)T^{n+1} \quad \text{or} \quad T=\left[\left(\frac{n+1}{A}\right)V\right]^{1/(n+1)} \quad (10)$$

Note that the case of  $n=-1$  is singular in the inverse transformation from  $V$  to  $T$ . This singularity results from the mathematical definition of the pseudotemperature  $V$  in Eqs. (8) and (9). It has no special physical significance and will be omitted in the following discussions. For the new variable  $V$  in the transformed space, the energy Eq. (5) becomes Laplacian

$$\nabla^2 V=0. \quad (11)$$

The boundary conditions (6) and (7), on the other hand, are transformed to

$$V=0 \quad \text{at} \quad \theta=\pi, \quad (12)$$

and

$$V_{,\theta}=0 \quad \text{at} \quad \theta=0. \quad (13)$$

Under the transformation defined by Eq. (10), Eqs. (12) and (13) are only applicable for the case with  $(n+1)$  being greater than zero, i.e.,  $n>-1$ . For the cases with  $n<-1$ , a zero temperature specified at the crack surfaces ( $T=0$ ) results in  $V$  having the value infinity. The need for a different approach is thus evident. In this section, therefore, we restrict our discussions to the case with  $n>-1$ .

In the transformed space  $V$ , Eqs. (11)–(13) are identical to those in the crack problem with a homogeneous and isotropic thermal conductivity (Tzou, 1991b). The equidimensionality in  $r$  of the Laplace equation allows the following form for  $V$ :

$$V(r, \theta)=\sum_{m=0}^{\infty} C_{1m} r^{\lambda_{m+1}} F_m(\theta). \quad (14)$$

By substituting Eq. (14) into Eqs. (11)–(13), a second-order ordinary differential equation for  $F_m$  results. Along with the homogeneous boundary conditions at  $\theta=0$  and  $\pi$ ,

$$F_{m,\theta}(0)=0 \quad \text{and} \quad F_m(\pi)=0, \quad (15)$$

the formulation thus renders an eigenvalue problem to be solved for  $\lambda_m$ . With all the details provided in the previous work (Tzou, 1991b), the results for eigenvalues are

$$\lambda_m=(m-2)/2 \quad \text{with} \quad m=0, 1, 2, \dots \quad (16)$$

Substituting Eq. (16) into Eq. (14), the asymptotic form for  $V(r, \theta)$  in the neighborhood of the crack tip is obtained:

$$V(r, \theta)=C_{11}\sqrt{r} \cos(\theta/2)+C_{12}r \sin(\theta/2)+C_{13}r^{3/2} \cos(3\theta/2)+\dots \quad (17)$$

The real temperature  $T$  thus results from substituting Eq. (17) into the inverse transformation (10). In the near-tip region with  $r$  approaching zero, the second term and thereafter in Eq. (17) will approach zero at a faster rate than the first term. This is evident by considering the limit of  $r^{j+1/2}/r^j \rightarrow 0$  as  $r \rightarrow 0$ . When closely approaching the crack tip, therefore, the near-tip temperature is proportional to  $\sqrt{r}$ . The temperature gradient  $T_{,r}$  can be obtained by direct differentiations:

$$T_{,r}=\left\{\frac{C_{11}^{1/(n+1)}}{2}\left(\frac{1}{n+1}\right)\left(\frac{n+1}{A}\right)^{-n/(n+1)}\right\}r^{-(2n+1)/2(n+1)}\times \cos^{-n/(n+1)}(\theta/2)-C_{11}^{-n/(n+1)}C_{12}\left[\left(\frac{n}{n+1}\right)^2\left(\frac{n+1}{A}\right)^{-n/(n+1)}+1\right]r^{-n/2(n+1)}\times \cos^{-n/(n+1)}(\theta/2)\sin(\theta/2)+O(r^{-n/2(n+1)}). \quad (18)$$

By the same ratio test,

$$\lim_{r \rightarrow 0} r^{-n/2(n+1)}/r^{-(2n+1)/2(n+1)}=\lim_{r \rightarrow 0} r^{1/2} \rightarrow 0, \quad (19)$$

we observe that the first term in Eq. (18) again dominates over the entire series. The temperature gradient in the near-tip region is therefore

$$T_{,r} \sim r^{-(2n+1)/2(n+1)} \cos^{-n/(n+1)}(\theta/2), \quad \text{for} \quad r \rightarrow 0. \quad (20)$$

For the thermal conductivity varying as a function of temperature according to Eq. (8), in summary, the temperature and its gradient in the near-tip region are, respectively,

$$T \sim r^{1/2(n+1)} \quad \text{and} \quad T_{,r} \sim r^{-(2n+1)/2(n+1)}, \quad \text{with} \quad n+1>0 \quad (21)$$

At the crack tip with  $r$  approaching zero, the temperature is bounded. It approaches zero as prescribed by the boundary condition. For the case with  $(n+1)>0$  and  $(2n+1)<0$ , i.e.,  $-1<n<-1/2$ , the temperature gradient vanishes at the crack tip ( $T_{,r}=0$  at  $r=0$ ). For a Fourier solid, the zero temperature gradient also implies diminution of the heat flux toward the crack tip. Although an abrupt change of geometric curvature still persists at the crack tip, the thermal energy could sufficiently dissipate into the surrounding media due to the strong effects from the thermal conductivity. For the case with  $n>-1/2$ , the temperature gradient presents a singularity at the crack tip. The power of singularity is  $(2n+1)/2(n+1)$ . The heat flux component in the  $r$  direction ( $q_r$ ) intensifies at the same rate toward the crack tip. As the value of  $n$  approaches zero, refer to Eq. (8), the thermal conductivity reduces to a constant. The power of singularity being  $1/2$  for homogeneous solids is thus retrieved (Tzou, 1991b). In the limiting case with  $n$  approaching infinity, the power of singularity approaches a limit value of 1. This result is shown graphically in Fig. 2. As a comparison, the eigenfunctions ( $\cos^{-n/(n+1)}(\theta/2)$ ) for typical values of  $n=-0.5$ ,  $-0.6$ , and  $-0.7$  are displayed in Fig. 3.

In the near-tip region, at this stage, influence of a temperature-dependent thermal conductivity on the singular behavior of the temperature gradient is clear. In passing to the effect of material inhomogeneity, however, we should notice that the case (a) introduced here is mainly for illustrating the asymptotic analysis. Not only is the functional form of  $k(T)$  assumed in Eq. (8) somewhat trivial, but some paradoxes also exist in this oversimplified model. The case of  $-1<n<-1/2$  for which the temperature gradient vanishes at the crack tip, for example, depicts a thermal conductivity decreasing with temperature.

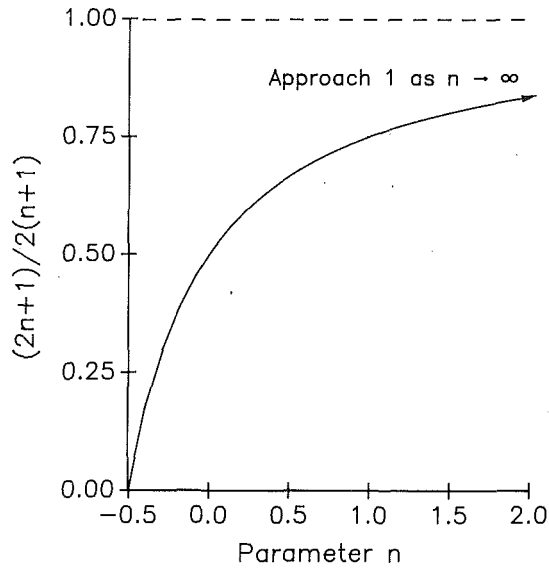


Fig. 2 The power of singularity  $p$  varying as a function of the material parameter  $n$ ; Eq. (23) for temperature-dependent thermal conductivity

In reality, this unusual behavior only exists in a very narrow range of temperature prior to melting. It has little value for engineering materials operated under normal conditions.

**(b) Nonhomogeneous Thermal Conductivity.** Thermal conductivity can also vary from one location to another in a thermal field. A typical example is the refined structure of the second-phase constituents in composites. For this type of material, the orientations and distributions of the second phased constituents dictate the local distribution of the thermal conductivity. Especially in a crisis situation where a crack is unavoidably initiated, a detailed understanding on the local distribution of the thermal energy around the crack tip is very useful in preventing the crack from growing. This knowledge not only provides an assessment for the postdamage performance of the structure in dissipating heat but also reveals the most efficient way to repair the crack.

The effects of nonhomogeneous thermal conductivity can be better understood by separately considering the variations in the radial and the angular directions. For a directional response in the radiation ( $r$ ) direction, a power-law type of variation

$$k(r) = Ar^n \quad (22)$$

could be used to model the thermal conductivity. The purpose, then, is to determine the physical domain of parameter  $n$  in which the singularity of the temperature gradient  $T_r$  vanishes at the crack tip. Substituting Eq. (22) into Eq. (5), the energy equation reduces to

$$\nabla^2 T + (n/r)T_r = 0. \quad (23)$$

Similarly, the polar coordinate system centered at the crack tip is used. The coefficient  $A$  in Eq. (22) has been eliminated in Eq. (23). As a result, it does not have any influence on the near-tip behavior. Assuming the same product form as Eq. (14) for temperature  $T$ , we observe that Eq. (23) is again equidimensional in  $r$ . The equation governing the angular distribution of  $F_m(\theta)$ , however, becomes

$$F_{m,\theta\theta} + [\lambda_m^2 + (2+n)\lambda_m + (n+1)]F_m = 0. \quad (24)$$

For  $n=0$ , the thermal conductivity reduces to a constant and Eq. (24) reduces to the form for solids with a homogeneous and isotropic thermal conductivity (Tzou, 1991b). The boundary conditions remain the same, as given by Eq. (15). The eigenvalue problem thus formulated, i.e., Eqs. (15) and (24), possesses an analytical solution:

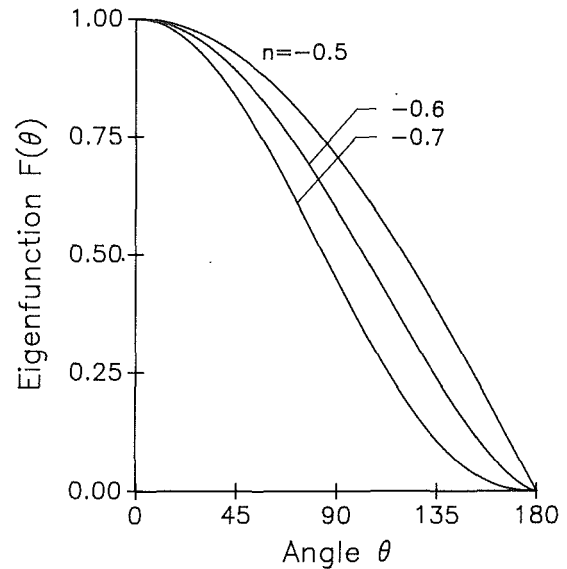


Fig. 3 The eigenfunctions  $\cos^{-n/(n+1)}(\theta/2)$  of the near-tip temperature for the cases with temperature-dependent thermal conductivity: the cases for  $n=0$  (homogeneous solid), 1, and 2

$$F_m(\theta) = C_{1m} \cos(\beta_m \theta), \quad (25)$$

with  $\beta_m = (2m+1)/2$  and  $m$  being all positive integers.

In relation to the eigenvalues  $\lambda_m$ , the coefficients  $\beta_m$  can be found as

$$\lambda_m = \left\{ -(2+n) + \sqrt{(2+n)^2 - 4[(n+1) - \beta_m^2]} \right\} / 2. \quad (26)$$

For  $n=0$ , the case with a homogeneous thermal conductivity, the lowest eigenvalue  $\lambda_0$  with  $m=0$  is  $-1/2$ . The power of singularity of temperature gradient being half ( $1/2$ ) is again retrieved. Superposition for all the eigenmodes of temperature then yields:

$$T(r, \theta) = \sum_{m=0}^{\infty} r^{\lambda_m+1} F_m(\theta) = C_{10} r^{\lambda_0+1} \cos(\theta/2) + C_{11} r^{\lambda_1+1} \cos(3\theta/2) + C_{12} r^{\lambda_2+1} \cos(5\theta/2) + \dots \quad (27)$$

The temperature gradient in the  $r$  direction, consequently, is

$$T_{,r} = C_{10}(\lambda_0+1)r^{\lambda_0} \cos(\theta/2) + C_{11}(\lambda_1+1)r^{\lambda_1} \cos(3\theta/2) + C_{12}(\lambda_2+1)r^{\lambda_2} \cos(5\theta/2) + \dots \quad (28)$$

with all the eigenvalues  $\lambda_m$  defined in Eq. (26). Two features are observed immediately: (i)  $\lambda_0+1$  is positive definite and (ii)  $\lambda_m < \lambda_{m+1}$ . The first condition leads to a zero temperature at  $r=0$  as required by the boundary condition at the crack surface. The second condition results in a ratio of

$$\lim_{r \rightarrow 0} \frac{r^{\lambda_{m+1}+1}}{r^{\lambda_m+1}} \rightarrow 0 \quad \text{as } r \rightarrow 0 \quad \text{for all the values of } m, \quad (29)$$

for determining the dominant terms in Eqs. (27) and (28). When approaching the crack tip at  $r=0$ , Eq. (29) implies that the first terms in Eqs. (27) and (28) dominate over the entire series. The asymptotic expressions for the near-tip temperature and its gradient, therefore, are

$$T(r, \theta) \sim C_{10} r^{\lambda_0+1} \cos(\theta/2), \quad \text{and}$$

$$T_{,r} \sim C_{10}(\lambda_0+1)r^{\lambda_0} \cos(\theta/2) \quad \text{as } r \rightarrow 0 \quad (30)$$

where  $\lambda_0$  has a value of  $[(n^2+1)^{1/2} - (n+2)]/2$  according to Eq. (26).

Again, the lowest eigenvalue  $\lambda_0$  depicts the singular behavior of the temperature gradient in the near-tip region. For  $\lambda_0 < 0$  or equivalently,



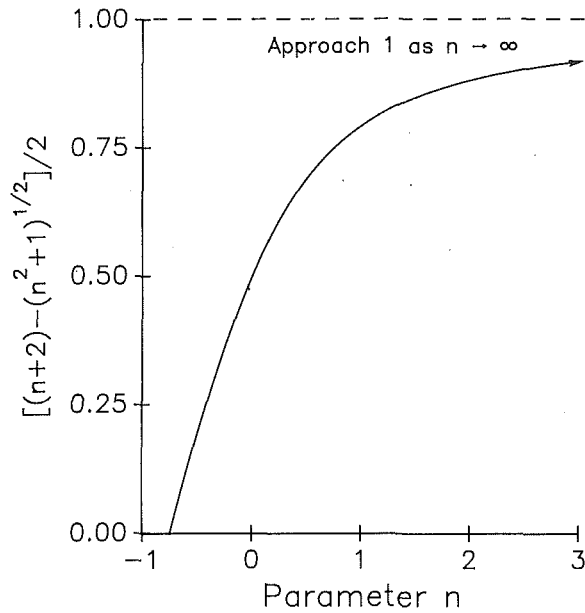


Fig. 4 The power of singularity  $-\lambda$  varying as a function of the material parameter  $n$ ; the case for nonhomogeneous thermal conductivity (Eq. (24)) and  $-\lambda = [(n+2) - (n^2+1)^{1/2}]/2$

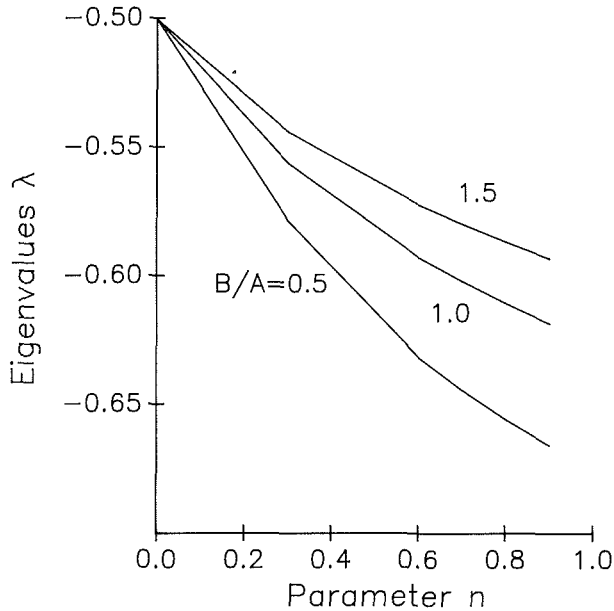


Fig. 5 The power of singularity  $-\lambda$  varying as a function of the material parameter  $n$ ; nonhomogeneous model of Eq. (35) with  $B/A = 0.5, 1.0,$  and  $1.5$

$$n > -3/4, \quad (31)$$

the temperature gradient is singular at the crack tip and the power of singularity is  $-\lambda_0 = [(n+2) - (n^2+1)^{1/2}]/2$ . Graphically, this condition is presented in Fig. 4. For  $n=0$ , the power of singularity being half (1/2) for homogeneous solids is retrieved. For  $n < -3/4$ , on the other hand, the temperature gradient vanishes at the crack tip. The thermal energy in this case efficiently dissipates into the surrounding elements before the geometric singularity at the crack tip comes into effect.

For the thermal conductivity varying in the angular direction, the asymptotic analysis can be applied in a parallel manner. Assuming an even function of  $k(\theta)$  about the axis of  $\theta=0$ ,

$$k(\theta) = A [\cos^n(\theta) + B/A], \quad (32)$$

the symmetric boundary condition in Eq. (15) still holds. The

Table 1 The lowest eigenvalue  $\lambda_0$  obtained by adopting four and ten nodes inside the field

| $n$ values  | $\lambda_0$ for four nodes | $\lambda_0$ for ten nodes |
|-------------|----------------------------|---------------------------|
| $B/A = 0.5$ |                            |                           |
| 0.          | -0.5021                    | -0.5006                   |
| 0.3         | -0.5742                    | -0.5788                   |
| 0.6         | -0.6294                    | -0.6315                   |
| 0.7         | -0.6440                    | -0.6444                   |
| 0.8         | -0.6569                    | -0.6557                   |
| 0.9         | -0.6684                    | -0.6659                   |
| $B/A = 1.0$ |                            |                           |
| 0.          | -0.5021                    | -0.5006                   |
| 0.3         | -0.5542                    | -0.5564                   |
| 0.6         | -0.5922                    | -0.5928                   |
| 0.7         | -0.6024                    | -0.6022                   |
| 0.8         | -0.6116                    | -0.6107                   |
| 0.9         | -0.6200                    | -0.6185                   |
| $B/A = 1.5$ |                            |                           |
| 0.          | -0.5021                    | -0.5006                   |
| 0.3         | -0.5430                    | -0.5442                   |
| 0.6         | -0.5724                    | -0.5725                   |
| 0.7         | -0.5804                    | -0.5799                   |
| 0.8         | -0.5877                    | -0.5868                   |
| 0.9         | -0.5945                    | -0.5933                   |

coefficient  $B$  is introduced here to scale the reference value of thermal conductivity at  $\theta=90$  deg. Now substituting Eq. (32) into Eq. (5), the energy equation becomes

$$\nabla^2 T(r, \theta) - (1/r^2) [An \cos^{n-1} \theta \sin \theta / (A \cos^n \theta + B)] T_{,\theta} = 0. \quad (33)$$

Assuming the same product form as Eq. (27), the eigenfunction  $F_m(\theta)$  in this case is governed by

$$F_{m,\theta\theta} - g(\theta) F_{m,\theta} + (\lambda_m + 1)^2 F_m = 0, \quad \text{with}$$

$$g(\theta) = n \cos^{n-1} \theta \sin \theta / (\cos^n \theta + B/A). \quad (34)$$

In addition to the parameter  $n$ , the eigenvalue problem for the present case also depends on the ratio of  $B/A$ . Along with the homogeneous boundary conditions (15), Eq. (34) is to be solved for the eigenvalues  $\lambda_m$ . Equation (34) is an ordinary differential equation with complicated variable coefficients. Numerical methods such as finite difference approximations are necessary for this case. For the  $j$ th node discretizing the functional space  $F_m$ , the central difference form of Eq. (34) is

$$[1/(\Delta\theta)^2 + g(\theta_j)/(2\Delta\theta)] F_{m,j-1} + [(\lambda_m + 1)^2 - 2/(\Delta\theta)^2] F_{m,j} + [1/(\Delta\theta)^2 - g(\theta_j)/(2\Delta\theta)] F_{m,j+1} = 0. \quad (35)$$

By incorporating the boundary conditions at the ends of  $\theta=0$  and  $\pi$ , Eq. (35) essentially leads to a determinant

$$|A_{ij}(\lambda_m; \Delta\theta, \theta_j, n)| = 0 \quad \text{for } i, j = 1, 2, 3, \dots, N \quad (36)$$

for nontrivial solutions. Based on selected values of the angular increment  $\Delta\theta$  and the parameter  $n$  in the thermal conductivity, obviously, the eigenvalue  $\lambda_m$  depends on the nodal number  $N$  discretizing the field. Similar to the previous cases, the lowest eigenvalue  $\lambda_0$  dominates the singular behavior of the temperature gradient at the crack tip. With reference to Eqs. (21) and (28), the value of  $-\lambda_0$  is actually the desired power of singularity.

For the present example with a smoothly varying thermal conductivity, Eq. (32), fast convergence for  $\lambda_0$  is achieved by using only four nodes ( $N=4$ ). Reliable solutions for the corresponding eigenfunctions  $F_\theta(\theta)$ , however, are obtained by employing 18 nodes. Table 1 summarizes the results of eigenvalues obtained by using four and ten nodes inside the field. For various values of  $B/A$ , variations of  $\lambda_0$  to the parameter  $n$  are shown in Fig. 5. The power of singularity ( $-\lambda_0$ ) increases when the value of  $n$  increases. At the same value of  $n$ , on the other hand, the power of singularity increases when the ratio of  $B/A$  decreases. When the value of  $n$  approaches zero (0), the thermal conductivity becomes homogeneous and the result of

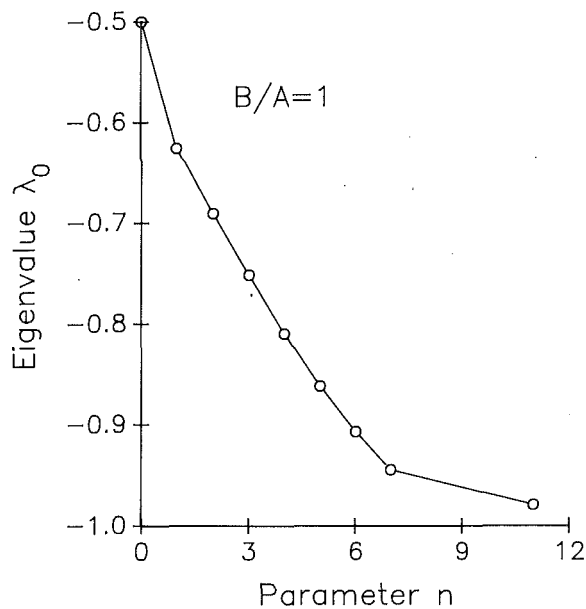


Fig. 6 Asymptotic variation of the power of singularity ( $-\lambda_0$ ) versus the parameter  $n$  in Eq. (22);  $B/A = 1$

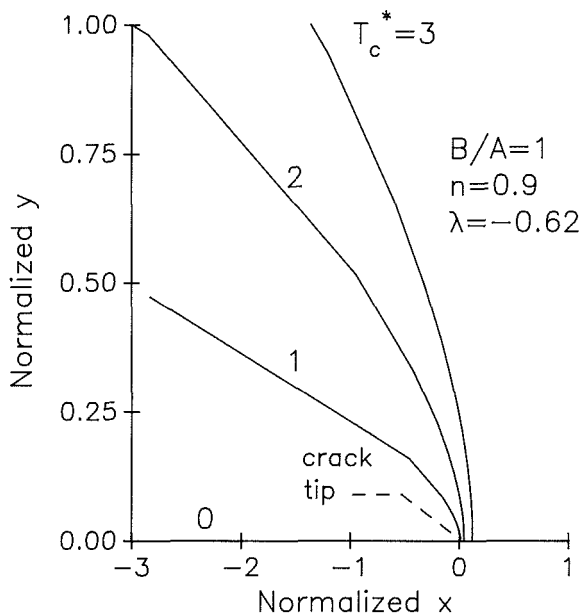


Fig. 7 Temperature contours in the neighborhood of the crack tip; homogeneous model of Eq. (35) with  $B/A = 1$  and  $n = 0$

$-\lambda_0$  being half (1/2) is retrieved for all the cases. When the value of  $n$  continuously increases, the power of singularity approaches a limit value of one (1). For a typical situation with  $B/A = 1$ , Fig. 6 shows this asymptotic behavior in the domain of  $n$  from 0 to 12. For the nonhomogeneous thermal conductivity shown by Eq. (32), therefore, a singularity in the temperature gradient  $T_r$  always exists at the crack tip.

For the present case, the temperature and its gradient are characterized by the lowest mode of eigenfunctions

$$T(r, \theta) = C_1 r^{\lambda_0 + 1} F_0(\theta), \quad T_r = C_1 (\lambda_0 + 1) r^{\lambda_0} F_0(\theta) \quad \text{for } r \rightarrow 0. \quad (37)$$

Such asymptotic forms also facilitate the representations by the contour patterns in the near-tip region. By slight rearrangements, we have

$$r = [T_c^*/F_0(\theta)]^{1/(\lambda_0 + 1)} \quad \text{for temperature and} \quad (38)$$

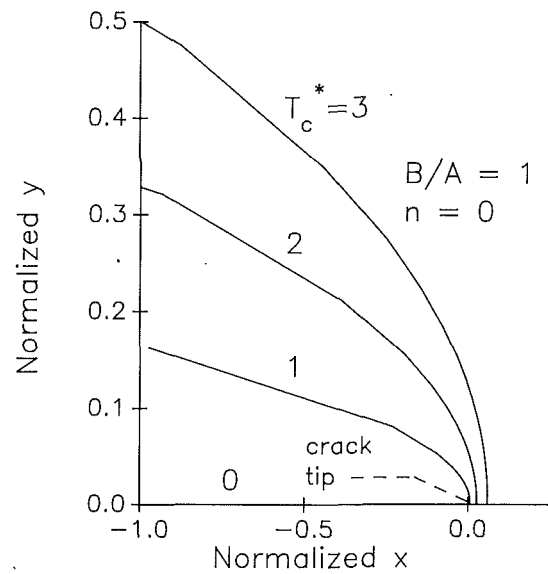


Fig. 8 Temperature contours in the neighborhood of the crack tip; nonhomogeneous model of Eq. (35) with  $B/A = 1$  and  $n = 0.9$  ( $\lambda \approx -0.62$ )

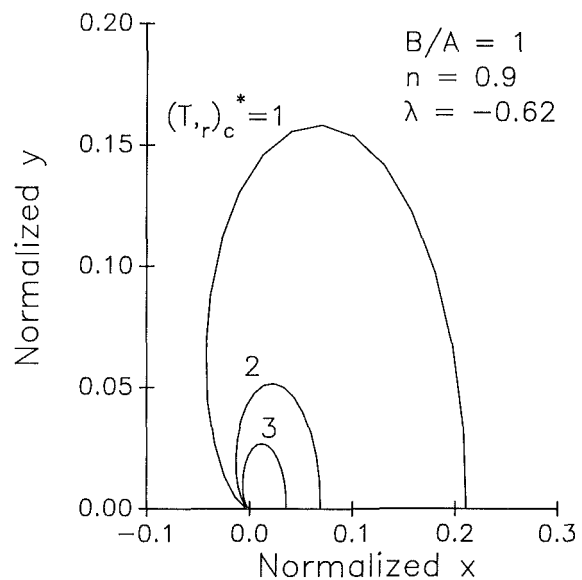


Fig. 9 Contours of temperature gradient  $T_r$  in the neighborhood of the crack tip; nonhomogeneous model of Eq. (35) with  $B/A = 1$  and  $n = 0.9$  ( $\lambda \approx -0.62$ )

$$r = [(\lambda_0 + 1)F_0(\theta)/(T_r)_c^*]^{1/|\lambda_0|} \quad \text{for temperature gradient.} \quad (39)$$

The quantities  $T_c^*$  and  $(T_r)_c^*$  in these equations are normalized with respect to the amplitude  $C_1$  of the eigenfunction and the crack length. Also, in Eq. (39), we have reciprocated the ratio to account for the nature of eigenvalues  $\lambda_0$  being always negative. For  $B/A = 1$ , Figs. 7 and 8 display the temperature contour patterns in the neighborhood of the crack tip for  $n = 0$  (homogeneous model) and 0.9. Due to symmetry of the problem, only the contour patterns in the upper-half plane need to be presented. The crack tip is at the position of (0, 0). The corresponding eigenvalues  $\lambda_0$  for  $n = 0$  and 0.9 are respectively  $-0.5$  and  $-0.62$ . For both cases, the temperature increases in the direction away from the crack surface. For the case with  $B/A = 1$  and  $n = 0.9$  ( $\lambda \approx -0.62$ ), the contour patterns of temperature gradient are shown in Fig. 9. Unlike the temperature contours, the isochromatic line of  $T_r$  forms closed loops in the vicinity of the crack tip. The intensity of the temperature

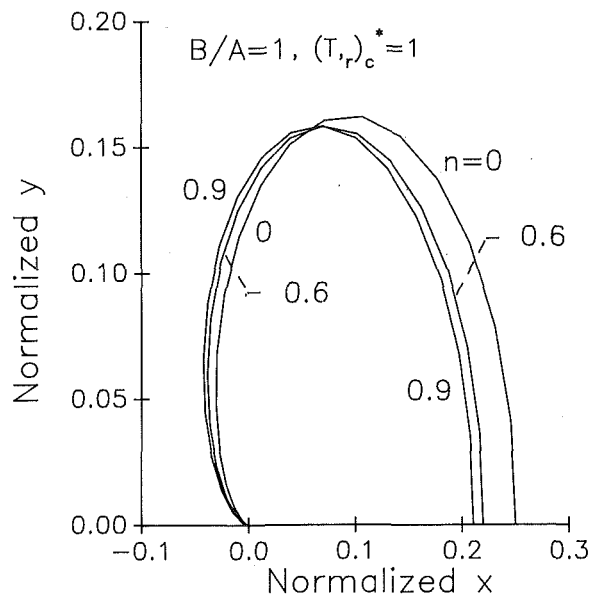


Fig. 10 Contours of temperature gradient  $T_r$  in the neighborhood of the crack tip; the effect of parameter  $n$  in Eq. (35)

gradient increases toward the crack tip and the localization of thermal energy is clear. Under the same value of  $(T_r)_c^* = 1$ , Figs. 10 and 11 show the effects of parameter  $n$  and conductivity ratio  $B/A$  on the contour patterns of  $T_r$ . Though insignificant, the isochromatic line of  $T_r$  shifts toward the crack surfaces as the value of  $n$  or  $B/A$  increases.

In case (a) where the thermal conductivity varies in the  $r$  direction, singularity of the temperature gradient at the crack tip sometimes can be eliminated. In case (b) where the thermal conductivity varies in the  $\theta$  direction, however, singularity in the temperature gradient always exists. With regard to avoiding the localization of thermal energy at the crack tip, therefore, a detailed control on the thermal conductivity varying in the  $r$  direction is more efficient. This result makes physical sense because the singular behavior only occurs in the  $r$  direction of the temperature gradient,  $T_r$ .

## Conclusion

Due to the abrupt change of geometric curvature at the crack tip, the temperature gradient usually presents a  $1/\sqrt{r}$ -type singularity. The presence of singularity in temperature gradient implies localization of thermal energy in heat conduction. This situation should be avoided for structures or devices designed primarily for dissipating heat. Localization of thermal energy in a structure would significantly degrade the overall performance in heat conduction. More seriously, it may induce excessive amounts of thermal stresses and promote catastrophic failure of the entire structure by thermal cracking. Associated with the aged use of structural components, obviously, an efficient way to control the energy localization is necessary.

This work has shown that the thermal conductivity is an important physical factor for dissipating the thermal energy accumulated at the crack tip. For example, the thermal conductivity varying in the  $r$  direction may eliminate the localization of thermal energy at the crack tip. The threshold value of  $n \approx -3/4$  in Eq. (22) further provides a specific way to repair the crack. Most importantly, it depicts that the patching material should be implemented in the radial direction of the crack tip. The thermal conductivity, moreover, should have a diminishing rate smaller than  $-3/4$  versus the radial distance. For aged devices used in an environment requiring controls with high accuracy, such specific knowledge is necessary to recover the heat transfer performance. For various models

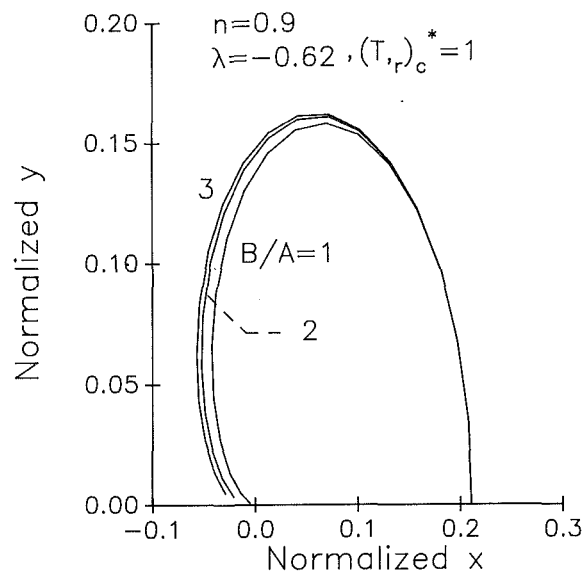


Fig. 11 Contours of temperature gradient  $T_r$  in the neighborhood of the crack tip; effect of conductivity ratio  $B/A$  in Eq. (35)

Table 2 Summary on the effect of thermal conductivity on the singular behavior of the near-tip temperature gradient

| Type of thermal conductivity                     | The physical domain in which singularity diminishes |
|--|---|
| Orthotropic                                      | $k_\theta > 4 k_r$ , Tzou (1990b)                   |
| Temperature-dependent<br>$k(T) = AT^n$           | $-1 < n < -1/2$ , Eq. (21)                          |
| Nonhomogeneous<br>$k(r) = Ar^n$                  | $n < -3/4$ , Eq. (31)                               |
| Nonhomogeneous<br>$k(\theta) = A \cos^n(\theta)$ | None  |

considered so far, Table 2 summarizes the effect of thermal conductivity on the diminution of the temperature gradient. In the near-tip region with  $r$  approaching zero, these results can also be extended to transient problems. As indicated before, the time-dependent behavior only influences the magnitude of the IFTG while the power of singularity remains the same (Tzou, 1990).

Engineering problems in reality usually involve much more complicated situations than those considered in this work. The finite element method is a popular approach for solving the problems with practical interest. In conjunction with this powerful method, the asymptotic solutions obtained in this work can be used to improve the accuracy and efficiency of the numerical algorithms. Conventionally, due to the presence of a singularity in the temperature gradient, a convergent mesh involving a lot of elements is needed to catch the rapid change toward the crack tip. The node-shifting technique (Tzou, 1991a), however, can implement the desired power of singularity by shifting the intermediate nodes to particular locations on the element edge. Such particular locations depend on the elements used in the analysis. For eight-node quadrilateral elements, for example, the particular location to implement a  $1/\sqrt{r}$  singularity of the temperature gradient is at the quarter (1/4) position toward the crack tip. For 12-node quadrilateral elements, on the other hand, the particular locations are at the 1/9 and 4/9 positions of the element edge. Under the same grid pattern used in the discretization, the node-shifting technique has shown to highly improve the accuracy of the near-tip solutions (Tzou, 1991a). For solids with a nonhomogeneous or an orthotropic thermal conductivity, the power of singularity depends on the physical parameters; refer to Table 2. The intermediate nodes, therefore, have to be re-allocated to

implement the required power of singularity. Generally speaking, the particular positions for these nodes also depend on the physical parameters involved in a special type of thermal conductivity.

## References

- Ames, W. F., 1965, *Nonlinear Partial Differential Equations in Engineering*, Chap. 2, Academic Press, New York.
- Florence, A. L., and Goodier, J. N., 1960, "Thermal Stresses Due to Disturbance of Uniform Heat Flow by an Insulated Ovaloid Hole," *ASME JOURNAL OF HEAT TRANSFER*, Vol. 82, pp. 635-639.
- Florence, A. L., and Goodier, J. N., 1963, "The Linear Thermoelastic Problem of Uniform Heat Flow Disturbed by a Penny-Shaped Insulated Crack," *International Journal of Engineering Science*, Vol. 111, pp. 533-540.
- Hildebrand, F. B., 1974, *Advanced Calculus for Applications*, Prentice-Hall, Englewood Cliffs, NJ, pp. 200-206.
- Kassir, M. K., 1971, "Thermal Crack Propagation," *ASME Journal of Basic Engineering*, Vol. 94, pp. 643-648.
- Loeb, A. L., 1954, "Thermal Conductivity: VIII, A Theory of Thermal Conductivity of Porous Materials," *Journal of American Ceramic Society*, Vol. 37, pp. 96-99.
- Morse, M., and Feshbach, H., 1953, *Methods of Theoretical Physics*, Vol. 1, McGraw-Hill, New York, pp. 978-985.
- Sih, G. C., 1965, "Heat Conduction in the Infinite Medium With Lines of Discontinuities," *ASME JOURNAL OF HEAT TRANSFER*, Vol. 87, pp. 293-297.
- Tzou, D. Y., 1985, "Intensification of Externally Applied Magnetic Field Around a Crack in Layered Composite," *Journal of Theoretical and Applied Fracture Mechanics*, Vol. 4, pp. 191-199.
- Tzou, D. Y., and Chen, E. P., 1990, "Overall Degradation of Conductive Solids With Mesocracks," *International Journal of Heat and Mass Transfer*, Vol. 33, pp. 2173-2182.
- Tzou, D. Y., 1990, "Thermal Shock Waves Induced by a Moving Crack," *ASME JOURNAL OF HEAT TRANSFER*, Vol. 112, pp. 21-27.
- Tzou, D. Y., 1991a, "On the Use of Node-Shifting Techniques for the Intensity Factor of Temperature Gradient at a Macrocrack Tip," *Numerical Heat Transfer*, Vol. 19(A), pp. 237-253.
- Tzou, D. Y., 1991b, "The Singular Behavior of the Temperature Gradient in the Vicinity of a Macrocrack Tip," *International Journal of Heat and Mass Transfer*, Vol. 33, pp. 2625-2630.
- Tzou, D. Y., 1991c, "The Effect of Internal Heat Transfer in Cavities on the Overall Thermal Conductivity," *International Journal of Heat and Mass Transfer*, Vol. 34, pp. 1839-1846.

B. T. F. Chung  
Professor.  
Fellow ASME

B. X. Zhang  
Graduate Assistant.  
Student Mem. ASME

Department of Mechanical Engineering,  
The University of Akron,  
Akron, OH 44325-3903

# Optimization of Radiating Fin Array Including Mutual Irradiations Between Radiator Elements

*The present study develops a new approach to minimize the weight of a radiating straight fin array so that the whole system of the fin array is optimized by minimizing the weight of the individual fin, which is subjected to radiation interaction with adjacent fins and base. The obtained system has the minimum weight possible, and also yields the best shape of the individual fins for a given total heat dissipation and uniform base temperature. Based on the present analysis, the optimum number of fins in a fin array is obtained.*

## Introduction

Radiating fins play an important role in thermal control of space vehicles and satellites. Since the weight and material cost are the major design considerations in heat exchangers, it is highly desirable to obtain an optimum design with respect to fin mass. As a consequence, minimization of individual fin mass has been the research topic of numerous investigators, e.g., Duffin (1959), Liu, (1962), Amadi and Razani (1973), Wilkins (1974), Maday (1974), Dhar and Arora (1976), Mikk (1980), Razelos and Imre (1983), etc. Relatively, a few authors dealt with minimization of the mass of a radiative fin array for which the mutual irradiation between fin-to-fin and fin-to-base should be taken into consideration. The only papers involving optimization of radiating fin array are those of Karlekar and Chao (1963) and Schnurr et al. (1976). Karlekar and Chao (1963) considered the trapezoidal fins with both rectangular and triangular fins as two limiting cases. However, the authors neglected fin-to-base interaction in their analysis. Schnurr et al. (1976) assumed that the emissivities of the primary surface and the extended surface are identical; furthermore, their results were restricted to the radiative fins of rectangular and triangular profiles only. A combined approach using the Fletcher-Reeves conjugate gradient method followed by a Hooke-Jeeves direct search was employed by Schnurr et al. (1976) to determine the optimum dimensions for either rectangular or triangular shape. Strictly speaking, none of the above profiles will yield a minimum mass; the optimum shape of the fin depends on the thermal properties, the environmental temperature, and the total dissipation from the base.

The purpose of the present work is to develop a totally different optimization approach as employed by Schnurr et al. (1976) to determine the minimum weight or mass of radiating straight fin array extending from a pipe.

## Analysis

Consideration hereby is given to a radiating fin array system for a unit axial length of cylinder as illustrated in Fig. 1. We wish to find the total minimum fin mass, optimum fin shape, and optimum number of fins of the system for a specified base temperature and a given amount of total heat dissipation,  $Q_o$ , of the system.

The present analysis is based on the following assumptions: (1) Steady state holds; (2) the temperature distribution in the fin is one dimensional, i.e., the fin is thin enough and the length of the fins along the axis of the base cylinder is much

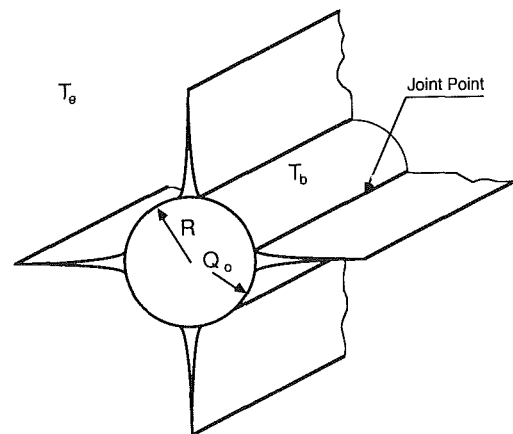


Fig. 1 Sketch of a fin array

larger than any other length dimension of the system; (3) no heat is transferred at the fin tip; (4) the pipe surface is isothermal (in reality, the fin acts like a heat sink and would normally depress its base temperature); (5) the fin thickness at the base is small as compared to the spacing between the adjacent fins; (6) the gray body assumption holds for all surfaces of fins and base; (7) the length of arc assumption applies, i.e., the curvature effect is neglected in deriving the energy equation ( $ds$  is replaced by  $dx$ ); (8) all the fins are identical in shape and dimensions and are equally spaced.

The optimization procedure includes two steps: First we optimize the system for a given arbitrary number of fins  $N$ ; second we determine an optimum number of fins,  $N_{opt}$ , that yields the minimum mass of the system. Essentially, the idea of our previous work (Chung and Zhang, 1991) is extended here to optimize the whole system of the fin array. In the case of fin array, as shown in Fig. 2, each fin is subjected to the radiative interaction with the base, the adjacent fins, and the space. Here  $q_o$ , the summation of the heat transferred by the fin and the base, is specified. Without loss of generality, we consider an arbitrary system consisting of a base and a single fin. The system is required to dissipate a total heat flow of  $q_o$ , which exceeds the dissipation capability of the base alone. Let  $q_b$  and  $q_{bs}$  represent the heat flow dissipated by the fin and the base, respectively; then we can write

$$q_o = q_b + q_{bs} \quad (1)$$

Besides Eq. (1), due to radiative interaction, another constraint must exist that determines the proportion between  $q_b$  and  $q_{bs}$ . This constraint may be symbolically expressed as

Contributed by the Heat Transfer Division for publication in the JOURNAL OF HEAT TRANSFER. Manuscript received by the Heat Transfer Division July 16, 1990; revision received March 7, 1991. Keywords: Finned Surfaces, Radiation, Radiation Interactions.

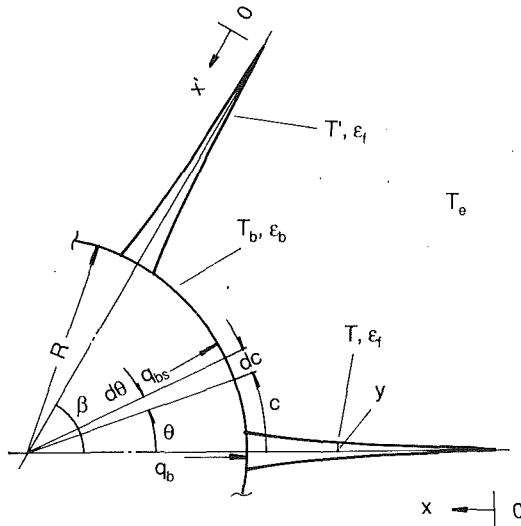


Fig. 2 Sketch of a portion of a fin array between two adjacent fins

$$F(q_{bs}) = 0 \quad (2)$$

Equation (2) is expressed more explicitly later by Eq. (26). The equations describing the heat transfer performance of the individual fin are

$$q(x) = 2k(T)y(x)\frac{dT}{dx} \quad (3)$$

$$dq = HdX \quad (4)$$

The associated boundary conditions are

$$q = 0 \quad \text{at } x = 0; \quad (5)$$

$$q = q_b, \quad T = T_b \quad \text{at } x = b \quad (6)$$

The fin profile area is given by

$$A_p = 2 \int_0^b y dx \quad (7)$$

Since the fin is involved in radiative heat exchange with the participating surfaces, the dissipation function,  $H$ , is both temperature and position dependent, i.e.,  $H = H(x, T)$ , which is known for any specified problem. Considering that  $T$  is a monotonic function of  $x$ , and  $x$  is a monotonic function of  $T$ , we can write  $H$  as  $H = H(x(T), T) = H(T)$ . Wilkins (1960) developed a similarity transformation that considerably simplifies the optimization procedure for an individual fin to dissipate the specified heat,  $q_b$ . To minimize the fin mass subjected to dissipating the total heat,  $q_o$ , from both of the fins and the base, we modify the transformation suggested by Wilkins (1960) as follows:

$$U(T) = \frac{1}{u_o} \int_{T^*}^T kH^2 dt \quad (8)$$

$$V = \left(\frac{q}{q_o}\right)^{3/2} \quad (9)$$

where  $V$  is a function of  $U$  only;  $T^*$  is defined as  $H(T^*) = 0$ ; and

$$u_o = \int_{T^*}^{T_b} kH^2 dT \quad (10)$$

Since no heat is transferred at  $x = 0$ , making the most efficient use of mass requires that the thickness of the fin at the tip be zero. As proved by Chung and Zhang (1991) and Wilkins (1960),  $T^*$  actually stands for the temperature at the fin tip. Thus, from Eqs. (3)–(10), the following relationships are obtained in terms of  $V$  and  $U$ :

$$dx = \frac{2}{3} q_o \frac{V^{-1/3}}{u_o} \frac{dV}{dU} kHdT \quad (11)$$

## Nomenclature

|   |  |   |
|---|--|---|
| $A_p$ = profile area of the individual fin, $m^2$                 | $k_b$ = conductivity at base temperature $T_b$ , $W/m \cdot K$                             | $T_b$ = base temperature, $K$                           |
| $A_{p_{min}}$ = minimum profile area of the individual fin, $m^2$ | $\bar{K} = K/K_b$  | $U, \bar{U}, \bar{U}_o$ = transformation variables      |
| $\bar{A} = A_{p_{min}} / (k_b / \sigma T_b^3)^2$                  | $N$ = number of fins in a fin array  | $u_o$ = transformation variables, $W^3/m^5$             |
| $\bar{A}_T = \bar{A} \cdot N$                                     | $N_{opt}$ = optimum number of fins in a fin array  | $V$ = transformation variable                           |
| $\bar{A}_{T_{opt}} = \bar{A} \cdot N_{opt}$                       | $q$ = local heat flow rate of individual fin, per unit axial length of the cylinder, $W/m$ | $x$ = coordinate of fin along length, $m$               |
| $b$ = length of fin, $m$  | $\bar{q} = q/q_b$  | $y$ = thickness of fin, $m$                             |
| $\bar{b} = b / (k_b / \sigma T_b^3)$                              | $q_b$ = net heat flow dissipated by one fin, $W/m$   | $\bar{X} = x / (k_b / \sigma T_b^3)$                    |
| $\bar{b}_R = \bar{b} / R$   | $q_{bs}$ = net heat flow dissipated by surface of base between two adjacent fins, $W/m$    | $\bar{X}_R = \bar{X} / R$                               |
| $c$ = coordinate of the base along the arc, $m$                   | $q_o = q_b + q_{bs}$ , $W/m$   | $\bar{Y} = y / (k_b / \sigma T_b^3)$                    |
| $\bar{C} = c / (k_b / \sigma T_b^3)$                              | $Q_o$ = total heat flow dissipated by fin array, $W/m$                                     | $\beta$ = angle between two adjacent fins               |
| $df_{dx-dc}$ = view factor from $dx$ to $dc$                      | $R$ = radius of base pipe, $m$   | $\gamma = q_b / (k_b T_b)$                              |
| $F_{dx-A_e}$ = view factor from $dx$ to space                     | $\bar{R} = r / (k_b / \sigma T_b^3)$   | $\gamma_{bs} = q_{bs} / (k_b T_b)$                      |
| $G$ = irradiation of fin, $W/m^2$                                 | $T$ = local temperature of fin, $K$  | $\bar{\gamma} = \gamma / R$                             |
| $G_b$ = irradiation of base, $W/m^2$                              | $T^*$ = temperature at tip of fin, $K$   | $\bar{\gamma}_{bs} = \gamma_{bs} / R$                   |
| $H$ = heat dissipation function, $W/m^2$                          | $T_e$ = environment temperature, $K$   | $\bar{\Gamma} = Q_o / (k_b T_b)$                        |
| $\bar{H} = H / (\sigma T_b^4)$                                    |  | $\bar{\Gamma} = \Gamma / R$                             |
| $J$ = radiosity of fin, $W/m^2$                                   |  | $\epsilon_f$ = emissivity of fin                        |
| $J_b$ = radiosity of base, $W/m^2$                                |  | $\epsilon_b$ = emissivity of base                       |
| $k$ = thermal conductivity, $W/m \cdot K$                         |  | $\theta$ = angular coordinate of pipe base              |
|   |  | $\xi = T/T_b$   |
|   |  | $\sigma$ = Stefan-Boltzmann constant, $W/m^2 \cdot K^4$ |
|   |  | $\phi = J / (\sigma T_b^4)$                             |

$$y = \frac{q_o^2}{3u_o} V^{1/3} H \frac{dV}{dU} \quad (12)$$

$$A_P = \frac{4q_o^3}{9u_o} \int_0^1 \left( \frac{dV}{dU} \right)^2 dU \quad (13)$$

From the fundamental theory of variational calculus, if a function  $V(U)$  is sought in order to minimize the intergral  $I$ ,  $I = \int_0^1 f(U, V, V') dU$ , it is equivalent to solve the Euler-Lagrange equation  $\partial f / \partial V - d(\partial f / \partial V') / dU = 0$  subject to the same boundary conditions. As can be seen in Eq. (13), the corresponding  $f$  is a function of only  $V'$ , i.e.,  $f(V') = V'^2$ . To minimize  $A_P$ , we apply the Euler-Lagrange equation mentioned above, which yield  $V = C_1 U + C_2$ . According to Eqs. (5), (6), and (8)–(10), the boundary conditions in terms of  $V$  and  $U$  are:  $V = 0$  at  $U = 0$ , and  $V = (q_b/q_o)^{3/2}$  at  $U = 1$ . Thus we obtain

$$V = \left( \frac{q_b}{q_o} \right)^{3/2} U \quad (14)$$

Substituting Eq. (14) into Eqs. (9) and (11)–(13), respectively, yields the optimum solutions

$$x = \frac{2q_b}{3u_o} \int_{T^*}^T k(T) H(x(T), T) U^{-1/3}(T) dT \quad (15)$$

$$y = \frac{q_b^2}{3u_o} U^{1/3} H \quad (16)$$

$$q = q_b U^{2/3} \quad (17)$$

$$A_{P_{\min}} = \frac{4q_b^3}{9u_o} \quad (18)$$

Equations (15)–(18) have exactly the same forms as the results from Chung and Zhang (1991). This implies that the best shape for the individual fin to dissipate the amount of heat  $q_b$  also represents the best shape of the individual fin for the whole system to dissipate the total amount of heat  $q_o$ . In our earlier work,  $q_b$  is given, while in the present case  $q_b$  has to be determined by Eqs. (1) and (2).

To apply the above results, we have to determine the dissipation function,  $H$ , the temperature of the fin tip,  $T^*$ , and the constraints of  $q_b$  and  $q_{bs}$ . From the local energy balance on the surfaces of the fin and the base, we can write

$$G = \sigma T_e^4 F_{dx-A_e} + \int_{f'} J' dF_{dx-dx'} + \int_b J_b dF_{dx-dc} \quad (19)$$

$$J = \epsilon_f \sigma T^4 + (1 - \epsilon_f) G \quad (20)$$

$$G_b = \sigma T_e^4 F_{dc-A_e} + \int_f J dF_{dc-dx} + \int_{f'} J' dF_{dc-dx'} \quad (21)$$

$$J_b = \epsilon_b \sigma T_b^4 + (1 - \epsilon_b) G_b \quad (22)$$

Solving Eqs. (19)–(22), and noting that  $H = 2(J - G)$ , we obtain the functions of  $H$  and  $J$ , respectively,

$$H[x(T), J(x(T), T), T] = 2\epsilon_f \left\{ \sigma T^4 - \sigma T_e^4 F_{dx-A_e} - \int_{f'} J' dF_{dx-dx'} - \int_b \left[ \epsilon_b \sigma T_b^4 + (1 - \epsilon_b) \left( \sigma T_e^4 F_{dc-A_e} + \int_f J dF_{dc-dx} + \int_{f'} J' dF_{dc-dx'} \right) \right] dF_{dx-dc} \right\} \quad (23)$$

$$J(x(T), T) = \epsilon_f \sigma T^4 + (1 - \epsilon_f) \left\{ \sigma T_e^4 F_{dx-A_e} + \int_{f'} J' dF_{dx-dx'} \right.$$

$$\left. + \int_b \left[ \epsilon_b \sigma T_b^4 + (1 - \epsilon_b) \left( \sigma T_e^4 F_{dc-A_e} + \int_f J dF_{dc-dx} + \int_{f'} J' dF_{dc-dx'} \right) \right] dF_{dx-dc} \right\} \quad (24)$$

In the above equations, the primes stand for “of the adjacent fin”;  $\int_b, \int_{f'}$  represents the integrations along the base between two fins, along the fin, and along the adjacent fin, respectively. Due to symmetry,  $J'$  is equal to  $J$  when  $x'$  and  $x$  have the same value. The associate view factors have been reported by Zhang (1990).

Setting  $H|_{x=0} = 0$  in Eq. (23) yields the temperature at the fin tip, which is necessary for evaluation of Eqs. (8), (10), and (15).

$$T^* = \left\{ T_e^4 F_{dx-A_e}|_{x=0} + \frac{1}{\sigma} \int_{f'} J' dF_{dx-dx'}|_{x=0} + \frac{1}{\sigma} \int_b \left[ \epsilon_b \sigma T_b^4 + (1 - \epsilon_b) \left( \sigma T_e^4 F_{dc-A_e} + \int_f J dF_{dc-dx} + \int_{f'} J' dF_{dc-dx'} \right) \right] dF_{dx-dc}|_{x=0} \right\}^{1/4} \quad (25)$$

The net heat transfer from the base surface between two fins is

$$q_{bs} = \int_b (J_b - G_b) dc = \int_b \epsilon_b \left( \sigma T_b^4 - \sigma T_e^4 F_{dc-A_e} - \int_f J dF_{dc-dx} - \int_{f'} J' dF_{dc-dx'} \right) dC \quad (26)$$

Equation (26) combining with the relation

$$Q_o = N(q_b + q_{bs}) \quad (27)$$

makes up the constraints that  $q_b$  and  $q_{bs}$  must satisfy.

Equations (8), (10), (15), and (23)–(27) can be written in the following dimensionless forms:

$$\bar{U}(\xi) = \frac{1}{\bar{U}_o} \int_{\xi^*}^{\xi} \bar{K}(\xi) \bar{H}^2(\bar{X}(\xi), \phi(\bar{X}(\xi), \xi), \xi) d\xi \quad (28)$$

$$\bar{U}_o = \int_{\xi^*}^1 \bar{K}(\xi) \bar{H}^2(\bar{X}(\xi), \phi(\bar{X}(\xi), \xi), \xi) d\xi \quad (29)$$

$$\bar{X}(\xi) = \frac{2\gamma}{3\bar{U}_o} \int_{\xi^*}^{\xi} \bar{K}(\xi) \bar{H}(\bar{X}(\xi), \phi(\bar{X}(\xi), \xi), \xi) \bar{U}^{-1/3} d\xi \quad (30)$$

$$\bar{H}(\bar{X}(\xi), \phi(\bar{X}(\xi), \xi), \xi) = 2\epsilon_f \left\{ \xi^4 - \xi_e^4 F_{d\bar{x}A_e} - \int_{f'} \phi' dF_{d\bar{x}-d\bar{x}'} - \int_b \left[ \epsilon_b + (1 - \epsilon_b) \left( \xi_e^4 F_{d\bar{c}-A_e} + \int_f \phi dF_{d\bar{c}-d\bar{x}} + \int_{f'} \phi' dF_{d\bar{c}-d\bar{x}'} \right) \right] dF_{d\bar{x}-d\bar{c}} \right\} \quad (31)$$

$$\phi(\bar{X}(\xi), \xi) = \epsilon_f \xi^4 + (1 - \epsilon_f) \left\{ \xi_e^4 F_{d\bar{x}-A_e} + \int_{f'} \phi' dF_{d\bar{x}-d\bar{x}'} + \int_b \left[ \epsilon_b + (1 - \epsilon_b) \left( \xi_e^4 F_{d\bar{c}-A_e} + \int_f \phi dF_{d\bar{c}-d\bar{x}} + \int_{f'} \phi' dF_{d\bar{c}-d\bar{x}'} \right) \right] dF_{d\bar{x}-d\bar{c}} \right\} \quad (32)$$

$$\xi^* = \left\{ \xi_e^4 F_{d\bar{x}-A_e} |_{\bar{x}=0} + \int_{f'} \phi' dF_{d\bar{x}-d\bar{x}'} |_{\bar{x}=0} + \int_b \left[ \epsilon_b + (1-\epsilon_b) \left( \xi_e^4 F_{d\bar{x}-A_e} + \int_{f'} \phi dF_{d\bar{c}-d\bar{x}} + \int_{f'} \phi' dF_{d\bar{c}-d\bar{x}'} \right) \right] \cdot dF_{d\bar{x}-d\bar{c}} |_{\bar{x}=0} \right\}^{1/4} \quad (33)$$

$$\gamma_{bs} = \int_b \epsilon_b \left( 1 - \xi_e^4 F_{d\bar{c}-A_e} - \int_{f'} \phi dF_{d\bar{c}-d\bar{x}} - \int_{f'} \phi' dF_{d\bar{c}-d\bar{x}'} \right) d\bar{c} \quad (34)$$

$$\Gamma = N(\gamma + \gamma_{bs}) \quad (35)$$

Equations (28)–(35) consist of a system of nonlinear integral equations, which yield the optimum individual fin of a fin array for any given number of fins,  $N$ . Once they are solved, the dimensionless minimum profile area,  $\bar{A}$ , can be obtained directly from

$$\bar{A} = \frac{4\gamma^3}{9\bar{U}_o} \quad (36)$$

and the total fin profile area,  $\bar{A}_T$ , is given by

$$\bar{A}_T = \frac{4\gamma^3}{9\bar{U}_o} N \quad (37)$$

By varying  $N$  from 3, 4, 5, ..., the minimum value of  $\bar{A}_T$ ,  $\bar{A}_{T_{\min}}$ , is chosen from the calculated series of  $\bar{A}_T$ 's. The corresponding  $N$  represents the optimum fin number,  $N_{\text{opt}}$ .

Dividing  $\bar{X}$ ,  $\gamma$ ,  $\gamma_{bs}$  and  $\Gamma$  by  $\bar{R}$  in Eqs. (30), (34), and (35), we obtain

$$\bar{X}_R(\xi) = \frac{2\bar{\gamma}}{3\bar{U}_o} \int_{\xi^*}^{\xi} \bar{K}(\xi) \bar{H}(\bar{X}_R(\xi), \phi(\bar{X}_R(\xi), \xi), \xi) \bar{U}^{1/3} d\xi \quad (30')$$

$$\bar{\gamma}_{bs} = \int_b \epsilon_b \left( 1 - \xi_e^4 F_{d\bar{c}-A_e} - \int_{f'} \phi dF_{d\bar{c}-d\bar{x}} - \int_{f'} \phi' dF_{d\bar{c}-d\bar{x}'} \right) d\theta \quad (34')$$

$$\bar{\Gamma} = N(\bar{\gamma} + \bar{\gamma}_{bs}) \quad (35')$$

If we divide all of the length dimensions in the view factors by  $\bar{R}$ , Eqs. (28), (29), and (31)–(33) are not influenced since all the view factors involved will remain unchanged. Investigating the system of equations including Eqs. (28), (29), (30'), (31)–(33), (34') (35'), and (37) reveals that the optimum number of fins,  $N_{\text{opt}}$ , is a function of  $\bar{\Gamma}$ ,  $\epsilon_b$ ,  $\epsilon_f$ ,  $\xi_e$ , and  $\bar{K}$ ; while  $\bar{A}_{T_{\min}}$  is a function of  $\bar{\Gamma}$ ,  $\bar{R}$ ,  $\epsilon_b$ ,  $\epsilon_f$ ,  $\xi_e$ , and  $\bar{K}$ . After the  $N_{\text{opt}}$  has been determined, the optimum parameters each individual fin, dimensionless thickness distribution,  $\bar{Y}$ , heat flow distribution,  $\bar{q}$ , are obtained from

$$\bar{Y}(\xi) = \frac{\bar{\gamma}^2}{3\bar{U}_o} \bar{U}^{1/3}(\xi) \bar{H}(\bar{X}(\xi), \phi(\bar{X}(\xi), \xi), \xi) \quad (38)$$

$$\bar{q}(\xi) = \bar{U}^{2/3}(\xi) \quad (39)$$

A mathematical difficulty arises when we evaluate  $\bar{H}|_{\bar{x}=\bar{b}}$  and  $\phi|_{\bar{x}=\bar{b}}$ , since the view factors  $dF_{d\bar{c}-d\bar{x}}$  and  $dF_{d\bar{x}-d\bar{c}}$  become indeterminate as both of  $\theta$  and  $\bar{b} - \bar{X}$  approach zero. Following the suggestion of Sparrow et al. (1961), we can overcome this difficulty using a physical argument, i.e., one half of the energy leaving the joint point (the corner of fin and its base; see Fig. 1), which belongs to the fin, arrives at the joint point, which belongs to the base, and vice versa. Thus from the energy balance at the joint point, the following equations can be established:

$$J|_{x=b} = \epsilon_f \sigma T_b^4 + (1 - \epsilon_f) G|_{x=b} \quad (40)$$

$$J_b|_{\theta=0} = \epsilon_b \sigma T_b^4 + (1 - \epsilon_b) G_b|_{\theta=0} \quad (41)$$

$$G|_{x=b} = \frac{1}{2} J_b|_{\theta=0} + \sigma T_e^4 F_{dx-A_e}|_{x=b} + \int_{f'} J' dF_{dx-dx'} |_{x=b} \quad (42)$$

$$G_b|_{\theta=0} = \frac{1}{2} J|_{x=b} + \sigma T_e^4 F_{dc-A_e}|_{\theta=0} + \int_{f'} J' dF_{dc-dx'} |_{\theta=0} \quad (43)$$

Solving the above four equations simultaneously, we obtain  $J|_{x=b}$ , in its dimensionless form

$$\phi|_{\bar{x}=\bar{b}} \left\{ \epsilon_f + (1 - \epsilon_f) \left[ \frac{1}{d} \epsilon_b + \frac{1}{2} (1 - \epsilon_b) \xi_e^4 F_{d\bar{c}-A_e} |_{\theta=0} + \frac{1}{2} (1 - \epsilon_b) \int_{f'} \phi' dF_{d\bar{c}-d\bar{x}'} |_{\theta=0} + \xi_e^4 F_{d\bar{x}-A_e} |_{\bar{x}=\bar{b}} + \int_{f'} \phi' dF_{d\bar{x}-d\bar{x}'} |_{\bar{x}=\bar{b}} \right] \right\} \div \left[ 1 - \frac{1}{4} (1 - \epsilon_f)(1 - \epsilon_b) \right] \quad (44)$$

and  $H|_{x=b}$  is solved from  $H|_{x=b} = 2(J|_{x=b} - G|_{x=b})$ , or in terms of dimensionless form, it is expressed by

$$\bar{H}|_{\bar{x}=\bar{b}} = 2\epsilon_f \left\{ 1 - \left[ \frac{1}{2} (\epsilon_b + (1 - \epsilon_b)) \left( \frac{1}{2} \phi|_{\bar{x}=\bar{b}} + \xi_e^4 F_{d\bar{c}-A_e} |_{\theta=0} + \int_{f'} \phi' dF_{d\bar{c}-d\bar{x}'} |_{\theta=0} \right) + \xi_e^4 F_{d\bar{x}-A_e} |_{\bar{x}=\bar{b}} + \int_{f'} \phi' dF_{d\bar{x}-d\bar{x}'} |_{\bar{x}=\bar{b}} \right] \right\} \quad (45)$$

Equations (44) and (45) are employed to determine the values of  $\phi$  and  $\bar{H}$  at the point of  $\bar{X} = \bar{b}$  in the computations. A rigorous mathematical approach can be also applied to obtain  $\phi|_{\bar{x}=\bar{b}}$ . Details of this mathematical approach are given in the appendix.

## Results and Discussion

Equations (28)–(35) are solved numerically and iteratively. The optimum number of fins,  $N_{\text{opt}}$ , is found to depend on five parameters, namely,  $\bar{\Gamma}$ ,  $\epsilon_b$ ,  $\epsilon_f$ ,  $\xi_e$ , and  $\bar{K}$ ; while the minimum total fin profile area,  $\bar{A}_{T_{\min}}$ , is controlled, similar to the case of individual fins considered earlier by Chung and Zhang (1991), by six parameters,  $\bar{\Gamma}$ ,  $\bar{R}$ ,  $\epsilon_b$ ,  $\epsilon_f$ ,  $\xi_e$ , and  $\bar{K}$ . A wide range of parameters is chosen in the calculations. Considering that the conductivity of most metals decreases with temperature,  $\bar{K}$  is assumed to be a linear decreasing function of  $\xi$ , i.e.,  $\bar{K} = 1 + C_k(1 - \xi)$ . Different  $C_k$ 's are selected to test the effect of  $\bar{K}$ . The optimum number of fins,  $N_{\text{opt}}$ , and the optimum fin length,  $\bar{b}_{R_{\text{opt}}}$ , versus various combinations of parameters are presented in Table 1. The results indicate that a decrease of any of the five parameters,  $\bar{\Gamma}$ ,  $\epsilon_b$ ,  $\epsilon_f$ ,  $\xi_e$ , and  $C_k$ , will result in an increase in the optimum number of fins. As expected, any factor weakening the interactions in the system will cause  $N_{\text{opt}}$  to rise.

Figure 3 shows how the dimensionless heat dissipation at the base,  $\bar{\Gamma}$ , influences  $\bar{A}_{T_{\min}}$  and  $N_{\text{opt}}$ . Note that no fin would be needed if  $\bar{\Gamma} \leq 2\pi \bar{R} \epsilon_b (\xi_b^4 - \xi_e^4)$ . In this figure, the circle represents the minimum total fin profile area at the corresponding number of fins, and hence also represents the optimum number of fins of the array,  $N_{\text{opt}}$ . As the total heat flow decreases, shorter fins are required to dissipate the heat, which weakens the radiation interactions between fin-to-fin and fin-to-base. If not mutual interaction existed in the system, the increase of the number of fins would certainly reduce the



Table 1  $N_{opt}$  and  $\bar{b}_{R_{opt}}$  under various conditions

| $\epsilon_f$ | $\epsilon_b$ | $\bar{\Gamma}$ | $\xi_e$ | $C_k$ | $N_{opt}$ | $\bar{b}_{R_{opt}}$ |
|--------------|--------------|----------------|---------|-------|-----------|---------------------|
| 0.9          | 0.9          | 50             | 0       | 0     | 4         | 23.6                |
| 0.9          | 0.9          | 20             | 0       | 0     | 4         | 7.77                |
| 0.9          | 0.9          | 10             | 0       | 0     | 5         | 2.32                |
| 0.9          | 0.9          | 8.33           | 0       | 0     | 5         | 1.48                |
| 0.9          | 0.9          | 6.67           | 0       | 0     | 6         | 0.605               |
| 1            | 0.9          | 10             | 0       | 0     | 5         | 2.11                |
| 0.9          | 0.9          | 10             | 0       | 0     | 5         | 2.32                |
| 0.75         | 0.9          | 10             | 0       | 0     | 5         | 2.74                |
| 0.4          | 0.9          | 10             | 0       | 0     | 6         | 4.52                |
| 0.9          | 1            | 10             | 0       | 0     | 4         | 2.29                |
| 0.9          | 0.9          | 10             | 0       | 0     | 5         | 2.32                |
| 0.9          | 0.75         | 10             | 0       | 0     | 5         | 2.59                |
| 0.9          | 0.5          | 10             | 0       | 0     | 6         | 2.86                |
| 0.4          | 0.9          | 10             | 0       | 0     | 6         | 4.52                |
| 0.4          | 0.75         | 10             | 0       | 0     | 7         | 4.81                |
| 0.4          | 0.5          | 10             | 0       | 0     | 9         | 5.11                |
| 0.9          | 0.9          | 50             | 0       | 0     | 4         | 23.6                |
| 0.9          | 0.5          | 50             | 0       | 0     | 5         | 23.2                |
| 0.5          | 0.9          | 50             | 0       | 0     | 8         | 32.1                |
| 0.9          | 0.9          | 6.67           | 0.5     | 0     | 5         | 0.841               |
| 0.9          | 0.9          | 6.67           | 0.4     | 0     | 5         | 0.730               |
| 0.9          | 0.9          | 6.67           | 0.3     | 0     | 6         | 0.629               |
| 0.9          | 0.9          | 6.67           | 0       | 0     | 6         | 0.605               |
| 0.9          | 0.9          | 6.67           | 0       | 4     | 5         | 0.793               |
| 0.9          | 0.9          | 6.67           | 0       | 2     | 5         | 0.734               |
| 0.9          | 0.9          | 6.67           | 0       | 1     | 5         | 0.698               |
| 0.9          | 0.9          | 6.67           | 0       | 0     | 6         | 0.605               |
| 0.4          | 0.5          | 6.67           | 0       | 0     | 10        | 2.51                |

total fin profile area for the same given amount of heat dissipation. Therefore less interaction in the system tends to increase the optimum number of fins. The numerical results of Schnurr et al. (1976) reveal that the optimum number of fins is independent of the total heat flow, which is not true in general, but is only sure when the lengths of the fins are relatively large as compared to the radius of the base. The fact may become clear by considering the following special case. If the fins are short enough so that the adjacent fins can't "see" each other, definitely adding more fins will reduce the total fin profile area, as is evident from Eq. (37). For long fins, the mutual interacting between two adjacent fins becomes "saturated." Hence, further increasing the length of the fin as a result of increase in heat dissipation will no longer intensify the interaction significantly. Schnurr et al. (1976) were correct in this sense. Increasing the radius of the base is equivalent to intensifying the capability of the base to dissipate heat; hence for a given  $\Gamma$ , a smaller amount of heat has to be dissipated by fins, and consequently a smaller mass of fins will be needed. Numerical computations reveal that the same ratios of  $\Gamma$  to  $\bar{R}$  (i.e.,  $\bar{\Gamma}$ ), yield the same optimum numbers of fins.

Numerical results indicate that  $N_{opt}$  tends to decrease with high values of  $\xi_e$ , as shown in Fig. 4, although the effect is not strong. Note that higher values of  $\xi_e$  result in longer fins and hence increase the radiation interaction in the system.

Figure 5 plots the minimum fin profile area against number of fins for different fin emissivities. A decrease of  $\epsilon_f$  weakens the radiation interaction in the fin array, even though that increases the length of the fins. It allows more fins to be added. Small  $\epsilon_f$  reduces the capability of the fins to dissipate heat, and hence leads to a larger  $\bar{A}_{T_{min}}$ .

Figure 6 illustrates the influence of  $\epsilon_b$  on  $N_{opt}$  and  $\bar{A}_{T_{min}}$  for both  $\epsilon_f = 0.4$  (right-hand-side scale) and  $\epsilon_f = 0.9$  (left-hand-side scale). Similar to the previous case, lower values of  $\epsilon_b$  also lead to an increase of both  $N_{opt}$  and  $\bar{A}_{T_{min}}$ . Low values of  $\epsilon_b$

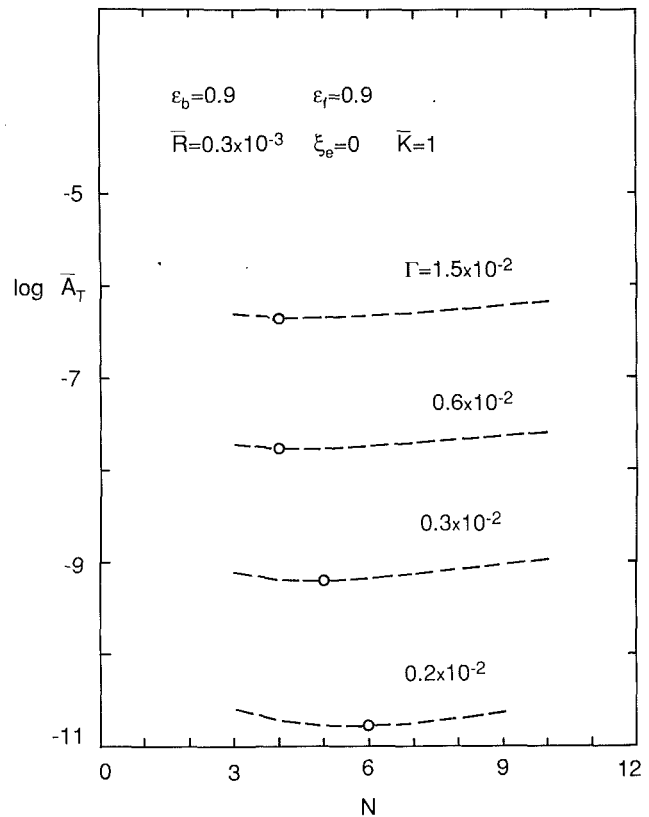


Fig. 3 Influence of  $\Gamma$  on  $N_{opt}$  and  $\bar{A}_{T_{min}}$

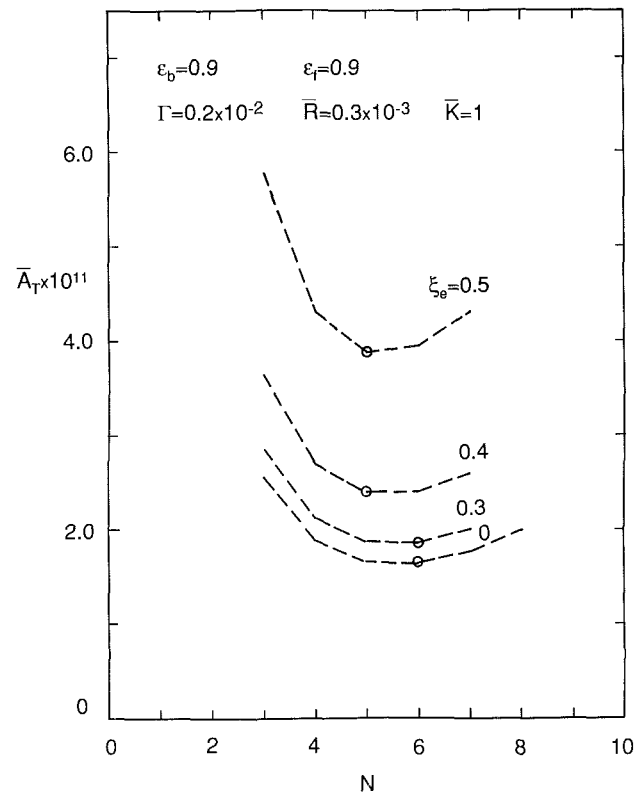


Fig. 4 Influence of  $\xi_e$  on  $N_{opt}$  and  $\bar{A}_{T_{min}}$

cause a weak radiative interaction for the whole system, which in turn raises the optimum number of fins. Since a higher fraction of heat has to be dissipated by the fins, a larger fin

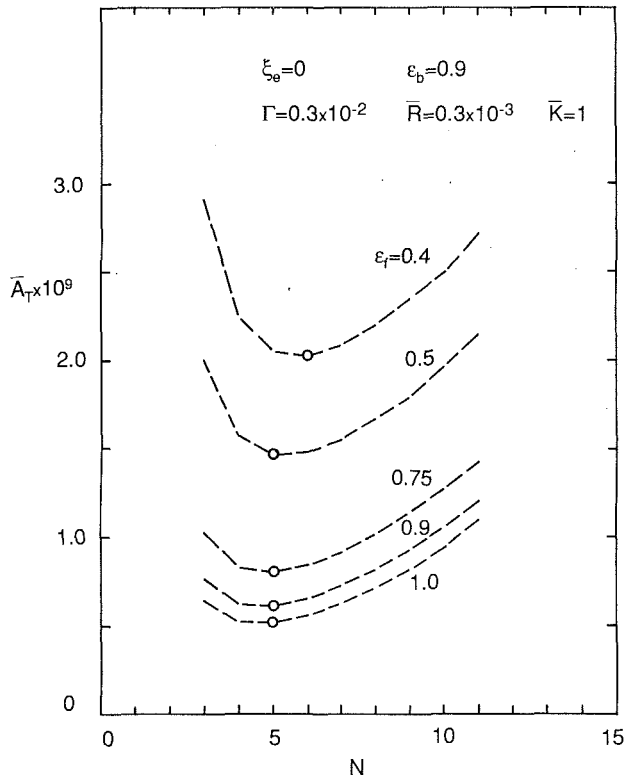


Fig. 5 Predicted  $N_{opt}$  and  $\bar{A}_{T_{min}}$  as functions of  $\epsilon_f$

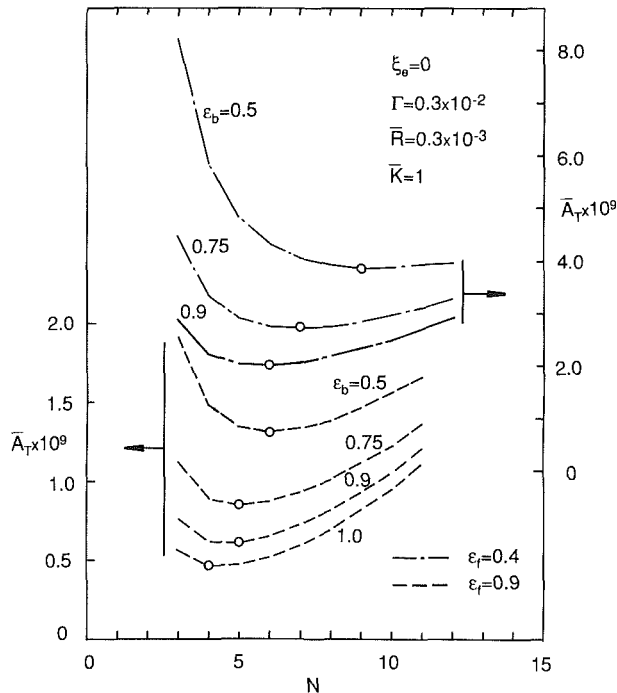


Fig. 6  $N_{opt}$  and  $\bar{A}_{T_{min}}$  as functions of  $\epsilon_b$  for different  $\epsilon_f$

profile area is therefore required. With low values of  $\epsilon_b$  combining with low values of  $\epsilon_f$  (the top curve), the optimum number of fins will increase further. As shown in this figure,  $N_{opt}$  is as high as nine for the data presented. It should be pointed out that the data selected to test the effects of  $\epsilon_b$  and  $\epsilon_f$ , shown in Figs. 5 and 6, are so chosen that the base and the fins have comparable dimensions.

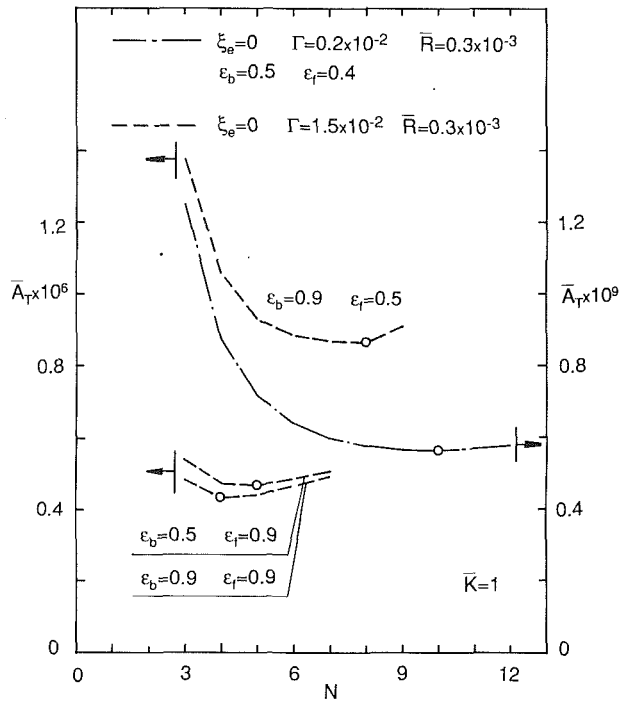


Fig. 7 Influence of  $\epsilon_f$  and  $\epsilon_b$  on  $N_{opt}$  and  $\bar{A}_{T_{min}}$  for high values of  $\Gamma$  and  $N_{opt}$  of the smallest possible parameters involved

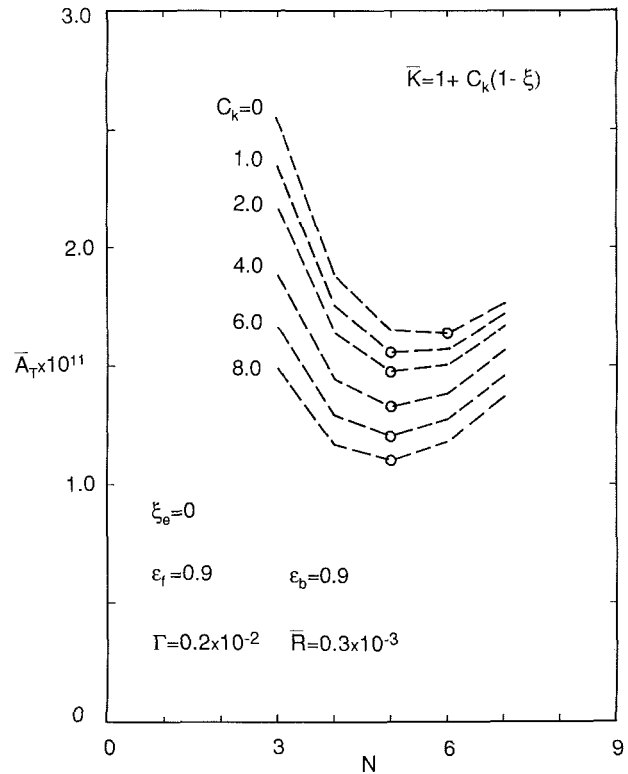


Fig. 8 Influence of  $C_k$  on  $N_{opt}$  and  $\bar{A}_{T_{min}}$

If the fin length is much larger than the radius of the base, a case given by the dashed lines of Fig. 7,  $N_{opt}$  will be more sensitive to  $\epsilon_f$  but less to  $\epsilon_b$ , as shown in this figure, because  $\epsilon_f$  becomes dominant in control of the intensity of interaction of the whole system. The broken line curve in this figure indicates that  $N_{opt}$  can be as large as ten for the combination of

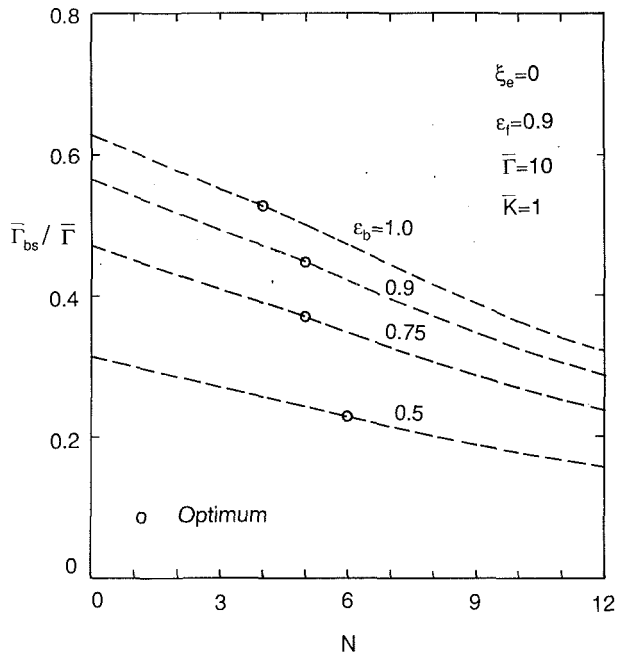


Fig. 9 Heat dissipated from base as a function of number of fins

the smallest values of  $\bar{\Gamma}$ ,  $\epsilon_b$ ,  $\epsilon_f$ , and  $\xi_e$  chosen in this investigation.

Assuming  $\bar{K}$  to be a linear function of  $\xi$ , the influence of  $\xi$  on  $\bar{K}$  is controlled by the parameter  $C_k$ . When  $C_k$  is taken as zero,  $\bar{K}$  reduces to one, which represents a constant conductivity. A positive value of  $C_k$  yields a decreasing linear relationship between  $\bar{K}$  and  $\xi$ . Figure 8 indicates the effect of assumed temperature-independent conductivity on  $\bar{A}_{T_{min}}$  and  $N_{opt}$ . A higher value of  $C_k$  results in a thinner fin thickness and a longer fin length. The latter increases the interaction in the system, which has the effect of reducing  $N_{opt}$ . On the other hand, the high value of  $C_k$  improves the conduction in the system, which helps to reduce  $\bar{A}_{T_{min}}$ .

Under the conditions of constant thermal conductivity, i.e.,  $\bar{K} = 1$ , carefully examining Eqs.(8), (10), (15)–(18), and (23)–(27) shows that both temperature and heat transfer distributions inside the optimum fin are independent of the conductivity. Consequently,  $N_{opt}$  is not a function of the conductivity if  $k$  is a constant. A similar conclusion was also implied from the results of Karlekar and Chao (1963) and Schnurr et al. (1976), although they did not mention this point explicitly.

Figure 9 describes the ratio of the heat dissipated by the base to the total heat flow,  $\bar{\Gamma}_{bs}/\bar{\Gamma}$ , as functions of  $N$  and  $\epsilon_b$  with  $\epsilon_f = 0.9$  and  $\bar{\Gamma} = 10$ . Interestingly,  $\bar{\Gamma}_{bs}/\bar{\Gamma}$  is almost a decreasing linear function of number of fins, although the governing equations involved are much more complicated. The circle represents the state of optimum design.

Figure 10 illustrates some typical optimum fin shapes under different design parameters. Note that the  $\bar{X}$  scale is much larger than the  $\bar{Y}$  scale. As can be seen, all optimum fins have a sharp tip, which may not be practical from the point of view of structure or manufacture. However, this weakness can be removed by specifying an acceptable minimum thickness. The method has been described in detail by Chung and Zhang (1991) and Wilkins (1960) and will not be repeated here. Figure 11 shows the temperature and heat flow distributions for one of the optimum designs shown in Fig. 10. Note that the tip temperature is not equal to the environment temperature ( $\xi_e = 0$ ) due to radiation interactions.

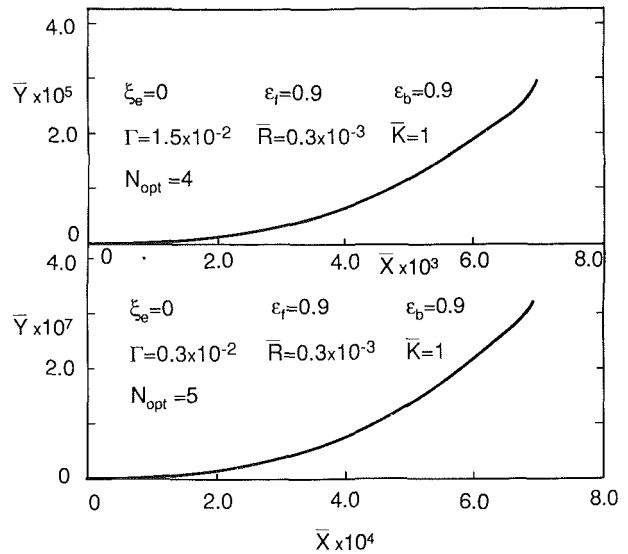


Fig. 10 Typical shapes of optimum fins

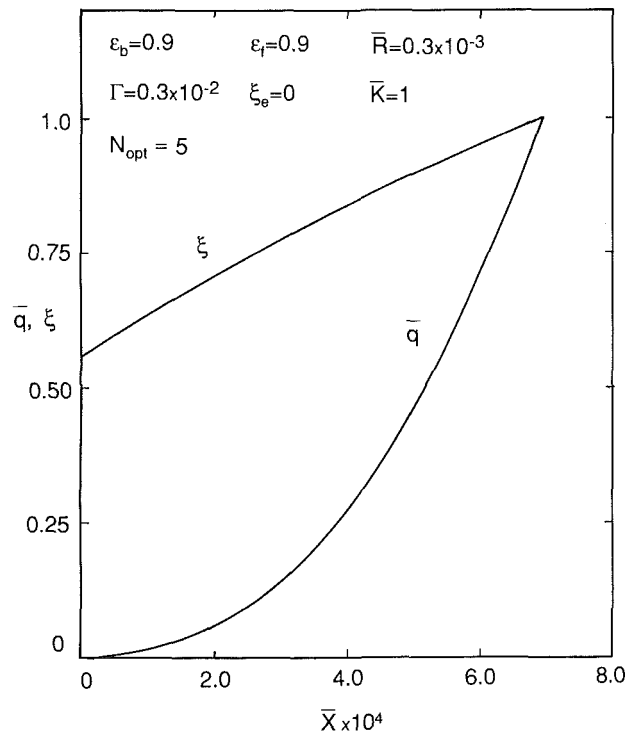


Fig. 11 Temperature and heat transfer distributions for one fin

Figure 12 compares the minimum total fin profile area with the results published earlier. Curves 1 and 2 are taken from the results of Karlekar and Chao (1963) and Schnurr et al. (1976), respectively. Both of them are triangular shapes. Curve 1 does not include the effect of radiation interaction at the base, while curve 2 takes account of this effect. Curves 1 and 2 are supposed to coincide at very large value of total heat flow (which yields a long fin), when the fin length is much larger than the radius of base. Curve 3 represents the present study, which yields the possible minimum fin profile area the system may have. For this set of parameters, the difference between curves 2 and 3 appears to be reasonably small if the heat transfer is not very large. This demonstrates that the triangular profile is a reasonable approximation in order to

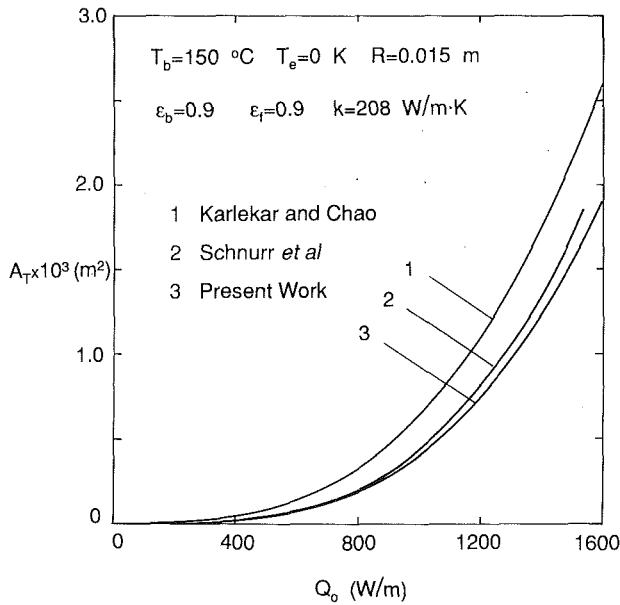


Fig. 12 Comparison of the total profile area with previous studies

minimize the fin mass. The figure also shows that the effect of radiation interaction at the base is very important, even for fins with a large length-to-radius ratio,  $\bar{b}_R$ .

### Conclusion

This study reveals that the optimum number of fins in a fin array depends on five major parameters, namely, the emissivity of the fins, the emissivity of the base, the dimensionless heat flow dissipation from the system  $\bar{\Gamma}$ , the environment to base temperature ratio, and the coefficient describing the temperature dependency of the conductivity,  $C_k$ . The present results indicate that the decrease of any of the five parameters mentioned above results in an increase in the optimum number of fins. Any factor weakening the radiation interactions in the system will cause the number of optimum fins to rise. The optimum number of fins usually is found to be between four to ten from a wide choice of parameters. The lower limit for the number of fins for any combination of the parameters is four, while the upper limit depends on how small the values of the parameters involved in the calculations are.

In agreement with the earlier work, the present study shows that all optimum fins have a sharp tip, which may not be practical from the point view of structure and manufacture. The present results further demonstrate the importance of the radiation interaction effect at the base.

### References

- Ahmadi, G., and Razani, A., 1973, "Some Optimization Problems Relating to Cooling Fins," *International Journal of Heat and Mass Transfer*, Vol. 16, pp. 2369-2375.
- Chung, B. T. F., and Zhang, B. X., 1991 "Minimum Mass Longitudinal Fins with Radiation Interaction at the Base," *Journal of the Franklin Institute*, Vol. 328, pp. 143-161.
- Dhar, P. L., and Arora, C. P., 1976, "Optimum Design of Finned Surfaces," *Journal of the Franklin Institute*, Vol. 301, pp. 379-392.
- Duffin, R. J., 1959, "A Variational Problem Relating to Cooling Fins," *Journal of Mathematics and Mechanics*, Vol. 8, pp. 47-56.
- Karlekar, B. V., and Chao, B. T., 1963, "Mass Minimization of Radiating Trapezoidal Fins With Negligible Base Cylinder Interaction," *International Journal of Heat and Mass Transfer*, Vol. 6, pp. 33-48.
- Liu, C. Y., 1962, "A Variational Problem With Applications to Cooling Fins," *Journal of the Society for Industrial and Applied Mathematics*, Vol. 10, pp. 19-29.
- Maday, C. J., 1974, "The Minimum Weight One-Dimensional Straight Fin," *ASME Journal of Engineering for Industry*, Vol. 97, pp. 161-165.

Mikk, I., 1980, "Convective Fin of Minimum Mass," *International Journal of Heat and Mass Transfer*, Vol. 22, pp. 707-711.

Razelos, P., and Imre, K., 1983, "Minimum Mass Convective Fins With Variable Heat Transfer Coefficients," *Journal of the Franklin Institute*, Vol. 315, pp. 269-282.

Schnurr, N. M., Shapiro, A. B., and Townsend, M. A., 1976, "Optimization of Radiating Fin Arrays With Respect to Weight," *ASME JOURNAL OF HEAT TRANSFER*, Vol. 98, pp. 643-648.

Sparrow, E. M., Eckert, E. R. G., and Irvine, T. F., Jr., 1961, "The Effectiveness of Radiating Fins With Mutual Irradiation," *Journal of the Aerospace Sciences*, Vol. 28, pp. 763-772.

Wilkins, J. E., 1960, "Minimum Mass Thin Fins for Space Radiators," *Proceedings of the 1960 Heat Transfer and Fluid Mechanics Institute*, D. M. Mason et al., eds., Stanford University Press, Stanford, CA, pp. 229-243.

Wilkins, J. E., 1974, "Optimum Shapes for Fin Rejection Heat by Convection and Radiation," *Journal of the Franklin Institute*, Vol. 297, pp. 1-6.

Zhang, B. X., 1990, "Minimum Mass of Longitudinal Fin and Fin Array With Radiative Interaction at the Base," M.S. Thesis, the University of Akron, Akron, OH.

## APPENDIX

### Mathematical Evaluation of Radiosity at the Joint Point of Fin and Base

The purpose of this section is to develop a mathematical approach to evaluate the value of  $J|_{x=b}$  (the dimensional form of  $\phi|_{x=\bar{b}}$ ).

By eliminating  $G$  and  $G_b$  from Eqs. (19)-(22), the radiosities of the fin and the pipe may be written as

$$J(x_1) = \epsilon_f \sigma T^4 + (1 - \epsilon_f) \left[ T_e^4 F_{dx-A_e} + \int_{f'} J' dF_{dx-dx'} + \int_b J_b dF_{dx-dc} \right] \quad (A-1)$$

$$J_b(c) = \epsilon_b \sigma T_b^4 + (1 - \epsilon_b) \left[ \sigma T_b^4 F_{dc-A_e} + \int_f J dF_{dc-dx} + \int_{f'} J' dF_{dc-dx'} \right] \quad (A-2)$$

Here  $J$  is treated as function of  $x_1$ , where  $x_1 = b - x$ ; and  $J_b$  is treated as function of  $c$ . Thus at the joint point we have  $x_1 = c = 0$ .

To remove the difficulty of evaluating the indeterminate values of  $dF_{dx-dc}$  and  $dF_{dc-dx}$  at the joint point, we rewrite Eqs. (A-1) and (A-2) in the following form:

$$J(x_1) = \epsilon_f \sigma T^4 + (1 - \epsilon_f) \left\{ \sigma T_e^4 F_{dx-A_e} + \int_{f'} J' dkF_{dx-dx'} + \int_b [J_b(c) - J_b(x_1)] dF_{dx-dc} + J_b(x_1) \int_b dF_{dx-dc} \right\} \quad (A-3)$$

$$J_b(c) = \epsilon_b \sigma T_b^4 + (1 - \epsilon_b) \left\{ \sigma T_e^4 F_{dc-A_e} + \int_{f'} J' dF_{dc-dx'} + \int_f [J(x_1) - J(c)] dF_{dc-dx} + J(c) \int_f dF_{dc-dx} \right\} \quad (A-4)$$

Fortunately, both of the analytical expressions for  $\int_b dF_{dx-dc}$  and  $\int_f dF_{dc-dx}$  can be obtained.

$$\int_b dKF_{dx-dc} = \frac{1}{2} R^2 \int_{\theta=0}^{\theta=\cos^{-1} \frac{R}{R+b-x}} \frac{\sin \theta [(b-x+R) \cos \theta - R] d\theta}{[(b-x+R)^2 + R^2 - 2(b-x+R)R \cos \theta]^{3/2}} = \frac{1}{2} \left[ 1 - \sqrt{1 - \frac{R^2}{(R+b-x)^2}} \right] \quad (A-5)$$

$$\int_f dF_{dc-dx} = \frac{1}{2} R \sin \theta \int_{x=0}^{x=R+b-\frac{R}{\cos \theta}} \frac{[(b-x+R) \cos \theta - R] dx}{[(b-x+R)^2 + R^2 - 2(b-x+R)R \cos \theta]^{3/2}} \\ = \frac{1}{2} \left[ 1 - \frac{(R+b) \sin \theta}{\sqrt{(R+b)^2 + R^2 - 2(R+b)R \cos \theta}} \right] \quad (\text{A-6})$$

Letting  $x_1$  be zero in Eq. (A-3) and  $c$  be zero in Eq. (A-4), we arrive at

$$J(0) = \epsilon_f \sigma T^4 + (1 - \epsilon_f) \{ \sigma T_e^4 F_{dx-A_e} |_{x_1=0} \\ + \int_{f'} J' dF_{dx-dx'} |_{x_1=0} + \int_b [J_b(c) - J_b(0)] dF_{dx-dc} |_{x_1=0} \\ + J_b(0) \int_b dF_{dx-dc} |_{x_1=0} \} \quad (\text{A-7})$$

$$J_b(0) = \epsilon_b \sigma T_b^4 + (1 - \epsilon_b) \{ \sigma T_e^4 F_{dc-A_e} |_{c=0} \\ + \int_{f'} J' dF_{dc-dx'} |_{c=0} + \int_f [J(x_1) \\ - J(0)] dF_{dc-dx} |_{c=0} + J(0) \int_f dF_{dc-dx} |_{c=0} \} \quad (\text{A-8})$$

From the above two equations, the following expressions are obtained:

$$\int_b [J_b(c) - J_b(0)] dF_{dx-dc} |_{x_1=0} = 0$$

$$\int_f [J(x_1) - J(0)] dF_{dc-dx} |_{c=0} = 0$$

and from Eqs. (A-5) and (A-6), the following results are obtained:

$$\int_b dF_{dx-dc} |_{x_1=0} = \frac{1}{2}$$

$$\int_f dF_{dc-dx} |_{c=0} = \frac{1}{2}$$

Noting that  $J(0) = J|_{x=b}$  and  $J_b(0) = J_b|_{\theta=0}$ , Eqs. (A-7) and (A-8) are reduced, respectively, to

$$J|_{x=b} = \epsilon_f \sigma T_b^4 + (1 - \epsilon_f) \left[ \sigma T_e^4 F_{dx-A_e} |_{x=b} \\ + \int_{f'} J' dF_{dx-dx'} |_{x=b} + \frac{1}{2} J_b|_{\theta=0} \right] \quad (\text{A-9})$$

$$J_b|_{\theta=0} = \epsilon_b \sigma T_b^4 + (1 - \epsilon_b) \left[ \sigma T_e^4 F_{dc-A_e} |_{\theta=0} \\ + \int_{f'} J' dF_{dc-dx} |_{\theta=0} + \frac{1}{2} J|_{x=b} \right] \quad (\text{A-10})$$

Equations (A-9) and (A-10) are identical to what will be obtained by eliminating  $G|_{x=b}$  and  $G_b|_{\theta=0}$  from Eqs. (40)–(43), which are directly derived from the physical arguments. Solving  $J|_{x=b}$  from Eqs. (A-9) and (A-10) results in the same expression of radiosity of the joint point given by Eq. (44), which is expressed in the dimensionless form of  $J|_{x=b}$ , i.e.,  $\phi|_{\bar{x}=\bar{b}}$ .

# Numerical Predictions of Local Entropy Generation in an Impinging Jet

M. K. Drost

Senior Research Engineer.

M. D. White

Research Engineer.

Pacific Northwest Laboratory,  
Richland, WA 99352

*Local entropy generation rates related to viscous dissipation and heat transfer across finite temperature differences can be calculated for isotropic and Newtonian fluids from the temperature and velocity fields in a thermal process. This study consisted of the development of a numerical procedure for the prediction of local entropy generation rates and the application of that procedure to convective heat transfer associated with a fluid jet impinging on a heated wall. The procedure involved expanding an existing computation fluid dynamics computer code to include the numerical calculation of local entropy generation. The modified code was benchmarked against analytical solutions and was then used to simulate a cold fluid jet impinging on a hot wall. The results show that the calculation of local entropy generation is feasible and can provide useful information.*

## 1.0 Introduction

A large number of texts and studies have shown that the valid measure of thermodynamic performance of a device or process is its irreversibility (or related measures of performance such as entropy generation or second-law efficiency) (Van Wylen and Sonntag, 1973; Bejan, 1982; Gaggioli, 1983). Second-law analysis techniques have been widely used to evaluate the sources of irreversibility in components and systems of components, but the evaluation of local sources of irreversibility in thermal processes has received limited attention. While some analytical procedures for evaluating local entropy generation were published in 1979 (Bejan, 1979a), applications have been limited to fluid flows with analytical solutions for the velocity and temperature fields. Inclusion of entropy generation calculations in computational fluid dynamics (CFD) codes would allow the evaluation of local entropy generation in more complicated thermal phenomena (Drost and Zaworski, 1988). The research documented here consists of incorporating local entropy generation calculations in an existing CFD code and then using the code to evaluate local entropy generation in an impinging jet. The specific objectives of the research included:

- Incorporating calculation of local entropy generation in an existing CFD code.
- Benchmarking the entropy generation calculations by comparison of numerical results with analytical calculations for laminar pipe flow.
- Using the modified CFD code to investigate the sources and distribution of local entropy generation in an impinging jet for a variety of fluids and a range of fluid velocities.

## 2.0 Previous Research

The application of partial differential equations describing local entropy generation to a convecting fluid has been proposed by Bejan (1979a). Bejan used this procedure to evaluate local entropy generation in several simple flow situations that had analytical solutions available for the velocity and temperature fields (Bejan, 1979a, 1982). Bejan's work is the only

example of using local entropy generation calculations to evaluate thermodynamic processes identified in the literature.

While the calculation of local entropy generation from the flow and temperatures fields has been limited, a number of investigators have used a lumped parameter approach to calculate entropy generation. Bejan has evaluated entropy generation in internal conduit flow, external flow, and in insulation systems using lumped parameters (Bejan, 1979a, 1979b, 1982). Dunbar (1982) has applied a one-dimensional lumped parameter analysis to the evaluation of a fuel cell, while Hutchinson and Lyke (1987) have used a similar approach to investigate irreversibilities in a Stirling engine regenerator. Two recent papers have presented one-dimensional lumped parameter evaluations of local entropy generation in heat exchangers (Liang and Kuehn, 1988; El-Sayed, 1988).

While one researcher has suggested that the calculation of local entropy generation can be used as a diagnostic for evaluating numerical entropy generation in a CFD code (Argrow et al., 1987), an extensive literature review did not identify any previous studies that actually incorporated entropy generation relationships in a CFD code and then used the code to evaluate a thermodynamic process.

## 3.0 Numerical Calculation of Local Entropy Generation

One theoretically correct measure of thermodynamic performance is the magnitude of thermodynamic irreversibilities associated with a component or process. It can be shown that the minimization of entropy generation also results in the maximum reduction in irreversibility (Govy, 1889; Stodola, 1910). The development of improved thermal designs will be enhanced by the ability to identify clearly the source and location of entropy generation. Systems of individual components can be optimized from estimates of net entropy generation for complete components, but the development of novel components and processes should benefit from knowing the distribution and sources of entropy generation on a local level.

**3.1 Modeling Methodology.** Equation (1) gives local entropy generation for a convecting fluid (Bejan 1979a, 1982), when the fluid is isotropic and Newtonian. Equation (1) is presented in rectangular Cartesian coordinates.

Contributed by the Heat Transfer Division for publication in the JOURNAL OF HEAT TRANSFER. Manuscript received by the Heat Transfer Division October 13, 1989; revision received April 23, 1991. Keywords: Jets, Numerical Methods, Thermodynamics and Second Law.

$$\dot{S}_{\text{gen}}'' = \frac{\kappa}{T^2} \left[ \left( \frac{\partial T}{\partial x} \right)^2 + \left( \frac{\partial T}{\partial y} \right)^2 + \left( \frac{\partial T}{\partial z} \right)^2 \right] + \frac{\epsilon}{T} \left\{ 2 \left[ \left( \frac{\partial u}{\partial x} \right)^2 + \left( \frac{\partial v}{\partial y} \right)^2 + \left( \frac{\partial w}{\partial z} \right)^2 \right] + \left( \frac{\partial u}{\partial y} + \frac{\partial v}{\partial x} \right)^2 + \left( \frac{\partial u}{\partial z} + \frac{\partial w}{\partial x} \right)^2 + \left( \frac{\partial v}{\partial z} + \frac{\partial w}{\partial y} \right)^2 \right\} \quad (1)$$

One important feature of Eq. (1) is that the impacts of different sources of entropy generation are clearly identified. The first bracketed term on the right-hand side of Eq. (1) is the entropy generation due to heat transfer across a finite temperature difference, whereas the second bracketed term is the local entropy generation due to viscous dissipation. When analytical expressions are available for the temperature and velocity fields, Eq. (1) can be evaluated to yield the local entropy generation. Total entropy generation can then be determined by integrating Eq. (1) over the region of interest.

Most practical problems are sufficiently complex that analytical solutions do not exist. In this case, a CFD code can be used to predict the velocity and temperature fields. The results of the computer simulation can then be used to calculate entropy generation numerically.

Equation (1) is valid for both laminar and turbulent flow; where the effective thermal conductivity is the sum of the molecular thermal conductivity and the eddy thermal conductivity, and the effective viscosity is the sum of the molecular viscosity and the eddy diffusivity. Local entropy generation rates are, therefore, dependent on the local spatial gradients of temperature and velocity and on the absolute local values of temperature, effective thermal conductivity, and viscosity. These quantities were estimated locally for fluid flow and convective heat transfer problems with the finite-difference based TEMPEST computer code (Trent et al., 1989a, 1989b).

The method for computing local entropy generation consisted of substituting the finite difference formulations for the partial derivative terms of Eq. (1) into TEMPEST and evaluating the resulting expression after each simulation time advance. TEMPEST is a three-dimensional, time-dependent computer program for hydrothermal analysis and it generates the velocity and temperature gradients required to compute the local entropy generation rate.

The evaluation of local entropy generation throughout the computational domain is decoupled from computation of the temperature, pressure, velocity, turbulent kinetic energy, and dissipation of turbulent kinetic energy. Conserving the first-order accuracy of the finite differencing scheme used in the TEMPEST code, the entropy generation equation was also differenced to first-order accuracy. The difference expressions for three of the twelve partial differential terms in Eq. (1) are presented below:

$$\left( \frac{\partial T}{\partial x} \right)^2 = \left\{ \frac{(\Delta x_{i-1} + \Delta x_i)T_{i+1} - (\Delta x_{i+1} + \Delta x_i)T_{i-1} + (\Delta x_{i+1} + \Delta x_{i-1})T_i}{(\Delta x_{i+1} + \Delta x_i)(\Delta x_{i-1} + \Delta x_i)} \right\}^2 \quad (2)$$

$$\left( \frac{\partial u}{\partial x} \right)^2 = \left( \frac{u_i - u_{i-1}}{\Delta x_i} \right)^2 \quad (3)$$

$$\left( \frac{\partial v}{\partial x} \right)^2 = \left\{ \left[ \frac{(\Delta x_{i-1} + \Delta x_i)(v_{i+1,j} + v_{i+1,j-1})}{2(\Delta x_{i+1} + \Delta x_i)(\Delta x_{i-1} + \Delta x_i)} \right] - \left[ \frac{(\Delta x_{i+1} + \Delta x_i)(v_{i-1,j} + v_{i-1,j-1})}{2(\Delta x_{i+1} + \Delta x_i)(\Delta x_{i-1} + \Delta x_i)} \right] + \left[ \frac{(\Delta x_{i+1} - \Delta x_{i-1})(v_j + v_{j-1})}{2(\Delta x_{i+1} + \Delta x_i)(\Delta x_{i-1} + \Delta x_i)} \right] \right\}^2 \quad (4)$$

The subscripts  $i$  and  $j$  are indices for the positive  $x$  and  $y$  Cartesian coordinate directions, respectively. The subscripting convention is to suppress all indices except for those indices that differ from the local cell  $(i, j, k)$ . The finite difference expression for entropy generation reflects the staggered grid arrangement used in TEMPEST where the scalar variables are cell centered and the velocities are positioned on the cell faces. The  $u$  velocity associated with the  $i, j, k$  cell is positioned on the face between the  $i, j, k$  and  $i + 1, j, k$  cells. The same indexing logic holds for the  $y$  and  $z$  Cartesian directions.

TEMPEST solves the three conservation equations governing mass, momentum, and energy, subject to several important assumptions. The fluid is modeled as single-phase, incompressible, and Newtonian. The Boussinesq approximation is assumed and the heating contribution caused by viscous dissipation is neglected in the energy equation. These assumptions combine to yield a loosely coupled momentum and energy equation where the coupling is through a thermodynamic state relationship. The coupling is important for simulations where natural convection is significant.

Neglecting viscous dissipation in the energy equation when the objective is to evaluate local entropy generation caused by viscous dissipation can appear to be inconsistent, but the evaluation of Eq. (1) only depends on accurately knowing the velocity and temperature fields and transport properties. Repeated benchmarking (Trent et al., 1989a, 1989b) has shown that the TEMPEST code can accurately predict velocity and temperature fields when viscous dissipation in the energy equation is neglected. This suggests that the results of the TEMPEST code can be used with Eq. (1) to predict local entropy generation even though viscous dissipation is not included in the energy equation.

The turbulent flow conservation equations are time averaged and Reynolds stresses are incorporated through appropriate

## Nomenclature

|   |   |  |
|---|---|--|
| $c_p$ = specific heat, J/K kg                       | $\dot{S}_{\text{gen}}''$ = entropy generation rate, W/Km <sup>2</sup> | of entropy generation, W/Km <sup>2</sup>   |
| $e_T$ = absolute error in temperature, K            | $T$ = temperature, K  | $\epsilon_{\text{sgv}}$ = error in viscous component entropy generation, W/Km <sup>2</sup> |
| $e_u$ = absolute error in the $u$ velocity, m/s     | $T_o$ = wall temperature, K   | $\kappa$ = effective thermal conductivity, W/Km  |
| $k$ = thermal conductivity, W/Km                    | $u, v, w$ = $x, y, z$ -direction velocity                             | $\mu$ = dynamic viscosity, Pa s  |
| $k_T$ = eddy thermal conductivity, W/Km             | $V$ = average flow velocity, m/s                                      | $\mu_T$ = eddy viscosity, Pa s   |
| $\dot{q}_o''$ = surface heat flux, W/m <sup>2</sup> | $x, y, z$ = Cartesian coordinate directions                           |  |
| $r$ = radius, m                                     | $\Delta x$ = node dimension in the $x$ direction, m                   | <b>Subscripts</b>  |
| $r_o$ = conduit radius, m                           | $\partial$ = partial derivative                                       | $i$ = $x$ direction node index   |
|   | $\epsilon$ = effective viscosity, Pa s                                | $j$ = $y$ direction node index   |
|   | $\epsilon_{\text{sgt}}$ = error in thermal component                  |  |

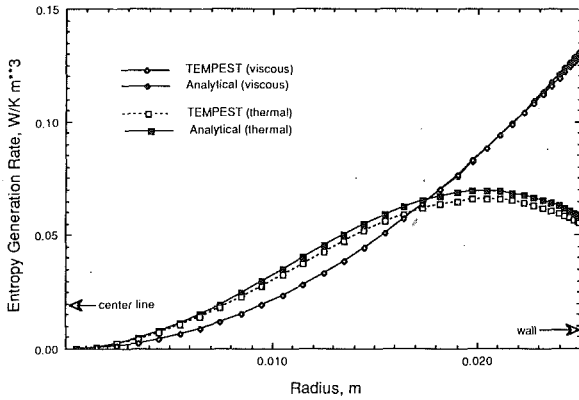


Fig. 1 Entropy generation for laminar flow with constant heat flux

eddy viscosity models. In the current version of TEMPEST, turbulent flow Reynolds stresses are modeled through an effective viscosity. The Prandtl-Kolmogorov hypothesis is used to relate the effective viscosity to a velocity and a length scale. In this approach, transport equations for turbulent kinetic energy and dissipation of turbulent kinetic energy are solved to determine the effective turbulent viscosity. The turbulent viscosity is then employed to compute the turbulent (eddy) thermal conductivity.

The TEMPEST solution procedure is a semi-implicit time marching finite-difference approach with all governing equations solved sequentially. For each time step the momentum equations are solved explicitly while the solution of the pressure equations uses an implicit formulation. Temperature, turbulent kinetic energy, dissipation of turbulent kinetic energy, and other scalar transport equations are solved using an implicit continuation procedure. The solution includes three phases. During the first phase, the three momentum equations are advanced in time to obtain approximations to the velocity field based on previous time step values of the pressure and density field. The initial velocity fields satisfy the momentum equation, but not necessarily the continuity equation. The implicit phase computes corrections to the velocity and pressure fields such that the adjusted quantities satisfy the continuity equation. With the implicit phase velocities computed, the scalar phase updates (time advances) the values of temperature and other scalar quantities. The solution is advanced in time by repeated application of the three solution phases described above.

It might appear that calculation of entropy generation could be included in the scalar phase; however, unlike some other scalar quantities, the entropy generation does not influence the solution of the momentum equation. The entropy generation quantities should, therefore, be considered as a postscalar phase.

For the steady-state solutions presented in this study, the concept of time stepping is somewhat artificial because the solution is brought to steady state from some arbitrary initial guess through a series of artificial transients.

**3.2 Benchmark Problem.** The procedure for calculating local entropy generation was benchmarked by comparing numerical results with an analytical solution for laminar flow in a circular duct with a constant wall heat flux. The problem was specifically structured so that the entropy generation caused by viscous dissipation and thermal gradients were of the same order. The benchmark problem involved the flow of 150°C helium at an average velocity of 8.75 m/s, through a circular duct with a diameter of 0.05 m. The duct was assumed to have a constant wall heat flux of 45 W/m<sup>2</sup>. The properties of helium were held constant for both the analytical and numerical evaluations. The analytical solutions for the velocity profile and

temperature profile are presented in Eqs. (5) and (6) (Kays and Crawford, 1980).

$$u = 2V \left( 1 - \frac{r^2}{r_o^2} \right) \quad (5)$$

$$T = T_o - \frac{\dot{q}_o''}{k} \left( \frac{3}{4} r_o + \frac{r^4}{4r_o^3} - \frac{r^2}{r_o} \right) \quad (6)$$

The local entropy generation rate then follows from the cylindrical form of Eq. (1) and is given by Eq. (7).

$$\dot{S}_{gen}'' = \frac{k \left\{ \frac{\dot{q}_o''}{k} \left( \frac{r^3}{r_o^3} - 2 \frac{r}{r_o} \right) \right\}^2}{\left\{ T_o - \frac{\dot{q}_o''}{k} \left( \frac{3}{4} r_o + \frac{r^4}{4r_o^3} - \frac{r^2}{r_o} \right) \right\}^2} + \frac{\mu \left( \frac{-4Vr}{r_o^2} \right)^2}{\left\{ T_o - \frac{\dot{q}_o''}{k} \left( \frac{3}{4} r_o + \frac{r^4}{4r_o^3} - \frac{r^2}{r_o} \right) \right\}^2} \quad (7)$$

The left and right portion of the right-hand side of the equation correspond to the entropy generation caused by the thermal gradients and viscous dissipation, respectively.

The benchmark problem was modeled with TEMPEST in two-dimensional cylindrical coordinates with an axis of symmetric around the duct centerline. An axial duct length of 36 m was used to assure that fully developed flow was being modeled. Uniform inlet flow and temperature profiles across the duct radius were assumed and the flow and temperature profiles were allowed to develop along the axial length of the duct. Local entropy generation profiles were computed at each of the radial nodes across the duct radius at the duct exit. The contributions to local entropy generation caused by thermal gradients and viscous dissipation were computed separately and then compared with the analytical solution. The wall temperature assumed for the analytical solution matched that used in the numerical simulation. Figure 1 presents a comparison of analytical and numerical local entropy generation across the duct radius.

The comparison demonstrates that both the TEMPEST code and the entropy generation subroutine function as expected for laminar flow. The (*k-e*) turbulence model used in TEMPEST has been thoroughly benchmarked for a variety of applications, and further benchmarking was not included in this study. Unlike laminar flow, analytical calculations of local entropy generation in turbulent flows were not identified in the literature. Therefore, the local entropy generation subroutine could not be benchmarked for turbulent flow. Instead, the local entropy generation subroutine was verified by comparing code results with manual calculations.

#### 4.0 Local Entropy Generation in an Impinging Jet

The calculation of local entropy generation provides an analyst with theoretically valid information on the spatial and temporal distribution of thermodynamic losses in a thermal process and on the tradeoffs associated with optimizing the process. We hypothesize that the availability of this information can be useful to an analyst by (1) focusing attention on significant sources of irreversibilities and (2) providing the objective function for optimizations. As part of this study, a sample problem was selected to demonstrate the calculation of local entropy generation in a complicated thermal process. The sample problem consisted of calculating the local entropy generation in an impinging jet. A schematic representation of the problem is shown in Fig. 2 and it consists of a jet of low-temperature fluid impinging on a heated wall. Impingement



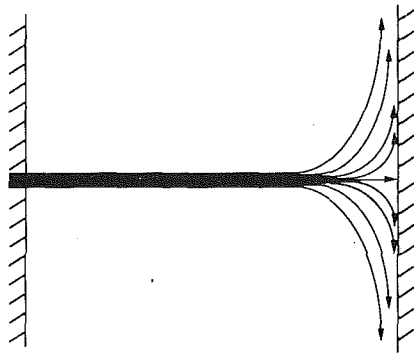


Fig. 2 Impinging jet

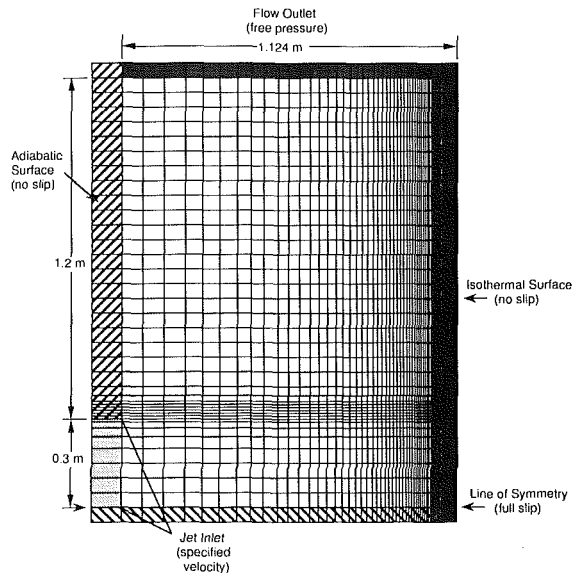


Fig. 3 Computational grid for the impinging jet problem

heat transfer has been used for turbine blade cooling, cooling of electronic components, and for air heating in solar thermal power applications. The goals of this evaluation were to:

- demonstrate the numerical calculation of local entropy generation in a complicated process
- demonstrate the application of the results by
  - evaluating the structure of local entropy generation
  - optimizing the jet Reynolds number.

**4.1 Problem Definition.** The impinging jet problem involves viscous dissipation near the jet inlet and along the impinging wall. This results in viscous entropy generation being concentrated in the same two regions. With surface heat transfer limited to the heated wall, the thermal entropy generation will primarily occur near the wall with turbulent mixing away from the wall producing local thermal gradients. Helium and glycerin were evaluated as heat transfer fluids. While helium is often used as a heat transfer fluid, glycerin was included as a limiting case where viscous dissipation becomes the dominant source of entropy generation, even at low velocities. Although TEMPEST and the associated entropy generation subroutine are fully transient and three dimensional, the impinging jet was modeled as a two-dimensional slot jet operating at steady state.

The physical arrangement and noding scheme used for evaluation of the impinging jet are shown in Fig. 3. The fluid jet enters the computational domain in the lower corner of the left vertical boundary with a uniform specified velocity. In the horizontal direction the computational domain is bounded by

Table 1 Simulation parameters

| No. | Fluid    | Jet Reynolds No.  | Prandtl No. | Thermal Boundary                 |
|-----|----------|-------------------|-------------|----------------------------------|
| 1a  | glycerin | $7.5 \times 10^2$ | 16610.0     | Isothermal                       |
| 1b  | glycerin | $7.5 \times 10^2$ | 16610.0     | Heat flux, 1830 W/m <sup>2</sup> |
| 2a  | helium   | $3.0 \times 10^3$ | 0.556       | Isothermal                       |
| 2b  | helium   | $3.0 \times 10^3$ | 0.556       | Heat flux, 150 W/m <sup>2</sup>  |
| 3a  | helium   | $3.0 \times 10^4$ | 0.556       | Isothermal                       |
| 3b  | helium   | $3.0 \times 10^4$ | 0.556       | Heat flux, 150 W/m <sup>2</sup>  |
| 4a  | helium   | $1.5 \times 10^5$ | 0.556       | Isothermal                       |
| 4b  | helium   | $1.5 \times 10^5$ | 0.556       | Heat flux, 150 W/m <sup>2</sup>  |
| 5a  | helium   | $3.0 \times 10^5$ | 0.556       | Isothermal                       |
| 5b  | helium   | $3.0 \times 10^5$ | 0.556       | Heat flux, 150 W/m <sup>2</sup>  |

two vertical walls, the left wall being an adiabatic, no-slip surface and the right wall being either an isothermal or constant heat flux, no-slip surface. The upper horizontal surface is an unspecified outflow/inflow boundary for which the flow conditions are computed. Due to the symmetry of the jet, only one-half of the jet needs to be simulated. This means that the lower boundary will be a line of symmetry located on the centerline of the jet. Therefore, the lower horizontal boundary is modeled as having a rigid free-slip flow condition, with an adiabatic surface. The inlet jet has a width of 0.3 m; the flow outlet covers the entire upper horizontal boundary with a width of 1.124 m. The vertical dimension of the computational domain was arbitrarily limited to 1.5 m.

The computational noding scheme consisted of a  $60 \times 40$  Cartesian grid with variable node spacing. The horizontal node spacing varied between 0.0711 m and 0.001 m, while the vertical node spacing varied between 0.05 m and 0.01 m. The high aspect ratio nodes were located near the vertical isothermal surface to capture the thermal and momentum boundary layers. Vertical node refinement was used to capture the shear layers of the jet as it entered the computational domain. All computations were performed on a Macintosh II computer configured either with a MC68020 processor, or a MC68030 processor and MC68882 coprocessor. Typical central processing unit (CPU) processing times for the latter machine were around 14 ms/time-step/cell.

The jet impingement problem was simulated using thermal property data for glycerin and helium. One glycerin and four helium jet velocities were evaluated. Two thermal boundary conditions were considered for each fluid type and inlet jet velocity: (1) an isothermal surface 10°C above the inlet jet temperature and (2) a constant surface heat flux. Viscosity, thermal conductivity, specific heat, and density were modeled as being independent of temperature. A total of 10 cases were simulated. The key parameters associated with the simulations are summarized on Table 1. The Reynolds number presented in Table 1 uses the diameter of the inlet jet as the characteristic length.

**4.2 Results.** The results from the 10 simulations are presented in three forms. First, the local entropy generation rate has been integrated over the complete computational domain for each of the simulations and the results have been tabulated. This is followed by a discussion of the structure of local entropy generation in several of the simulations. The last section presents the results of an error analysis.

The discussion of the results will focus on the insights afforded by computing and visualizing local entropy generation rates associated with an impinging jet. The graphic representations presented in this article were created by a procedure that converts the color image into a pseudo-gray-scale image through a palette of interconnected symbols. Where relevant, the palette, with its associated scale, is shown below each figure.

**4.2.1 Integrated Entropy Generation.** The results of local entropy generation analysis can be used to optimize a device because the local entropy generation rate can be integrated

**Table 2 Integrated entropy generation rates**

| No. | Viscous, W/K           | Thermal, W/K            | Total, W/K              | Flux, W/m <sup>2</sup> |
|-----|------------------------|-------------------------|-------------------------|------------------------|
| 1a  | 0.233                  | 0.145                   | 0.377                   | 1830                   |
| 1b  | 0.233                  | 0.129                   | 0.362                   | 1830                   |
| 2a  | $0.551 \times 10^{-5}$ | $0.2397 \times 10^{-1}$ | $0.2397 \times 10^{-1}$ | 275                    |
| 2b  | $0.551 \times 10^{-5}$ | $0.637 \times 10^{-2}$  | $0.638 \times 10^{-2}$  | 150                    |
| 3a  | $0.105 \times 10^{-2}$ | $0.865 \times 10^{-1}$  | $0.872 \times 10^{-1}$  | 944                    |
| 3b  | $0.105 \times 10^{-2}$ | $0.207 \times 10^{-2}$  | $0.313 \times 10^{-2}$  | 150                    |
| 4a  | 0.129                  | 0.149                   | 0.278                   | 1840                   |
| 4b  | 0.129                  | $0.998 \times 10^{-3}$  | 0.131                   | 150                    |
| 5a  | 0.921                  | 0.209                   | 1.130                   | 2740                   |
| 5b  | 0.921                  | $0.644 \times 10^{-3}$  | 0.933                   | 150                    |

over the complete process to yield one objective function that combines the impact of different thermodynamic losses. In the case of the impinging jet, the integrated total entropy generation can be used to optimize the design thermodynamically (minimizing irreversibilities). A component such as an impinging jet heat exchanger should be optimized as part of a complete system. By evaluating a completing system, impact on entropy generation in other components caused by design modifications to the jet can be determined. In this study, we are focusing on entropy generation within the impinging jet heat exchanger and have chosen to bound the problem by modeling and optimizing the jet as if it were an isolated component and have not considered its interaction with other components.

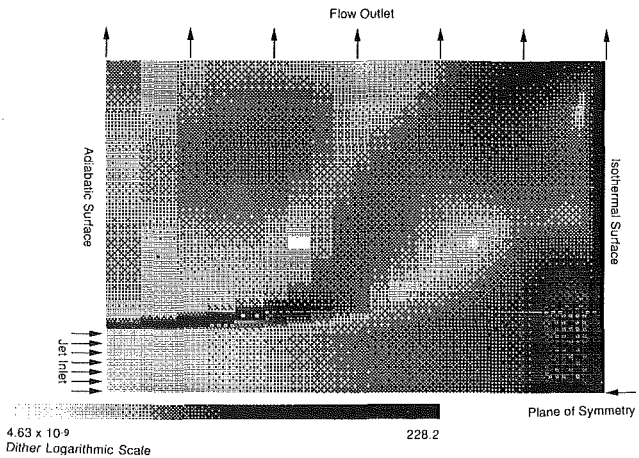
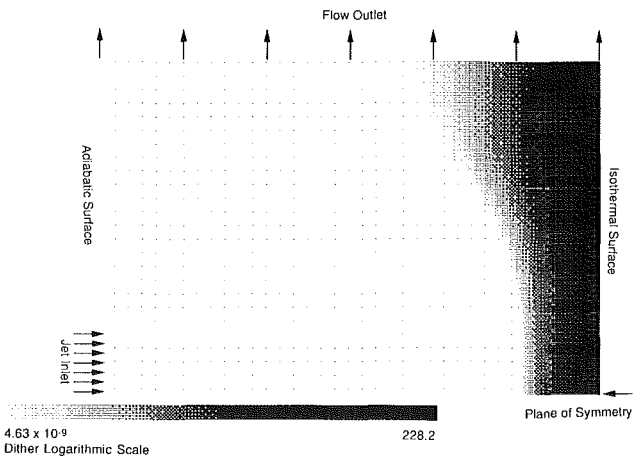
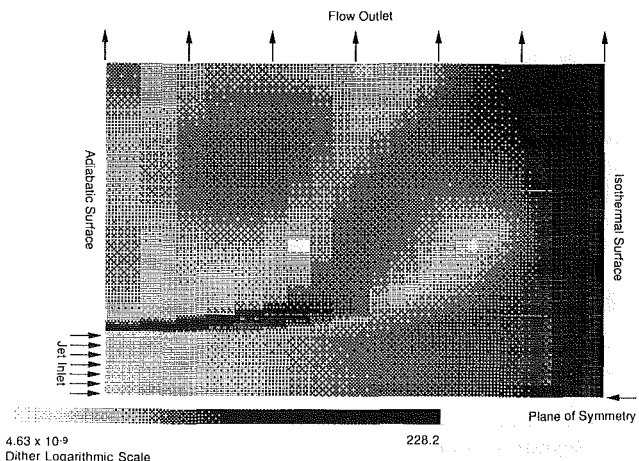
In this evaluation, the impact of three design variables on thermodynamic performance was explored. First, the influence of the heated wall boundary conditions on the integrated total entropy generation was investigated. The second evaluation examined the impact of the jet velocity (or jet Reynolds number) on total integrated entropy generation. The final evaluation compared helium with glycerin as a heat transfer fluid for an impinging jet.

Table 2 summarizes the integrated entropy generation rates resulting from the 10 simulations. The second through fourth columns in Table 2 present the local entropy generation rates integrated over the computational domain for entropy generation associated with viscous dissipation and thermal gradients, and total integrated entropy generation. The fifth column presents the average surface heat flux from the heat surface. For isothermal simulations the local heat flux was a complex function of the vertical wall position, fluid properties, and jet Reynolds number, with the maximum heat fluxes occurring at the jet center line.

A review of the results in Table 2 demonstrates several applications for local entropy generation calculations. There are three significant findings:

- **Boundary Conditions.** Simulations 1(a) and 1(b) have similar heat fluxes, allowing a meaningful comparison of integrated entropy generation. The comparison shows that for the conditions being considered, the boundary conditions have a negligible impact on the integrated entropy generation.

- **Optimum Jet Reynolds Number.** One of the objectives of the study was to determine the optimum jet Reynolds number. It was anticipated that the entropy generation due to viscous dissipation would increase with the jet Reynolds number, while the entropy generation due to thermal gradients would decrease, resulting in an optimum Reynolds number. A comparison of simulations 2(b), 3(b), 4(b), and 5(b) shows this to be the case. As expected, the integrated entropy generation caused by viscous dissipation increases with increasing Reynolds number as the integrated entropy generation caused by thermal gradients decreases. The minimum integrated total entropy generation occurs at a Reynolds number of approximately  $3.0 \times 10^4$ . This suggests that if the designer of an impinging jet heat exchanger wants to minimize thermodynamic losses in a heat exchanger with the characteristics of the

**Fig. 4 Viscous component of local entropy generation, W/K m<sup>3</sup> (No. 3a)****Fig. 5 Thermal component of local entropy generation, W/K m<sup>3</sup> (No. 3a)****Fig. 6 Total local entropy generation, W/K m<sup>3</sup> (No. 3a)**

sample problem, the device should be designed to operate with a jet Reynolds number around  $3.0 \times 10^4$ .

- **Heat Transfer Fluid Selection.** Simulations 1(a) and 4(a) were used to compare helium with glycerin as a heat transfer fluid because the integrated heat flux is similar for both simulations. The results show that the total entropy generation associated with using glycerin as the heat transfer fluid is significantly larger than the entropy generation rate associated with using helium. The results suggest that glycerin is not an

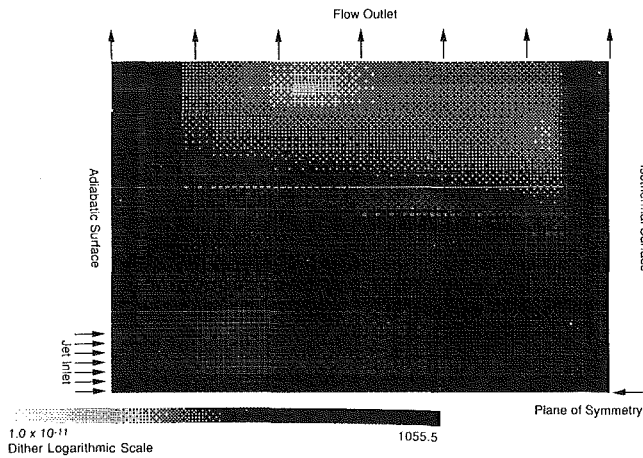


Fig. 7 Viscous component of local entropy generation, W/K m<sup>3</sup> (No. 1a)

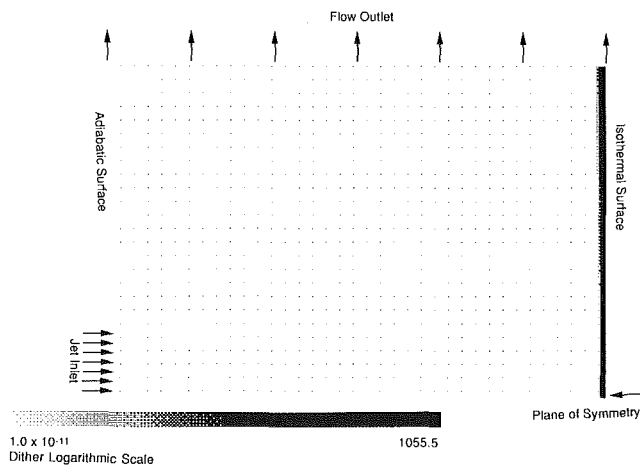


Fig. 8 Thermal component of local entropy generation, W/K m<sup>3</sup> (No. 1a)

attractive candidate for use in impingement heat exchangers when the heat exchanger is being optimized as an isolated component. While a rigorous comparison of heat transfer fluids was beyond the scope of this study, the use of integrated total entropy generation can provide a method of comparing alternative fluids.

Other design variables, such as the spacing between the jet and the heated wall and the angle of incident for the jet, could also be optimized using local entropy generation analysis, but the limited scope of this demonstration prevented further investigations.

**4.2.2 Local Entropy Generation.** The local entropy generation results are presented for two simulations. The first three figures show the components of local entropy generation and total entropy generation for case 3(a) (a helium jet with a jet Reynolds number of  $3.0 \times 10^4$ ). The last two figures show entropy generation due to viscous dissipation and thermal gradients for case 1(a) (a glycerin jet with a jet Reynolds number  $7.5 \times 10^2$ ).

Figures 4, 5, and 6 depict fields of local entropy generation rates for simulation 3(a), separated into the viscous dissipation component, thermal gradient component, and total entropy generation rate. The three figures are equivalently scaled using the natural logarithm of the entropy generation. The logarithmic scale ranges from  $4.63 \times 10^{-9}$  W/K m<sup>3</sup> to 228.2 W/K m<sup>3</sup>. The local entropy generation caused by viscous dissipation is shown in Fig. 4. The results show that local entropy generation caused by viscous dissipation is concentrated in the

shear layers near the jet inlet and the vertical wall boundary layers. Without logarithmic scaling, the detail in the figure is lost, with the perceivable entropy generation collapsing to a thin shear and boundary layer. Local entropy generation caused by thermal gradients is shown in Fig. 5, where it appears as an enlarged boundary layer along the heated vertical surface. The relatively high entropy generation rates that occur within the entrance shear layers of the jet result from the recirculating helium at elevated temperatures mixing with the cooler inlet jet fluid. The spatial distribution of total local entropy generation is presented in Fig. 6 and it shows that entropy generation caused by viscous dissipation dominates in the jet entrance shear region, while the thermal gradient component of local entropy generation dominates the boundary layer along the vertical heated wall. As one would expect, the observed distribution is strongly dependent on the flow structure and thermal boundary conditions.

The impinging jet was also simulated using glycerin as the heat transfer fluid. The components of local entropy generation for a glycerin jet impinging on an isothermal heated surface (simulation 1a) are depicted in Figs. 7 and 8. Figures 7 and 8 are scaled by the natural logarithm of entropy generation. The viscous dissipation component of local entropy generation is shown in Fig. 7 and it is quite different from its counterpart for the helium jet. A significant amount of entropy generation occurs in the glycerin jet as it decelerates upon entering the computational domain. Moreover, a more equal distribution of viscous dissipation is occurring along the adiabatic and heated vertical surfaces. This is in contrast to the helium jet simulation where the viscous dissipation was confined to the entrance shear region and the impingement wall boundary layer. These differences in the viscous dissipation fields are attributed to the differences between jet Reynolds numbers and fluid physical properties.

The results of the local entropy generation analysis show the structure of entropy generation. When helium is the jet fluid, the results show that entropy generation is concentrated in the boundary layer and that the analyst can understand the distribution of entropy generation by understanding the behavior of the boundary layer. When glycerin is used, entropy generation in the shear layer becomes much more important.

Local entropy generation has an additional application because it can be viewed as the fundamental source of cost generation in a process. While this issue was beyond the scope of the current study, in theory, it should be possible to assign a cost to each component of entropy generation. It would then be possible to produce figures similar to Figs. 4–8 that show the spatial distribution of cost generation.

**4.2.3 Error Analysis.** An estimate of the relationship between errors in the primitive variables of temperature and velocity, and errors in the entropy generation components may be made with a few assumptions. For the viscous dissipation component, it is assumed that:

$$\frac{\partial u}{\partial x} = \frac{\partial u}{\partial y} = \frac{\partial v}{\partial x} = \frac{\partial v}{\partial y}; \quad \text{and } \epsilon_u = \epsilon_v; \quad (8)$$

Then, an estimate of the error in the viscous component of entropy generation that corresponds to a level error in the velocity field may be expressed as follows, for a first-order finite difference scheme:

$$\epsilon_{sgv} = 32 \frac{\mu}{T} \left\{ \frac{\epsilon_v}{\Delta x} \frac{\Delta u}{\Delta x} + \frac{\epsilon_v^2}{\Delta x^2} \right\} \quad (9)$$

If the velocity gradient  $\Delta u/\Delta x$  is approximated by the gradient across the turbulent momentum boundary layer on the heated surface at the volume exit,  $\Delta x$  is approximated by the average node spacing, and the second term of Eq. (9) is ignored, a relation between an error in velocity and the viscous component

**Table 3 Relation between primitive errors and entropy errors**

| Jet Reynolds No.  | Viscous relation                                  | Thermal relation                                  |
|-------------------|---|---|
| $3.0 \times 10^3$ | $\epsilon_{sgv} = 2.97 \times 10^{-4} \epsilon_u$ | $\epsilon_{sgt} = 5.05 \times 10^{-2} \epsilon_T$ |
| $3.0 \times 10^4$ | $\epsilon_{sgv} = 4.74 \times 10^{-3} \epsilon_u$ | $\epsilon_{sgt} = 8.77 \times 10^{-2} \epsilon_T$ |
| $1.5 \times 10^4$ | $\epsilon_{sgv} = 3.28 \times 10^{-2} \epsilon_u$ | $\epsilon_{sgt} = 1.21 \times 10^{-1} \epsilon_T$ |
| $3.0 \times 10^5$ | $\epsilon_{sgv} = 7.54 \times 10^{-2} \epsilon_u$ | $\epsilon_{sgt} = 1.40 \times 10^{-1} \epsilon_T$ |

of entropy generation may be obtained. These relations are summarized in Table 3 for the helium simulations.

A similar analysis was performed on the error in the thermal component of entropy generation with dependence on the error in the temperature field. For the thermal error analysis it was assumed that

$$\frac{\partial T}{\partial x} = \frac{\partial T}{\partial y}; \quad (10)$$

The thermal gradient  $\Delta T/\Delta x$  was approximated by the gradient across the thermal boundary layer on the heated surface at the volume exit;  $\Delta x$  was approximated by the average node spacing; and the analogous term to the second term of Eq. (9) was ignored. The relations between an error in temperature and thermal component of entropy generation are also summarized in Table 3 for the helium simulations.

In all cases the error resulting from the first-order finite difference scheme is small compared to the calculated entropy generation.

## 5.0 Conclusions

The results of this study confirm the feasibility of numerical calculation of local entropy generation in complicated thermal processes. Specific conclusions concerning the feasibility of numerical calculation of local entropy generation include:

- The integration of local entropy generation calculations into an existing CFD code proved to be straightforward and did not significantly increase run time.
- The comparison of numerical and analytical results for a simple benchmarking problem was successful.

Specific conclusions concerning the usefulness of numerical calculation of local entropy generation include:

- Numerical calculations allowed the investigation of the structure of local entropy generation in thermal processes. The results showed that for the sample problem, entropy generation is concentrated in the boundary layer. To a great extent, understanding the boundary layer will allow an understanding of local entropy generation.
- Numerical calculations were used to optimize the design of the impinging jet heat exchanger. The results of the study showed that there is an optimum jet Reynolds number that minimizes the entropy generation in the impinging jet and suggests a procedure for evaluating heat transfer fluids.

Based on the results of this study, we have made several recommendations for future research:

- Given the simplicity and potential usefulness of including local entropy generation calculations in CFD codes, CFD code developers should be encouraged to incorporate local entropy generation calculation in a wide range of simulation tools.
- Local entropy generation calculations should be expanded to involve more complicated processes including multiple phases, multiple components, reacting flows, compressible flows, and radiation heat transfer.

## Acknowledgments

Pacific Northwest Laboratory is operated for the U.S. Department of Energy by Battelle Memorial Institute under Contract No. DE-AC06-76RL0 1830. Funding for the research presented in the paper was provided by the U.S. Department of Energy's Energy Conversion and Utilization Technology Program.

## References

- Argrow, B. M., Emanuel, G., and Rasmussen, M. L., 1987, "Entropy Production in Nonsteady General Coordinates," *AIAA Journal*, Vol. 25, pp. 1629-1631.
- Bejan, A., 1979a, "A Study of Entropy Generation in Fundamental Convective Heat Transfer," *ASME JOURNAL OF HEAT TRANSFER*, Vol. 101, pp. 718-725.
- Bejan, A., 1979b, "Second Law Analysis in Heat Transfer," presented at workshop on "The Second Law of Thermodynamics," George Washington University, Washington, DC, Aug. 14-16.
- Bejan, A., 1982, *Entropy Generation Through Heat and Fluid Flow*, Wiley Interscience, New York.
- Drost, M. K., and Zaworski, J. R., 1988, "A Review of Second Law Analysis Techniques Applicable to Basic Thermal Science Research," in: *Thermodynamic Analysis of Chemically Reactive Systems*, ASME, New York, pp. 7-12.
- Dunbar, W. R., 1982, "Computer Simulation of a High Temperature Solid Electrolyte Fuel Cell," M.S. Thesis, Marquette University, Milwaukee, WI.
- El-Sayed, Y., 1988, "On Exergy and Surface Requirements for Heat Transfer Processes Involving Binary Mixtures," in: *Second Law Analysis in Heat/Mass Transfer and Energy Conversion*, ASME, New York, pp. 19-24.
- Gaggioli, R. A., 1983, "Second Law Analysis for Process and Energy Engineering," in: *Efficiency and Costing, Second Law Analysis of Processes*, ACS 235, American Chemical Society, Washington, DC.
- Govy, M., 1889, "Sur l'Énergie Utilisable," *J. Physics*, Vol. 8, p. 501.
- Hutchinson, R. A., and Lyke, S. E., 1987, "Microcomputer Analysis of Regenerative Heat Exchangers for Oscillating Flows," in: *Proceedings: 1987 ASME/JSME Thermal Engineering Joint Conference*, Vol. 2, ASME, New York, p. 653.
- Kays, M. W., and Crawford, M. E., 1980, *Convective Heat and Mass Transfer*, 2nd ed., McGraw-Hill Company, New York.
- Liang, H., and Kuehn, T. H., 1988, "Irreversibility Analysis of a Water to Water Mechanical Compression Heat Pump," in: *Analysis and Applications of Heat Pumps*, ASME, New York, pp. 31-36.
- Stodola, A., 1910, *Steam and Gas Turbines*, McGraw-Hill, New York.
- Trent, D. S., Eyler, L. L., and Budden, M. J., 1989a, *TEMPEST—A Three-Dimensional Time-Dependent Computer Program for Hydrothermal Analysis, Vol. 1: Numerical Methods and User Input*, PNL-4348, Vol. 1, Rev. 2, Pacific Northwest Laboratory, Richland, WA.
- Trent, D. S., Eyler, L. L., and Budden, M. J., 1989b, *TEMPEST—A Three-Dimensional Time-Dependent Computer Program for Hydrothermal Analysis, Vol. 2: Assessment and Verification Results*, PNL-4348, Vol. 2, Rev. 2, Pacific Northwest Laboratory, Richland, WA.
- Van Wylen, J. G., and Sonntag, R. E., 1973, *Fundamentals of Classical Thermodynamics*, Wiley, New York.

# Analysis of Matrix Heat Exchanger Performance

G. Venkatarathnam

S. Sarangi

Process Equipment and Design Laboratory,  
Cryogenic Engineering Centre,  
Indian Institute of Technology,  
Kharagpur—721302, India

Matrix heat exchangers, invented forty years ago, have found widespread applications during the last two decades. Because of their unique construction, they satisfy the diverse requirements of high compactness, high transfer coefficient, low axial conductivity, and uniform flow distribution. The heat transfer mechanism in these exchangers is quite complex. Convective heat transfer takes place in the pores as well as in the front and rear faces of the plates. Conduction heat transfer takes place in two directions: between the streams through the perforated plates, and along the separating wall in the axial direction. The five sources of heat transfer are strongly coupled with each other. The governing equations have been derived and simplified using well-justified assumptions. The discrete structure of the exchanger helps in reducing the partial differential equations to sets of algebraic and ordinary differential equations. A numerical scheme is presented for solving these equations. Its use is illustrated with two examples.

## Introduction

A matrix heat exchanger (MHE) essentially consists of a stack of perforated plates of high-conductivity metal (e.g., copper, aluminum) alternating with spacers made of a low-conductivity material (e.g., plastics, stainless steel). The spacers are cut out of solid sheets in such a way that two or more passages are created for the fluid streams. The alternate layers of perforated plates and spacers are bonded together along with a suitable header at each end. The resulting monoblock unit contains two or more passages through which fluid streams can flow in a countercurrent fashion exchanging heat with each other through the conducting plates. The spacers serve the multiple purposes of providing seals between the channels, reducing axial heat conduction, promoting turbulence by interrupting boundary layer growth, and eliminating flow maldistribution by providing intermediate headering. Figure 1 illustrates the geometry of a typical matrix heat exchanger.

Matrix heat exchangers, first introduced by McMahon et al. (1950), have changed considerably during the last four decades. While they were originally conceived for use in large air separation systems, today they are used mainly, though not exclusively, in small refrigerators operating at liquid helium temperature. Commercially available punched sheets have been replaced by custom-designed perforated plates manufactured by chemical milling processes; neoprene gaskets and steel tie rods have given way to exotic plastic spacers and epoxy adhesives (Fleming, 1969). Diffusion-bonded all-metal heat exchangers (Bova et al., 1978; Harada et al., 1986) using copper perforated plates and stainless steel spacers have enhanced operating pressures, leak tightness, and reliability. In coming years they are expected to play a significant role in the development of compact and efficient cryorefrigerators utilizing reciprocating and turbine expanders.

The heat transfer process in a matrix heat exchanger is quite complex. The total heat transfer resistance between the two fluid streams is composed of the following parts:

- convective heat transfer between the hot fluid stream and perforated plates;
- conduction along the perforated plates up to the separating wall;
- conduction across the separator;

- conduction along the perforated plates from the separator; and
- convective heat transfer between perforated plate and cold fluid stream.

This description appears similar to that of a conventional heat exchanger with fins on both sides. The peculiarities of the matrix exchanger are manifested when one tries to find the heat transfer correlations, fin efficiencies, and the role of the separator.

## Definition of the Problem

The plates of the MHE have often been considered as fins with an efficiency between 0.4 and 0.6 (Fleming, 1969). There is a considerable temperature gradient along the plates and the fin formula does not represent the heat transfer process cor-

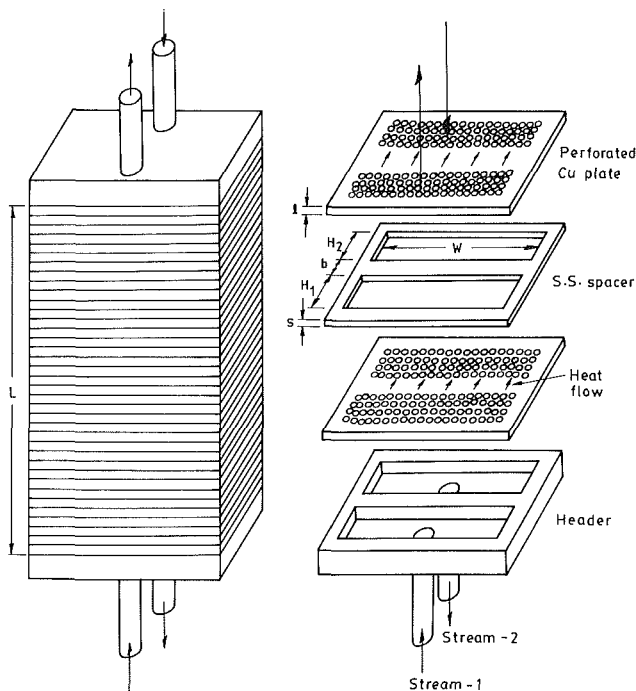


Fig. 1 Schematic of a perforated plate matrix heat exchanger showing different dimensions

Contributed by the Heat Transfer Division for publication in the JOURNAL OF HEAT TRANSFER. Manuscript received by the Heat Transfer Division December 15, 1989, revision received December 24, 1990. Keywords: Cryogenics, Heat Exchangers, Modeling and Scaling.

rectly. The plate and fluid temperatures vary in both axial and lateral directions. In addition, the wall is heterogenous and the number of plates is finite. Because of the above factors, standard heat exchanger formulas cannot be directly applied to matrix heat exchangers. The governing equations have to be integrated to predict the performance of these exchangers under any particular set of conditions.

In forthcoming sections, governing equations have been derived for heat transfer in a matrix heat exchanger with two parallel rectangular channels. The system of partial differential equations has been simplified using justifiable assumptions. The partial differential equations are reduced to sets of algebraic and ordinary differential equations. These equations have been solved for some specific inputs and the results have been compared with results obtained by other methods available in the literature.

## Review of Literature

The first major attempt toward modeling matrix heat exchangers was the work of Fleming (1969). Fleming's approach was to use standard heat exchanger relations, the perforated plate being considered as the secondary surface or a fin with a certain fin efficiency. However, unlike the standard problem where a fin is exposed to a fixed fluid temperature, Fleming assumed a constant temperature difference between the fin and the fluid. Instead of the usual hyperbolic tangent expression for the fin efficiency, he derived the following relation:

$$\eta_{\text{fin}} = \left[ 1 + \frac{m^2 H^2}{3} \right]^{-1} \quad (1)$$

where  $m^2 = hA'''/k_p$ ;  $h$  = transfer coefficient;  $k_p$  = effective thermal conductivity of the plates in the transverse direction;  $H$  = plate height (fin height); and  $A'''$  = heat transfer area per unit volume of the plate.

Although an MHE is made up of plates and spacers, it is often treated as being essentially uniform in the axial direction. An alternative approach, where the MHE was treated as a discrete set of plate-spacer pairs, was adopted by Sarangi and Barclay (1984). They assumed that the full temperature drop in the axial direction took place over the spacers, neglecting any temperature gradient along the plates. They used the prin-

ciple of superposition to suggest the following expressions for the effectiveness of a high- $N_{tu}$  exchanger with  $n$  plates:

$$\epsilon = \frac{1 - p^n}{1 - \nu p^n} + \frac{1 - \nu q^{n-1}}{1 - \nu^2 q^{n-1}} - \frac{1 - \nu^n}{1 - \nu^{n+1}} \quad (2)$$

with

$$p = \frac{\mu + \alpha_1}{1 + \mu\alpha_2}; \quad q = \frac{\nu(1 + n\lambda)}{1 + \nu n\lambda} \quad \text{and} \quad \mu = \frac{1 - \alpha_1}{1 - \alpha_2} \nu$$

where  $\alpha = \exp(-N_{tu}/n)$  is the  $N_{tu}$  per plate for each side,  $\nu$  = heat capacity rate ratio, and  $\lambda$  is an axial conduction parameter.

For balance flow operation, Eq. (2) reduces to:

$$\epsilon = \frac{n(1 - \alpha_1)(1 - \alpha_2)}{n(1 - \alpha_1)(1 - \alpha_2) + (1 - \alpha_1\alpha_2)} + \frac{n(1 + \lambda)}{1 + n(1 + 2\lambda)} - \frac{n}{n + 1} \quad (3)$$

The derivation of these formulas is based on the principle that in high-effectiveness exchangers the ineffectiveness due to different sources can be added to give the total ineffectiveness. Based on Eqs. (2) and (3), Sarangi and Barclay (1984) have shown that there is a limit to the effective  $N_{tu}$  of a matrix heat exchanger and that the limit is 1.0 per plate for balanced flow operation. Experimental results, recently reported by Hubbel and Cain (1986), support this conclusion. It should be noted that Hubbel and Cain have incorrectly attempted to fit a straight line to their experimental data ignoring the effect of finite number of plates. Sarangi and Barclay (1984) imply a perfect fin (i.e.,  $\eta_{\text{fin}} = 1$ ) and ignore the temperature gradient in the lateral direction.

The most extensive analytical studies on matrix heat exchanger performance are from Babak and co-workers. In their initial model (1983) the authors neglected axial conduction and considered the exchanger as a homogeneous medium with fixed transverse conductivity. The authors define an effective conductivity  $k_e$ , which includes the conductivity of the perforated plates as well as the convective film coefficient in the perforations. This enables them to represent both the matrix and the fluid by a single temperature, which is a function of the axial coordinate  $z$  and the transverse coordinate  $y$ . By performing an energy balance over a differential control volume  $Wdzdy$ , the authors derive the equation:

## Nomenclature

$A'''$  = heat transfer area/unit volume of plates,  $\text{m}^2/\text{m}^3$   
 $b$  = spacer width, m  
 $C$  =  $WHGc_p$  = heat capacity, rate W/K  
 $c_p$  = fluid specific heat at constant pressure, J/kg·K  
 $d$  = perforation diameter, m  
 $F$  = constant = +1 for stream 1; -1 for stream 2  
 $G$  = mass velocity in header, kg/ $\text{m}^2 \cdot \text{s}$   
 $h$  = heat transfer coefficient, W/ $\text{m}^2 \cdot \text{K}$   
 $H$  = plate height, m  
 $k$  = thermal conductivity, W/m·K  
 $l$  = plate thickness, m  
 $L$  = overall length of the exchanger, m  
 $m$  = fin parameter,  $\text{m}^{-1}$   
 $n$  = number of plates in the exchanger  
 $N_{tu}$  = number of heat transfer units

$P$  = porosity of plate  
 $q$  = heat transfer rate at the plate-separator interface, W  
 $s$  = thickness of spacer, m  
 $t$  = fluid temperature, K  
 $T$  = plate temperature, K  
 $y$  = transverse coordinate, m  
 $W$  = plate width, m  
 $z$  = axial coordinate, m  
 $\alpha$  =  $\exp(-N_{tu}/n)$   
 $\epsilon$  = heat exchanger effectiveness  
 $\eta_{\text{fin}}$  = fin efficiency  
 $\eta$  = dimensionless transverse coordinate defined by Eq. (12)  
 $\theta$  = dimensionless fluid temperature defined by Eq. (12)  
 $\lambda_s$  = axial conduction parameter per plate defined by Eq. (28)  
 $\lambda$  =  $\lambda_s/n$  = overall axial conduction parameter  
 $\lambda_p$  = spacer lateral conduction parameter defined by Eq. (28)

$\nu$  =  $C_1/C_2$  = heat capacity rate ratio  
 $\tau$  = dimensionless plate temperature defined by Eq. (12)  
 $\phi$  = plate conduction parameter defined by Eq. (12)  
 $\chi$  = dimensionless heat transfer rate at the separator-plate interface defined by Eq. (18)

### Subscripts

$e$  = effective  
 $f$  = fluid  
 $i$  = fluid stream index  
 $is$  = plate-separator interface of  $i$ th channel  
 $j$  = plate index  
 $p$  = plate (perforated region)  
 $P$  = plate (unperforated region), plate material  
 $s$  = separating wall  
 $1, 2$  = fluid streams (1: smaller heat capacity rate)

$$(Gc_p)_i \frac{\partial T_i}{\partial z} = k_{e,i} \frac{\partial^2 T_i}{\partial y^2}, \quad i = 1, 2 \quad (4)$$

with appropriate boundary conditions. In this relation  $G$  is the mass velocity in the header,  $c_p$  the fluid specific heat at constant pressure, and  $k_e$  the effective thermal conductivity of the perforated plate. The subscript  $i$  refers to the channel number.

Equations (4) have been solved analytically by separation of variables. Using a "series solution" approach Babak and co-workers have expressed the performance of the exchanger in terms of four dimensionless quantities:  $X$ ,  $Y$ ,  $Z$ , and  $P$ . Many limiting cases have been worked out in detail. This model may be termed a "continuum model," because it does not take into account the "discrete" nature that typifies a matrix heat exchanger.

In subsequent publications (1985a, 1986) these authors have further extended this technique to many different cases and presented the results graphically (1986). By considering about 20 terms in the series and using a computer, they determined the effective  $N_{tu}$  of the MHE with an accuracy of better than 2 percent (1985a). The expressions are quite complex. Unlike simpler analytical relations these expressions do not provide any physical insight into the heat transfer process.

In a later paper (1985b) the authors have utilized the finite difference method instead of the analytical approach in solving the equations. However, instead of considering the entire exchanger, they considered only one channel subjected to a constant heat flux (independent of axial coordinate). In that analysis, the discrete structure of the exchanger has been ignored and convective heat transfer resistance has not been considered separately. They have, however, considered axial conduction in the separating wall. Since the plates and spacers are in parallel for lateral conduction but in series for axial conduction, the effective conductivities in these two directions are different.

$$k_{\text{transverse}} = \frac{lk_p + sk_s}{s+l} \quad (5a)$$

$$k_{\text{axial}} = (s+l) / \left( \frac{l}{k_p} + \frac{s}{k_s} \right) \quad (5b)$$

The results of this numerical model are in reasonable agreement with the experimental data of Mikulin et al. (1979).

A review of the available literature shows that a detailed analysis of the complete exchanger, which considers both convective and conductive resistances including axial conduction, as well as the distinctively discrete nature of the MHE, was yet to be attempted. Such an analysis is required not only for rating and sizing of matrix heat exchangers, but also to evolve a proper procedure for reducing the experimental data on heat transfer coefficients. The present paper is an effort in that direction.

## Mathematical Model

Let us consider a matrix heat exchanger consisting of  $n$  perforated plates each of thickness  $l$ , separated by spacers of thickness  $s$ . The diameter of the holes in the plates is  $d$ . Two rectangular slots of dimensions  $W \times H_i$  are cut in the spacers,  $H$  being the dimension in the heat flow direction. The two channels are separated by the separator of width  $b$  and the overall length of the exchanger is  $L$ . These dimensions are illustrated in Fig. 1.

**Heat Transfer in the Plates.** In practice, matrix heat exchangers are made of thin plates of highly conducting materials. Plate thickness and hole diameter are typically in the range of 0.5 to 2 mm. The Nusselt number for the flow generally lies in the range of 4 to 40. Considering the plates to be made of copper (conductivity  $k_p = 400$  W/mK) and the working fluid to be helium gas ( $k_f = 0.15$  W/mK), a reasonable

estimate of the Biot number in the fluid flow direction is given as

$$\text{Bi} = \frac{hl}{k_p} = \text{Nu} \frac{l}{d} \frac{k_f}{k_p} \quad (6)$$

Substituting the figures given above,

$$\text{Bi} = (40)(1) \left( \frac{0.15}{400} \right) = 0.015$$

At such small values of Bi, the plates can be considered isothermal in the fluid flow direction, which has been experimentally confirmed by Kirpikov and Leifman (1972). Thus, the temperature of any particular plate in channel ( $i$ ), designated by its serial number  $j$  counted from the entrance of channel (1), can be represented by the function  $T_{i,j}(y)$ ,  $y$  being the transverse coordinate.

Plate temperature changes from plate to plate over the spacer elements. Fluid temperature changes as it flows through the perforations, remaining constant over the space between the plates.  $t_{i,j}(y)$  represents the temperature of the fluid in stream  $i$  at transverse coordinate  $y$  as it enters the  $j$ th plate. It leaves the  $j$ th plate with temperature  $t_{i,j+1}(y)$ . Let  $t(y, z)$  represent the fluid temperature inside the plates. Figure 2 shows a longitudinal section of the heat exchanger highlighting the energy balance over two control volumes. The positive  $z$  direction is in the direction of fluid stream 1 and the positive  $y$  direction is from stream 1 to stream 2.  $y_1$  is 0 at the boundary and  $H_1$  at the separator.  $y_2$  is 0 at the separator and  $H_2$  at the boundary. Figure 2(a) shows a differential control volume  $Wdydz$  in the flow passages, whereas Fig. 2(b) shows a differential control volume in the separating wall. The energy balance over the control volumes yields the governing equations.

An energy balance over the fluid contained in the differential volume element  $Wdydz$  (Fig. 2a) in either of the channels gives:

$$\frac{\partial t}{\partial z} = F \left( \frac{hA''}{Gc_p} \right)_i (T_{i,j} - t) \quad (7)$$

where  $h$  = heat transfer coefficient;  $G$  = fluid mass velocity;  $c_p$  = fluid specific heat; and  $F$  is a constant equal to +1 for stream 1 and -1 for stream 2. An energy balance over the same volume element  $Wdydz$  containing both the fluid and the matrix yields:

$$\frac{d^2 T_{i,j}}{dy_i^2} = \left( F \frac{Gc_p}{k_p} \right)_i \frac{\partial t}{\partial z} \quad (8)$$

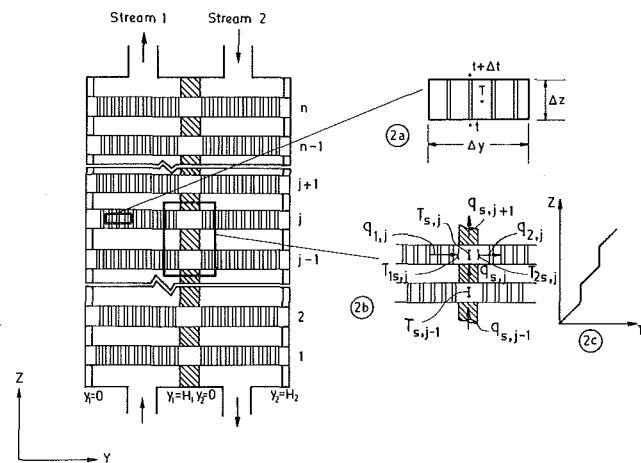


Fig. 2 Longitudinal section of a MHE. Inset (2a) shows the control volume for energy balance in the plates and inset (2b) shows the control volume for energy balance in the separating wall. Figure (2c) shows the temperature profile along the center line

where  $k_p$  is the effective thermal conductivity of the matrix in the heat flow direction, which is normal to the fluid flow direction. Conduction heat transfer in the  $z$  direction is ignored because of the isothermal condition of the plate.

Equations (7) and (8) are the governing differential equations over a single plate. They do not represent the space between the plates. Integrating Eq. (7) for a fixed value of  $y$  over a particular plate ( $j$ th plate), i.e., within the limits  $z = 0$  to  $z = l$ , we obtain the following relation between the fluid temperatures on both sides of a single plate:

$$\frac{t_{i,j+1} - T_{i,j}}{t_{i,j} - T_{i,j}} = \exp\left(\frac{F - hA''l}{Gc_p}\right) \quad (9)$$

Equation (9) is valid for both individual streams. Defining  $N_{u,f,i} = (hA''l/Gc_p)_i$  as the "Nu on one side of a single plate," we can express Eq. (9) as:

$$t_{1,j+1} = T_{1,j} + \exp(-N_{u,f,1})(t_{1,j} - T_{1,j}) \quad (10a)$$

and

$$t_{2,j} = T_{2,j} + \exp(-N_{u,f,2})(t_{2,j+1} - T_{2,j}) \quad (10b)$$

Equation (10) provides two different expressions for stream 1 and stream 2. For stream 1 the recurrence relation is in increasing order of  $j$  and for stream 2 it is the reverse, to match the different fluid flow directions. These equations are valid for any value of the transverse coordinate  $y$ .

Integration of Eq. (8) in the  $z$  direction for  $z = 0$  to  $z = l$  over a plate element gives:

$$\frac{d^2 T_{i,j}}{dy_i^2} = F \left( \frac{Gc_p}{k_p l} \right) (t_{i,j+1} - t_{i,j})$$

which, when combined with Eq. (10), reduces to the following pair of equations:

$$\frac{d^2 T_{1,j}}{dy_1^2} = \left( \frac{Gc_p}{k_p l} \right) [1 - \exp(-N_{u,f,1})] (T_{1,j} - t_{1,j}) \quad (11a)$$

$$\frac{d^2 T_{2,j}}{dy_2^2} = \left( \frac{Gc_p}{k_p l} \right) [1 - \exp(-N_{u,f,2})] (T_{2,j} - t_{2,j+1}) \quad (11b)$$

Equations (10) and (11) are the governing equations for both channels of the heat exchanger. Before developing these equations further, let us express them in dimensionless form utilizing the following dimensionless variables and parameters:

$$\theta = \frac{t - t_{2,in}}{t_{1,in} - t_{2,in}}; \quad \tau = \frac{T - t_{2,in}}{t_{1,in} - t_{2,in}}; \quad \eta_i = \frac{y}{H_i};$$

$$N_{u,p,i} = \frac{k_p l}{(Gc_p H^2)_i} \text{ and } \phi_i = \frac{N_{u,p,i}}{N_{u,f,i}} \quad (12)$$

$N_{u,p,i}$  may be termed as the plate conduction  $N_{u,p}$  for the  $i$ th channel and  $\phi_i$ , a plate conduction parameter.

Equations (10) and (11) can be written as:

$$\theta_{1,j+1} = \tau_{1,j} + \exp(-N_{u,f,1}) (\theta_{1,j} - \tau_{1,j}) \quad (13a)$$

$$\theta_{2,j+1} = \tau_{2,j} + \exp(-N_{u,f,2}) (\theta_{2,j+1} - \tau_{2,j}) \quad (13b)$$

and

$$\frac{d^2 \tau_{1,j}}{d\eta_1^2} = \frac{1 - \exp(-N_{u,f,1})}{\phi_1 N_{u,f,1}} (\tau_{1,j} - \theta_{1,j}) \quad (14a)$$

$$\frac{d^2 \tau_{2,j}}{d\eta_2^2} = \frac{1 - \exp(-N_{u,f,2})}{\phi_2 N_{u,f,2}} (\tau_{2,j} - \theta_{2,j+1}) \quad (14b)$$

Equations (13) are two sets of  $n$  algebraic equations in dimensionless fluid temperature  $\theta_{i,j}$  ( $2 \leq j \leq n + 1$  for stream 1 and  $n \geq j \geq 1$  for stream 2), for any value of the transverse coordinate  $\eta$ . Since the two fluid inlet temperatures  $T_{1,in}$  and  $T_{2,in}$  are specified, we have:

$$\theta_{1,1} = 1 \text{ and } \theta_{2,n+1} = 0 \quad (15)$$

Equations (14) are two sets of a second-order ordinary differential equation in  $\tau_{i,j}$  ( $j = 1$  to  $n$  and  $i = 1$  to  $2$ ). Because the boundaries  $y_1 = 0$  and  $y_2 = H_2$  are insulated, the boundary conditions are given by the relations

$$\frac{dT_{1,j}}{dy_1} = 0 \text{ at } y_1 = 0 \text{ and } \frac{dT_{2,j}}{dy_2} = 0 \text{ at } y_2 = H_2$$

which in dimensionless form become

$$\frac{d\tau_{1,j}}{d\eta_1} = 0 \text{ at } \eta_1 = 0 \text{ and } \frac{d\tau_{2,j}}{d\eta_2} = 0 \text{ at } \eta_2 = 1 \quad (16)$$

At the other boundaries, i.e., at  $\eta_1 = 1$  and at  $\eta_2 = 0$ , the boundary conditions are closely related to the heat transfer process in the separator.

The heat transfer rate from or to the  $i$ th stream through the  $j$ th plate is given as

$$q_{i,j} = -k_p W l \frac{dT_{i,j}}{dy_i} \quad (17)$$

where  $dT_{i,j}/dy_i$  is computed at the separator boundary, i.e., at  $y_1 = H_1$  and at  $y_2 = 0$ . Defining a dimensionless heat flow rate,

$$\chi_{i,j} = q_{i,j} / (WHGc_p)_i (t_{1,in} - t_{2,in}) \quad (18)$$

Eq. (17) can be rewritten as

$$\chi_{i,j} = -N_{u,p,i} \frac{d\tau_{i,j}}{d\eta_i} = -\phi_i N_{u,f,i} \frac{d\tau_{i,j}}{d\eta_i} \quad (19)$$

$d\tau_{i,j}/d\eta_i$  is computed at  $\eta_1 = 1$  and at  $\eta_2 = 0$ . For convenience, let us define the two boundary temperatures  $T_{is,j}$  as follows:

$$T_{1s,j} = T_{1,j} (y_1 = H) \text{ and } T_{2s,j} = T_{2,j} (y_2 = 0) \quad (20)$$

In dimensionless form,

$$\tau_{1s,j} = \tau_{1,j} (\eta_1 = 1) \text{ and } \tau_{2s,j} = \tau_{2,j} (\eta_2 = 0) \quad (21)$$

**Heat Transfer in the Separator.** If the separating wall is considered uniform in all directions, the standard Fourier conduction equation can be written as:

$$k_{s,y} \frac{\partial^2 T_s}{\partial y^2} + k_{s,z} \frac{\partial^2 T_s}{\partial z^2} = 0 \quad (22)$$

where  $k_{s,y}$  and  $k_{s,z}$  are the effective mean conductivity in the transverse and longitudinal directions, respectively (see Eqs. (5)).

Formulation of the heat transfer process in the separator in terms of the continuum approach described above leads to some difficulties. The plates have been assumed isothermal in the  $z$  direction over the length  $l$ , whereas Eq. (22) predicts a finite temperature change over the same distance. It is also difficult to state the boundary conditions correctly. Although these difficulties can be circumvented with suitable approximations, we have chosen an alternative approach, which makes the solution of the problem substantially simpler while still maintaining sufficient overall accuracy. The following assumptions are made:

1 The temperature of a plate is constant over its thickness ( $z$  direction). The whole temperature drop occurs along the spacer elements.

2 Inside the separator, temperature profiles in the plates are linear in the transverse direction.

3 For the purpose of estimating axial conduction effects, an average of the temperature on both sides of the separator ( $y_s = 0$  and  $y_s = b$ ) is taken as the temperature of the separator at any cross section.

Temperatures on both sides of the wall of the  $j$ th plate are related to the average heat flux by the relation:

$$\frac{q_{1,j} + q_{2,j}}{2} = \frac{k_p W l}{b} (T_{1s,j} - T_{2s,j}) \quad (23)$$



Defining the axial heat flow  $q_{s,j}$  as the rate of heat flow into the separator portion of the  $j$ th plate from the  $(j-1)$ th plate and considering an energy balance over the separator portion of the  $j$ th plate (Fig. 2b) results in

$$q_{1,j} - q_{2,j} = q_{s,j+1} - q_{s,j} \quad (24)$$

$$q_{s,j} = \frac{k_s W b}{s} (T_{s,j-1} - T_{s,j}) \quad (25a)$$

where using assumption (3),  $T_{s,j} = (T_{1s,j} + T_{2s,j})/2$ .

Since the two ends of the exchanger are insulated,

$$q_{s,1} = 0 \quad \text{and} \quad q_{s,n+1} = 0 \quad (25b)$$

Substituting Eqs. (25) into Eq. (24) and expressing the results in dimensionless form gives the following relations:

$$\chi_{1,j} - \frac{\chi_{2,j}}{\nu} = \lambda_s (2\tau_{s,j} - \tau_{s,j-1} - \tau_{s,j+1}) \quad 2 \leq j \leq n-1 \quad (26a)$$

$$\chi_{1,1} - \frac{\chi_{2,1}}{\nu} = \lambda_s (\tau_{s,1} - \tau_{s,2}) \quad (26b)$$

$$\chi_{1,n} - \frac{\chi_{2,n}}{\nu} = \lambda_s (\tau_{s,n} - \tau_{s,n-1}) \quad (26c)$$

Equation (23) can also be expressed in dimensionless form as

$$\chi_{1,j} + \frac{\chi_{2,j}}{\nu} = 2\lambda_p (\tau_{1s,j} - \tau_{2s,j}) \quad (27)$$

where  $\nu$  is the capacity rate  $(WHGC_p)_1 / (WHGC_p)_2$  and  $\lambda_p$  and  $\lambda_s$  are lateral and axial conduction parameters of the separator defined as

$$\lambda_p = \frac{k_p l}{(bHGc_p)_1} \quad \text{and} \quad \lambda_s = \frac{k_s b}{(sHGc_p)_1} \quad (28)$$

$\lambda_s$  is related to the overall axial conduction parameter  $\lambda$  (Sarangi and Barclay, 1984; Kroeger, 1967) as  $\lambda_s = n\lambda$ .

The partial differential Eq. (22) has now been replaced by the two sets of algebraic Eqs. (26) and (27). These equations, in fact, serve as the boundary conditions for the two sets of differential equations in Eq. (14).

**Governing Equations.** The governing equations for the entire exchanger can now be summarized as follows (this rearrangement helps in framing the proper solution procedure):

#### Stream 1

$$\theta_{1,j+1} = \tau_{1,j} + \exp(-N_{tu,f,1}) (\theta_{1,j} - \tau_{1,j}) \quad (13a)$$

and

$$\frac{d^2 \tau_{1,j}}{d\eta_1^2} = \frac{1 - \exp(-N_{tu,f,1})}{\phi_1 N_{tu,f,1}} (\tau_{1,j} - \theta_{1,j}) \quad (14a)$$

with the boundary conditions:

$$\frac{d\tau_{1,j}}{d\eta_1} = 0 \quad \text{at} \quad \eta_1 = 0 \quad \text{and} \quad \theta_{1,1} = 1$$

$$\tau_{1s,j} = \tau_{1,j} \quad (\eta_1 = 1) \quad \text{and} \quad \chi_{1,j} = -\phi_1 N_{tu,f,1} \frac{d\tau_{1,j}}{d\eta_1} \quad (\eta_1 = 1)$$

#### Stream 2

$$\theta_{2,j} = \tau_{2,j} + \exp(-N_{tu,f,2}) (\theta_{2,j+1} - \tau_{2,j}) \quad (13b)$$

$$\frac{d^2 \tau_{2,j}}{d\eta_2^2} = \frac{1 - \exp(-N_{tu,f,2})}{\phi_2 N_{tu,f,2}} (\tau_{2,j} - \theta_{2,j+1}) \quad (14b)$$

with the boundary conditions:

$$\frac{d\tau_{2,j}}{d\eta_2} = 0 \quad \text{at} \quad \eta_2 = 1 \quad \text{and} \quad \theta_{2,n+1} = 0$$

$$\tau_{2s,j} = \tau_{2,j} \quad (\eta_2 = 0) \quad \text{and} \quad \chi_{2,j} = -\phi_2 N_{tu,f,2} \frac{d\tau_{2,j}}{d\eta_2} \quad (\eta_2 = 0)$$

#### Separating Wall

$$\chi_{1,j} + \frac{\chi_{2,j}}{\nu} = 2\lambda_p (\tau_{1s,j} - \tau_{2s,j}); \quad 1 \leq j \leq n \quad (27)$$

$$\chi_{1,j} - \frac{\chi_{2,j}}{\nu} = \lambda_s (2\tau_{s,j} - \tau_{s,j-1} - \tau_{s,j+1}); \quad 2 \leq j \leq n-1 \quad (26a)$$

$$\chi_{1,1} - \frac{\chi_{2,1}}{\nu} = \lambda_s (\tau_{s,1} - \tau_{s,2}) \quad (26b)$$

$$\chi_{1,n} - \frac{\chi_{2,n}}{\nu} = \lambda_s (\tau_{s,n} - \tau_{s,n-1}) \quad (26c)$$

Equations (13), (14), (26), and (27), along with appropriate boundary conditions, fully describe the heat exchanger. Since the equations are parabolic and linear, their solution is quite straightforward (Venkatarathnam, 1991). The variables  $\theta_{1,j}$ ,  $\theta_{2,j}$ ,  $\tau_{1,j}$ , and  $\tau_{2,j}$  are strongly coupled and the set of equations must be solved simultaneously. An efficient and stable algorithm is required for an iterative solution of this system.

**Solution Algorithm.** Many different algorithms have been applied to solve the equations developed for the heat exchanger. Some of the schemes are unstable and some lack efficiency. The method that has been found to be most suitable consists of the following steps:

1 Assume a complete temperature profile for the channel 1-separator interface, i.e.,  $\tau_{1s,j} : 1 \leq j \leq n$ . In subsequent iterations use the profile computed in step (7).

2 Using Eqs. (13a) and (14a) and the temperature boundary condition assumed in step (1), compute the fluid and matrix temperatures throughout channel 1. Determine the heat transfer rates  $\chi_{1,j}$  at the channel 1-separator interface.

3 Calculate  $\chi_{2,j}$  and  $\tau_{2s,j}$  using separator Eqs. (26) and (27) as well as the  $\tau_{1s,j}$  and  $\chi_{1,j}$  computed in step (2).

4 Using Eqs. (13b) and (14b) and the boundary heat flow rates ( $\chi_{2,j}$ ) calculated in step (3), compute fluid and matrix temperatures throughout channel 2. Determine the temperatures  $\tau_{2s,j}$  and heat transfer rates  $\chi_{2,j}$  at the channel 2-separator interface.

5 Using  $\chi_{1,j}$  calculated in step (2),  $\chi_{2,j}$  and  $\tau_{2s,j}$  calculated in step (4), and Eqs. (27) calculate the temperature profile on the channel 1-separator interface.

6 Compare the computed temperature profile with the assumed profile used in step (2) of this iteration. If the two profiles match within a certain convergence parameter, go to step (8). Otherwise go to step (7).

7 Compute a new temperature profile for the channel 1-separator interface  $\tau_{1s,j}$  from the one assumed in step (2) and the one computed in step (5) by using a relaxation factor. We have generally used a relaxation factor between 0.3 and 0.4 in our computations.

8 Once the iterations are completed, the average exit temperatures of the fluid streams, effectiveness, and effective  $N_{tu}$  of the heat exchanger can be calculated.

The most significant aspect of this method is the retention of the heat transfer rates  $\chi_{2,j}$  while discarding the interface temperatures  $\tau_{2,j}$  in step (4). This approach, ensuring the conservation of energy at all intermediate stages, is responsible for the stability of the iteration scheme.

#### Results and Discussion

Based on the formalism developed in the last section, we have written a computer program to predict the performance of perforated plate matrix heat exchangers with rectangular geometry. The effectiveness is expressed in terms of an "effective  $N_{tu}$  ( $=N_{tu,eff}$ )" given by the relation:

$$N_{tu,eff} = \frac{-1}{1-\nu} \ln \frac{1-\epsilon}{1-\nu\epsilon} \quad (29a)$$

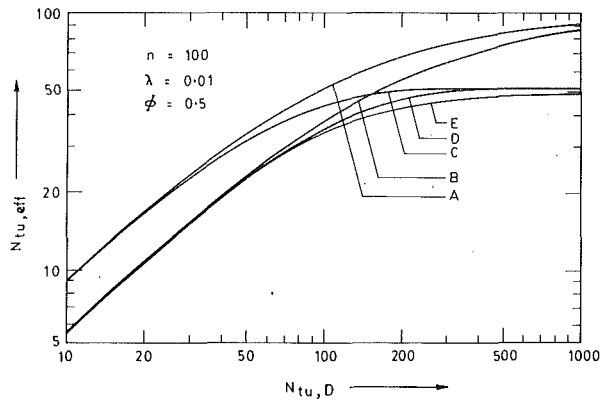


Fig. 3 Effective  $N_{tu}$  ( $= N_{tu,eff}$ ) shown as a function of design  $N_{tu}$  ( $= N_{tu,D}$ ) for given number of plates  $n$ , axial conduction parameter  $\lambda$ , and plate conduction parameter  $\phi$ : (A) Continuum approach, axial conduction included (Kroeger, 1967); (B) Fleming's model with axial conduction effects (Fleming, 1969; Kroeger, 1967); (C) Sarangi and Barclay formulation (1984); (D) modified Sarangi and Barclay formulation; (E) present work

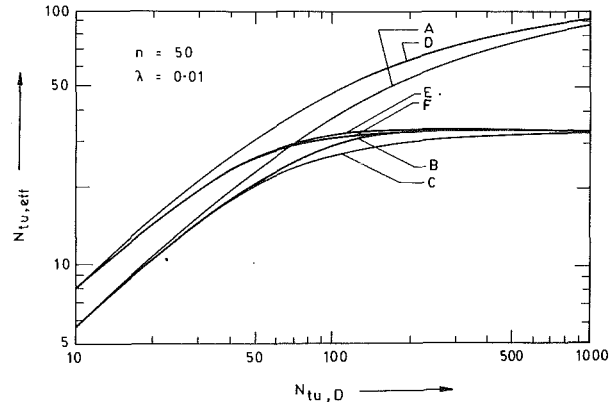


Fig. 4 Effective  $N_{tu}$  ( $= N_{tu,eff}$ ) shown as a function of design  $N_{tu}$  ( $= N_{tu,D}$ ) and plate conduction parameter  $\phi$  for  $\phi = 0.5$  (A, B, C) and  $\phi = 2.5$  (D, E, F): (A, D) Fleming's model with axial conduction effects (Fleming, 1969; Kroeger, 1967); (B, E) modified Sarangi and Barclay formulation (Sarangi and Barclay, 1984); (C, F) present work

which reduces to:

$$N_{tu,eff} = \epsilon / (1 - \epsilon) \quad (29b)$$

for balanced flow ( $\nu = 1$ ) units. Effective  $N_{tu}$  is the  $N_{tu}$  of a hypothetical exchanger, which has the same effectiveness  $\epsilon$  as the one being studied but none of the irreversibilities except convective resistance. The design  $N_{tu}$  ( $= N_{tu,D}$ ), on the other hand is the conventional  $N_{tu}$  given by the relation

$$\frac{N_{tu,D}}{n} = \left[ \frac{1}{N_{tu,f,1}} + \frac{\nu}{N_{tu,f,2}} \right]^{-1}$$

The inputs to this program are the seven dimensionless variables  $N_{tu,f,1}$ ,  $N_{tu,f,2}$ ,  $\phi_1$ ,  $\phi_2$ ,  $\nu$ ,  $\lambda_p$ , and  $\lambda_s$  and the number of plates  $n$ . As an example, results for a typical set of balanced flow ( $\nu = 1$ ) heat exchangers are presented here. The exchangers have balanced design, i.e.,  $N_{tu,f,1} = N_{tu,f,2} = 2 N_{tu,D} / n$  and  $\phi_1 = \phi_2 = \phi$ ; transverse resistance of the separator is neglected ( $\lambda_p = \infty$ ). Calculations have been performed for  $n = 50$  and  $100$ ,  $\phi = 0.5$  and  $2.5$ , and  $10 \leq N_{tu,D} \leq 1000$ . The computed results are plotted in Fig. 3 for  $n = 100$ ,  $\phi = 0.5$ , and in Fig. 4 for  $n = 50$ ,  $\phi = 0.5$  and  $2.5$  along with calculations based on the methods of Kroeger (1967), Fleming (1969), and Sarangi and Barclay (1984).

Kroeger's (1967) formulation considers the effect of axial conduction but ignores the effects of plate conduction as well as that of the discrete structure of the exchanger. Fleming's approach expresses plate conduction effects by an equivalent fin efficiency, which reduces the effective heat transfer area. From Eqs. (1) and (12) it can be seen that Fleming's fin efficiency is related to our plate conduction parameter by the relation

$$\eta_{fin} = \left[ 1 + \frac{1}{3\phi} \right]^{-1} \quad (31)$$

In Fig. 3, while curve A considers only axial conduction, curve B considers both axial conduction and fin efficiency. While the two curves differ at low  $N_{tu,D}$  by the fin efficiency factor, at high  $N_{tu,D}$  they approach each other with both being limited by axial conduction effects.

The approach of Sarangi and Barclay (1984) places an emphasis on the effect of a finite number of plates along with that of axial conduction. If the number of plates is high ( $n \gg 1/\lambda$ ), the curve coincides with that of Kroeger (1967). But if  $n$  is small, the effective  $N_{tu}$  approaches  $n$  as  $N_{tu,D}$  is increased indefinitely. The effect of plate conduction can be incorporated into the formulation of Sarangi and Barclay by replacing  $N_{tu,D}$  in Eqs. (3) and (4) by  $N_{tu,D} / (1 + 1/3\phi)$ . This is the basis of the

modified Sarangi and Barclay approach shown in Figs. 3 and 4. The present numerical method has most features in common with the modified Sarangi and Barclay method and consequently the two curves agree very well over the entire range of  $N_{tu,D}$ , except near  $N_{tu,D} \approx n$ , where a small deviation is observed. This deviation is caused by the method of superposition used by Sarangi and Barclay (1984). The deviation is greater for small values of  $\phi$  (Fig. 4) because at small  $N_{tu,D}$  the plate temperature profile has a larger temperature gradient in the lateral direction and influences the fluid temperature profile.

In conclusion, the following observations can be made from Figs. 3 and 4:

1 At low  $N_{tu,D}$  the effectiveness is fairly independent of the number of plates  $n$  and the axial conduction parameter  $\lambda$ . The effective  $N_{tu}$  is adequately given by  $N_{tu,D} / (1 + 1/3\phi)$ .

2 At high  $N_{tu,D}$  the effectiveness is limited by  $n$  and  $\lambda$  instead of  $N_{tu,D}$  or  $\phi$ . If  $n < 1/\lambda$ ,  $n$  is the controlling factor; otherwise the effective  $N_{tu}$  is determined by the axial conduction parameter  $\lambda$ .

3 Replacement of  $N_{tu,D}$  in the Sarangi and Barclay relation [Eqs. (2) and (3)] with  $N_{tu,D} / (1 + 1/3\phi)$  is sufficient in most cases to predict the performance of matrix heat exchangers of rectangular geometry.

The numerical technique described in this paper is, however, much more general and can be used for exchangers of circular or arbitrary cross sections.

## Acknowledgments

This study was supported by the Department of Non-Conventional Energy Sources, Ministry of Energy, Government of India under the project, Liquid Hydrogen: Production, Storage, and Transfer.

## References

- Babak, V. N., Babak, T. B., Kholpanov, L. P., and Malyusov, V. A., 1983, "On the Computation of a Matrix Heat Exchanger From Perforated Plates," *Theor. Osno. Khim. Tekh.*, Vol. 17, pp. 347-360; translation: *Theor. Found. Chem. Eng.*, Vol. 17, pp. 236-248.
- Babak, V. N., Babak, T. B., Kholpanov, L. P., and Malyusov, V. A., 1985a, "Design of a Sectional Heat Exchanger Made of Perforated Plates With a Highly Conductive Wall," *Theor. Osno. Khim. Tekh.*, Vol. 19, pp. 762-767; translation: *Theor. Found. Chem. Eng.*, Vol. 19, pp. 484-489.
- Babak, T. B., Zablotskaya, N. S., Babak, V. N., Kholpanov, L. P., and

- Malyusov, V. A., 1985b, "Applicability of the Convective Heat Transfer Equation for Design of Matrix Heat Exchangers," *Theor. Osno. Khim. Tekh.*, Vol. 19, pp. 488-494; translation: *Theor. Found. Chem. Eng.*, Vol. 19, pp. 314-321.
- Babak, V. N., Babak, T. B., Kholpanov, L. P., and Malyusov, V. A., 1986a, "A Procedure for Calculating Matrix Heat Exchangers From Perforated Plates," *Inzhenerno Fizicheskii Zhurnal*, Vol. 50, pp. 457-458; translation: *J. Eng. Physics*, Vol. 50, pp. 330-335.
- Babak, V. N., Babak, T. B., Kholpanov, L. P., and Malyusov, V. A., 1986b, "Calculation of Compact Matrix Heat Exchanger With Plane-Parallel Channels," *Theor. Osno. Khim. Tekh.*, Vol. 20, pp. 327-331; translation: *Theor. Found. Chem. Eng.*, Vol. 20, pp. 201-205.
- Bova, V. I., Zablotskaya, N. S., Vaselov, V. A., and Samusenkov, N. V., 1978, "Development of Efficient Regenerators for Air-Fractionating Units," *Khim. Neft. Mash.*, No. 7, pp. 11-12; translation: *Chem. Petr. Eng.*, No. 4, pp. 309-313.
- Fleming, R. B., 1969, "A Compact Perforated Plate Heat Exchanger," in: *Advances in Cryogenic Eng.*, K. D. Timmerhaus, ed., Plenum, Vol. 14, pp. 197-204.
- Harada, S., Matsuda, T., Saito, S., and Ihara, K., 1986, "Small Size Helium Refrigerator With Micro Turbine Expanders," *Proceedings of International Cryocooler Conference*, Easton, MD, Sept. 25-26.
- Hubbell, R., and Cain, C. L., 1986, "New Heat Transfer and Friction Factor Design Data for Perforated Heat Exchangers," *Advances in Cryogenic Eng.*, Plenum, R. W. Fast, ed., Vol. 31, pp. 383-390.
- Kroeger, P. G., 1967, "Performance Deterioration in High-Effectiveness Heat Exchangers Due to Axial Heat Conduction Effects," *Advances in Cryogenic Eng.*, K. D. Timmerhaus, ed., Plenum, Vol. 12, pp. 363-372.
- Kirpikov, V. A., and Leifman, I. I., 1972, "Calculation of the Temperature Profile of a Perforated Fin," *Inzhenerno Fizicheskii Zhurnal*, Vol. 23, pp. 316-321; translation: *J. Eng. Physics*, Vol. 23, pp. 1024-1027.
- McMahon, H. O., Bowen, R. J., and Bley, G. A., Jr., 1950, "A Perforated Plate Heat Exchanger," *Trans. ASME*, Vol. 72, pp. 623-632.
- Mikulin, E. I., Shevich, Yu. A., and Potapov, U. N., 1979, "Efficiency of Perforated Plate Array Heat Exchangers," *Khim. Neft. Mashin.*, No. 5, pp. 13-15; translation: *Chem. Petr. Eng.*, pp. 514-519.
- Sarangi, S., and Barclay, J. A., 1984, "An Analysis of Compact Heat Exchanger Performance," *Cryogenic Processes and Equipment—1984*, ASME, P. J. Kerney et al., eds., pp. 37-44.
- Venkatarathnam, G., and Sarangi, S., 1990, "Matrix Heat Exchangers and Their Application in Cryogenic Systems," *Cryogenics*, Vol. 30, pp. 907-918.
- Venkatarathnam, G., 1991, "Matrix Heat Exchangers," Ph.D. Dissertation, Indian Institute of Technology, Kharagpur.

# Simultaneously Developing, Laminar Flow, Forced Convection in the Entrance Region of Parallel Plates

T. V. Nguyen

Principal Research Scientist,  
CSIRO Division of Mineral and  
Process Engineering,  
Clayton, Australia

I. L. Maclaine-cross

Senior Lecturer,  
School of Mechanical and  
Manufacturing Engineering,  
University of New South Wales,  
Kensington, NSW 2033, Australia

*This paper reports on a numerical study of simultaneously developing flow in the entrance region of a cascade of thin parallel horizontal plates with a uniform flow at upstream infinity. Results obtained by ADI solution of finite difference equations for the Navier-Stokes and energy partial differential equations are extrapolated to zero mesh size with extended Richardson extrapolation. Nusselt numbers, incremental heat transfer number, and thermal entrance length are presented for Reynolds numbers between 40 and 2000;  $Pr = 0.2, 0.7, 2, 7, 10$  and 100; and constant wall temperature and heat flux boundary conditions.*

## 1 Introduction

In gas-to-surface heat transfer at low temperature differences in air conditioning applications, the cost savings are greater from high heat transfer with low pressure drop. For a given passage cross-sectional area, this is easier to achieve with a high ratio of Nusselt number to Fanning friction factor times Reynolds number,  $Nu/(fRe)$ . Two heat transfer boundary conditions are of primary interest: constant wall temperature, which is approximated in evaporative coolers; and constant heat flux, which is approximated in rotary regenerative heat and mass exchangers. Constant wall temperature is denoted here by the subscript  $T$  and constant wall heat flux by  $H$ . For laminar fully developed flow, the parallel plate passage geometry (Fig. 1) has  $Nu_T = 7.54070$ ,  $Nu_H = 140/17$ , and  $fRe = 24$  giving a higher  $Nu/(fRe)$  than any other cross sections (Shah and London, 1978).

Parallel plate exchangers are used with numbers of transfer units for a flow stream  $4(x \times Nu + N)$  between 1 and 40 depending on application (Dunkle et al., 1980). The number of transfer units for flow development  $4(L \times Nu + N) \approx 0.6$  is significantly less than this so flow is always fully developed. The incremental heat transfer number  $N$  may, however, contribute up to about 15 percent of the heat transfer, so accurate knowledge of its value is important to performance prediction. The exchangers are operated with passage Reynolds numbers between 100 and 1000 so flow is laminar. The Prandtl number  $Pr$  is about 0.7 and the analogous Schmidt number for mass transfer 0.6. The ratio of Grashof to Reynolds number squared ( $Gr/Re^2$ ) is less than  $10^{-4}$ , so natural convection has an insignificant effect on heat transfer and pressure drop (Shah and London, 1978). The parallel plate thickness is less than 10 percent of their spacing. The width of the plates is typically 200 times the plate spacing, which is very uniform due to the tension used to hold the plates in position. Viscous dissipation, flow work, thermal sources within the fluid, and mass transfer coupling to fluid heat transfer are negligible or nonexistent in these devices.

In making performance predictions, theoretical fully developed high aspect ratio rectangular passage  $Nu$  and  $fRe$  are used with zero thickness parallel plate incremental heat transfer  $N$  and pressure drop numbers  $K$  (Shah and London, 1978).  $Nu$  and  $fRe$  are corrected for variable property effects but not

$N$  or  $K$ . The pressure drop is corrected for finite thickness using Bernoulli's equation at the entrance and the momentum equation at the exit. The agreement with experiment (Dunkle et al., 1980; Ambrose et al., 1983; Maclaine-cross and Ambrose, 1980) has been satisfactory from a practical viewpoint even though considerable uncertainty surrounds the correct value of  $N$ . For experimental, parallel plate, regenerative dehumidifiers, based on the commercial, parallel plate, heat exchanger design (Dunkle et al., 1980), significant solid side resistance to heat and mass transfer has been inferred from overall transfer coefficient measurements (Maclaine-cross and Pesaran, 1986). More accurate knowledge of the air side resistance would give improved knowledge of the solid side resistance.

Laminar flow over flat plates with zero pressure gradient has a higher  $Nu/(fRe)$  than laminar fully developed flow between parallel plates. This suggests that the entrance region of parallel plates may have superior performance to the fully developed region. If this were true on an integrated rather than a local basis, it may be possible to develop staggered parallel strip matrices (Maclaine-cross and Pesaran, 1986) with higher  $Nu/(fRe)$  than parallel plates.

Incremental pressure drop,  $K$ , and heat transfer,  $N_T$ ,  $N_H$ , numbers for parallel plates are thus of considerable practical as well as theoretical interest, and especially the fully developed flow values,  $K(\infty)$ ,  $N_T(\infty)$ , and  $N_H(\infty)$ . The boundary conditions required are simultaneous development of velocity and temperature profiles, which, far upstream of the entrance, are assumed uniform. The effect of axial diffusion on  $K$ ,  $N_T$ , and  $N_H$  is negligible only at very high Reynolds and Peclet numbers,

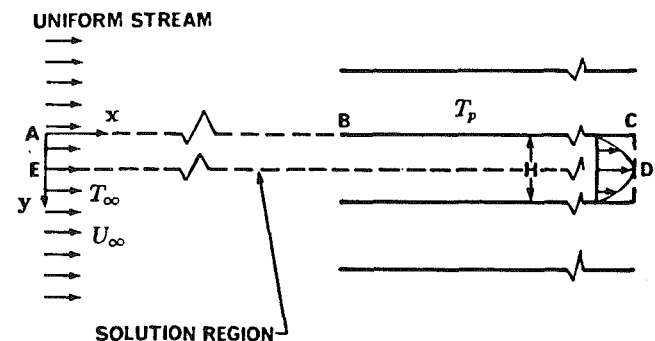


Fig. 1 Boundary conditions and solution region for parallel plate cascade

Contributed by the Heat Transfer Division for publication in the JOURNAL OF HEAT TRANSFER. Manuscript received by the Heat Transfer Division November 3, 1989; revision received April 9, 1991. Keywords: Forced Convection, Heat Exchangers, Numerical Methods.

because of the rapid change in axial velocity and temperature gradients near the entrance. Consequently,  $K$  is a function of  $Re$ , and  $N_T$  and  $N_H$  are functions of  $Pe$ .  $N_T$  and  $N_H$  are also functions of Prandtl number  $Pr$ .

Nguyen and Maclaine-cross (1988), assuming constant properties, numerically solved the Navier–Stokes equations both far upstream and downstream of the entrance to a cascade of very thin parallel plates (Fig. 1). They extrapolated their results to zero grid size using three finite grid sizes to reduce discretization error substantially. Their correlating equation

$$K(\infty) = 0.6779 + 4.5914/Re \quad (1)$$

was within 1 percent of their extrapolated  $K(\infty)$  and their dimensionless entrance length  $L_{hy}^+$ , defined by  $K(L_{hy}^+) = 0.99 K(\infty)$ , was within 1 percent of 0.01378 for  $40 \leq Re \leq 2000$ . The equation is in excellent agreement with Shah and London's (1978) recommendation for large Reynolds numbers  $K(\infty) = 0.674$  and with the Lundgren et al. (1964) approximate analytic value 0.686 used for rotary heat exchanger predictions (Maclaine-cross and Ambrose, 1980).

For  $Pr = 0$ , the fluid is inviscid and the fluid velocity remains constant and is fully developed at the inlet. This is sometimes called plug flow. The fully developed temperature profiles for plug flow give higher Nusselt numbers,  $Nu_T = \pi^2$ ,  $Nu_H = 12$ , than those above for a fully developed velocity profile. For  $Pe \gg 1$ , the differential equation and boundary conditions approach those for one-dimensional diffusion into a finite slab for which many solutions are known (Carslaw and Jaeger, 1963). From these solutions may be calculated the incremental heat transfer numbers,  $N_T(\infty) = 0.0525046$  and  $N_H(\infty) = 0.1086$ , for  $Pr = 0$  and  $Pe = \infty$ .

For  $Pr \gg 1$ , the velocity profile develops much more rapidly than the temperature profile; and for large  $Pe$ , the simultaneously developing flow problem approximates the Graetz–Nusselt problem, which has been solved by a variety of methods. Shah (1975) has calculated  $N$  for developing flow, and for fully developed flow obtained  $N_T(\infty) = 0.02348$  and  $N_H(\infty) = 0.0364$  with  $Pr = Pe = \infty$ . The higher values of  $Nu$  and  $N$  for  $Pr = 0$  suggest that as  $Pr$  falls,  $N$  will increase. Large values of  $N$  are likely for  $Pr \ll 1$ , when plug flow is approximated for a substantial distance from the entrance.

For  $Pr \approx 1$ , the simultaneous flow development problem has been solved for  $Pe \gg 1000$ , which makes the assumption of uniform flow at the entrance a satisfactory approximation. For short ducts, agreement between various solution methods is within 5 percent for  $Nu_{m,T}$  but values of  $Nu_{x,H}$  differ by up to 16 percent (Shah and London, 1978). The correlating equation used by Mercer et al. (1967) for  $Nu_{m,T}$  implies  $N_T(\infty) = 0$ , which suggests errors in  $Nu_{m,T}$  may be significant for longer ducts. For design of many parallel plate exchangers, values of

incremental heat transfer number  $N$  with  $70 \leq Pe \leq 700$  are desired, but only the values mentioned in the previous paragraphs are available.

This paper presents values of  $N$  for parallel plates with uniform flow far upstream of the entrance and constant properties. The velocities are calculated using a finite difference scheme consistent with the Navier–Stokes equations (Nguyen and Maclaine-cross, 1988), and temperatures using a related finite difference scheme consistent with the energy equation (Section 2). Discretization error is reduced by extrapolating three mesh sizes to zero mesh size giving excellent agreement with previous accurate solutions for special values (Section 3). Values and correlations of incremental heat transfer numbers are given for constant wall temperature (Section 4) and constant wall heat flux (Section 5). These results resolve some literature problems (Section 6) but further work is still of interest (Section 7).

## 2 Equations and Their Solution

In Fig. 1 fluid is pictured as flowing through an array of horizontal parallel plates, which are a centerline distance  $H$  apart. Both the temperature  $T_\infty$  and velocity  $U_\infty$  are uniform at upstream infinity. The plates are either kept at the same uniform temperature  $T_p$  or the heat flux is constant. The flow becomes fully developed far downstream. Dimensionless Cartesian coordinates are chosen such that the plate spacing is unity.

The equations of motion are written in terms of the stream function  $\psi$  and vorticity  $\zeta$ , defined by

$$u = \frac{\partial \psi}{\partial y}, \quad v = -\frac{\partial \psi}{\partial x}, \quad \text{and} \quad \zeta = \frac{\partial v}{\partial x} - \frac{\partial u}{\partial y}, \quad (2)$$

where  $u$ ,  $v$  are velocity components in the  $x$ ,  $y$  directions.

The dimensionless governing equations for vorticity, stream function, and temperature, derived from the Navier–Stokes equations and subject to the usual Boussinesq approximations, are

$$\frac{\partial \zeta}{\partial t} = -u \frac{\partial \zeta}{\partial x} - v \frac{\partial \zeta}{\partial y} + \frac{1}{Re} \left( \frac{\partial^2 \zeta}{\partial x^2} + \frac{\partial^2 \zeta}{\partial y^2} \right) \quad (3)$$

$$0 = \left( \frac{\partial^2 \psi}{\partial x^2} + \frac{\partial^2 \psi}{\partial y^2} \right) + \zeta \quad (4)$$

$$\frac{\partial \theta}{\partial t} = -u \frac{\partial \theta}{\partial x} - v \frac{\partial \theta}{\partial y} + \frac{1}{RePr} \left( \frac{\partial^2 \theta}{\partial x^2} + \frac{\partial^2 \theta}{\partial y^2} \right) \quad (5)$$

in which  $\theta = (T - T_\infty)/(T_p - T_\infty)$ ,  $Re = U_\infty H/\nu$ , and  $Pr = \nu/\alpha$ . Here  $H$ ,  $\nu$ , and  $\alpha$  denote, respectively, the pitch of the plates, the kinetic viscosity, and the thermal diffusivity.

## Nomenclature

$D_h$  = hydraulic diameter  
 $f$  = Fanning friction factor  
 $Gr$  = Grashof number  
 $H$  = channel width  
 $K$  = incremental pressure drop number  
 $K(\infty)$  = fully developed incremental pressure drop number  
 $L_{hy}^+$  = hydrodynamic entrance length  
 $L_{th}^*$  = thermal entrance length  
 $n$  = number of interior mesh points  
 $N$  = incremental heat transfer number  
 $N(\infty)$  = fully developed incremental heat transfer number  
 $Nu$  = Nusselt number  
 $Pe$  = Peclet number  
 $Pr$  = Prandtl number  
 $Re$  = Reynolds number =  $D_h U_\infty/\nu$

$t$  = time  
 $\Delta t$  = time step  
 $T$  = temperature  
 $u$  =  $x$  component of velocity  
 $U_\infty$  = upstream velocity  
 $v$  =  $y$  component of velocity  
 $x$  = coordinate along the plates  
 $x_t$  = transformed coordinate along the plates  
 $y$  = coordinate normal to the plates  
 $\alpha$  = thermal diffusivity  
 $\alpha_\phi$  = false transient factor  
 $\epsilon$  = convergence factor  
 $\zeta$  = vorticity  
 $\theta$  = dimensionless temperature  
 $\nu$  = kinetic viscosity  
 $\psi$  = stream function

**Table 1 Incremental heat transfer number  $N_T(\infty)$**

| Re   | 6x81    | 11x161  | 21x321  | Extrapolated | Diff.(%) |
|------|---------|---------|---------|--------------|----------|
| 40   | 0.02208 | 0.03278 | 0.03745 | 0.03938      | 0.96     |
| 50   | 0.01971 | 0.02965 | 0.03405 | 0.03588      | 1.01     |
| 60   | 0.01848 | 0.02777 | 0.03199 | 0.03377      | 1.07     |
| 80   | 0.01744 | 0.02572 | 0.02968 | 0.03137      | 1.15     |
| 100  | 0.01708 | 0.02468 | 0.02844 | 0.03005      | 1.19     |
| 150  | 0.01689 | 0.02349 | 0.02696 | 0.02812      | 1.07     |
| 200  | 0.01686 | 0.02314 | 0.02631 | 0.02767      | 1.10     |
| 300  | 0.01685 | 0.02279 | 0.02575 | 0.02701      | 1.04     |
| 600  | 0.01685 | 0.02257 | 0.02534 | 0.02652      | 0.96     |
| 1000 | 0.01685 | 0.02252 | 0.02524 | 0.02640      | 0.94     |
| 2000 | 0.01685 | 0.02250 | 0.02522 | 0.02637      | 0.94     |

**Table 2 Incremental heat transfer number  $N_H(\infty)$**

| Re   | 6x81    | 11x161  | 21x321  | Extrapolated | Diff.(%) |
|------|---------|---------|---------|--------------|----------|
| 40   | 0.09185 | 0.07106 | 0.06101 | 0.05674      | 1.62     |
| 50   | 0.08534 | 0.06556 | 0.05741 | 0.05408      | 1.12     |
| 60   | 0.08202 | 0.06351 | 0.05549 | 0.05217      | 0.82     |
| 80   | 0.07901 | 0.05977 | 0.05365 | 0.05136      | 0.49     |
| 100  | 0.07776 | 0.05851 | 0.05283 | 0.05078      | 0.35     |
| 150  | 0.07665 | 0.05731 | 0.05203 | 0.05019      | 0.16     |
| 200  | 0.07629 | 0.05687 | 0.05172 | 0.04995      | 0.11     |
| 300  | 0.07603 | 0.05651 | 0.05143 | 0.04970      | 0.08     |
| 600  | 0.07588 | 0.05621 | 0.05112 | 0.04939      | 0.07     |
| 1000 | 0.07585 | 0.05613 | 0.05100 | 0.04926      | 0.07     |
| 2000 | 0.07583 | 0.05610 | 0.05095 | 0.04919      | 0.08     |

**Table 3 Comparison of  $Nu_x$  for  $Pr = 100$  and  $Re = 2000$**

| $x^*$    | $Nu_{x,T}$ |         | $Nu_{x,H}$ |                |
|----------|------------|---------|------------|----------------|
|          | Present    | Brown   | Present    | Sparrow et al. |
| 0.0      | 53.2801    | -       | 49.1681    | -              |
| 0.000754 | 13.9169    | 13.9517 | 16.3676    | 16.8149        |
| 0.001527 | 11.0975    | 11.3514 | 13.4247    | 13.6102        |
| 0.002320 | 9.9699     | 10.1424 | 11.9913    | 12.0984        |
| 0.003136 | 9.2952     | 9.4133  | 11.1012    | 11.1705        |
| 0.003974 | 8.8396     | 8.9225  | 10.4832    | 10.5321        |
| 0.004837 | 8.5114     | 8.5708  | 10.0260    | 10.0618        |
| 0.006641 | 8.0826     | 8.1151  | 9.3969     | 9.4179         |
| 0.008562 | 7.8359     | 7.8541  | 8.9939     | 9.0068         |
| 0.010615 | 7.6952     | 7.7055  | 8.7263     | 8.7345         |
| 0.015203 | 7.5764     | 7.5799  | 8.4284     | 8.4311         |
| 0.020629 | 7.5460     | 7.5479  | 8.3009     | 8.3018         |
| 0.027271 | 7.5407     | 7.5416  | 8.2530     | 8.2533         |
| 0.035833 | 7.5407     | 7.5407  | 8.2386     | 8.2386         |
| 0.047900 | 7.5407     | 7.5407  | 8.2356     | 8.2356         |
| 0.068529 | 7.5407     | 7.5407  | 8.2353     | 8.2353         |

Figure 1 shows the region ABCDE within which these equations were solved. The solution region is extended to infinity both upstream and downstream of the entry to the channels. Uniform flow was imposed on section AE:  $u = 1$ ;  $v = 0$ ;  $\theta = 0$ ;  $\zeta = 0$ . Since the solution region represents the upper half of a channel formed by two parallel plates, the boundary conditions on sections AB and DE are:  $v = 0$ ;  $\partial u / \partial y = 0$ ;  $\zeta = 0$ . On section BC, the velocities are zero and the stream function is constant.

The coordinates and partial differential Eqs. (3), (4), and (5) were transformed both upstream and downstream of the entrance using a function related to the downstream decay (Maclaine-cross, 1974). The transformed coordinate  $x_t$  is dimensionless and  $-1 \leq x_t \leq 1$ . It may be calculated from the dimensionless coordinate  $x$  in Eqs. (3), (4), and (5) using

$$x_t = \frac{(1 - \exp(-|x|/(0.089275RePr)))x}{|x|} \quad (6)$$

The transformed coordinates give a more equal change in dependent variables over each grid element and points at upstream and downstream infinity. The number of grid elements required for a given discretization error is greatly reduced at the expense of slightly more computation per grid element.

Finite difference equations were derived from the transformed nonlinear partial differential equations. Forward differences were used for the time derivatives and central differences for space derivatives. Quadratic upstream interpolation for convective kinematics (QUICK) (Leonard, 1979) was used for the convective terms in both the momentum and energy equations to give stability with a discretization error of the order of the square of the mesh size.

The alternating direction implicit (ADI) iterative method was used to solve the nonlinear finite difference equations simultaneously. Convergence was measured by calculating

$$\epsilon_\phi = \frac{1}{n\phi_{\max}} \sum \frac{\phi^{n+1} - \phi^n}{\alpha_\phi \Delta t} \quad (7)$$

where  $n$  is the number of interior mesh points,  $\phi_{\max}$  is the maximum magnitude of  $\phi$ ,  $\alpha_\phi$  is the false transient factor, and  $\Delta t$  is the time step. Iteration was repeated until  $\epsilon_\zeta$ ,  $\epsilon_\psi$ ,  $\epsilon_\theta$  were all less than  $10^{-9}$  so that the error in solving the finite difference equations was negligible and independent of grid size.

The dimensionless groups used in the present work are defined as follows:

- the local Nusselt number,

$$Nu_x = 2 \left( \frac{\partial \theta}{\partial y} \right)_{y=0} / (\theta_p - \theta_m) \quad (8)$$

where  $\theta_m$  is the fluid bulk mean temperature;

- the mean Nusselt number,

$$Nu_m = \frac{1}{x} \int_0^x Nu_x dx \quad (9)$$

- the incremental heat transfer number,

$$N_{bc}(x) = Nu_{m,bc} x^* - Nu_{bc} x^* \quad (10)$$

The suffix *bc* represents the associated thermal boundary conditions (*T* or *H*) and  $Nu_{bc}$  is the Nusselt number for fully developed flow.

Discretization error is the difference between the exact solution of the finite difference equations and the exact solution of the consistent partial differential equations. For the finite difference equations used here this is of the order of the grid size squared. It may be reduced to fourth order by extrapolation to zero grid size of the finite difference equation solutions for three different grid size. Each grid is solved with the same parameters and boundary conditions. The three grids chosen were  $6 \times 81$ ,  $11 \times 161$ , and  $21 \times 321$  mesh points in the  $y$  and  $x$  directions, respectively, making each grid size half its predecessor. The following extrapolation formula was calculated from the general expression of Maclaine-cross (1974):

$$A = A_3 - \frac{(A_3 - A_1) - 12(A_3 - A_2)}{21} \quad (11)$$

where  $A_3$  is the value at the smallest grid size, etc. Other details of the solution method are discussed elsewhere (Nguyen, 1980; Nguyen et al., 1981).

### 3 Error Estimate and Previous Solutions

The extrapolated values of  $N_T(\infty)$  and  $N_H(\infty)$  at  $Pr = 0.7$  are given in Tables 1 and 2, respectively, together with the values for the three grid meshes used in calculating them. The difference between two-point and three-point extrapolation is

**Table 4 Comparison of  $Nu_{m,T}$  and  $Nu_{x,H}$  for  $Pr = 10$  and  $0.7$  and  $Re = 2000$**

| $x^*$   | $Nu_{m,T} (Pr=10)$ |         | $x^*$   | $Nu_{x,H} (Pr=0.7)$ |         |
|---------|--------------------|---------|---------|---------------------|---------|
|         | Shah and London    | Present |         | Hwang and Fan       | Present |
| 0.002   | 15.44              | 13.9555 | 0.00179 | 15.11               | 14.9411 |
| 0.00313 | 13.40              | 12.3847 | 0.00625 | 10.03               | 9.9441  |
| 0.00625 | 11.01              | 10.4878 | 0.0107  | 8.901               | 8.8747  |
| 0.00938 | 9.978              | 9.6318  | 0.0286  | 8.239               | 8.2548  |
| 0.0125  | 9.402              | 9.153   | 0.0893  | 8.221               | 8.2353  |
| 0.0250  | 8.474              | 8.3528  |         |                     |         |
| 0.0406  | 8.106              | 8.0404  |         |                     |         |
| 0.0656  | 7.878              | 7.8494  |         |                     |         |

**Table 5 Incremental heat transfer number  $N_T(\infty)$  at  $Re = 2000$**

| Pr            | 0.2     | 0.7     | 2       | 7       | 10      | 100     |
|---------------|---------|---------|---------|---------|---------|---------|
| $N_T(\infty)$ | 0.04052 | 0.02637 | 0.02225 | 0.02046 | 0.02021 | 0.02007 |

**Table 6 Thermal entrance length  $L_{th,T}^*$  at  $Re = 2000$**

| Pr           | 0.2     | 0.7      | 2        | 7        | 10       | 100      |
|--------------|---------|----------|----------|----------|----------|----------|
| $L_{th,T}^*$ | 0.01187 | 0.007840 | 0.007248 | 0.007635 | 0.007714 | 0.007788 |

**Table 7 Extrapolated  $Nu_{m,T}$  as a function of  $x^*$  and Pr for  $Re = 2000$**

| $x^*$  | Pr=0.2  | Pr=0.7  | Pr=2    | Pr=7    | Pr=10   | Pr=100  |
|--------|---------|---------|---------|---------|---------|---------|
| .00153 | 18.0883 | 17.8277 | 16.4740 | 15.1587 | 14.9391 | 14.6018 |
| .00314 | 15.5477 | 14.2252 | 13.1876 | 12.4687 | 12.3788 | 12.2585 |
| .00484 | 13.6736 | 12.4001 | 11.6295 | 11.1793 | 11.1281 | 11.0621 |
| .00664 | 12.3995 | 11.2931 | 10.6935 | 10.3821 | 10.3482 | 10.3049 |
| .00856 | 11.5047 | 10.5445 | 10.0630 | 9.8317  | 9.8074  | 9.7758  |
| .01061 | 10.8465 | 10.0037 | 9.6097  | 9.4305  | 9.4100  | 9.3855  |
| .01520 | 9.9503  | 9.2802  | 9.0051  | 8.8860  | 8.8699  | 8.8534  |
| .02062 | 9.3711  | 8.8243  | 8.6233  | 8.5363  | 8.5245  | 8.5124  |
| .02727 | 8.9598  | 8.5110  | 8.3598  | 8.2942  | 8.2852  | 8.2761  |
| .03583 | 8.6424  | 8.2787  | 8.1638  | 8.1139  | 8.1070  | 8.1001  |
| .04790 | 8.3771  | 8.0924  | 8.0065  | 7.9691  | 7.9640  | 7.9597  |
| .06852 | 8.1308  | 7.9159  | 7.8658  | 7.8397  | 7.8362  | 7.8331  |
| .08916 | 7.9952  | 7.8364  | 7.7903  | 7.7702  | 7.7674  | 7.7652  |

**Table 8 Incremental heat transfer number  $N_H(\infty)$  at  $Re = 2000$**

| Pr            | 0.2     | 0.7     | 2       | 7       | 10      | 100     |
|---------------|---------|---------|---------|---------|---------|---------|
| $N_H(\infty)$ | 0.08210 | 0.04919 | 0.04034 | 0.03573 | 0.03505 | 0.03352 |

given in the last column. The largest difference for  $N_T$  is 1.19 percent at  $Re = 100$  and for  $N_H$ , 1.62 percent at  $Re = 40$ . It is believed that the residual discretization error in the three-point extrapolations is less than 1.62 percent.

If the finite difference equations were solved exactly with a grid size so small that the discretization error was negligible, it is still possible that the result would not be an accurate solution of the Navier-Stokes and energy equations for the parallel plate boundary conditions but of some other partial differential equations or boundary conditions. This could result from an error in deriving or coding the finite difference equations or inconsistency between them and the partial differential equations (Carnahan et al., 1969). Derivation, coding, and consistency can be tested by comparison with established solutions and values for very large Reynolds number as follows.

Local Nusselt numbers  $Nu_x$  calculated using the finite difference method in Section 2 for  $Pr = 100$  and  $Re = 2000$  are compared in Table 3 with previous analytic series solutions (Brown, 1960; Sparrow et al., 1963) for  $Pr = Pe = \infty$ . The agreement is to five significant figures for higher values of  $x^*$  for both constant wall temperature and constant wall heat flux. Dimensionless thermal entry length  $L^*$  as defined by Shah and London (1978) is a function of  $Nu_x$  and is consequently the same for both solutions. This agreement suggests that the finite difference representation of the energy equation (Section 2) is consistent with the partial differential equation.

**Table 9 Thermal entrance length  $L_{th,H}^*$**

| Pr           | 0.2     | 0.7     | 2       | 7       | 10      | 100     |
|--------------|---------|---------|---------|---------|---------|---------|
| $L_{th,H}^*$ | 0.02031 | 0.01282 | 0.01156 | 0.01148 | 0.01148 | 0.01147 |

**Table 10 Extrapolated  $Nu_{x,H}$  as a function of  $x^*$  and Pr for  $Re = 2000$**

| $x^*$    | Pr=0.2  | Pr=0.7  | Pr=2    | Pr=7    | Pr=10   |
|----------|---------|---------|---------|---------|---------|
| 0.       | 79.4008 | 69.8981 | 62.3635 | 56.6410 | 55.3640 |
| 0.000754 | 21.1910 | 20.4510 | 18.6304 | 16.9856 | 16.7081 |
| 0.001527 | 17.2620 | 15.8783 | 14.4469 | 13.5773 | 13.4924 |
| 0.002320 | 15.2366 | 13.5761 | 12.5482 | 12.0422 | 12.0148 |
| 0.003136 | 13.7672 | 12.2231 | 11.4304 | 11.1241 | 11.1133 |
| 0.003974 | 12.6668 | 11.3179 | 10.6851 | 10.4961 | 10.4907 |
| 0.004837 | 11.8436 | 10.6663 | 10.1524 | 10.0344 | 10.0312 |
| 0.006641 | 10.7245 | 9.7934  | 9.4486  | 9.4012  | 9.3997  |
| 0.008562 | 10.0105 | 9.2460  | 9.0166  | 9.0166  | 8.9956  |
| 0.010615 | 9.5260  | 8.8862  | 8.7372  | 8.7279  | 8.7274  |
| 0.015203 | 8.9435  | 8.4879  | 8.4312  | 8.4286  | 8.4284  |
| 0.020629 | 8.6385  | 8.3200  | 8.3018  | 8.3010  | 8.3009  |
| 0.027271 | 8.4675  | 8.2578  | 8.2532  | 8.2530  | 8.2530  |
| 0.035833 | 8.3630  | 8.2393  | 8.2386  | 8.2386  | 8.2386  |
| 0.047900 | 8.2947  | 8.2356  | 8.2355  | 8.2355  | 8.2355  |
| 0.068529 | 8.2521  | 8.2353  | 8.2353  | 8.2353  | 8.2353  |
| 0.089159 | 8.2403  | 8.2353  | 8.2353  | 8.2353  | 8.2353  |

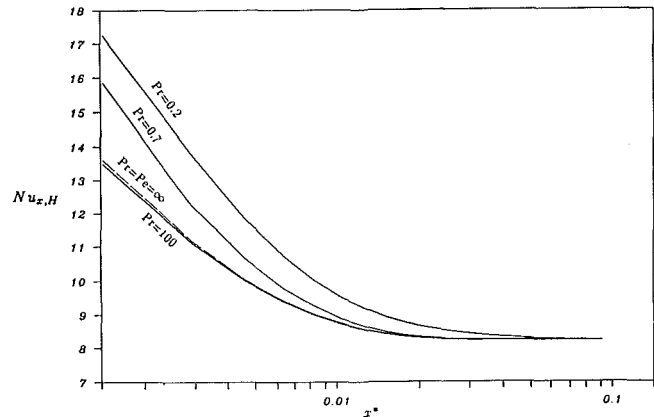


**Fig. 2  $Nu_{x,H}$  as a function of  $x^*$  and Pr**

For various Pr, Shah and London (1978) have provided finite difference solutions for  $Nu_{m,T}$ , and Hwang and Fan (1963) for  $Nu_{x,H}$ . For  $Pr = 10$  and  $0.7$ , Table 4 compares these with values interpolated from the authors' solutions for  $Re = 2000$ . The accuracy of interpolation over the authors' first downstream element was uncertain so comparisons were made only for points downstream of  $x^* = 0.001527$ . The present fully developed flow values agree to five significant figures with classical analytic solutions. The previous values in Table 4 appear to agree with these analytic solutions to two significant figures. They confirm the present values to two significant figures at shorter passage lengths.

#### 4 Constant Wall Temperature Results

Fully developed incremental heat transfer numbers for constant wall temperature  $N_T(\infty)$  are given in Table 5 for  $Re = 2000$  and  $Pr = 0.2, 0.7, 2, 7, 10$ , and  $100$ . For  $Pr = 0.7$  and  $40 \leq Re \leq 2000$ , Eqs. (12) and (13) correlate the values in Table 1 with a maximum error of 1.2 percent at  $Re = 2000$ .

$$N_T(\infty) = 0.02320 + 0.6417/Re, \text{ for } 40 \leq Re \leq 80 \quad (12)$$

$$N_T(\infty) = 0.02583 + 0.4217/Re, \text{ for } 80 \leq Re \leq 2000 \quad (13)$$

For  $0.2 \leq Pr \leq 100$  and  $Re = 2000$ , Eq. (14) correlates

these values with a maximum error of 1.65 percent at  $Pr = 0.7$ .

$$N_T(\infty) = 0.02005 + 0.00412/Pr \quad (14)$$

The thermal entry length  $L_{th}^*$ , defined by  $Nu_{x,T}(L_{th}^*, T) = 1.05Nu_T$ , for the parameter values in Table 5, are given in Table 6.

$Nu_{m,T}$  is given in Table 7 for  $Re = 2000$  at each axial coarse mesh station for  $Pr = 0.2, 0.7, 2, 7, 10, \text{ and } 100$ .

## 5 Constant Wall Heat Flux Results

Fully developed incremental heat transfer numbers for constant wall heat flux  $N_H(\infty)$  are given in Table 8 for  $40 \leq Re \leq 2000$  and  $Pr = 0.2, 0.7, 2, 7, 10, \text{ and } 100$ . For  $Pr = 0.7$  and  $40 \leq Re \leq 2000$ , Eqs. (15) and (16) correlate the values in Table 2 with a maximum error of 0.2 percent at  $Re = 100$ .

$$N_H(\infty) = 0.04308 + 0.5471/Re, \text{ for } 40 \leq Re \leq 60 \quad (15)$$

$$N_H(\infty) = 0.04906 + 0.1821/Re, \text{ for } 60 \leq Re \leq 2000 \quad (16)$$

For  $0.2 \leq Pr \leq 100$  and  $Re = 2000$ , Eqs. (17) and (18) correlate these values with a maximum error of 0.63 percent at  $Pr = 100$ .

$$N_H(\infty) = 0.03582 + 0.00926/Pr, \text{ for } 0.2 \leq Pr \leq 2 \quad (17)$$

$$N_H(\infty) = 0.03359 + 0.01362/Pr, \text{ for } 2 \leq Pr \leq 100 \quad (18)$$

The thermal entry length  $L_{th,H}^*$  defined by  $Nu_{x,H}(L_{th,H}^*) = 1.05 Nu_H$ , for the parameter values in Table 8, are given in Table 9.

Local heat transfer numbers are less dependent on entrance conditions than integrated values and so are more useful in comparing solutions.  $Nu_{x,H}$  is given in Table 10 for  $Re = 2000$  at each axial coarse mesh station for  $Pr = 0.2, 0.7, 2, 7, \text{ and } 10$  (for values of  $Nu_{x,H}$  at  $Pr = 100$ , see Table 3).  $Nu_{x,H}$  is plotted in Fig. 2 with the  $Pr = Pe = \infty$  curve dashed.

## 6 Comments on Results

Many of the data from previous solutions discussed in Sections 1 and 3 have assumed one or another form of uniform flow at the entrance. This condition is approximated only at very high  $Re$  by a cascade of parallel plates with uniform flow far upstream of the entrance. For the  $Re$  considered here, heat transfer and deceleration and acceleration of fluid particles effectively begins about one plate pitch upstream of the entrance. The boundary condition of zero velocity on the plate at the entrance is satisfied with finite velocity and temperature gradients. The friction factors and heat transfer coefficients on the leading edges of the plate are high but finite. The entrance lengths and incremental numbers are slightly less than for the uniform entrance assumption.

For air-to-air parallel plate exchangers, Dunkle and Maclaine-cross (1970) recommended calculating the pressure drop using  $K(\infty)$  from Lundgren et al. (1964) and the number of transfer units using the fully developed value of  $Nu_H/fRe = 0.3431$ . For  $Pr = 0.7, Re = 300$ , and ten transfer units in a flow stream,  $x^* = 0.297561$  and the results above give  $Nu_{m,H}/f_{app}Re = 0.3383$ . The recommendation from Dunkle and Maclaine-cross (1979) is 1.4 percent too high for this example.

The results in the previous sections allow comparison of heat transfer to pressure drop ratio in the entrance with that for fully developed flow. The fully developed flow measures of this are  $Nu_T/fRe = 0.3142$  and  $Nu_H/fRe = 0.3431$ . For  $Pr = 0.7$  and  $Re = 300, K(\infty) = 0.6938$  (Nguyen and Maclaine-cross, 1988),  $N_T(\infty) = 0.02701$ , and  $N_H(\infty) = 0.04950$ . The portion of  $K(\infty)$  recoverable at the exit may be estimated as 0.4 by assuming the velocity profile is fully developed just upstream of the exit and applying the momentum equation. The irrecoverable part of  $K(\infty)$  is thus 0.2938. To obtain one transfer unit for a flow stream  $x_1^* = 0.0295715$  and  $x_2^* =$

0.0243464. The fully developed values of  $Nu/fRe$  to produce one transfer unit with the same flow rate and pressure loss  $(Nu/fRe)_1$  may be calculated as  $(Nu_T/fRe)_1 = 0.3069$  and  $(Nu_H/fRe)_1 = 0.3627$ . These  $Nu/fRe$  are, respectively, 2.3 percent lower and 5.7 percent higher than for fully developed flow.

Figure 2 shows clearly that heat transfer is higher in the entrance region. This is however at the expense of pressure loss and could also be obtained with reduced plate spacing. For air conditioning the previous paragraph shows that only in the case of constant heat flux is there a possibility of gaining a small improvement. This improvement could alternatively be obtained by using a 2.8 percent larger passage free flow area. The cost of this could be much smaller than manufacturing a heat exchanger whose passages consist of ten widely spaced cascades of parallel strips (Maclaine-cross and Pesaran, 1986) to obtain ten transfer units with a 5.7 percent reduction in pressure loss.

## 7 Conclusion

The Navier-Stokes and energy equations have been solved more accurately than previously for a cascade of semi-infinite thin parallel plates with uniform flow far upstream of the entrance. Equations (12)–(18) give fully developed incremental heat transfer number  $N(\infty)$  for  $0.2 < Pr < 100$  and  $40 \leq Re \leq 2000$  for use in design of air-conditioning parallel plate devices with maximum expected errors of 1.2, 1.6, 0.2, and 0.6 percent, respectively. Except at  $Pr = 10$  and  $Re = 2000$ , the values are significantly greater than for the classical Graetz type solutions with  $Pr = Pe = \infty$ . They are not as large as previously surmised (Section 6). The authors have assumed constant properties, idealized constant boundary conditions, and that finite thickness can be corrected for by using Bernoulli's equation and that the flow just upstream of the exit is fully developed. For the flow just upstream of the exit to be fully developed, the upstream passage must be long and also  $Re$  must be large so that effects downstream of the exit do not propagate upstream of it. The authors believe that  $Re \geq 40$  is sufficient but this remains to be investigated. The effect of these assumptions could be studied and assessed using methods related to those described in Section 2. Also of interest are closely spaced cascades of parallel strips, which may offer better performance than widely spaced cascades (Section 6).

## References

- Ambrose, C. W., Maclaine-cross, I. L., and Robson, E. B., 1983, "The Use of Rotary Regenerative Heat Exchangers for the Conservation of Energy in Buildings," Final Report NERDDC Project 109, Department of Primary Industry and Energy, Canberra, Australia.
- Brown, G. M., 1960, "Heat or Mass Transfer in a Fluid in a Laminar Flow in a Circular or Flat Conduit," *AIChE J.*, Vol. 6, pp. 179–183.
- Carnahan, A. B., Luther, C. D., and Wilkes, E. F., 1969, *Applied Numerical Methods*, 1st ed., Wiley, New York.
- Carslaw, H. S., and Jaeger, J. C., 1963, *Operations Methods in Applied Mathematics*, Dover.
- Dunkle, R. V., and Maclaine-cross, I. L., 1970, "Theory and Design of Rotary Regenerators for Air Conditioning," *Trans. Mech. and Chem. Eng.*, Institution of Engineers, Australia, Vol. MC6(1), pp. 1–6.
- Dunkle, R. V., Banks, P. J., and Maclaine-cross, I. L., 1980, "Wound Parallel Plate Exchangers for Air-Conditioning Applications," *Compact Heat Exchangers*, R. K. Shah et al., eds., ASME HTD-Vol. 10, pp. 65–71.
- Hwang, C. I., and Fan, F. T., 1963, "Finite Difference Analysis of Forced-Convection Heat Transfer in Entrance Region of a Flat Rectangular Duct," *Appl. Sci. Res.*, Section A, Vol. 13, p. 401.
- Leonard, B. P., 1979, "A Stable and Accurate Convective Modelling Procedure Based on Quadratic Upstream Interpolation," *Comp. Meth. in Applied Mech. and Eng.*, Vol. 19, pp. 59–98.
- Lundgren, T. S., Sparrow, E. M., and Starr, J. B., 1964, "Pressure Drop Due to the Entrance Region in Ducts of Arbitrary Cross Section," *ASME Journal of Basic Engineering*, Vol. 86, No. 3, pp. 620–626.



Maclaine-cross, I. L., 1974, "A Theory of Combined Heat and Mass Transfer in Regenerators," Ph.D. thesis, Department of Mechanical Engineering, Monash University, Australia.

Maclaine-cross, I. L., and Ambrose, C. W., 1980, "Predicted and Measured Pressure Drop in Parallel Plate Rotary Regenerators," *ASME Journal of Fluids Engineering*, Vol. 102, No. 1, pp. 59-63.

Maclaine-cross, I. L., and Pesaran, A. A., 1986, "Heat and Mass Transfer Analysis of Dehumidifiers Using Adiabatic Transient Tests," presented at the AIAA/ASME 4th Thermophysics and Heat Transfer Conference, Boston, MA.

Mercer, W. E., Pearce, W. M., and Hitchcock, J. E., 1967, "Laminar Forced Convection in the Entrance Region Between Parallel Flat Plates," *ASME JOURNAL OF HEAT TRANSFER*, Vol. 89, p. 251.

Nguyen, T. V., 1980, "Parallel Plate Heat Exchangers," Ph.D. thesis, School of Mechanical and Industrial Engineering, University of New South Wales, Australia.

Nguyen, T. V., Maclaine-cross, I. L., and de Vahl Davis, G., 1981, in: *Numerical Methods in Heat Transfer*, R. W. Lewis, K. Morgan, and O. C. Zienkiewicz, eds., Wiley, pp. 349-372.

Nguyen, T. V., and Maclaine-cross, I. L., 1988, "Incremental Pressure Drop Number in Parallel-Plate Heat Exchangers," *ASME Journal of Fluids Engineering*, Vol. 110, No. 1, pp. 93-96.

Shah, R. K., 1975, "Thermal Entry Length Solutions for the Circular Tube and Parallel Plates," *Proc. Natl. Heat Mass Transfer Conf., 3rd*, Indian Inst. Technol., Bombay, Vol. 1, Paper No. HMT-11-75.

Shah, R. K., and London, A. L., 1978, "Laminar Flow Forced Convection in Ducts," *Advances in Heat Transfer*, T. F. Irvine and J. P. Harnett, eds., Academic Press.

Sparrow, E. M., Novotny, J. M., and Lin, S. H., 1963, "Laminar Flow of a Heat-Generating Fluid in a Parallel-Plate Channel," *AICHE J.*, Vol. 9, pp. 797-804.

# Influence of High Mainstream Turbulence on Leading Edge Heat Transfer

A. B. Mehendale  
Research Assistant.

J. C. Han  
Professor.  
Fellow ASME

S. Ou  
Research Assistant.

Turbine Heat Transfer Laboratory,  
Mechanical Engineering Department,  
Texas A&M University,  
College Station, TX 77843-3123

*The influence of high mainstream turbulence on leading edge heat transfer was studied. High mainstream turbulence was produced by a bar grid ( $Tu = 3.3$ – $5.1$  percent), passive grid ( $Tu = 7.6$ – $9.7$  percent), and jet grid ( $Tu = 12.9$ – $15.2$  percent). Experiments were performed using a blunt body with a semicylinder leading edge and flat sidewalls. The mainstream Reynolds numbers based on leading edge diameter were 25,000, 40,000, and 100,000. Spanwise and streamwise distributions of local heat transfer coefficients on the leading edge and flat sidewall were obtained. The results indicate that the leading edge heat transfer increases significantly with increasing mainstream turbulence intensity, but the effect diminishes at the end of the flat sidewall because of turbulence decay. Stagnation point heat transfer results for high turbulence intensity flows agree with the Lowery and Vachon correlation, but the overall heat transfer results for the leading edge quarter-cylinder region are higher than their overall correlation for the entire circular cylinder region. High mainstream turbulence tends not to shift the location of the separation-reattachment region. The reattachment heat transfer results are about the same regardless of mainstream turbulence levels and are much higher than the turbulent flat plate correlation.*

## Introduction

The trend in advanced aeroengine design for high thermal efficiency and high power density is toward high entry gas temperature. Highly sophisticated cooling technologies such as film cooling and augmented internal cooling are employed for airfoils of advanced gas turbine engines. To provide a better cooling design it is necessary to understand the convective heat transfer characteristics between a high-temperature gas stream and turbine airfoil. Important parameters that affect turbine airfoil heat transfer are mainstream turbulence, pressure gradient, surface curvature, roughness, and film cooling. This investigation focuses on the influence of high mainstream turbulence on leading edge heat transfer.

Consider convective heat transfer in the case of turbulent flow over a flat plate. Studies by Simonich and Bradshaw (1978) and Hancock and Bradshaw (1983) on effects of mainstream turbulence on heat transfer showed that for every 1 percent increase in turbulence intensity the heat transfer coefficient increases about 5 percent. Blair (1983a, 1983b) did extensive work in finding the effect of grid-generated turbulence on flat plate heat transfer and reported that for a turbulence intensity of 6 percent the heat transfer coefficient increases by 18 percent as compared to that without grid. Han and Young (1988) and Young et al. (1991) studied the effect of jet-grid-generated turbulence on flat plate heat transfer and reported that for a turbulence intensity of 15 percent, the heat transfer coefficient increases by 50 percent as compared to the zero turbulence correlation in the fully turbulent region.

Consider heat transfer in the case of flow over a circular cylinder. O'Brien and VanFossen (1985) studied the effect of jet-grid-generated turbulence on heat transfer from the leading edge of a circular cylinder in crossflow. At a turbulence intensity of 10–12 percent, the heat transfer coefficient increased by 37–53 percent over the zero turbulence intensity case for Reynolds numbers 48,000–180,000. They reported that the

stagnation point heat transfer results were 10–15 percent lower than the frequency used Lowery and Vachon correlation (1975). Morehouse and Simoneau (1986) studied the effects of grid and wake-generated turbulence on the local heat transfer for the forward half of a circular cylinder. They found that the stagnation point heat transfer results for the grid-generated turbulence agreed with the Lowery and Vachon correlation, while the stagnation heat transfer results for the wake-generated turbulence were 10–25 percent lower than the correlation.

Consider heat transfer in the case of flow over a blunt body with a circular leading edge and a flat afterbody. Ota and Kon (1974, 1980) studied heat transfer in the separated and reattached flow on blunt flat plates. They found that for a low mainstream turbulence intensity of about 0.5 percent, the heat transfer downstream of reattachment relaxes to the common turbulent state. Ota and Kon (1979) studied the effect of nose (leading edge) shape on heat transfer in the separated, reattached, and redeveloped regions for Reynolds numbers lower than 20,000. Zelenka and Loehrke (1983) also studied the effect of leading edge bluntness for Reynolds numbers less than 4000. Bellows and Mayle (1986) examined heat transfer downstream of a leading edge separation bubble on a blunt body. They measured the free-stream and boundary layer velocity profiles for a low mainstream turbulence intensity of about 0.4 percent and found that a small separation bubble existed where the leading edge merged with the flat afterbody. They also reported that the surface heat transfer through the separation region increased by almost an order of magnitude and, near reattachment, was about 50 percent higher than that predicted by the turbulent flat plate correlation.

This study focuses on the effect of high mainstream turbulence on leading edge heat transfer. A blunt body with a semicylinder leading edge and a flat afterbody, similar to that used by Bellows and Mayle (1986), is used. Mainstream turbulence is produced by a bar grid with an incident turbulence intensity of 3.3–5.1 percent, a passive grid with an incident turbulence intensity of 7.6–9.7 percent, and a jet grid (similar to that used by Han and Young, 1988; Young et al., 1991)

Contributed by the Heat Transfer Division for publication in the JOURNAL OF HEAT TRANSFER. Manuscript received by the Heat Transfer Division March 14, 1990; revision received April 23, 1991. Keywords: Forced Convection, Turbines, Turbulence.

with an incident mainstream turbulence intensity of 12.9–15.2 percent. Spanwise and streamwise distributions of local heat transfer from the leading edge to the end of the flat afterbody are obtained for three incident mainstream Reynolds numbers of 25,000, 40,000, and 100,000 based on the leading edge diameter. The main objectives of the study are to determine: (1) whether the stagnation point heat transfer under high mainstream turbulence and moderate Reynolds numbers agrees with the Lowery and Vachon correlation that was developed for moderate mainstream turbulence levels and very high Reynolds numbers ( $Re_D = 109,000$  to  $302,000$ ), (2) whether high mainstream turbulence affects heat transfer at separation and reattachment, and (3) whether high mainstream turbulence affects the separation and reattachment locations.

This paper represents part of the results from the research program "Influence of High Mainstream Turbulence on Leading Edge Film Cooling and Heat Transfer." Additional information on the present investigation may be found from Mehendale (1991) and Mehendale and Han (1990).

### Test Apparatus and Instrumentation

A schematic of the low-speed, open circuit wind tunnel is shown in Fig. 1. The test apparatus was designed as a suction type wind tunnel to avoid uncontrolled turbulence in the discharge of the 7.5 kW (10 hp) blower. A flow straightener made of honeycombed plastic straws assured uniform and parallel flow going into the nozzle. The one-dimensional, 3:1 contraction nozzle produced a uniform flow entering the test channel. The test channel was 25.4 cm high, 76.2 cm wide in cross section, and 183 cm in length. Flow velocity could be varied by controlling a sliding gate on the discharge end of the blower and was continuously monitored by a pitot probe located inside the test channel. The inlet air temperature was maintained within  $\pm 1^\circ\text{C}$  of the desired value by a central air conditioning unit.

Three turbulence grids were fabricated to generate different levels of turbulence intensities. The turbulence grids are shown in Fig. 1. The first was a relatively lower turbulence bar grid, the second a high turbulence passive grid, and the third was an even higher turbulence jet grid. All three grids had an open area of 54 percent. The bar grid was made of stainless steel bars, 0.5 cm square in cross section and 1.9 cm apart. The passive grid was made of hollow brass tubes, 1.3 cm square in cross section and 4.8 cm apart. The passive grid also served as the jet grid as it had 96 holes 0.5 mm in diameter located at the grid nodes. Holes were drilled in vertical tubes and

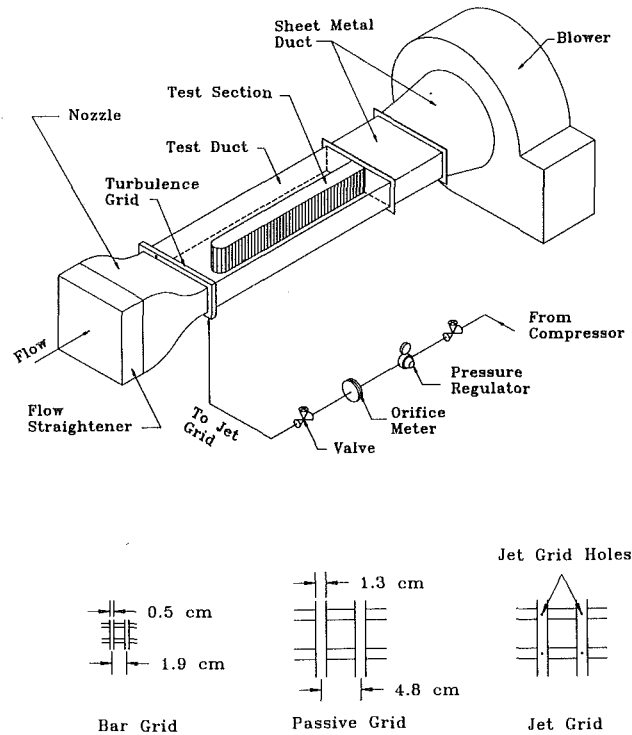


Fig. 1 Schematic of the test rig

pointed downstream of the grid. These vertical tubes were connected at the top and bottom to two injection plenums. To use the passive grid as a jet grid, compressed air was supplied to the injection plenums, which distribute the air evenly. The injection plenums had four inlet ports. Velocity distributions, in a plane normal to the flow direction at  $X/b = 20$ , showed that the jet centerline velocities were within  $\pm 5$  percent of the average velocity (based on the mass flow rate supplied to the injection plenums). The compressed air passed through the hollow brass tubes and was subsequently injected in the downwind (downstream) direction. Tests were performed to find the optimum injection ratio for the jet grid. It was found that as the injection ratio was increased, the turbulence intensity increased and then tapered off. The beginning point of taper was used as the optimum point and the corresponding optimum injection ratio was used. The optimum injection ratio (injection

### Nomenclature

$b$  = passive grid width  
 $D$  = leading edge diameter  
 $h$  = convective heat transfer coefficient  
 $L_e^u$  = dissipation length scale  
 $Nu_D$  = local Nusselt number based on leading edge diameter  
 $\overline{Nu_D}$  = spanwise-averaged Nusselt number  
 $\overline{Nu_D}$  = leading edge overall Nusselt number (spanwise and streamwise-averaged)  
 $q''$  = convective heat flux  
 $q''_{\text{cond}}$  = conduction heat loss flux  
 $q''_{\text{gen}}$  = generated surface heat flux  
 $q''_{\text{rad}}$  = radiation heat loss flux  
 $R$  = leading edge radius

$Re_D$  = Reynolds number based on incident mainstream velocity ( $U_\infty$ ) and leading edge diameter  
 $Re_x$  = Reynolds number based on local mainstream velocity and streamwise distance measured from stagnation point  
 $St$  = Stanton number based on local mainstream velocity and streamwise distance measured from stagnation point  
 $\overline{St}$  = spanwise averaged Stanton number  
 $Tu$  = local streamwise turbulence intensity  $(u'^2)^{1/2}/U$

$T_{aw}$  = adiabatic wall (foil) temperature  
 $T_w$  = measured wall (foil) temperature  
 $T_\infty$  = incident mainstream air temperature  
 $U$  = local mainstream velocity  
 $U_\infty$  = incident mainstream velocity at  $X/b = 20$  without any grid  
 $u'$  = local streamwise fluctuating velocity  
 $(u'^2)^{1/2}$  = rms of fluctuating velocity component  
 $X$  = axial distance measured from grid  
 $x$  = streamwise distance measured from stagnation  
 $Z$  = spanwise distance

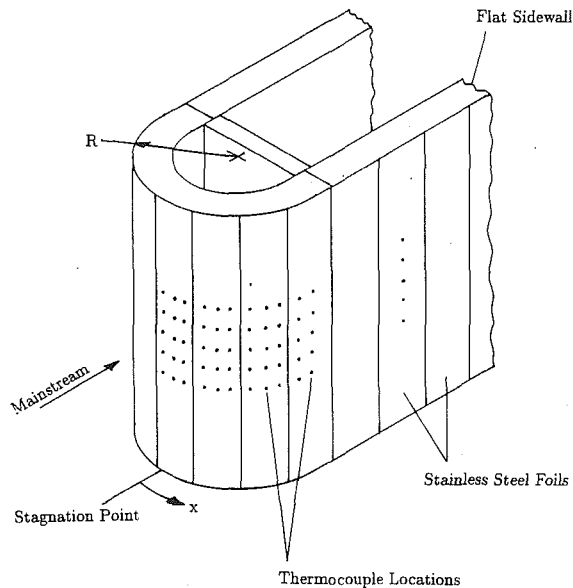


Fig. 2 Schematic of leading edge with detailed thermocouple distributions

mass flow rate/mainstream flow rate) was 2.5–3.0 percent depending on the Reynolds number under consideration.

As shown in Fig. 2, the test model was a blunt body with a semicylinder leading edge and a flat afterbody. It simulates the leading edge of a gas turbine vane. The leading edge was 15.2 cm in diameter and 25.4 cm in height, which created a flow blockage of 20 percent. At  $\pm 90$  deg from the stagnation line, the leading edge profile merged with two 158-cm-long and 25.4-cm-high flat walls running parallel to the end of the test model. High-quality oak wood pieces were laminated together to form the test model. The wood was 2.8 cm thick throughout. Tiny holes were drilled at strategic locations in the test model to let thermocouple wires through. To assure uniform approaching flow and turbulence, the leading edge of the test model was positioned at a distance of 47.6 cm downstream of the grid in the test channel ( $X/b = 37$ ).

Forty-five strips of 0.005-cm-thick stainless steel foil were cemented vertically on the outer surface of the test model. Each strip was 25 cm long, 3.8 cm wide, and separated from the others by 0.8 mm. The foils were connected in a serpentine manner, by means of copper bus bars, to form a series circuit. To eliminate local disturbances caused by the 0.8-mm gaps, the gaps were filled with silicone caulk until the surface was smooth and flush with the foil surface. This prevented the flow from tripping at the upstream edge of each foil and reduced the risk of accidental electric contact between foils. The surface acted as a constant heat flux test surface when a voltage source was applied across it; otherwise, it acted as an adiabatic surface. An autotransformer was used to generate the desired amount of constant heat flux in the foils. Circuit voltage and current were measured by a HP digital multimeter. Seventy calibrated, 36-gage copper-constantan thermocouples were centered on the underside of the foils. Fifty-five were distributed in the semicylinder leading edge region as shown in Fig. 2. The thermocouples in the leading edge region were spaced 1.6 cm and 1.3 cm in the spanwise and streamwise directions, respectively. Additional thermocouples were attached on the inner wall of the test model to estimate conduction heat loss. All thermocouples were connected to a 100-channel Fluke 2280A data logger interfaced with an IBM PC.

A four-channel TSI IFA 100 constant temperature anemometer (CTA) and a four-channel TSI IFA 200 high-speed digitizer were connected to an IBM PC through a TSI DMA connector to record hot-wire data. A calibrated single hot wire

Table 1 Reference turbulence intensities with different turbulence grids for different Reynolds numbers

| $Re_D$  | No Grid | Bar Grid | Passive Grid | Jet Grid |
|---------|---------|----------|--------------|----------|
| 100,000 | 0.75%   | 5.07%    | 9.67%        | 12.9%    |
| 40,000  | 0.73%   | 4.66%    | 7.59%        | 15.2%    |
| 25,000  | 1.37%   | 3.31%    | 8.53%        | No Tests |

was used to measure streamwise mainstream velocity and turbulence intensity distributions. An HP 3478A multimeter monitored true rms fluctuations in the CTA output. This was used to double check the computer display of calibrated rms values, which was based on the five sets of 1032 readings from the TSI IFA 200 digitizer. Pitot probes, 2 mm in diameter, were used to measure velocity profiles, set desired Reynolds number flow, and constantly monitor it. These probes were connected to a Dwyer microtector with a least count of 0.025 mm.

### Test Conditions and Data Analysis

Before conducting heat transfer tests it was assured that mainstream flow velocities at corresponding locations on the left and right sides of the test model flat sidewalls were the same. This assured that the test model was centrally located within the test channel, i.e., flow symmetry existed. Heat transfer tests were conducted at Reynolds numbers of 100,000, 400,000, and 25,000 based on leading edge diameter ( $D$ ) and incident mainstream velocity ( $U_\infty$ ).

Mainstream streamwise turbulence intensity in the test channel without insertion of any turbulence grid (the no-grid case) was about 0.75 percent. Higher streamwise turbulence intensities were generated by inserting the appropriate turbulence grid in the mainstream flow at the nozzle exit. Centerline turbulence intensity decayed with distance from the grid but, as the flow approached the stagnation line, a decrease in mainstream velocity caused an increase in turbulence intensity. It was seen that as the Reynolds number was changed the same grid would produce a different level of streamwise turbulence intensity distribution. The point of minimum turbulence intensity, before the stagnation effect caused it to go up, varied with grid and Reynolds number. Because of this, it was very difficult to say which value of turbulence intensity should be considered as the reference value, the value at a fixed location downstream of the grid or the minimum value for a given upstream condition. In this study, the minimum value of the centerline decay curve was chosen as the reference turbulence intensity. The reference values of percent turbulence intensities for different Reynolds numbers and grids are shown in Table 1. This will be discussed further in Fig. 3.

The mainstream temperature was maintained at about 25°C. The total heat loss for all cases of Reynolds numbers and grids was maintained at similar levels by sustaining similar levels of surface temperature distribution, ranging from 40 to 50°C, over the entire test model. This was achieved by controlling the input voltage. It took an average of 3½ to 4 hours to reach steady state for each test case. Three sets of temperature distribution data at one-minute intervals were recorded when steady state was reached. The data were averaged to reduce the effects of minor surface temperature fluctuations.

The local heat transfer coefficient,  $h$ , is defined as:

$$h = q'' / (T_w - T_{aw}) \quad (1)$$

where  $q''$  is the convective heat flux from the foil surface,  $T_w$  is the local steady-state foil temperature, and  $T_{aw}$  is the adiabatic wall temperature.

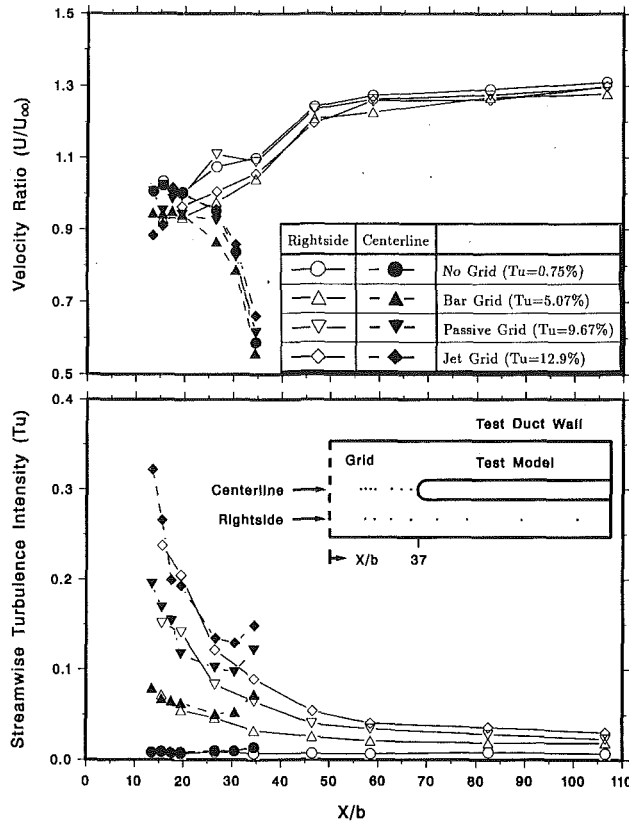


Fig. 3 Streamwise distributions of normalized mainstream velocity and turbulence intensity

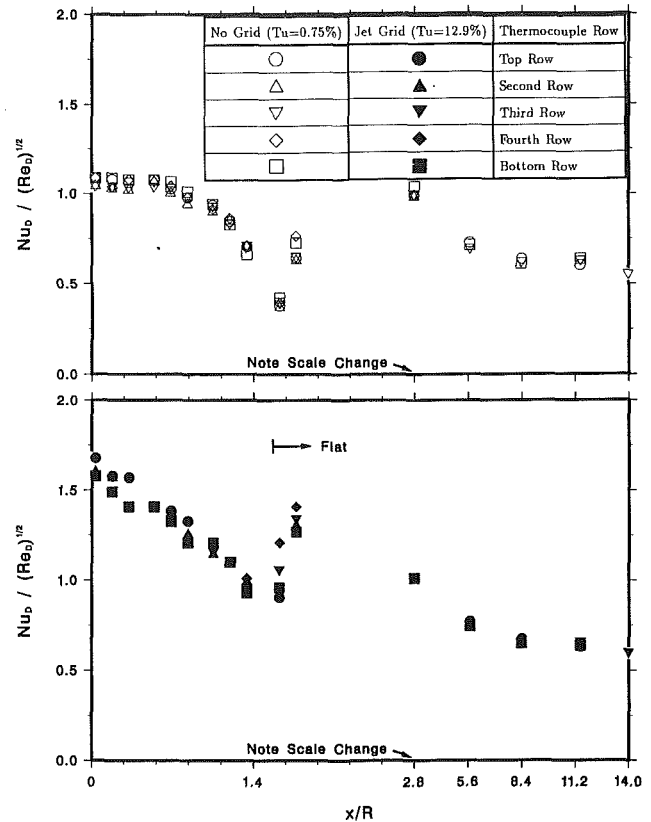


Fig. 4 Local Nusselt number distributions for  $Re_D = 100,000$ : (a)  $Tu = 0.75$  percent, (b)  $Tu = 12.9$  percent

To take into account the conduction and radiation heat losses, the local heat transfer coefficient  $h$  was calculated using:

$$h = (q''_{gen} - q''_{cond} - q''_{rad}) / (T_w - T_{aw}) \quad (2)$$

where  $q''_{gen}$  is the generated surface heat flux from voltage-current calculations,  $q''_{cond}$  is the conduction loss flux through the test model and to the surroundings, and  $q''_{rad}$  is the radiation loss flux to the test channel walls.

Uniform foil resistance produced an almost constant surface heat flux boundary condition. Loss tests were performed for a no-flow condition to determine total heat loss from the test model. The loss calibration was performed by supplying a small amount of power to the test model. The surface temperature distribution, power input, and ambient temperature were recorded when steady state was reached. A different level of power was then supplied and the procedure was repeated. This was done several times to obtain the loss curve. This was used to estimate the total loss.

Radiation heat loss was estimated using the Stefan-Boltzmann equation with an assumed value of emissivity of 0.22 for stainless steel foils at  $45^\circ\text{C}$ . Thus, knowing the two, conduction loss was estimated. The conduction and radiation loss fluxes were about 3 and 10 percent of the generated surface heat flux. Heat conduction within the thin heater foils was less than 0.1 percent and was not considered. Heat loss through the thermocouple wires was less than 0.1 percent and was also negligible.

An uncertainty analysis was carried out based on the method of Kline and McClintock (1953). The uncertainties in  $h$ ,  $Nu$ , and  $Re$  were 1.1, 2.2, and 3.4 percent, respectively. This resulted in an overall uncertainty of about 3 percent in the  $Nu/(Re)^{1/2}$  results for the most conservative case of  $Re_D = 25,000$ .

## Results and Discussion

Velocity and turbulence intensity distributions in the test

channel were measured to check the oncoming mainstream flow conditions. The vertical and horizontal velocity profiles at midplane were measured by traversing a pitot probe 1.5 diameters upstream of the leading edge. The results show that the oncoming mainstream velocity profiles were fairly uniform over the entire  $Y$ - $Z$  midplane (Mehendale, 1991). Figure 3 shows local velocity and turbulence intensity distributions along the centerline and right-side line of the test channel for a Reynolds number of 100,000. It is seen that the ratio of local mainstream velocity to incident mainstream velocity ( $U/U_\infty$ ) is 1.0 to 20 grid diameters ( $X/b = 20$ ) downstream of the grid, i.e., 1.5 diameters upstream of the leading edge of the test model. The incident mainstream velocity ( $U_\infty$ ) is 10 m/s at  $X/b = 20$  with the no-grid condition. Downstream of this point, local mainstream velocities along the centerline decrease sharply because of approaching leading edge stagnation. However, they increase along the right-side line because of the test model blockage effect. These curves then taper off, but the small increase is because of the growing boundary layer.

Although the mainstream velocity distributions along the centerline and right-side line do not vary much with upstream turbulence conditions, it is not so for the turbulence intensity distributions. The results show that for the bar, passive, and jet-grid cases, the streamwise turbulence intensity along the right-side line decreases monotonically with increasing distance from the grid. The streamwise turbulence intensity along the centerline also decreases at a higher rate than that along the right-side line. It then starts increasing as the mainstream velocity starts decreasing because of the stagnation effect. As indicated earlier, these minimum values are used as reference turbulence intensities (see Table 1). For  $Re_D = 100,000$ , the reference turbulence intensities are 5.07 percent for the bar grid, 9.67 percent for the passive grid, and 12.9 percent for the jet grid. The corresponding dissipation length scales at the same location are estimated to be about 1.0 cm ( $L_t^*/D = 0.066$ ),

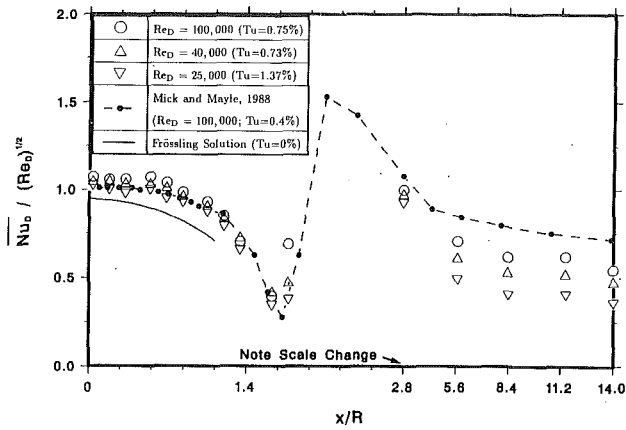


Fig. 5 Effect of Reynolds number on spanwise-averaged Nusselt number distributions for  $Tu = 0.75$  percent

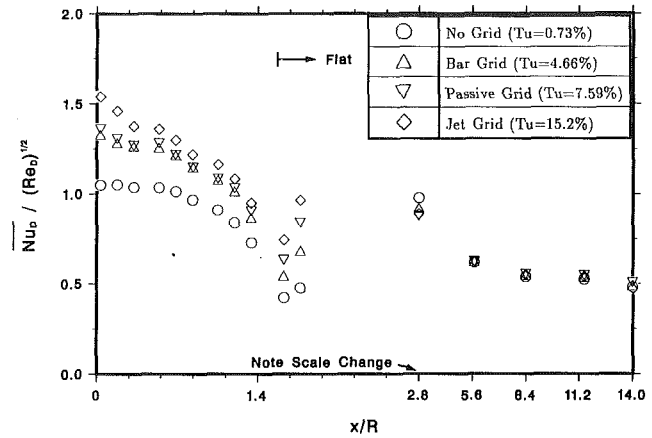


Fig. 7 Effect of turbulence intensity on spanwise-averaged Nusselt number distributions for  $Re_D = 40,000$

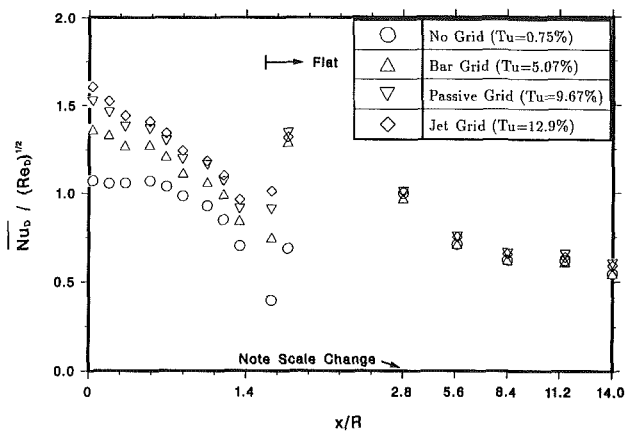


Fig. 6 Effect of turbulence intensity on spanwise-averaged Nusselt number distributions for  $Re_D = 100,000$

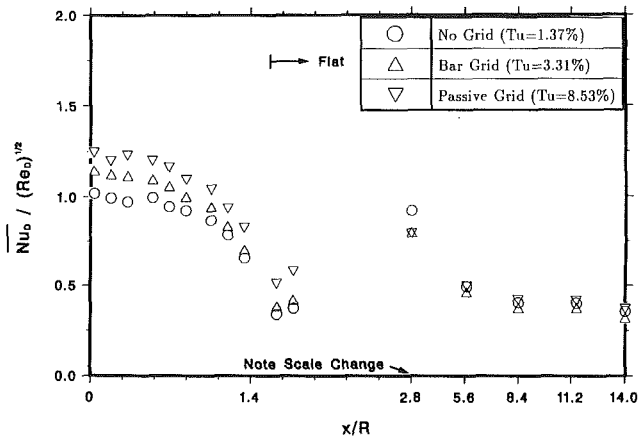


Fig. 8 Effect of turbulence intensity on spanwise-averaged Nusselt number distributions for  $Re_D = 25,000$

1.5 cm ( $L_e^u/D = 0.099$ ), and 1.7 cm ( $L_e^u/D = 0.112$ ), respectively. The dissipation length scale is determined based on the method proposed by Hancock and Bradshaw (1983). The dissipation length scale is calculated from the streamwise mean and fluctuating velocity measurements as  $L_e^u = -(\bar{u}'^2)^{3/2}/(U\bar{u}'^2/dx)$ .

Figure 4 shows the spanwise variation of  $Nu_D/(Re_D)^{1/2}$  at all streamwise locations ( $x/R$ ) for the no-grid and jet-grid cases at  $Re_D = 100,000$ . The spanwise variation for the no-grid case is as expected within  $\pm 2$  percent of average at all locations. There is an increase in the spanwise variation for the jet-grid high-turbulence case. The grid-generated high-turbulence flow contains many different sizes of vortex. These vortices may give rise to spanwise variations and account for the increase in leading edge region heat transfer. This spanwise variation is larger in the separation region ( $x/R \approx 1.6$ ). However, the turbulence intensity does not affect the spanwise variation on the flat sidewall region.

Figure 5 shows that for  $Re_D = 100,000$ , the spanwise-averaged heat transfer results  $\bar{Nu}_D/(Re_D)^{1/2}$  follow those obtained by Mick and Mayle (1988). In their paper, the decrease and rapid rise of a Nusselt number around  $x/R = 1.6$  is the result of a separating leading edge laminar boundary layer followed by a turbulent reattachment. The present data are slightly higher in the leading edge region and lower on the flat portion of the test model. The wind tunnel in the present study had an inherent turbulence intensity of 0.75 percent, which is higher than the 0.4 percent in Mick and Mayle's case. This may be the reason that our results appear slightly higher in the leading edge region. In the present study, for the same approaching mainstream Reynolds number flow, the mainstream velocity

on the flat sidewall portion is 20 percent lower than Mick and Mayle's because of lower blockage. For this reason the boundary layer on the flat sidewall is thicker and can explain the lower heat transfer coefficients on the flat sidewall. The Frössling solution for the stagnation region heat transfer for zero turbulence intensity mainstream flow (O'Brien and VanFossen, 1985) is shown for comparison with the analysis results. Figure 5 also shows streamwise variations of spanwise-averaged Nusselt numbers for the no-grid case and for  $Re_D = 40,000$  and 25,000. It is seen that there is a downward shift in the entire distribution curve with decreasing Reynolds numbers. The effect of the Reynolds number on heat transfer is not as severe in the leading edge region as in the flat sidewall region. This is because the boundary layer in the leading edge region is quite thin due to stagnation and accelerating flow, but the difference in boundary layer growth is appreciable on the flat sidewall region.

Figure 6 shows the effect of mainstream turbulence intensity on spanwise-averaged heat transfer results for  $Re_D = 100,000$ . As the mainstream turbulence intensity increases, the spanwise-averaged heat transfer on the leading edge region also increases. The jet grid causes an increase as high as 50 percent near the stagnation region in the heat transfer results. Due to different mainstream turbulence intensity flows, the spread in  $Nu_D$  at a given location ( $x$ ) reduces with increasing streamwise distance to the point of separation ( $x/R \approx 1.6$ ) where the spread is quite large. At the point of reattachment ( $x/R \approx 1.7$ ), the effect of jet, passive, or bar grid on heat transfer is negligible but the results are much higher than that for the no-grid case. The effect of upstream turbulence conditions on the flat sidewall region is insignificant and may be due to the decay

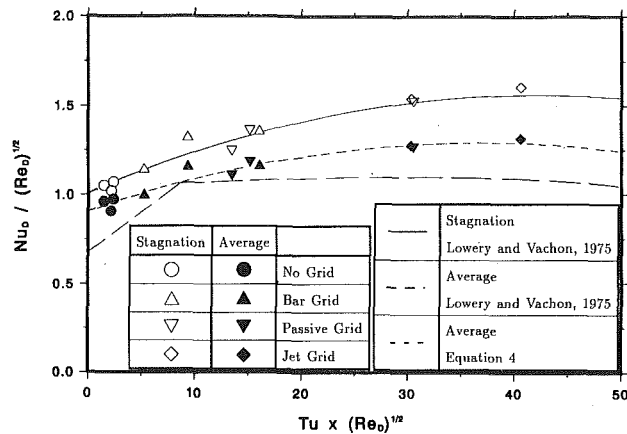


Fig. 9 Comparison of leading edge heat transfer data with high turbulence to frequently used correlation

of turbulence intensity and the turbulent boundary layer. Figure 7 shows the effect of mainstream intensity for the case of  $Re_D = 40,000$ . The effect of jet grid in the leading edge region has been reduced slightly as compared to  $Re_D = 100,000$ . The effect of passive grid is reduced considerably compared to the jet grid. The bar grid and passive grid produce very similar heat transfer results. This pattern stays the same until the point of separation when more spread is observed as in  $Re_D = 100,000$ . The effect of upstream turbulence on the flat sidewall region is not evident. Jet grid tests were not performed for a Reynolds number of 25,000. The heat transfer results for the rest of the turbulence grids are shown in Fig. 8. There is a clear distinction between the results for the bar grid and passive grid. As expected, the passive grid produces the highest heat transfer on the leading edge. As observed in the previous cases, there is little effect of upstream turbulence intensity on the flat sidewall region.

A comparison of Figs. 6, 7, and 8 shows that for  $Re_D = 40,000$ , the enhancement in heat transfer from bar grid to passive grid is not as distinct as for  $Re_D = 25,000$  and 100,000. The reason for this is seen in Table 1. The mainstream turbulence intensity for the bar grid increases with increasing Reynolds numbers, but such is not the case for the passive grid where the turbulence intensity for  $Re_D = 40,000$  is the minimum of all three Reynolds numbers. The increments in turbulence intensity, from bar grid to passive grid for  $Re_D = 100,000$ , 40,000, and 25,000, are 4.60, 2.93, and 5.22 percent, respectively. Since  $Re_D = 40,000$  has the least increment, the heat transfer enhancement from bar grid to passive grid is the minimum for  $Re_D = 40,000$ .

Lowery and Vachon (1975) presented the following equation for stagnation point heat transfer:

$$\overline{Nu}_D / (Re_D)^{1/2} = 1.01 + 2.624[Tu(Re_D)^{1/2}/100] - 3.07[Tu(Re_D)^{1/2}/100]^2 \quad (3)$$

The effect of  $Tu(Re_D)^{1/2}$  on the stagnation region heat transfer and overall leading edge heat transfer is shown in Fig. 9. Reference values of turbulence intensities, shown in Table 1, have been used to evaluate the parameter  $Tu(Re_D)^{1/2}$ . The stagnation region results are spanwise-averaged heat transfer data for the first column of thermocouples near the stagnation line. The overall leading edge results are spanwise and then streamwise-averaged heat transfer data over the entire leading edge quarter-cylinder region. The results for stagnation point heat transfer follow the stagnation point heat transfer correlation by Lowery and Vachon (1975). Lowery and Vachon used a large mesh grid (0.2 cm diameter, 2.52 cm pitch, 1-3 percent turbulence intensity) and a wooden dowel grid (1.58 cm diameter, 3.15 cm pitch, 5-14 percent turbulence intensity) in their experiments for Reynolds numbers between 109,000

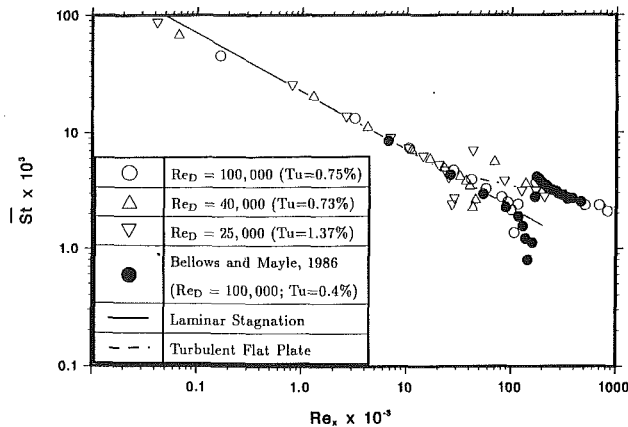


Fig. 10 Spanwise-averaged Stanton number distributions for  $Tu = 0.75$  percent

and 302,000. Overall heat transfer results for the entire leading edge are slightly higher than those obtained by Lowery and Vachon. This is possibly because only the front half of the leading edge is considered, whereas, in other studies, the entire cylinder with lower heat transfer coefficients on the back half are considered. The following equation represents the overall leading edge heat transfer data:

$$\overline{Nu}_D / (Re_D)^{1/2} = 0.902 + 2.14[Tu(Re_D)^{1/2}/100] - 2.89[Tu(Re_D)^{1/2}/100]^2 \quad (4)$$

Another important consideration is the variation of the spanwise-averaged Stanton number ( $St$ ) with  $Re_x$  based on streamwise distance from stagnation, the local mainstream velocity ( $U$ ), and properties based on boundary conditions. The heat transfer results for  $Re_D = 100,000$ , 40,000, and 25,000 for the no-grid case are shown in Fig. 10. Heat transfer results for  $Re_D = 100,000$  and the mainstream turbulence intensity of 0.4 percent from Bellows and Mayle (1986) are also included. Also plotted are the laminar solution for two-dimensional stagnation flow

$$St = 0.57Pr^{-0.6}Re_x^{-0.5} \quad (5)$$

and the turbulent flat plate correlation for a constant heat flux surface

$$St = 0.0307Pr^{-0.4}Re_x^{-0.2} \quad (6)$$

where  $Pr$ , the Prandtl number, is assumed to be 0.707. In Fig. 10 it is seen that even though the points of separation from the three Reynolds numbers, based on diameter, are physically very close to each other ( $x/R = 1.6$  from Fig. 5), when plotted against  $Re_x$  there are three distinct minima. Prior to the points of minimum heat transfer, all the points follow the laminar stagnation solution very well except for a slight variation on the stagnation point. Heat transfer results are higher than the turbulent correlation when flow reattaches on the surface. After reattachment, heat transfer results on the flat sidewall region follow the turbulent flat plate correlation pattern except they are slightly lower than the correlation. The present data agree with Bellows and Mayle (1986) for  $Re_D = 100,000$ .

Figure 11 shows the effect of mainstream turbulence intensity on the Stanton number for  $Re_D = 100,000$ . The results for the no-grid case follow the laminar solution until the separation point but are always slightly higher. The Stanton number for a given location goes up with increasing mainstream turbulence intensity. It should be noted that as  $Re_x$  goes up, the spread in Stanton number decreases, i.e., the effect of mainstream turbulence intensity is reduced. Locations for flow separation and reattachment are not affected by mainstream turbulence levels. After reattachment all points seem to fall

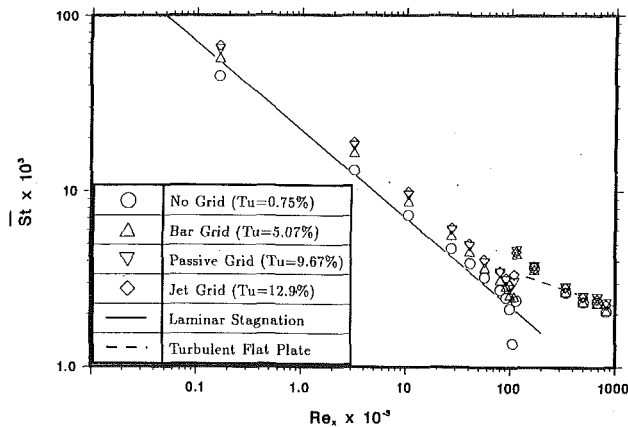


Fig. 11 Effect of turbulence intensity on spanwise-averaged Stanton number distributions for  $Re_D = 100,000$

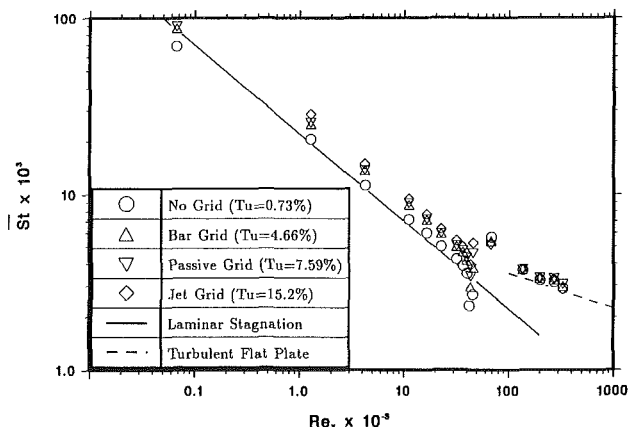


Fig. 12 Effect of turbulence intensity on spanwise-averaged Stanton number distributions for  $Re_D = 40,000$

together for any given location and are on the turbulent flat plate curve. As seen in Fig. 12, for  $Re_D = 40,000$ , the heat transfer results for the no-grid case follow the curve more closely than the previous case to the point of separation. An increase in mainstream turbulence intensity increases the Stanton number at any given location. As in the previous case, because of upstream turbulence conditions, the Stanton number variation at a given location reduces with increasing  $Re_x$ . The results at the reattachment region are higher than the turbulent flat plate curve. This is consistent with  $Re_D = 100,000$  because the flow probably has not yet developed into a fully developed turbulent flow. In the case of  $Re_D = 25,000$ , shown in Fig. 13, the no-grid case heat transfer results fall on the laminar stagnation curve before the point of separation. The effect of mainstream turbulence in increased heat transfer is as previously seen. Unlike the previous two cases, the heat transfer results on the flat sidewall are slightly lower than the turbulent flat plate correlation.

### Concluding Remarks

The influence of high mainstream turbulence on leading edge heat transfer has been investigated. Streamwise distributions of the local heat transfer coefficient are obtained under four mainstream turbulence levels for three mainstream Reynolds numbers. The main findings are:

1 Heat transfer in the leading edge region increases significantly with increasing mainstream turbulence levels for the three Reynolds numbers studied. The effect diminishes at the end of the flat sidewall due to decay of mainstream turbulence.

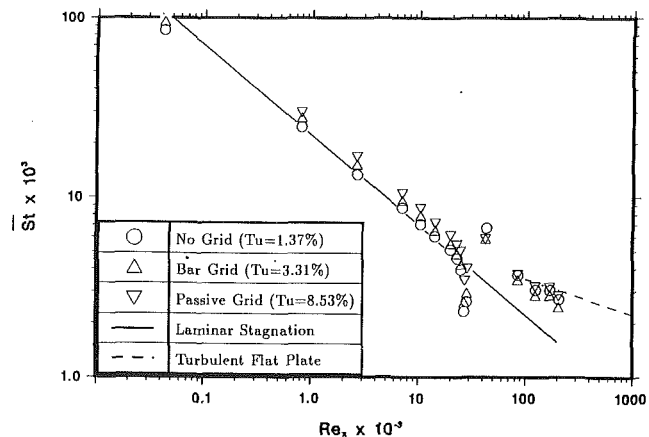


Fig. 13 Effect of turbulence intensity on spanwise-averaged Stanton number distributions for  $Re_D = 25,000$

2 Stagnation point heat transfer (results for all four mainstream turbulence levels and three Reynolds numbers studied) agrees with the correlation developed by Lowery and Vachon. Overall heat transfer results for the entire leading edge quarter-cylinder region are higher than those obtained by Lowery and Vachon for the entire circular cylinder region.

3 Separation and reattachment locations (at the leading edge merging with the flat plate) are not affected by mainstream turbulence levels. Heat transfer results at the reattachment point for all four mainstream turbulence levels are about the same and are higher than the turbulent flat plate correlation for each of the three Reynolds numbers studied.

4 Heat transfer results for all four mainstream turbulence levels fall together far downstream from reattachment on the turbulent flat plate correlation. However, heat transfer data are lower than the turbulent correlation for the case  $Re_D = 25,000$ .

### Acknowledgments

The turbulence portion was supported through Dr. Richard B. Rivir of the U.S. Air Force Wright-Patterson Air Force Base under contract #F33615-86-C-2723. The test model was associated with the Film Cooling Project sponsored by Textron Lycoming through contract #H164150. Their support is gratefully acknowledged.

### References

- Bellows, W. J., and Mayle, R. E., 1986, "Heat Transfer Downstream of a Leading Edge Separation Bubble," *ASME Journal of Turbomachinery*, Vol. 108, pp. 131-136.
- Blair, M. F., 1983a, "Influence of Free-Stream Turbulence on Turbulent Boundary Layer Heat Transfer and Mean Profile Development, Part I—Experimental Data," *ASME JOURNAL OF HEAT TRANSFER*, Vol. 105, pp. 33-40.
- Blair, M. F., 1983b, "Influence of Free-Stream Turbulence on Turbulent Boundary Layer Heat Transfer and Mean Profile Development, Part II—Analysis of Results," *ASME JOURNAL OF HEAT TRANSFER*, Vol. 105, pp. 41-47.
- Han, J. C., and Young, C. D., 1988, "The Influence of Jet-Grid Turbulence on Turbulent Boundary Layer Flow and Heat Transfer," *Transport Phenomena in Turbulent Flows*, M. Hirata and N. Kasagi, eds., Hemisphere Publishing Corporation, New York, pp. 501-514.
- Hancock, P. E., and Bradshaw, P., 1983, "The Effect of Free-Stream Turbulence on Turbulent Boundary Layers," *ASME Journal of Fluids Engineering*, Vol. 105, pp. 284-289.
- Kline, S. J., and McClintock, F. A., 1953, "Describing Uncertainties in Single Sample Experiments," *Mechanical Engineering*, Jan.
- Lowery, G. W., and Vachon, R. I., 1975, "The Effect of Turbulence on Heat Transfer From Heated Cylinders," *International Journal of Heat and Mass Transfer*, Vol. 18, pp. 1229-1242.
- Mehendale, A. B., 1991, "Effect of High Mainstream Turbulence on Leading Edge Heat Transfer and Film Cooling," Ph.D. Dissertation, Texas A&M University.
- Mehendale, A. B., and Han, J. C., 1990, "Influence of High Mainstream Turbulence on Leading Edge Film Cooling Heat Transfer," *ASME Paper No. 90-GT-9*; accepted for publication in the *ASME Journal of Turbomachinery*.



- Mick, W. J., and Mayle, R. E., 1988, "Stagnation Film Cooling and Heat Transfer, Including Its Effect Within the Hole Pattern," *ASME Journal of Turbomachinery*, Vol. 110, pp. 66-72.
- Morehouse, K. A., and Simoneau, R. J., 1986, "Effect of a Rotor Wake on the Local Heat Transfer on the Forward Half of a Circular Cylinder," *Proceedings of the International Heat Transfer Conference*, San Francisco, CA, pp. 1249-1255.
- O'Brien, J. E., and VanFossen, G. J., 1985, "The Influence of Jet-Grid Turbulence on Heat Transfer From the Stagnation Region of a Cylinder in Crossflow," ASME Paper No. 85-HT-58.
- Ota, T., and Kon, N., 1974, "Heat Transfer in the Separated and Reattached Flow on a Blunt Flat Plate," *ASME JOURNAL OF HEAT TRANSFER*, Vol. 96, pp. 459-462.
- Ota, T., and Kon, N., 1979, "Heat Transfer in the Separated and Reattached Flow Over Blunt Flat Plates—Effects of Nose Shape," *International Journal of Heat and Mass Transfer*, Vol. 22, pp. 197-206.
- Ota, T., and Kon, N., 1980, "Turbulent Transfer of Momentum and Heat in a Separating and Reattaching Flow Over a Blunt Flat Plate," *ASME JOURNAL OF HEAT TRANSFER*, Vol. 102, pp. 749-754.
- Simonich, J. C., and Bradshaw, P., 1978, "Effect of Free-Stream Turbulence on Heat Transfer Through a Turbulent Boundary Layer," *ASME JOURNAL OF HEAT TRANSFER*, Vol. 100, pp. 671-677.
- Young, C. D., Han, J. C., Huang, Y., and Rivir, R. B., 1991, "Influence of Jet-Grid Turbulence on Flat Plate Turbulent Boundary Layer Flow and Heat Transfer," presented at the Third ASME/JSME Thermal Engineering Joint Conference, Reno, NV; *ASME JOURNAL OF HEAT TRANSFER*, in press.
- Zelenka, R. L., and Loehrke, R. I., 1983, "Heat Transfer From Interrupted Flat Plates," *ASME JOURNAL OF HEAT TRANSFER*, Vol. 105, pp. 172-177.

# Local Heat/Mass Transfer Distributions on the Surface of a Wall-Mounted Cube

M. K. Chyu

Associate Professor,  
Mem. ASME

V. Natarajan

Graduate Assistant.

Department of Mechanical Engineering,  
Carnegie Mellon University,  
Pittsburgh, PA 15213

*Local mass transfer from the surface of a wall-mounted cube is studied using the naphthalene sublimation technique. The streakline pattern on each face of the cube is visualized using the oil-graphite method. A horseshoe vortex system near the endwall, in conjunction with the separated shear layers initiated at sharp edges, determines the transport characteristics around the cube. As a direct influence of the flowfield, the local mass transfer distributions reflect features of three-dimensional flow separation that are significantly different from their two-dimensional counterparts existing in the midsection of a long prism. According to several previous studies, average mass transfer over the rear surface of a square prism without end effects is the highest among all surfaces. However, it is the lowest for the present case with a wall-mounted cube. The cube side wall has the highest average mass transfer overall. This is a result of the elevated local mass transfer existing in the lower portion of the surface, near which a horseshoe vortex system prevails. In addition to local data, correlations of average Sherwood number with Reynolds number are also presented for various surfaces.*

## Introduction

Separated flow over a bluff body is one of the most actively researched topics in modern fluid dynamics and transport phenomena. This is due mainly to its eminent importance in both engineering applications and the fundamental features involved. Aerodynamics researchers have devoted significant efforts to studying the drag and lift forces acting on various airfoil configurations. Heat transfer on the surface of circular cylinders in crossflow has been an important subject for development of compact heat exchangers. However, most of these research efforts have been concerned with two-dimensional bluff bodies located in a free stream of infinite extent, and much less attention has been given to its three-dimensional counterpart that is mounted on a plane wall. For the latter, the body-endwall interaction aggravates the complexity of the flow structure and associated convection transport. This is exemplified by the well-known "horseshoe" vortex near the base of a wall-mounted circular cylinder (Schlichting, 1979). Such a flow generally induces a very nonuniform heat or mass transfer distribution in the region (Goldstein and Karni, 1984; Goldstein et al., 1985).

Features of the three-dimensional flow separation and heat transfer induced by a wall-mounted cube are experimentally investigated in the present study. Particular emphasis lies in characterization of the local heat transfer distribution over the entire surface of the cube. Only limited study of this topic has been performed in the past. This is probably due to the cumbersome procedures involved in setting up local measurement and thermal insulations. Transport information relating to flow around a cuboidal body is useful in a variety of applications including roughness effects on turbulent boundary layer, wind and thermal loads on buildings or man-made structures, cooling of electronic components, pollutant dispersion, etc.

The aerodynamics aspects of a wall-mounted cube have been studied mainly by flow visualization, surface static pressure measurements, and, to some extent, through analytical means.

Counihan et al. (1974), using a momentum-deficit approach, analytically investigated the far wake region behind a cube. Castro and Robins (1977) performed a study with pressure measurements, which provided a good insight into the flow structure. Sakamoto et al. (1982) later reported similar but more detailed pressure results. Using both flow visualization with smoke tracer and kinematic analysis, Woo et al. (1977), Hunt et al. (1978), and Peterka et al. (1985) reported a series of work concerning wind flow around buildings. Figure 1 provides a sketch representing a typical mean flowfield based on these studies. Here several counterrotating horseshoe vortices similar to those observed with a wall-mounted cylinder prevail in the vicinity of the cube base. The presence of sharp edges induces complex separation-reattachment patterns on both the top and side walls. One of the most intriguing features lies in the flow near the rear side of cube where an inverted U-shaped vortex exists within a separation cavity. The postseparation flow may be very sensitive to the flow conditions upstream. In fact, results obtained from the present study that are to be elaborated later exhibit a significantly different flow pattern from that shown in Fig. 1, particularly near the side and top walls.

In the literature, heat transfer studies with flow separation induced by a square bluff body generally used a tall prism with its largest dimension extended from the endwall and normal to the free stream. Igarashi (1985, 1986) investigated the surface

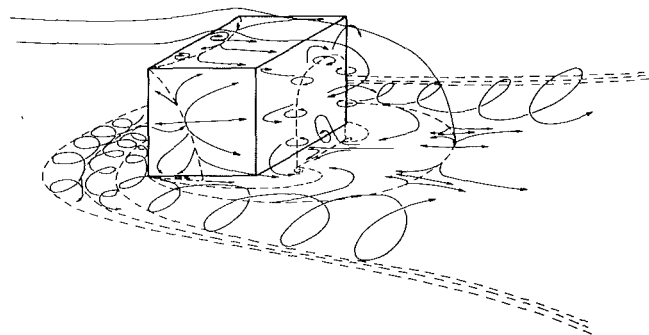


Fig. 1 Projected flow pattern around a wall-mounted cube

Contributed by the Heat Transfer Division for publication in the JOURNAL OF HEAT TRANSFER. Manuscript received by the Heat Transfer Division October 5, 1990; revision received February 19, 1991. Keywords: Analog Techniques, Flow Separation, Forced Convection.

heat transfer in the midsection (two-dimensional regime) of a prism with various flow angles of attack. Goldstein et al. (1990) obtained local mass transfer distributions both in the midsection and near the prism endwall (three-dimensional regime). Their three-dimensional results display a great similarity to those found earlier with a circular cylinder (Goldstein and Karni, 1984; Goldstein et al., 1985). Heat transfer with exactly cubic geometry has recently been reported by Olsen et al. (1989). In their study, however, only two of the five participating surfaces were heated, and results on the top and rear surfaces were excluded.

The complex flowfield around a cube is expected to induce a highly nonuniform surface heat transfer with large spatial gradients. Conventional thermal measurements may be insufficient to resolve such a local phenomenon. Thus the present study adopts an analogous mass transfer system using the naphthalene sublimation technique. The mass transfer results may be transformed into their heat transfer counterparts by invoking an analogy between these two transport processes (Eckert, 1976). Local mass transfer distributions are obtained by measurements of surface profiles before and after an exposure to the wind-tunnel airstream. To ensure data quality, the current technique requires a rapid data acquisition rate and accurate specimen-repositioning capability. As suggested by Goldstein et al. (1985) and Chyu (1986), a computer-controlled, surface profile measurement system can fulfill these requirements. In addition to local study, an integration of the local data measured yields the average mass transfer of each participating surface, and its dimensionless counterpart is correlated with the Reynolds number. An auxiliary flow visualization using graphite-oil film, which shows the distribution of shear stress and streakline pattern, is also performed on each surface.

### Heat and Mass Transfer Analogy

The usual definition of heat transfer coefficient comes from the equation

$$h = q / (T_w - T_\infty) \quad (1)$$

Correspondingly, the mass transfer coefficient is given by

$$h_m = \dot{m} / (\rho_{v,w} - \rho_\infty) \quad (2)$$

Analogy between Eqs. (1) and (2) implies that  $(T_w - T_\infty)$  and  $q$  in heat transfer correspond to  $(\rho_{v,w} - \rho_\infty)$  and  $\dot{m}$  in mass transfer. In the present study, the naphthalene vapor concentration in the free stream is zero and Eq. (2) reduces to

$$h_m = \dot{m} / \rho_{v,w} \quad (3)$$

As the mass transfer system is essentially isothermal, the naphthalene vapor pressure and vapor concentration at the wall are

constant. This is equivalent to a constant temperature wall boundary condition in heat transfer study.

Local mass transfer from a naphthalene plate can be evaluated from the change of surface elevation, which is equivalent to the change in naphthalene thickness. The change of elevation or thickness due to sublimation is given by

$$dy = \dot{m} dt / \rho_s \quad (4)$$

where  $\rho_s$  is the density of solid naphthalene. Note that  $dy$  and  $\dot{m}$  are functions of local coordinates of the mass transfer active surface. Combining Eqs. (3) and (4) and integrating over the test duration yields

$$h_m = (\rho_s \Delta y) / (\rho_{v,w} \Delta t) \quad (5)$$

The dimensionless mass transfer coefficient, or Sherwood number, is defined by

$$\text{Sh} = h_m d / \mathcal{D} \quad (6)$$

where  $\mathcal{D}$  is the naphthalene-air diffusion coefficient, which is determined by taking the Schmidt number equal to 1.87 suggested by Chen (1988); i.e.,

$$\text{Sc} = \nu / \mathcal{D} \quad (7)$$

Since naphthalene concentration in the boundary layer is extremely small, the kinematic viscosity,  $\nu$ , uses the value of air under the operating conditions. By analogy, the Sherwood number can be transformed to its heat transfer counterpart, Nusselt number (Nu), using the relation

$$\text{Nu} / \text{Sh} = (\text{Pr} / \text{Sc})^n \quad (8)$$

where Pr is the Prandtl number and the power index  $n$ , according to Igarashi (1986), is approximately equal to 1/3.

It is often the case that the wall temperature varies slightly during a test run. Thus a sensible value of  $\rho_{v,w}$  must be the time-averaged naphthalene concentrations at the surface. This is done first by evaluating the time-averaged naphthalene vapor pressure using a correlation proposed by Ambrose et al. (1974); from this,  $\rho_{v,w}$  is evaluated using the ideal gas law and the wall temperature.

### Experimental Apparatus and Procedures

The tests are performed in an open-loop, variable-speed wind tunnel operated in a suction mode. The test section, made of transparent plexiglass, is 1.2 m long and 0.3 m square in cross section. A series of turbulence-reducing screens are positioned at the inlet of the wind tunnel. This is followed by a 16:1 contraction section. A 3-mm wire trip is located at the outlet of the contraction. An exhaust pipe guides the wind tunnel discharge out of the laboratory, ensuring that the inlet air is free from naphthalene. The test cube with its surface coated

### Nomenclature

|  |  |  |
|--|--|--|
| $\mathcal{D}$ = naphthalene-air diffusion coefficient      | $q$ = heat flux from wall  | $x, y, z$ = coordinate system, see Fig. 2  |
| $d$ = cube height  | $\text{Re} = \text{Reynolds number} = Ud/\nu$  | $\alpha$ = thermal diffusivity   |
| $h$ = heat transfer coefficient, Eq. (1)                   | $\text{Sc} = \text{naphthalene-air Schmidt number} = \nu/\mathcal{D}$                | $\Delta$ = finite difference operator  |
| $h_m$ = naphthalene mass transfer coefficient, Eq. (2)     | $\text{Sh} = \text{naphthalene mass transfer Sherwood number} = h_m d / \mathcal{D}$ | $\nu$ = kinematic viscosity of air   |
| $k$ = thermal conductivity                                 | $\overline{\text{Sh}}$ = surface-resolved average Sherwood number                    | $\rho_{v,w}$ = vapor mass concentration or density of naphthalene at wall                                    |
| $\dot{m}$ = mass transfer flux of naphthalene from surface | $T_w$ = temperature of wall  | $\rho_\infty$ = vapor mass concentration or density of naphthalene in free stream, zero in the present study |
| $n$ = power index  | $T_\infty$ = temperature of free stream  | $\rho_s$ = density of solid naphthalene  |
| $\text{Nu} = \text{Nusselt number} = hd/k$                 | $t$ = time   |  |
| $\text{Pr} = \text{Prandtl number} = \nu/\alpha$           | $U$ = velocity of free stream  |  |

with naphthalene has a side of 50.8 mm and is located approximately 0.48 m from the end of the contraction section. Less than 3 percent of the flow area is blocked by the cube. At this location, the mean velocity profile of the boundary layer without the cube present is measured using an impact tube associated with wall pressure taps and an inclined manometer. For all test cases, the boundary layer thickness ranges between 10 and 13 mm, which is equivalent to approximately 1/4 of the cube height. The boundary layer is turbulent in nature following nearly a 1/6 power-law profile over the test section. The free-stream turbulence intensity as measured by a hot-wire anemometer is less than 0.3 percent over the entire test range of air speed. Based on the cube height and free-stream velocity, the Reynolds numbers studied are  $3.1 \times 10^4$ ,  $5.8 \times 10^4$ ,  $8.2 \times 10^4$  and  $1.1 \times 10^5$ . Two copper-constantan thermocouples are used: One measures the free-stream temperature and the other, attached to the cube top wall, measures the naphthalene surface temperature. The temperature reading of the latter is generally lower, by about  $0.2^\circ\text{C}$ , possibly due to the latent heat involved in the process of sublimation.

The cube is an assembly of six flat aluminum plates. Five of the six plates designated for airstream exposure are coated with naphthalene, and the sixth plate is the base for mounting purposes. Each of the mass transfer plates is connected to its adjacent plates by means of L-shaped brackets inside the cube. These brackets ensure a tight fit of the various plates to one another, thereby forming a perfect cube. The complete assembled units is mounted onto the indented tunnel floor via the base plate. Except very near the edge of each mass transfer surface, an approximately 3-mm recess is provided on each of the surfaces to facilitate casting of naphthalene. An 0.8-mm-wide aluminum strip is kept on the edges of each plate. The purpose of keeping the edge metallic is twofold; first, to provide reference points for the local measurement, and second, to retain a perfect sharp-edged configuration unaffected by the sublimation process. The tradeoff is that the metallic section is mass transfer inactive. This effect, however, is considered to be rather insignificant as its width is less than 2 percent of the cube dimension. For flow visualization, a solid aluminum block is used instead of the naphthalene-coated cube.

The naphthalene-coated cube surfaces are stored in a sealed plastic box for at least eight hours to attain thermal equilibrium with the wind tunnel room. A test starts with the profile measurement of these surfaces using an automated data acquisition system similar to that described by Goldstein et al. (1985) and Chyu (1986). The local measurement uses a  $21 \times 21$  uniform grid on each surface, which gives a 2.2-mm spacing between any two adjacent measurement points. Once all the surfaces are measured, they are then weighed individually by a high-precision electronic balance (Sartorius 4001 MP) that has an accuracy of  $\pm 10^{-6}$  g. This is done to check the surface-resolved average mass transfer with the corresponding integrated average of the locally measured values. The assembled cube is exposed to the wind tunnel airstream for about 45 minutes, during which time thermocouple readings are recorded every minute. At the completion of the test, the cube is disassembled and each of the surface profiles is measured and the plates are weighed again. Estimated uncertainty for the local Sherwood number is approximately  $\pm 3$  percent, based on the method of Kline and McClintock (1953). The local data all repeat within 7 percent.

## Results and Discussion

To facilitate the following discussion, the surfaces are classified as front (impingement) wall, side (left and right) walls, top wall, and rear wall. Figure 2 gives a sketch of the coordinate system. The orientation of left and right is determined as one faces downstream. Due to symmetry, only the left-wall results are presented instead of both side walls. However, data on

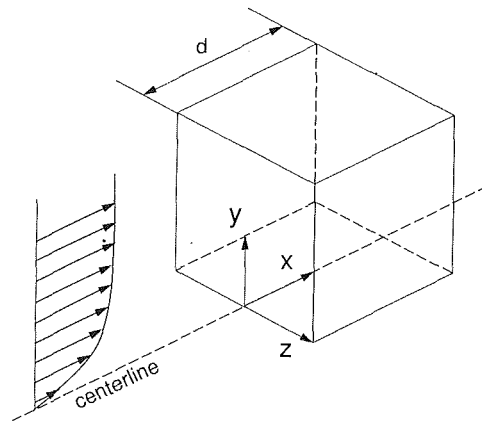


Fig. 2 Cube and its coordinate system

both side walls are obtained and compared in actual test, and a nearly perfect symmetry is always observed. The local Sherwood number ( $Sh$ ) distributions on various surfaces, in the form of both contours and line plots on selected locations, are presented in Figs. 3 and 4, respectively. Figure 5 shows photographs of oil streak patterns. The near-wall flowfield may be understood based on the level of brightness displayed on these photos. A dark area where graphite powders accumulate represents a low-speed zone or separated flow region. On the contrary, a bright spot implies high-speed flow or shear-layer reattachment. Note that this somewhat qualitative approach may be incapable of resolving other critical features (e.g., saddle points) involved in a three-dimensional flow separation. Each of Figs. 3 to 5 consists of four subfigures marked as (a)–(d), representing the corresponding results for the front wall, the side wall, the top wall, and the rear wall, respectively.

The general trends of  $Sh$  on each surface for all five Reynolds numbers presently investigated are found to be quite similar, and hence only the results of a representative Reynolds number at  $8.2 \times 10^4$  are presented to detail. Front-wall  $Sh$  contours shown in Fig. 3(a) display excellent symmetry with respect to the centerline along the direction normal to the endwall ( $y$  axis). Relatively uniform mass transfer distributions ( $Sh \approx 300$  to  $350$ ) are observed over the central portion of the surface. Such a trend is also clearly seen in Fig. 4(a); i.e., for a given spanwise location ( $x/d$ ), the values of  $Sh$  remain almost constant over  $0.3 \leq y/d \leq 0.8$ . Olsen et al. (1989) have reported a similar observation for flow with smaller values of Reynolds number. This domain of nearly uniform mass transfer coincides with the high-pressure zone, due to direct flow impingement, reported by Sakamoto et al. (1982). Examining the flow visualization photo shown in Fig. 5(a) reveals that a more or less uniformly dark region in the upper central part of the surface corresponds to this high-pressure zone. The stagnation pressure forces the impinging flow to spread both downward and outward toward all edges. The effects of flow acceleration and high speed result in sharp increases in mass transfer near the outer edges. Mass transfer of the outmost points measured ( $0.02d$  away from the actual edge) is approximately 50 percent higher than that over the central zone.

Very high mass transfer exists near the lower corner of the front surface, where the predominant flow feature is the horseshoe vortex. As shown in Figs. 3(a) and 4(a), the maximum  $Sh$  in the corner region occurs at the data point closest to the endwall; i.e.,  $y/d = 0.02$ . Similar findings have been reported by Goldstein et al. for both square prism (1990) and circular cylinder (1984). They have argued that the maximum in mass transfer is caused by a compact, but very intense, corner vortex embedded underneath the primary horseshoe vortex. Coincidentally, Sakamoto et al. (1982) reported an unusual rise in pressure at exactly the same location. The mag-

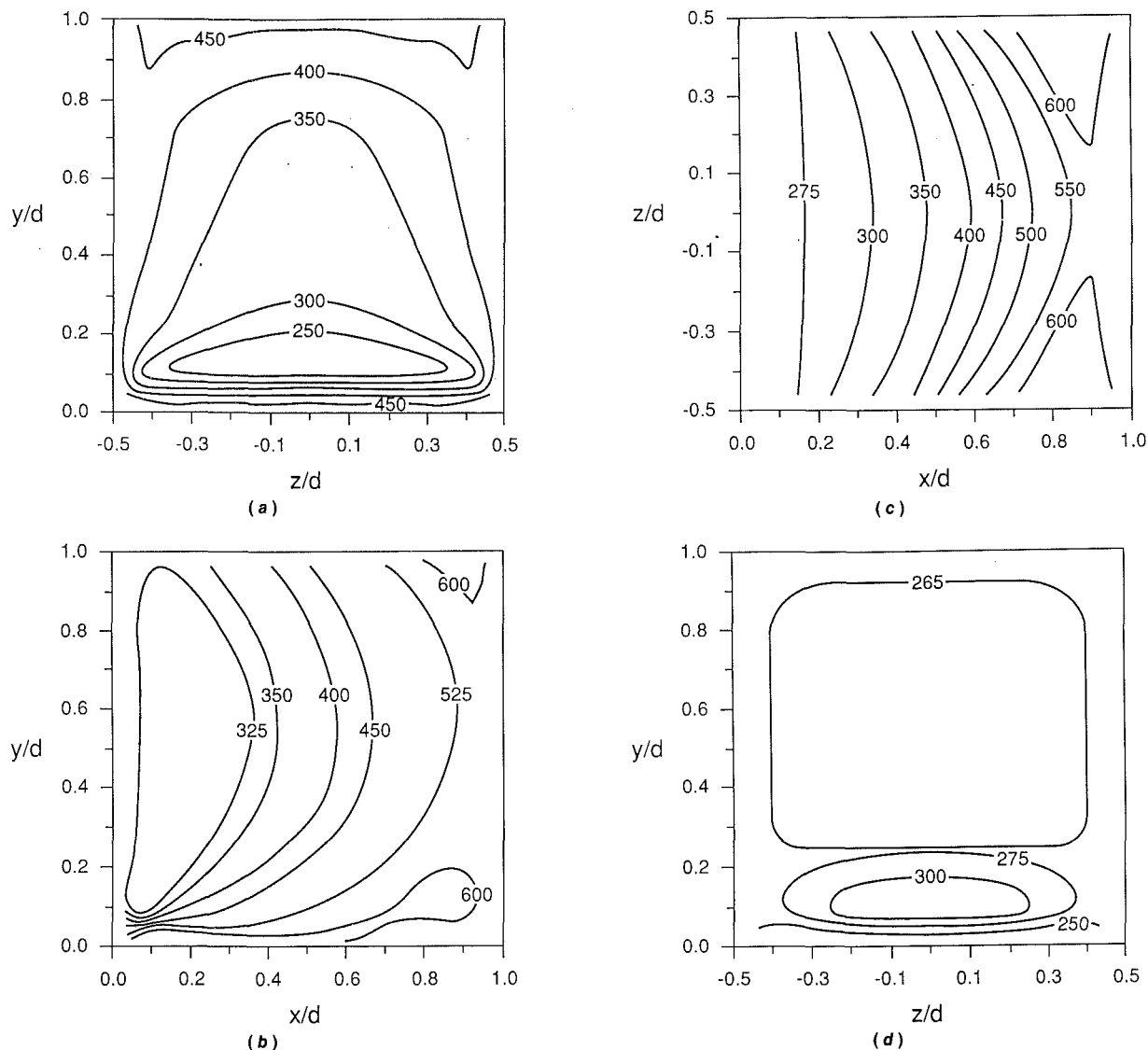


Fig. 3 Local Sherwood number contour plots: (a) front face; (b) left face; (c) top face; (d) rear face

nitude of  $Sh$  drops sharply with an increase in  $y$  coordinate until it reaches a local minimum ( $Sh \approx 200$  to  $250$ ) at  $y/d \approx 0.1$  to  $0.15$ . An upwash of the corner vortex in conjunction with a downwash from the central region, thus forming a separation zone, is considered to be responsible for this minimum in mass transfer. Such a feature is clearly displayed in Fig. 5(a) as a dark band marked across the entire surface span. The region below the dark band is much brighter, illustrating strong shear stress induced by the corner vortex, within which a maximum  $Sh$  prevails. The location of the aforementioned  $Sh$  minimum, again, is in excellent agreement with the prism data of Goldstein et al. (1990). In their study, however, a second but moderate peak of mass transfer is found by  $y/d \approx 0.07$ . Such a second peak is not observed in the present data. This difference may be attributable to the distinctions in both hydrodynamic aspects of the pre-separated flow and geometry. Besides, the present measurement grid may be too coarse to resolve such a phenomenon.

Results concerning the cube (left) side wall are presented in Figs. 3(b), 4(b), and 5(b). The local Sherwood number along the streamwise direction ( $x$ ) generally decreases from the upstream edge, reaches a minimum at  $x/d \approx 0.1$ , and then increases progressively toward the downstream edge. Meanwhile, mass transfer near the top edge or the base is higher than that

of the central region. The region very close to the front corner,  $y/d \leq 0.1$  and  $x/d \leq 0.1$ , has both the highest magnitude and gradient in  $Sh$ , due mainly to the horseshoe vortex prevailing in the vicinity. It is also very likely that the strong secondary vortex that produces the maximum  $Sh$  near the lower corner of the front face continues to dominate this small corner region. To a great extent, the present mass transfer characteristics on the cube side wall are similar to that near the base of a square prism reported by Goldstein et al. (1990).

Observations based on the mass transfer distributions and the flow visualization (Fig. 5(b)) suggest that the entire side wall of the cube is enclosed in a separation zone. The same speculation has been reported in many recent studies (Sakamoto et al., 1982; Igarashi, 1985, 1986; Olsen et al., 1989). This implies that the present cube-flow patterns are fundamentally different from those in Fig. 1, wherein the flow distinctly reattaches to the side wall. This dissimilarity undoubtedly arises due to the differences in flow conditions. An intriguing and somewhat unexpected feature revealed in the oil-streak pattern of Fig. 5(b) consists of two dark bands oriented in nearly perpendicular fashion and intersecting near the upstream lower corner. The vertical band near the leading edge is apparently a separation zone and the surface streaks generally move from the leading edge toward the band. The hor-

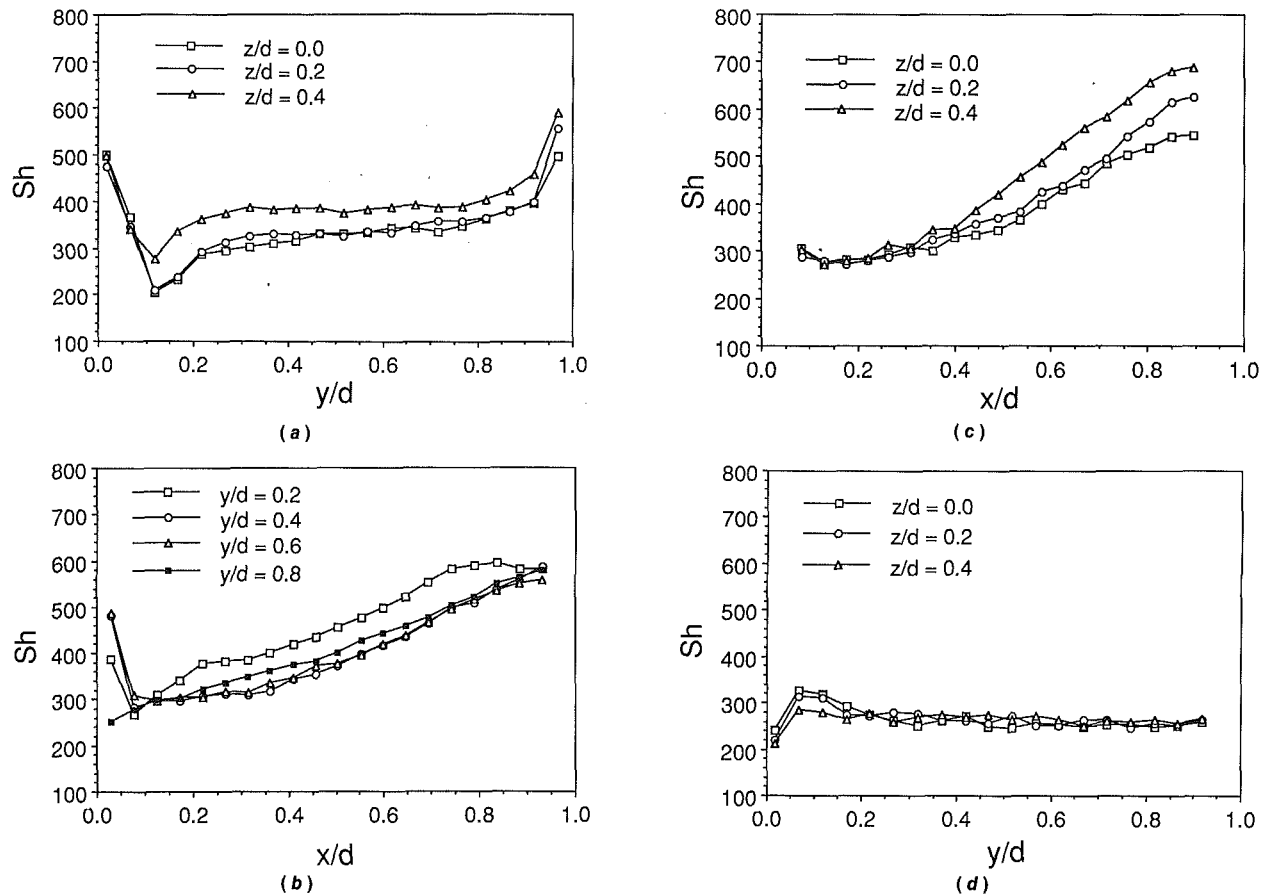


Fig. 4 Local Sherwood number line plots: (a) front face; (b) left face; (c) top face; (d) rear face

horizontal band also represents a separation zone, and it is caused by a downwash from the downstream upper corner and upwash from the downstream lower corner. An observation throughout the actual development of the flow pattern reveals that the two merging streaks both possess a velocity component along the negative- $x$  direction. The dark band itself, in fact, is very dynamic in nature. It moves along its own course from the downstream edge toward upstream and eventually merges with the vertically oriented separation zone near the upstream lower corner. At the merge of the two dark bands, the streak pattern appears to be very unsteady and bursts away from the cube toward the free stream periodically. This unsteady mechanism is considered to be one of the primary causes for the increased mass transfer existing in the region, as Figs. 3(b) and 4(b) show.

Figures 3(c) and 4(c) present mass transfer distributions for the top surface of the cube. Observe that  $Sh$  increases monotonically toward downstream from  $x/d \approx 0.2$ . Due to sharp-edge effects, the mass transfer immediately adjacent to the leading edge is expected to be high, although it is not noticeable within the present measurement domain. Inferences based on the mass transfer characteristics and the flow visualization suggest, as in the case of the side wall, that a separation zone engulfs the top surface completely. According to the streak pattern shown in Fig. 5(c), the dark band near the upstream part of the surface, representing a separation zone, further attests to this speculation. This at least implies that the surface streaks migrate from both upstream and downstream edges toward the separation zone. Note that the dark band is thinner (along the  $x$  direction) at the central region ( $-0.2 \leq z/d \leq 0.2$ ) of the surface, and it increases in thickness toward the side edges. The actual shape of the dark band is found to be

Reynolds number dependent. A decrease in Reynolds number reduces the spanwise size (in the  $z$  direction) of the thinner region and makes the band shape more uneven across the surface span. Correspondingly it is also found that the spanwise variation of  $Sh$  versus  $z/d$  is less prominent with an increase in Reynolds number. The spanwise variation of  $Sh$  for the case presented in Figs. 3(c) and 4(c) (i.e.,  $Re = 8.2 \times 10^4$ ) is very insignificant.

The transport phenomena near the rear surface are expected to be influenced by a highly complex recirculation structure behind the cube. As a result of active mixing adjacent to the surface, Figs. 3(d) and 4(d) show that the mass transfer over a majority of the surface is very uniform ( $Sh \approx 270$ ). A light rise in local Sherwood number exists near the base at  $y/d \approx 0.1$ . This is, in part, caused by the horseshoe vortex that emanates from the base of the front surface and entrains into the rear side of cube. Correspondingly, the flow visualization photo displayed in Fig. 5(d) has a nearly equal level of brightness in the region of  $0.2 \leq y/d \leq 0.8$  and is slightly brighter below it. The sketch shown in Fig. 1 reveals that near both side edges and slightly downstream of the rear surface, the entrained horseshoe vortex interacts with the recirculating wake and forms an uprising vortex with its initial rotation axis parallel to the  $y$  axis. Kinematically, the vortices on both sides rotate in an opposite sense, meet near the upper part of the surface. The system is then convected downstream by the separated shear layer initiated near the leading edge of the top surface. The envelope of this flow motion forms an arch, the so-called inverted U-shaped vortex. An auxiliary study on visualizing the flow streaks on the endwall (not shown) indicates that the rotating axis of the inverted U-shaped vortex is located at  $0.5d$  downstream from the rear surface and  $x/d = \pm 0.4$  approx-

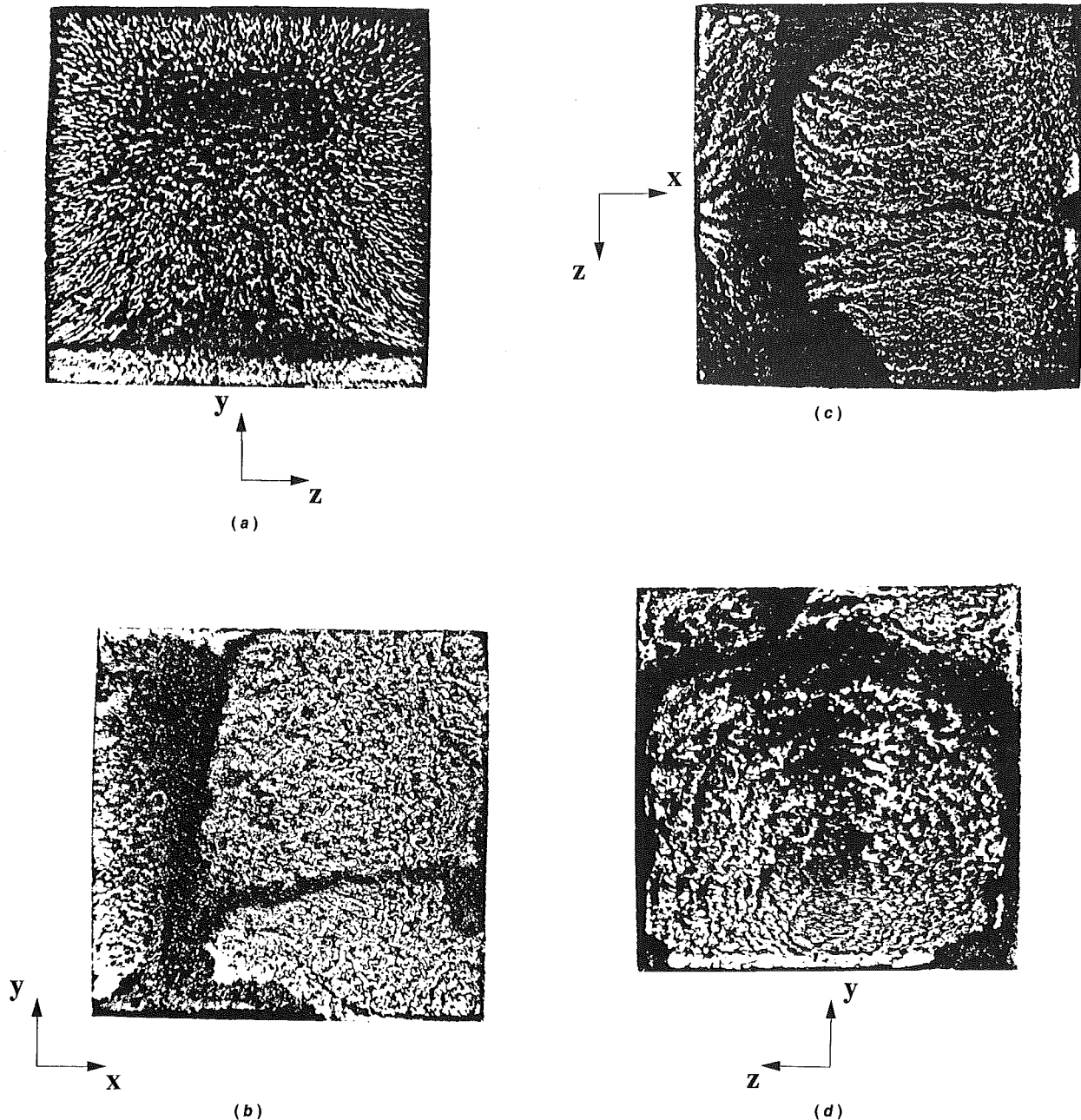


Fig. 5 Wall streakline patterns: (a) front face; (b) left face; (c) top face; (d) rear face

imately. Besides, a dark arch near the top of the surface shown in Fig. 5(d) may result from such a vortex motion. This phenomenon is more visible as the Reynolds number increases.

Attention is now turned to the surface-resolved average mass transfer. The surface-averaged mass transfer coefficient is obtained by a numerical integration of the local data on each surface. As indicated earlier, to countercheck the accuracy of the current local data, the per-surface average mass transfer is also obtained using the weighing technique. The difference between these two approaches is less than 6 percent, which is considered to be very satisfactory. Within the present test range, i.e.,  $3.1 \times 10^4 \leq Re \leq 1.1 \times 10^5$ , the average mass transfer Sherwood numbers ( $\overline{Sh}$ ) are correlated with the Reynolds number as follows:

$$\begin{aligned} \text{Front: } \overline{Sh} &= 0.868 Re^{0.538} \\ \text{Right: } \overline{Sh} &= 0.278 Re^{0.652} \\ \text{Left: } \overline{Sh} &= 0.246 Re^{0.666} \end{aligned}$$

$$\begin{aligned} \text{Top: } \overline{Sh} &= 0.247 Re^{0.657} \\ \text{Rear: } \overline{Sh} &= 0.196 Re^{0.661} \\ \text{Overall: } \overline{Sh} &= 0.343 Re^{0.626} \end{aligned}$$

For a given  $Re$ , either side wall has the highest average mass transfer, followed by the top wall, the front wall, and the rear wall. Each of the side surfaces contributes about 20 to 25 percent of the overall average mass transfer, and, on the other hand, the rear surface contributes less than 17 percent.

In terms of Reynolds number dependency, all the present correlations compare favorably with those by Igarashi (1985, 1986) for crossflow around a two-dimensional prism. He proposed that the per-surface average Nusselt number for both the side walls and the rear surface is correlated well with the Reynolds number to a  $2/3$  power. In addition, the power index reduces to  $1/2$  for the front face. However, as a contrast to the present finding, his data indicate that the rear surface has a consistently higher heat transfer than both the side walls and

the front walls. The vortex shedding accompanied with the separated shear layer induced upstream is considered to be the prime cause for elevating the transport characteristics near the rear wall. A rough average of the local data of Goldstein et al. (1990) also reveals the same trend in the two-dimensional flow regime. Hence it is apparent that features involved in the three-dimensional separation, particularly those existing behind the cube, have hindered the convection transport as compared to the two-dimensional case. The flow structures are fundamentally different between these two cases.

## Conclusions

Local mass transfer data are obtained from the various surfaces of a cube for Reynolds number ranging from  $3.1 \times 10^4$  to  $1.1 \times 10^5$ . The naphthalene sublimation technique provides a viable means to conduct this study. A horseshoe vortex system, in conjunction with separated shear layers induced by sharp edges, predominates the transport characteristics around the cube. Strong nonuniformities are portrayed in the front and the two side faces. Existence of a primary and a smaller, but very intense, corner vortex is inferred from both the flow visualization and the mass transfer profiles. Such a corner vortex induces high mass transfer in the upstream corner of the side surfaces. The side and the top surfaces are engulfed completely in a separation zone. An inclined downwash of recirculating flow merging with a roll-up of the horseshoe vortex results in a complex separation pattern near the side walls. This has elevated the mass transfer significantly in the region. Mass transfer from the top surface shows an almost linear increase in transport coefficient along the steamwise direction. Active wake mixing behind the cube causes a highly uniform distribution of mass transfer on the rear surface. Correlations of surface-resolved Sherwood number with Reynolds number are obtained and compared to the corresponding two-dimensional results. Good agreement in terms of the Reynolds number dependency is observed. A contradicting fact is that average mass transfer on the rear surface is the lowest, as opposed to the two-dimensional case wherein the rear face has the highest transfer coefficient. Thus conclusions based on two-dimensional flow regime may be inapplicable to their three-dimensional counterparts.

## Acknowledgments

The local mass transfer measurement system used in this

study, in part, is constructed under an equipment grant from NSF, No. CBT-8506827.

## References

- Ambrose, D., Lawrenson, I. J., and Sparke, C. H. S., 1975, "The Vapor Pressure of Naphthalene," *J. Chem. Thermodynamics*, Vol. 7, pp. 1173-1176.
- Castro, I. P., and Robins, A. G., 1977, "The Flow Around a Surface-Mounted Cube in Uniform and Turbulent Streams," *J. Fluid Mech.*, Vol. 79, pp. 307-335.
- Chen, P. H., 1988, "Measurement of Local Mass Transfer From a Gas Turbine Blade," Ph.D Thesis, University of Minnesota, Minneapolis, MN.
- Chyu, M. K., 1986, "Influence of Roughness Elements on Local Mass Transfer From a Flat Surface," Ph.D Thesis, University of Minnesota, Minneapolis, MN.
- Counihan, J., Hunt, J. C. R., and Jackson, P. S., 1974, "Wakes Behind Two-Dimensional Surface Obstacles in Turbulent Boundary Layers," *J. Fluid Mech.*, Vol. 76, pp. 529-563.
- Eckert, E. R. G., 1976, "Analogies to Heat Transfer Processes," *Measurements in Heat Transfer*, E. R. G. Eckert and R. J. Goldstein, eds., Hemisphere Publication, Washington, DC.
- Goldstein, R. J., and Karni, J., 1984, "The Effect of a Wall Boundary-Layer on Local Mass Transfer From a Cylinder in Crossflow," *ASME JOURNAL OF HEAT TRANSFER*, Vol. 106, pp. 260-267.
- Goldstein, R. J., Chyu, M. K., and Hain, R. C., 1985, "Measurement of Local Mass Transfer in the Region of the Base of a Protruding Cylinder With a Computer-Controlled Data Acquisition System," *International Journal of Heat and Mass Transfer*, Vol. 28, pp. 977-985.
- Goldstein, R. J., Yoo, S. Y., and Chung, M. K., 1990, "Convective Mass Transfer From a Square Cylinder and Its Base Plateau," *International Journal of Heat and Mass Transfer*, Vol. 33, pp. 9-18.
- Hunt, J. C. R., Abell, C. J., Peterka, J. A., and Woo, H. G. C., 1978, "Kinematical Studies of the Flows Around Free or Surface-Mounted Obstacles; Applying Topology to Flow Visualization," *J. Fluid Mech.*, Vol. 86, pp. 179-200.
- Igarashi, T., 1985, "Heat Transfer From a Square Prism to an Air Stream," *International Journal of Heat and Mass Transfer*, Vol. 28, pp. 175-181.
- Igarashi, T., 1986, "Local Heat Transfer From a Square Prism to an Air-stream," *International Journal of Heat and Mass Transfer*, Vol. 29, pp. 777-784.
- Kline, S. J., and McClintock, 1953, "Describing Uncertainty in Single-Sample Experiments," *Mech. Engrg.*, Vol. 75, pp. 3-8.
- Olsen, J., Webb, B. W., and Queiroz, M., 1989, "Local Three-Dimensional Heat Transfer From a Heated Cube," presented at the ASME Winter Annual Meeting, San Francisco.
- Peterka, J. A., Meroney, R. N., and Kothari, K. M., 1985, "Wind Flow Patterns About Buildings," *J. Wind Engrg. and Ind. Aero.*, Vol. 21, pp. 21-38.
- Sakamoto, H., Moriya, M., Taniguchi, S., and Arie, M., 1982, "The Form Drag of Three-Dimensional Bluff Bodies Immersed in Turbulent Boundary Layers," *ASME Journal of Fluids Engineering*, Vol. 104, pp. 326-334.
- Schlichting, H., 1979, *Boundary Layer Theory*, 7th ed., McGraw-Hill, New York.
- Woo, H. G. C., Peterka, J. A., and Cermak, J. E., 1977, "Wind-Tunnel Measurements in the Wakes of Structures," NASA CR-2806.



# Surface Curvature Effect on Slot-Air-Jet Impingement Cooling Flow and Heat Transfer Process

C. Gau

C. M. Chung

Institute of Aeronautics and Astronautics,  
National Cheng Kung University,  
Tainan, Taiwan 700

*Experiments are performed to study surface curvature effects on the impingement cooling flow and the heat transfer processes over a concave and a convex surface. A single air jet issuing from different size slots continuously impinges normally on the concave side or the convex side of a heated semicylindrical surface. An electrical resistance wire is used to generate smoke, which allows us to visualize the impinging flow structure. The local heat transfer Nusselt number along the surfaces is measured. For impingement on a convex surface, three-dimensional counterrotating vortices on the stagnation point are initiated, which result in the enhancement of the heat transfer process. For impingement on a concave surface, the heat transfer Nusselt number increases with increasing surface curvature, which suggests the initiation of Taylor-Görtler vortices along the surface. In the experiment, the Reynolds number ranges from 6000 to 350,000, the slot-to-plate spacing from 2 to 16, and the diameter-to-slot-width ratio  $D/b$  from 8 to 45.7. Correlations of both the stagnation point and the average Nusselt number over the curved surface, which account for the surface curvature effect, are presented.*

## 1 Introduction

Impingement cooling has been widely used to cool a heat transfer component exposed to a high temperature or a high heat flux environment. The impingement cooling jet has the advantage that it is readily moved to the location of interest and removes a large amount of heat. It has been widely used in such industrial systems as high-temperature gas turbines, paper drying, glass manufacturing, and high-density electronic equipment. The impinging jet used in these systems is air. Over the past 30 years, impingement cooling heat transfer has been extensively studied. Good review articles are available (Martin, 1977; Becko, 1976). The impinging flow structure (Donaldson and Snedeker, 1971a, 1971b), the local heat transfer, and the correlations of average Nusselt number in terms of relevant parameters have been well studied (Gardon and Cobonpue, 1963; Gardon and Akfirat, 1966; Korger and Krizek, 1965; Zumbrennen et al., 1989).

However, the impingement cooling studied in the past was on a flat plate. The situation of impingement cooling over a curved surface may frequently be encountered. However, the studies of impingement cooling on a curved surface are relatively few. Chupp et al. (1969) studied the impingement cooling heat transfer for an array of round jets impinging on a concave surface. The geometric configuration studied is very similar to the case for cooling of the leading edge of a gas turbine airfoil. They measure the local Nusselt number and correlate the average Nusselt number in terms of the Reynolds number, the nozzle-to-plate spacing, and some nondimensional parameters of geometry. However, the local heat transfer obtained is actually an average over a relatively large space. A similar geometry is also studied by Metzger et al. (1969, 1972) and Hrycak (1978, 1981). Tabakoff and Clewenger (1972) study three different configurations of impinging jets on a concave surface: the single slot jet, the one-dimensional row of round jets, and the two-dimensional array of jets. Both the local and the average Nusselt number are determined. However, the local heat transfer Nusselt number obtained is again an average over a relatively large space. A few correlations of average Nusselt numbers for slot jet impingement cooling over a concave or a

convex surface are presented in the report of Becko (1976). However, the surface curvature effect on the local and the average Nusselt number is not reported. The detailed mechanism causing the heat transfer process on a curved surface, which is different from the case on the flat plate, is not understood. Therefore, the objective of the present study is to report the curvature effect on the impinging jet flow structure and the detailed local heat transfer process along a curved surface. By using a nondimensional analysis, the surface curvature effect can be deduced to be represented by the value of a nondimensional parameter that is the ratio of the curved surface diameter to the slot width. In the experiment, the study of surface curvature effect on the impinging flow and the heat transfer process along a curved surface is achieved by using different size slots that impinge cool air on a heated concave or a convex surface. Both the flow visualization and the heat transfer coefficient measurements along the surface are made and compared with published results. Correlations of both the stagnation point and the average Nusselt number, which accounts for the surface curvature effect, are presented.

## 2 Experimental Apparatus and Procedures

The impinging air jet issuing from the nozzle is supplied with a high-pressure blower system, which can furnish a maximum air flow of  $10 \text{ m}^3/\text{min}$ . To ensure air quality, a settling chamber with a honeycomb and different size meshes is made and used to reduce the turbulence intensity and maintain a uniform air flow at the exit. The nozzle is made convergent and curved smoothly, which allows rapid acceleration of fluid without occurrence of flow separation and generation of turbulence. Therefore, a uniform velocity profile associated with relatively low turbulence intensity across the nozzle width at the exit is obtained. The streamwise turbulence intensity at the nozzle exit is measured with a hot-wire anemometer and is found less than 0.7 percent for the Reynolds number ranging from 6000 to 35,000. The jet velocity is measured with a Pitot tube. Different size rectangular nozzles are made, 0.35 cm, 0.6 cm, 1 cm, 1.5 cm, and 2 cm in width. To ensure that the second dimension of the nozzle slot does not affect the slot jet flow, all the nozzles are made long in the direction perpendicular to the nozzle axis, which is 15 cm in length.

Contributed by the Heat Transfer Division for publication in the JOURNAL OF HEAT TRANSFER. Manuscript received by the Heat Transfer Division August 6, 1990; revision received March 7, 1991. Keywords: Forced Convection, Turbines.

Both the concave and the convex surface are made from a cylindrical plexiglass tube, which is 1 cm in thickness, 16 cm in inside diameter, and 16 cm in length. The cylindrical tube is cut in half. The concave surface can be made inside the tube while the convex surface can be made outside. The surface is adhered with a 0.015 mm thin stainless steel foil, which can be heated by passing through electric current. Since the steel foil is so thin and the plexiglass tube has a very low thermal conductivity, the heat conduction along the tube wall in both the circumferential and the axial direction is negligibly small. To reduce heat loss to the ambient, the heated surface is well insulated on the back. To account for the additional radiation heat loss directly from the steel foil, the total heat loss to the ambient is estimated at less than 3 percent.

To measure the temperature distribution along the heated wall in the circumferential direction, a total of 51 thermocouples are inserted individually into equally spaced small holes drilled in the tube wall in order that the thermocouple junction can attach to the heated steel foil. One additional thermocouple is used to measure the jet temperature at the slot exit. All the temperature signals are acquired with a data logger and sent into a PC for data processing and plotting. Before the experiments, all the thermocouples are calibrated in a constant temperature bath to ensure the measurement accuracy of  $\pm 0.1^\circ\text{C}$ .

To ensure that the stainless steel foil is heated uniformly, the entire foil is cut into a number of long strips that are circumferential. Each strip is heated individually with an equal amount of d-c power. With the desired voltage  $V$  and current  $I$  passing through the thin strip, the heat flux along the surface can be calculated and is equal to  $VI/A$ , where  $A$  is the area of the strip. The local heat transfer coefficient can be determined with the following equation:

$$h_t = q / (T_w - T_\infty) \quad (1)$$

When the air velocity is so high that the wall-air friction can heat up the wall and raise the wall temperature, Eq. (1) needs to be modified slightly to account for the viscous heating effect. The viscous heating effect becomes noticeable when the impinging jet velocity is greater than 40 m/s. At this time, the  $T_\infty$  in Eq. (1) is replaced with  $T_{aw}$ . The adiabatic wall temperature along the surface is measured when the foil heater is turned off.

### 3 Results and Discussion

Before starting to perform the heat transfer experiments, one has to select the correct number of nondimensional parameters that affect the heat transfer process along the surface. The number of nondimensional parameters for impingement cooling over a flat surface have been used frequently in the literature. However, for impingement cooling over the curved surfaces, a number of nondimensional parameters need to be derived. Starting from the governing equations and boundary

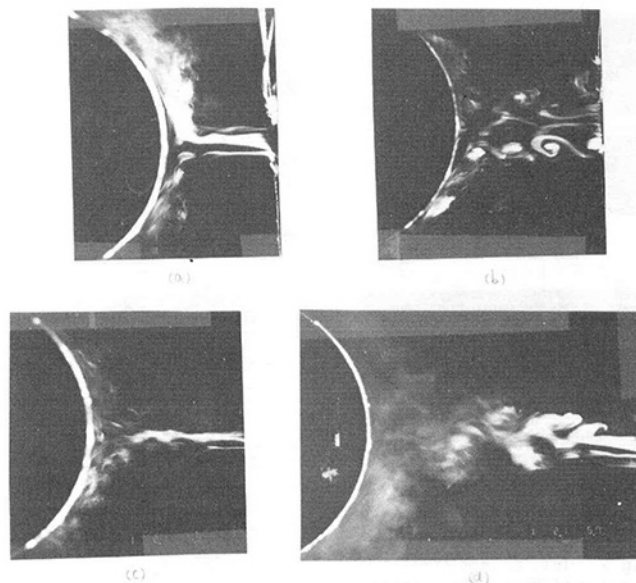


Fig. 1 Impinging jet flow structure on a convex surface for the cases of (a)  $Z/b=4$ ,  $D/jb=16$ , and  $Re=1200$ , (b)  $Z/b=4$ ,  $D/jb=8$  and  $Re=2000$ , (c)  $Z/b=8$ ,  $D/jb=16$ ,  $Re=1200$ , and (d)  $Z/b=12$ ,  $D/jb=16$ ,  $Re=1200$

conditions of the system, the nondimensional parameters can be readily derived (Chung, 1989). It has been found that  $Nu = f(Re, Pr, x/b, Z/b, D/b)$ . The nondimensional parameter that can be used to study the curvature effect on the heat transfer process is  $D/b$ . Since during the experiments, the slot width  $b$  is much easier to change than the diameter of surface, the slot width is selected to vary and used to study the curvature effect on the heat transfer process along a concave or a convex surface.

#### 3.1 Flow Visualization

**3.1.1 Convex Surface.** Figure 1 shows the flow structure of an impinging jet normal to the convex surface at slot-to-plate spacings of  $Z/b=4$ , 8, and 12, respectively. According to the descriptions by Martin (1977), the jet has a potential core of approximately  $4b$  in length. Therefore, for the case when the slot-to-plate spacing is less than  $4b$ , a wall jet of laminar boundary flow in the region close to the stagnation point is expected. This can be inferred from Fig. 1(a), where the smoke trace around the stagnation point does not indicate a strong mixing process and disappears. At the same time, Fig. 1(a) shows that the entire jet maintains its structure and does not have a significant mixing with the ambient air. It is expected that the impinging velocity on the convex surface is approximately the same as the slot exit velocity. However, far down-

#### Nomenclature

|   |  |                                       |
|---|--|---------------------------------------|
| $A$ = area of heater strip                      | $Nu$ = Nusselt number = $h_t b/k$                        | $Z$ = slot-to-plate spacing           |
| $b$ = slot width                                | $\bar{Nu}$ = average Nusselt number = $\bar{h}_t b/k$    | $\alpha$ = thermal diffusivity        |
| $c_p$ = specific heat                           | $Pr$ = Prandtl number = $c_p \mu/k$                      | $\mu$ = kinematic viscosity           |
| $D$ = diameter of the curved surface            | $q$ = heat flux  | $\nu$ = dynamic viscosity             |
| $D_m$ = species diffusion coefficient           | $Re$ = Reynolds number = $U_j b/\nu$                     |                                       |
| $d$ = diameter of round jet nozzle              | $Sh$ = Sherwood number = $h_m b/D_m$                     |                                       |
| $h_t$ = convective heat transfer coefficient    | $Sc$ = Schmidt number = $c_p \mu/D_m$                    |                                       |
| $\bar{h}_t$ = average heat transfer coefficient | $T$ = temperature  |                                       |
| $h_m$ = convective mass transfer coefficient    | $U$ = streamwise velocity                                |                                       |
| $I$ = current                                   | $V$ = voltage  |                                       |
| $k$ = thermal conductivity                      | $x$ = circumferential distance from the stagnation point |                                       |
|   |  | <b>Subscripts</b>                     |
|   |  | $aw$ = refers to adiabatic wall       |
|   |  | $c$ = refers to concave surface       |
|   |  | $j$ = refers to jet flow at slot exit |
|   |  | $o$ = refers to stagnation point      |
|   |  | $v$ = refers to convex surface        |
|   |  | $\infty$ = refers to ambient air      |

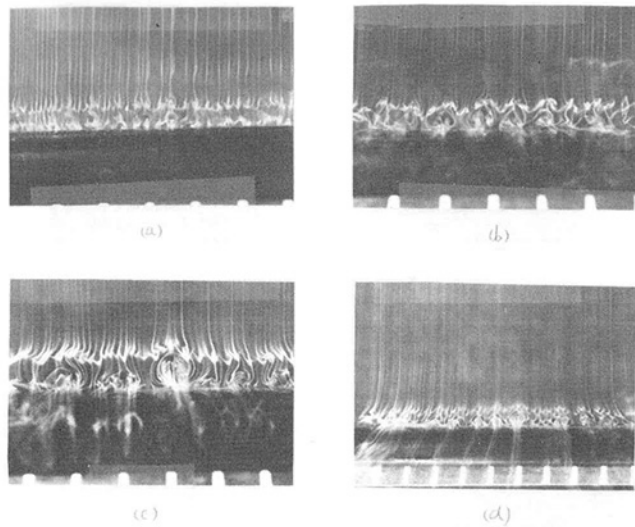


Fig. 2 Three-dimensional rotating vortices on the stagnation point for the case of  $Z/b = 4$ ,  $Re = 2000$  and (a)  $D/b = 16$ , (b)  $D/b = 10.7$ , (c)  $D/b = 8$ , and (d)  $D/b = 16$  (photo taken at different angle)

stream along the wall, the flow is turbulent. It appears that a transition from laminar to turbulent boundary layer occurs when a critical Reynolds number is exceeded. However, due to the occurrence of a centrifugal force, the entire flow over the convex surface is stable (Schlichting, 1979), and no initiation of three-dimensional vortices in the downstream region is found. For a wider slot, the vortex formation and pairing due to the mixing of free jet with ambient air can be observed, as shown in Fig. 1(b). The vortex formation can still be observed at a distance far from the stagnation point before flow becomes turbulent. However, the vortex formation is hardly observed when the slot width is small. It appears that the increase in slot width causes an earlier initiation of vortices in the mixing region of the jet, which can increase the rate of mixing of jet flow with ambient air and result in an earlier termination of the potential core. Therefore, an increase in the momentum transport in the jet flow and the enhancement of the heat transfer process along the wall, especially on the stagnation point, can be expected. However, the Reynolds number effect on the impinging jet flow structure is not as significant as the slot width. The flow structure for  $Re = 2000$  is almost the same as for  $Re = 1200$ . For the case at spacings of  $Z/b = 8$  and 12, significant mixing of jet flow with ambient air occurs. The jet flow, before arriving at the surface, becomes wide and fully turbulent, as shown in Figs. 1(c) and 1(d). It appears that at a large slot-to-plate spacing, the jet impinging velocity on the wall decreases significantly, which can result in the decrease in heat transfer rate. By viewing the jet flow in a direction perpendicular to the axis of the semicylindrical surface, as the jet flow approaches the convex surface, a series of three-dimensional counterrotating vortices on the stagnation point can be observed, as shown in Fig. 2. Kestin and Wood (1970), based on a stability analysis and confirmed by experiments, conclude that the flow approaching a blunt body is not stable and can become a series of three-dimensional counterrotating vortices due to the random disturbance carried by the free stream. The current finding agrees with the previous results. However, the size of the counterrotating vortices increases when the slot width increases as shown in Figs. 2(b) and 2(c). The diameter of the vortices is estimated to be approximately half the slot width. In addition, each pair of vortices can produce a streamline, as shown in Fig. 2(d), which flows circumferentially along the wall. When the slot-to-plate spacing increases, i.e.,  $Z/b = 8$  and 12, the jet flow, before arriving at the surface, is turbulent, and the three-dimensional

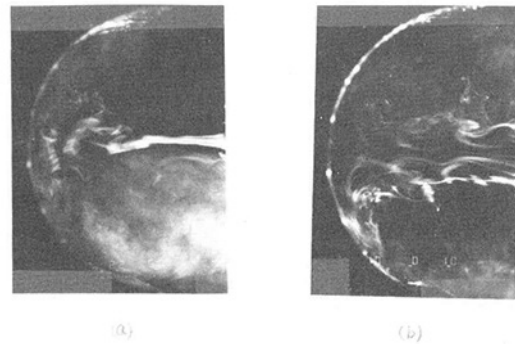


Fig. 3 Impinging jet flow structure on a concave surface for the cases of (a)  $Z/b = 8$ ,  $D/b = 16$ , and  $Re = 1200$ , (b)  $Z/b = 4$ ,  $D/b = 8$ , and  $Re = 2000$

vortices could not be observed. It is expected that the appearance of counterrotating vortices can increase the momentum and energy exchange in the flow, which can enhance the heat transfer along the wall. In the later presentation of local heat transfer measurements, it can be inferred from the results of the Nusselt number measurements that the three-dimensional vortices still exist when the approaching jet flow becomes turbulent.

**3.1.2 Concave Surface.** In the case of an impinging jet on a concave surface, the flow structure before reaching the wall is very similar to the case of impinging jet on a convex surface. Figure 3(b) shows that for a wide impinging jet ( $b = 20$  mm), vortex formation due to jet mixing with ambient air can be clearly observed. It appears again that the increase in slot width causes an earlier initiation of vortices in the mixing region of the jet, which can result in an earlier termination of potential core. Therefore, an increase in the momentum transport in the flow and the heat transfer process along the wall, especially on and around the stagnation point, can be expected. However, on the stagnation point, no initiation of three-dimensional vortices is found. In the downstream region, the entire wall jet is turbulent, and the flow structure could hardly be observed. However, it has been found (Schlichting, 1979) that for flow over a concave surface, a centrifugal force generated due to the curvature effect can destabilize the flow and lead to a type of instability that is referred to as a Taylor-Görtler vortex. A series of Taylor-Görtler vortices with axes parallel to the streamwise direction extends over the entire concave surface. It has been found (Mayle et al., 1981; Thomann, 1968) that the generation of Taylor-Görtler vortices can significantly increase the momentum and energy exchange in the flow and enhance the heat transfer on the wall. The enhancement of the heat transfer along a concave surface can be found in the later figures of the local heat transfer data, which concludes the generation of Taylor-Görtler vortices along the concave surface.

## 3.2 Heat Transfer

**3.2.1 Flat Plate.** When the slot width is small ( $d = 6$  mm) and  $D/b = 45.7$ , both the local Nusselt number along the concave and the convex surface are plotted in Fig. 4(a) for  $Z/b = 4$  and Fig. 4(b) for  $Z/b = 8$ . The maximum uncertainty of the measured local Nusselt number is  $\pm 7.1$  percent. Since the Nusselt number along both surfaces is almost identical, it appears that the curvature effect on the heat transfer process along the wall is not significant when the slot width is small and  $D/b = 45.7$ . It should be noted that when the slot is close to the surface, some portion of the potential core can reach the surface so that the wall jet can experience a transition from laminar to turbulent flow, which can result in a sudden increase in the Nusselt number, as shown in Fig. 4(a). As the turbulent boundary layer develops, the Nusselt number decreases gradually downstream. When slot-to-plate spacing is large, the

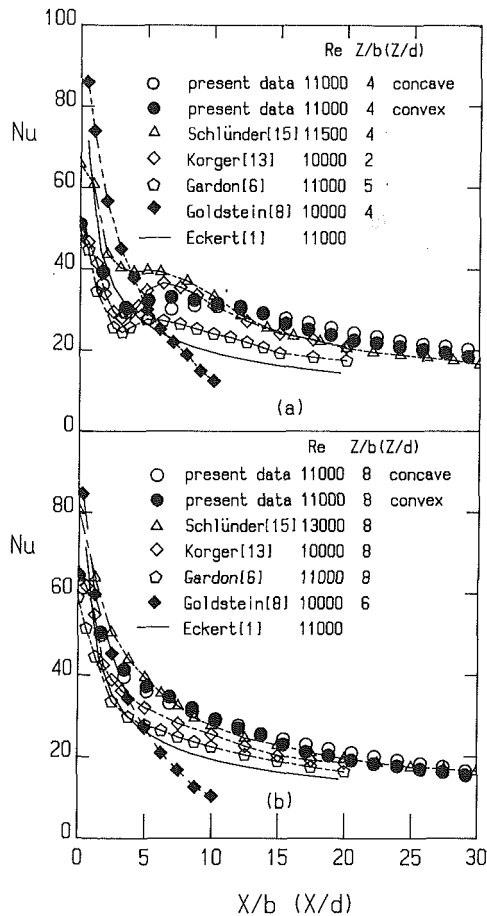


Fig. 4 Comparison of local heat transfer Nusselt number between the present data for the small curvature surfaces  $Dc/b = 45.7$  and the published results for the flat plate

potential core of the jet is not long enough to reach the surface, and the jet flow approaching the wall is turbulent. Therefore, a significantly higher Nusselt number on the stagnation point and a monotonic decrease in the downstream region can be expected, as shown in Fig. 4(b). Comparison is also made in the same figure between the present results and the published data available for impingement cooling over a flat plate. The closest agreement is found with the results from Karger and Krizek (1965) around the stagnation point and Schlünder (in Martin, 1977) in the region far from the stagnation points, who have performed the mass transfer experiments and obtained the mass transfer Sherwood number in their results is transformed into the heat transfer Nusselt number with the relation  $Nu = (Pr/Sc)^{0.42}$  as suggested by Schlünder. Gardon and Akfirat (1966) have performed the heat transfer experiment for slot jet cooling. However, their data are significantly lower than the current data. Becko (1976) mentions that the data from Gardon and Akfirat are 20 percent lower due to an experimental error. Therefore, a 20 percent increase of Gardon and Akfirat's data can make their results approach the current ones. Comparison is also made with the results from Goldstein and Franchett (1988) who use a metallic-foil heater similar to the current one to heat the top flat plate. However, their results are for the case of round jet cooling. Their data are higher in the region around the stagnation point and lower far downstream than the current one. The higher heat transfer rate for Goldstein and Franchett's data in the region around the stagnation point is probably attributed to the higher jet turbulence intensity at the nozzle exit, which can enhance the heat transfer. However, the jet turbulence intensity is not described in their report. It is suspected that the air supply system and the type of nozzle

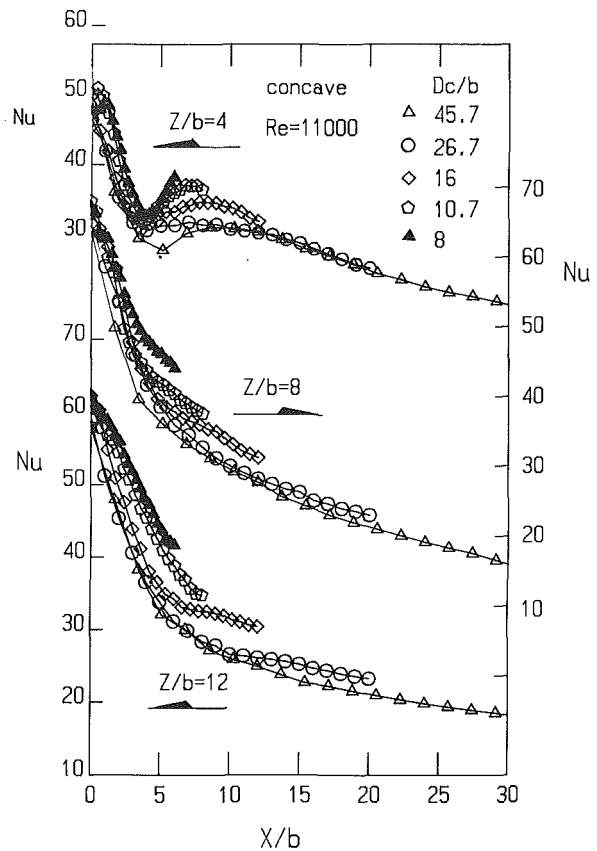


Fig. 5 Effect of concave surface curvature on the local heat transfer Nusselt number for the case of  $Re = 11,000$  and  $Z/b = 4, 8,$  and  $12$

(with sudden contraction inside) used in their experiment can produce a jet with a higher turbulence intensity. In the case of impinging jet with relatively low turbulence intensity, the stagnation point Nusselt number for the circular jet approaches that for the slot jet. In the far downstream region the total mass and momentum available to cool the surface for the case of round jet cooling are significantly less than in the case of slot jet cooling. Therefore, the heat transfer coefficient for the round jet cooling is lower. Eckert (Becko, 1976) obtains the correlation of Nusselt number based on a laminar boundary layer analysis. Therefore, his results exhibit a monotonic decrease and are lower than those of Goldstein and Franchett.

**3.2.2 Concave Surface.** Comparison of local heat transfer results along a concave surface at different diameter-to-slot-width ratios is shown in Fig. 5 for the cases of  $Z/b = 4, 8,$  and  $12,$  respectively. Since the current experiments are performed on a concave surface at a fixed diameter, the heat transfer data at the far downstream region could not be obtained when the slot width is large. However, in general, the heat transfer Nusselt number increases with increasing surface curvature. The increase of the Nusselt number of the concave surface is attributed to the initiation of a series of Taylor-Görtler vortices, which extend over the entire surface. It has been found (Mayle et al., 1981; Thomann, 1968) that for flow over a concave surface, a series of Taylor-Görtler vortices can be initiated that can significantly increase the momentum and energy exchange near the wall and enhance the heat transfer along the wall. Kottke (1986) found that different size meshes positioned in the free stream before the concave surface can produce different size Taylor-Görtler vortices, which lead to different levels in the enhancement of the heat transfer process. In the current experiment, the increase in Nusselt number with increasing surface curvature suggests that the size of the Tay-

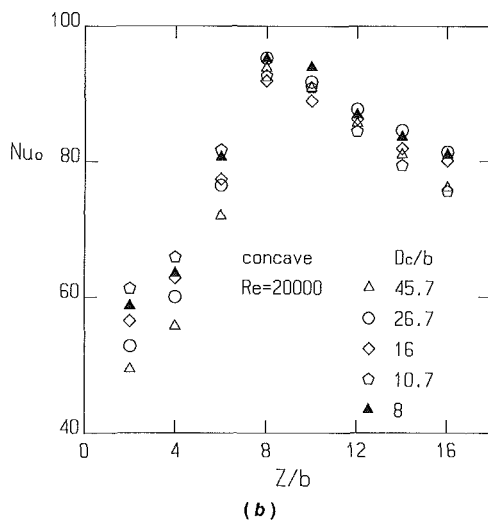
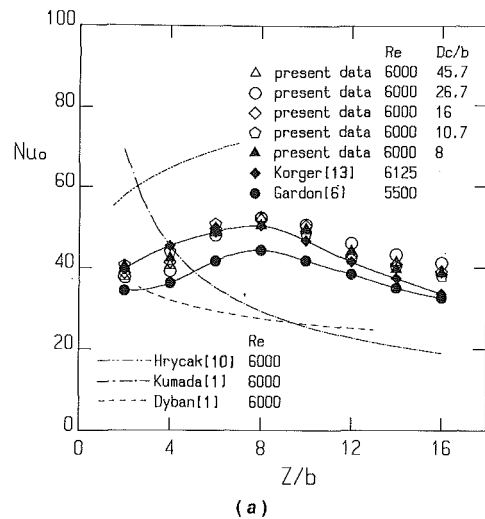


Fig. 6 Effect of concave surface curvature on the stagnation point Nusselt number and comparison with published results for (a)  $Re = 6000$  and (b)  $Re = 20,000$

lor-Görtler vortices increases with increasing surface curvature. However, it is interesting to be able to visualize how the flow structure of Taylor-Görtler vortices varies with curvature. However, this relies on a more detailed flow visualization experiment, which could not be provided with the current flow visualization facilities. Of particular interest is the stagnation point heat transfer and the laminar boundary layer heat transfer in the region close to the stagnation point when the slot-to-plate spacing is not large, which also increases with increasing surface curvature. It should be noted that the increase in the surface curvature is due to the increase in the slot width. The Taylor-Görtler vortices could not be initiated on and around the stagnation point. Therefore, the increase in the Nusselt number with increasing surface curvature is attributed to the earlier initiation of vortices in the mixing region of a wider jet, which results in an earlier termination of the potential core and the enhancement in the momentum transport in the flow and the heat transfer process along the wall, especially on the stagnation point. For the case of impinging jet over a flat plate, the enhancement in the heat transfer for a wider jet is also observed (Gardon and Akfirat, 1966).

The stagnation point Nusselt number  $Nu_o$  versus the slot-to-plate spacing at different diameter-to-slot-width ratios is plotted and compared with published results as shown in Fig. 6. The present data are in closest agreement with Korger and Krizek's results and are higher than Gardon and Akfirat's.

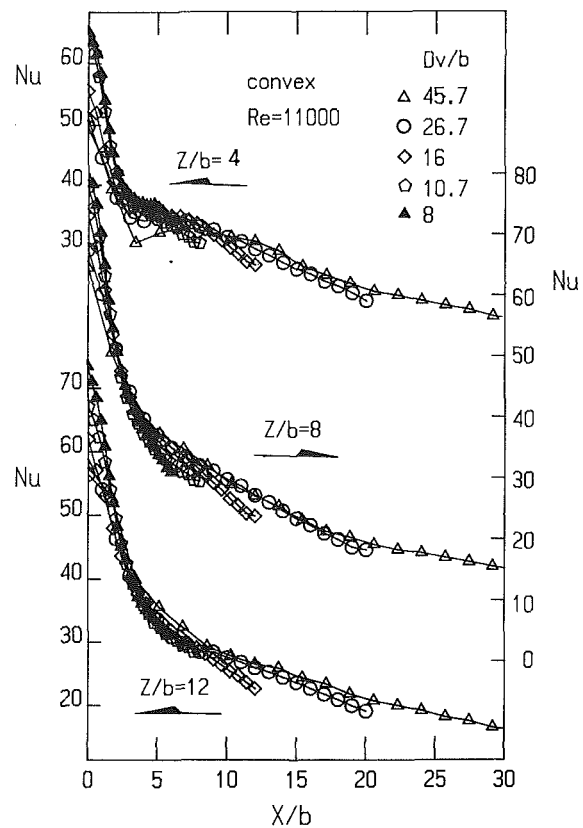


Fig. 7 Effect of convex surface curvature on the local heat transfer Nusselt number for the case of  $Re = 11,000$  and  $Z/b = 4, 8,$  and  $12$

After accounting for 20 percent experimental error in Gardon and Akfirat's data, agreement with the current data is good. Both the previously published results and the current data indicate that the maximum stagnation point heat transfer occurs at  $Z/b = 8$ . The results from Hrycak for round jet cooling on a flat plate are valid only in the region  $2 \leq Z/b \leq 7$  and are significantly higher than the case for the slot jet cooling. Hrycak (1981) mentions that his data have also been compared with an experimentally obtained expression for  $Nu_o$  in the report (Hrycak, 1978) and are 81 percent higher. The higher stagnation point Nusselt number has been attributed to the high turbulence intensity in the jet flow, which has been estimated to be 18 percent. Therefore, a higher Nusselt number than the current one is expected. However, the experimental results from Kumada and the theoretical analysis from Dyban (in Becco, 1976) for the case of slot jet cooling are significantly lower.

At a low Reynolds number, the surface curvature does not have a significant effect on the  $Nu_o$  number. It appears that at a low Reynolds number the earlier or the later initiation of vortices in the jet does not have a significant effect on the momentum and the heat transfer process along the surface. However, at a higher Reynolds number, the  $Nu_o$  number increases with increasing surface curvature for  $Z/b < 8$  as shown in Fig. 6(b). For the case of  $Z/b > 8$ , the curvature effect on  $Nu_o$  could not be concluded from the current data. This effect suggests that the earlier initiation of vortices in the mixing region of a wider jet can effect and increase the stagnation point heat transfer only when the slot-to-plate spacings is not large ( $Z/b < 8$ ). When the slot-to-plate spacing is large and jet flow becomes turbulent, the earlier initiation of vortices does not have a significant effect on the heat transfer process along the wall. The lower stagnation Nusselt number at  $D_c/b = 8$  is attributed to the fact that the maximum Nusselt number does not occur at the stagnation point but at a small distance from the stagnation point. This fact can be observed in Fig. 5(a).

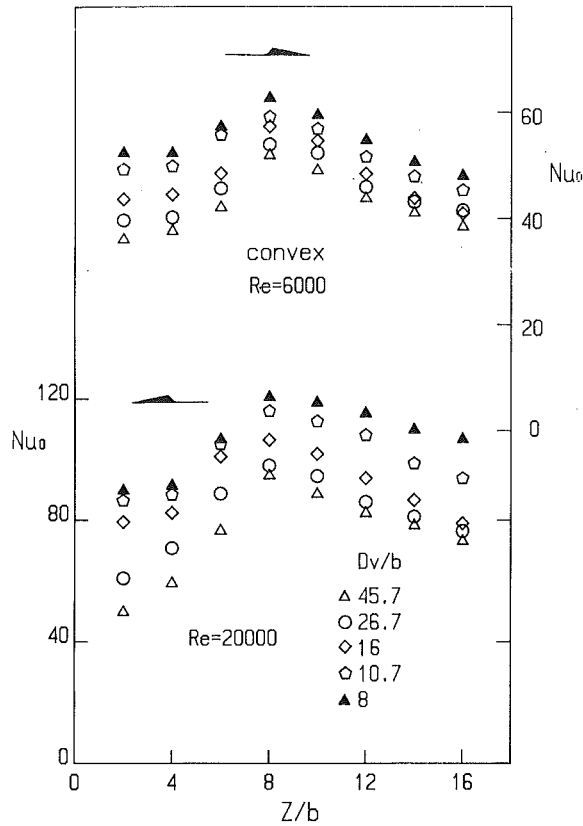


Fig. 8 Effect of convex surface curvature on the stagnation point Nusselt number for both  $Re = 6000$  and  $Re = 20,000$

A similar shift of the maximum Nusselt number beside the stagnation point for the cases of large surface curvature  $2.8 < D_c/b < 4$  is also reported by Dyban and Mazur (in Becko, 1976).

**3.2.3 Convex Surface.** For the case of impingement cooling on a convex surface, the curvature effect on the  $Nu_0$  number is significant, as shown in Fig. 7, while its effect on the local Nusselt number in the region far from the stagnation point is small. On the stagnation point,  $Nu_0$  increases with increasing curvature. The increase of  $Nu_0$  with increasing curvature is attributed to the occurrence of three-dimensional vortices on the stagnation point, which can increase in size with increasing surface curvature (as shown in the previous flow visualization experiment) and enhance the heat transfer process. However, far downstream from the stagnation point, it has been found (Schlichting, 1979; Mayle et al., 1981) that the surface curvature has the effect of stabilizing the flow and reducing the momentum and energy transport near the wall, which results in the decrease of Nusselt number. In addition, the increase in slot width can cause an earlier initiation of vortices in the jet, which can terminate the potential core at an earlier time and enhance the momentum and the heat transfer process along the wall. However, Fig. 7 shows that the local Nusselt number in the downstream region decreases slightly with increasing curvature. It appears that the earlier initiation of vortices for a wider jet does not have a significant effect on the heat transfer process in the downstream region.

The stagnation point Nusselt number versus  $Z/b$  at various curvatures is plotted in Fig. 8. The stagnation point Nusselt number increases monotonically with increasing surface curvature at both low and high  $Re$  number. Correlations of  $Nu_0$  in terms of the Reynolds number, the diameter-to-slot-width, and the slot-to-plate spacing are obtained as follows:

For  $2 \leq Z/b \leq 8$ ,

$$Nu_0 = 0.729 Re^{0.5} (D_v/b)^{-0.14} (Z/b)^{0.16} \quad (2)$$

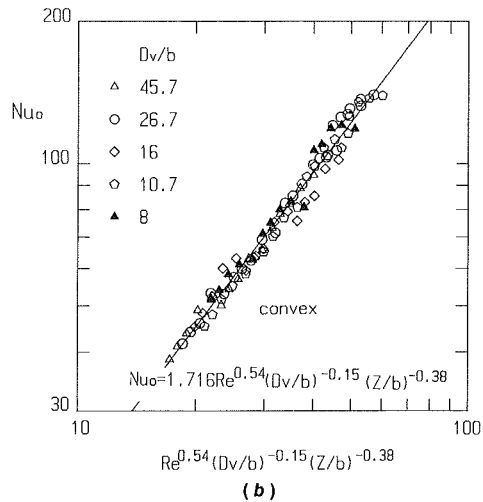
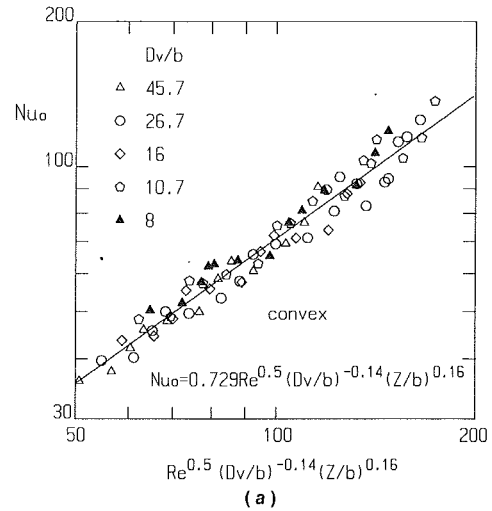


Fig. 9 Correlations of the stagnation point Nusselt number on the convex surface for  $6000 \leq Re \leq 35,000$ ,  $8 \leq D_v/b \leq 45.7$ , and (a)  $2 \leq Z/b \leq 8$  and (b)  $8 \leq Z/b \leq 16$

with a standard deviation of 2.8 percent.

For  $8 \leq Z/b \leq 16$ ,

$$Nu_0 = 1.716 Re^{0.54} (D_v/b)^{-0.15} (Z/b)^{-0.38} \quad (3)$$

with a standard deviation of 2.3 percent.

The above correlations are valid for  $6000 \leq Re \leq 35,000$  and  $8 \leq D_v/b \leq 45.7$ . The least-square fit of data is presented in Fig. 9. The fact that the  $Nu_0$  number is proportional to the Reynolds number to the one half power for  $Z/b \leq 8$  agrees with the analysis from Hrycak (1981) and the experimental correlation of others (Hoogendoorn, 1977) for the case of the flat plate.

**3.2.4 Average Nusselt Number.** An average heat transfer coefficient is obtained by dividing the average heat flux around the curved surface by the mean temperature difference between the wall and the ambient. The average Nusselt number, which is defined as  $\bar{h}_i b/k$ , is also correlated with the Reynolds number, the diameter-to-slot-width, and the slot-to-plate spacing for  $6000 \leq Re \leq 35,000$  and  $8 \leq D_v/b \leq 45.7$ .

For concave surface and  $2 \leq Z/b \leq 8$ ,

$$\bar{Nu} = 0.251 Re^{0.68} (D_c/b)^{-0.38} (Z/b)^{0.15} \quad (4)$$

with standard deviation of 2.4 percent.

For concave surface and  $8 \leq Z/b \leq 16$ ,

$$\bar{Nu} = 0.394 Re^{0.68} (D_c/b)^{-0.38} (Z/b)^{-0.32} \quad (5)$$

with standard deviation of 2.9 percent.

For convex surface and  $2 \leq Z/b \leq 8$ ,

$$\bar{Nu} = 0.221 Re^{0.65} (D_v/b)^{-0.33} (Z/b)^{0.1} \quad (6)$$

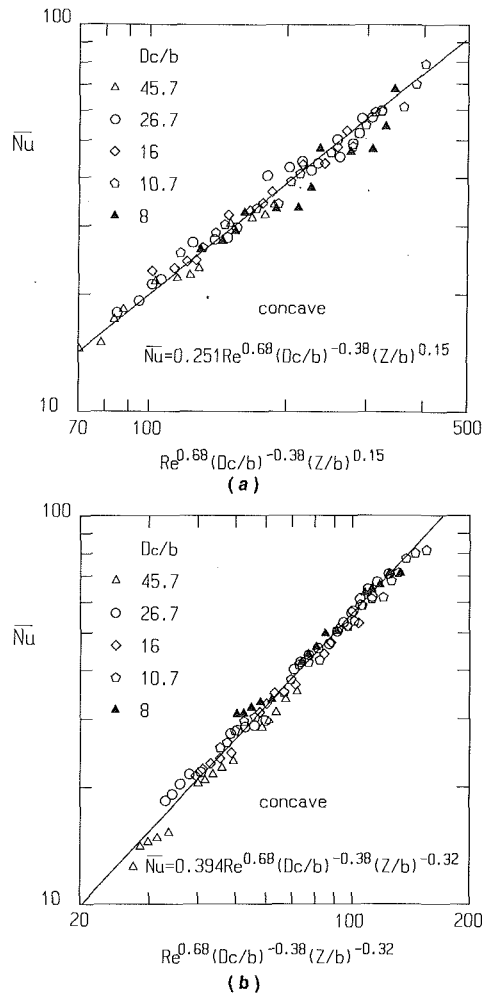


Fig. 10 Correlations of the average Nusselt number on the concave surface for  $6000 \leq Re \leq 35,000$ ,  $8 \leq D_c/b \leq 45.7$ , and (a)  $2 \leq Z/b \leq 8$  and (b)  $8 \leq Z/b \leq 16$

with standard deviation of 2.8 percent.

For a convex surface and  $8 \leq Z/b \leq 16$ ,

$$\bar{Nu} = 0.308 Re^{0.65} (D_c/b)^{-0.38} (Z/b)^{0.2} \quad (7)$$

with a standard deviation of 2.5 percent.

Typical results of least-square fit to the data are presented in Fig. 10.

#### 4 Conclusions

The surface curvature effect on the impinging flow structure and the heat transfer along a concave and a convex surface are studied experimentally. For the case of impingement cooling on a convex surface, a series of three-dimensional counterrotating vortices are initiated near the wall on the stagnation point, which can increase the momentum transport in the flow and enhance the heat transfer process on the wall. The increase of surface curvature can increase the size of the counterrotating vortices, which results in further increase of the stagnation point Nusselt number. In the region away from the stagnation point, the centrifugal force due to the surface curvature can stabilize the flow and reduce the heat transfer.

In the case of impingement cooling on a concave surface, no three-dimensional vortices in the stagnation point are observed. The flow structure in the region far from the stagnation point is turbulent and could hardly be observed. However, the heat transfer measurements indicate that the local Nusselt number increases with increasing surface curvature. This fact is attributed to the generation of Taylor-Görtler vortices, which can increase the momentum transport in the flow and enhance

the heat transfer process along the surface. The earlier initiation of vortices in the mixing region of a wiser jet can cause an earlier termination of potential core, which results in an increase in the heat transfer on and around the stagnation point.

The local heat transfer Nusselt number measured for the case when surface curvature effect is small is compared with the published results for the case of impingement cooling on a flat surface. Good agreement is obtained. Both the stagnation point Nusselt number and the averaged Nusselt number determined are well correlated in terms of relevant nondimensional parameters.

#### Acknowledgments

This research was sponsored by the National Science Council of Taiwan under contract No. NSC 79-0401-E-006-52.

#### References

- Becko, Y., 1976, "Impingement Cooling—A Review," Von Karman Institute for Fluid Dynamics, Lecture series 83.
- Chung, C. M., 1989, "Impingement Cooling on a Concave and a Convex Surface," M.S. Thesis, Institute of Aeronautics and Astronautics, National Cheng Kung University, Taiwan.
- Chupp, R. E., Helms, H. E., McFadden, P. W., and Brown, T. P., 1969, "Evaluation of Internal Heat-Transfer Coefficients for Impingement-Cooled Turbine Airfoils," *Journal of Aircraft*, Vol. 6, pp. 203-208.
- Donaldson, C. D., and Snedeker, R. S., 1971a, "A Study of Free Jet Impingement. Part 1. Mean Properties of Free and Impinging Jets," *Journal of Fluid Mechanics*, Vol. 45, Part 2, pp. 281-319.
- Donaldson, C. D., and Snedeker, R. S., 1971b, "A Study of Free Jet Impingement. Part 2. Free Jet Turbulent Structure and Impingement Heat Transfer," *Journal of Fluid Mechanics*, Vol. 45, Part 3, pp. 477-512.
- Gardon, R., and Cobonpue, J., 1963, "Heat Transfer Between a Flat Plate and Jets of Air Impinging on It," in: *International Developments in Heat Transfer*, Proceedings of the 2nd International Heat Transfer Conference, ASME, New York, pp. 454-460.
- Gardon, R., and Akfirat, J. C., 1966, "Heat Transfer Characteristics of Impinging Two-Dimensional Air Jets," *ASME JOURNAL OF HEAT TRANSFER*, Vol. 88, pp. 101-108.
- Goldstein, R. J., and Frachett, M. E., 1988, "Heat Transfer From a Flat Surface to an Oblique Impinging Jet," *ASME JOURNAL OF HEAT TRANSFER*, Vol. 110, pp. 84-89.
- Hoogendoorn, C. J., 1977, "The Effect of Turbulence on Heat Transfer at a Stagnation Point," *International Journal of Heat and Mass Transfer*, Vol. 20, pp. 1333-1338.
- Hrycak, P., 1978, "Heat Transfer From a Row of Jets Impinging on Concave Semicylindrical Surface," *Proceedings of 6th International Heat Transfer Conference*, Vol. 2, pp. 67-72, EC-11, Toronto, Canada.
- Hrycak, P., 1981, "Heat Transfer From a Row of Impinging Jets to Concave Cylindrical Surfaces," *International Journal of Heat and Mass Transfer*, Vol. 24, pp. 407-419.
- Kestin, J., and Wood, R. T., 1970, "On the Stability of Two-Dimensional Stagnation Flow," *Journal of Fluid Mechanics*, Vol. 44, pp. 461-479.
- Korger, M., and Krizek, F., 1965, "Mass-Transfer Coefficient in Impingement Flow From Slotted Nozzles," *International Journal of Heat and Mass Transfer*, Vol. 9, pp. 337-344.
- Kottke, V., 1986, "Taylor-Görtler Vortices and Their Effect on Heat and Mass Transfer," *Proceedings of 8th International Heat Transfer Conference*, C. L. Tien et al., eds., pp. 1139-1144.
- Martin, H., 1977, "Heat and Mass Transfer Between Impinging Gas Jets and Solid Surfaces," in: *Advances in Heat Transfer*, J. Hartnett and T. Irvine, Jr., eds., Vol. 13, pp. 1-60.
- Mayle, R. E., Blair, M. F., and Kopper, F. C., 1981, "Turbulent Boundary Layer Heat Transfer on Curved Surfaces," *ASME JOURNAL OF HEAT TRANSFER*, Vol. 101, pp. 521-525.
- Metzger, D. E., Yamashita, T., and Jenkins, C. W., 1969, "Impingement Cooling of Concave Surfaces With Lines of Circular Air Jets," *ASME Journal of Engineering for Power*, Vol. 91, pp. 149-158.
- Metzger, D. E., Baltzer, R. T., and Jenkins, C. W., 1972, "Impingement Cooling Performance in Gas Turbine Airfoils Including Effects of Leading Edge Sharpness," *ASME Journal of Engineering for Power*, Vol. 94, pp. 219-225.
- Schlichting, H., 1979, *Boundary-Layer Theory*, 7th ed., McGraw-Hill, New York.
- Tabakoff, W., and Clevenger, W., 1972, "Gas Turbine Blade Heat Transfer Augmentation by Impingement of Air Jets Having Various Configurations," *ASME Journal of Engineering for Power*, Vol. 94, pp. 51-60.
- Thomann, H., 1968, "Effect of Streamwise Wall Curvature on Heat Transfer in a Turbulent Boundary Layer," *Journal of Fluid Mechanics*, Vol. 33, Part 2, pp. 283-292.
- Zumbrunnen, D. A., Incropera, F. P., and Viskanta, R., 1989, "Convective Heat Transfer Distributions on a Plate Cooled by Planar Water Jets," *ASME JOURNAL OF HEAT TRANSFER*, Vol. 111, pp. 889-896.

# Heat Transfer in a Staggered Tube Array for a Gas-Solid Suspension Flow

D. B. Murray

J. A. Fitzpatrick

Mem. ASME

Department of Mechanical Engineering,  
Trinity College,  
Dublin 2, Ireland

*The crossflow heat transfer characteristics of a tube array subject to a dilute gas-solid suspension flow have been investigated. For a tube located in the first row of the array, the results indicate that an increase in the thermal capacity of the mixture is the dominant influence on heat transfer and a correlation for predicting the Nusselt number enhancement is developed. At the second row, the Nusselt number is influenced by thermal property changes and delayed boundary layer separation, whereas heat transfer in the third and later rows is determined by a combination of thermal capacity effects and changes in the flow structure and turbulence levels within the array.*

## Introduction

The effect on heat transfer of solid particles suspended in a gas flow is of considerable interest in the design of heat exchangers for fluidized bed applications. For crossflow-type systems, the heat transfer is generally considered to be enhanced by the presence of the particles. For example, increased heat transfer performance has been reported by both Wood et al. (1980) for tubes located in the splash zone immediately above a fluidized bed and by Byam et al. (1981) who examined the heat transfer of dilute suspension flows for various locations in the freeboard. The heat transfer characteristics of a crossflow heat exchanger were investigated by Woodcock and Worley (1966) for mass loading ratios from 2 to 8 kg/kg. Their results showed an enhancement of the Nusselt number for the complete tube bank with a strong dependence on the solids loading. For the solids circulation type boilers described by Marshall (1988), heat exchangers are located high in the freeboard, where the mass loading ratio is less than 1 kg/kg and there are few experimental data for heat exchangers operating in such dilute concentration flows.

A number of studies have been carried out for gas-solid suspension flows in pipes as described, for example, by Depew and Kramer (1972) and Sadek (1972). The presence of the solid phase resulted in higher rates of heat transfer for the same flow temperature conditions and this was considered to be due to increased volumetric heat capacity of the fluid. The higher enhancement with smaller particles observed by Farbar and Morley (1957) has been attributed to more effective heat transfer resulting from higher surface area to volume ratios. Conductive heat transfer between the surface and contacting particles was identified by Reising (1965) and Kurosaki et al. (1986) as an important factor in the improved heat transfer performance, although Depew and Kramer (1972) and Tien (1961) have suggested that direct heat transfer from the wall to the solid phase is usually negligible.

Changes in the turbulent structure and the boundary layer characteristics of the flow can also affect the heat transfer. The Nusselt number in a pipe flow with a loading ratio of around 1 kg/kg was found to be reduced or unaffected by the presence of the particles by Shimizu et al. (1988) and by Kane and Pfeffer (1985). The latter considered the reduction to be a consequence of suppression of the turbulence of the carrier fluid. Owen (1969) considered the effect of solid particles on

turbulent flows and derived approximate expressions for turbulence suppression based on the ratio of particle response time to a characteristic time scale for the eddies. Gas-particle turbulence interaction has also been assessed on the basis of the ratio of the relative particle to eddy size by Gore and Crowe (1989) and in terms of the particle Reynolds number by Hetsroni (1988). Thus, particles can suppress turbulence and reduce heat transfer for some gas-particle flows. In addition to turbulence effects, changes in boundary layer profiles have been measured by Lee and Durst (1982) and by Fitzpatrick et al. (1990) for gas-particle suspension flows in pipes and across a circular cylinder respectively. For both of these, reductions in the boundary layer physical thickness were observed with higher velocity gradients at the wall so that higher local heat transfer coefficients would be expected. This type of heat transfer enhancement will be less significant at higher Reynolds numbers as noted by Farbar and Morley (1957).

This paper reports the results from an experimental study aimed at assessing the influence of particles on the local and overall heat transfer performance for a tube array of the type used in fluidized bed systems. A series of tests have been conducted in which the effect of location, particle size and concentration, and flow velocity have been examined. The results suggest that, for particles in the range 40–200  $\mu\text{m}$  with mass loading ratios of less than 1 kg/kg, increased thermal capacity gives a net enhancement of heat transfer in the first row and over the front of a second row tube, whereas additional effects such as turbulence suppression and a delay in boundary layer separation cause reductions in Nusselt number for the remainder of the array.

## Experimental Facilities and Instrumentation

**Main Flow Circuit.** The tests were conducted in a closed-loop recirculating wind tunnel with a particle feed and collection system, as shown in Fig. 1. Vanes and honeycomb are included upstream of the test section to give a uniform air flow distribution across the section at all flow rates, as was confirmed by pitot static tube measurements. The test section is 0.4 m square and the 10 row by 8 column array used in the present study is triangular with a tube pitch to diameter ratio of 2.0 and tube diameter of 25 mm. One heated tube is used for the heat transfer measurements, as this has been shown by Aiba and Yamazaki (1976) to give adequate results for tube array studies. The volumetric flow rate through the tunnel is monitored by a venturi meter located on the down leg of the

Contributed by the Heat Transfer Division for publication in the JOURNAL OF HEAT TRANSFER. Manuscript received by the Heat Transfer Division November 12, 1990; revision received April 19, 1991. Keywords: Forced Convection, Heat Exchangers, Multiphase Flows.





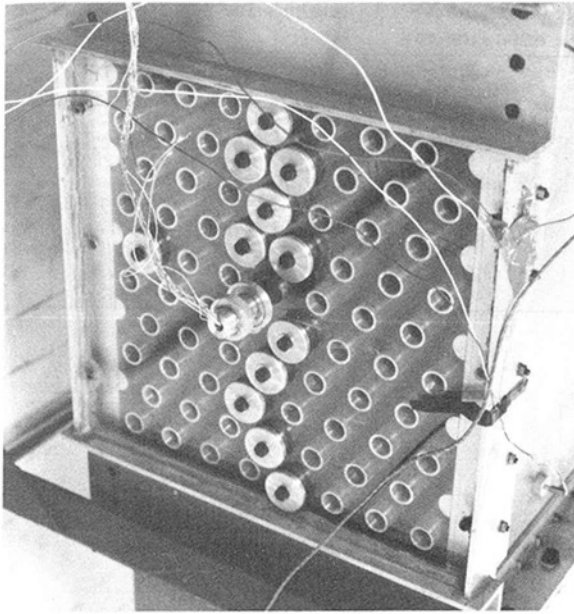


Fig. 2 Instrumented tube in tube array

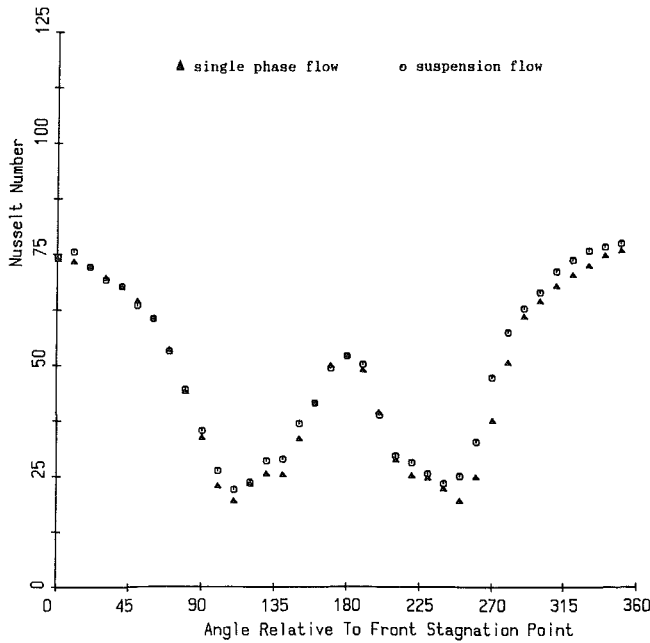


Fig. 3 Local Nusselt numbers for a tube in the first row:  $Re = 5000$ ,  $d_p = 150 \mu m$ ,  $S_L = 0.64$

suspension flow cases at a given sensor location and if the statistical variation in the local heat transfer measurement was more than  $\pm 3$  percent, further tests were conducted to ensure consistent results. Thus, although the differences between suspension and single-phase Nusselt numbers were sometimes less than the uncertainty limit on absolute values, the relative values were repeatable.

### Results and Observations

**Effect of Location.** At the first row, it can be seen from Fig. 3 that the local Nusselt number exhibits a small increase at all measurement points around the tube. From Fig. 4, similar trends are observed around the front of the tube in the second row with increases of around 7 percent for local heat transfer coefficients. However, decreases of up to 25 percent are evident

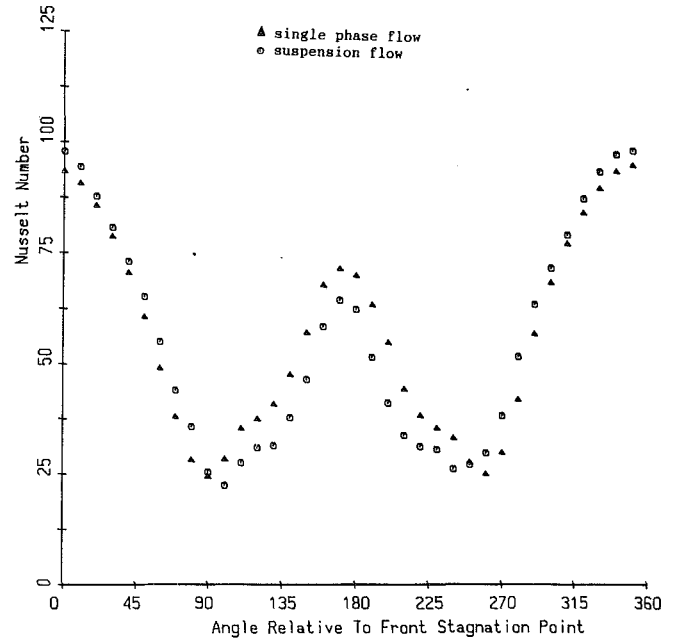


Fig. 4 Local Nusselt numbers for a tube in the second row:  $Re = 5000$ ,  $d_p = 150 \mu m$ ,  $S_L = 0.64$

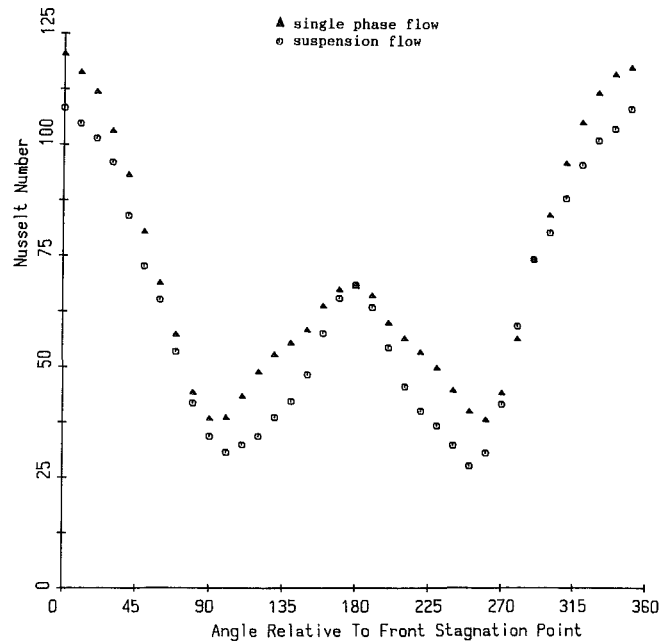


Fig. 5 Local Nusselt numbers for a tube in the third row:  $Re = 5000$ ,  $d_p = 150 \mu m$ ,  $S_L = 0.64$

in the wake of the tube with a rearward shift of up to 10 deg in the position of the minimum Nusselt number. The consequence is a decrease of some 2 percent in the overall Nusselt number at this location. At the third row, it is evident from Fig. 5 that there is a marked decrease in the local heat transfer coefficients around the tube for these conditions with the greatest reductions evident close to the front stagnation point and in the secondary vortex region after separation. The minimum Nusselt number occurs almost 10 deg later for the suspension flow, which contributes to a reduction of about 30 percent in the secondary vortex region. In the main wake, the suspension Nusselt number rises more strongly and at 180 deg the two curves coincide. Similar results were obtained at the fourth row, although the drop in heat transfer is not quite so great.

**Table 1 Mean Nusselt numbers for suspension and single-phase tests: effect of location within array**

| Test No. | Row | Re (approx) | $S_L$ , kg/kg | $d_p$ , $\mu\text{m}$ | Mean $Nu_a$ | Mean $Nu_{su}$ | Change, percent |
|----------|-----|-------------|---------------|-----------------------|-------------|----------------|-----------------|
| 1        | 1   | 5000        | 0.65          | 150                   | 49.2        | 51.5           | +4.5            |
| 2        | 2   | 5000        | 0.65          | 150                   | 55.7        | 54.7           | -1.9            |
| 3        | 3   | 5000        | 0.65          | 150                   | 67.1        | 59.7           | -11.1           |
| 4        | 4   | 5000        | 0.65          | 150                   | 66.6        | 61.6           | -7.5            |
| 5        | 5   | 5000        | 0.65          | 150                   | 65.9        | 61.6           | -6.6            |
| 6        | 6   | 5000        | 0.65          | 150                   | 63.6        | 62.1           | -2.4            |
| 7        | 8   | 5000        | 0.65          | 150                   | 64.2        | 62.9           | -2.0            |
| 8        | 10  | 5000        | 0.65          | 150                   | 64.9        | 64.1           | -1.2            |

**Table 2 Mean Nusselt numbers for suspension and single-phase tests: first row**

| Test No. | Row | Re (approx) | $S_L$ , kg/kg | $d_p$ , $\mu\text{m}$ | Mean $Nu_a$ | Mean $Nu_{su}$ | Change, percent |
|----------|-----|-------------|---------------|-----------------------|-------------|----------------|-----------------|
| 9        | 1   | 5000        | 0.43          | 150                   | 47.6        | 48.7           | +2.4            |
| 10       | 1   | 5000        | 0.27          | 150                   | 46.8        | 47.5           | +1.7            |
| 11       | 1   | 5000        | 0.20          | 150                   | 47.0        | 48.0           | +2.1            |
| 12       | 1   | 10000       | 0.46          | 150                   | 59.7        | 59.8           | +0.1            |
| 13       | 1   | 10000       | 0.20          | 150                   | 59.5        | 59.7           | -0.3            |
| 14       | 1   | 5000        | 0.66          | 65                    | 47.8        | 54.7           | +14.5           |
| 15       | 1   | 5000        | 0.18          | 65                    | 47.9        | 51.1           | +6.6            |
| 16       | 1   | 10000       | 0.47          | 65                    | 58.9        | 62.3           | +5.8            |
| 17       | 1   | 10000       | 0.21          | 65                    | 59.1        | 60.5           | +2.5            |

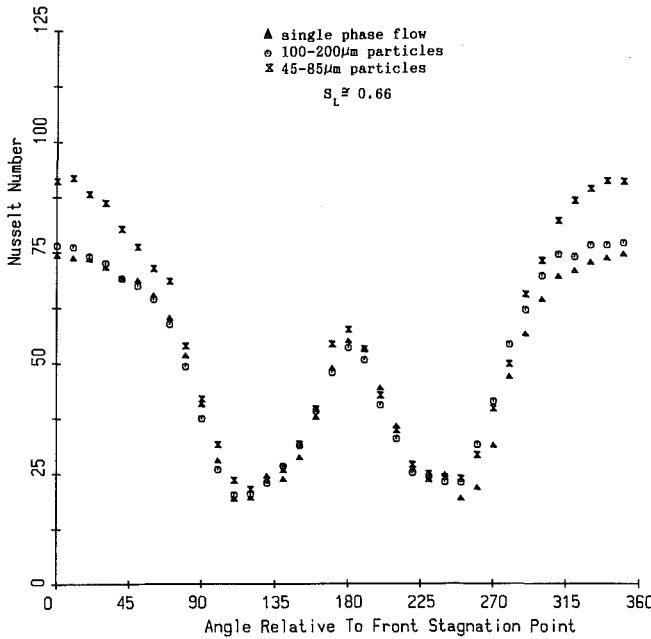


**Fig. 6 Effect of particle size on Nusselt number: first row: Re = 5000**

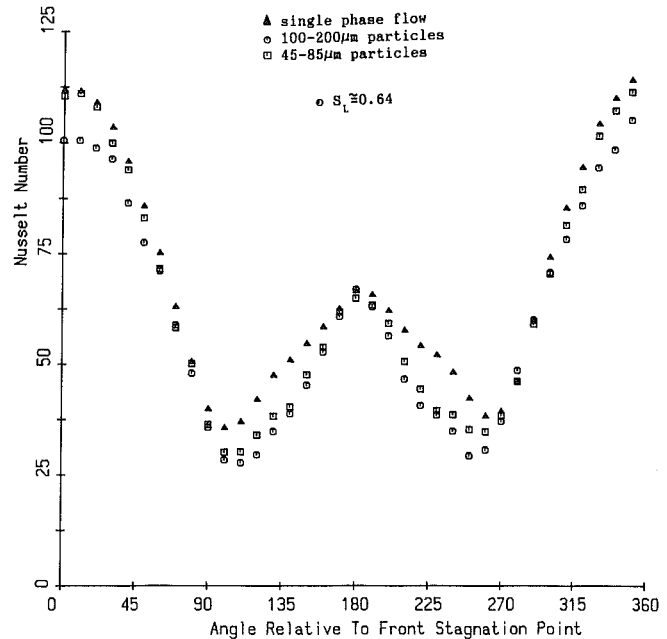


**Fig. 7 Effect of particle size on Nusselt number: third row: Re = 5000**

From the fifth row onward, the reduction in heat transfer due to the solid particles becomes less marked until, at the tenth row, a slight reduction observed in local heat transfer at the front of the tube is virtually compensated by a small increase in the wake. This can be seen from Table 1, where the changes in mean Nusselt number, along with details of the test conditions, are shown. Although the overall changes in mean Nusselt are, in many cases, less than the expected uncertainty in the measurements, the mean results have been determined by integrating the local values and the variation in these individual readings was considerably greater than the experimental uncertainty.

These results indicate that the suspension heat transfer progresses from a small enhancement at the first row to a significant decrease in Nusselt number at the third row. In order to examine the possible reasons for these differences in heat transfer performance, the Reynolds number and particle size and concentration were varied for tests at the first and third rows.

**First Row.** The effect of particle size on the local heat transfer measurements for the first row tube is shown in Fig. 6, where data points obtained using particles with a mean diameter of  $65 \mu\text{m}$  are compared with the results from the  $150 \mu\text{m}$  particles using similar concentrations. The results for a single-phase flow are included for comparison. From Fig. 6, the local enhancement close to the front stagnation point averages approximately 25 percent for the smaller particles compared with 3–5 percent for the larger particles. The local Nusselt number in the wake region is slightly increased by the presence

of the fine solids, which contrasts with the small decrease observed in the flow containing the larger particles. Overall, the mean Nusselt number with the suspension of small particles is 14.5 percent higher than that of the equivalent air-only case as compared with 4.5 percent higher for the large particles.

A similar particle size effect was observed at a Reynolds number of 10,000 with an enhancement of approximately 5.8 percent in the mean Nusselt number for the  $65 \mu\text{m}$  particles, whereas no change was measured for the large particle suspension. The influence of particle concentration was investigated for each particle size at both Reynolds numbers. The mean Nusselt numbers are summarized in Table 2 and it can be seen that the increase in mean heat transfer coefficient is related to the concentration of particles in the flow. At both Reynolds numbers it was found that the increase in Nusselt number over the front of the tube was most sensitive to the solids concentration. Once again, it should be recalled that the changes in the mean values have been determined from local coefficients, which showed greater variation.

**Third Row.** For the third row, the results in Fig. 7 show the effect of particle size at a Reynolds number of 5000. The local Nusselt number is reduced over most of the tube circumference with values of 11.1 and 6.5 percent, respectively, for the large and small particles. From Fig. 7, the greatest difference for the particle sizes occurs over the front of the tube, a very small decrease being recorded for the  $65 \mu\text{m}$  particles compared with a substantial reduction for the  $150 \mu\text{m}$  case.

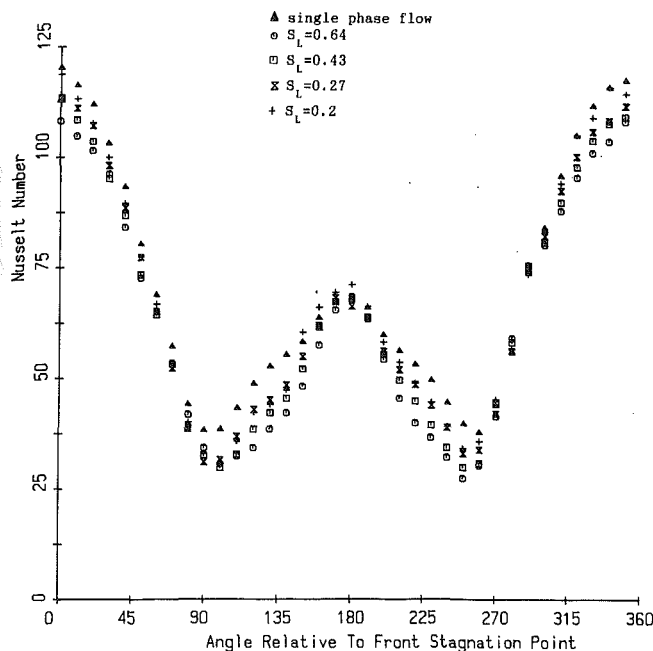


Fig. 8 Effect of mass loading ratio on Nusselt number: third row:  $Re = 5000$ ;  $d_p = 150 \mu m$

Similar reductions were recorded for both particle sizes in the wake where the pattern of variation is very similar to that recorded for the second row. The effect of varying the solids mass loading ratio for both particle sizes was also investigated. From the data shown in Fig. 8 for the  $150 \mu m$  particles, it can be seen that heat transfer in the regions most influenced by the particles, namely the zone around the front stagnation point and the secondary vortex region, is strongly dependent on the solids concentration.

At a Reynolds number of 10,000, it was found that the differences in heat transfer over the front of the tube were less significant but that the results elsewhere were very similar to those recorded at the lower Reynolds number. The influence of particle concentration was also examined for each particle size at the Reynolds number of 10,000. For the  $150 \mu m$  particles, heat transfer over the front of the tube and in the secondary vortex region is influenced by the mass loading ratio, whereas there is little evidence of a dependence on concentration for the fine particles. A summary of the results for the mean Nusselt numbers recorded at the third row is given in Table 3.

## Discussion

From the results described in the previous section, it is evident that the particles enhance the heat transfer at the first row, cause local increases and decreases for the tube in the second row, and reduce the local and overall Nusselt numbers for the third and subsequent rows. The discussion is subdivided to address these specific differences.

**First Row.** The general trend observed from the results presented for the first row is an increase in heat transfer, which is most significant over the front of the tube and in the region close to separation of the boundary layer. Although factors such as turbulence suppression and changes in the boundary layer profile can influence convective heat transfer for suspension flows, a detailed analysis of the first row trends by Murray (1989) has shown that an increase in the volumetric thermal capacity of the fluid can account for the measured increases at this location.

Although a number of correlations have been proposed for

Table 3 Mean Nusselt numbers for suspension and single-phase tests: third row

| Test No. | Row | Re (approx) | $S_L$ , kg/kg | $d_p$ , $\mu m$ | Mean $Nu_a$ | Mean $Nu_{su}$ | Change, percent |
|----------|-----|-------------|---------------|-----------------|-------------|----------------|-----------------|
| 18       | 3   | 5000        | 0.43          | 150             | 66.5        | 60.7           | -8.8            |
| 19       | 3   | 5000        | 0.27          | 150             | 68.1        | 63.7           | -6.4            |
| 20       | 3   | 5000        | 0.20          | 150             | 67.4        | 64.7           | -4.0            |
| 21       | 3   | 10000       | 0.46          | 150             | 88.4        | 79.1           | -10.6           |
| 22       | 3   | 10000       | 0.20          | 150             | 88.2        | 82.4           | -6.7            |
| 23       | 3   | 5000        | 0.65          | 65              | 68.0        | 63.6           | -6.5            |
| 24       | 3   | 5000        | 0.18          | 65              | 68.4        | 65.3           | -4.4            |
| 25       | 3   | 10000       | 0.47          | 65              | 84.9        | 77.3           | -9.0            |
| 26       | 3   | 10000       | 0.21          | 65              | 84.7        | 77.7           | -8.2            |

suspension Nusselt numbers in pipe or in-line tube array flows, there is no correlation available for crossflow heat transfer applications. By considering the suspension as a homogeneous fluid, the standard correlation for the mean Nusselt number of a single tube in crossflow given by Zukauskas (1972) can be used, as shown by Murray (1989), to give the ratio of the suspension flow Nusselt number to the single-phase Nusselt number as:

$$Nu_{su}/Nu_a = \{1 + S_L c_{pr}\}^{0.37} \quad (1)$$

where  $S_L$  is the solids mass loading ratio in kg/kg and  $c_{pr}$  is the ratio of the specific heat of the solids to that of the gas phase.

$\{1 + S_L c_{pr}\}$  is usually referred to as the convective capacity parameter and is important in assessing the dependence of the Nusselt number on the thermal properties. This indicates that an exponent of 0.37 for the convective capacity parameter is appropriate for assessing the increased thermal capacity effect. Thus, the enhancement of Nusselt number due to the increased volumetric thermal capacity of a suspension of infinitely fine particles results from an increase in the effective Prandtl number of the fluid. However, observed particle size and Reynolds number effects are still not accounted for by this expression.

The effect of particle size can be incorporated into the convective capacity parameter by considering the ability of particles of different sizes to realize their full thermal capacity, i.e., to achieve a new uniform temperature close to that of the surrounding air. Contact heat transfer is not considered important in the current tests as the findings of Tien (1961), Depew and Kramer (1972), and Kurosaki et al. (1986) have shown it to be negligible for air-glass suspensions in duct and impinging jet flows. Convective heat transfer from the gas to the particle is governed by the thermal relaxation time (first-order time constant), which is defined as:

$$t_{rel} = \frac{d_p \rho_p c_{pp}}{6h_p} \quad (2)$$

where  $d_p$  is the particle diameter,  $\rho_p$  is the particle density,  $c_{pp}$  is the specific heat of the solid, and  $h_p$  is the heat transfer coefficient between the particle and the gas, determined from an appropriate correlation such as that of Hughmark (1967). Clearly, small particles will respond more rapidly as there is a greater surface area to volume ratio. Thus, the thermal relaxation time,  $t_{rel}$ , can be used to determine the ability of a particular suspension of solids in a gas flow to realize its full thermal capacity. If the particle thermal relaxation times are longer than the particle residence time close to the heat transfer surface, then the heat transferred to the particles will be reduced accordingly. An approximate residence time can be obtained as the diameter of the heated tube divided by the average upstream air flow velocity. The ratio of this characteristic residence time to the thermal relaxation time can be used as

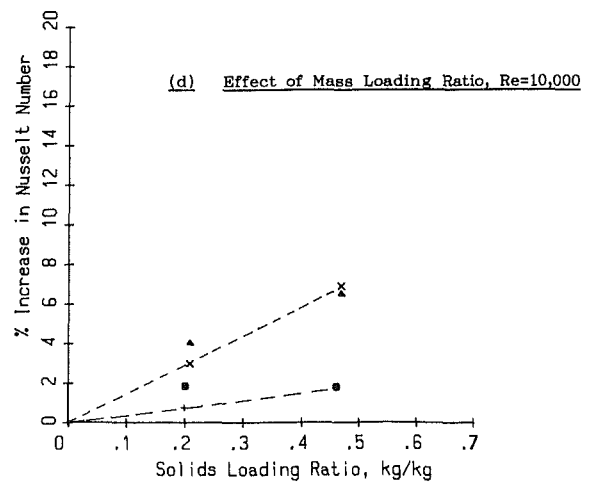
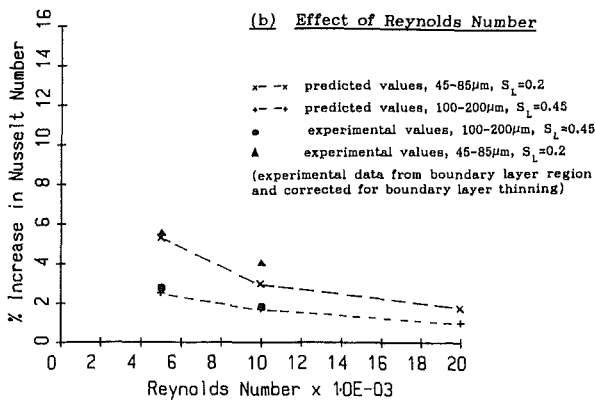
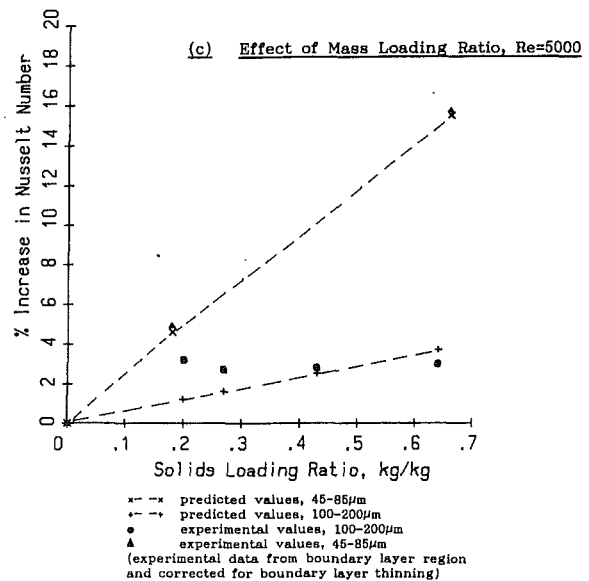
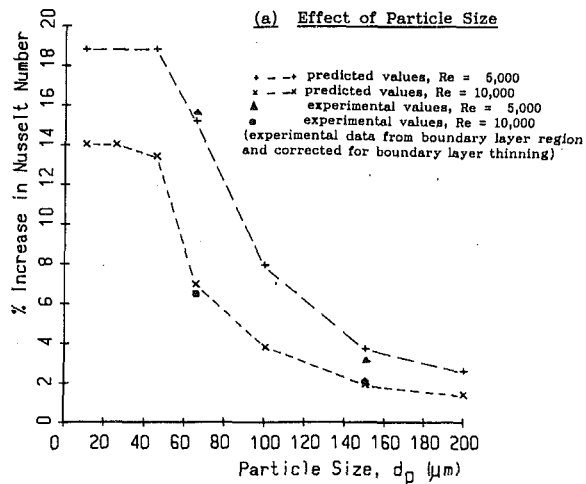


Fig. 9 Experimental and predicted thermal enhancement trends: first row

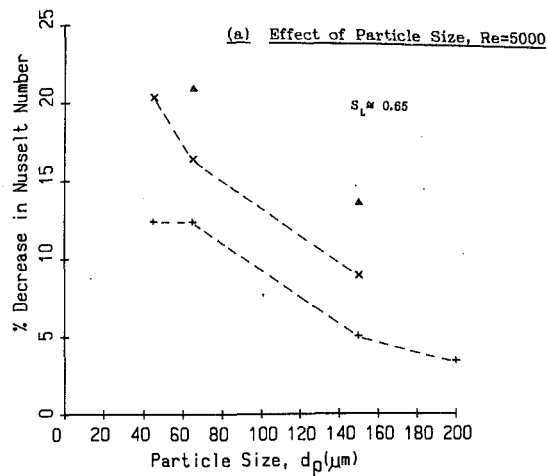
a "thermal effectiveness factor" given by  $\eta_t = (t_{char}/t_{rel})$ . This can then be used to estimate the heat transfer enhancement by modifying the convective capacity parameter to give a new thermal enhancement prediction as:

$$Nu_{su}/Nu_a = [1 + \eta_t S_L C_{pr}]^{0.37} \quad (3)$$

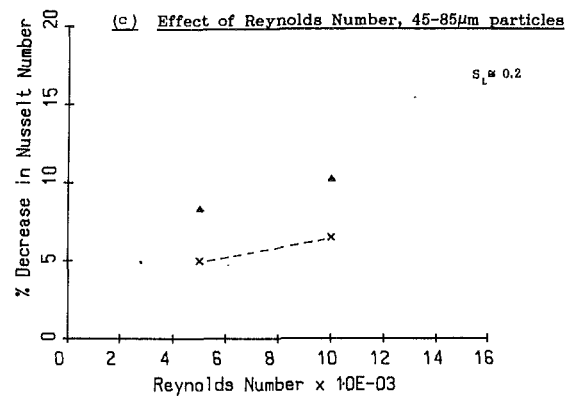
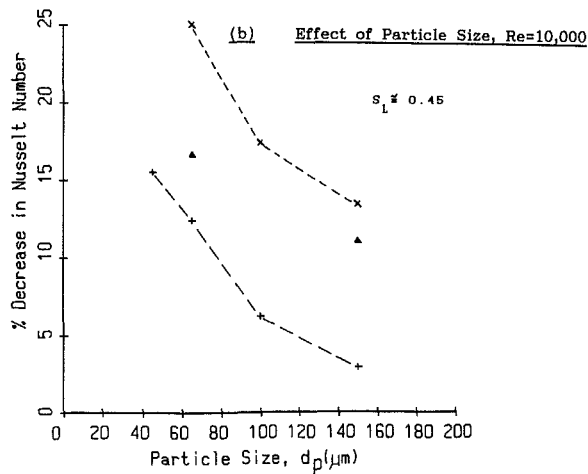
(It is understood, of course, that the maximum value for  $\eta_t$  is 1.0.)

For a flow where particles have thermal relaxation times less than the characteristic residence time, this analysis implies that the enhancement of heat transfer will be the same as that for an equivalent homogeneous fluid. In practice, particles of finite size will lag behind the temperature of the fluid at any point in the thermal boundary layer and, therefore, the effective thermal capacity and Prandtl number at that point will be less than the ideal value corresponding to the homogeneous fluid. This indicates that the Nusselt number increase predicted using Eq. (3) should be considered as an upper limit. Nonetheless, finite sized particles may enter the thermal "control zone" more than once as result of impact and rebound from the cylinder and subsequent re-entrainment in the impinging fluid. This process can be considered as an effective turbulent transport of heat, which is present in particulate flows only and is likely to lead to additional enhancement of heat transfer. Specific experiments would be required to determine the characteristics of particle residence times around the tube.

The predictions for percentage increase in Nusselt number based on Eq. (3) are shown in Fig. 9 as a function of Reynolds number and particle size and concentration. Although the general applicability of this correlation has yet to be assessed, it is considered to be valid for particles of 20  $\mu\text{m}$  to 200  $\mu\text{m}$  in size and for solid mass loading ratios of up to 1 kg/kg. Tube array flows with Reynolds numbers from 3000 to 30,000 may be investigated. The experimental data shown in Fig. 9 relate solely to the nonseparated flow region and have been modified by assuming that the increase in Nusselt number close to separation results exclusively from boundary layer thinning, which is discussed later. The relationship between particle size and increase in Nusselt number is displayed in Fig. 9(a) for Reynolds numbers of 5000 and 10,000. Although the experimental data are limited, good agreement exists between the measured and predicted results. The upper limit to the potential enhancement shown on Fig. 9(a) is considered to be due to the approximations made in deriving Eq. (3). Figure 9(b) shows the effect of Reynolds number on enhancement for both particle sizes and again it is obvious that the predicted and experimental values show the same trends. The influence of solids mass loading ratio on the increase in Nusselt number is shown in Figs. 9(c) and 9(d) for Reynolds numbers of 5000 and 10,000, respectively. The agreement between measured and predicted values is not as good at the lower mass loading ratios where the changes in Nusselt number are small but the general trend



x - x predicted decrease, relative size  
 + - + predicted decrease, relative time  
 ▲ experimental decrease  
 (experimental data from boundary layer region,  
 third row)



x - x predicted decrease, relative time  
 ▲ experimental decrease  
 (experimental data from boundary layer region,  
 third row)

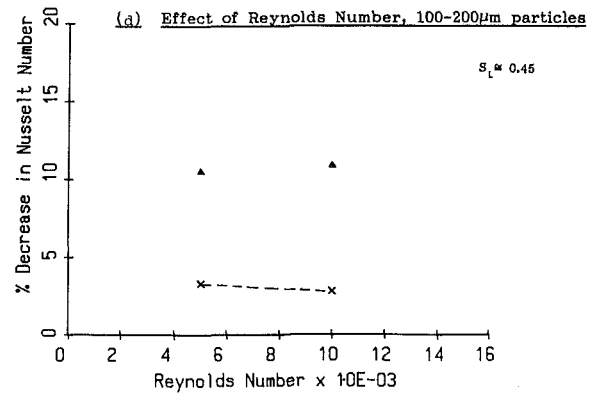


Fig. 10 Experimental and predicted Nusselt number reductions due to turbulence suppression: third row

of higher enhancement with an increase in solid concentration is well predicted.

**Second Row.** At the second row, an increase in the local Nusselt number over the front of the tube was recorded but the heat transfer in the wake decreased sharply. Furthermore, the minimum Nusselt number occurred later for the suspension flow with apparent delay of the separation point by some 5 to 10 deg. For both first and second row tests, specific local enhancement of heat transfer was evident in the near separation region and this would seem to indicate that the particles are influencing the local boundary layer thickness. In an experimental study of the effect of particles on the boundary layer in the near separation region for a tube in crossflow, Fitzpatrick et al. (1991) have reported a reduction in the local boundary layer thickness. This would explain the increase in local heat transfer in this region. In addition, it was reported that the separation point for a tube in the second row of an array section geometrically similar to that used here moved from 85 to 90 deg when 0.5 kg/kg of 150 μm particles were added to the flow. This would result in a shift in the minimum Nusselt number position for the second row and reduce heat transfer at the rear of the tube due to the narrower wake region as observed in the experimental data. Thus, for the tube in the second row, the increase in heat transfer due to the thermal capacity effects at the front of the tube is countered by a

decrease at the rear as a consequence of delayed boundary layer separation. The overall effect of local boundary layer thinning for both the first and second rows contributes little to the overall heat transfer coefficient, although local changes of up to 20 percent can occur.

**Third and Subsequent Rows.** For the tube located in the third row, a reduction in Nusselt number was recorded for all particle sizes, concentrations, and flow Reynolds numbers. In a single-phase flow, this is the location of maximum heat transfer generally attributed to high turbulence levels at this location in the array. It seems that the observed changes may be a direct consequence of a local reduction in the turbulence of the gas phase. In order to assess the effect of particles on the local turbulence levels, the relative time hypothesis of Owen (1969) can be used. The work done by an eddy on interacting with a particle is estimated as a function of the particle response time,  $t^*$ , relative to a characteristic eddy time,  $t_e$ . For very small particles where  $t^* < t_e$ , it was suggested that the rate of turbulent dissipation would be increased compared to single-phase flow by a factor of  $(1 + S_L)^{1/2}$ . For larger particles with  $t^* > t_e$ , this factor was modified to  $[1 + (S_L)(t_e/t^*)]^{1/2}$ . For very large particles with  $t^* \gg t_e$ , the particles are sensitive to very low frequency turbulent fluctuations only and were considered to make little contribution to this type of turbulence dissipation. The particle response times can be estimated from

**Table 4 Turbulence suppression estimates for the tube array flow**

| $S_{L_s}$ ,<br>kg/kg | $d_p$ ,<br>$\mu\text{m}$ | Re     | $t_{etb}$ , s | $t^*$ , s | $t_{etb}/t^*$ | $(U'_{su}/U'_a)_{tb}$ |
|----------------------|--------------------------|--------|---------------|-----------|---------------|-----------------------|
| 0.65                 | 150                      | 5,000  | 0.048         | 0.173     | 0.277         | 0.922                 |
| 0.43                 | 150                      | 5,000  | 0.048         | 0.173     | 0.277         | 0.948                 |
| 0.27                 | 150                      | 5,000  | 0.048         | 0.173     | 0.277         | 0.967                 |
| 0.20                 | 150                      | 5,000  | 0.048         | 0.173     | 0.277         | 0.975                 |
| 0.46                 | 150                      | 10,000 | 0.024         | 0.173     | 0.139         | 0.970                 |
| 0.2                  | 150                      | 10,000 | 0.024         | 0.173     | 0.139         | 0.988                 |
| 0.65                 | 65                       | 5,000  | 0.048         | 0.033     | 1.455         | 0.776                 |
| 0.18                 | 65                       | 5,000  | 0.048         | 0.033     | 1.455         | 0.921                 |
| 0.47                 | 65                       | 10,000 | 0.024         | 0.033     | 0.727         | 0.863                 |
| 0.21                 | 65                       | 10,000 | 0.024         | 0.033     | 0.727         | 0.932                 |

Note:  $t_{etb}$  denotes eddy within tube bank; \* denotes particle response time.

Stokes law and characteristic eddy times for the turbulence were evaluated from a range of Strouhal numbers reported by Weaver et al. (1987) for a geometrically similar array.

Table 4 shows the estimated time constants together with the predicted decrease in turbulence intensity for the tube array flow, based solely on direct eddy-particle turbulent interaction.

Using the correlations of Morgan (1975) and Lowery and Vachon (1975), which relate the free-stream turbulence intensity to overall and local heat transfer of a tube in crossflow, it is possible to estimate the effect of these changes in turbulence on heat transfer. Thus, the greatest decrease in heat transfer as a consequence of turbulence suppression would be expected at the third row for the 65  $\mu\text{m}$  particles. However, the experimental results show a greater reduction in the Nusselt number for the larger particles. This apparent anomaly can be explained by considering the enhancement due to thermal capacity effects, which will be much greater for the small particles. Using the correlation suggested, the estimated change in heat transfer without turbulence effects would be an increase of 15 percent. The experimental results show an overall decrease of 6.5 percent, indicating that a significant reduction in heat transfer has occurred. The only mechanisms that can account for this reduction are turbulence suppression in the vicinity of the third row tube, along with some influence of delayed boundary layer separation.

The similarity in trends between predicted changes in Nusselt number as a result of turbulence suppression and the experimental data can be seen from Fig. 10 where the experimental results have been modified to take account of the expected enhancement of Nusselt number resulting from thermal property effects and localized boundary layer thinning. The modified experimental data are compared with the predicted changes determined from the relative time turbulence suppression analysis of Owen (1969) and also with some projected figures based on the relative size investigation of Gore and Crowe (1989). The results shown compare data from the boundary layer region of the third row tube with the changes predicted for local heat transfer around the front stagnation point and show that the measured data correctly reflect the trends in heat transfer reduction with changes in Reynolds number and particle size. However, it is evident from Fig. 10 that the experimental data suggest a greater turbulence suppression effect than expected from the analysis of eddy-particle interaction.

One factor that may account for this is the wake narrowing associated with delayed boundary layer separation for the tube in the second row. This not only influences heat transfer over the wake of the second row tube but also influences the third and later rows because the turbulence generation upstream of these rows is now reduced. This wake narrowing effect, combined with the direct eddy-particle turbulent interaction, will result in a larger reduction in heat transfer than predicted above. The validity of this hypothesis is supported by the fact that the greatest reduction in Nusselt number is experienced

for the tube in the third row, which is most strongly affected by turbulence generated from the second row tube.

## Conclusions

A series of heat transfer tests has been conducted for a dilute gas-solid suspension flow through a staggered tube array. Glass beads of 65  $\mu\text{m}$  and 150  $\mu\text{m}$  nominal diameters were used at mass loading ratios from 0.2 to 0.65 kg/kg and with tube array Reynolds numbers of 5000 and 10,000. Although the range of Reynolds number, particle size, and solid concentration is limited, and the analysis of heat transfer mechanisms is elementary, it is possible to identify some important trends from the results obtained. The following conclusions were reached:

1 The local and overall heat transfer coefficients for a tube in the first row of the array have been shown to increase with the greatest enhancement achieved for the highest concentration of fine particles at the lower Reynolds number. A correlation based on the increased thermal capacity effect has been derived and shown to give good agreement with the limited experimental data. Further detailed experiments to assess the general applicability of the correlation are required.

2 At the second row, a local enhancement of heat transfer over the front of the tube and a significant reduction in the wake region was observed. The enhancement has been considered to result from the increased thermal capacity effects and the reduction over the rear has been attributed to delayed boundary layer separation and resultant wake narrowing.

3 The dominant influence on heat transfer for a tube in the third row has been shown to be suppression of turbulence by the particles. This has caused an overall decrease in the mean Nusselt number with the greatest effect due to the 65  $\mu\text{m}$  particles. These trends are consistent with the predictions of Owen (1969). The decrease in Nusselt number is greatest for the tube in the third row and then reduces with depth in the array.

## Acknowledgments

The authors would like to acknowledge the assistance of A. Reid with the development and construction of the experimental rig. Financial support for this work was provided by DGXII of the E.C. under research grant EN3F/44/IRL.

## References

- Aiba, S., and Yamazaki, K., 1976, "An Experimental Investigation of Heat Transfer Around a Tube in a Bank," *ASME JOURNAL OF HEAT TRANSFER*, Vol. 98, pp. 503-508.
- Byam, J., Pillai, K. K., and Roberts, A. G., 1981, "Heat Transfer to Cooling Coils in the Splash Zone of a Pressurised Fluidised Bed Combustor," *AICHE Symposium Series*, Vol. 77, No. 208, pp. 351-358.
- Depew, C. A., and Kramer, T. J., 1972, "Heat Transfer to Flowing Gas-Solid Mixtures," *Advances in Heat Transfer*, Vol. 9, Academic Press, pp. 113-180.
- Farbar, L., and Morley, M. J., 1957, "Heat Transfer to Flowing Gas-Solids Mixtures in a Circular Tube," *Ind. Eng. Chem.*, Vol. 49, pp. 1143-1150.
- Fitzpatrick, J. A., Lambert, B., and Murray, D. B., 1991, "Measurements in the Separation Region of a Gas-Particle Cross Flow," *Experiments in Fluids*, in press.
- Gore, R. A., and Crowe, C. T., 1989, "Effect of Particle Size on Modulating Turbulence Intensity," *Int. J. Multiphase Flow*, Vol. 15, No. 2, pp. 279-285.
- Hetsroni, G., 1988, "Particles-Turbulence Interaction," *Proc. 3rd Int. Symp. on Liquid-Solid Flows*, ASME FED-Vol. 75, pp. 1-12.
- Hughmark, G. A., 1967, "Mass and Heat Transfer From Rigid Spheres," *AICHE Journal*, Vol. 13, pp. 1219-1221.
- Jepson, G., Poll, A., and Smith, W., 1963, "Heat Transfer From Gas to Wall in a Gas-Solids Transport Line," *Trans. I. Chem. E.*, Vol. 41, pp. 207-211.
- Kane, R. S., and Pfeffer, R., 1985, "Heat Transfer in Gas-Solids Drag Reducing Flow," *ASME JOURNAL OF HEAT TRANSFER*, Vol. 107, pp. 570-574.
- Kurosaki, Y., Murasaki, T., Satoh, I., and Kashiwagi, T., 1986, "Study on

- Heat Transfer Mechanism of a Gas-Solid Suspension Impinging Jet (Effect of Particle Sizes and Thermal Properties)," *Proc. 8th International Heat Transfer Conference*, San Francisco, CA, Vol. 5, pp. 2587-2592.
- Lee, S. L., and Durst, F., 1982, "On the Motion of Particles in Turbulent Duct Flows," *Int. J. Multiphase Flow*, Vol. 8, pp. 125-146.
- Lowery, G. W., and Vachon, R. I., 1975, "The Effect of Turbulence on Heat Transfer From Heated Cylinders," *Int. J. Heat Mass Transfer*, Vol. 18, pp. 1229-1242.
- Marshall, A. R., 1988, "Reduced NO<sub>x</sub> Emissions and Other Phenomena in Fluidised Bed Combustion," in: *Fluidised Bed Combustor Design, Construction and Operation*, P. F. Sens and J. K. Wilkinson, eds., Elsevier, pp. 114-123.
- Morgan, V. T., 1975, "The Overall Convective Heat Transfer From Smooth Circular Cylinders," *Advances in Heat Transfer*, Vol. 11, pp. 199-264.
- Murray, D. B., and Fitzpatrick, J. A., 1988, "Local Heat Transfer Coefficients for a Tube Array Using a Micro-Foil Heat Flow Sensor," *Proc. 2nd U.K. Nat. Conf. on Heat Transfer*, Vol. 2, Glasgow, pp. 1635-1649.
- Murray, D. B., 1989, "The Effect of Solid Particles on Cross Flow Heat Transfer," Ph.D. thesis, University of Dublin, Ireland.
- Nikitin, A. V., Sapozhnikov, V. V., and Bogachev, V. V., 1976, "Heat Transfer in Dust-Laden Gas Flows," *Heat Transfer—Soviet Research*, Vol. 8, No. 5, pp. 87-93.
- Owen, P. R., 1969, "Pneumatic Transport," *J. Fluid Mech.*, Vol. 39, pp. 407-432.
- Reising, G. F. S., 1965, "Dust Suspension—A Novel Heat Transfer Medium," *Chemical and Process Engineering*, pp. 436-443.
- Sadek, S. E., 1972, "Heat Transfer to Air-Solids Suspensions in Turbulent Flow," *I&EC Process Design and Development*, Vol. 11, No. 1, pp. 133-135.
- Saxena, S. C., Grewal, N. S., and Gabor, J. D., 1978, "Heat Transfer Between a Gas Fluidised Bed and Immersed Tubes," *Advances in Heat Transfer*, Vol. 14, pp. 149-247.
- Shimizu, A., Hasegawa, S., and Tanaka, H., 1988, "Flow and Heat Transfer Characteristics of Gaseous Solid Suspension Medium Within Circular Riser Tubes," *JSME International Journal, Series II*, Vol. 31, No. 3, pp. 451-460.
- Tien, C. L., 1961, "Heat Transfer by a Turbulently Flowing Fluid-Solids Mixture in a Pipe," *ASME JOURNAL OF HEAT TRANSFER*, Vol. 83, pp. 183-188.
- Weaver, D. S., Fitzpatrick, J. A., and ElKashlan, M., 1987, "Strouhal Numbers for Heat Exchanger Tube Arrays in Cross Flow," *ASME Journal of Pressure Vessel Technology*, Vol. 109, pp. 219-223.
- Wood, R. T., Kuwata, M., and Staub, F. W., 1980, "Heat Transfer to Horizontal Tube Banks in the Splash Zone of a Fluidised Bed of Large Particles," in: *Fluidization*, J. R. Grace and J. M. Matsen, eds., Plenum, New York, pp. 235-242.
- Woodcock, M. T., and Worley, N. G., 1966, "Gas-Solid Suspensions as Heat Transfer Media," *Proc. I. Mech. E.*, Vol. 181, Pt. 31, pp. 17-33.
- Zukauskas, A., 1972, "Heat Transfer From Tubes in Cross Flow," *Advances in Heat Transfer*, Vol. 8, pp. 93-160.



# Simultaneous Heat and Mass Transfer From a Two-Dimensional, Partially Liquid-Covered Surface

Y.-X. Tao<sup>1</sup>

M. Kaviany

Department of Mechanical Engineering  
and Applied Mechanics,  
The University of Michigan,  
Ann Arbor, MI 48109

*Simultaneous heat and mass transfer from partially liquid-covered surfaces is examined experimentally using a surface made of cylinders with the voids filled with liquid. The steady-state evaporation rate, surface temperature of the liquid and exposed solid, and location of meniscus are measured for various ambient air velocities and temperatures. Using these, we examine the effect of the extent to which the liquid covers the surface on the evaporation mass transfer rate resulting from the convective heat transfer from the ambient gas to this surface. The results show strong Bond and Reynolds number effects. For small Bond and Reynolds numbers, the presence of dry (exposed solid) surface does not influence the mass transfer rate. As the Bond or Reynolds number increases, a critical liquid coverage is found below which the mass transfer begins to decrease. Heat transfer from the exposed solid to the liquid is also examined using the measured surface temperature, a conduction model, and an estimate of the liquid and solid surface areas (using a static formation for the liquid meniscus). The results show that at the liquid surface an analogy between heat and mass transfer does not exist.*

## 1 Introduction

One of the interfacial transport problems is that of simultaneous heat and mass transfer at the interface of a partially saturated porous medium and a plain medium. For porous media with random structure, this interface is partially liquid covered and the liquid phase does not occupy every surface indentation (or surface pore), but isolated collections of these indentations are partially covered by the liquid. The heat is transferred between the ambient (plain medium) and the interface through these liquid surfaces and also through the exposed solid matrix while the evaporation occurs only from the liquid surfaces.

When the surface pores are small or the equivalent particles making up the matrix are small, the molecules leaving the liquid surfaces can diffuse sideways, and therefore, the mass transfer can be nearly equal to that from a fully liquid-covered surface. For this to occur, the ratio of the mean free path of the vapor molecules (we neglect the effect of the noncondensibles) to the particle radius,  $\lambda/R$ , should not be too small (i.e., the Knudsen number  $Kn = \lambda/R$ , should not be too small). Schlünder (1988) discusses this case and presents a one-dimensional mass diffusion model. For surfaces that satisfy these conditions, the mass transfer rate (and for solid matrices with thermal conductivities similar to those of the liquid occupying them, the heat transfer rate) does not change as the surface saturation decreases (this is the familiar constant drying rate observed for solid matrices with small pores).

For larger pores, the extent of the liquid coverage does influence the heat and mass transfer rate. This is shown for planar surfaces by Plumb and Wang (1982) and by Rogers and Kaviany (1990) for packed beds of spheres. The sideways diffusion does not result in complete coverage of the dry surfaces, and the surface indentations and protuberances are large enough to influence the hydrodynamics. The complete description of this problem and the predictions of the effect of the surface saturation on the transfer rates require specification of:

- Gas motion adjacent to the interface of porous/plain media, including the effects of surface evaporation (similar to blowing) and buoyancy (due to variation of temperature and vapor concentration).
- Heat transfer from the gaseous phase to the protruding solid and the subsequent transfer of this heat to the adjacent liquid bodies and the solid substrate.
- Motion within the liquid caused by the surface tension gradient (Marangoni convection), buoyancy, and wind shear.

The simultaneous specification of all of these is a difficult task and is not attempted here. A two-dimensional, numerical simulation of the gas-side convection from a surface made of cylinders (with flow perpendicular to the axis of these cylinders) and the space between these cylinders partially filled with a liquid has been done by Kaviany (1989). The results show that as the Reynolds number,  $Re_R = u_a R / \nu_a$ , becomes larger than 10, a vortex is formed in the surface indentations and that as the liquid meniscus recedes, the mass transfer rate decreases. Inclusion of the substrate conduction is rather straightforward. The liquid motion has been studied by Cook et al. (1981), and Mirzamoghadam and Catton (1988) for perfectly wetting liquids (contact angle equal to zero). In their studies the convection heat transfer from the solid substrate to the liquid was neglected, and the liquid has a meniscus that extends over the solid surface forming an adsorbed layer (or film). They note that when the surface is heated just slightly above the boiling point (no nucleation occurring), the motions produced by the van der Waals force and the surface tension gradient cause a large heat transfer rate near the interline (the line separating adsorbed and evaporating films). For partially wetting liquids where the heat transfer is from the adjacent solid surfaces and also from the ambient gas, no analysis or experimental results are yet available.

In the following, we consider a simple, two-dimensional surface made of a single layer of cylinders, where their radius is  $R$  and the distance between their centers is  $l$  (i.e.,  $l$  is the unit-cell size). We perform experiments on such a surface where the cylinders are made of glass and constitute the upper surface of a cavity filled with liquid ethanol. This upper surface is placed at the bottom of a wind tunnel where heated air is blown over it. In these steady-state experiments, we vary the extent to which the liquid covers the cylinders from fully cov-

<sup>1</sup>Present address: Department of Mechanical Engineering, University of Saskatchewan, Saskatoon, Saskatchewan, S7N 0W0, Canada.

Contributed by the Heat Transfer Division for publication in the *JOURNAL OF HEAT TRANSFER*. Manuscript received by the Heat Transfer Division September 12, 1990; revision received July 1, 1991. Keywords: Conjugate Heat Transfer, Evaporation, Forced Convection.

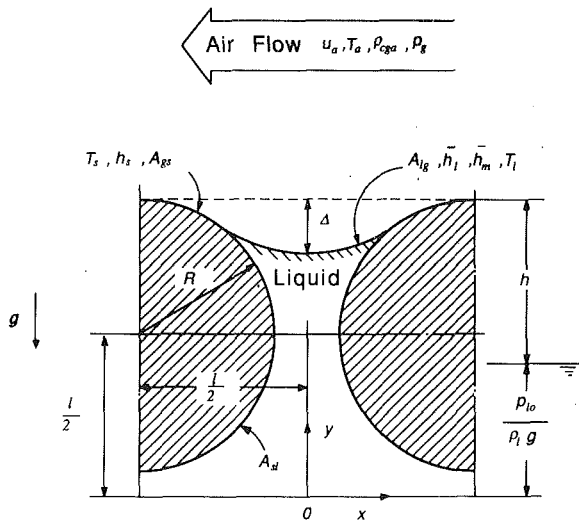


Fig. 1 Coordinate system used for the meniscus between two adjacent cylinders

ered to below the center. We measure the mass transfer rate and the surface temperature of the liquid and the exposed solid (using an infrared imager). We also measure the capillary pressure and the location of the meniscus (its lowest point). In order to make a rough estimation of the meniscus contour, including the contact points, we use the Young-LaPlace static formation, i.e., we neglect the liquid motion, evaporation, surface adsorption, and any contact angle hysteresis. As will be shown, these assumptions are not justifiable, as they result in liquid contours that are lower than what the experiments indirectly indicate. We present the experimental results for the evaporation rate as a function of the extent of the liquid coverage, and we point out the complexities in determining the liquid meniscus position.

A schematic of the unit cell is given in Fig. 1. The unit cell has a length (along the flow)  $l$ , a height (perpendicular to flow)  $l/2 + R$ , and a depth of a unit length. Here we have chosen

$$\frac{2R}{l} = 0.8165.$$

This makes for a cylinder of radius  $R$ , having the same unit cell volume as a sphere of radius  $l/2$ . This choice was made

## Nomenclature

$A$  = area,  $m^2$   
 $a$  = area per unit cylinder length,  $m^2/m$   
 $Bo$  = Bond number =  $g\rho_l R^2/\sigma$   
 $c_p$  = specific heat at constant pressure,  $J/kg\cdot K$   
 $d$  = diameter,  $m$   
 $D$  = binary mass diffusivity,  $m^2/s$   
 $g$  = gravitational constant,  $m/s^2$   
 $h$  = heat transfer coefficient,  $W/m^2\cdot K$ ; measured liquid height,  $m$   
 $\bar{h}_{l,a}$  = average heat transfer coefficient based on heat and mass transfer analogy,  $W/m^2\cdot K$   
 $h_m$  = mass transfer coefficient,  $m/s$   
 $i_{lg}$  = enthalpy of evaporation,  $J/kg$   
 $k$  = thermal conductivity,  $W/m\cdot K$   
 $L$  = length of the evaporation surface (planar) along the flow,  $m$   
 $l$  = unit cell length,  $m$

$Le$  = Lewis number =  $\alpha/D$   
 $\dot{m}$  = mass flow rate,  $kg/m^2\cdot s$   
 $Ma$  = Marangoni number =  $(d\sigma/dT)/\mu_l\alpha_l$   
 $Pr$  = Prandtl number =  $\nu/\alpha$   
 $q$  = heat flux,  $W/m^2$   
 $Q$  = heat transfer rate,  $W$   
 $r$  = radial coordinate,  $m$   
 $R$  = radius,  $m$   
 $Ra$  = Rayleigh number =  $(g\beta\Delta T l^3)/\nu\alpha$   
 $Re$  = Reynolds number =  $u_a l/\nu$   
 $s$  = saturation  
 $T$  = temperature,  $K$   
 $u$  = velocity,  $m/s$   
 $x$  = horizontal coordinate,  $m$   
 $y$  = vertical coordinate,  $m$   
 $\alpha$  = thermal diffusivity,  $m^2/s$   
 $\Delta$  = meniscus position,  $m$   
 $\epsilon$  = emissivity

$\lambda$  = mean free path of gas molecules,  $m$   
 $\mu$  = dynamic viscosity,  $Pa\cdot s$   
 $\nu$  = kinematic viscosity,  $m^2/s$   
 $\rho$  = density,  $kg/m^3$   
 $\theta$  = tangential coordinate,  $deg$   
 $\theta_c$  = contact angle,  $deg$   
 $\sigma$  = surface tension,  $N/m$ ; or Stefan-Boltzmann constant,  $W/m^2\cdot K^4$

## Superscripts

$\bar{\quad}$  = average  
 $*$  = dimensionless

## Subscripts

$a$  = ambient  
 $g$  = gaseous phase  
 $l$  = liquid phase  
 $o$  = subcooling  
 $rad$  = radiation  
 $s$  = solid phase; surface

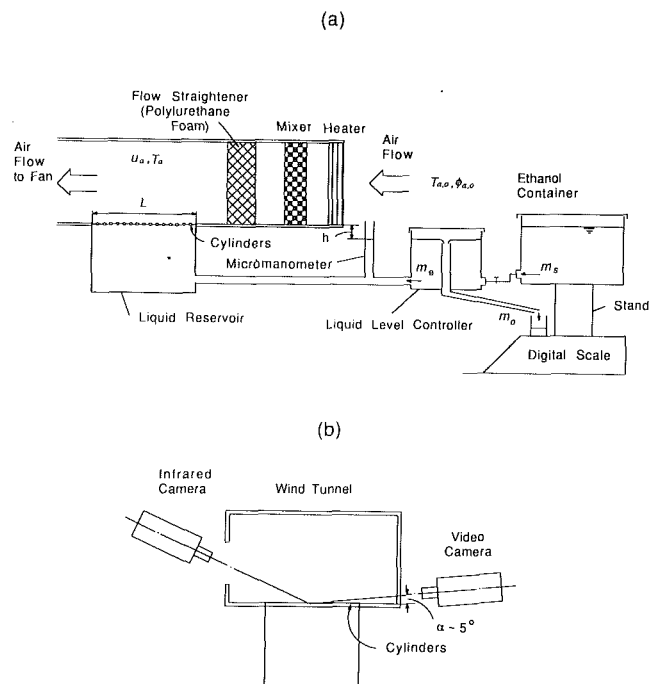


Fig. 2 (a) A schematic of the apparatus, and (b) a side view of the apparatus

mostly to fix the distance between the centers of the cylinders (i.e., not to use it as a variable). In connection with any application to the interfacial transport between partially saturated porous and plain media, we also define a surface saturation as

$$s_1 = \frac{\text{volume of liquid in the unit cell}}{\text{total void volume of the unit cell}}$$

A further discussion on two-phase flow and heat transfer in porous media can be found from Kaviany (1991).

## 2 Experiment

Figure 2(a) shows a schematic of the experimental apparatus by which the evaporation of ethanol from the surface made of a single-layer of cylinders (with the interstices filled with

**Table 1 Experimental conditions**

| Material | $d$ (mm) | $Bo$ | $u_a$     | $Re_L$      | $Re_R$    | $T_o(^{\circ}C)$ | $T_a(^{\circ}C)$ |
|----------|----------|------|-----------|-------------|-----------|------------------|------------------|
| Glass    | 0.501    | 0.02 | 0.5 ~ 1.5 | 3300 ~ 9000 | 16 ~ 44   | 24.0             | 70 ± 2           |
| Glass    | 1.499    | 0.20 | 0.5 ~ 1.5 | 3300 ~ 9000 | 48 ~ 133  | 23.9             | 70 ± 2           |
| Glass    | 3.277    | 0.98 | 0.5 ~ 1.5 | 3300 ~ 9000 | 106 ~ 290 | 24.3             | 70 ± 2           |

$L = 10.2$  cm,  $\sigma = 0.02$  N/m.

ethanol) to a forced convection air flow was measured. The planar surface of the evaporation surface is  $0.011$  m<sup>2</sup>. This surface is made of about 116 cylinders when diameter is 0.5 mm. Efforts have been made to minimize the vertical and horizontal offsets of the cylinders. However, some nonuniformity in the arrangement of the small diameter cylinders (e.g., 0.5 mm) exists due to the large length-to-diameter ratio. The cylinders assembly is mounted in a plexiglass reservoir and placed at the bottom of a plexiglass channel that has a cross section of  $10 \times 20$  cm (the 10 cm side is placed vertically). The air supply to the channel is heated with an 1800 W heater located at the entrance to the channel. A passive mixer is used to ensure uniformity of the temperature field, and a porous foam is used to produce a uniform velocity field; therefore, the effects due to flow and thermal boundary layers are minimized.

The velocity field above the surface of the cylinders is measured using a laser-Doppler anemometer (Dantec). A humidifier is used to provide the seeding. Turbulent flows at velocities  $\geq 0.7$  m/s are observed (mostly due to the presence of the foam and the mixer). The ambient temperature above the cylinders is measured by three thermocouples placed in the channel and at different vertical locations. The variation of temperature with time and position is found to be within  $\pm 2^{\circ}C$ . Once the air speed and temperature in the channel are set to the desired values, liquid ethanol is continuously supplied to the cavity in order to maintain the menisci at a desired location (by monitoring the liquid surface and the capillary pressure). In order to minimize the effect of system impurities on the surface tension, the entire liquid supply system was cleaned using pure liquid ethanol and the unused pure ethanol was then added to the system before each test run. The container and connecting tubes are chosen for handling of organic solutions. High purity ethanol is used and the effect of the absorbed water vapor on the surface tension is expected to be small. The ranges for the parameters studied are listed in Table 1. The evaporated ethanol mass,  $m_e$ , which equals the difference between the supplied mass,  $m_s$ , and the overflow mass,  $m_o$ , is then measured by a digital scale. A video camera (Fig. 2b) records the lowest meniscus position  $\Delta$ . (Due to the light reflection near the liquid/solid interface, the exact position of the contact line is difficult to measure.) The slope of the mass-versus-time curve determined by the least-square approximation method gives the evaporation rate of ethanol under a given set of air velocity, temperature, and meniscus position (or saturation). The measurements of the mass and the meniscus position are made for air velocities ranging from 0.56 to 1.51 m/s for liquid levels from fully covered (flooded) to the lowest position possible (which does not result in formation of air bubbles underneath the cylinders). The desired saturation is achieved by always starting from the fully liquid-covered condition. Therefore, the contact angle  $\theta_c$  should have a value close to the receding contact angle [the difference between the receding and the advancing contact angle can be as high as 50 deg (Chappuis, 1982)]. The measurement of the static contact

angle,  $\theta_c$ , is done using the tilted plate method. Theoretically, this angle is near zero for a smooth, clean glass surface. The measured value is about 11 deg, which is used in the calculation of the static meniscus contour, as will be discussed. The room temperature and humidity are also measured. The air temperature in the wind channel is kept at approximately  $70^{\circ}C$ .

The repeatability for the air velocity measurements is  $\pm 2$  percent, and the digital scale is accurate to 0.01 g. Because the measured evaporation rate is in the range of 0.5 to 1.0 g/min, the measuring time interval is kept greater than 2 min in order to minimize the error due to the drifting of the electronic scale. The total uncertainty in the evaporation rate measurement is within 1 to 5 percent. The higher uncertainty corresponds to the lower evaporation rates.

For a given liquid level (i.e., surface saturation), the capillary pressure is expressed as

$$p_c = p_g - p_l = p_g - (p_{lo} - \rho_l g y), \quad (1)$$

where the coordinates are shown in Fig. 1. With  $p_g = 0$  (as the reference point),  $p_c$  can be found from the measured  $h$  and  $\Delta$ , i.e.,

$$p_c = (h - \Delta)\rho_l g, \quad (2)$$

where  $h$  is measured using a micro-manometer with a resolution of 0.001 in.

After steady-state conditions are reached and the evaporation rate is recorded, the plate covering the circular opening on one side of the channel is removed to allow the cylinder/liquid surface temperature to be measured. The measurement is made with an infrared imager that records the two-dimensional temperature field. The accuracy of the instrument (liquid nitrogen cooled) is  $0.5^{\circ}C$  of the measured temperature for high emissivity targets. (Emissivity uncertainties considerably increase measurement uncertainties for low-emissivity targets.) The total hemispherical emissivity of liquid ethanol is estimated using the method described by Siegel and Howell (1981) and is found to be 0.94. The surface temperature over the entire surface is examined. The variation of the surface temperature from one cell (cylinder-liquid) to another is found not noticeable.

In summary, the measurements detailed above are

$$\begin{aligned} \dot{m} &= \dot{m}(\Delta, u_a, T_a), \\ T_s(x) &= T_s(x, \Delta, u_a, T_a), \\ p_c &= p_c(\Delta, u_a, T_a), \end{aligned}$$

and  $\theta_c$ .

### 3 Analysis

**3.1 Meniscus Contour.** In the following, we estimate the liquid surface area (and the surface saturation) using the Young-LaPlace formulation and the measured  $\Delta$  and  $\theta_c$ . This formulation is based on the inclusion of the surface and gravitational potential energy only. The stability of the meniscus is discussed by Saez (1983), and it is expected that the meniscus will be stable for the conditions specified here. We note that due to surface contamination and hysteresis, even the isothermal meniscus cannot be predicted by this method with a reasonable accuracy (Saez and Carbonell, 1985). For non-isothermal liquid bodies we expected this formulation to predict the meniscus contour only for very small deviations from the ideal conditions upon which it is based.

According to the coordinate system in Fig. 1, any point  $(x, y)$  on the meniscus obeys the following equation (Saez, 1983):

$$y^{*''} = - \left( p_{lo}^* - Bo \frac{l^2}{4R^2} y^* \right) (1 + y^{*'}{}^2)^{1.5}, \quad (3)$$

where

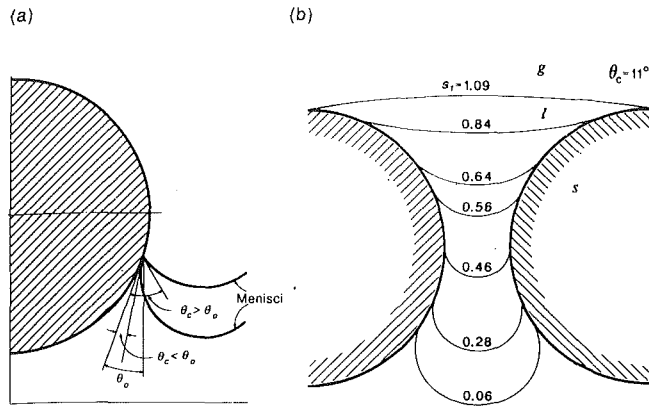


Fig. 3 (a) Analysis of a meniscus forming below the neck of two adjacent cylinders, and (b) meniscus contours for the contact angle of 11 deg

$$y^* = \frac{y}{l/2}, \quad p_{lo}^* = \frac{p_{lo} l/2}{\sigma}, \quad Bo = \frac{g \rho l^2}{4\sigma}, \quad x^* = \frac{x}{l/2},$$

and the prime and double primes are the first and second derivatives of  $y$  with respect to  $x$ , and an asterisk indicates dimensionless variables.

Equation (3) is valid for the meniscus that lies above the plane passing through the centers of two adjacent cylinders ( $y_s^* \geq 1$ ). When the starting point of the meniscus falls below this center plane and the contact angle is small, then the dependent variable  $y$  is double-valued for  $x^* \leq x_s^*$  (shown in Fig. 3a). For such cases, i.e.,  $\theta < \theta_o$  ( $\theta_o$  is defined in Fig. 3), the integration domain can be divided into three domains:

Domain I:

$$x^{*''} = - \left( p_{lo}^* - Bo \frac{l^2}{4R^2} y^* \right) (1 + x^{*'}{}^2)^{1.5}, \quad x^* \leq |x_s^*|; \quad (4)$$

Domain II:

$$y^{*''} = - \left( p_{lo}^* - Bo \frac{l^2}{4R^2} y^* \right) (1 + y^{*'}{}^2)^{1.5}, \quad -|x^*| \leq x^* \leq -|x_s^*|; \quad (5)$$

Domain III:

$$x^{*''} = \left( p_{lo}^* - Bo \frac{l^2}{4R^2} y^* \right) (1 + x^{*'}{}^2)^{1.5}, \quad x^* \geq -|x_s^*|. \quad (6)$$

In Domains I and III, integration can be done with  $y^*$  as the independent and  $x^*$  as the dependent variable. At the junction of the two domains, we have  $x^{*'} = 1/y^{*'}$ . The starting point ( $x_s^*$ ,  $y_s^*$ ) is bounded by

$$y_s^* = 1 \pm \sqrt{\frac{l^2}{4R^2} - (1 + x_s^{*'})^2}. \quad (7)$$

Integration of Eqs. (3) to (4)–(6) is done using the fourth-order Runge-Kutta method (as an initial value problem) for a given  $\theta_c$ ,  $Bo$ , and  $p_{lo}$  (since  $l^2/4R^2$  is a constant). When the value of  $x_s^*$  is estimated and  $y_s^*$  is given by Eq. (7), the profile is computed by marching in  $x^*$  until  $y^*$  reaches the right-hand side cylinder where the angle of intersection (i.e., the contact angle) is checked against the prescribed value. If they do not agree, a new guess for  $x_s^*$  is made. Iterations are performed until convergence is obtained to within 0.1 percent of  $\theta_c$ . Figure 3(b) shows the contours for  $\theta_c = 11$  deg and  $Bo = 0.02$ . From these profiles, the saturation and the liquid surface area can be determined numerically. The exposed solid surface area per unit cylinder length for one unit cell and for a given saturation is given by

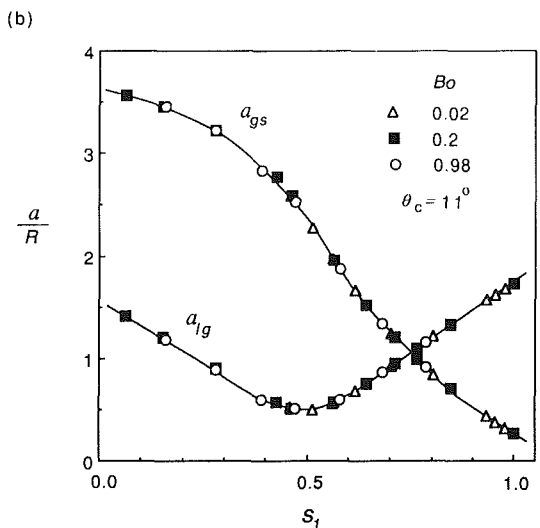
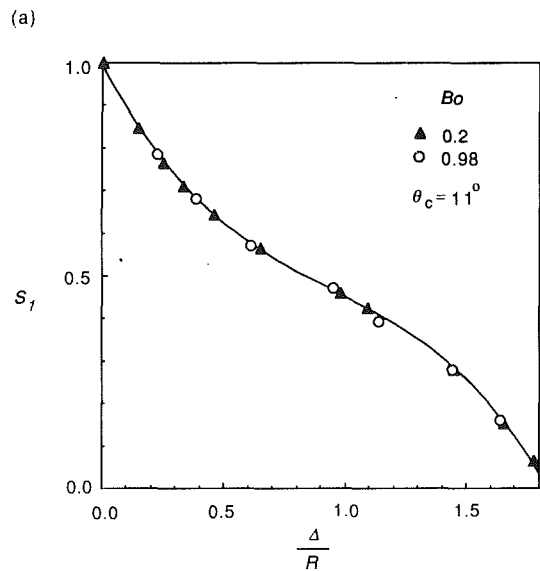


Fig. 4 (a) Variation of the surface saturation with respect to the depth  $\Delta$ , and (b) variation of the liquid and solid surface areas (per unit cylinder length) with respect to surface saturation for different Bond numbers

$$a_{lg} = 2R \left[ \frac{\pi}{2} + \tan^{-1} \left( \frac{\sqrt{l^2/4R^2 - (1 + x_s^{*'})^2}}{1 + x_s^{*'}} \right) \right]. \quad (8)$$

In Fig. 4(a) the variation of  $s_1$  with respect to  $\Delta/R$  is shown for  $\theta_c = 11$  deg and two values of  $Bo$ . The results fall on a single curve because surface tension dominates in the range of Bond numbers ( $Bo < 1$ ). The same is true for the results shown in Fig. 4(b), where the liquid and solid surface areas per unit cylinder length are given as a function of  $s_1$ .

In summary, the static formulation gives us

$$p_c = p_c \left( \Delta, Bo, \frac{2R}{l} \right),$$

$$s_1 = s_1 \left( \Delta, Bo, \frac{2R}{l} \right).$$

Therefore, the capillary pressure can be predicted once  $\Delta$  and the cylinder radius are known. If the surface evaporation, the liquid motion, and meniscus hysteresis are negligible, then the predicted  $p_c$  will be very close to that measured. As will be shown, this is not the case here. In general due to the surface conditions that influence wettability, even for isothermal men-

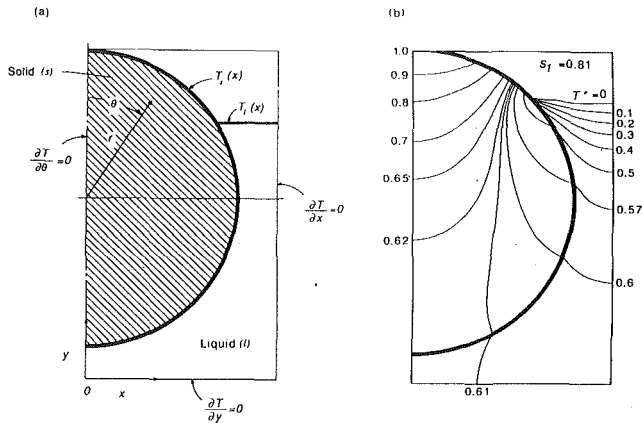


Fig. 5 (a) The boundary conditions for the conduction formulation, and (b) typical example of the distributed temperature field within the cylinder and liquid

isci the predicted and measured  $p_c$  do not agree unless empiricism is introduced (Saez and Carbonell, 1985).

**3.2 Conduction Through Solid and Liquid.** Now we undertake to estimate the amount of heat transferred from the gaseous phase to the solid cylinders  $q_{gs}$ . This heat is in turn transferred from the cylinders to the surrounding liquid and contributes to the required heat for the evaporation (the remainder of the required evaporation heat is supplied directly from the gaseous phase). As we will show, the measured liquid and solid surface temperatures for the  $d = 1.5$  and  $3.3$  mm cylinders are not uniform. We use the measured  $T_s(x)$  along with a conduction model for the solid and liquid phases in the unit cell in order to estimate the rate of heat transfer through the solid  $q_{gs}$ . Again, the conduction approximation is limited to small  $\partial\sigma/\partial x$ ,  $T_s - T_l$ , and  $u_a R/\nu_a$ , and these limits are not realized in all of the experiments.

We use the contact line obtained from the meniscus calculation and then treat the liquid surface as planar. Using the actual curved liquid surface does not change  $q_{gs}$  noticeably. At the bottom of the unit cell ( $y = 0$ ), we use the adiabatic boundary condition, and we use symmetry about  $x = l/2$ . Figure 5(a) depicts the conduction problem and Fig. 5(b) shows a typical temperature distribution. The mathematical specification of the conduction problem is given below.

In the cylinder

$$\frac{\partial}{\partial r^*} \left( r^* \frac{\partial T^*}{\partial r^*} \right) + \frac{1}{r^*} \frac{\partial^2 T^*}{\partial \theta^2} = 0, \quad (9)$$

$$T^* = T^*(\theta), \text{ for } r^* = \frac{R}{l/2}, \quad 0 \leq \theta \leq \theta_o,$$

$$T^* = \text{finite}, \text{ for } r^* = 0, \quad 0 \leq \theta \leq \pi,$$

$$\frac{\partial T^*}{\partial \theta} = 0, \text{ for } \theta = 0, \quad 0 \leq r^* \leq \frac{R}{l/2},$$

$$\frac{\partial T^*}{\partial \theta} = 0, \text{ for } \theta = \pi, \quad 0 \leq r^* \leq \frac{R}{l/2}.$$

In the liquid

$$\frac{\partial^2 T^*}{\partial x^{*2}} + \frac{\partial^2 T^*}{\partial y^{*2}} = 0, \quad (10)$$

$$T^* = T^*(x^*), \text{ for } y^* = y_s^*, \quad x_s^* \leq x^* \leq 1,$$

$$\frac{\partial T^*}{\partial y^*} = 0, \text{ for } y^* = 0, \quad 0 \leq x^* \leq 1,$$

$$\frac{\partial T^*}{\partial x^*} = 0, \text{ for } x^* = 1, \quad 0 \leq y^* \leq y_s^*,$$

where

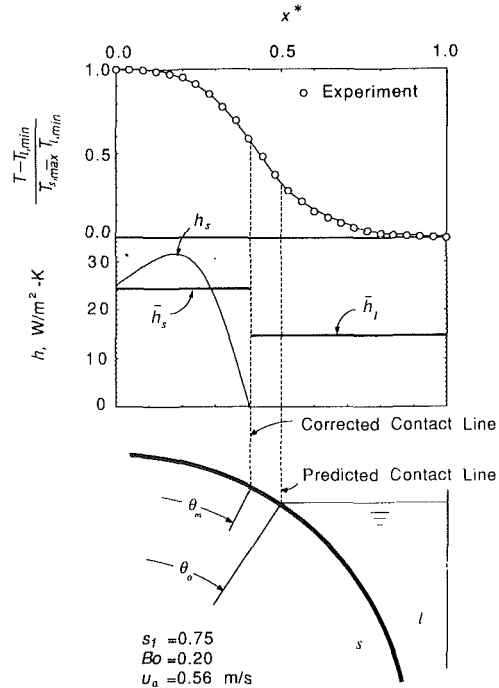


Fig. 6 A typical example of the surface temperature distribution and heat transfer coefficients on a cylinder

$$T^* = \frac{T - T_{l,\min}}{T_{s,\max} - T_{l,\min}}, \quad r^* = \frac{r}{l/2},$$

and  $T_{l,\min}$  is the lowest temperature on the liquid surface, and  $T_{s,\max}$  is the highest temperature on the exposed solid surface.

The above formulation is solved using the finite-difference approximation techniques. Cylindrical grids are used for the cylinder, and rectangular grids are used for the liquid. A linear interpolation is used at the interface of two domains. The system of equations is solved by iteration using the overrelaxation method. The criterion for the convergence is that any variable is considered to have the final value if its deviation from the previously iterated value is within 0.2 percent. The energy balance is examined and found to be satisfied to within 1 percent (the difference between the heat flow in and heat flow out divided by the heat flow in).

The local heat flux at the solid surface is

$$q_{gs}(x) = k \left( \frac{\partial T}{\partial r} \right)_{r=R}. \quad (11)$$

The local heat transfer coefficient along this surface is defined as

$$h_s(x) = \frac{q_{gs}(x) - q_{rad}}{T_a - T_s(x)}, \quad (12)$$

where  $q_{rad}$  is the radiation heat flux from the surroundings (assumed black) and is taken as

$$q_{rad}(x) = \epsilon\sigma [T_a^4 - T_s(x)^4].$$

Under experimental conditions,  $q_{rad}$  is about 20 percent of  $q_{gs}$  and, therefore, cannot be neglected in the calculation of  $h_s$ . A typical variation of  $h_s$  with respect to  $x$  is shown in Fig. 6. Since  $T_s(x)$ ,  $T_l(x)$ , and  $(x_s, y_s)$  are specified independently, the position at which  $h_s$  changes sign (i.e., where to the left of this position heat arrives at the solid through the gas and to the right of it heat leaves from the solid to the liquid) may not be at  $(x_s, y_s)$ . This is true in the results given in Fig. 6. Here we correct the contact line to the position where  $h_s$  changes sign. We associate this error in the prediction of  $(x_s, y_s)$  to the idealization in the static formulation.

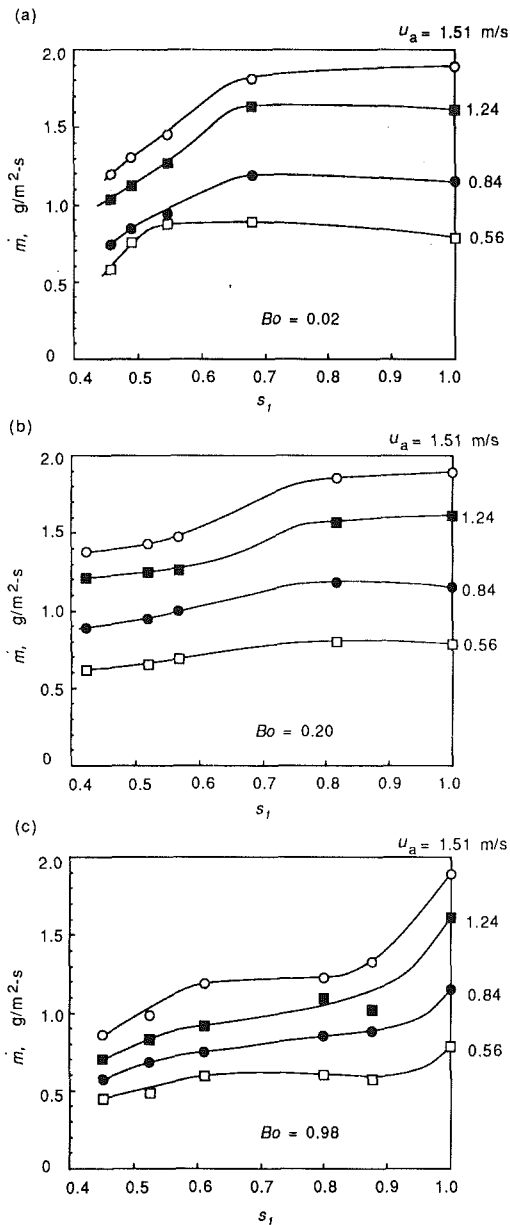


Fig. 7 Experimental results for variation of the evaporation rate with respect to surface saturation for different Bond numbers

Then, the total heat transfer from the gaseous phase to the solid (per unit cylinder length) becomes

$$Q_{gs} = k_s \int_0^{\theta_m} \left( \frac{\partial T}{\partial r} \right)_{r=R} R d\theta, \quad (13)$$

and  $\theta_m$  is the angular position where  $(\partial T / \partial r)_{r=R} = 0$ . The heat arriving at the solid surface leaves as

$$Q_{sl} = -k_s \int_{\theta_m}^{\pi} \left( \frac{\partial T}{\partial r} \right)_{r=R} R d\theta. \quad (14)$$

This completes the conduction problem.

The average mass transfer coefficient is determined using the measured mass transfer rate per unit area of the planar surface,  $\dot{m}$ , i.e.

$$\bar{h}_m = \frac{\dot{m}}{A_{lg}(\rho_{cgo} - \rho_{cga})}, \quad (15)$$

where  $A_{lg}$  is the modified liquid surface area and includes the

arc between  $\theta_m$  and  $\theta_1$ , and  $\rho_{cgo}$  is evaluated at the mean temperature  $\bar{T}_l$  over  $A_{lg}$ .

Now, applying an overall energy balance, we have

$$\dot{m} A_{lg} i_{lg} = Q_{lg} + Q_{gs} + Q_{rad}. \quad (16)$$

Since

$$Q_{lg} = \bar{h}_l A_{lg} (T_a - \bar{T}_l), \quad (17)$$

we have

$$\bar{h}_l = \frac{1}{(T_a - \bar{T}_l)} \left[ \dot{m} i_{lg} - \frac{1}{A_{lg}} (Q_{gs} - Q_{rad}) \right], \quad (18)$$

where

$$Q_{rad} = \int_{A_{gs} + A_{lg}} q_{rad}(x) dA.$$

For comparison, the heat transfer coefficient based on the validity of the analogy between convection heat and mass transfer is also found. This gives (Incropera and DeWitt, 1985)

$$\bar{h}_{l,a} = \bar{h}_m \rho_g c_{pg} Le^{2/3}. \quad (19)$$

Finally, the average heat transfer coefficient for the solid surface is

$$\bar{h}_s = \frac{Q_{sg} - Q_{rad,s}}{A_{gs}(T_a - \bar{T}_s)}, \quad (20)$$

where

$$Q_{rad,s} = \int_{A_{gs}} q_{rad}(x) dA.$$

In the above treatment, the buoyancy and the surface tension driven flows in the liquid have been neglected. These assumptions are justified if the liquid Rayleigh and Marangoni numbers are below certain values. For  $R = 1.63$  mm (the largest linear dimension used in this study), we have  $Bo = 0.98$ . The largest temperature difference between the liquid and solid encountered for this radius was  $1.5^\circ\text{C}$ ; therefore,  $Ra$  based on  $R$  is about 800 and  $Ma$  based on  $R$  is about -3000. For low saturations, it may be more reasonable to use  $l/2 - R$  as the length scale. Based on this,  $Ra$  becomes about 10 and  $Ma$  becomes about -670. Since no analysis of the natural and thermocapillary convection is available for this particular geometry, the critical values for  $Ra$  and  $Ma$  marking the transition from the conduction regime to convection regime are not known. In addition, for  $R = 0.75$  and  $1.63$  mm, liquid motions due to wind shear have been observed. For  $R = 0.5$  mm, the cylinders could not be placed parallel to each other and in the same plane to as satisfactory extent (an average offset of 10 percent of the cylinder diameter exists). Therefore, we mention again that the use of a static meniscus and the conduction treatments for the idealized surface structure, which do not include those real effects, is a simplified approach.

## 4 Results and Discussion

We now present the measured  $\dot{m}$ , i.e., the average mass flux, and show how it varies with respect to  $R$  (or Bond number) and  $\Delta$ , for a given  $u_a$  and  $T_a$ . Next, we show that the measured  $\rho_c$  is much smaller than that predicted. Also using the measured  $T_s(x)$  and the conduction model (including the correction made to the contact line), we estimate the average heat transfer coefficient for the solid and the liquid surfaces, i.e.,  $\bar{h}_s$  and  $\bar{h}_l$ . Since the heat and mass transfer surfaces are different and the Knudsen number is small, we also point out the lack of an analogy between the heat and mass transfer for this interfacial transport.

### 4.1 Effect of Bond Number and Surface Saturation on Mass Transfer Rate.

The experimental conditions are given

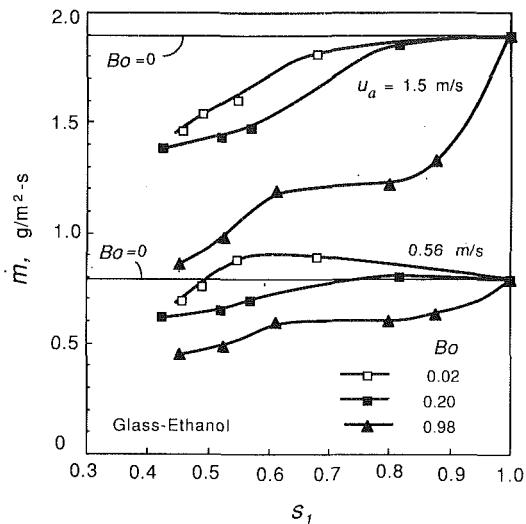


Fig. 8 Comparison of evaporation rates between high and low air velocities for different Bond numbers

in Table 1, and as shown,  $T_a$  is kept the same for all the experiments. For each  $R$ , four different  $u_a$  are used, namely 0.56, 0.84, 1.24, and 1.51 m/s. As was mentioned, all the measurements are made under steady-state conditions. The results are in the form  $\dot{m} = \dot{m}(u_a, Bo)$ , where the Bond numbers are 0.02 to 0.98. In light of the static formulation, these Bond numbers are considered low, because the cylinder size is small enough to enable the surface tension to dominate, as compared to the gravity potential, in determining the meniscus contour. This was evident in Figs. 4(a) and 4(b) where the surface saturation was found to be only a function of  $\Delta/R$ , i.e.,  $s_1$  did not depend on  $Bo$ . This surface saturation,  $s_1$ , is used instead of  $\Delta/R$  in the presentation of the average mass transfer rates, i.e., we use  $D = D(Bo, u_a, s_1)$ . In the experiments, the surface saturation ranges from slightly above 0.4 to 1.0 (flooded). Figure 7(a)–(c) shows  $\dot{m}(s_1)$  for three Bond numbers. As expected for large  $Bo$ , the mass flux increases with  $u_a$ . For smaller  $Bo$ , the mass flux becomes independent of  $s_1$  (for large  $s_1$ ). As we mentioned, for  $Bo \rightarrow 0$ , i.e., very small particles,  $\lambda/R$  is not very small [this depends also on the ratio of the concentration boundary-layer thickness to  $R$  (Schlünder, 1988)], and therefore,  $\dot{m}$  becomes independent of  $s_1$ . Then, the trend found in Figs. 7(a)–(b) is in agreement with the previous observation/descriptions of the saturation independence for small  $R$  or large  $s_1$ . (Large  $s_1$  implies smaller linear dimension for the exposed solid surface.) Figures 7(a)–(b) show that as  $s_1$  decreases, a transition saturation  $s_{1t}$  is reached below which the mass flux begins to drop. This transition is marked with

$$\frac{\dot{m}(s_1)}{\dot{m}(s_1=1)} = 1, \text{ for } s_1 \geq s_{1t}.$$

The transition saturation increases with an increase in  $Bo$ , and for  $Bo = 0.98$  its value is unity. Then, we have

$$s_{1t} = 1, \text{ for } Bo \geq 1, \\ s_{1t} \rightarrow 0, \text{ for } Bo \rightarrow 0.$$

We note that  $s_{1t}$  also depends on  $u_a$ , and the results of Figs. 7(a)–(c) show that

$$s_{1t} \rightarrow 0 \text{ as } u_a \rightarrow 0.$$

This is expected because the sideways diffusion becomes as significant as the lateral (outward from the surface) diffusion as  $u_a \rightarrow 0$ .

We generalize these observations slightly by using  $Re_R = u_a R / \nu_a$  instead of  $u_a$  and give

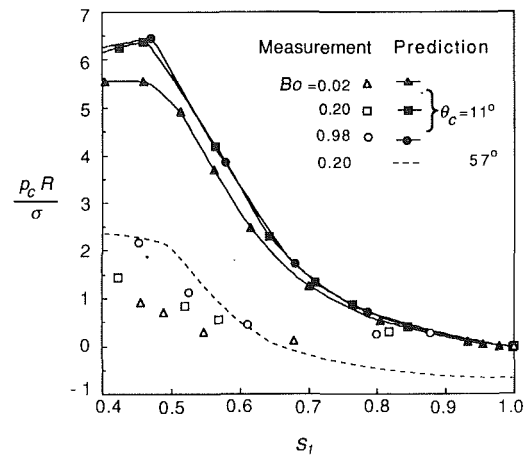


Fig. 9 Variation of capillary pressure with respect to surface saturation for different Bond numbers

$$s_{1t} = s_{1t}(Bo, Re_R),$$

with

$$s_{1t} \rightarrow 0 \text{ as } Re_R \rightarrow 0.$$

We then suggest

$$\frac{\dot{m}(s_1 \geq s_{1t})}{\dot{m}(s_1 = 1)} = 1, \text{ and } s_{1t} = f(Bo)g(Re_R),$$

with

$$f(Bo) = \begin{cases} 0, & \text{for } Bo \rightarrow 0 \\ 1, & \text{for } Bo \geq 1 \end{cases}$$

and

$$\frac{\partial f}{\partial Bo} = 0, \text{ for } Bo \rightarrow 0, \\ g(Re_R) = 1, \text{ for } Re_R \rightarrow 0, \\ \frac{\partial g}{\partial Re_R} = 0, \text{ for } Re_R \rightarrow 0.$$

In addition, we note that for  $0 \leq s_1 \leq s_{1t}$  both functions  $f$  and  $g$  are single-valued. Due to the limited experimental results we do not attempt to find the empirical correlations for  $f$  and  $g$ .

The results presented in Figs. 7(a)–(c) are replotted in Fig. 8 using only two of the values of  $u_a$ . The zero Bond number asymptotes (saturation independence) are also shown. A slight increase in  $\dot{m}$  with a decrease in  $s_1$  for  $Bo = 0.02$  can be the result of a combination of the surface roughness caused by partial exposure of the solid and the sidewise diffusion. Note that as  $u_a$  decreases, the decrease in  $\dot{m}$  with a decrease in  $s_1$  is less significant (as mentioned, because diffusion becomes more significant). Also, note the rather significant difference present between the results for  $Bo = 0.2$  and  $0.98$  for  $u_a = 1.51$  m/s. We have not attempted to present the results given in Figs. 7 and 8 in dimensionless forms (i.e., Sherwood, Reynolds, Schmidt numbers), because the experimental results are limited to one fluid. The static formulation given in the last section does not predict any significant change in meniscus contour when  $Bo$  is changed between these two values. We except that this change in  $\dot{m}$  is due to a combined effect of a hydrodynamic transition in the gas-side (due to increase in  $R$ ) and the dynamics of the meniscus (liquid motion, heated contact line, and hysteresis). We now examine this deviation from the static behavior.

**4.2 Validity of Static Formulation.** The capillary pressure is predicted by the static formulation as  $p_c = p_c(\Delta, Bo, \theta_c)$ , and here it is also measured (as described in section 2). In Fig. 9, the predicted and the measured values are compared. The measured values are lower, and this difference is very large

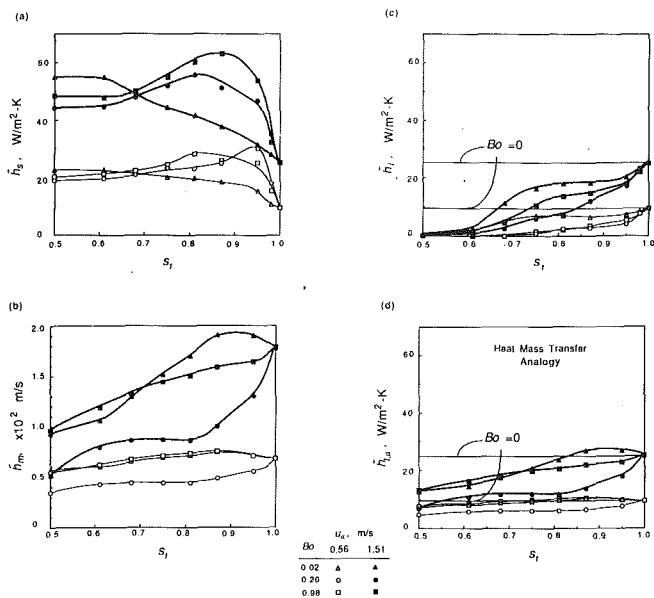


**Fig. 10** (a) Average heat transfer coefficients from the solid, (b) mass transfer coefficients, (c) average heat transfer coefficients from the liquid surface, and (d) liquid heat transfer coefficients based on heat and mass transfer analogy

at small saturations. We have given several reasons for this difference. We also note that for the liquid to flow to the surface for evaporation, a pressure gradient must exist. This gradient is largest at  $y = l/2$  for (for  $\Delta < R$ ). This upflow causes an increase in the radius of curvature of the meniscus. Visual observations also support this meniscus flatness, although they could not be quantified. Another reason for the deviation from the static formulation is that in the experiments, there exists an uncertainty in the actual intercylinder distance  $l$  and the offset of the cylinder centers (up to 10 percent of the cylinder diameter for the small cylinders). However, an uncertainty analysis shows that the errors due to the geometry only make a small contribution to the uncertainty in the measured capillary pressure. For example, a 10 percent uncertainty in the planar position of the cylinder (offset) results in less than 5 percent uncertainty in  $\Delta$  and less than 3 percent uncertainty in  $s_1$ . Therefore, it is believed that dynamic effects on the meniscus contour, especially on the contact angle, may be the main reason for the difference between the predicted and measured capillary pressure. As an exercise, we use  $\theta_c = 57$  deg for  $Bo = 0.2$  and for low saturations ( $0.4 < s_1 < 0.7$ ), we find the predicted capillary pressure is much closer to the measured values. The results for  $\theta_c = 57$  deg are also shown in Fig. 9. Note that this static contact angle is not that measured and our visual observations of the meniscus does not support such high  $\theta_c$ . Further study of the dynamic aspects of the meniscus is required for the accurate description of the capillary pressure. As expected, this can be a major undertaking. However, noting that the predicted surface areas  $A_{gs}$  and  $A_{lg}$  involve some uncertainties and can deviate from the experimental results, we proceed to use  $T(x)$  to estimate  $\bar{h}_s$  and  $\bar{h}_l$ .

**4.3 Average Heat and Mass Transfer Coefficients.** Using  $T_s(x)$ , the conduction model, the corrected contact position, and liquid and solid surface areas, we can determine  $h_s$  and  $\bar{h}_s$ . Knowing  $\dot{m}$  and the heat required for evaporation,  $i_{lg}\dot{m}$ , we can determine the average mass transfer coefficient  $\bar{h}_m$  and the average heat transfer coefficient for the liquid surface  $\bar{h}_l$ . We can also use  $\bar{h}_m$  in Eq. (19) to determine a heat transfer

coefficient  $\bar{h}_{l,a}$  for this surface, assuming that the analogy holds. These results are given in Figs. 10(a)–(d).

For  $\bar{h}_s$  at  $s_1 = 1$ , we have used  $\bar{h}_l(s_1 = 1)$  because the heat transfer coefficient is not expected to be significantly different between a planar liquid-covered surface and a planar solid surface although, because of the evaporation velocity and the variation in properties, some difference is expected (Greiner and Winter, 1978). The results show that as  $s_1$  decreases, initially  $\bar{h}_s$  increases. This can be due to the surface roughness effect, which for large  $s_1$  more than compensates for the decrease in the local  $h_s$  in the indentation. (An example of the distribution of  $h_s$  is given in Fig. 6.) As  $s_1$  decreases further, these two gas-side hydrodynamic effects seem to cancel each other.

The mass transfer coefficient calculated using Eq. (15) is given in Fig. 10(b). It has a behavior similar to  $\dot{m}$  (given in Figs. 7 and 8). For large velocities, a significant transition occurs between  $Bo = 0.2$  and  $0.98$ . For low velocities,  $s_{1l}$  becomes smaller.

The average heat transfer coefficient  $\bar{h}_l$  calculated for the liquid surface using Eq. (18) is given in Fig. 10(c). Note that unlike  $\bar{h}_s$ ,  $\bar{h}_l$  decreases monotonically with  $s_1$ . This is an expected behavior for a receding liquid surface and is in agreement with the observations of Rogers and Kaviany (1990) in their transient experiment with packed beds. Note that for a given  $s_1$ , the magnitudes of  $\bar{h}_s$  and  $\bar{h}_l$  are significantly different with  $\bar{h}_l$  being smaller.

Finally, we examine the existence of an analogy between the heat and mass transfer from the liquid surface by comparing  $\bar{h}_l$  with  $\bar{h}_{l,a}$  [determined from Eq. (19)]. The results are given in Fig. 10(d). We note that  $\bar{h}_l$  given in Fig. 10(c) is different from  $\bar{h}_{l,a}$  for  $s_1 < 1$ , i.e., the analogy between the heat and mass transfer does not exist on the liquid surface. This is expected, because near the surface the temperature field (heat is transported to both the liquid and the solid surfaces) is different from the concentration field (mass transfer from the liquid surface only). We also note that  $\bar{h}_l > \bar{h}_{l,a}$  shows a trend similar to  $\dot{m}$ . As was mentioned, here we will not attempt to present the results in dimensionless form (i.e., Sherwood, Nusselt, Reynolds, Prandtl, Schmidt numbers), because of the limited particle size and the single fluid used.

The transfer coefficients given above are based on a very simple conduction model with the surface areas based on yet another simple model. Therefore, we present these results as suggestive and note that further study of the gas-side and substrate transports is needed for any definitive conclusions.

## 5 Conclusions

We have examined the influence of the extent to which a surface is covered by the liquid phase (saturation effect) on the evaporation rate from a two-dimensional surface undergoing simultaneous heat and mass transfer. The experimental results show that a transition saturation exists above which the mass transfer rate is not affected by the saturation. This transition (or critical) saturation decreases with a decrease in the Bond number and increases with an increase in the Reynolds number based on the particle (cylinder) size. We used the static formulation for the meniscus contour and showed that the dynamics effects present in the experiments cause significant deviations from this prediction (i.e.,  $p_c$ ,  $A_{lg}$ ,  $A_{gs}$ , and  $s_1$  are different). Using estimates for the surface areas, a conduction model, and the measured surface temperature, we point out the lack of an analogy between the heat and mass transfer at the liquid surface. The analyses performed do not include some significant dynamic, real effects that must be included when more accurate predictions of the effect of surface saturation on the evaporation rate are required.



## References

- Chappuis, J., 1982, "Contact Angles," *Multiphase Science and Technology*, McGraw-Hill, Vol. 1, p. 387.
- Cook, R., Tung, C. Y., and Wayner, P. C., 1981, "Use of Scanning Microphotometer to Determine the Evaporation Heat Transfer Characteristics of the Contact Region," *Int. J. Heat Mass Transfer*, Vol. 19, pp. 487-492.
- Greiner, M., and Winter, R. F., 1978, "Forced Flow Evaporation at High Mass Transfer Rates," *Ger. Chem. Eng.*, Vol. 1, pp. 352-360.
- Incropera, F. P., and DeWitt, D. P., 1985, *Fundamentals of Heat Transfer*, Wiley, New York, p. 285.
- Kaviany, M., 1989, "Forced Convection Heat and Mass Transfer From a Partially Liquid Covered Surface," *Num. Heat Transfer*, Vol. 15A, pp. 445-469.
- Kaviany, M., 1991, *Principles of Heat Transfer in Porous Media*, Springer-Verlag, New York.
- Mirzamoghadam, A., and Catton, I., 1988, "A Physical Model of the Evaporating Meniscus," *ASME JOURNAL OF HEAT TRANSFER*, Vol. 110, pp. 201-207.
- Plumb, O. A., and Wang, C.-C., 1982, "Convective Mass Transfer From Partially Wetted Surfaces," ASME Paper No. 82-HT-59.
- Rogers, J., and Kaviany, M., 1990, "Variation of Heat and Mass Transfer Coefficients During Drying of Granular Beds," *ASME JOURNAL OF HEAT TRANSFER*, Vol. 112, pp. 668-674.
- Saez, A. E., 1983, "Hydrodynamics and Lateral Thermal Dispersion for Gas-Liquid Concurrent Flow in Packed Beds," Ph. D. Thesis, University of California, Davis.
- Saez, A. E., and Carbonell, R. G., 1985, "Hydrodynamic Parameters for Gas-Liquid Concurrent Flow in Packed-Beds," *AIChE J.*, Vol. 31, pp. 52-62.
- Schlünder, E. U., 1988, "On the Mechanism of Constant Drying Rate period and Its Relevance to Diffusion Controlled Catalytic Gas Phase Reaction," *Chem. Eng. Science*, Vol. 43, pp. 2685-2688.
- Siegel, R., and Howell, J. R., 1981, *Thermal Radiation Heat Transfer*, 2nd ed., Hemisphere, pp. 104-105.

# The Aspect Ratio Effect on Natural Convection in an Enclosure With Protruding Heat Sources

M. Keyhani

L. Chen

D. R. Pitts

Department of Mechanical and Aerospace  
Engineering,  
The University of Tennessee,  
Knoxville, TN 37996-2110

*The aspect ratio effect on natural convection heat transfer in a rectangular enclosure with protruding heat sources has been experimentally investigated. Five protruding heaters were mounted with uniform vertical spacing on one vertical wall. The vertical wall opposite to the wall on which heated sections were mounted was movable so that the enclosure width could be adjusted to the desired value. The top surface of the test enclosure was an isothermal heat sink. All other surfaces except the two end vertical surfaces were insulated. The five heaters were identical with each having horizontal protuberance of  $L_3 = 9$  mm and vertical height of  $L_1 = 15$  mm. The vertical spacing between the heaters was  $L_2 = 15$  mm. The enclosure width was varied in experiments from  $W = 13.5$  mm to 45 mm. The experiments were conducted for six values of cavity width resulting in variations in the cavity height-to-width ratios (aspect ratios) and cavity width-to-protruding heater height ratios of 3.67 to 12.22 and 1.5 to 5.0, respectively. Ethylene glycol was used as the convective medium. Flow visualization pictures and heat transfer data indicate that the starting point of core flow directly affects the local heat transfer coefficient of the bottom heater, while the secondary flow cell between the top heated section and the top sink surface influences the heat transfer coefficient of the top heater. Cavity width variation influences the heat transfer process mainly through altered flow patterns. This influence is weak when the ratio of width-to-protruding height is 4.0 and negligible when this ratio is 5.0 or more. Based on the local height length scale (measured from the bottom of the cavity) the data for all the cavity widths are correlated and an explicit relation for the aspect ratio effect on local Nusselt number is reported. The correlation of local Nusselt number versus local modified Rayleigh number is independent of the number of heaters in the vertical array, cavity width-to-heater protrusion height ratio,  $W/L_3$ , and vertical height location of the heaters. This conclusion is based on the present results and previously reported data and is valid for the following conditions:  $1.5 \leq W/L_3 \leq 5.0$ ;  $3.67 \leq \text{aspect ratio} \leq 1.22$ ; vertical height of heater from 8 to 15 mm; and number of heated sections from 5 to 10.*

## Introduction

Effective cooling of micro-electronic components by means of natural convection has recently been accepted as a viable alternative to forced cooling in some circumstances. Natural convection provides simple, low-cost, reliable, maintenance-free and electronic-interference-free cooling (Johnson, 1986). Therefore, research work on natural convection in fluid-filled enclosures is of current interest (Yang, 1987). A brief summary of the related recent research work on natural convection in enclosures follows.

**Cooled Vertical Surface.** Keyhani et al. (1988a) performed experiments on natural convection heat transfer in a tall vertical cavity with eleven alternately heated and unheated, flush-mounted sections of equal height on a vertical wall. Another paper by Keyhani et al. (1988b) extended the previous work with an experimental and a numerical study of the problem in an enclosure having an aspect ratio of 4.5 and three heated sections. The authors indicated that the Nusselt numbers for a dielectric fluid ( $Pr = 25$ ) were nearly the same as those for ethylene glycol ( $Pr = 166$ ) under otherwise identical conditions. Moreover, the flow patterns for the two fluids were nearly identical at a given modified Rayleigh number. Thus for  $Pr = 25$  to 166, the results of the experimental research with ethylene glycol appear to be applicable to immersion

cooling with dielectric fluids. Kuhn and Ooshuizen (1986) conducted a numerical study of three-dimensional, transient, natural convective flow in a rectangular enclosure with localized heating. They pointed out that the three-dimensional flow increased the local heat transfer coefficient at the edge of the element and caused the average Nusselt number to be higher than that in the corresponding two-dimensional flow.

**Cooled Top and Bottom Horizontal Surfaces.** Kelleher et al. (1987) and Lee et al. (1987) presented experimental and numerical results respectively for natural convection in a water-filled, rectangular enclosure with one small heater protruding from a vertical wall. Experiments were conducted with the heater at three different locations: near the top, in the middle, and near the bottom of the wall. Their results indicated that for a given Rayleigh number, the local Nusselt number decreased as the heater was raised in the cavity. Very little research work has focused specifically on the effect of geometric factors on natural convection heat transfer. Liu et al. (1987) numerically studied three-dimensional, convective cooling of a  $3 \times 3$  array of protruding chips mounted on one vertical wall of an enclosure. They reported that the temperature and flow characteristics in the enclosure with a width of  $W = 30$  mm were similar to those for  $W = 18$  mm, except that the maximum chip surface temperature was reduced by  $4^\circ\text{C}$ . They also indicated that boundary layer and stratification behavior were valid for  $W/L_3 \geq 3.0$ . Joshi et al. (1990) conducted an experimental study of natural convection cooling of a  $3 \times 3$  array of heated protrusions in a rectangular enclosure filled with

Contributed by the Heat Transfer Division and presented at the AIAA/ASME Thermophysics and Heat Transfer Conference, Seattle, Washington, June 18–20, 1990. Manuscript received by the Heat Transfer Division July 19, 1990; revision received February 25, 1991. Keywords: Natural Convection, Enclosure Flows, Electronic Equipment.

dielectric fluid FC75. They obtained data for a single geometry and presented a single correlation for the Nusselt numbers of the nine heated components.

**Cooled Top Horizontal Surface.** Chen et al. (1988) experimentally studied the flow structure and heat transfer characteristics of natural convection in an enclosure with ten protruding heaters. They reported that the transfer coefficients for all the heated sections could be represented by a single correlation when the Nusselt and modified Rayleigh numbers were calculated based on the length scale of local heater height. The local heater height was measured from the bottom of the cavity to the midheight of a given heated section. Carmona and Keyhani (1989) conducted an experimental investigation of the cavity width effect on immersion cooling of five flush heaters on one vertical wall of an enclosure. Six cavity widths were studied covering an aspect ratio range of 3.67 to 12.2. The experiments were conducted with ethylene glycol and FC75. Based on the length scale proposed by Chen et al., they correlated their data for all the cavity widths and reported an explicit relation for the aspect ratio effect on local Nusselt number.

The objective of the present work is to extend the work of Chen et al. and that of Carmona and Keyhani. Specifically, the objective is to determine the aspect ratio effect on natural convection heat transfer in a rectangular enclosure with five protruding heat sources (horizontal strips), and explore the mechanism of such influence. It is hoped that the results of the present study with a protrusion height of 9 mm along with Carmona and Keyhani's results will provide the limiting values for the local Nusselt numbers, and describe the influence of the aspect ratio on them.

## Experimental Apparatus

The test cell for the present study was identical to that used by Carmona and Keyhani, with the exception of a finite protrusion height of 9 mm for the heated sections. Therefore, a brief discussion of the apparatus will be presented here, and further details can be found from Carmona and Keyhani (1989). The schematic of the enclosure and the details of the experimental apparatus are given in Figs. 1 and 2, respectively.

In order to have sufficient space for a wide variation in the width of the actual enclosure under study, an outer rectangular box with inner dimensions of  $H = 171.35$  mm,  $D = 141$  mm, and  $W = 139.7$  mm was made of 25.4-mm-thick plexiglass sheet. The vertical endwalls of the box ( $z$  direction) were made out of 6.35-mm-thick, ground plate glass. The top surface covering the cavity was a copper heat exchanger plate. A constant temperature water bath circulator maintained the top plate at a constant temperature to within  $0.15^\circ\text{C}$ . Seven 30 AWG (copper-constantan) thermocouples were placed in wells that were within 1 mm of the bottom surface of the plate to verify that the copper heat exchanger was maintained at a constant temperature.

The actual experimental enclosure was formed by placing a "movable" vertical plate and the "hot" plate inside the rectangular box enclosure formed by the outer plexiglass plates and the two glass endwalls (see Fig. 2 for details). In order to minimize heat losses, the "movable" vertical plate, the "hot" plate, and the bottom plate were instrumented with silicone-rubber thermofoil guard heaters. These plates were instrumented with differential thermopiles to determine the conduction heat loss. The voltages supplied to the "guard" heaters were adjusted such that the outputs of the differential thermopiles were reduced to a level so that the total heat loss was below 2 percent of the total power input.

The phenolite wall containing the protruding heaters was 177.8 mm high and 141 mm wide. Five identical rows of protruding heated sections were mounted on this plate. These heated sections were distributed such that identical rows of flush unheated and protruding heated sections were obtained. Details of the construction of the heated sections are given in Fig. 2. A silicon rubber thermofoil heater with a thickness of 0.25 mm was attached on a phenolite block. The heater-phenolite block assembly was inserted in an aluminum frame that was 3 mm thick in the  $x$  direction and 1.15 mm thick on the top and bottom surface ( $y$  direction). The protruding heated sections were attached to the frontal phenolite sheet with glue and screws. Seventeen 30 AWG copper-constantan thermocouples (type T) were placed on the vertical, top, and bottom horizontal surfaces of the protruding heaters to measure the temperatures. On heater 3, two more thermocouples were located on the two ends of the protruding heater in the spanwise

## Nomenclature

|  |  |   |
|--|--|---|
| $A$ = aspect ratio = $H/W$   | $N$ = heater row number (starting from the bottom)   |   |
| $A_h$ = surface area of the heated section, $\text{m}^2$   | $\text{Nu}$ = Nusselt number = $h$ [length scale]/ $k$   | $\text{Ra}^*$ = modified Rayleigh number = $\text{NuRa}$  |
| $A_T$ = area of top sink surface, $\text{m}^2$   | $\text{Pr}$ = Prandtl number = $\nu/\alpha$  | $T$ = temperature, $\text{K}$   |
| $C$ = isobaric specific heat, $\text{J}/\text{kg}\cdot\text{K}$  | $q$ = convective heat flux per heated section = $(Q - Q_l - Q_{sc})/A_h$ , $\text{W}/\text{m}^2$ | $x, y, z$ = Cartesian coordinates, $\text{m}$   |
| $D$ = depth of the enclosure in the $z$ direction, $\text{m}$  | $q_T$ = convective heat flux at the top surface = $(Q_T - Q_{l,T})/A_T$ , $\text{W}/\text{m}^2$  | $W$ = width of the cavity, $\text{m}$   |
| $g$ = acceleration due to gravity, $\text{m}/\text{s}^2$   | $Q$ = power input per heated section, $\text{W}$   | $\alpha$ = thermal diffusivity = $k/\rho C$ , $\text{m}^2/\text{s}$   |
| $h$ = local heat transfer coefficient = $q/(T_h - T_c)$ , $\text{W}/\text{m}^2\cdot\text{K}$                             | $Q_l$ = heat loss per heated section, $\text{W}$   | $\rho$ = density, $\text{kg}/\text{m}^3$  |
| $h_T$ = heat transfer coefficient at the top sink surface = $q_T/(\bar{T}_h - T_c)$ , $\text{W}/\text{m}^2\cdot\text{K}$ | $Q_{l,T}$ = total heat loss from the enclosure to the environment, $\text{W}$                    | $\nu$ = kinematic viscosity, $\text{m}^2/\text{s}$  |
| $H$ = height of the enclosure, $\text{m}$  | $Q_{sc}$ = substrate conduction heat transfer per heated section, $\text{W}$                     | $\sigma$ = standard error of estimate   |
| $k$ = thermal conductivity, $\text{W}/\text{m}\cdot\text{K}$   | $Q_T$ = total power input, $\text{W}$  |   |
| $L_1$ = height of the heated section, $\text{m}$   | $\text{Ra}$ = Rayleigh number = $g\beta(T_h - T_c)$ [length scale] $^3/\alpha\nu$                | <b>Subscripts</b>   |
| $L_2$ = height of the unheated section, $\text{m}$   |  | $c$ = cold wall   |
| $L_3$ = protruding thickness, $\text{m}$   |  | $h$ = heated section  |
|  |  | $L_1$ = based on the heated section height  |
|  |  | $y$ = based on the local height, measured from the bottom of the cavity to the mid-height of a heated section |
|  |  | <b>Superscripts</b>   |
|  |  | $(\bar{\quad})$ = average   |

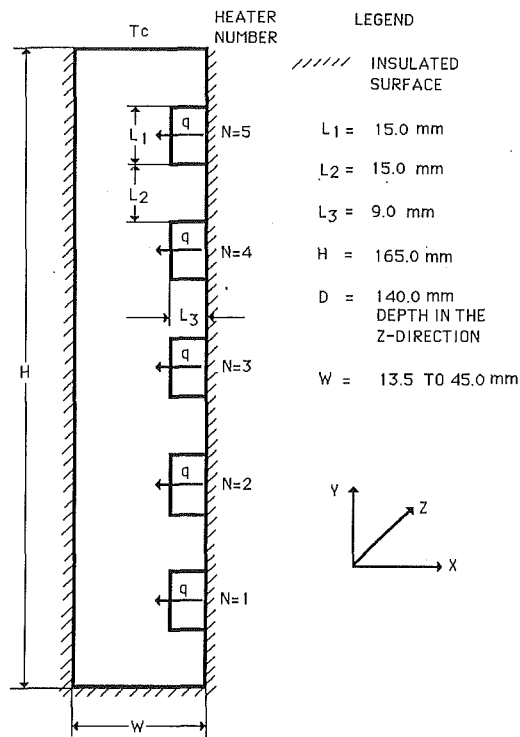


Fig. 1 Schematic of the enclosure

direction to measure the end effects. The unheated sections of the phenolite plate were also instrumented with 30 AWG thermocouples for temperature measurements.

Visualization experiments were conducted with ethylene glycol to investigate the flow structure. A thin plane of light was projected through a transparent gap on the movable wall to illuminate the midspan section of the test enclosure. Aluminum powder (5 to 30  $\mu\text{m}$  in size) was used as tracer particles. Still photographs were taken for each cavity width at several power inputs.

A power panel containing a voltage regulator, a step-down transformer and five variacs was used to measure and control the voltage and current in each circuit. The data were collected and analyzed with a data acquisition package consisting of a Hewlett-Packard control unit (HP 3497A), a digital voltmeter (HP 3456A), an extender (HP 3498A) and a system voltmeter (HP 3437A). All digital information were collected via a Hewlett-Packard 9817A desktop computer and stored for subsequent data reduction and analysis.

### Data Reduction

The thermophysical properties of ethylene glycol were evaluated at the arithmetic average of temperatures  $T_h$  and  $T_c$ , where  $T_h$  is the average temperature of each heated surface and  $T_c$  is the temperature of the top heat sink. The local convective heat transfer coefficient  $h$  for a specific heated section is defined by

$$h = \frac{q}{T_h - T_c} \quad (1)$$

and the convected heat flux is calculated via

$$q = \frac{Q - Q_l - Q_{sc}}{A_h} \quad (2)$$

where  $Q$  is the power input to each heater,  $Q_l$  is the heat loss per heater to the laboratory environment by conduction through the enclosure walls, and  $Q_{sc}$  is the substrate conduction heat transfer convected from the unheated sections. In Eq. (2),  $A_h$  is the total exposed surface area of each protruding heater.

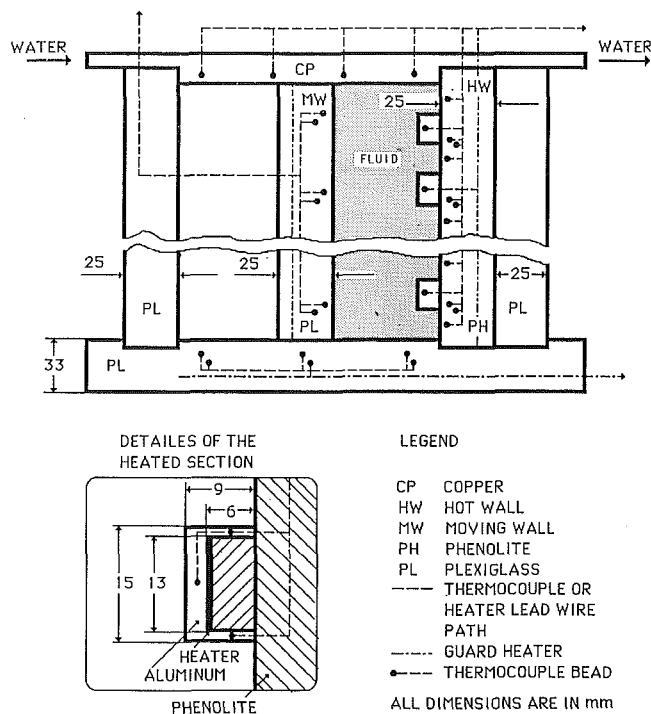


Fig. 2 Details of the experimental apparatus

The ratio  $Q_{sc}/(Q - Q_l)$  depends on enclosure width, power input, and heater location. By numerical analysis of the substrate conduction problem, the ratios corresponding to each heater at different widths and power inputs were calculated. The ratio range was from 3 to 9 percent.

A heat transfer coefficient for the top sink surface is defined as

$$h_T = (Q_T - Q_{l,T}) / A_T (\bar{T}_h - T_c) \quad (3)$$

where  $Q_T$  is the total power input,  $Q_{l,T}$  is the total heat loss to the laboratory environment,  $\bar{T}_h$  is the average temperature of all the heated sections, and  $A_T$  is the top sink surface area. It should be noted that the convected energy at the top surface includes the energy convected from the unheated section. The Nusselt and modified Rayleigh numbers are defined as

$$\text{Nu} = h[\text{length scale}] / k \quad (4)$$

$$\text{Ra}^* = g\beta q[\text{length scale}]^4 / \nu\alpha \quad (5)$$

The length scales of local heater height,  $y$ , and the heated section height,  $L_1$ , are employed in the presentation of the results.

### Uncertainty Analysis

The thermocouple outputs were measured to  $\pm 0.1 \mu\text{V}$ , which corresponds to a sensitivity of  $0.0025^\circ\text{C}$ . A reasonable limit of the accuracy of the temperature measurement is  $\pm 0.15^\circ\text{C}$ . This estimation includes the errors introduced by reference junction compensation ( $\pm 0.02^\circ\text{C}$ ), temperature difference along terminals, thermal offset, voltage-to-temperature conversion errors, and DVM inaccuracy. The voltage input to each heater circuit was measured with a sensitivity of 1 mV and an accuracy of 0.1 percent. Comparison between the original resistance of each heater circuit accurately measured before the experiments and the average resistance after being heated indicated that the maximum uncertainty for resistances could be conservatively estimated as  $\pm 2$  percent. The uncertainty of length scale was  $\pm 0.25 \text{ mm}$ . The uncertainties of thermophysical properties of the ethylene glycol were estimated as  $\pm 2$  percent, which was based on the variations reported in the literature.

Table 1 The geometric parameters covered in the present study

| W (mm)           | 13.5  | 18   | 22.5 | 27   | 36   | 45   |
|------------------|-------|------|------|------|------|------|
| H/W              | 12.22 | 9.17 | 7.33 | 6.11 | 4.58 | 3.67 |
| W/L <sub>3</sub> | 1.5   | 2.0  | 2.50 | 3.0  | 4.0  | 5.0  |

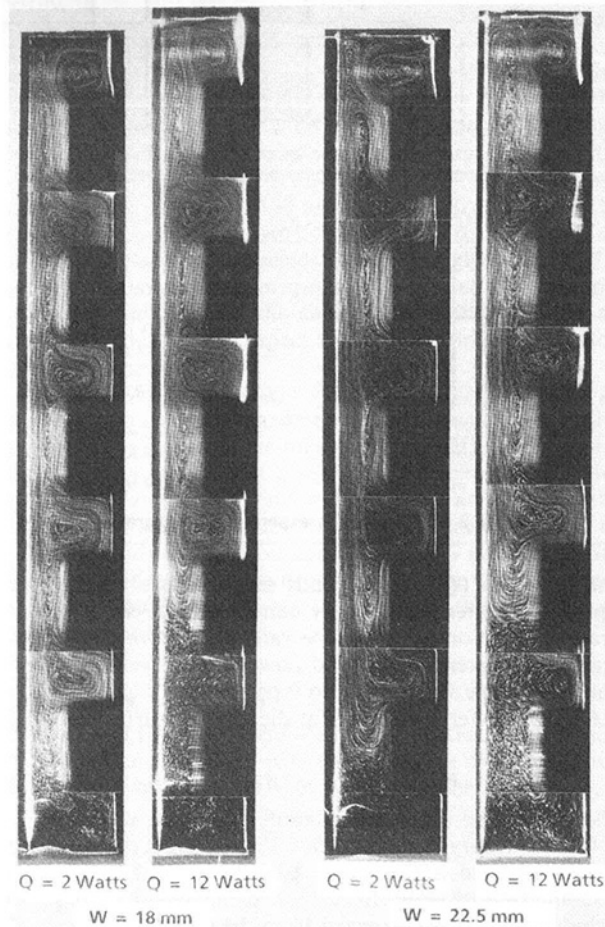


Fig. 3 Streak photographs of the entire cavity at average modified Rayleigh numbers of (from left to right)  $Ra_{t1}^* = 5.16 \times 10^5$ ,  $5.64 \times 10^6$ ,  $4.65 \times 10^5$ , and  $5.06 \times 10^6$

The uncertainties in the Nusselt and modified Rayleigh numbers are strongly dependent on the power input. A low power input results in higher uncertainties due to small temperature differences. As the power input is increased, the uncertainty in the experimental data is decreased. Uncertainty analyses using the standard Kline-McClintock method indicates that the uncertainties of  $Nu_c$  and  $Ra_{t1}^*$  were 4.2 to 5 percent and 5.4 to 7 percent, respectively. For detailed discussions of the data reduction procedure and the uncertainty analysis, please refer to Chen (1989).

## Results and Discussion

Eighty-five (85) experimental runs with ethylene glycol as working medium were conducted for power inputs of 2 W to 13 W per heated section with six values of enclosure width. The experiments covered a local modified Rayleigh number  $Ra_{t1}^*$  range of  $2.5 \times 10^6$  to  $4.6 \times 10^{10}$ , while the local Prandtl number varied from 110 to 62. The geometric parameters covered in the present study are presented in Table 1.

**Flow Visualization.** Figures 3, 4, and 5 present the photographs of flow patterns within the entire enclosure for var-

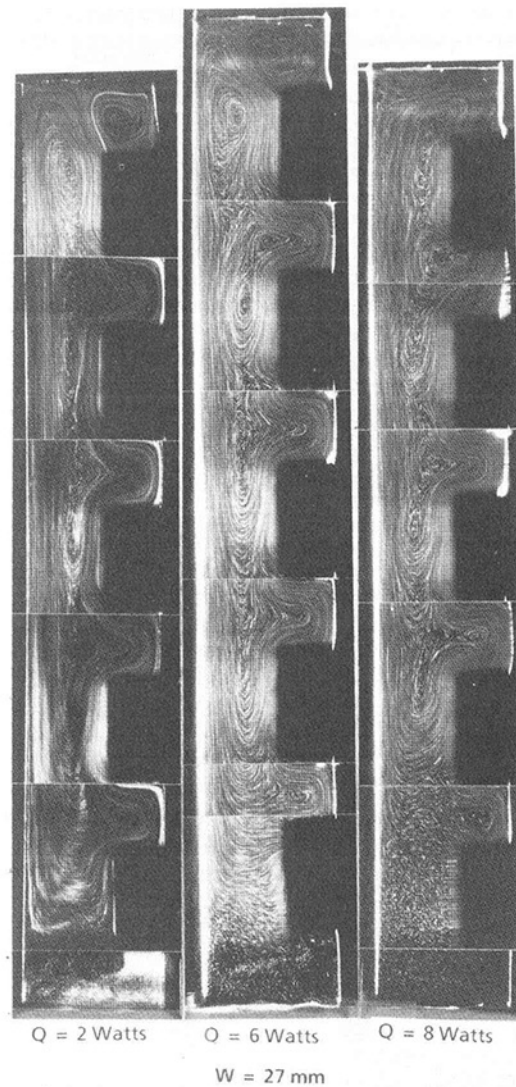


Fig. 4 Streak photographs of the entire cavity at average modified Rayleigh numbers of (from left to right)  $Ra_{t1}^* = 4.82 \times 10^5$ ,  $1.71 \times 10^6$ , and  $2.56 \times 10^6$

ious widths and power inputs. It should be mentioned that the apparent difference between the heights of the heated and the unheated sections is an optical effect. In these photographs, near the "hot" wall (heated and unheated sections) and the opposing vertical wall thick layers of primary flows are observed. Between these layers there exists a long and narrow core flow, which consists of secondary flow cells. This core flow, which begins at a height depending on the power input, ends near the top surface of the enclosure. When power input is low, the core flow starts from a low region of heater 1. When power input is increased, the location of the bottom of the core flow moves up and finally reaches the middle of heater 2 at  $Q = 12$  W per heater (Fig. 3).

Below the core flow, fluid flows much faster than that in the core flow and directly impinges on the heater 1 surface. The streamlines in this part are not smooth and exhibit characteristics of unsteady flow. Due to a higher observed velocity and lower measured fluid temperature, the local heat transfer coefficient for heater 1 is higher than that for the other heated sections. Moreover, in the case of high power input this lower portion of the flow is elongated (Figs. 3, 4), and it covers the entire height of heater 1. Hence, the difference between the local heat transfer coefficients of heaters 1 and 2 increases with power input. Another observed fact is that the fluid ve-

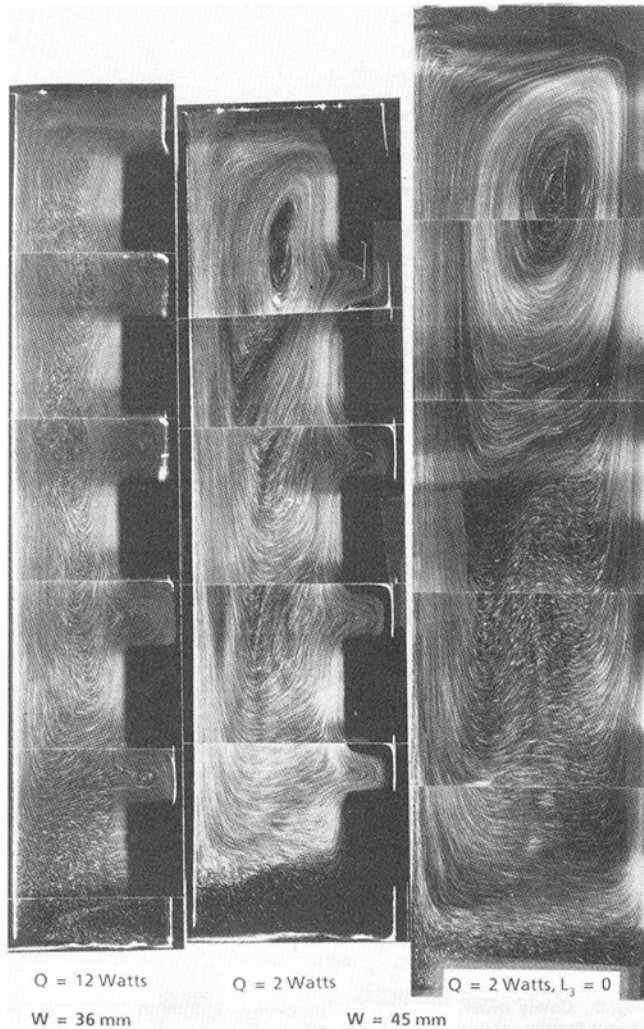


Fig. 5 Streak photographs of the entire cavity at average modified Rayleigh numbers of (from left to right)  $Ra_m^* = 4.72 \times 10^5$ ,  $4.43 \times 10^5$ , and  $7.86 \times 10^5$ ; the photograph with  $L_3 = 0$  is from Carmona and Keyhani (1989)

locity in the region below the core flow increases with decreasing  $W$ . Therefore, the difference between the local heat transfer coefficients of heaters 1 and 2 will increase with a decrease in  $W$ .

On the top of heater 5, as can be seen in the photographs (Figs. 4 and 5), there is a large secondary flow cell. This cell exchanges energy directly from heater 5 to the top surface and enhances the heat transfer coefficient of this heater. However, as the power input and  $W$  are increased (Figs. 4 and 5), this secondary flow gradually disappears, thus altering the heat transfer coefficient of heater 5. The contact area between the core flow and the top sink surface is increasing while this cell is shrinking, which enhances the heat transfer process for heaters below heater 5. Therefore, for large cavity width and high power input the heat transfer coefficient at heater 5 would be smaller than that of heater 4.

It is evident that the core flow can be described as consisting of two different portions. One portion is between the heated sections and the opposing vertical wall and is narrow and consists of several small secondary flow cells. The other part is between the unheated sections and the opposing vertical wall and consists of a single secondary flow cell. With increase of  $W$ , the secondary flow cells adjacent to the heated and unheated sections become weaker (as shown in Figs. 3, 4, and 5) and essentially disappear at  $W/L_3 = 5$ . Figure 5(a) shows the

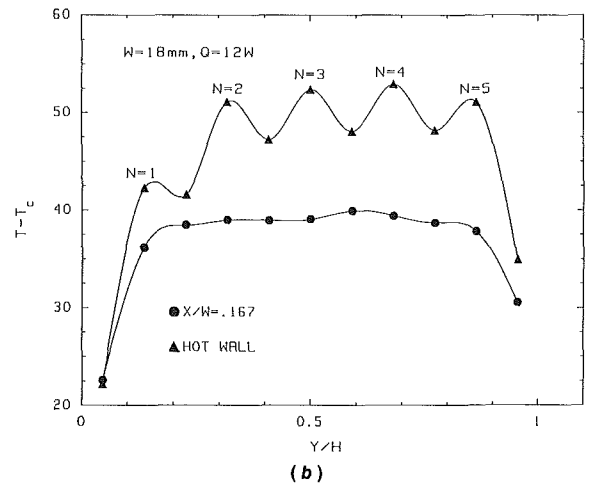
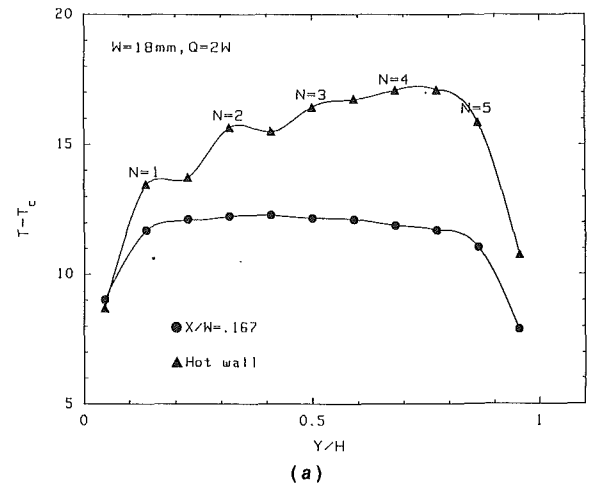


Fig. 6 Temperature distribution,  $T - T_c$ , in the fluid and along the "hot wall" for  $W = 18$  mm: (a)  $Q = 2$  W; and (b)  $Q = 12$  W

flow pattern for  $W/L_3 = 4$  and  $Q = 12$  W. With the exception of a single secondary flow cell that can be seen at the top portion of the cavity, no secondary flow cells adjacent to the unheated and heated sections are observed in this picture. Figure 5(b) shows the flow pattern for the case of  $W/L_3 = 5$  and  $Q = 2$  W. In this case the core flow is smooth, and only one secondary flow cell can be observed between heater 5 and the opposing vertical wall. Essentially this flow pattern is similar to that observed by Carmona and Keyhani (1989) with  $L_3 = 0$ , flush-heated sections, as shown in Fig. 5(c). This fact indicates that when  $W/L_3 \geq 5.0$ , the influence of protrusion on the flow pattern is negligible.

**Temperature Distribution.** Figures 6, 7, and 8 present excess temperatures ( $T - T_c$ ) of the heated and unheated sections and the core fluid temperature for various values of cavity widths and power inputs. Figure 6 shows the measured temperatures for  $W = 18$  mm with 2 and 12 W power input per heater. The excess temperature distribution for the core fluid is nearly constant with the exception of the top and bottom values. At all power inputs the temperatures of the top and bottom unheated sections are much lower than those of other unheated and heated sections. The temperature at the bottom unheated section is close to that of the core fluid.

The effect of an increase in the power input, at a fixed cavity width, on the temperature distribution on the "hot" wall can be seen in Fig. 6. For a given power input, the bottom heater ( $N = 1$ ) has the lowest temperature among the heated sections. Moreover, a steady increase in the temperature of the heaters from  $N = 1$  to 4 is observed. The top heater ( $N = 5$ ) has a

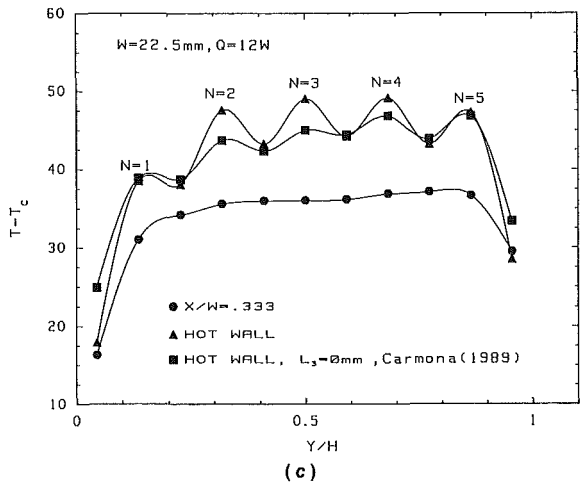
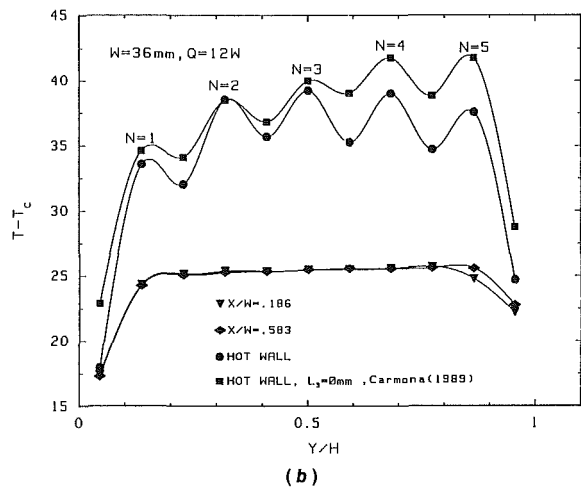
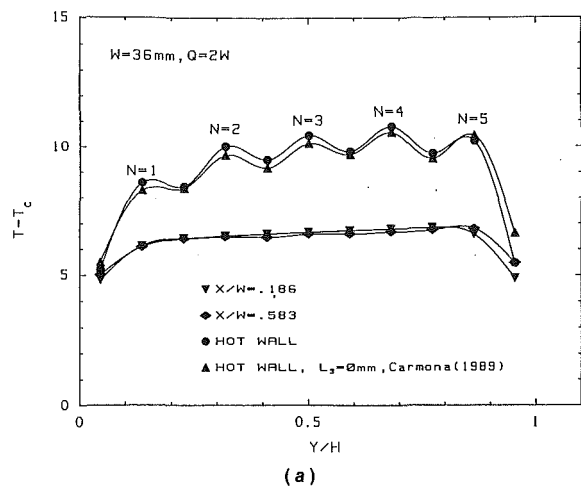


Fig. 7 Comparison of the present temperature distributions with the flush-heated case (Carmona and Keyhani, 1989): (a)  $W = 36$  mm,  $Q = 2$  W; (b)  $W = 36$  mm,  $Q = 12$  W; and (c)  $W = 22.5$  mm,  $Q = 12$  W

lower temperature than that of heater 4 due to its proximity to the top sink surface. A comparison of Figs. 6(a) and 6(b) shows that the relative difference between  $(T_h - T_c)$  of heaters 1 and 2 is increased as  $Q$  is increased from 2 to 12 W per heater. This trend is due to the change in the flow pattern in the vicinity of heater 1 as discussed earlier (please refer to the discussion of Fig. 3). Another effect of increase in  $Q$  on the  $(T_h - T_c)$  distribution is the reduction of the difference between the temperatures of heaters 2 to 4 and a corresponding increase in the differences between the temperatures of the heated and unheated sections.

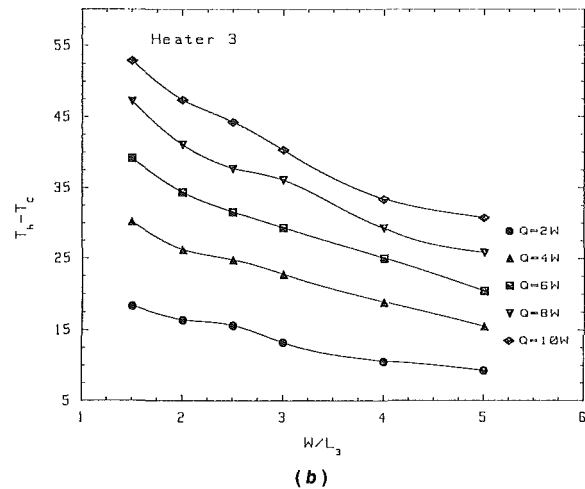
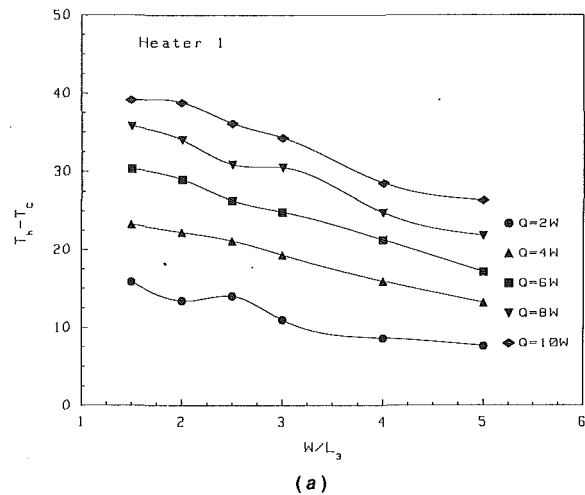


Fig. 8 Cavity width effect on heated section temperatures at various power inputs: (a) heater 1; (b) heater 3

Comparisons of the temperature distributions along the “hot” wall with protruding heated sections and the flush-heated case (Carmona and Keyhani, 1989) are made in Figs. 7(a), 7(b), and 7(c). It should be noted that the enclosure used by Carmona and Keyhani was identical to that of the present investigation with the exception of  $L_3 = 0$ . Therefore, the  $A_h$  for the present problem is 2.2 times larger than that of the flush-heater case. For  $W = 36$  mm and  $Q = 2$  W, the temperatures of the heated and unheated sections of the protruding wall and flush wall, with the exception of the top unheated section, are nearly the same (Fig. 7(a)). In general the protruding case temperatures are slightly higher than those for the flush case. As the power input is increased to  $Q = 12$  W (Fig. 7(b)), the difference between the two profiles increases, and the flush-heated wall temperatures are in general substantially higher than the protruded values. Figures 7(a) and 7(b) also show the excess core temperature distributions for the protruding case at  $x/W = 0.186$  and  $x/W = 0.583$ . These two profiles are nearly the same, which is indicative of the quality of the imposed adiabatic boundary condition at the opposing vertical wall. Moreover, this shows that the region of nearly constant vertical temperature distribution in the core fluid is at least 14.3 mm wide ( $x/W = 0.186$  to 0.583).

The effect of change in  $W$  from 36 mm to 22.5 mm on the temperature profiles of the two cases of protruding and flush-heated walls can be observed in Figs. 7(b) and 7(c). A comparison of Figs. 7(b) and 7(c) shows that the decrease in the cavity width results in a pronounced change in the differences between the temperatures of heaters 2 to 5 of the two cases. The increase in the aspect ratio has resulted in a decrease in

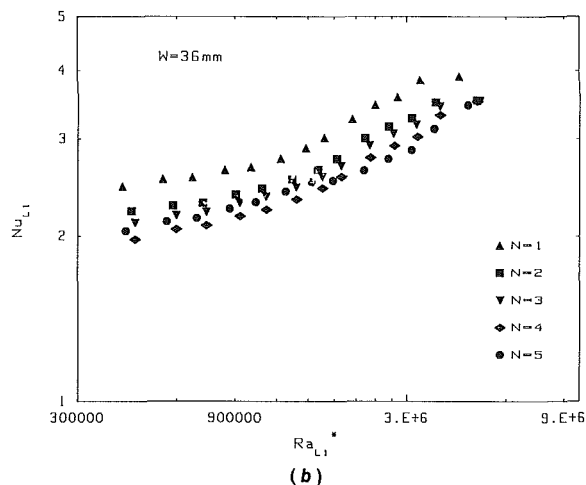
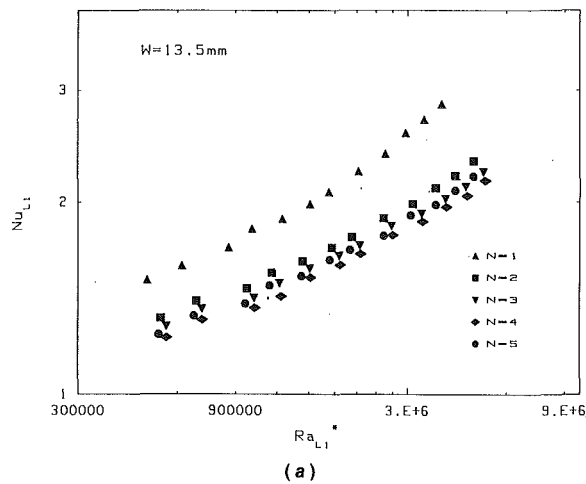


Fig. 9 Heated section Nusselt numbers ( $Nu_{L1}$ ) as a function of  $Ra_{L1}^*$ : (a)  $W = 13.5$  mm; (b)  $W = 36$  mm

the difference between the temperatures of the top heated sections of the two cases to an extent that they are nearly the same. Moreover, the higher aspect ratio has resulted in protruded temperatures for heaters  $N = 2, 3,$  and  $4,$  which are higher than those for the flush case, which is opposite to the results observed with  $W = 36$  mm. A partial explanation for this behavior may be the fact that the aspect ratio effect is more pronounced in the protruded case.

The influence of cavity width parameter ( $W/L_3$ ) on the temperature of the heated sections  $N = 1$  and  $3$  at power inputs of  $Q = 2, 4, 6, 8,$  and  $10$  W per heater is shown in Figs. 8(a) and 8(b). As discussed earlier, changes in  $W$  for a fixed  $Q$  and variation in  $Q$  for a fixed  $W$  each have pronounced and distinct effects on the flow pattern, which varies from one heated section to another. The data suggest that the effect of  $W/L_3$  on  $(T_h - T_c)$  at all power inputs is rather complicated for  $1.5 \leq W/L_3 \leq 3$ . Moreover, it is clear that the influence of  $W/L_3$  on the temperature of the heated sections is weak for  $W/L_3 > 3$  and negligible for  $W/L_3 > 4$ .

**Heat Transfer.** Figure 9 presents the Nusselt number as a function of modified Rayleigh number based on protruding height  $L_1$  for all the heaters at  $W = 13.5$  and  $36$  mm, respectively. Since  $L_1$  is constant in the present experiments, this plot directly shows the dependence of local heat transfer coefficient for each heater on the power input. It is observed that heater 1 has the highest heat transfer coefficient. Moreover, the difference between  $Nu_{L1}$  of heaters 1 and 2 increases with power input ( $Ra_{L1}^*$ ) and decreases when cavity width is increased (decreasing aspect ratio). For  $W = 13.5$  mm and  $Q = 2$  W per

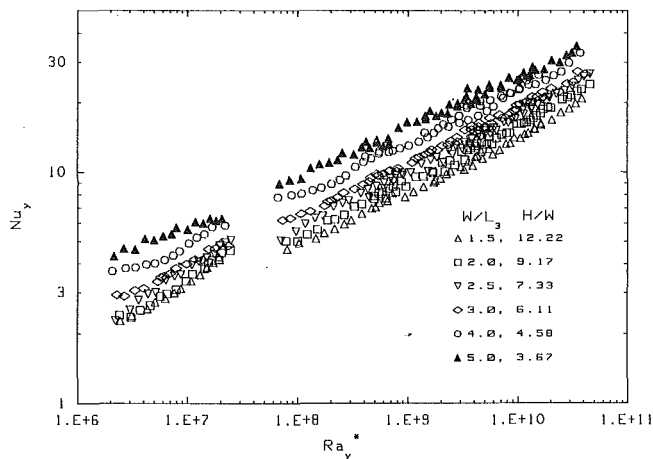


Fig. 10 Local Nusselt number ( $Nu_y$ ) as a function of local modified Rayleigh number ( $Ra_y^*$ ) for all the cavity widths

Table 2 Coefficients  $c$ , exponents  $m$ , and standard errors of estimates  $\sigma$  for heat transfer correlations

| W (mm) | c     | m                   | $\sigma$ |
|--------|-------|---------------------|----------|
| 13.5   | 0.095 | $0.216 \pm 0.00267$ | 0.263    |
| 18.0   | 0.084 | $0.227 \pm 0.00265$ | 0.275    |
| 22.5   | 0.089 | $0.229 \pm 0.00267$ | 0.277    |
| 27.0   | 0.1   | $0.228 \pm 0.00269$ | 0.273    |
| 36.0   | 0.132 | $0.223 \pm 0.00272$ | 0.267    |
| 45.0   | 0.18  | $0.216 \pm 0.00273$ | 0.258    |

heater, the  $Nu_{L1}$  of heater 1 is 14.5 percent higher than that of heater 2, while at  $Q = 11$  W per heater the corresponding difference is increased to 22.8 percent. However, as the cavity width is increased from 13.5 mm to 18 mm and to 27 mm (data not shown in Fig. 9), the corresponding difference between  $Nu_{L1}$  of heaters 1 and 2 decreases from 14.5 to 11.5 and 10 percent, respectively. The increase of  $Nu_{L1}$  of heater 1 as a result of an increase in the power input, at a fixed cavity width, is mainly due to the higher local height of starting point of the core flow. It was observed that a decrease in the cavity width results in a higher velocity in this region, which enhances the heat transfer coefficient of heater 1.

With increase in the heater number (local height),  $Nu_{L1}$  decreases up to heater 4, which has the lowest value. At heater 5,  $Nu_{L1}$  increases over that of heater 4. However, for  $W = 36$  mm and high modified Rayleigh number  $Ra_{L1}^*$ , the lowest value of Nusselt number moves to heater 5. This fact supports the previous discussion of the flow visualization results. As stated earlier, for large enclosure widths (36 and 45 mm) the secondary flow cell between heater 5 and the top sink surface gradually becomes smaller and finally disappears as the power input is increased (Figs. 4, 5). This phenomenon of course weakens the convection process at heater 5 and enhances the heat transfer at heaters below heater 5 due to larger contact area between the primary flow and the top surface.

The presentation of the Nusselt numbers in terms of  $Nu_{L1}$  for all of the heated sections and cavity widths would require several graphs and 30 correlations. Chen et al. (1988) have shown that the choice of length scale of local height  $y$  substantially simplifies the task of the presentation and discussion of the results. The present data based on the length of scale  $y$  are presented in Fig. 10. It is interesting to note that for each cavity width, the log-log plot of  $Nu_y$  versus  $Ra_y^*$  for all the heated sections forms a straight line. Moreover, the data for



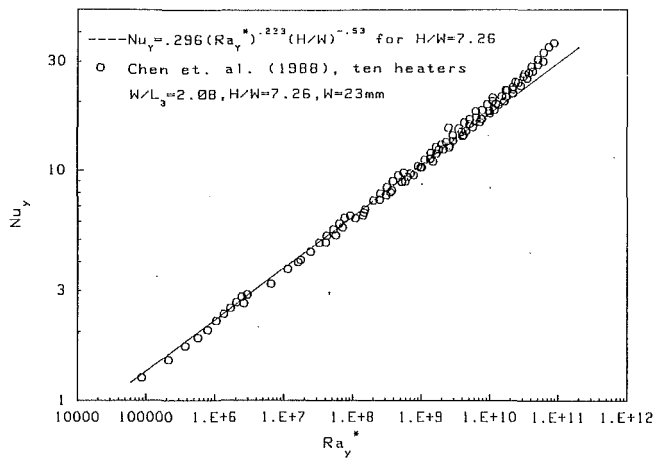


Fig. 11 Comparison of present correlation with previous data (Chen et al., 1988)

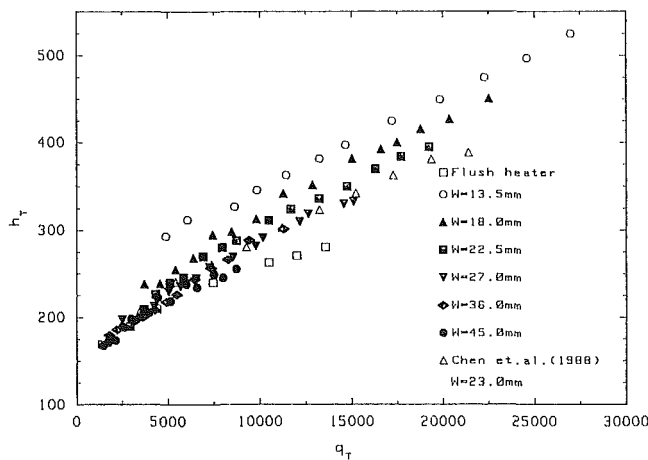


Fig. 12 Heat transfer coefficient (based on the top cooling area) versus the heat flux based at the top cooling surface (flush heater data of Carmona and Keyhani are for  $W = 45$  mm)

each cavity width can be correlated with a standard error of less than 0.28. It is obvious that the task of analysis of cooling problems is substantially simplified when one can unify the data via local height scaling. The local Nusselt number of the heated sections  $Nu_y$  for each width is correlated in terms of its respective local modified Rayleigh number  $Ra_y^*$  in the form of

$$Nu_y = c(Ra_y^*)^m \quad (6)$$

where the constants,  $c$ , exponents,  $m$ , and the standard errors of estimates,  $\sigma$ , are tabulated in Table 2. These correlations represent the experimental data with an average deviation of 2.8 percent. The percent average deviation represents the sum of the absolute percent deviations of the predicted values from the experimental values divided by the number of data points. A general correlation for all the widths studied was also obtained as:

$$Nu_y = 0.296(Ra_y^*)^{0.223}(A)^{-0.53} \quad (7)$$

The average deviation of experimental data from this correlation is 4.5 percent.

Figure 11 presents a comparison of the present general correlation, Eq. (7), with the data reported by Chen et al. (1988). It is encouraging that the above correlation can predict those data very well. It should be pointed out that the data of Chen et al. (1988) were for  $A = 7.26$  and  $W/L_3 = 2.09$  ( $W = 23$  mm,  $L_3 = 11$  mm, and  $H = 167$  mm). Although the dimensions of  $W$  and  $H$  of that study and the present one are close, the other geometric parameters are quite different. The previous

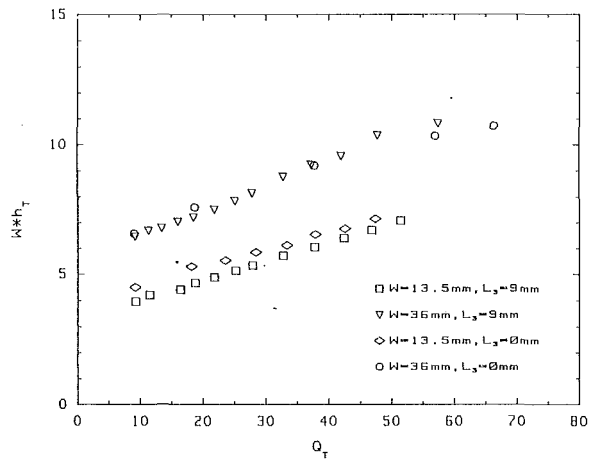


Fig. 13 Comparison of  $Wh_T$  of the present study with the flush-heated case (Carmona and Keyhani, 1989)

experiment was with ten heaters having  $L_3 = 11$  mm and  $L_1 = L_2 = 8$  mm, while the present experiment has five heaters with  $L_3 = 9$  mm,  $L_1 = L_2 = 15$  mm. This fact reveals an interesting and important characteristic of this class of problems. The correlation of the local Nusselt number  $Nu_y$  in terms of the local modified Rayleigh number  $Ra_y^*$  is independent of the number of heaters for  $5 \leq N \leq 10$ , the heater vertical height  $L_1 = 8$  to 15 mm, and the protruding height when  $1.5 \leq W/L_3 \leq 5.0$ ,  $3.67 \leq A \leq 12.22$  and  $L_1 = L_2$ . For this range of parameters, the aspect ratio of the enclosure ( $H/W$ ) is the primary geometric factor. This conclusion is true for the experimental conditions stated and a range of  $Ra_y^*$  from  $8.7 \times 10^4$  to  $8.7 \times 10^{10}$ .

Carmona and Keyhani (1989) used an otherwise identical apparatus to that of the present study except for flush-mounted heated sections. They reported the following general correlation for the aspect ratio effect in the flush-heater case:

$$Nu_y = 0.437(Ra_y^*)^{0.227}(A)^{-0.416} \quad (8)$$

It is interesting to note that the exponent of  $Ra_y^*$  of the present study and that of Eq. (8) are nearly the same. However, the aspect ratio effect in the protruding case is stronger than that of the flush-heated case. A stronger aspect ratio effect in the case of protruding heated sections is not contrary to intuitive expectations. A comparison of the present results and the flush-heated case shows that the flush-heated case heat transfer coefficients are higher than those of the protruded case. For  $W = 13.5$  and 45 mm the ratios of the present  $Nu_y$  to those of the flush-heated case at  $Ra_y^* = 10^7$  are 48 and 53.6 percent, respectively.

The total energy convected from the heated and unheated sections is transferred to the top sink surface. The heat transfer coefficient  $h_T$  at the top surface as defined by Eq. (3) is plotted against the total convective heat flux at the top surface  $q_T$  in Fig. 12. This figure shows that  $h_T$  increases with decreasing cavity width. It should be noted that for a given power input the highest fluid velocity was observed at the smallest cavity width during the flow visualization experiments. Liu et al. (1987) reported a similar finding in their numerical study dealing with convection cooling of an array of heated protrusions in a cavity. The data by Chen et al. (1988) and the flush case (Carmona and Keyhani, 1989) are also presented in this figure. Since the cavity width for the Chen et al. (1988) data was 23 mm, their  $h_T$  values are between the present data for  $W = 22.5$  mm and  $W = 27$  mm, and are closer to the former. For  $W = 45$  mm, the Carmona and Keyhani data for  $L_3 = 0$  at low  $q_T$  values are almost equal to those for  $L_3 = 9$  mm of the present study. Unfortunately, at high  $q_T$  values there are no data for  $L_3 = 9$  mm to compare with the Carmona and Keyhani

data. A comparison of  $Wh_T$  versus  $Q_T$  between the two cases of  $L_3 = 9$  and  $L_3 = 0$  with  $W = 13.5$  mm and  $W = 36$  mm is presented in Fig. 13. At  $W = 13.5$  mm the product of  $Wh_T$  for the flush case is about 13 percent higher than  $Wh_T$  for  $L_3 = 9$  mm, while at  $W = 36$  mm the  $Wh_T$  values of the two cases are nearly the same. The present results cannot be compared with the predictions of Liu et al. or the data of Joshi et al. due to differences in the range of parameters investigated. Moreover, it should be noted that those studies are for cooled top and bottom surfaces, while the present study is for a cooled top surface. For design purposes, we believe that the present correlation along with that reported by Carmona and Keyhani (1989) for flush-heaters, for the range of parameters investigated, can provide bounding limits on the local heat transfer coefficients.

## Conclusion

Experiments have been carried out to investigate the aspect ratio effect on natural convection in a rectangular enclosure with multiple protruding heaters. Ethylene glycol was used as the working fluid. Photographs of the flow patterns, heat transfer correlations, and the aspect ratio effect on heat transfer coefficients are presented and discussed. A summary of concluding statements follows.

- The bottom heated section has the highest local heat transfer coefficient, and thereafter the values decrease up to heater 4. However, at  $Ra_y^* > 6.69 \times 10^9$  the minimum local value is observed at the top heater.
- Between the primary flow layers there is a narrow and long core flow consisting of secondary flow cells, and along most of the height of the core flow the fluid temperature is nearly constant.
- The height at which core flow begins moves up with an increase in the power input and thus enhances the heat transfer coefficient of the bottom heater.
- The secondary flow cell between the top heater and the top sink surface influences the heat transfer coefficient of this heater. With increasing values of cavity width and power input this secondary flow cell becomes small and finally disappears. Thus, the heat transfer coefficient of the top heater is decreased. Meanwhile, the contact area between the primary flow and the top sink surface is increased, which is a positive factor influencing heat transfer coefficients of heaters below the top heater.
- The fluid velocity decreases with an increase in the cavity width resulting in a lower heat transfer coefficient at the top surface. However, the top cooling area is increased such that the product term,  $Wh_T$ , is enhanced, resulting in a lower average temperature difference.
- Based on the local height  $y$  of each heater, all the data

are well represented by a single correlation. This correlation includes an explicit aspect ratio effect and is independent of the number of heaters, protruding height and the heater vertical height (under experimental conditions of  $1.5 \leq W/L_3 \leq 5.0$ ,  $3.67 \leq A \leq 12.22$ ,  $8 \text{ mm} \leq L_1 = L_2 \leq 15 \text{ mm}$ , and number of heated sections from 5 to 10).

- With  $L_3 = 9$  mm, the heat transfer coefficients of the heated sections are lower than those of the flush heater case, and the difference diminishes as the aspect ratio decreases.

## References

- Carmona, R., 1989, "The Aspect Ratio Effect on Immersion Cooling in an Enclosure With Discrete Heaters," Master Thesis, The University of Tennessee, Knoxville, TN, May.
- Carmona, R., and Keyhani, M., 1989, "The Cavity Width Effect on Immersion Cooling of Discrete Flush-Heaters on One Vertical Wall of an Enclosure Cooled From the Top," *Proceedings of the 1989 AIChE/ASME National Heat Transfer Conference*, ASME HTD-Vol. 107, pp. 207-219; also *ASME Journal of Electronic Packaging*, Vol. 111, pp. 268-276.
- Chen, L., Keyhani, M., and Pitts, D. R., 1988, "An Experimental Study of Natural Convection Heat Transfer in a Rectangular Enclosure With Protruding Heaters," *Proceedings, 25th AIChE/ASME National Heat Transfer Conference*, Houston, TX, HTD-96, Vol. 2, pp. 125-133; also *Journal of Thermophysics and Heat Transfer*, Vol. 5, No. 2, 1991, pp. 217-223.
- Chen, L., 1989, "The Aspect Ratio Effect on Natural Convection in an Enclosure With Protruding Heat Sources," Ph.D. Thesis, The University of Tennessee, Knoxville, TN, Aug.
- Johnson, C. F., 1986, "Evaluation of Correlation for Natural Convection Cooling of Electronic Equipment," *Heat Transfer in Electronic Equipment—1986*, ASME HTD-Vol. 57, pp. 103-111.
- Joshi, Y., Kelleher, M. D., and Benedict, T. J., 1990, "Natural Convection Immersion Cooling of an Array of Simulated Electronic Components in an Enclosure Filled With Dielectric Fluid," *Heat Transfer in Electronic and Microelectronic Equipment*, A. E. Bergles, ed., Hemisphere, New York, pp. 445-468.
- Kelleher, M. D., Knock, R. H., and Yang, K. T., 1987, "Laminar Natural Convection in a Rectangular Enclosure Due to a Heated Protrusion on One Vertical Wall Part I: Experimental Investigation," *Proceedings, 2nd ASME/JSME Thermal Engineering Joint Conference*, Honolulu, HI, Vol. 2, pp. 169-177.
- Keyhani, M., Prasad, V., and Cox, R., 1988a, "An Experimental Study of Natural Convection in a Vertical Cavity With Discrete Heat Sources," *ASME JOURNAL OF HEAT TRANSFER*, Vol. 110, pp. 616-624.
- Keyhani, M., Prasad, V., Shen, R., and Wong, T.-T., 1988b, "Free Convection Heat Transfer From Discrete Heat Sources in a Vertical Cavity," *Natural and Mixed Convection in Electronic Equipment Cooling*, R. A. Wirtz, ed., ASME HTD-Vol. 100, pp. 12-24.
- Kuhn, D., and Oosthuizen, P. H., 1986, "Three-Dimensional Transient Natural Convective Flow in a Rectangular Enclosure With Localized Heating," *Natural Convection in Enclosures—1986*, R. S. Figliola and I. Catton, eds. ASME HTD-Vol. 63, pp. 55-62.
- Lee, J. J., Liu, V. K., Yang, K. T., and Kelleher, M. D., 1987, "Laminar Natural Convection in a Rectangular Enclosure Due to a Heated Protrusion on One Vertical Wall Part II: Numerical Simulation," *Proceedings, 2nd ASME/JSME Thermal Engineering Joint Conference*, Honolulu, HI, Vol. 2, pp. 179-185.
- Liu, K. V., Yang, K. T., and Kelleher, M. D., 1987, "Three-Dimensional Natural Convection Cooling of an Array of Heated Protrusions in an Enclosure Filled With a Dielectric Fluid," *Proceedings, International Symposium on Cooling Technology for Electronic Equipment*, Honolulu, HI, pp. 486-497.
- Yang, K. T., 1987, "Natural Convection in Enclosures," *Handbook of Single Phase Convection Heat Transfer*, S. Kakac, R. K. Shah, and W. Aug, eds., Wiley, New York.

# Natural Convection in a Square Cavity With Thin Porous Layers on Its Vertical Walls

P. Le Breton

J. P. Caltagirone

E. Arquis

M.A.S.T.E.R.—ENSCP,  
Université de Bordeaux I,  
F.33405 Talence, France

*Natural convection in a square cavity in which differentially heated vertical walls are covered with thin porous layers is studied by using a control volume formulation and a SIMPLER algorithm for pressure-velocity coupling. Comparisons with benchmark solutions for natural convection in fluid-filled cavities are first presented for Rayleigh numbers up to  $10^8$ . The problem of the square cavity with thin porous layers on its vertical walls is then studied by using a modified form of the Navier-Stokes equations by addition of a Darcy term. It is shown that the main effect of the introduction of porous layers is to produce a large decrease of the overall Nusselt number when the permeability is reduced. The higher the Rayleigh number is, the stronger is the decrease, and obviously the decrease also increases with the layer thickness. Moreover, porous layers having a thickness of the order of the boundary layer thickness are sufficient, and taking thicker ones only induces a small decrease of the heat transfer. The main effect of porous layers is to reduce the upwind flow and then to decrease the convective heat transfer.*

## I Introduction

The problem of the natural convection in a rectangular cavity with differentially heated, isothermal vertical walls and insulated horizontal surfaces has been the subject of numerous numerical and experimental studies. In many applications of natural convection, for example, in thermal insulation, or in geothermal systems, the fluid flow is in interaction with a porous medium. In a wide variety of such problems, the physical system can be represented by a two-dimensional rectangular enclosure partially filled with a homogeneous porous medium.

Some studies have been directed on this subject. Somerton and Catton (1982) studied convective instabilities in the case of a horizontal fluid layer superposed above a porous layer and heated from below, using one set of equations for each layer. The porous medium was modeled by a Brinkman extension of the Darcy law. Poulikakos and Bejan (1983) considered a vertical rectangular enclosure filled with vertical porous layers of different permeabilities. They used momentum equations based on the Darcy flow model with a space variation of permeability. Lauriat and Mesguich (1984) investigated natural convection and radiation in vertical rectangular enclosures that were vertically divided into a fluid and a porous layer, the two layers being separated by a permeable wall. Arquis and Caltagirone (1987) studied a square vertical cavity with a porous layer centered or adjacent to a wall, by considering the porous medium as a "special" fluid by solving the same set of equations in the entire domain. These equations are a modified form of the Navier-Stokes equations with a Darcy term. The transition from the fluid to the porous layer has been achieved by a continuous space variation of permeability and other physical properties. Beckermann et al. (1987, 1988) numerically and experimentally studied the problem of a square cavity with a large porous layer which was adjacent to one of the vertical walls (1987, 1988), centered (1988), or adjacent to the horizontal bottom wall (1988). They also combined the governing equations of each medium in order to solve only one set of equations for the two regions. In addition,

they incorporated the Forchheimer extension to account for inertia effects in the porous media.

The present study is motivated by two remarks. None of the presented works deal with a very thin porous layer. Then, in the air-filled square cavity problem very thin boundary layers are developing along the vertical walls. Their thickness decreases when the Rayleigh number increases and it is known that the vertical velocities have very high values very close to the walls and a great part of convective heat transfer occurs here. This is why it is of interest to study the effects of the introduction of thin porous layers on the vertical walls and especially on the evolution of the global heat transfer. The flow is modeled by considering the porous medium as a "special" fluid, referring to Arquis and Caltagirone (1987). Only one set of equations is then solved for both media. The influence of the Rayleigh number and porous layer's permeability, thickness, and conductivity will be analyzed. Before that, our results for a square cavity filled with air will be presented and compared to the previous results.

## II Formulation and Resolution

**II.1 Physical Model.** The problem considered is the two-dimensional natural convection flow in a vertical square cavity with adiabatic horizontal walls and isothermal vertical sides at  $T_H$  and  $T_C$ . The horizontal walls are separated by a distance  $H$  and the horizontal ones by a height  $L$ . The aspect ratio  $A = H/L$  defines the geometric similarity. Both velocity components are equal to zero on the boundaries. The vertical walls are covered with thin porous layers. The porous substratum of porosity  $\epsilon$  and permeability  $K$  is saturated by a Boussinesq, Newtonian fluid of kinematic viscosity  $\nu$ , coefficient of thermal expansion  $\beta$ , density  $\rho$ , thermal conductivity  $\kappa_f$ , and heat capacity  $(\rho c)_f$ . The saturated porous medium is similar to an artificial fluid of heat capacity  $(\rho c)_p = \epsilon(\rho c)_f + (1 - \epsilon)(\rho c)_s$  and thermal conductivity  $\kappa_p$  (see Fig. 1). The porous material used in this study is supposed to have a porosity close to one and its heat capacity is then equal to the fluid one.

**II.2 Mathematical Model.** Instead of solving one set of equations for each region, the equations could be combined into a unique set of equations valid at all points. These equations are a modified form of Navier-Stokes equations with

Contributed by the Heat Transfer Division for publication in the JOURNAL OF HEAT TRANSFER. Manuscript received by the Heat Transfer Division April 25, 1990; revision received December 6, 1990. Keywords: Enclosure Flows, Natural Convection, Porous Media.

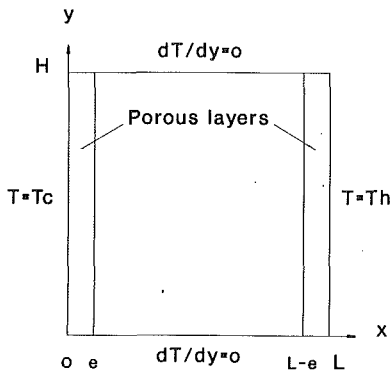


Fig. 1 Physical model

introduction of a Darcy term (Arquis and Caltagirone, 1987; Beckermann et al., 1987, 1988; Turki and Lauriat, 1990). Both media are then treated with this set of equations, introducing a variation in space of the physical parameters (thermal conductivity and permeability):

$$\nabla \cdot \mathbf{V} = 0 \quad (1)$$

$$(\rho c)_f \frac{\partial T}{\partial t} + (\rho c)_f \mathbf{V} \cdot \nabla T = \nabla \cdot (\kappa(x, y) \nabla T) \quad (2)$$

$$\rho_f \frac{\partial \mathbf{V}}{\partial t} + \rho_f \mathbf{V} \cdot \nabla \mathbf{V} = \mu \nabla^2 \mathbf{V} - \frac{\mu}{K(x, y)} \mathbf{V} - \nabla p + \rho_f g \quad (3)$$

It must be noticed that we do not introduce the Forchheimer's extension, which permits us to take into account the inertia effects in the porous media. In our configuration the pore Reynolds number is close to one and in this case the inertia effects can be neglected.

The variation in space of the thermal conductivity and permeability are written as follows:

$$\begin{cases} \kappa(x, y) = \kappa_f \\ K(x, y) = \infty \end{cases} \text{ for } e < x < L - e \quad (4)$$

$$\begin{cases} \kappa(x, y) = \kappa_p \\ K(x, y) = K_p \end{cases} \text{ for } 0 < x < e \text{ and } L - e < x < L \quad (5)$$

We use the following nondimensional variables:

$$T^* = \frac{T - T_0}{T_H - T_C} \quad x^*, y^* = \frac{x, y}{L}$$

$$u^*, v^* = u, v \frac{L}{\alpha} \quad p^* = p \frac{L^2}{\rho \alpha^2} \quad t^* = t \frac{\alpha}{L^2}$$

where  $T_0 = (T_H - T_C)/2$  and  $\alpha$  is the fluid thermal diffusivity.

We also introduce the following nondimensional parameters:

Rayleigh number:

$$Ra = \frac{g\beta(T_H - T_C)L^3}{\nu\alpha}$$

Prandtl number:

$$Pr = \frac{\nu}{\alpha}$$

Darcy number:

$$Da = \frac{K}{L^2}$$

Conductivity ratio:

$$R = \frac{\kappa_p}{\kappa_f}$$

Aspect ratio:

$$A = \frac{H}{L}$$

Dimensionless thickness:

$$B = \frac{e}{L}$$

and the following dimensionless properties:

Dimensionless conductivity:

$$\kappa^* = \frac{\kappa}{\kappa_f}$$

Dimensionless permeability:

$$K^* = \frac{K}{K_f}$$

We obtain this set of dimensionless equations:

$$\nabla \cdot \mathbf{V}^* = 0 \quad (6)$$

$$\frac{\partial T^*}{\partial t^*} + \mathbf{V}^* \cdot \nabla T^* = \nabla \cdot (\kappa^*(x, y) \nabla T^*) \quad (7)$$

$$\frac{\partial \mathbf{V}^*}{\partial t^*} + \mathbf{V}^* \cdot \nabla \mathbf{V}^* = Pr \nabla^2 \mathbf{V}^* - \frac{Pr}{K^*(x, y) Da} \mathbf{V}^* - \nabla p^* + Ra Pr T^* \quad (8)$$

In the following the asterisks are omitted.

## Nomenclature

$A$  = cavity aspect ratio =  $H/L$   
 $B$  = dimensionless porous layer thickness  
 $c$  = isobaric specific heat, J/kg·K  
 $C$  = expansion of irregular grid  
 $D$  = constant in the irregular grid definition  
 $Da$  = Darcy number =  $K/L^2$   
 $e$  = porous layer thickness, m  
 $H$  = cavity height, m  
 $g$  = acceleration due to gravity,  $m/s^2$   
 $K$  = permeability,  $m^2$   
 $L$  = cavity width, m  
 $Nu$  = overall Nusselt number  
 $Nu_x$  = local Nusselt number

$p$  = pressure, Pa  
 $p, q$  = irregular grid coordinates, m  
 $Pr$  = Prandtl number =  $\nu/\alpha$   
 $R$  = conductivity ratio =  $\kappa_p/\kappa_f$   
 $Ra$  = Rayleigh number =  $g\beta\Delta TL^3/\nu\alpha$   
 $Ra^*$  = filtration Rayleigh number =  $RaDa$   
 $t$  = time, s  
 $T$  = temperature, K  
 $u$  = dimensionless velocity in  $x$  direction  
 $v$  = dimensionless velocity in  $y$  direction  
 $V$  = velocity vector, m/s  
 $x, y$  = Cartesian coordinates, m

$\alpha$  = thermal diffusivity =  $k/\rho c$ ,  $m^2/s$   
 $\beta$  = isobaric coefficient of thermal expansion of fluid  
 $\epsilon$  = porous media porosity  
 $\kappa$  = thermal conductivity,  $W/m \cdot K$   
 $\mu$  = dynamic viscosity of fluid,  $kg/m \cdot s$   
 $\rho$  = density,  $kg/m^3$   
 $\psi$  = dimensionless stream function

## Subscripts

$c$  = cooled surface  
 $f$  = fluid  
 $h$  = heated surface  
 $p$  = porous media  
 $s$  = solid

The boundary conditions are:

$$T = +0.5 \text{ and } u = v = 0 \text{ at } x = 0$$

$$T = -0.5 \text{ and } u = v = 0 \text{ at } x = 1$$

$$\partial T / \partial y = 0 \text{ and } u = v = 0 \text{ at } y = 0, A$$

**II.3 Numerical Procedure.** The transient equations are solved to obtain a steady-state solution. When a rather convergent result is approached, the transient terms vanish and the steady-state equations are solved. This formulation moreover allows us to detect instabilities.

The differential equations are discretized in space with the finite volume method. The physical model is discretized with three interlacing staggered meshes. The one for the scalar quantities ( $T$  and  $p$ ) is chosen so that the fluid boundaries lay on scalar points.

The SIMPLER algorithm, proposed by Patankar (1980), is used to solve the velocity-pressure coupling. At each iteration, five linear systems have to be solved: the momentum and energy equations and two pressure equations. They are all treated the same way. The temporal integration is done using an alternate direction implicit method. Each tridiagonal system is then solved according to the Thomas algorithm. The pressure equation and the pressure correction equation are written using an instantaneous form and are solved iteratively.

Each time step requires between  $2 \times 10^{-4}$  and  $5 \times 10^{-4}$  CPU seconds for each grid point on a CRAY II. A large part of this CPU time is spent solving the pressure and pressure correction equations. For  $Ra = 10^7$ , about 100 iterations for both pressure equations are required at each time step during the first iterations. If this number is reduced, the total number of time steps is increased. Indeed, it appears necessary to have a quite good value of pressure at each time step to accelerate the convergence. The choice of the criterion for the convergence of those equations is then particularly important. A good compromise between the number of iterations on the pressure equations and the total number of time steps must be found.

For high Rayleigh numbers, thin momentum boundary layers are seen near the vertical walls, whereas the fluid is nearly stagnant in the central region. The thickness of this layer decreases with the Rayleigh number. Use of nonuniform grids permits the presence of several discretization points in the boundary layer without introducing an excessive number of grid points, which would induce high CPU costs. The functions used to define the mesh size permit the introduction of a fine grid size near the surfaces and a coarse one in the core region. These functions also allow us to consider very thin porous layers. For both the  $x$  and  $y$  directions the stretching functions are:

$$x, y = D(e^{Cp,q} - 1) \text{ for } 0 \leq x, y \leq L/2 \quad (9)$$

$$x, y = 1 - D(e^{C(1-p,q)} - 1) \text{ for } L/2 \leq x, y \leq L \quad (10)$$

where  $x$  and  $y$  are the irregular grid coordinates and  $p$  and  $q$  are the regular ones.  $C$  is the grid expansion and the constant  $D$  is given by:

$$D = 0.5 / (e^{C/2} - 1) \quad (11)$$

It is known that the formal truncation error deteriorates when using nonuniform meshes, especially for abrupt changes in mesh spacing. Hence, the stretching parameter should be carefully chosen according to the number of grid points and boundary layer thickness. That is why in our calculations the ratio of the maximum and minimum values of the space interval does not exceed 7.

### III Code Validation

In order to validate this code, our result in a square enclosure

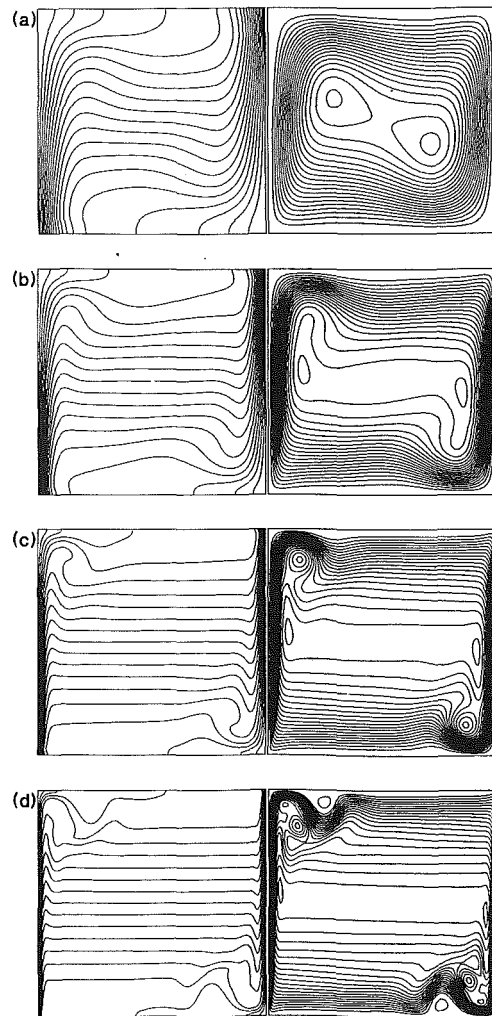


Fig. 2 Isotherms and streamlines: (a)  $Ra = 10^5$ ; (b)  $Ra = 10^6$ ; (c)  $Ra = 10^7$ ; (d)  $Ra = 10^8$

filled with air ( $Pr = 0.71$ ), without any porous layer has been compared to the benchmark solutions reported in the literature.

Figure 2 shows temperature and stream function fields for Rayleigh values from  $10^5$  to  $10^8$ . It should be noted that  $Ra = 10^8$  is close to the critical Rayleigh number for the onset of oscillatory flows ( $Ra = 2 \times 10^8$ ; Paolucci and Chenoweth, 1989). For this reason we have not been able to obtain a really steady solution for this Rayleigh number. In spite of this point, the flow structure is in good agreement with the results of Le Quéré (1987) who used a spectral method. The "hydraulic jump," which is one of the dominant features of natural convection flows in differentially heated cavities with adiabatic endwalls at high Rayleigh numbers, can especially be seen.

Numerical solutions are then presented and compared with benchmark solutions in Table 1 for  $Ra$  ranging from  $10^5$  to  $10^8$ . The following grid sizes were used:

$$Ra = 1 \times 10^5: \quad 48 \times 48 \quad C = 3$$

$$Ra = 1 \times 10^6: \quad 64 \times 64 \quad C = 3$$

$$Ra = 1 \times 10^7: \quad 80 \times 80 \quad C = 3$$

$$Ra = 1 \times 10^8: \quad 80 \times 80 \quad C = 3$$

and the following results are supplied:

$\overline{Nu}$  = average Nusselt number defined as follows:

$$\overline{Nu} = \int Nu_x \cdot dx \text{ where } Nu_x = \int \left( uT - \frac{\partial T}{\partial x} \right) \cdot dy;$$

**Table 1 Comparison of results in the case of the air-filled cavity**

|               | $\bar{Nu}$ | $U_{max}$ | $V_{max}$ | $\psi_{max}$ | $\psi_{mil}$ |
|---------------|------------|-----------|-----------|--------------|--------------|
| $Ra = 10^5$   |            |           |           |              |              |
| De Vahl Davis | 4.517      | 34.81     | 68.22     | 9.644        | 9.142        |
| Le Quéré      | 4.523      | 34.75     | 68.64     | 9.619        | 9.112        |
| Abrous        | 4.584      | 34.41     | 69.32     | —            | —            |
| Present work  | 4.521      | 33.63     | 68.53     | 9.544        | 9.08         |
| $Ra = 10^6$   |            |           |           |              |              |
| De Vahl Davis | 8.798      | 65.33     | 216.75    | 16.96        | 16.53        |
| Le Quéré      | 8.826      | 64.83     | 220.56    | 16.81        | 16.39        |
| Abrous        | 9.052      | 69.01     | 222.7     | —            | —            |
| Present work  | 8.794      | 64.07     | 219.82    | 16.82        | 16.53        |
| $Ra = 10^7$   |            |           |           |              |              |
| Upson         | 16.34      | 147.56    | 728.23    | 29.69        | —            |
| Le Quéré      | 16.51      | 148.8     | 699.3     | 29.87        | 29.27        |
| Abrous        | 16.18      | 130       | 675       | —            | —            |
| Present work  | 16.38      | 141.09    | 694.2     | 30.17        | 29.03        |
| $Ra = 10^8$   |            |           |           |              |              |
| Markatos      | 32.04      | 514.43    | 1812      | —            | —            |
| Le Quéré      | 30.28      | 316       | 2222      | 53.76        | 52.07        |
| Abrous        | 32.84      | 544       | 2036      | —            | —            |
| Present work  | 29.39      | 271.88    | 2205      | 51.62        | 51.34        |

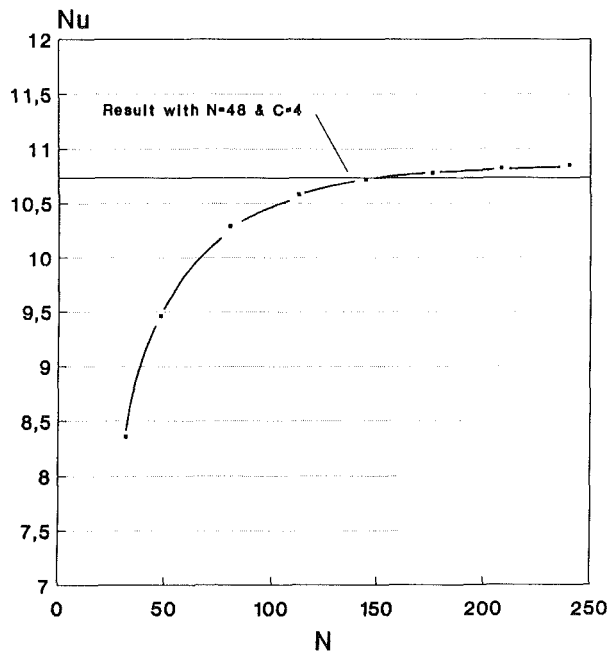


**Fig. 3 Evolution of Nusselt number with grid size for  $Ra = 10^7$ ,  $Da = 10^{-4}$ , and  $B = 0.1$**

$U_{max}$  = maximum horizontal velocity on the vertical midplane;  
 $V_{max}$  = maximum vertical velocity on the horizontal midplane;  
 $\psi_{max}$  = maximum stream function;  
 $\psi_{mild}$  = stream function at the midpoint of the cavity.

For  $Ra = 10^5$  and  $Ra = 10^6$  we report the benchmark solution of de Vahl Davis (1983), and those published by Le Quéré (1987), and Abrous and Emery (1989) who used a control volume finite difference technique based on the SIMPLE algorithm. Our results are in excellent agreement with them.

For higher Rayleigh number,  $10^7$  and  $10^8$ , our results are compared with the ones published by Upson et al. (1981), who used a finite element method, and those of Markatos and Pericleous (1984) using a finite volume method. It is to be noted that Abrous and Emery (1989) and Markatos and Pericleous (1984) use a  $k-\epsilon$  model to account for turbulence for  $Ra \geq 10^7$ . Since the end of the steady laminar regime occurs at about  $Ra \cong 2 \times 10^8$ , a turbulence model is useless before this value. As can be shown, our results are in better agreement with those given by Upson and Le Quéré, who did not use any turbulence model.

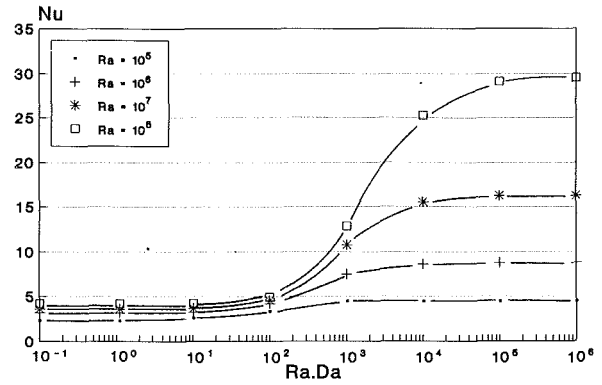


**Fig. 4 Variations of Nusselt number with  $Ra \cdot Da$  for  $Ra = 10^5$ ;  $Ra = 10^6$ ;  $Ra = 10^7$ , and  $Ra = 10^8$ , and  $B = 0.1$**

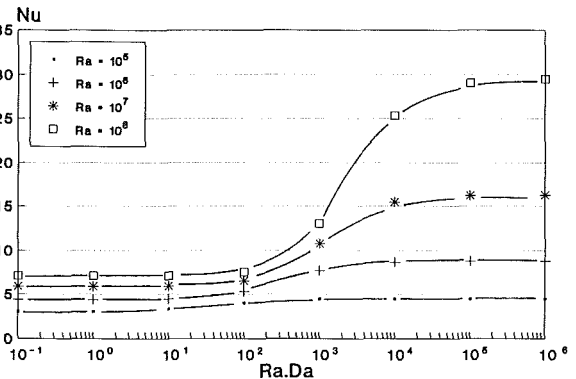


**Fig. 5 Variations of Nusselt number with  $Ra \cdot Da$  for  $Ra = 10^5$ ;  $Ra = 10^6$ ;  $Ra = 10^7$ , and  $Ra = 10^8$ , and  $B = 0.05$**

In order to verify the numerical accuracy of the results we have refined a uniform grid from  $32^2$  up to  $208^2$  points. Figure 3 presents the values of  $Nu$  obtained by using the different grids for  $Ra = 10^7$ ,  $Da = 10^{-4}$ , and  $e = 0.1$ . It appears that increasing the number of grid points from  $128^2$  and  $240^2$  only induces an increase of 1.7 percent of the Nusselt number. It means that the  $128^2$  grid already gives an accurate solution.

For the calculations carried out on nonuniform grids of  $48^2$  nodes, an expansion  $C = 4$  was used. It corresponds to a ratio of 6.8 between the greatest and the lowest interval space. The value of Nusselt number obtained in this configuration is plotted on Fig. 3. An accuracy of the same order as for a uniform grid of 150 nodes is obtained. This grid is then used for the following calculations.

#### IV Results and Conclusion in the Case of the Cavity With Thin Layers on Its Vertical Sides

The main effect of the introduction of the porous layers on the vertical sides of the cavity is to decrease the overall heat transfer between the hot and the cold wall. The influence of four parameters is analyzed here, namely: Rayleigh number, Darcy number, layer thickness, and conductivity ratio. The fluid considered is the air of Prandtl number 0.71 and the aspect ratio is  $A = 1$ . The Rayleigh number is increased from  $10^5$  up to  $10^8$ .

**IV.1 Influence of Rayleigh Number.** The variations of the Nusselt number with the product of Rayleigh and Darcy numbers,  $Ra$  and  $Da$ , are reported on Figs. 4 and 5 for four Rayleigh numbers ( $10^5$ ,  $10^6$ ,  $10^7$ , and  $10^8$ ) and two porous layer thicknesses (0.1 and 0.05). In the following, the product  $Ra \times Da$  will be called filtration Rayleigh number and will be noted  $Ra^*$ .

It can be seen that the higher the Rayleigh number, the stronger the decrease of the Nusselt number. For a thickness

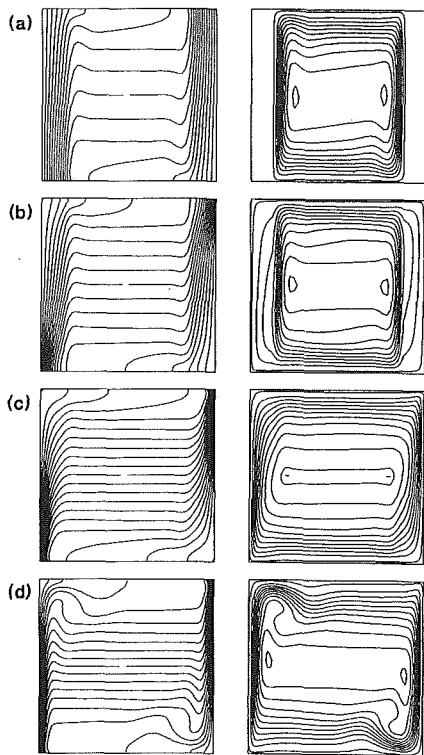


Fig. 6 Isotherms and streamlines for  $Ra = 10^7$  and  $B = 0.1$ : (a)  $Ra \cdot Da = 10^{-1}$ , (b)  $Ra \cdot Da = 10^2$ , (c)  $Ra \cdot Da = 10^3$ , (d)  $Ra \cdot Da = 10^4$

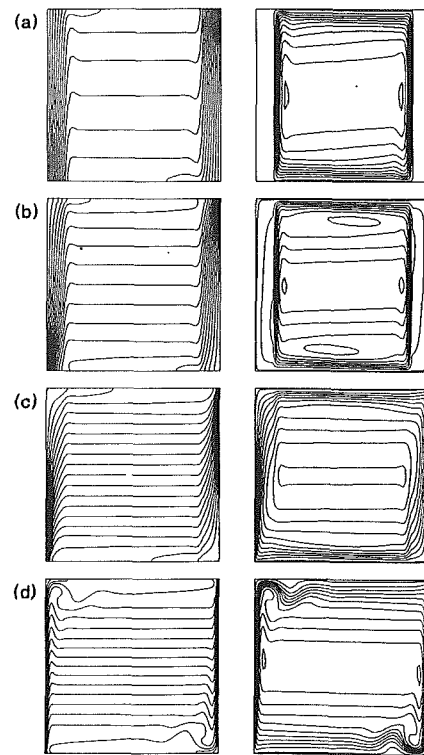


Fig. 7 Isotherms and streamlines for  $Ra = 10^8$  and  $B = 0.1$ : (a)  $Ra \cdot Da = 10^{-1}$ , (b)  $Ra \cdot Da = 10^2$ , (c)  $Ra \cdot Da = 10^3$ , (d)  $Ra \cdot Da = 10^4$

value of 0.1, the fall is about 78 percent for  $Ra = 10^7$  and 86 percent for  $Ra = 10^8$ . Accordingly, the porous layers have a more important influence for the high Rayleigh number values. When the permeability is small enough to consider that there is no convection in the porous layers, the heat flux transferred by conduction and natural convection through the composite cavity could be estimated from the thermal resistance concept. The nondimensional heat flux is given by:

$$Nu = \frac{1}{2B + 1/q} \quad (12)$$

The expression of  $q$ , the convective heat transfer, is then:

$$q = \frac{Nu}{1 - 2BNu} \quad (13)$$

In order to have a positive value of  $q$  the Nusselt number must satisfy

$$Nu < \frac{1}{2B} \quad (14)$$

For example, for  $B = 0.1$  the maximum value of  $Nu$  is 5, and for  $B = 0.05$  it is 10. This can be verified in Figs. 4 and 5. This means that even for very high Rayleigh numbers, when the permeability is very small, the Nusselt number cannot be greater than this value.

This remark is important in a lot of real applications, particularly in the case of thermal insulation problem where Rayleigh numbers are generally greater than  $10^8$ . In a room that is three meters width, in which the hot wall is  $20^\circ\text{C}$  and the cold one  $0^\circ\text{C}$ , the Rayleigh number is about  $10^{11}$ . It has been noted before that the transition between steady laminar flow and unsteady flow occurs at about  $Ra = 10^8$ , which means that the flow is often turbulent in building insulation applications and a turbulence model would be necessary to study those cases. It will be the subject of a future study. However, even if our numerical code does not permit us to conclude for very high Rayleigh number applications, we know that the

Nusselt number will not exceed 5 for  $B = 0.1$  and 10 for  $B = 0.05$  for low permeabilities. It means that the relative reduction due to the porous layers will be very strong for high Rayleigh numbers. Hence, the porous layers will be efficient when they are really necessary.

**IV.2 Influence of Permeability.** Figures 4 and 5 show the variation of Nusselt number with permeability. Indeed, the Darcy number is defined as the ratio of the permeability to the square of the cavity width, and thereby  $Ra^*$  increases with the permeability. Three zones can be distinguished in Figs. 4 and 5. When the filtration Rayleigh number  $Ra^*$  is lower than 100, it has a relatively weak impact on the heat transfer. In this case, the porous medium has such a small permeability that it acts almost like a solid material. In the second zone, where  $Ra^*$  is between 100 and 10,000, the Nusselt number increases strongly with  $Ra^*$ . The porous layers are then really efficient. Finally, for  $Ra^*$  greater than 10,000, the Nusselt number remains nearly constant. The porous medium is too permeable to have a significant impact on the heat transfer and it has a "fluid behavior."

Those three zones can also be distinguished on the flow patterns shown on Figs. 6 and 7 for two Rayleigh numbers ( $10^7$  and  $10^8$ ), and for an increase of the Darcy number. For a low  $Ra^*$  value, the flow takes place in the fluid part of the cavity, and the heat is only transferred by conduction in the porous medium. Consequently the temperature profile is linear in the porous layers. The porous medium has a "solid behavior." For increasing values of  $Ra^*$ , the fluid penetrates into the porous layers and a significant change in the flow pattern can be seen. When the permeability is very high, the flow pattern is similar to the one in the square cavity without any porous media.

The vertical velocity profiles on the horizontal midplane, reported in Figs. 8 and 9, for  $Ra = 10^8$  show the transition that occurs between the values  $10^2$  and  $10^3$  of  $Ra^*$ . In this area, two velocity peaks can be seen. The first one takes place in

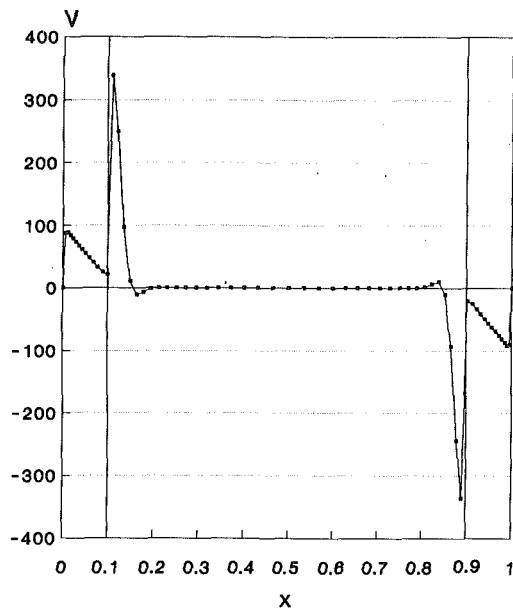


Fig. 8 Vertical velocity on the horizontal midplane:  $Ra = 10^8$ ,  $Ra \cdot Da = 10^2$ ,  $B = 0.1$

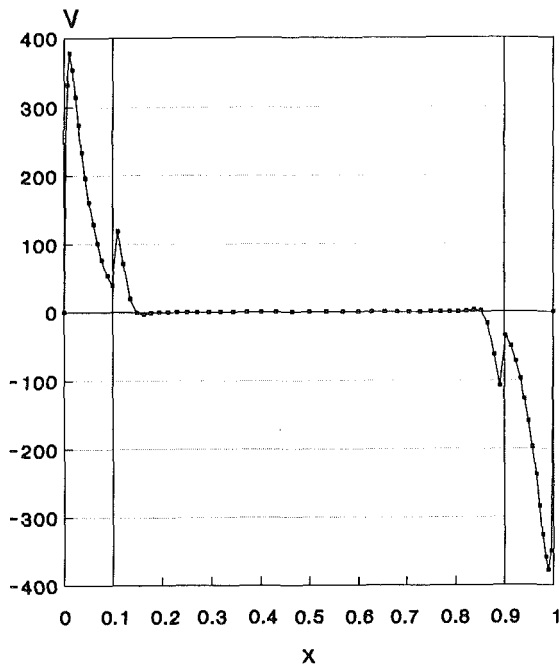


Fig. 9 Vertical velocity on the horizontal midplane:  $Ra = 10^8$ ,  $Ra \cdot Da = 10^3$ ,  $B = 0.1$

the porous layer and corresponds to the boundary layer at the wall-porous medium interface. The second one takes place in the boundary layer at the fluid-porous media interface.

For  $Ra^* = 10^2$  (Fig. 8), the absolute maximum value of vertical velocity takes place in the fluid part. Moreover, the velocity profile is linear in the porous layer and follows the Darcy law except near the wall. It can be noted that, according to the Brinkman model, the boundary layer thickness,  $\delta'$ , is theoretically of the order of  $\sqrt{K_p}$ . For  $Ra = 10^8$ , the permeability is  $10^{-6}$ , and  $\delta'$  should be about  $10^{-3}$ . It can be approximately verified in Fig. 10.

For  $Ra^* = 10^3$  (Fig. 9), the permeability is increased, and there is a better fluid penetration in the porous layer. The boundary layer in the porous medium is like a fluid boundary layer, and the absolute maximum value takes place in it. Nevertheless, there still exists a second fluid boundary layer at the

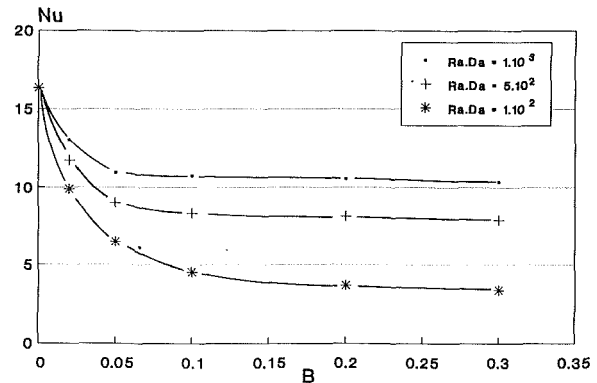


Fig. 10 Variations of Nusselt number with thickness  $e$  and Darcy number  $Da$

fluid-porous medium interface, but this second velocity peak is lower than the first one.

Between those two values of  $Ra^*$ , there is a point where both vertical velocity peak on the horizontal midplane have the same value. This point corresponds, on Figs. 4 and 5, to the area in which the Nusselt number strongly begins to increase with the permeability.

Recently, Beckermann et al. (1987) found experimentally and numerically that the penetration into the porous layer is significant if the filtration Rayleigh number  $Ra^*$  is greater than about 50. It must be noted that they studied the case of a square cavity with a large porous layer adjacent to one of the vertical walls. In our configuration, the penetration of the fluid is significant for  $Ra^*$  greater than about 100.

**IV.3 Influence of Porous Layer Thickness.** Figures 4 and 5 show that the decrease of the heat transfer increases with the porous layer thickness value. For  $Ra = 10^8$  and  $Da = 10^{-6}$ , for example, the fall is about 26 percent for  $B = 0.05$  and 17 percent for  $B = 0.1$ .

Nevertheless, it can be shown that it is not necessary to introduce a very high thickness of porous medium to obtain a significant decrease of the heat transfer. Figure 10 shows the variations of Nusselt number with the porous layer thickness  $B$ , for  $Ra^* = 1 \times 10^3$ ,  $5 \times 10^2$ , and  $1 \times 10^2$  and for a fixed Rayleigh number  $Ra = 10^7$ . The Darcy values are chosen in order to have a filtration Rayleigh number between  $10^2$  and  $10^3$ . This interval corresponds to the zone in which the transition "fluid behavior" to "solid behavior" occurs. For a thickness value greater than 0.1, the Nusselt number decreases very slowly for an increasing thickness, whereas for a thickness lower than 0.1, a small addition of porous medium causes a sharp decrease in the Nusselt number. It can also be noted that the decrease of the Nusselt number is more pronounced for the lowest value of permeability. To explain the first observation, let us come back to the fluid cavity problem. A thickness  $\delta$  can be defined as the length between the wall and the first point where the vertical median velocity is zero. For  $Ra = 10^7$ , this thickness is 0.1. Then, it can be deduced that in order to have a significant decrease of the Nusselt number, a porous layer thickness equal to  $\delta$  is sufficient. When the Rayleigh number is  $10^8$ , the  $\delta$  value is 0.05. The role of the porous layer is actually to flatten the vertical velocity profile near the vertical walls and to reduce the upwind flow and then to reduce the convective heat transfer in the area where it is the strongest. When the layer thickness becomes greater than  $\delta$ , the Nusselt number has a nearly constant value, which corresponds to the case of a porous cavity. This means that introducing porous material in the core region in which the flow is not very dynamic only induces a very small decrease of the heat transfer. Hence, because the boundary layer thickness decreases for high Rayleigh numbers, the porous layer thick-



ness needed to obtain a significant decrease of Nu will also decrease for high Rayleigh numbers. This is interesting for real applications in which the Rayleigh number is often high, because it will not be necessary to introduce thick layers to have a strong decrease of the heat transfer.

**IV.4 Influence of Conductivity Ratio.** Figure 11 presents the variations of the global heat transfer with the conductivity ratio  $R$  for several values of  $Ra^*$ . It shows a great influence of the porous medium conductivity on the Nusselt number. The decrease of heat transfer shown on Figs. 4 and 5 is obviously less important when the conductivity ratio becomes greater than one. For example, when  $Ra^*$  is decreased from an infinite value to  $Ra^* = 10^3$  for  $Ra = 10^7$ , the decrease of Nusselt number is 64 percent for  $R = 1$ , whereas it is only 50 percent for  $R = 2$ , and 20 percent for  $R = 5$ .

But for practical applications like thermal insulation of buildings, this point is not really important. The most permeable glass wool, usually used in such applications, has a permeability equal to about  $10^{-8} \text{ m}^2$ . If the characteristic length is 1 m, the Darcy number is  $10^{-8}$ , and then the filtration Rayleigh number is equal to 0.1. Figure 4 shows that for this value of  $Ra^*$ , the porous medium acts as a solid material. It is known that the conductivity of such a material does not exceed about two times the air conductivity. This means that Figs. 4 and 5 can be used for practical applications even if no variation of the conductivity ratio was introduced.

**IV.5 Decrease in Temperature Difference of the Facing Surfaces.** The radiative heat transfer between the hot and cold walls can be evaluated as the product of a heat transfer coefficient and the difference of the opposing surfaces temperatures. In the case of a fluid cavity this temperature difference corresponds to the difference between the hot wall temperature  $T_H$  and the cold one  $T_C$  (i.e.,  $+0.5$  and  $-0.5$ ). When the porous layers are introduced, the facing surfaces are not isothermal, as can be seen in Figs. 6 and 7. Nevertheless, the radiative heat transfer can be approximated by the difference of their average temperature. For example, for  $Ra = 10^7$  and  $Da = 10^{-5}$ , the average temperature is about 0.1 for a layer thickness of  $e = 0.1$  (the cold one is  $-0.1$ ). This means that the radiative heat transfer will be considerably decreased.

## V Conclusions

An accurate numerical solution for the high Rayleigh number laminar natural convection flow in the square cavity heated from the vertical side is presented, and is in excellent agreement with the previous results. The effects of introduction of thin porous layers along vertical walls are then studied.

It is shown that the reduction of overall Nusselt number increases with Rayleigh number and becomes really significant for high Rayleigh numbers corresponding to real applications. The decrease of global heat transfer also decreases with the layer thickness. It is nevertheless of no use to take thicknesses greater than the fluid boundary layer width to have a significant reduction. The role of porous media is to reduce very high values of vertical velocities that occur in boundary layers. An increase of the layer thickness only induces a low decrease of Nusselt number and is only due the reduction of the cavity width. We also show that the global heat transfer decreases for a decreasing permeability.

Finally, the heat transfer decrease is less strong when a conductivity ratio is taken into account. But it has been shown that the material used in practical applications may have a very low permeability together with a low conductivity.

As a conclusion, another interesting effect of porous layers may be pointed out. It is especially important in the case of the thermal insulation of a room in which one wall is cold and the other is hot, both being covered with a thin porous layer.

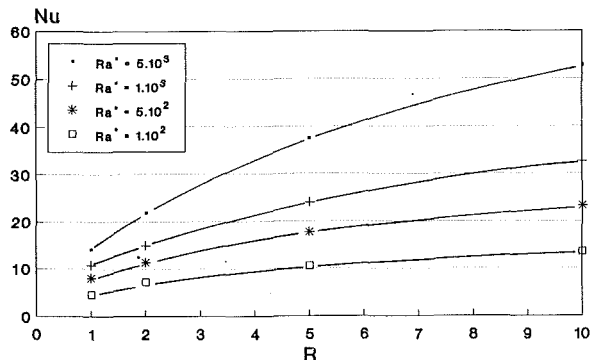


Fig. 11 Variations of Nusselt number with conductivity ratio  $R$  and Darcy number  $Da = 10^7$

Their effects will be of three types. The first, which have already been shown, are the reduction of Nusselt number and radiative heat transfer. The third is a consequence of the last shown effect and deals with a notion of comfort. We have shown that the difference of the average temperature of the opposing vertical surfaces is considerably reduced by the adjunction of porous layers. It is obvious that a room in which there is a little difference of temperature between the two vertical walls is more comfortable than one where temperature gradient is important.

## Acknowledgments

Computation means have been granted by the C.C.V.R. Scientific Committee. The authors also wish to thank the C.N.U.S.C. for the facilities we were given.

## References

- Abrous, A., and Emery, A. F., 1989, "Turbulent Free Convection in Square Cavities With Mixed Boundary Conditions," *Heat Transfer in Convective Flows*, ASME HTD-Vol. 107.
- Arquis, E., and Caltagirone, J. P., 1987, "Interacting Convection Between Fluid and Open Porous Layers," ASME Paper No. 87-WA/HT-24.
- Beckermann, C., Ramadhyani, S., and Viskanta, R., 1987, "Natural Convection Flow and Heat Transfer Between a Fluid Layer and a Porous Layer Inside a Rectangular Enclosure," ASME JOURNAL OF HEAT TRANSFER, Vol. 109, pp. 363-370.
- Beckermann, C., Viskanta, R., and Ramadhyani, S., 1988, "Natural Convection in Vertical Enclosures Containing Simultaneously Fluid and Porous Layers," *Journal of Fluid Mechanics*, Vol. 186, pp. 257-284.
- De Vahl Davis, G., 1983, "Natural Convection of Air in a Square Cavity: A Bench Mark Numerical Solution," *International Journal of Numerical Methods in Fluids*, Vol. XX, pp. 227-248.
- Le Quéré, P., 1987, "Etude de la Transition à l'Instationnarité des Ecoulements de Convection Naturelle en Cavité Verticale Différentiellement Chauffée par des Méthodes Spectrales Chebyshev," Thesis, Université de Poitiers, France.
- Lauriat, G., and Mesguich, F., 1984, "Natural Convection and Radiation in an Enclosure Partially Filled With a Porous Insulation," ASME Paper No. 84-WA/HT-101.
- Markatos, N. C., and Pericleous, K. A., 1984, "Laminar and Turbulent Natural Convection in an Enclosed Cavity," *International Journal of Heat and Mass Transfer*, Vol. 28, pp. 125-138.
- Paolucci, S., and Chenoweth, D. R., 1989, "Transition to Chaos in a Differentially Heated Vertical Cavity," *Journal of Fluid Mechanics*, Vol. 201, pp. 379-410.
- Patankar, S. V., 1980, *Numerical Heat Transfer and Fluid Flow*, Hemisphere Publishing Corp., Washington, DC.
- Poulikakos, D., and Bejan, A., 1983, "Natural Convection in Vertically and Horizontally Layered Porous Media Heated From the Side," *International Journal of Heat and Mass Transfer*, Vol. 26, pp. 1805-1814.
- Somerton, C. W., and Catton, I., 1982, "On the Thermal Instability of Superposed Porous and Fluid Layers," ASME JOURNAL OF HEAT TRANSFER, Vol. 104, pp. 160-165.
- Turki, S., and Lauriat, G., 1990, "An Examination of Two Numerical Procedures for Natural Convection in Composite Enclosures," *Numerical Heat Transfer*, ASME HTD-Vol. 130, pp. 107-113.
- Upton, C. D., Gresho, P. M., and Lee, R. L., 1981, "Finite Element Simulations of Thermally Induced Convection in an Enclosed Cavity," *Numerical Solutions for a Comparison Problem on Natural Convection in an Enclosed Cavity*, United Kingdom Atomic Energy Authority, HARWELL.

# On the Low Rayleigh Number Asymptote for Natural Convection Through an Isothermal, Parallel-Plate Channel

L. Martin

G. D. Raithby  
Mem. ASME

M. M. Yovanovich  
Fellow ASME

Department of Mechanical Engineering,  
University of Waterloo,  
Waterloo, Ontario, Canada N2L 3G1

*The problem of natural convection through a channel formed by isothermal, parallel plates forms a cornerstone of our understanding of a class of natural convection flows. Following the pioneering study of Elenbaas, it is widely accepted that there is a fully developed régime, at low Rayleigh number, in which the Nusselt number becomes directly proportional to the Rayleigh number. This paper gives a detailed analysis of heat transfer in this régime. It is concluded that the previous numerical studies, which appeared to confirm this asymptote, used inappropriate boundary conditions, and that the asymptotic behavior should, in fact, not be expected except under very special conditions.*

## Introduction

Heat release in a cavity that has openings to cooler surroundings induces a natural convection flow. There are many examples of such flows (e.g., chimneys, parallel plate fins, computer boards, etc.), but probably the most extensively studied and well understood is the natural convection flow induced by parallel heated isothermal plates. A definition sketch for this problem appears in Fig. 1(A); the objective is to predict the total heat flow  $Q$  to the fluid from the surfaces of the plates that face each other.

Elenbaas (1942) did an exhaustive pioneering study of this problem. By analyzing a simplified set of equations, and by adjusting constants to fit experimental data, he proposed the following equation for the Nusselt number:

$$Nu = \frac{Ra^*}{3} [1 - e^{-35/16 Ra^*}]^{3/4} \quad Ra^* = Ra \frac{b}{L_c} \quad (1)$$

This relation is plotted in Fig. 2. One remarkable feature of the expression is that the channel aspect ratio,  $L_c/b$ , does not appear explicitly, but has been absorbed into a modified Rayleigh number,  $Ra^*$ , called the Elenbaas Rayleigh number. Equation (1) also yields the two asymptotes

$$Nu \rightarrow Nu_{bl} = 0.60 Ra^{*1/4} \quad Ra^* \rightarrow \infty \quad (2A)$$

$$Nu \rightarrow Nu_{fd} = \frac{1}{3} Ra^* \quad Ra^* \rightarrow 0 \quad (2B)$$

where  $Nu_{bl}$  is the Nusselt number for the boundary layer régime and  $Nu_{fd}$  is the Nusselt number for fully developed flow throughout the flow passage. Elenbaas provided an impressive collection of data that confirmed Eq. (1) over the range  $10^{-1} < Ra^* < 10^5$ .

Raithby and Hollands (1975) derived a different relation that also captures both limiting cases. Bar-Cohen and Rohsenow (1984) provided a comprehensive review of this and related problems. Bar-Cohen and Rohsenow (1984), and Raithby and Hollands (1985) correlated the heat transfer results using a blending function of the type proposed by Churchill and Usagi (1972). After modifying the coefficient in Eq. (2A)

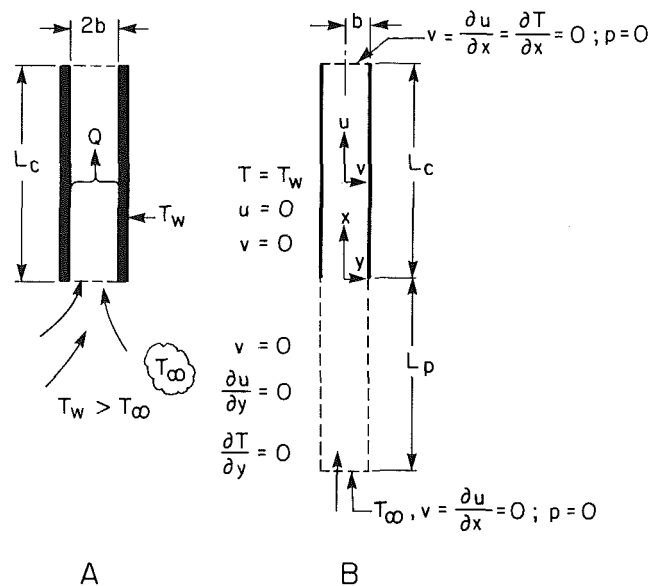


Fig. 1 Definition sketch for the generic parallel plate problem (A) and the specific problem analyzed in this paper (B)

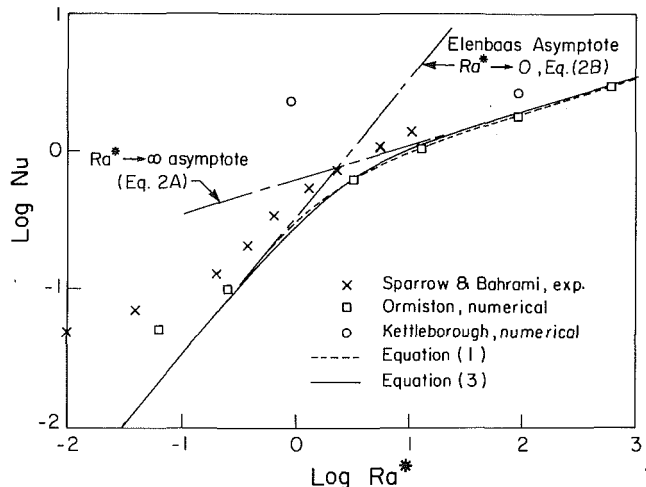


Fig. 2 Average heat transfer from a vertical parallel plate channel

Contributed by the Heat Transfer Division for publication in the JOURNAL OF HEAT TRANSFER. Manuscript received by the Heat Transfer Division March 7, 1990; revision received November 30, 1990. Keywords: Electronic Equipment, Natural Convection.

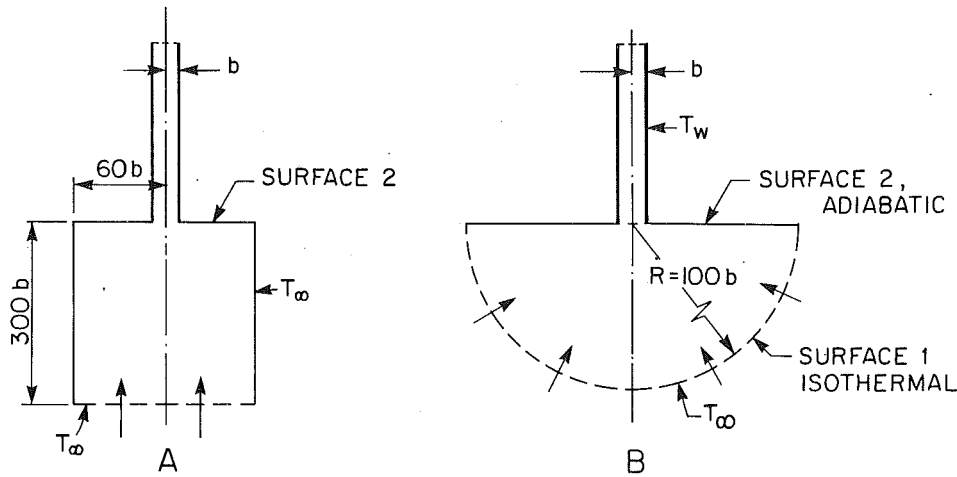


Fig. 3 Configurations assumed in numerical studies by Kettleborough (1972) and Nakamura et al. (1982), (A), and by Ormiston (1983), (B); solid and dotted lines represent impermeable and permeable boundaries, respectively

to agree with the measurements of Aung et al. (1972), the blended function is

$$Nu = (Nu_{fd}^m + Nu_{bl}^m)^{1/m}; \quad m = -1.9 \quad (3A)$$

where

$$Nu_{fd} = \frac{1}{3} Ra^* \quad (3B)$$

$$Nu_{bl} = 0.62 Ra^{*1/4} \quad (3C)$$

Equation (3) agrees closely with Eq. (1), as seen in Fig. 2.

Besides the experimental verification of Elenbaas (1942), Eqs. (1) and (3) are in close agreement with the parabolic solution reported by Bodia and Osterle (1962). Aihara (1973) carefully examined the effect of different inlet conditions for the parabolic problem and his predictions also agree closely with Eqs. (1) and (3).

Based on these and other confirmations, the current conclusion seems to be that natural convection heat transfer in an isothermal parallel-plate channel is a fully resolved problem, at least for the laminar flow régime.

There have been the disquieting pieces of evidence, however,

that suggest major discrepancies with the Elenbaas' asymptote for fully developed heat transfer, Eq. (3B). Sparrow and Bahrami (1980), using the naphthalene sublimation technique, measured a higher transfer rate in this régime; their data, converted to equivalent heat transfer, are shown in Fig. 2. They argued that the large corrections Elenbaas used to account for radiation and edge effects had caused fortuitous agreement with the theoretical fully developed asymptote. During the sublimation process, however, heat must be absorbed by the solid naphthalene, and this must be drawn from both the plates and the gas. If a significant portion of the heat transfer comes from the gas, the buoyancy forces induced by the cooling can be shown to be of the same order as the buoyancy forces due to concentration changes. It can be argued, therefore, that this effect could account for the discrepancy between their measurements and Elenbaas' data.

Kettleborough (1972) and Nakamura et al. (1982) solved the full (elliptic) equations of motion for the geometry shown in Fig. 3(A). Kettleborough's predicted heat transfer was much higher than Elenbaas' curve (Fig. 2). The predictions of Nakamura et al. (1982) for the same geometry were in reasonable

## Nomenclature

|  |   |   |
|--|---|---|
| $b$ = half-width of channel, Fig. 1  | upstream plenum boundary  | $T_\infty$ = temperature of the ambient fluid and of the inlet of the plenum, K |
| $c_p$ = specific heat at constant pressure, J/kg K                           | $Nu_{CONV}$ = Nu for the case $L_p^* \rightarrow \infty$              | $u, v$ = velocity components in the $x$ and $y$ directions, m/s                 |
| $g$ = gravitational acceleration, $m/s^2$                                    | $Nu_{fd}$ = Nu for the fully developed régime: Eq. (3B) or (24)       | $u_r$ = reference velocity = $L_c^* k / \rho c_p b$                             |
| $k$ = thermal conductivity, W/mK   | $\tilde{Nu}$ = $Nu(L_c^*)^2$  | $\bar{u}$ = average $u$ velocity in the channel                                 |
| $L_c$ = channel length, Fig. 1(B)  | $p$ = pressure, Pa  | $u^*, v^*$ = dimensionless velocities: $u^* = u/u_r, v^* = v/v_r$               |
| $L_c^*$ = $L_c/b$  | $p^*$ = $p/\rho u_r^2$  | $v_r$ = reference velocity = $k/\rho c_p b$                                     |
| $L_p$ = plenum length, Fig. 1(B)   | $Pe$ = Peclet number = $\rho b \bar{u} c_p / k$                       | $x, y$ = coordinates, see Fig. 1(B)   |
| $L_p^*$ = $L_p/b$  | $Pr$ = Prandtl number = $\mu c_p / k$                                 | $x^*$ = $x/L_c$   |
| $m$ = mass flow rate through the channel, per unit depth = $\rho \bar{u} 2b$ | $Q$ = total heat transfer from both plates, per unit depth of channel | $y^*$ = $y/b$   |
| $Nu$ = Nusselt number = $[Q/2L_c(T_w - T_\infty)](b/k)$                      | $Ra$ = Rayleigh number = $g\beta(T_w - T_\infty)b^3/\nu\alpha$        | $\beta$ = thermal expansion coefficient, $1/K$                                  |
| $Nu_{bl}$ = Nusselt number for the laminar boundary layer régime, Eq. (3c)   | $Ra^*$ = Elenbaas Rayleigh number = $Ra(b/L_c)$                       | $\theta$ = nondimensional temperature = $(T - T_\infty)/(T_w - T_\infty)$       |
| $Nu_{COND}$ = Nu for conduction between the plates and the                   | $\tilde{Ra}$ = modified Rayleigh number = $Ra^*(L_c^*)^2$             | $\mu$ = dynamic viscosity, kg/ms  |
|  | $T$ = temperature, K  | $\rho$ = fluid density, $kg/m^3$  |
|  | $T_w$ = temperature of the isothermal plates, K                       |   |

agreement with Eq. (1) or (3) but only one predicted point fell in the fully developed régime. Ormiston (1983) predicted flow and heat transfer for the geometry shown in Fig. 3(B). He was able to show that counterflow heat conduction, out the inlet, caused his Nusselt numbers (see Fig. 2) to lie well above the fully developed prediction of Elenbaas for low values of  $Ra^*$ , even when the semicircular inflow boundary (Fig. 3B) was far removed from the plates. These results exhibit the trends already seen in Sparrow and Bahrami's data, and the questions concerning the validity of both Elenbaas' data and the earlier analyses for low Rayleigh numbers become more difficult to dismiss.

Because the problem of natural convection through parallel plate channels is arguably the most important cornerstone problem of the open-cavity type, it is imperative that the flow and heat transfer at low Rayleigh numbers be understood. The purpose of this paper is to explore this low Rayleigh number régime.

## Description of Problem

Because the purpose of this study is to enhance understanding, it is helpful to select the simplest geometric arrangement that still contains the relevant physics. The flow is therefore taken to be steady and two dimensional (no variation normal to the plane of Fig. 1A). If there is a large array of plates (such as a stack of circuit boards) at the same temperature, the flow and heat transfer in the channels in the central portion of the array will be the same, so it is sufficient to analyze one channel. Further assuming that the plates are thin, the problem reduces to that shown in Fig. 1(B). On the channel boundaries (solid lines) the velocity will be zero and the temperature fixed at  $T_w$ . In the plenum upstream of the channel, sheltering by neighboring plates will result in symmetry along the vertical dotted lines ( $v = \partial u / \partial y = \partial T / \partial y = 0$ ). The flow is assumed to enter the upstream plenum boundary at temperature  $T_\infty$ . Fully developed conditions ( $v = \partial u / \partial x = \partial T / \partial x = 0$ ) are prescribed at the downstream boundary, but the limitations of these conditions are discussed later. Furthermore, the pressure at one point on the inlet and exit plane are set to the same value.

**Equations of Motion and Their Numerical Solution.** The two-dimensional equations of motion for steady flow of a Newtonian fluid with constant properties are

$$\frac{\partial u}{\partial x} + \frac{\partial v}{\partial y} = 0 \quad (4)$$

$$\frac{\partial}{\partial x}(\rho u u) + \frac{\partial}{\partial y}(\rho v u) = -\frac{\partial p}{\partial x} + \mu \left( \frac{\partial^2 u}{\partial x^2} + \frac{\partial^2 u}{\partial y^2} \right) + \rho \beta (T - T_\infty) g \quad (5)$$

$$\frac{\partial}{\partial x}(\rho u v) + \frac{\partial}{\partial y}(\rho v v) = -\frac{\partial p}{\partial y} + \mu \left( \frac{\partial^2 v}{\partial x^2} + \frac{\partial^2 v}{\partial y^2} \right) \quad (6)$$

$$\frac{\partial}{\partial x}(\rho c_p u T) + \frac{\partial}{\partial y}(\rho c_p v T) = k \left( \frac{\partial^2 T}{\partial x^2} + \frac{\partial^2 T}{\partial y^2} \right) \quad (7)$$

These equations were discretized on a Cartesian mesh, with the flexibility to concentrate the mesh along the walls and near the channel inlet where gradients in the dependent variables are expected to be greatest. The computational method used (see Martin, 1988) was a variant of the methods described by Patankar (1980) and Van Doormaal and Raithby (1984).

It is necessary to add to the boundary condition specification already given that the pressure was specified as zero (relative to atmospheric pressure) at only the center node on the inlet and exit planes. To accommodate this pressure specification,

one control-volume mass conservation equation was removed; this is permitted (in fact desirable—see Van Doormaal and Raithby, 1984) because the velocity boundary conditions make one control-volume continuity equation redundant on each of these planes.

An exhaustive study was undertaken by Martin (1988) to ensure that the code was free of errors and that the mesh was sufficiently fine to provide accurate predictions. For low  $Ra^*$ , solutions were obtained on a sequence of grids, and the value of  $Nu$  at zero grid spacing was estimated by extrapolation. The  $Nu$  values reported in this study used grids for which  $Nu$  is within 1 percent of this asymptote. For  $Ra^* \rightarrow 0$ , the  $Nu$  values obtained by the code were checked against results from a conduction analysis. At  $Ra^* = 229$ , where the boundary layer assumptions are expected to be valid, the present code predictions were found to agree with Aihara's (1973) predictions to within 1.1 percent. Based on these and other studies, all solutions reported in this paper give heat transfer and mass through flow rates that are believed accurate to within about 2 percent, with the accuracy of most results well within this bound. These predictions will be presented in later sections.

**Dimensional Analysis.** Introducing the nondimensional variables defined in the Nomenclature, Eqs. (4)–(7) become

$$\frac{\partial u^*}{\partial x^*} + \frac{\partial v^*}{\partial y^*} = 0 \quad (8)$$

$$u^* \frac{\partial u^*}{\partial x^*} + v^* \frac{\partial u^*}{\partial y^*} = -\frac{\partial p^*}{\partial x^*} + \text{Pr} \left( \left( \frac{1}{L_c^*} \right)^2 \frac{\partial^2 u^*}{\partial x^{*2}} + \frac{\partial^2 u^*}{\partial y^{*2}} \right) + Ra^* \text{Pr} \theta \quad (9)$$

$$u^* \frac{\partial v^*}{\partial x^*} + v^* \frac{\partial v^*}{\partial y^*} = -(L_c^*)^2 \frac{\partial p^*}{\partial y^*} + \text{Pr} \left( \left( \frac{1}{L_c^*} \right)^2 \frac{\partial^2 v^*}{\partial x^{*2}} + \frac{\partial^2 v^*}{\partial y^{*2}} \right) \quad (10)$$

$$u^* \frac{\partial \theta}{\partial x^*} + v^* \frac{\partial \theta}{\partial y^*} = \left( \frac{1}{L_c^*} \right)^2 \frac{\partial^2 \theta}{\partial x^{*2}} + \frac{\partial^2 \theta}{\partial y^{*2}} \quad (11)$$

The boundary conditions are

$$y^* = \pm 1; \quad 0 \leq x^* \leq 1: \quad u^* = v^* = 0 \quad \theta = 1 \quad (12A)$$

$$y^* = \pm 1; \quad -\frac{L_p^*}{L_c^*} \leq x^* \leq 0: \quad v^* = \frac{\partial u^*}{\partial y^*} = \frac{\partial \theta}{\partial y^*} = 0 \quad (12B)$$

$$x^* = -\frac{L_p^*}{L_c^*}, \quad -1 < y^* < 1: \quad v^* = \frac{\partial u^*}{\partial x^*} = \theta = 0; \quad p^* = 0(\text{1point}) \quad (12C)$$

$$x^* = 1, \quad -1 < y^* < 1: \quad v^* = \frac{\partial u^*}{\partial x^*} = \frac{\partial \theta}{\partial x^*} = 0; \quad p^* = 0(\text{1point}) \quad (12D)$$

If the parabolic approximation is made, all diffusion effects in the  $x$  direction are ignored ( $\partial^2(\ )/\partial x^{*2} = 0$ ), and the  $y$ -momentum equation is replaced by  $p^*(x, y) = p^*(x)$ . Because there is no diffusion in the  $x$  direction, there will be no change in the solution in the inlet region;  $-(L_p/L_c) < x^* < 0$ , so the solution of Eqs. (8)–(12) becomes independent of  $L_p^*$  and  $L_c^*$ . This results in the following functional dependence of the nondimensional heat transfer and flow rate

$$Nu = Nu(Ra^*, \text{Pr}); \quad \text{Pe} = \text{Pe}(Ra^*, \text{Pr}) \quad (13)$$

These are the dependencies suggested, but not proved, by Elenbaas (1942).

At low  $Ra^*$  (fully developed régime) one must expect that diffusion in the  $x$  direction will be comparable to convection, so that  $\partial^2(\ )/\partial x^{*2}$  terms should not be dropped from Eqs. (8)–(12). If the inlet plenum is very long ( $L_p^* \rightarrow \infty$ ), the following dependence is deduced:

$$Nu = Nu(Ra^*, Pr, L_c^*); \quad Pe = Pe(Ra^*, Pr, L_c^*) \quad (14)$$

For the fully developed régime, this dimensional analysis does not support Elenbaas' conclusion (that Eq. (13) is valid) except when  $L_c^*$  becomes asymptotically large.

At values of  $Ra^*$  that are small enough for  $x$  diffusion to be important, and if  $L_p^*$  is not asymptotically large, the solution to Eqs. (8)–(12) will also depend on the plenum length,  $L_p^* = L_p/b$ . The dependencies of the dimensionless average heat transfer and mass flow rates for the general problem in Fig. 1(B) are therefore

$$Nu = Nu(Ra^*, Pr, L_c^*, L_p^*) \quad Pe = Pe(Ra^*, Pr, L_c^*, L_p^*) \quad (15)$$

From dimensional analysis, it is therefore concluded that Elenbaas' asymptote, Eq. (3B), is not correct at low values of  $Ra^*$  unless  $L_p^* \rightarrow \infty$  and  $L_c^* \rightarrow \infty$ . It remains to establish the actual  $Ra^*$  range over which the effects of  $L_c^*$  and  $L_p^*$  become important.

### Fully Developed Asymptote $L_p^* \rightarrow \infty$

Before giving the results of a numerical study, some guidance (relating to the question of the behavior of  $Nu$  in the  $Ra^*$  domain over which  $x$ -diffusion is important) is obtained from an approximate analysis. The case of a long inlet plenum,  $L_p^* \rightarrow \infty$ , is considered first, where the functional relation (14) is expected to be valid.

When there was no flow through the channel in Fig. 1(B), the temperature on the  $x=0$  plane would vary from  $T_w$  at  $y = \pm b$  to a slightly smaller value near  $y=0$ . Any flow will cause this temperature to decrease toward  $T_\infty$ . Specification of  $T = T_w$  on  $x=0$  is therefore an upper bound on the temperature on the inlet plane that becomes approximately correct as  $Pe \rightarrow 0$  (i.e., in the fully developed régime). In this régime, the dynamic pressure variations are small, so that the  $u$  velocity in the inlet plenum can be approximated as uniform at  $\bar{u}$ .

In the fully developed régime, the upper bound on the temperature distribution in the plenum is therefore described approximately by

$$\rho c_p \bar{u} \frac{dT}{dx} = k \frac{d^2 T}{dx^2} \quad (16)$$

$$x=0 \quad T = T_w$$

$$x = -L_p \approx -\infty \quad T = T_\infty$$

The nondimensional plenum temperature distribution is therefore given by

$$\theta = \exp(Pe L_c^* x^*) \quad x^* \leq 0 \quad (17)$$

$$\theta = 1 \quad x^* \geq 0$$

The total buoyancy force inducing flow through the channel and plenum, per unit depth (i.e., distance normal to the plane of Fig. 1) of channel and for  $L_p^* \rightarrow \infty$ , is

$$F_B = 2\rho g \beta (T_w - T_\infty) L_c b \int_{-\infty}^1 \theta dx^* \quad (18)$$

Equating this to the viscous drag force on the wall over the domain  $0 \leq x^* \leq 1$ , assuming the velocity profile to be parabolic, results in the velocity

$$\bar{u} = \frac{\rho g \beta (T_w - T_\infty) b^2}{3\mu} \left[ 1 + \frac{1}{L_c^* Pe} \right] \quad (19)$$

The second term in Eq. (19) is a correction to the Elenbaas equation for velocity. This is an implicit equation for  $\bar{u}$ , because  $Pe$  contains  $\bar{u}$ , which can be solved to yield

$$Pe = \frac{Ra}{6} \left[ 1 + \sqrt{1 + \frac{12}{L_c^* Ra}} \right] \quad (20)$$

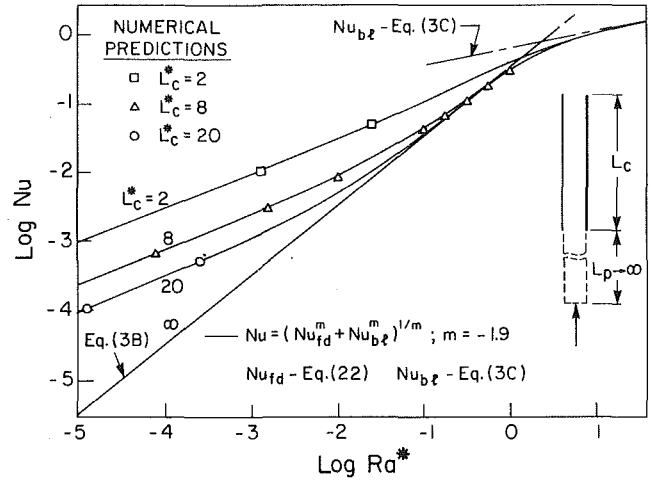


Fig. 4 Heat transfer predictions for various channel heights,  $L_c^*$ , and for a large plenum length,  $L_p^* \rightarrow \infty$

Table 1 Values of  $Nu_{COND}$

| $L_p/L_c$ | $L_c^* = 8$ | $L_c^* = 10$ |
|-----------|-------------|--------------|
| 1         | 0.01481     | 0.009574     |
| 0.5       | 0.02814     | 0.01838      |
| 0.25      | 0.05120     | 0.03400      |
| 0.10      | 0.1007      | 0.06939      |

Performing an energy balance on the channel and plenum, the total heat flow from the plates,  $Q$ , is

$$Q = \dot{m} c_p (T_w - T_\infty) \quad (21)$$

The average Nusselt number is therefore

$$Nu_{fd} = \frac{Pe}{L_c^*} = \frac{Ra}{6L_c^*} \left[ 1 + \sqrt{1 + \frac{12}{L_c^* Ra}} \right] \quad (22)$$

This equation is the appropriate fully developed asymptote for the problem in Fig. 1(B) for the special case:  $L_p^* \rightarrow \infty$ .

To obtain an equation for the Nusselt number that spans the fully developed and boundary layer régime, it is appropriate to use Eq. (3), but with Eq. (3B) replaced by Eq. (22). This equation is plotted in Fig. 4 for  $Ra^* < 50$ . For  $L_c^* \leq 10$  (short channels) it is seen that there is no range in  $Ra^*$  over which the Elenbaas asymptote, Eq. (3B), is valid. As  $L_c^*$  increases, the range in  $Ra^*$  over which the Elenbaas asymptote is approached becomes wider. The  $L_c^* \rightarrow \infty$  curve is the Elenbaas asymptote ( $Nu_{fd} \rightarrow Ra^*/3$  in Eq. (22) as  $L_c^* \rightarrow \infty$ ).

The symbols that appear in Fig. 4 are predictions based on the numerical solution of the full equations of motion (4)–(7). The agreement between these and the approximate solution just presented is seen to be excellent.

### New Nusselt and Rayleigh Numbers for the Fully Developed Régime

If a new Nusselt and Rayleigh numbers are defined as follows:

$$\tilde{Nu}_{fd} = (L_c^*)^2 Nu_{fd} \quad \tilde{Ra} = L_c^* Ra = (L_c^*)^2 Ra^* \quad (23)$$

Eq. (22) becomes

$$\tilde{Nu}_{fd} = \frac{\tilde{Ra}}{6} \left[ 1 + \sqrt{1 + \frac{12}{\tilde{Ra}}} \right] \quad (24)$$

This equation is significant because there is no separate dependence on  $L_c^*$ ; that is, all predictions in the fully developed régime should fall on a single curve of  $\tilde{Nu}$  versus  $\tilde{Ra}$ .

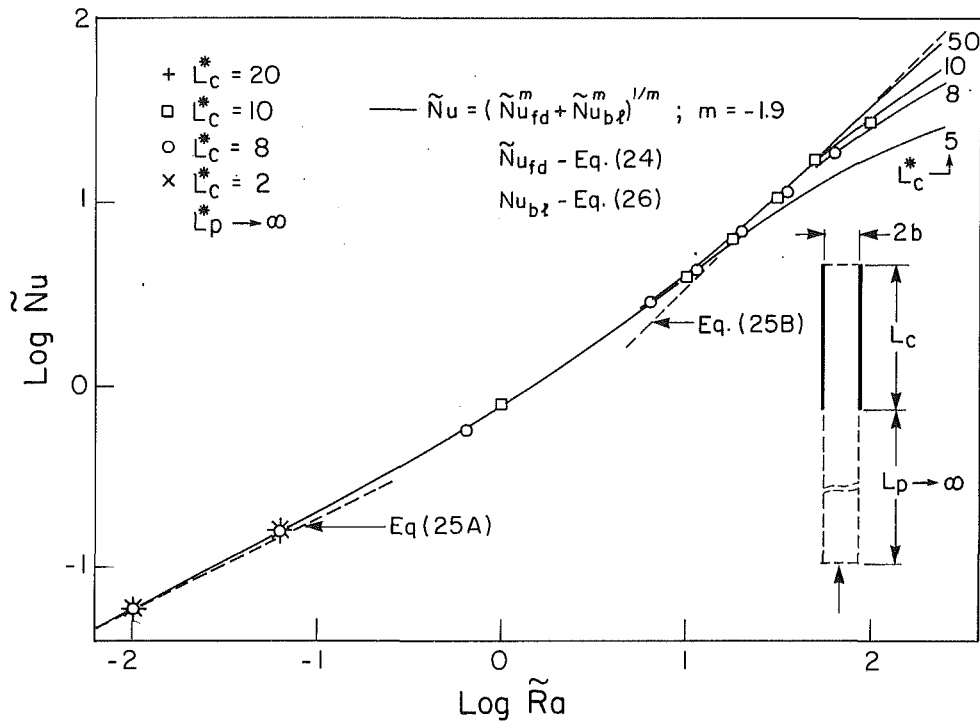


Fig. 5 New coordinates that collapse all predictions in the fully developed régime onto a single curve

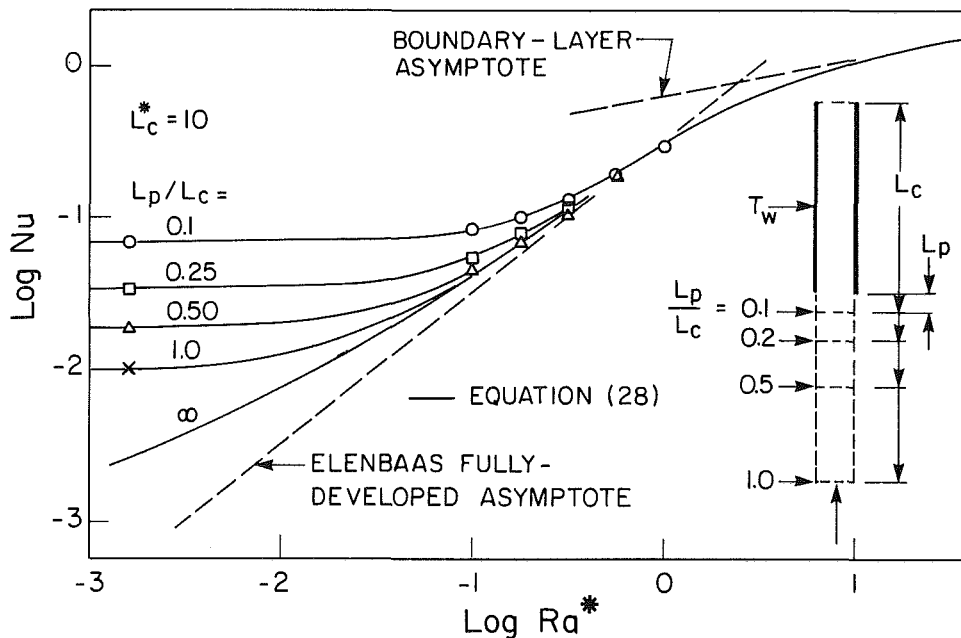


Fig. 6 Heat transfer for a fixed channel length,  $L_c^* = 10$ , and for various inlet plenum lengths,  $L_p^*$

Equation (24) has two asymptotes

$$\tilde{Nu}_{fd} \rightarrow \sqrt{\frac{\tilde{Ra}}{3}} \quad \text{as } \tilde{Ra} \rightarrow 0 \quad (25A)$$

$$\tilde{Nu}_{fd} \rightarrow \frac{\tilde{Ra}}{3} \quad \text{as } \tilde{Ra} \rightarrow \infty \quad (25B)$$

The second of these is the Elenbaas equation, Eq. (3B). The first, Eq. (25A), represents a new asymptote that accounts for the effect of upstream conduction. Because of transition to the boundary layer régime, the range of Ra over which the Elenbaas asymptote is valid is limited; the previous section

showed, in fact, that there is no Ra range over which it is valid for short channels ( $L_c^* \leq 10$ ).

In order to obtain an equation in these coordinates that spans the fully developed and boundary layer régime, Eq. (3C) is transformed to

$$\tilde{Nu}_{bl} = 0.62 \tilde{Ra}^{1/4} (L_c^*)^{3/2} \quad (26)$$

and Eqs. (24) and (26) are substituted into the blending relation

$$\tilde{Nu} = (\tilde{Nu}_{fd}^m + \tilde{Nu}_{bl}^m)^{1/m} \quad m = -1.9 \quad (27)$$

Equation (27), using Eq. (24) for  $\tilde{Nu}_{fd}$  and Eq. (26) for  $\tilde{Nu}_{bl}$ , is plotted in Fig. 5. Also shown are the two fully developed asymptotes given by Eqs. (25A) and (25B).

Numerical predictions obtained for  $L_p^* \rightarrow \infty$  are plotted in  $\tilde{Nu}-\tilde{Ra}$  coordinates in Fig. 5. This figure confirms that these coordinates indeed collapse all the predictions, for different  $L_c^*$ , onto a single curve in the fully developed régime. The boundary layer asymptote (in these coordinates) now depends on the value of  $L_c^*$ ; Eq. (27) predicts the correct  $\tilde{Ra}$  at which results break away from the fully developed régime toward the boundary layer régime.

### Effect of Upstream Conduction to Plenum Boundary (Finite $L_p^*$ )

In all the results just presented, as  $Ra \rightarrow 0$  the Nusselt number approaches zero. In any real situation this will not occur because there will always be some heat conduction to surrounding surfaces. For the boundary conditions shown in Fig. 1(B), as  $Ra \rightarrow 0$ , the Nusselt number will approach that for conduction from the plates at  $T_w$  to the upstream boundary at  $T_\infty$ . As  $L_p^* \rightarrow \infty$ , this limiting heat transfer approaches zero (the case reported in the previous sections). Note that the boundary conditions allow no conduction through the  $x=L_c$  boundary in Fig. 1(B), a point still to be addressed.

In this section, the Nusselt number for the  $L_p^* \rightarrow \infty$  case is given the new notation,  $Nu_{CONV}$  (i.e.,  $Nu_{CONV}$  is given by Eq. (3A), using Eq. (3C) for  $Nu_{bl}$  and Eq. (22) for  $Nu_{fd}$ ). The Nusselt number for conduction to the plenum inlet boundary, at  $x = -L_p$ , is denoted by  $Nu_{COND}$ .

The solution to the pure conduction problem, given by Gibbs (1958), requires elliptic integrals and related functions that can be easily calculated using theta functions, as outlined by Lemczyk and Yovanovich (1988). The values of  $Nu_{COND}$  for the conduction limit are given in Table 1. Note that as  $L_p \rightarrow \infty$ ,  $Nu_{COND} \rightarrow 1/(L_p^* L_c^*)$ .

The Nusselt number, including conduction, can again be approximated by the blending equation

$$Nu = (Nu_{COND}^n + Nu_{CONV}^n)^{1/n} \quad n = 1.9 \quad (28)$$

Equation (28) is plotted in Fig. 6 for four values of  $L_p/L_c$  between 0.1 and 1.0, all for  $L_c^* = 10$ . Heat conduction to the upstream boundary is seen to have a pronounced effect on the heat transfer from the plates, even when the inlet channel has a length equal to the plate length ( $L_p/L_c = 1.0$ ).

The results of numerical predictions are also shown in Fig. 6. For the limited range of parameters examined, there is good agreement with Eq. (28).

### Discussion

For the geometrically simple case shown in Fig. 1(B), upstream conduction can have an important effect on the heat transfer from the plates. For  $L_p \rightarrow \infty$ , the upstream conduction preheats the fluid before it enters the channel causing the effective height of the buoyant column to increase; this, in turn, induces a higher throughflow and therefore a higher heat transfer from the plates.

For a short inlet plenum, heat transfer is further augmented by conduction to the upstream boundary. The combined effects of higher effective height of the buoyant column and of heat conduction to the boundary can result in heat transfer rates that are very much larger than those predicted by the low Rayleigh number Elenbaas asymptote.

For other shapes of inlet channel, upstream conduction will play a different, but important, role. For the geometry shown in Fig. 3(B), upstream conduction is much more important than for the geometry of this study (Fig. 1B) for a given distance between the channel entrance and the upstream boundary. This is because the area for the flow increases with distance upstream, which has the dual effect of decreasing the velocity that moves counter to the upstream heat conduction and of decreasing the resistance to conduction. Even for  $R/b = 100$ ,

the results of Ormiston (1983), shown in Fig. 2, indicate a very significant contribution to the low-Ra heat transfer.

In reality, Surface 2 in Fig. 3(B) could not be maintained adiabatic for gas flows. The heat flow path from the channel to Surface 2 is much shorter than the path to Surface 1, so that heat transfer from the plates to this surface would likely be very important at low Ra. This would further increase the discrepancy between observed heat transfer and the Elenbaas asymptote. It is, therefore, concluded that Elenbaas' low Rayleigh number asymptote will not be observed except under extremely special conditions.

Since the parabolic solutions (e.g., Bodoia and Osterle, 1962) have been one of the key pieces of supporting evidence for the Elenbaas asymptote, one must now enquire as to why these solutions are also incorrect. The answer seems to be that the parabolic flow assumptions are invalid at low Ra. Certainly axial diffusion is important at low Ra, and clearly the specification of  $T = T_\infty$  at  $x^* = 0$  is incorrect. In fact, if axial diffusion were retained with this boundary condition specification, asymptotically large heat transfer would be found for  $Ra \rightarrow 0$  because of the thermal short circuit where the inlet plane intersects the plates. It is only because of a partial cancellation of simplifying approximations that the parabolic solutions yield reasonable results at all.

The remaining questions relate to the disagreement among different sets of experimental data. It now seems that Sparrow and Bahrami (1980) measured high (equivalent) heat transfer at low Ra partly because of the cooling that accompanied the sublimation and partly because upstream diffusion at the inlet both augmented buoyancy and transferred mass to fluid that never passed through the channel. It also appears that Elenbaas' data yielded reasonable agreement with his low-Ra asymptote partly because his  $L_c^*$  were large, but also because the large corrections to the data (see Sparrow and Bahrami, 1980) resulted in fortuitous agreement.

The present study has analyzed the heat transfer from the parallel plates for two-dimensional flow, for one channel in an infinite stack of channels, and for zero heat conduction from the top of the channel. For the analysis and discussion in this paper, the heat transfer is expected to be much different for one, or only a few, channels because the upstream diffusion will be different. (The present analysis should not, therefore, be expected to agree with the Sparrow and Bahrami data.) For low Ra, neither the depth of the plates nor the number of channels would be sufficient to prevent three-dimensional conduction effects at the inlet. Furthermore, the fully developed boundary condition on temperature at the duct outlet ( $\partial T/\partial x = 0$  at  $x=L_c$ ) often becomes inappropriate at low Ra, especially if there are nearby cool surfaces to which the plates can conduct. While the problem analyzed in the present study has been educational, the conclusion of this study is that these predictions will only be valid under restrictive conditions. In general, the low-Ra heat transfer will depend on the particular inlet and outlet configuration used.

### Summary and Conclusions

The problem of flow and heat transfer by natural convection through a channel formed by parallel isothermal plates is central to our understanding of open-cavity flows. Despite some scattered experimental and numerical evidence to the contrary, there is wide acceptance that the Elenbaas fully developed régime exists at low Rayleigh numbers, in which the Nusselt number becomes directly proportional to the Rayleigh number.

This paper has presented a numerical study, a simple analysis, and correlation equations for natural convection through an array of large parallel, vertical, heated plates. The Elenbaas fully developed régime is shown to exist only as a very special limiting case. For the problem studied, new asymptotic (fully developed) relations are presented for this particular problem.

From the analysis presented, it becomes clear that the heat transfer at low Rayleigh number will depend on the shape and boundary conditions of the inlet and outlet plenums. In particular, Elenbaas' asymptotic expression for low Rayleigh numbers will not be valid except under extremely special circumstances.

### Acknowledgments

This work was partially supported by the Manufacturing Research Corporation of Ontario (MRCO) and partially by an operating grant to the second author from the Natural Sciences and Engineering Research Council (NSERC) of Canada.

### References

- Aihara, T., 1973, "Effects of Inlet Boundary Conditions on Numerical Solutions of Free Convection Between Vertical Parallel Plates," *Rep. Inst. High Speed Mech.*, Vol. 28, No. 258.
- Aung, W., Fletcher, L. S., and Sernas, V., 1972, "Developing Laminar Free Convection Between Flat Plates With Asymmetric Heating," *Int. J. Heat Mass Transfer*, Vol. 15, pp. 2293-2308.
- Bar-Cohen, A., and Rohsenow, W. M., 1984, "Thermally Optimum Spacing of Vertical, Natural Convection Cooled, Parallel Plates," *ASME JOURNAL OF HEAT TRANSFER*, Vol. 106, pp. 116-123.
- Bodoia, J. R., and Osterle, J. F., 1962, "The Development of Free Convection Between Heated Vertical Plates," *ASME JOURNAL OF HEAT TRANSFER*, Vol. 84, pp. 40-44.
- Churchill, S. W., and Usagi, R., 1972, "A General Expression for the Correlation of Rates of Transfer and Other Phenomena," *AIChE J.*, Vol. 18, pp. 1121-1128.
- Elenbaas, W., 1942, "Heat Dissipation of Parallel Plates by Free Convection," *Physica*, Vol. 9, pp. 1-28.
- Gibbs, W. J., 1958, *Conformal Transformations in Electrical Engineering*, The British Thompson-Houston Co. Ltd.
- Kettleborough, C. F., 1972, "Transient Laminar Free Convection Between Heated Vertical Parallel Plates Including Entrance Effects," *Int. J. Heat Mass Transfer*, Vol. 15, pp. 883-896.
- Lemczyk, T. F., and Yovanovich, M. M., 1988, "Efficient Evaluation of Incomplete Elliptic Integrals and Functions," *Comp. Math. Applic.*, Vol. 16, No. 9, pp. 747-757.
- Martin, L. C., 1988, "A Numerical Study of Natural Convection Cooling of Parallel Plates at Low Rayleigh Number," M.A.Sc. Thesis, Dept. of Mechanical Engineering, University of Waterloo, Ontario, Canada.
- Nakamura, H., Asako, Y., and Naitou, T., 1982, "Heat Transfer by Free Convection Between Two Parallel Flat Plates," *Numerical Heat Transfer*, Vol. 5, pp. 95-106.
- Ormiston, S. J., 1983, "A Numerical Study of Two Dimensional Natural Convection in a Trombe Wall System Including Vent and Room Effects," M.A.Sc. Thesis, Dept. of Mechanical Engineering, University of Waterloo, Ontario, Canada.
- Patankar, S. V., 1980, *Numerical Heat Transfer and Fluid Flow*, McGraw-Hill, New York.
- Raithby, G. D., and Hollands, K. G. T., 1975, "A General Method of Obtaining Approximate Solutions to Laminar and Turbulent Free Convection Problems," *Advances in Heat Transfer*, T. F. Irvine, Jr., and J. P. Hartnett, eds., Vol. 11, Academic Press, New York, pp. 265-315.
- Raithby, G. D., and Hollands, K. G. T., 1985, "Natural Convection," *Handbook of Heat Transfer*, W. M. Rohsenow, J. P. Hartnett, and E. N. Granic, eds., Chap. 6, McGraw-Hill.
- Sparrow, E. M., and Bahrami, P. A., 1980, "Experiments on Natural Convection From Vertical Parallel Plates With Either Open or Closed Edges," *ASME JOURNAL OF HEAT TRANSFER*, Vol. 102, pp. 221-227.
- Shewen, E. C., 1986, "A Peltier-Effect Technique for Natural Convection Heat Flux Measurement Applied to the Rectangular Open Cavity," PhD Thesis, Dept. Mechanical Engineering, University of Waterloo, Waterloo, Ontario, Canada.
- Van Doormal, J. P., and Raithby, G. D., 1984, "Enhancements of the SIMPLE Method for Predicting Incompressible Fluid Flows," *Numerical Heat Transfer*, Vol. 7, pp. 147-163.



# Three-Dimensional Laminar Natural Convection in an Inclined Air Slot With Hexagonal Honeycomb Core

Y. Asako

H. Nakamura

Z. Chen

Department of Mechanical Engineering,  
Tokyo Metropolitan University,  
Tokyo, 192-03 Japan

M. Faghri

Department of Mechanical Engineering,  
University of Rhode Island,  
Kingston, RI 02881

*Numerical solutions are obtained for a three-dimensional natural convection heat transfer problem in an inclined air slot with a hexagonal honeycomb core. The air slot is assumed to be long and wide such that the velocity and temperature fields repeat themselves in successive enclosures. The numerical methodology is based on an algebraic coordinate transformation technique, which maps the complex cross section onto a rectangle, coupled with a calculation procedure for fully elliptic three-dimensional flows. The calculations are performed for Rayleigh numbers in the range of  $10^3$  to  $10^5$ , inclination angles in the range of  $-90$  to  $80$  deg, Prandtl number of  $0.7$ , and for five values of the aspect ratio. Three types of thermal boundary condition for the honeycomb side walls are considered. The average Nusselt number results are compared with those for a rectangular two-dimensional enclosure.*

## Introduction

A vertical air slot with a hexagonal honeycomb core is often used as an insulating wall. Inside such a slot the main mechanisms of heat transfer are natural convection and radiation. A summary of the literature in buoyancy-induced flows has been recently brought together by Gebhart et al. (1988). This includes a chapter about natural convection in enclosures and partial enclosures. From a study of this information, it is evident that three-dimensional natural convection inside enclosures has been limited to simple geometries such as a rectangular box and a horizontal cylinder. This was the motivation to start a number of studies by Asako et al. (1989, 1990) for natural convection in a vertical air slot with a hexagonal honeycomb core. In the present study, the natural convection in an inclined air slot with a hexagonal honeycomb core is investigated.

The numerical methodology used in this study utilizes an algebraic coordinate transformation developed previously in a paper by Faghri et al. (1984), which maps an irregular cross section into a rectangle. This method was extended to fully three-dimensional problems by Asako et al. (1989). The numerical solutions are obtained for three types of thermal boundary condition for the honeycomb side walls. These are the conductive, adiabatic, and no-thickness thermal boundary conditions. These conditions exist when the honeycomb core is a good conductor, thermally insulated, and a poor conductor and thin, respectively. The effect of the angle of inclination on the heat transfer characteristics is investigated in the range of  $-90$  to  $80$  deg, for the three values of Rayleigh number ( $Ra = 10^3$ ,  $10^4$ , and  $10^5$ ), for five values of aspect ratio ( $H/L = 0.25$ ,  $0.5$ ,  $1$ ,  $2$ , and  $5$ ), and for a Prandtl number of  $0.7$ . The results are presented in the form of axial and vertical velocity profiles and average and local heat transfer coefficients and they are compared with the corresponding values for two-dimensional rectangular enclosures.

## Formulation

**Description of the Problem.** The problem to be considered

in this study is schematically depicted in Fig. 1. It involves the determination of three-dimensional heat transfer for laminar natural convection in an inclined hexagonal honeycomb enclosure. If the air slot is very long and wide in both the vertical and the horizontal directions, the velocity and temperature fields repeat themselves in successive enclosures, except at the end boundaries of the enclosure. Then, it is possible to solve the natural convection problem in only one honeycomb en-

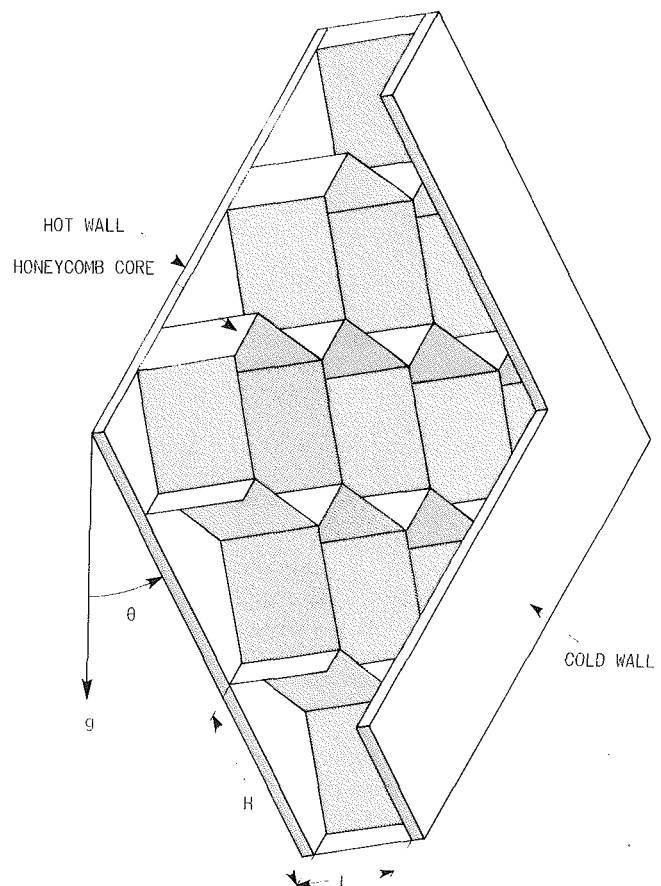


Fig. 1 Schematic diagram of an inclined air slot with honeycomb core

Contributed by the Heat Transfer Division and presented at the Joint AIAA/ASME Thermophysics and Heat Transfer Conference, Seattle, Washington, June 18-20, 1990. Manuscript received by the Heat Transfer Division July 23, 1990; revision received May 13, 1991. Keywords: Enclosure Flows, Natural Convection, Numerical Methods.

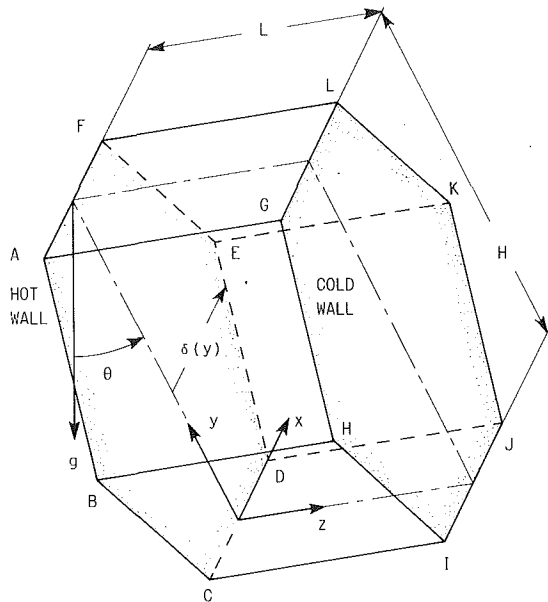


Fig. 2 Schematic diagram of an inclined honeycomb enclosure

closure with an appropriate thermal boundary condition as illustrated in Fig. 2. As seen in this figure, the two hexagonal end walls of the honeycomb enclosure are kept at uniform temperatures  $t_H$  and  $t_c$ , respectively. The side walls can be modeled as good conductors and thick, thermally insulated, or poor conductors and thin. The angle of inclination denoted by  $\theta$  is 0 when the air slot stands vertically and takes a positive value when the hot end wall is lower than the cold end wall. The geometry of the problem is specified by the height ( $H$ ) and the length ( $L$ ). The solution domain, with the assumption of symmetry, is confined to the right half of the honeycomb enclosure. The mathematical expression for the width of this honeycomb,  $\delta(y)$ , is derived in an earlier paper by Asako et al. (1989).

**The Conservation Equations.** The governing equations to be considered are the continuity, momentum, and energy equations. Constant thermophysical properties are assumed except for the density in the buoyancy force term. The following dimensionless variables are used:

$$\begin{aligned} X &= x/L, & Y &= y/L, & Z &= z/L, \\ U &= u/(\nu/L), & V &= v/(\nu/L), & W &= w/(\nu/L), \\ P &= p/\rho(\nu/L)^2, & T &= (t - t_m)/(t_H - t_c) \end{aligned} \quad (1)$$

where  $t_m$  is the average temperature of end walls and is expressed by  $t_m = (t_H + t_c)/2$ . Then, upon introduction of the dimensionless variables and parameters, the governing equations take the following forms:

**Continuity Equation:**

$$\partial U/\partial X + \partial V/\partial Y + \partial W/\partial Z = 0 \quad (2)$$

**Momentum Equations:**

$$U(\partial U/\partial X) + V(\partial U/\partial Y) + W(\partial U/\partial Z) = -\partial P/\partial X + \nabla^2 U \quad (3)$$

$$U(\partial V/\partial X) + V(\partial V/\partial Y) + W(\partial V/\partial Z) = -\partial P/\partial Y + \nabla^2 V + (Ra/Pr)T \cos \theta \quad (4)$$

$$U(\partial W/\partial X) + V(\partial W/\partial Y) + W(\partial W/\partial Z) = -\partial P/\partial Z + \nabla^2 W + (Ra/Pr)T \sin \theta \quad (5)$$

**Energy Equation:**

$$U(\partial T/\partial X) + V(\partial T/\partial Y) + W(\partial T/\partial Z) = (1/Pr) \nabla^2 T \quad (6)$$

where

$$\nabla^2 = \partial^2/\partial X^2 + \partial^2/\partial Y^2 + \partial^2/\partial Z^2 \quad (7)$$

To complete the formulation of the problem, it remains to discuss the boundary conditions. These are:

$$\text{at all walls:} \quad U = V = W = 0$$

$$\text{at the symmetry plane } (X=0): \quad U = \partial V/\partial X = \partial W/\partial X = 0 \quad (8)$$

The thermal boundary conditions on the hot and cold end walls are

$$\text{hot wall:} \quad t = t_H$$

$$\text{cold wall:} \quad t = t_c \quad (9)$$

The corresponding dimensionless form of the boundary conditions are

$$\text{hot wall:} \quad T = 0.5$$

$$\text{cold wall:} \quad T = -0.5 \quad (10)$$

As mentioned earlier, three types of thermal boundary condition for the side walls are considered. The first boundary condition is the so-called conductive condition. This condition exists when the honeycomb walls are good conductors and thick. In this condition, the temperature of the side wall varies linearly in the  $z$  direction. The mathematical expression for this condition is

$$t = t_H - (t_H - t_c)(z/L) \quad (11)$$

## Nomenclature

|   |  |   |
|---|--|---|
| $a$ = thermal diffusivity                             | $P$ = dimensionless pressure                               | $w$ = axial velocity component                        |
| $C_p$ = specific heat of the fluid                    | $p$ = pressure   | $X, Y$ = dimensionless coordinates = $x/L, = y/L$     |
| $H$ = height of a hexagonal honeycomb enclosure       | $Q$ = total heat transfer rate from hot wall               | $x, y$ = coordinates                                  |
| $h$ = local heat transfer coefficient [Eq. (16)]      | $q$ = heat flux from hot wall                              | $Z$ = dimensionless axial coordinate = $z/L$          |
| $h_m$ = average heat transfer coefficient [Eq. (17)]  | $Ra$ = Rayleigh number = $g\beta L^3(t_H - t_c)/\nu\alpha$ | $z$ = axial coordinate                                |
| $k$ = thermal conductivity                            | $T$ = dimensionless temperature                            | $\delta(y)$ = half width of a hexagonal enclosure     |
| $L$ = axial length of a hexagonal honeycomb enclosure | $t_m$ = averaged temperature = $(t_H + t_c)/2$             | $\eta$ = transformed coordinate = $X/\{\delta(y)/L\}$ |
| $Nu$ = local Nusselt number [Eq. (20)]                | $t_H$ = hot wall temperature                               | $\theta$ = angle of inclination                       |
| $Nu_m$ = average Nusselt number [Eq. (21)]            | $t_c$ = cold wall temperature                              | $\mu$ = viscosity                                     |
| $Pr$ = Prandtl number                                 | $U, V$ = dimensionless velocity components [Eq. (1)]       | $\nu$ = kinematic viscosity                           |
|   | $u, v$ = velocity components                               | $\xi$ = transformed coordinate = $Y$                  |
|   | $W$ = dimensionless axial velocity component [Eq. (1)]     | $\rho$ = density of the fluid                         |

The corresponding dimensionless form of Eq. (11) can be easily obtained as

$$T = 0.5 - Z \quad (12)$$

The second boundary condition for the side walls is that of the adiabatic condition. This condition exists when the side walls are thermally insulated and is expressed as:

$$\partial T / \partial N = 0 \quad (13)$$

where  $N$  is the dimensionless coordinate directed along the outward normal to the walls. The third boundary condition for the side walls is the so-called "no-thickness" wall condition, which indicates that conduction is negligible along the walls as the walls are thin. Therefore, the heat flux through the top wall (AGLF) becomes equal to that through the bottom wall (CIJD); the heat flux through one of the upper side walls (ABHG) becomes equal to that through the lower side walls (EDJK). From the assumption of symmetry, the heat flux through the right upper wall (FEKL) becomes equal to that through the left upper wall (ABHG). The mathematical expressions for these conditions are as follows:

$$T_{AGLF} = T_{CIJD}, \quad (\partial T / \partial N)_{AGLF} = -(\partial T / \partial N)_{CIJD}$$

$$T_{FEKL} = T_{EDJK}, \quad (\partial T / \partial N)_{FEKL} = -(\partial T / \partial N)_{EDJK} \quad (14)$$

**Numerical Solutions.** A simple algebraic coordinate transformation is used that maps the hexagonal cross section onto a rectangle. Specifically, the  $X, Y$  coordinates are transformed into  $\eta, \xi$  coordinates by the relations

$$\eta = X / [\delta(y) / L], \quad \xi = Y \quad (15)$$

In terms of the new coordinates, the solution domain is bounded by  $0 < \eta < 1, 0 < \xi < H/L$ . The transformed equations and their discretization and solutions for the conductive and adiabatic thermal boundary conditions, and for the "no-thickness" thermal boundary condition, are documented in earlier papers by Asako et al. (1989, 1990), respectively. The discretized procedure of the equations is based on the control volume based power-law scheme of Patankar (1981), and the discretized equations are solved by using a line-by-line method. The pressure and velocities are linked by the SIMPLE algorithm of Patankar (1980). All computations were performed with  $(16 \times 30 \times 22)$  grid points. These grid points are distributed uniformly over the solution domain in the  $\eta, \xi$ , and  $Z$  coordinate directions. The effect of grid size on the Nusselt number result for the vertical air slot has already been examined and illustrated in the paper by Asako et al. (1989).

The convergence criterion used in these computations is that the value of the mass flux residuals (mass flow) divided by the total mass flow in each control volume is under  $10^{-9}$ . The underrelaxation factors for the velocity and pressure are set to 0.5 and 0.8, respectively. About 200 to 800 iterations are required to obtain a converged solution. The number of iterations depends on the aspect ratio, the Rayleigh number, and the angle of inclination. The computations for higher aspect ratios, higher Rayleigh numbers, and higher angles of inclination require a larger number of iterations.

From an examination of the governing Eqs. (2)–(6), it can be seen that there are two parameters whose values have to be specified prior to the initiation of the numerical solutions. These are the Prandtl number,  $Pr$ , and the Rayleigh number,  $Ra$ . In this paper, a value of 0.7 is chosen for  $Pr$ , and the values chosen for the Rayleigh number are in the range from  $10^3$  to  $10^5$ . Aside from  $Pr$  and  $Ra$ , there are two geometric parameters and the angle of inclination that have to be specified. These are the height ( $H$ ), the length of the enclosure ( $L$ ), and the angle ( $\theta$ ). If the  $L$  is used as a reference length, then  $H/L$  needs to be specified as the geometric parameter. The selected values of  $H/L$  are 0.25, 0.5, 1, 2, and 5.

Two-dimensional natural convection in an inclined rectangular enclosure has been investigated both experimentally and

theoretically by Ozoe et al. (1974a, 1974b). The mode of convection in the rectangular enclosure was found to be a two-dimensional roll cell with its axis in the long dimension of the enclosure for an angle of inclination below 80 deg. Between 80 and 90 deg (horizontal), complex flow patterns were observed. The mode of convection was found to be multiple roll cell. Therefore, the values chosen for the angle of inclination  $\theta$  for the present computations are in the range from  $-90$  to 80 deg. However, the convergence of the computation for the combination of higher angles of inclination ( $\theta > 45$  deg), higher Rayleigh numbers ( $Ra > 10^5$ ), and higher aspect ratios ( $H/L > 2$ ) was very slow and the solution for some cases could not be obtained due to a possible bifurcation of the problem. Extension of the present work to a case where the converged solution is not obtainable is the subject of the continuation of this work.

**Nusselt Numbers.** The local and average heat transfer coefficients on the hot wall are defined as

$$h = q / (t_H - t_c) \quad (16)$$

$$h_m = Q / [A_H (t_H - t_c)] \quad (17)$$

where  $q$  is the local heat flux,  $A_H$  is the area of the hexagonal hot wall equal to  $(3/2)H^2 \tan(\pi/6)$ ,  $Q$  is the total heat transfer rate from the hot wall. The local heat flux,  $q$  and the total heat transfer rate,  $Q$ , can be expressed by the temperature gradient at the hot wall as

$$q = -k(\partial t / \partial z)_H \quad (18)$$

$$Q = -k \int_{A_H} (\partial t / \partial z)_H dA$$

$$= -2k \int_0^H \int_0^\delta (\partial t / \partial z)_H dx dy \quad (19)$$

The Nusselt number expressions are as follows:

$$Nu = h L / k = -(\partial T / \partial Z)_H \quad (20)$$

$$Nu_m = h_m L / k =$$

$$- \int_0^{H/L} \int_0^1 (\partial T / \partial Z)_H (\delta / L) d\eta d\xi / [(3/4)(H/L)^2 \tan(\pi/6)] \quad (21)$$

## Results and Discussion

**Velocity Profiles.** The axial velocity component,  $W$  at  $x$ - $y$  planes of  $Z = 0.05, 0.2, 0.35, 0.5, 0.65, 0.8$ , and  $0.95$  and for conduction side wall boundary condition are presented in Fig. 3 for  $H/L = 1, Ra = 10^3, \theta = 45$  deg and in Fig. 4 for  $H/L = 1, Ra = 10^5, \theta = 45$  deg. The locations of the  $x$ - $y$  planes are speckled in Fig. 5. The corners of the hexagonal cross section are marked with the letters  $a_1, b_1, \dots$  in the figures. Although the solution domain is confined to the right half of the enclosure, the velocity profiles of the left half of the enclosure are also presented by using the symmetry of the problem. The computations are performed in the transformed domain, but the results are transformed back to the physical plane. A general-purpose solid graphic utility is used for this purpose. The values at the graphic grid points were interpolated from the computational grid point values.

In earlier papers by Asako et al. (1989, 1990) for a vertical air slot, it was evident that the axial velocity component profile,  $W$ , was classified into two types. Namely, type  $A$  refers to Fig. 3 where the fluid on the vertical symmetry line ( $X = 0$ ) is moving faster than other locations at the same elevation. Type  $M$  refers to Fig. 4 where the velocity profile has two peaks at the same elevation. As seen from Figs. 3 and 4, the velocity profile changes in shape from type  $A$  to type  $M$  with increasing Rayleigh number. The classification of the velocity profile is summarized in Table 1. It is noteworthy that the

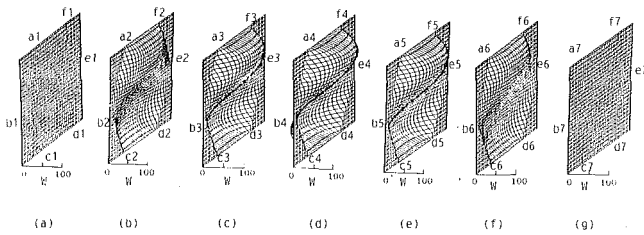


Fig. 3 Axial velocity profiles at  $x$ - $y$  planes for  $H/L = 1$ ,  $Ra = 10^3$ , and  $\theta = 45$  deg: (a)  $Z = 0.05$ ; (b)  $Z = 0.2$ ; (c)  $Z = 0.35$ ; (d)  $Z = 0.5$ ; (e)  $Z = 0.65$ ; (f)  $Z = 0.8$ ; (g)  $Z = 0.95$

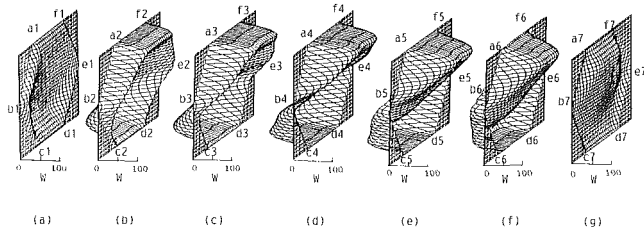


Fig. 4 Axial velocity profiles at  $x$ - $y$  planes for  $H/L = 1$ ,  $Ra = 10^5$ , and  $\theta = 45$  deg: (a)  $Z = 0.05$ ; (b)  $Z = 0.2$ ; (c)  $Z = 0.35$ ; (d)  $Z = 0.5$ ; (e)  $Z = 0.65$ ; (f)  $Z = 0.8$ ; (g)  $Z = 0.95$

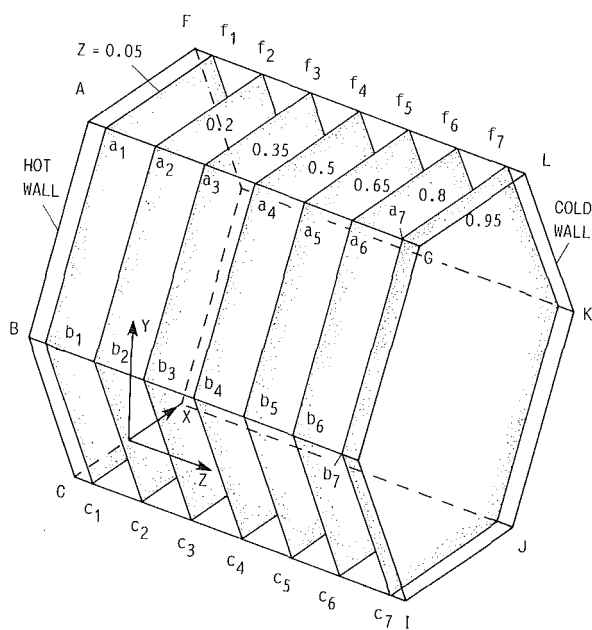


Fig. 5 Schematic view of the location of  $x$ - $y$  planes in Figs. 3 and 4

Table 1 Classification of axial velocity profile  $W$

| $H/L$ | $Ra$   | $-90^\circ$ | $-80^\circ$ | $-60^\circ$ | $-45^\circ$ | $-30^\circ$ | $0^\circ$ | $30^\circ$ | $45^\circ$ | $60^\circ$ | $80^\circ$ |
|-------|--------|-------------|-------------|-------------|-------------|-------------|-----------|------------|------------|------------|------------|
| 0.25  | $10^3$ | A           | A           | A           | A           | A           | A         | A          | A          | A          | A          |
|       | $10^4$ | A           | A           | A           | A           | A           | A         | A          | A          | A          | A          |
|       | $10^5$ | A           | A           | A           | A           | A           | A         | A          | A          | A          | A          |
| 0.5   | $10^3$ | A           | A           | A           | A           | A           | A         | A          | A          | A          | A          |
|       | $10^4$ | A           | A           | A           | A           | A           | A         | A          | A          | A          | A          |
|       | $10^5$ | A           | A           | A           | A           | A           | A         | A          | A          | A          | A          |
| 1     | $10^3$ | A           | A           | A           | A           | A           | A         | A          | A          | A          | A          |
|       | $10^4$ | A           | A           | A           | A           | A           | A         | A          | A          | A          | A          |
|       | $10^5$ | M           | M           | M           | M           | M           | M         | M          | M          | M          | M          |
| 2     | $10^3$ | A           | A           | A           | A           | A           | A         | A          | A          | A          | A          |
|       | $10^4$ | M           | M           | M           | M           | M           | M         | M          | M          | M          | M          |
|       | $10^5$ | M           | M           | M           | M           | M           | M         | M          | M          | M          | -          |
| 5     | $10^3$ | M           | M           | M           | M           | M           | M         | M          | M          | M          | M          |
|       | $10^4$ | M           | M           | M           | M           | M           | M         | M          | M          | -          | -          |
|       | $10^5$ | M           | M           | M           | M           | M           | M         | -          | -          | -          | -          |

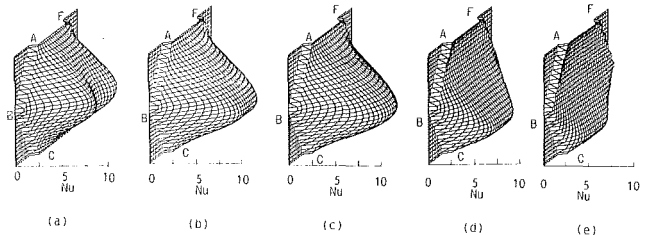


Fig. 6 Local Nusselt number on the hot wall for  $H/L = 1$  and  $Ra = 10^5$  for the conduction side wall boundary condition

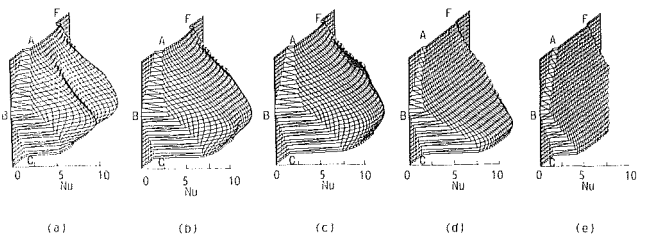


Fig. 7 Local Nusselt number on the hot wall for  $H/L = 1$  and  $Ra = 10^5$  for the adiabatic side wall boundary condition

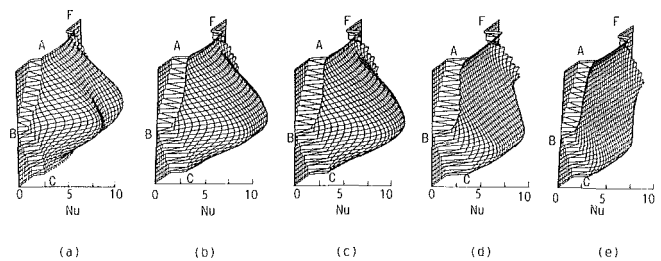


Fig. 8 Local Nusselt number on the hot wall for  $H/L = 1$ , and  $Ra = 10^5$  for the no-thickness side wall boundary condition

thermal boundary conditions on the side walls do not influence this classification. Although only the results for  $\theta = 45$  deg are shown in the figures, the maximum velocity of the circulation can be observed between 30 and 60 deg of inclination under the same Rayleigh number and aspect ratio. The trends for the velocity profiles for the adiabatic side boundary condition and for the no-thickness side boundary condition are similar to those for the conduction side boundary condition.

**Local Nusselt Number.** The local Nusselt numbers on the hot wall for  $H/L = 1$ ,  $Ra = 10^5$ , and for the conduction side wall boundary condition, the adiabatic side wall boundary condition, and the no-thickness side wall boundary condition are presented in Figs. 6, 7, and 8, respectively. In each figure, the Nusselt numbers for angles of inclination  $\theta = 80, 45, 30, -30$ , and  $-60$  deg are shown in Figs. (a), (b), (c), (d), and (e), respectively. As seen from these figures, the local Nusselt number value at the hot wall for conduction boundary condition approaches unity by definition. For the no-thickness side boundary condition, the local Nusselt number value at one side of the hot wall coincides with the value at the opposite side from the periodicity condition. For any thermal boundary condition for the side wall, the local Nusselt number value approaches unity for  $\theta = -90$  deg. This result indicates that the heat is transferred only by heat conduction for  $\theta = -90$  deg. From the study of the local Nusselt number profiles in Figs. 6 and 7, and 8, it is evident that the local Nusselt number profile is also classified into two types. The one-peak type refers to Fig. 6(b), where the local Nusselt number on the symmetric plane ( $X = 0$ ) takes the highest value at the same elevation, and the two-peak type refers to Fig. 6(a), where the local Nusselt number profile has two peaks at the same elevation. As seen from Figs. 6, 7, and 8, the local Nusselt

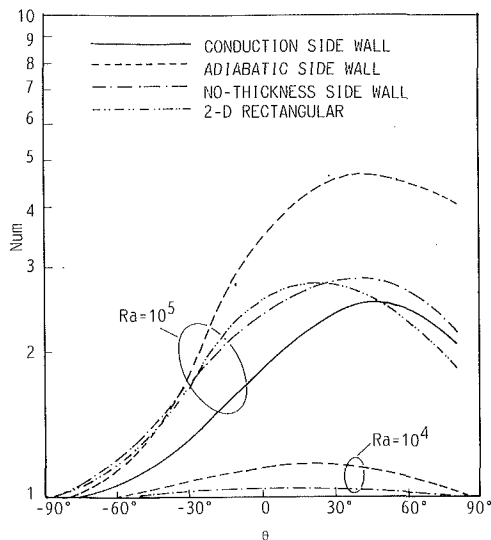


Fig. 9 Average Nusselt number,  $Nu_m$ , for  $H/L = 0.5$  as a function of the angle of inclination

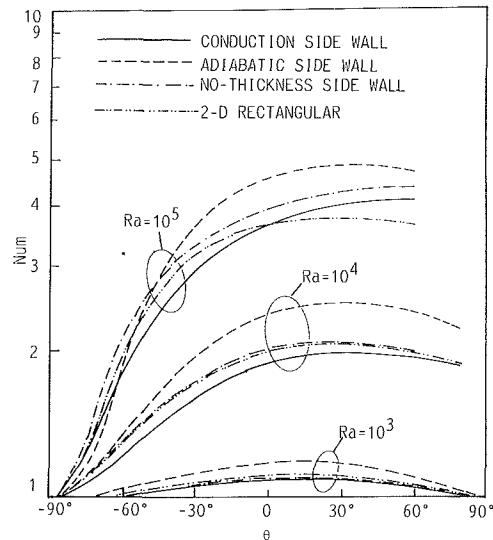


Fig. 11 Average Nusselt number,  $Nu_m$ , for  $H/L = 2$  as a function of the angle of inclination

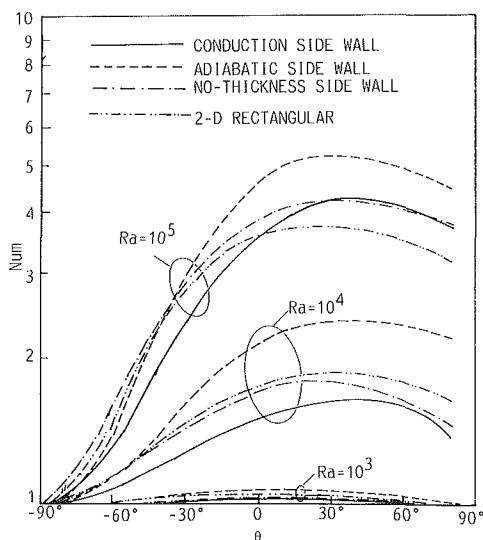


Fig. 10 Average Nusselt number,  $Nu_m$ , for  $H/L = 1$  as a function of the angle of inclination

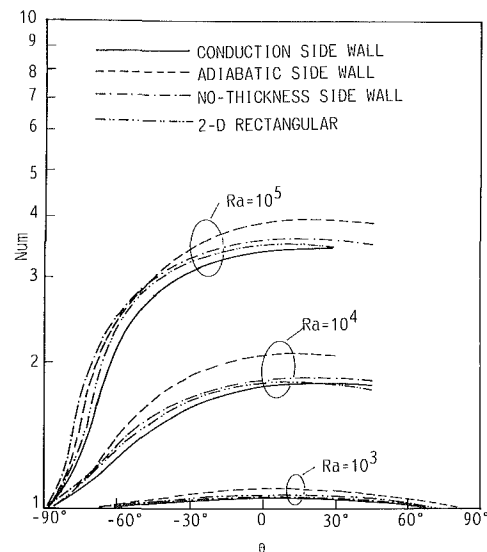


Fig. 12 Average Nusselt number,  $Nu_m$ , for  $H/L = 5$  as a function of the angle of inclination

number profile changes in shape from one peak to two peaks with increasing angle of inclination. This result corresponds to the presence of the two peaks in the axial velocity profile.

**Average Nusselt Number.** The average Nusselt numbers for the aspect ratios  $H/L = 0.5, 1, 2,$  and  $5$  are plotted as a function of the inclination angle, with the Rayleigh number as the curve parameter in Figs. 9, 10, 11, and 12, respectively. Since the value of the average Nusselt number for  $H/L = 0.25$  is less than 1.14, the figure for  $H/L = 0.25$  is not shown in this paper. As seen from these figures, the average Nusselt number increases with increasing angle of inclination until it reaches a peak value near  $\theta = 30$  deg depending on the aspect ratio and the Rayleigh number and decreases with increasing angle of inclination. Comparing these figures, it is seen that, among the three types of thermal boundary condition, the adiabatic side wall boundary condition yields the highest average Nusselt number.

The full three-dimensional computation requires extensive computing time. Therefore, it would be helpful if the average Nusselt number could be predicted from a two-dimensional model. To investigate this, supplementary two-dimensional

computations for a rectangular enclosure of height  $H$  and horizontal length  $L$  were performed. The results for only the conduction side wall boundary condition are plotted in Figs. 9, 10, 11, and 12 by two-dotted chain lines. The widely known two-dimensional computer code "SIMPLE" is used for the computations. Computations were performed with  $(30 \times 22)$  grid points. The grid points were distributed uniformly over the solution domain in the  $Y$  and  $Z$  directions. As seen from these figures, the two and three-dimensional results agree very well for higher aspect ratios. On the other hand, slight differences can be seen for the cases of  $H/L = 0.5$  and  $1$  because of the side wall effect. The friction caused by the side walls affects the circulation of the fluid, which in turn affects the heat transfer. Therefore, the side wall effect is accentuated for lower aspect ratios. Although the results for the other side wall boundary conditions are not shown in these figures, similar trends can be observed in the results of the two-dimensional model with other thermal boundary conditions.

### Concluding Remarks

Three-dimensional laminar natural convection heat transfer

characteristics in an inclined air slot with a hexagonal honeycomb core are obtained numerically by a coordinate transformation technique. The computations were performed for angles of inclination in the range of  $-90$  to  $80$  deg, Rayleigh numbers in the range of  $10^3$  to  $10^5$ , Prandtl number of  $0.7$ , and five values of aspect ratio. The main conclusions of the results are: (a) The axial velocity profiles can be classified into two types depending on the angle of inclination, the Rayleigh number, and the aspect ratio of the enclosure. (b) The average Nusselt number increases with increasing angle of inclination, and it takes the highest value near  $\theta = 30$  deg. The highest values of the average Nusselt number among the three types of thermal boundary condition are those for the adiabatic side wall boundary condition. (c) The average Nusselt number can be predicted by a two-dimensional model depending on the values of the aspect ratio and the Rayleigh number.

## References

- Asako, Y., Nakamura, H., and Faghri, M., 1989, "Three-Dimensional Laminar Natural Convection in Horizontal Hexagonal Honeycomb Enclosure," *Numerical Heat Transfer*, Vol. 15, pp. 67-86.
- Asako, Y., Nakamura, H., and Faghri, M., 1990, "Three-Dimensional Laminar Natural Convection in Vertical Air Slot With Hexagonal Honeycomb Core," *ASME JOURNAL OF HEAT TRANSFER*, Vol. 112, pp. 130-136.
- Bejan, A., and Tien, C. L., 1978, "Laminar Natural Convection Heat Transfer in a Horizontal Cavity With Different End Temperature," *ASME JOURNAL OF HEAT TRANSFER*, Vol. 100, pp. 641-647.
- Faghri, M., 1984, "Slot Jet Impingement on a Cylinder," *Proceedings of the ASME/AIChE Heat Transfer Conference*, Paper No. 84-HT-7.
- Faghri, M., Sparrow, E. M., and Prata, A. T., 1984, "Finite Difference Solutions of Convection-Diffusion Problems in Irregular Domains Using a Non-orthogonal Coordinate Transformation," *Numerical Heat Transfer*, Vol. 7, pp. 183-209.
- Faghri, M., and Asako, Y., 1987, "Numerical Determination of Heat Transfer and Pressure Drop Characteristics for a Converging-Diverging Flow Channel," *ASME JOURNAL OF HEAT TRANSFER*, Vol. 109, pp. 606-612.
- Gebhart, B., Jaluria, Y., Mahajan, R. L., and Sammakia, B., 1988, *Buoyancy-Induced Flows and Transport*, Hemisphere Publishing Corp., Washington, DC.
- Nakamura, H., Asako, Y., and Aoki, H., 1987, "Natural Convection Heat Transfer in a Vertical Air Slot Partitioned by Corrugated Plates," *Numerical Heat Transfer*, Vol. 11, pp. 77-94.
- Ozoe, H., Sayama, H., and Churchill, S. W., 1974a, "Natural Convection in an Inclined Square Channel," *International Journal of Heat and Mass Transfer*, Vol. 17, pp. 401-406.
- Ozoe, H., Yamamoto, K., Sayama, H., and Churchill, S. W., 1974b, "Natural Convection in an Inclined Rectangular Channel Heated on One Side and Cooled on the Opposing Side," *International Journal of Heat and Mass Transfer*, Vol. 17, pp. 1209-1217.
- Patankar, S. V., 1980, *Numerical Heat Transfer and Fluid Flow*, Hemisphere Publishing Corp., Washington, DC.
- Patankar, S. V., 1981, "A Calculation Procedure for Two-Dimensional Elliptic Situations," *Numerical Heat Transfer*, Vol. 4, pp. 409-425.

# Natural Convection in Vertically Vented Enclosures

D. M. Sefcik

B. W. Webb

H. S. Heaton

Heat Transfer Laboratory,  
Brigham Young University,  
Provo, UT 84602

*Steady, laminar natural convection in vertically vented two-dimensional enclosures has been investigated both experimentally and analytically. A vertically vented enclosure is one in which the buoyancy-driven flow and heat transfer are restricted by vents in the top and bottom bounding walls of the enclosure. The local heat transfer along the heated wall was determined using Mach-Zehnder interferometry, and the flow structure was determined using a smoke generation flow visualization technique. Analytically, the governing conservation equations were solved numerically using a control volume-based finite difference technique. The results reveal strongly non-uniform local heat transfer along the isothermal wall as a result of the blockage at the inlet. A local maximum and minimum occur in the lower half of the enclosure. The flow visualization and analytical predictions for the flow field reveal that these heat transfer extrema are attributed to separated flow effects near the inlet gap with the associated primary inlet flow impingement and bifurcation at the heated wall. The analysis predicts well the flow structure and local and average heat transfer data. The results show asymptotic behavior to the classical vertical parallel plate result in the limit as the vent gap approaches the enclosure width.*

## Introduction

Natural convection cooling techniques continue to play a dominant role in the cooling of electronic equipment because of their low cost, ease of maintenance, and absence of electromagnetic interference and operating noise. In many passive cooling situations the heat sources are mounted on arrays of vertically configured boards. The entrance and exit of the vertical channels formed by these arrays may be obstructed as a protection measure. The situation is then one of natural convection from a heated wall in a vertically vented enclosure. The vertical venting designation indicates that the buoyancy-driven flow and heat transfer are restricted by vents in the top and bottom bounding walls of the enclosure. This research was aimed at the investigation of the natural convection heat transfer process and the corresponding flow patterns, which are anticipated to be strongly dependent on the size of the blockage that exists at the inlet and exit.

The vertically vented enclosure begins to resemble a traditional (unvented) enclosure as the vent gap spacings are reduced. As the gap spacings decrease to zero, the geometry considered in this study becomes a fully enclosed cavity. Since all the walls except for the heated surface were adiabatic, the gap spacing was maintained finite as no other cooling mechanism was provided. Natural convection characteristics of differentially heated enclosures have been studied quite extensively, and a recent review of the prior work in this area is available (Gebhart et al., 1988). When the gap spacing is increased so that it is equal to the width of the enclosure, the vertically vented enclosure becomes a vertical parallel plate channel. Such a configuration has also been extensively studied both numerically and experimentally (Aung et al., 1972; Bar-Cohen and Rohsenow, 1984; Sparrow et al., 1984). Buoyancy-driven flow and heat transfer in two-dimensional fully or partially open enclosures has also been a topic of current research (LeQuere et al., 1981; Penot, 1982; Hess and Henze, 1984; Chan and Tien, 1985, 1986; Chen et al., 1985; Humphrey and To, 1986; Clausing et al., 1987; Miyamoto et al., 1989).

The foregoing review of previous work has revealed little research in the area of natural convection heat transfer in

vertically vented enclosures. The purpose of this study is to characterize the flow and heat transfer in a vertically vented enclosure containing one isothermally heated wall. This problem is approached using experimental and analytical methods.

## Experimental Apparatus and Method

Figure 1 shows schematically a side view of the enclosure used for the experimental arm of the study. The heated vertical wall at the right was maintained at a constant temperature while the remaining walls were insulated. The isothermally heated wall was constructed of pure copper. Heated water was circulated from a Neslab RTE-220 constant-temperature bath through channels that were milled in a counterflow arrangement inside the copper wall. Five thermocouples were mounted just below the heated surface to verify that the wall was nearly isothermal. The maximum surface temperature variation was found to be less than 1.5 percent of the minimum difference between the ambient and heated wall temperature. The horizontal surfaces and the vertical wall opposite the heated wall were maintained adiabatic. The horizontal walls were constructed of 1.6-mm-thick balsa wood. The movable inlet and exit vent walls were also balsa wood, and were 5.1 cm long

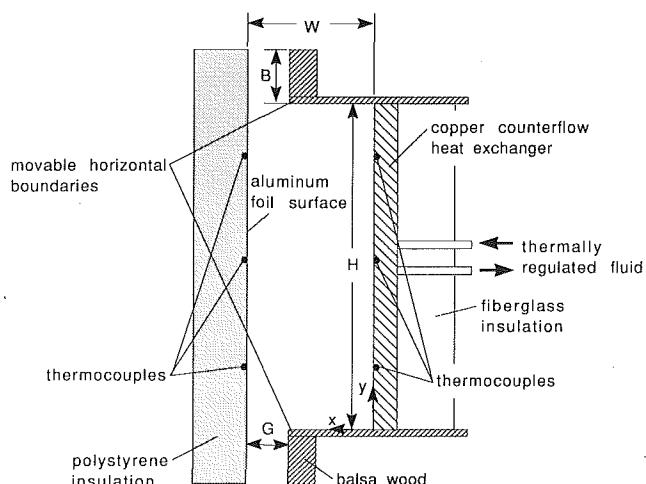


Fig. 1 Schematic of experimental apparatus and definition of geometric parameters

Contributed by the Heat Transfer Division for publication in the JOURNAL OF HEAT TRANSFER. Manuscript received by the Heat Transfer Division August 24, 1990; revision received June 21, 1991. Keywords: Electronic Equipment, Natural Convection.

and 4.8 mm thick. The vertical adiabatic side wall at left was constructed of 15.2-cm-thick closed-pore extruded polystyrene insulation. Five thermocouples were placed below the surface of the adiabatic wall to assess when steady-state conditions were achieved. Optical quality glass was placed at the spanwise ends of the enclosure, forming the remaining vertical boundaries of the cavity. This allowed optical access to the convecting air medium for the Mach-Zehnder interferometric studies.

The height of the heated wall,  $H$ , was maintained constant at 19.05 cm. The width of the enclosure,  $W$ , was varied between 1.9 cm and 10.2 cm. The vent gap spacing,  $G$ , was adjusted through a range of 1.9 mm to 10.2 cm. The length of the inlet and exit vent,  $B$ , was held constant at 5.1 cm. The depth of the enclosure in the spanwise direction (normal to the plane of Fig. 1) was 30.5 cm. This cavity depth was a compromise between two-dimensionality of the flow and heat transfer in the enclosure and unacceptably high interference fringe density. Smoke visualization revealed the flow to be two-dimensional for all but the smallest gap spacing,  $G/W = 0.1$ , where some three-dimensional fluid motion was observed.

To minimize the radiative heat transfer in the cavity, aluminum foil was mounted on the insulated side wall and the isothermal wall was polished to a mirror finish. Using a zonal analysis, the net radiation heat transfer to the adiabatic side wall was estimated to be less than 6 percent of the average convective heat transfer from the isothermal surface.

Each of the dimensional geometric parameters was normalized by the width of the enclosure: aspect ratio,  $H/W$ , normalized gap spacing,  $G/W$ , and the normalized vent length,  $B/W$ . The Grashof number,  $Gr$ , and the Nusselt number,  $Nu$ , used in this study were also based on the width of the enclosure. This choice of characteristic length was made because of its use in the limiting case of natural convection in vertical parallel plate channels,  $G/W \rightarrow 1$  (Aung et al., 1972; Sparrow et al., 1984).

A Mach-Zehnder Interferometer (MZI) was used to quantify the temperature field of the convecting air within the enclosure. This interferometer utilized 30.5-cm-dia mirrors with a Spectra Physics Model 124 B 15 mW helium-neon laser as the light source. The MZI is of 60 deg parallelogram design to optimize the field of view. The interferometer was used in infinite fringe mode. A 10.2 cm  $\times$  12.7 cm format camera was used to photograph the images produced by the interferometer. The camera was used without a lens and the image was focused directly on the negative using the MZI optical system. The fringe pattern and the temperature at the surface of the vertical adiabatic wall were monitored to ascertain when steady-state conditions prevailed. Data were not collected until the fringe pattern remained fixed and the temperatures at different locations of the wall ceased to change, at least 8 hours after heating was initiated.

Established optical techniques were used to determine the

local heat transfer along the isothermal wall from the Mach-Zehnder interferograms (Hauf and Griggull, 1970). The temperature difference between adjacent fringes in Mach-Zehnder interferograms to be presented was approximately 3.3°C; however, this difference is dependent on the local absolute temperature. The perpendicular distance from the heated surface to the fringes near the isothermal wall was determined using a measuring microscope with 12.7  $\mu$ m resolution. The change in temperature versus distance from the wall was plotted and curve fitted. The results generated using first, second, and third-order regression polynomials to curve fit the data were investigated. The linear fit inaccurately represented the curvature at the wall, while the third-order fit yielded anomalously low gradients. The second-order polynomial was, therefore, used to curve fit the data in all results reported here. The temperature of the isothermal wall was limited to a minimum of 40°C and to a maximum of 90°C due to fringe density considerations. At least five fringes were used in the curve fit for the determination of the local convective heat flux; fewer than five resulted in unacceptable inaccuracies. For small differences between the heated wall and inlet temperature, it was necessary to make measurements at each half fringe, while for large temperature differences only measurements at every other fringe were used. The local convective heat flux was then calculated from the Fourier-Biot law by evaluating the differentiated polynomial expression at the heated wall. Fringe displacement due to refraction effects (Eckert and Goldstein, 1976) resulted in a maximum local temperature measurement error of 5 percent of  $(T_w - T_o)$ ; the measurement error was usually 2 percent or less for most conditions.

The average Nusselt number,  $\bar{Nu}$ , for each test case was calculated according to its definition for an isothermal surface

$$\bar{Nu} = \int_0^1 Nu d(y/H) \quad (1)$$

In practice, the integration of Eq. (1) was approximated for the experiments using the local data at discrete points.

Local and average Nusselt numbers were obtained experimentally for enclosures with four different aspect ratios,  $H/W = 1.88, 2.5, 5.0, \text{ and } 10.0$ . The aspect ratio was varied by adjusting the spacing between the isothermal wall and the adiabatic side wall while the height of the enclosure was maintained constant. Dimensionless gap spacings,  $G/W$ , of 0.10, 0.33, 0.67, and 1.0 were studied for each of the aspect ratios considered. In addition,  $G/W = 0.20$  and 0.50 were studied for  $H/W = 5.0$ . The inlet and exit vent gap spacings were identical. The foregoing test cases were completed with  $T_w = 65^\circ\text{C}$ , which corresponds to nominal Grashof numbers  $Gr = 4.22(10^6), 1.81(10^6), 2.27(10^5), \text{ and } 2.79(10^4)$  for  $H/W = 1.88, 2.5, 5.0, \text{ and } 10$ , respectively. In addition,  $H/W = 5.0, G/W = 0.33$  and 0.67; and  $H/W = 5.0, G/W = 0.67$  configurations were studied for  $T_w = 40, 50, \text{ and } 90^\circ\text{C}$ . These wall temper-

## Nomenclature

|   |   |   |
|---|---|---|
| $B$ = length of vent inlet and exit vents, Fig. 1                 | $p_o$ = local ambient hydrostatic pressure                    | $W$ = width of the enclosure, Fig. 1                          |
| $G$ = width of inlet and exit vent gaps, Fig. 1                   | $P$ = dimensionless pressure defect = $(p - p_o)/\rho(v/W)^2$ | $(X, Y)$ = dimensionless coordinates = $(x, y)/W$             |
| $H$ = height of enclosure, Fig. 1                                 | $Pr$ = Prandtl number = $\nu/\alpha$                          | $\beta$ = volumetric coefficient of thermal expansion         |
| $Gr$ = Grashof number = $g\beta(T_w - T_o)W^3/\nu^2$              | $q$ = local convective heat flux along heated wall            | $\theta$ = dimensionless temperature, $(T - T_o)/(T_w - T_o)$ |
| $k$ = thermal conductivity  | $Ra$ = Rayleigh number = $GrPr$                               | $\nu$ = kinematic viscosity                                   |
| $Nu$ = local Nusselt number along heated wall = $qW/k(T_w - T_o)$ | $T_o$ = fluid inlet temperature                               | $\rho$ = fluid density  |
| $\bar{Nu}$ = average Nusselt number, Eq. (1)                      | $T_w$ = isothermal heated wall temperature                    | <b>Subscripts</b>   |
|   | $(U, V)$ = dimensionless velocities = $(u, v)W/\nu$           | $H$ = based on cavity height                                  |



atures expressed as nominal Grashof numbers are  $Gr = 1.06(10^5)$ ,  $1.7(10^5)$ , and  $2.96(10^5)$  for  $H/W = 5.0$  and  $Gr = 8.54(10^5)$ ,  $1.22(10^6)$ , and  $2.33(10^6)$  for  $H/W = 2.5$ . The maximum height-based Grashof number,  $Gr_H = Gr(H/W)^3$ , was  $3.7(10^7)$ . This is well below the traditional limit of  $Ra_H \approx 10^9$  for the onset of turbulence for free convection from an isolated vertical plate. Chen et al. (1985) reported unsteady transport for buoyancy-driven flow in a cavity with fully open side at  $Gr_H \approx 4.4(10^7)$ , while Hess and Henze (1984) documented the onset of turbulence only for  $Gr_H > 3.0(10^{10})$  for the same geometry. Unsteady flow was not observed in this study for  $Gr_H < 3.7(10^7)$  where the side-facing opening of the cavity was shrouded by an adiabatic wall except for the  $G/W = 0.1$  configuration.

Flow visualization experiments were conducted to correlate the flow structure with the local heat transfer data, and to verify the accuracy of the analytical model. The basic optical components of a shadowgraph system with 30.5 cm mirrors were used. The parallel light eliminated optical irregularities, such as taper and curvature, which were found to be present when conventional background lighting was used. To generate smoke for the flow visualization studies, steel wire pulled taut and attached to electrically insulating struts was positioned parallel to, and below the lower vent gap. The wire was coated with glycerine and a small voltage potential was momentarily imposed along it. As the wire heated due to electrical resistance, smoke was generated from the glycerine. The smoke was entrained into the enclosure due to buoyancy. The smoke patterns were then photographed with a 35 mm camera. The imposed voltage was maintained low so that the buoyancy force generated by the heated wire was low relative to the forces in the enclosure. By pulsing the transformer repeatedly, a series of photographs were taken illustrating the flow in the various spatial regions of the cavity. A composite flow map for a given geometric configuration and heating rate was then constructed from the series of photographs. Flow visualization was conducted for an aspect ratio,  $H/W = 5.0$ , at a nominal Grashof number  $Gr = 3.0(10^5)$  for vent gap spacings  $G/W = 0.10$ ,  $0.33$ , and  $0.67$ .

An analysis of possible errors in the experimental measurements revealed a maximum uncertainty in the local Nusselt and Grashof numbers of 8.5 and 12.7 percent, respectively. The maximum uncertainty in normalized gap spacing was found to be 6 percent with the exception of the  $G/W = 0.1$  configuration, where the uncertainty may be as high as 19 percent for the smallest enclosure width.

## Analysis

The partial differential equations governing conservation of mass, momentum, and energy in the vented enclosure were discretized and solved numerically. The dimensionless equations that govern steady, laminar, buoyancy-driven flow for a fluid admitting the Boussinesq approximation are

*Continuity:*

$$\frac{\partial U}{\partial X} + \frac{\partial V}{\partial Y} = 0 \quad (2)$$

*X-Momentum:*

$$\frac{\partial UU}{\partial X} + \frac{\partial VU}{\partial Y} = -\frac{\partial P}{\partial X} + \frac{\partial^2 U}{\partial X^2} + \frac{\partial^2 U}{\partial Y^2} \quad (3)$$

*Y-Momentum:*

$$\frac{\partial UV}{\partial X} + \frac{\partial VV}{\partial Y} = -\frac{\partial P}{\partial Y} + \frac{\partial^2 V}{\partial X^2} + \frac{\partial^2 V}{\partial Y^2} + Gr \theta \quad (4)$$

*Energy:*

$$\frac{\partial U\theta}{\partial X} + \frac{\partial V\theta}{\partial Y} = \frac{1}{Pr} \left( \frac{\partial^2 \theta}{\partial X^2} + \frac{\partial^2 \theta}{\partial Y^2} \right) \quad (5)$$

These equations were solved subject to the following boundary conditions. The side wall opposite the heated wall and the top and bottom walls were considered adiabatic. The heated wall was regarded as isothermal at  $\theta = 1$ . No-slip boundary conditions were imposed along all walls of the enclosure. Pressure boundary conditions are imposed at the inlet and exit vents as has been done for predictions of natural convection in vertical parallel plate channels (Aihara, 1973; Chappidi and Eno, 1990). The pressure at the entrance of the lower vent gap was considered to be uniform and equal to that of the local ambient fluid less the dynamic pressure,  $P = -\bar{V}^2/2$ , due to the acceleration of stagnant ambient fluid into the inlet gap. The pressure at the exit of the upper vent gap was also considered to be uniform and equal to that of the local ambient fluid,  $P = 0$  (i.e.,  $p = p_o$ ).

Natural convection in the vertical parallel plate channel configuration has traditionally been solved using a parabolic marching scheme (Aung et al., 1972). Pressure and arbitrary mean velocity information is provided at the inlet and the solution proceeds by marching in the streamwise direction until the pressure returns to the local ambient level. The channel length is thus determined for the arbitrary imposed inlet velocity. It was not possible to employ a marching scheme to generate a solution for the vertically vented enclosure, however, since the presence of recirculating flow renders the problem elliptic. Consequently, pressure boundary conditions listed in the analytical problem formulation above were imposed at the inlet and exits. Equations (2)–(5) were solved numerically using a control volume-based finite difference method. The SIMPLER algorithm was used to treat the coupling between momentum and continuity, and the power-law scheme was employed to model the combined effects of advection and diffusion (Patankar, 1980). With the imposed pressure boundary conditions at the inlet and exit vent gaps, the average inlet velocity was an outcome of the solution. It is this unique inlet velocity for which the buoyancy forces are balanced by the viscous and other drag forces in the cavity.

A nonuniform grid was used within the enclosure cavity, which clustered the majority of the nodes according to a power-law function near the bottom of the heated cavity. Grid sizes of  $42 \times 52$ ,  $52 \times 62$ ,  $62 \times 72$ , and  $72 \times 82$  were investigated for several geometric configurations to determine the resolution needed to yield a grid independent solution. As the resolution of the grid was increased above the  $62 \times 72$  grid, the predictions for Nu differed by less than 0.2 percent for both small and large aspect ratio enclosures. Thus it was determined that a  $62 \times 72$  grid size yielded an acceptable compromise between grid resolution and required computing time.

## Results and Discussion

The predicted flow structure is compared with that obtained during the flow visualization studies in Fig. 2 for the experimental conditions  $Gr = 3.0(10^5)$ ,  $H/W = 5.0$ ,  $G/W = 0.33$ . The composite flow structure of Fig. 2(b) was constructed from multiple photographic images similar to the example shown in Fig. 2(c). The smoke generation wire was positioned at many different locations in the inlet vent to reveal the pattern of flow in the entire enclosure. The predicted streamlines are in qualitative agreement with the flow structure observed experimentally. The figure reveals that a clockwise-rotating recirculation zone exists in the lower section of the enclosure, which results from a separation of the flow at the inlet vent. The recirculation zone is largely isolated from the remainder of the flow. Such a recirculation zone has been theoretically predicted and observed experimentally in fully open cavities for higher Rayleigh numbers,  $Ra_H \approx 10^7$  (Humphrey and To, 1986; Chen et al., 1985; Chan and Tien, 1985, 1986). Indeed, Chen et al. found outflow near  $y = 0$  at the aperture plane of an open cavity for  $H/W = 0.5$  and  $1.0$  that penetrated the flow outside

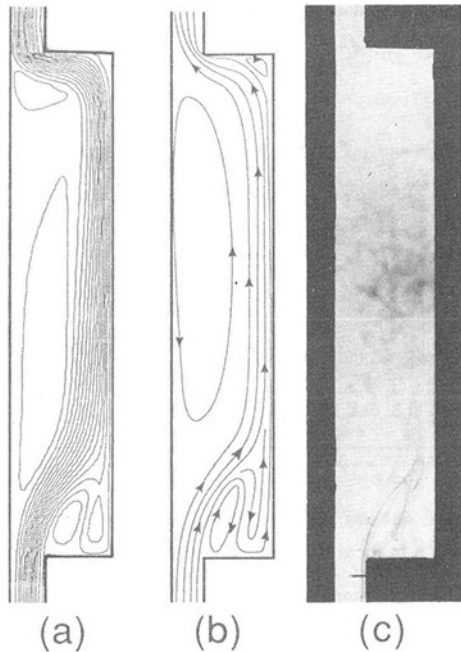


Fig. 2 Flow structure for  $H/W = 5.0$ ,  $G/W = 0.33$ ,  $Gr = 3.0(10^5)$ : (a) theoretical predictions, (b) experimental flow visualization composite sketch, and (c) flow visualization photograph

the enclosure. The outflow was found to increase in size with increasing Rayleigh number and decreasing cavity aspect ratio,  $H/W$ . It appears that the presence of the shrouding wall, as demonstrated here, prevents the recirculation in the cavity bottom from penetrating flow beyond the gap due to the relatively high-velocity inlet.

The primary inlet flow approaches the heated vertical wall near  $y/H = 0.15$ . The approaching flow splits, with a small portion proceeding downward along the right side of the recirculation zone. Upon reaching the lower wall, this flow turns toward the heated wall and proceeds upward, joining the remainder of the primary inlet fluid in a relatively thin boundary layer. Note also that a recirculation zone of significant extent is both observed and predicted along the adiabatic wall. Typical velocities were very low in this large recirculating region, and were only observed sporadically in the flow visualization experiments. Flow visualization experiments for other gap spacings revealed that as  $G/W$  was increased, the size of the recirculation zone was reduced, with a larger fraction of the inlet flow initiating boundary layer development at  $y/H = 0$  (Sefcik, 1990). The recirculation zone near the inlet vanishes for  $G/W \geq 0.7$ , an observation that is corroborated by numerical predictions (Sefcik et al., 1991). As will be seen shortly, the complex flow structure illustrated in Fig. 2 is coupled intimately to the local heat transfer along the isothermal wall.

Mach-Zehnder interferograms are shown in Fig. 3 for dimensionless gap spacings  $G/W = 0.2, 0.5$ , and  $0.67$  at  $H/W = 5.0$  and a nominal Grashof number  $2.27(10^7)$ . Study of these test cases reveals general thermal characteristics that were present in all of the tests. The interferograms reveal that the majority of the isotherms are clustered near the heated wall for each case, indicating highest heat transfer in the boundary layer. The spacing between the isotherms adjacent to the upper half of the heated wall ( $y/H > 0.3$ ) increases in the vertical direction for all configurations tested, indicating a monotonic decrease with  $y$  coordinate in the heat transfer in that region. However, for  $G/W \leq 0.5$  (Figs. 3a and 3b), a local maximum and minimum in the temperature gradient exist near  $y/H \approx 0.2$ . The interferograms show that the isotherms are closely spaced at the bottom of the heated surface, but the spacing between fringes increases at locations farther up the heated wall. The

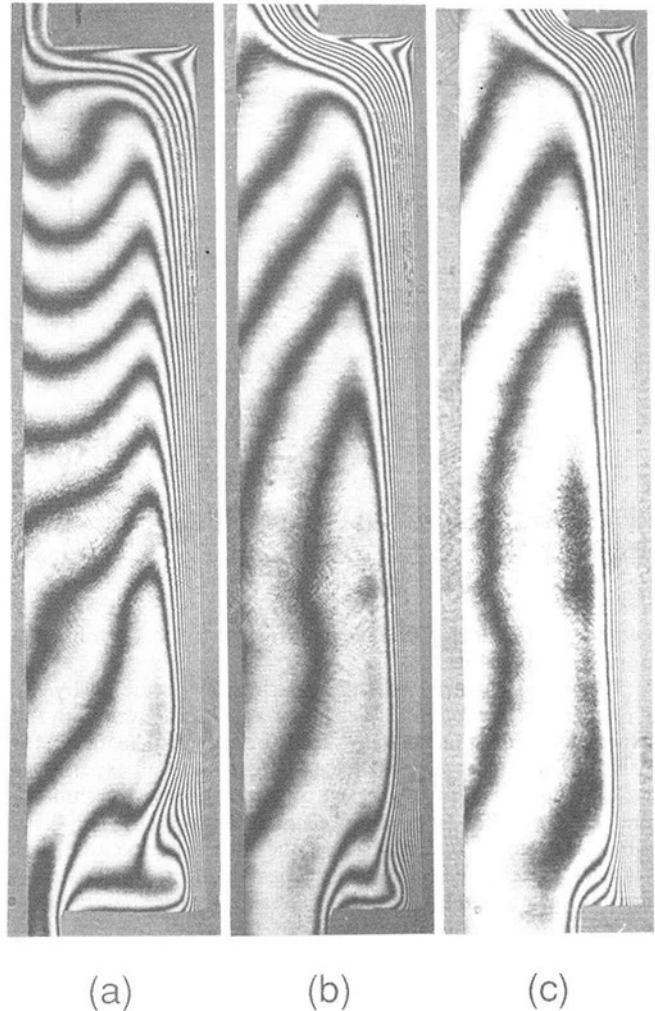


Fig. 3 Mach-Zehnder interferograms for  $H/W = 5.0$  and  $Gr = 2.27(10^5)$ : (a)  $G/W = 0.2$ , (b)  $G/W = 0.5$ , and (c)  $G/W = 0.67$ ; adiabatic and isothermal vertical walls are on the left and right, respectively

spacing between fringes subsequently decreases back to a local minimum somewhere between  $y/H = 0.1$  and  $0.5$ . The exact locations and the magnitudes of the local minimum and maximum heat transfer were found to vary for different geometric parameters (Sefcik, 1990). Note that for an increased gap spacing of  $G/W = 0.67$  (Fig. 3c) the extrema in local heat transfer near  $y/H \approx 0.2$  have nearly vanished.

Experimental and theoretically predicted local heat transfer profiles are shown in Fig. 4 for the conditions  $H/W = 5.0$ ,  $G/W = 0.33$ , and  $Gr = 1.08(10^5)$ ; and  $H/W = 2.5$ ,  $G/W = 0.33$ , and  $Gr = 1.83(10^6)$ . The large variations in heat transfer profiles below  $y/H \approx 0.5$  are evident for both cases. The local Nusselt number is relatively high at  $y/H = 0$  due to locally thin thermal boundary layer in this region (see Fig. 3). The local heat flux decreases as the thermal boundary layer grows. An increase in  $Nu$  then occurs slightly above the recirculation zone where the cool inlet fluid flowing around the top of the recirculation zone penetrates the growing thermal boundary layer. This local maximum heat transfer is reminiscent of the flow and heat transfer in open cavities, where the inlet flow impinges against the vertical heated wall (LeQuere et al., 1981). The highly nonuniform local heat transfer pattern seen in this study was found to be largely dependent on the size of the vent gap spacing and the aspect ratio of the enclosure. The local Nusselt number profiles of Fig. 4 also show that the heat transfer decreases sharply in the region next to the upper one-tenth of the heated wall. This is a result of the air being forced

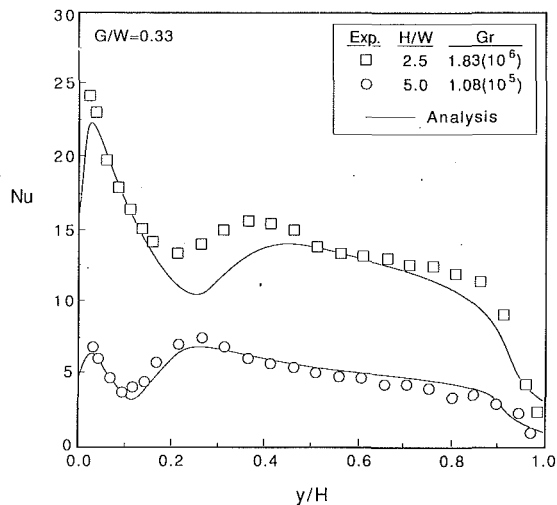


Fig. 4 Comparison of experimental and theoretically predicted local heat transfer profiles

away from the heated surface as it turned to flow around the upper horizontal wall.

The flow structure and the heat transfer predicted by the model and presented in Figs. 2 and 4 agree quite well with the experimental thermal and flow structure and local heat transfer results. The discrepancies between predictions and experimental data lie largely in the region of primary flow attachment, and were found to be even more significant for  $G/W = 0.10$ , where the model underpredicted the local and average heat transfer (Sefcik, 1990). This is believed due to (i) unsteady and three-dimensional flow effects observed experimentally for  $G/W = 0.1$ , and (ii) sensitivity of the predicted flow and thermal structure to the hydrodynamic and thermal boundary conditions particularly for small gap spacings.

**Vent Gap Spacing.** Figure 5 illustrates the variation in experimentally determined local Nusselt number with vertical location along the heated wall for  $H/W = 5.0$  at a nominal Grashof number  $Gr = 2.27(10^5)$  for vent gap spacings,  $G/W$ , between 0.1 and 1.0. The profiles of the local Nusselt number are found to be nearly identical in the region  $0.3 \leq y/H \leq 0.9$  for  $G/W \geq 0.33$ . The sharp decrease in the Nusselt number for the region above  $y/H = 0.9$  for all the test cases except  $G/W = 1.0$  is due to the presence of the upper horizontal wall as was discussed previously. The enclosures for which  $G/W = 0.10$  and  $0.20$  exhibit lower heat transfer over the region of the heated wall  $0.3 \leq y/H \leq 0.9$  than the other four configurations. For these cases the vent gap produces a more severely constricted flow condition at the inlet, which reduces the amount of fluid drawn into the enclosure.

The local variation in the heat transfer coefficient near the lower three-tenths of the isothermal wall is seen to be strongly dependent on the vent gap spacing. This is a result of the significant changes in the flow structure observed during the flow visualization studies for the vent gap spacings investigated. It was found that the point of primary inlet flow attachment on the heated surface was strongly dependent on the size of the vent gap. The inset panel of Fig. 5 illustrates the vertical position on the heated wall where the maximum and minimum Nusselt number are found experimentally,  $(y/H)_{\max}$  and  $(y/H)_{\min}$ , respectively. Also shown in the inset is the location of primary flow attachment on the heated vertical wall, as revealed by the flow visualization photographs. As is evident, there is a clear correlation between the location of locally maximum heat transfer and the position of primary flow attachment. This suggests that the primary inlet flow carries relatively cool fluid to the heated wall, which penetrates the

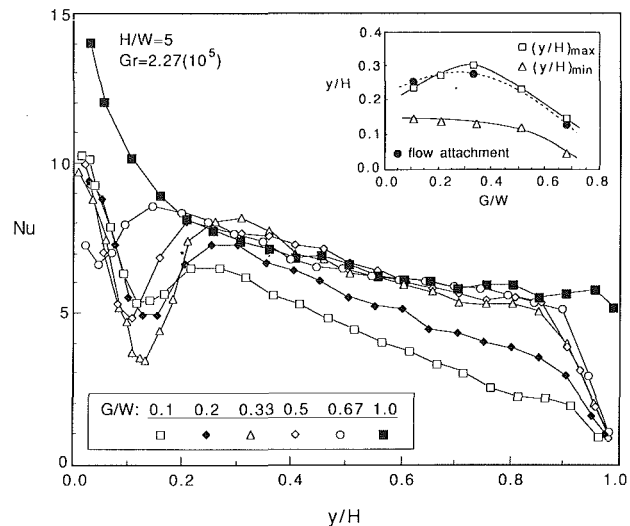


Fig. 5 Variation in local Nusselt number with vertical location along the heated wall for  $H/W = 5.0$ ,  $G/W = 0.10, 0.20, 0.33, 0.5, 0.67$ , and  $1.0$  at a nominal Grashof number  $Gr = 2.27(10^5)$

thermal boundary layer, resulting in a local heat transfer increase there.

Figure 5 reveals that, as the dimensionless gap spacing is varied from 0.10 to 0.33 for  $H/W = 5.0$ , the difference between the magnitudes of the peak and the valley of the heat transfer profile increases. This is accompanied by an increase in the distance separating their corresponding locations (see inset, Fig. 5). This is believed due to increasing velocities of the primary inlet flow for increasing  $G/W$ , which impinges on the heated wall. The inlet mass flow is restricted for  $G/W < 0.33$ . As the vent gap spacing is increased beyond  $G/W = 0.33$ , the difference between the peak and valley in the Nusselt number profile decreases. This is due to an increase in the fraction of fluid that is drawn around the recirculation zone (which shrinks for increasing  $G/W$ ), and flows toward the heated wall at the bottom of the enclosure,  $y/H = 0$ . The magnitude of the local minimum increases significantly for the larger vent gap. With a greater fraction of inlet flow initiating boundary layer flow at the bottom of the heated wall, the increase in local heat transfer is reduced near  $y/H \approx 0.2$  where the inlet flow would otherwise impinge. Note that for  $G/W = 1.0$  the extrema vanish and the Nusselt number profile exhibits characteristics of a vertical parallel plate channel (Aung et al., 1972).

The effect of the vent gap spacing on the average Nusselt number,  $\bar{Nu}$ , is shown in Fig. 6. For each aspect ratio, increasing the vent gap spacing tends generally to increase the average heat transfer coefficient. However, the drastic variations in the local Nusselt number with changes in vent gap spacing seen in Fig. 5 yield only modest changes in the average Nusselt number (generally less than 25 percent). The largest increase in  $\bar{Nu}$  with  $G/W$  is seen to occur between  $G/W = 0.1$  and  $0.33$ . As  $G/W$  is increased above 0.1, the severe inlet mass flow restriction is relaxed, and the local heat transfer along the upper portion of the heated surface increases above the relatively low values prevalent for  $G/W < 0.33$ . Generally, only slight increases in the average heat transfer are observed for  $G/W > 0.33$ .

The data of Fig. 6 suggest a correlation for average Nusselt number as a function of dimensionless gap spacing. Although the experimental data are too sparse to develop a generalized correlation  $\bar{Nu} = f(H/W, G/W, Gr)$ , average Nusselt numbers for  $H/W = 5.0$  and  $Gr = 2.3(10^5)$  were found to correlate well with

$$\bar{Nu}/Gr^{0.25} = 0.289(G/W)^{0.19} \quad (6)$$

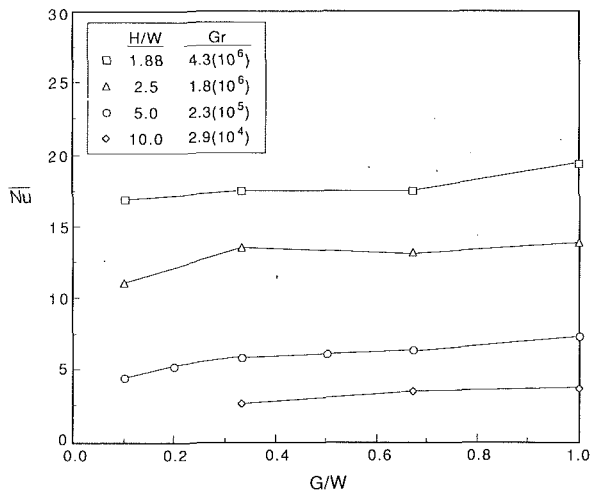


Fig. 6 Effect of the vent gap spacing on the average Nusselt number,  $\bar{Nu}$

for  $0.3 < G/W < 1.0$ . Data for  $G/W = 0.1$  could not be correlated satisfactorily; as has been noted, the  $G/W = 0.1$  data suffered from unsteady and three-dimensional flow effects. The exponent on the Grashof number was imposed arbitrarily based on the limiting case behavior for laminar free convection from a vertical, isothermal wall (Ostrach, 1953), which reveals a dependence on  $Gr^{0.25}$ . A parametric numerical study of natural convection in vertically vented enclosures (Sefcik et al., 1991) has predicted an average Nusselt number dependence on gap spacing of  $(G/W)^{0.18}$  for enclosures of aspect ratio  $H/W = 5.0$ . The correlation exponents from the experimental and theoretical investigations are in good agreement. The correlation of Eq. (6) reveals only a moderate decrease (less than 15 percent) in heat transfer for dimensionless gap spacings greater than  $G/W = 0.5$ .

**Grashof Number.** A general increase in the magnitude of the Nusselt number occurs as the Grashof number increases. However, the shapes of the local heat transfer profiles along the isothermal wall are similar for each test case, and the locations of the peak and valley in the heat transfer remain nearly the same (Sefcik, 1990). Since the shape of the heat transfer profiles remained nearly the same for all Grashof numbers studied, it was concluded that the wall temperature did not significantly change the flow structure within the enclosure for the temperature range studied. Rather, it is suggested that increasing the isothermal wall temperature raises the velocities and the resulting inlet mass flow of the convecting medium due to the increased buoyant force. This is corroborated by the analytical predictions of Sefcik et al. (1991).

The effect of Grashof number on average heat transfer is shown in Fig. 7. Good agreement is observed between theoretical predictions and experimental data; less than 10 percent variation exists between the experimental and predicted values of the average Nusselt number for identical configurations. A general increase in  $\bar{Nu}$  occurs for increasing values of  $Gr$ . Figure 7 also includes the parallel plate correlations of Bar-Cohen and Rohsenow (1984) for the appropriate channel aspect ratio,  $H/W$ . Theoretical predictions for  $G/W = 1.0$  using the model presented here (not shown) were lower than the Bar-Cohen and Rohsenow correlation, albeit with a maximum deviation of less than 10 percent (Sefcik, 1990). The approximate dependence of the average Nusselt number on  $Gr^{0.25}$  is evident for all aspect ratios and vent gap spacings studied. Figure 7 also illustrates the dependence of average Nusselt number on Grashof number for fully open square ( $H/W = 1$ ) cavities (Miyamoto et al., 1989; LeQuere et al., 1981). These results show significantly lower average heat transfer than the results

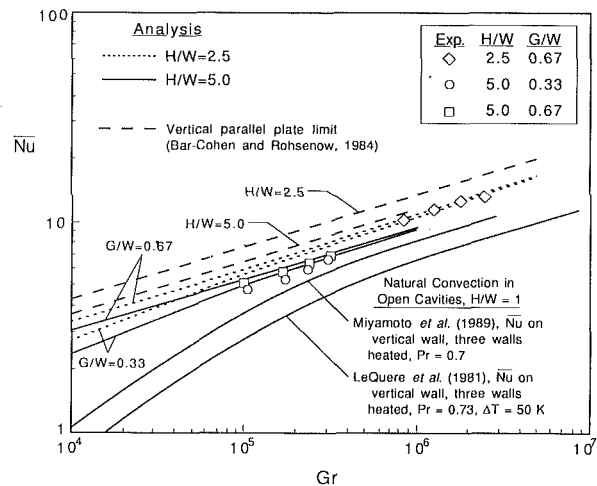


Fig. 7 Variation of the average Nusselt number with Grashof number

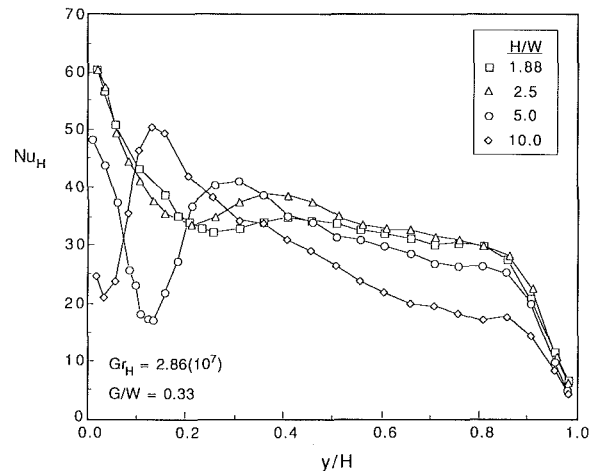


Fig. 8 Effect of enclosure aspect ratio on height-based local Nusselt number for  $G/W = 0.33$ ,  $Gr_H = 2.86(10^7)$ ,  $H/W = 1.88, 2.5, 5.0$ , and  $10.0$

of this study. However, it should be noted that the open cavity results and those of this study are for different  $H/W$ ; it was demonstrated that the open cavity vertical wall heat transfer increases with an increase in  $H/W$  (Humphrey and To, 1986).

**Enclosure Aspect Ratio.** In order to compare the heat transfer coefficients quantitatively for enclosures with varying aspect ratios, the Nusselt number is redefined such that the characteristic length used for each test case is identical. The Nusselt number based on channel height,  $Nu_H = Nu(H/W)$ , bases the Nusselt number on the height of the heated wall rather than the width of the enclosure. Likewise, a Grashof number based on channel height,  $Gr_H = Gr(H/W)^3$ , was used for purposes of comparison. The height-based Grashof number is the same for identical imposed temperature differences. Hence, the heat transfer coefficient results of experiments with the same imposed temperature difference but different cavity widths may be compared directly by examining  $Nu_H$ .

Significant changes in the local heat transfer occur for variable cavity aspect ratio. Local height-based Nusselt number profiles are shown in Fig. 8 for all aspect ratios studied at a nominal  $Gr_H = 2.86(10^7)$ . Generally, for a given dimensionless gap spacing, the inlet impingement flow and resulting locally higher heat transfer become more pronounced as  $H/W$  is increased (shallower cavities). The proximity of the heated wall to the recirculation zone near the inlet influences in a more direct way the local heat transfer in the bottom portion of the cavity. This is consistent with open cavity results, where the recessed (vertical) wall heat transfer was found to increase with

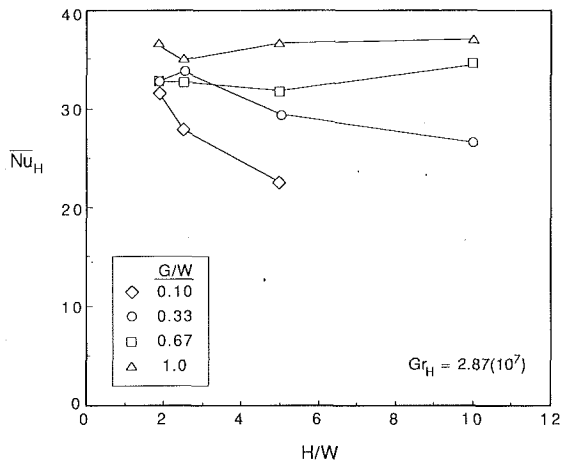


Fig. 9 Influence of enclosure aspect ratio on height-based average Nusselt number for  $Gr_H = 2.87(10^7)$  and  $G/W = 0.10, 0.33, 0.67,$  and  $1.0$

increasing  $H/W$ , and was explained by more intense impingement of the separated inlet flow on the heated wall (Humphrey and To, 1986).

The average Nusselt number based on enclosure height,  $\overline{Nu}_H$ , is plotted as a function of enclosure aspect ratio for  $G/W = 0.10, 0.33, 0.67,$  and  $1.0$  in Fig. 9. The data show that as the gap spacing increases, the relative change in  $\overline{Nu}_H$  decreases for variable aspect ratios. For  $G/W = 0.10$  and  $0.33$  a general decrease in the average modified Nusselt number is seen for increasing aspect ratios. These decreases are due to the mass flow restriction at the inlet and the associated relatively low heat transfer along most of the isothermal wall. Generally, a modest increase in  $\overline{Nu}_H$  occurs as the aspect ratio increases for gap spacings  $G/W = 0.67$  and  $1.0$ . For these gap spacings and at large aspect ratios the recirculation zone near the bottom of the enclosure was either very small or nonexistent. In addition,  $G/W$  is large enough that a severe restriction of the inlet mass flow probably does not occur as the aspect ratio increases. The small increase in  $\overline{Nu}_H$  most likely results from the decreased distance between the inlet vent and the heated wall as the aspect ratio increases. It should be noted, however, that the increases in  $\overline{Nu}_H$  with increasing  $H/W$  for  $G/W > 0.33$  are actually within the experimental uncertainty of the data.

## Conclusions

Buoyancy-driven flow and heat transfer in a vertically vented enclosure have been investigated experimentally and analytically. The effects of the vent gap spacing, enclosure aspect ratio, and Grashof number on the flow structure and local and average heat transfer were examined. A complex flow pattern, which includes a large recirculation zone near the inlet vent, was found to be highly dependent on the gap spacing. The local heat transfer was discovered to be very nonuniform along the lower half of the heated wall as a result of the split inlet flow above the recirculation zone. The flow visualization and analytical predictions for the flow field reveal that the local variations in heat transfer in this region are attributed to the complex flow structure in the lower half of the cavity, which are strongly dependent on the vent gap. The results show that asymptotic behavior to the classical vertical parallel plate re-

sults in the limit as the vent gap approaches the enclosure width. The analysis was seen to predict well the flow structure and local and average heat transfer data.

## Acknowledgments

Financial support of this work under U.S. National Science Foundation Grant CBT-8552493 is gratefully acknowledged.

## References

- Aihara, T., 1973, "Effects of Inlet Boundary Conditions on Numerical Solutions of Free Convection Between Parallel Plates," *Report of the Institute of High Speed Mechanics*, Vol. 28, pp. 1-27.
- Aung, W., Fletcher, L. S., and Sernas, V., 1972, "Developing Laminar Free Convection Between Vertical Plates and Asymmetric Heating," *International Journal of Heat and Mass Transfer*, Vol. 16, pp. 2293-2308.
- Bar-Cohen, A., and Rohsenow, W. M., 1984, "Thermally Optimum Spacing of Vertical Natural Convection Cooled, Parallel Plates," *ASME JOURNAL OF HEAT TRANSFER*, Vol. 106, pp. 116-123.
- Chan, Y. L., and Tien, C. L., 1985, "A Numerical Study of Two-Dimensional Natural Convection in Square Open Cavities," *Numerical Heat Transfer*, Vol. 8, pp. 65-80.
- Chan, Y. L., and Tien, C. L., 1986, "Laminar Natural Convection in Shallow Open Cavities," *ASME JOURNAL OF HEAT TRANSFER*, Vol. 108, pp. 305-309.
- Chappidi, P. R., and Eno, B. E., 1990, "A Comparative Study of the Effect of Inlet Conditions on a Free Convective Flow in a Vertical Channel," *ASME JOURNAL OF HEAT TRANSFER*, Vol. 112, pp. 1082-1085.
- Chen, K. S., Humphrey, J. A. C., and Sherman, F. S., 1985, "Free and Mixed Convective Flow of Air in a Heated Cavity of Variable Rectangular Cross-Section and Orientation," *Philosophical Transactions of the Royal Society*, Vol. A316, pp. 57-84.
- Clausing, A. M., Waldvogel, J. M., and Lister, L. D., 1987, "Natural Convection From Isothermal Cubical Cavities With a Variety of Side-Facing Apertures," *ASME JOURNAL OF HEAT TRANSFER*, Vol. 109, pp. 407-412.
- Eckert, E. R. G., and Goldstein, R. J., 1976, "Optical Measurement of Temperature," in: *Measurements in Heat Transfer*, R. J. Goldstein, ed., Hemisphere Publishing Co., Washington, D. C.
- Gebhart, B., Jaluria, Y., Mahajan, R. L., and Sammakia, B., 1988, *Buoyancy-Induced Flows and Transport*, Hemisphere Publishing Co., New York.
- Hauf, W., and Grigull, U., 1970, "Optical Methods in Heat Transfer," in: *Advances in Heat Transfer*, J. P. Hartnett and T. F. Irvine, Jr., eds., Academic Press, New York.
- Hess, C. F., and Henze, R. H., 1984, "Experimental Investigation of Natural Convection Losses From Open Cavities," *ASME JOURNAL OF HEAT TRANSFER*, Vol. 106, pp. 333-338.
- Humphrey, J. A. C., and To, W. M., 1986, "Numerical Simulation of Buoyant, Turbulent Flow, Part 2. Free and Mixed Convection in a Heated Cavity," *International Journal of Heat and Mass Transfer*, Vol. 29, pp. 593-610.
- LeQuere, P., Humphrey, J. A. C., and Sherman, F. S., 1981, "Numerical Calculation of Thermally Driven Two-Dimensional Unsteady Laminar Flow in Cavities of Rectangular Cross Section," *Numerical Heat Transfer*, Vol. 4, pp. 249-283.
- Miyamoto, M., Kuehn, T. H., Goldstein, R. J., and Katoh, Y., 1989, "Two-Dimensional Laminar Natural Convection Heat Transfer From a Fully or Partially Open Square Cavity," *Numerical Heat Transfer, Part A*, Vol. 15, pp. 411-430.
- Ostrach, S., 1953, "An Analysis of Laminar Free Convection Flow and Heat Transfer About a Flat Plate Parallel to the Direction of the Generating Body Force," National Advisory Committee For Aeronautics, Report 111.
- Patankar, S. V., 1980, *Numerical Heat Transfer and Fluid Flow*, McGraw-Hill, New York.
- Penot, F., 1982, "Numerical Calculation of Two-Dimensional Natural Convection in Isothermal Open Cavities," *Numerical Heat Transfer*, Vol. 5, pp. 421-437.
- Sefcik, D. M., 1990, "Natural Convection Heat Transfer in a Vertically-Vented Enclosure," M. S. Thesis, Department of Mechanical Engineering, Brigham Young University, Provo, UT.
- Sefcik, D. M., Webb, B. W., and Heaton, H. S., 1991, "Analysis of Natural Convection in Vertically-Vented Enclosures," *International Journal of Heat and Mass Transfer*, in press.
- Sparrow, E. M., Chrysler, G. M., and Azevedo, L. F., 1984, "Observed Flow Reversals and Measured-Predicted Nusselt Numbers for Natural Convection in a One-Sided Heated Vertical Channel," *ASME JOURNAL OF HEAT TRANSFER*, Vol. 106, pp. 325-332.

# Turbulent Natural Convection in a Horizontal Layer of Small-Prandtl-Number Fluid

F. B. Cheung

S. W. Shiah

Department of Mechanical Engineering,  
The Pennsylvania State University,  
University Park, PA 16802

D. H. Cho

L. Baker, Jr.

Reactor Analysis and Safety Division,  
Argonne National Laboratory,  
Argonne, IL 60439

*Turbulent natural convection in a horizontal layer of liquid metal confined between two infinite rigid plates is studied theoretically. The layer, with uniformly distributed energy sources in the fluid, is heated from below and cooled from above. An approximate analysis of the Boussinesq equations of motion is performed for the case of small-Prandtl-number fluids to determine the temperature profiles in three different thermal regions of the layer. By matching these profiles in the regions of overlap, analytical expressions are derived for the lower and upper surface Nusselt numbers and the dimensionless turbulent core temperature as functions of the internal and external Rayleigh numbers defined respectively in terms of the volumetric heating rate and surface-to-surface temperature difference of the layer. Comparison of the present results with heat transfer data for liquid mercury is made and found to be good.*

## Introduction

In recent years, uranium metal and uranium/aluminum alloys have been used as the fuel material for some advanced and special purpose nuclear reactors. During a postulated core-meltdown accident in such reactors, a significant amount of core material could become molten. The core melt could relocate downward into the lower plenum region of the reactor vessel, and a layer of molten metal (i.e., core melt) could form above a horizontal steel structure. In most cases, the molten layer is heated internally at high decay power levels, and turbulent natural convection is the likely mode of heat transfer in the molten phase. To assess the extent of thermal attack of the steel structure by the core melt, it is necessary to determine the surface heat fluxes from the boundaries of the molten layer. This calls for the study of turbulent natural convection in a horizontal layer of heat-generating liquid metal.

Many studies of turbulent natural convection in internally heated fluid layers have been performed in the past, as can be seen in the review article by Cheung and Chawla (1987). For the case in which the natural convection process is induced entirely by volumetric heating of the layer, corresponding to the case of a horizontal heat-generating layer with an adiabatic lower boundary, experimental results have been presented by Fiedler and Wille (1971), Kulacki and Nagle (1975), and Kulacki and Emara (1977). They employed electrolytically heated water layers to measure the upper surface Nusselt number,  $Nu_1$ , as a function of the internal Rayleigh number,  $Ra_I$ , defined in terms of the layer depth and the rate of volumetric heat generation. Their results were presented in the form

$$Nu_1 = \text{const} \times Ra_I^m$$

Fiedler and Wille reported a value of  $m = 0.228$  in the range of  $2 \times 10^5 \leq Ra_I \leq 6 \times 10^8$ ; Kulacki and Nagle reported a value of  $m = 0.239$  in the range of  $1.5 \times 10^5 \leq Ra_I \leq 2.5 \times 10^9$ ; Kulacki and Emara reported a value of  $m = 0.227$  in the range of  $1.89 \times 10^3 \leq Ra_I \leq 2.17 \times 10^{12}$ . A theoretical study of the problem has also been performed by Cheung (1980). He found that  $m$  had a value very close to 0.227 in the range of  $1 \times 10^5 \leq Ra_I \leq 1 \times 10^{11}$ . However, for  $Ra_I \geq 1 \times 10^{23}$ ,  $m$  ap-

proached asymptotically a value of 0.25. All of the above studies were limited to moderate-Prandtl-number fluids, and thus the results cannot be applied directly to a heat-generating layer of liquid metal. So far, there are no experimental data for an internally heated layer of small-Prandtl-number fluid.

A closely related problem that has also been investigated quite extensively is the turbulent Rayleigh-Bénard problem concerning natural convection in a horizontal fluid layer heated from below and cooled from above. In this problem, there is no volumetric heating of the fluid, and the natural convection process is induced by bottom or external heating of the layer. Among others, experimental results have been presented by Globe and Dropkin (1959), Chu and Goldstein (1973), Garon and Goldstein (1973), and Threlfall (1975). Globe and Dropkin employed silicone oil, water, and mercury as the working fluids; Chu and Goldstein as well as Garon and Goldstein employed water as the working fluid; Threlfall employed gaseous helium as the working fluid. Their results were presented in the form

$$Nu_E = \text{const} \times Ra_E^n$$

where  $Nu_E$  is the lower and upper surface Nusselt number for the externally heated layer and  $Ra_E$  the external Rayleigh number defined in terms of the layer depth and the surface-to-surface temperature difference of the layer. Globe and Dropkin reported a value of  $n = 0.333$  in the range of  $1.51 \times 10^5 \leq Ra_E \leq 6.76 \times 10^8$ ; Chu and Goldstein reported a value of  $n = 0.278$  in the range of  $2.76 \times 10^5 \leq Ra_E \leq 1.05 \times 10^8$ ; Garon and Goldstein reported a value of  $n = 0.293$  in the range of  $1.34 \times 10^7 \leq Ra_E \leq 3.29 \times 10^9$ ; Threlfall reported a value of  $n = 0.280$  in the range of  $4 \times 10^5 \leq Ra_E \leq 2 \times 10^9$ . Note that the mercury data of Globe and Dropkin represent only available heat transfer data for liquid metal.

In this study, a theoretical investigation is made of turbulent natural convection in a horizontal layer of heat-generating liquid metal heated from below, following an approach similar to that of Kraichnan (1962) and Cheung and Chawla (1986). The main objective is to derive correlating equations for the lower and upper surface Nusselt numbers that are applicable to both externally heated and internally heated layers. The theoretical results are validated using the mercury data of Globe and Dropkin (1959) for an externally heated layer, and the final results are then applied to the case of an internally heated liquid metal layer.

Contributed by the Heat Transfer Division for publication in the JOURNAL OF HEAT TRANSFER. Manuscript received by the Heat Transfer Division August 28, 1990; revision received May 2, 1991. Keywords: Enclosure Flows, Liquid Metals, Natural Convection.

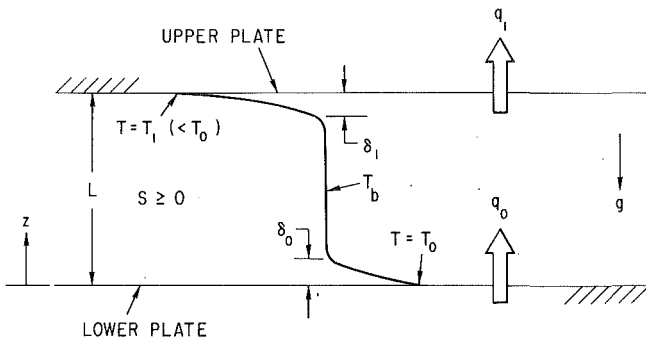


Fig. 1 Schematic of the heat-generating fluid layer heated from below and cooled from above

### Problem Formulation

Consider the process of turbulent natural convection in a horizontal layer of heat-generating liquid metal heated from below and cooled from above, as shown in Fig. 1. The layer, bounded by two rigid surfaces, is infinite in the horizontal extent. The strength,  $S$ , of the volumetric heat generation, the bottom heating rate,  $q_0$ , and the top cooling rate,  $q_1$ , are assumed to be uniform and constant so that a statistically steady one-dimensional transport is maintained in the layer. The properties of the fluid are assumed to be constant except density variation in the buoyancy force. Using the Boussinesq approximation, the governing equations are

$$\nabla \cdot \mathbf{u} = 0 \quad (1)$$

$$\left( \frac{\partial}{\partial t} - \nu \nabla^2 \right) \mathbf{u} = -(\mathbf{u} \cdot \nabla) \mathbf{u} - \rho_0^{-1} \nabla P + \mathbf{k} g \beta T \quad (2)$$

$$\left( \frac{\partial}{\partial t} - \alpha \nabla^2 \right) T = -(\mathbf{u} \cdot \nabla) T + S / \rho_0 C_p \quad (3)$$

where  $\mathbf{k}$  is a unit vector in the vertical direction and the other symbols are defined in the nomenclature.

For statistically stationary one-dimensional flow, the dependent variables may be decomposed into the mean and fluctuating parts, i.e.,

$$T = \bar{T} + \theta, \quad \bar{T} = \bar{T}(z), \quad \bar{\theta} = \bar{\mathbf{u}} = 0 \quad (4)$$

where  $z$  is the vertical coordinate measured upward from the lower surface. The governing equations become

$$\alpha \frac{d^2 \bar{T}}{dz^2} = \frac{d}{dz} \overline{w\theta} - \frac{S}{\rho_0 C_p} \quad (5)$$

$$\left( \frac{\partial}{\partial t} - \nu \nabla^2 \right) \mathbf{u} = -(\mathbf{u} \cdot \nabla) \mathbf{u} - \rho_0^{-1} \nabla p + \mathbf{k} g \beta \theta \quad (6)$$

$$\left( \frac{\partial}{\partial t} - \alpha \nabla^2 \right) \theta = -w \frac{d\bar{T}}{dz} - [(\mathbf{u} \cdot \nabla) \theta - \overline{(\mathbf{u} \cdot \nabla) \theta}] \quad (7)$$

where  $p = P - \bar{P} - \rho_0 \bar{w}^2$  is the fluctuating pressure and  $\overline{w\theta}$  the eddy heat transport rate. Using the heat flux condition at the lower boundary, Eq. (5) can be integrated to give

$$-\alpha \frac{d\bar{T}}{dz} + \overline{w\theta} = \frac{1}{\rho_0 C_p} (Sz + q_0) \quad (8)$$

From dimensional considerations of Eqs. (6)–(8), it can be shown that the lower and upper surface Nusselt numbers,  $Nu_0$

### Nomenclature

|   |   |   |
|---|---|---|
| $B_i$ = universal constant ( $i = 1, 2$ )   | $T$ = local fluid temperature   | $\theta_b$ = dimensionless turbulent core temperature, Eq. (9)              |
| $C_i$ = integration constant ( $i = 1, 2, 3, 4, 5$ )                              | $T_0$ = lower surface temperature   | $\lambda$ = thermal conductivity of the fluid                               |
| $C_p$ = specific heat   | $T_1$ = upper surface temperature   | $\nu$ = kinematic viscosity of the fluid                                    |
| $D_i$ = universal constant ( $i = 1, 2$ )   | $T_b$ = bulk core temperature   | $\xi$ = dimensionless lower thermal boundary layer thickness = $\delta_0/L$ |
| $f_0$ = unknown function of $\eta$ for the lower thermal boundary layer, Eq. (13) | $\bar{T}_{\delta_0}$ = mean local temperature of the lower thermal boundary layer                     | $\xi$ = dimensionless upper thermal boundary layer thickness, $\delta_1/L$  |
| $f_1$ = unknown function of $\eta$ for the upper thermal boundary layer, Eq. (30) | $\bar{T}_{\delta_1}$ = mean local temperature of the upper thermal boundary layer                     | $\rho_0$ = density of the fluid   |
| $g$ = acceleration due to gravity   | $\mathbf{u}$ = velocity vector  | $\chi_0$ = dimensionless parameter for the lower thermal boundary, Eq. (22) |
| $\mathbf{k}$ = unit vector in the vertical direction                              | $w$ = vertical component of velocity  | $\chi_1$ = dimensionless parameter for the upper thermal boundary, Eq. (38) |
| $L$ = depth of the fluid layer  | $\overline{w\theta}$ = eddy heat flux   | $\langle \rangle$ = root-mean-square quantity                               |
| $Nu_0$ = lower surface Nusselt number, Eq. (9)                                    | $z$ = vertical coordinate measured upward from the lower surface                                      |   |
| $Nu_1$ = upper surface Nusselt number, Eq. (9)                                    | $\alpha$ = thermal diffusivity of the fluid   |   |
| $Nu_E$ = surface Nusselt number for the case of $Ra_I = 0$ , Eq. (46)             | $\beta$ = isobaric thermal expansion coefficient of the fluid   |   |
| $p$ = fluctuating pressure  | $\delta_0$ = lower thermal boundary layer thickness   |   |
| $P$ = local pressure  | $\delta_1$ = upper thermal boundary layer thickness   |   |
| $Pr$ = Prandtl number of the fluid, Eq. (10)                                      | $\Delta T_c$ = temperature drop across the turbulent core   |   |
| $q_0$ = lower surface heat flux   | $\Delta T_{\delta_0}$ = temperature drop across the lower thermal boundary layer                      |   |
| $q_1$ = upper surface heat flux   | $\Delta T_{\delta_1}$ = temperature drop across the upper thermal boundary layer                      |   |
| $Ra_E$ = external Rayleigh number, Eq. (10)                                       | $\eta$ = dimensionless local spatial variable for the lower boundary layer = $z/\delta_0$             |   |
| $Ra_I$ = internal Rayleigh number, Eq. (10)                                       | $\tilde{\eta}$ = dimensionless local spatial variable for the upper boundary layer = $(L-z)/\delta_1$ |   |
| $S$ = rate of volumetric heating of the fluid layer                               | $\theta$ = fluctuating temperature  |   |
| $t$ = time  |   |   |

and  $Nu_1$ , respectively, and the dimensionless turbulent core temperature,  $\theta_b$ , are functions of the internal Rayleigh number,  $Ra_I$ , the external Rayleigh number,  $Ra_E$  and the fluid Prandtl number,  $Pr$ . These quantities are defined by

$$Nu_0 = \frac{q_0 L}{\lambda(T_0 - T_1)}, Nu_1 = \frac{q_1 L}{\lambda(T_0 - T_1)}, \theta_b = \frac{T_b - T_1}{T_0 - T_1} \quad (9)$$

$$Ra_I = \frac{g\beta SL^5}{2\lambda\alpha\nu}, Ra_E = \frac{g\beta(T_0 - T_1)L^3}{\alpha\nu}, Pr = \frac{\nu}{\alpha} \quad (10)$$

From an overall energy balance of the layer as a whole, we have  $q_1 = q_0 + SL$ . Thus, the upper and lower surface Nusselt numbers are related by

$$Nu_1 = Nu_0 + \frac{2Ra_I}{Ra_E} \quad (11)$$

The above relation is valid as long as the turbulent transport process is statistically steady.

### Analysis

For  $Pr \ll 1$ , the viscous boundary layer is very thin compared to the thermal boundary layer. To determine the functional dependence of  $Nu_0$ ,  $Nu_1$ , and  $\theta_b$  on  $Ra_I$ ,  $Ra_E$ , and  $Pr$ , we seek the temperature behavior in three different thermal regions of the layer (see Fig. 1). These are: (i) the lower thermal boundary layer region where  $0 < z < \delta_0$ , (ii) the well-mixed thermal core region where  $\delta_0 < z < (L - \delta_1)$ , and (iii) the upper thermal boundary layer region where  $(L - \delta_1) < z < L$ .

In the lower thermal boundary layer region, thermal transport is dominated by conduction. Equation (8) may be approximated by

$$\Theta \left( \alpha \frac{dT}{dz} \right) \sim \frac{q_0}{\rho_0 C_p} \text{ or } \frac{\lambda \Delta T_{\delta_0}}{\delta_0} \sim q_0 \quad (12)$$

where  $\Theta$  represents the order of magnitude,  $\Delta T_{\delta_0}$  the temperature drop across the lower thermal boundary layer of thickness  $\delta_0$ , and  $q_0$  the lower surface heat flux. In writing Eq. (12), we have assumed  $\delta_0/L \ll 1$  so that the term involving  $Sz$  in Eq. (8) may be ignored. The validity of this assumption will be examined later. In terms of  $\Delta T_{\delta_0}$ , a near-field temperature profile may be constructed for the lower thermal boundary layer as

$$\bar{T}_{\delta_0} = T_0 - \Delta T_{\delta_0} f_0(\eta) \quad (13)$$

where  $T_0$  is the lower surface temperature,  $\eta = z/\delta_0$  the dimensionless local spatial variable, and  $f_0$  an unknown function of  $\eta$  to be determined during the course of analysis. Substituting Eq. (12) into Eq. (13), we obtain

$$\bar{T}_{\delta_0} = T_0 - \frac{q_0 L}{\lambda} \xi f_0(\eta) \quad (14)$$

where  $\xi = \delta_0/L$  is the dimensionless lower thermal boundary layer thickness, and the proportionality constant of Eq. (12) has been absorbed in the unknown function  $f_0(\eta)$ .

In the well-mixed thermal core region, eddy transport dominates molecular transport. Neglecting the conduction term in Eq. (8), we get

$$\Theta(\overline{w\theta}) \sim \frac{q_0}{\rho_0 C_p} \left( 1 + \frac{Sz}{q_0} \right) \text{ or } \langle w \rangle \langle \theta \rangle \sim \frac{q_0}{\rho_0 C_p} \left( 1 + \frac{Sz}{q_0} \right) \quad (15)$$

where  $\langle \rangle$  denotes the root-mean-square values of the turbulence fluctuating quantities. In Eq. (15), the magnitude of the term  $\overline{w\theta}$  is taken to be on the same order of the product  $\langle w \rangle$  and  $\langle \theta \rangle$ . However, they are not quantitatively identical. The symbol “ $\sim$ ” is used to indicate that the left-hand side is proportional to the right-hand side. Meanwhile, a balance between the inertia term and the buoyancy term in Eq. (6) gives

$$\Theta(\mathbf{u} \cdot \nabla \mathbf{u}) \sim \Theta(g\beta\theta) \text{ or } \frac{\langle w \rangle^2}{z} \sim g\beta \langle \theta \rangle \quad (16)$$

where a mixing length scale on the order of  $z$  has been chosen relative to the lower surface. The use of this mixing length scale for the turbulent core region is adequate as long as  $\delta_0/L \ll 1$ . Similarly, a balance between the advection term and the production term in Eq. (7) leads to

$$\Theta(\mathbf{u} \cdot \nabla \theta) \sim \Theta \left( w \frac{dT}{dz} \right) \text{ or } \Delta T_c \sim \langle \theta \rangle + C_1 \quad (17)$$

where  $\Delta T_c = \bar{T}_c - T_b$  is the temperature drop across the thermal core region,  $\bar{T}_c$  the local fluid temperature,  $T_b$  the bulk fluid temperature at the center of the layer, and  $C_1$  an integration constant, which may be a function of the lower surface heat flux and the local acceleration due to gravity. From Eqs. (15)–(17), we have

$$\Delta T_c \sim (g\beta)^{-1/3} \left( \frac{q_0}{\rho_0 C_p} \right)^{2/3} L^{-1/3} \left[ C_2 + \left( \frac{z}{L} \right)^{-1/3} \left( 1 + \frac{Sz}{q_0} \right)^{2/3} \right] \quad (18)$$

where  $C_2$  is a true constant, independent of  $z$ ,  $q_0$ , and  $g$ . With the above expression for  $\Delta T_c$ , a far-field temperature profile relative to the lower surface may be constructed as

$$\bar{T}_c = T_b + C_3 (g\beta)^{-1/3} \left( \frac{q_0}{\rho_0 C_p} \right)^{2/3} L^{-1/3} \left[ C_2 + (\eta\xi)^{-1/3} \left( 1 + \frac{SL}{q_0} \eta\xi \right)^{2/3} \right] \quad (19)$$

where  $C_3$  is a proportionality constant. Since molecular transport is not important in the thermal core region,  $C_3$  is independent of  $Pr$ . Note that the bulk core temperature,  $T_b$ , is an unknown quantity that needs to be determined in the course of analysis.

We may now determine the lower thermal boundary layer characteristics by matching the expressions for the near-field and far-field temperatures in the region of overlap where  $\eta \sim 1$  and  $\xi \ll 1$ . The existence of such an overlap region is conceivable if we argue that molecular conductivity and eddy conductivity are equally important in the overlap region. From Eqs. (14) and (19), we obtain

$$T_0 - \frac{q_0 L}{\lambda} \xi f_0(\eta) = T_b + C_3 (g\beta)^{-1/3} \left( \frac{q_0}{\rho_0 C_p} \right)^{2/3} L^{-1/3} \{ C_2 + (\eta\xi)^{-1/3} [1 + \Theta(\xi)] \} \quad (20)$$

By manipulating Eqs. (9), (10), and (20), the following relation is obtained:

$$(1 - \theta_b) - Nu_0 \xi f_0(\eta) = C_3 \chi_0 \{ C_2 + (\eta\xi)^{-1/3} [1 + \Theta(\xi)] \} \quad (21)$$

where  $\chi_0$  is given by

$$\chi_0 = Pr^{-1/3} Ra_E^{-1/3} Nu_0^{2/3} = \chi_0(\xi, Pr) \quad (22)$$

Differentiating Eq. (21) with respect to  $\eta$  and ignoring the higher-order term involving  $\Theta(\xi)$ , we get

$$Nu_0 \xi \frac{df_0}{d\eta} = \frac{C_3}{3} \chi_0 \xi^{-1/3} \eta^{-4/3} \quad (23)$$

Rearranging, we have

$$\eta^{4/3} \frac{df_0}{d\eta} = \frac{C_3}{3} \frac{\chi_0}{Nu_0} \xi^{-4/3} \quad (24)$$

Since the left-hand side of the above equation is a function of  $\eta$  only and the right-hand side is a function of  $\xi$  alone, both sides must be equal to the same constant, say  $C_4$ . This leads to

$$f_0(\eta) = C_5 - 3C_4 \eta^{-1/3} \text{ and } \xi = \left( \frac{C_3 \chi_0}{3C_4 Nu_0} \right)^{3/4} \quad (25)$$



where  $C_5$  is an integration constant. Substituting the above results into Eq. (21) and again ignoring the higher-order term involving  $\Theta(\xi)$ , we get

$$1 - \theta_b = C_2 C_3 \chi_0 + C_5 \text{Nu}_0 \left( \frac{C_3 \chi_0}{3 C_4 \text{Nu}_0} \right)^{3/4} \quad (26)$$

From Eqs. (22) and (26), an expression for the lower surface Nusselt number can be derived as

$$\text{Nu}_0 = \frac{(1 - \theta_b)^{4/3} \text{Pr}^{1/3} \text{Ra}_E^{1/3}}{[B_0 + D_0 (\text{Pr} \text{Ra}_E \text{Nu}_0)^{-1/12}]^{4/3}} \quad (27)$$

where  $B_0 = C_5 (C_3/3C_4)^{3/4}$  and  $D_0 = C_2 C_3$  are new constants. Note from Eqs. (22) and (25) that the dimensionless thickness of the lower thermal boundary layer is given by

$$\xi = \delta_0/L = A_0 (\text{Pr} \text{Ra}_E \text{Nu}_0)^{-1/4} \quad (28)$$

where  $A_0 = (C_3/3C_4)^{3/4}$  is a new constant. Evidently, the assumption of  $\xi \ll 1$  is valid if  $\text{Ra}_E \text{Nu}_0 \gg \text{Pr}^{-1}$ . In reactor safety studies,  $\text{Ra}_E$  has a typical value of  $1 \times 10^8$ ,  $\text{Nu}_0$  has a typical value of  $1 \times 10^2$ , and  $\text{Pr} \sim 1 \times 10^{-2}$  for liquid metals. Thus  $\xi$  or  $\delta_0/L$  is on the order of  $1 \times 10^{-2}$ , which is much less than unity. This demonstrates that the above analysis is self-consistent.

To complete the analysis, the upper surface Nusselt number needs to be determined by considering the heat transfer in the upper thermal boundary layer region where  $(L - \delta_1) < z < L$ . Assuming  $\delta_1/L \ll 1$ , Eq. (8) may be approximated by

$$\Theta \left( \alpha \frac{dT}{dz} \right) \sim \frac{q_1}{\rho C_p} \text{ or } \frac{\lambda \Delta T_{\delta_1}}{\delta_1} \sim q_1 \quad (29)$$

where  $\Delta T_{\delta_1}$  is the temperature drop across the upper thermal boundary layer of thickness  $\delta_1$  and  $q_1$  is the upper surface heat flux. In terms of  $\Delta T_{\delta_1}$ , a near-field temperature profile may be constructed for the upper thermal boundary layer as

$$\bar{T}_{\delta_1} = T_1 + \Delta T_{\delta_1} f_1(\tilde{\eta}) \quad (30)$$

where  $T_1$  is the upper surface temperature,  $\tilde{\eta} = (L - z)/\delta_1$  the dimensionless local spatial variable, and  $f_1$  an unknown function of  $\tilde{\eta}$  to be determined during the course of analysis. Substituting Eq. (29) into Eq. (30), we obtain

$$\bar{T}_{\delta_1} = T_1 + \frac{q_1 L}{\lambda} \tilde{\xi} f_1(\tilde{\eta}) \quad (31)$$

where  $\tilde{\xi} = \delta_1/L$  is the dimensionless upper thermal boundary layer thickness.

In the well-mixed thermal core region, eddy transport dominates molecular transport. From Eqs. (6)–(8), we have

$$\langle w \rangle \langle \theta \rangle \sim \frac{q_1}{\rho C_p} \left[ 1 - \frac{S(L - z)}{q_1} \right] \quad (32)$$

$$\frac{\langle w \rangle^2}{L - z} \sim g\beta \langle \theta \rangle \text{ and } \Delta T_c \sim \langle \theta \rangle + \tilde{C}_1 \quad (33)$$

where  $\tilde{C}_1$  is an integration constant and a mixing length scale on the order of  $(L - z)$  has been chosen relative to the upper surface. The above expressions lead to

$$\Delta T_c \sim (g\beta)^{-1/3} \left( \frac{q_1}{\rho C_p} \right)^{2/3} L^{-1/3} \left\{ \tilde{C}_2 + \left( 1 - \frac{z}{L} \right)^{-1/3} \left[ 1 - \frac{S(L - z)}{q_1} \right]^{2/3} \right\} \quad (34)$$

where  $\tilde{C}_2$  is a constant. With the above expression for  $\Delta T_c$ , a far-field temperature profile relative to the upper surface may be constructed as

$$\bar{T}_c = T_b - \tilde{C}_3 (g\beta)^{-1/3} \left( \frac{q_1}{\rho C_p} \right)^{2/3} L^{-1/3} \left[ \tilde{C}_2 + (\tilde{\eta} \tilde{\xi})^{-1/3} \left( 1 - \frac{SL}{q_1} \tilde{\eta} \tilde{\xi} \right)^{2/3} \right] \quad (35)$$

where  $\tilde{C}_3$  is another constant of proportionality.

For  $\tilde{\eta} \sim 1$  and  $\tilde{\xi} \ll 1$ , we may match the near-field and far-field temperatures given by Eqs. (31) and (35), respectively, to yield

$$T_1 + \frac{q_1 L}{\lambda} \tilde{\xi} f_1(\tilde{\eta}) = T_b - \tilde{C}_3 (g\beta)^{-1/3} \left( \frac{q_1}{\rho C_p} \right)^{2/3} L^{-1/3} \{ \tilde{C}_2 + (\tilde{\eta} \tilde{\xi})^{-1/3} [1 - \Theta(\tilde{\xi})] \} \quad (36)$$

By manipulating Eqs. (9), (10), and (36), the following relation is obtained:

$$\theta_b - \text{Nu}_1 \tilde{\xi} f_1(\tilde{\eta}) = \tilde{C}_3 \chi_1 \{ \tilde{C}_2 + (\tilde{\eta} \tilde{\xi})^{-1/3} [1 - \theta(\xi)] \} \quad (37)$$

where  $\chi_1$  is given by

$$\chi_1 = \text{Pr}^{-1/3} \text{Ra}_E^{-1/3} \text{Nu}_1^{2/3} = \chi_1(\tilde{\xi}, \text{Pr}) \quad (38)$$

Differentiating Eq. (37) with respect to  $\tilde{\eta}$  and ignoring the higher-order term involving  $\Theta(\tilde{\xi})$ , we get

$$\text{Nu}_1 \tilde{\xi} \frac{df_1}{d\tilde{\eta}} = \frac{\tilde{C}_3}{3} \chi_1 \tilde{\xi}^{-1/3} \tilde{\eta}^{-4/3} \quad (39)$$

Rearranging, we have

$$\tilde{\eta}^{4/3} \frac{df_1}{d\tilde{\eta}} = \frac{\tilde{C}_3}{3} \frac{\chi_1}{\text{Nu}_1} \tilde{\xi}^{-4/3} = \tilde{C}_4 \quad (40)$$

where  $\tilde{C}_4$  is a constant, independent of  $\tilde{\eta}$  and  $\tilde{\xi}$ . This leads to

$$f_1(\tilde{\eta}) = \tilde{C}_5 - 3\tilde{C}_4 \tilde{\eta}^{-1/3} \text{ and } \tilde{\xi} = \left( \frac{\tilde{C}_3 \chi_1}{3\tilde{C}_4 \text{Nu}_1} \right)^{3/4} \quad (41)$$

where  $\tilde{C}_5$  is an integration constant. From Eqs. (37), (38), and (40), we have

$$\tilde{\xi} = \delta_1/L = A_1 (\text{Pr} \text{Ra}_E \text{Nu}_1)^{-1/4} \quad (42)$$

and

$$\text{Nu}_1 = \frac{\theta_b^{4/3} \text{Pr}^{1/3} \text{Ra}_E^{1/3}}{[B_1 + D_1 (\text{Pr} \text{Ra}_E \text{Nu}_1)^{-1/12}]^{4/3}} \quad (43)$$

where  $A_1 = (\tilde{C}_3/3\tilde{C}_4)^{3/4}$ ,  $B_1 = \tilde{C}_5 A_1$ , and  $D_1 = \tilde{C}_2 \tilde{C}_3$  are new constants. Note that we have  $\tilde{\xi} \ll 1$  for  $\text{Ra}_E \text{Nu}_1 \gg \text{Pr}^{-1}$ , which is the case for high-Rayleigh-number turbulent convection. Again, the analysis is self-consistent.

Substituting Eqs. (27) and (43) into Eq. (11), the following relation can be derived:

$$\frac{\theta_b^{4/3} \text{Pr}^{1/3} \text{Ra}_E^{1/3}}{[B_1 + D_1 (\text{Pr} \text{Ra}_E \text{Nu}_1)^{-1/12}]^{4/3}} = \frac{(1 - \theta_b)^{4/3} \text{Pr}^{1/3} \text{Ra}_E^{1/3}}{[B_0 + D_0 (\text{Pr} \text{Ra}_E \text{Nu}_0)^{-1/12}]^{4/3}} + \frac{2\text{Ra}_I}{\text{Ra}_E} \quad (44)$$

For given values of  $\text{Ra}_r$ ,  $\text{Ra}_E$ , and  $\text{Pr}$ , Eqs. (27), (43), and (44) give a unique set of values for  $\theta_b$ ,  $\text{Nu}_0$ , and  $\text{Nu}_1$ . Note that the above correlations are considerably different from those obtained by Cheung (1978) based on a semi-empirical boundary layer model.

## Results and Discussion

There are four universal constants ( $B_0$ ,  $B_1$ ,  $D_0$ , and  $D_1$ ) resulting from the analysis that need to be determined by experimental data. As mentioned in the introduction section, the only available heat transfer data for liquid metals are those reported by Globe and Dropkin (1959). To make use of these valuable experimental results, the limiting case of turbulent Rayleigh-Bénard convection in a horizontal fluid layer without internal energy sources is considered. The objective is to es-

estimate the values of the universal constant based on the data of Globe and Dropkin (1959). The results may then be applied to the case of an internally heated layer. Note that there is a strong experimental support for the similarity in turbulent thermal convection between an externally heated layer and an internally heated layer. Based on the data for water and helium reported by various researchers, Bergholz et al. (1979) have clearly demonstrated that the heat transfer characteristics of turbulent Rayleigh-Bénard convection and convection driven by internal energy sources can be derived one from the other. Evidently, the data based on an applied  $\Delta T$  (i.e., an externally heated layer) can be used to construct a model for internal energy generation (i.e., an internally heated layer).

In the absence of internal energy sources, we have  $S = 0$  or  $Ra_I = 0$ . It follows that  $q_0 = q_1$  and  $\theta_b = 0.5$ . From Eq. (44) we obtain

$$B_0 + D_0(\text{Pr}Ra_E \text{Nu}_E)^{-1/12} = B_1 + D_1(\text{Pr}Ra_E \text{Nu}_E)^{-1/12} \quad (45)$$

where

$$\text{Nu}_E = \lim_{Ra_I \rightarrow 0} \text{Nu}_0 = \lim_{Ra_I \rightarrow 0} \text{Nu}_1 \quad (46)$$

For Eq. (45) to be valid for different values of  $Ra_E$  and  $\text{Pr}$ , we require

$$B_0 = B_1 = B \text{ and } D_0 = D_1 = D \quad (47)$$

Thus only two independent universal constants,  $B$  and  $D$ , need to be determined. Equation (27) becomes the same as Eq. (43), which can be written as

$$\text{Nu}_E = \frac{2^{-4/3} \text{Pr}^{1/3} Ra_E^{1/3}}{[B + D(\text{Pr}Ra_E \text{Nu}_E)^{-1/12}]^{4/3}} \quad (48)$$

Rearranging the above expression, we get

$$0.5 \text{Nu}_E^{-2/3} Ra_E^{1/3} \text{Pr}^{1/3} = D + B(\text{Nu}_E Ra_E \text{Pr})^{1/12} \quad (49)$$

Thus, the plot of  $(0.5 \text{Nu}_E^{-2/3} Ra_E^{1/3} \text{Pr}^{1/3})$  versus  $(\text{Nu}_E Ra_E \text{Pr})^{1/12}$  should be a straight line if  $B$  and  $D$  are indeed universal constants.

To determine the values of  $B$  and  $D$ , the heat transfer data for mercury ( $\text{Pr} = 0.024$ ) reported by Globe and Dropkin (1959) are employed. This set of data includes a total of 24 data points, covering the range of  $3.6 \times 10^5 < Ra_E < 3.1 \times 10^7$ . Unfortunately, the experimental results were presented only in a graphic form. The raw data were not given in the journal article. To obtain the numerical values of  $Ra_E$  and  $\text{Nu}_E$  for each data point, the original figure presented by Globe and Dropkin was enlarged photographically. Results are listed in Table 1. Using these values of  $Ra_E$  and  $\text{Nu}_E$ , the corresponding values of  $(\text{Nu}_E Ra_E \text{Pr})^{1/12}$  and  $(0.5 \text{Nu}_E^{-2/3} Ra_E^{1/3} \text{Pr}^{1/3})$  were calculated, and are also listed in Table 1. The 24 data points obtained are plotted in Fig. 2, with  $(0.5 \text{Nu}_E^{-2/3} Ra_E^{1/3} \text{Pr}^{1/3})$  being treated as a function of  $(\text{Nu}_E Ra_E \text{Pr})^{1/12}$ . A straight line is obtained using a least-squares technique. Evidently, the experimental data lend support to the present theory. Both  $B$  and  $D$  are universal constants, independent of  $Ra_E$ . The values of these two constants that best fit the data are found to be  $B = 1.490$  and  $D = 0.923$ . Thus Eq. (48) becomes

$$\text{Nu}_E = \frac{0.233 \text{Pr}^{1/3} Ra_E^{1/3}}{[1 + 0.619(\text{Pr}Ra_E \text{Nu}_E)^{-1/12}]^{4/3}} \quad (50)$$

The above equation is qualitatively similar to the results obtained by Long (1976) for an externally heated layer based on the data of Garon and Goldstein (1973) and Threlfall (1975). It should be noted that the plot of  $(0.5 \text{Nu}_E^{-2/3} Ra_E^{1/3} \text{Pr}^{1/3})$  versus  $(\text{Nu}_E Ra_E \text{Pr})^{1/12}$  greatly amplifies the errors associated with the experimental measurement. As a result, the data appear to be quite scattered. In the conventional plot of  $\text{Nu}_E$  versus  $Ra_E$ , as shown in Fig. 3, the data are fairly well correlated over the entire range of  $3.6 \times 10^5 < Ra_E < 3.1 \times 10^7$ . Equation (50),

Table 1 Heat Transfer data for liquid mercury ( $\text{Pr} = 0.024$ ) from Globe and Dropkin (1959)

| $Ra_E$     | $\text{Nu}_E$ | $(\text{Nu}_E Ra_E \text{Pr})^{1/12}$ | $0.5 \text{Nu}_E^{-2/3} Ra_E^{1/3} \text{Pr}^{1/3}$ |
|------------|---------------|---------------------------------------|---|
| 0.3656E+06 | 2.966         | 2.333                                 | 4.996   |
| 0.3692E+06 | 3.210         | 2.350                                 | 4.755   |
| 0.4400E+06 | 3.614         | 2.409                                 | 4.658   |
| 0.5194E+06 | 4.581         | 2.491                                 | 4.203   |
| 0.5839E+06 | 3.911         | 2.483                                 | 4.856   |
| 0.7599E+06 | 4.491         | 2.567                                 | 4.835   |
| 0.8627E+06 | 5.582         | 2.642                                 | 4.363   |
| 0.8970E+06 | 5.261         | 2.637                                 | 4.599   |
| 0.9511E+06 | 4.861         | 2.633                                 | 4.943   |
| 0.1250E+07 | 6.285         | 2.752                                 | 4.562   |
| 0.1275E+07 | 6.041         | 2.747                                 | 4.714   |
| 0.1549E+07 | 5.582         | 2.774                                 | 5.303   |
| 0.2117E+07 | 7.217         | 2.909                                 | 4.959   |
| 0.2334E+07 | 7.658         | 2.947                                 | 4.924   |
| 0.3127E+07 | 8.126         | 3.035                                 | 5.218   |
| 0.3316E+07 | 6.538         | 2.995                                 | 6.151   |
| 0.3414E+07 | 7.967         | 3.052                                 | 5.444   |
| 0.3448E+07 | 7.508         | 3.039                                 | 5.682   |
| 0.4804E+07 | 8.288         | 3.150                                 | 5.942   |
| 0.4899E+07 | 9.708         | 3.197                                 | 5.383   |
| 0.5401E+07 | 9.518         | 3.218                                 | 5.634   |
| 0.8797E+07 | 10.716        | 3.385                                 | 6.125   |
| 0.1549E+08 | 13.585        | 3.619                                 | 6.315   |
| 0.3037E+08 | 16.553        | 3.892                                 | 6.928   |

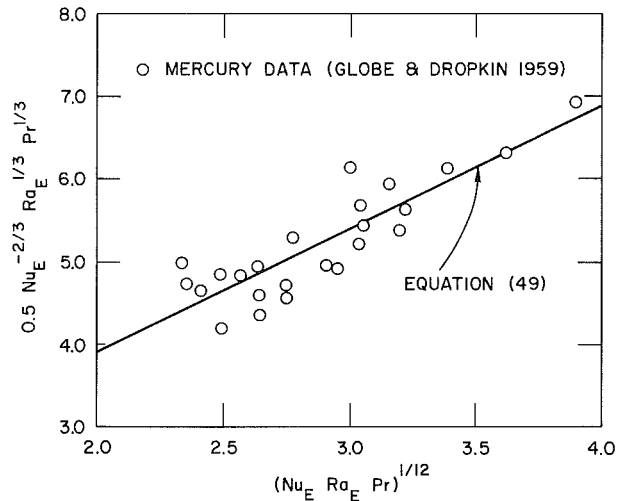


Fig. 2 Correlation of the mercury data ( $\text{Pr} = 0.024$ ): determination of the universal constants

which is given by the solid line, represents the best fit of the data. Using the values of  $B = 1.490$  and  $D = 0.923$ , Eqs. (27), (43), and (44) become

$$\text{Nu}_0 = \frac{0.588(1 - \theta_b)^{4/3} \text{Pr}^{1/3} Ra_E^{1/3}}{[1 + 0.619(\text{Pr}Ra_E \text{Nu}_0)^{-1/12}]^{4/3}} \quad (51)$$

$$\text{Nu}_1 = \frac{0.588 \theta_b^{4/3} \text{Pr}^{1/3} Ra_E^{1/3}}{[1 + 0.619(\text{Pr}Ra_E \text{Nu}_1)^{-1/12}]^{4/3}} \quad (52)$$

$$\frac{(1 - \theta_b)^{4/3} \text{Pr}^{1/3} Ra_E^{1/3}}{[1 + 0.619(\text{Pr}Ra_E \text{Nu}_0)^{-1/12}]^{4/3}} = \frac{\theta_b^{4/3} \text{Pr}^{1/3} Ra_E^{1/3}}{[1 + 0.619(\text{Pr}Ra_E \text{Nu}_1)^{-1/12}]^{4/3}} - \frac{3.4 Ra_I}{Ra_E} \quad (53)$$

For a given set of  $\text{Pr}Ra_E$ , and  $Ra_I$ , the above coupled equations can be solved numerically to determine the values of  $\theta_b$ ,  $\text{Nu}_0$ ,

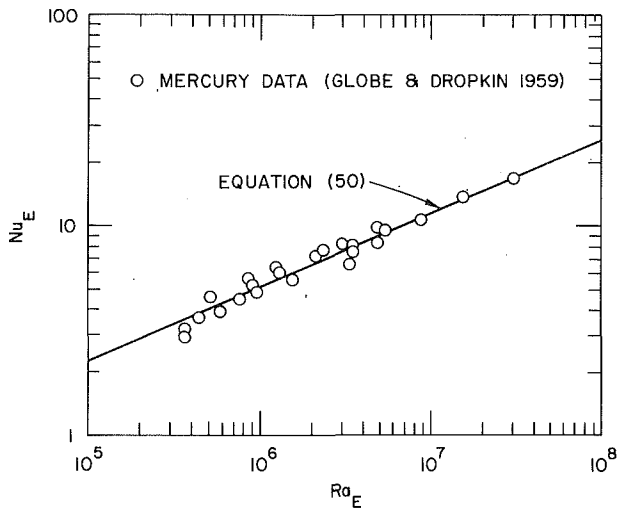


Fig. 3 The Nusselt number-Rayleigh number relation for liquid mercury ( $Pr = 0.024$ )

and  $Nu_1$ . Note that the dependence of the Nusselt numbers on the Prandtl number is substantially different from that obtained for moderate to large Prandtl numbers (Cheung, 1986). Typical results for the case of  $Pr = 0.01$  are depicted in Figs. 4 and 5. In Fig. 4, the dimensionless core temperature  $\theta_b$  is plotted against the external Rayleigh number  $Ra_E$ , with the internal Rayleigh number as a parameter. For the special case of  $Ra_I = 0$ , corresponding to the case of turbulent Rayleigh-Bénard convection,  $\theta_b$  has a constant value of 0.5. For the case of  $Ra_I > 0$ , the situation is quite different. If  $Ra_I$  is less than  $0.5 Ra_E$ , the value of  $\theta_b$  remains almost unchanged at 0.5, indicating a negligible effect of internal heat generation. On the other hand, if  $Ra_I$  is larger than  $0.5 Ra_E$ , the value of  $\theta_b$  becomes greater than 0.5. In fact,  $\theta_b$  would approach unity as  $Ra_I$  becomes much larger than  $Ra_E$  (not shown in the figure). Note that the slopes of the curves are very steep as the limit of  $\theta_b = 1$  is approached. This is not included in Fig. 4 since the main objective of the figure is to show how the curves deviate from the case of  $Ra_I = 0$ . The condition for  $\theta_b = 1$ , corresponding to the special case of heat source-driven turbulent convection with no external heating, will be discussed later.

Figure 5 shows the variations of the lower and upper surface Nusselt numbers,  $Nu_0$  and  $Nu_1$ , respectively, with the external and internal Rayleigh numbers. For the special case of  $Ra_I = 0$ , both  $Nu_0$  and  $Nu_1$  have the same value of  $Nu_E$ , given by

$$Nu_E = \frac{0.05 Ra_E^{1/3}}{[1 + 0.91 (Ra_E Nu_E)^{-1/2}]^{4/3}} \quad (54)$$

For  $Ra_I < 0.5 Ra_E$ , the values of  $Nu_0$  and  $Nu_1$  remain almost the same as  $Nu_E$ , indicating a negligible effect of internal heat generation. On the other hand, for  $Ra_I > 0.5 Ra_E$ ,  $Nu_1$  can become much larger than  $Nu_E$  whereas  $Nu_0$  can become much smaller than  $Nu_E$ .

It is of interest to consider the limiting case of heat source-driven turbulent convection with no external heating. In this case, the fluid layer is thermally insulated from below and the natural convection process is induced entirely by internal heating alone. Under this asymptotic condition, we have  $q_0 = 0$ ,  $Nu_0 = 0$  and  $q_1 = SL$ . It follows from Eqs. (9) and (27) that

$$Nu_1 = \frac{SL^2}{\lambda(T_0 - T_1)} \quad \text{and} \quad \theta_b = 1 \quad (55)$$

Thus the upper surface heat flux  $q_1$  is a given quantity, the unknown of the problem being the bottom surface temperature  $T_0$ . From Eqs. (11) and (43), we have

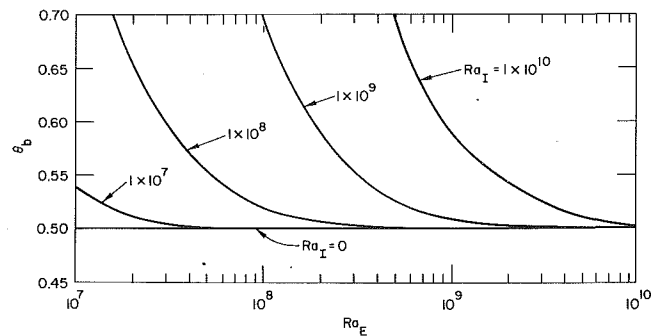


Fig. 4 Variation of the dimensionless turbulent core temperature with the external and internal Rayleigh numbers ( $Pr = 0.01$ )

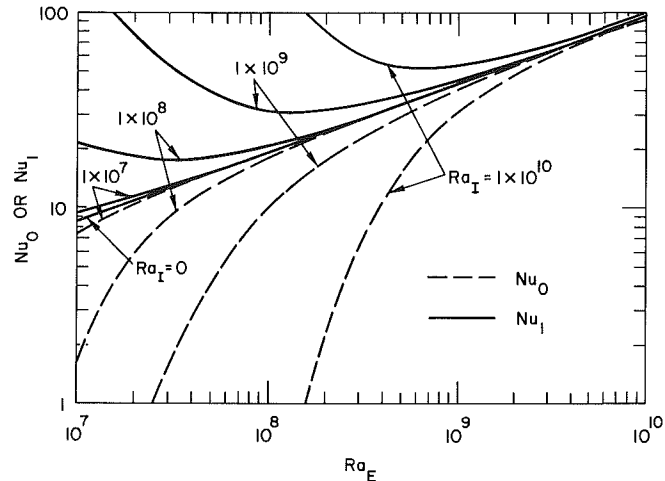


Fig. 5 Variations of the lower and upper surface Nusselt numbers with the external and internal Rayleigh numbers ( $Pr = 0.01$ )

$$Nu_1 = \frac{0.798 Pr^{1/4} Ra_I^{1/4}}{1 + 0.584 (Pr Ra_I)^{-1/12}} \quad (56)$$

The above expression is qualitatively similar to the result obtained by Cheung (1980) for an internally heated layer based on the data of Kulacki et al. (1975, 1977). Note that the external Rayleigh number defined by Eq. (10) is also an unknown quantity in this special case since the bottom surface temperature  $T_0$  is not given. From Eqs. (11) and (56), the following expression for  $Ra_E$  can be derived:

$$\lim_{Nu_0 \rightarrow 0} Ra_E = \frac{1 + 0.584 (Pr Ra_I)^{-1/12}}{0.399 Pr^{1/4} Ra_I^{-3/4}} \quad (57)$$

For a given value of  $Pr$ , the above  $Ra_E - Ra_I$  relationship uniquely defines the conditions for which  $Nu_0 = 0$  and  $\theta_b = 1$ .

## Summary and Conclusions

An approximate analysis of the Boussinesq equations of motion governing the process of natural convection in a horizontal layer of small-Prandtl-number fluid has been performed. Closed-form analytical expressions for the lower and upper surface heat transfer have been derived involving only two independent universal constants. The values of these constants have been determined using the available heated transfer data for liquid mercury with no internal energy sources. Since the present theory applies to both externally heated and internally heated layers, the results can be employed to predict the heat transfer behavior of a horizontal layer of liquid metal with internal heat generation.

It is found that at high external Rayleigh numbers (i.e.,  $Ra_E > 1 \times 10^7$ ) the effect of heat generation is not important for  $Ra_I < 0.5Ra_E$ . Both the lower and upper surface Nusselt numbers have about the same value, and the dimensionless core temperature is approximately equal to 0.5. On the other hand, for  $Ra_I > 0.5Ra_E$ , the upper surface Nusselt number can be considerably larger than the lower surface Nusselt number, whereas the dimensionless core temperature can be considerably greater than 0.5. Under the asymptotic conditions given by Eq. (57), the lower surface becomes thermally insulated and the dimensionless core temperature has a value of unity. In this limiting case, the lower surface Nusselt number is identically zero and the upper surface Nusselt number is a function of the Prandtl number and the internal Rayleigh number alone, as given by Eq. (56). The present results should be useful in the safety studies of advanced and special purpose nuclear reactors.

### Acknowledgments

The work performed by the first author was supported by the Reactor Engineering Division of the Argonne National Laboratory. The authors wish to thank Dr. Bruce Spencer for his interest in this work and Mrs. Eileen Stephenson for typing the manuscript.

### References

Bergholz, R. F., Chen, M. M., and Cheung, F. B., 1979, "Generalization of Heat Transfer Results for Turbulent Free Convection Adjacent to Horizontal Surfaces," *Int. J. Heat Mass Transfer*, Vol. 22, pp. 763-769.

Cheung, F. B., 1978, "Correlation Equations for Turbulent Thermal Convection in a Horizontal Fluid Layer Heated Internally and From Below," *ASME JOURNAL OF HEAT TRANSFER*, Vol. 100, pp. 416-422.

Cheung, F. B., 1980, "Heat-Source-Driven Thermal Convection at Arbitrary Prandtl Number," *J. Fluid Mech.*, Vol. 97, pp. 743-758.

Cheung, F. B., and Chawla, T. C., 1986, "A Unified Theory of Turbulent Thermal Convection in a Horizontal Fluid Layer," *Proc. Eighth Int. Heat Transfer Conf.*, Vol. 3, pp. 1359-1364.

Cheung, F. B., and Chawla, T. C., 1987, "Complex Heat Transfer Processes in Heat-Generating Fluid Layers," *Annual Review of Numerical Fluid Mechanics and Heat Transfer*, Vol. 1, pp. 403-448.

Chu, T. Y., and Goldstein, R. J., 1973, "Turbulent Convection in a Horizontal Layer of Water," *J. Fluid Mech.*, Vol. 60, pp. 141-159.

Fiedler, H., and Wille, R., 1971, "Wärmetransport bei freier Konvektion in einer horizontalen Flüssigkeitsschicht mit Volumenheizung, Teil 1: Integraler Wärmetransport," *Rep. Deutsche Forschungs Versuchsanstalt Luft-Raumfahrt*, Inst. Turbulenzforschung, Berlin.

Garon, A. M., and Goldstein, R. J., 1973, "Velocity and Heat Transfer Measurements in Thermal Convection," *Phys. Fluids*, Vol. 16, pp. 1818-1825.

Globe, S., and Dropkin, D., 1959, "Natural Convection Heat Transfer in Liquid Confined by Two Horizontal Plates and Heated From Below," *ASME JOURNAL OF HEAT TRANSFER*, Vol. 81, pp. 24-30.

Kraichnan, R. M., 1962, "Turbulent Thermal Convection at Arbitrary Prandtl Number," *Phys. Fluids*, Vol. 5, pp. 1374-1389.

Kulacki, F. A., and Nagle, M. E., 1975, "Natural Convection in a Horizontal Layer, With Volumetric Energy Sources," *ASME JOURNAL OF HEAT TRANSFER*, Vol. 97, pp. 204-211.

Kulacki, F. A., and Emara, A. A., 1977, "Steady Transient Thermal Convection in a Fluid Layer With Volumetric Energy Sources," *J. Fluid Mech.*, Vol. 83, pp. 375-395.

Long, R. R., 1976, "The Relation Between Nusselt Number and Rayleigh Number in Turbulent Thermal Convection," *J. Fluid Mech.*, Vol. 73, pp. 445-451.

Threlfall, D. C., 1975, "Free Convection in Low-Temperature Gaseous Helium," *J. Fluid Mech.*, Vol. 67, pp. 17-28.

# Simultaneous Hydrodynamic and Thermal Development in Mixed Convection in a Vertical Annulus With Fluid Property Variations

W. Aung  
Adjunct Professor.

H. E. Moghadam  
Research Assistant.

Department of Mechanical Engineering,  
Howard University,  
Washington, DC

F. K. Tsou  
Professor,  
Department of Mechanical Engineering,  
Drexel University,  
Philadelphia, PA 19104

*This paper concerns a theoretical investigation of forced and mixed convection heat transfer in a vertical concentric annulus. An implicit finite difference technique is developed to study the effects of temperature-dependent fluid properties, which are represented by power law relations. The fluid under consideration in this study is air, which is an ideal gas with  $Pr=0.72$ . Computations are made with a radius ratio of 0.25. The inner wall is heated at UHF, and the outer wall is heated at UHF or is insulated. The axial distribution of the wall-to-bulk temperature ratio is found to undergo a maximum or minimum, depending on whether the wall is heated or insulated. Fluid property variations enhance the local Nusselt numbers. It is shown that, depending on the length of the duct, heat transfer can be appreciably affected by fluid property variation. For the UHF cases studied here, free convection effects enhance the local Nusselt numbers at intermediate axial distances.*

## Introduction

During the laminar flow of fluids in channels with high heating rates, two effects are worthy of attention. These are related to buoyancy and temperature-dependent fluid properties. The former leads to mixed convection flow, which could be substantially different from pure forced convection (Aung, 1987), and this subject has been the focus in an increasing number of recent studies.

Several studies are available for the limiting cases of circular tubes and parallel plates where the fluid properties are considered to be temperature dependent. For the circular tube, existing studies include those of Worsoe-Schmidt and Leppert (1965), Worsoe-Schmidt (1966), and Bankston and McEligot (1970). An extensive review of heat transfer in variable property forced convection in circular tubes has been given by Bergles (1983a, 1983b). For the parallel-plate duct, early investigations such as those by Swearingen and McEligot (1971) and McEligot et al. (1977) were motivated by the need to understand the effects of mixture composition and gas property variation for heating or cooling in regenerative heat exchangers of gas turbine cycles.

In the case of the concentric circular annular duct, the current knowledge concerning heat transfer with fluid property variation is very limited. While the case of constant fluid property was considered more than twenty years ago (Heaton et al., 1964), only a few studies have been reported that deal with variable property flow. Shumway (1969) studied the laminar gas flow in an annulus ( $r^*=0.25$ ) with variation of fluid properties for both fully developed and uniform entry velocity profiles. The study that is most often cited is that by Shumway and McEligot (1971). For high heating rates they studied both fully developed and uniform entry velocity profiles with emphasis on the former. They did not include buoyancy effects in their study. Maitra and Subba Raju (1975) obtained a closed-form solution of the velocity profile for a fully developed upward flow with constant properties. El-Shaarawi and Sarhan (1980) studied free convection effects on the developing flow of air in vertical concentric annuli. Malik and Pletcher (1980)

utilized an explicit finite difference scheme for the prediction of laminar and turbulent convective heat transfer in straight annular passages. Particular emphasis was given to the effects of buoyancy on vertically upward flow. In their calculation only the case of fully developed velocity profile at the inlet was considered. More recently, Jambunathan et al. (1987) studied numerically the effects of variable properties on heat transfer in hydrodynamically and thermally developing laminar flow through annular ducts having aspect ratios of 0.3, 0.5, and 0.7. Curve fits of available experimental data were employed to account for fluid property variations.

The present study deals with a theoretical investigation of laminar mixed convection in a vertical, concentric annulus with temperature-dependent fluid properties. A simultaneous development of the velocity and temperature fields is considered by employing boundary layer-type equations of motion and energy. Results are presented for forced convection with variable properties, and the effects of mixed convection are also considered. These results are not available in the existing literature.

## Mathematical Statement of the Problem

The heat transfer phenomena to be investigated here are described by the conservation equations for two-dimensional laminar flow of a fluid in a vertical annulus. The fluid is assumed to be an ideal gas; hence, its density is given by the ideal gas equation of state, and the enthalpy is simply a function of the specific heat and temperature. Power law relations are used to relate the remaining fluid properties as functions of temperature. The fluid is assumed to approach the channel with a uniform velocity and temperature, and flows vertically upward.

In the following, the governing equations, boundary conditions, and starting conditions are given in dimensionless forms.

### Continuity Equation

$$\frac{\partial}{\partial x^+} (\rho^+ u^+) + \frac{1}{r^+} \frac{\partial}{\partial r^+} (r^+ \rho^+ v^+) = 0 \quad (1)$$

Contributed by the Heat Transfer Division for publication in the JOURNAL OF HEAT TRANSFER. Manuscript received by the Heat Transfer Division October 10, 1989; revision received August 14, 1990. Keywords: Heat Exchangers, Mixed Convection, Numerical Methods.

### Axial Momentum Equation

$$\rho^+ \left( u^+ \frac{\partial u^+}{\partial x^+} + v^+ \frac{\partial u^+}{\partial r^+} \right) = - \frac{Gr_e}{Re_e} Pr_e \rho^+ + \frac{dP}{dx^+} + Pr_e \frac{1}{r^+} \frac{\partial}{\partial r^+} \left( r^+ \mu^+ \frac{\partial u^+}{\partial r^+} \right) \quad (2)$$

### Energy Equation

$$\rho^+ \left( u^+ \frac{\partial H^+}{\partial x^+} + v^+ \frac{\partial H^+}{\partial r^+} \right) = \frac{1}{r^+} \frac{\partial}{\partial r^+} \left( r^+ \frac{k^+}{c_p^+} \frac{\partial H^+}{\partial r^+} \right) \quad (3)$$

### Equation for Cross-Sectional Mass Conservation

$$\int_{r_{iw}^+}^{r_{ow}^+} \rho^+ u^+ r^+ dr^+ = \frac{1}{8} \frac{1+r^*}{1-r^*} \quad (4)$$

**Boundary Conditions.** For  $x^+ > 0$ , on both walls:

$$u^+ = 0, v^+ = 0, -\frac{\partial H^+}{\partial r^+} = \frac{c_p^+}{k^+} q^+ \quad (5)$$

**Starting Conditions.** At  $x^+ = 0$ ,  $r_{iw}^+ < r^+ < r_{ow}^+$ :

$$u^+ = 1, v^+ = 0, H^+ = 0, P = 0. \quad (6)$$

### Numerical Approach

The system of equations given by Eqs. (1)–(4) is solved using an implicit finite difference technique in which each of the equations is replaced by an algebraic equation. A marching procedure is employed for solution. In this, unknowns in the first row of nodes inside the duct are solved for in the beginning of the solution process, and the procedure is repeated for succeeding rows using results for the previous row. To obtain the solution for each row, the algebraic (“difference”) forms

of Eqs. (2) and (4) are solved simultaneously for  $u^+$  and  $P$ . This is followed by solving the algebraic form of Eq. (3) for  $H^+$ . The following equation is then used to calculate temperature:

$$T^+ = [1 + (1+a)H^+]^{1/(1+a)} \quad (7)$$

Next, densities are calculated using the ideal gas law; i.e.,

$$\rho^+ = p^+ / T^+ \quad (8)$$

Radial velocities are computed from explicit expressions, which are derived from the difference form of Eq. (1).

Next, the following power law relations are employed to obtain the fluid properties:

$$\begin{aligned} c_p^+ &= (T^+)^a \\ \mu^+ &= (T^+)^b \\ k^+ &= (T^+)^c \end{aligned} \quad (9)$$

The exponents  $a$ ,  $b$ , and  $c$  used here are given in the Nomenclature, and are very close to those employed by Swearingen and McEligot (1971). Local Nusselt numbers are computed from

$$Nu_w = \frac{q_w^+}{k_b^+ (T_w^+ - T_b^+)} \quad (10)$$

where

$$T_b^+ = \frac{\int_{r_{iw}^+}^{r_{ow}^+} \rho^+ u^+ c_p^+ T^+ r^+ dr^+}{\int_{r_{iw}^+}^{r_{ow}^+} \rho^+ u^+ c_p^+ r^+ dr^+}, \quad k_b^+ = (T_b^+)^c$$

The friction results are represented by the product of total

### Nomenclature

|   |   |  |
|---|---|--|
| $a = 0.095$ ; exponent in power law for specific heat                     | $p$ = absolute pressure   | $\mu$ = viscosity  |
| $b = 0.670$ ; exponent in power law for viscosity                         | $p^+$ = nondimensional pressure = $p/p_e$   | $\mu^+$ = nondimensional viscosity = $\mu/\mu_e$   |
| $c = 0.805$ ; exponent in power law for thermal conductivity              | $Pr_e$ = Prandtl number = $\mu_e c_{p,e}/k_e$   | $\mu_m$ = mean viscosity = $\int_{r_{iw}}^{r_{ow}} \mu r dr / \int_{r_{iw}}^{r_{ow}} r dr$             |
| $c_p$ = specific heat at constant pressure                                | $q''$ = heat flux at either wall  | $\rho$ = density   |
| $c_p^+$ = nondimensional specific heat = $c_p/c_{p,e}$                    | $q^+$ = nondimensional heat flux = $q''_w r_w / (k_e T_e)$                                  | $\rho^+$ = nondimensional density = $\rho/\rho_e$  |
| $D_h$ = hydraulic diameter = $2(r_{ow} - r_{iw})$                         | $r$ = radial coordinate   | $\rho_m$ = mean density = $\int_{r_{iw}}^{r_{ow}} \rho r dr / \int_{r_{iw}}^{r_{ow}} r dr$             |
| $f$ = friction factor = $\tau_w / [\rho_m u_m^2 / 2]$                     | $r^+$ = nondimensional radial coordinate = $r/D_h$  | $\tau_w$ = wall shear stress = $-\left(\mu \frac{\partial u}{\partial r}\right)_w$                     |
| $f_s$ = total friction factor = $(r^* \cdot f_{iw} + f_{ow}) / (1 + r^*)$ | $r^*$ = radius ratio = $r_{iw}/r_{ow}$  |  |
| $Gr_e$ = modified Grashof number = $g D_h^3 / \nu_e^2$                    | $Re_e$ = Reynolds number = $\rho_e u_e D_h / \mu_e$   |  |
| $g$ = acceleration of gravity   | $Re_m$ = Reynolds number = $\rho_m u_m D_h / \mu_m$   |  |
| $H$ = enthalpy  | $T$ = absolute temperature  |  |
| $h$ = local heat transfer coefficient = $q''_w / (T_w - T_b)$             | $T^+$ = nondimensional temperature = $T/T_e$  |  |
| $H^+$ = nondimensional enthalpy = $(H - H_e) / (c_{p,e} T_e)$             | $u$ = axial velocity  |  |
| $k$ = thermal conductivity  | $u^+$ = nondimensional axial velocity = $u/u_e$   |  |
| $k^+$ = nondimensional heat conductivity = $k/k_e$                        | $u_m$ = mean axial velocity = $\int_{r_{iw}}^{r_{ow}} u r dr / \int_{r_{iw}}^{r_{ow}} r dr$ |  |
| $Nu$ = local Nusselt number = $h \cdot r_w / k_b$                         | $v$ = radial velocity   |  |
| $P$ = pressure defect = $(p_e - p) / (\rho_e u_e^2)$                      | $v^+$ = nondimensional radial velocity = $(v/u_e) Re_e Pr_e$                                |  |
|   | $x$ = axial coordinate  |  |
|   | $x^+$ = nondimensional axial coordinate = $(x/D_h) / (Re_e Pr_e)$                           |  |
|   |   | <b>Subscripts</b>  |
|   |   | $b$ = bulk quantity  |
|   |   | $e$ = for gas properties, reference value at $x=0$ ; for nondimensional parameters, evaluated at $x=0$ |
|   |   | $iw$ = inner wall  |
|   |   | $ow$ = outer wall  |
|   |   | $w$ = either wall  |
|   |   | <b>Superscript</b>   |
|   |   | $+$ = nondimensional quantities  |

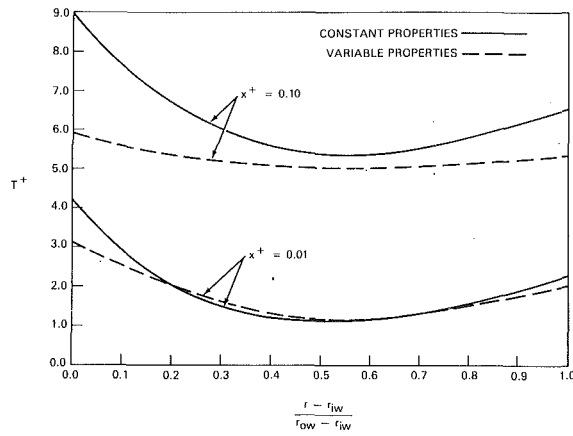


Fig. 1 Temperature profiles for pure forced convection;  $q_{iw}^+ = q_{ow}^+ = 5$

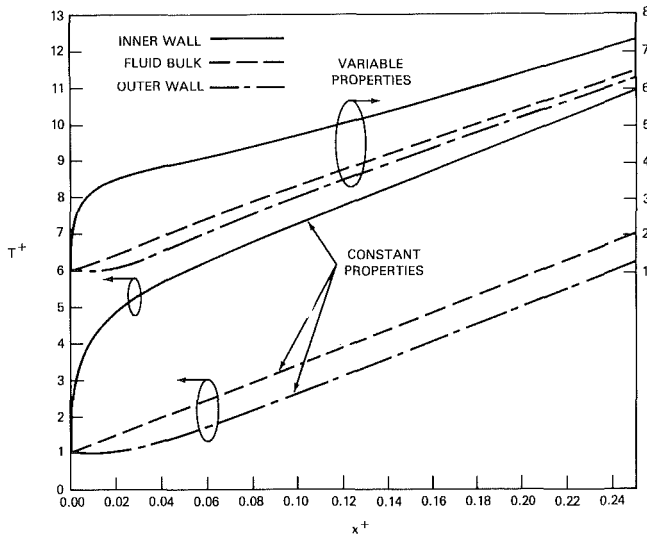


Fig. 2 Temperature distributions for pure forced convection;  $q_{iw}^+ = 5$ ,  $q_{ow}^+ = 0$

friction factor and the Reynolds number ( $f_s \cdot \text{Re}_m$ ). For instance, for the inner wall we can write:

$$f_{iw} \cdot \text{Re}_m = \frac{2 \left( \mu^+ \frac{\partial u^+}{\partial r^+} \right)_{iw}}{\mu_m^+ u_m^+} \quad (11)$$

A more detailed description of the present numerical method is presented elsewhere by Moghadam and Aung (1990).

### Numerical Accuracy

The accuracy of the present method has been investigated by first performing a grid independency test. This led to the choice of 321 equally spaced grids in the transverse direction at the beginning of the computation; that is, at the channel entrance. The method is then applied to study known cases for comparison with the existing literature. The existing solutions are the constant property results of Heaton et al. (1964) and the constant as well as variable property forced convection results of Shumway and McEligot (1971) and Shumway (1969).

The present solutions are indistinguishable from the two existing studies for constant property flow (Heaton et al., 1964; Shumway and McEligot, 1971). For variable property flow with simultaneous development of velocity and temperature profiles, the present results are about 5 percent higher in the development region than the limited numerical results published by Shumway and McEligot (1971). The case being con-

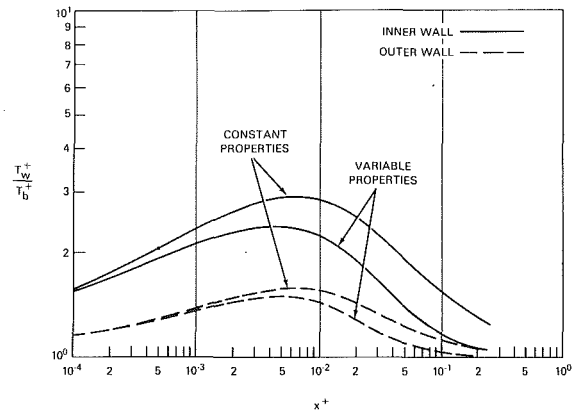


Fig. 3 Wall-to-bulk temperature ratios for pure forced convection;  $q_{iw}^+ = q_{ow}^+ = 5$

sidered is for  $q_{iw}^+ = 20$ , and  $q_{ow}^+ = 0$ . The discrepancy is believed to be caused by the use of much finer mesh spacing in the present method. As mentioned previously, a total of 321 nodes are used near the entrance of the channel in the present study, whereas Shumway and McEligot used 84 radial nodes throughout their study.

### Results

Calculations have been carried out for forced and mixed convection in a vertical annulus having  $r^* = 0.25$ . The velocity and temperature profiles are simultaneously developing. The present results are obtained with UHF boundary conditions.

**Variable Property Effects.** Temperature profiles as a function of axial distance are shown in Fig. 1. Clearly, transverse temperature distribution is more uniform, and axial increase in temperature is slowed as a result of property variation. Noticeable differences in the temperature profiles between constant and variable properties may be noted, and wall temperature gradients are evidently smaller in variable property flow. This trend is not reflected to the same pronounced degree in the derived heat transfer parameters such as the Nusselt number, as will be discussed. The reason is that in variable property flow, a decrease in the wall temperature gradient is countered by an increase in the thermal conductivity.

Axial distributions in the inner and outer wall temperatures and the bulk temperature are plotted in Fig. 2. This figure quantifies the effect already qualitatively shown in Fig. 1; i.e., rates of temperature increase are reduced and transverse differences are also decreased. These trends are shown by the smaller slopes of the variable properties curves and the fact that they are bunched closer together.

Results for wall-to-bulk temperature ratios are given in Fig. 3 for  $q_{iw}^+ = q_{ow}^+ = 5$ . In the case of constant properties, up to  $x^+ = 0.006$ , the rates of increase of the inner and outer wall temperatures are higher than the bulk temperature; therefore, the magnitude of the ratio  $T_w^+ / T_b^+$  is ascending with  $x^+$ . The trend is just the opposite when  $x^+$  is greater than 0.006. In the case of variable properties, for the inner wall, this ratio reaches a maximum value of about 2.4 at  $x^+ = 0.004$ . At this location, the local Nusselt number for the inner wall also exhibits the maximum deviation, by 22.6 percent, from the constant property results (see Fig. 6). For the outer wall, the maximum value of the wall-to-bulk temperature ratio is about 1.5.

When the outer wall is insulated, i.e.,  $q_{iw}^+ = 5$ ,  $q_{ow}^+ = 0$ , the trend for axial distribution of the wall-to-bulk temperature ratio remains unchanged for the heated (inner) wall, but the ratio for the unheated (outer) wall is altered. To see this, one may refer to Fig. 4. Here, the inner wall curves for both constant and variable properties go through maxima. By con-

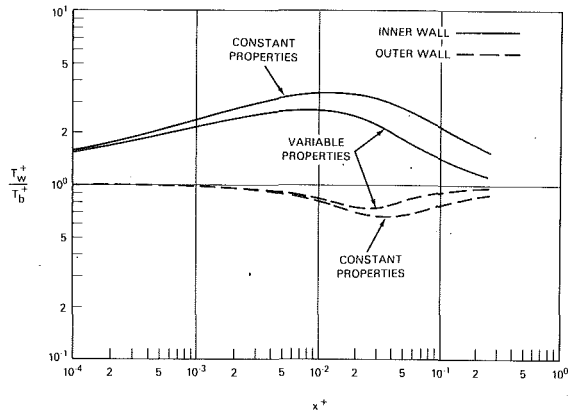


Fig. 4 Wall-to-bulk temperature ratios for pure forced convection;  $q_{iw}^+ = 5, q_{ow}^+ = 0$

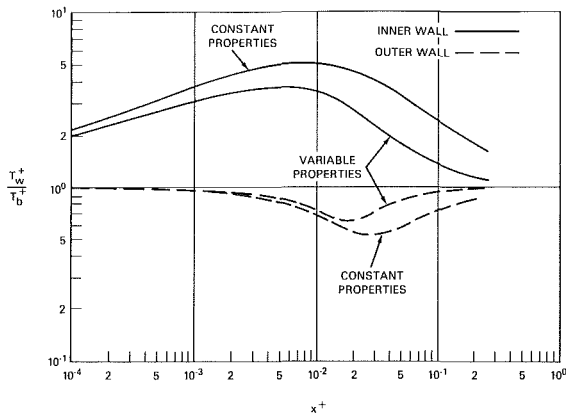


Fig. 5 Wall-to-bulk temperature ratios for pure forced convection;  $q_{iw}^+ = 10, q_{ow}^+ = 0$

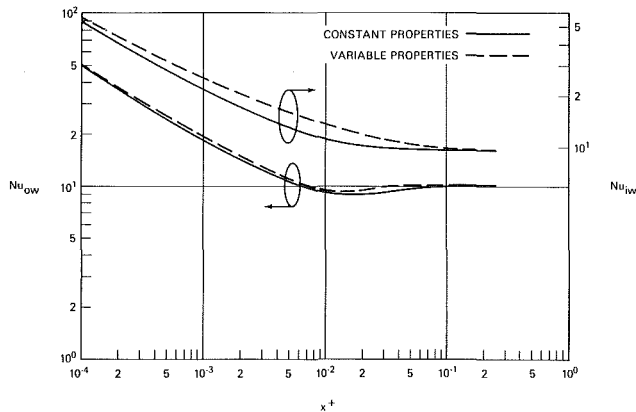


Fig. 6 Inner and outer wall local Nusselt numbers for pure forced convection;  $q_{iw}^+ = q_{ow}^+ = 5$

trast, the outer wall curves have minima. The trends are the same when the inner wall heat flux is doubled, as shown in Fig. 5. Thus, wall heating conditions have a significant bearing on the axial distributions of the wall-to-bulk temperature ratio, which is an important parameter for heat transfer in channel flow.

Irrespective of the magnitude of the heat flux, temperature dependent fluid properties tend to bring these ratios closer for the inner and outer walls.

**Variable Property Effects on the Nusselt Numbers.** Inner and outer wall Nusselt numbers are displayed in Fig. 6. It is noted that the effect of fluid property variation is almost negligible on the outer wall even when both walls are heated. On

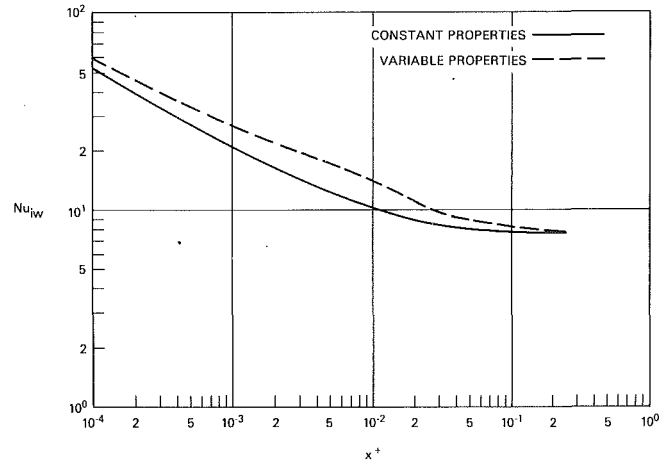


Fig. 7 Inner wall local Nusselt numbers for pure forced convection;  $q_{iw}^+ = 10, q_{ow}^+ = 0$

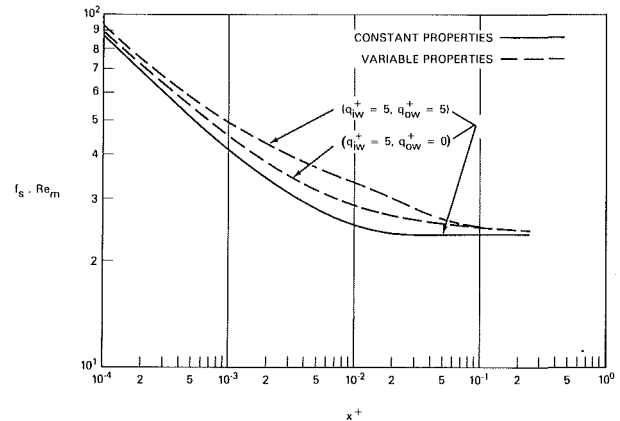


Fig. 8 Total friction factor—Reynolds number product for pure forced convection;  $q_{iw}^+ = q_{ow}^+ = 5$  and  $q_{iw}^+ = 5, q_{ow}^+ = 0$

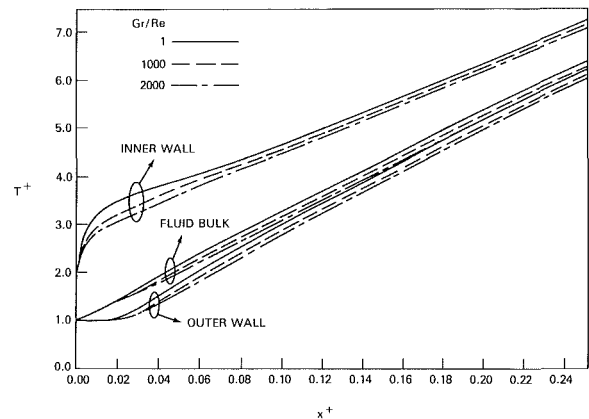


Fig. 9 Temperature distributions for mixed convection with variable properties;  $q_{iw}^+ = 5, q_{ow}^+ = 0$

the inner wall, deviations between constant and variable property results range from small to negligible near the channel entrance and far downstream from it. Local deviations become appreciable in the neighborhood of  $x^+ = 0.01$ . Although the dimensional heat fluxes are identical on both walls, the use of a different characteristic length in the definition of each leads to an actual (dimensional) heat flux on the inner wall that is four times that of the outer wall. (Recall that the radius ratio is 0.25 in the present study.) The higher heating, and hence, higher temperature on the inner wall gives rise to a



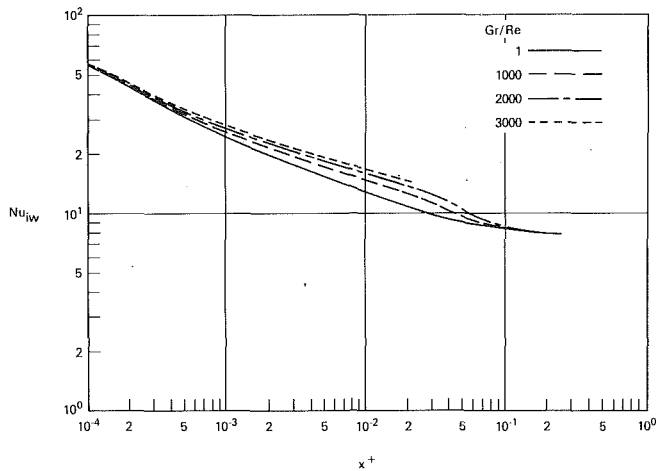


Fig. 10 Inner wall local Nusselt numbers for mixed convection with variable properties;  $q_{iw}^+ = 5$ ,  $q_{ow}^+ = 0$

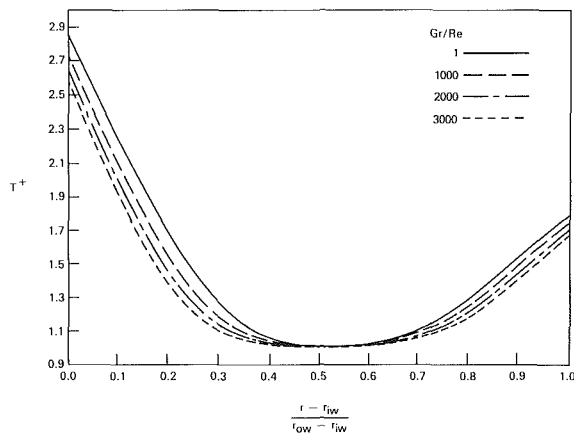


Fig. 11 Temperature profiles at axial location  $x^+ = 0.005$  for mixed convection with variable properties;  $q_{iw}^+ = q_{ow}^+ = 5$

greater degree of property variations; consequently, the departure from constant property values for the inner wall Nusselt number due to property variation is noticeably greater.

Even so, the maximum departure from constant property results, due to temperature-dependence of fluid properties, is less than 20 percent for the specific heating conditions ( $q_{iw}^+ = q_{ow}^+ = 5$ ) shown on Fig. 6. When the dimensionless heat flux on the inner wall is doubled ( $q_{iw}^+ = 10$ ,  $q_{ow}^+ = 0$ ), the deviation could be as much as 50 percent, as illustrated in Fig. 7. The implication is that temperature-dependent fluid properties could have an appreciable influence on the local Nusselt number.

**Effect on the Total Friction Factor.** Figure 8 displays the axial variation of the total friction factor–Reynolds number product for two sets of boundary conditions. Curves for constant and variable fluid properties are shown for comparison. Note that all curves tend to the same constant value at large values of  $x^+$ . Further, the discrepancies between constant and variable properties become larger when the outer wall is heated.

**Mixed Convection Results.** Inner, outer, and bulk temperature distributions for an insulated outer wall are shown in Fig. 9 for three values of  $Gr/Re$ . An increase in this parameter results in a reduction in temperature. At  $x^+ = 0.02$ , there is a decrease of 12 percent in the inner wall temperature with a decrease of only 2.3 percent downstream. The corresponding inner wall local Nusselt numbers are shown in Fig. 10. At  $x^+ = 0.02$ , buoyancy forces cause an increase of about 34 percent. The interruption in the curve for the highest  $Gr/$

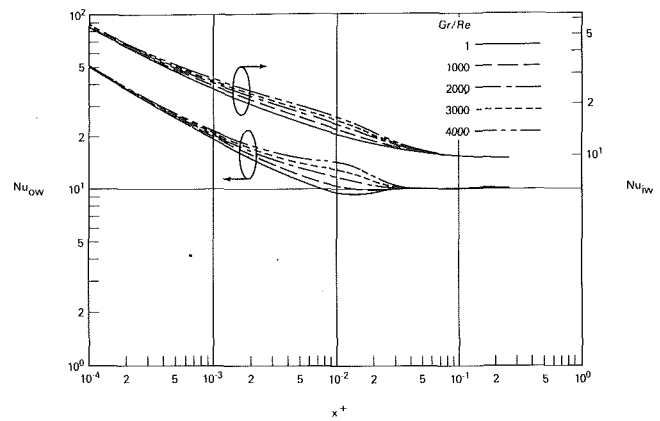


Fig. 12 Inner and outer wall local Nusselt numbers for mixed convection with variable properties;  $q_{iw}^+ = q_{ow}^+ = 5$

$Re$  is caused by the breakdown of the solution due to the onset of flow reversal since the outer wall is relatively cooler (insulated).

For a UHF outer wall, the temperature profiles at an axial location of  $x^+ = 0.005$  are shown in Fig. 11. In the middle of the annular gap where the fluid is cool buoyancy has no effect, whereas elsewhere it causes a decrease in temperature. At the inner and outer walls there are reductions of about 10 and 7 percent, respectively. Inner and outer wall local Nusselt numbers are illustrated in Fig. 12. At  $x^+ = 0.01$ , one can observe increases of 25 and 50 percent, respectively. Note that the asymptotic values of the Nusselt number are higher than those for an insulated outer wall (see Fig. 10).

## Conclusions

In the present study we have presented a detailed account of the effects of temperature-dependent fluid properties on laminar forced and mixed convection in a concentric circular vertical annulus. This problem contains many parameters, and hence, only typical cases have been presented for discussion in this paper. It is believed that these cases have served to shed additional light on variable property and mixed convection effects in vertical, concentric annular ducts. The conclusions arising from this study may be summarized as follows:

- 1 The overall effect of thermal fluid property variations is to decrease temperature gradients in the channel.
- 2 Temperature-dependent properties cause the local Nusselt number to increase over the constant property value. The increase is negligible on an insulated wall but becomes larger with higher heating and could be as much as 50 percent. Extrapolating from this, it would appear that variable property effects can be very significant in high heating rate situations.
- 3 The wall-to-bulk temperature ratio exhibits a maximum on the heated wall and a minimum on an insulated wall.
- 4 For the UHF boundary conditions studied here, buoyancy forces cause a reduction in temperatures while they enhance the local Nusselt numbers at relatively short distances from the inlet. These effects were found to be negligible near the entrance and far downstream.

## References

- Aung W., 1987, "Mixed Convection in Internal Flow," *Handbook for Single-Phase Convective Heat Transfer*, S. Kakac, R. Shah, and W. Aung, eds., Wiley, Chap. 15, pp. 15.1–15.51.
- Bankston, C. A., and McEligot, D. M., 1970, "Turbulent and Laminar Heat Transfer to Gases With Varying Properties in the Entry Region of Circular

Tubes," *International Journal of Heat and Mass Transfer*, Vol. 13, pp. 319-344.

Bergles, A. E., 1983a, "Prediction of the Effects of Temperature-Dependent Fluid Properties on Laminar Heat Transfer," *Low Reynolds Number Flow Heat Exchangers*, S. Kakac, R. K. Shah, and A. E. Bergles, eds., Hemisphere Publishing Corp., pp. 451-471.

Bergles, A. E., 1983b, "Experimental Verification of Analyses and Correlation of the Effects of Temperature-Dependent Fluid Properties on Laminar Heat Transfer," *Low Reynolds Number Flow Heat Exchangers*, S. Kakac, R. K. Shah, and A. E. Bergles, eds., Hemisphere Publishing Corp., pp. 473-486.

El-Shaarawi, M. A. I., and Sarhan, A., 1980, "Free Convection Effects on the Developing Laminar Flow in Vertical Concentric Annuli," *ASME JOURNAL OF HEAT TRANSFER*, Vol. 102, pp. 617-622.

Heaton, H. S., Reynolds, W. C., and Kays, W. M., 1964, "Heat Transfer in Annular Passages: Simultaneous Development of Velocity and Temperature Fields in Laminar Flow," *International Journal of Heat and Mass Transfer*, Vol. 7, pp. 763-781.

Jambunathan, K., Edwards, R. J., Pritchard, J. G., and Bland, J., 1987, "A Computational Study of Developing Laminar Annular Fluid Flow With Heat Transfer," presented at the National Heat Transfer Conference, Pittsburgh, PA, Aug. 9-12; ASME Paper No. 87-HT-13.

Maitra, D., and Subba Raju, K., 1975, "Combined Free and Forced Convection Laminar Heat Transfer in a Vertical Annulus," *ASME JOURNAL OF HEAT TRANSFER*, Vol. 97, pp. 135-137.

Malik, M. R., and Pletcher, R. H., 1980, "Calculation of Variable Property Heat Transfer in Ducts of Annular Cross Section," *Numerical Heat Transfer*, Vol. 3, pp. 241-257.

McEligot, D. M., Taylor, M. F., and Durst, F., 1977, "Internal Forced Convection to Mixtures of Inert Gases," *International Journal of Heat and Mass Transfer*, Vol. 20, pp. 475-486.

Moghadam, H., and Aung, W., 1990, "Numerical Method for Laminar Convection in Concentric Vertical Annular Duct With Variable Properties," *Numerical Heat Transfer*, Part A, Vol. 18, pp. 357-370.

Shumway, R. W., 1969, "Variable Properties Laminar Gas Flow Heat Transfer and Pressure Drop in Annuli," Ph.D. Dissertation, Aerospace and Mechanical Engineering Department, University of Arizona, Tempe, AZ.

Shumway, R. W., and McEligot, D. M., 1971, "Heated Laminar Gas Flow in Annuli With Temperature-Dependent Transport Properties," *Nuclear Science and Engineering*, Vol. 46, pp. 394-407.

Swearingen, T. B., and McEligot, D. M., 1971, "Internal Laminar Heat Transfer With Gas-Property Variation," *ASME JOURNAL OF HEAT TRANSFER*, Vol. 93, pp. 432-440.

Worsoe-Schmidt, P. M., and Leppert, G., 1965, "Heat Transfer and Friction for Laminar Flow of Gas in a Circular Tube at High Heating Rate," *International Journal of Heat and Mass Transfer*, Vol. 8, pp. 1281-1301.

Worsoe-Schmidt, P. M., 1966, "Heat Transfer and Friction for Laminar Flow of Helium and Carbon Dioxide in a Circular Tube at High Heating Rate," *International Journal of Heat and Mass Transfer*, Vol. 9, pp. 1291-1295.

S. Venkateswaran  
Research Assistant.

S. T. Thynell  
Assistant Professor.  
Mem. ASME

C. L. Merkle  
Distinguished Alumni Professor.  
Mem. ASME

Department of Mechanical Engineering,  
The Pennsylvania State University,  
University Park, PA 16802

# A Study of Thermal Radiation Transfer in a Solar Thruster

*Combined convective and radiative heat transfer in an axisymmetric solar thruster is analyzed. In a solar thruster, focused solar energy is converted into thermal energy by volumetric absorption, resulting in a significant increase in the temperature of the propellant gas. The heated gas is then expanded through a propulsive nozzle in order to generate thrust. In the present theoretical analysis, submicron size particles are employed for providing the mechanism of solar energy absorption. The two-dimensional radiation problem is solved using both an exact integral method and the  $P_1$ -approximation. The overall energy transfer is solved iteratively by numerical means. The computational model is used to perform parametric studies of the effects of Boltzmann number, optical dimensions of the medium, and wall emissivity. The overall performance of the solar thruster is assessed by determining the thrust levels and the specific impulses of the device under different operating conditions.*

## Introduction

In recent years, there has been an interest in employing solar energy as the energy source for the propellant working fluid in an otherwise conventional rocket engine (Shoji, 1984; Rault, 1985; Venkateswaran et al., 1990). The application of this advanced propulsion concept is in space-based systems, where solar energy is readily available. In a solar thermal rocket, concentrated solar energy is beamed directly into the propellant (usually hydrogen) and converted into thermal energy by volumetric absorption. A highly efficient absorption of the sun's energy can be achieved by seeding the hydrogen gas with small amounts of either alkali vapors or submicron size particles (Hull and Hunt, 1984; Wang and Yuen, 1986). The high-temperature gas may then be expanded in a rocket nozzle in order to produce thrust. Solar thrusters are capable of delivering moderate thrusts (100 to 1000 N) at relatively high specific impulses (above 500 s) compared to conventional chemical systems. This promise of high specific impulse makes solar propulsion an attractive alternative to chemical propulsion.

Previous studies of this problem have employed relatively simplified approaches for treating the overall energy transport problem. One-dimensional studies have been employed (Palmer, 1978; Rault, 1985) to predict solar-sustained plasmas in alkali vapors; however, these studies result in completely misleading estimates for the mass flux through the nozzle and provide no means for predicting the heat load on the peripheral wall surface. The first two-dimensional analysis of the problem was performed by Thynell and Merkle (1989), who used the  $P_1$ -approximation to model the radiative transfer for a gray medium. Recently, Venkateswaran et al. (1990) employed a two-dimensional analysis that included a realistic model for the absorption coefficient of alkali vapors, whose spectral behavior is extremely variable; however, the use of the  $P_1$ -approximation as a solution to the nongray radiation problem requires substantial computer times, particularly since it has to be iteratively coupled to the overall energy equation. Therefore, a thick-thin approximation, calibrated with  $P_1$  solutions, was employed to perform parametric surveys. In this regard, it is important to note that although the  $P_1$ -approximation has been widely used in a variety of engineering situations, its accuracy and validity in modeling the complex radiation problem within a solar thruster are uncertain.

Contributed by the Heat Transfer Division and presented at the Joint AIAA/ASME Thermophysics and Heat Transfer Conference, Seattle, Washington, June 18-20. Manuscript received by the Heat Transfer Division April 10, 1990; revision received February 22, 1991. Keywords: Radiation, Radiation Interactions, Solar Energy.

The primary objective of this work is to assess the performance of the solar propulsion concept by means of a two-dimensional model. We concentrate on the concept of solar energy absorption by submicron size particles suspended in the gaseous propellant (hydrogen). In our study, we use an exact solution technique for the radiation problem because the accurate estimation of the temperature fields and radiative wall fluxes is of particular importance. It is well known that the  $P_1$ -approximation often yields satisfactory results for optically thick media, but it may become very inaccurate in optically thin cases, in particular in two- and three-dimensional geometries (Modest, 1990). To achieve efficient solar absorption, it may be preferable to employ working fluids whose optical dimensions fall in the intermediate range because the use of optically thick media may result in significant re-emission losses. The accuracy of the  $P_1$ -approximation over intermediate opacities in the presence of locally strong energy reemission within the medium and highly asymmetric boundary conditions is not well documented in the literature. For this reason, we use an exact integral method to perform parametric studies and to evaluate thrust and specific impulse capabilities of the thruster. As a result, the secondary objective of this work is to compare the results of the exact method with the results from the  $P_1$ -approximation.

## Analysis

**Physical Model.** The general picture of a conceived solar thruster is depicted in Fig. 1. Both the concentrated solar beam from the collector and the working fluid (typically hydrogen gas) enter the thruster from the upstream inlet end. The working fluid contains small, submicron size carbon particles to

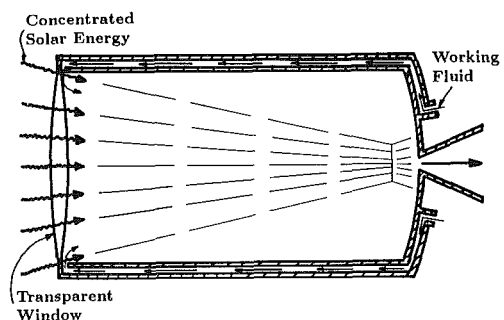


Fig. 1 Concept of solar rocket thruster

ensure absorption of the solar radiation within the thruster. The hot gas is then accelerated through a supersonic nozzle at the downstream end in order to produce thrust. Typically, the inlet working fluid is circulated around the walls of the thruster for cooling purposes as shown in Fig. 1.

**Assumptions.** To develop a mathematical model for the interaction problem described previously, the following additional simplifying assumptions are introduced:

1 A steady state exists, and the medium is in local thermodynamic equilibrium (LTE).

2 The solar thruster has a two-dimensional cylindrical interior geometry, as shown in Fig. 2, and all quantities remain invariant under translation around the  $z$  axis, i.e., the problem involves two-dimensional cylindrical geometry. Since the ratio of the nozzle throat diameter to the thruster diameter is about 0.03 or smaller, the effect of the downstream geometry on the radiation problem is assumed negligible.

3 The calculations are performed only over the inlet region of the solar thruster, which is essentially the region where heat addition occurs. The choked nozzle throat region is not included in the present calculations.

4 The radial velocity component is negligible, and the axial velocity component is uniform. (This assumption could be relaxed at the expense of solving the complete fluid dynamic equations; however, the present approximate field is qualitatively correct and enables us to investigate the details of the radiation problem much more efficiently.)

5 The specific heat  $c_p$  and absorption coefficient  $\kappa$  are independent of position. This assumption implies that the thermodynamic and radiative properties are temperature independent.

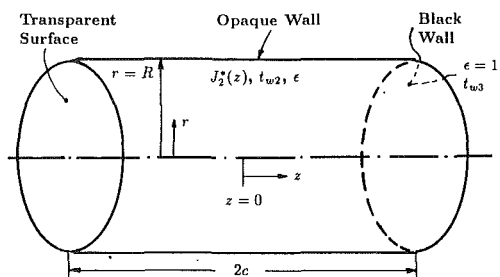


Fig. 2 Geometry and coordinates of thruster model

6 The scattering effects by the suspended particles within the medium are negligible. This is a very good approximation for small particles ( $\pi D_p/\lambda < 1$ ), which are considered in the present work as the absorption mechanism of the radiant energy. By using 0.1- $\mu\text{m}$ -size carbon particles, which have been employed in experiments (Hull and Hunt, 1984), and by considering a characteristic wavelength of 0.707  $\mu\text{m}$ , it is easily shown using the Mie theory (Özsisik, 1973) that the single scattering albedo is about 0.05.

7 The absorption coefficient  $\kappa$  is independent of wavelength. For small particles, the absorption coefficient is approximately inversely proportional to wavelength (Siegel and Howell, 1981). To account for such wavelength dependence more accurately, it should be possible to incorporate a Gaussian quadrature scheme, such as the one discussed by Edwards (1981), but multiple radiation solutions are required. To keep the computational effort within reason, we assume a gray absorption coefficient.

8 The upstream boundary surface at  $z = -c$  (the lens

## Nomenclature

|  |  |  |
|--|--|--|
| $B_i$ = expansion coefficients to radiosity of surface at $r = R$  | $q_{\hat{e}_z}^*(r, z) = q_{\hat{e}_z}(r, z)/\pi I_b(T_{\text{ref}})$<br>= dimensionless net axial heat flux | $\overline{VK}_n(r, r', u)$ = integral defined by Thynell (1990) |
| $Bo$ = Boltzmann number, Eq. (3a)  | $Q_r$ = dimensionless radiant heat loss along wall at $r = R$  | $V_n(r, u)$ = integral defined by Thynell (1990)                 |
| $c$ = half the axial optical depth   | $r$ = optical radial coordinate  | $\overline{WK}(r, z - z')$ = integral defined by Thynell (1990)  |
| $c_p$ = specific heat  | $R$ = optical radius   | $W_i(r, z)$ = integral defined by Thynell (1990)                 |
| $D_p$ = diameter of particles  | $\overline{RK}_n(r, z - z')$ = integral defined by Thynell (1990)  | $\overline{ZK}_n(r, r', u)$ = integral defined by Thynell (1990) |
| $G(r, z)$ = incident radiation   | $t$ = dimensionless fluid temperature, Eq. (3c)  | $z$ = axial optical coordinate                                   |
| $I_b$ = blackbody emission   | $t_0$ = dimensionless fluid temperature at $z = -c$  | $\epsilon$ = emissivity  |
| $I_0^*(r) = I_0(r)/\pi I_b(T_{\text{ref}})$ = dimensionless flux at inlet                                  | $t_{w2}$ = prescribed wall temperature at $r = R$  | $\eta$ = absorption efficiency                                   |
| $I_0(r)$ = flux at inlet of thruster   | $t_{w3}$ = prescribed wall temperature at $z = c$  | $\theta$ = polar angle   |
| $I(r, z, \theta, \phi)$ = radiation intensity  | $T$ = fluid temperature  | $\kappa$ = absorption coefficient                                |
| $I_{sp}$ = specific impulse  | $Th$ = approximate nozzle thrust   | $\lambda$ = wavelength   |
| $J_2^*(z) = J_2(z)/\pi I_b(T_{\text{ref}})$ = dimensionless radiosity of surface at $r = R$                | $T_0$ = fluid temperature at $z = -c$  | $\rho_f$ = density of fluid                                      |
| $k$ = thermal conductivity of gas  | $T_{\text{ref}}$ = reference temperature   | $\sigma$ = Stefan-Boltzmann constant                             |
| $N$ = conduction to radiation parameter  | $u$ = axial fluid velocity   | $\phi$ = azimuth angle   |
| $q_{\hat{e}_r}^*(r, z) = q_{\hat{e}_r}(r, z)/\pi I_b(T_{\text{ref}})$ = dimensionless net radial heat flux |  |  |
|  |  | <b>Subscripts</b>  |
|  |  | $f$ = fluid  |
|  |  | ref = reference  |
|  |  | 0 = inlet condition  |
|  |  | <b>Superscripts</b>  |
|  |  | * = dimensionless quantity                                       |

material) is completely transparent to radiation incident from within the medium.

9 The opaque bounding surface at  $r = R$  is diffusely emitting and diffusely reflecting. Since the bounding surface at  $r = R$  is assumed opaque diffuse and gray, Kirchhoff's law is applicable.

10 The surface at  $z = c$  is treated as a perfect absorber,  $\epsilon = 1$ .

11 The refractive index of the medium is unity, which for most gases is a very good approximation.

**Energy Equation.** The quasi-one-dimensional flow assumption simplifies the fluid mechanics such that only the energy equation needs to be solved. The energy equation in two-dimensional cylindrical co-ordinates in dimensionless form is given as (Özsisik, 1973)

$$\text{Bo} \frac{\partial t(r, z)}{\partial z} = N \frac{\partial^2 t(r, z)}{\partial z^2} + \frac{N}{r} \frac{\partial}{\partial r} \left( r \frac{\partial t(r, z)}{\partial r} \right) - 4t^4(r, z) + G_e^*(r, z) + G_{\text{sun}}^*(r, z), \quad -c < z < c, \quad 0 < r < R, \quad (1)$$

where the independent optical variables  $(r, z)$  are related to the physical variables by  $r = \kappa r_p$  and  $z = \kappa z_p$ . The boundary conditions on the energy equation are given by

$$t(r, -c) = t_0, \quad z = -c, \quad 0 \leq r < R, \quad (2a)$$

$$\frac{\partial^2 t}{\partial z^2} = 0, \quad z = c, \quad 0 \leq r < R, \quad (2b)$$

$$\frac{\partial t}{\partial r} = 0, \quad r = 0, \quad -c < z < c, \quad (2c)$$

$$t = t_{w2}, \quad r = R, \quad -c < z < c. \quad (2d)$$

Here, the temperature is specified at the inlet and at the wall boundaries, and a symmetry condition is applied at the centerline. The imposed downstream boundary condition, Eq. (2b), requires further clarification. First, the fluid flow field calculations near the nozzle region are not performed. Second, the conduction-to-radiation parameter  $N$  is extremely small ( $\approx 10^{-4}$ ) for the present gas flow situation, which practically makes the problem first order and the inlet condition of primary importance. Therefore we employ a downstream condition analogous to the ones that are often employed in solutions to the Navier-Stokes equations for similar flow conditions (Venkateswaran et al., 1990). It should also be noted that the choked nozzle sets the mass flow rate in the thruster, which requires us to consider the mass flow rate as a parameter (Bo number). The dimensionless variables are defined as

$$\text{Bo} = \frac{\rho u c_p T_{\text{ref}}}{\pi I_b(T_{\text{ref}})}, \quad (3a)$$

$$N = \frac{\kappa k T_{\text{ref}}}{\pi I_b(T_{\text{ref}})}, \quad (3b)$$

$$t(r, z) = \frac{T(r, z)}{T_{\text{ref}}}, \quad (3c)$$

$$G_e^*(r, z) = \frac{G_e(r, z)}{\pi I_b(T_{\text{ref}})}, \quad (3d)$$

$$G_{\text{sun}}^*(r, z) = \frac{G_{\text{sun}}(r, z)}{\pi I_b(T_{\text{ref}})}. \quad (3e)$$

Here,  $\rho$  is the density,  $u$  the velocity,  $c_p$  the specific heat,  $T(r, z)$  the temperature of the fluid,  $I_b(T)$  the Planck blackbody function,  $G_e(r, z)$  the incident radiation due to emission by the medium, and  $G_{\text{sun}}(r, z)$  the incident radiation due to the solar irradiation. That is, the radiation heat transfer is split up into two parts: (1) that due to solar irradiation and (2) that due to re-emission. The reference temperature of the medium,

$T_{\text{ref}}$ , is related to the efficiency of the external collection of the sun's energy. Here it is assumed to be 3500 K.

The dimensionless incident radiation  $G_e^*(r, z)$  and  $G_{\text{sun}}^*(r, z)$  are related to the radiation intensity by

$$G_e^*(r, z) = \int_{\phi=0}^{2\pi} \int_{\theta=0}^{\pi} I_e^*(r, z, \theta, \phi) \sin \theta d\theta d\phi, \quad (4a)$$

$$G_{\text{sun}}^*(r, z) = \int_{\phi=0}^{2\pi} \int_{\theta=0}^{\pi} I_{\text{sun}}^*(r, z, \theta, \phi) \sin \theta d\theta d\phi. \quad (4b)$$

To obtain expressions for these functions, it is necessary to solve the equation of radiative transfer for the radiation intensity. The solution to these problems are discussed in the following sections.

**Radiative Transfer Due to the Medium Emission.** A schematic of the physical model and coordinates is illustrated in Fig. 2. As shown recently (Thynell, 1989), it is possible to transform the equation of radiative transfer into an equivalent integral form of the Fredholm type. In problems involving a multidimensional, absorbing-emitting medium bounded by gray-diffuse surfaces, the transformation yields a system of coupled integral equations, whose dependent variables are the radiosities. In general, there is one significant advantage for solving such a system of integral equations rather than the equation of transfer: The number of independent variables is reduced. In the present case, we reduce the number of independent variables in the emission problem from four  $(r, z, \theta, \phi)$  to one  $(z)$ . That is, the dependent variable in the radiation problem is the radiosity of the peripheral surface  $J_2^*(z)$  rather than the intensity  $I_e^*(r, z, \theta, \phi)$ . Once a solution has been obtained for  $J_2^*(z)$ , then the incident radiation and the net radiant heat fluxes can be computed. Furthermore, if the peripheral surface is black, then we obtain an explicit expression for the incident radiation and the net radiative fluxes in terms of surface and volume integrals over the wall and medium temperatures, respectively. The mathematical formulation to the radiation problem involving the radiosity is given by (Thynell, 1990)

$$J_2^*(z) = \epsilon t_{w2}^4 + (1 - \epsilon) \int_{-c}^c J_2^*(z') \overline{RK}_4(R, z - z') dz' + (1 - \epsilon) [t_{w3}^4 V_{4,0}(R, c - z) + \overline{SQ}_r(R, z)], \quad (5)$$

where explicit expressions for the kernels of the integral equation  $\overline{RK}_n(r, z - z')$ , and  $\overline{VK}_n(r, r', u)$  have been specified elsewhere (Thynell, 1990), and

$$\overline{SQ}_r(r, z) = \int_{-c}^c \int_0^R t^4(r', z') \overline{VK}_3(r, r', z - z') r' dr' dz'. \quad (6)$$

Assuming that the temperatures of the boundary surfaces are constant, we employ a standard power series representation of the radiosity given by

$$J_2^*(z) = \sum_{i=0}^I B_i z^i. \quad (7)$$

To solve for the unknown expansion coefficients  $B_i$ ,  $i = 0, 1, \dots, I$ , Eq. (7) is substituted into Eq. (5) and a collocation strategy based on the zeroes of the Chebyshev polynomials is employed to set up a system of  $I + 1$  linear algebraic equations for the unknown expansion coefficients. A standard routine is employed to solve the system of equations. We should note that if the wall emissivity is unity, then the radiosity is the blackbody emissive power and the problem is simplified significantly.

Once a solution is obtained to the expansion coefficients, the dimensionless net radiant heat fluxes in the axial and radial directions at the inlet, along the peripheral surface, and downstream are, respectively, computed from (Thynell, 1990)

$$q_{\bar{e}_z}^*(r, -c) = \sum_{i=0}^I B_i W_i(r, -c) - t_{w3}^4 F_{4,0}(r, 2c) + \overline{SQ}_z(r, -c), \quad (8a)$$

$$q_{\bar{e}_r}^*(R, z) = -\epsilon t_{w2}^4 + \epsilon \sum_{i=0}^I B_i H_{4,i}(R, z) + \epsilon t_{w3}^4 V_{4,0}(R, c-z) + \epsilon \overline{SQ}_r(R, z), \quad (8b)$$

$$q_{\bar{e}_z}^*(r, c) = -t_{w3}^4 + \sum_{i=0}^I B_i W_i(r, c) + \overline{SQ}_z(r, c), \quad (8c)$$

where

$$\overline{SQ}_z(r, z) = \int_{-c}^c \int_0^R t^4(r', z') \overline{ZK}_3(r, r', z-z') r' dr' dz', \quad (9)$$

and explicit expressions for the functions  $W_i(r, z)$ ,  $F_{n,i}(r, u)$  and  $H_{n,i}(r, z)$  have been defined in a previous work (Thynell, 1990). Similarly, the evaluation of the dimensionless incident radiation in the interior of the medium is performed by using the expression given by (Thynell, 1990)

$$G_z^*(r, z) = \sum_{i=0}^I B_i H_{3,i}(r, z) + t_{w3}^4 F_{3,0}(r, c-z) + \overline{SG}(r, z), \quad 0 \leq r < R, -c < z < c, \quad (10)$$

where

$$\overline{SG}(r, z) = \int_{-c}^c \int_0^R t^4(r', z') \overline{ZK}_2(r, r', z-z') r' dr' dz'. \quad (11)$$

Evaluation of Eq. (10) at the bounding surfaces requires a modification since some of the integrals are undefined. In this work, however, the evaluation of the incident radiation at the bounding surfaces are not needed and thus the corresponding expressions are not included.

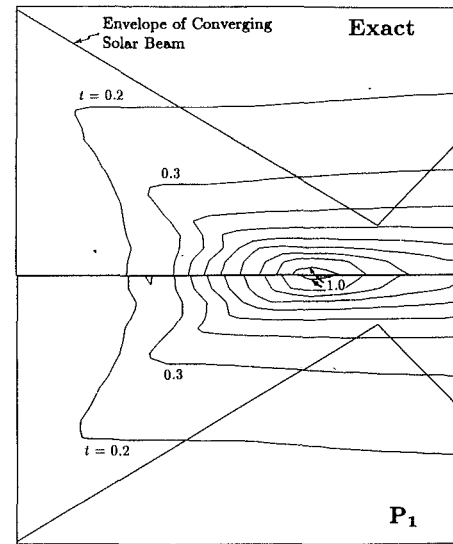
The radiation problem described above is also solved using the well-known  $P_1$ -approximation (Özsisik, 1973). Since this technique has been discussed in many previous works, it is not necessary to include the details here. However, it should be pointed out that this technique changes the character of the radiative transfer from one in which the radiation intensity at a point is influenced by all other points directly, to another in which the radiation "diffuses" through the medium and is thus dependent only on local gradients.

**Beam Absorption Model.** The absorption of the incoming converging solar beam is computed by employing a ray-tracing technique. To implement this technique, the law of geometric optics is used to split up the collimated beam at each radial point at the thruster inlet. The overall shape of the beam, however, is set by the focal spot size and the  $f$ -number of the converging lens (or the collector mirror arrangement). Along each ray, the intensity is determined by using

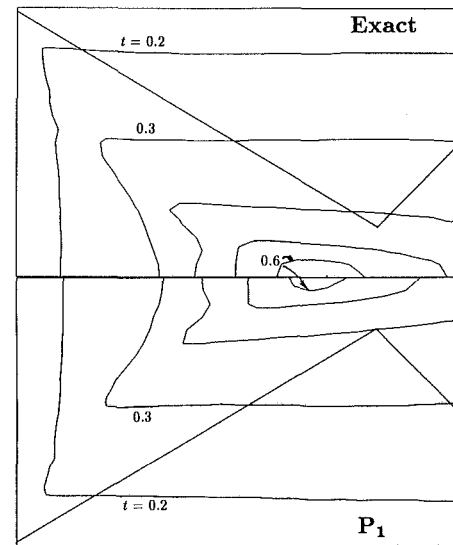
$$\frac{dI_{m,\text{sun}}^*}{ds} = -\kappa I_{m,\text{sun}}^* \quad (12a)$$

$$I_{m,\text{sun}}^*(0) = I_0^*(r), \quad (12b)$$

where  $m$  implies the  $m$ th ray and  $I_0^*(r)$  is the dimensionless irradiation due the sun at the inlet. Equation (12a) is solved directly along the path  $s$ , which is related to a cell in the computational domain. Once Eq. (12a) has been solved for all rays passing through that cell, an integration over the solid angles as defined by Eq. (4b) gives the incident radiation due to the focused energy from the sun. We note that the component of the incident radiant that is transmitted through the flowing medium is absorbed by the black downstream boundary; hence, no reflection effects are considered. In addition, we also assume that the sun's irradiation is not incident on the peripheral surface.



(a)



(b)

Fig. 3 Temperature distributions calculated by both the exact and the  $P_1$ -approximation for a medium bounded by a black peripheral wall,  $B_0 = 1.37$  and  $R = 1.33c$ ; (a)  $R = 1$ , and (b)  $R = 3$

**Numerical Solution Procedure.** The two-dimensional energy equation may be solved by a conventional finite difference scheme. We chose to use a time-iterative procedure that marches Eq. (1) in time until a steady state is established. An Alternating Direction Implicit (ADI) procedure was employed in conjunction with this scheme in order to simplify the two-dimensional operator. Between each iterative step on the energy equation, the radiation problem is solved to obtain a new estimate on the incident radiation at each point due to emission. In this work, the functions  $\overline{SQ}_r(r, z)$ ,  $\overline{SQ}_z(r, z)$ , and  $\overline{SG}(r, z)$  are evaluated using either a 20-point or a 40-point Gauss-Legendre quadrature. The medium emissive power, that is the temperature, at the quadrature points is obtained by using a two-dimensional interpolation scheme.

## Results and Discussion

The objective of this work is to assess the overall performance potential of the proposed solar thruster concept. In the following section, we study the effects of various system parameters on the absorption efficiency and temperature distribution within the thruster. The parameters varied are the

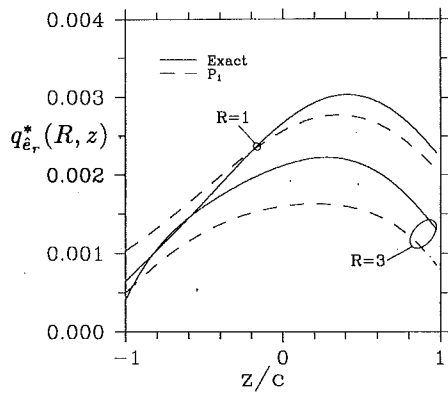


Fig. 4 Comparison of the net radiant heat fluxes along the peripheral wall using both the exact and the  $P_1$ -approximation;  $Bo = 1.37$ ,  $R = 1$ , and  $\epsilon = 1$

Boltzmann number (or mass flux), the optical thickness of the medium, and the radiative properties of the peripheral wall. In addition, thrust levels and available specific impulses of the thruster are determined over a range of operating conditions. As a secondary objective, we also compare the results of the exact method and the  $P_1$ -approximation. The comparison is performed for different optical dimensions and thruster operating conditions.

In our calculations, the power in the inlet solar beam is taken to be 1 MW with a concentration ratio of  $10^4:1$  of the collection system (Palmer, 1978). The geometry of the thruster is fixed corresponding to the optical dimensions of  $R = 1.33c$ ; the window diameter is set equal to the solar beam diameter at the thruster inlet (1 m) and the focal point is described by a unit  $f$ -number lens such that it is located near the center of the downstream exit. For all cases presented, we assume a fixed value of the conduction-to-radiation parameter  $N = 0.7 \times 10^{-3}$ . The selected value of  $N$  is a representative value for molecular gases and the characteristics of the present problem. Given the small value of  $N$ , we expect that conduction is negligible compared to radiation, except perhaps near the boundary where large temperature gradients may occur. The wall temperature was maintained such that  $t_{w2} = t_{w3} = 0.14$  in all the calculations. The following results have been obtained by using either 20 or 40 point Gauss-Legendre quadratures in the evaluation of Eq. (6), and a  $31 \times 21$  grid in the evaluation of Eq. (1). For the  $P_1$ -approximation, a  $41 \times 41$  grid was used. Here, it is necessary to use grid-stretching near the boundaries and in regions of steep gradients in order to ensure that the resulting solutions are grid independent.

In Figs. 3(a) and 3(b), we show contours of the dimensionless medium temperatures for two different opacities of  $R = 1.33c = 1$  and 3. All other conditions are maintained constant with  $Bo = 1.37$  and  $\epsilon = 1$ . In each figure, results from both the exact and the  $P_1$  solutions are included for comparison. Inspection of the figures reveals several interesting features. In Fig. 3(a), the incoming converging solar beam produces significant temperature gradients in the region of the focus (the envelope of the incident beam is shown superimposed on the temperature contours). The peak gas temperature is about 1 (which corresponds to 3500 K). Further, the use of the  $P_1$  method is seen to yield results that are in close agreement with the exact solution method. The maximum discrepancy occurs at the central core of the heated gas, where the remission effects are significant; but, even in this region, the  $P_1$ -approximation only slightly underpredicts the medium temperatures.

In the case of optically thin media, only a small portion of the solar radiation is absorbed before the beam is incident on the rear wall of the thruster chamber. Clearly, such a situation is undesirable in the solar thruster and is not of interest. However, the effect of increasing the optical dimensions needs to

be investigated. Figure 3(b) shows the results for one such case. Compared to the result in Fig. 3(a), we find that a greater portion of the incident radiation is absorbed near the inlet window (upstream of the beam focus). At the focal plane, the intensity of incident radiation is therefore lower; consequently, the peak gas temperature (which still occurs in the region of the focus) is considerably lower at about 0.7 (2450 K). For even higher optical thicknesses, a larger portion of the energy is absorbed near the inlet window itself. This leads to larger reradiation losses through the inlet window, thereby resulting in poorer energy conversion efficiencies. Thus, for a solar thruster, feasible opacities are likely to be in the intermediate range ( $R = 1.33c = 1$  to 3).

The results from the use of the  $P_1$  method illustrated in Fig. 3(b) show a greater degree of disagreement with the exact solution than the earlier case shown in Fig. 3(a). At the center of the hot gas core, where the maximum error occurs, the  $P_1$ -approximation underpredicts the temperature by about 12 percent. The reason for this underprediction is due to the  $P_1$ -approximation's failure in accurately modeling the re-emission problem, which is strongly directional. Furthermore, the diffusion character of the  $P_1$ -approximation also produces larger net radiation fluxes near the focal point than does the exact solution. The larger radiant fluxes require lower convective transports of sensible energy, since the overall energy balance must be satisfied; hence, lower medium peak temperatures are predicted using the  $P_1$ -approximation.

Figure 4 illustrates the net dimensionless radiant heat flux along the peripheral wall for the above two cases. The accurate prediction of the flux along the wall (and the inlet window) is important because adequate wall cooling must be provided. Figure 4 shows that the peripheral flux is larger for the  $R = 1$  case than for the  $R = 3$  case. This effect is due to the higher medium temperature (which leads to more re-emission) as is evident from Figs. 3. Also shown on Fig. 4 are the results of the  $P_1$ -approximation for the two cases. The  $P_1$ -approximation underpredicts the net radiant heat transfer except near the inlet window for the  $R = 1$  case. The maximum discrepancy is about 20 percent, even though the medium temperature is predicted more accurately. There may be several reasons for the observed underprediction. First, the radiation intensity is a highly discontinuous function near the wall; the radiation field emerging from the interior is much stronger than that emanating from the walls. Second, the boundary conditions in the  $P_1$  solution are interpreted according to the Marshak projection scheme; no rigorous theory exists on how to construct the boundary conditions for the  $P_1$ -approximation. Finally, the diffusion character of the  $P_1$  formulation overpredicts the absorption of the radiant energy emerging from the interior; this effect is readily apparent on examining the results shown by Özisik (p. 443, 1973) of the transmissivity of radiant energy emitted from a hot wall through a cold medium to a cold wall.

In Figs. 5(a) and 5(b), we show the effect of the Boltzmann number on the dimensionless temperature contours with  $R = 1$ ,  $c = 0.75$ ,  $\epsilon = 1$ ,  $Bo = 0.68$  and  $2.74$ , respectively. Inspection of Fig. 5(a) reveals that the case of  $Bo = 0.68$ , which may be obtained by reducing the speed of the fluid, results in extremely large temperature gradients within the fluid. The maximum temperature in this case is  $t_{max} = 1.15$ , which corresponds to 4025 K. However, an increase in the Boltzmann number to  $2.74$  (Fig. 5b) reduces the established temperatures within the fluid as a result of a reduction of the residence time of the fluid within the thruster. In this case, the maximum temperature is approximately  $t_{max} = 0.83$ , which corresponds to 2905 K. By noting that the maximum temperature in Fig. 3(a) is 1 (3500 K), we deduce that the maximum temperature decreases monotonically with increasing  $Bo$  number.

In Fig. 6, we illustrate the effects of the peripheral wall emissivity and the Boltzmann number on the dimensionless

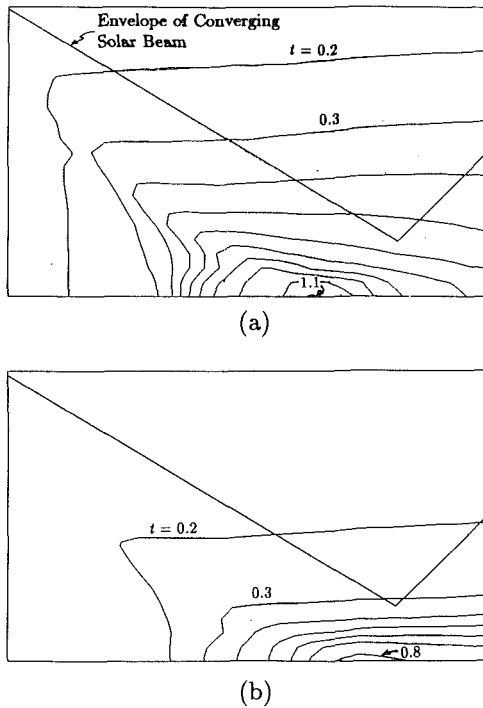


Fig. 5 The effect of Boltzmann number on the temperature distribution using the exact solution technique for a medium whose peripheral bounding surface is black and  $R = 1$ ; (a)  $Bo = 0.68$ , and (b)  $Bo = 2.74$

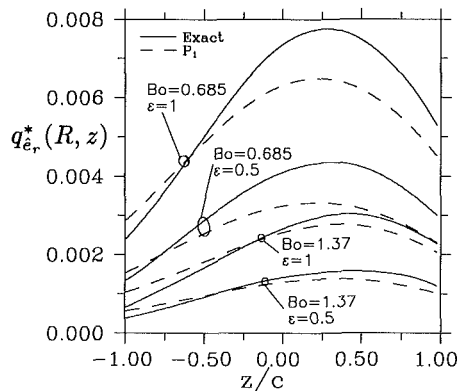


Fig. 6 The influence of the peripheral wall emissivity and Boltzmann number  $Bo$  on the dimensionless net radiant heat flux along the peripheral wall;  $Bo = 0.68$  and  $1.37$ ,  $R = 1$

net radiant heat flux along the peripheral wall for the case of  $R = 1$ ,  $c = 0.75$ , and  $Bo = 0.68$  and  $1.37$ , respectively. It is clearly shown in this figure that the peripheral wall heat flux decreases significantly as the Boltzmann number increases. Such an increase is of course expected since the medium temperatures decrease with increasing Boltzmann numbers. Since the radiative fluxes to the walls decrease with  $Bo$  number, we may anticipate the energy conversion efficiencies will increase with increasing  $Bo$  number. We also observe that the diffusely reflecting peripheral wall reduces the net radiant heat flux in proportion to the reduction in the wall emissivity. This effect is also expected since the peripheral wall heat transfer is only a small fraction of the overall heat transfer; that is, for the cases considered most of the absorbed energy is convected through the outlet and the energy reflected from peripheral wall back into the medium does not change the medium temperature distribution to any significant extent. We also note in Fig. 6 that the  $P_1$ -approximation consistently underpredicts the peripheral radiant heat flux, as mentioned previously in conjunction with the discussion of the results in Fig. 4.

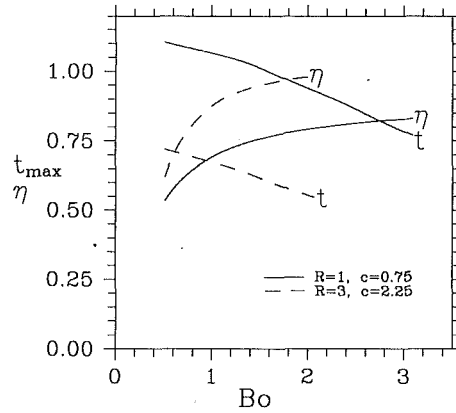


Fig. 7 The effects of the Boltzmann number and optical dimensions on the absorption efficiency  $\eta$  and maximum temperature of the medium  $t_{max}$ ;  $R = 1$  and  $3$ , and  $\epsilon = 1$

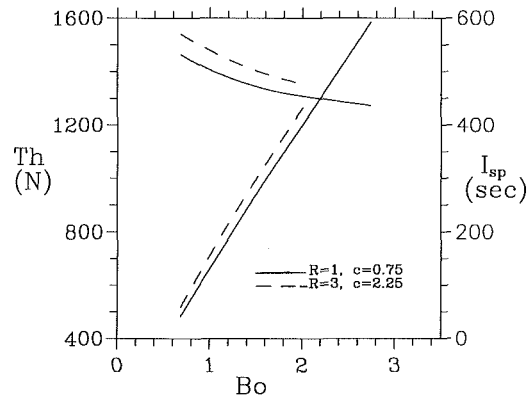


Fig. 8 The effects of Boltzmann number and optical dimensions on the performance of the solar thruster

Finally, we consider the overall performance of the solar thruster. In particular, we are interested in determining the overall absorption efficiency ( $\eta$ ), peak temperatures as well as operating thrust ( $Th$ ) and specific impulse ( $I_{sp}$ ) of the thruster. Here, the predictions of the thrust and specific impulse should only be considered as reasonable first-order approximations of the thruster's capabilities, since the time-consuming nozzle calculations are not considered. To obtain such first-order analysis, we assume that the enthalpy of the fluid (hydrogen) is completely converted into kinetic energy, i.e., an isentropic expansion. The enthalpy is computed at the exit plane of the absorption region using numerical integration.

In Fig. 7, we depict the effects of Boltzmann number and optical dimensions on the absorption efficiency  $\eta$  and maximum fluid temperature  $t_{max}$  for the case of  $\epsilon = 1$ . The absorption efficiency is defined as the ratio of the energy convected through the outlet to the total amount of energy that is incident on the working fluid. Examination of this figure reveals that the larger absorption efficiencies are obtained for the larger  $Bo$  numbers. This result is due to the reduction in the radiative losses for the larger  $Bo$  numbers as noted above. It should be noted that in an actual thruster the  $Bo$  number or the mass flux is set by the choked nozzle throat. In addition, in Fig. 7 the absorption efficiencies are lower for the smaller optical dimensions, because a portion of the focused solar energy is transmitted through rather than absorbed by the working fluid.

In Fig. 8, we illustrate the effects of the Boltzmann number and optical dimensions on the predictions of the thrust and the specific impulse for  $\epsilon = 1$ . Clearly, thrust increases linearly with Boltzmann number or, in other words, the mass flow rate. Also, for the case with a higher optical thickness, a slightly



higher thrust is obtained. This is a consequence of the higher absorption efficiencies evidenced in Fig. 7 for the larger optical dimensions. On the other hand, specific impulse decreases somewhat with flow rate. This is because the mean temperature of the fluid at the exit of the absorption region decreases with increase in flow rate. We note that, over the range of operating conditions examined, specific impulses in the range of 400 to 600 seconds are obtained, thereby promising good overall performance of the solar thruster.

### Summary and Conclusions

Combined convection and radiation in an absorbing, emitting, axisymmetric solar thruster has been examined. The absorption of the solar energy has been achieved by mixing submicron-size particles within a hydrogen gas. The overall energy equation has been solved by using a finite difference technique whereas the radiation problem has been solved by using both an exact integral method and the standard  $P_1$ -approximation. Based on the results for a 1 MW thruster, the following conclusions have been reached:

1 High overall thermal efficiencies (up to 90 percent or more) are obtained in the thruster for intermediate optical thickness of the medium. The thermal efficiency increases with increasing Boltzmann number.

2 Peak gas temperatures in the thruster range from 2500 to 4000 K. Peak gas temperatures are higher for lower Bo numbers and smaller optical dimensions.

3 Wall radiation fluxes decrease with increasing Boltzmann numbers and increasing reflectivity of the peripheral wall.

4 The solar thruster is capable of delivering thrusts in the range of 500 to 1500 N.

5 The specific impulses of the thruster range from 400 to 600 s. The specific impulse increases with optical dimensions but decreases with Bo number.

6 The  $P_1$ -approximation yields reasonably good results over the opacities of interest. For larger optical dimensions, the peak temperature is underpredicted by about 10 percent, and the radiant heat fluxes along the wall are underpredicted by about 20 percent.

### Acknowledgments

S. T. Thynell gratefully acknowledges the partial support received from the Office of Naval Research, Grant No. N00014-86-K-0468. C. L. Merkle gratefully acknowledges the support received from the Air Force Office of Scientific Research under contract No. 89-0312.

### References

- Edwards, D. K., 1981, *Radiation Heat Transfer Notes*, Hemisphere, Washington, DC, p. 210.
- Hull, P. G., and Hunt, A. J., 1984, "A Reciprocating Solar-Heated Engine Utilizing Direct Absorption by Small Particles," *ASME Journal of Solar Energy Engineering*, Vol. 106, pp. 29-34.
- Mattick, A. T., 1978, "Absorption of Solar Radiation by Alkali Vapors," *Radiation Energy Conversion in Space*, K. W. Billman, ed., Progress in Astronautics and Aeronautics, Academic Press, New York, Vol. 61, pp. 159-171.
- Modest, M. F., 1990, "The Improved Differential Approximation for Radiative Transfer in Multi-dimensional Media," *ASME JOURNAL OF HEAT TRANSFER*, Vol. 112, No. 3, pp. 819-821.
- Özisik, M. N., 1973, *Radiative Transfer*, Wiley, New York.
- Palmer, A. J., 1978, "Radiatively Sustained Cesium Plasmas for Solar Electric Conversion," *Third NASA Conference on Radiation Energy Conversion*, Progress in Astronautics and Aeronautics, Vol. 61, pp. 201-210.
- Rault, D. F. G., 1985, "Radiation Energy Receiver for Solar Propulsion Systems," *J. Spacecraft and Rockets*, Vol. 22, pp. 642-648.
- Shoji, J. M., 1984, "Potential of Advanced Solar Thermal Propulsion," *Orbit Raising and Maneuvering Propulsion: Research Status and Needs*, L. H. Caveny, ed., Progress in Astronautics and Aeronautics, Academic Press, New York, Vol. 89, pp. 30-47.
- Siegel, R., and Howell, J. R., 1981, *Thermal Radiation Heat Transfer*, 2nd ed., McGraw-Hill, New York.
- Thynell, S. T., 1989, "The Integral Form of the Equation of Transfer in Finite, Two-Dimensional Cylindrical Media," *J. Quant. Spectrosc. Radiat. Transfer*, Vol. 42, No. 2, pp. 117-136.
- Thynell, S. T., and Merkle, C. L., 1989, "Analysis of Volumetric Absorption of Solar Energy and Its Interaction With Convection," *ASME JOURNAL OF HEAT TRANSFER*, Vol. 111, No. 4, pp. 1006-1014.
- Thynell, S. T., 1990, "Treatment of Radiation Heat Transfer in Absorbing, Emitting, Scattering, Two-Dimensional Cylindrical Media," *Numerical Heat Transfer*, Part A, Vol. 4, pp. 449-472.
- Venkateswaran, S., Merkle, C. L., and Thynell, S. T., 1990, "An Analysis of Solar Thermal Rocket Propulsion," AIAA Paper No. 90-0136; *AIAA J. Propulsion and Power* (in press).
- Wang, K. Y., and Yuen, W. W., 1986, "Rapid Heating of Gas/Small-Particle Mixture," *Radiation in Energy Systems*, ASME HTD-Vol. 55, pp. 17-23.

# Determination of Radiative Fluxes in an Absorbing, Emitting, and Scattering Vapor Formed by Laser Irradiation

P. Erpelding

A. Minardi

P. J. Bishop

Department of Mechanical Engineering  
and Aerospace Sciences,  
University of Central Florida,  
Orlando, FL 32816-0993

*A two-dimensional computer model is developed to determine the radiative heat flux distributions within the vapor formed above a metal target irradiated by a laser beam. An axisymmetric cylindrical enclosure containing a radiatively participating medium is considered. Scattering is assumed to be isotropic and allowances are made for variation of the radiative properties of the medium and boundaries. The P-1 and P-3 spherical harmonics approximations are used to solve the integro-differential radiative transfer equation. The resulting equations are then solved for the radial and axial heat fluxes using a finite-difference algorithm. The most significant factors affecting the results obtained from both the P-1 and P-3 approximations were the optical thickness of the medium and the type of laser profile incident upon the medium. Using different wall reflectivities and scattering albedos had a smaller effect. Changing the medium temperature had an insignificant effect as long as medium temperatures were below 20,000 K.*

## Introduction

When a laser beam strikes a metal surface, the events that follow are functions of both the laser beam intensity and thermal characteristics of the metal. At low intensities, a laser beam striking a metal surface will initially result in absorption of the radiation from the laser, heating of the surface, and eventually, conduction within the material. One of the earliest reports of absorption by a laser beam was made by Reedy (1965). When the surface reaches its melting temperature, a liquid pool is formed. At high intensities, the liquid metal will vaporize and partially ionize, forming a plasma. The research objective was to develop a two-dimensional computer model to analyze the radiative heat transfer within the vapor or plasma formed when a metal target is irradiated by a laser beam having different spatial variations. Figure 1 illustrates the general physical description.

Laser-plasma-target interactions strongly affect the energy delivery to a target surface. Reported experiments have shown conditions under which the delivery of laser radiation to a surface has been substantially higher than surface absorption,  $\alpha I_c$ . Although this phenomenon, called thermal coupling, has been widely observed by a number of researchers (McKay and Schriempf, 1979; Hettche et al., 1976; Maher and Hall, 1980; Marcus et al., 1976; von Allmen, 1976; Walters and Clauer, 1978), the mechanisms for the additional energy transfer are not fully understood. Researchers have measured thermal coupling coefficients ranging from values substantially lower than the absorptivity to values substantially greater than the absorptivity (Maher and Hall, 1980).

The prevalent theory to explain enhanced thermal coupling suggests that a plasma formed above the surface plays a significant role in the energy delivery process. This plasma can absorb, scatter, and re-emit incident laser energy. This theory states that interactions between the incident radiation, plasma, and surface result in enhancement of energy delivered to the surface while the plasma is in close contact with the surface. Within a certain range of intensities, the plasma will have a moderate optical thickness. Some of the energy will be atten-

uated (scattered or absorbed) by the plasma and some will be transmitted through the plasma. It is hypothesized that for these moderate optical thicknesses enhanced thermal coupling occurs.

Proponents of this theory include Marcus et al. (1976), Neilson (1979), McKay and Schriempf (1979), Maher and Hall (1980), Walters et al. (1981), Bass (1987), Minardi and Bishop (1989), and Minardi et al. (1990). McKay and Schriempf (1979) report that there are some researchers, such as Walters and Clauer (1978), Basov et al. (1969), and Batanov et al. (1973), who believe that enhanced thermal coupling does not depend on the presence of a plasma. These researchers believe that enhanced thermal coupling is due to metal-dielectric transition at the surface.

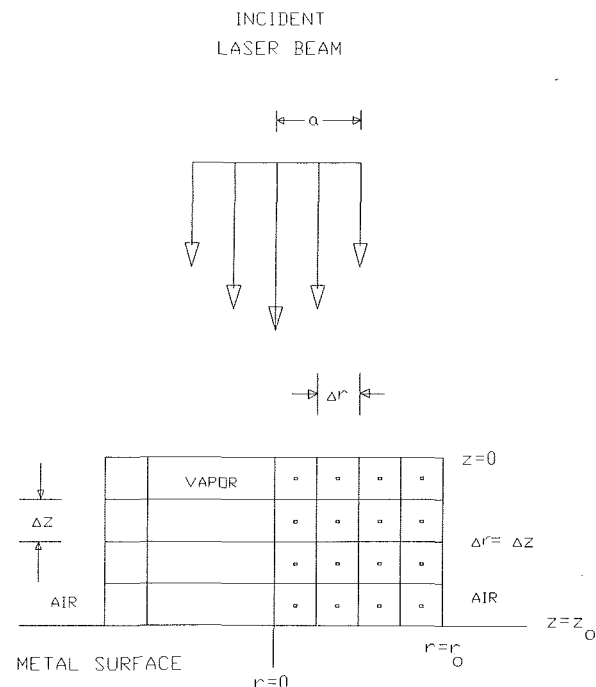


Fig. 1 Numerical modeling of a laser beam interacting with a metal plasma

Contributed by the Heat Transfer Division for publication in the JOURNAL OF HEAT TRANSFER. Manuscript received by the Heat Transfer Division June 11, 1990; revision received April 23, 1991. Keywords: Laser Processing, Materials Processing and Manufacturing Processes, Radiation Interactions.

It is essential to understand the radiative heat transfer mechanisms within the plasma to explain thermal coupling. The differential models to analyze radiative heat transfer, which include the Eddington, moment, and spherical harmonics approximations, have attracted considerable attention. This is due primarily to their ability to provide acceptable solutions to complicated problems without having large computer storage or time requirements. The two-dimensional moment method has been investigated by Stone and Gaustad (1961) and by Cheng (1964). Analytical, exact solutions to two-dimensional radiative heat transfer have been obtained by Cheng (1972) for rectangular and Dua and Cheng (1975) for cylindrical geometries.

More recently, Ratzel and Howell (1983) have analyzed two-dimensional radiative transfer in rectangular enclosures using the P-1 and P-3 spherical harmonics approximations. Menguc and Viskanta (1986) investigated the radiative heat transfer in finite cylindrical enclosures using the P-1 and P-3 spherical harmonics approximations.

Efforts have also been directed toward the effects of an external collimated beam incident upon an enclosure surface. The effects of a collimated beam and multiple scattering have been studied by Kim and Lee (1989), Yuen et al. (1988), and Gerstl et al. (1987). Crosbie and Schrenker (1985) and Tan and Howell (1990) have predicted radiative heat fluxes for rectangular enclosures with a constant collimated laser irradiation at the top surface. Crosbie and Farrell (1984) have developed integral equations for the source terms and heat fluxes for cylindrical enclosures with diffuse or collimated radiation at the top surface. For these studies the laser beam strikes the entire top surface.

In an effort to understand the role of the plasma in enhanced thermal coupling, we have developed a model of the radiative

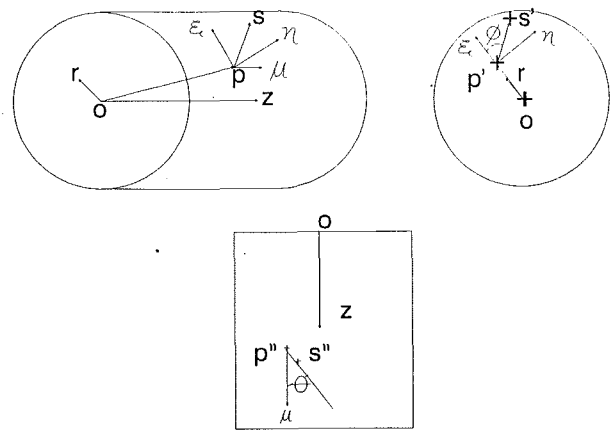


Fig. 2 Coordinate system and nomenclature for an external incident collimated flux on the boundary at  $z=0$

heat transfer mechanisms within the plasma. It is assumed that the vapor and eventual plasma that forms above the target is axisymmetric like the laser beam. Due to the axisymmetric laser profile, material will be removed from the surface in a circularly shaped area that expands. The vapor shape is assumed cylindrical, and its dimensions will increase as time increases. The plasma itself is very close to the surface and relatively stationary while enhanced thermal coupling is occurring. Fluid dynamic considerations are neglected since plasma-laser-target interactions occur rapidly while the vapor is in contact with the surface. Temperatures of the plasma have been determined experimentally (Knutson et al., 1987) to be about 7000 to 8000 K with an electron density of  $10^{17}/\text{cm}^3$  for a laser irradiation intensity of from threshold to  $5 \times 10^7 \text{ W/}$

## Nomenclature

|  |   |  |
|--|---|--|
| $a$ = laser beam radius, cm  | $K_0, K_{11}, K_{13}, K_{33}$ = defined in appendix                         | $z_0$ = medium (enclosure) depth, cm   |
| $F_0, F_i, F_{ij}, F_{ijk}$ = defined in appendix                                      | $l_1 = \xi = \sin \theta \cos \phi$ (direction cosine in $r$ direction)     | $\alpha(r, z)$ = medium absorption coefficient, $\text{cm}^{-1}$                                   |
| $h_w$ = defined by Eq. (8)   | $l_2 = \eta = \sin \theta \sin \phi$ (direction cosine in $\phi$ direction) | $\beta(r, z)$ = extinction coefficient, $\text{cm}^{-1}$   |
| $I$ = radiation intensity, $\text{W}/\text{cm}^2\text{-sr}$                            | $l_3 = \mu = \cos \theta$ (direction cosine in $z$ direction)               | $\delta_{ij}$ = Kronecker delta  |
| $I_b = (\sigma T^4/\pi)n^2$ = Planck's black-body function, $\text{W}/\text{cm}^2$     | $n$ = index of refraction   | $\epsilon_w$ = emissivity of boundary surface  |
| $I_c$ = incident uniform laser beam intensity, $\text{W}/\text{cm}^2$                  | $n_j$ = normal directional cosine   | $\theta$ = angle between intensity and $z$ axis, Fig. 2  |
| $I_j$ = moment of intensity in the inward normal direction to the surface              | $p$ = point in the medium, Fig. 2   | $\theta_c$ = angle between collimated beam and $z$ axis  |
| $I_0/4\sigma T^4$ = normalized $I_0$ moment  | $p', p''$ = projections of point $p$  | $\theta_H$ = high value of $\theta$  |
| $I_1/\sigma T^4$ = normalized radial heat flux   | $r$ = radial dimension  | $\theta_L$ = low value of $\theta$   |
| $I_3/\sigma T^4$ = normalized axial heat flux  | $\bar{r} = r/r_0$ = normalized radial dimension                             | $\rho_w$ = reflectivity of boundary surface  |
| $I_{11}, I_{13}, I_{33}$ = second moments of intensity                                 | $r_0$ = medium (enclosure) radius, cm                                       | $\sigma$ = Stefan-Boltzmann constant = $(5.6699 \times 10^{-12} \text{ W}/\text{cm}^2\text{-K}^4)$ |
| $J_0$ = zeroth moment of source term   | $r_d$ = disk radius, Fig. 3   | $\tau_0(r, z)$ = optical thickness   |
| $J_i, J_{ij}, J_{ijk}$ = first, second, and third moments of source term, respectively | $s$ = a point in the medium, Fig. 2   | $\phi$ = defined in Fig. 2   |
|  | $s', s''$ = projections of point $s$  | $\phi_c$ = angle between projection of collimated beam on $\xi$ - $\eta$ plane and $\xi$ axis      |
|  | $T$ = temperature, K  | $\omega(r, z)$ = scattering albedo   |
|  | $z$ = axial dimension   | $\Omega$ = solid angle   |
|  | $\bar{z} = z/r_0$ = normalized axial dimension                              |  |

cm<sup>2</sup>. For aluminum at this intensity level, singly and doubly ionized Al was observed within the plasma.

### Analysis

In this study, the vapor formed above a metal irradiated by a spatially varying laser is modeled (Erpelding, 1990) as a cylindrical enclosure with a transparent top, peripheral surfaces, and a diffusely emitting and reflecting bottom surface (interface of vapor and metal). The laser irradiation is only incident over a certain area of the top surface defined by the laser beam size. Since thermal coupling occurs when the metal is in contact with the vapor, it is assumed that the vapor has a small velocity at this point in time. Figure 2 illustrates the coordinate systems used in this study.

For an absorbing, emitting, and isotropically scattering gas mixture in local thermodynamic equilibrium, the time-independent radiative transfer equation for a two-dimensional axisymmetric cylindrical enclosure with isotropic scattering is given by (Ozisik, 1973)

$$\left[ \frac{1}{\beta(r, z)} \left( \xi \frac{\partial}{\partial r} - \eta \frac{1}{r} \frac{\partial}{\partial \phi} + \mu \frac{\partial}{\partial z} \right) + 1 \right] I(r, z, \theta, \phi) = J(r, z) + \frac{\omega(r, z)}{4\pi} \int_0^{2\pi} \int_0^\pi I(r, z, \theta', \phi') \sin \theta' d\theta' d\phi' \quad (1)$$

The source function is given by

$$J(r, z) = [1 - \omega(r, z)] I_b + \frac{\omega(r, z)}{4\pi} I_c e^{-\int \beta dz / \cos \theta_c} \quad (2)$$

This study uses a collimated beam normal to the top surface ( $z=0$ ), and therefore,  $\theta_c=0$ . For constant properties  $\int \beta dz = \beta z$ .

Since the top surface is transparent, the collimated laser beam passes through a limited region of the plasma with its associated direction ( $\theta_c, \phi_c$ ) (Tan and Howell, 1990; Crosbie and Farrell, 1984; Crosbie and Schrenker, 1985). Only positions within this region will have a value of  $I_c$ . Otherwise,  $I_c$  is zero.

Following a lengthy procedure using the P-1 and P-3 spherical harmonic approximations, detailed by Menguc (1985) and Menguc and Viskanta (1986) for cylindrical, and Ratzel and Howell (1983) for rectangular systems, and applying the appropriate moments to the energy equation, Eq. (1), and the source function, Eq. (2), the governing differential equation in terms of moments of the intensity can be written. The P-1 approximation is reduced to a single partial differential equation in terms of  $I_0$ .

$$\frac{\partial^2 I_0}{\partial \bar{r}^2} + \frac{1}{\bar{r}} \frac{\partial I_0}{\partial \bar{r}} + \frac{\partial^2 I_0}{\partial \bar{z}^2} = 3\tau_0 \left[ \frac{\partial J_1}{\partial \bar{r}} + \frac{1}{\bar{r}} J_1 + \frac{\partial J_3}{\partial \bar{z}} \right] + 3\tau_0^2 [I_0(1 - \omega) - J_0] \quad (3)$$

The P-3 approximation is written as four partial differential equations in terms of  $I_0, I_{11}, I_{13},$  and  $I_{33}$ .

$$\begin{aligned} \frac{4}{5} \frac{\partial^2 I_0}{\partial \bar{r}^2} + \frac{4}{5} \frac{\partial^2 I_0}{\partial \bar{z}^2} - \frac{3}{5\bar{r}} \frac{\partial I_0}{\partial \bar{r}} - \frac{6}{\bar{r}^2} I_0 - 7\tau_0^2 I_0 + \frac{7}{3} \omega \tau_0^2 I_0 \\ - \frac{\partial^2 I_{11}}{\partial \bar{z}^2} + \frac{6}{\bar{r}} \frac{\partial I_{11}}{\partial \bar{r}} + \frac{12}{\bar{r}^2} I_{11} + 7\tau_0^2 I_{11} - \frac{\partial^2 I_{33}}{\partial \bar{r}^2} + \frac{6}{\bar{r}^2} I_{33} \\ + 7\tau_0^2 I_{33} + 2 \frac{\partial^2 I_{13}}{\partial \bar{r} \partial \bar{z}} + \frac{6}{\bar{r}} \frac{\partial I_{13}}{\partial \bar{z}} = K_0 \end{aligned} \quad (4a)$$

$$\begin{aligned} 6 \frac{\partial^2 I_{11}}{\partial \bar{r}^2} + \frac{\partial^2 I_{11}}{\partial \bar{z}^2} + \frac{12}{\bar{r}} \frac{\partial I_{11}}{\partial \bar{r}} - \frac{12}{\bar{r}^2} I_{11} - \frac{3}{5} \frac{\partial^2 I_0}{\partial \bar{r}^2} - \frac{1}{5} \frac{\partial^2 I_0}{\partial \bar{z}^2} \\ - \frac{26}{5\bar{r}} \frac{\partial I_0}{\partial \bar{r}} + \frac{6}{\bar{r}^2} I_0 + \frac{\partial^2 I_{33}}{\partial \bar{z}^2} + \frac{5}{\bar{r}} \frac{\partial I_{33}}{\partial \bar{r}} - \frac{6}{\bar{r}^2} I_{33} + 6 \frac{\partial^2 I_{13}}{\partial \bar{r} \partial \bar{z}} \\ + \frac{2}{\bar{r}} \frac{\partial I_{13}}{\partial \bar{z}} - 7\tau_0^2 I_{11} + \frac{7}{3} \omega \tau_0^2 I_0 = K_{11} \end{aligned} \quad (4b)$$

$$\begin{aligned} \frac{\partial^2 I_{33}}{\partial \bar{r}^2} + 6 \frac{\partial^2 I_{33}}{\partial \bar{z}^2} + \frac{2}{\bar{r}} \frac{\partial I_{33}}{\partial \bar{r}} - \frac{1}{5} \frac{\partial^2 I_0}{\partial \bar{r}^2} - \frac{3}{5} \frac{\partial^2 I_0}{\partial \bar{z}^2} \\ - \frac{6}{5\bar{r}} \frac{\partial I_0}{\partial \bar{r}} + \frac{\partial^2 I_{11}}{\partial \bar{r}^2} + \frac{3}{\bar{r}} \frac{\partial I_{11}}{\partial \bar{r}} + 6 \frac{\partial^2 I_{13}}{\partial \bar{r} \partial \bar{z}} + \frac{6}{\bar{r}} \frac{\partial I_{13}}{\partial \bar{z}} \\ - 7\tau_0^2 I_{33} + \frac{7}{3} \tau_0^2 \omega I_0 = K_{33} \end{aligned} \quad (4c)$$

$$\begin{aligned} 3 \frac{\partial^2 I_{13}}{\partial \bar{r}^2} + 3 \frac{\partial^2 I_{13}}{\partial \bar{z}^2} + \frac{3}{\bar{r}} \frac{\partial I_{13}}{\partial \bar{r}} - \frac{3}{\bar{r}^2} I_{13} - 7\tau_0^2 I_{13} \\ \frac{2}{5} \frac{\partial^2 I_0}{\partial \bar{r} \partial \bar{z}} - \frac{2}{\bar{r}} \frac{\partial I_0}{\partial \bar{z}} + 2 \frac{\partial^2 I_{11}}{\partial \bar{r} \partial \bar{z}} + \frac{4}{\bar{r}} \frac{\partial I_{11}}{\partial \bar{z}} \\ + 2 \frac{\partial^2 I_{33}}{\partial \bar{r} \partial \bar{z}} + \frac{2}{\bar{r}} \frac{\partial I_{33}}{\partial \bar{z}} = K_{13} \end{aligned} \quad (4d)$$

The values of  $K_0, K_{11}, K_{33}, K_{13}$  are given in the appendix.

The  $I_1$  and  $I_3$  moments have physical significance (Cheng, 1964) and represent the radiative heat fluxes in the  $r$  and  $z$  directions, respectively. For the P-1 approximation

$$I_1 = J_1 - \frac{1}{3\tau_0} \frac{\partial I_0}{\partial \bar{r}} \quad (5a)$$

$$I_3 = J_3 - \frac{1}{3\tau_0} \frac{\partial I_0}{\partial \bar{z}} \quad (5b)$$

For the P-3 approximation

$$I_1 = J_1 - \frac{1}{\tau_0} \frac{\partial I_{11}}{\partial \bar{r}} - \frac{1}{\tau_0 \bar{r}} (I_{11} - I_{22}) - \frac{1}{\tau_0} \frac{\partial I_{13}}{\partial \bar{z}} \quad (6a)$$

$$I_3 = J_3 - \frac{1}{\tau_0} \frac{\partial I_{13}}{\partial \bar{r}} - \frac{1}{\tau_0 \bar{r}} I_{13} - \frac{1}{\tau_0} \frac{\partial I_{33}}{\partial \bar{z}} \quad (6b)$$

For lower order spherical harmonics approximations (P-1 and P-3), Marshak's boundary conditions yield the best results (Davison, 1958). Marshak's boundary condition is obtained by taking the integral of the intensity over appropriate hemispheres and is given by

$$\begin{aligned} \int_{2\pi} I(r, z, \theta, \phi) l_i \sin \theta d\theta d\phi \\ = \int_{2\pi} h_w(r, z, \theta, \phi) l_i \sin \theta d\theta d\phi \end{aligned} \quad (7a)$$

for P-1 and

$$\begin{aligned} \int_{2\pi} I(r, z, \theta, \phi) l_i l_j l_k \sin \theta d\theta d\phi \\ = \int_{2\pi} h_w(r, z, \theta, \phi) l_i l_j l_k \sin \theta d\theta d\phi \end{aligned} \quad (7b)$$

for P-3 where  $h_w$  depends on the type of boundary condition. For an emitting and diffusely reflecting wall, such as a metal target at  $z=z_0$ ,

$$\begin{aligned} h_w(r, z, \theta, \phi) = \epsilon_w I_b \\ = \frac{\rho_w}{\pi} \int_{2\pi} \left( I(r, z, \theta', \phi') + \frac{I_j}{\pi} \right) n_j \sin \theta' d\theta' d\phi' \end{aligned} \quad (8)$$

Equation (8) is used to solve for  $h_w$  in terms of moments, and then is substituted into either Eq. (7a) or (7b) to yield an expression for the boundary condition at the bottom surface.

The values for the various coefficients in Eqs. (7a) and (8) depend on the surfaces for which the boundary conditions are being developed and are found in Table 1.

For a uniformly distributed, externally collimated flux, incident on the  $z=0$  surface, the moments of the source function can be expressed as (Menguc, 1985)

**Table 1 Coefficients and limits for P-1 boundary conditions**

| Boundary  | $\theta$ range | $\phi$ range   | $l_i$ | $n_i$  | $I_j$  |
|-----------|----------------|----------------|-------|--------|--------|
| $r = r_0$ | $0-\pi$        | $\pi/2-3\pi/2$ | $\xi$ | $-\xi$ | $I_1$  |
| $z = 0$   | $0-\pi/2$      | $0-2\pi$       | $\mu$ | $\mu$  | $-I_3$ |
| $z = z_0$ | $\pi/2-\pi$    | $0-2\pi$       | $\mu$ | $-\mu$ | $I_3$  |

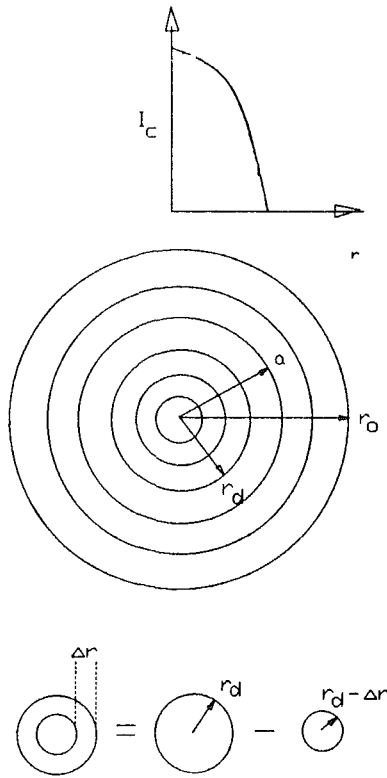


**Fig. 3 Schematic representation of finite rings used to determine the source term for varying laser profiles**

$$J_0(\bar{r}, \bar{z}) = 4\pi(1 - \omega)I_b + F_0 \quad (9a)$$

$$J_i(\bar{r}, \bar{z}) = F_i \quad (9b)$$

$$J_{ij}(\bar{r}, \bar{z}) = \delta_{ij} \frac{4}{3} \pi(1 - \omega)I_b + F_{ij} \quad (9c)$$

$$J_{ijk}(\bar{r}, \bar{z}) = F_{ijk} \quad (9d)$$

The moments of the source function given by Eq. (9) were developed for use with a uniform incident intensity. This condition is met by a laser profile of constant intensity, although most laser profiles are Gaussian, not constant. The computer solution allows for three different laser profiles to be selected (Minardi and Bishop, 1988). These include constant, parabolic, and gaussian distributions. To account for the varying laser profile, a superposition scheme of finite rings is used. It is assumed that there are a number of rings that form the laser beam where each ring thickness is small enough that the laser intensity is assumed constant over the ring area. These rings are constructed by the difference in size of consecutive disks. Each disk has a constant intensity equal to that of the ring. Figure 3 shows these rings and disks and the geometry associated with determining the source function for each ring.

The solutions arise by solving Eq. (3) for the P-1 approximation and Eq. (4) for the P-3 approximation using a finite differencing scheme. Results of the P-1 approximation are used as starting values for the P-3 approximation, which is solved

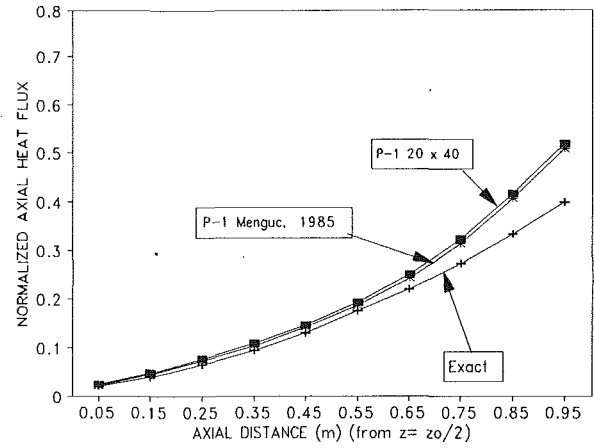


**Fig. 4 Normalized axial heat flux as a function of axial distance for  $r_0 = 1$  m,  $z_0 = 2$  m,  $T_w = 0$ ,  $r = 1$  m,  $\epsilon_w = 1$ ,  $\tau_0 = 1$**

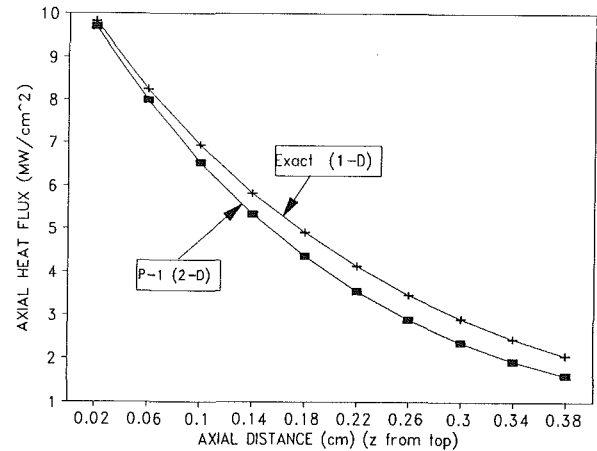


**Fig. 5 Axial heat flux as a function of axial distance for  $r_0 = 0.4$  cm,  $z_0 = 0.4$  cm,  $r = 0$  cm,  $T = 7500$  K,  $\alpha = 2.5$  cm $^{-1}$ ,  $\epsilon_w = 1$ ,  $\tau_0 = 1.0$**

by an iterative technique. The next solution is obtained by evaluating new moment values at each grid point based on previous values. These values are recalculated until a predetermined convergence criterion has been satisfied. Heat fluxes in the radial and axial directions are then computed using the finite difference form of Eqs. (5) and (6).

## Results and Discussion

The P-1 approximation is compared with analytical results obtained by Dua and Cheng (1975) for a finite, cylindrical, black wall enclosure containing an absorbing and emitting medium with no incident laser beam. Figure 4 shows the normalized axial heat flux,  $I_3/\sigma T^4$ , increasing with axial distance from  $z = z_0$ . Similar results were obtained by Menguc (1985) using a finite element method to evaluate the P-1 approximation.

In order to evaluate the method developed for the conditions applied at the top and bottom surfaces of a medium irradiated by a laser beam, the P-1 approximation is compared with a one-dimensional analytical solution (Erpelding, 1990). The analytical solution derived for an absorbing and emitting medium is given by

$$I_0 = \frac{6(I_c - \sigma T^4)}{\sqrt{3} + 3/2} \exp(-\sqrt{3}\alpha z) + 4\sigma T^4 \quad (10a)$$

$$I_3 = \frac{2\sqrt{3}}{\sqrt{3} + 3/2} (I_c - \sigma T^4) \exp(-\sqrt{3}\alpha z) \quad (10b)$$

Figure 5 compares values generated at  $r = 0$  by the two-dimensional solution with those generated by the one-dimen-

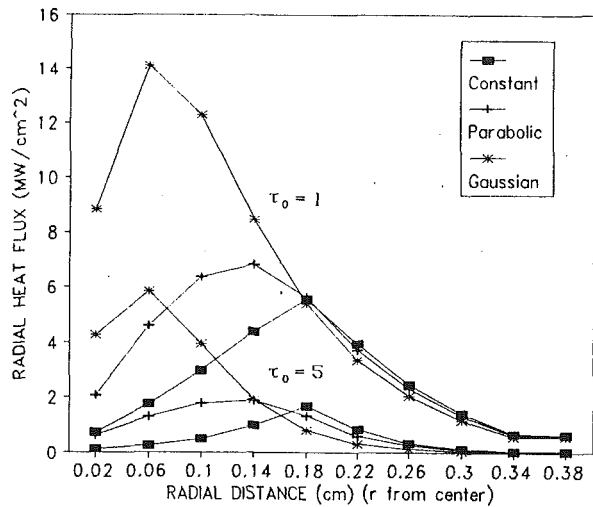


Fig. 6 Radial heat flux as a function of radial distance using three different laser profiles for  $r_0 = 0.4$  cm,  $z_0 = 0.4$  cm,  $a = 0.2$  cm,  $z = 0.06$  cm,  $T = 7500$  K,  $\omega = 0.2$ ,  $\epsilon_w = 0.1$

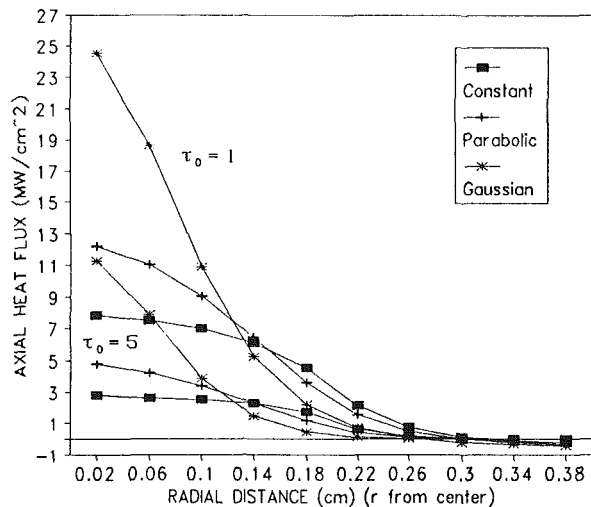


Fig. 7 Axial heat flux as a function of radial distance using three different laser profiles for  $r_0 = 0.4$  cm,  $z_0 = 0.4$  cm,  $a = 0.2$  cm,  $z = 0.06$  cm,  $T = 7500$  K,  $\omega = 0.2$ ,  $\epsilon_w = 0.1$

sional solution for axial heat flux. Figure 5 implies correct treatment of the source function and boundary conditions.

Many simulation studies were performed to evaluate the effects of varying material and laser properties on the radial and axial heat fluxes predicted by the P-1 approximation. Each test run consisted of a laser beam ( $a = 0.2$  cm) irradiating the top surface of a cylindrical enclosure of 0.4 cm radius. The laser beam profiles examined had the same energy fluency based upon a constant intensity of  $10 \text{ MW/cm}^2$ . The spot center intensity is  $10 \text{ MW/cm}^2$  for the constant profile,  $20 \text{ MW/cm}^2$  for the parabolic profile, and  $80 \text{ MW/cm}^2$  for the gaussian profile (Minardi and Bishop, 1988).

Figure 6 provides a comparison of the radial heat flux in two media having different optical thicknesses. The peak values of the radial heat flux obtained are significantly lower than the incident spot center due to attenuation by absorption and scattering. The peak value of radial heat flux, independent of optical thickness, occurs at 0.06 cm for the gaussian profile, at 0.14 cm for the parabolic profile, and at 0.18 cm for the constant profile. The boundary conditions at the centerline and edge of the enclosure result in peak values not occurring at spot center for all three profiles.

At the edge of the laser beam the radial heat flux profiles cross over one another. This is noted to a greater extent when the medium is optically thick. The crossing over occurs in the

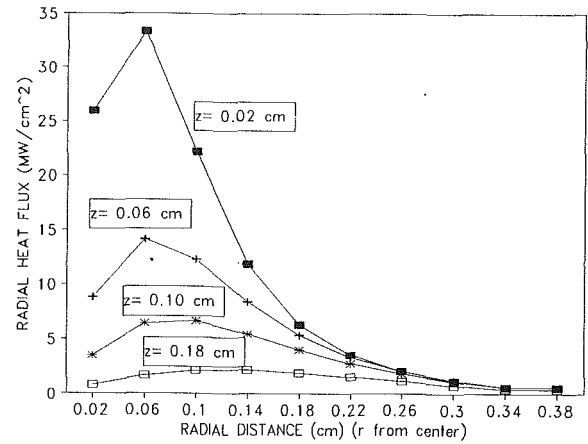


Fig. 8(a) Radial heat flux as a function of radial distance for a gaussian profile at various depths for  $r_0 = 0.4$  cm,  $z_0 = 0.4$  cm,  $a = 0.2$  cm,  $T = 7500$  K,  $\omega = 0.2$ ,  $\epsilon_w = 0.1$ ,  $\tau_0 = 1.0$

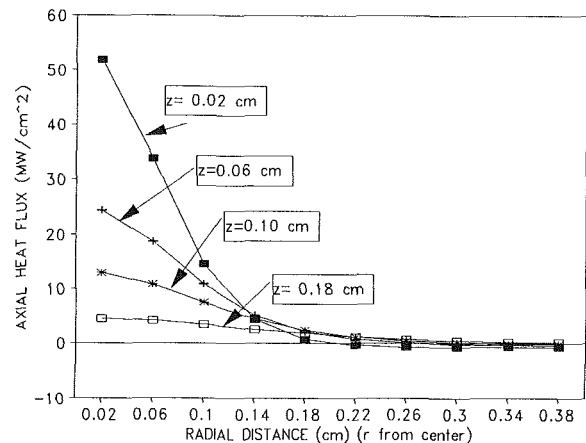


Fig. 8(b) Axial heat flux as a function of radial distance for a gaussian profile at various depths for  $r_0 = 0.4$  cm,  $z_0 = 0.4$  cm,  $a = 0.2$  cm,  $T = 7500$  K,  $\omega = 0.2$ ,  $\epsilon_w = 0.1$ ,  $\tau_0 = 1.0$

intensity profiles since the laser beam profiles all have the same energy fluency. The magnitudes of radial heat flux decrease significantly when the optical thickness of the medium is increased. In addition, the values of radial heat flux vary to a greater extent at the edge of the laser beam when the medium is optically thick. Nevertheless, changing the optical thickness of the medium does not affect the general shapes of the curves.

Figure 7 provides a comparison of the axial heat flux for the three different laser profiles in two media having different optical thicknesses. The different laser profiles yield axial heat fluxes, which closely resemble the incident laser beam profile. The greatest magnitude of axial heat flux occurs at the center of the enclosure and laser beam for all three profiles. The peak values are significantly lower than corresponding spot center values due to attenuation. Once again, the magnitudes of axial heat flux decrease significantly when the optical thickness of the medium is increased. Nevertheless, changing the optical thickness of the medium does not affect the general shapes of the curves.

Figure 8(a) provides a comparison of the radial heat flux for a gaussian profile at various depths in the enclosure. The most noticeable changes in radial heat flux are near the top surface 0.06 cm from the centerline of the enclosure. At depths approaching the bottom of the enclosure, only slight variations are noticed. In addition, the shapes of the curves change with depth as well. Attenuation by scattering and absorption accounts for these results.

Figure 8(b) provides a comparison of the axial heat flux for a gaussian profile at various depths in the enclosure. The most

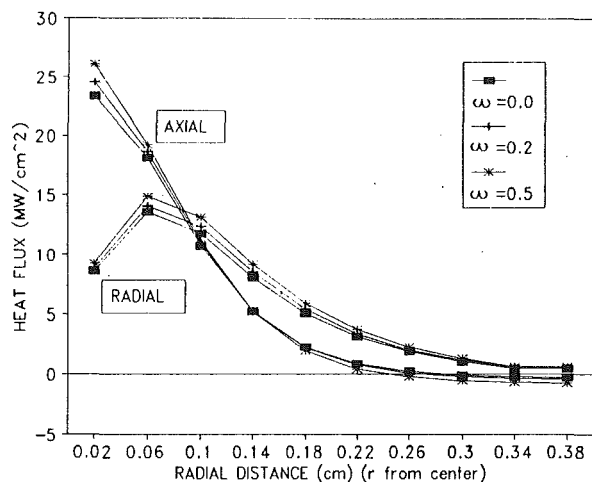


Fig. 9 Radial and axial heat flux as a function of radial distance for a gaussian profile using different scattering albedos for  $r_0 = 0.4$  cm,  $z_0 = 0.4$  cm,  $a = 0.2$  cm,  $z = 0.06$  cm,  $T = 7500$  K,  $\epsilon_w = 0.1$ ,  $\tau_0 = 1.0$

noticeable changes in axial heat flux are near the top surface and centerline of the enclosure. The large gradients noted at the uppermost layers are similar to the laser beam profile. At depths approaching the bottom of the enclosure, only slight variations are apparent due to the attenuation.

Figure 9 illustrates the effects of changing the scattering albedo with constant attenuation on the radial and axial heat flux. Increasing the magnitude of the scattering albedo results in an increase in the radial heat flux along the entire radial dimension. The radial heat flux in a medium with  $\omega = 0.5$  exceeds the radial heat flux in a nonscattering medium by a maximum of 10 percent and occurs at a radial distance of 0.06 cm.

The effects on the axial heat flux are not as apparent. The axial heat flux increases a maximum of 5 percent at radial distances less than the laser beam radius. At radial distances outside the laser beam radius, the axial heat flux is more negative by as much as 50 percent.

Figure 10 illustrates the effects of changing wall reflectivity at the bottom surface of the enclosure on the radial and axial heat flux. Increasing the magnitude of wall reflectivity results in a maximum 9 percent increase in radial heat flux. This point occurs at the edge of the laser beam at a radial distance of 0.18 cm. As wall reflectivity is increased, more energy is reflected back into the medium, thus increasing the radial heat flux.

Increasing the magnitude of wall reflectivity results in an overall 50 percent decrease in axial heat flux. The axial heat flux varied by the same fraction along the entire radial distance. As wall reflectivity is increased, more energy is reflected back into the medium and the majority of this is reflected back toward the enclosure. Axial heat flux decreases in order to compensate for the increase in reflected energy. Of course, the effect on axial heat flux is greater since the bottom reflecting surface is perpendicular to the  $z$  axis.

The effect of changing the medium temperature on the axial heat flux was investigated. Increasing the temperature well beyond the experimental value of 7500 K (Knudtson et al., 1987) has an insignificant effect on the radial and axial heat fluxes. Only at extremely high temperatures ( $T = 50,000$  K) were there changes in the axial heat flux.

Similar effects were noted using the P-3 approximation. This is to be expected since the P-1 approximation is the starting point for the P-3 approximation. Significant variations occurred in the magnitude of the axial heat flux, particularly at the top surface of the enclosure where the greatest gradients exist. Figure 11 illustrates these differences between results predicted by the P-1 and P-3 approximations.

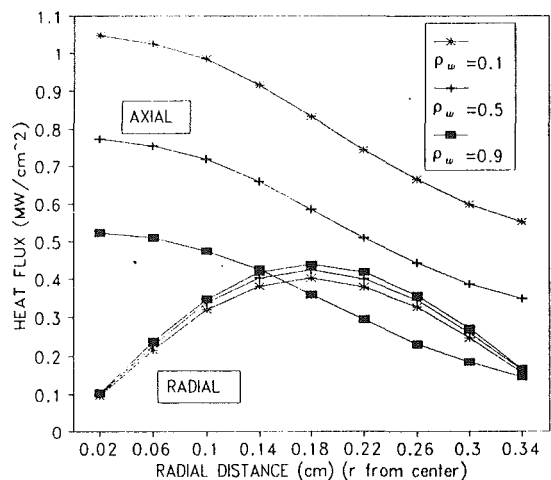


Fig. 10 Radial and axial heat flux as a function of radial distance for a gaussian profile using different wall reflectivities and emissivities for  $r_0 = 0.4$  cm,  $z_0 = 0.4$  cm,  $a = 0.2$  cm,  $z = 0.34$  cm,  $T = 7500$  K,  $\omega = 0.2$ ,  $\tau_0 = 1.0$

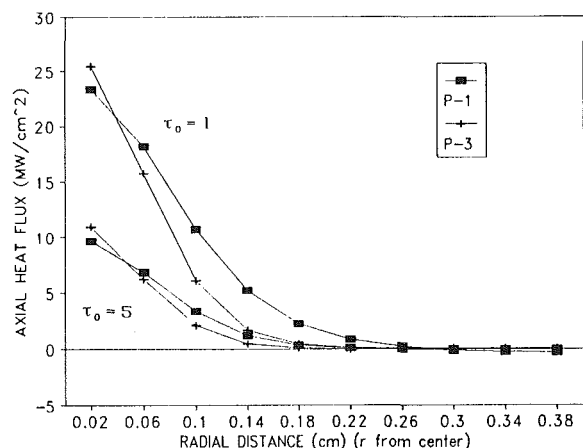


Fig. 11 Axial heat flux as a function of radial distance for a gaussian profile using the P-1 and P-3 approximations for  $r_0 = 0.4$  cm,  $z_0 = 0.4$  cm,  $a = 0.2$  cm,  $T = 7500$  K,  $\alpha = 2.5$  cm<sup>-1</sup>,  $\epsilon_w = 0.1$ ,  $\tau_0 = 1.0$ ,  $\tau_0 = 5.0$

Figure 11 compares the axial heat flux for a gaussian profile using the P-1 and P-3 approximations for two different optical thicknesses. The P-1 approximation overpredicts the P-3 approximation by 10 percent along the majority of the radial distance. The P-3 approximation models the steep gradient of the laser profile more closely than does the P-1 approximation. When the optical thickness increases, the P-1 and P-3 approximations agree much more closely. The P-1 approximation overpredicts the P-3 approximation by a maximum of 5 percent. The better agreement noted between the P-1 and P-3 approximations for an optically thick medium is consistent with other studies (Menguc and Viskanta, 1986; Ratzel and Howell, 1983).

## Conclusions

A two-dimensional cylindrical finite differencing computer model has been developed using P-1 and P-3 approximations to solve the radiative transfer equation. The program models an absorbing, emitting, and isotropically scattering medium contained in a cylindrical enclosure irradiated by a laser beam at the top surface. This physically models the radiative fluxes in a vapor formed during laser material processing.

The most significant factors affecting the results obtained from both the P-1 and P-3 approximations were the optical thickness of the medium and the laser profile incident upon the medium. Using different wall reflectivities and scattering albedos had much less of an effect. Changing the medium

temperature had an insignificant effect as long as medium temperatures were below 20,000 K.

It is, therefore, very important that the laser profile and medium optical thickness be known to a certain degree of accuracy so that meaningful results are obtained. The other factors mentioned above do not play as significant a role in the determination of radial and axial heat flux, thus allowing approximate values to suffice.

The P-1 and P-3 approximations are only limited in their ability to model media that are optically thin. For a laser beam irradiating a medium within an enclosure, optical thicknesses of less than one should be avoided when using the P-1 approximation. Optical thicknesses less than 0.5 should be avoided when using the P-3 approximation (Menguc, 1985).

## References

- Basov, Boiko, Krokhin, Semenov, and Skilzkov, 1969, *Journal of Soviet Physics*, Vol. 13 (cited by McKay and Schriempf).
- Bass, M., 1987, "Laser-Material Interactions," *Encyclopedia of Physical Science and Technology*, Vol. 7, Academic Press Inc., pp. 129-145.
- Batanov, Bunkin, Prokhorov, and Federov, 1973, *Soviet Physics—JETP*, Vol. 36 (cited by McKay and Schriempf).
- Cheng, P., 1964, "Two Dimensional Radiating Gas Flow by a Moment Method," *AIAA Journal*, Vol. 2, No. 9, pp. 1662-1664.
- Cheng, P., 1972, "Exact Solutions and Differential Approximations for Multi-dimensional Radiative Transfer in Cartesian Configurations," *Progress in Astronautics and Aeronautics*, Vol. 31, pp. 269-308.
- Crosbie, A. L., and Farrell, J. B., 1984, "Exact Formulation of Multiple Scattering in a Three-Dimensional Cylindrical Geometry," *J. Quant. Spectrosc. Radiat. Transfer*, Vol. 31, No. 5, pp. 397-416.
- Crosbie, A. L., and Schrenker, R. G., 1985, "Multiple Scattering in a Two Dimensional Rectangular Medium Exposed to Collimated Radiation," *J. Quant. Spectrosc. Radiat. Transfer*, Vol. 33, No. 2, pp. 101-125.
- Davison, B., 1958, *Neutron Transport Theory*, Clarendon Press, Oxford, United Kingdom.
- Dua, S. S., and Cheng, P., 1975, "Multi-dimensional Radiative Transfer in Non-isothermal Bounding Walls," *International Journal of Heat and Mass Transfer*, Vol. 18, pp. 245-259.
- Erpelding, P., 1990, "Modeling Radiative Heat Transfer in an Absorbing Emitting, and Scattering Medium," Master's Thesis, University of Central Florida, Orlando, FL.
- Gerstl, S., Zardecki, A., Wesley, P. U., Stupin, D. M., Stokes, G. H., and Eliot, N. E., "Off-Axis Multiple Scattering of a Laser Beam in Turbid Media: Comparison of Theory and Experiment," *Applied Optics*, Vol. 26, No. 5, pp. 779-785.
- Hetteche, L. R., et al., 1976, "Mechanical Response and Thermal Coupling of Metallic Targets to High-Intensity 1.06  $\mu\text{m}$  Laser Radiation," *Journal of Applied Physics*, Vol. 47, No. 4, pp. 1415-1421.
- Kim, T. K., and Lee, H. S., 1989, "Radiative Transfer in Two-Dimensional Anisotropic Scattering Media With Collimated Incidence," *J. Quant. Spectrosc. Radiat. Transfer*, Vol. 42, No. 3, pp. 225-238.
- Knudtson, J. T., Green, W. B., and Sutton, D. G., 1987, "The UV-Visible Spectroscopy of Laser-Produced Aluminum Plasmas," *Journal of Applied Physics*, Vol. 61, No. 10, pp. 4771-4780.
- Maher, W. E., and Hall, R. B., 1980, "Pulsed Laser Heating Profile Width and Changes in Total Coupling With Pulse Length and Pressure," *Journal of Applied Physics*, Vol. 51, No. 3m, pp. 1338-1344.
- Marcus, S., Lowder, J. E., and Mooney, D. L., 1976, "Large-Spot Thermal Coupling of CO<sub>2</sub> Laser Radiation to Metallic Surfaces," *Journal of Applied Physics*, Vol. 47, No. 7, pp. 2966-2968.
- McKay, J. A., and Schriempf, J. T., 1979, "Anomalous Infrared Absorptance of Aluminum Under Pulsed 10.6  $\mu\text{m}$  Laser Irradiation in a Vacuum," *Applied Physics Letters*, Vol. 35, pp. 433-434.
- Menguc, M. P., 1985, "Modeling of Radiative Heat Transfer in Multi-dimensional Enclosures Using Spherical Harmonics Approximation," Ph.D. Thesis, Purdue University, W. Lafayette, IN.
- Menguc, M. P., and Viskanta, R., 1986, "Radiative Transfer in Axisymmetric, Finite Cylindrical Enclosures," *ASME JOURNAL OF HEAT TRANSFER*, Vol. 108, pp. 271-276.
- Minardi, A., and Bishop, P. J., 1988, "Two-Dimensional Transient Temperature Distribution Within a Metal Undergoing Multiple Phase Changes Caused by Laser Irradiation at the Surface," *ASME JOURNAL OF HEAT TRANSFER*, Vol. 110, pp. 1009-1011.
- Minardi, A., and Bishop, P. J., 1989, "Temperature Distribution Within a Metal Subjected to Irradiation by a Laser of Spatially Varying Intensity," *Heat Transfer in Manufacturing and Materials Processing*, HTD-Vol. 113, pp. 39-44.
- Minardi, A., Bishop, P. J., Mills, T. E., Morrison, K. M., and Pearson, I. K., 1990, "Mass Removal and Hole Profile Characteristics for Drilling Using Continuous and Pulsed Lasers," *Heat Transfer in Space Systems*, ASME HTD-Vol. 135, pp. 117-123.
- Neilson, P. E., 1979, "High-Intensity Laser Matter Coupling in a Vacuum," *Journal of Applied Physics*, Vol. 50, pp. 3938-3943.

Ozisik, M. N., 1973, *Radiative Transfer and Interactions With Conduction and Convection*, Wiley, New York.

Ratzel, A. C. III, and Howell, J. R., 1983, "Two-Dimensional Radiation in Absorbing-Emitting-Scattering Media Using the P-N Approximation," *ASME JOURNAL OF HEAT TRANSFER*, Vol. 105, pp. 333-340.

Ready, J. F., 1965, "Effects Due to Absorption of Laser Radiation," *Journal of Applied Physics*, Vol. 36, No. 2, pp. 462-468.

Stone, P. H., and Gaustad, J. E., 1961, "The Application of a Moment Method to the Solution of Non-Gray Radiative Transfer Problems," *Journal of Astrophysics*, Vol. 134, No. 2, pp. 456-468.

Tan, Z., and Howell, J. R., 1990, "Two-Dimensional Radiative Heat Transfer in an Absorbing, Emitting, and Linearly Anisotropically Scattering Medium Exposed to a Collimated Source," *1990 AIAA/ASME Thermophysics and Heat Transfer Conference*, ASME HTD-Vol. 137, pp. 101-106.

Von Allmen, M., 1976, "Laser Drilling Velocity in Metals," *Journal of Applied Physics*, Vol. 47, No. 12, pp. 5460-5463.

Walters, C. T., and Clauer, A. H., 1978, "Materials Research Society Symposium on Laser-Solid Interactions and Laser Processing," Boston (unpublished); *Applied Physics Letters*, Vol. 33, 1978 (cited by McKay and Schriempf).

Walters, C. T., Tucker, T. R., Ream, S. L., Clauer, A. H., and Gallant, D. J., 1981, "Thermal Coupling of CO<sub>2</sub> Laser Radiation to Metals," *Lasers in Metallurgy, Proceedings of the 110th AIME Annual Meeting*, Chicago, IL.

Yuen, W. W., Hsu, I. C., Olsted, S. J., and Cunningham, G. R., 1988, "Effects of Multiple Scattering on the Optical Transmission of a Collimated Radiative Energy Beam in an Anisotropically Scattering Medium," Paper No. AIAA-88-2626.

## APPENDIX

The functions  $K$  to the governing equations for the P-3 approximation are given as

$$K_0 = 7\tau_0 \left[ \frac{\partial J_1}{\partial \bar{r}} + \frac{\partial J_3}{\partial \bar{z}} - \frac{\partial J_{111}}{\partial \bar{r}} - \frac{\partial J_{133}}{\partial \bar{r}} - \frac{\partial J_{113}}{\partial \bar{z}} - \frac{\partial J_{333}}{\partial \bar{z}} + \frac{3}{\bar{r}} J_{122} \right] + 7\tau_0^2 [J_{11} + J_{33} - J_0]$$

$$K_{11} = 7\tau_0 \left[ \frac{3}{\bar{r}} J_{111} + \frac{2}{\bar{r}} J_{133} - \frac{2}{\bar{r}} J_1 + \frac{\partial J_{111}}{\partial \bar{r}} + \frac{\partial J_{113}}{\partial \bar{z}} \right] - 7\tau_0^2 J_{11}$$

$$K_{33} = 7\tau_0 \left[ \frac{1}{\bar{r}} J_{133} + \frac{\partial J_{133}}{\partial \bar{r}} + \frac{\partial J_{333}}{\partial \bar{z}} \right] - 7\tau_0^2 J_{33}$$

$$K_{13} = 7\tau_0 \left[ \frac{2}{\bar{r}} J_{113} + \frac{1}{\bar{r}} J_{333} - \frac{1}{\bar{r}} J_3 + \frac{\partial J_{113}}{\partial \bar{r}} + \frac{\partial J_{133}}{\partial \bar{z}} \right] - 7\tau_0^2 J_{13}$$

The functions  $F$  to the source function for the P-1 and P-3 approximations are given as

$$F_0 = I_c \frac{\omega}{4\pi} e^{-\beta dz / \cos \theta_c} \int_0^{2\pi} \int_{\theta_L}^{\theta_H} \sin \theta d\theta d\phi = I_c \frac{\omega}{4\pi} e^{-\beta dz / \cos \theta_c} \int_{\Omega} d\Omega$$

$$F_i = I_c \frac{\omega}{4\pi} e^{-\beta dz / \cos \theta_c} \int_0^{2\pi} \int_{\theta_L}^{\theta_H} l_i \sin \theta d\theta d\phi = I_c \frac{\omega}{4\pi} e^{-\beta dz / \cos \theta_c} \int_{\Omega} l_i d\Omega$$

$$F_{ij} = I_c \frac{\omega}{4\pi} e^{-\beta dz / \cos \theta_c} \int_0^{2\pi} \int_{\theta_L}^{\theta_H} l_{ij} \sin \theta d\theta d\phi = I_c \frac{\omega}{4\pi} e^{-\beta dz / \cos \theta_c} \int_{\Omega} l_{ij} d\Omega$$

$$F_{ijk} = I_c \frac{\omega}{4\pi} e^{-\beta dz / \cos \theta_c} \int_0^{2\pi} \int_{\theta_L}^{\theta_H} l_{ijk} \sin \theta d\theta d\phi = I_c \frac{\omega}{4\pi} e^{-\beta dz / \cos \theta_c} \int_{\Omega} l_{ijk} d\Omega$$

For a collimated beam normal to the top surface,  $\theta_c = 0$ ,  $\theta_L = 0$ , and  $\theta_H = \pi$ .



# Nongray Radiative Gas Analyses Using the S-N Discrete Ordinates Method

T. K. Kim

Energy Laboratory,  
Korea Institute of Energy and Resources,  
Dae Jeon, South Korea

J. A. Menart

H. S. Lee<sup>1</sup>

Department of Mechanical Engineering,  
University of Minnesota,  
Minneapolis, MN 55455

*The S-N discrete ordinates method is applied to analyze radiative heat transfer in nongray gases. Spectral correlation between the terms in the equation of transfer is considered for black or nearly nonreflecting walls. Formulations to apply the S-N method using a narrow-band or the exponential wide-band model are presented. The net radiative wall heat fluxes and the radiative source distributions are obtained for uniform, parabolic, and boundary layer type temperature profiles, as well as for a parabolic concentration profile. The narrow- and wide-band nongray solutions are compared with gray-band approximations using the same band models. The computational speed of the gray-band approximation is obtained at the expense of accuracy in the internal fluxes and radiative source distributions. The wall radiative flux predictions by the gray-band approximation are satisfactory.*

## Introduction

Modeling radiative heat transfer in nongray gases is difficult because the absorption and emission characteristics of participating gases are strong functions of wavenumber. Accurate computation techniques for nongray gases are required to predict the heat transfer characteristics of boilers, furnaces, rocket engines, and other high-temperature systems.

The present study investigates the use of the *S-N* discrete ordinates method (Carlson and Lathrop, 1968; Kim and Lee, 1988) for nongray heat transfer analyses. Fiveland and Jamaluddin (1989) utilized the *S-N* method with only the gray-band approximation. Both nongray and gray-band solutions are considered in this study. The exponential wide-band model (Edwards, 1976) and Mayer and Goody's statistical narrow-band model (Goody, 1964) are used in the analysis, because they are physically realistic models with reasonable computation cost. Both models account for the effects of the discrete line structure of the bands, and the effects of the band wings with varying pressure and path length.

The band models chosen for this study are not as accurate as the line-by-line calculations. Taine and co-workers carried out line-by-line calculations for single absorption bands of H<sub>2</sub>O (Hartmann et al., 1984) and CO<sub>2</sub> (Soufiani et al., 1985). The line-by-line results are used to check their tabulated data for statistical narrow-band parameters. They found excellent agreement for the statistical narrow-band model with an exponential-tailed-inverse line-strength distribution. Many of their calculations also compared favorably to high resolution spectra. Soufiani and Taine (1989) performed experiments with H<sub>2</sub>O and CO<sub>2</sub> flowing in a rectangular channel and compared their experimental results to a numerical calculation using the narrow-band model mentioned above. Excellent agreement was reported between experimental and numerical results.

Although the line-by-line calculations are theoretically the most precise way to treat radiative heat transfer in a gas, large computation resources are required. Obtaining molecular absorption data needed for the calculation can also be difficult. Since the narrow-band models can compare favorably to the limited line-by-line data available, they are generally used as the standard for comparison (Mengüç and Viskanta, 1986; Grosshandler, 1980; Grosshandler and Nguyen, 1985). The

statistical narrow-band model with an exponential-tailed-inverse line-strength distribution is used in this work. The band parameters, based on line-by-line calculations, are directly from Hartmann et al. (1984) and Soufiani et al. (1985).

Wide-band models are extensively used in gas radiative heat transfer analyses (Cess et al., 1967; Buckius, 1982). By far the most popular wide-band model is that of Edwards (1976). Edwards and co-workers have successfully used this model (Edwards and Menart, 1964; Edwards and Babikian, 1989), as well as other investigators (Thynell, 1989). Because of its general acceptance, this is the wide-band model used in this study.

Since the purpose of this investigation is to apply the *S-N* technique along with nongray band models, a simple one-dimensional slab of pure H<sub>2</sub>O gas or a mixture of H<sub>2</sub>O and N<sub>2</sub> is considered for analysis. Radiative analyses are performed for temperature profiles that are uniform, a boundary layer type, a parabolic type, as well as for a parabolic concentration profile. The Curtis-Godson approach is used to handle non-isothermal or inhomogeneous gases (Godson, 1953). The radiative transfer quantities of interest in this study are both the net radiative wall flux and the radiative source distribution inside the medium. The gas pressure is always kept at one atmosphere, but the path length is varied from 0.1 to 1.0 m. To check the accuracy of the nongray *S-N* analysis, comparisons are made to the correlated results of Zhang et al. (1988) who use the discrete direction method in their analysis. Results are also obtained by an implementation of the flux method presented by Soufiani et al. (1985) for additional verification.

## Formulation

**Narrow-Band Formulation.** The *S-N* discrete ordinates method is a powerful numerical technique for solving the equation of transfer in absorbing, emitting, and anisotropically scattering media. Formulation of the nongray equation of transfer for an absorbing and emitting medium for use with the *S-N* method and the narrow-band model is presented in this section.

The wavenumber-averaged, differential form of the equation of transfer is written as

$$\frac{\partial \bar{I}_\nu(s, \Omega)}{\partial s} + \bar{a}_\nu(s) \bar{I}_\nu(s, \Omega) = \bar{a}_\nu(s) \bar{I}_{b\nu}(s), \quad (1)$$

where the process of averaging over a bandwidth  $\Delta\nu$  is indicated by an overbar symbol. The emission term on the right-hand

<sup>1</sup> Present address: NASA-Lewis Research Center, Cleveland, OH 44135.

Contributed by the Heat Transfer Division and presented at the Joint AIAA/ASME Thermophysics and Heat Transfer Conference, Seattle, Washington, June 18–20, 1990. Manuscript received by the Heat Transfer Division January 3, 1990; revision received March 8, 1991. Keywords: Radiation.

side is separately averaged since the Planck function  $I_{b\nu}(s)$  is smooth over the wavenumber spectrum; a constant value,  $\bar{I}_{b\nu}(s)$ , is used within a narrow  $\Delta\nu$  interval.

Special attention to the spectral correlation is required in evaluating the remaining average in the equation of transfer (Edwards, 1962; Zhang et al., 1988). There are hundreds of major absorption lines even in a  $25\text{ cm}^{-1}$  spectral interval, and the intensity traversing the gas medium also has a similar number of peaks. These strong spectral dependencies of the radiating gas property  $a_\nu(s)$  and the intensity  $I_\nu(s, \Omega)$  cause strong correlations between them.

The average  $a_\nu(s)I_\nu(s, \Omega)$  is obtained by considering the integrated form of the equation of transfer along a line of sight, multiplied by  $a_\nu(s)$ ;

$$\overline{a_\nu(s)I_\nu(s, \Omega)} = \overline{I_{w\nu}(s_w, \Omega) a_\nu(s)\tau_\nu(s_w \rightarrow s)} + \int_{s_w}^s \overline{a_\nu(s)a_\nu(s')\tau_\nu(s' \rightarrow s)\bar{I}_{b\nu}(s')} ds', \quad (2)$$

where  $s_w$  is a point at a wall,  $s$  is a point in the absorbing-emitting medium, and  $s_w \rightarrow s$  is the path from  $s_w$  to  $s$ . The spectral transmittance between  $s'$  and  $s$  is defined as

$$\tau_\nu(s' \rightarrow s) \equiv \exp\left\{-\int_{s'}^s a_\nu(s'') ds''\right\}. \quad (3)$$

The boundary wall intensity in Eq. (2) can be expressed for a diffuse, gray wall as

$$I_{w\nu}(s_w, \Omega) = \epsilon_w \bar{I}_{b\nu\nu}(s_w) + \frac{1-\epsilon_w}{\pi} \int_{\hat{n} \cdot \Omega' < 0} |\hat{n} \cdot \Omega'| I_{w\nu}(s_w, \Omega') d\Omega', \text{ for } \hat{n} \cdot \Omega > 0. \quad (4)$$

The reflected portion of the wall intensity can have as strong a wavenumber dependence as  $\tau_\nu(s_w \rightarrow s)$  and usually cannot be averaged separately over  $\Delta\nu$ . If, however, just the wall emission is considered,  $I_{w\nu}(s_w, \Omega)$  is essentially constant over a narrow band and may be taken out of the spectral integral. Otherwise, fully correlated treatment of the wall reflected intensity is re-

quired (Edwards, 1962; Nelson, 1979). For high-emissivity walls ( $\epsilon_w \rightarrow 1.0$ ), the simplification

$$\overline{I_{w\nu}(s_w, \Omega) a_\nu(s)\tau_\nu(s_w \rightarrow s)} \approx \bar{I}_{w\nu}(s_w, \Omega) \overline{a_\nu(s)\tau_\nu(s_w \rightarrow s)} \quad (5)$$

can be used with no noticeable loss in accuracy for narrow band widths.

The remaining averages in Eq. (2),  $\overline{a_\nu(s)\tau_\nu(s_w \rightarrow s)}$  and  $\overline{a_\nu(s)a_\nu(s')\tau_\nu(s' \rightarrow s)}$ , can be determined by differentiating the average transmittance appropriately. The nongray equation of transfer then becomes

$$\frac{\partial \bar{I}_\nu(s, \Omega)}{\partial s} = \frac{\partial \tau_\nu(s' \rightarrow s)}{\partial s'} \bigg|_{s'=s} \bar{I}_{b\nu}(s) + \bar{I}_{w\nu}(s_w, \Omega) \frac{\partial}{\partial s} \{\bar{\tau}_\nu(s_w \rightarrow s)\} + \int_{s_w}^s \frac{\partial}{\partial s} \left( \frac{\partial \tau_\nu(s' \rightarrow s)}{\partial s'} \right) \bar{I}_{b\nu}(s') ds', \quad (6)$$

where

$$\frac{\partial \tau_\nu(s' \rightarrow s)}{\partial s'} \bigg|_{s'=s} = \bar{a}_\nu(s). \quad (7)$$

This notation is consistent with the narrow-band gas models, which give gas transmittances rather than absorption coefficients. The nongray equation of transfer [Eq. (6)] can also be obtained by first spectrally averaging the integrated equation of transfer along a line of sight, and then differentiating it with respect to  $s$  using the Leibniz rule.

For narrow-band S-N calculations Eq. (6) is discretized as

$$\{\bar{I}_{\nu, n, i+1} - \bar{I}_{\nu, n, i}\} = (1 - \bar{\tau}_{\nu, n, i-i+1}) \bar{I}_{b\nu, i+1/2} + \bar{C}_{\nu, n, i+1/2}, \quad (8)$$

where

$$\bar{C}_{\nu, n, i+1/2} = \bar{I}_{w\nu, n, 1} (\bar{\tau}_{\nu, n, 1-i+1} - \bar{\tau}_{\nu, n, 1-i}) + \sum_{k=1}^{i-1} [(\bar{\tau}_{\nu, n, k+1-i+1} - \bar{\tau}_{\nu, n, k+1-i}) - (\bar{\tau}_{\nu, n, k-i+1} - \bar{\tau}_{\nu, n, k-i})] \bar{I}_{b\nu, k+1/2}. \quad (9)$$

The angular discretization is indicated by the subscript  $n$ , and the spatial discretization is indicated by the subscript  $i$ .

## Nomenclature

$A_j$  = band absorption,  $\text{cm}^{-1}$   
 $A_j^*$  = nondimensional band absorption  
 $a$  = absorption coefficient,  $\text{m}^{-1}$   
 $\bar{C}_\nu$  = spectral source term,  $\text{kW}/(\text{m}^2 \cdot \text{sr} \cdot \text{cm}^{-1})$   
 $C^T$  = total source term,  $\text{kW}/(\text{m}^2 \cdot \text{sr})$   
 $c_n$  = weighting coefficient for S-N solution  
 $-dq/dx$  = radiative source distribution,  $\text{kW}/\text{m}^3$   
 $F$  = blackbody fraction  
 $f$  = species molar fraction  
 $I_\nu$  = spectral radiative intensity,  $\text{kW}/(\text{m}^2 \cdot \text{sr} \cdot \text{cm}^{-1})$   
 $I^T$  = total radiative intensity,  $\text{kW}/(\text{m}^2 \cdot \text{sr})$   
 $I_j$  = integrated  $j$ th band radiative intensity,  $\text{kW}/(\text{m}^2 \cdot \text{sr})$   
 $J$  = number of wide-bands  
 $\bar{k}_\nu$  = mean line-intensity to spacing ratio,  $\text{cm}^{-1} \text{atm}^{-1}$   
 $L$  = slab thickness, m  
 $L_{MB}$  = mean beam length of the entire slab, m

$M$  = number of grid points  
 $\hat{n}$  = inward normal vector to walls  
 $N$  = order of S-N discrete ordinates approximation  
 $p$  = pressure, atm  
 $q$  = radiative heat flux,  $\text{kW}/\text{m}^2$   
 $s, s'$  = position variables, m  
 $T$  = absolute temperature, K  
 $u$  = pressure-path length parameter,  $\text{atm} \cdot \text{m}$   
 $x$  =  $x$ -coordinate, m  
 $\bar{\beta}_\nu$  = mean line-width to spacing ratio  
 $\bar{\gamma}_\nu$  = mean half-width of an absorption line,  $\text{cm}^{-1}$   
 $\bar{\delta}_\nu$  = equivalent line spacing,  $\text{cm}^{-1}$   
 $\Delta x$  = width of a sublayer, or a control volume, m  
 $\Delta\nu$  = wavenumber interval,  $\text{cm}^{-1}$   
 $\epsilon_w$  = wall emissivity  
 $\theta$  = polar angle  
 $\mu$  =  $x$ -direction cosine =  $\cos \theta$   
 $\nu$  = wavenumber,  $\text{cm}^{-1}$

$\sigma$  = Stefan-Boltzmann constant,  $\text{kW}/(\text{m}^2 \cdot \text{K}^4)$   
 $\tau$  = transmittance  
 $\tau_H$  = optical depth at the head of a wide-band  
 $\phi$  = azimuthal angle  
 $\Omega$  = solid angle,  $(\theta, \phi)$

### Superscripts

' or '' = integration variable  
 $(\bar{\quad})$  = spectrally averaged quantity over  $\Delta\nu$

### Subscripts

$b$  = blackbody  
 $e$  = equivalent parameter  
 $i$  = spatial index  
 $j$  = wide-band number index  
 $k$  = dummy spatial index  
 $l$  = lower spectral limit  
 $M$  = grid point at upper wall  
 $n$  = angular index  
 $u$  = upper spectral limit  
 $w$  = wall  
 $\nu$  = spectral  
 $1$  = grid point at lower wall

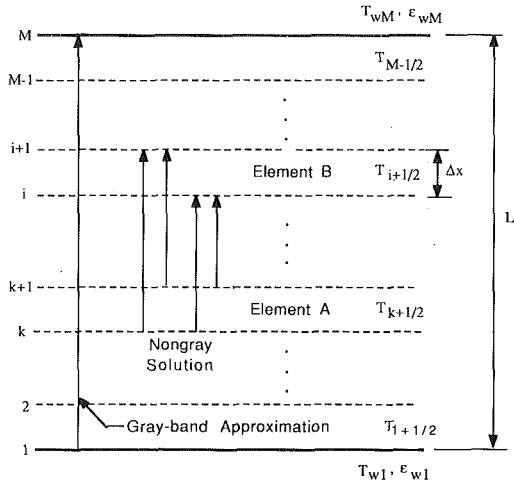


Fig. 1 Schematic of the slab geometry and length scales

The grid numbering scheme is shown in Fig. 1. Equations (8) and (9) are written for  $i=1$  to  $M$ , and  $n=1$  to  $N/2$  for the positive  $\mu_n$  directions. For the negative  $\mu_n$  directions similar equations can be written, which must be solved simultaneously. The intensities at the control volume edges with subscripts  $i$  or  $i+1$  are related to the control volume center intensity with subscript  $i+1/2$  by an auxiliary equation,  $\bar{I}_{\nu,n,i+1/2} = (1-c_n)\bar{I}_{\nu,n,i} + c_n\bar{I}_{\nu,n,i+1}$ . The diamond difference scheme sets  $c_n = 0.5$ . The spatial weights  $c_n$  vary between 0.5 and 1 and are determined using the positive scheme suggested by Carlson and Lathrop (1968). The subscripts used for the transmittances indicate  $\bar{\tau}_{\nu,n,k-i+1} \equiv \bar{\tau}_{\nu}(x_k/|\mu_n| - x_{i+1}/|\mu_n|)$ . The wall and gas emission terms,  $I_{w\nu}$  and  $I_{b\nu}$ , are evaluated at the band center.

An existing  $S-N$  code developed by the authors for gray, absorbing, emitting, and anisotropic scattering media is used for the nongray radiation solution (Kim and Lee, 1988), treating the spectral source term  $\bar{C}_{\nu,n,i+1/2}$  like an anisotropic scattering source term.

The statistical narrow-band model with an exponential-tailed-inverse line-strength distribution gives the average transmittance over a narrow wavenumber interval. For an isothermal and homogeneous path length ( $s' \rightarrow s$ ) of a molar fraction  $f$  and a total pressure  $p$  (Ludwig et al., 1973), the average transmittance is

$$\bar{\tau}_{\nu}(s' \rightarrow s) = \exp \left[ -\frac{\bar{\beta}_{\nu}}{\pi} \left( \sqrt{1 + \frac{2\pi u \bar{k}_{\nu}}{\bar{\beta}_{\nu}}} - 1 \right) \right], \quad (10)$$

where the pressure-path length  $u$  is  $fp|s \rightarrow s'|$  and the average line-width to spacing ratio is given as  $\bar{\beta}_{\nu} = 2\pi\bar{\gamma}_{\nu}/\delta_{\nu}$ . The mean band parameters  $\bar{k}_{\nu}$  and  $1/\delta_{\nu}$  for  $H_2O$  vapor over the spectral range of  $\nu = 150-8000 \text{ cm}^{-1}$  are obtained for this study from the narrow-band data based on line-by-line calculations published by Hartmann et al. (1984) and Soufiani et al. (1985). The mean half-width  $\bar{\gamma}_{\nu}$  is obtained using the parameters suggested by Zhang et al. (1988). A band width of 25 or  $50 \text{ cm}^{-1}$  is used in the calculations.

For a nonisothermal and inhomogeneous medium, the average transmittance is obtained by using the Curtis-Godson formal method (Godson, 1953). This method approximates the nonisothermal and inhomogeneous medium with an equivalent isothermal and homogeneous medium. The equivalent band parameters  $\bar{\beta}_{\nu,e}$  and  $\bar{k}_{\nu,e}$  are obtained by averaging the band parameters over the pressure-path length  $u$  of the nonisothermal, inhomogeneous medium as

$$u(s' \rightarrow s) = \int_s^{s'} p(s'') f(s'') ds'', \quad (11)$$

$$\bar{k}_{\nu,e}(s' \rightarrow s) = \frac{1}{u} \int_s^{s'} p(s'') f(s'') \bar{k}_{\nu}(s'') ds'', \quad (12)$$

and

$$\bar{\beta}_{\nu,e}(s' \rightarrow s) = \frac{1}{u \bar{k}_{\nu,e}} \int_s^{s'} p(s'') f(s'') \bar{k}_{\nu}(s'') \bar{\beta}_{\nu}(s'') ds''. \quad (13)$$

The equivalent properties are then used in place of the isothermal and homogeneous properties in Eq. (10).

After the spectral intensity field is calculated, the total net radiative flux is obtained as

$$q(\dot{x}) = \sum_{\text{all } \Delta\nu's} \left[ \int_{4\pi} \mu \bar{I}_{\nu}(x, \Omega) d\Omega \right] \Delta\nu. \quad (14)$$

The radiative source term used in the energy equation for combined mode heat transfer problems,  $-dq/dx$ , can be obtained from the net fluxes using a finite differencing technique.

An alternate way to obtain the total heat transfer quantities is first to integrate the equation of transfer [Eq. (1)] over the entire spectral domain before the narrow-band approximation is applied. This method is quicker computationally, because the  $S-N$  portion of the program only has to be performed once. This alternate approach is similar to the wide-band formulation presented in the following section.

**Wide-Band Formulation.** A general form of the total, or wavenumber-integrated, equation of transfer can be written as

$$\begin{aligned} \frac{\partial I^T(s, \Omega)}{\partial s} = & \int_0^{\infty} \frac{\partial \tau_{\nu}(s' \rightarrow s)}{\partial s'} \Big|_{s'=s} I_{b\nu}(s) d\nu \\ & + \int_0^{\infty} I_{w\nu}(s_w, \Omega) \frac{\partial}{\partial s} \{ \tau_{\nu}(s_w \rightarrow s) \} d\nu \\ & + \int_0^{\infty} \int_{s_w}^s \frac{\partial}{\partial s} \left( \frac{\partial \tau_{\nu}(s' \rightarrow s)}{\partial s'} \right) I_{b\nu}(s') ds' d\nu, \end{aligned} \quad (15)$$

where the total intensity is written with a superscript  $T$ . Equation (15) is analogous to Eq. (6) for the narrow-band formulation, because the derivations are similar.

In order to evaluate the total intensity, a wide-band model must be incorporated into the analysis. For this study, the exponential wide-band model is applied. The band absorption for the exponential wide-band model is derived from Goody's narrow-band model by assuming that the line intensity to line spacing ratio has an exponential distribution (Edwards, 1976). The  $j$ th band absorption,  $A_j(s' \rightarrow s)$ , for an isolated band is defined to be

$$A_j(s' \rightarrow s) \equiv \int_{\nu_{lj}}^{\nu_{uj}} [1 - \tau_{\nu}(s' \rightarrow s)] d\nu, \quad (16)$$

where  $\nu_{lj}$  and  $\nu_{uj}$  are assigned at or somewhere outside the perceptible limits of the band.

The spectral integrals in Eq. (15) are approximated by summations over all the gas bands (making the band approximation), and  $I_{b\nu}$  and  $I_{w\nu}$  are assumed essentially constant over each band. The terms involving gas transmittances are rewritten using the band absorption definition, e.g.,

$$\partial A_j(s' \rightarrow s) / \partial s = - \int_{\nu_{lj}}^{\nu_{uj}} [\partial \tau_{\nu}(s' \rightarrow s) / \partial s] d\nu. \quad \text{The final form of}$$

the total equation of transfer with the exponential wide-band is

$$\begin{aligned} \frac{\partial I^T(s, \Omega)}{\partial s} = & - \sum_{j=1}^J \frac{\partial A_j(s' \rightarrow s)}{\partial s'} \Big|_{s'=s} \bar{I}_{bj}(s) \\ & - \sum_{j=1}^J \bar{I}_{wj}(s_w, \Omega) \frac{\partial A_j(s_w \rightarrow s)}{\partial s} \\ & - \sum_{j=1}^J \int_{s_w}^s \frac{\partial}{\partial s} \left[ \frac{\partial A_j(s' \rightarrow s)}{\partial s'} \right] \bar{I}_{bj}(s') ds', \end{aligned} \quad (17)$$

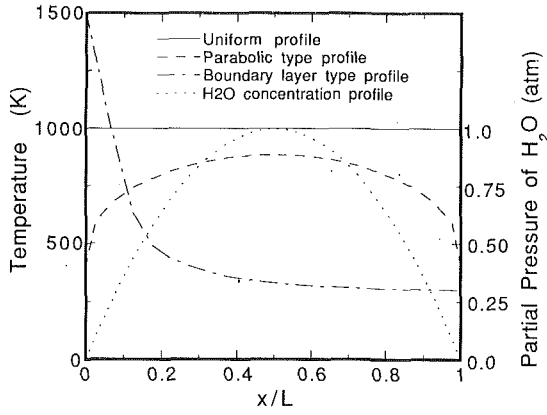


Fig. 2 Temperature and concentration profiles

where the  $j$  subscript symbolizes the value of that quantity for the  $j$ th band, and the total number of bands under consideration is  $J$ .

The discretized form of Eq. (17) for  $S$ - $N$  calculations is

$$\{I_{n,i+1}^T - I_{n,i}^T\} = \sum_{j=1}^J A_{j,n,i-i+1} \bar{I}_{bj,i+1/2} + C_{n,i+1/2}^T, \quad (18)$$

where  $C_{n,i+1/2}^T$  is the total source term, and the subscripts on the band absorptances indicate  $A_{j,n,k-i+1} = A_j(x_k/l | \mu_n | \rightarrow x_{i+1} | \mu_n |)$ .

The bandwidths in the wide-band model can become quite large, on the order of  $1000 \text{ cm}^{-1}$ . It is therefore more accurate to use some suitable average of  $\bar{I}_{wj}$  and  $\bar{I}_{bj}$  instead of the band-center values. One option, which is accurate for large optical depths at the band centers, is to use  $A_j$  as the bandwidth along with blackbody fractions,  $F$ . For  $\bar{I}_{bj}$  averaged over the band

$$\bar{I}_{bj,k+1/2} A_{j,n,k-i+1} = \frac{\sigma T_{k+1/2}^4}{\pi} F_{j,n,k-i+1}, \quad (19)$$

where

$$F_{j,n,k-i+1} \equiv F_{0-(\nu_c - A_{j,n,k-i+1/2})T_{k+1/2}} - F_{0-(\nu_c + A_{j,n,k-i+1/2})T_{k+1/2}} \quad (20)$$

if the band center  $\nu_c$  is given. Similar expressions to Eq. (20) can be written if the lower or upper limit of the band is specified instead of the band center. The resulting discretized, total equation of transfer is

$$\{I_{n,i+1}^T - I_{n,i}^T\} = \frac{\sigma T_{i+1/2}^4}{\pi} \sum_{j=1}^J F_{j,n,i-i+1} + C_{n,i+1/2}^T, \quad (21)$$

where the total source term is

$$C_{n,i+1/2}^T = -\frac{\sigma T_w^4}{\pi} \sum_{j=1}^J (F_{j,n,1-i+1} - F_{j,n,1-i}) - \sum_{k=1}^{i-1} \frac{\sigma T_{k+1/2}^4}{\pi} \sum_{j=1}^J [(F_{j,n,k+1-i+1} - F_{j,n,k+1-i}) - (F_{j,n,k-i+1} - F_{j,n,k-i})]. \quad (22)$$

In these equations the spectral integration must be performed on the  $F_j$  values first, because of the varying bandwidths with path length. The total heat flux is then determined by one call to the  $S$ - $N$  solution routine. Band overlap is handled in a manner suggested by Edwards and Balakrishnan (1973). That is, if two or more bands overlap, the minimum and maximum values of all the bands involved in the overlap are retained while others are discarded. The region of overlap bands is then treated as one band. In Eqs. (21) and (22),  $J$  is the total number of bands treating the overlapped bands as one band. The recommendations of Edwards (1976) in equations (196), (197),

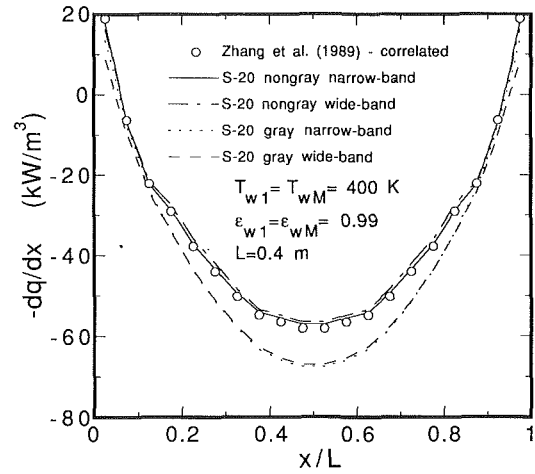


Fig. 3 The radiative source for the parabolic type temperature profile

and (198) of his paper are used for obtaining equivalent properties for a nonisothermal or inhomogeneous path.

**Gray-Band Formulation.** For the gray-band calculations the following forms of Eq. (1) are solved for the narrow- and wide-band calculations, respectively:

$$\frac{\partial \bar{I}_v(s, \Omega)}{\partial s} + \bar{a}_v(s) \bar{I}_v(s, \Omega) = \bar{a}_v(s) \bar{I}_{bv}(s) \quad (23)$$

and

$$\frac{\partial I_j(s, \Omega)}{\partial s} + \bar{a}_j(s) I_j(s, \Omega) = \frac{\partial T^4(s)}{\pi} (F_{0-\nu_j T(s)} - F_{0-\nu_{uj} T(s)}), \quad (24)$$

where  $I_j$  is the integrated intensity over the  $j$ th band, and the  $F$ 's are blackbody fractions. In both of these equations some suitably averaged absorption coefficient is used in place of a correlated average of  $\bar{a}_v(s) \bar{I}_v(s, \Omega)$ . After Eq. (23) is solved for each narrow-band, the total heat fluxes are obtained using Eq. (14). The total heat fluxes from Eq. (24) are obtained by adding the  $I_j$ 's for each band together and then performing an angular integration.

For this study, the averaged absorption coefficient is evaluated based on the same narrow- and wide-band models used in the nongray analysis. The  $\bar{a}_v$  and  $\bar{a}_j$  are computed from the transmittances of the entire layer (see Fig. 1). The layer is first converted into an equivalent isothermal, homogeneous medium by the appropriate nonisothermal band theory, and the mean beam length of the layer is calculated based on the overall thickness. An equivalent narrow-band-averaged absorption coefficient is obtained as

$$\bar{a}_v = \frac{1}{\Delta \nu} \int_{\Delta \nu} a_\nu d\nu \cong -\frac{\ln \bar{\tau}_\nu(L_{MB})}{L_{MB}}, \quad (25)$$

where the mean beam length for the planar slab is taken to be  $1.9L$ . This same equation is used for the wide-band-averaged absorption coefficient with the  $\nu$  subscript replaced by the band subscript  $j$ . Equation (10) is used to calculate the transmittance from narrow-band data, while that used to get a transmittance from the wide-band model is (Edwards, 1976)

$$\bar{\tau}_j = \frac{\tau_{H,j}}{A_j^*} \frac{dA_j^*}{d\tau_{H,j}} \quad \text{for } \bar{\tau}_j \leq 0.90. \quad (26)$$

In this equation  $\tau_H$  is the optical depth at the band head, and  $A_j^*$  is the band absorption divided by the exponential decay width,  $A_j^*$  is based on  $L_{MB}$ . If the value from Eq. (26) is greater than 0.9, the transmittance is set equal to 0.90.

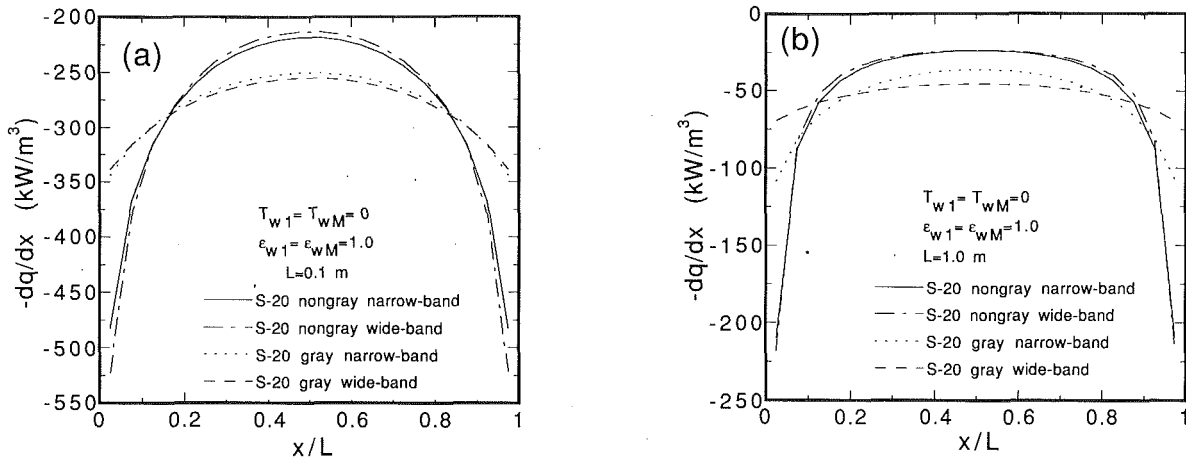


Fig. 4 The radiative source for the uniform temperature profile

The wide-band limits in Eqs. (24) and (25) are determined from

$$\nu_{uj} - \nu_{lj} = A_j / (1 - \bar{\tau}_j), \quad (27)$$

and the band head location is given by Edwards (1976) along with other fundamental data for the exponential wide-band model. Band overlap is handled by creating a new band for each overlapped region, where the transmissivity of the overlapped region is equal to the product of all the band transmissivities involved in the overlap. The block calculation procedure described by Edwards (1976) is used for the gray, wide-band calculations. The narrow-band  $\Delta\nu$  in Eqs. (23) and (25) are 25 or 50  $\text{cm}^{-1}$ .

From Fig. 1 it is easy to see the simplification provided by the gray-band approximation. The overall slab width, and the control volume sizes,  $\Delta x$ , are the only length scales required for the calculation. For the nongray solution, however, four length scales are needed to determine the effect of element A on element B, and this has to be done for all the combinations of gas elements for every direction. The other simplification offered by the gray-band approximation is that the equation of transfer formulation is similar to a gray gas formulation.

## Results and Discussion

Three different temperature profiles for a uniform composition of pure  $\text{H}_2\text{O}$  vapor at 1 atm between two infinite parallel plates are studied using the  $S$ - $N$  solution method. The temperature profiles used are shown in Fig. 2. Also shown in the figure is a parabolic  $\text{H}_2\text{O}$  concentration profile for a mixture of  $\text{H}_2\text{O}$  and  $\text{N}_2$  at 1 atm. For the uniform temperature profile the gas temperature is chosen to be 1000 K, while the walls are held at 0 K. This uniform temperature profile is used with the pure  $\text{H}_2\text{O}$  case for two different path lengths and also with the parabolic  $\text{H}_2\text{O}$  concentration profile. The parabolic type temperature profile shown in Fig. 2 was obtained from Zhang et al. (1988) and was chosen so that the results obtained from this work can be compared to their published results. This type of temperature profile is also important because it is similar to that found in fully developed duct flows. The third temperature profile was taken from a combined radiation and convection boundary layer solution for a gray gas (Lee et al., 1990) and is indicated as the boundary layer type temperature profile.

All the results presented in this section were obtained using a 20 direction Gaussian quadrature set. Higher order quadrature sets did not influence the resulting total quantities significantly. The overall slab is divided into 20 sublayers for all the calculations. The methods used to obtain the presented

results are the nongray and gray-band  $S$ - $N$  method, and the flux method outlined by Soufiani et al. (1985).

All the gray wall emissivities are  $\epsilon_w = 1.0$ , except with the parabolic type temperature profile where both walls have  $\epsilon_w = 0.99$ . A wall emissivity of 0.99 for this case allows for a direct comparison with Zhang et al. (1988) who also use the approximation shown in Eq. (5) for the reflected component.

Figure 3 shows the radiation source results for the parabolic type temperature profile. The nongray  $S$ - $N$  result using the narrow-band data agrees very well with the published data of Zhang et al. (1988) and the nongray wide-band results. The gray narrow- and wide-band results are in close agreement with each other but fall approximately 18 percent below the other results at the center of the slab.

The narrow-band calculation for Fig. 3 only goes up to 4200  $\text{cm}^{-1}$  and uses the same narrow-band data actually used by Zhang et al. (1988), which is a slightly different and updated version of the band data published earlier in Hartmann et al. (1984) and Soufiani et al. (1985). This new data set was obtained via direct correspondence with Taine and Soufiani (1990) and is not published at this time. To compare with these narrow-band results, the wide-band results only account for the rotational, 6.3  $\mu\text{m}$ , and 2.7  $\mu\text{m}$  bands of  $\text{H}_2\text{O}$ . All other results shown in this paper use the data published by Hartmann et al. (1984) and Soufiani et al. (1985) and include all  $\text{H}_2\text{O}$  bands.

Figures 4(a) and 4(b) show  $-dq/dx$  obtained for the uniform temperature case with slab thickness of 0.1 and 1.0 m. The gray-band results fall below the nongray narrow- and wide-band results at the center of the layer and are well above these results at the edges. The nongray results show that a step change in the temperature has a big effect on the radiation source distribution, especially as the medium becomes more optically thin. When the medium becomes more optically thick,  $-dq/dx$  at the center of the slab approaches zero as it does in Fig. 4(b). Again, the respective narrow- and wide-band solutions agree very well with each other. The gray-band solutions using the narrow-band model are closer to the nongray solutions than the gray, wide-band solutions. This is more apparent in the gray-band solutions for  $L = 1.0$  m (Fig. 4b). As  $\Delta\nu$  gets closer to the line-by-line scale, the general trend should be that the gray-band approximation using the narrow-band data gets closer to the nongray results.

Figure 5 presents results of the four methods for a boundary layer type of temperature profile. For a boundary layer profile with a hot wall, the gas goes from a net emitter near the wall to a net absorber away from the wall. Far from the wall the gas becomes uniform in temperature, and  $-dq/dx$  gradually approaches zero. The gray-band solutions do not predict the large peak in the radiative source term near the wall. The gray-

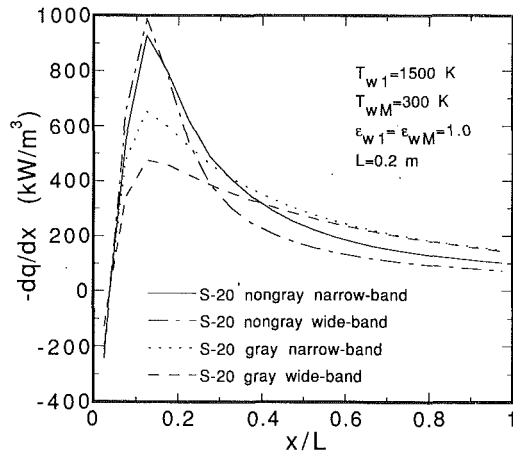


Fig. 5 The radiative source for the boundary layer type temperature profile

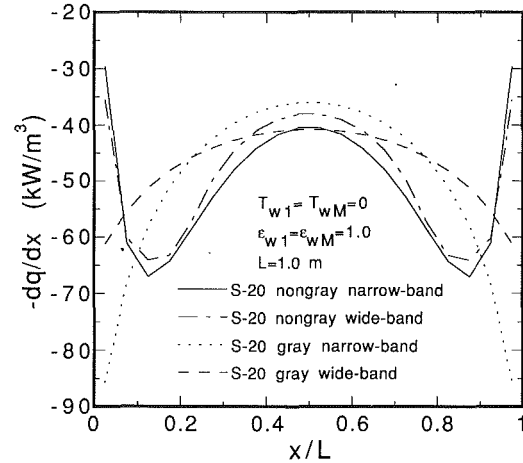


Fig. 6 The radiative source for the parabolic H<sub>2</sub>O concentration profile with the uniform temperature profile

Table 1 Net wall fluxes (kW/m<sup>2</sup>)

|   | S-20 Method |           |           |           | Flux Method (Soufiani et al.) |           |
|---|-------------|-----------|-----------|-----------|-------------------------------|-----------|
|   | Narrow-band |           | Wide-band |           | Narrow-band                   | Wide-band |
|   | Nongray     | Gray-band | Nongray   | Gray-band | Nongray                       | Nongray   |
| Parabolic $T$                             | -6.7        | -8.0      | -6.6      | -8.1      | -6.8                          | -6.5      |
| Uniform $T$ ;<br>$L = 0.1$ m              | -14.3       | -14.0     | -14.4     | -14.1     | -14.2                         | -14.3     |
| Uniform $T$ ;<br>$L = 1.0$ m              | -28.2       | -27.7     | -27.6     | -26.3     | -28.1                         | -27.4     |
| Boundary layer $T$                        | 277.4       | 278.5     | 277.0     | 281.7     | 277.7                         | 276.7     |
| Uniform $T$ with<br>concentration profile | -25.4       | -25.1     | -24.6     | -23.6     | -25.3                         | -24.6     |

band approximation with the wide-band model shows the most smoothing of the radiative source curves. The agreement between the narrow- and wide-band solutions is not as good as was seen for the other temperature profiles. This is believed to be due to the rapid changes in  $-dq/dx$ .

The results for the varying H<sub>2</sub>O concentration with a uniform temperature profile are shown in Fig. 6. The gray-band approximation fails to predict some interesting features near the walls, where the largest errors were already observed in Fig. 4(b) for uniform H<sub>2</sub>O concentration. In fact, the gray-band results are the same as those that would be obtained for a uniform slab of H<sub>2</sub>O at an average concentration representing the parabolic distribution. This shows that a gray-band approximation with its mean beam length tends to average out the effects of the concentration and temperature profiles. The exponential wide-band model does not predict such sharp peaks as the statistical narrow-band model.

There are physical justifications for the features shown by the nongray solutions in Fig. 6. First, since the H<sub>2</sub>O concentration at the walls goes to zero there can be no absorption by the gas, and  $-dq/dx$  must go to zero. In the figure,  $-dq/dx$  does not quite reach zero, since the data at the walls are not available as a result of using 20 control volumes in the computation. Secondly,  $-dq/dx$  will tend to zero at the centerline as the gas becomes optically thick. The W type shape shown in Fig. 6 is not seen at small optical depths. For a very small optical depth just a U shape is observed. Thirdly,  $-dq/dx$  cannot be positive for these conditions. These three considerations together say that two humps will be present in these data for large optical depths;  $-dq/dx$  must decrease from the edges, and for large enough optical depths, it must decrease from the center as well.

Table 1 shows the net radiative wall fluxes obtained for the

cases presented in Figs. 3–6. The gray-band approximation, which is easier to formulate and therefore much quicker computationally (on the order of 0.1 to 1.0 s Cray-2 CPU time), gives almost the same wall heat fluxes as the other solutions. The small differences would disappear, if the absorption coefficient shown in Eq. (25) were based on the actual lengths for each angle through the medium instead of on the mean beam length. However, since the gray-band approximation will never give the correct results for the intermediate fluxes or the  $-dq/dx$  profile, calculating one absorption coefficient based on the overall mean beam length of the slab is sensible for this approximation.

The data obtained from a flux method of solution outlined by Soufiani et al. (1985) are also presented in Table 1. The radiation source distributions calculated by the flux method were not shown in Figs. 3–6, because they fall on top of the corresponding nongray  $S-N$  solutions. The solutions obtained from this flux method served as another check on the nongray  $S-N$  solutions. Computationally the flux method is only slightly slower than the gray-band method. The advantage of the  $S-N$  method is that it can be extended to two dimensions, using the code already developed for two-dimensional, anisotropically scattering media (Kim and Lee, 1988).

Larger computation times are required for the nongray  $S-N$  method solutions (on the order of 10 seconds Cray-2 CPU time). The time-consuming portion of the narrow-band solution is in reading the narrow-band data for transmittance calculations. There are much fewer data to read into the wide-band model, but the computation time to get each band absorptance can be significant with the exponential wide-band model, which is the most complicated of the wide-band models.

Computation time savings of over a factor of two can be achieved by evaluating the  $S-N$  nongray source terms using the

mean beam length concept. The mean beam lengths of all four length scales required by the nongray solution must be evaluated. Still, this allows for a single calculation of the source term at each  $x$  location, rather than separate calculations at every direction. For the narrow-band calculations, the nongray mean-beam-length wall fluxes were more accurate than those from the corresponding gray-band approximation. More importantly, the internal radiation source distribution is still accurately predicted.

## Conclusions

Existing  $S-N$  codes for gray, absorbing, emitting, and scattering media can be adapted to handle nongray gas radiation accurately. Formulations of the equation of transfer using a narrow- or wide-band model define a spectral source term that is similar to an anisotropic scattering source term. Significant amounts of computer time are generally required to handle nongray gas radiation. One way to reduce this computational time is to use the gray-band approximation; however, accuracy in the internal fluxes and radiative source distribution is lost. The loss in accuracy is particularly noticeable in regions of rapid temperature and concentration changes. The net wall radiative fluxes are, however, predicted with reasonable accuracy.

## Acknowledgments

This work was supported in part by the National Science Foundation Grant No. NSF/CBT-8451076. Support from the Minnesota Supercomputer Institute is also gratefully acknowledged.

## References

Buckius, R. O., 1982, "The Effect of Molecular Gas Absorption on Radiative Heat Transfer With Scattering," *ASME JOURNAL OF HEAT TRANSFER*, Vol. 104, pp. 580-586.

Carlson, B. G., and Lathrop, K. D., 1968, "Transport Theory—the Method of Discrete Ordinates," *Computing Methods in Reactor Physics*, H. Greenspan, C. N. Kelber, and D. Okrent, eds., Gordon & Breach, New York, pp. 166-266.

Cess, R. D., Mighdoll, P., and Tiwari, S. N., 1967, "Infrared Radiative Heat Transfer in Nongray Gases," *International Journal of Heat and Mass Transfer*, Vol. 10, pp. 1521-1532.

Edwards, D. K., 1962, "Radiation Interchange in a Nongray Enclosure Containing an Isothermal Carbon-Dioxide-Nitrogen Gas Mixture," *ASME JOURNAL OF HEAT TRANSFER*, Vol. 84, pp. 1-11.

Edwards, D. K., and Menard, W. A., 1964, "Comparison of Models for Correlation of Total Band Absorption," *Applied Optics*, Vol. 3, pp. 621-625.

Edwards, D. K., and Balakrishnan, A., 1973, "Thermal Radiation by Combustion Gases," *International Journal of Heat and Mass Transfer*, Vol. 16, pp. 25-40.

Edwards, D. K., 1976, "Molecular Gas Band Radiation," *Advances in Heat Transfer*, Vol. 12, Academic Press, New York, pp. 115-193.

Edwards, D. K., and Babikian, P. S., 1989, "Radiation From a Nongray Scattering, Emitting and Absorbing SRM Plume," Paper No. AIAA-89-1721.

Fiveland, W. A., and Jamaluddin, A. S., 1989, "Three-Dimensional Spectral Radiative Heat Transfer Solutions by the Discrete-Ordinates Method," *Heat Transfer Phenomena in Radiation, Combustion, and Fires*, R. K. Shah, ed., ASME HTD-Vol. 106, pp. 43-48.

Godson, W. L., 1953, "The Evaluation of Infrared Radiation Fluxes Due to Atmospheric Water Vapor," *Quarterly Journal of Royal Meteorological Society*, Vol. 79, pp. 367-379.

Goody, R. M., 1964, *Atmospheric Radiation*, Clarendon Press, Oxford, pp. 122-170.

Grosshandler, W. L., 1980, "Radiative Heat Transfer in Nonhomogeneous Gases: A Simplified Approach," *International Journal of Heat and Mass Transfer*, Vol. 23, pp. 1447-1459.

Grosshandler, W. L., and Nguyen, H. D., 1985, "Application of the Total Transmittance Nonhomogeneous Radiation Model to Methane Combustion," *ASME JOURNAL OF HEAT TRANSFER*, Vol. 107, pp. 455-450.

Hartmann, J. M., Levi De Leon, R., and Taine, J., 1984, "Line-by-Line and Narrow-Band Statistical Model Calculations for H<sub>2</sub>O," *Journal of Quantitative Spectroscopy and Radiative Transfer*, Vol. 32, No. 2, pp. 119-127.

Kim, T. K., and Lee, H. S., 1988, "Effect of Anisotropic Scattering on Radiative Heat Transfer in Two Dimensional Rectangular Enclosures," *International Journal of Heat and Mass Transfer*, Vol. 31, pp. 1711-1721.

Lee, H. S., Menart, J. A., and Fakheri, A., 1990, "A Multilayer Radiation Solution for Boundary Layer Flow of Gray Gases," *Journal of Thermophysics and Heat Transfer*, Vol. 4, pp. 180-185.

Ludwig, C. B., Malkmus, W., Reardon, J. E., and Thompson, J. A. L., 1973, *Handbook of Infrared Radiation From Combustion Gases*, NASA SP-3080, Scientific and Technical Information Office, Washington, DC.

Mengüç, M. P., and Viskanta, R., 1986, "An Assessment of Spectral Radiative Heat Transfer Predictions for a Pulverized Coal-Fired Furnace," *Proceedings of the Eighth International Heat Transfer Conference*, San Francisco, Vol. 2, pp. 815-820.

Nelson, D. A., 1979, "Band Radiation Within Diffuse-Walled Enclosures, Part I: Exact Solutions for Simple Enclosures," *ASME JOURNAL OF HEAT TRANSFER*, Vol. 101, pp. 81-89.

Soufiani, A., Hartmann, J. M., and Taine, J., 1985, "Validity of Band-Model Calculations for CO<sub>2</sub> and H<sub>2</sub>O Applied to Radiative Properties and Conductive-Radiative Transfer," *Journal of Quantitative Spectroscopy and Radiative Transfer*, Vol. 33, No. 3, pp. 243-257.

Soufiani, A., and Taine, J., 1989, "Experimental and Theoretical Studies of Combined Radiative and Convective Transfer in CO<sub>2</sub> and H<sub>2</sub>O Laminar Flows," *International Journal of Heat and Mass Transfer*, Vol. 32, No. 3, pp. 447-486.

Taine, J., and Soufiani, A., 1990, Private communication, Mar.

Thynell, S., 1989, "Effect of Either CO<sub>2</sub> and H<sub>2</sub>O and Particles on Radiation in a One-Dimensional Cylinder," Paper No. AIAA 89-1718.

Zhang, L., Soufiani, A., and Taine, J., 1988, "Spectral Correlated and Non-correlated Radiative Transfer in a Finite Axisymmetric System Containing an Absorbing and Emitting Real Gas-Particle Mixture," *International Journal of Heat and Mass Transfer*, Vol. 31, pp. 2261-2272.

# Optical Diagnostics and Radiative Properties of Simulated Soot Agglomerates

J. C. Ku

Assistant Professor.  
Mem. ASME

K.-H. Shim

Research Assistant.

Mechanical Engineering Department,  
Wayne State University,  
Detroit, MI 48202

*The effect of agglomeration on the optical diagnostics and radiative properties of simulated soot agglomerates is investigated, using results from the Jones solution. It is found that agglomeration has a very strong effect on scattering, but only a weak effect on extinction ( $\cong$  absorption). An accurate relation has been developed, based on near-forward scattering coefficients, for inferring the number of primary particles in soot agglomerates. General models for both total and differential scattering coefficients have also been established. These results are in general agreement with those predicted for fractal aggregates having a large number of particles. Because of the effect of agglomeration, scattering may not be negligible in treating radiative transport from soot agglomerates.*

## Introduction

Soot particles formed in hydrocarbon-fueled combustion systems have long been of interest to research scientists and engineers. Of particular interest are the gas-to-solid particulate formation process and the increase in heat transfer due to thermal radiation from soot particles. These aspects are difficult to analyze because they are interconnected with other aspects of combustion and transport processes. There have been studies addressing various aspects of flame soots including sooting chemistry (Cole et al., 1984; Weissman and Benson, 1989), particulate formation modeling (Moss et al., 1988; Megaridis and Dobbins, 1990a), particle inception (Harris and Weiner, 1988), soot oxidation (Neoh et al., 1984; Garo et al., 1990), and mass and energy transport (Gore and Faeth, 1986; Kent and Honnery, 1990).

Optical diagnostics and radiative properties are important subjects in the investigation of flame soot particles. Models for the soot formation process are usually verified by comparing with such data as particle size and number density obtained from optical diagnostics. For calculating radiation heat transfer from soot particles, the extinction coefficient, single-scattering albedo, and phase function are needed in the visible and near-infrared wavelengths. Both these subjects are applications of the absorption and scattering of light by small particles. Particulate diagnostics is an inverse problem in that fundamental physical properties such as size, number density, and complex refractive index of particles are inferred from extinction and scattering measurements using a pertinent light scattering theory. Conversely, the calculation of radiative properties is a forward problem. But since soot particles typically exist as agglomerates, the treatment of both subjects becomes more difficult.

Wersborg et al. (1973) observed, through electron microscopy, a noticeable level of agglomeration even for soot particles in their earliest stage of formation. Detailed size analyses and some of the most revealing micrographs of soot agglomerates have been reported by Megaridis and Dobbins (1989, 1990b). The effect of agglomeration on the optical diagnostics of soot particles is probably first reported by Dalzell et al. (1970). They found that angular scattering patterns of soot agglomerates cannot be curve-fitted to the Mie solution with any combination of equivalent diameter and effective refractive

indices, and inferred diameters are much larger than the ones observed from micrographs. It is clear that the effect of agglomeration is significant on both optical diagnostics and radiative properties of soot particles, but it has been intentionally overlooked in most of the earlier works.

Sensible models have been developed recently based on the fractal aggregate theories, and successfully applied on aggregates of gold, silica, and polystyrene (Berry and Percival, 1986; Freltoft et al., 1986; Chen et al., 1988; Lin et al., 1990). However, these models may be applicable only to fractal aggregates that have self-similarity in shape and large number (say, hundreds) of primary particles. Attempts to apply these models on soot agglomerates have been made through computer simulation (Dobbins and Megaridis, 1990), morphological description (Megaridis and Dobbins, 1990b), and analysis of optical measurements (Dobbins et al., 1990). We decide to take a different approach and study the light scattering and absorption of randomly oriented chainlike agglomerates with smaller number of primary particles using the Jones solution (1979a, 1979b). The same approach was taken by Felske et al. (1986), Ku and Flower (1987), and Kumar and Tien (1989). However, the numerical results in Felske et al. (1986) are questionable due to errors in the Jones solution, which were later found by Kumar and Tien (1989) and Ku (1991), whereas Kumar and Tien (1989) in essence applied the weak-coupling (or first-order Born) approximation of the Jones solution.

The objectives of this study are twofold: first, to examine the effect of agglomeration on the optical diagnostics and radiative properties of soot agglomerates by comparing their extinction and scattering coefficients with those of single spheres. Since the Jones solution is implicit and computationally intensive, a second and more important objective is to formulate simple but accurate models for the absorption and scattering of light by soot agglomerates. In addition to three different chainlike morphologies, variations in primary particle size, refractive indices, and number per agglomerate will all be considered in the analysis.

## Optical Diagnostics and Radiative Properties of Small Particles

Optical measurements obtained from a particulate suspension, such as a sooty flame, can be used to calculate the local extinction and differential scattering coefficients ( $\sigma_e$  and  $\sigma_s$ , respectively) of particles (D'Alessio, 1981). When the particle

Contributed by the Heat Transfer Division and presented at the ASME Winter Annual Meeting, Dallas, Texas, November 25-30, 1990. Manuscript received by the Heat Transfer Division August 7, 1990; revision received January 31, 1991. Keywords: Fire/Flames, Radiation, Thermophysical Properties.



number density is sufficiently low such that it is in the single-scattering regime, these coefficients are given as the product of number density  $N_D$  and optical cross section  $C$  of individual particles by

$$\sigma = N_D \bar{C}, \quad (1)$$

where the overbar denotes a mean value averaged over a particle size distribution  $P(D)$  ( $D$  = diameter) according to

$$\bar{C} = \int_0^{\infty} CP(D)dD. \quad (2)$$

For spherical particles, these cross sections depend on the size distribution  $P(D)$  and complex refractive index  $m$  according to the Mie or Rayleigh solution (Bohren and Huffman, 1983). The differential scattering cross section also depends on the scattering angle  $\theta$ . For agglomerated particles, these cross sections further depend on the morphology of agglomerates.

In optical diagnostics, the objective is to infer  $N_D$ ,  $P(D)$ , and  $m$  from the measurements, whereas in heat transfer analysis, radiative properties are usually calculated from the known  $N_D$ ,  $P(D)$ , and  $m$ . In addition to the extinction coefficient  $\sigma_e$ , other radiative properties needed are single-scattering albedo  $\Omega_0$  and phase function  $\Phi(\theta)$  defined as (Siegel and Howell, 1981)

$$\Omega_0 = \frac{C_{s,t}}{C_e}, \quad (3)$$

$$\Phi(\theta) = \frac{4\pi C_s(\theta)}{C_{s,t}}, \quad (4)$$

respectively. Here  $C_{s,t}$  is the total scattering cross section.

The Rayleigh solution, though applicable only to nonagglomerated small spherical particles, has been adopted in most published works on soot diagnostics and radiative properties. In the Rayleigh solution the various cross sections are given as

$$C_e = \left(\frac{\lambda^2}{\pi}\right) x^3 E, \quad (5)$$

$$C_{s,t} = \left(\frac{2\lambda^2}{3\pi}\right) x^6 F, \quad (6)$$

$$C_{s,vv} = \left(\frac{\lambda}{2\pi}\right)^2 x^6 F, \quad (7)$$

$$C_{s,hh}(\theta) = C_{s,vv} \cos^2 \theta, \quad (8)$$

where

$$E = -\text{Im}(A), \quad F = |A|^2, \quad A = \frac{m^2 - 1}{m^2 + 2}. \quad (9)$$

Here,  $\text{Im}$  denotes the imaginary part of a complex quantity, and the double subscripts  $vv$  (vertical) and  $hh$  (horizontal) specify the direction of polarization of the incident and scattered lights. In the Rayleigh limit, as can be seen from Eqs. (7) and (8), differential scattering cross sections at all angles and for both polarizations are explicitly coupled in such a way that a single scattering measurement provides complete information about the angular distribution of the scattered light. Therefore, for particles in the Rayleigh limit, there are only two independent data points, one extinction and one differential light scattering, available at each wavelength. Yet there could be as many as five parameters to be inferred: number density, mean size, standard deviation in size, and the real and imaginary parts of complex refractive index.

Assuming that particles of all sizes have the same refractive indices, then the effect of size distribution can be analyzed through a mean diameter  $D_{mn}$  defined as

$$D_{mn} = \left[ \int_0^{\infty} D^m P(D)dD / \int_0^{\infty} D^n P(D)dD \right]^{1/(m-n)}. \quad (10)$$

With the refractive indices known (or assumed to be known), the mean diameter  $D_{63}$  and the number density  $N$  can be inferred from the measured  $\sigma_e$  and  $\sigma_{s,vv}$  according to (Dobbins et al., 1984; Felske et al., 1986)

$$D_{63} = \lambda \left( \frac{4\sigma_{s,vv}}{\pi^2 \sigma_e} \right)^{1/3} \left( \frac{E}{F} \right)^{1/3}, \quad (11)$$

$$N = \left( \frac{1}{4\lambda^2} \right) \left( \frac{D_{63}}{D_{30}} \right)^3 \left( \frac{\sigma_e^2}{\sigma_{s,vv}} \right) \left( \frac{F}{E^2} \right), \quad (12)$$

respectively. Some analyses only need the volume fraction  $f_v$ ,

## Nomenclature

|                |  |
|----------------|--|
| $A$            | = function of complex refractive index = $(m^2 - 1)/(m^2 + 2)$ |
| $C, C'$        | = extinction or scattering cross section of a particle         |
| $D$            | = particle diameter  |
| $D_{mn}$       | = mean diameter of particles defined by Eq. (10)               |
| $E$            | = function of complex refractive index = $-\text{Im}(A)$       |
| $\mathbf{E}$   | = electrical field   |
| $\mathbf{E}_o$ | = amplitude of the sinusoidal incident field                   |
| $f_v$          | = volume fraction of particles                                 |
| $F$            | = function of complex refractive index = $ A ^2$               |
| $k$            | = wave number = $2\pi/\lambda$                                 |
| $l$            | = overall length of an agglomerate                             |
| $m$            | = complex refractive index                                     |
| $N_D$          | = number density of particles                                  |
| $N$            | = number of spheres in an agglomerate                          |
| $P(D)$         | = size distribution function                                   |

|                |  |
|----------------|--|
| $r$            | = radial distance of a particle, spherical coordinate          |
| $\bar{T}_{ij}$ | = $3 \times 3$ matrix, introduced in Eq. (17)                  |
| $x$            | = particle size parameter = $\pi D/\lambda$                    |
| $z$            | = direction of light propagation, Cartesian coordinate         |
| $\beta$        | = angle whose definition is found below Eq. (18)               |
| $\theta$       | = polar angle of the scattered light, spherical coordinate     |
| $\lambda$      | = wavelength of radiation                                      |
| $\sigma$       | = extinction or scattering coefficient of particles            |
| $\phi$         | = azimuthal angle of the scattered light, spherical coordinate |
| $\Phi$         | = scattering phase function                                    |
| $\Omega_0$     | = single-scattering albedo                                     |

### Superscripts

|     |                  |
|-----|------------------|
| $a$ | = agglomerate    |
| $s$ | = single spheres |

### Subscripts

|          |   |
|----------|---|
| $a$      | = absorption                                      |
| $e$      | = extinction                                      |
| $hh$     | = horizontally polarized incidence and scattering |
| $i, j$   | = index for particle identification               |
| $inc$    | = incident radiation                              |
| $p$      | = direction of polarization                       |
| $s$      | = differential scattering                         |
| $s, t$   | = total scattering                                |
| $vv$     | = vertically polarized incidence and scattering   |
| $\theta$ | = spherical coordinate component                  |
| $\phi$   | = spherical coordinate component                  |

### Symbols

|               |  |
|---------------|--|
| $\bar{\quad}$ | = averaged over a size distribution function |
| $\hat{\quad}$ | = directional unit vector                    |

which can be inferred directly from the extinction measurement by

$$f_v = \left(\frac{\lambda}{6\pi}\right) \sigma_e \left(\frac{1}{E}\right). \quad (13)$$

Following the same format, the radiative properties of particles at a given wavelength can be expressed as

$$\sigma_e = \left(\frac{\pi^2}{\lambda}\right) N D_{30}^3 E, \quad (14)$$

$$\Omega_0 = \left(\frac{2\pi^3}{3\lambda^3}\right) D_{63}^3 \left(\frac{F}{E}\right), \quad (15)$$

$$\Phi(\theta) = \frac{3}{4} (1 + \cos^2\theta). \quad (16)$$

In Eqs. (11)–(16), the effect of refractive indices on the diagnostics and radiative properties of particles is reflected through those terms containing  $E$  and/or  $F$ , and the effect of size distribution through those terms containing  $D_{mn}$ . For soot particles, comprehensive numerical results of these effects for a given range of refractive indices and size distribution have been reported by Ku and Shim (1990). Some other results can be found from Dobbins et al. (1984) and Felske et al. (1986).

### Absorption and Scattering of Light by Agglomerated Particles

A solution for the absorption and scattering of light by agglomerated particles is needed to analyze their optical diagnostics and radiative properties. Ku and Shim (1991) have compared some of the solutions and concluded that the Jones solution is reasonably accurate for agglomerates of small absorbing spheres such as soot particles. Results calculated from the Jones solution will be used to examine the effect of agglomeration in this study. In addition, an attempt will be made to establish simple but reasonably accurate models for the absorption and scattering of light by soot agglomerates.

In the Jones solution, first the internal field of each sphere,  $\mathbf{E}_i$ , is solved from a system of linear algebraic equations

$$\mathbf{E}_i = \left(\frac{3}{m^2 + 2}\right) \mathbf{E}_{\text{inc}, i} - \frac{i}{3} \left(\frac{m^2 - 1}{m^2 + 2}\right) \sum_{\substack{j=1 \\ j \neq i}}^N x_j^3 \bar{T}_{ij} \mathbf{E}_j, \quad (17)$$

Here, the incident field is set to propagate along the  $z$  axis and represented by  $\mathbf{E}_{\text{inc}} = \mathbf{E}_0 \exp(-ikz)$  with  $k = 2\pi/\lambda$  being the wave number,  $x_j$  is the size parameter of the  $j$ th sphere,  $\bar{T}_{ij}$  is a  $3 \times 3$  matrix in terms of spherical Bessel and associated Legendre functions ( $h_n^{(2)}$  and  $P_n^m$ , respectively), and  $N$  is the total number of spheres in an agglomerate. As pointed out by Kumar and Tien (1989), Jones did not realize that his derivation was actually based on  $C = A + iB$  ( $i = \sqrt{-1}$ ) sign convention. The correct solution corresponding to  $C = A - iB$  sign convention, which is adopted in this paper, requires a sign change in all the terms involving  $i$  and consequently leads to a spherical Bessel function  $h_n^{(2)}$ . Equation (17) represents a system of  $3N$  equations since each  $\mathbf{E}_i$  has three components. In the equation, the first term on the right-hand side represents the primary field induced by the incident radiation (i.e., phase difference), whereas the second term represents the field interaction among spheres (i.e., multiple/dependent scattering). For the case where all the spheres have the same refractive index and size parameter, the extinction and differential scattering cross sections are given as

$$C'_e = -\frac{\lambda^2}{\pi} \frac{x^3}{3E_0^2} \text{Im} \left[ (m^2 - 1) \sum_{i=1}^N \exp(ikz_i) (\mathbf{E}_0 \cdot \mathbf{E}_i) \right], \quad (18)$$

$$C'_{s,pp}(\theta, \phi)$$

$$= \left(\frac{\lambda}{2\pi}\right)^2 \frac{|m^2 - 1|^2}{9} x^6 \left| \sum_{i=1}^N \exp(ikr_i \cos\beta_i) (E_{i,\hat{\theta}} \hat{\theta} + E_{i,\hat{\phi}} \hat{\phi})_{pp} \right|^2, \quad (19)$$

respectively. Here,  $\hat{\theta}$  and  $\hat{\phi}$  are unit vectors in the spherical coordinate system,  $\theta$  and  $\phi$  specify the direction of the scattered light,  $(r_i, \theta_i, \phi_i)$  is the position of a sphere,  $\cos\beta_i = \cos\theta_i \cos\theta + \sin\theta_i \sin\theta \cos(\phi_i - \phi)$ , and the subscript  $p$  denotes the direction of polarization. The term  $\exp(ikz_i)$  in Eq. (18) is the correction made by Ku (1991). To simulate soot agglomerates in flames, random orientation is assumed and the average cross section is calculated from

$$C = \frac{1}{4\pi} \int_0^{2\pi} \int_0^\pi C' \sin\theta d\theta d\phi. \quad (20)$$

To study the effect of agglomeration, the coefficient for an agglomerate ( $\sigma^a = C^a$ ) is compared to that for single spheres of the same number ( $\sigma^s = N C^s$ ). In the theoretical limit, when both phase difference and multiple scattering among particles are negligible, Eqs. (17)–(19), predict that

$$\sigma_e^a = \sigma_e^s \quad [C_e^a = N C_e^s], \quad (21)$$

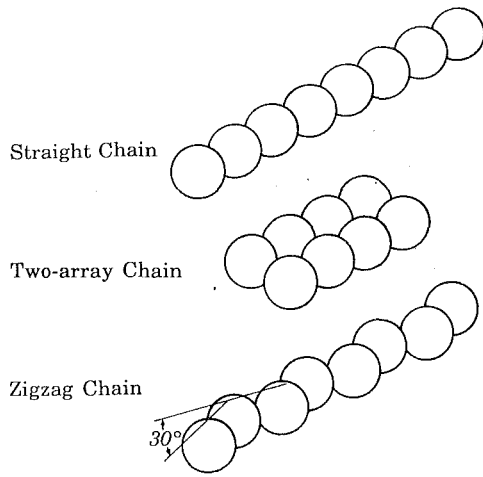
$$\sigma_s^a = N \sigma_s^s \quad [C_s^a = N^2 C_s^s], \quad (22)$$

where the superscript  $a$  and  $s$  denote agglomerate and single spheres, respectively. Equation (22) applies to both differential and total scattering coefficients. Therefore, in the limit, between an agglomerate and  $N$  single spheres, the extinction stays the same, whereas the scattering is multiplied by a factor of  $N$  for an agglomerate. In Eqs. (11)–(16), we evaluate each term involving  $\sigma$  for an agglomerate and for the same number of spheres; then the ratio between the two values represents the effect of agglomeration on respective properties. These ratios could be interpreted as the error in inferring data for agglomerates using the Rayleigh solution. For instance, in the limit, the particle size will be overestimated by a factor of  $N^{1/3}$ , whereas the volume fraction will not be affected.

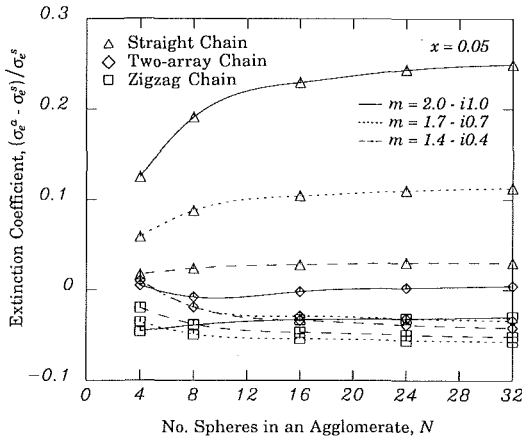
### Numerical Results

When phase difference and multiple scattering become significant, deviations from Eqs. (21) and (22) are expected. This is demonstrated by calculations made for three basic morphologies shown in Fig. 1(a): straight chain, two-array chain, and zigzag chain of up to 32 spheres. They are chosen because they resemble the fundamental structure of flame soot agglomerates seen in the micrographs of Megaridis and Dobbins (1989, 1990b). The primary sphere has a size parameter of  $x = (0.05, 0.1, 0.2)$  and a refractive index of  $m = (1.4 - i0.4, 1.7 - i0.7, 2.0 - i1.0)$ , both values covering the typical range for soot particles (Ku and Shim, 1990). For two-array and zigzag chains, an additional average is taken after rotating them by 90 deg about the chain axis. Detailed results are shown in Fig. 1(b–f).

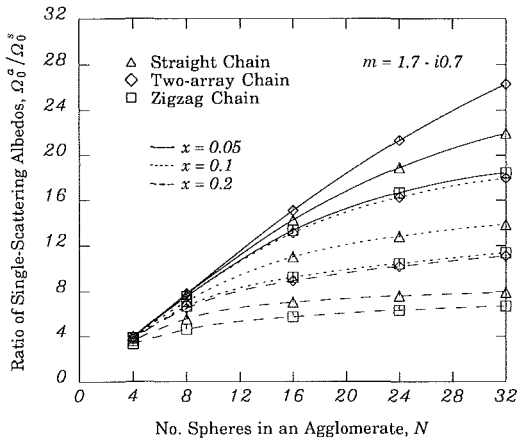
Figure 1(b) shows that the difference between extinction coefficients for agglomerates and single spheres of the same number is less than 10 percent for the most part. Consequently, the inversion for volume fractions and the calculation of extinction coefficients of soot particles are only slightly affected by the effect of agglomeration. Only the results for  $x = 0.05$  are shown because the others are nearly identical, indicating a decoupling of the primary particle size effect. Physically, this is expected because for agglomerates of small absorbing particles such as soot, the extinction is mostly due to absorption and the absorption will not be significantly affected by the agglomeration. Analytically, after substituting Eq. (17) into Eq. (18), it can be argued that the phase difference effect is of little significance because of the cancellation of  $\exp(-ikz)$



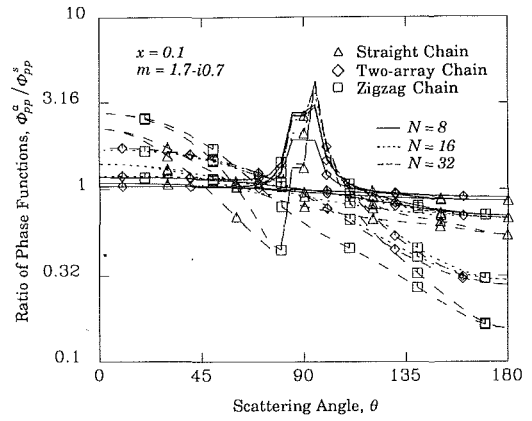
(a) Agglomerate morphologies which were investigated



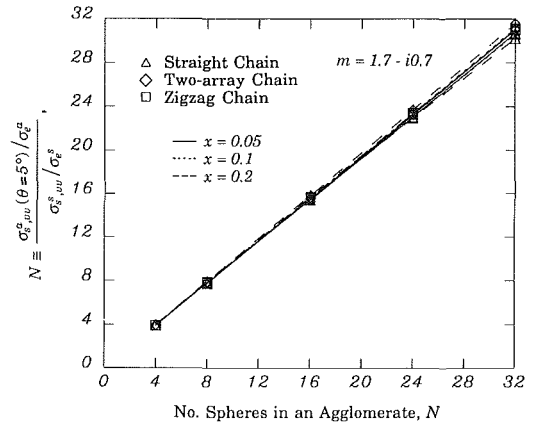
(b) Difference in Extinction Coefficients



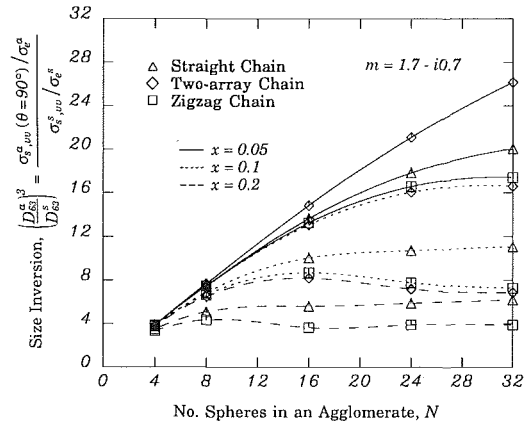
(c) Ratio of Single-Scattering Albedos



(d) Ratio of Phase Functions



(e) Determination of  $N$



(f) Ratio of Inferred Sizes

**Fig. 1 (a) Agglomerate morphologies investigated, and the effect of agglomeration on: (b) extinction coefficient, (c) single-scattering albedo, (d) phase function, (e) determination of  $N$ , and (f) size inversion**

in  $\mathbf{E}_{inc}$  in Eq. (17) and  $\exp(ikz)$  in Eq. (18) and the multiple scattering effect is also insignificant because of its  $x^4$  dependence. However, the increase in deviation due to increasing  $m$  for straight chains seems to suggest the relative dominance of the multiple scattering effect since  $(m^2 - 1)/(m^2 + 2)$  increases as  $m$  increases. But for two-array and zigzag chains that have additional structure, due to additional averaging and probably offsetting deviations between different effects, the overall deviation is reduced. In conclusion, it seems reasonable to suggest

that the effect of agglomeration cause no more than 10 percent deviation in extinction measurements of real soot agglomerates in flames.

The phase difference effect becomes more important in analyzing scattering coefficients since  $\exp(-ikz)$  and  $\exp(ikr\cos\theta)$  in Eq. (19) do not cancel out. Figure 1(c) shows the ratio between single-scattering albedos for agglomerates and for single spheres of the same number as a function of the number of single spheres. The deviation from Eq. (22) generally be-

comes larger as the overall size parameter, defined as  $\pi l/\lambda$  ( $l$  = overall length), increases. Except that a zigzag chain, which has a smaller overall size parameter, actually shows larger deviation than a straight chain. This indicates that scattering coefficients have a weak dependence on the morphology. Only results for  $m = 1.7 - i0.7$  are shown in the figure. Results for other refractive indices are quite similar because comparisons are made on ratios and therefore the refractive index dependence is more or less factored out.

The ratio of phase functions,  $\Phi(\theta)$ , is shown in Fig. 1(d). Only results for one refractive index ( $m = 1.7 - i0.7$ ) and one size parameter ( $x = 0.1$ ) are shown because they are quite insensitive to refractive index variations and they depend only on the overall size parameter for a given agglomerate (i.e., a chain with 16 spheres at  $x = 0.2$  has a curve very similar to the one with 32 spheres at  $x = 0.1$ ), which again supports a decoupling of the primary particle size effect. A strong dependence on the overall size and a weak dependence on the morphology are clearly seen. It has been shown that the phase function for simulated agglomerates cannot be fitted to the Mie solution even by allowing for any reasonable equivalent diameter and effective refractive indices (Ku and Flower, 1987), which is consistent with the observation of Dalzell et al. (1970) on experimental data.

A careful examination of the angular scattering results reveals that Eq. (22) holds true for near-forward scattering angles, say,  $\theta < 10$  deg, regardless of complex refractive indices and size parameters. This is shown in Fig. 1(e), which can be put into equation form as

$$N \cong \frac{\sigma_{s,vv}^a(\theta < 10 \text{ deg})/\sigma_e^a}{\sigma_{s,vv}^s/\sigma_e^s} \quad (23)$$

This equation can be used to infer the number of spheres in a chainlike agglomerate when their size and refractive index are known. It should be pointed out that the same trends are observed for ratios based on  $\sigma_{s,vv}$  alone. The advantage of ratioing based on  $\sigma_{s,vv}/\sigma_e$  is that the number density will be factored out when treating actual experimental data. On the other hand, if one forces the inversion for particle diameter from agglomerate data using Eq. (11) with  $\sigma_{s,vv}$  (90 deg), the error is really unpredictable, as can be seen from Fig. 1(f). However, it is clear that the diameter will almost definitely be overestimated this way. This is consistent with the experimental observations of Dalzell et al. (1970) wherein inferred diameters were many times larger than the actual primary particle size observed through electron microscopy.

## Concluding Remarks

In summary, for agglomerates of small absorbing spheres such as soot, agglomeration only has a weak effect on extinction ( $\cong$  absorption) coefficients. For scattering coefficients, the effect of agglomeration has been demonstrated to be much more significant. It is found that both total and differential scattering coefficients of agglomerates are functions of single sphere's coefficients, number of spheres per agglomerate ( $N$ ), overall size parameter, and agglomeration morphology. Because the scattering for agglomerates is approximately  $N$  times that of single spheres of the same number, its effect may not be negligible when compared to the extinction, as usually assumed in most published works, in analyzing radiative transfer from soot agglomerates. A set of more generalized models is proposed in the form of

$$\sigma_e^a \cong \sigma_e^s [\sigma_e \cong \sigma_a], \quad (24)$$

$$\sigma_{s,t}^a \cong N \sigma_{s,t}^s f(\pi l/\lambda), \quad (25)$$

$$\sigma_{s,pp}^a(\theta) \cong N \sigma_{s,pp}^s(\theta) g(\theta, \pi l/\lambda) \text{ where } g(\theta \rightarrow 0 \text{ deg}) \cong 1, \quad (26)$$

wherein the subscript  $a$  denotes absorption,  $l$  is the overall length of an agglomerate, and the explicit functional forms of  $f$  and  $g$  are to be determined after more comprehensive studies. One potential candidate for these functions is a series of Legendre polynomials. These models are expected to have a weak dependence on refractive indices and agglomerate morphologies, both of which will be purposely ignored in order to retain their generality.

It is worthwhile pointing out that Eqs. (24)–(26) agree very well with the theoretical predictions for fractal aggregates (Berry and Percival, 1986; Freltoft et al., 1986; Chen et al., 1988; Lin et al., 1990). The function  $g$  is the equivalent of structure factor, whereas the overall length  $l$  is replaced by the radius of gyration, in fractal aggregate theories. This is noteworthy because the Jones solution is intended for finite  $N$  whereas fractal aggregates theoretically have  $N \rightarrow \infty$ . In addition to the conclusion drawn from this study on simulated soot agglomerates, the analyses by Dobbins et al. (1990) and Megaridis and Dobbins (1990b) on experimental data also support the applicability of fractal aggregate models on agglomerates with as few as five primary particles.

## Acknowledgments

This study was supported by the National Science Foundation, under Grant No. RII-8805070.

## References

- Berry, M. V., and Percival, I. C., 1986, "Optics of Fractal Clusters Such as Smoke," *Optica Acta*, Vol. 33, pp. 577–591.
- Bohren, C. F., and Huffman, D. R., 1983, *Absorption and Scattering of Light by Small Particles*, Wiley, New York.
- Chen, Z., Sheng, P., Weitz, D. A., Lindsay, H. M., and Lin, M. Y., 1988, "Optical Properties of Aggregate Clusters," *Phys. Rev. B*, Vol. 34, pp. 5232–5235.
- Cole, J. A., Bittner, J. D., and Howard, J. B., 1984, "Radical Pathways in Soot Formation," *Symposium on Combustion Chemistry*, T. Sloane, ed.
- D'Alessio, A., 1981, "Light Scattering and Fluorescence Diagnostics of Rich Flames Produced by Gaseous and Liquid Fuels," *Particulate Carbon*, D. C. Siegla and G. W. Smith, eds., Plenum Press, New York, pp. 207–259.
- Dalzell, W. H., Williams, G. C., and Hottel, H. C., 1970, "A Light Scattering Method for Soot Concentration Measurements," *Comb. Flame*, Vol. 14, pp. 161–170.
- Dobbins, R. A., Santoro, R. J., and Semerjian, H. G., 1984, "Interpretation of Optical Measurements of Soot in Flames," *Prog. Astro. Aero.*, Vol. 92, pp. 208–237.
- Dobbins, R. A., and Megaridis, C. M., 1990, "Absorption and Scattering of Light by Polydisperse Fractal Aggregates," presented at the 2nd Int'l Cong. Optical Particles Sizing, Tempe, Arizona; *Applied Optics*, in press.
- Dobbins, R. A., Santoro, R. J., and Semerjian, H. G., 1990, "Analysis of Light Scattering From Soot Using Optical Cross Sections for Agglomerates," *23rd Symp. (Int'l) Comb.*, in press.
- Felske, J. D., Hsu, P.-F., and Ku, J. C., 1986, "The Effect of Soot Particle Optical Inhomogeneity and Agglomeration on the Analysis of Light Scattering Measurements in Flames," *J. Quant. Spectrosc. Radiat. Transfer*, Vol. 35, pp. 447–465.
- Freltoft, T., Kjems, J. K., and Sinha, S. K., 1986, "Power-Law Correlations and Finite-Size Effects in Silica Particle Aggregates Studied by Small-Angle Neutron Scattering," *Phys. Rev. B*, Vol. 33, pp. 269–275.
- Garó, A., Prado, G., and Lahaye, J., 1990, "Chemical Aspects of Soot Particles Oxidation in a Laminar Methane-Air Diffusion Flame," *Comb. Flame*, Vol. 79, pp. 226–233.
- Gore, J. P., and Faeth, G. M., 1986, "Structure and Spectral Radiation Properties of Turbulent Ethylene/Air Diffusion Flames," *21st Symp. (Int'l) Comb.*, pp. 1521–1531.
- Harris, S. J., and Weiner, A. M., 1988, "A Picture of Soot Particle Inception," *22nd Symp. (Int'l) Comb.*, pp. 333–342.
- Jones, A. R., 1979a, "Electromagnetic Wave Scattering by Assemblies of Particles in the Rayleigh Approximation," *Proc. Roy. Soc. London A*, Vol. 366, pp. 111–127.
- Jones, A. R., 1979b, "Scattering Efficiency Factors for Agglomerates of Small Spheres," *J. Phys. D: Appl. Phys.*, Vol. 12, pp. 1661–1672.
- Kent, J. H., and Honnery, D. R., 1990, "A Soot Formation Rate Map for a Laminar Ethylene Diffusion Flame," *Comb. Flame*, Vol. 79, p. 287–298.
- Ku, J. C., and Flower, W. L., 1987, "In-Situ Morphology of Soot Agglomerates From Laser Light Scattering," presented at The Combustion Institute (Eastern States) and NBS Combined Meetings, Gaithersburg, MD.
- Ku, J. C., and Shim, K.-H., 1990, "The Effects of Refractive Indices, Size Distribution and Agglomeration on the Diagnostics and Radiative Properties of

- Flame Soot Particles," *Heat and Mass Transfer in Fires and Combustion Systems*, W. L. Grosshandler and H. G. Semerjian, eds., ASME HTD-Vol. 148, pp. 105-115.
- Ku, J. C., 1991, "Correction for the Extinction Efficiency Factors Given in the Jones Solution for Electromagnetic Scattering by Agglomerates of Small Spheres," *J. Phys. D: Appl. Phys.*, Vol. 24, pp. 71-75.
- Ku, J. C., and Shim, K.-H., 1991, "A Comparison of Solutions for Light Scattering and Absorption by Agglomerated or Arbitrarily Shaped Particles," submitted to *J. Quant. Spectrosc. Radiat. Transfer*.
- Kumar, S., and Tien, C. L., 1989, "Effective Diameter of Agglomerates for Radiative Extinction and Scattering," *Comb. Sci. Tech.*, Vol. 66, pp. 199-216.
- Lin, M. Y., Lindsay, H., Weitz, D., Ball, R., Klein, R., and Meakin, P., 1990, "Universal Reaction-Limited Colloid Aggregates," *Phys. Rev. A*, Vol. 41, pp. 2005-2020.
- Megaridis, C. M., and Dobbins, R. A., 1989, "Comparison of Soot Growth and Oxidation in Smoking and Non-smoking Ethylene Diffusion Flames," *Comb. Sci. Tech.*, Vol. 66, pp. 1-16.
- Megaridis, C. M., and Dobbins, R. A., 1990a, "A Bimodal Integral Solution of the Dynamic Equation for an Aerosol Undergoing Simultaneous Particle Inception and Coagulation," *Aerosol Sci. Tech.*, Vol. 12, pp. 240-255.
- Megaridis, C. M., and Dobbins, R. A., 1990b, "Morphological Description of Flame-Generated Materials," *Comb. Sci. Tech.*, Vol. 77, pp. 95-109.
- Moss, J. B., Stewart, C. D., and Syed, K. J., 1988, "Flowfield Modeling of Soot Formation at Elevated Pressure," *22nd Symp. (Int'l) Comb.*, pp. 413-423.
- Neoh, K. G., Howard, J. B., and Sarofim, A. F., 1984, "Effect of Oxidation on the Physical Structure of Soot," *20th Symp. (Int'l) Comb.*, pp. 951-957.
- Siegel, R., and Howell, J. R., 1981, *Thermal Radiation Heat Transfer*, Hemisphere, New York.
- Weissman, M., and Benson, S. W., 1989, "Mechanism of Soot Initiation in Methane Systems," *Prog. Energy Comb. Sci.*, Vol. 15, pp. 273-285.
- Wersborg, B. L., Howard, J. B., and Williams, G. C., 1973, "Physical Mechanisms in Carbon Formation in Flames," *14th Symp. (Int'l) Comb.*, pp. 929-940.

# Combustion of a Fuel Droplet Surrounded by Oxidizer Droplets

**Tsung Leo Jiang**  
Associate Professor.

**Huei-Huang Chiu**  
Director and Professor.

Institute of Aeronautics and Astronautics,  
National Cheng Kung University,  
Tainan, Taiwan

*The interaction between a burning fuel droplet and satellite oxidizer droplets is studied analytically. The effects of droplet spacing and droplet size ratio on the flame configuration of a burning fuel droplet with a satellite oxidizer droplet are analyzed in a high-temperature oxidizing environment by using the bispherical coordinate system. Three combustion modes including normal combustion, conjugate combustion, and composite combustion are identified at appropriate droplet size ratio and droplet spacing. The burning rate of the fuel droplet is found to be greater than that of an isolated burning fuel droplet, and to increase with the decreasing distance between two droplets. This result has shown a positive effect on the interaction between fuel and oxidizer droplets, in contrast to that of two interacting fuel droplets where the burning rate decreases with decreasing droplet spacing. The combustion configuration of a fuel droplet surrounded by six satellite oxidizer droplets symmetrically is also examined by the method of images. The flame that encloses the fuel droplet is found to be "compressed" and distorted to a nonspherical shape due not only to the group effect among oxidizer droplets but also to the interaction of bipropellant droplets. The results indicate that the burning rate of a fuel droplet increases and the flame size decreases significantly as a result of an increased supply of oxidizer vapor provided by the surrounding oxidizer droplets. Therefore properly optimized bipropellant combustion is potentially able to achieve a desired combustion performance with a much smaller combustor than a conventional spray burner.*

## Introduction

It has been well recognized that external or internal group combustion may occur when a dense fuel droplet cloud produces a fuel-rich nonflammable mixture surrounding fuel droplets so that an envelope flame encloses the vaporizing fuel droplets (Suzuki and Chiu, 1971; Chiu and Liu, 1977; Chiu et al., 1982). The occurrence of external or internal group combustion reduces the total burning rate of droplets in spray combustion and leads to the incomplete combustion of droplets. Furthermore, interaction between burning fuel droplets also causes the reduction of individual droplet burning rates (Brzustowski et al., 1979; Umemura et al., 1981a, 1981b; Labowsky, 1980a). One of the remedies for these phenomena is to inject liquid oxidizer into the fuel spray to create a near-stoichiometric droplet cluster in order to produce a flammable gas mixture and promote oxidation in a smaller space. This effect can be shown in the bipropellant liquid rocket engine combustor, where liquid oxidizer and fuel droplets are mixed to burn in the highly reactive environment. However, the combustion phenomena caused by the coexistence of fuel and oxidizer droplets are so complicated that previous research work in the area of liquid rocket engine combustors attacked this subject very little. Recently Chiu (1986) proposed the bipropellant droplet combustion theory. In addition to the normal combustion of fuel droplets in the classical droplet combustion theory, two new combustion modes termed "conjugate combustion" and "composite combustion" were defined phenomenologically in this theory. Conjugate combustion is simply defined as the oxidizer droplet combustion occurring in the fuel-rich environment to be differentiated from normal combustion, which is defined as the fuel droplet combustion in the oxidizer-rich environment. Because of the coexistence of fuel and oxidizer droplets, the conjugate combustion of oxidizer

droplets can be enclosed by the normal flame of fuel droplets, or the normal combustion of fuel droplets can be embedded in the conjugate flame of oxidizer droplets. This combustion mode includes both conjugate combustion and normal combustion, and is classified as composite combustion. This theory has been further extended by Jiang and Chiu (1986), and applied to the analysis of a liquid rocket engine combustor to assess the effects of collective interaction of bipropellant droplets under various atomization conditions. However, without the detailed study of bipropellant droplet interaction, the droplet vaporization model used to determine the droplet vaporization rates of both fuel and oxidizer droplets can only follow the classical droplet vaporization theory (Williams, 1985).

The objective of the present paper is therefore to examine the interactive effects of coexisting bipropellant droplets on the droplet burning rate and the flame configuration. The discrete droplet model, which was used to investigate the interaction between two burning fuel droplets (Brzustowski et al., 1979; Umemura et al., 1981a, 1981b) and the interaction among the arrayed burning fuel droplets (Labowsky, 1980a), is adopted since it is able to provide insight into droplet interaction. In the discrete droplet model, the droplets are always placed in a homogeneous gas-phase environment with the environmental conditions at infinity prescribed. To study the interaction of burning fuel droplets, the problem was usually treated by the assumption that the Stefan flow effect, which yields nonlinear terms in the governing equations, is negligible (Brzustowski et al., 1979), or that the mass flux field is irrotational and can be represented by a potential function (Umemura et al., 1981a, 1981b; Labowsky, 1980a, 1980b). For bipropellant droplet burning, combustion intensity is anticipated to be much stronger and the Stefan flow effect may not be negligible. Furthermore, the assumption of a potential mass flux field due to the droplet vaporization associated with the usual Shvab-Zeldovich formulation would lead to a conflict solution. The physically asymmetric phenomenon associated with different vaporization sources of fuel and oxidizer droplets cannot be described by a mathematically symmetric for-

Contributed by the Heat Transfer Division and presented at the Joint ASME/JSME Thermal Engineering Conference, Honolulu, Hawaii, March 22-26, 1987. Manuscript received by the Heat Transfer Division November 9, 1989; revision received November 22, 1990. Keywords: Combustion, Evaporation, Phase-Change Phenomena.

mulation from a unified mass potential and Shvab-Zeldovich variable. To overcome this difficulty, the present study assumes that the mass flux field is irrotational only locally around the fuel and oxidizer droplets, and ought to be represented by two different potential functions accounting for both fuel and oxidizer vaporizing droplet sources. Two Shvab-Zeldovich variables are then defined around the fuel and oxidizer droplet regions, respectively. The final solutions are obtained by matching these two solutions at the junction of two regions.

### Assumptions

The following assumptions, commonly used in the study of multidroplet interaction, are also adopted for the present analysis of bipropellant multidroplet interaction:

- 1 The droplet burning process is completely quasi-steady. This means that the droplet radii vary very slowly with time. This assumption is valid along with the assumption that the ambient pressure is far below the critical point of liquid droplets.
- 2 The far-field conditions are uniform and prespecified.
- 3 The effects of radiation, forced convection, and natural convection are neglected.
- 4 The bipropellant droplets are fixed in space. Under the framework of quasi-steady analysis, no transient effects are studied even though the droplet spacings may vary.
- 5 The conditions at the droplet surfaces are uniform, and local thermodynamic equilibrium between phases exists at the surface of each droplet.
- 6 The shape of each droplet is assumed to be spherical throughout the whole burning process.
- 7 The Lewis number ( $Le \equiv k/\rho DC_p$ ) is unity.

### Formulation

A conjugate doublet configuration, consisting of a fuel droplet and an oxidizer droplet, is first studied in a high-temperature, oxidizing environment by using the bispherical coordinate system (Fig. 1). The configuration of a burning fuel droplet surrounded by six oxidizer droplets symmetrically (Fig. 2) is then examined by the method of images to study the interaction between the fuel droplet and the satellite oxidizer droplets. The detailed formulation for both configurations is given as follows.

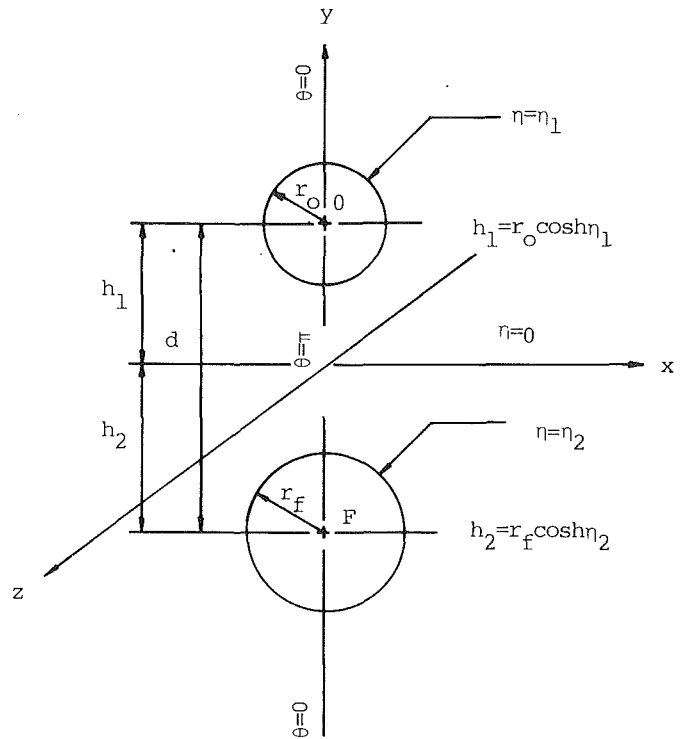


Fig. 1 Schematic diagram of a bipropellant doublet configuration and the associated bispherical coordinates

**Conjugate Doublet Configuration.** The conservation equations governing the mass and Shvab-Zeldovich concentration variable are given in the following vector forms:

$$\nabla \cdot (\rho \bar{v}) = 0 \quad (1)$$

$$\nabla \cdot (\rho \bar{v} \beta - \rho D \nabla \beta) = 0 \quad (2)$$

where  $\beta = \beta_f = \bar{Y}_f - \bar{Y}_o/\nu$  around the fuel droplet and  $\beta = \beta_o = \bar{Y}_o - \bar{Y}_f \nu$  around the oxidizer droplet.

The mass flux vector is assumed to be locally irrotational in the regions near the droplets; therefore, it can be represented by the gradient of a scalar potential. Two scalar potential

### Nomenclature

|   |  |  |
|---|--|--|
| $A$ = integration constant in equation (4)  | $k$ = thermal conductivity                                   | $\beta$ = Shvab-Zeldovich variable   |
| $B_f$ = transfer number for the fuel droplet  | $L$ = latent heat  | $\eta, \theta, \psi$ = bispherical coordinates                                       |
| $B_o$ = transfer number for the oxidizer droplet  | $Le$ = Lewis number $\equiv k/\rho DC_p$                     | $\lambda$ = correction factor of droplet vaporization rate $= \dot{m}/\dot{m}_{iso}$ |
| $C_n$ = integration constant in equation (14)   | $\dot{m}$ = droplet evaporation rate                         | $\nu$ = stoichiometric coefficient ratio (oxidizer/fuel)                             |
| $C_p$ = specific heat   | $O$ = oxidizer droplet                                       | $\rho$ = density   |
| $D$ = diffusivity   | $Q^o$ = heat of reaction per unit mass of oxidizer consumed  | $\phi$ = potential function  |
| $d$ = droplet central distance  | $r$ = droplet radius   | $\bar{\phi}$ = nondimensional potential function                                     |
| $F$ = fuel droplet  | $\bar{r}$ = position vector                                  | $\Phi = \exp(\phi/\rho D)$   |
| $H$ = integration constant in equation (4)  | $\bar{s}$ = droplet surface area vector                      |  |
| $h_1$ = distance between oxidizer droplet center and coordinate origin as shown in Fig. 1 | $\bar{v}$ = velocity vector                                  |  |
| $h_2$ = distance between fuel droplet center and coordinate origin as shown in Fig. 1     | $x, y, z$ = Cartesian coordinates                            |  |
| $K_n$ = integration constant in equation (14)   | $X$ = nondimensional coordinate $= x/r_f$                    |  |
|   | $Y$ = nondimensional coordinate $= y/r_f$                    |  |
|   | $\bar{Y}$ = nondimensional coordinate $= (y + h_2)/r_f$      |  |
|   | $\bar{Y}$ = species mass fraction                            |  |
|   | $Z$ = nondimensional coordinate $= z/r_f$                    |  |
|   | $\alpha_i$ = potential function coefficient in equation (20) |  |
|   |  | <b>Subscripts</b>  |
|   |  | $c$ = intersection of droplet centerline and flame surface                           |
|   |  | $f$ = fuel   |
|   |  | $iso$ = isolated single droplet  |
|   |  | $l$ = liquid fuel or oxidizer  |
|   |  | $o$ = oxidizer   |
|   |  | $s$ = droplet surface  |
|   |  | $\infty$ = infinity  |

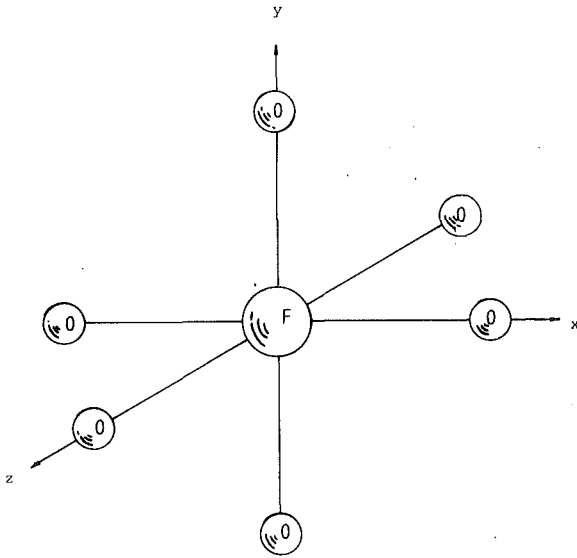


Fig. 2 Configuration of a burning fuel droplet surrounded by six oxidizer droplets symmetrically and the associated Cartesian coordinates

functions are given to account for the vaporization of fuel and oxidizer droplets, respectively, i.e.,

$$\rho \bar{v} = \nabla \phi = \nabla \phi_f \text{ around the fuel droplet}$$

$$\rho \bar{v} = \nabla \phi = \nabla \phi_o \text{ around the oxidizer droplet}$$

The scalar potential functions  $\phi_f$  and  $\phi_o$  satisfy the Laplace equation by virtue of equation (1), whereas  $\beta$  obeys the Fokker-Planck equation, given by

$$\nabla \cdot (\beta \nabla \phi - \rho D \nabla \beta) = 0 \quad (3)$$

which has the following particular solution:

$$\beta = A + H \exp(\phi / \rho D) \quad (4)$$

where  $A$  and  $H$  are integration constants and will be determined by the boundary conditions. The concentration of fuel vapor and oxidizer vapor on the surface of the droplets is assumed to be homogeneous and constant. This assumption is usually adopted in the discrete droplet model and is consistent with the assumption of irrotational flow. With  $\bar{Y}_f = 0$  on the oxidizer droplet surface,  $\bar{Y}_o = 0$  on the fuel droplet surface, and  $\phi = 0$  at infinity,  $A$  and  $H$  are given by

$$A_f = (\beta_{f,\infty} \Phi_{f,f} - \beta_{f,f}) / (\Phi_{f,f} - 1) \quad (5a)$$

$$H_f = (\beta_{f,f} - \beta_{f,\infty}) / (\Phi_{f,f} - 1)$$

$$A_o = (\beta_{o,\infty} \Phi_{o,o} - \beta_{o,o}) / (\Phi_{o,o} - 1) \quad (5b)$$

$$H_o = (\beta_{o,o} - \beta_{o,\infty}) / (\Phi_{o,o} - 1)$$

where  $\Phi = \exp(\phi / \rho D)$ . The potential values on the fuel and oxidizer droplet surface  $\phi_{f,f}$  and  $\phi_{o,o}$  are to be determined by applying the mass conservation law on the droplet surface, i.e.,

$$(\rho \bar{v} \beta - \rho D \nabla \beta)_s = (\rho \bar{v})_s \quad (6)$$

With  $\rho \bar{v} = \nabla \phi$  and  $\beta = A + H \exp(\phi / \rho D)$ , equation (6) can be further reduced to

$$(\beta_s - \beta_\infty) \Phi_s / (\Phi_s - 1) = \beta_s - 1$$

or

$$\Phi_s = (\beta_s - 1) / (\beta_\infty - 1) \quad (7)$$

Therefore,  $\phi_s = \rho D \ln[(\beta_s - 1) / (\beta_\infty - 1)]$  and

$$\phi_{f,f} = \rho D \ln[(\beta_{f,f} - 1) / (\beta_{f,\infty} - 1)] \quad (8a)$$

$$\phi_{o,o} = \rho D \ln[(\beta_{o,o} - 1) / (\beta_{o,\infty} - 1)] \quad (8b)$$

$\beta_{f,f}$  and  $\beta_{o,o}$  then need to be determined. They can be obtained by the following procedure. First the coupling function

$$\beta_T = \frac{C_p(T - T_s)}{Q^o} + \bar{Y}_o \text{ for the fuel droplet}$$

or

$$\beta_T = \frac{C_p(T - T_s)}{Q^o} + \bar{Y}_f \nu \text{ for the oxidizer droplet}$$

which is governed by  $\nabla \cdot (\rho \bar{v} \beta_T - \rho D \nabla \beta_T) = 0$ , is solved with the boundary conditions:

at infinity:

$$\beta_T = \beta_{T,\infty} = \frac{C_p(T_\infty - T_s)}{Q^o} + \bar{Y}_{o,\infty} \text{ for the fuel droplet}$$

$$= \frac{C_p(T_\infty - T_s)}{Q^o} + \bar{Y}_{f,\infty} \nu \text{ for the oxidizer droplet,}$$

on the droplet surface:

$$\beta_T = \beta_{T,s} = 0$$

where  $\bar{Y}_o = 0$  on the fuel droplet surface and  $\bar{Y}_f = 0$  on the oxidizer droplet surface have been assumed. By an approach similar to the solution of  $\beta$ , the solution of  $\beta_T$  is obtained as

$$\beta_T = \beta_{T,\infty} (\Phi_s - \Phi) / (\Phi_s - 1) \quad (9)$$

As the droplet phase change (vaporization) occurs, the heat transfer is assumed to provide the necessary latent heat for the droplet evaporation only. Namely, the energy balance is observed at the droplet surface as

$$\left(\frac{k}{C_p}\right) \nabla \beta_T = \rho \bar{v} \left(\frac{L}{Q^o}\right)$$

or

$$\nabla \beta_T = \rho D \nabla \phi \left(\frac{L}{Q^o}\right) \quad (10)$$

where the unitary Lewis number has been applied. Therefore,

$$\Phi_s = L / (L + Q^o \beta_{T,\infty}) \quad (11)$$

By equating equations (7) and (11), we can obtain

$$\beta_s = 1 - L(1 - \beta_\infty) / (L + Q^o \beta_{T,\infty}) \quad (12)$$

We define  $\bar{\phi}_f = \phi_f / \phi_{f,f}$  and  $\bar{\phi}_o = \phi_o / \phi_{o,o}$ . The mathematical problem is then reduced to solving two Laplace equations with imposed boundary conditions, i.e.,

$$\nabla^2 \bar{\phi}_f = 0 \quad (13a)$$

$$\nabla^2 \bar{\phi}_o = 0 \quad (13b)$$

with

$$\bar{\phi}_f = 1, \quad \bar{\phi}_o = \bar{\phi}_{o,f} \text{ on the fuel droplet surface} \quad (13c)$$

$$\bar{\phi}_o = 1, \quad \bar{\phi}_f = \bar{\phi}_{f,o} \text{ on the oxidizer droplet surface} \quad (13d)$$

and

$$\bar{\phi}_f = \bar{\phi}_o = 0 \text{ at infinity.} \quad (13e)$$

The Laplace equations are solved by using the bispherical coordinate system  $\eta, \theta, \psi$  (Brzustowski et al., 1979). The general solution to the Laplace equations in the bispherical coordinate system is given by

$$\bar{\phi} = (\cosh \eta - \cos \theta)^{1/2} \sum_{n=0}^{\infty} [C_n \cosh(n + 1/2)\eta + K_n \sinh(n + 1/2)\eta] P_n(\cos \theta) \quad (14)$$

Applying the boundary conditions imposed on the droplet surface and at infinity,  $C_n$  and  $K_n$  are determined as

$$C_{n,f} = \sqrt{2} [(\sinh \alpha_1 \cosh \alpha_2 - \bar{\phi}_{f,o} \sinh \alpha_2 \cosh \alpha_1)] \quad (15a)$$



$$K_{n,f} = -\sqrt{2}[(\bar{\phi}_{o,f} \sinh \alpha_1 \sinh \alpha_2 + \bar{\phi}_{f,o} \sinh \alpha_1 \cosh \alpha_2) / \sinh(\alpha_1 - \alpha_2) + (1 - \bar{\phi}_{f,o}) \cosh \alpha_1 \cosh \alpha_2] / \sinh(\alpha_1 - \alpha_2) \quad (15b)$$

$$C_{n,o} = \sqrt{2}[(\bar{\phi}_{o,f} \sinh \alpha_1 \cosh \alpha_2 - \sinh \alpha_2 \cosh \alpha_1) / \sinh(\alpha_1 - \alpha_2) + (1 + \bar{\phi}_{o,f}) \sinh \alpha_1 \sinh \alpha_2] / \sinh(\alpha_1 - \alpha_2) \quad (15c)$$

$$K_{n,o} = -\sqrt{2}[(\bar{\phi}_{o,f} \sinh \alpha_2 \cosh \alpha_1 + \sinh \alpha_1 \cosh \alpha_2) / \sinh(\alpha_1 - \alpha_2) + (\bar{\phi}_{o,f} - 1) \cosh \alpha_1 \cosh \alpha_2] / \sinh(\alpha_1 - \alpha_2) \quad (15d)$$

where  $\alpha_i = (n + 1/2)\eta_i$ ,  $i = 1, 2$ . In order to determine the unknowns  $\bar{\phi}_{o,f}$  and  $\bar{\phi}_{f,o}$ , the matching conditions of two regions are applied at the junction that separates the two regions, i.e.,

$$\beta_f = -\frac{\beta_o}{\nu} \quad (16a)$$

$$\rho \bar{v} \beta_f - \rho D \nabla \beta_f = \frac{-1}{\nu} [\rho \bar{v} \beta_o - \rho D \nabla \beta_o] \quad (16b)$$

The assumption of homogeneous concentration on the droplet surface leads to a single potential value on the droplet surface. Therefore, matching conditions are applied at one junction point to obtain the potential values  $\bar{\phi}_{o,f}$  and  $\bar{\phi}_{f,o}$  within the present approximation. The selected point most able to account for the interaction between the bipropellant droplets is the junction point  $c$  located at the intersection of the droplet centerline and the flame surface. With the thin-flame sheet assumption, the flame surface is determined where the stoichiometric condition is satisfied or  $\beta = 0$ . Thus, the matching conditions in terms of  $\phi_f$  and  $\phi_o$  at the point  $c$  are given by

$$\bar{\phi}_f = \bar{\phi}_{f,c} = (\rho D / \phi_{f,j}) \ln[(\beta_{f,\infty} \Phi_{f,j} - \beta_{f,j}) / (\beta_{f,\infty} - \beta_{f,j})] \quad (17a)$$

$$\bar{\phi}_o = \bar{\phi}_{o,c} = (\rho D / \phi_{o,o}) \ln[(\beta_{o,\infty} \Phi_{o,o} - \beta_{o,o}) / (\beta_{o,\infty} - \beta_{o,o})] \quad (17b)$$

and

$$(\nabla \bar{\phi}_j)_c = (-\phi_{o,o} / \phi_{f,j}) (\nabla \bar{\phi}_o)_c \quad (18)$$

The potential values  $\bar{\phi}_{f,o}$ ,  $\bar{\phi}_{o,f}$  and the junction point  $c$  can be determined iteratively such that the above matching conditions are satisfied. Once the potential values  $\bar{\phi}_{f,o}$  and  $\bar{\phi}_{o,f}$  are obtained, the flame position is determined at the locations where  $\beta_f = 0$ . The burning rates of droplets can be obtained by taking the integration of mass flux around droplets, i.e.,

$$\begin{aligned} \dot{m}_l &= \int_l \rho \bar{v} \cdot d\bar{s} \\ &= \phi_{l,l} \int_l \nabla \bar{\phi}_l \cdot d\bar{s} \\ &= \dot{m}_{l,iso} \frac{1}{4\pi r_{l,j}} \int_l \nabla \bar{\phi}_l \cdot d\bar{s} \\ &= \dot{m}_{l,iso} \lambda_l \end{aligned} \quad (19)$$

where  $l = o$  or  $f$ , and

$$\begin{aligned} \lambda_f &= \frac{1}{4\pi r_{f,j}} \int_f \nabla \bar{\phi}_f \cdot d\bar{s} \\ &= \frac{1}{4\pi r_{f,j}} \left\{ -2\pi r_{f,j} - 2\sqrt{2}\pi r_{f,j} \sinh \eta_2 \sum_{n=0}^{\infty} [C_{n,f} \sinh(n + 1/2)\eta_2] \right. \\ &\quad \left. + K_{n,f} \cosh(n + 1/2)\eta_2 [\cosh(n + 1/2)\eta_2 + \sinh(n + 1/2)\eta_2] \right\} \\ \lambda_o &= \frac{1}{4\pi r_{o,o}} \int_o \nabla \bar{\phi}_o \cdot d\bar{s} \\ &= \frac{1}{4\pi r_{o,o}} \left\{ 2\pi r_{o,o} + 2\sqrt{2}\pi r_{o,o} \sinh \eta_1 \sum_{n=0}^{\infty} [C_{n,o} \sinh(n + 1/2)\eta_1] \right. \\ &\quad \left. + K_{n,o} \cosh(n + 1/2)\eta_1 [\cosh(n + 1/2)\eta_1 - \sinh(n + 1/2)\eta_1] \right\} \end{aligned}$$

**Many-Droplet Configuration.** For the configuration of a burning fuel droplet surrounded by many droplets symmetrically, the formulation described in the previous section for the doublet configuration is still valid, except that the solutions to the Laplace equations based on the bispherical coordinates are not applicable. Labowsky (1980a, 1980b), however, has successfully used the method of images to solve Laplace equations for the multidroplet array. This method is also adopted here for the bipropellant many-droplet configuration. Following the formulation for the doublet system, the effort required for the present configuration is to solve the Laplace equations for a many-droplet system.

The solutions to the Laplace equations are constructed by superimposing the fields from properly distributed point sources and sinks such that the boundary conditions are satisfied. A set of sources and sinks, which are located inside the droplets, is first determined for each droplet such that the potential value is unity on the corresponding droplet surface and is zero on the surface of the other droplets. The method to determine those sources and sinks is simply to place a source in the center of a droplet such that the potential value on the droplet surface is unity in the first generation. This would raise the potential value on the other droplet surfaces. The second effort is therefore to suppress the raised values by placing sinks in the droplets in the second generation. The procedure is continued until the surface conditions of droplets are satisfied and an infinite series of sources and sinks are produced. The details of this procedure were given by Labowsky (1980b). Practically, only a finite number of sources and sinks are obtained when the convergent value of the series is reached approximately. In the present analysis, four generations have produced acceptable convergent results with the limitation of computational cost. By expressing the potential field, determined by each set of sources and sinks, with  $\alpha_i(\bar{r})$ , where  $\alpha_i(\bar{r}) = 1$  on the surface of the  $i$ th droplet, and  $\alpha_i(\bar{r}) = 0$  at infinity and on the surface of all other droplets, the potential function with imposed boundary conditions  $\bar{\phi}_j$  on the surface of the  $j$ th droplet is then given by

$$\bar{\phi} = \sum_{i=1}^N \alpha_i \bar{\phi}_i \quad (20)$$

The same procedure as that being used in determining  $\bar{\phi}_{f,o}$ ,  $\bar{\phi}_{o,f}$ , and the junction point  $c$  for the doublet configuration is employed for the many-droplet system. The droplet burning rate is more easily estimated by applying the Gauss theorem (Labowsky, 1980b) and is given by

$$\begin{aligned} \dot{m}_l &= \int_l \rho \bar{v} \cdot d\bar{s} \\ &= \phi_{l,l} \int_l \nabla \bar{\phi}_l \cdot d\bar{s} \\ &= \dot{m}_{l,iso} \frac{1}{4\pi r_{l,j}} \int_l \nabla \bar{\phi}_l \cdot d\bar{s} \\ &= \dot{m}_{l,iso} \lambda_l \end{aligned} \quad (21)$$

where  $l = o$  or  $f$ , and

$$\begin{aligned} \lambda_l &= \frac{1}{4\pi r_{l,j}} \int_l \nabla \bar{\phi}_l \cdot d\bar{s} \\ &= \frac{1}{4\pi r_{l,j}} \sum_{i=1}^N [(\text{sum of source strengths inside the } l\text{th} \\ &\quad \text{droplet associated with the } \alpha_j \text{ field}) \times \bar{\phi}_{l,j}] \end{aligned}$$

It is noted that sources have positive source strengths but sinks have negative source strengths.

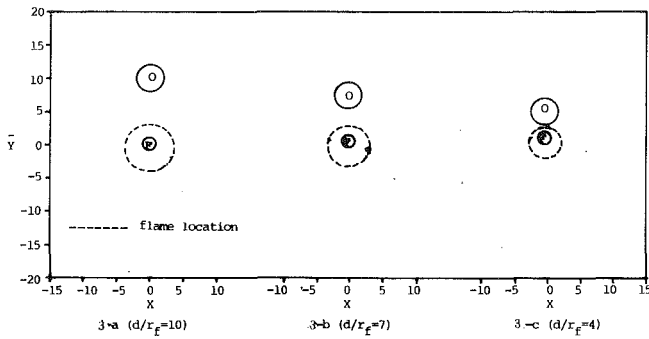


Fig. 3 Flame configuration of a bipropellant doublet at different droplet spacings ( $r_o/r_f = 2$ )

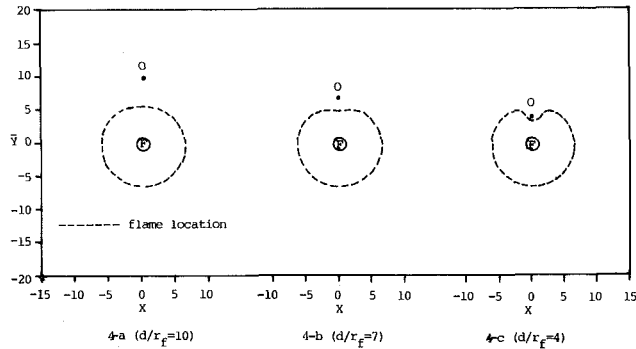


Fig. 4 Flame configuration of a bipropellant doublet at different droplet spacings ( $r_o/r_f = 0.1$ )

## Results and Discussion

**Conjugate Doublet Configuration.** For the configuration of conjugate doublet, the following input data are given:  $\bar{Y}_{0,\infty} = 0.2$ ,  $\bar{Y}_{f,\infty} = 0.0$ , and  $\nu = 1.0$ . The transfer numbers for fuel and oxidizer droplets are defined as:  $B_f = 1/L_f[C_p(T_\infty - T_{s,f}) + Q^o \bar{Y}_{0,\infty}]$  and  $B_o = 1/L_o[C_p(T_\infty - T_{s,o}) + Q^o \nu \bar{Y}_{f,\infty}]$ . They account for both far-field conditions and droplet properties. In the present case, the values of transfer numbers are specified as:  $B_f = 2.4375$  and  $B_o = 1.5$ .

The flame configuration for the different droplet size ratios in this sample calculation is shown in Figs. 3(a-c) and Figs. 4(a-c). In Figs. 3(a-c) the oxidizer droplet radius is two times the fuel droplet radius and the droplet center distance is 10.0, 7.0, and 4.0 times the fuel droplet radius, respectively. It is observed that the present flame shape is much smaller than that of an isolated burning fuel droplet with the same far-field conditions by the classical droplet-combustion theory, which is 6.77 times the fuel droplet radius (Williams, 1985). The size of the flame shape is observed to decrease with decreasing droplet spacings. The theoretical predictions of a flame stand-off distance of a burning fuel droplet in an oxidizing atmosphere have been reported to be greater than experimental observations (Brzustowski et al., 1979). The lack of experimental data on the bipropellant droplet combustion configuration, such as treated in the present study, makes it rather difficult to assess the accuracy of the prediction of exact flame size. Nevertheless, the nature of bipropellant multidroplet interaction has been demonstrated through the present results. In Figs. 4(a-c) the oxidizer droplet is much smaller than the fuel droplet. The radius of the oxidizer droplet is just one-tenth of the fuel droplet radius. Therefore, the influence of the existence of an oxidizer droplet on fuel droplet burning is much less than that in the previous case. The flame is not distorted much when the oxidizer droplet is located seven times the fuel droplet radius away from the fuel droplet, which is beyond the flame size of an isolated burning fuel droplet. However, when the

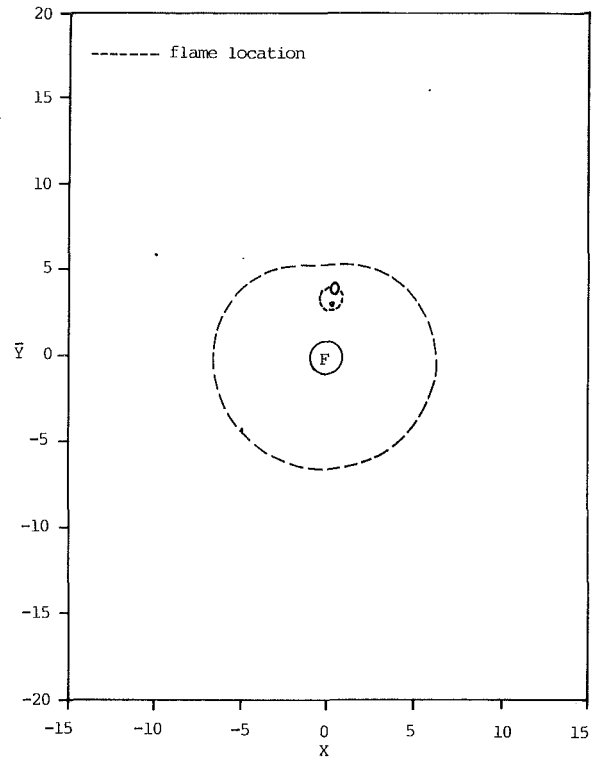


Fig. 5 Composite combustion of a bipropellant doublet ( $r_o/r_f = 0.1$ ,  $d/r_f = 3$ )

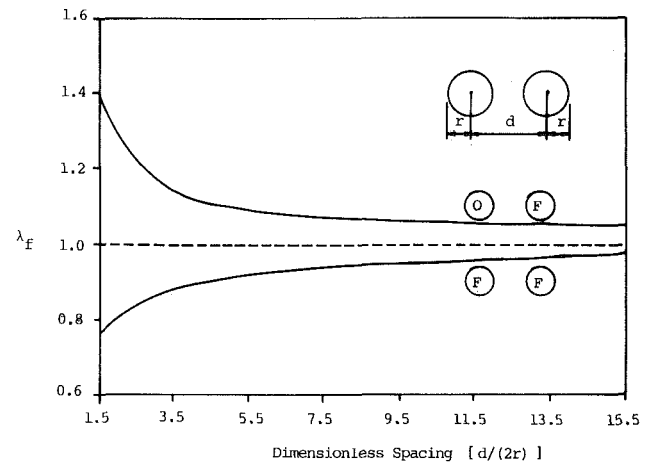
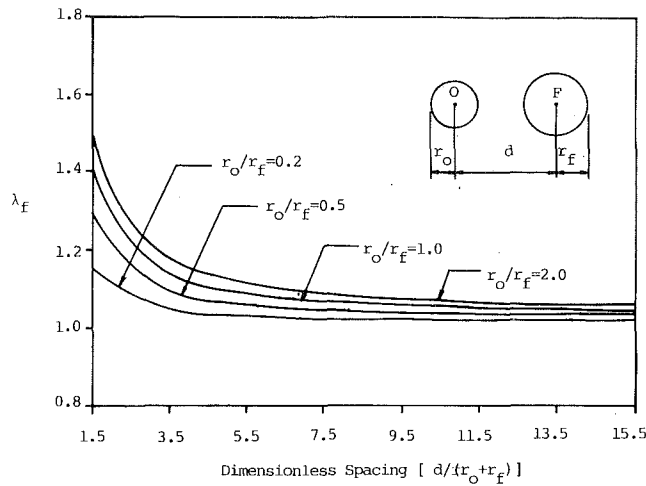


Fig. 6 Effects of bipropellant droplet combustion on the fuel droplet burning rates

droplet center distance is reduced to four times the fuel droplet radius, the flame is greatly "pushed" and shaped just like an apple. Further decrease of the droplet center distance to three times the fuel droplet radius makes the small oxidizer droplet penetrate the flame surface into the fuel-rich zone and burn by itself as conjugate combustion shown in Fig. 5. Conjugate combustion of an oxidizer droplet and the surrounding normal flame of a fuel droplet constitutes the so-called composite combustion.

The effect of bipropellant droplet interaction on the fuel droplet burning rate is shown in Fig. 6 for the bipropellant doublet of the same size in comparison with the case of combustion of two fuel droplets of the same size. The correction factor, which is defined as the ratio of the fuel droplet burning rate to that of an isolated burning fuel droplet, is shown to be greater than unity for bipropellant combustion in contrast



**Fig. 7** Effects of bipropellant droplet spacings on the fuel droplet burning rates

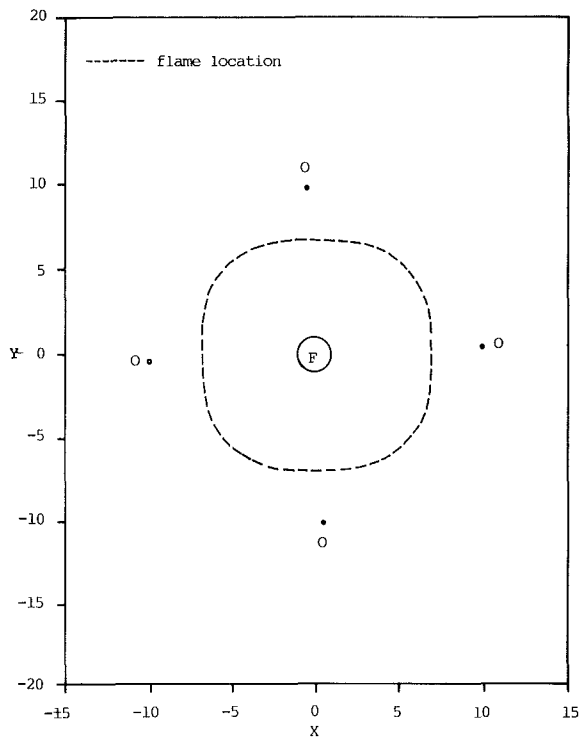


**Fig. 8** Flame configuration of a burning fuel droplet surrounded by six oxidizer droplets at the section of  $Z=0.0$  ( $r_O/r_F=0.1$ ,  $d/r_F=10.0$ )

to combustion of two fuel droplets, which always has a correction factor smaller than unity. Furthermore, the correction factor is shown to increase with increasing droplet spacings for bipropellant droplet combustion because the interaction of bipropellant droplets is more intensive with decreasing droplet spacings. On the other hand, the intensified interaction due to the decreasing droplet spacings of two burning fuel droplets could make the correction factor even less (Umemura et al., 1981a). The droplet size ratio is also a major parameter in multidroplet interaction. The effect of the bipropellant droplet size ratio (defined as the ratio of the oxidizer droplet radius to the fuel droplet radius) on the fuel droplet burning rate is shown in Fig. 7. The larger droplet size ratio can lead to a higher fuel droplet burning rate because the larger oxidizer droplet is able to provide more oxidizer vapor for burning of the fuel droplet. However, in the combustion of two fuel droplets,

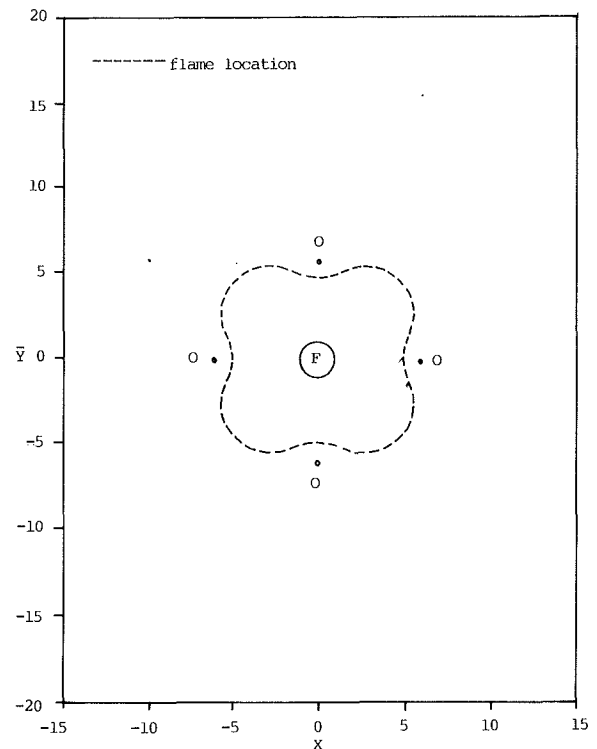


**Fig. 9** Flame configuration of a burning fuel droplet surrounded by six oxidizer droplets at the section of  $Z=0.0$  ( $r_O/r_F=0.1$ ,  $d/r_F=6.0$ )

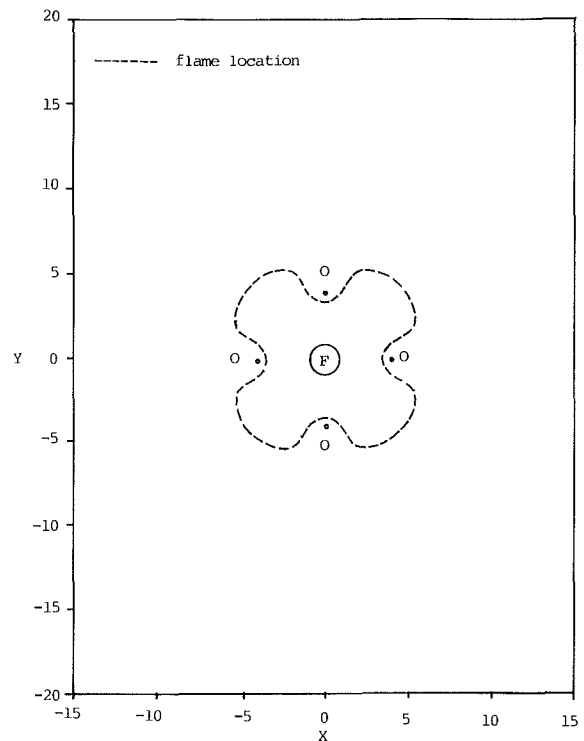


**Fig. 10** Flame configuration of a burning fuel droplet surrounded by six oxidizer droplets at the section of  $Z=0.0$  ( $r_O/r_F=0.1$ ,  $d/r_F=4.0$ )

lets, the larger fuel droplet tends to block the vaporization of the other fuel droplet such that the fuel droplet burning rate is reduced (Umemura et al., 1981b). The comparison of bipropellant droplet combustion and combustion of two fuel droplets reveals that the interaction between bipropellant droplets always enhances droplet burning, while the interaction between two fuel droplets would diminish fuel droplet burning.

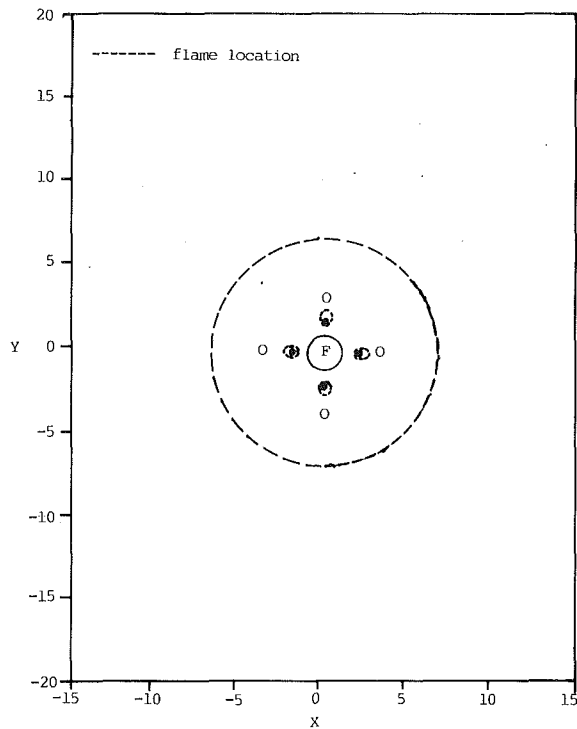


Fig. 11 Composite combustion of a burning fuel droplet surrounded by six oxidizer droplets at the section of  $Z=0.0$  ( $r_o/r_f=0.1$ ,  $d/r_f=2.0$ )

**Many-Droplet Configuration.** The input data for the configuration of a burning fuel droplet surrounded by six oxidizer droplets symmetrically are given as follows:  $\tilde{Y}_{o,\infty}=0.1$ ,  $\tilde{Y}_{f,\infty}=0.0$ ,  $\nu=1$ ,  $B_f=1.9688$ , and  $B_o=1.5$ . The distortion of flame shape due to the interaction between fuel and oxidizer droplets in a many-droplet configuration is shown in Figs. 8–10. In this numerical example, the spacings between the fuel droplet and the oxidizer droplets are 10, 6, and 4 times the fuel droplet radius, respectively. In Fig. 8 the interaction between bipropellant droplets causes a flattened flame surface and the original spherical flame shape becomes a cubelike box. When the droplet center distance is further reduced, the flame shape is “compressed” to a smaller size and “pushed” toward the central fuel droplet by the oxidizer droplets as shown in Figs. 9 and 10. When the droplet center distance is decreased to 2 times the fuel droplet radius, composite combustion is shown in this structured configuration, as shown by Fig. 11, where the oxidizer droplets burn by themselves as conjugate combustion embedded inside the normal flame of a fuel droplet. This normal flame of a fuel droplet is nearly spherically shaped with the flame size about 7 times the fuel droplet radius.

For an isolated single droplet burning, the flame size is 11.4 times the fuel droplet radius with the same far-field conditions by the classical droplet combustion theory. Therefore, the flame size of the fuel droplet surrounded by oxidizer droplets obviously shrinks because of the penetration of the oxidizer droplets that consume part of the fuel vapor. This result implies that the combustion zone in various combustors can be possibly reduced with the injection of oxidizer droplets into the fuel sprays.

## Conclusion

The bipropellant droplet interaction has been studied analytically with the bispherical coordinates for the doublet system and the method of images for the many-droplet configuration. Three combustion modes, including normal combustion, conjugate combustion, and composite combustion, have been identified. The results have shown the enhancement of fuel droplet burning and the shrinking of fuel droplet flame size due to the presence of satellite oxidizer droplets. This conclusion may suggest the positive effects of bipropellant droplet combustion by its higher combustion intensity and more compact combustion space requirement. These advantages would be able to aid in the design of an efficient compact combustor for high-thrust and low-weight-penalty space propulsion engines.

## References

- Brzustowski, T. A., Twardus, E. M., Wojcicki, S., and Sobiesiak, A., 1979, “Interaction of Two Burning Fuel Droplets of Arbitrary Size,” *AIAA J.*, Vol. 17, pp. 1234–1242.
- Chiu, H. H., and Liu, T. M., 1977, “Group Combustion of Liquid Droplets,” *Comb. Sci. Technol.*, Vol. 17, pp. 127–142.
- Chiu, H. H., Kim, H. Y., and Croke, E. J., 1982, “Internal Group Combustion of Liquid Droplets,” *19th Symp. (Int.) on Combustion*, pp. 971–980.
- Chiu, H. H., 1986, “Theory of Bipropellant Combustion, Part I—Conjugate, Normal and Composite Combustion Phenomena,” presented at the AIAA 24th Aerospace Science Meeting, Reno, NV, Paper No. AIAA-86-0260.
- Jiang, T. L., and Chiu, H. H., 1986, “Theory of Bipropellant Combustion, Part II—Conjugate, Normal and Composite Combustion in a Liquid Propellant Rocket Combustion Chamber,” presented at the AIAA 24th Aerospace Science Meeting, Reno, NV, Paper No. AIAA-86-0261.
- Labowsky, M., 1980a, “Calculation of the Burning Rates of Interacting Fuel Droplets,” *Comb. Sci. Technol.*, Vol. 22, pp. 217–226.
- Labowsky, M., 1980b, “Transfer Rate Calculations for Compositionally Dissimilar Interacting Particles,” *Chem. Eng. Sci.*, Vol. 35, pp. 1041–1048.
- Suzuki, T., and Chiu, H. H., 1971, “Multi-droplet Combustion of Liquid Propellant,” *Proceedings of 9th Int. Conf. on Space Technology and Science*, Tokyo, Japan, pp. 145–154.
- Umemura, A., Ogawa, S., and Oshima, N., 1981a, “Analysis of the Interaction Between Two Burning Fuel Droplets,” *Comb. Flame*, Vol. 41, pp. 45–55.
- Umemura, A., Ogawa, S., and Oshima, N., 1981b, “Analysis of the Interaction Between Two Burning Fuel Droplets With Different Sizes,” *Comb. Flame*, Vol. 43, pp. 111–119.
- Williams, F. A., 1985, *Combustion Theory*, The Benjamin/Cummings Publishing Company, Inc.

# A Model for Correlating Flow Boiling Heat Transfer in Augmented Tubes and Compact Evaporators

S. G. Kandlikar<sup>1</sup>

Visiting Scientist,  
Mechanical Engineering Department and  
Plasma Fusion Center,  
Massachusetts Institute of Technology,  
Cambridge, MA 02139

*The additive model for the convective and nucleate boiling components originally suggested by Bergles and Rohsenow (1964) for subcooled and low-quality regions was employed in the Kandlikar correlation (1990a) for flow boiling in smooth tubes. It is now extended to augmented tubes and compact evaporators. Two separate factors are introduced in the convective boiling and the nucleate boiling terms to account for the augmentation effects due to the respective mechanisms. The fin efficiency effects in the compact evaporator geometry are included through a reduction in the nucleate boiling component over the fins due to a lower fin surface temperature. The agreement between the model predictions and the data reported in the literature is within the uncertainty bounds of the experimental measurements.*

## Introduction

Augmented tubes and specially designed compact heat exchanger surfaces are being increasingly employed in flow boiling applications. Some of the augmented tube geometries used in the refrigeration industry include microfin, microgrooved, low-fin, and inserts such as helical wires and twisted tapes. In automotive air conditioning evaporators and in many low-temperature two-phase applications, compact heat exchangers of plate-fin construction are employed. The compact heat exchangers with low-temperature fluid stream boiling during its passage are usually called compact evaporators.

The use of augmented surfaces and compact heat exchangers in refrigeration air conditioning and process industries is justified on the basis of the overall reductions in material cost, weight, size, and/or pumping power in some instances. In calculating the potential savings, and also in the actual design, accurate estimates of the heat transfer coefficients are needed.

A number of investigators have conducted experiments to determine the flow boiling heat transfer coefficients in a variety of augmented tube geometries. Their experimental data are generally reported in a tabular or graphic form. Since there are no adequate predictive techniques available for these geometries, a designer is usually faced with using the data from tables and graphs. The resulting loss in accuracy is generally compensated by the use of generous safety factors.

Some of the recent experimental investigations on compact evaporators are aimed toward understanding the flow patterns and heat transfer mechanisms in these highly enhanced geometries. Damainides and Westwater (1988) report the flow patterns observed in a staggered fin heat exchanger with air-water flow. Cohen and Carey (1990) conducted experiments with R-113 flowing in single cross-ribbed channels of four different geometric configurations. The channels were constructed from a copper block, which was heated with electrical heaters. The top side of the channel was covered with a transparent Lexan cover plate to observe the liquid film behavior. Revealing information was obtained by Cohen and Carey on the existence of nucleate boiling in certain preferred locations

in the channel. They also obtained local flow boiling data, which were correlated by modifying the Chen (1966) correlation. The two-phase multiplier  $F$  was correlated as a function of the Martinelli parameter  $X_{tt}$  for each geometry tested. A similar dependence of  $F$  on  $X_{tt}$  was observed with an earlier correlating scheme developed by Carey and Mandrusiak (1986) based on the annular film model.

Robertson and Lovegrove (1983) conducted flow boiling experiments with R-11 in an electrically heated serrated-fin test section. The local heat transfer coefficients were correlated as a function of flow rate and quality. The contribution from nucleate boiling was not included in their correlating scheme.

A recent correlation developed by Kandlikar (1990a) for flow boiling in smooth circular tubes is able to correlate the data for refrigerants, cryogenics, and water within an average error ranging from  $\pm 10$  to  $\pm 20$  percent. The correlation is based on an additive model for the convective boiling and the nucleate boiling contributions represented by the convection number,  $Co$ , and the boiling number,  $Bo$ . These dimensionless numbers were proposed earlier by Shah (1982) in his chart correlation. In another paper, Kandlikar (1991) presented a flow boiling map in which the parametric relationships between the heat transfer coefficient and the major variables were presented in terms of dimensionless parameters. Specific maps for water, R-22 and R-134a were prepared by Kandlikar (1990b) for estimating the heat transfer coefficient under a given set of operating conditions for these fluids.

The basic model developed by Kandlikar (1990a) in arriving at the smooth tube correlation is now extended to cover augmented tubes and compact evaporator geometries. The details of the model and the results of a comparison with the available experimental data are reported in this paper.

## Objectives of the Present Work

1 Develop a model for flow boiling heat transfer in augmented tube and compact evaporator geometries based on the additive concept for the convective and the nucleate boiling contributions.

2 Provide a quantitative measure for the type of augmentation (convective or nucleate boiling) occurring in a given geometry.

3 Compare the model predictions with the experimental data reported in literature.

<sup>1</sup>Current address: Professor, Mechanical Engineering Department, Rochester Institute of Technology, Rochester, NY 14623.

Contributed by the Heat Transfer Division for publication in the *JOURNAL OF HEAT TRANSFER*. Manuscript received by the Heat Transfer Division July 30, 1990; revision received January 8, 1991. Keywords: Augmentation and Enhancement, Boiling, Heat Exchangers.

## Development of the Flow Boiling Model

The correlation developed by Kandlikar (1990a) for smooth tubes is used as the starting point. The correlation for vertical tubes, or for horizontal tubes with Froude number,  $Fr_{lo} > 0.04$ , is given by:

Smooth tube, Kandlikar correlation:

$$h_{TP} = \text{larger of } \begin{cases} h_{TP,NBD} \\ h_{TP,CBD} \end{cases} \quad (1)$$

where the subscripts NBD and CBD refer to the nucleate boiling dominant and the convective boiling dominant regions, for which the  $h_{TP}$  values are given as:

$$h_{TP,NBD} = 0.6683 Co^{-0.2}(1-x)^{0.8}h_{lo} + 1058.0 Bo^{0.7}(1-x)^{0.8}F_{fl}h_{lo} \quad (2)$$

and

$$h_{TP,CBD} = 1.1360 Co^{-0.9}(1-x)^{0.8}h_{lo} + 667.2 Bo^{0.7}(1-x)^{0.8}F_{fl}h_{lo} \quad (3)$$

The Dittus-Boelter correlation was originally employed by Kandlikar (1990a) for calculating  $h_{lo}$  in smooth tubes. In a subsequent paper, Kandlikar (1990b) recommended the Petukhov-Popov (1963) and the Gnielinski (1976) correlations, which are able to account for the Prandtl number effect of different fluids more accurately than the Dittus-Boelter correlation.

The first terms on the right-hand side of Eqs. (2) and (3) represent the convective boiling components while the second terms represent the nucleate boiling components.  $F_{fl}$  is a fluid-dependent parameter, which is applied as a multiplier in the nucleate boiling terms. Table 1 lists the values of  $F_{fl}$  as reported by Eckels and Pate (1990) for R-134a, and by Kandlikar (1990a) for water and other refrigerants.  $F_{fl}$  for nitrogen was also reported by Kandlikar (1990a), but is likely to undergo further changes due to a wide scatter in the flow boiling data for nitrogen available at the present time.

*A Model for Augmented Tubes.* It is postulated that the and

Table 1 Fluid-dependent parameter,  $F_{fl}$ , in the Kandlikar (1990b) correlation

| Fluid  | $F_{fl}$ |
|--------|----------|
| Water  | 1.00     |
| R-11   | 1.30     |
| R-12   | 1.50     |
| R-13B1 | 1.31     |
| R-22   | 2.20     |
| R-113  | 1.30     |
| R-114  | 1.24     |
| R-134a | 1.63     |
| R-152a | 1.10     |

A material dependence of  $F_{fl}$  is reported by Kandlikar (1991b). Above values are applicable to copper tubes only, for stainless steel tubes, use  $F_{fl} = 1.0$  for all fluids.

effects of  $x$ ,  $G$ ,  $q$ , and fluid properties on  $h_{TP}$  in augmented tubes and compact evaporators are similar to those in smooth tubes as represented by Eqs. (1)–(3); one however needs to take into account the variation of heat flux over the extended surfaces. The augmentation in  $h_{TP}$  is considered to be occurring due to two separate effects, represented by the augmentation factors  $E_{CB}$  and  $E_{NB}$  in the convective and the nucleate boiling terms, respectively. For augmented tubes with microscale protrusions (fin efficiency close to 100 percent), Eq. (1) is applied with the following equations for  $h_{TP,NBD}$  and  $h_{TP,CBD}$ :

*Augmented tubes:*

$$h_{TP,NBD} = 0.6683 Co^{-0.2}(1-x)^{0.8}h_{lo}E_{CB} + 1058.0 Bo^{0.7}(1-x)^{0.8}F_{fl}h_{lo}E_{NB} \quad (4)$$

## Nomenclature

|  |   |  |
|--|---|--|
| $A$ = area, $m^2$  | $F_{fl}$ = fluid-dependent parameter given in Table 1   | $q$ = heat flux defined by Eq. (15), $W/m^2$                                       |
| $Bo$ = boiling number, $q/(Gi_g)$  | $Fr_{lo}$ = Froude number with all flow as liquid = $G^2/(\rho_l g D)$                                      | $Re$ = Reynolds number = $GD/\mu$  |
| $c_p$ = specific heat, $J/kg K$  | $G$ = mass flux, $kg/m^2 s$   | $St$ = Stanton number = $h/(Gc_p)$   |
| $Co$ = convection number = $(\rho_g/\rho_l)^{0.5}((1-x)/x)^{0.8}$  | $h_{lo}$ = single-phase heat transfer coefficient with all flow as liquid, $W/m^2 K$                        | $t$ = fin thickness  |
| $D$ = diameter of a smooth tube, root diameter of a microfin tube, or hydraulic diameter of a compact evaporator flow channel, $m$ | $h_{TP}$ = two-phase heat transfer coefficient, $W/m^2 K$   | $\Delta T_{p-sat}$ = difference between the prime and saturation temperatures, $K$ |
| $E_{CB}$ = augmentation factor for convective boiling contribution   | $h_{TP,\eta}$ = two-phase heat transfer coefficient in a compact evaporator, defined by Eq. (14), $W/m^2 K$ | $x$ = quality  |
| $E'_{CB}$ = modified augmentation factor for convective boiling to include the constant from the unknown single-phase correlation  | $i_{lg}$ = latent heat of vaporization, $J/kg$  | $\eta$ = fin efficiency  |
| $E_{NB}$ = augmentation factor for nucleate boiling contribution   | $j$ = $j$ factor = $StPr^{2/3}$   | $\mu$ = viscosity, $kg/m s$  |
| $E'_{NB}$ = modified augmentation factor for nucleate boiling to include the constant from the unknown single-phase correlation    | $k$ = thermal conductivity, $W/m K$   | $\rho$ = density, $kg/m^3$   |
|  | $L$ = fin height, $m$   |  |
|  | $m$ = defined by Eq. (26), $m^{-1}$   |  |
|  | $n$ = exponent of $Re_{lo}$ for augmented tubes, Eqs. (18) and (19)   |  |
|  | $Pr$ = Prandtl number = $c_p \mu / k$   |  |
|  | $Q$ = heat transfer rate, $W$   |  |
|  |   | <b>Subscripts</b>  |
|  |   | CBD = convective boiling dominant region   |
|  |   | $F$ = fin  |
|  |   | $g$ = vapor  |
|  |   | $l$ = liquid   |
|  |   | $lg$ = latent  |
|  |   | $lo$ = with all flow as liquid   |
|  |   | NBD = nucleate boiling dominant region   |
|  |   | $P$ = prime surface  |

$$h_{TP,CBD} = 1.1360 Co^{-0.9}(1-x)^{0.8} h_{i0} E_{CB} + 667.2 Bo^{0.7}(1-x)^{0.8} F_{fl} h_{i0} E_{NB} \quad (5)$$

The enhancement factors  $E_{CB}$  and  $E_{NB}$  are assumed to be characteristics of the augmented tube geometry, and independent of the operating parameters. The numerical constants appearing in Eqs. (4) and (5) are the same as those in the Kandlikar correlation for smooth tubes.

The heat transfer coefficient  $h_{i0}$  in Eqs. (4) and (5) is obtained from the single-phase correlation for the augmented geometry with total flow as liquid. One of the essential requirements for the single-phase correlation is to provide the correct Reynolds number relationship applicable to the augmented tube. In situations where a reliable single-phase correlation is not available, the Reynolds number exponent  $n$  in a Dittus-Boelter type correlation is treated as a third constant along with  $E_{CB}$  and  $E_{NB}$ , and their values are determined from the experimental flow boiling data.

**A Model for Compact Evaporators.** The flow boiling heat transfer in compact evaporators differs from that in smooth tubes in two ways. Firstly, the geometries employed in compact evaporators are highly augmented with the use of cross ribs, interrupted plate fins, or other similar flow channels. Secondly, the nucleate boiling contribution varies considerably over the channel surfaces due to nonuniform fin surface temperature.

The model presented here utilizes the single-phase heat transfer correlation for compact evaporators to describe the dependence of the heat transfer coefficient on  $Re$  and  $Pr$ . The presence of fins is assumed to affect the nucleate boiling component as it is dependent on the local fin temperature, while the convective boiling component is assumed to be uniform over the entire fin and the prime surfaces at a given section. The resulting equations are given as follows:

For prime surface:

$$h_{TP,P} = \text{larger of } \begin{cases} h_{TP,P,NBD} \\ h_{TP,P,CBD} \end{cases} \quad (6)$$

where

$$h_{TP,P,NBD} = 0.6683 Co^{-0.2}(1-x)^{0.8} h_{i0} E_{CB} + 1058.0 Bo_P^{0.7}(1-x)^{0.8} F_{fl} h_{i0} E_{NB} \quad (7)$$

and

$$h_{TP,P,CBD} = 1.1360 Co^{-0.9}(1-x)^{0.8} h_{i0} E_{CB} + 667.2 Bo_P^{0.7}(1-x)^{0.8} F_{fl} h_{i0} E_{NB} \quad (8)$$

For fin surface:

$$h_{TP,F} = \text{larger of } \begin{cases} h_{TP,F,NBD} \\ h_{TP,F,CBD} \end{cases} \quad (9)$$

where

$$h_{TP,F,NBD} = 0.6683 Co^{-0.2}(1-x)^{0.8} h_{i0} E_{CB} + 1058.0 Bo_F^{0.7}(1-x)^{0.8} F_{fl} h_{i0} E_{NB} \quad (10)$$

and

$$h_{TP,F,CBD} = 1.1360 Co^{-0.9}(1-x)^{0.8} h_{i0} E_{CB} + 667.2 Bo_F^{0.7}(1-x) F_{fl} h_{i0} E_{NB} \quad (11)$$

In Eqs. (6)–(11),  $h_{i0}$  is the single-phase heat transfer coefficient in the compact evaporator with all flow as liquid. The values of  $F_{fl}$  and the numerical constants are the same as those in the Kandlikar correlation for smooth tubes. The boiling numbers on the prime surface,  $Bo_P$ , and on the fins,  $Bo_F$ , are different due to the differences in the respective heat fluxes,  $q_P$  and  $q_F$  (average heat flux over the fins).  $E_{CB}$  and  $E_{NB}$  are the augmentation factors for the convective boiling and the nucleate boiling terms, respectively, and are assumed to be characteristics of the compact evaporator geometry.

The overall heat transfer coefficient  $h_{TP,\eta}$  is defined in terms

of the total heat transfer rate  $dQ$  in an element and the temperature difference  $\Delta T_{P-sat}$  between the prime surface and the saturation temperature

$$dQ = h_{TP,\eta}(dA_P + dA_F)\Delta T_{P-sat} \quad (12)$$

Also,

$$dQ = (h_{TP,P}dA_P + h_{TP,F}dA_F\eta_F)\Delta T_{P-sat} \quad (13)$$

where  $\eta_F$  is the fin efficiency.

From Eqs. (12) and (13),  $h_{TP,\eta}$  may be expressed as

$$h_{TP,\eta} = [h_{TP,P} + h_{TP,F}(A_F/A_P)\eta_F]/(1 + A_F/A_P) \quad (14)$$

The average heat flux  $q$  may be expressed as

$$q = dQ/(dA_P + dA_F) = h_{TP,\eta}\Delta T_{P-sat} \quad (15)$$

The heat fluxes  $q_P$  and  $q_F$  on the prime and fin surfaces, respectively, are given by

$$q_P = h_{TP,P}\Delta T_{P-sat} = q(h_{TP,P}/h_{TP,\eta}) \quad (16)$$

and

$$q_F = h_{TP,F}\Delta T_{P-sat}\eta_F = q(h_{TP,F}/h_{TP,\eta})\eta_F \quad (17)$$

The values of  $Bo_P$  and  $Bo_F$  in Eqs. (6)–(11) are not known initially, and an iterative scheme with Eqs. (16) and (17) is needed when the average heat flux  $q$  is specified. The predicted value of  $h_{TP,\eta}$  is then obtained from Eq. (14).

It may be noted that all heat transfer coefficient and heat flux values are local at any given section in the compact evaporator.

## Comparison With Experimental Data

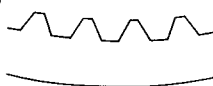
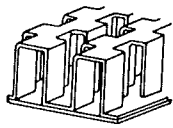


The flow boiling models presented earlier are compared here with the experimental data. For this purpose, three experimental investigations have been selected from the literature based on the completeness of the reported results and accuracy of measurements. Table 2 lists the details of the experimental conditions and an estimate of the errors involved in various measurements.

**Results With Augmented Tube Data.** The augmented tube correlation is checked with the data obtained by Khanpara et al. (1987). They report the flow boiling data in a microfin tube with two refrigerants, R-113 and R-22. The microfin tube dimensions and other experimental details are given in Table 2.

In the correlation developed here, the root diameter is used as the characteristic dimension for calculating  $Re$  and  $Nu$ , while the heat transfer coefficients  $h_{TP}$  and  $h_{i0}$  are based on the actual inside surface area of the microfin tube.

Equations (1), (4), and (5) require information on the single-phase heat transfer coefficient with liquid flow for augmented tubes. The experimental results reported by Khanpara (1986) on the single-phase heat transfer coefficient with R-113 in the microfin tube indicate that  $Nu/Pr^{0.4}$  is proportional to  $Re^{1.7}$  in the  $Re$  range from 6000 to 10,000, while the data for R-22 in the range 12,000 to 15,000 are well below the extension of the R-113 line. Also, the R-22 data are scattered by as much as a factor of 2 for a given  $Re$ . The scatter is believed to be due to wall temperature fluctuations caused by swirling/vortex shedding near the wall of the micro-fin tube. The two-phase data however do not exhibit such a scatter. For these reasons, the single-phase data could not be correlated with any reasonable accuracy. To overcome this problem, the Reynolds number exponent  $n$  is introduced as an additional constant in the Dittus-Boelter type single-phase correlation. The augmentation factors  $E_{CB}$  and  $E_{NB}$  in Eqs. (4) and (5) were modified to  $E_{CB}$  and  $E_{NB}$  to include the unknown leading constant (in place of 0.023) from the single phase correlation. The resulting equations take the following form:

**Table 2 Details of experiments conducted by previous investigators for generating data on a microfin tube and compact evaporators employed in testing the proposed model**

| Investigator                       | Geometry  | Tube or evaporator Geometry   | Test Fluid and Parameter Ranges   | Details of Experimental Set up  |
|------------------------------------|---|---|---|---|
| Khanpara, Pate and Bergles, (1987) |  | Microfin tube, copper, ID=8.75mm, electrically heated, Fin height=0.22 mm, Fin pitch=0.455mm, $A_{aug}/A_{smooth}=1.54$ , Fin geometry-rounded tip-and flat valley (width 0.203mm)                        | R-113; $x$ : 0.025-0.74, $P$ : 324-343 kPa, $G$ : 248-600 kg/m <sup>2</sup> s, $q$ : 8.1-39.7 kW/m <sup>2</sup><br>R-22; $x$ : 0.020-0.78, $P$ : 848-969 kPa, $G$ : 280-533, $q$ : 7.1-12.8 kW/m <sup>2</sup> | Horizontal flow; Measurement accuracy: $q$ - ±4%, $h_{TP}$ - ±15%; Radial guard heater                              |
| Robertson and Lovegrove, (1983)    |  | Serrated aluminum fin compact evaporator, single channel heated electrically from top and bottom, Fin thickness = 0.2mm, Fin height=6.15 mm, $D_i=2.65$ mm, $A_f/A_p=4.06$                                | R-11; $x$ : 0.01-0.8, $P$ : 304-720 kPa, $G$ : 34.4-159 kg/m <sup>2</sup> s, $q$ : 1.3-3.0 kW/m <sup>2</sup>  | Horizontal flow; Measurement accuracy: $T$ - ±0.2 K, Heat leak- 5%; Rotameter- <1%, $h_{TP}$ : 10-15%               |
| Cohen and Carey (1990); Geometry 1 |  | Cross-ribbed copper plate fin compact evaporator, single channel electrically heated from one side, rib angle=30°, rib pitch=28.6mm, rib height=3.2mm, rib thickness=1.6mm, $D_i=6.78$ mm, $A_f/A_p=0.56$ | R-113; $x$ : 0.02-0.75, $P$ : 101 kPa, $G$ : 111.3 kg/m <sup>2</sup> s, $q$ : 56-133 kW/m <sup>2</sup>  | Vertical up flow, electrically heated copper block; Measurement accuracy: $Q$ - ±6%, $T$ - ±0.06 K, $h_{TP}$ - ±11% |
| Cohen and Carey (1990); Geometry 3 |  | Cross-ribbed copper plate fin compact evaporator, single channel electrically heated from one side, rib angle=60°, rib pitch=17.1mm, rib height=3.2mm, rib thickness=1.6mm, $D_i=6.83$ mm, $A_f/A_p=0.54$ | R-113; $x$ : 0.06-0.75, $P$ : 101 kPa, $G$ : 110.7 kg/m <sup>2</sup> s, $q$ : 47-159 kW/m <sup>2</sup>  | same as above   |

**Table 3 Comparison between the experimental data and model predictions**

| Investigators  | RMS % | Mean % | Abs. Mean % |
|--|-------|--------|-------------|
| Khanpara et al. (1987), Micro-fin Tube; $n=0.4$ , $E'_{CB}=82.0$ , $E'_{NB}=72.0$                  | 10.8  | 8.3    | +1.8        |
| Robertson and Lovegrove, (1983) Compact Evaporator, Serrated fin; $E_{CB}=1.20$ , $E_{NB}=0.77$    | 5.4   | 7.4    | -4.3        |
| Cohen and Carey, (1990), Compact Evaporator, Cross-ribs, Geometry 1; $E_{CB}=2.45$ , $E_{NB}=0.63$ | 8.2   | 6.1    | +0.2        |
| Cohen and Carey, (1990), Compact Evaporator, Cross-ribs, Geometry 3; $E_{CB}=3.00$ , $E_{NB}=0.30$ | 3.6   | 2.9    | -0.2        |

% Error = 100 (Experimental-Predicted)/Experimental

*Augmented tube:*

$$h_{TP,NBD} = 0.6683 Co^{-0.2}(1-x)^{0.8} Re_{lo}^n Pr_l^{0.4} E'_{CB} + 1058.0 Bo^{0.7}(1-x)^{0.8} F_{fl} Re_{lo}^n Pr_l^{0.4} E'_{NB} \quad (18)$$

and

$$h_{TP,CBD} = 1.1360 Co^{-0.9}(1-x)^{0.8} Re_{lo}^n Pr_l^{0.4} E'_{CB} + 667.2 Bo^{0.7}(1-x)^{0.8} F_{fl} Re_{lo}^n Pr_l^{0.4} E'_{NB} \quad (19)$$

A total of 26 data points were reported by Khanpara (1986) for R-113 and 34 data points for R-22 for the microfin geometry listed in Table 2. These data points were used in determining

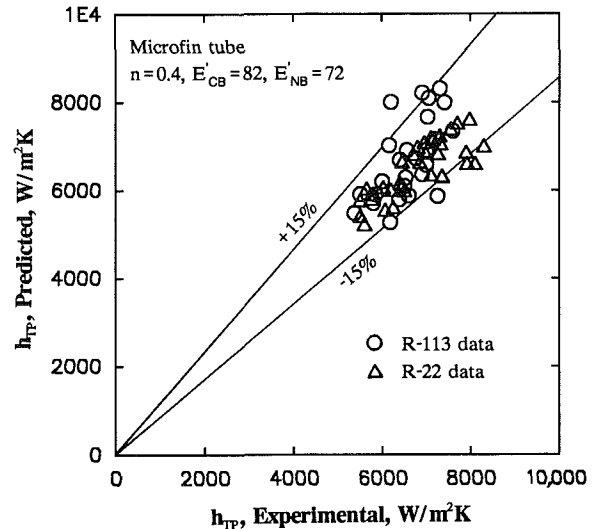


**Fig. 1 Comparison between the model predictions and experimental data by Khanpara et al. (1987) for flow boiling of R-22 and R-113 inside a microfin tube**

the constants  $n$ ,  $E'_{CB}$ , and  $E'_{NB}$  in Eqs. (18) and (19). The combination of the three constants yielding the lowest rms error for both refrigerant data sets was selected.

The values of the constants for the microfin tube determined from the data are  $n=0.4$ ,  $E'_{CB}=82.0$ , and  $E'_{NB}=72.0$ . These values are specific to the microfin geometry listed in Table 2. The rms, mean, and absolute mean differences between the experimental and the predicted values for R-113 and R-22 are given in Table 3. Figure 1 shows a plot of the predicted versus experimental values of  $h_{TP}$  for the microfin tube. The limits of the reported experimental uncertainty of ±15 percent are also shown on the plot. Out of a total of 60 data points, 75 percent of the points are correlated to within ±10 percent, 90



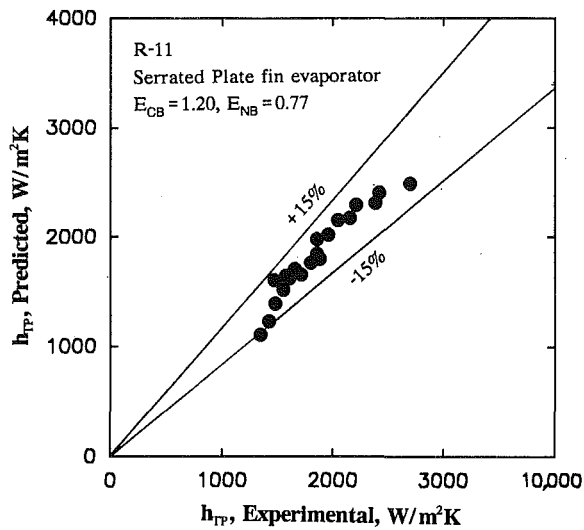


Fig. 2 Comparison between the model predictions and experimental data by Lovegrove and Robertson (1983) for flow boiling of R-11 inside a serrated fin compact evaporator

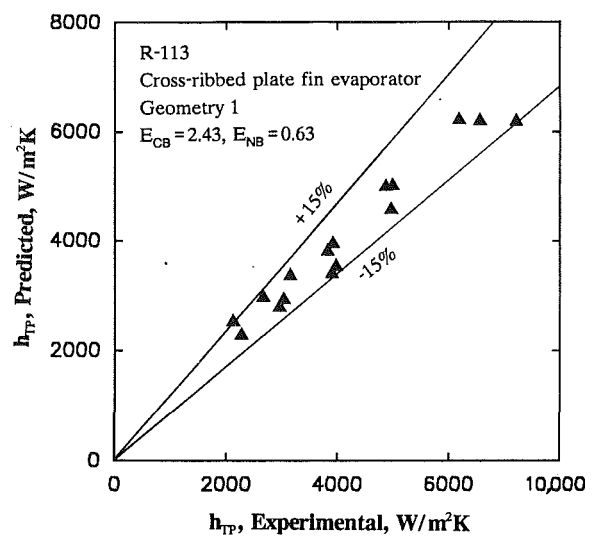


Fig. 3 Comparison between the model predictions and experimental data by Cohen and Carey (1990) for flow boiling of R-113 inside a cross-ribbed compact evaporator (geometry 1)

percent within  $\pm 15$  percent, and only one data point lies beyond  $\pm 18$  percent. Considering the experimental uncertainty and the scatter in the experimental data sets, the agreement is seen to be very good.

It may be noted that the same values of the augmentation factors  $E'_{CB}$  and  $E'_{NB}$  were able to correlate both R-113 and R-22 data sets obtained with the same microfin tube. These factors therefore are believed to be characteristic of the microfin tube in the range of parameters tested. Since the constant from the single-phase correlation is absorbed in these factors, only the ratio of the convective to the nucleate boiling augmentation can be obtained as  $E'_{CB}/E'_{NB} = 82/72 = 1.14$ . This indicates that in the microfin tube tested, the convective augmentation is slightly higher than the nucleate boiling augmentation. Such information could be used in developing augmentation techniques suitable for specific applications. Incorporating small-scale surface changes on the tube surface such as re-entrant cavities and narrow grooves will enhance nucleate boiling and  $E'_{NB}$  will increase, while the convective component and  $E'_{CB}$  will increase if the tube surface offers large-scale disturbances due to fins, wires, ridges, and grooves.

**Results With Compact Evaporator Data.** The flow boiling model given by Eqs. (6)–(11), (14), (16), and (17) was tested with the data reported by Robertson and Lovegrove (1983) for R-11 in a serrated plate fin evaporator, and by Cohen and Carey (1990) for two rib geometries of cross-ribbed channels. Some of the details of the experimental setup and measurement accuracy of the two investigations are given in Table 2.

In the correlations presented for compact evaporators, Nu and Re are based on the hydraulic diameter of the flow channel, and the heat transfer coefficients  $h_{TP,\eta}$ ,  $h_{TP,P}$  and  $h_{TP,F}$  are defined by Eqs. (12), (16), and (17), respectively.

The single-phase heat transfer coefficients for the evaporators are obtained from Eqs. (20)–(23), which are derived from the experimental  $j$ -Re plots.

*Serrated fin geometry, Robertson and Lovegrove (1983):*

$$\text{StPr}^{2/3} = 0.2106 \text{Re}^{-0.38} \quad (20)$$

*Cross-ribbed geometry, No. 1, Cohen and Carey (1990):*

$$\text{StPr}^{2/3} = 0.418 \text{Re}^{-0.37} \quad (21)$$

*Cross-ribbed geometry, No. 3, Cohen and Carey (1990):*

$$\text{StPr}^{2/3} = 0.341 \text{Re}^{-0.30} \quad (22)$$

$h_{lo}$  is then obtained from the corresponding  $\text{St}_{lo}$  with all liquid flow as:

$$h_{lo} = \text{St}_{lo} G c_p \quad (23)$$

The fin efficiency expressions are as follows:

*Serrated fin geometry, Robertson and Lovegrove (1983):*

$$\eta_F = \tanh(mL)/mL \quad (24)$$

*Cross-ribbed fin geometry, Cohen and Carey (1990):*

$$\eta_F = \{ \tanh(mL) + h_{TP,F}/(k_F m) \} / \{ m(L + t/2) [1 + \tanh(mL)h_{TP,F}/(k_F m)] \} \quad (25)$$

where  $m$  in Eqs. (24) and (25) is given by

$$m = [2h_{TP,F}/(k_F t)]^{0.5} \quad (26)$$

A procedure similar to that explained for the augmented tubes was followed in obtaining the constants  $E_{CB}$  and  $E_{NB}$  from the experimental data. A total of 22 data points reported by Robertson and Lovegrove (1983) were utilized for the serrated plate fin evaporator, and 18 data points for geometry 1 and 14 data points for geometry 3 reported by Cohen and Carey (1990) were employed for the cross-rib geometry. The experimental data were first reduced to yield the value of  $h_{TP,\eta}$  as defined by Eq. (14).

The rms, mean and absolute mean differences between the experimental and the predicted values are given in Table 3. Also, the values of the constants obtained from the data analysis are included.

Comparisons of the experimental and predicted values of the heat transfer coefficients for each data set are presented in Figs. 2, 3, and 4. Two lines indicating the approximate accuracy limits of the experimental data are also drawn in Figs. 2–4. It can be seen that the model predictions are in excellent agreement with the experimental data.

The values of the convective boiling and the nucleate boiling augmentation factors are given in Figs. 2–4 as well as in Table 3 for each geometry investigated. It can be seen that the convective boiling augmentation  $E_{CB}$  in compact evaporators is quite large compared to the nucleate boiling augmentation  $E_{NB}$ .

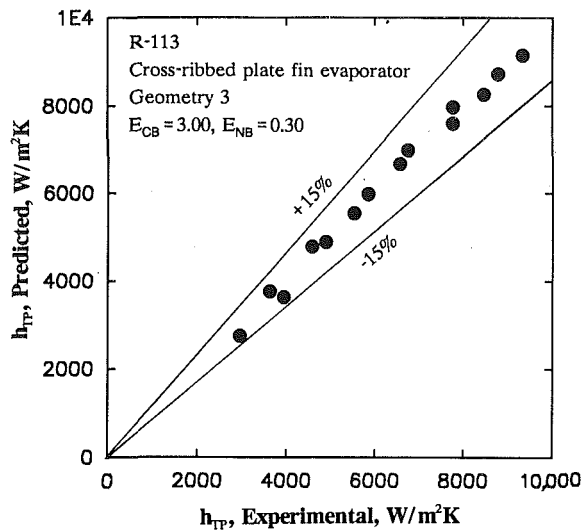


Fig. 4 Comparison between the model predictions and experimental data by Cohen and Carey (1990) for flow boiling of R-113 inside a cross-ribbed compact evaporator (geometry 3)

This is to be expected since the geometries considered do not have any special surface structure to enhance the nucleate boiling, whereas the complex flow passages provide a high degree of convective augmentation. In fact, the nucleate boiling is significantly suppressed ( $E_{NB} < 1$ ) in these geometries due to the presence of a high wall shear stress. Additional discussion on the suppression effects due to wall shear stress is presented by Kandlikar (1990c).

Further comparison can be made between the two geometries tested by Cohen and Carey. The nucleate boiling enhancement factor for geometry 1 ( $E_{NB} = 0.63$ ) is higher than that for geometry 3 ( $E_{NB} = 0.30$ ). This is in agreement with the visual observations made by Cohen and Carey (1990) through the top transparent cover on the flow channels. They observed a number of nucleation sites in the channel with geometry 1, while there were only a few small bubbles seen in the corner regions in geometry 3. On the other hand, the convective enhancement factor  $E_{CB}$  for geometry 1 ( $E_{CB} = 2.43$ ) is lower than that for geometry 3 ( $E_{CB} = 3.0$ ). A closer look at the two geometries described in Table 2 and the single-phase correlations given by Eqs. (21) and (22) reveals that the flow passages for geometry 3 are more tortuous and yield a higher heat transfer coefficient than that for geometry 1. From the above discussion, it can be seen that the model developed here is able to provide important clues regarding the mechanisms during flow boiling inside augmented tubes and compact evaporators.

### Additional Remarks

The results presented in this paper indicate that it is possible to extend the additive model employed in the Kandlikar (1990a) correlation for different geometries by critically evaluating the additional effects. Another area where these concepts could be employed is the flow boiling of multicomponent mixtures in smooth and enhanced tubes, and in compact evaporator geometries. Because of the additional complexity introduced due to mass transfer effects, the problem is unquestionably more challenging. The two aspects where attention should be focused are: (i) changes in properties with concentration and its effect on the convective and the nucleate boiling components, and (ii) the complex effect of heat flux on the nucleate boiling component due to diffusion of one or more volatile components through the mixture. Results based on this approach are presented by Kandlikar (1991) for binary refrigerant systems.

A general comment seems appropriate here regarding the way in which the experimental heat transfer data are reported by the investigators of compact evaporators. They generally plot their  $h_{TP}$  versus  $x$  data on a log-log scale. A linear scale for  $x$  however seems more appropriate since the changes in  $x$  are linearly related to the enthalpy changes (under constant system pressure assumption) along the evaporator. Further, the quality range from 0.01–0.1 is greatly expanded on a log-log plot, occupying almost half the width, while the range from 0.5 onward is compressed. The low-quality range is not used in the refrigeration evaporator, whereas the heat transfer and dryout considerations are of major importance in the high-quality region of an evaporator. It is therefore recommended that a linear scale be used for  $x$ . The log scale for  $h_{TP}$  may be justified when the post-dryout data, which are usually an order of magnitude lower than the wet surface data, are also shown on the same plot.

### Conclusions

The additive model employed in the Kandlikar (1990) correlation is extended to cover the flow boiling heat transfer in augmented tubes and compact evaporators. Two separate augmentation factors are introduced in the convective and the nucleate boiling terms. In the case of compact evaporators, effects due to fin efficiency are included by using appropriate heat fluxes over the prime and the fin surfaces. Experimental data obtained by Khanpara et al. (1987) for R-22 and R-113 boiling in a microfin tube have been correlated with an average deviation of 8.3 percent. The augmentation factors have been found to be specific to the tube geometry and independent of the refrigerant or operating conditions over the range of parameters investigated. The compact evaporator data obtained by Robertson and Lovegrove (1983) for flow boiling of R-11 in a serrated plate-fin geometry, and by Cohen and Carey (1990) for flow boiling of R-113 in two cross-rib geometries were correlated with average deviations of 7.4, 6.1, and 2.9 percent respectively. The enhancement factors  $E_{CB}$  and  $E_{NB}$  in case of augmented tubes, and  $E'_{CB}$  and  $E'_{NB}$  in case of compact evaporators, were able to provide important clues regarding the type of enhancement (convective or nucleate boiling) occurring in the channel during flow boiling.

### References

- Bergles, A. E., and Rohsenow, W. M., 1964, "The Determination of Forced Convection, Surface Boiling Heat Transfer," *ASME JOURNAL OF HEAT TRANSFER*, Vol. 86, pp. 365–372.
- Carey, V. P., and Mandrusiak, G. D., 1986, "Annular Film-Flow Boiling of Liquids in a Partially Heated Vertical Channel With Offset Strip Fins," *International Journal of Heat and Mass Transfer*, Vol. 29, pp. 927–939.
- Chen, J. C., 1966, "A Correlation for Boiling Heat Transfer to Saturated Fluids in Convective Flow," *Industrial and Engineering Chemistry, Process Design and Development*, Vol. 5, pp. 322–329.
- Cohen, M., and Carey, V. P., 1990, "A Comparison of the Flow Boiling Performance Characteristics of Partially-Heated Cross-Ribbed Channels With Different Rib Geometries," *International Journal of Heat and Mass Transfer*, in press.
- Damainides, C. A., and Westwater, J. W., 1988, "Two-Phase Flow Patterns in a Compact Heat Exchanger and in Small Tubes," *Proceedings of the Second UK National Conference on Heat Transfer*, Vol. II, pp. 1257–1268.
- Eckels, S. J., and Pate, M. B., 1990, "An Experimental Comparison of Evaporation and Condensation Heat Transfer Coefficients for HFC-134a and CFC-12," *International Journal of Refrigeration*, Nov., pp. xx-oo.
- Gnielinski, V., 1976, "New Equations for Heat and Mass Transfer in Turbulent Pipe and Channel Flow," *International Chemical Engineer*, Vol. 16, pp. 359–368.
- Kandlikar, S. G., 1989, "Development of a Flow Boiling Map for Subcooled and Saturated Boiling of Different Fluids Inside Circular Tubes," in: *Heat Transfer With Phase Change*, X. X. Habib et al., eds., Vol. 114, pp. 51–62; also accepted for publication in the *ASME JOURNAL OF HEAT TRANSFER*.
- Kandlikar, S. G., 1990a, "A General Correlation for Saturated Two-Phase Flow Boiling Heat Transfer Inside Horizontal and Vertical Tubes," *ASME JOURNAL OF HEAT TRANSFER*, Vol. 112, pp. 219–228.
- Kandlikar, S. G., 1990b, "Flow Boiling Maps for Water, R-22 and R-134a in the Saturated Region," presented at the 9th International Heat Transfer Conference, Jerusalem, Aug.

Kandlikar, S. G., 1990c, "A Mechanistic Model for Saturated Flow Boiling Heat Transfer," *Single and Multiphase Convective Heat Transfer*, M. A. Ebdian, K. Vafai, and A. Lavine, eds., ASME HTD-Vol. 145, pp. 61-69.

Kandlikar, S. G., 1991, "Correlating Flow Boiling Heat Transfer Data in Binary Systems," *Phase Change Heat Transfer*, E. Hensel et al., eds., ASME HTD-Vol. 159.

Khanpara, J. C., 1986, "Augmentation of In-Tube Evaporation and Condensation With Micro-Fin Tubes," Ph.D. Dissertation, Iowa State University, Ames, IA.

Khanpara, J. C., Pate, M. B., and Bergles, A. E., 1987, "Local Evaporation Heat Transfer in a Smooth Tube and a Micro-fin Tube Using Refrigerants 22

and 113," in: *Boiling and Condensation in Heat Transfer Equipment*, E. G. Ragi et al., eds., ASME HTD-Vol. 85, pp. 31-40.

Petukhov, B. S., and Popov, V. N., 1963, "Theoretical Calculation of Heat Exchange and Frictional Resistance in Turbulent Flow in Tubes of an Incompressible Fluid With Variable Physical Properties," *Teplofiz. Vysok. Temperatur (High Temperature Heat Physics)*, Vol. 1, No. 1.

Robertson, J. M., and Lovegrove, P. C., 1983, "Boiling Heat Transfer With Freon 11 (R11) in Brazed Aluminum Plate-Fin Heat Exchangers," *ASME JOURNAL OF HEAT TRANSFER*, Vol. 105, pp. 605-610.

Shah, M. M., 1982, "Chart Correlation for Saturated Boiling Heat Transfer: Equations and Further Study," *American Society of Heating, Refrigerating and Air Conditioning Engineers Transactions*, Vol. 88, Part 1, pp. 185-196.

# Bubble Dynamics in Boiling Under High Heat Flux Pulse Heating

A. Asai

Associate Scientist,  
Canon Inc. Research Center,  
5-1 Morinosato-Wakamiya,  
Atsugi, Kanagawa 243-01, Japan

*A new theoretical model of bubble behavior in boiling under high heat flux pulse is presented. The essence of the model is nucleation in the superheated liquid followed by instantaneous formation of a vapor film, rapid bubble growth due to the pressure impulse, and cavitation bubble collapse. To check the model, boiling of methanol under 5 ~ 50 MW m<sup>-2</sup> heat flux pulse using a small thin film heater has been experimentally investigated. When the heat flux was relatively low (< 20 MW m<sup>-2</sup>), a bubble grew in a hemispherical shape. When the heat flux was extremely high (> 20 MW m<sup>-2</sup>), many small bubbles nucleated and combined into a vapor film. The bubble behavior in the latter case is explained well by the model.*

## Introduction

The boiling of a liquid under an extremely high heat flux pulse differs from the usual nucleate boiling in many points (Skripov, 1974). First, the boiling process is initiated at a higher temperature close to the theoretically expected superheat limit. Second, the boiling process is more explosive because the initial bubble pressure is very large. Third, the boiling process is more reproducible because the boiling mechanism is mainly governed by the property of liquids, not by the surface state. This phenomenon has been effectively used in investigating the superheat of liquids (Skripov, 1974).

The pulse heating of liquids under extremely high heat flux is not only an experimental technique but also a practical technology to realize explosive boiling reproducibly. The bubble jet (or thermal ink jet) printing technology is an example, in which boiling is used as a means to generate pressure to eject ink drops from small nozzles (Hara and Endo, 1982; Allen et al., 1985). In a typical bubble jet printer, ink is heated by the electrical pulses applied to thin film resistors placed in nozzles, under the condition of ~ 100 MW m<sup>-2</sup> in heat flux, 1 ~ 10 μs in pulse width, and up to 1 ~ 10 kHz in frequency.

In designing an apparatus that utilizes the boiling under extremely high heat flux pulse, such as a bubble jet printer, it is important to predict the bubble behavior. Skripov (1974) showed a condition (impact condition) to realize the spontaneous nucleation in pulse heating and clarified the basic characteristics of the boiling under extremely high heat flux pulse. Asai (1989) showed a numerical method to predict the nucleation process in pulse heating. Asai et al. (1987) showed a numerical method to predict the bubble growth after the vapor film is formed. From the practical point of view, however, further investigations are needed because no analytical model is available to predict the bubble behavior under extremely high heat flux pulse.

In this paper, a new theoretical model of nucleation and bubble growth in boiling under extremely high heat flux is presented. As for the nucleation characteristics, an analytical expression of the nucleation probability in the time-dependent temperature field is obtained, by integrating the nucleation rate in time and space. As for the bubble growth characteristics, an analytical expression of the time-dependent bubble pressure is obtained, by treating the initial bubble growth as an impulsive motion of a thin vapor film. These analytical expressions give a basic understanding of the phenomenon.

To check the validity of the model, an experiment was also done. Boiling of methanol under 5 ~ 50 MW m<sup>-2</sup> heat flux pulse was investigated using a thin film heater. The experi-

mentally observed bubble characteristics were explained well by the model.

## Theoretical Model

**Nucleation Probability.** In usual situations, boiling is initiated by the growth of gas or vapor trapped in the cavity of the heating wall. In boiling under extremely high heat flux pulse heating, however, the dominant bubble generation mechanism is the spontaneous nucleation due to thermal motion of liquid molecules (Skripov, 1974). This is because the liquid temperature rises so rapidly that vapor or gas nuclei, which may be trapped on the heating surface, do not grow large before the spontaneous nucleation occurs. In the following discussion, we consider an ideal case of spontaneous nucleation and neglect the effect of the growth of pre-existing nuclei. Actually, the pre-existing nuclei may have an influence on the boiling incipience, especially when the heating surface is not smooth.

According to the classical nucleation theory, the homogeneous nucleation rate (probability)  $J_{ho}$  per unit time and volume due to the thermal fluctuation of a liquid of temperature  $T$  is given by (Van Stralen and Cole, 1979)

$$J_{ho}(T) = N_l \left( \frac{3\sigma_l(T)}{\pi m_l} \right)^{1/2} \exp[G(T)],$$

$$G(T) = - \frac{16\pi\sigma_l(T)^3}{3k_B T (p_v(T) - p_{amb})^2},$$

$$p_v(T) = p_{sat}(T) \exp \left[ \frac{p_{sat}(T) - p_{amb}}{N_l k_B T} \right], \quad (1)$$

where  $N_l$  and  $m_l$  are the number density and the mass of the liquid molecule, respectively,  $\sigma_l$  is the surface tension of the liquid,  $k_B$  is the Boltzmann constant,  $p_{amb}$  is the ambient pressure,  $p_v$  is the equilibrium vapor pressure in the critical size bubble, and  $p_{sat}$  is the saturated vapor pressure at a flat interface. The heterogeneous nucleation rate (probability)  $K_{he}$  per unit time and area at a heating surface due to the thermal fluctuation of a liquid of temperature  $T$  is given by (Van Stralen and Cole, 1979)

$$K_{he}(T, \theta) = N_l^{2/3} \psi \left( \frac{3\sigma_l(T)}{\pi m_l} \right)^{1/2} \exp[\phi G(T)],$$

$$\phi \equiv (2 + 3 \cos \theta - \cos^3 \theta) / 4,$$

$$\psi \equiv (1 + \cos \theta) / 2, \quad (2)$$

where  $\theta$  is the contact angle of the liquid at the heating surface.

When a liquid is heated on a flat wall, with a uniform heat flux area,  $S_h$ , the temperature distribution near the heating

Contributed by the Heat Transfer Division and presented at the 3rd ASME/JSME Thermal Engineering Joint Conference, Reno, Nevada, March 17-22, 1991. Manuscript received by the Heat Transfer Division August 13, 1990; revision received May 23, 1991. Keywords: Boiling, Modeling and Scaling, Transient and Unsteady Heat Transfer.

surface is approximately one dimensional, as long as the following condition is satisfied:

$$2\sqrt{a_l t} \ll d_h \quad (3')$$

where  $a_l$  is the thermal diffusivity of the liquid and  $d_h$  is the size of the heating area. Thus the total nucleation rate (probability)  $K(t)$  per unit time and area at the heating surface ( $z = 0$ ) due to the homogeneous and heterogeneous nucleation is given by

$$K(t) = \int_0^\infty J_{ho}(T(z, t)) dz + K_{he}(T_w, \theta) - K_{he}(T_w, 0), \quad (3)$$

where  $z$  is the coordinate perpendicular to the wall and  $T_w$  is the temperature of the liquid at  $z = 0$ . The last term of Eq. (3) is added so that the effect of the heterogeneous nucleation vanishes when  $\theta = 0$ . In order to calculate the integral in Eq. (3), we apply the linear approximation to the temperature field. This approximation is justified because the nucleation rate is an exponentially increasing function and only  $z \sim 0$  contribute to the integral. We approximate the temperature field with a linear form (Skripov, 1974)

$$T(z, t) = T_w(t) - q_w(t)z/k_l, \quad (4)$$

and expand  $G(T)$  around  $T_w(t)$ :

$$G(T(z, t)) \approx G(T_w(t)) - G'(T_w(t))q_w(t)z/k_l.$$

If we neglect the temperature dependence of the factor before the exponential function in Eq. (1), we obtain

$$J_{ho}(T(z, t)) = J_{ho}(T_w(t)) \exp[-q_w(t)G'(T_w(t))z/k_l],$$

$$K(t) = \frac{k_l J_{ho}(T_w(t))}{q_w(t)G'(T_w(t))}, \quad (5)$$

where  $k_l$  is the heat conductivity of the liquid and  $q_w(t)$  is the heat flux from the wall to the liquid. Since the effect of the heterogeneous nucleation is small as long as the heating surface is flat and  $\theta < \pi/2$ , we neglect the last two terms of Eq. (3) in the following analysis.

Since the probability,  $F(t)$ , that the nucleation occurs up to time  $t$  after the heat pulse is turned on satisfies

$$\begin{aligned} dF(t)/dt &= S_h K(t) (1 - F(t)), \\ F(t) &= 0, \quad \text{for } t = 0, \end{aligned} \quad (6)$$

we obtain

$$F(t) = 1 - \exp \left[ -S_h \int_0^t K(t) dt \right]. \quad (7)$$

We approximate the change of the temperature  $T_w(t)$  near  $t = t_g$  with a linear form (Skripov, 1974)

$$T_w(t) = T_g + \dot{T}_w(t_g)(t - t_g),$$

$$T_g = T_w(t_g),$$

$$\dot{T}_w(t_g) \equiv d/dt, \quad (8)$$

and expand  $G(T_w(t))$  around  $T_g$ :

$$G(T_w(t)) = G(T_g) + G'(T_g)\dot{T}_w(t_g)(t - t_g).$$

If we neglect the time dependence of variables out of the exponential function in Eq. (5), we obtain

$$K(t) = \frac{k_l J_{ho}(T_g)}{q(t_g)G'(T_g)} \exp[G'(T_g)\dot{T}_w(t_g)(t - t_g)]. \quad (9)$$

If we choose the time  $t_g$  so that

$$\frac{S_h k_l J_{ho}(T_g)}{q(t_g)\dot{T}_w(t_g)G'(T_g)^2} = 1, \quad (10)$$

we obtain

$$F(t) = 1 - \exp[-n(t)],$$

$$n(t) \equiv S_h \int_0^t K(t) dt \quad (11)$$

$$= \exp[G'(T_g)\dot{T}_w(t_g)(t - t_g)].$$

The function  $n(t)$  represents the typical number of nuclei at a time  $t$ .

The value of  $n(t)$  may differ from the experimental data because the temperature field is disturbed after the nucleation occurs. The probability  $F(t)$ , on the other hand, allows the comparison with the experimental data, because it depends only on the temperature field before the nucleation occurs.

Since  $n(t_g) = 1$  and the probability distribution of the incipient time of nucleation,  $dF/dt$ , is maximum at  $t = t_g$ , we define the homogeneous nucleation temperature as the tem-

## Nomenclature

$A$  = inertance,  $\text{kg m}^{-4}$   
 $a$  = thermal diffusivity,  $\text{m}^2 \text{s}^{-1}$   
 $d$  = length,  $\text{m}$   
 $F$  = probability  
 $f(\zeta)$  = function defined by the solution of Eq. (26)  
 $G$  = exponent in the expression of the nucleation rate  
 $H$  = enthalpy,  $\text{J}$   
 $J$  = nucleation rate per unit time and volume,  $\text{m}^{-3} \text{s}^{-1}$   
 $K$  = nucleation rate per unit time and area,  $\text{m}^{-2} \text{s}^{-1}$   
 $k$  = thermal conductivity,  $\text{W m}^{-1} \text{K}^{-1}$   
 $k_B$  = Boltzmann constant,  $1.38 \times 10^{-23} \text{ J K}^{-1}$   
 $L$  = heat of vaporization,  $\text{J kg}^{-1}$   
 $m$  = mass of a molecule,  $\text{kg}$   
 $N$  = number density,  $\text{m}^{-3}$   
 $n$  = number  
 $\mathbf{n}$  = unit normal vector

$p$  = pressure,  $\text{Pa}$   
 $q$  = heat flux,  $\text{W m}^{-2}$   
 $R$  = radius,  $\text{m}$   
 $S$  = area,  $\text{m}^2$   
 $T$  = temperature,  $\text{K}$   
 $t$  = time,  $\text{s}$   
 $t_0$  = time when nuclei contact each other,  $\text{s}$   
 $t_1 = 3q_h S_h A_l / (2\rho_g \rho_l L_g), \text{ s}$   
 $t_2 = \pi(\alpha_g \beta_g T_g k_l)^2 / (4q_h^2 a_l), \text{ s}$   
 $t_3$  = time when the heat flux  $q_w(t)$  becomes maximum,  $\text{s}$   
 $t_e$  = time constant of bubble pressure decrease,  $\text{s}$   
 $\mathbf{u}$  = velocity,  $\text{m s}^{-1}$   
 $V$  = volume,  $\text{m}^3$   
 $\alpha_g = 1 - \rho_g / \rho_l$   
 $\beta_g = p_g / (\rho_g L_g)$   
 $\gamma_g = 1 - p_{\text{amb}} / p_g$   
 $\delta_0, \delta_1$  = dimensionless constants defined in Eq. (24)  
 $\theta$  = contact angle,  $\text{rad}$

$\lambda$  = dimensionless parameter in Eq. (27)  
 $\rho$  = density,  $\text{kg m}^{-3}$   
 $\sigma$  = surface tension,  $\text{N m}^{-1}$   
 $\tau$  = heat pulse width,  $\text{s}$   
 $\Phi$  = solution of Eq. (17)  
 $\phi = (2 + 3 \cos \theta - \cos^3 \theta) / 4$   
 $\psi = (1 + \cos \theta) / 2$

## Subscripts

amb = ambient  
col = collapse  
 $g$  = generation (nucleation)  
 $h$  = heater  
 $he$  = heterogeneous  
 $ho$  = homogeneous  
 $l$  = liquid  
max = maximum  
sat = saturation  
 $v$  = vapor  
 $w$  = wall

perature  $T_g$  by Eq. (10). It is noted that the value of  $T_g$  does not change so much if we use another definition of  $T_g$  such as the average of the incipient nucleation temperature or the temperature at the time when  $F(t) = 0.5$ , because the nucleation rate increases exponentially as the temperature increases.

If the contact angle  $\theta$  is large ( $\theta > \pi/2$ ) and the effect of heterogeneous nucleation dominates, then

$$K(t) \approx K_{he}(T_w(t), \theta). \quad (9')$$

In this case, we should choose  $t_g$  so that

$$\frac{S_h K_{he}(T_g, \theta)}{\phi G'(T_g) \dot{T}_w(t_g)} = 1, \quad (10')$$

and we obtain

$$F(t) = 1 - \exp[-n(t)],$$

$$n(t) = \exp[\phi G'(T_g) \dot{T}_w(t_g) - (t - t_g)]. \quad (11')$$

**Bubble Growth in the Early Stage.** When the homogeneous nucleation occurs, the initial bubble radius,  $2\sigma_l(T_g)/[p_v(T_g) - p_{amb}]$ , is very small (1 ~ 10 nm for methanol, ethanol, and water) and the initial bubble pressure,  $p_v(T_g)$ , is very high (1 ~ 10 MPa for methanol, ethanol, and water). Thus the bubble growth in the early stage before the cooling effect becomes significant is approximated by the asymptotic Rayleigh bubble growth rate (Rayleigh, 1917):

$$\dot{R} = [2(p_{sat}(T_g) - p_{amb})/(3\rho_l)]^{1/2}, \quad (12)$$

where  $R$  is the radius of a nucleus, and  $\rho_l$  is the density of the liquid.

If we use Eq. (12) as the bubble growth rate, the typical time  $t_0$  when bubbles contact can be estimated by the solution of the equation

$$S_h = n(t_0) \pi \dot{R}^2 (t_0 - t_g)^2. \quad (13)$$

It is noted that Eq. (13) is not accurate because the cooling effect may affect the bubble growth rate before bubbles contact. If the heat pulse width  $\tau$  is longer than  $t_0$  and heat flux  $q_w$  is so large that  $n(t_0) \gg 1$  is satisfied, the surface is instantly covered by many small nuclei and they combine into a thin vapor film before they grow large. In this case, the effect of the evaporating microlayer is small and the bubble growth process may be idealized by the growth of a very thin vapor film created at  $t \approx t_g$ . In the following discussion of this section, we assume this idealization and set the origin of time at  $t = t_g$ .

In the early stage of bubble growth, the liquid velocity is small and the effect of convection and viscosity can be neglected (Batchelor, 1967). If we further neglect the compressibility of the liquid, the liquid motion is described by

$$\nabla \cdot \mathbf{u} = 0, \quad (14)$$

$$\rho_l \partial \mathbf{u} / \partial t + \nabla p = 0,$$

where  $\mathbf{u}$  and  $p$  are the velocity and pressure of the liquid, respectively. This approximation is valid if the following conditions are satisfied:

$$u_v t \ll d,$$

$$2\sqrt{\nu t} \ll d, \quad (14')$$

$$v_l t \gg d,$$

where  $u_v$  is the velocity of the liquid-vapor boundary,  $d$  is a typical size of the system,  $\nu$  is the kinematic viscosity, and  $v_l$  is the sound velocity in the liquid.

We neglect the effect of the surface tension at the bubble boundary, assuming that the following condition is satisfied:

$$\sigma_l/d_h \ll p_v - p_{amb}, \quad (15')$$

where  $p_v$  is the initial pressure of the bubble. If we further assume that the pressure in the vapor film is uniform and neglect the discontinuity of pressure at the liquid-vapor interface, the bubble volume  $V_v$  satisfies the following equation:

$$d^2 V_v(t)/dt^2 = (p_v(t) - p_{amb})/A_l, \quad (15)$$

$$V_v(t) = dV_v(t)/dt = 0, \quad \text{for } t = 0.$$

Here  $A_l$  is the inertance (Olson, 1957) of the liquid region, defined by

$$A_l \equiv -\rho_l \left[ \int_{S_h} \nabla \Phi \cdot \mathbf{n} dS_h \right]^{-1}, \quad (16)$$

where  $\mathbf{n}$  is the outward unit normal vector at the heating surface. Here  $\Phi$  is the solution of the differential equation

$$\nabla^2 \Phi = 0,$$

$$\Phi = 1, \quad \text{on } S_h, \quad (17)$$

$$\Phi = 0, \quad \text{on } S_{amb},$$

where  $S_{amb}$  is the open boundary of the liquid region at which  $p = p_{amb}$ . The value of  $A_l$  strongly depends on the shape of the liquid region. If the heater is a square of sides  $d_h$  located on a flat wall and the liquid is filled in a semi-infinite region defined by the wall and the infinite open boundary, the inertance of the semi-infinite region is  $\approx 0.43 \rho_l/d_h$ .

We assume that the heat flux from the heater to the liquid is suddenly turned on at  $t = 0$  and turned off immediately after the vapor film is formed. This assumption is justified if the liquid is directly heated by a thin film heater deposited on a wall. The first law of thermodynamics yields

$$dH(t)/dt = S_h q_v(t) + V_v(t) dp_v/dt, \quad (18)$$

where  $H$  is the total enthalpy of the bubble and the liquid-vapor interface and  $q_v$  is the heat flux from the liquid to the bubble. Here the heat flux from the heater to the bubble is neglected because the heat pulse is turned off and the residual heat from the thin film heater is small compared to the heat from the superheated liquid.

Since

$$dH(t)/dt = \rho_g L_g dV_v(t)/dt + o(t),$$

$$dV_v(t)/dt = p_g \gamma_g t / A_l + o(t), \quad (19)$$

$$V_v(t) dp_v(t)/dt = o(t),$$

$$\gamma_g \equiv 1 - p_{amb}/p_g,$$

as  $t \rightarrow 0$ , we obtain

$$q_v(t) = \frac{p_g \rho_g L_g \gamma_g t}{S_h A_l} + o(t), \quad t \rightarrow 0, \quad (20)$$

where  $p_g$ ,  $\rho_g$ , and  $L_g$  are vapor pressure, vapor density, and the heat of vaporization at the temperature  $T_g$ . Since the temperature field near the bubble boundary is approximately one dimensional, the temperature of the bubble surface  $T_v$  is given by

$$T_v(t) \approx T_g - \frac{2}{k_l} \left( q_h + \frac{2p_g \rho_g L_g t}{3S_h A_l} \right) \left( \frac{a_l t}{\pi} \right)^{1/2}, \quad (21)$$

where  $a_l$  is the thermal diffusivity of the liquid and  $q_h$  is the average heat flux from the heater to the liquid before the vapor film is formed.

Since the thickness of the vapor film is thin and the liquid velocity is small in the early stage, the pressure in the vapor film,  $p_v$ , can be approximated by the saturated vapor pressure at the temperature  $T_v$ . The Clausius-Clapeyron equation yields

$$\begin{aligned}
p_v &= p_g \exp [(1 - T_g/T_v)/(\alpha_g \beta_g)], \\
\alpha_g &\equiv 1 - \rho_g/\rho_l, \\
\beta_g &\equiv p_g/(\rho_g L_g).
\end{aligned} \tag{22}$$

Substituting Eq. (21) into Eq. (22) we obtain

$$\begin{aligned}
p_v &= p_g \exp \left[ - \left( 1 + \frac{t}{t_1} \right) \left( \frac{t}{t_2} \right)^{1/2} \right], \\
t_1 &\equiv \frac{3q_h S_h A_l}{2p_g \rho_g L_g}, \\
t_2 &\equiv \frac{\pi (\alpha_g \beta_g T_g k_l)^2}{4q_h^2 a_l}.
\end{aligned} \tag{23}$$

Equation (23) is valid only at the early stage when the heat flux  $q_v$  is described by the linear expression (20). The upper limit of the time when Eq. (23) can be used is estimated by the time  $t_3$  when the heat flux  $q_v$  becomes maximum. Substituting Eq. (23) into Eqs. (15) and (18), we obtain

$$\begin{aligned}
q_v(t) &= \frac{p_g \rho_g L_g \gamma_g t}{S_h A_l} \left[ 1 - \left( \delta_0 + \delta_1 \frac{t}{t_1} \right) \left( \frac{t}{t_2} \right)^{1/2} \right] + o(t^{2.5}), \\
\delta_0 &\equiv \frac{5}{4} \left( 1 - \alpha_g \beta_g + \frac{8}{15\gamma_g} \right) - \frac{\beta_g}{4}, \\
\delta_1 &\equiv \frac{7}{4} \left( 1 - \alpha_g \beta_g + \frac{8}{35\gamma_g} \right) - \frac{3\beta_g}{4},
\end{aligned} \tag{24}$$

and

$$t_3 \approx \frac{3\delta_0 t_1}{5\delta_1} f \left( \frac{2}{3\delta_0} \left( \frac{5\delta_1 t_2}{3\delta_0 t_1} \right)^{1/2} \right), \tag{25}$$

where  $f(\zeta)$  is the solution of an algebraic equation with a parameter  $\zeta$ :

$$(1+f)\sqrt{f} = \zeta. \tag{26}$$

**Bubble Growth in the Later Stage.** In the later stage, the bubble pressure is no longer approximated by Eq. (23). We use a kind of profile method because it is difficult to obtain an analytical expression of the bubble pressure in the later stage. Since it is expected that the bubble pressure decreases rapidly as long as the heat pulse is short and the superheated liquid layer is thin (Asai et al., 1987), we assume the following time profile of the bubble pressure:

$$p_v(t) = [p_g - p_{\text{sat}}(T_{\text{amb}})] \exp[-(t/t_e)^\lambda] + p_{\text{sat}}(T_{\text{amb}}), \tag{27}$$

where  $T_{\text{amb}}$  is the ambient temperature,  $t_e$  is the time constant of pressure decrease, and  $\lambda$  is a parameter. Expression (27) has the property that  $p_v(0) = p_g$  and  $p_v(t) \rightarrow p_{\text{sat}}(T_{\text{amb}})$  as  $t \rightarrow \infty$ . If we impose the condition that Eq. (27) agrees with Eq. (23) at  $t = t_3$ , we obtain the equation to determine  $t_e$ :

$$t_e = t_3(1 + t_3/t_1)^{-1/\lambda} (t_3/t_2)^{-1/(2\lambda)}. \tag{28}$$

The parameter  $\lambda$  may depend on the thermal property of the liquid, heating condition, and the magnitude of  $A_l$ . Although the value of  $\lambda$  is expected to be 0.5 ~ 1.5 from Eq. (23), the precise value cannot be determined by the present model, because the assumptions used in the model are valid only in the early stage of bubble growth. At present, the value of  $\lambda$  should be determined by experimental bubble growth data, as is demonstrated in subsequent sections.

We consider the case when the heat pulse duration is so short and the superheated liquid layer is so thin that the temperature and the pressure of the bubble rapidly decrease before the vapor film grows large. In such a highly subcooled condition, the liquid is given an initial supply of kinetic energy by the

pressure impulse and thereafter the bubble growth and collapse process are dynamically controlled by the pressure difference and the liquid inertia (Bankoff, 1966). If we assume  $p_{\text{amb}} \ll p_g$ , the pressure impulse  $P$  and the work  $W$  done by the bubble to the liquid are given by

$$\begin{aligned}
P &\approx p_g t_e/\lambda, \\
W &\approx P^2/(2A_l).
\end{aligned} \tag{29}$$

If we further assume that the bubble pressure decreases rapidly to the value  $p_{\text{sat}}(T_{\text{amb}})$  and that the liquid motion stops when the bubble volume  $V_v$  becomes the maximum value,  $V_{\text{max}}$ , we obtain

$$V_{\text{max}} \approx W/[p_{\text{amb}} - p_{\text{sat}}(T_{\text{amb}})]. \tag{30}$$

If we define the equivalent bubble radius  $R_v(t)$  by the radius of a hemisphere of volume  $V_v(t)$ , the maximum equivalent bubble radius  $R_{\text{max}}$  is given by

$$R_{\text{max}} = [3V_{\text{max}}/(2\pi)]^{1/3}. \tag{31}$$

The above discussion on the bubble pressure and the maximum bubble radius can be applied to any geometry of the liquid region. The bubble growth curve, however, depends on the shape of the liquid region. In the following discussion, we will consider the simplest case when the heater is located on a flat wall and the liquid is filled in a semi-infinite region defined by the wall and the infinite open boundary. We approximate the time profile of the bubble pressure by an idealized impulse:

$$p_v(t) = P\delta(t) + p_{\text{sat}}(T_{\text{amb}}), \tag{32}$$

where  $\delta(t)$  is the delta function. This approximation is valid if we are interested in the bubble growth curve in the later stage. We further neglect the effect of viscosity and surface tension.

In the bubble growth phase, the bubble motion can be approximated by a one-dimensional growth of a vapor film. Thus the bubble volume,  $V_v(t)$ , satisfies the following equation:

$$d^2 V_v/dt^2 = -(p_{\text{amb}} - p_{\text{sat}}(T_{\text{amb}}))/A_l, \tag{33}$$

$$V_v(t) = 0, \quad dV_v(t)/dt = P/A_l, \quad \text{for } t = 0.$$

This equation is easily solved:

$$V_v(t) = W(2\xi - \xi^2)/(p_{\text{amb}} - p_{\text{sat}}(T_{\text{amb}})), \tag{34}$$

$$\xi \equiv (p_{\text{amb}} - p_{\text{sat}}(T_{\text{amb}}))t/P.$$

The bubble behavior after it reaches its maximum volume can be treated as a cavitation bubble (Rayleigh, 1917):

$$R_v(t) \frac{d^2 R_v}{dt^2} + \frac{3}{2} \left( \frac{dR_v(t)}{dt} \right)^2 = -\frac{p_{\text{amb}} - p_{\text{sat}}(T_{\text{amb}})}{\rho_l}. \tag{35}$$

The time  $t_{\text{col}}$  required by the bubble to collapse is given by

$$t_{\text{col}} = 0.915 R_{\text{max}} [\rho_l/(p_{\text{amb}} - p_{\text{sat}}(T_{\text{amb}}))]^{1/2}. \tag{36}$$

## Experimental Method

To check the validity of the theoretical model, the bubble behavior in boiling of methanol under electrical pulse heating using a thin film heater was observed. The structure of the heater is shown in Fig. 1. The resistance of the heater was 24.3  $\Omega$ . A small glass cell (8 mm  $\times$  12 mm  $\times$  6 mm) of four sides was installed on the substrate. The cell was filled with methanol and covered by a glass plate. The methanol used in the experiment was a commercially available reagent of superior quality grade. The experiment was done under the atmospheric pressure ( $\approx$  100 kPa) and the room temperature ( $\approx$  296 K). A schematic diagram of the experimental apparatus is shown in Fig. 2. The heat pulses were rectangular pulses of constant voltage at the frequency of 1 Hz. Voltage values were chosen so that bubbles were formed for pulse widths of about 5, 10, 20, 50, 100, 200, and 500  $\mu$ s, respectively. For each voltage value, pulse width was adjusted so that the pulse was turned

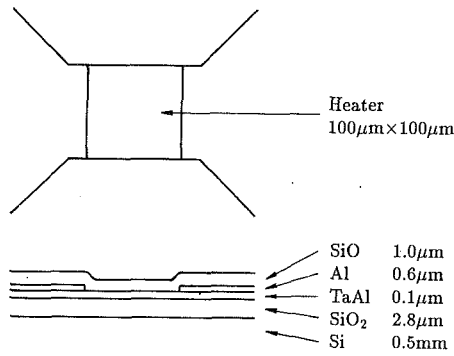


Fig. 1 Structure of the thin film heater: A TaAl resistor, Al electrodes, and an SiO passivation layer are deposited on a surface oxidized Si substrate

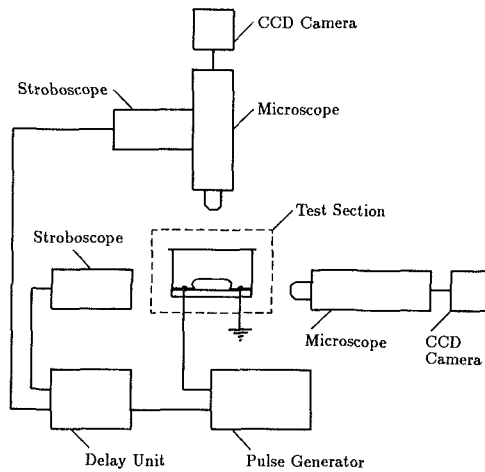


Fig. 2 Schematic diagram of the experimental apparatus

off immediately after the vapor film was formed. Bubbles were observed from top and side by stroboscopic lighting, synchronized to the heating pulse. Bubble shape at any moment can be observed by setting an appropriate delay time to the trigger signal for the stroboscope.

The nucleation probability  $F$  was measured by counting the number of events,  $n$ , when a vapor bubble was formed under 100 observations, for each heating condition. This observation yields the standard deviation of  $(F(1-F)/100)^{1/2}$  for the value of  $F$ . The dependence of  $F$  on the time  $t$  can be measured by changing the pulse width  $\tau$ , since the liquid temperature decreases rapidly after the heat pulse is turned off. The bubble volume was calculated as the volume of an ellipsoid of revolution,  $2\pi(w/2)^2h/3$ , where  $w$  and  $h$  are width and height of the side view of the bubble. This approximation may involve an error of about 20 percent in the equivalent bubble radius, defined by the radius of a hemisphere of equal volume.

The heat flux and the temperature at the heating surface before bubble generation were calculated by solving the three-dimensional heat conduction equation. The thermal properties used in the calculation are shown in Table 1. The values were taken from *JSME Data Book* (JSME, 1986) at 300 K. The thermal conductivity of the SiO passivation layer, which may differ greatly from the bulk value, was assumed to be  $75 \pm 25$  percent of that of quartz glass.

## Results and Discussion

The nucleation probabilities measured for various heating conditions are plotted in Fig. 3, together with the theoretical values calculated by Eq. (11). The physical properties of methanol are taken from *JSME Data Book* (JSME, 1983). The time

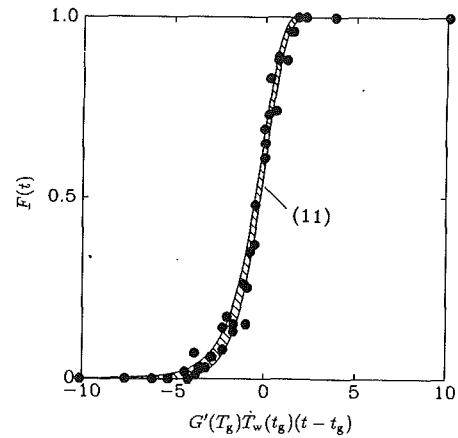


Fig. 3 Nucleation probability  $F$ , as a function of a dimensionless variable  $G'(T_g)\bar{T}_w(t_g)(t-t_g)$

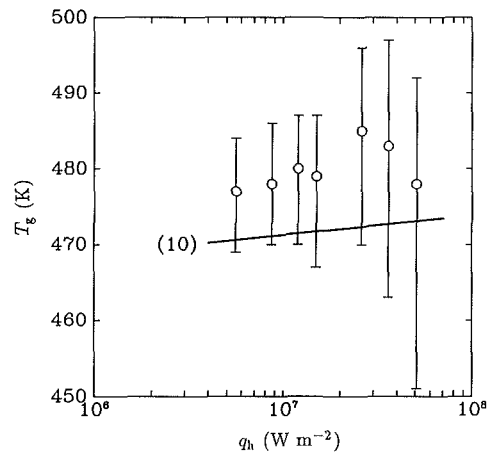


Fig. 4 Nucleation temperature  $T_g$  as a function of heat flux  $q_h$

Table 1 Thermal properties used in the calculation

| Material | Thermal conductivity, $W m^{-1} K^{-1}$ | Specific heat, $J kg^{-1} K^{-1}$ | Density, $kg m^{-3}$ |
|----------|---|-----------------------------------|----------------------|
| Methanol | $2.02 \times 10^{-1}$                   | $2.54 \times 10^3$                | $7.85 \times 10^2$   |
| SiO*     | $1.04 \pm 0.34$                         | $7.4 \times 10^2$                 | $2.19 \times 10^3$   |
| Al       | $2.37 \times 10^2$                      | $9.05 \times 10^2$                | $2.69 \times 10^3$   |
| TaAl†    | $1.44 \times 10^2$                      | $2.38 \times 10^2$                | $9.93 \times 10^3$   |
| SiO2     | 1.38                                    | $7.4 \times 10^2$                 | $2.19 \times 10^3$   |
| Si       | $1.48 \times 10^2$                      | $7.13 \times 10^2$                | $2.33 \times 10^3$   |

\*Estimated from quartz glass.

†Estimated from Ta and Al.

$t_g$  for the experiment is determined so that the experimentally observed  $F(t_g)$  agrees with the theoretical value,  $1 - 1/e$ . Thus the agreement in experimental and theoretical data in Fig. 3 does not mean the absolute agreement on  $t_g$ , but the relative agreement on the dependence of  $F$  on  $t - t_g$ . The shaded area of the theoretical values of  $F$  corresponds to the standard deviation of the measured probability,  $(F(1-F)/100)^{1/2}$ .

The nucleation temperature  $T_g$  for each heat flux, measured as the temperature of the heating surface at  $t = t_g$ , is plotted in Fig. 4, together with the theoretical value of the homogeneous nucleation temperature defined by Eq. (10). Experimental values deviate from the theoretical value by 5 ~ 15 K. Experimental errors come from the uncertainty in the thermal properties, applied voltage, and the resistance of the heater.

Top view photographs of bubbles in the early stage, under various heat fluxes  $q_h$  and pulse widths  $\tau$ , are shown in Fig. 5. As expected from Eqs. (13) and (11), the number of nuclei



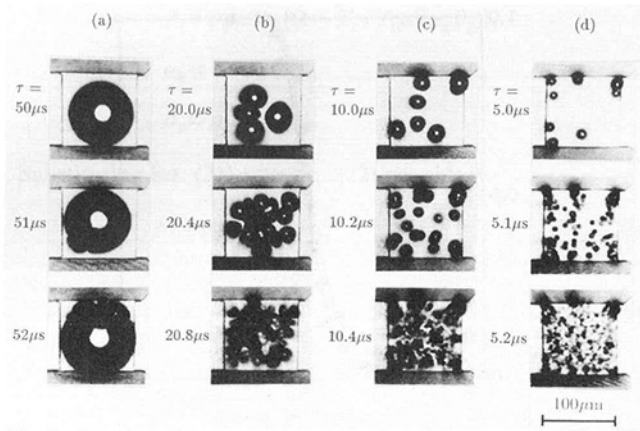


Fig. 5 Top view photographs of bubbles in the early stage: (a)  $q_h = 16 \text{ MW m}^{-2}$ , (b)  $q_h = 25 \text{ MW m}^{-2}$ , (c)  $q_h = 35 \text{ MW m}^{-2}$ , (d)  $q_h = 51 \text{ MW m}^{-2}$ .

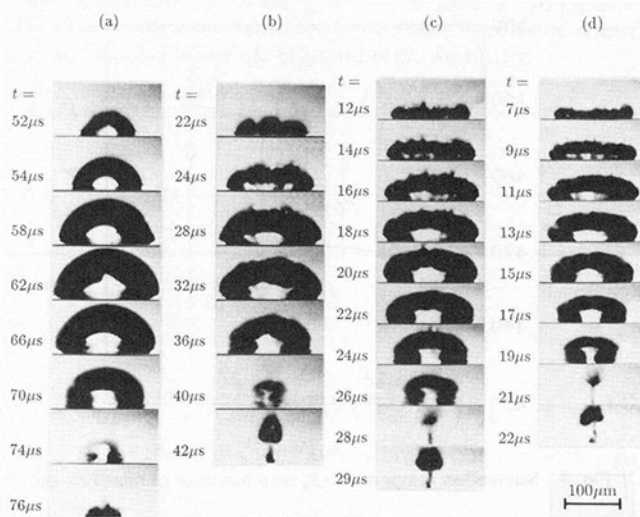


Fig. 6 Side view photographs of bubbles in the later stage: (a)  $q_h = 16 \text{ MW m}^{-2}$ ,  $\tau = 52 \mu\text{s}$ , (b)  $q_h = 25 \text{ MW m}^{-2}$ ,  $\tau = 20.8 \mu\text{s}$ , (c)  $q_h = 35 \text{ MW m}^{-2}$ ,  $\tau = 10.4 \mu\text{s}$ , (d)  $q_h = 51 \text{ MW m}^{-2}$ ,  $\tau = 5.2 \mu\text{s}$ . The origin of time is taken at the beginning of the heat pulse.

increased as the heat flux or the pulse width was increased. Similar bubble behaviors were also observed for ethanol and water. The effect of the heat flux and the pulse width had also been investigated numerically by Asai (1989). It was observed that most nucleation sites changed randomly from event to event although several sites were more likely to be activated than other sites. It is conjectured that these weak sites appeared because vapor or gas is trapped on the surface, or the heat flux or the surface was not uniform.

Side view photographs of bubbles under various heat fluxes are shown in Fig. 6. The shape of the bubble was spheroidal or hemispherical in the case of a higher or lower heat flux, respectively. This is because many nuclei combine into a vapor film in a higher heat flux case and a few nuclei grow before other nucleation sites are activated in a lower heat flux case. The irregularity of the bubble boundary in the early stage of bubble growth is due to the individual growth of nuclei at the initial stage as shown in Fig. 5. As shown in Fig. 6, the bubble expanded again in a mushroom shape after the bubble collapsed in higher heat flux cases. This phenomenon is considered to be the cavitation rebound (Hammitt, 1980). The bubble disappeared before the next heat pulse was applied.

The experimental data of bubble radius versus time for  $q_h = 16, 25, 35,$  and  $51 \text{ MW m}^{-2}$  are plotted in Fig. 7, together with the theoretical curves. The theoretical bubble growth and collapse curves are obtained by solving Eqs. (33) and (35),

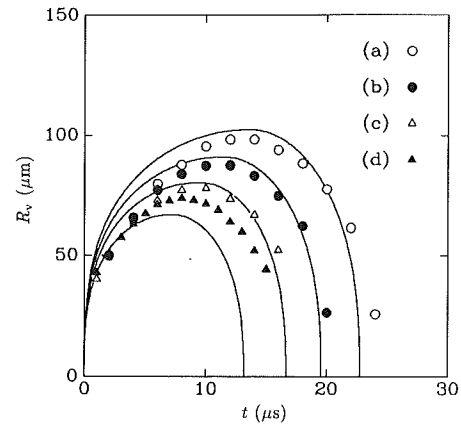


Fig. 7 Bubble radius versus time, compared with the model: (a)  $q_h = 16 \text{ MW m}^{-2}$ ,  $\tau = 52 \mu\text{s}$ , (b)  $q_h = 25 \text{ MW m}^{-2}$ ,  $\tau = 20.8 \mu\text{s}$ , (c)  $q_h = 35 \text{ MW m}^{-2}$ ,  $\tau = 10.4 \mu\text{s}$ , (d)  $q_h = 51 \text{ MW m}^{-2}$ ,  $\tau = 5.2 \mu\text{s}$

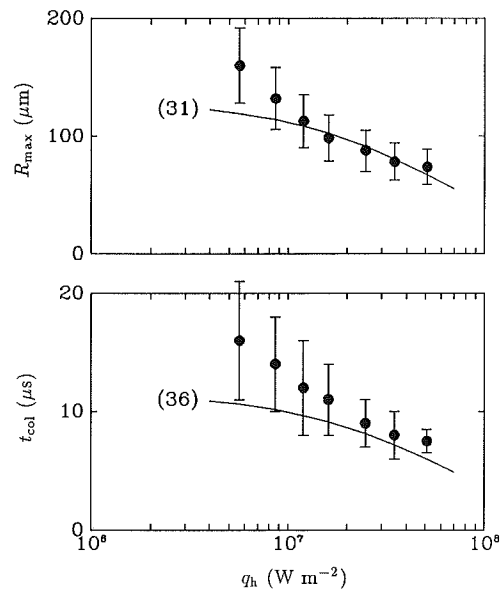


Fig. 8 Maximum bubble radius  $R_{\text{max}}$  and bubble collapse time  $t_{\text{col}}$  as functions of heat flux  $q_h$

respectively. The value of the parameter  $\lambda$  was chosen to 0.6. The theoretical model explains the experimentally observed asymmetry of the bubble behavior in growth and collapse phases.

The maximum equivalent bubble radius and the bubble collapse time under various heat fluxes are plotted in Fig. 8, together with the theoretical curves calculated by Eqs. (31) and (36). The experimental data agree with the model within 20 percent in the region  $q_h > 20 \text{ MW m}^{-2}$ . It is noted that the cases of  $q_h < 20 \text{ MW m}^{-2}$  cannot be treated by the present model because the vapor film is not formed.

The agreement of experimental and theoretical values in Figs. 3 and 4, together with the randomness of the nucleation sites, implies that the dominant bubble generation mechanism is the spontaneous nucleation of liquids due to the thermal fluctuation, described by the homogeneous nucleation theory. The agreement of experimental and theoretical values in Fig. 8 implies that the basic mechanism of bubble growth is the explosive bubble growth under a high-pressure impulse followed by the cavitation bubble collapse, described by the present model.

The present model not only gives a basic understanding of the bubble dynamics in boiling under extremely high heat flux pulse, but also has a practical value in that the bubble dynamics

is reduced to the fluid dynamics of the liquid. That is, the bubble behavior in the later stage is analyzed as fluid dynamics of the liquid, by using the bubble pressure Eq. (27) or (32) as a boundary condition. In some cases, however, the fluid dynamics Eqs. (33) and (35) should be modified. In a bubble jet printer, for example, the bubble grows in a small nozzle, so that the effect of viscosity and surface tension should be considered (Asai et al., 1987).

### Conclusions

The bubble behavior in boiling under extremely high heat flux pulse heating is explained well by the theoretical model. The essence of the model is nucleation in the superheated liquid followed by instantaneous formation of a vapor film, rapid bubble growth due to the pressure impulse, and cavitation bubble collapse.

### Acknowledgments

The author is grateful to Prof. Susumu Kotake, the University of Tokyo, for discussions on the model. He also thanks Atsushi Shiozaki, Isao Kimura, and Tetsuya Kaneko, Canon Inc., for preparing the thin film heater.

### References

- Allen, R. R., Meyer, J. D., and Knight, W. R., 1985, "Thermodynamics and Hydrodynamics of Thermal Ink Jets," *Hewlett-Packard J.*, Vol. 36, No. 5, pp. 21-27.
- Asai, A., Hara, T., and Endo, I., 1987, "One-Dimensional Model of Bubble Growth and Liquid Flow in Bubble Jet Printers," *Jpn. J. Appl. Phys.*, Vol. 26, pp. 1794-1801.
- Asai, A., Hirasawa, S., and Endo, I., 1988, "Bubble Generation Mechanism in the Bubble Jet Recording Process," *J. Imaging Technol.*, Vol. 14, pp. 120-124.
- Asai, A., 1989, "Application of the Nucleation Theory to the Design of Bubble Jet Printers," *Jpn. J. Appl. Phys.*, Vol. 28, pp. 909-915.
- Bankoff, S. G., 1966, "Diffusion-Controlled Bubble Growth," *Adv. Chem. Eng.*, Vol. 6, pp. 1-60.
- Batchelor, G. K., 1967, *An Introduction to Fluid Mechanics*, Cambridge University Press, London, United Kingdom.
- Hammit, F. G., 1980, *Cavitation and Multiphase Flow Phenomena*, McGraw-Hill, New York.
- Hara, T., and Endo, I., 1982, "Bubble Jet Recording," *J. Inst. Image Electron. Engrs. Jpn.*, Vol. 11, pp. 66-71 [in Japanese].
- JSME, 1986, *JSME Data Book: Heat Transfer*, 4th ed., Jpn. Soc. Mech. Engrs., Tokyo [in Japanese].
- JSME, 1983, *JSME Data Book: Thermophysical Properties of Fluids*, Jpn. Soc. Mech. Engrs., Tokyo [in Japanese].
- Olson, H. F., 1957, *Acoustical Engineering*, D. Van Nostrand Company, Inc., London, United Kingdom.
- Rayleigh, Lord, 1917, "On the Pressure Developed in a Liquid During the Collapse of a Spherical Cavity," *Philos. Mag.*, Vol. 34, pp. 94-98.
- Skrpov, V. P., 1974, *Metastable Liquids*, J. Wiley, New York.
- Van Stralen, S., and Cole, R., 1979, *Boiling Phenomena*, Vol. 1, Hemisphere Publishing Corp., Washington, DC.

# Temperature Uniformity Across the Surface in Transition Boiling

Y. Haramura

Associate Professor,  
Department of Mechanical Engineering,  
Kanagawa University,  
Yokohama 221, Japan

The condition under which temperature is kept uniform across the surface in transition boiling is investigated theoretically and numerically. Analysis of three-dimensional heat conduction indicates that an unstable mode emerges depending on the gradient of a boiling curve and dimension and properties of a heater block in steady-state runs. A thinner heated block for the same diameter or larger diameter for the same thickness loses uniformity for a shallower boiling curve in transition boiling. Simulation of a transient run and another analysis indicates that the surface is always kept sufficiently uniform in transient runs without control of heat input. The analysis also reveals the rapid change in the surface temperature in transient runs.

## Introduction

Owing to the development of control techniques, stationary transition boiling can be maintained by controlled electrical heating as reported by Peterson and Zaalouk (1971), Sakurai and Shiotsu (1974), Nakamura et al. (1986), and Haramura (1988, 1990). There have been many studies on transition boiling carried out using transient runs (e.g., Witte and Lienhard, 1982; Bui and Dhir, 1985; Maracy and Winterton, 1988) to obtain information on transition boiling. Because higher heat flux occurs at lower wall temperatures in transition boiling, higher heat flow emanates from cold spots that happen to be formed. This is an unstable situation, which can result in a large temperature gradient along the heating surface. This situation is similar to that reported by Farber and Scorah (1948). They observed simultaneous nucleate and film boiling on different areas of an electrically heated wire. Their apparatus could not have maintained the transition regime in a steady-state manner; in an apparatus that is able to operate in stable transition boiling, such a situation would be mistaken for transition boiling. So it is important to make clear the conditions under which surface temperature may be kept uniform, to avoid such mistakes.

## Analysis for Uniform Surface Temperature Condition

**Assumptions.** To simplify the problem, it is assumed that properties of the heater block are constant at all temperatures and boiling heat flux,  $q$ , is described linearly as

$$q = h(\theta_w - \theta_\infty) \quad (1)$$

with wall temperature  $\theta_w$ , where  $h$  is the slope of the boiling curve (negative in transition boiling), and  $\theta_\infty$  is the temperature at which the extension line of the boiling curve crosses the wall temperature axis (see Fig. 1). A uniform heat flux,  $q_w$ , is applied from the opposite surface. It may be controlled to maintain steady-state transition boiling, and it is adequate to assume it constant, because when the temperature is controlled sufficiently, heat input as well as the temperature settles down.

**Mode Analysis.** Heat conduction is described by the following equation in cylindrical coordinates ( $r, \phi, z$ ):

$$\frac{\partial \theta}{\partial t} = \alpha \left( \frac{\partial^2 \theta}{\partial r^2} + \frac{1}{r} \frac{\partial \theta}{\partial r} + \frac{1}{r^2} \frac{\partial^2 \theta}{\partial \phi^2} + \frac{\partial^2 \theta}{\partial z^2} \right) \quad (2)$$

with boundary conditions:

$$\theta|_{r=0} = \text{finite}, \quad (3)$$

$$\left. \frac{\partial \theta}{\partial r} \right|_{r=R_0} = 0 \quad (4)$$

$$\theta|_{\phi=2\pi} = \theta|_{\phi=0} \quad (5)$$

$$-\lambda \left. \frac{\partial \theta}{\partial z} \right|_{z=-H} = q_w \text{ (const)} \quad (6)$$

$$-\lambda \left. \frac{\partial \theta}{\partial z} \right|_{z=0} = h(\theta|_{z=0} - \theta_\infty) \quad (7)$$

where  $\alpha$  is the thermal diffusivity,  $\lambda$  the thermal conductivity,  $R_0$  the radius, and  $H$  the thickness of the block.

Since the stationary and uniform solution of Eq. (2) is

$$\theta - \theta_\infty = q_w(-z)/\lambda + q_w/h, \quad (8)$$

we can separate the variables as

$$\theta - \theta_\infty = T(t)R(r)\Phi(\phi)Z(z) + q_w(-z)/\lambda + q_w/h \quad (9)$$

and obtain

$$\Phi'' + s^2\Phi = 0 \quad (10)$$

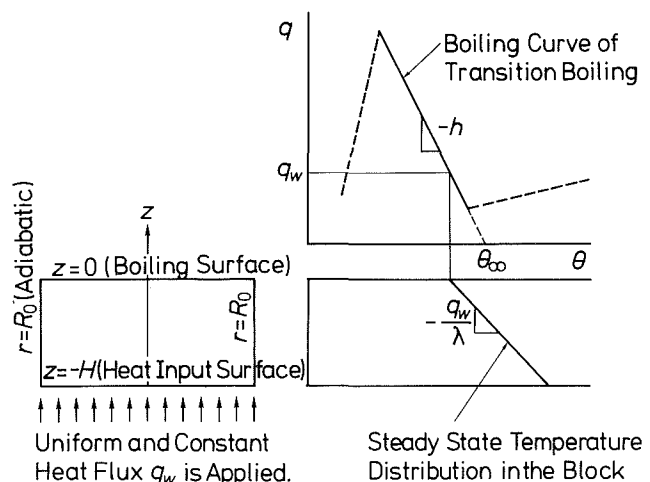


Fig. 1 Diagram of heating block and assumed boiling curve in the analysis

<sup>1</sup>Cyclic heat input (a-c heating) may cause a different kind of problem for a very thin heater block. But it is not necessary to account for this in most cases in which uniform temperature is realized. The only case where the effect should be considered is that for a very small surface (less than 2 mm in diameter).

Contributed by the Heat Transfer Division for publication in the JOURNAL OF HEAT TRANSFER. Manuscript received by the Heat Transfer Division August 7, 1990; revision received March 13, 1991. Keywords: Boiling, Conduction.

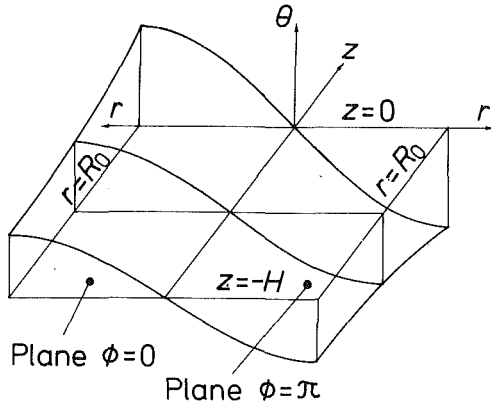


Fig. 2 Temperature profile of the most dangerous mode 1-1-1

$$R'' + \frac{1}{r}R' + \left(k^2 - \frac{s^2}{r^2}\right)R = 0 \quad (11)$$

$$T' - (\beta + i\omega)T = 0 \quad (12)$$

$$Z'' - \left(k^2 + \frac{\beta}{\alpha} + i\frac{\omega}{\alpha}\right)Z = 0 \quad (13)$$

with boundary conditions

$$R(0): \text{finite}, \quad (3')$$

$$R'(R_0) = 0, \quad (4')$$

$$\Phi(2\pi) = \Phi(0), \quad (5')$$

$$Z'(-H) = 0, \quad (6')$$

$$Z'(0) + \frac{h}{\lambda}Z(0) = 0. \quad (7')$$

Because of boundary condition (5')  $\Phi$  must be sinusoidal and  $s$  must be an integer. The solution of Eq. (11) with boundary conditions (3') and (4') must be a Bessel function  $J_s(k_{sj}r)$ , where  $k_{sj}$  is the  $j$ th smallest positive solution that satisfies

$$J'_s(k_{sj}R_0) = 0. \quad (14)$$

Let the coefficients in Eq. (13) be replaced by real constants  $\gamma$  and  $m$  as

$$k^2 + \frac{\beta}{\alpha} + i\frac{\omega}{\alpha} = (\gamma + im)^2. \quad (15)$$

To satisfy boundary conditions (6') and (7'),  $\gamma$  and  $m$  must satisfy the characteristic equation:

$$(\gamma + im)\{e^{(\gamma+im)H} - e^{-(\gamma+im)H}\} + \frac{h}{\lambda}\{e^{(\gamma+im)H} + e^{-(\gamma+im)H}\} = 0 \quad (16)$$

The solutions for negative  $h$  are as follows:

$$\gamma H \tanh(\gamma H) = -hH/\gamma, \quad m = 0 \quad (17)$$

$$\gamma = 0, \quad mH \tan(mH) = -hH/\lambda \quad (18)$$

Once  $h$  is given,  $\gamma_l$  and  $m_l$  are determined by Eqs. (17) and

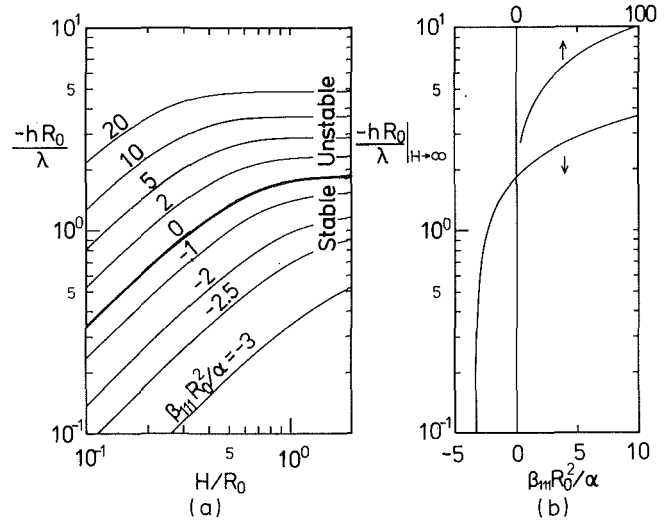


Fig. 3 Growth rate of the most dangerous disturbance mode of temperature

(18) ( $l$  denotes the  $l$ th axial mode) and the temperature disturbance growth rate  $\beta_{sjl}$  is determined by

$$\beta_{sjl} = \alpha(\gamma_l^2 - m_l^2 - k_{sj}^2) \quad (19)$$

for each mode of  $s$  (circumferential mode) and  $j$  (radial mode). The solutions other than that of Eq. (17) are not important here because they always give stable modes. To keep the surface temperature uniform, all of the  $\beta_{sjl}$ 's must be negative. This condition implies that  $k_{11}$ , which is the smallest  $k_{sj}$  of all, is larger than the value of  $\gamma_l$  given by Eq. (17). Since  $k_{11} = 1.841/R_0$  ( $k_{sj}R_0$ 's satisfy Eq. (14)), the condition is written as

$$\gamma R_0 < 1.841 \quad (20)$$

$$\gamma H \tanh(\gamma H) = -hH/\lambda \quad (21)$$

These two equations give the stable condition of the most dangerous mode 1-1-1 illustrated in Fig. 2.

#### Growth Rate of the Most Dangerous Mode 1-1-1.

Equations (20) and (21) tell us the following about the uniformity:

(A) For a thin block ( $\tanh(\gamma H) \approx \gamma H$ ), the condition necessary to keep the surface temperature uniform is given by

$$-h < 3.390 \frac{H}{R_0} \cdot \frac{\lambda}{R_0} \quad (22)$$

which means that the thicker block of constant diameter, or the smaller diameter block of constant thickness, makes for uniform temperature on the boiling face.

(B) For a sufficiently thick block ( $\tanh(\gamma H) \approx 1$ ), the condition is

$$-h < 1.841 \frac{\lambda}{R_0} \quad (23)$$

### Nomenclature

$c_p$  = specific heat, J kg<sup>-1</sup> K<sup>-1</sup>  
 $H$  = thickness of the heated block, m  
 $h$  = slope of boiling curve, W m<sup>-2</sup> K<sup>-1</sup>  
 $i$  = the imaginary unit  
 $k$  = wavenumber, m<sup>-1</sup>  
 $m$  = parameter defined in Eq. (15), m<sup>-1</sup>  
 $q$  = heat flux, W m<sup>-2</sup>

$R_0$  = radius of the heated block, m  
 $r$  = radial coordinate, m  
 $z$  = axial coordinate, m  
 $\alpha$  = thermal diffusivity, m<sup>2</sup> s<sup>-1</sup>  
 $\beta$  = temperature disturbance growth rate, s<sup>-1</sup>  
 $\gamma$  = parameter defined in Eq. (15), m<sup>-1</sup>  
 $\xi$  = temperature change rate, s<sup>-1</sup>

$\phi$  = circumferential coordinate  
 $\theta$  = temperature, K  
 $\lambda$  = thermal conductivity, W m<sup>-1</sup> K<sup>-1</sup>  
 $\rho$  = density, kg m<sup>-3</sup>

#### Subscripts

$j$  = radial mode  
 $l$  = axial mode  
 $s$  = circumferential mode

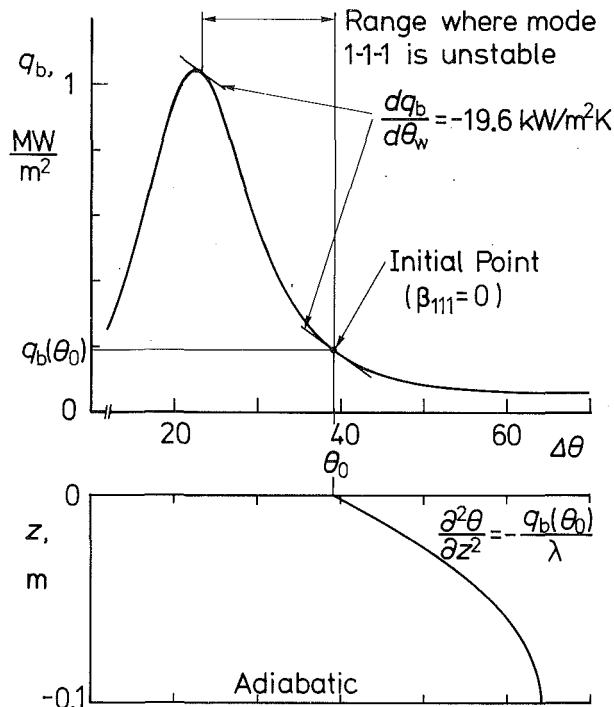


Fig. 4 Initial temperature distribution in the simulation

Thickness does not affect the limitation any more if  $H$  is thicker than  $R_0$ .

Figure 3(a) shows the limitation of  $h$  for a given  $H/R_0$ . When  $-h$  is in the area under the thick curve indicated by the equation  $\beta_{111}R_0^2/\alpha = 0$ , the heated surface is kept uniform. On the other hand, when  $-h$  is above the curve, hot or cold spots tend to grow. Steady-state runs should therefore be carried out under the condition where  $-h$  is under the curve. It is sufficient that transient runs be performed under the condition that the growth time constant,  $1/\beta_{111}$ , is sufficiently long compared to the period in which transition boiling takes place. Figure 3(b) refers to the limiting case of an infinitely thick block, which gives the largest  $-h$  for a given  $R_0$ . Figure 3(b) can be used for interpolation in Fig. 3(a).

### Simulation of a Transient Run

The analysis indicates that temperature disturbances grow or decay depending on the slope of the boiling curve, and the dimensions and material of the heated block. So it seems that if the growth time constant,  $1/\beta_{111}$ , is much smaller than the transition boiling period in a transient run, temperature disturbances will grow and a large temperature gradient will appear across the surface. Therefore, a simulation of a transient run is carried out to examine whether this is true, for a block with large thermal mass.

**Method of Simulation.** The boiling curve is assumed to be described by the equation

$$q_b = 750(\Delta\theta) + \frac{150(\Delta\theta)^3}{1 \times 10^{-11}(\Delta\theta)^8 + 1} \quad (24)$$

simulating saturation boiling of water at atmospheric pressure, where the heat flux,  $q_b$ , is measured in  $W/m^2$ , wall superheat,  $\Delta\theta = \theta_w - \theta_{sat}$ , in K. The heated block is a copper block, adiabatic on the opposite surface. The diameter of the block is 75 mm and thickness 100 mm. The initial temperature distribution is a superposition of the following two:

(A) Temperature distribution when surface temperature is  $\theta_0$ , while the block is cooling at constant rate given by  $q_b(\theta_0)$ , where  $\theta_0$  is the temperature at which the gradient of boiling

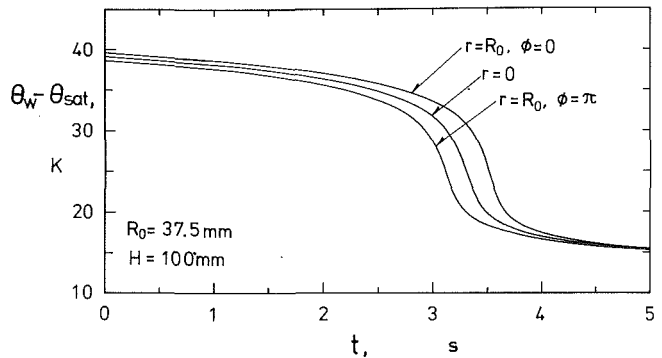


Fig. 5 Cooling curve of the simulation

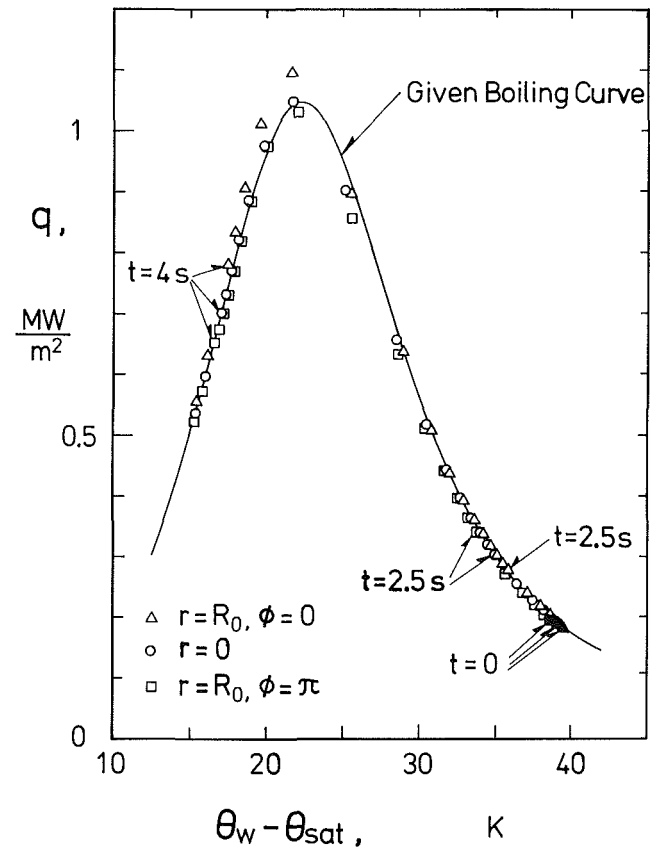


Fig. 6 Boiling curve of the simulation

curve makes the growth rate,  $\beta_{111}$ , zero near the film boiling regime (see Fig. 4).

(B) Temperature distribution of mode 1-1-1 (see Fig. 2) with 0.5 K amplitude (at two opposing points,  $\phi = 0$  and  $\phi = \pi$ , on the periphery of the boiling surface).

The temperature distribution of (A) makes the conclusion clear because the distribution does not change relatively in position, only decreasing at a constant rate. Modes other than 1-1-1 decay. So, it is sufficient to take only mode 1-1-1 into account.

The simulation is divided into two steps. The first is the calculation of the temperature change in the block using a finite difference method. Here the values of node spacing  $\Delta r$ ,  $\Delta\phi$ ,  $\Delta z$ , and  $\Delta t$  were taken to be 2.5 mm, 15 deg, 2.5 mm, and 0.05 s, respectively, and a central difference was taken for all variables. The calculation error was found to be less than 0.05 K based on comparison of results for different  $\Delta r$ ,  $\Delta\phi$ ,  $\Delta z$ , and  $\Delta t$ .

The second step is the calculation of wall superheat and wall heat flux. The temperatures at two points given by the previous

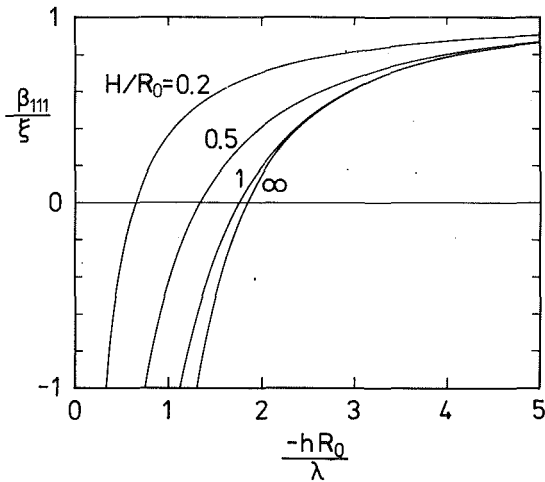


Fig. 7 Ratio of temperature disturbance growing rate to temperature changing rate

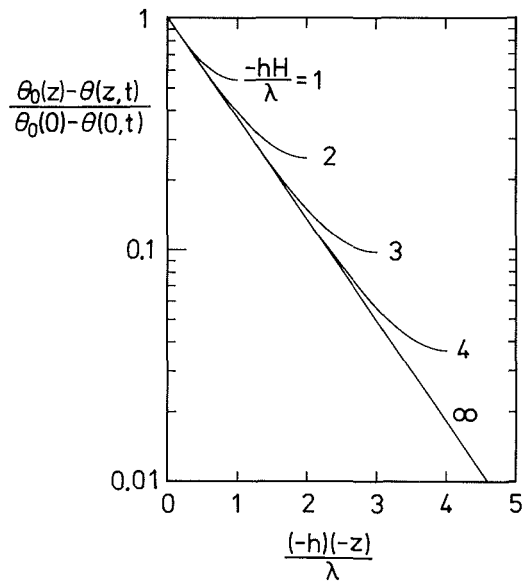


Fig. 8 Influence of the surface temperature on the temperature in a heater block in transition boiling

step are used as boundary conditions. Depths of two points at which temperatures are given are selected as 2.5 mm and 20 mm; the  $\Delta z$  and  $\Delta t$  are taken as 2.5 mm and 0.1 s, respectively. One-dimensional heat flow is assumed and the implicit method is taken. Errors in prediction must be less than 0.2 K.

**Results.** Figure 5 is the cooling curve obtained from this simulation. Wall superheats at three points (two of them are at the periphery and the other is at the center) are shown. As superheat decreases, the slope of boiling curve becomes steeper, so the amplitude of the mode increases with time until transition boiling disappears. In the nucleate boiling regime even the most dangerous mode is stable and decays rapidly. It should be noted that if the block is cooled at a uniform rate throughout, the cooling rate would be  $q/(\rho c_p H)$ , which is calculated to be less than 3 K/s. The cooling rate of the simulation is ten times greater than this.

The boiling curve, the relationship between superheat and heat flux at a given time and location, is shown in Fig. 6. The three different symbols represent location. They are plotted every 0.5 s between  $t=0$  s and  $t=5$  s except between  $t=2.5$  s and  $t=4$  s where they are plotted every 0.1 s. The full line represents the given boiling curve. It has a much steeper slope in transition boiling than those obtained through any transient

studies for saturated liquid. In spite of this fact, an accurate enough boiling curve is obtained assuming one-dimensional heat flow at all points. This is caused by the rapid decrease in wall temperature, which results in insufficient time for growth of temperature disturbance.

### Surface Cooling Rate in Transient Transition Boiling

As mentioned above, surface temperature decreases rapidly in transient transition boiling even for a large thermal mass. Therefore, when discussing the uniformity in transient runs, the actual cooling rate must be known.

One-dimensional heat conduction is described by the basic equation

$$\frac{\partial \theta}{\partial t} = \alpha \frac{\partial^2 \theta}{\partial z^2} \quad (25)$$

with boundary conditions

$$-\lambda \frac{\partial \theta}{\partial z} = q_w \quad \text{for } z = -H \text{ (heat input surface)} \quad (26)$$

$$-\lambda \frac{\partial \theta}{\partial z} = h(\theta - \theta_\infty) \quad \text{for } z = 0 \text{ (boiling surface)}. \quad (27)$$

A linear boiling curve given by Eq. (1) as well as negative  $h$  in transition boiling are assumed again. The initial condition is selected as

$$\theta = \theta_\infty - \frac{q_w}{(-h)} + \frac{q_w}{\lambda} (-z) - \theta_1 \cdot f(z) \quad (28)$$

which describes a small temperature shift  $\theta_1$  from the temperature distribution prevailing for steady-state conduction of heat flux  $q_w$ .  $f(z)$ , a function of  $z$ , is determined to be an eigenfunction. Then we obtain the solution

$$\theta - \theta_0(z) = -\theta_1 e^{\xi t} \cosh \left( \sqrt{\frac{\xi}{\alpha}} (H+z) \right) \quad (29)$$

where

$$\left( \sqrt{\frac{\xi}{\alpha}} H \right) \tanh \left( \sqrt{\frac{\xi}{\alpha}} H \right) = \frac{-hH}{\lambda} \quad (30)$$

$$\theta_0(z) = \theta_\infty + \frac{q_w}{h} - \frac{q_w}{\lambda} z \quad (31)$$

Equation (30) denotes only one unstable mode, and the other modes give negative  $\xi$ . In the case of a transient cooling,  $\theta_1$  is positive, and for a transient heating  $\theta_1$  is negative. In either case, surface temperature changes exponentially with time according to the growth rate  $\xi$ .

For  $h = -70$  kW/m<sup>2</sup>K,  $\xi$  is calculated to be  $3 \text{ s}^{-1}$ . Since  $d\theta/dt$  equals  $\xi(\theta - \theta_0)$  at any fixed point, and  $\theta - \theta_0$  on the boiling surface ( $z=0$ ) will be the order of 10 K at the latest period of transition boiling, the maximum rate of decrease of temperature, in the case simulated in the previous section, will be about 30 K/s, which agrees with the result of the simulation. The ratio of  $\beta_{111}$  to  $\xi$  shown in Fig. 7 indicates that  $\beta_{111}$  is always smaller than  $\xi$ . Therefore, there cannot be enough time for growth of any temperature disturbance in transient transition boiling without control of input heat flux.

When solving inverse heat conduction problems using measured temperatures, results may be affected by measurement errors. This is caused by shallow temperature penetration depth as shown in Fig. 8. The curves represent  $\theta$  given by Eq. (29).  $\theta_0(0) - \theta(0, t)$  is of the order of 10 K at the end of a transition boiling period and errors in temperature measurement are at least 0.1 K. The ratio of measurement error to actual change in temperature at the measuring point,  $\theta_0(z) - \theta(z, t)$ , gives the relative error of surface temperature and heat flux. If 10 per-

cent error is allowed, the depth of the shallower measuring point,  $z_1$ , must satisfy

$$\frac{(-h)(-z_1)}{\lambda} < 2 \quad (32)$$

and the shallower, the better for accurate calculation. If  $h$  obtained by solving inverse problem does not satisfy Eq. (32), the results are meaningless. They do not represent heat transfer characteristics, but represent the limitations of the system.

### Conclusion

The condition under which temperature is kept uniform across a surface in transition boiling has been studied.

The condition for steady-state runs is described in which the most dangerous mode of the three-dimensional heat conduction equation is attenuated, which results in Eq. (20) with Eq. (21). This condition must be satisfied in steady-state experiments. The ratio of thickness to diameter of a heater block directly affects the criterion of the stability for a thin block as described with Eq. (22). Its limitation is represented by Eq. (23), and corresponds to increasing the thickness of the block up to approximately the radius of the block.

Simulation of a transient run and analysis of one-dimensional heat conduction have been carried out to reveal the condition for transient runs. The simulation indicates that nonuniform temperature distribution across the surface causes only a negligible effect on wall superheat and wall heat flux calculated from inside temperatures assuming one-dimensional

heat flow in a transient run. The analysis indicates that there cannot be enough time for growth of even the most dangerous mode. Therefore, the boiling surface is kept sufficiently uniform in any transient runs without control of heat input. They also indicate that the surface temperature changes rapidly in transition boiling.

### References

- Bui, T. D., and Dhir, V. K., 1985, "Transition Boiling Heat Transfer on a Vertical Surface," *ASME JOURNAL OF HEAT TRANSFER*, Vol. 107, pp. 756-763.
- Farber, E. A., and Scoria, R. L., 1948, "Heat Transfer to Water Boiling Under Pressure," *Transactions of the ASME*, Vol. 70, pp. 369-384.
- Haramura, Y., 1988, "Heat Transfer Characteristics of Steady State Transition Boiling on a Horizontal Plate," *Proceedings, 25th National Heat Transfer Symposium of Japan*, pp. 271-273.
- Haramura, Y., 1990, "Heat Transfer Characteristics of Transition Boiling on a Horizontal Plate," *Proceedings, 27th National Heat Transfer Symposium of Japan*, pp. 328-330.
- Maracy, M., and Winterton, R. H. S., 1988, "Hysteresis and Contact Angle Effects in Transition Boiling of Water," *Int. J. Heat Mass Transfer*, Vol. 31, pp. 1443-1449.
- Nakamura, S., Kuroda, M., and Matushima, T., 1986, "Feedforward Temperature Control of Heating Surfaces for Boiling Experiment (1st Report, Basic Study)," *Transactions of the Japan Society of Mechanical Engineers*, Vol. 52, pp. 3293-3299.
- Peterson, W. C., and Zaalouk, M. G., 1971, "Boiling Curve Measurements From a Controlled Heat Transfer Process," *ASME JOURNAL OF HEAT TRANSFER*, Vol. 93, pp. 408-412.
- Sakurai, A., and Shiotsu, M., 1974, "Temperature-Controlled Pool-Boiling Heat Transfer," *Proceedings, 5th International Heat Transfer Conference*, Vol. 4, B3.1, pp. 81-85.
- Witte, L. C., and Lienhard, J. H., 1982, "On the Existence of Two 'Transition' Boiling Curves," *Int. J. Heat Mass Transfer*, Vol. 25, pp. 771-779.

# Vapor Dynamics of Heat Pipe Start-Up

F. Issacci

Assoc. Mem. ASME

I. Catton

Fellow ASME

N. M. Ghoniem

Professor.

Mechanical, Aerospace,  
and Nuclear Engineering,  
University of California—Los Angeles,  
Los Angeles, CA 90024-1509

*Vapor dynamics of heat pipes during the start-up phase of operation is analyzed. The vapor flow is modeled by a two-dimensional, compressible viscous flow in an enclosure with inflow and outflow boundary conditions. For high-input heat fluxes, a compression wave is created in the evaporator early in the operation. A nonlinear filtering technique, along with the centered difference scheme, is used to capture the shocklike wave and overcome the cell Reynolds number problem. Multiple wave reflections are observed in the evaporation and adiabatic regions. These wave reflections cause a significant increase in the local pressure and flow circulations, which grow with time. It is shown that the maximum and maximum-averaged pressure drops oscillate periodically because of the wave reflections. Although the pressure drops converge to a constant value at steady state, they are significantly higher than their steady-state value at the initiation of the process. The time for the vapor core to reach a steady-state condition was found to be on the order of seconds.*

## Introduction

The behavior of vapor flow during the start-up phase of heat pipe operation has been analyzed in order to examine the flow patterns for low and high-input heat fluxes. Here, start-up is the process through which the heat pipe starts its operation from a static condition and arrives at steady-state operation. The response of the vapor flow may be an important design issue in dynamic thermal systems where a heat pipe is used to transfer heat following sudden increases in the heat load. The importance of the transient phase, of course, depends on many factors not considered here.

During a start-up, the working fluid of a heat pipe may initially be very cold or frozen in the wick. Here, the liquid is assumed to be very cold and the vapor, which is thermodynamically in equilibrium with the liquid, is at very low pressure. The vapor core response to a sudden-input heat flux or a sudden change in the condenser temperature is the primary focus of this work.

The vapor flow in heat pipes is a complicated problem because of the nonlinear nature of the describing equations and because of the inflow and outflow boundaries in the evaporator and condenser. Different approaches have been used to simplify the problem. In most previous work, the vapor flow is analyzed under steady-state conditions as a one-dimensional (1D) flow (e.g., Edwards and Marcus, 1971) and a 2D flow (Tien and Rohani, 1974; Faghri, 1986; Faghri et al., 1989; Peterson and Tien, 1987). In studies of the dynamic behavior of heat pipes, the vapor flow is modeled either as a quasi-steady flow (Jang et al., 1989) or as a 1D transient vapor flow along with friction coefficients approximated from a steady-state 2D model (Bowman, 1987). It has been shown by steady-state 2D analysis that the 1D vapor-flow model is not able accurately to predict the axial heat and mass transfer and pressure drop (Bankston and Smith, 1973). Furthermore, 2D steady-state studies indicate that flow reversal takes place in the condensation section under high heat flux (Issacci et al., 1989). It is, therefore, important to establish the conditions for this mode during transient operations.

In a theoretical study using a 1D transient model, Bystrov and Goncharov (1983) showed that the time steps in the numerical calculations that are necessary to satisfy stability re-

quirements are small (order of  $10^{-7}$  s). The numerical scheme used in this work is fully implicit, which allows larger time steps (up to order of  $10^{-2}$  s). The vapor dynamics of heat pipes was also studied by Issacci et al. (1989) using a 2D transient model with the SIMPLER method (Patankar, 1980). The primary advantage of SIMPLER is the staggered grid, which makes the numerical scheme stable and, consequently, the computational time low. Although this method yielded interesting results, the resulting computational code was limited to low-compressibility flows. However, in the start-up mode of a heat pipe, there are regions of high as well as low compressibility. Existing numerical codes for highly compressible flows, on the other hand, are only able to handle steady-state conditions because of their small allowable time steps and, furthermore, they are not stable for low-Mach-number problems.

Several theoretical studies have recently been carried out to model heat pipes at start-up from the frozen state (Bowman et al., 1990; Chow and Zhong, 1990; Hall and Doster, 1988, 1990; Jang et al., 1989; Rao et al., 1990). In these different approaches, the vapor core has been modeled as a 1D quasi-steady or 1D unsteady state flow.

As can be seen, the past 2D studies were limited to incompressible flows and compressible flow studies were limited to 1D. At UCLA, the study of dynamic behavior of heat pipes began by analyzing the liquid and vapor phases separately (Roche, 1988; Issacci et al., 1988). The objective was to develop very detailed computer codes for each phase and then to combine them in a comprehensive code. Roche (1988) developed a numerical code for the liquid phase in the start-up mode with the vapor phase assumed to be at a constant temperature and pressure. He used a kinetic theory approach to model the phase change at the liquid-vapor interface.

The objective of this work is to investigate thoroughly the dynamic behavior of the vapor flow in heat pipes during the start-up phase of its operation. Efforts have been directed toward understanding of the vapor flow patterns under very low pressure and high input heat flux conditions. In heat pipes under the transient mode of operations, the vapor flow is the most complicated process. A simple model of this phase is, however, needed for a fast computer code. A simple and accurate model would only be achievable if the complete vapor process was understood in detail. The studies carried out in this paper are aimed at this understanding.

The fully compressible describing equations of the vapor flow are numerically solved using a transient 2D model. The

Contributed by the Heat Transfer Division for publication in the JOURNAL OF HEAT TRANSFER. Manuscript received by the Heat Transfer Division March 27, 1990; revision received March 8, 1991. Keywords: Heat Pipes and Thermosyphons, Numerical Methods, Transient and Unsteady Heat Transfer.



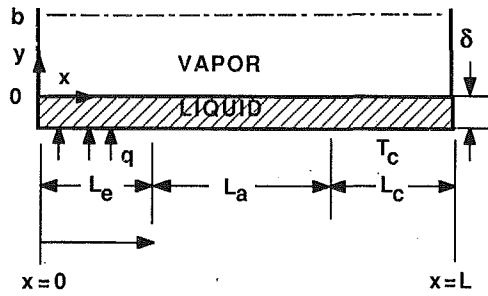


Fig. 1 Vapor flow model in a heat pipe

numerical scheme is fully implicit using a staggered grid, and it is stable for all Mach numbers between zero and one, a suitable range for the start-up transient mode. The effect of wall and wick structure is not included here. As mentioned above, the main concern is the detailed study of vapor phase to be coupled later to other phases in the heat pipe. The transient characteristics of the wall and wick structure affect the vapor flow patterns. However, the results of the vapor phase study will help significantly in the complete model of heat pipes.

## 2 Describing Equations

Vapor flow in the heat pipe core is modeled as channel flow, as is shown in Fig. 1. The bottom boundary of the channel is a thin porous medium, which contains the liquid. The input heat flux to the evaporator and the temperature of the outer surface of the condenser are specified. The planar side walls are assumed adiabatic.

The equations describing the vapor flow are the continuity, momentum, and energy equations, which are time dependent, viscous, and compressible. An equation of state (EOS) is used to relate pressure, density, and temperature within the vapor core. These equations in Cartesian coordinates  $(x, y)$  are

*Continuity*

$$\frac{\partial \rho}{\partial t} + \frac{\partial(\rho u)}{\partial x} + \frac{\partial(\rho v)}{\partial y} = 0 \quad (1)$$

*x Momentum*

$$\begin{aligned} \frac{\partial(\rho u)}{\partial t} + \frac{\partial(\rho u u)}{\partial x} + \frac{\partial(\rho u v)}{\partial y} = & \\ & - \frac{\partial p}{\partial x} + \frac{\partial}{\partial x} \left( \mu \frac{\partial u}{\partial x} \right) + \frac{\partial}{\partial y} \left( \mu \frac{\partial u}{\partial y} \right) \\ & + \left[ \frac{\partial}{\partial x} \left( \mu \frac{\partial u}{\partial x} \right) + \frac{\partial}{\partial y} \left( \mu \frac{\partial v}{\partial x} \right) - \frac{2}{3} \frac{\partial}{\partial x} \left( \mu \frac{\partial u}{\partial x} + \mu \frac{\partial v}{\partial y} \right) \right] \end{aligned} \quad (2)$$

*y Momentum*

$$\begin{aligned} \frac{\partial(\rho v)}{\partial t} + \frac{\partial(\rho u v)}{\partial x} + \frac{\partial(\rho v v)}{\partial y} = & \\ & - \frac{\partial p}{\partial y} + \frac{\partial}{\partial x} \left( \mu \frac{\partial v}{\partial x} \right) + \frac{\partial}{\partial y} \left( \mu \frac{\partial v}{\partial y} \right) \\ & + \left[ \frac{\partial}{\partial x} \left( \mu \frac{\partial u}{\partial y} \right) + \frac{\partial}{\partial y} \left( \mu \frac{\partial v}{\partial y} \right) - \frac{2}{3} \frac{\partial}{\partial y} \left( \mu \frac{\partial u}{\partial x} + \mu \frac{\partial v}{\partial y} \right) \right] \end{aligned} \quad (3)$$

*Energy*

$$\begin{aligned} C_p \left[ \frac{\partial(\rho T)}{\partial t} + \frac{\partial(\rho u T)}{\partial x} + \frac{\partial(\rho v T)}{\partial y} \right] = \frac{\partial p}{\partial t} + & \\ & u \frac{\partial p}{\partial x} + v \frac{\partial p}{\partial y} + \frac{\partial}{\partial x} \left( k \frac{\partial T}{\partial x} \right) \\ & + \frac{\partial}{\partial y} \left( k \frac{\partial T}{\partial y} \right) + \mu \left[ 2 \left( \frac{\partial u}{\partial x} \right)^2 + 2 \left( \frac{\partial v}{\partial y} \right)^2 + \left( \frac{\partial u}{\partial y} + \frac{\partial v}{\partial x} \right)^2 \right] \end{aligned} \quad (4)$$

*EOS*

$$p = \rho R T \quad (5)$$

Here, the vapor flow is assumed to be a perfect gas; however, Eq. (5) can be replaced by a more realistic EOS with no major difficulty in calculations.

**2.1 Initial and Boundary Conditions.** The working liquid is assumed initially to be at a low temperature (close to the freezing point). Further, there is no input heat and the stagnant vapor is in thermodynamic equilibrium with the liquid. The boundaries of the vapor core are shown in Fig. 1. A no-slip and impermeable condition for the velocity and an adiabatic condition for the temperature are assumed on the side walls, i.e., at  $x = 0$  and  $x = L$  as

$$u = 0, \quad v = 0, \quad \partial T / \partial x = 0 \quad (6)$$

On the centerline the symmetry condition implies, at  $y = b$ ,

$$\partial u / \partial y = 0, \quad v = 0, \quad \partial T / \partial y = 0 \quad (7)$$

The boundary conditions at the liquid-vapor interface are the challenging ones. The liquid flow is assumed to be in a porous medium of thickness  $\delta$ , which is much smaller than the vapor core thickness  $b$ . The axial velocity is assumed zero on this boundary, i.e., at  $y = 0$ ,

$$u = 0 \quad (8)$$

To assign boundary conditions for the temperature and vertical velocity, the liquid-vapor interface is divided into three regions. In the evaporation zone the input flux,  $\dot{q}''$ , is a given parameter and the input flow is approximated at  $y = 0$  and  $0 < x \leq L_e$  by

$$\rho v = \dot{m}'' \approx \dot{q}'' / h_{fg}(T), \quad T = T_{\text{sat}}(p) \quad (9)$$

where  $h_{fg}$  is the heat of vaporization and  $\dot{m}''$  is the input mass

## Nomenclature

$b$  = channel width

$C_p$  = specific heat

$h_{fg}$  = latent heat

$k$  = thermal conductivity

$L$  = heat pipe length

$L_a$  = adiabatic section length

$L_c$  = condenser length

$L_e$  = evaporator length

$\dot{m}''$  = mass flux

$N_x$  = number of grid points in  $x$  direction

$N_y$  = number of grid points in  $y$  direction

$p$  = pressure

$\dot{q}''$  = input heat flux

$R$  = gas constant

$Re$  = Reynolds number

$T$  = temperature

$t$  = time

$u$  = axial velocity

$v$  = vertical velocity

$x$  = axial coordinate

$y$  = vertical coordinate

$\delta$  = liquid layer thickness

$\Delta t$  = time increment

$\lambda$  = constant factor

$\mu$  = viscosity

$\rho$  = density

$\phi$  = general dependent variable

$\phi^r$  = referenced value of  $\phi$

### Subscripts

$c$  = condenser

$eff$  = effective

$o$  = initial value

$sat$  = saturation

flux. Conduction in the liquid layer is neglected. It should be noted that this boundary condition ignores the thermal characteristics of the heat pipe wall and the working fluid-wick layer. The temperature is assumed to be the saturation temperature  $T_{\text{sat}}(p)$  of the liquid corresponding to the interface pressure. In the adiabatic zone, the boundary conditions at  $y = 0$  and  $L_e < x \leq (L_e + L_a)$  are

$$v = 0, \quad \partial T / \partial y = 0 \quad (10)$$

In the condensation zone the temperature  $T_c$  of the outer surface is given.  $T_c$  could well vary with time, as it is usually related to the ambient temperature by convection and/or radiation heat transfer. Here,  $T_c$  is assumed fixed, which is the equivalent to assuming very good heat transfer to the surroundings. By equating the heat of evaporation to the heat conduction in the liquid layer, the outflow from this region is approximated at  $y = 0$  and  $(L_e + L_a) < x \leq L$ , by

$$\rho v = \dot{m}'' \approx - \frac{k_{\text{eff}}}{\delta} \left( \frac{T - T_c}{h_{fg}(T)} \right), \quad T = T_{\text{sat}}(p) \quad (11)$$

where  $k_{\text{eff}}$  is the effective conductivity of the liquid layer and the temperature is assumed to be the saturation temperature corresponding to the pressure at the interface. This neglects transient conduction in the fluid layer, which may be an important contribution to the process.

### 3 Solution Method

The five describing Eqs. (1)–(5), with the initial and boundary conditions given by Eqs. (6)–(11), have been numerically solved for the five variables  $\rho$ ,  $\rho u$ ,  $\rho v$ ,  $T$ , and  $p$ . A finite-difference method has been used with backward Euler discretization in time and centered differences in space. Dealing with a wide range of input heat fluxes, the method deals effectively with the cell Reynolds number problem as well as shock-capturing complexity. Discretization of the advective terms in this problem plays a significant role. The centered-difference scheme (CDS) is ill-behaved for grid Reynolds numbers larger than two because the coefficients of the difference equations are not necessarily positive. As a consequence, solutions to the difference equations may not be unique, resulting in non-physical spatial oscillations. In a study of the 1D forms of the describing Eqs. (1)–(5) by Issacci et al. (1990b), standard methods such as upwinding and power law and a more recent scheme, CONDIF, were examined. It was shown that these schemes are well-behaved but that they cause oscillations and overshoot at high compressibility and, except for CONDIF, they cause numerical diffusion at low compressibility as well. The CONDIF scheme was used by Issacci et al. (1990a) in a study of the start-up transient process in heat pipes. It was shown that for input heat fluxes greater than  $1 \text{ kW/m}^2$  in an Na-filled heat pipe, a shocklike wave is created in the evaporation region. Therefore, the CONDIF scheme was found to be unsuitable for shock capturing.

Recently developed methods for shock capturing that use field-by-field decomposition and flux limiting, e.g., Harten (1983) or Chakravarthy and Osher (1982), are able to capture a sharp discontinuity without oscillations. However, these methods are complicated and are not numerically efficient. Different filters have also been used in shock capturing; cf. Harten and Zwas (1972). The major problem in filtering is the low accuracy and smearing of the shock front. Recently, Engquist et al., (1989) proposed a nonlinear filter to capture accurately a shock without oscillations. The algorithms for this filtering are simple to implement and are more efficient than earlier methods with comparable abilities.

A filtering technique, based on the concept introduced by Engquist et al. (1989), was used in a study of 1D compressible vapor dynamics by Issacci et al. (1990b). It was shown that CDS used with nonlinear filtering yields a second-order, stable

solution in cell Reynolds problems and is able to capture a shock without oscillations. In the present work the same technique has been used to solve the 2D form of the describing equations for a compressible vapor flow.

The describing equations are nonlinear and coupled. An iterative method is used to solve Eqs. (1)–(5) for  $\rho$ ,  $\rho u$ ,  $\rho v$ ,  $T$ , and  $p$  separately. The SOR method is used to solve the differenced equations. Iteration on the equations was stopped after convergence of all the variables. This iteration method required the least storage and fewest calculations.

### 4 Results

A computer code was written to implement the numerical procedure described above. The boundary conditions of inflow and outflow at different locations on the same boundary are nonlinear. Furthermore, the exit point of the evaporator and the entrance point to the condenser, on the bottom boundary, are mathematically singular points. The boundary conditions at these points have sharp gradients, which perturb the numerical scheme. In order to avoid this problem, the inflow and outflow mass fluxes are multiplied by the factor  $\tanh \lambda(x - x_0)$ . In the evaporator and the condenser,  $x_0 = 0$  and  $2$ , respectively. Depending on  $\lambda$ , this factor makes the gradients smoother at the singular points. In practice, the vapor phase is coupled to the liquid phase in the heat pipe and the heat flux applied to the liquid phase will not produce a step-shape profile at the liquid-vapor interface.

For the results shown in this section, the working fluid is liquid sodium at, initially,  $P_0 = 10^3 \text{ N/m}^2$  and  $T_0 = 800 \text{ K}$ . The geometry dimensions are  $b = 5 \text{ cm}$ ,  $L_e = L_a = L_c = b$ , and  $\lambda = 5$ . The results are shown in the following sections for low- and high-input heat fluxes and for the pressure drops along different sections of the heat pipe.

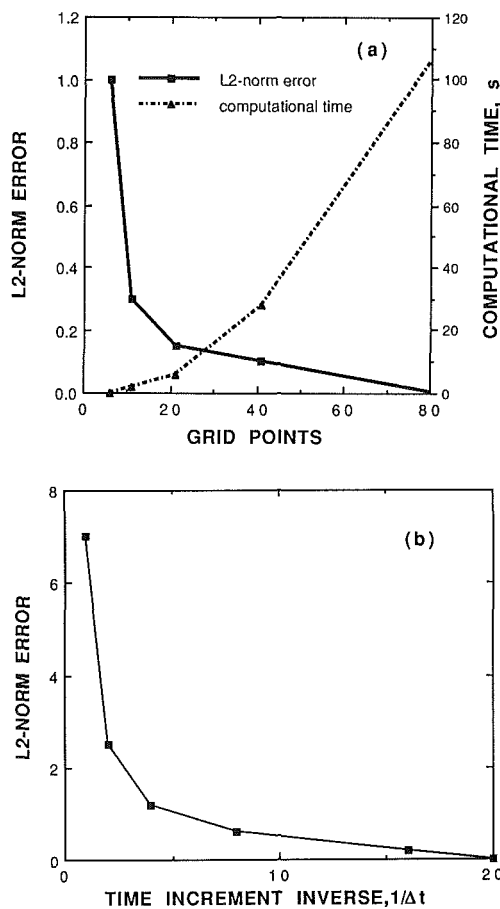


Fig. 2  $L^2$ -norm error and computational time

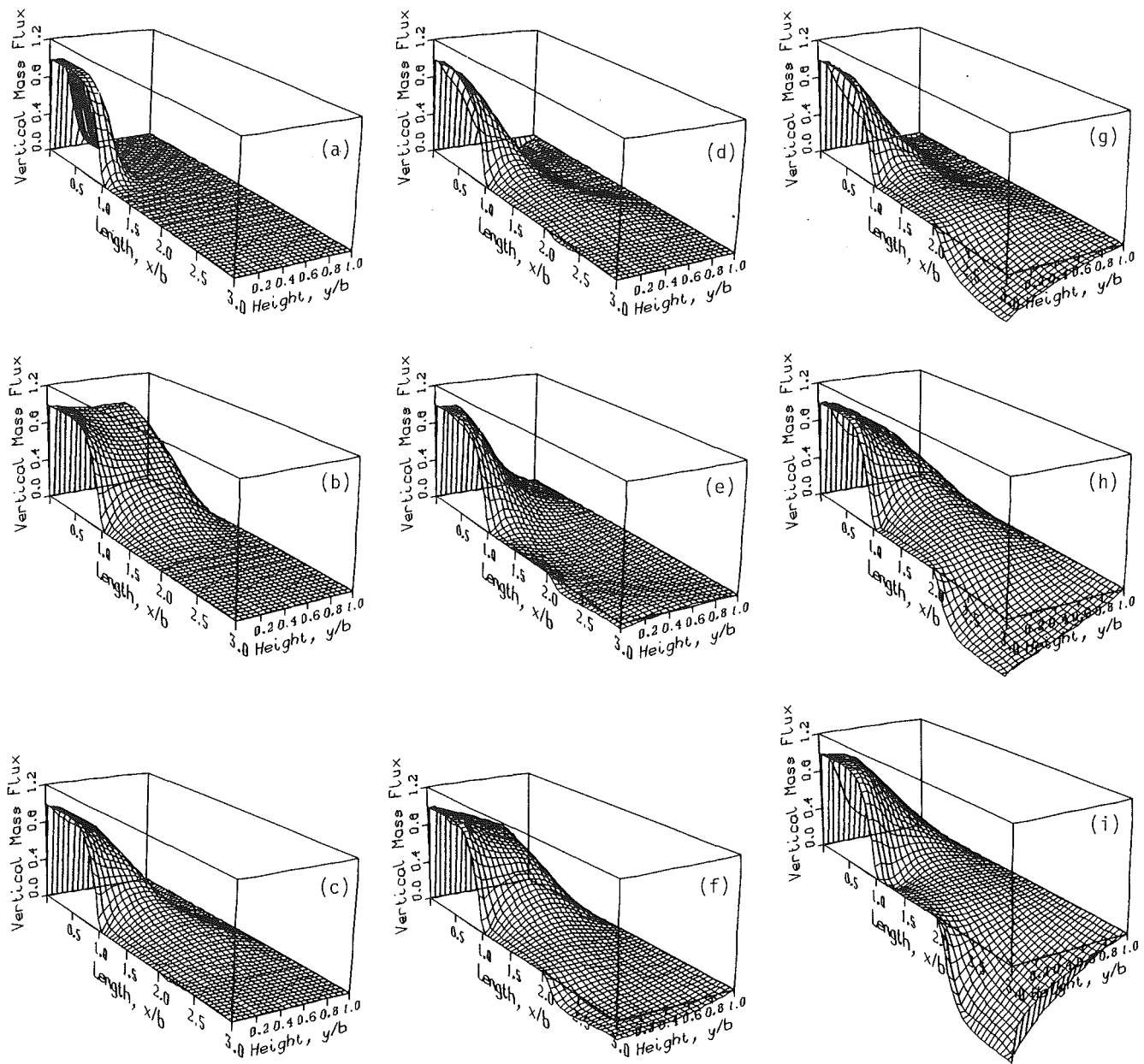


Fig. 3 Transient development of the vertical mass flux for a low-input heat flux

The calculational grid for each computation was chosen by inspection of the calculated  $L^2$ -norm error. The  $L^2$ -norm is defined as

$$L^2 - \text{norm} = \left[ \frac{1}{N_x N_y} \sum_{i,j} \left( \frac{\phi_{i,j} - \phi_{i,j}^r}{\phi_{i,j}^r} \right)^2 \right]^{1/2} \quad (12)$$

where  $N_x$  and  $N_y$  are numbers of grid points in the  $x$  and  $y$  directions, respectively. Here,  $\phi$  is one of the dependent variables ( $\rho$ ,  $\rho u$ ,  $\rho v$ ,  $T$ , or  $P$ ) and  $\phi^r$  is the calculated  $\phi$  on the finest mesh of calculations. The results of the error analysis for a sample calculation are shown in Fig. 2. With an increase in grid points, the  $L^2$ -norm error decreases exponentially; however, the computational time increases (Fig. 2a). In this sample analysis, for grid points greater than 21, the error does not decrease by much, whereas the corresponding computational time increases significantly. Therefore, for this case, the optimized grid point is 21.

The same error analysis is also carried out for time incre-

ments  $\Delta t$  using Eq. (12). In this case,  $\phi^r$  is the result of calculations according to the smallest  $\Delta t$ . The  $L^2$ -norm error for different time increments is shown in Fig. 2(b). As expected, the error decreases as  $\Delta t$  decreases. The sample error analysis, described above, was carried out for different input conditions in order to choose the corresponding optimized grid points and time increments.

**4.1 Low-Input Heat Flux.** Figure 3 shows the flow patterns in the vapor core for a low-input heat flux,  $\dot{q}_0'' = 10^5$  W/m<sup>2</sup>. The Reynolds number based on the vapor thickness is  $Re = 100$  and the computations were done for an optimized grid of  $21 \times 61$ . The transient development of the vertical mass flux  $\rho v$  at different times is shown in Fig. 3. At  $t = 0$ , the vapor is stagnant. Evaporation takes place as the input heat flux is applied. Since the input heat flux is relatively high, a compression wave is created (Fig. 3a). The vapor flow develops above the evaporator and in the adiabatic region and the wave travels above the evaporator until it hits the upper boundary (Fig. 3b) where the vertical mass flux is blocked,  $\rho v$

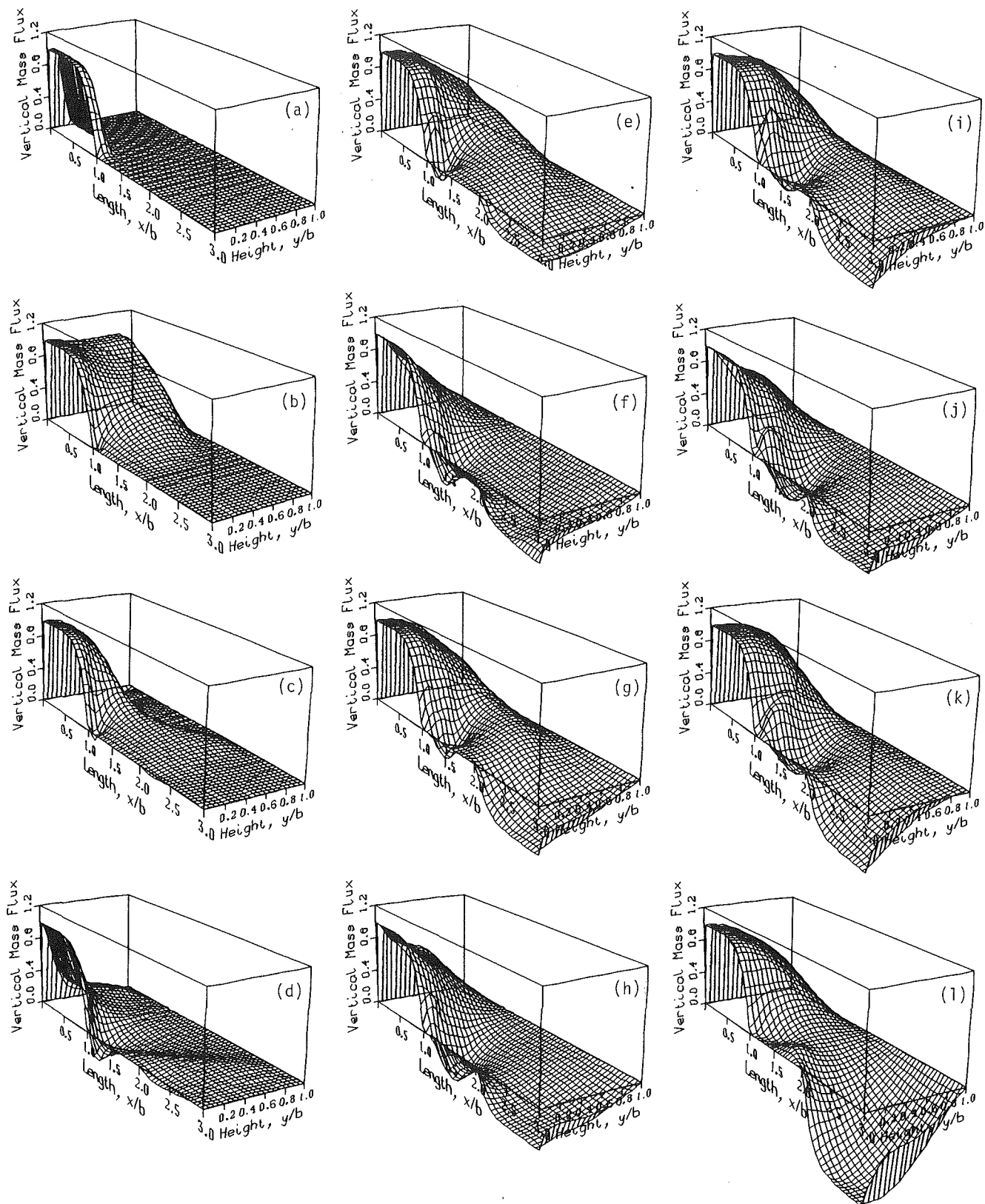
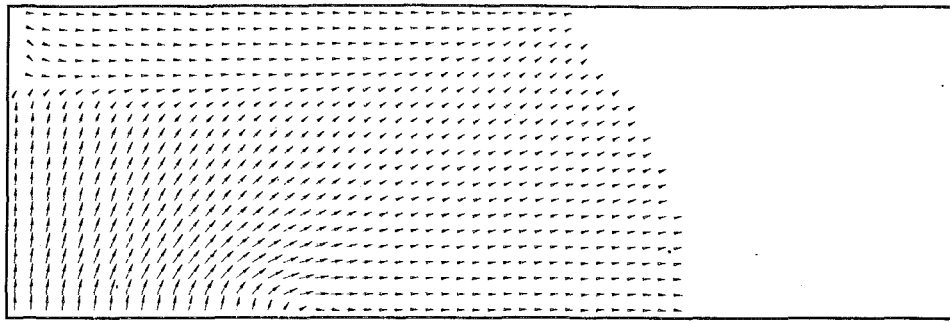


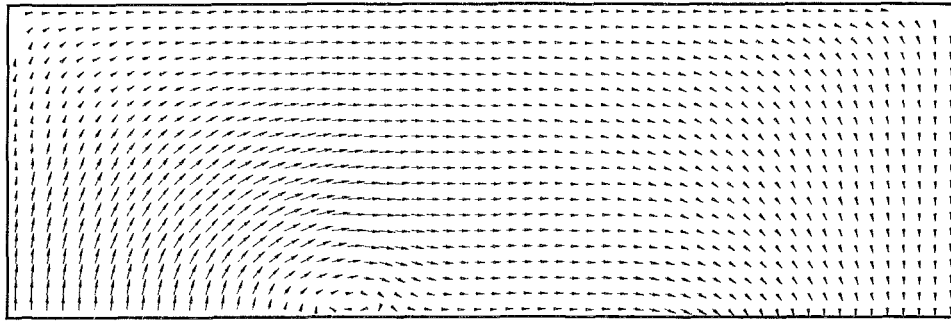
Fig. 4 Transient development of the vertical mass flux for a high-input heat flux

= 0. At this point, the vapor is compressed and the vapor pressure increases, which causes a positive vertical pressure gradient and the wave reflects back (Fig. 3c). The figure also shows reverse flow in the top left corner, which is caused by wave reflection. When the reflected wave reaches the lower

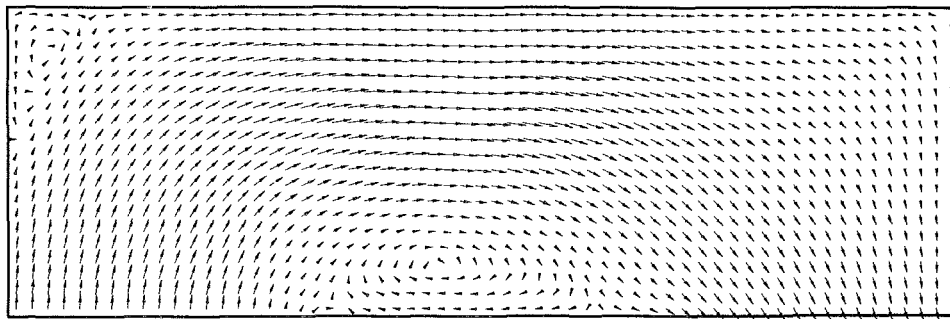
boundary (Fig. 3d) and the vapor is compressed within the evaporation region, the vertical pressure gradient is reduced and the inflow mass flux tries again to fill the evaporation region (Fig. 3e). As the vapor fills the evaporation region (Fig. 3f), another wave reflection occurs and the flow reverses in



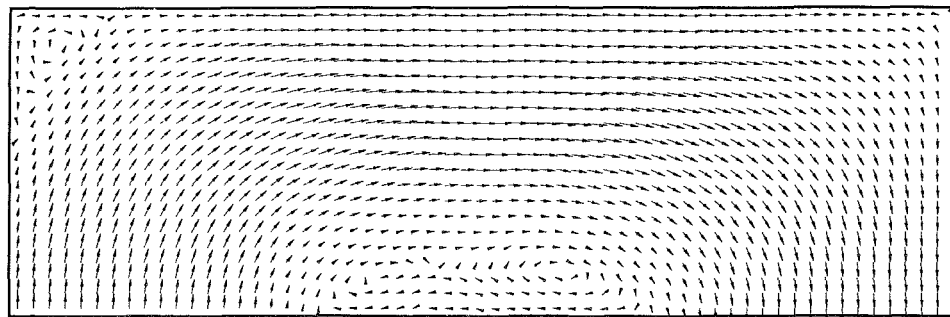
(a)



(b)



(c)



(d)

Fig. 5 Vapor flow fluids at different time levels (arrows indicate direction; tail indicates magnitude)

the top left corner (Fig. 3g). Comparing Figs. 3(d) and 3(g), the reverse flow after the second reflection is weaker than that in the first reflection. About eight to ten cycles of refill and reflection of mass flow are observed in the evaporation region before the process becomes steady (Fig. 3i). At each cycle the

reverse flow is weaker and after four cycles there is no reverse flow. The vertical gradient in the mass flux  $\rho v$  also decreases with each cycle.

The transient flow pattern in the condensation region,  $2 < x/b \leq 3$ , is also illustrated in Fig. 3. At early stages of the

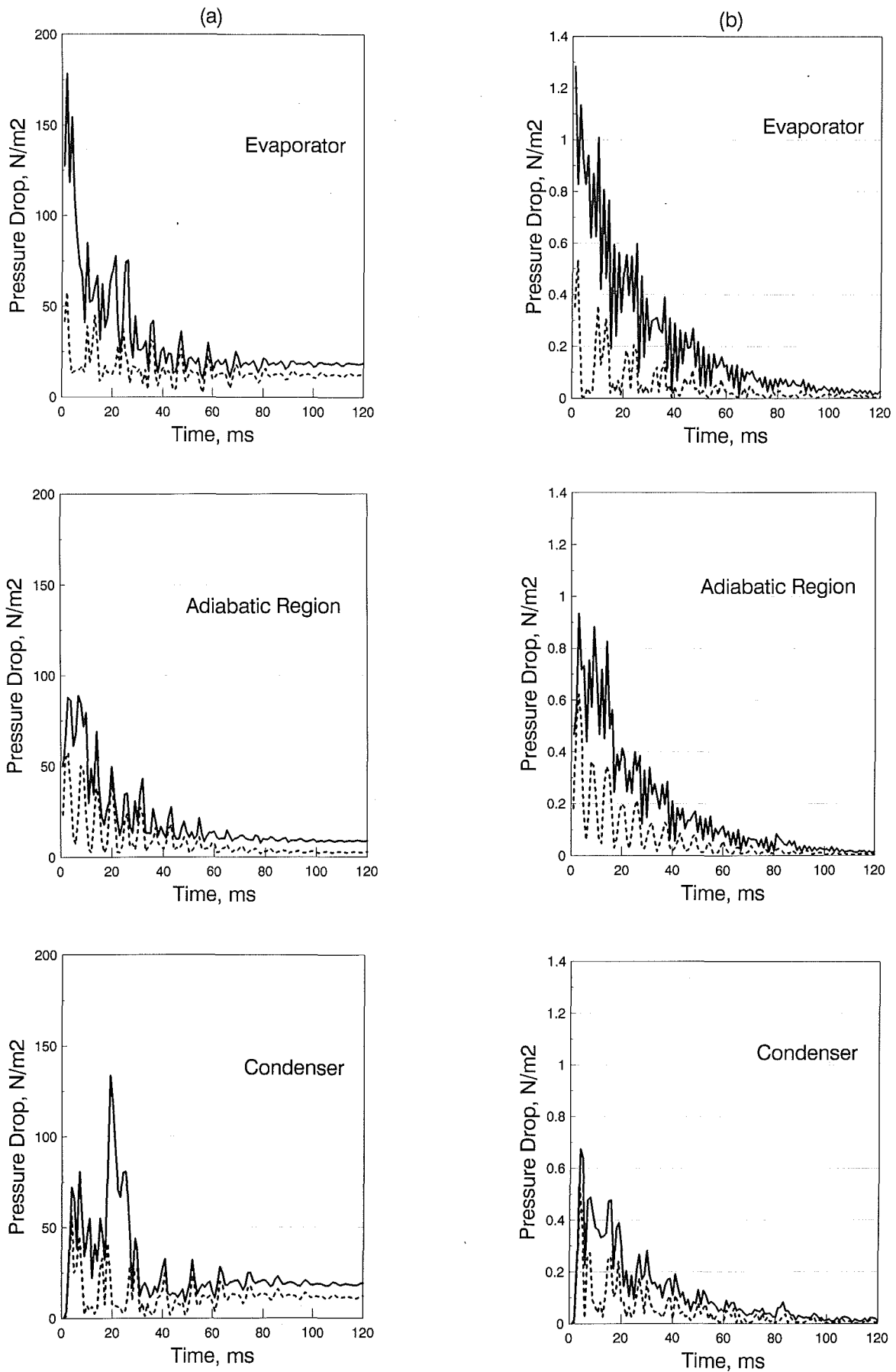


Fig. 6 Calculated pressure drops for (a) high- and (b) low-input heat fluxes (— and ··· denote maximum and maximum averaged pressure drops, respectively)

start-up transient process, the vapor is at the same temperature as the liquid and, therefore, there is no condensation (Figs. 3*a* and 3*b*). When vapor at the higher temperature flows from the evaporation to the condensation region, the vapor temperature on the condenser increases. A temperature gradient is then established along the liquid layer since the temperature at the outer surface of the liquid layer is kept fixed, and condensation takes place (Fig. 3*c*). The vapor temperature in the condenser increases with time and, consequently, the condensation rate increases. At steady state, shown in Fig. 3*i*, the mass flow through the evaporator equals the mass flow out of the condenser.

**4.2 High-Input Heat Flux.** The transient flow patterns for a relatively high heat flux,  $\dot{q}_0'' = 10^6 \text{ W/m}^2$ , are shown in Fig. 4. The corresponding Reynolds number in this case is  $Re = 1000$  and the optimized grid in this case in  $41 \times 121$ . The transient development of the vertical flow  $\rho v$  at different times is shown (Fig. 4). In the evaporator region, multiple wave reflection and refill of vapor is observed to be the same as that for the low-input heat flux discussed above. In this case, however, the reversed flow caused by the wave reflection develops with time and is sustained as the process reaches steady-state operation.

At high-input heat flux, the flow pattern in the adiabatic region,  $1 < x/b \leq 2$ , is significantly different from that for lower heat fluxes. Figure 4(*d*) shows that when the reflected wave reaches the lower boundary of the evaporator, circulation is initiated in the adiabatic region. This circulation ceases when the vapor flow refills the evaporator region (Fig. 4*e*). However, the second reflection will cause a stronger circulation in the adiabatic region, as shown in Fig. 4(*f*). Figures 4(*g*)–4(*l*) demonstrate the subsequent sets of reflection and refill of the vapor flow with circulation strength increasing with time. When the process reaches steady-state conditions, circulation occupies a significant portion of the region. Circulation in the adiabatic region was also found and reported by Issacci et al. (1989) in an analysis of the operational transient mode of heat pipes.

In order to show the overall picture of flow pattern development, Fig. 5 was prepared to depict the vapor flow fields at different times. Figure 5(*a*) shows the flow field at an early stage of the transient process after the first wave reflection. Here the wave reflection in the left top corner of the evaporation region is shown. The wave reflection initiates flow circulation at the entrance to the adiabatic region shown in Fig. 5(*b*). Vortex formation in the adiabatic region develops with time to a stronger flow circulation (Fig. 5*c*) and another vortex can be seen in the left corner of the evaporation region. In the flow field at steady state (Fig. 5*d*), it is seen that flow circulation in the adiabatic region develops to two vortices.

**4.3 Pressure and Pressure Drop.** One of the major issues in designing a heat pipe is to calculate correctly the pressure drop along the vapor core in different sections of the pipe. The correlations widely used in these calculations are based on a simple 1D steady-state analysis. In this section, the pressure drops in different sections of the heat pipe are shown as functions of time. The calculated pressure drops for high- and low-input ( $\dot{q}_0'' = 10^6 \text{ W/m}^2$  and  $10^4 \text{ W/m}^2$ , respectively) heat fluxes are shown in Fig. 6 for different times during the transient phase. Solid lines show the maximum pressure drop in a specific region of the pipe. Averaging the pressure along the vertical cross section of the pipe and then calculating the maximum-averaged pressure drop yields interesting results, which are shown by dotted lines for different times in different sections. Both the maximum and the maximum-averaged pressure drops display nearly periodic oscillation until they converge to a constant value at steady state. Pressure oscillations are caused by multiple wave reflections in the evaporation region (Figs.

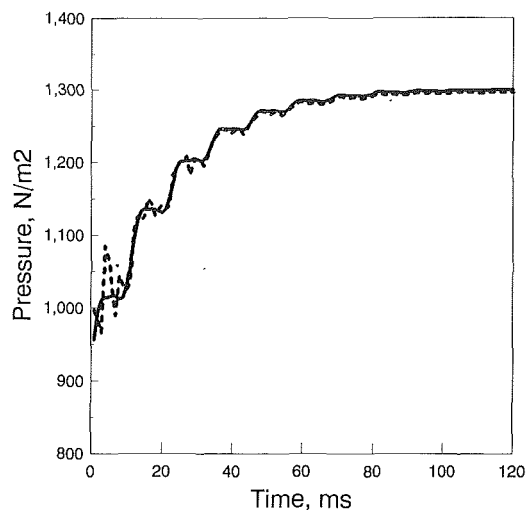


Fig. 7 Averaged (—) and saturated (···) vapor pressures in the evaporator

3 and 4) and at each wave reflection, the local pressure increases significantly. Consequently, a large pressure difference is created along the pipe. The same type of oscillation in the vapor pressure, caused by reflection of compression waves, was also reported by Bowman and Hitchcock (1988).

Another interesting result that can be seen in Fig. 6 is that the pressure drop is significantly higher during the initial period of the start-up transient of heat pipe operation. The mean value of the pressure drop decreases with time, and at steady state its value is less than 10 percent of the initial pressure drop. Therefore, if a heat pipe is designed to operate in the transient mode, the use of steady-state correlations may result in significant errors.

Tien and Rohani (1974) showed that the cross-sectional averaged pressure difference along a heat pipe is greater than the pressure difference calculated by Bankston and Smith (1973) using a 1D analysis. Here we compare the cross-sectional averaged pressure with the calculated 2D pressure by comparing the maximum pressure drops in both cases. Although the maximum-averaged pressure drops (dotted lines on Fig. 6) converge to the maximum pressure drops as the process approaches steady state, it is significantly lower during the initial transient time. This emphasizes the need for a 2D vapor flow model in an overall heat pipe transient analysis.

The pressure drop along the pipe, as mentioned before, plays an important role in the design of a heat pipe. In addition, the pressure in the evaporator may cause limitations on heat pipe operations. When a wave reflects in the evaporation region and the local pressure increases, the increase in the overall pressure of the evaporator may affect the evaporation rate. In order to study this aspect, the averaged (solid lines) and the saturated vapor pressures (dotted lines) in the liquid-vapor interface in the evaporator are shown as functions of time in Fig. 7. Here again, the periodic behavior of pressure is evident. During early transient times, the averaged pressure in the evaporator is sometimes larger than the saturated pressure. This will affect the evaporation process by decreasing the evaporation rate. Furthermore, whenever the vapor pressure is greater than the saturated pressure, condensation takes place by nucleation of mists in the vapor. In this case the flow is not homogeneous and a two-phase flow analysis should be incorporated. We have not done so.

**4.4 Friction Factor.** In order to design a heat pipe, it is necessary to calculate the friction factor coefficients of liquid on the vapor core. The averaged friction factor at the liquid-vapor interface along the pipe is calculated by

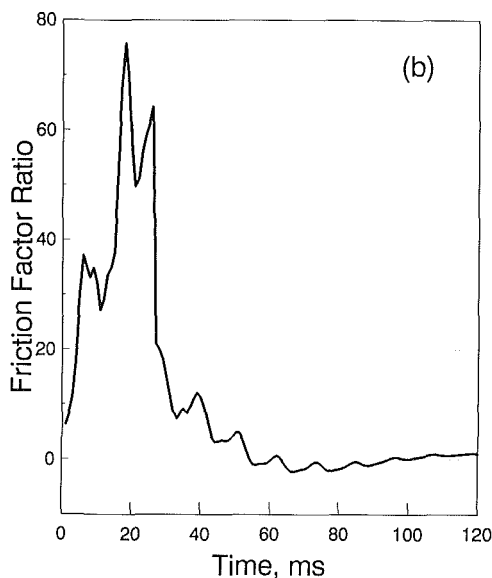
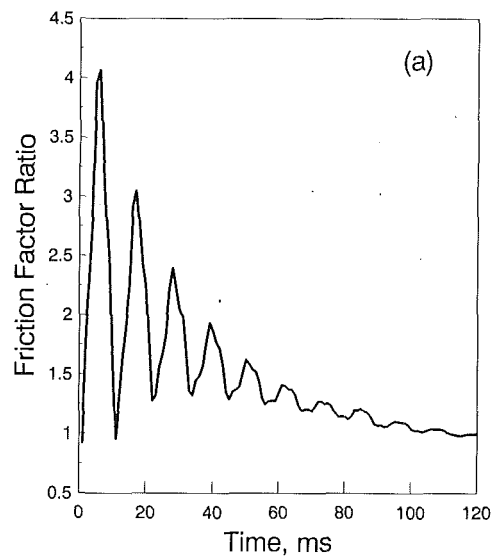


Fig. 8 Friction factors for (a) low- and (b) high-input heat fluxes

$$C_f(t) = \frac{\frac{1}{L} \int_0^L \tau_w dx}{\frac{1}{2} \rho u^2} = \frac{\frac{1}{L} \int_0^L \mu \frac{du}{dy} \Big|_{y=0} dx}{\frac{1}{2} \rho u^2} \quad (13)$$

The ratio of the averaged friction factor and its value at steady state,  $C_f(t)/C_f(\infty)$ , for low- and high-input heat fluxes are shown in Figs. 8(a) and 8(b), respectively. The friction factor oscillates periodically because of the wave reflections, and converges to a constant value at steady state. Figure 8(a) shows that for low-input heat flux ( $\dot{q}_o'' = 10^4 \text{ W/m}^2$ ), the maximum friction factor during the transient phase is about 50 percent more than its value at steady state. Note that during the times the friction factor is high, the wick could dry out. For high-input heat flux ( $\dot{q}_o'' = 10^6 \text{ W/m}^2$ ), the friction factor is about 35 times more than its steady-state value (Fig. 8b). This implies that in designing a heat pipe for transient operations, the steady-state correlations may cause a significant error.

**4.5 Temperature, Pressure, and Axial Mass Flux.** The variations of the averaged vapor temperature and pressure of the pipe are shown in Figs. 9 and 10, respectively. At an early stage of operation the temperature difference between the

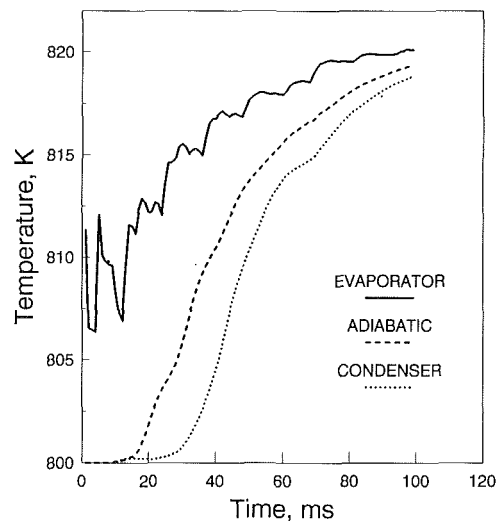


Fig. 9 Averaged vapor temperature

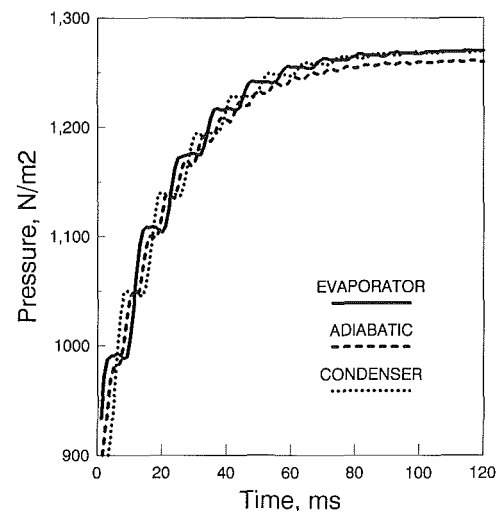


Fig. 10 Averaged vapor pressure

evaporator and the condenser is about 12 K, whereas at steady state, the temperature difference decreases to about 2 K. The effects of multiple reflections of the compression waves in the evaporator are also observed in these figures.

The development of the axial mass flux of the vapor flow with time is shown in Fig. 11 for the middle of the evaporator,  $x = 0.5$ , and for the middle of the pipe,  $x = 1.5$ . The vapor axial mass flux in the evaporator, Fig. 11(a), develops to a parabolic profile. However, in the adiabatic region, Fig. 11(b), a reverse flow is shown to grow with time.

## 5. Summary and Conclusions

A nonlinear filtering technique has been used to analyze the start-up vapor dynamics in heat pipes. Large variations in vapor compressibility during the transient phase render it inappropriate to use the SIMPLER scheme or to use standard schemes for the advective terms.

For a high heat flux, the start-up transient phase involves multiple wave reflections from the line of symmetry in the evaporator region. Each wave reflection causes a significant increase in the local pressure and a large pressure drop along the heat pipe. Furthermore, wave reflections cause flow reversal in the evaporation region and flow circulations in the adiabatic region. The vapor vortex formation in the evaporator is only transient and is observed to disappear as steady state



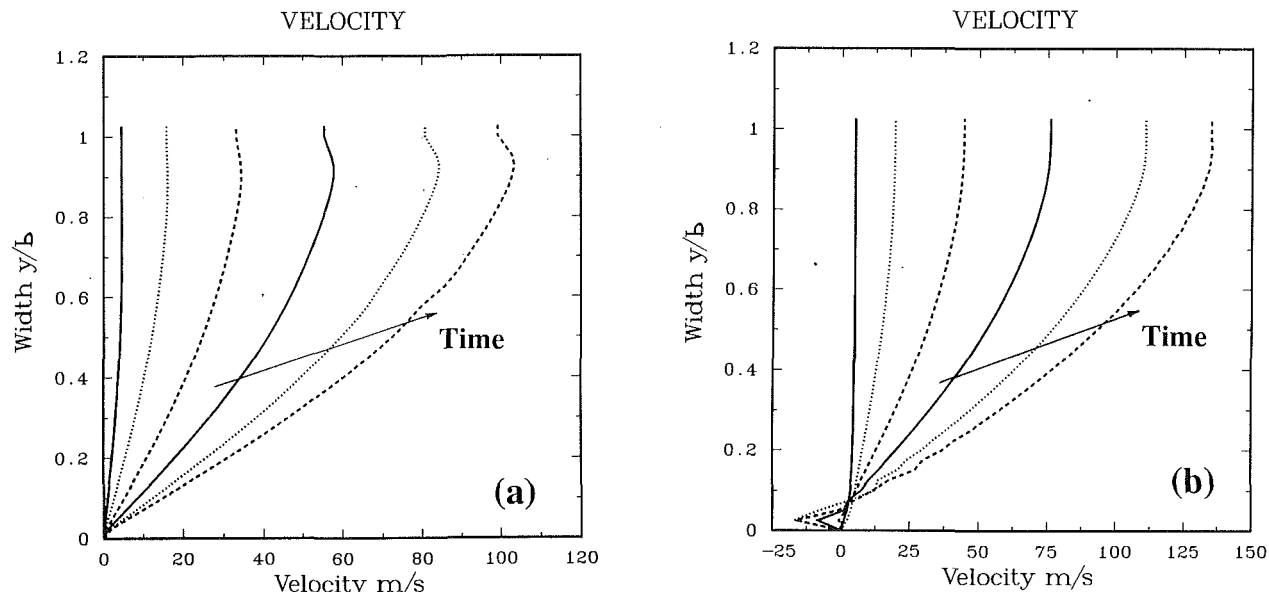


Fig. 11 Axial mass flux; (a) evaporator, (b) adiabatic region

is approached. However the circulation in the adiabatic region grows with time, and in the steady-state condition the circulation occupies a significant portion of the region.

The maximum and maximum-averaged pressure drops in different sections of the heat pipe oscillate periodically with time because of the multiple wave reflections in the evaporator. The pressure drops converge to a constant value at steady state. However, they are significantly higher than their steady-state value at the initiation of the start-up transient.

The pressure increase due to wave reflection may cause the overall pressure of the evaporator to be greater than the saturated vapor pressure. When this occurs, condensation takes place by mist nucleation in the vapor. Therefore, the condensation rate is expected to decrease.

The time for the vapor core to reach a steady-state condition depends on the input heat flux, the heat pipe geometry, the working fluid, and the condenser conditions. However, the vapor transient time is of the order of seconds. Depending on the time constant for the overall system, the vapor transient time may be very short. Therefore, the vapor core may be assumed quasi-steady in transient analysis of a heat pipe operation.

### Acknowledgments

This work was supported by NASA-Lewis under Contract No. NAG3-899 and NASA Dryden under Contract No. NCC2-374 Supp. 2, and by the U.S. Department of Energy, Office of Fusion Energy, Grant No. DE-FG03-86ER52126, with UCLA.

### References

Bankston, C. A., and Smith, H. J., 1973, "Vapor Flow in Cylindrical Heat Pipes," *ASME JOURNAL OF HEAT TRANSFER*, Vol. 95, pp. 371-376.

Bystrov, P. I., and Goncharov, V. F., 1983, "Starting Dynamics of High Temperature Gas-Filled Heat Pipes," *High Temperature*, Vol. 21, pp. 927-936.

Bowman, W. J., 1987, "Simulated Heat Pipe Vapor Dynamics," Ph.D. Dissertation, Air Force Institute of Technology.

Bowman, W. J., and Hitchcock, J. E., 1988, "Transient, Compressible Heat-Pipe Vapor Dynamics," *Proceedings, 24th National Heat Transfer Conference*, Vol. 1, pp. 329-337, Houston, TX.

Bowman, W. J., McClure, W. C., and Towne, M., 1990, "Transient Heat-Pipe Modeling, Paper 2," AIAA Paper No. 90-0061.

Chakravarthy, S., and Osher S., 1982, "Numerical Experiments With the Osher Upwind Scheme for the Euler Equations," *Proceedings, Joint Fluids, Plasma, Thermophysics and Heat Transfer Conference*, AIAA/ASME, St. Louis, MO.

Chow, L., and Zhong, J., 1990, "Analysis of Heat Pipe Start-Up From the Frozen State," presented at the AIAA/ASME 5th Joint Thermophysics and Heat Transfer Conference, Seattle, WA.

Edwards, D. K., and Marcus, B. D., 1972, "Heat and Mass Transfer in the Vicinity of the Vapor-Gas Front in a Gas-Loaded Heat Pipe," *ASME JOURNAL OF HEAT TRANSFER*, Vol. 94, No. 2, pp. 155-162.

Engquist, B., Lötstedt, P., and Sjögreen, B., 1989, "Nonlinear Filters for Efficient Shock Computation," *J. Math. Comp.*, Vol. 52, No. 186, pp. 509-537.

Faghri, A., 1986, "Vapor Flow Analysis in a Double-Walled Concentric Heat Pipe," *Numerical Heat Transfer*, Vol. 10, pp. 583-596.

Faghri, A., Chen, M.-M., and Mahefkey, E. T., 1989, "Simultaneous Axial Conduction in the Fluid and the Pipe Wall for Forced Convective Laminar Flow With Blowing and Suction at the Wall," *Int. J. Heat Mass Transfer*, Vol. 32, No. 2, pp. 281-288.

Hall, M. L., and Doster, J. M., 1988, "The THROPUT Code: Thermohydraulic Heat Pipe Modeling," *Proceedings, 5th Symposium on Space Nuclear Power Systems*, Institute for Space Nuclear Power Studies, University of New Mexico.

Hall, M. L., and Doster, J. M., 1990, "A Sensitivity Study of the Effects of Evaporation/Condensation Accommodation Coefficients on Transient Heat Pipe Modeling," *Int. J. Heat Mass Transfer*, Vol. 33, No. 3, pp. 465-481.

Harten, A., and Zwas, G., 1972, "Switched Numerical Shuman Filters for Shock Calculations," *J. Engrg. Math.*, Vol. 6, pp. 207-216.

Harten, A., 1983, "High Resolution Schemes for Hyperbolic Conservation Laws," *J. Comp. Phys.*, Vol. 49, pp. 357-393.

Issacci, F., Roche, G. L., Klein, D. B., and Catton, I., 1988, "Heat Pipe Vapor Dynamics," University of California—Los Angeles, Report No. UCLA-ENG-88-28.

Issacci, F., Catton, I., Heiss, A., and Ghoniem, N. M., 1989, "Analysis of Heat Pipe Vapor Flow Dynamics," *Chem. Eng. Comm.*, Vol. 85, pp. 85-94.

Issacci, F., Catton, I., and Ghoniem, N. M., 1990a, "Vapor Dynamics of Heat Pipe Start-Up," *Proceedings, 7th Symposium on Space Nuclear Power Systems*, Vol. 2, pp. 1002-1007, Institute for Space Nuclear Power Studies, University of New Mexico.

Issacci, F., McDonough, J. M., Catton, I., and Ghoniem, N. M., 1990b, "Nonlinear Filtering for Shock Capturing and Cell-Reynolds Number Problems in Compressible Vapor Dynamics," submitted to *J. Comp. Phys.*

Jang, J. H., Faghri, A., Chang, W. S., and Mahefkey, E. T., 1989, "Mathematical Modeling and Analysis of Heat Pipe Startup From the Frozen State," in: *Heat Transfer With Phase Change*, ASME HTD-Vol. 114.

Patankar, S. V., 1980, *Numerical Heat Transfer and Fluid Mechanics*, McGraw-Hill, New York.

Peterson, P. F., and Tien, C. L., 1987, "Gas-Concentration Measurements and Analysis for Gas-Loaded Thermosyphons," *Proceedings, International Symposium on Natural Circulation*, ASME HTD, Boston, MA.

Rao, D. V., El-Genk, M. S., and Juhasz, A. J., 1990, "Transient Model of High Temperature Heat Pipes," *Proceedings, 7th Symposium on Space Nuclear Power Systems*, Institute for Space Nuclear Power Studies, University of New Mexico.

Roche, G. L., 1988, "Analytical Studies of the Liquid Phase Transient Behavior of a High Temperature Heat Pipe," M. S. Thesis, University of California—Los Angeles.

Runchal, A. K., 1987, "CONDIF: A Modified Central-Difference Scheme for Convective Flows," *Int. J. Numer. Methods Eng.*, Vol. 24, No. 8, pp. 1593-1608.

Tien, C. L., and Rohani, A. R., 1974, "Analysis of the Effects of Vapor Pressure Drop on Heat Pipe Performance," *Int. J. Heat Mass Transfer*, Vol. 17, pp. 61-67.

# Transient Multidimensional Analysis of Nonconventional Heat Pipes With Uniform and Nonuniform Heat Distributions

Y. Cao

Graduate Research Assistant

A. Faghri

Brage Golding Distinguished Professor

Wright State University,  
Department of Mechanical and  
Materials Engineering,  
Dayton, OH 45435

*A numerical analysis of transient heat pipe performance including nonconventional heat pipes with nonuniform heat distributions is presented. A body-fitted grid system was applied to a three-dimensional wall and wick model, which was coupled with a transient compressible quasi-one-dimensional vapor flow model. The numerical results were first compared with experimental data from cylindrical heat pipes with good agreement. Numerical calculations were then made for a leading edge heat pipe with localized high heat fluxes. Performance characteristics different from conventional heat pipes are illustrated and some operating limits concerning heat pipe design are discussed.*

## Introduction

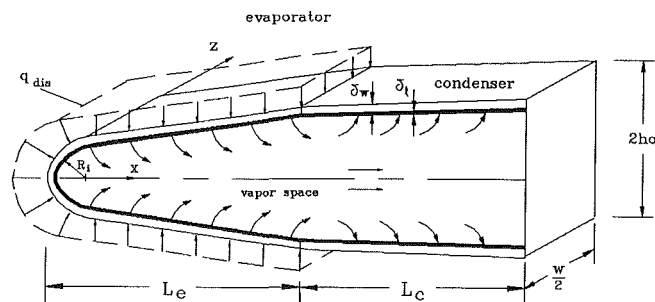
The study of heat pipe dynamics is important in many areas such as the design and operation of space satellite radiators, cooling the leading edges of re-entry vehicles and hypersonic aircraft, electronic equipment cooling, and the cooling of nuclear and isotope reactors.

Since the heat pipe is a very complex system that involves many heat transfer modes, it is very difficult to obtain a generalized analytical solution for the heat pipe dynamics. In recent years, researchers have concentrated on the numerical analysis of transient heat pipe operation. These include Chang and Colwell (1985), Hall and Doster (1990), Bowman and Hitchcock (1988), Jang et al. (1990), and Cao and Faghri (1990). The numerical models involve different assumptions and are at different stages of development. However, most of these numerical analyses deal with conventional cylindrical heat pipes with heat distributions that are uniform around the circumference. Jang (1988) was the only numerical study related to a leading edge heat pipe using a finite element method. Mathematical models have been developed for heat pipe startup from the frozen state. The emphasis of Jang's study was the early transient period of heat pipe startup involving the change of phase in the wick. Neither the coupling of the vapor flow with the wick and wall nor the continuum transient vapor analysis was completed.

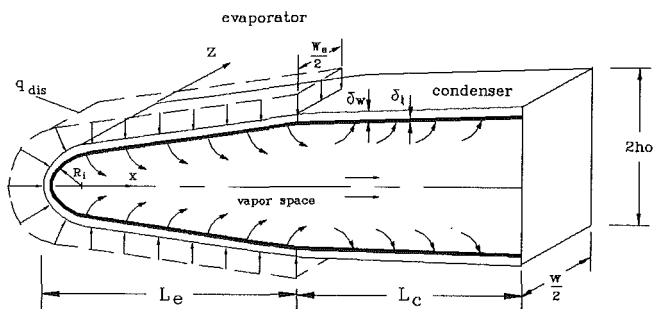
The configuration of a leading edge heat pipe is shown in Fig. 1, which is considered to be one of the most promising candidates for cooling the leading edges of re-entry vehicles and hypersonic aircraft. In the basic concept, the heat pipe covers the leading edge to be protected. The intense aerodynamic heat is absorbed mainly at the leading edge, and transported through the heat pipe to the condenser, where it is rejected by radiation or convection. This nonconventional heat pipe differs from the conventional cylindrical heat pipe in several aspects:

1 The special geometric configuration of the heat pipe makes it difficult to simulate the heat pipe operation with the Cartesian or cylindrical coordinate systems since the vapor cross-sectional area changes along the heat pipe length. In this case, one has to resort to the finite element or the finite difference method with body-fitting coordinates.

Contributed by the Heat Transfer Division for publication in the JOURNAL OF HEAT TRANSFER. Manuscript received by the Heat Transfer Division September 27, 1990; revision received April 11, 1991. Keywords: Conjugate Heat Transfer, Phase-Change Phenomena, Thermal Energy Storage.



a) Uniform heating along the heat pipe width



b) Nonuniform heating along the heat pipe width

Fig. 1 Schematic of the leading edge heat pipe

2 Extremely high heat fluxes at the leading edge make the thickness or the thermal conductivity of the heat pipe wall and wick to be one of the dominant factors of the heat pipe operation. For the conventional heat pipe with a moderate heat flux, the temperature drop across the wall and wick can be neglected without causing a significant error when analyzing the heat pipe operation. However, this is not the case for leading edge heat pipes.

3 The heat distribution at the leading edge is usually not uniform. This makes the heat transfer in the wall and wick generally three dimensional.

In this paper, a numerical modeling for the transient analysis

of nonconventional heat pipes with variable cross-sectional areas and nonuniform heat distributions is presented that implemented the above concerns. The numerical results are compared with the relevant experimental data for conventional cylindrical heat pipes, and then the numerical results for a leading edge heat pipe are elaborated.

### Mathematical Modeling

The mathematical formulation for the conventional heat pipe has been given by Jang et al. (1990) and Cao and Faghri (1990). However, neither study solved the governing equations completely because of the complexity of the problem. The effect of the liquid flow in the wick structure was neglected and the wick structure was assumed to be saturated by the working substance. These assumptions were justified because the thermal conductivity of the liquid metal is high and the wick is very thin. This does not mean that the liquid flow in the porous wick is not important. While the liquid flow has a negligible influence on the temperature distribution in the wick, it is very important in the determination of the capillary limit of the heat pipe. In the present study, the liquid flow in the porous wick was considered as a decoupled process and Darcy's law was applied to determine the capillary limit.

As for the transient vapor flow, most of the previous works used one-dimensional models, which incorporated friction coefficients found from two-dimensional numerical results or experiments. Cao and Faghri (1990) employed a two-dimensional transient vapor flow model coupled with a two-dimensional wall and wick model. Unfortunately, the scheme could not be directly applied to the present problem because of the nonconventional configuration as well as the three-dimensional heat transfer in the wall and wick. For the multidimensional modeling of the present transient vapor flow, a body-fitting system is needed that would result in a very complicated numerical model. Another concern for the multidimensional modeling of the vapor was that although it eliminated the need for friction coefficients, the computational time needed was dramatically increased. Based on the above arguments and the fact that the vapor temperature in the transverse directions is rather uniform, a transient compressible quasi-one-dimensional vapor flow model with variable cross-sectional area coupled with a three-dimensional heat transfer model in the wall and wick was chosen in the present study.

To simplify the analysis for the wall and the wick, the heat pipe was assumed to be symmetric about the stagnation line

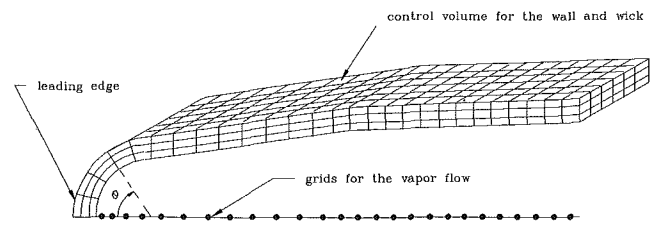


Fig. 2 Body-fitted grids for the wall and wick region (not to scale)

so that only the upper half of the heat pipe was considered. A typical vapor space channel with width  $W$  was considered for the mathematical formulation with the symmetric thermal boundary condition applied on both sides.

**Heat Pipe Wall and Wick.** A body-conforming coordinate system using a multiblock approach was employed in which the region of interest was split into two blocks, each of which was mapped separately with different coordinates. When lower-order blending functions were used, the grid lines usually had some kinks at the nonphysical boundaries. Solution techniques, particularly those based on the Taylor series expansion, might be sensitive to kinks in the grid lines. The finite control-volume methods used here were found to be less sensitive since they are based on flux balances in the cells (Karki, 1986). The body-fitted grid for the heat pipe wall and wick is shown in Fig. 2. A cylindrical coordinate system was used at the leading edge up to  $\theta = 90$  deg. The energy equation in this region is

$$(c_{p\rho}) \frac{\partial T}{\partial t} = \frac{1}{r} \frac{\partial}{\partial r} \left( rk \frac{\partial T}{\partial r} \right) + \frac{1}{r^2} \frac{\partial}{\partial \theta} \left( k \frac{\partial T}{\partial \theta} \right) + \frac{\partial}{\partial z} \left( k \frac{\partial T}{\partial z} \right) \quad (1)$$

For the rest of the heat pipe, a Cartesian system is used. The corresponding energy equation is

$$(c_{p\rho}) \frac{\partial T}{\partial t} = \frac{\partial}{\partial x} \left( k \frac{\partial T}{\partial x} \right) + \frac{\partial}{\partial y} \left( k \frac{\partial T}{\partial y} \right) + \frac{\partial}{\partial z} \left( k \frac{\partial T}{\partial z} \right) \quad (2)$$

where

$$k = \begin{cases} k_w & \text{for the wall} \\ k_{\text{eff}} & \text{for the wick} \end{cases} \quad (3)$$

$$(c_{p\rho}) = \begin{cases} c_{w\rho w} & \text{for the wall} \\ \omega(c_{p\rho})_l + (1-\omega)(c_{p\rho})_s & \text{for the wick} \end{cases} \quad (4)$$

### Nomenclature

|  |  |  |
|--|--|--|
| $a$ = coefficient in Eq. (17)  | $k$ = thermal conductivity, W/(m-K)  | $R$ = gas constant, kJ/(kg-K)  |
| $A$ = cross-sectional area of the vapor channel, $\text{m}^2$                | $K$ = wick permeability, $\text{m}^2$  | $\text{Re}$ = Reynolds number = $UD/\nu$   |
| $B$ = source term in Eq. (17)  | $L$ = total length of the heat pipe, m   | $R_i$ = leading edge radius, m   |
| $c_p$ = specific heat at constant pressure, J/(kg-K)                         | $L_a$ = length of the adiabatic section, m   | $R_m$ = radius of curvature of the meniscus in Eq. (16), m                               |
| $D$ = diameter of the heat pipe, m   | $L_c$ = length of the condenser, m   | $R_v$ = vapor core radius, m   |
| $D_h$ = hydraulic diameter, m  | $L_e$ = length of the evaporator, m  | $r$ = radial coordinate or capillary radius, m   |
| $f$ = friction coefficient = $2\tau_w/\rho U^2$                              | $m_i$ = mass flux at the liquid-vapor interface, $\text{kg}/(\text{m}^2\text{-s})$ | $r_c$ = effective capillary radius of the wick pores at the liquid-vapor interface, m    |
| $G$ = liquid mass flow rate in the wick, $\text{kg}/\text{s}$                | $M$ = Mach number = $U/\sqrt{\gamma p/\rho_v}$                                     | $r_n$ = initial radius of the vapor bubble at formation, m                               |
| $h$ = convective heat transfer coefficient, $\text{W}/(\text{m}^2\text{-K})$ | $p$ = vapor pressure, $\text{N}/\text{m}^2$  | $S$ = channel wall surface area between the leading edge and position $x$ , $\text{m}^2$ |
| $h_{fg}$ = latent heat of evaporation, J/kg                                  | $p'$ = pressure correction, $\text{N}/\text{m}^2$                                  | $t$ = time, s  |
| $h_o$ = half-thickness of the leading edge heat pipe, m                      | $q$ = heat flux, $\text{W}/\text{m}^2$   | $T$ = temperature, K   |
|  | $q_s$ = heat source term, $\text{W}/\text{m}^2$                                    |  |
|  | $Q$ = heat input at the outer wall of the evaporator, W                            |  |

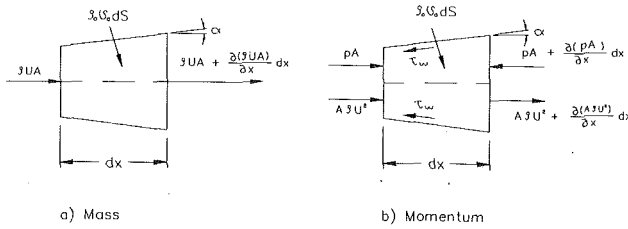


Fig. 3 Vapor control volume for the conservation of mass and momentum

**Transient Compressible Quasi-One-Dimensional Vapor Flow.** A stationary vapor control volume with width  $dx$  is represented in Fig. 3, along with the terms that appear in the conservation equations. The control volume was drawn on the vapor side of the liquid-vapor interface. The axial velocity was taken to be the average vapor velocity. It was also assumed that the injection or suction vapor velocity at the liquid-vapor interface was perpendicular to the heat pipe wall.

The conservation of mass equation is

$$\frac{\partial(\rho A)}{\partial t} + \frac{\partial(\rho UA)}{\partial x} = v_o \rho_o \frac{dS}{dx} \quad (5)$$

where  $A = A(x)$  is the cross-sectional area of the vapor channel.  $S = S(x)$  is the channel wall surface area between the leading edge and position  $x$ . For a circular heat pipe  $dS/dx$  reduces to  $\pi D$ .

The conservation of momentum equation for the same control volume is

$$\frac{\partial}{\partial t} (A \rho U) + \frac{\partial}{\partial x} (A \rho U^2) = -A \frac{\partial}{\partial x} \left( p - \frac{4}{3} \mu \frac{\partial U}{\partial x} \right) - \frac{1}{2} f \rho U^2 \frac{dS}{dx} \cos \alpha + \rho_o v_o^2 \frac{dS}{dx} \sin \alpha \quad (6)$$

where  $f = 2 \tau_w / \rho U^2$  is the friction coefficient at the wall.

The perfect gas law is employed to account for the compressibility of the vapor. The equation of state is

$$p = \rho RT_v \quad (7)$$

The vapor temperature and pressure are related by the Clausius-Clapeyron equation:

$$\frac{dp}{p} = \frac{h_{fg}}{R} \frac{dT_v}{T_v^2} \quad (8)$$

This approach corresponds to the equilibrium two-phase model (Levy, 1968) with vapor quality  $x' = 1$ . It was shown by Levy that the equilibrium two-phase model was realistic and  $x'$  was approximately equal to unity along the heat pipe. Ivanovskii et al. (1982) also used this model with  $x' = 1$  to analyze the steady-state one-dimensional vapor flow, and found that the numerical results agreed well with the experimental data.

**Boundary Conditions and Friction Coefficients.** At both ends of the heat pipe, the no-slip condition for the vapor velocity was applied; i.e., at  $x = 0$  and  $L$ ,  $U = 0$ . For the wall and wick regions, the adiabatic symmetry boundary conditions were applied except at the outer wall surface and the inner liquid-vapor interface, which will be described separately.

At the outer wall surface of the evaporator section, a distributed heat flux  $q_{dis}$  was specified. At the outer wall surface of the condenser section, either a convective or a radiative boundary condition was specified:

$$q_c = \begin{cases} h(T_w - T_f) & \text{(convection)} \\ \sigma \epsilon T_w^4 & \text{(radiation)} \end{cases} \quad (9)$$

where  $h$  is the convective heat transfer coefficient,  $T_f$  is the bulk cooling fluid temperature,  $T_w$  is the outer wall temperature of the condenser,  $\epsilon$  is the emissivity, and  $\sigma$  is the Stefan-Boltzmann constant.

The boundary condition at the liquid-vapor interface is more involved because this couples the wick and the vapor flow. The interface temperature at the evaporator and adiabatic sections was assumed to be the vapor temperature obtained by the Clausius-Clapeyron equation. Since in the present study the working temperature is relatively high, the assumption is valid as shown by Dunn and Reay (1982) and by Groll et al. (1984).

The blowing or suction mass velocity  $v_o \rho_o$  in Eqs. (5) and (6) was found from the interface relation:

$$\rho_o v_o = \frac{k_{eff}}{h_{fg}} \frac{\partial T_l}{\partial r} \begin{cases} > 0 & \text{blowing} \\ < 0 & \text{suction} \end{cases} \quad (10)$$

where  $\partial T_l / \partial r$  can be calculated from the temperature distribution in the wick.

At the condenser interface, vapor condenses and releases its latent heat energy. In order to simulate this process, a heat source

$$q_s = h_{fg} \rho_o v_o \quad (11)$$

## Nomenclature (cont.)

$T_w$  = outer wall surface temperature, K

$U$  = axial velocity, m/s

$U^*$  = axial velocity based on the guessed pressure  $p^*$ , m/s

$v$  = radial velocity, m/s

$W$  = width of the heat pipe for numerical calculation, m

$W_e$  = heating width in  $z$  direction, m

$x$  = axial coordinate, m

$x'$  = vapor quality

$z$  = width direction in Fig. 1

$\alpha$  = slope of the heat pipe wall, rad

$\gamma$  = ratio of specific heats =  $c_p / c_v$

$\delta$  = wall or liquid-wick thickness, m

$\epsilon$  = emissivity

$\theta$  = tangential coordinate at the leading edge

$\nu_l$  = liquid kinematic viscosity,  $m^2/s$

$\xi$  = dummy variable in Eq. (15)

$\rho$  = density,  $kg/m^3$

$\sigma$  = Stefan-Boltzmann constant,  $W/(m^2 \cdot K^4)$

$\sigma_l$  = liquid surface tension, N/m

$\phi$  = general variable in Eq. (17)

$\omega$  = porosity

### Subscripts

$a$  = adiabatic

$b$  = vapor bubble

$c$  = condenser or capillary

$e$  = evaporator

$E$  = "east" neighbor of grid  $P$

eff = effective

$f$  = fluid

$i$  = vapor-liquid interface or initial condition

$l$  = liquid or liquid-wick

$L$  = latent heat

max = maximum

min = minimum

$o$  = properties of the injected or extracted fluid at the liquid-vapor interface

$P$  = grid point

$s$  = saturation or wick structure material

$v$  = vapor

$w$  = wall

$W$  = "west" neighbor of grid  $P$

was applied at the grids next to the interface on the wick side. The suction mass flux  $v_o\rho_o$  in Eq. (11) can be obtained by using the conservation of mass Eq. (5) for a given vapor flow distribution along the  $x$  direction.

The friction coefficient  $f$  for the vapor flow used in this paper is described below. At the evaporator, the vapor flow is always laminar as indicated by Bowman and Hitchcock (1988). The skin-friction coefficient for a circular pipe is  $f = 16/\text{Re}$ . If the Reynolds number was greater than 2000, the flow at the condenser was considered to be turbulent, and the skin-friction coefficient was taken to be  $f = 0.079/\text{Re}^{0.25}$ . Bowman and Hitchcock (1988) studied the transient compressible flow of air in a simulated heat pipe and proposed a friction correlation that takes into account the effect of mass removal at the liquid-vapor interface on the friction coefficient. In a later paper, Bowman (1990) pointed out that when their proposed correlation and the skin-friction coefficients were used to model two identical heat-pipe transients, very little difference could be seen. For the leading edge heat pipe shown in Fig. 1, the vapor channel is rectangular. The skin-friction coefficient  $f$  at the evaporator was taken to be  $f = \eta/\text{Re}_h$ , where  $\text{Re}_h$  is the Reynolds number based on the hydraulic diameter  $D_h$  of the vapor channel and  $\eta$  was taken from the chart for rectangular tubes (Chi, 1976). At the condenser,  $f = 0.079/\text{Re}_h^{0.25}$ .

**Limits to Heat Transport.** Since the compressible vapor flow coupled with the wick and wall was solved, the sonic limit (Mach number approaches unity) was part of the vapor flow solution, so no special effort was needed to describe the analytical relations here. Therefore, the relations for the capillary limit and the boiling limit are emphasized.

**Capillary Limit.** In order for the heat pipe to operate, the maximum capillary pumping head  $(\Delta p_c)_{\max}$  must be greater than the total pressure drop in the heat pipe. Upon neglecting the gravitational head, this relation can be expressed as

$$(\Delta p_c)_{\max} = \frac{2\sigma_l}{r_c} \geq \Delta p_l + \Delta p_v \quad (12)$$

where  $r_c$  is the effective capillary radius of the wick pores at the liquid-vapor interface.

The vapor pressure drop  $\Delta p_v$  was found from the vapor solution at each time step. For  $\Delta p_l$ , a quasi-steady-state assumption and Darcy's law were applied, with the positive  $x$ -direction opposite to the liquid flow direction:

$$\frac{dp_l}{dx} = \frac{\nu_l G}{KA_w} \quad (13)$$

where  $K$  is the wick permeability, which may be a function of  $x$ .  $A_w$  is the wick cross-sectional area, and  $G$  is the local axial mass flow rate of the liquid. Equation (13) can be integrated to obtain the liquid pressure drop  $\Delta p_l$  in Eq. (12). Therefore,

$$\int_0^{x_{\min}} \frac{\nu_l G}{KA_w} dx + \Delta p_v \leq \frac{2\sigma_l}{r_c} \quad (14)$$

where  $x_{\min}$  is the location where the capillary pressure is minimum and equal to zero.

The local liquid mass flow rate  $G = G(x)$  was obtained by numerically integrating  $m_l(x) = v_o\rho_o$  along the liquid-vapor interface at time  $t$

$$G(x) = \int_0^x v_o\rho_o W d\xi \quad (15)$$

**Boiling Limit.** The boiling limit occurs at the evaporator with high radial heat fluxes. Because of the existence of the capillary wick, the boiling process is more complicated than that for smooth surfaces. Analysis of the boiling limit involves the theory of nucleate boiling, which involves two processes:

the formation of bubbles (nucleation), and the subsequent growth and motion of these bubbles. A generally acceptable relation for the boiling limit is

$$\Delta T_{cr} = \frac{2T_v\sigma_l}{h_{fg}\rho_v} \left( \frac{1}{r_n} - \frac{1}{R_m} \right) \quad (16)$$

where  $r_n$  is the initial radius of the vapor bubble at its formation, and  $R_m$  is the radius of the liquid-vapor interface. In the absence of sufficient data, a conservative approach suggested by Chi (1976) would be to use the values of  $r_n$  equal to  $2.54 \times 10^{-5}$  and  $2.54 \times 10^{-7}$  m for the gas-loaded and conventional heat pipes, respectively.  $R_m$  was taken to be approximately  $r_c$  in the calculation.

## Numerical Procedure

The governing equations along with the boundary conditions were solved by employing the control-volume finite-difference approach described by Patankar (1980, 1988). For the wall and wick regions, an energy balance was directly applied to the control volume to obtain the discretization equations for temperature  $T$ . For the vapor flow, the one-dimensional SIMPLE algorithm was employed. To deal with the compressible flow, the pressure was chosen as a dependent variable and the density was obtained by directly applying the equation of state.

The discretization equations for  $U$  and  $p'$  have the general form

$$a_p\phi_p = a_E\phi_E + a_W\phi_W + B \quad (17)$$

which was described by Patankar (1980). For the present one-dimensional formulation, the source term  $B$  contains the blowing and suction contributions at the liquid-vapor interface, which appear in Eqs. (5) and (6).

At both ends of the heat pipe, the no-slip boundary condition leads to the prescribed velocity boundary conditions with  $U = 0$ . Since no boundary pressure is specified, and all the boundary coefficients in the pressure correction  $p'$  equation will be zero, the  $p'$  equation is left without any means of establishing the absolute value of  $p'$ . A direct tridiagonal matrix algorithm would encounter a singular matrix and not be able to give a solution. In this case, the value of  $p'$  at the condenser end was assigned to zero. The absolute value of the vapor pressure at the condenser end point was calculated using the temperature of the liquid-vapor interface at the liquid side and the Clausius-Clapeyron equation. The absolute values of the vapor pressure along the heat pipe were also adjusted according to the value at the end point during the iterations. The sequence of numerical steps was as follows:

- 1 Initialize the temperature, velocity, and pressure fields. The density values for the vapor are obtained from the current vapor pressure and temperature fields through the equation of state.
- 2 Calculate the vapor-liquid interface mass velocity  $v_o\rho_o$  using Eq. (10).
- 3 Solve the vapor momentum equation to obtain  $U^*$ .
- 4 Solve the  $p'$  equation and update the current vapor pressure field.
- 5 Calculate  $U$ 's from their starred values using the velocity correction formulas.
- 6 Calculate the vapor temperature using the Clausius-Clapeyron equation.
- 7 Calculate the heat source term, Eq. (11), using the conservation of mass (Eq. (5)) and the present vapor velocity solution.
- 8 Solve the temperature field for the wick and wall region.
- 9 Update the interface temperature at the evaporator and adiabatic sections with the present vapor temperature, and steps (1)–(9) are repeated until convergence is reached for each time step.

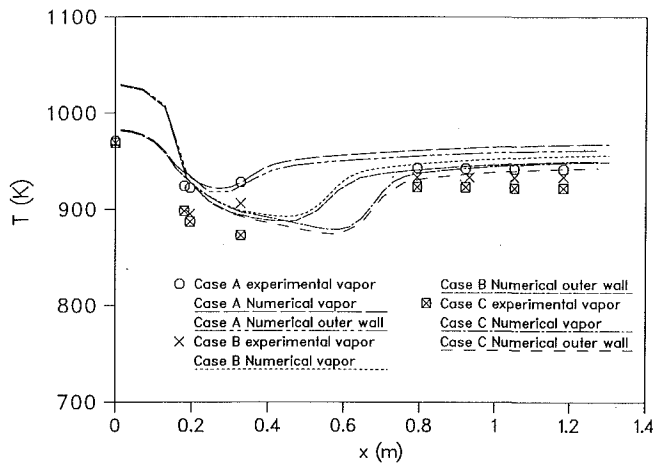


Fig. 4 The axial temperature profiles along the sodium heat pipe compared with the experimental data by Kemme (1969)

### Numerical Results and Discussion

In order to validate the present model, the computer code was first written for a conventional cylindrical heat pipe, and the numerical results were compared with the experimental data by Kemme (1969). The heat pipe studied by Kemme was 1.3 m long with  $L_e = 0.143$  m,  $L_c = 1.08$  m, and i.d. 5.7 mm with a screen wrap wick of thickness  $\delta_w = 0.15$  mm and stainless steel wall of thickness  $\delta_w = 0.9$  mm. During the experiment, the heat input was fixed to 6.4 kW. At a temperature near 800°C, the heat pipe was nearly isothermal so that the temperature profile was essentially flat. The operating temperature was then reduced by changing the cooling condition so that the choked condition could be reached. As the cooling rate at the condenser was increased in steps, three different sets of steady-state experimental data were obtained for subsonic (case A), sonic (case B), and supersonic (case C) vapor flow in the sodium heat pipe. In order to simulate the experimental conditions, a convective heat transfer boundary condition was specified at the outer wall surface of the heat pipe condenser,  $q_c = h(T_w - T_f)$ . The numerical calculation was first made to reach the steady state with a vapor working temperature of 800°C. Then, the heat transfer coefficient  $h$  was increased in steps, and three steady-state vapor temperature curves corresponding to the experimental data were obtained. The numerical results were compared with the experimental data in Fig. 4. Also shown in the figure are numerical outer wall temperature distributions. As can be seen, the agreement between the experimental data and the numerical results is reasonable.

The grid size used in the above numerical calculation was 8 (3 radial wick + 5 radial wall)  $\times$  48 (axial). The numerical results were essentially independent of grid size. A change of grid size from 8  $\times$  40 to 8  $\times$  80 resulted in a change in the numerical results of less than 3 percent. It should be pointed out that the numerical scheme used in this paper has some restriction on the radial grid size for the wick and wall. The blowing or suction mass velocity  $v_{o\rho_o}$  was calculated using the temperature distribution in the wick (Eq. (10)) during the iteration. If the grid size was too small and the effective thermal conductivity was high, the temperature at a particular grid would be very close to the temperatures of the neighboring grids. As a consequence, a serious round-off error would be produced when evaluating the temperature gradient in the wick. However, the heat pipe wick and wall are very thin (usually on the order of 1 mm), so a smaller number of grids in the wick and wall would not produce any significant discretization or truncation errors, especially when the control volume approach was used.

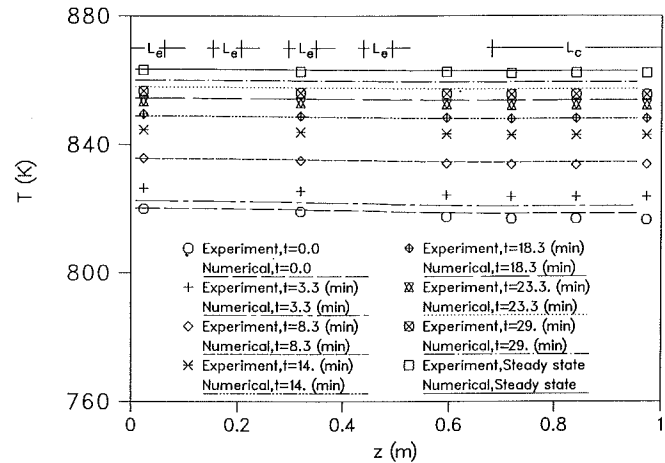


Fig. 5 The vapor temperature for different time periods compared with the experimental data by Faghri et al. (1991)

The numerical results were also compared with the transient experimental data by Faghri et al. (1991). The heat pipe was a 1-m-long multiple heat source sodium/stainless steel heat pipe with a vapor core radius  $R_v = 10.75$  mm, a wrapped screen wick of thickness  $\delta_l = 0.456$  mm, and stainless steel wall of thickness  $\delta_w = 2.15$  mm. The heat pipe was initially at steady state with each of the four heaters having a power input of  $Q_1 = 90$  W. At time  $t = 0$ , the power input was increased to  $Q_2 = 115$  W for each heater. Since the sodium heat pipe assembly included additional heat capacities such as those of the coiled heaters, radiation shielding, and supports, there existed an additional thermal inertia for a power increase to the heat pipe. To account for the additional heat capacities, a transient heat input  $Q_t = Q_1 + (Q_2 - Q_1) [1 - \exp(-t/\tau_o)]$  was specified at the outer wall surface of the evaporator section. The characteristic time  $\tau_o$ , which is the time needed for the outer surface of the heater to reach its maximum temperature after the power increase, was about 8 min from the experimental data. The boundary condition at the condenser was a radiative boundary condition,  $q_c = \epsilon \sigma T_w^4$ . The emissivity  $\epsilon$  was taken from the experiment to be  $\epsilon = 0.6$ . The numerical results for the vapor temperature were compared with the experimental data by Faghri et al. (1991) for six different times as well as two steady states in Fig. 5 with good agreement.

After testing the numerical method in the above two cases, attention was turned to the leading edge heat pipe shown in Fig. 1. In the following numerical calculation, the emphasis was put on the leading edge heat pipe with an extremely high heat input at the evaporator to demonstrate the performance characteristics that were different from conventional heat pipes. The numerical calculation was first made for a lithium leading edge heat pipe in Fig. 1(a) with a uniform heat input at the evaporator,  $q_{dis} = 3 \times 10^7$  W/m<sup>2</sup>. The dimensions and the properties of the heat pipe are  $L_e = 0.054$  m,  $L_c = 0.051$  m,  $W = 0.00630$  m,  $h_o = 0.00521$  m,  $R_i = 0.0015$  m,  $\delta_w = \delta_l = 0.380$  mm,  $(c_p\rho)_w = 4.94 \times 10^5$  J/(m<sup>3</sup>-K),  $(c_p\rho)_{eff} = 6.8 \times 10^5$  J/(m<sup>3</sup>-K),  $k_{eff} = 55$  W/(m-K),  $k_w = 40$  W/(m-K). At the condenser, a convective boundary condition was specified with  $q_c = h(T_w - T_f)$ . In this case,  $T_f$  and  $h$  were taken to be 500 K and 60,000 W/(m<sup>2</sup>-K), respectively. The initial condition for the heat pipe is  $T_v = T_w = 1200$  K,  $p_i = 2050$  N/m<sup>2</sup> and  $U = 0$  with a thawed working fluid. At  $t = 0$ ,  $q_{dis}$  was applied at the evaporator surface and the heat pipe startup was initiated. Figure 6 shows the vapor Mach number distribution along the heat pipe length during the startup process. The heat pipe reached the sonic limit in a very short time. For a conventional heat pipe, startup may be inhibited only when the heat pipe is initially in the frozen state and the heat transfer

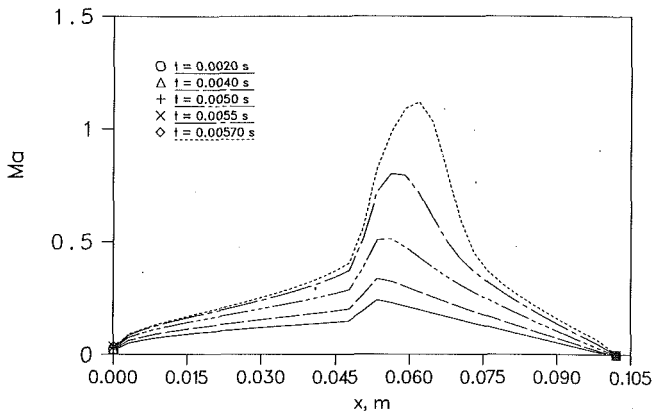


Fig. 6 The startup axial Mach number along the leading edge heat pipe with uniform heating and high heat transfer coefficient

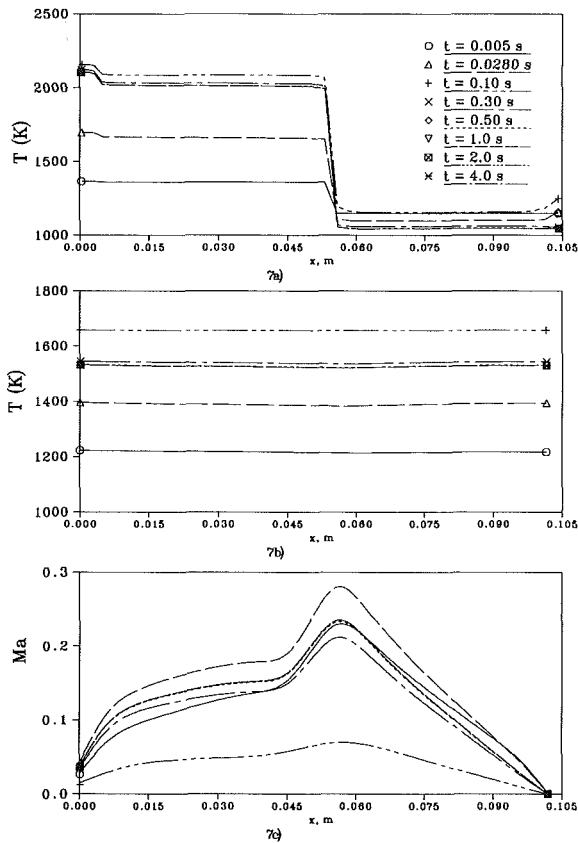


Fig. 7 The leading edge heat pipe with uniform heating at evaporator: (a) outer wall temperature; (b) vapor temperature; (c) axial Mach number

coefficient at the condenser is very high. However, for the present heat pipe with an extremely high power input at the evaporator and a small geometric dimension, startup difficulties may occur even when the heat pipe initially has a fairly high temperature. The calculation was made again with an initially lower heat transfer coefficient,  $h_i = 15,000 \text{ W}/(\text{m}^2\text{-K})$ , at the condenser, which was gradually increased to  $h = 60,000 \text{ W}/(\text{m}^2\text{-K})$  after  $t = 0.05 \text{ s}$ . The corresponding outer wall surface temperature, vapor temperature, and vapor Mach number are presented in Fig. 7. The heat pipe started successfully without encountering the sonic limit, and reached steady state in about 4 s. The transient periods for the present heat pipe were much shorter than those of conventional heat pipes, which have a transient period on the order of 10 min for a pulsed heat input as indicated by Cao and Faghri (1990).

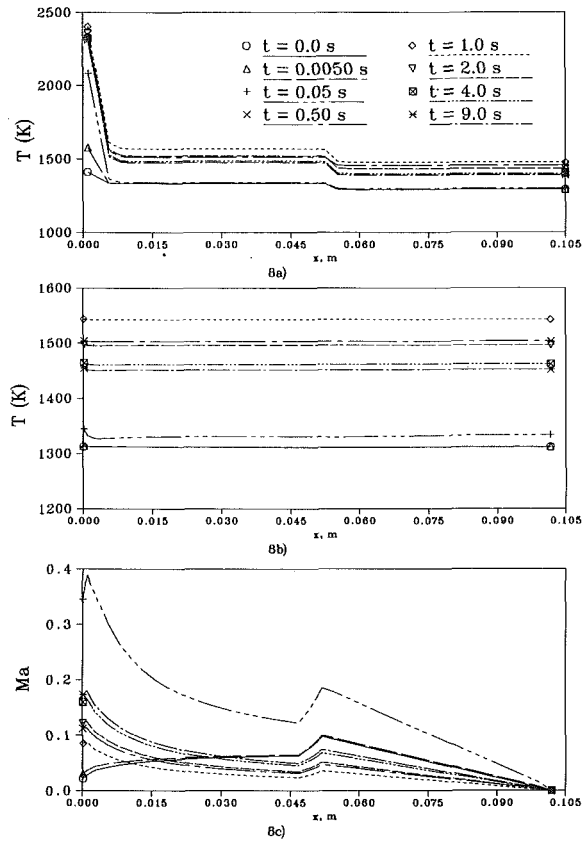


Fig. 8 The heat pipe with the line source at the leading edge: (a) outer wall temperature; (b) vapor temperature; (c) axial Mach number

Since the present heat pipe has a much smaller geometric dimension and therefore a smaller heat capacity, it is understandable that the heat pipe has a short transient period under a heavy heat load. Another performance characteristic worth noting is that although the vapor temperature is relatively uniform along the heat pipe length, large outer wall temperature gradients exist at the leading edge and near the evaporator-condenser junction.

A leading edge heat pipe with different heat inputs at the evaporator and a different wall and wick was then studied. The dimensions and properties of the tungsten wall and wick were  $\delta_i = 0.508 \text{ mm}$ ,  $\delta_w = 0.762 \text{ mm}$ ,  $(c_p\rho)_w = 2.1 \times 10^7 \text{ J}/(\text{m}^3\text{-K})$ ,  $(c_p\rho)_{\text{eff}} = 2.60 \times 10^6 \text{ J}/(\text{m}^3\text{-K})$ ,  $k_{\text{eff}} = 80 \text{ W}/(\text{m-K})$ ,  $k_w = 112 \text{ W}/(\text{m-K})$ , with the rest of the dimensions and working fluid of the heat pipe being the same as the previous one. The heat pipe was initially working at steady state with a uniform power input of  $q_{\text{dis}} = 2 \times 10^6 \text{ W}/\text{m}^2$  at the evaporator. At  $t = 0$ , a line heat source with a total heat input of  $Q = 2.06 \text{ kW}$  was added at the outer wall surface of the leading edge  $\left(-\frac{\pi}{2} \leq \theta \leq \frac{\pi}{2}\right)$ . The heat flux distribution was assumed

linear at the leading edge with a maximum heat flux of  $75 \times 10^6 \text{ W}/\text{m}^2$  at  $\theta = 0$ . The initial steady-state working condition at  $t = 0$  and the subsequent transient response are illustrated in Fig. 8. The convective heat transfer coefficient at the condenser was initially  $h = 2000 \text{ W}/(\text{m}^2\text{-K})$  corresponding to the initial steady state ( $t = 0$ ) and was gradually increased to  $h = 6000 \text{ W}/(\text{m}^2\text{-K})$  after  $t = 0.2 \text{ s}$  to reduce the heat pipe working temperature. Both the vapor temperature and the wall temperature rose to a maximum as the additional heat input was applied at the leading edge, and then dropped off because of the increase of the heat transfer coefficient at the condenser, reaching another steady state in about 9 s. The vapor velocity

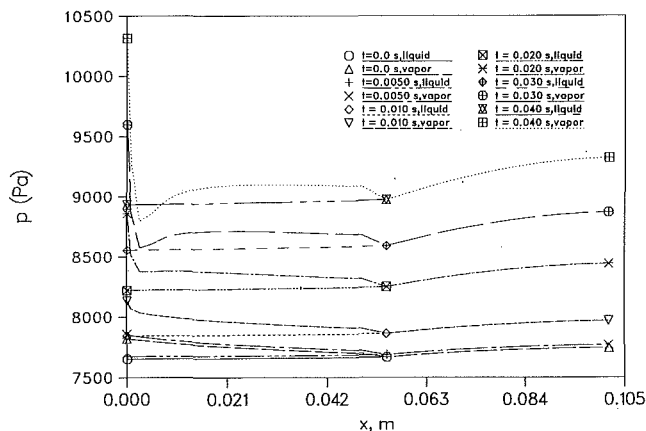


Fig. 9 The liquid and vapor pressure distributions along the heat pipe for different time periods

distribution along the heat pipe length with a uniform heat input at the evaporator was not much different from those of conventional cylindrical heat pipes as indicated by the case  $t = 0.0$  in Fig. 8(c). As the intense heat flux was applied at the leading edge ( $0 \leq x \leq R_m = 0.0015$  m), the vapor velocity increased sharply at the leading edge region, and then began to decrease in the slope region ( $R_m \leq x \leq L_e$ ). In this region, the area of the vapor flow space increased significantly with much less intense evaporation at the liquid-vapor interface; therefore, the vapor velocity actually decreased. Near the evaporator-condenser junction, the vapor velocity increased to another peak value and then gradually decreased to zero along the condenser.

The capillary and boiling limits were also calculated for this heat pipe configuration. The heat pipe wick considered was a wrapped screen wick with a permeability  $K = 6.0 \times 10^{-9} \text{ m}^2$  and an effective capillary radius  $r_c = 3.81 \times 10^{-4} \text{ m}$ . The  $x_{\min}$  in Eq. (14) was chosen as the location in the condenser near the evaporator-condenser junction. Figure 9 shows the liquid and vapor pressure distributions along the heat pipe at different time periods. Even for a uniform heat flux  $q_{\text{dis}} = 2 \times 10^6 \text{ W/m}^2$  (the steady state labeled with  $t = 0.0$  s), the liquid pressure drop constituted only a small portion of the total capillary pressure in Eq. (14). As the additional power was applied at the leading edge, the vapor pressure drop increased dramatically. At  $t = 0.004$  s, the vapor pressure at some location near the leading edge was even lower than the liquid pressure. Shortly after this, the capillary limit was reached. This means that a special design is needed for a leading edge heat pipe with heavy heat loads to increase the total capillary pressure available, or increase the vapor flow space at the leading edge. It should be pointed out that  $x_{\min}$ , where the vapor and liquid pressures are equal, was chosen at the location near the evaporator-condenser junction because of the large vapor pressure recovery at the condenser. Ernst (1967) pointed out that if the pressure recovery in the condenser region is greater than the liquid pressure drop, then the meniscus in the wick will be convex. While this is possible in principle under normal heat pipe operation, there is excess liquid in the condenser region so that this condition cannot occur. For this reason, it is usually assumed the meniscus in the wick is flat and the liquid and vapor pressures are equal in the condenser region, as shown in Fig. 9.

It should also be mentioned that the numerical results in Fig. 8 were obtained with the assumption that the capillary wick had been perfectly designed without encountering the capillary limits, while in reality this is not always the case. If the capillary limit was encountered, the outer wall temperature of the heat pipe would be too high and the heat pipe would be burned out.

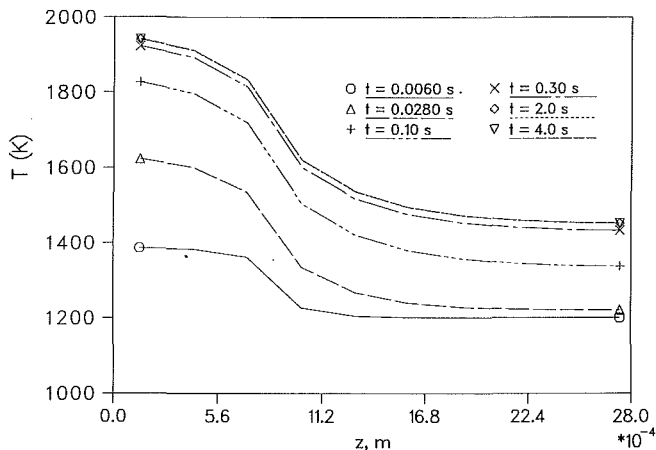


Fig. 10 The outer wall temperature along the stagnation line for the case of nonuniform heating

The boiling limitation in Eq. (16) is heavily dependent on  $r_n$ , the initial radius of the vapor bubbles at formation. In the absence of sufficient experimental data, Chi (1976) suggested that a value of  $r_n = 2.54 \times 10^{-7} \text{ m}$  be used. With this value, the boiling limitation would not be encountered in most cases except when the vapor temperature was very high and the lithium vapor pressure approached  $10^5 \text{ Pa}$ . However, the value of  $r_n = 2.54 \times 10^{-7} \text{ m}$  can only be used when the heat pipe has been carefully processed to eliminate all noncondensable gases. In the presence of noncondensable gases, a much larger value ranging from  $2.54 \times 10^{-6} \text{ m}$  to  $2.54 \times 10^{-5} \text{ m}$  should be used. In this case, the boiling limitation might be encountered with heavy heat loads.

Calculations were also made with a nonuniform heating condition along the width of the leading edge heat pipe shown in Fig. 1(b). The distributed heat flux was  $q_{\text{dis}} = 3 \times 10^7 \text{ W/m}^2$  with  $W_e = 1.90 \text{ mm}$ . The heat pipe configuration and the initial condition were the same as those of the first leading edge heat pipe examined. In this case, the heat transfer in the wall and wick was three dimensional. Figure 10 shows the outer wall temperature along the stagnation line in the width direction. As can be seen, heat conduction in the width direction is evident because of the nonuniform heating. However, the heat conduction effects are limited to a region about  $2(\delta_l + \delta_w)$  wide.

## Conclusions

The numerical method presented in this paper proves to be flexible and capable of dealing with conventional and non-conventional heat pipes. The numerical results have been compared with two sets of experimental data with good agreement. The numerical results for the leading edge heat pipe demonstrated the following performance characteristics:

- 1 For a leading edge heat pipe with an extremely high heat load at the evaporator and a small geometric dimension, difficulties with start-up at a relatively high temperature may be encountered when the cooling rate at the condenser is not low enough.

- 2 The leading edge heat pipe reached the steady state very quickly because of the high heat load and small heat capacity of the heat pipe.

- 3 When the heat load was very high at the leading edge, the vapor pressure drop was a dominant factor for the capillary limit consideration. An increase in the vapor space at the leading edge is recommended.

- 4 Even though the vapor temperature was relatively uniform along the heat pipe length, large temperature gradients existed at the outer wall surface of the heat pipe. These tem-



perature gradients may result in large thermal stresses, which may limit the life of the heat pipe.

5 Since temperature drops across the wick at the leading edge were as high as several hundreds of degrees, the boiling limit may be encountered in spite of the liquid-metal working fluid. More effort is needed to predict the boiling limit more accurately.

All these performance characteristics mentioned above add additional challenges to heat pipe applications, and further study is definitely needed.

### Acknowledgments

Funding for this work was provided by a joint effort of the NASA Lewis Research Center and the Thermal Energy Group of the Aero Propulsion Laboratory of the U.S. Air Force under contract No. F33615-88-C-2820.

### References

- Bowman, W. J., and Hitchcock, J., 1988, "Transient, Compressible Heat Pipe Vapor Dynamics," *Proc. 25th ASME National Heat Transfer Conf.*, Houston, TX, pp. 329-337.
- Bowman, W. J., 1990, "Transient Heat-Pipe Modeling, the Frozen Start-Up Problem," *Proc. AIAA/ASME 5th Joint Thermophysics and Heat Transfer Conference*, AIAA Paper No. 90-1773, Seattle, WA.
- Cao, Y., and Faghri, A., 1990, "A Transient Two-Dimensional Compressible Analysis for High Temperature Heat Pipes With a Pulsed Heat Input," *Numerical Heat Transfer, Part A*, Vol. 18, pp. 483-502.
- Chang, W. S., and Colwell, G. T., 1985, "Mathematical Modeling of the Transient Operating Characteristics of a Low-Temperature Heat Pipe," *Numerical Heat Transfer*, Vol. 8, pp. 169-186.
- Chi, S. W., 1976, *Heat Pipe Theory and Practice*, Hemisphere Publishing Corp., Washington, DC.
- Dunn, P. D., and Reay, D. A., 1982, *Heat Pipes*, 3rd ed., Pergamon Press, Oxford, United Kingdom.
- Ernst, D. M., 1967, "Evaluation of Theoretical Heat Pipe Performance," presented at the Thermionic Conversion Specialist Conf., Palo Alto, CA.
- Faghri, A., Buchko, M., and Cao, Y., 1991, "A Study of High Temperature Heat Pipes With Multiple Heat Sources and Sinks, Part I and II," *Proc. 27th National Heat Conf.*, also ASME JOURNAL OF HEAT TRANSFER, this issue.
- Groll, M., Brost, O., Mack, H., and Shevchuk, E. N., 1984, "Evaporation Heat Transfer of Sodium From Capillary Structures," *Research and Development of Heat Pipe Technology*, Supplement, pp. 21-27.
- Hall, M. L., and Doster, J. M., 1990, "A Sensitivity Study of the Effects of Evaporation/Condensation Accommodation Coefficients on Transient Heat Pipe Modeling," *Int. J. Heat Mass Transfer*, Vol. 33, pp. 465-481.
- Ivanovskii, M. N., Sorokin, V. P., and Yagodkin, I. V., 1982, *The Physical Principles of Heat Pipes*, Clarendon Press, Oxford, United Kingdom.
- Jang, J. H., 1988, "An Analysis of Start-Up From the Frozen State and Transient Performance of Heat Pipes," Ph.D. Dissertation, Georgia Institute of Technology, Atlanta, GA.
- Jang, J. H., Faghri, A., Chang, W. S., and Mahefkey, E. T., 1990, "Mathematical Modeling and Analysis of Heat Pipe Start-Up From the Frozen State," ASME JOURNAL OF HEAT TRANSFER, Vol. 112, No. 3, pp. 586-594.
- Karki, K. C., 1986, "A Calculation Procedure for Viscous Flows at All Speeds in Complex Geometries," Ph.D. Dissertation, University of Minnesota, Minneapolis, MN.
- Kemme, J. E., 1969, "Ultimate Heat-Pipe Performance," *IEEE Transactions on Electronic Devices*, Vol. ED16, No. 8, pp. 717-723.
- Levy, E. K., 1968, "Theoretical Investigation of Heat Pipes Operating at Low Vapor Pressure," ASME Journal of Engineering for Industry, Vol. 90, Series B, No. 4, pp. 547-552.
- Patankar, S. V., 1980, *Numerical Heat Transfer and Fluid Flow*, McGraw-Hill, New York.
- Patankar, S. V., 1988, "Elliptic Systems: Finite-Difference Method I," in: *Handbook of Numerical Heat Transfer*, W. J. Minkowycz et al., eds., Wiley, New York.

A. Faghri  
Brage Golding Distinguished Professor.

M. Buchko<sup>1</sup>  
Graduate Research Assistant.

Y. Cao  
Research Associate.

Department of Mechanical and Materials  
Engineering,  
Wright State University,  
Dayton, OH 45435

# A Study of High-Temperature Heat Pipes With Multiple Heat Sources and Sinks: Part I—Experimental Methodology and Frozen Startup Profiles

*A high-temperature sodium/stainless steel heat pipe with multiple heat sources and sinks was fabricated, processed, and tested. Experimental results from tests performed both under vacuum and in air are presented. The startup behavior of the heat pipe from the frozen state was investigated for various heat loads and input locations, with both low and high heat rejection rates at the condenser. No startup evaporator dryout failures were found, although the heat pipe was sonic-limited during startup in air.*

## Introduction

The use of high-temperature heat pipes has been proposed for cooling the leading edges and nose cones of re-entry vehicles, cooling rail guns, and laser mirrors, as well as for the thermal management of future hypersonic vehicle structures. These applications will require an understanding of the behavior and performance of liquid metal heat pipes with multiple nonuniform heat inputs. In general, the analytical and experimental analyses developed for single evaporator heat pipes cannot be applied to multiple evaporator heat pipes with nonuniform heat loads.

A high-temperature heat pipe is a closed-system heat transfer device that operates between 300 and 1500°C and contains a capillary wick structure with a liquid metal working fluid such as potassium or sodium. When a numerical model of high-temperature heat pipe behavior is proposed, the model must be compared to existing experimental data for verification. For comparison with experimental data, detailed information on the heat pipe operating system is needed. These data should include the type and shape of evaporator heat source, condenser cooling method, heat pipe instrumentation, and measurements of the evaporator and condenser heat fluxes. The type of test performed, such as startup, transient, or steady state, is also important. Unfortunately, most of the previous high-temperature heat pipe investigations with a single evaporator were presented in conference proceedings and many of the above experimental details were not reported.

Experimental investigation of the operating characteristics of a multiple heat source high-temperature heat pipe was necessary for several reasons:

1 A literature search did not reveal any experimental data for multiple heat source high-temperature high pipes, and the startup behavior for such a heat pipe was expected to differ from that with a single evaporator.

2 Vapor temperatures and therefore the vapor pressures were usually deduced from wall thermocouples, which can be influenced by the type of thermocouple used and the thermocouple mounting method. The wall thermocouple wires may absorb reflected radiation, or act as a small fin at high tem-

peratures, which can cause a steep temperature gradient along the thermocouple wire and inaccurate temperature readings. Direct measurement of the vapor temperatures is the most accurate approach for determining the startup behavior from the frozen state.

3 Many researchers report only the heat input to the evaporator or the heat output from the condenser, and an accurate energy balance for the heat pipe system cannot be attained. Heat losses from the evaporator and transport sections are significant, even with insulation.

4 Convection losses due to operation in air need to be determined for accurate system energy balances.

5 The conventional analytical predictions of Dunn and Reay (1982) and Chi (1976) for the capillary limits of heat pipes are often inaccurate and cannot be extended to multiple heat source heat pipes. Therefore, the capillary limits for multiple heat source heat pipes must be determined experimentally or by using a detailed numerical simulation model. In terrestrial applications the experimental data can be used in designing commercial heat pipes.

6 Accurate and detailed experimental results for the operating behavior of a high-temperature heat pipe with multiple evaporators will be required for verification of future numerical simulation models.

## Experimental Apparatus and Procedure

The high-temperature heat pipe was a sodium/stainless steel heat pipe designed to operate at a vapor temperature range of 500–800°C. The compatibility of 304L stainless steel with sodium is well-documented in heat pipe literature. No attempt was made to design a high-capacity heat pipe since the main objective was to obtain detailed and accurate experimental data related to the frozen startup operating characteristics with multiple heat sources.

The heat pipe shell and end caps were fabricated from Type 304L stainless steel. The heat pipe shell was 1000 mm in length, with an outside diameter of 26.7 mm, and a wall thickness of 2.15 mm. The ends of the heat pipe shell were machined so that the end caps fit snugly. All of the heat pipe parts were carefully fitted and cleaned using standard procedures. The heat pipe shell, end caps, and wick material were degreased with 1,1,1-trichloroethane, rinsed in deionized water, then rinsed in methanol and allowed to air dry.

A simple circumferential screen wick consisting of two wraps

<sup>1</sup>Present address: NASA Goddard Space Flight Center, Greenbelt, MD 20771.

Contributed by the Heat Transfer Division and presented at the National Heat Transfer Conference, Minneapolis, Minnesota, July 28–31, 1991. Manuscript received by the Heat Transfer Division December 20, 1990; revision received June 4, 1991. Keywords: Heat Pipes and Thermosyphons, High-Temperature Phenomena, Transient and Unsteady Heat Transfer.

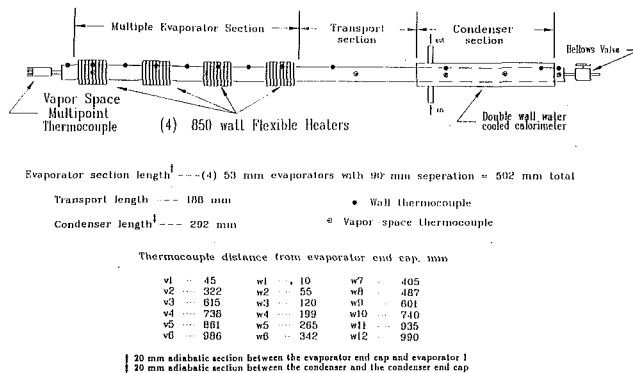


Fig. 1 High-temperature heat pipe thermocouple locations

of 100 mesh Type 304 stainless steel was installed to provide a liquid return path to the evaporators. The wick was rolled on a 19-mm mandrel with a slight offset that resulted in a shallow spiral in the wick. This slight spiral does not affect the thickness of the wick, but does provide a positive tension in the wick against the heat pipe wall. The vapor core diameter is 21.5 mm. The screen wire diameter and screen wick thickness are 0.114 and 0.456 mm, respectively.

The end caps were TIG welded to the heat pipe shell, and the interior of the heat pipe was protected from oxidation during the welding process by a cover layer of nitrogen. A high-temperature bellows-type valve was attached to the heat pipe fill tube to facilitate sealing, purging, and charging of the fluid inventory.

The heat pipe had four independently controlled heaters in the evaporator section. After consideration of several heat sources, Inconel 600 Aerorod BXX flexible electric heaters manufactured by ARi Industries were chosen since they were judged most reliable for the heat pipe performance tests. An important advantage of these flexible heaters was their ability to withstand high watt densities at temperatures up to 1000°C. Each evaporator consisted of one 850-W heater coiled around the heat pipe circumference, giving an individual evaporator length of 53 mm, with 90-mm adiabatic sections separating each evaporator (Fig. 1). One problem with coil-on heaters is a large temperature drop between the heater elements and the heat pipe wall due to poor thermal contact. In order to minimize the thermal contact resistance, a stainless steel clamp was mounted around each heater. Power input to each heater was supplied by a 120-V variable a-c transformer. The electrical current and voltage to each heater were measured with a Fluke 77 multimeter, which has an uncertainty of  $\pm 2$  percent of the reading.

Heat pipe vapor and wall temperatures were measured with Type K thermocouples, which were calibrated with an accuracy of  $\pm 0.3^\circ\text{C}$ . There were twelve wall thermocouples, six vapor space thermocouples, and one thermocouple on the top of each heater (Fig. 1). Wall thermocouples in the adiabatic, transport, and condenser sections were spot-welded to the heat pipe wall. One sheathed thermocouple was located in a shallow groove underneath each heater coil. A 4.7-mm-dia, Type 316 stainless steel sheathed multipoint thermocouple mounted axially within the heat pipe vapor space provided vapor temperatures at six locations. The multipoint thermocouple exited the heat pipe through a tube in the evaporator end cap and was locked in place with a compression fitting to provide a leak-tight seal. Temperature data were monitored with a Fluke 2285B Datalogger interfaced with an IBM personal computer for data storage and were typically recorded every two to five minutes.

The evaporator section of the heat pipe was insulated with a specially fabricated clamshell radiation heat shield unit in

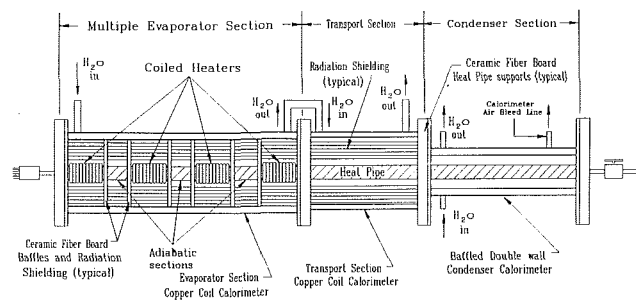


Fig. 2 High-temperature heat pipe assembly

order to minimize the radiation losses. The evaporator radiation shield consisted of six individual shields arranged concentrically around the heat pipe. The shields were fabricated from 0.127-mm Type 304 stainless steel shim-stock, and were mounted to a stainless steel jacket 127 mm in diameter and 1.6 mm thick (Fig. 2). The radiation shield also included internal ceramic baffles to separate the evaporators from the adjacent adiabatic sections. The adiabatic transport section of the heat pipe was insulated with six concentric radiation shields in the same manner as the evaporator section. Both the evaporator and transport sections were fitted with water-cooled calorimeters to measure the actual heat losses occurring in each section. The evaporator calorimeter was fabricated by soldering a continuous line of copper tubing to the outer wall of the radiation shield jacket. For the transport section calorimeter a jacket was fabricated from 127-mm-dia 1.6-mm wall copper pipe, and a continuous line of copper tubing was then soldered to the outer wall of the jacket. The evaporator and transport section calorimeter coolant supply lines were connected in series.

Heat was removed from the condenser section by radiation to a water-cooled double-wall calorimeter fabricated from copper. The calorimeter was 292 mm long, with an inner radius of 32 mm, leaving a gap of 19 mm between the heat pipe wall and the calorimeter surface. The calorimeter was equipped with internal baffles to improve the heat transfer between the inner wall and the coolant flow, and was fitted with an air bleed valve located at the top of the outer wall to ensure complete filling of the calorimeter.

Type K thermocouples located in the calorimeter inlets and outlets and measurements of the coolant mass flow rate through the calorimeters allowed the heat losses from each section of the heat pipe to be calculated. An accurate energy balance for the heat pipe could be computed by adding the heat losses from the evaporator, transport, and condenser sections and comparing the total heat loss to the electrical power input. The heat load transported by the heat pipe was defined as the power output from the condenser calorimeter.

After the installation of all thermocouples and heaters the heat pipe was mounted to an adjustable height support frame with ceramic fiberboard brackets. The heat pipe was then processed on a specially built heat pipe filling station. The heat pipe was evacuated to a pressure of  $10^{-7}$  torr and was initially filled with 43 g of Grade T3N5 sodium. It was necessary to push the sodium into the heat pipe with argon gas, so the heat pipe was hot-processed to remove the noncondensable gas. The hot-processing procedure was performed by reattaching the sodium fill chamber to the heat pipe fill valve, connecting the fill chamber to a high vacuum source, and operating the heat pipe with the fill valve open until isothermal vapor temperatures were observed. The fill valve was then closed, and the heat pipe was ready for testing.

The high-temperature heat pipe with multiple heat sources was tested at Wright State University in a stainless steel vacuum chamber. The vacuum chamber eliminates convection losses,

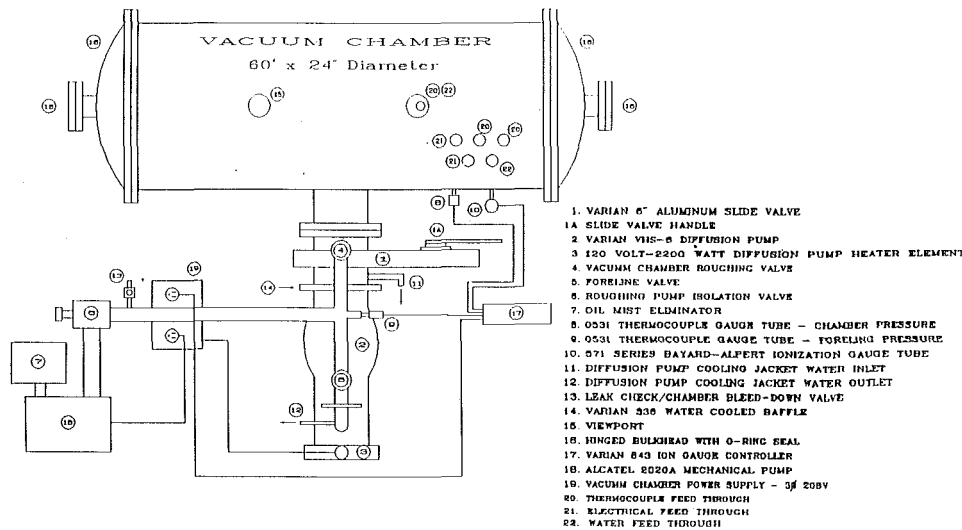


Fig. 3 Vacuum chamber operating system

prevents external oxidation of the heat pipe wall, and provides a physical barrier between the heat pipe and laboratory in case of containment failure. Stainless steel is a standard material used in vacuum chamber construction because it exhibits very low outgassing characteristics under high vacuum, and vacuum tight welds are easily attainable when TIG welding is used. Chamber dimensions were chosen to provide sufficient room inside the chamber for the heat pipe instrumentation and the heater power leads, and to allow testing at various evaporator elevations. The chamber was built with hinged bulkheads at each end to allow easy access to the chamber interior; the bulkheads were sealed with neoprene O-rings. The vacuum chamber evacuation system consisted of a 152-mm diffusion pump with a water-cooled baffle, an aluminum slide valve, and a 480 LPM mechanical pump. Vacuum pressure was monitored by a Bayard-Alpert type ionization gage and a thermocouple gage mounted to the chamber wall. Vacuum ports welded to the chamber wall were fitted with feed-throughs for the heater power leads, calorimeter water supply lines, and the heat pipe thermocouples. The chamber was also fitted with viewports to allow visual observation of the heat pipe during testing. Figure 3 shows the vacuum chamber operating system and auxiliary equipment used in the testing of the high-temperature heat pipe.

## Results and Discussion

The high-temperature heat pipe with multiple heat sources was tested under many different operating conditions. The startup behavior for single and multiple evaporator operation both under vacuum and in air was investigated. The heat pipe was operated with two different fluid charges (30 and 43 g), and was tested with evaporator elevations of 0, 1.4, 3.0, and 5.7 arc deg against gravity. A complete summary of tests completed is given in Table 1. The conditions contained in Table 1 are given for the steady state, although the results presented here are for frozen startup (part I) and continuum transient and steady-state operation (part II), and include the following:

- (A) the electrical input power to each active heater;
- (B) the individually measured power outputs from the evaporator, transport, and condenser section calorimeters;
- (C) the transport section vapor temperature;
- (D) the heat pipe fluid charge and evaporator elevation against gravity.

The legend at the beginning of Table 1 contains explanations for the superscript notations used to identify specific operating conditions reached during each case. Superscripts 1 and 2 modify the case number, and indicate when continuum flow ( $T^*$

= 395°C) was reached in the entire vapor space, and when isothermal operation was attained, respectively. The superscripts 3, 4, and 5 are located adjacent to individual evaporator heater power listings, and indicate that the notated evaporator overheated from wick dryout, the heater reached the maximum allowable temperature (900°C), or the maximum power output from the power supply was reached, respectively.

An experimental uncertainty analysis indicated that the major sources of uncertainty were in measuring the power input to each heater and the vapor temperature. The uncertainty in measuring the power input, as mentioned before, was about 2 percent. The vapor temperature measurement using the multipoint thermocouple probe involved velocity, radiation, and conduction errors. Each error was analyzed by applying the standard method described by Moffat (1962). The maximum uncertainty involved in the measurement of vapor temperature is the sum of the absolute value of each individual error, which is about 3.4 percent.

Repeatability tests were also performed for several cases to check the reliability of the experimental setup. In all the tests, good repeatability was demonstrated. For example, a heat pipe startup test was performed with a total power input of 241 W and the heat pipe reached the steady state with a transport vapor temperature of 456.9°C. The startup performance was repeated with the same total power input. The heat pipe reached steady state with a transport vapor temperature of 456.3°C.

The startup behavior of the high-temperature heat pipe in vacuum was always frontal in nature, with a sharp dropoff in temperature across the vapor front, and no pressure recovery in the condenser. This startup mode is well established for a radiation-cooled condenser, being observed by Merrigan et al. (1986), and Ponnappan (1990), among others. Deverall et al. (1970) concluded that heat rejected by radiation is a self-compensating system and automatically controls the heat-rejection rate. In other words, the active length of the condenser is determined by the surface area necessary to reject the applied heat load. Even though sonic velocities may occur in the condenser, the heat pipe startup is not sonic limited for a radiation-cooled condenser. No startup failures were found during testing in vacuum, even with initial power input levels of 1263 W to the heaters (case 9a). The time necessary to reach steady state from a frozen startup was found to be strictly dependent upon the initial heat load on the heat pipe because the input heat flux determined the evaporation rate at the liquid-vapor interface and the subsequent axial heat transport. The thermal mass of the heat pipe mounting assembly, radiation shields, calorimeters, and the thermal lag in the evaporator heaters also affected the startup time.

**Table 1 High temperature heat pipe with multiple heat sources: steady-state test results in vacuum and air**

All Powers Listed are given in watts

Superscript Legend

1 – continuum flow condition reached in vapor space ( $T^* = 395^\circ\text{C}$ )  
 2 – isothermal flow condition reached in vapor space ( $\Delta T_v < 10^\circ\text{C}$ )  
 3 – dryout condition reached in evaporator  
 4 – maximum allowable heater temperature reached ( $900^\circ\text{C}$ ), test halted  
 5 – maximum output from power supply

| Case               | Power to Evaporator Heater | 1                | 2                | 3                | 4                | Power out (evap.) | Power out (trans.) | Power out (cond.) | Transport Vapor Temp. ( $^\circ\text{C}$ ) | Angle Against Gravity | Fluid Charge | All Powers Listed are given in watts |        |                  |                  |                   |                    |                   |  |                       |              |                |     |
|--------------------|----------------------------|------------------|------------------|------------------|------------------|-------------------|--------------------|-------------------|--|-----------------------|--------------|--------------------------------------|--------|------------------|------------------|-------------------|--------------------|-------------------|--|-----------------------|--------------|----------------|-----|
|                    |                            |                  |                  |                  |                  |                   |                    |                   |  |                       |              | 1                                    | 2      | 3                | 4                | Power out (evap.) | Power out (trans.) | Power out (cond.) | Transport Vapor Temp. ( $^\circ\text{C}$ ) | Angle Against Gravity | Fluid Charge |                |     |
| 14a <sup>1</sup>   | Vacuum                     | 507              | –                | –                | –                | 214               | 15                 | 240               | 466.9                                      | 3 <sup>0</sup>        | 30g          | 14b <sup>1</sup>                     | Vacuum | 605              | –                | –                 | –                  | 244               | 20   | 296                   | 498.2        |                |     |
| 14c <sup>2</sup>   | Vacuum                     | 678 <sup>4</sup> | –                | –                | –                | 267               | 20                 | 340               | 518.2                                      |                       |              | 15a                                  | Vacuum | –                | 205              | –                 | –                  | 127               | 10   | 60                    | 404.6        | 3 <sup>0</sup> | 30g |
| 15a <sup>1</sup>   | Vacuum                     | –                | 205              | –                | –                | 127               | 10                 | 60                | 404.6                                      | 3 <sup>0</sup>        | 30g          | 15b                                  | Vacuum | –                | 301              | –                 | –                  | 155               | 12   | 131                   | 429.7        |                |     |
| 15b <sup>1</sup>   | Vacuum                     | –                | 301              | –                | –                | 155               | 12                 | 131               | 429.7                                      |                       |              | 15c <sup>1</sup>                     | Vacuum | –                | 402              | –                 | –                  | 181               | 14   | 205                   | 447.6        |                |     |
| 15c <sup>1</sup>   | Vacuum                     | –                | 402              | –                | –                | 181               | 14                 | 205               | 447.6                                      |                       |              | 15d                                  | Vacuum | –                | 490              | –                 | –                  | 203               | 16   | 262                   | 476.2        |                |     |
| 15d                | Vacuum                     | –                | 490              | –                | –                | 203               | 16                 | 262               | 476.2                                      |                       |              | 15e                                  | Vacuum | –                | 562 <sup>4</sup> | –                 | –                  | 228               | 20   | 306                   | 500.1        |                |     |
| 15e                | Vacuum                     | –                | 562 <sup>4</sup> | –                | –                | 228               | 20                 | 306               | 500.1                                      |                       |              | 16a                                  | Vacuum | –                | –                | 203               | –                  | 127               | 10   | 66                    | 405.2        | 3 <sup>0</sup> | 30g |
| 16a                | Vacuum                     | –                | –                | 203              | –                | 127               | 10                 | 66                | 405.2                                      | 3 <sup>0</sup>        | 30g          | 16b                                  | Vacuum | –                | –                | 303               | –                  | 157               | 12   | 131                   | 430.6        |                |     |
| 16b                | Vacuum                     | –                | –                | 303              | –                | 157               | 12                 | 131               | 430.6                                      |                       |              | 16c <sup>1</sup>                     | Vacuum | –                | –                | 403               | –                  | 179               | 14   | 197                   | 448.1        |                |     |
| 16c <sup>1</sup>   | Vacuum                     | –                | –                | 403              | –                | 179               | 14                 | 197               | 448.1                                      |                       |              | 16d                                  | Vacuum | –                | –                | 504 <sup>4</sup>  | –                  | 209               | 18   | 262                   | 479.5        |                |     |
| 16d                | Vacuum                     | –                | –                | 504 <sup>4</sup> | –                | 209               | 18                 | 262               | 479.5                                      |                       |              | 17a                                  | Vacuum | –                | –                | –                 | 207                | 118               | 14   | 69                    | 406.8        | 3 <sup>0</sup> | 30g |
| 17a                | Vacuum                     | –                | –                | –                | 207              | 118               | 14                 | 69                | 406.8                                      | 3 <sup>0</sup>        | 30g          | 17b                                  | Vacuum | –                | –                | –                 | 300                | 151               | 18   | 118                   | 425.8        |                |     |
| 17b                | Vacuum                     | –                | –                | –                | 300              | 151               | 18                 | 118               | 425.8                                      |                       |              | 17c <sup>1</sup>                     | Vacuum | –                | –                | –                 | 401                | 179               | 22   | 181                   | 441.9        |                |     |
| 17c <sup>1</sup>   | Vacuum                     | –                | –                | –                | 401              | 179               | 22                 | 181               | 441.9                                      |                       |              | 17d                                  | Vacuum | –                | –                | –                 | 480 <sup>4</sup>   | 201               | 22   | 230                   | 459.0        |                |     |
| 17d                | Vacuum                     | –                | –                | –                | 480 <sup>4</sup> | 201               | 22                 | 230               | 459.0                                      |                       |              | 18a <sup>1</sup>                     | Vacuum | 210              | –                | 210               | –                  | 190               | 13   | 206                   | 447.8        | 3 <sup>0</sup> | 30g |
| 18a <sup>1</sup>   | Vacuum                     | 210              | –                | 210              | –                | 190               | 13                 | 206               | 447.8                                      | 3 <sup>0</sup>        | 30g          | 18b <sup>2</sup>                     | Vacuum | 306              | –                | 304               | –                  | 250               | 18   | 320                   | 505.9        |                |     |
| 18b <sup>2</sup>   | Vacuum                     | 306              | –                | 304              | –                | 250               | 18                 | 320               | 505.9                                      |                       |              | 18c                                  | Vacuum | 405              | –                | 401               | –                  | 324               | 32   | 437                   | 561.5        |                |     |
| 18c                | Vacuum                     | 405              | –                | 401              | –                | 324               | 32                 | 437               | 561.5                                      |                       |              | 18d                                  | Vacuum | 507              | –                | 503               | –                  | 403               | 39   | 555                   | 607.7        |                |     |
| 18d                | Vacuum                     | 507              | –                | 503              | –                | 403               | 39                 | 555               | 607.7                                      |                       |              | 19a <sup>1</sup>                     | Vacuum | 208              | –                | –                 | 207                | 190               | 19   | 197                   | 443.3        | 3 <sup>0</sup> | 30g |
| 19a <sup>1</sup>   | Vacuum                     | 208              | –                | –                | 207              | 190               | 19                 | 197               | 443.3                                      | 3 <sup>0</sup>        | 30g          | 19b <sup>2</sup>                     | Vacuum | 302              | –                | –                 | 303                | 244               | 26   | 314                   | 496.6        |                |     |
| 19b <sup>2</sup>   | Vacuum                     | 302              | –                | –                | 303              | 244               | 26                 | 314               | 496.6                                      |                       |              | 19c                                  | Vacuum | 399              | –                | –                 | 401                | 311               | 34   | 427                   | 550.8        |                |     |
| 19c                | Vacuum                     | 399              | –                | –                | 401              | 311               | 34                 | 427               | 550.8                                      |                       |              | 19d                                  | Vacuum | 479              | –                | –                 | 473 <sup>4</sup>   | 366               | 38   | 510                   | 587.3        |                |     |
| 19d                | Vacuum                     | 479              | –                | –                | 473 <sup>4</sup> | 366               | 38                 | 510               | 587.3                                      |                       |              | 20a                                  | Vacuum | –                | –                | 98                | 100                | 109               | 11   | 82                    | 417.2        | 0 <sup>0</sup> | 43g |
| 20a                | Vacuum                     | –                | –                | 98               | 100              | 109               | 11                 | 82                | 417.2                                      | 0 <sup>0</sup>        | 43g          | 20b                                  | Vacuum | –                | –                | 141               | 143                | 151               | 15   | 129                   | 431.2        |                |     |
| 20b                | Vacuum                     | –                | –                | 141              | 143              | 151               | 15                 | 129               | 431.2                                      |                       |              | 20c <sup>1</sup>                     | Vacuum | –                | –                | 180               | 181                | 168               | 15   | 176                   | 447.9        |                |     |
| 20c <sup>1</sup>   | Vacuum                     | –                | –                | 180              | 181              | 168               | 15                 | 176               | 447.9                                      |                       |              | 20d                                  | Vacuum | –                | –                | 219               | 220                | 195               | 18   | 222                   | 472.7        |                |     |
| 20d                | Vacuum                     | –                | –                | 219              | 220              | 195               | 18                 | 222               | 472.7                                      |                       |              | 20e <sup>2</sup>                     | Vacuum | –                | –                | 260               | 258                | 225               | 20   | 278                   | 505.9        |                |     |
| 20e <sup>2</sup>   | Vacuum                     | –                | –                | 260              | 258              | 225               | 20                 | 278               | 505.9                                      |                       |              | 21a                                  | Vacuum | –                | 100              | 101               | –                  | 127               | 8  | 68                    | 409.3        | 0 <sup>0</sup> | 43g |
| 21a                | Vacuum                     | –                | 100              | 101              | –                | 127               | 8                  | 68                | 409.3                                      | 0 <sup>0</sup>        | 43g          | 21b                                  | Vacuum | –                | 139              | 140               | –                  | 155               | 10   | 121                   | 430.8        |                |     |
| 21b                | Vacuum                     | –                | 139              | 140              | –                | 155               | 10                 | 121               | 430.8                                      |                       |              | 21c <sup>1</sup>                     | Vacuum | –                | 182              | 182               | –                  | 179               | 12   | 181                   | 452.0        |                |     |
| 21c <sup>1</sup>   | Vacuum                     | –                | 182              | 182              | –                | 179               | 12                 | 181               | 452.0                                      |                       |              | 21d                                  | Vacuum | –                | 220              | 219               | –                  | 195               | 14   | 227                   | 480.8        |                |     |
| 21d                | Vacuum                     | –                | 220              | 219              | –                | 195               | 14                 | 227               | 480.8                                      |                       |              | 21e <sup>2</sup>                     | Vacuum | –                | 260              | 264               | –                  | 229               | 17   | 282                   | 511.6        |                |     |
| 21e <sup>2</sup>   | Vacuum                     | –                | 260              | 264              | –                | 229               | 17                 | 282               | 511.6                                      |                       |              | 22a                                  | Air    | 529              | –                | –                 | –                  | 272               | 33   | 196                   | 438.5        | 3 <sup>0</sup> | 30g |
| 22a                | Air                        | 529              | –                | –                | –                | 272               | 33                 | 196               | 438.5                                      | 3 <sup>0</sup>        | 30g          | 22b                                  | Air    | 627              | –                | –                 | –                  | 301               | 33   | 267                   | 449.9        |                |     |
| 22b                | Air                        | 627              | –                | –                | –                | 301               | 33                 | 267               | 449.9                                      |                       |              | 22c <sup>1</sup>                     | Air    | 727 <sup>5</sup> | –                | –                 | –                  | 314               | 37   | 325                   | 460.8        |                |     |
| 22c <sup>1</sup>   | Air                        | 727 <sup>5</sup> | –                | –                | –                | 314               | 37                 | 325               | 460.8                                      |                       |              | 23a                                  | Air    | –                | 394              | –                 | –                  | 249               | 26   | 99                    | 424.4        | 3 <sup>0</sup> | 30g |
| 23a                | Air                        | –                | 394              | –                | –                | 249               | 26                 | 99                | 424.4                                      | 3 <sup>0</sup>        | 30g          | 23b                                  | Air    | –                | 505              | –                 | –                  | 282               | 30   | 180                   | 437.2        |                |     |
| 23b                | Air                        | –                | 505              | –                | –                | 282               | 30                 | 180               | 437.2                                      |                       |              | 23c                                  | Air    | –                | 603              | –                 | –                  | 314               | 37   | 252                   | 449.5        |                |     |
| 23c                | Air                        | –                | 603              | –                | –                | 314               | 37                 | 252               | 449.5                                      |                       |              | 23d <sup>1</sup>                     | Air    | –                | 661 <sup>5</sup> | –                 | –                  | 333               | 37   | 296                   | 457.7        |                |     |
| 23d <sup>1</sup>   | Air                        | –                | 661 <sup>5</sup> | –                | –                | 333               | 37                 | 296               | 457.7                                      |                       |              | 24a                                  | Air    | –                | –                | 400               | –                  | 251               | 26   | 115                   | 432.8        | 3 <sup>0</sup> | 30g |
| 24a                | Air                        | –                | –                | 400              | –                | 251               | 26                 | 115               | 432.8                                      | 3 <sup>0</sup>        | 30g          | 24b                                  | Air    | –                | –                | 509               | –                  | 268               | 25   | 191                   | 444.5        |                |     |
| 24b                | Air                        | –                | –                | 509              | –                | 268               | 25                 | 191               | 444.5                                      |                       |              | 24c                                  | Air    | –                | –                | 604               | –                  | 304               | 22   | 257                   | 465.1        |                |     |
| 24c                | Air                        | –                | –                | 604              | –                | 304               | 22                 | 257               | 465.1                                      |                       |              | 24d <sup>1</sup>                     | Air    | –                | –                | 703 <sup>3</sup>  | –                  | 331               | 26   | 335                   | 466.2        |                |     |
| 24d <sup>1</sup>   | Air                        | –                | –                | 703 <sup>3</sup> | –                | 331               | 26                 | 335               | 466.2                                      |                       |              | 25a                                  | Air    | –                | –                | –                 | 397                | 214               | 36   | 148                   | 433.5        | 3 <sup>0</sup> | 30g |
| 25a                | Air                        | –                | –                | –                | 397              | 214               | 36                 | 148               | 433.5                                      | 3 <sup>0</sup>        | 30g          | 25b                                  | Air    | –                | –                | –                 | 502                | 258               | 37   | 200                   | 441.6        |                |     |
| 25b                | Air                        | –                | –                | –                | 502              | 258               | 37                 | 200               | 441.6                                      |                       |              | 25c                                  | Air    | –                | –                | –                 | 601                | 287               | 46   | 265                   | 453.8        |                |     |
| 25c                | Air                        | –                | –                | –                | 601              | 287               | 46                 | 265               | 453.8                                      |                       |              | 25d <sup>1</sup>                     | Air    | –                | –                | –                 | 727 <sup>5</sup>   | 324               | 50   | 338                   | 470.9        |                |     |
| 25d <sup>1</sup>   | Air                        | –                | –                | –                | 727 <sup>5</sup> | 324               | 50                 | 338               | 470.9                                      |                       |              | 26a                                  | Air    | 199              | –                | 201               | –                  | 254               | 28   | 129                   | 430.1        | 3 <sup>0</sup> | 30g |
| 26a                | Air                        | 199              | –                | 201              | –                | 254               | 28                 | 129               | 430.1                                      | 3 <sup>0</sup>        | 30g          | 26b                                  | Air    | 307              | –                | 302               | –                  | 283               | 32   | 272                   | 458.8        |                |     |
| 26b                | Air                        | 307              | –                | 302              | –                | 283               | 32                 | 272               | 458.8                                      |                       |              | 26c <sup>1,2</sup>                   | Air    | 405              | –                | 407               | –                  | 344               | 40   | 419                   | 504.6        |                |     |
| 26c <sup>1,2</sup> | Air                        | 405              | –                | 407              | –                | 344               | 40                 | 419               | 504.6                                      |                       |              | 26d                                  | Air    | 504              | –                | 505               | –                  | 408               | 49   | 513                   | 551.8        |                |     |
| 26d                | Air                        | 504              | –                | 505              | –                | 408               | 49                 | 513               | 551.8                                      |                       |              | 26e                                  | Air    | 603              | –                | 600               | –                  | 486               | 57   | 628                   | 593.2        |                |     |
| 26e                | Air                        | 603              | –                | 600              | –                | 486               | 57                 | 628               | 593.2                                      |                       |              | 26f                                  | Air    | 695              | –                | 696 <sup>3</sup>  | –                  | 555               | 61   | 716                   | 628.1        |                |     |
| 26f                | Air                        | 695              | –                | 696 <sup>3</sup> | –                | 555               | 61                 | 716               | 628.1                                      |                       |              | 27a                                  | Air    | 205              | –                | –                 | 207                | 235               | 33   | 130                   | 433.6        | 3 <sup>0</sup> | 30g |
| 27a                | Air                        | 205              | –                | –                | 207              | 235               | 33                 | 130               | 433.6                                      | 3 <sup>0</sup>        | 30g          | 27b                                  | Air    | 305              | –                | –                 | 303                | 273               | 37   | 287                   | 461.7        |                |     |
| 27b                | Air                        | 305              | –                | –                | 303              | 273               | 37                 | 287               | 461.7                                      |                       |              | 27c <sup>1,2</sup>                   | Air    | 403              | –                | –                 | 404                | 327               | 48   | 412                   | 502.2        |                |     |
| 27c <sup>1,2</sup> | Air                        | 403              | –                | –                | 404              | 327               | 48                 | 412               | 502.2                                      |                       |              | 27d                                  | Air    | 504              | –                | –                 | 507                | 401               | 55   | 522                   | 548.5        |                |     |

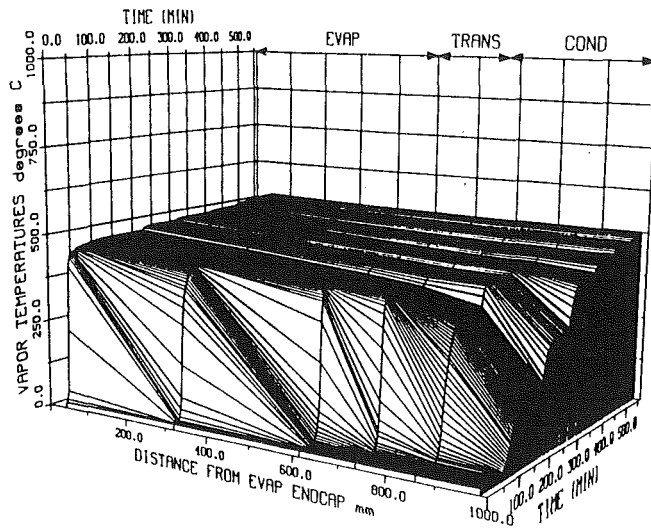


Fig. 4a Case 11, in vacuum

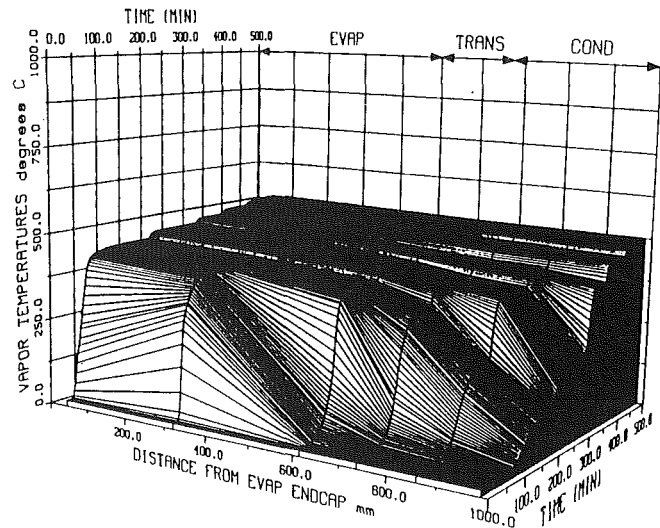


Fig. 5a Case 15, in vacuum

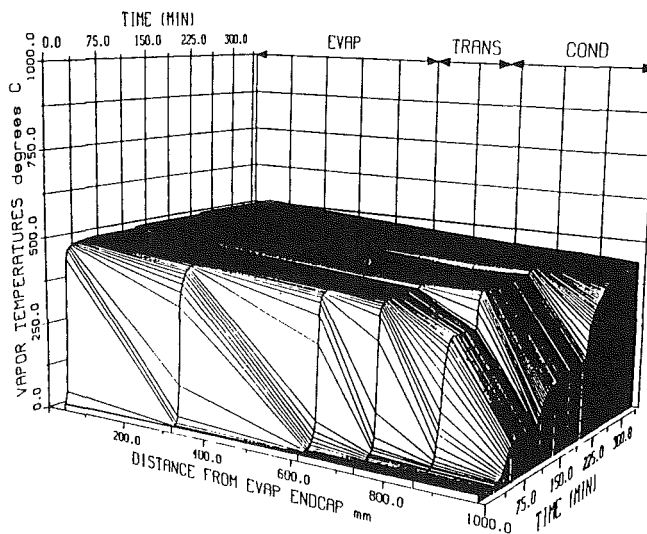


Fig. 4b Case 22, in air

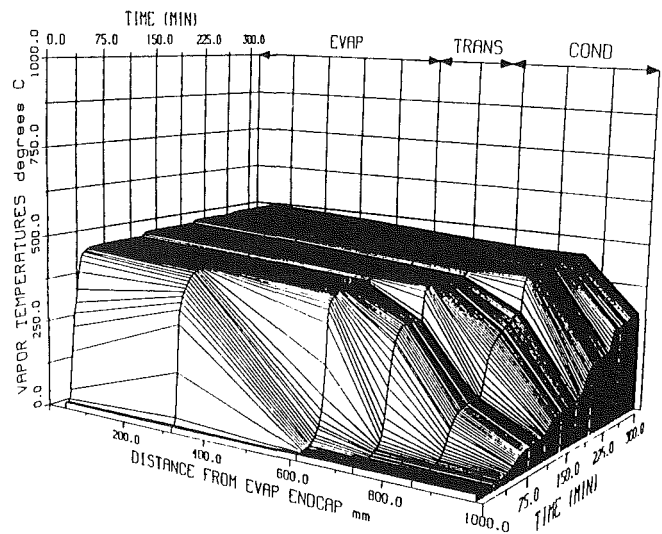


Fig. 5b Case 23, in air

Fig. 4 Transient axial vapor temperature profiles with evaporator 1 active

Fig. 5 Transient axial vapor temperature profiles with evaporator 2 active

Since no startup failures were found during testing in vacuum, several tests were conducted with the heat pipe operating in air, which increased the heat rejection rate at the condenser by the addition of convection heat losses. Figures 4(a) and 4(b) present three-dimensional transient vapor temperature profiles during operation under vacuum (case 11) and in air (case 22) with only evaporator 1 active. Figures 5(a) and 5(b) are similar graphs during operation under vacuum (case 15) and in air (case 23) with only evaporator 2 active. Both sets of figures clearly show how the startup behavior of the heat pipe changed with the increased heat rejection at the condenser. The startup power inputs for the cases in air (529 and 394 W) were much higher than those for startup under vacuum (311 and 205 W), the axial temperature gradient in the condenser was much more pronounced, and supersonic vapor flow occurred within the condenser region. No startup failures were found during operation in air, although much higher power levels were required to attain continuum flow in the entire vapor space. It is important to note that the total energy balance for the heat pipe was maintained during operation in air. This was due to the radiation shield insulation in the evaporator and transport

sections, which effectively eliminated air exchange between the room and the heat pipe assembly, so there were minimal convection losses from the heat pipe assembly to the environment. Also, the heat pipe itself was mounted on ceramic board supports, so very little heat was lost by conduction.

Figure 6(a) presents the transient vapor temperatures versus time for a high-power startup with only evaporator 1 active under vacuum (case 14a), and in air (case 22a). The six vapor space thermocouples are given curve labels V1, V2, V3, . . . , etc., and each specific case is identified by the number to the right of the hyphen, i.e., V2-14 specifies vapor thermocouple #2 for case 14. Exact vapor space thermocouple locations are given in Fig. 1. The transient vapor temperature profiles for the thermocouples located within the evaporator section, the transport section, and at the beginning of the condenser (V1, V2, V3, V4) show identical trends up to approximately 35 minutes from the initial power input, both under vacuum and in air. The heat pipe is well insulated in the evaporator and transport sections, and the presence of air within the insulation apparently has a negligible effect on the heat losses in these sections. The increased heat rejection rate at the condenser

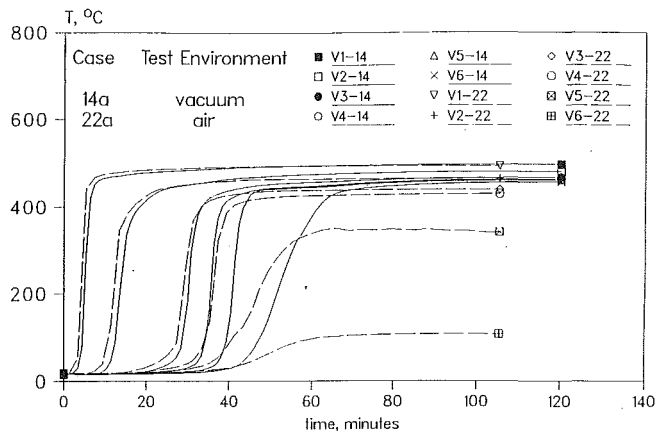


Figure 6a. Evaporator 1 active

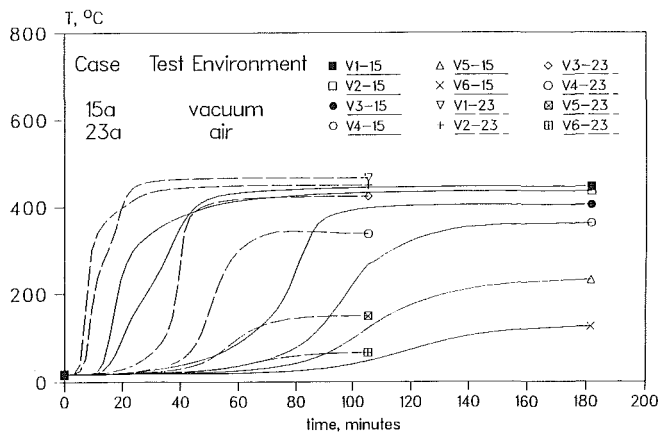


Figure 6b. Evaporator 2 active

Fig. 6 Effect of test environment on transient vapor temperatures during startup

during operation in air has a noticeable effect on the vapor temperatures within the condenser, shown by curves V5 and V6. Continuum flow was established in the entire heat pipe for startup under vacuum (case 14a), but during operation in air (case 22a) the end of the condenser is barely above the melting temperature of sodium. The startup of the heat pipe for single evaporator operation in air was definitely sonic limited, and the pressure drop in the condenser, as indicated from the steep dropoff in the vapor temperatures, shows that supersonic vapor flow existed within the condenser.

Figure 6(b) is a plot of transient vapor temperatures for startup with evaporator 2 active under vacuum (case 15a) and in air (case 23a). The vapor profiles show no similarities between the two cases, except for the first thermocouple located in the evaporator section (V1). Although an input power level of 205 W was insufficient to reach continuum flow in the entire heat pipe for startup in vacuum, the final steady-state evaporator vapor temperatures were nearly the same as for case 23 (in air), which had a startup power level of 394 W. The time necessary to reach steady state under vacuum was almost twice as long as that in air because of the smaller heat rejection rate at the condenser. The slope of the transient condenser vapor temperatures for startup under vacuum shows the slower temperature rise to the final steady state. The case in air reached steady state within 105 minutes, but the vapor front became essentially stationary at a time of about 70 minutes, when the front entered the condenser and supersonic vapor flow occurred. The low condenser heat rejection rate during operation in vacuum apparently prevented supersonic vapor velocities

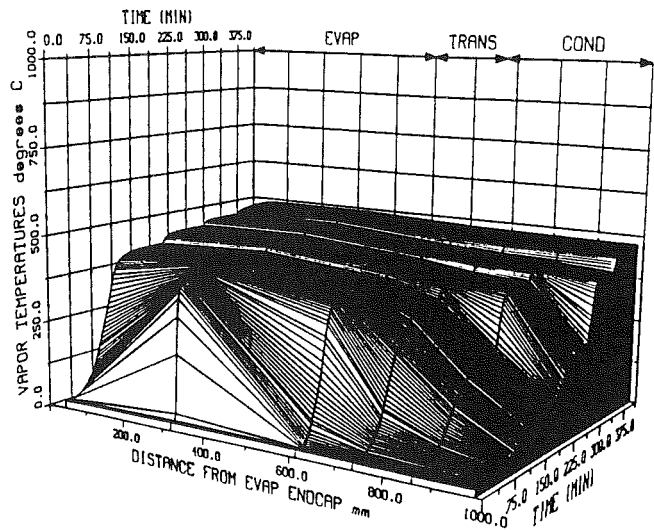


Fig. 7a Case 16, evaporator 3 active

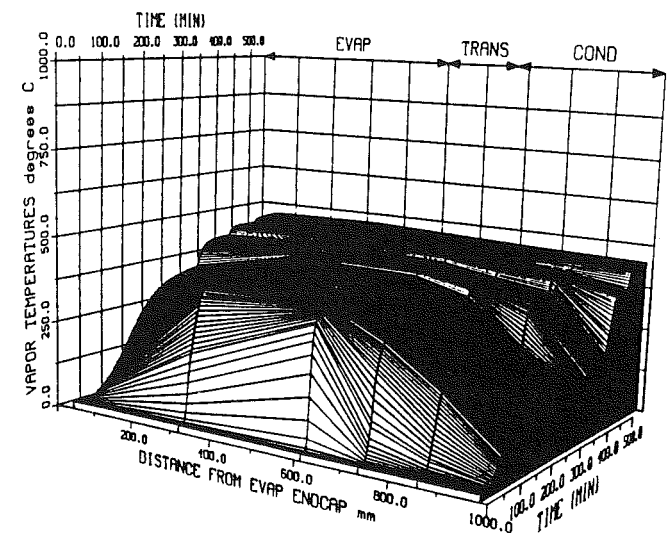


Fig. 7b Case 17, evaporator 4 active

Fig. 7 Transient axial vapor temperature profiles for one-evaporator operation in vacuum

and allowed the condenser to rise slowly in temperature to the final steady-state condition.

The startup behavior of the heat pipe with evaporators 3 or 4 active was quite different from a standard configuration heat pipe, where the evaporator is located at one end of the heat pipe. Figures 7(a) and 7(b), three-dimensional plots of the transient axial vapor temperature profiles for cases 16 and 17, demonstrate that during startup with an evaporator located near the middle of the heat pipe, the vapor flowed toward both the condenser and the evaporator end caps. When continuum flow was established in the entire evaporator section, the vapor flow assumed a "normal" profile, where the evaporator section was nearly isothermal and a temperature gradient existed in the condenser section.

The transient axial vapor temperature profiles for some two-evaporator startups are given in Figs. 8(a) and 8(b). Figure 8(a) (case 19, evaporators 1 and 4 active) indicates that a large temperature drop existed between the two active evaporators during startup due to the sudden heat flux applied to the evaporator sections, and the heat losses in the inactive evaporator sections. The axial vapor temperature gradients in Fig.

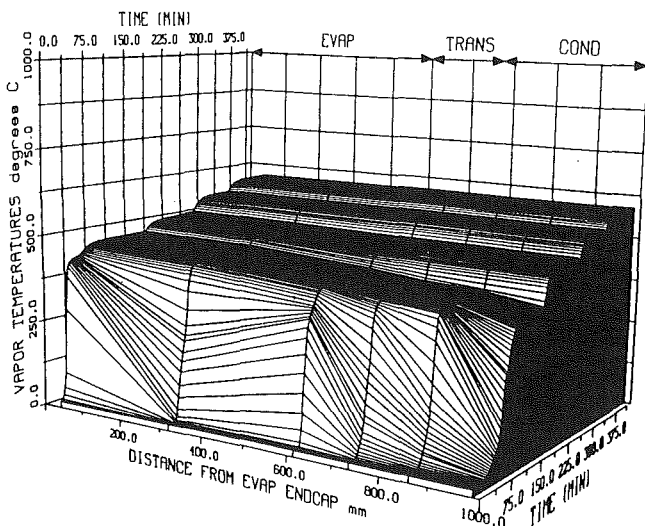


Fig. 8a Case 19, evaporators 1 and 4 active

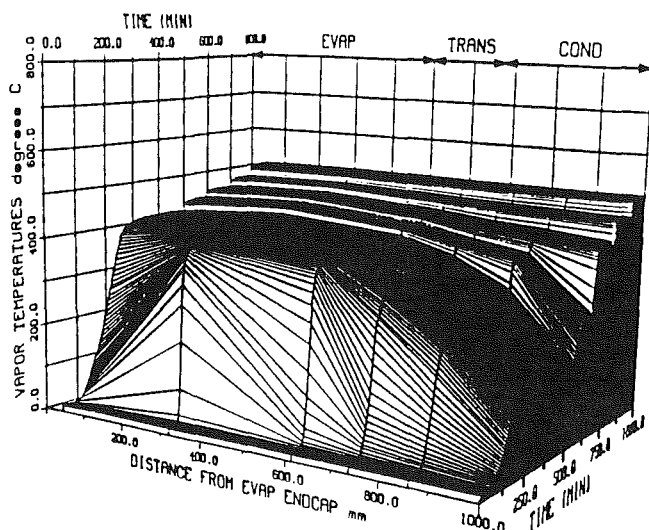


Fig. 8b Case 20, evaporators 3 and 4 active

Fig. 8 Transient axial vapor temperature profiles for two-evaporator operation in vacuum

8(b) (case 20, evaporators 3 and 4 active) shows that during startup in vacuum the vapor flow reached supersonic velocities in both directions, i.e., toward the evaporator end and toward the condenser end. The experimental setup had a certain effect on the degree of two-way vapor flow. The evaporator section of the heat pipe was insulated, but not truly adiabatic, so condensation occurred in the inactive areas of the evaporator section. The heat losses in the evaporator section contributed to the extreme temperature gradients between the active evaporators during startup. The three-dimensional two-evaporator

startup graphs clearly show that after continuum flow was reached in the evaporator section, the evaporator vapor temperature remained relatively constant as the vapor front moved down the heat pipe. This behavior has also been observed by Sockol and Forman (1970) for a radiation-cooled lithium heat pipe.

## Conclusions

A sodium/stainless steel heat pipe with a simple circumferential screen wick and multiple heat sources was successfully fabricated, processed, and tested, both in air and under vacuum. Detailed measurements of the heat pipe wall and vapor temperatures, multiple evaporator heat inputs, and steady-state heat losses from the evaporator, transport, and condenser sections were made. These tests showed that the startup behavior of a liquid metal heat pipe from the frozen state was greatly dependent upon the heat rejection rate at the condenser. Supersonic vapor velocities occurred in the condenser section during startup, and two-way vapor flow was observed in the evaporator section during several two-evaporator startups. No startup failures (evaporator dryout) were found for single or multiple evaporator operation in air or under vacuum, although startup in air was sonic limited until isothermal operation was reached.

The coil-on sheathed electrical resistance heaters used in the evaporator section were the primary limitation to finding the maximum heat transport capacity of the heat pipe, because approximately 40 percent of the input power to the heaters was lost, and not transported to the heat pipe condenser. Even with radiation shield insulation, heat losses from the evaporator and transport sections were significant, but water-cooled calorimeters installed on each section of the heat pipe allowed energy balances approaching 100 percent to be made during steady-state testing.

## Acknowledgments

Funding for this work was provided by a joint effort of the NASA Lewis Research Center and Thermal Energy Group of the Aero Propulsion Laboratory of the U.S. Air Force under contract No. F33615-89-C-2820.

## References

- Chi, S. W., 1976, *Heat Pipe Theory and Practice*, Hemisphere Publishing Corp., New York.
- Deverall, J. E., Kemme, J. E., and Florschuetz, L. W., 1970, "Sonic Limitations and Startup Problems of Heat Pipes," Los Alamos Scientific Laboratory Report LA-4518, Los Alamos, NM.
- Dunn, P. D., and Reay, D. A., 1982, *Heat Pipes*, 3rd ed., Pergamon Press, New York.
- Merrigan, M. A., Keddy, E. S. and Sena, J. T., 1986, "Transient Performance Investigation of a Space Power System Heat Pipe," AIAA Paper No. 86-1273.
- Moffat, R. J., 1962, "Gas Temperature Measurement," in: *Temperature, Its Measurement and Control in Science and Industry*, Vol. 3, Part 2, Reinhold Publishers, NY.
- Ponnappan, R., 1990, "Comparison of Vacuum and Gas Loaded Mode Performances of a LMHP," AIAA Paper No. 90-1755.
- Sockol, P. M., and Forman, R., 1970, "Re-examination of Heat Pipe Startup," *Proc. 9th IEEE Thermionic Conversion Specialist Conference*, pp. 571-573.



# A Study of High-Temperature Heat Pipes With Multiple Heat Sources and Sinks: Part II—Analysis of Continuum Transient and Steady-State Experimental Data With Numerical Predictions

A. Faghri

Brage Golding Distinguished Professor.

M. Buchko<sup>1</sup>

Graduate Research Assistant.

Y. Cao

Research Associate.

Department of Mechanical and Materials  
Engineering,  
Wright State University,  
Dayton, OH 45435

*The experimental data presented in Part I were analyzed concerning the heat pipe performance characteristics and design. Postexperiment examination of the loosely wrapped screen wick revealed annular gaps both between the wick and the heat pipe wall and between adjacent screen layers, which greatly enhanced the maximum heat capacity of the heat pipe compared to the analytical capillary limit for a tightly wrapped screen wick. A numerical simulation for transient heat pipe performances including the vapor region, wick structure, and the heat pipe wall is given. Numerical results for continuum transient and steady-state operations with multiple heat sources were compared with experimental results and found to be in good agreement.*

## Introduction

Experimental profiles for heat pipe startup from the frozen state have been presented in Part I of this paper. One of the objectives of the experimental study was to understand the transient and steady-state performance characteristics of the heat pipe, which are very important to heat pipe design and fabrication. In this part of the paper, the experimental results of the performance characteristics for the continuum transient and steady-state operation of the heat pipe are presented and analyzed, and the performance limits for operation with varying heat fluxes and locations are determined. Another objective of the experimental study was to provide accurate and complete experimental results for the development and verification of numerical simulation models.

Transient thermal analyses of heat pipes are categorized in three basic types: vapor flow in the core region including both continuum transient and free molecular conditions; transient liquid flow in the wick with the possibility of melting inside the wick as well as evaporation and condensation at the vapor/liquid interface; and transient heat conduction in the heat pipe wall. A recent detailed literature survey concerning the thermal analysis of heat pipes was given by Chen and Faghri (1990). This review covered both transient and steady-state operations as well as one- or two-dimensional modeling.

Jang et al. (1990) developed a comprehensive mathematical model and analysis of heat pipe startup from the frozen state. Different startup periods were described and the general mathematical formulation for each period was given. In an attempt to solve the governing equations, the liquid flow in the porous media was neglected, and the vapor flow was assumed to be one-dimensional. No comparison was made with experimental results.

Cao and Faghri (1990) developed a transient one-dimensional compressible analysis for high-temperature heat pipes

with a pulsed heat input. In this model, they also neglected the liquid flow in the wick by assuming the wick to be a pure conduction problem with an effective thermal conductivity.

All of the previous transient models either were not compared to any experimental data or were only compared to a simulated heat pipe using air flow in a porous pipe. In this paper, the numerical model of Cao and Faghri (1990) was adapted to the high-temperature heat pipe with multiple heat sources and sinks. The compressible two-dimensional transient mass, momentum, and energy equations in vapor region, and the energy equations in the wick and wall regions were solved as a conjugate problem. This model also eliminated the use of any empirical model for friction coefficients used in the one-dimensional transient vapor flow models. The transient experimental results for the vapor temperature along the heat pipe with multiple heat sources and sinks are also compared with the proposed model.

## Characteristics of Continuum Transient and Steady-State Operations

The experimental heat pipe (Part I) was operated with two different fluid charges (30 and 43 g). At first it appeared that the change in the fluid charge had a major effect on the steady-state operating temperature of the heat pipe. Figure 1 shows steady-state axial vapor temperature profiles for four-evaporator operation in vacuum before and after the removal of the excess sodium. The steady-state vapor temperature was about 25°C colder with a fluid charge of 30 g versus the same test with 43 g. The actual cause of the lower temperatures in the 30 g fluid charge cases was a slight increase in the emissivity of the heat pipe wall. Sodium was removed from the heat pipe during isothermal operation in air, and an oxide with a higher emissivity was formed on the heat pipe wall. Any effect of the fluid charge on the steady-state vapor temperatures would be negligible since the temperature of a thin liquid pool in the condenser would be close to the equilibrium temperature. Although the operating temperature was found to be a function of the wall emissivity, the total time necessary for startup from

<sup>1</sup> Present address: NASA Goddard Space Flight Center, Greenbelt, MD 20771.

Contributed by the Heat Transfer Division and presented at the National Heat Transfer Conference, Minneapolis, Minnesota, July 28–31, 1991. Manuscript received by the Heat Transfer Division December 20, 1990; revision received June 4, 1991. Keywords: Heat Pipes and Thermosyphons, Numerical Methods, Transient and Unsteady Heat Transfer.

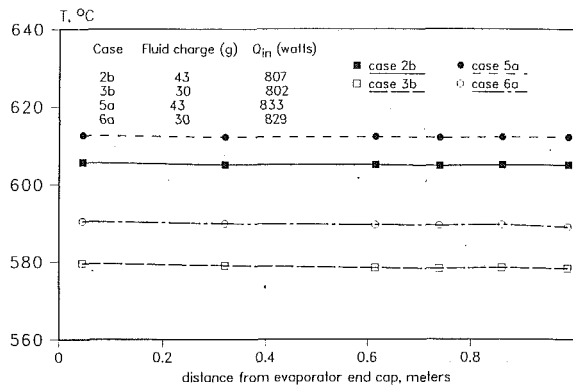


Fig. 1 Effect of emissivity on steady-state axial vapor temperature profiles

the frozen state to a steady-state condition did not change by any significant amount for the two fluid charges, since the heat capacity of the excess sodium was quite small when compared to the thermal mass of the heat pipe assembly.

A frequently encountered problem when testing heat pipes is the apparent sensitivity of the heat pipe to sudden increases in the applied heat loads, although the problem is more likely to occur in an arterial or composite wick heat pipe. The multiple heat source heat pipe had a simple circumferential screen wick, and showed no sensitivity to the startup input power level, or to large power increases from a steady-state condition. Figure 2(a) presents steady-state axial vapor temperature profiles for four-evaporator operation in vacuum, and shows that the final steady-state temperature reached was independent of the startup power level. Figure 2(b) shows the same phenomenon for single evaporator operation in air. The fact that the initial power level and the size of subsequent power increases had no effect on the final steady-state temperature of the heat pipe (with the final boundary conditions being the same) proves that the experimental results are repeatable.

Figures 3 and 4 are plots of the steady-state condenser power output versus the transport section vapor temperature during operation both in air and under vacuum for single-evaporator cases, and their corresponding steady-state vapor temperature profiles. Also shown are the condenser radiation heat transfer limit (calculated as the maximum radiation heat transfer from

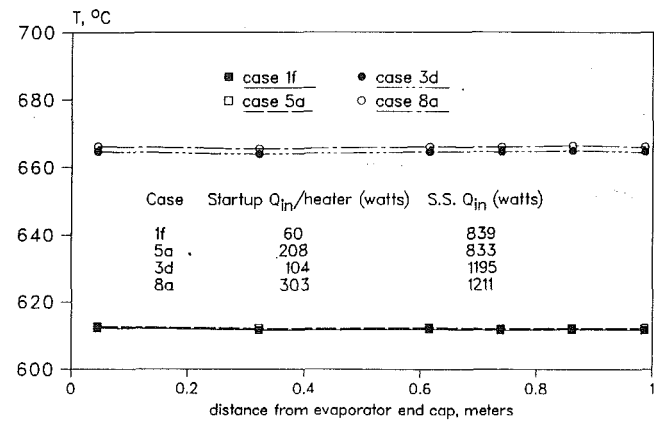


Fig. 2(a) Four evaporator operation

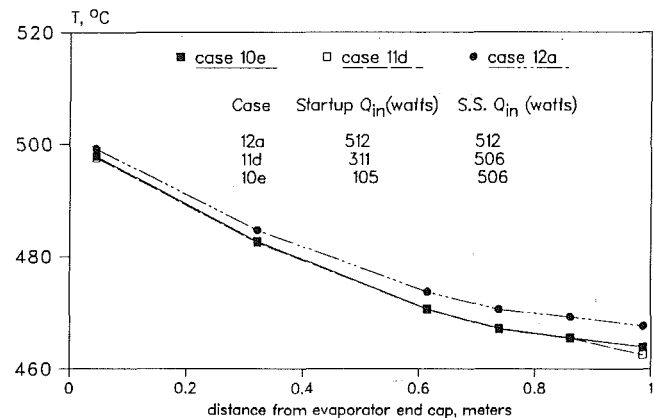


Fig. 2(b) One evaporator operation

Fig. 2 Effect of startup power levels on steady-state axial vapor temperature profiles

the condenser surface area for a given condenser wall temperature), and the heat pipe entrainment, sonic, and capillary limit curves. The heat pipe operating limits were calculated from the standard equations found from Chi (1976), assuming that only one evaporator was active. During startup in vacuum the heat pipe operated along the sonic limit until isothermal

## Nomenclature

$a$  = coefficient in Eq. (17)  
 $b$  = source term in Eq. (17)  
 $c_p$  = specific heat at constant pressure, J/(kg K)  
 $h$  = convective heat transfer coefficient, W/(m<sup>2</sup> K)  
 $h_{fg}$  = latent heat of evaporation, J/kg  
 $k$  = thermal conductivity, W/(m K)  
 $L$  = total length of the heat pipe, m  
 $p$  = vapor pressure, N/m<sup>2</sup>  
 $p'$  = pressure correction  
 $Q_{in}$  = heat input rate at the evaporator section, W  
 $Q_{out}$  = heat output rate at the condenser, W  
 $q$  = heat flux, W/m<sup>2</sup>  
 $R$  = gas constant, J/(kg K)  
 $R_v$  = vapor space radius, m  
 $R_w$  = wick-wall interface radius, m

$R_o$  = outer pipe wall radius, m  
 $Re$  = axial Reynolds number  
 $r$  = radial coordinate, m  
 $t$  = time, s  
 $T$  = temperature, K  
 $T_a$  = environmental temperature, K  
 $T_w$  = outer wall surface temperature, K  
 $v$  = radial velocity, m/s  
 $v^*$  = radial velocity based on the guessed pressure  $p^*$ , m/s  
 $v_i$  = radial vapor velocity at the liquid-vapor interface, m/s  
 $w$  = axial velocity, m/s  
 $w^*$  = axial vapor velocity based on the guessed pressure  $p^*$ , m/s  
 $z$  = axial coordinate, m  
 $\delta$  = wall or liquid-wick thickness, m  
 $\epsilon$  = emissivity  
 $\mu$  = dynamic viscosity, kg/(m s)

$\rho$  = density, kg/m<sup>3</sup>  
 $\sigma$  = Stefan-Boltzmann constant, W/(m<sup>2</sup> K<sup>4</sup>)  
 $\phi$  = general variable in Eq. (17)  
 $\omega$  = wick porosity

## Subscripts

$a$  = adiabatic  
 $c$  = condenser  
 $E$  = "east" neighbor of grid  $P$   
 $e$  = evaporator  
 $eff$  = effective  
 $i$  = liquid-vapor interface  
 $l$  = liquid or liquid-wick  
 $N$  = "north" neighbor of grid  $P$   
 $P$  = grid point  
 $S$  = "south" neighbor of grid  $P$   
 $s$  = wick structure material  
 $v$  = vapor  
 $W$  = "west" neighbor of grid  $P$   
 $w$  = wall

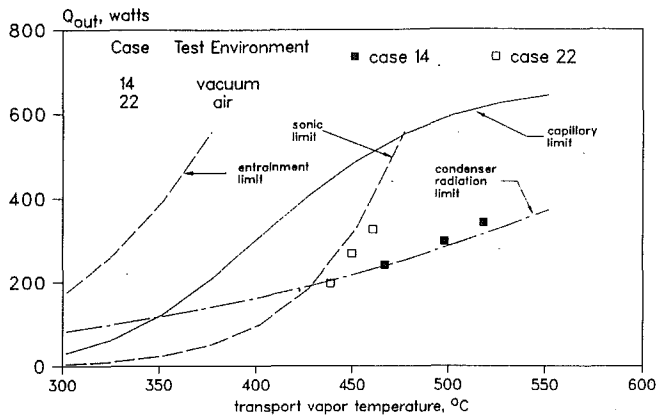


Fig. 3a Axial heat transfer limits versus transport vapor temperature

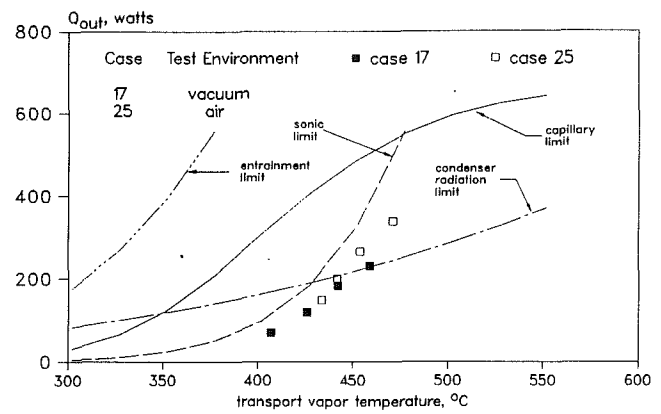


Fig. 4a Axial heat transfer limits versus transport vapor temperature

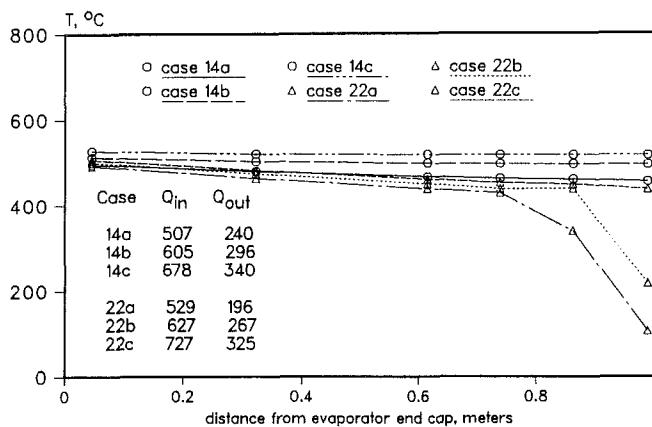


Fig. 3b Steady-state axial vapor temperature profiles

Fig. 3 Axial heat transfer limits and steady-state vapor temperature for operation in air and vacuum with evaporator 1 active

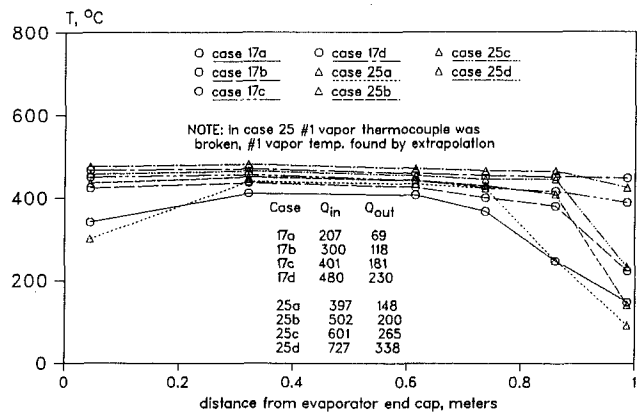


Fig. 4b Steady-state axial vapor temperature profiles

Fig. 4 Axial heat transfer limits and steady-state vapor temperature for operation in air and vacuum with evaporator 4 active

axial vapor temperatures were achieved (shown in Figs. 3a and 4a), then followed the condenser radiation heat transfer limit. Startup in air always followed the sonic limit curve, even after isothermal vapor temperatures were achieved because of additional heat losses at the condenser due to natural convection.

One of the primary interests in testing the high-temperature heat pipe with multiple heat sources was to determine the capillary limits for operation with varying heat fluxes and locations. Since the capillary limit was not found with the heat pipe horizontal, it was necessary to decrease the available capillary pressure in the wick. This was accomplished by raising the evaporator end of the heat pipe and operating against gravity. Tests were performed with evaporator elevations of 1.4, 3.0, and 5.7 arc deg. Initial design calculations, based on the standard equations contained in Chi (1976), indicated that the maximum capillary limit for the heat pipe, operating horizontally with evaporator 1 active, should have been approximately 250 W. The highest condenser power output attained for one-evaporator operation was 357 W, at an evaporator elevation of 1.4 deg (case 13d), but heater temperature limitations prevented any further power increases. In case 28h, operation in air at an evaporator elevation of 5.7 deg, it appeared that the capillary limit was found for four-evaporator operation. At the time evaporator 1 started to overheat, as shown in Fig. 5, the total heat input to the heat pipe was 2409 W. The condenser power output peaked at 1309 W, then suddenly began to drop off, while the evaporator calorimeter output and the evaporator 1 wall temperature continued to rise. The dryout limit data were somewhat tainted by the fact that a pocket of gas started to appear at the end of the con-

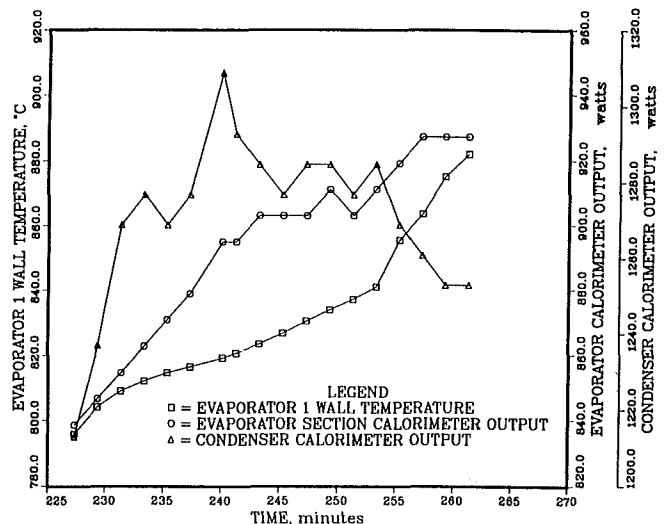


Fig. 5 Evaporator 1 dryout for case 28h: total power in 2409 W, operation in air with 5.7 deg evaporator elevation

denser vapor space. The test was immediately halted, and an attempt was made to remove this gas from the heat pipe. During the gas removal procedure an even larger quantity of gas suddenly appeared within the condenser vapor space, indicating a possible leak in the heat pipe. Since the heat pipe was being operated in air, any oxygen that entered the heat pipe through the apparent leak would immediately oxidize the sodium and effectively ruin the heat pipe, so all testing was stopped. The

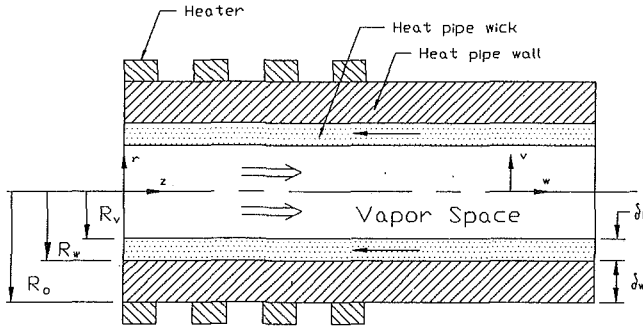


Fig. 6 The multiple evaporator heat pipe and coordinate system

heat pipe was disassembled, and the sodium was dissolved with methanol. The heat pipe container and end cap welds were leak-checked with a helium mass-spectrometer leak-detector and no leaks were found.

Postexperiment examination of the heat pipe wick showed that uneven annular gaps existed between the wick and the heat pipe wall, and in places between adjacent layers of screen. The existence of an annulus meant that the heat capacity of the heat pipe was much higher than the design power level, and the heaters were undersized as a result. Examination of the wick under evaporator 1 revealed slight corrosion and a contaminant deposit approximately 7 mm in diameter on the wick surface. A qualitative elemental identification on the contamination was made at Wright State University using a Transmission Electron Microscope, and the contaminant was determined to be composed of copper. The sodium used in the high-temperature heat pipe with multiple heat sources was delivered with a copper content of 5–20 ppm, according to the manufacturer. Given the quantity of copper contamination found in the heat pipe wick, it is not plausible that the copper content of the sodium was the sole source of the contamination. At some point in the heat pipe fabrication or fluid loading procedures, a small piece of copper must have been introduced to the heat pipe system. Merrigan et al. (1984), Keddy and Martinez (1982), and Tanaka et al. (1990) have previously reported that severe damage can occur in a screen wick from local dryout and evaporator overheating. The combination of the copper contamination and the wick dryout must have led to the formation of the noncondensable gas and the wick corrosion observed in the heat pipe. It should be noted that no gas was observed in the heat pipe prior to the case 28h wick dryout.

### Numerical Modeling and Predictions

The multiple-evaporator heat pipe configuration and coordinate system for the numerical modeling is schematically shown in Fig. 6. The wick is saturated with the liquid phase of the working fluid and the remaining volume of the pipe contains the vapor phase. Heat applied in the evaporators causes the liquid to vaporize into the vapor space. The vapor flows to the condenser and releases the latent heat as it condenses. The released heat is rejected into the environment by radiation or convection from the outer condenser surface.

**Governing Equations.** The experiment conducted by Bowman (1987) showed that the vapor flow was always laminar in the evaporator, while it might become turbulent at the condenser when the axial Reynolds number  $Re$  is relatively high ( $Re > 2000$ ). For the experiment conducted in this paper, the Reynolds number of the vapor flow is relatively low (on the order of 200); therefore, the vapor flow can be assumed to be laminar along the entire heat pipe. The governing equations for transient compressible laminar vapor flow with constant viscosity are given as follows (Ganic et al., 1985):

$$\frac{\partial \rho}{\partial t} + \frac{1}{r} \frac{\partial}{\partial r} (\rho r v) + \frac{\partial}{\partial z} (\rho w) = 0 \quad (1)$$

$$\frac{\partial (\rho v)}{\partial t} + \frac{1}{r} \frac{\partial}{\partial r} (\rho r v^2) + \frac{\partial}{\partial z} (\rho v w) = -\frac{\partial p}{\partial r} + \frac{4}{3} \mu \frac{1}{r} \frac{\partial}{\partial r} \left( r \frac{\partial v}{\partial r} \right) + \mu \frac{\partial^2 v}{\partial z^2} + \mu \left( \frac{1}{3} \frac{\partial^2 w}{\partial z \partial r} - \frac{4 v}{3 r^2} \right) \quad (2)$$

$$\frac{\partial (\rho w)}{\partial t} + \frac{1}{r} \frac{\partial}{\partial r} (\rho r v w) + \frac{\partial}{\partial z} (\rho w^2) = -\frac{\partial p}{\partial z} + \frac{\mu}{r} \frac{\partial}{\partial r} \left( r \frac{\partial w}{\partial r} \right) + \frac{4}{3} \mu \frac{\partial^2 w}{\partial z^2} + \frac{1}{3} \mu \left( r \frac{\partial v}{\partial z} + \frac{\partial^2 v}{\partial z \partial r} \right) \quad (3)$$

$$\rho c_p \left( \frac{\partial T}{\partial t} + v \frac{\partial T}{\partial r} + w \frac{\partial T}{\partial z} \right) = k \left[ \frac{1}{r} \frac{\partial}{\partial r} \left( r \frac{\partial T}{\partial r} \right) + \frac{\partial^2 T}{\partial z^2} \right] + \frac{Dp}{Dt} + \mu \Phi \quad (4)$$

where the viscous dissipation term  $\Phi$  is

$$\Phi = 2 \left[ \left( \frac{\partial v}{\partial r} \right)^2 + \left( \frac{v}{r} \right)^2 + \left( \frac{\partial w}{\partial z} \right)^2 \right] + \left( \frac{\partial v}{\partial z} + \frac{\partial w}{\partial r} \right)^2 - \frac{2}{3} \left[ \frac{1}{r} \frac{\partial}{\partial r} (r v) + \frac{\partial w}{\partial z} \right]^2$$

The equation of state is given by

$$p = \rho R T \quad (5)$$

The heat transfer through the heat pipe wall is purely by conduction. The corresponding governing equation is:

$$(\rho c_p)_w \frac{\partial T}{\partial t} = k_w \left[ \frac{1}{r} \frac{\partial}{\partial r} \left( r \frac{\partial T}{\partial r} \right) + \frac{\partial^2 T}{\partial z^2} \right] \quad (6)$$

The analysis of Cao and Faghri (1990) showed that the liquid flow in the wick had a negligible effect on the temperature distribution in the heat pipe. In this paper, the model of Cao and Faghri (1990) is adopted, and the governing equations for the wick region can be written as

$$(\rho c_p)_{\text{eff}} \frac{\partial T}{\partial t} = k_{\text{eff}} \left[ \frac{1}{r} \frac{\partial}{\partial r} \left( r \frac{\partial T}{\partial r} \right) + \frac{\partial^2 T}{\partial z^2} \right] \quad (7)$$

where

$$(\rho c_p)_{\text{eff}} = \omega (\rho c_p)_l + (1 - \omega) (\rho c_p)_s$$

$$k_{\text{eff}} = k_l [k_l + k_s - (1 - \omega) (k_l - k_s)] / [k_l + k_s + (1 - \omega) (k_l - k_s)]$$

**Boundary Conditions.** At both ends of the heat pipe, the no-slip condition for velocity and the adiabatic condition for temperature are applied. At  $z=0$  and  $L$ :

$$v = w = 0, \quad \frac{\partial T}{\partial z} = 0 \quad (8)$$

At the centerline,  $r=0$ , the symmetry condition implies:

$$\frac{\partial w}{\partial r} = 0, \quad v = 0, \quad \frac{\partial T}{\partial r} = 0 \quad (9)$$

The temperature at the vapor-liquid interface is assumed to be the saturation temperature corresponding to the interface pressure:

$$T_i = 1 \left/ \left( \frac{1}{T_o} - \frac{R}{h_{fg}} \ln \frac{p_i}{p_o} \right) \right. \quad (10)$$

where  $p_o$  and  $T_o$  are the reference saturation temperature and pressure.

The interface velocities at  $r=R_v$  are:

$$v_i = \left( -k_{\text{eff}} \frac{\partial T_i}{\partial r} + k_v \frac{\partial T_v}{\partial r} \right) / h_{fg} \rho_i, \quad w = 0 \quad (11)$$

The term  $k_v (\partial T_v / \partial r)$  in Eq. (11) can be neglected by an order

of magnitude analysis. At the condenser interface, vapor condenses and releases its latent heat energy. In order to simulate this process, a heat source

$$q_i = h_{fg} \rho_i v_i \quad (12)$$

was applied at the interface grids on the wick side. The suction mass flux  $\rho_i v_i$  can be obtained by a mass balance over the interface grids on the vapor side.

The boundary condition at the wick-wall interface  $r = R_w$  is:

$$k_w \frac{\partial T}{\partial r} = k_{\text{eff}} \frac{\partial T}{\partial r} \quad (13)$$

For the outer pipe wall surface  $r = R_o$ :

*Evaporator:*

$$k_w \left. \frac{\partial T}{\partial r} \right|_{r=R_o} = q_e \quad (14)$$

*Adiabatic:*

$$\left. \frac{\partial T}{\partial r} \right|_{r=R_o} = 0 \quad (15)$$

*Condenser:*

$$-k_w \left. \frac{\partial T}{\partial r} \right|_{r=R_o} = \begin{cases} h(T_w - T_a) & \text{(convection)} \\ \sigma \epsilon T_w^4 & \text{(radiation)} \end{cases} \quad (16a) \quad (16b)$$

where  $h$  is the convective heat transfer coefficient,  $T_w$  and  $T_a$  are the outer wall surface and environment temperatures, respectively,  $\epsilon$  is the emissivity of the heat pipe wall, and  $\sigma$  is the Stefan-Boltzmann constant.

**Numerical Procedure.** The vapor flow was solved by employing the SIMPLE algorithm (Patankar, 1980, 1988). The discretization equations for  $w$ ,  $v$ ,  $T$ , and  $p'$  have the general form

$$a_p \phi_p = a_E \phi_E + a_W \phi_W + a_N \phi_N + a_S \phi_S + b \quad (17)$$

A combination of the direct method (TDMA) and the Gauss-Seidel method was employed to solve the discretization equations. The pressure was chosen as a dependent variable and the equation of state  $\rho = p/RT$  was directly applied to obtain the vapor density while iterating.

At both ends of the heat pipe, the no-slip boundary condition leads to the prescribed velocity boundary conditions with  $w = v = 0$ . Since no boundary pressure is specified, and all the boundary coefficients in the pressure correction  $p'$  equation are zero, the  $p'$  equation is left without any means of establishing the absolute value of  $p'$ . In this case, the interface value of  $p'$  at the condenser end was assigned to zero. The absolute value of the vapor pressure at this point was calculated using the temperature of the liquid-vapor interface at the liquid side and the Clausius-Clapeyron equation. The absolute values of the vapor pressure along the heat pipe were also adjusted according to the value at this point during the iterations. The sequence of numerical steps was as follows:

- 1 Initialize the temperature, velocity, and pressure fields. The density values for the vapor are obtained from the current vapor pressure and temperature fields through the equation of state.
- 2 Calculate the vapor-liquid interface mass velocity  $v_i \rho_i$  using Eq. (11) and the previous temperature field. Calculate the interface vapor temperature using the Clausius-Clapeyron equation (Eq. (10)).
- 3 Solve the vapor momentum equation to obtain  $v^*$  and  $w^*$ .
- 4 Solve the  $p'$  equation and update the current vapor pressure field.
- 5 Calculate  $v$ ,  $w$  from their starred values using the velocity correction formulas.

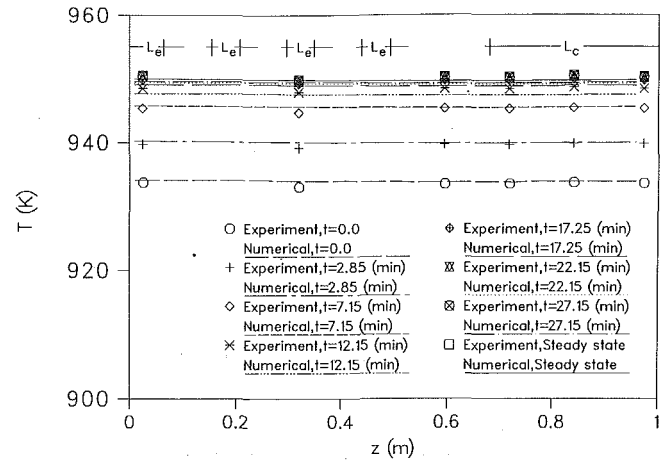


Fig. 7 The vapor temperature for different time periods compared with the experimental data for cases 6b and 6c

- 6 Calculate the heat source term, Eq. (12), applying the mass balance over the interface grids on the vapor side to obtain mass flux  $v_i \rho_i$ .
- 7 Solve the temperature field for the wick, wall, and vapor regions.
- 8 Steps (1)–(7) are repeated until convergence is reached for each time step.

**Numerical Predictions.** The numerical calculations for the transient heat pipe performance were made with the heat pipe configuration shown in Fig. 1 presented in Part I of this paper. The left end of evaporator 1 was taken to be  $z=0$ , and the right end of the condenser calorimeter was taken to be  $z=L$ , which made the total length of the numerically simulated heat pipe to be 0.96 m. Different grid sizes for the same problem were tested and it was proven that the numerical solutions were essentially independent of grid size used. A change from a grid size of  $(14 \times 36)$  to  $(24 \times 72)$ , for example, resulted in a maximum change in vapor and wall temperatures of less than 1 percent. A further refinement of grid size to  $(26 \times 108)$  resulted in a maximum change in vapor and wall temperatures of less than 0.5 percent. It should be pointed out that the present numerical scheme has some restrictions on the radial grid size, especially in the wick structure region. The interface velocities are computed using Eq. (11). If the effective thermal conductivity  $k_{\text{eff}}$  is large, the temperature difference between the adjacent grids in the wick is very small. As a result, a large numerical error may arise when estimating the temperature gradients in the wick. However, this is not a problem in practice. Since the radius of the vapor core and the thickness of the wick are very small (about 10 mm and 0.5 mm, respectively), a relatively small number of grids in these regions will simulate the heat pipe performance with sufficient accuracy.

Figure 7 compares the numerical vapor temperatures for different time periods with the experimental data for cases 6b–6c presented in Part I of this paper. The curve labeled with  $t=0.0$  is the steady-state condition corresponding to case 6b. In this case, the four evaporators were active with a total net power input of  $Q_{\text{in}} = 684$  W. The boundary condition at the condenser was radiative corresponding to Eq. (16b). At  $t=0$ , the power input at the evaporators was suddenly increased to  $Q_{\text{in}} = 737$  W. The transient response of the vapor temperature is presented in the same figure. After about 30 minutes, the heat pipe reached another steady state corresponding to case 6c. It can be seen that the numerical solutions agree very well with the experimental data. The above numerical calculations were made with a grid size of  $54$  (axial)  $\times$   $[10$  (radial vapor region)  $+ 4$  (radial wick region)  $+ 4$  (radial wall region)], and a heat pipe wall emissivity  $\epsilon = 0.645$  calculated from experi-

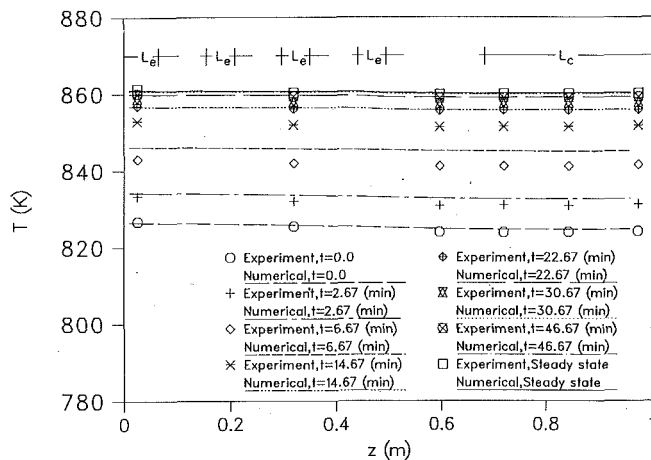


Fig. 8 The vapor temperature for different time periods compared with the experimental data for cases 19c and 19d

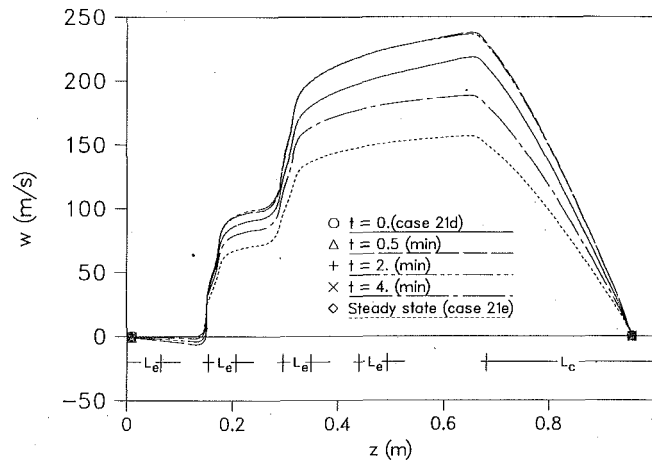


Fig. 10 The axial velocity profile along the centerline for different time periods with cases 21d and 21e

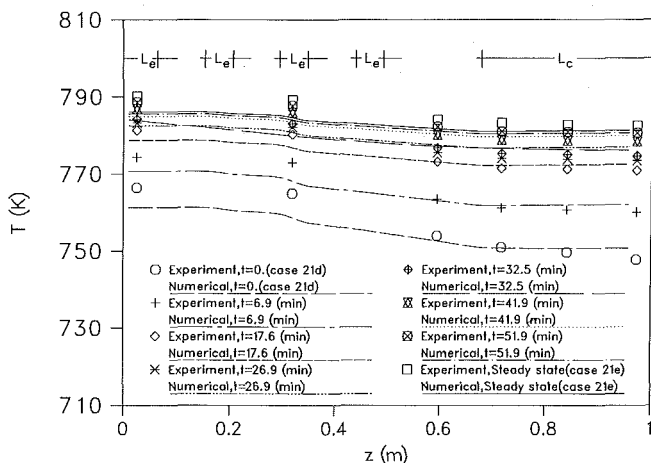


Fig. 9 The vapor temperature for different time periods compared with the experimental data for cases 21d and 21e

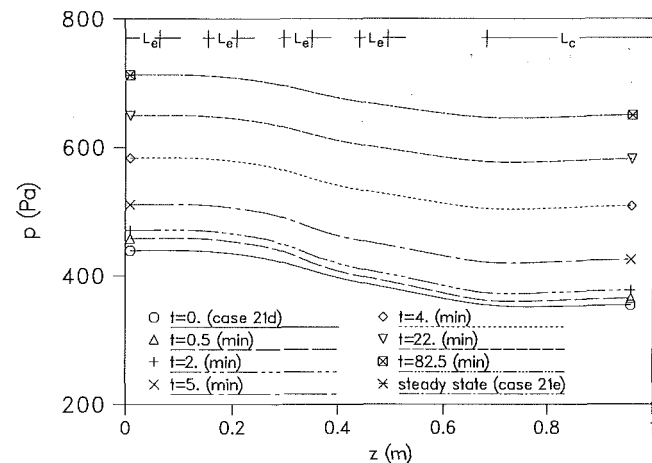


Fig. 11 The axial pressure profile along the centerline of the heat pipe for different time periods with cases 21d and 21e

mental data. It took about 1.5 hours CPU time on a VAX 6420 to run the case. For the emissivity calculation, an equation similar to that for radiation heat transfer between two concentric cylinders was used.

$$Q = [A_1 \sigma (T_1^4 - T_2^4)] / \left[ \frac{1}{\epsilon_1} + \left( \frac{1}{\epsilon_2} - 1 \right) \frac{d_1}{d_2} \right]$$

where  $T_1$  is the heat pipe wall temperature,  $T_2$  is the calorimeter heat sink temperature. The calorimeter was coated with graphite, which has an emissivity  $\epsilon_2 \approx 0.9$ . From the experiment,  $Q$ ,  $T_1$ , and  $T_2$  are known. Therefore, the emissivity,  $\epsilon_1$ , for the heat pipe condenser can be determined by the experimental results and the above equation.

The vapor temperatures for different time periods are compared with the experimental data for cases 19c and 19d in Fig. 8 with evaporators 1 and 4 active. The agreement between the numerical solutions and the experimental data is also good.

The numerical interface vapor temperatures are compared with the corresponding experimental data for cases 21d and 21e in Fig. 9. The numerical axial velocity and pressure profiles along the centerline of the heat pipe for the same cases are also given in Figs. 10 and 11. It is of interest to examine the axial velocity curves in Fig. 10. Since only evaporators 2 and 3 are active, the axial velocity curves are stepwise in the evaporator section. Also, the two-way vapor flow was observed near the left end of the evaporator section during the transient period. This was due to the sudden heat input increase to the

active evaporators, which caused the temperature in the active part of the evaporator section to be higher than that in the inactive part. However, after steady state was reached, the two-way vapor flow phenomenon disappeared due to the adiabatic boundary condition imposed on the inactive part of the evaporator section. Another trend worth notice was that shortly after the power input was increased from case 21d, the magnitude of the axial velocity increased slightly and then decreased gradually to another steady state condition. This trend was also observed by Cao and Faghri (1990). Unlike the velocity curves, the vapor pressure increased monotonically from a lower level to a higher level as the power input at the evaporator section was increased. Also, near the left end of the inactive part of the evaporator section, the pressure curves were relatively flat.

In the numerical modeling, the vapor flow was assumed to be laminar along the whole heat pipe. The numerical results above revealed that the axial vapor flow Reynolds number at the transport section in the heat pipe is in the range of 200 to 400, indicating that the laminar assumption is valid for the numerical simulation.

## Conclusions

Steady-state tests showed that a change in the emissivity of the heat pipe wall can have a significant effect on the operating temperature of the heat pipe. The final steady-state operating temperature of the heat pipe was found to be independent of

the startup power levels and the size of the subsequent power increases. A capillary limit for four-evaporator steady-state operation was found while testing in air, at a evaporator elevation of 5.7 deg. A combination of the evaporator 1 wick dryout and copper contamination of the working fluid caused noncondensable gas to be formed within the heat pipe, and corrosion was found in the wick under evaporator 1. Postexperiment examination of the heat pipe wick revealed that the loosely wrapped circumferential screen wick contained significant annular gaps between the wick and the heat pipe wall, and between adjacent screen layers. The annular gaps enhanced the maximum heat transport capability of the heat pipe, but increased the difficulty in predicting the capillary limits and in calculating the optimal heat pipe fluid charge.

The numerical results agree favorably with the experimental vapor temperature, proving that the numerical model presented in this paper is capable of simulating heat pipe performance and would be very useful for heat pipe design.

### Acknowledgments

Funding for this work was provided by a joint effort of the NASA Lewis Research Center and Thermal Energy Group of the Aero Propulsion Laboratory of the U.S. Air Force under contract No. F33615-89-C-2820.

### References

- Bowman, W. J., 1987, "Simulated Heat Pipe Vapor Dynamics," Ph.D. Dissertation, Air Force Institute of Technology.
- Cao, Y., and Faghri, A., 1990, "A Transient Two-Dimensional Compressible Analysis for High Temperature Heat Pipes With a Pulsed Heat Input," *Numerical Heat Transfer*, Part A, Vol. 18, No. 4, pp. 483-502.
- Chen, M. M., and Faghri, A., 1990, "An Analysis of the Vapor Flow and the Heat Conduction Through the Liquid-Wick and Pipe Wall in a Heat Pipe With Single or Multiple Heat Sources," *International Journal of Heat and Mass Transfer*, Vol. 33, No. 9, pp. 1945-1955.
- Chi, S. W., 1976, *Heat Pipe Theory and Practice*, Hemisphere Publishing Corp., New York.
- Ganic, E. N., Hartnett, J. P., and Rohsenow, W. M., 1985, "Basic Concepts of Heat Transfer," in: *Handbook of Heat Transfer Fundamentals*, W. M. Rohsenow et al., eds., McGraw-Hill, New York.
- Jang, J. H., Faghri, A., Chang, W. S., and Mahefkey, E. T., 1990, "Mathematical Modeling and Analysis of Heat Pipe Start-Up From the Frozen State," *ASME JOURNAL OF HEAT TRANSFER*, Vol. 112, No. 3, pp. 586-594.
- Keddy, E. S., and Martinez, H. E., 1982, "Development of High Temperature Liquid Metal Heat Pipes for Isothermal Irradiation Assemblies," *Proc. 17th Intersociety Energy Conversion Engineering Conference*, pp. 58-62.
- Merrigan, M. A., Keddy, E. S., and Runyan, J. R., and Martinez, H. E., 1984, "Development and Extended Operation of a High Power Radiation Loaded Heat Pipe," Los Alamos Scientific Laboratory Report LA-UR-84-1950, Los Alamos, NM.
- Patankar, S. V., 1980, *Numerical Heat Transfer and Fluid Flow*, McGraw-Hill, New York.
- Patankar, S. V., 1988, "Elliptic Systems: Finite-Difference Method I," in: *Handbook of Numerical Heat Transfer*, W. J. Minkowycz et al., eds., Wiley, New York.
- Tanaka, Y., Yamamoto, T., Matsumoto, S., Hirano, S., Ikeda, Y., Mochizuki, M., and Sugihara, S., 1990, "Container Failure of Sodium Heat Pipe Due to Local Dry-out," *Proceedings of 7th International Heat Pipe Conference*, Minsk, USSR.

This section contains shorter technical papers. These shorter papers will be subjected to the same review process as that for full papers.

## Numerical Analysis of Two-Dimensional Transient Freezing in a Spheroidal Capsule

Y. Asako,<sup>1</sup> H. Nakamura,<sup>1</sup> S. Toyoda,<sup>1</sup> and M. Faghri<sup>2</sup>

### Nomenclature

$a$  = thermal diffusivity  
 $c$  = specific heat  
 $Fo$  = Fourier number =  $at/L^2$   
 $L$  = reference length =  $\{\delta_0 \delta_{\pi/2}^2\}^{1/3}$   
 $Ste$  = Stefan number =  $c(T_f - T_w)/\lambda$   
 $T$  = temperature  
 $t$  = time  
 $\delta\tau$  = dimensionless time interval  
 $\lambda$  = latent heat of fusion  
 $\rho$  = density

### Introduction

The moving interface problem of freezing a liquid inside a container is of interest in a wide range of applications, such as casting of metals and glass, freeze drying of food stuffs, and storage of thermal energy. Previous numerical and analytical studies in the literature are for simple geometries such as spheres and cylinders. Examples are the work by Tien and Churchill (1965), who developed a numerical method for freezing outside an isothermal cylinder, and Tao (1967), who obtained numerical solutions inside cylinders and spheres. Analytical solutions for cylinders and spheres were obtained by Shih and Tsay (1971) and Stewartson and Waechter (1976), respectively. The focus of the present research is to obtain a numerical solution for freezing inside a complex geometry such as a spheroidal capsule. The liquid is initially at fusion temperature and freezing is initiated when the wall temperature is decreased to a fixed lower value.

Faghri et al. (1984) proposed an algebraic coordinate transformation that transforms an irregular solution domain onto a rectangle. In the present work, this method is extended to axisymmetric problems by mapping an irregular cross section of the solidified zone onto concentric spheres. The calculations are performed for the Stefan number in the range of 0.03 to

0.36, and for several values of the dimensionless geometric parameter characterizing the spheroidal capsule. The results are presented in form of the solid-liquid interface shapes and the ratios of the solidification zone volume to the capsule volume.

### Formulation

**Description of the Problem.** The problem to be considered is schematically depicted in Fig. 1, which shows an axisymmetric spheroidal capsule initially filled with a liquid at fusion temperature. Freezing is initiated when the wall temperature is suddenly decreased to a fixed lower value. Since the liquid is at fusion temperature, buoyancy-driven convection does not occur in the liquid. Therefore, attention is focused only on heat conduction in the solidified material with a moving boundary. This is a two-dimensional Stefan problem in spheroidal geometry.

The solution domain is composed of a core of unfrozen liquid and a shell of solidified material. These zones are re-

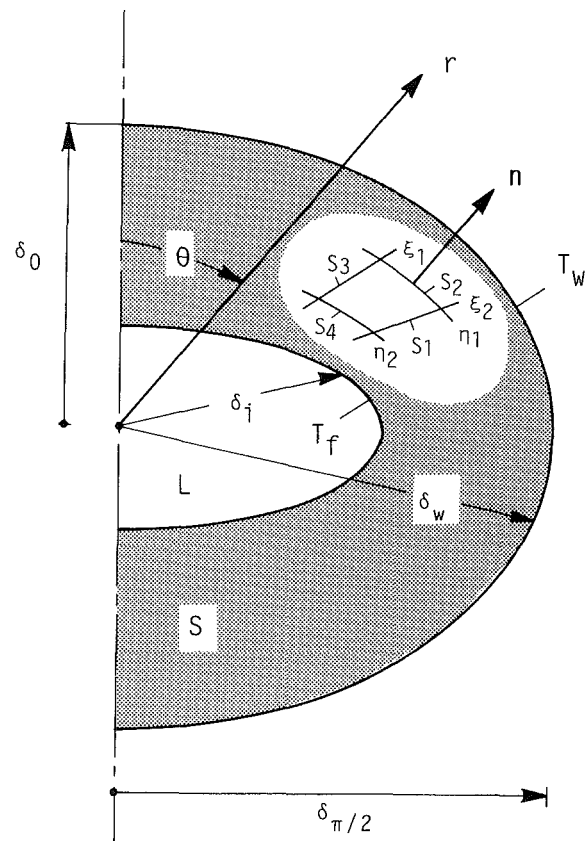


Fig. 1 Schematic diagram of the spheroidal capsule

<sup>1</sup>Department of Mechanical Engineering, Tokyo Metropolitan University, Tokyo, 158 Japan.

<sup>2</sup>Department of Mechanical Engineering, University of Rhode Island, Kingston, RI 02881.

Contributed by the Heat Transfer Division and presented at the AIAA/ASME Thermophysics and Heat Transfer Conference, Seattle, Washington, June 18-20, 1990. Manuscript received by the Heat Transfer Division July 23, 1990; revision received April 24, 1991. Keywords: Numerical Methods, Phase-Change Phenomena.



spectively designated as  $L$  and  $S$  in Fig. 1. With the assumption of symmetry, this domain is confined to a quarter of the spheroidal capsule. The radial coordinate of the solid-liquid interface is denoted by  $\delta_i$ . In general, at a given time,  $\delta_i$  varies with the angle  $\theta$ , and as freezing proceeds, it varies with time. The radial coordinate of the capsule wall is denoted by  $\delta_w$ , which is a function of  $\theta$ . The mathematical expression for  $\delta_w$  is given by

$$\delta_w(\theta) = \delta_0 \delta_{\pi/2} / [(\delta_0 \cos \theta)^2 + (\delta_{\pi/2} \sin \theta)^2]^{1/2} \quad (1)$$

where  $\delta_0$  and  $\delta_{\pi/2}$  are the radial coordinates of the capsule wall at  $\theta=0$  and  $\pi/2$ , respectively.

**Conservation Equation.** The governing equation in the solidified zone is the two-dimensional conduction equation. Assuming constant thermophysical properties and using the following dimensionless variables:

$$R = r/L, \quad \Theta = (T - T_w) / (T_f - T_w),$$

$$\tau = \{at/L^2\} \{c(T_f - T_w)/\lambda\} = \text{Fo Ste} \quad (2)$$

where  $L$  is a reference length, which is the radius of a sphere whose volume equals the spheroidal capsule, the governing equation takes the following form:

$$\text{Ste}(\partial\Theta/\partial\tau) = \nabla^2\Theta \quad (3)$$

where

$$\nabla^2 = (1/R^2)\partial\{R^2(\partial/\partial R)\}/\partial R + (1/R^2 \sin \theta)\partial\{\sin \theta(\partial/\partial\theta)\}/\partial\theta \quad (4)$$

The boundary conditions are

$$\begin{aligned} \text{on the solid-liquid interface } (R = \delta_i/L): \quad & \Theta = 1 \\ \text{on the capsule wall } (R = \delta_w/L): \quad & \Theta = 0 \\ \text{for symmetry } (\theta = 0 \text{ and } \pi/2): \quad & \partial\Theta/\partial\theta = 0 \end{aligned} \quad (5)$$

**Coordinate Transformation.** A simple algebraic coordinate transformation is introduced that maps the physical domain onto a spherical shell. Specifically,  $R, \theta$  coordinates are transformed into  $\eta$  and  $\xi$  coordinates by the relations

$$\eta = (R - \delta_i/L) / \{(\delta_w - \delta_i)/L\} = R/\Delta_d - \Delta_o, \quad \xi = \theta$$

$$\text{where } \Delta_d = (\delta_w - \delta_i)/L, \quad \Delta_o = (\delta_i/L) / \{(\delta_w - \delta_i)/L\} \quad (6)$$

In terms of the new coordinates, the solution domain is defined by  $0 < \eta < 1$ , and  $0 < \xi < \pi/2$ .

**Integral Forms.** The dimensionless form of the energy Eq. (3) is integrated over a control volume in physical space bounded by lines of constant  $\eta$  and  $\xi$  as illustrated in Fig. 1. Using the divergence theorem, it reduces to

$$\text{Ste} \int_v (\partial\Theta/\partial\tau) dv = \int_s \mathbf{n} \cdot \nabla\Theta ds \quad (7)$$

where  $v$  and  $s$  represent the dimensionless volume and surface of the control volume, respectively. Equation (7) can be expressed in  $\eta$  and  $\xi$  coordinates as

$$\begin{aligned} \text{Ste} \int_v (\partial\Theta/\partial\tau)(\eta + \Delta_o)^2 \Delta_d^3 \sin \xi d\eta d\xi \\ = \int_1 (\gamma + \psi) \Delta_d \sin \xi d\eta + \int_2 (\Omega + \Lambda)(\eta + \Delta_o) \Delta_d \sin \xi d\xi \\ - \int_3 (\gamma + \psi) \Delta_d \sin \xi d\eta - \int_4 (\Omega + \Lambda)(\eta + \Delta_o) \Delta_d \sin \xi d\xi \end{aligned} \quad (8)$$

where

$$\begin{aligned} \Omega = \alpha(\eta + \Delta_o)(\partial\Theta/\partial\eta), \quad \gamma = (\partial\Theta/\partial\xi) \\ \Lambda = -\beta(\partial\Theta/\partial\xi) \quad \psi = -\beta(\eta + \Delta_o)(\partial\Theta/\partial\eta) \end{aligned} \quad (9)$$

With regard to the volume integral, both  $\Delta_o$  and  $\Delta_d$  are independent of time during each of the computational time intervals. In this paper, a fully implicit treatment is adopted

for the discretization of Eq. (8). The derivatives  $\partial\Theta/\partial\eta$  and  $\partial\Theta/\partial\xi$ , which are contained in  $\Omega, \gamma, \Lambda$ , and  $\psi$ , are regarded as corresponding to time  $(\tau^0 + \delta\tau)$  during the representative time interval extending from  $\tau^0$  to  $(\tau^0 + \delta\tau)$ .

**Interface Energy Balance.** At any point on the solid-liquid interface, an energy balance yields

$$\mathbf{q}_i \cdot \mathbf{n} = -\rho\lambda\mathbf{u}_s \cdot \mathbf{n} \quad (10)$$

where  $\mathbf{q}_i$  is the heat flux from the interface into the solid,  $\mathbf{u}_s$  is the interface velocity, which is negative, and  $\mathbf{n}$  is the unit vector normal to the interface. The discretized form of Eq. (10) can be written as

$$\Delta_i = \{(\Delta_i^0)^2 + 2\Delta_o^0(\partial\Theta/\partial\eta)_i \delta\tau\alpha\}^{1/2} \quad (11)$$

where  $\Delta_i = \delta_i/L$ . In this equation,  $(\partial\Theta/\partial\eta)_i$  is evaluated at  $(\tau^0 + \delta\tau)$ , whereas  $\Delta_i^0$  and  $\Delta_o^0$  are obtained at  $\tau^0$ . Therefore, Eq. (11) enables us to evaluate  $\Delta_i$  at  $(\tau^0 + \delta\tau)$  without iteration.

**Numerical Solutions.** From an examination of the governing equation, it can be seen that the value of the Stefan number  $\text{Ste}$  has to be specified prior to the initiation of the numerical solutions. The values chosen for  $\text{Ste}$  are in the range of 0.03 to 0.36. Apart from  $\text{Ste}$ , two geometric parameters, the radial coordinates  $\delta_0$  and  $\delta_{\pi/2}$  of the spheroidal capsule, have to be specified. If the radius of a sphere whose volume equals a spheroid is selected as a reference length,  $L = \{\delta_0 \delta_{\pi/2}^2\}^{1/3}$ , then there exists a relation between  $\delta_0/L$  and  $\delta_{\pi/2}/L$  as  $(\delta_{\pi/2}/L) = (\delta_0/L)^{-1/2}$ . The values for  $\delta_0/L$  and  $\delta_{\pi/2}/L$  are selected such that the surface area ratio of the spheroidal to spherical capsules,  $S_{\text{spheroid}}/S_{\text{sphere}}$ , ranges from 1.2 to 1.6. It should be noted that there exist a prolate spheroid and an oblate spheroid that have identical surface area ratios. The computations were done for both prolate and oblate spheroids. The geometric parameters of the spheroidal and spherical capsules tested are listed in Table 1.

All computations were performed with  $(42 \times 22)$  grids. These grids are distributed in a uniform manner over the solidified zone. Supplementary runs for the oblate spheroid of  $S_{\text{spheroid}}/S_{\text{sphere}} = 1.4$  and  $\text{Ste} = 0.12$  were performed with  $(27 \times 17)$ ,  $(42 \times 22)$ , and  $(82 \times 42)$  grids to investigate the control volume size effect. The maximum difference in the ratio of solidified zone volume to capsule volume,  $V_s/V_{\text{cap}}$ , between the coarse mesh  $(27 \times 17)$  and the medium mesh  $(42 \times 22)$  is 0.56 percent, and the maximum difference between the medium mesh and the fine mesh  $(82 \times 42)$  is 0.23 percent. The grid size effect was also tested with grids that are distributed in a nonuniform manner with higher concentration of grids closer to the interface at both ends in the  $\theta$  direction. The maximum difference between the uniform and nonuniform grids is 0.19 percent, which is small.

A very thin solidified layer thickness of 1 percent of the radius  $\delta_0$  and  $\delta_{\pi/2}$  was initially assumed for the prolate and oblate spheroidal capsules, respectively. The effect of this initial thickness was tested for the oblate spheroidal capsule of

Table 1 Geometric parameters of the spheroidal capsule

| Type    | $S_{\text{spheroid}}/S_{\text{sphere}}$ | $\delta_0/L$ | $\delta_{\pi/2}/L$ |
|---------|---|--------------|--------------------|
| sphere  | 1                                       | 1            | 1                  |
| oblate  | 1.2                                     | 0.5202       | 1.386              |
| oblate  | 1.4                                     | 0.4079       | 1.566              |
| oblate  | 1.6                                     | 0.3417       | 1.711              |
| prolate | 1.2                                     | 2.162        | 0.6801             |
| prolate | 1.4                                     | 3.086        | 0.5693             |
| prolate | 1.6                                     | 4.096        | 0.4941             |

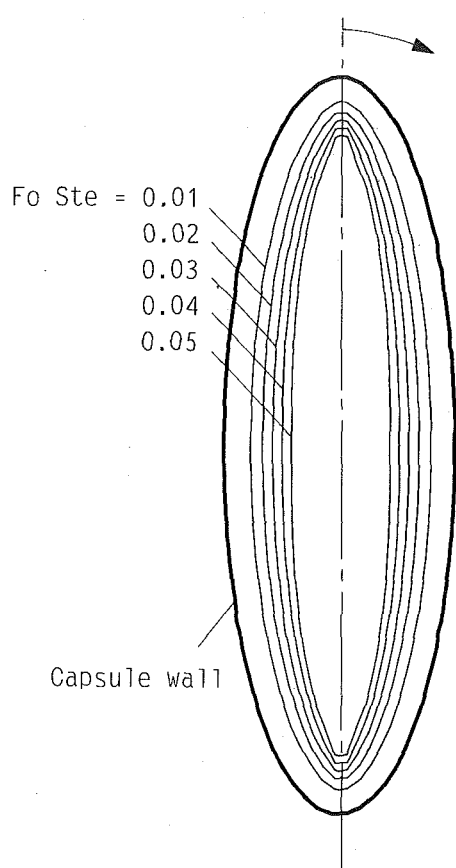


Fig. 2 Solid-liquid interface shapes for prolate spheroid with  $S_{\text{spheroid}}/S_{\text{sphere}} = 1.2$  and  $Ste = 0.12$

$S_{\text{spheroid}}/S_{\text{sphere}} = 1.4$  and  $Ste = 0.12$  with 0.5 percent of the radius  $\delta_{\pi/2}$  as the initial thickness. The maximum difference in the ratio of the solidified zone volume to the capsule volume,  $V_s/V_{\text{cap}}$ , was 0.5 percent.

Attention will now be focused on the time interval. The first dimensionless time interval is taken as  $\delta\tau = 10^{-7}$ . Starting with this value, the time interval is increased to  $\delta\tau = 10^{-5}$  at  $\tau = 10^{-3}$ . Computation was terminated when the volume of the solidified zone reached 90 percent of the capsule volume.

## Results and Discussion

**Interface Shapes.** The representative interface shapes for the prolate and oblate spheroidal capsules of  $S_{\text{spheroid}}/S_{\text{sphere}} = 1.2$  and  $Ste = 0.12$  are presented in Figs. 2 and 3, respectively. Although the solution domain is confined to a quarter of the capsule, the interface shapes for the whole capsule are presented by the symmetry of the problem for time intervals of 0.01. It is assumed that the volumes and the surface areas of the prolate and oblate spheroidal capsule are identical. As seen from Figs. 2 and 3 for  $Fo Ste < 0.04$ , the solidified thickness is uniform. However, for  $Fo Ste > 0.04$ , there is a localized decrease in the thickness of the frozen region at the small ends of the spheroids and also an increase in the thickness of frozen region near the flat horizontal portion for oblate spheroid. The "zig-zag" profile or the decrease in the thickness at the ends of the spheroids was improved by refinement of the grids. However, the maximum difference in the solidified thickness at  $\theta = 0$  between  $(42 \times 22)$  uniform grids and  $(82 \times 42)$  nonuniform grids is less than 0.5 percent. Therefore, the increase in the solidified thickness at  $\theta = 0$  is not caused by the grid resolution in the oblate capsule. The physical reason for this behavior is not clear. However, it can be caused by numerical "false diffusion." This is because at  $Fo Ste > 0.04$ , the

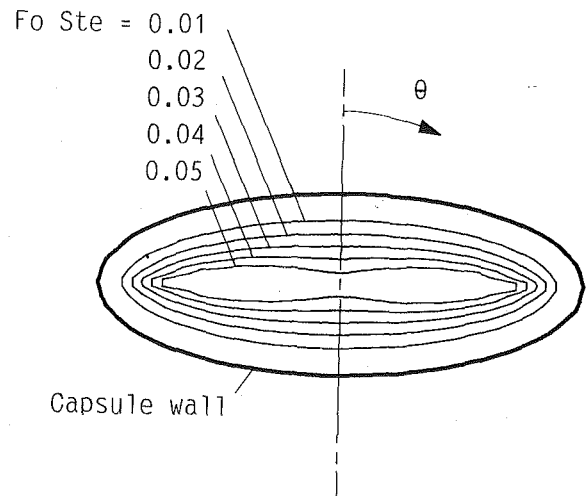


Fig. 3 Solid-liquid interface shapes for oblate spheroid with  $S_{\text{spheroid}}/S_{\text{sphere}} = 1.2$  and  $Ste = 0.12$

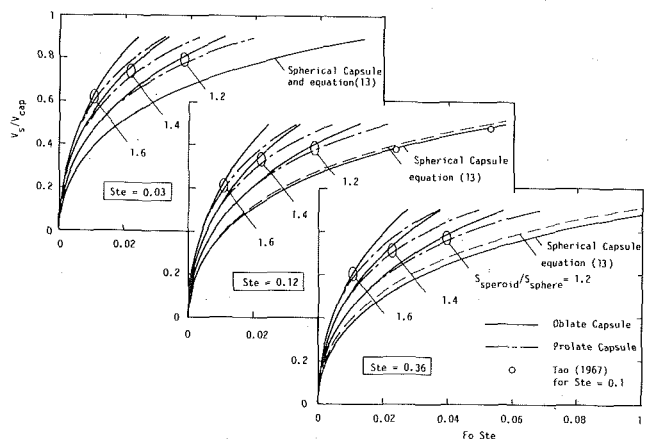


Fig. 4 Solidified zone volume as a function of  $Fo Ste$

computational zone is confined to a narrow horizontal gap where the grids are highly skewed and nonorthogonal.

**Solidified Volume.** The ratios of the solidified zone volume to the capsule volume,  $V_s/V_{\text{cap}}$ , are plotted in Fig. 4 as a function of the  $Fo Ste$  number with surface area ratio of the spheroidal to spherical capsules,  $S_{\text{spheroid}}/S_{\text{sphere}}$ , as a curve parameter for  $Ste = 0.13, 0.12$ , and  $0.36$ . The solid and dashed lines in this figure refer to the oblate and prolate spheroidal capsules, respectively. The present numerical results for the spherical capsule are also plotted in the figure together with the numerical results for the spherical capsule for  $Ste = 0.1$  by Tao (1967), which shows a very good agreement even though the  $Ste$  is slightly different.

As seen from Fig. 4, the speed of solidification for both oblate and prolate spheroidal capsules is higher than that for the spherical capsule. This trend is accentuated with increasing surface area ratio,  $S_{\text{spheroid}}/S_{\text{sphere}}$ , in both spheroidal capsules. It is also seen that the speed of solidification for the oblate capsule is slightly higher than that for the prolate capsule. It is noteworthy that the speed of solidification for the oblate capsule of  $S_{\text{spheroid}}/S_{\text{sphere}} = 1.6$  is about three times higher than that for the spherical capsule. This shows that the oblate spheroidal capsule is superior to the spherical capsule in transient heat storage characteristics.

Attention will now be focused on a limiting case where the specific heat of the solidified medium is extremely low such that the Stefan number approaches zero. Then, Eq. (3) reduces to

$$0 = \nabla^2 \theta \quad (12)$$

In the case of the spherical capsule, it is easy to obtain an analytical solution. The ratio of the solidified zone volume to the capsule volume,  $V_s/V_{\text{cap}}$ , can be written as

$$\text{Fo Ste} = (1 - V_s/V_{\text{cap}})/3 - (1 - V_s/V_{\text{cap}})^{2/3}/2 + 1/6 \quad (13)$$

An analytical value of  $V_s/V_{\text{cap}}$  for the limiting case of  $\text{Ste} = 0$  from Eq. (13) is also plotted in Fig. 4. A good agreement can be seen between the analytical and numerical results for  $\text{Ste} = 0.03$ .

From the examination of the governing equation, the solidified zone volume is function of the Fourier number, Fo, and the Stefan number, Ste. However, comparing the results for  $\text{Ste} = 0.03, 0.12,$  and  $0.36$ , it is evident that the solidified zone volume can be approximately expressed as a function of (Fo Ste) in the range of  $\text{Ste} = 0.03$  to  $0.36$  with an error of less than 15 percent.

### Concluding Remarks

A transient two-dimensional freezing of a phase-change medium contained in a spheroidal capsule has been investigated numerically. The main conclusions of the results are as follows:

1 The speed of solidification of the spheroidal capsule is higher than that for the spherical capsule. This trend is accentuated with increasing surface area ratio,  $S_{\text{spheroid}}/S_{\text{sphere}}$ .

2 The speed of solidification of the spheroidal capsule mainly depends on the surface area ratio of the spheroidal capsule,  $S_{\text{spheroid}}/S_{\text{sphere}}$ . For  $S_{\text{spheroid}}/S_{\text{sphere}} = 1.6$ , it is about three times higher than for the spherical capsule.

3 The speed of solidification for the oblate spheroidal capsule is slightly higher than that for the prolate capsule.

4 The solidified zone volume for the spheroidal capsule can be approximately expressed as a function of (Fo Ste) in the range of  $\text{Ste} = 0.03$  to  $0.36$  with an error of less than 15 percent.

### References

- Faghri, M., Sparrow, E. M., and Prata, A. T., 1984, "Finite-Difference Solutions of Convection-Diffusion Problems in Irregular Domains, Using a Nonorthogonal Coordinate Transformation," *Numerical Heat Transfer*, Vol. 7, pp. 183-209.
- Shih, Y. P., and Tsay, S. Y., 1971, "Analytical Solutions for Freezing a Saturated Liquid Inside or Outside Cylinders," *Chemical Engineering Science*, Vol. 26, pp. 809-816.
- Stewartson, K., and Waechter, R. T., 1976, "On Stefan's Problem for Spheres," *Proc. R. Soc. Lond. A.*, Vol. 348, pp. 415-426.
- Tao, L. C., 1967, "Generalized Numerical Solutions for Freezing a Saturated Liquid in Cylinders and Spheres," *AIChE Journal*, Vol. 13, No. 1, pp. 165-169.
- Tien, L. C., and Churchill, S. W., 1965, "Freezing Front Motion and Heat Transfer Outside an Infinite, Isothermal Cylinder," *AIChE Journal*, Vol. 11, No. 5, pp. 790-793.

## The Effect of the Thermal Boundary Condition on Heat Transfer From a Cylinder in Crossflow

J. W. Baughn<sup>1</sup> and N. Saniei<sup>2</sup>

### Nomenclature

$A$  = area of gold coating

<sup>1</sup>Professor, Department of Mechanical, Aeronautical, and Materials Engineering, University of California, Davis, CA 95616; Fellow ASME.

<sup>2</sup>Assistant Professor, Department of Mechanical Engineering, Southern Illinois University, Edwardsville, IL 62026-1275; Mem. ASME.

Contributed by the Heat Transfer Division of the AMERICAN SOCIETY OF MECHANICAL ENGINEERS. Manuscript received by the Heat Transfer Division September 24, 1990; revision received June 4, 1991. Keywords: Augmentation and Enhancement, Flow Separation, Instrumentation.

- $C$  = pitot tube multiplier (used in uncertainty analysis to account for uncertainty in the velocity measurement)
- $D$  = cylinder diameter
- $f$  = ratio of local electrical heating to average heating (used in uncertainty analysis to account for nonuniformity of the gold coating)
- $h$  = heat transfer coefficient
- $I$  = gold coating current
- $L$  = cylinder length
- $\text{Nu}$  = local Nusselt number based on  $D$
- $q_c$  = convective heat flux
- $q_l$  = heat flux loss due to conduction
- $\text{Re}$  = Reynolds number based on  $D$
- $T_a$  = air temperature
- $T_{lc}$  = liquid crystal temperature
- $V$  = voltage across gold coating
- $x_i$  = measurand  $i$  (used in uncertainty analysis)
- $\delta x_i$  = uncertainty of measurand  $x_i$  (20:1 odds)
- $\epsilon$  = emissivity of liquid crystal surface
- $\theta$  = angle around pin fin or cylinder as measured from the front
- $\sigma$  = Stefan-Boltzmann constant

### Introduction

There have been numerous studies, both experimental and analytical, of the heat transfer from or to a cylinder in crossflow. Zukauskas and Ziugzda (1985) have reviewed the experimental and analytical techniques that have been used in these studies and have summarized many of the important results and conclusions. Many different effects on the heat transfer are considered in their book and in the many papers that have been published on this topic. These include the flow regime, cylindrical shape, surface roughness, fluid physical properties, blockage, and free stream turbulence. One effect that has received relatively little attention is the effect of the thermal boundary condition on the local heat transfer distribution on a cylinder in crossflow. Perhaps this is because in many other flow conditions the thermal boundary condition has a small effect. For example, Siegel and Sparrow (1960) concluded that for turbulent flow in a duct the heat transfer is quite insensitive to the two different wall thermal boundary conditions of uniform wall heat flux and uniform wall temperature. This is often not the case when there is thermal boundary layer development, such as occurs on a flat plate or cylinder in crossflow. For a flat plate boundary layer, Taylor et al. (1989) have recently shown that the thermal boundary condition has a significant influence on heat transfer. For cylinders in crossflow, Papell (1981) and O'Brien et al. (1986) show that the local heat transfer distribution on the front half, with its laminar boundary layer, is significantly affected by the thermal boundary condition. This is also confirmed by the numerical study of Mariani (1985).

The objective of the present work is to provide low-turbulence, low-blockage, and high-resolution measurements of heat transfer on a cylinder in crossflow using a uniform heat flux boundary condition. These measurements are for comparison to earlier measurements in the same wind tunnel under identical conditions except with a uniform wall temperature. This comparison is made in order to demonstrate the effect of the thermal boundary condition. The measurements presented have a lower free-stream turbulence, a longer cylinder, less blockage, and provide a higher spatial resolution and lower uncertainty than the earlier cylinder measurements of Papell (1981) and those of O'Brien et al. (1986).

### Experimental Techniques

Both the uniform wall temperature and uniform wall heat

$$0 = \nabla^2 \theta \quad (12)$$

In the case of the spherical capsule, it is easy to obtain an analytical solution. The ratio of the solidified zone volume to the capsule volume,  $V_s/V_{\text{cap}}$ , can be written as

$$\text{Fo Ste} = (1 - V_s/V_{\text{cap}})/3 - (1 - V_s/V_{\text{cap}})^{2/3}/2 + 1/6 \quad (13)$$

An analytical value of  $V_s/V_{\text{cap}}$  for the limiting case of  $\text{Ste} = 0$  from Eq. (13) is also plotted in Fig. 4. A good agreement can be seen between the analytical and numerical results for  $\text{Ste} = 0.03$ .

From the examination of the governing equation, the solidified zone volume is function of the Fourier number, Fo, and the Stefan number, Ste. However, comparing the results for  $\text{Ste} = 0.03, 0.12,$  and  $0.36$ , it is evident that the solidified zone volume can be approximately expressed as a function of (Fo Ste) in the range of  $\text{Ste} = 0.03$  to  $0.36$  with an error of less than 15 percent.

### Concluding Remarks

A transient two-dimensional freezing of a phase-change medium contained in a spheroidal capsule has been investigated numerically. The main conclusions of the results are as follows:

1 The speed of solidification of the spheroidal capsule is higher than that for the spherical capsule. This trend is accentuated with increasing surface area ratio,  $S_{\text{spheroid}}/S_{\text{sphere}}$ .

2 The speed of solidification of the spheroidal capsule mainly depends on the surface area ratio of the spheroidal capsule,  $S_{\text{spheroid}}/S_{\text{sphere}}$ . For  $S_{\text{spheroid}}/S_{\text{sphere}} = 1.6$ , it is about three times higher than that for the spherical capsule.

3 The speed of solidification for the oblate spheroidal capsule is slightly higher than that for the prolate capsule.

4 The solidified zone volume for the spheroidal capsule can be approximately expressed as a function of (Fo Ste) in the range of  $\text{Ste} = 0.03$  to  $0.36$  with an error of less than 15 percent.

### References

- Faghri, M., Sparrow, E. M., and Prata, A. T., 1984, "Finite-Difference Solutions of Convection-Diffusion Problems in Irregular Domains, Using a Nonorthogonal Coordinate Transformation," *Numerical Heat Transfer*, Vol. 7, pp. 183-209.
- Shih, Y. P., and Tsay, S. Y., 1971, "Analytical Solutions for Freezing a Saturated Liquid Inside or Outside Cylinders," *Chemical Engineering Science*, Vol. 26, pp. 809-816.
- Stewartson, K., and Waechter, R. T., 1976, "On Stefan's Problem for Spheres," *Proc. R. Soc. Lond. A.*, Vol. 348, pp. 415-426.
- Tao, L. C., 1967, "Generalized Numerical Solutions for Freezing a Saturated Liquid in Cylinders and Spheres," *AIChE Journal*, Vol. 13, No. 1, pp. 165-169.
- Tien, L. C., and Churchill, S. W., 1965, "Freezing Front Motion and Heat Transfer Outside an Infinite, Isothermal Cylinder," *AIChE Journal*, Vol. 11, No. 5, pp. 790-793.

## The Effect of the Thermal Boundary Condition on Heat Transfer From a Cylinder in Crossflow

J. W. Baughn<sup>1</sup> and N. Saniei<sup>2</sup>

### Nomenclature

$A$  = area of gold coating

<sup>1</sup>Professor, Department of Mechanical, Aeronautical, and Materials Engineering, University of California, Davis, CA 95616; Fellow ASME.

<sup>2</sup>Assistant Professor, Department of Mechanical Engineering, Southern Illinois University, Edwardsville, IL 62026-1275; Mem. ASME.

Contributed by the Heat Transfer Division of the AMERICAN SOCIETY OF MECHANICAL ENGINEERS. Manuscript received by the Heat Transfer Division September 24, 1990; revision received June 4, 1991. Keywords: Augmentation and Enhancement, Flow Separation, Instrumentation.

- $C$  = pitot tube multiplier (used in uncertainty analysis to account for uncertainty in the velocity measurement)
- $D$  = cylinder diameter
- $f$  = ratio of local electrical heating to average heating (used in uncertainty analysis to account for nonuniformity of the gold coating)
- $h$  = heat transfer coefficient
- $I$  = gold coating current
- $L$  = cylinder length
- $\text{Nu}$  = local Nusselt number based on  $D$
- $q_c$  = convective heat flux
- $q_l$  = heat flux loss due to conduction
- $\text{Re}$  = Reynolds number based on  $D$
- $T_a$  = air temperature
- $T_{lc}$  = liquid crystal temperature
- $V$  = voltage across gold coating
- $x_i$  = measurand  $i$  (used in uncertainty analysis)
- $\delta x_i$  = uncertainty of measurand  $x_i$  (20:1 odds)
- $\epsilon$  = emissivity of liquid crystal surface
- $\theta$  = angle around pin fin or cylinder as measured from the front
- $\sigma$  = Stefan-Boltzmann constant

### Introduction

There have been numerous studies, both experimental and analytical, of the heat transfer from or to a cylinder in crossflow. Zukauskas and Ziugzda (1985) have reviewed the experimental and analytical techniques that have been used in these studies and have summarized many of the important results and conclusions. Many different effects on the heat transfer are considered in their book and in the many papers that have been published on this topic. These include the flow regime, cylindrical shape, surface roughness, fluid physical properties, blockage, and free stream turbulence. One effect that has received relatively little attention is the effect of the thermal boundary condition on the local heat transfer distribution on a cylinder in crossflow. Perhaps this is because in many other flow conditions the thermal boundary condition has a small effect. For example, Siegel and Sparrow (1960) concluded that for turbulent flow in a duct the heat transfer is quite insensitive to the two different wall thermal boundary conditions of uniform wall heat flux and uniform wall temperature. This is often not the case when there is thermal boundary layer development, such as occurs on a flat plate or cylinder in crossflow. For a flat plate boundary layer, Taylor et al. (1989) have recently shown that the thermal boundary condition has a significant influence on heat transfer. For cylinders in crossflow, Papell (1981) and O'Brien et al. (1986) show that the local heat transfer distribution on the front half, with its laminar boundary layer, is significantly affected by the thermal boundary condition. This is also confirmed by the numerical study of Mariani (1985).

The objective of the present work is to provide low-turbulence, low-blockage, and high-resolution measurements of heat transfer on a cylinder in crossflow using a uniform heat flux boundary condition. These measurements are for comparison to earlier measurements in the same wind tunnel under identical conditions except with a uniform wall temperature. This comparison is made in order to demonstrate the effect of the thermal boundary condition. The measurements presented have a lower free-stream turbulence, a longer cylinder, less blockage, and provide a higher spatial resolution and lower uncertainty than the earlier cylinder measurements of Papell (1981) and those of O'Brien et al. (1986).

### Experimental Techniques

Both the uniform wall temperature and uniform wall heat

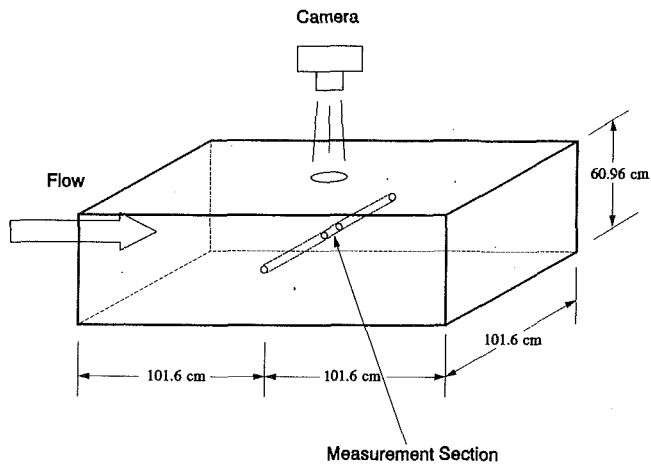


Fig. 1 Diagram of duct arrangement

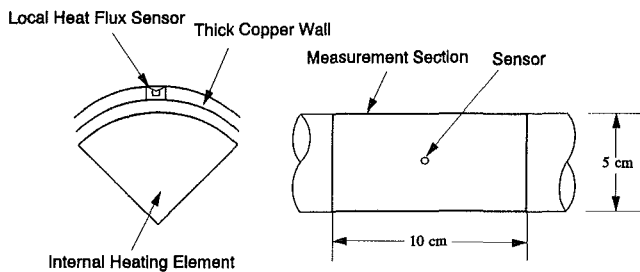


Fig. 2(a) Diagram of uniform temperature cylinder

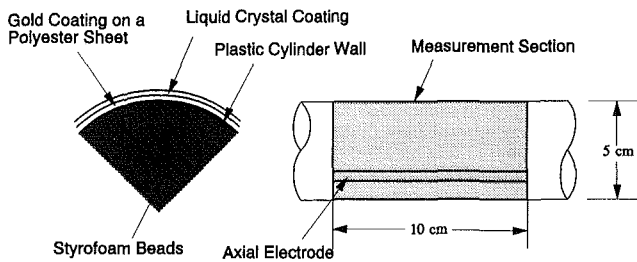


Fig. 2(b) Diagram of uniform heat flux cylinder

flux measurements presented here were done in the same air wind tunnel. This wind tunnel has a large diverging/converging entrance, which produces a uniform velocity, low-turbulence (less than 0.5 percent) air flow in a rectangular duct. The duct test section is 61 cm high and 102 cm across. The cylinders were 5 cm in diameter and were mounted across the duct as shown in Fig. 1. Blockage in both cases was low (8 percent).

The thermal test section of the cylinders was a 10-cm length of the cylinder at the center of the duct. Since the boundary layers are thin compared to the diameter and length of the heated section, two-dimensional flow effects are small.

Both sets of measurements used a Reynolds number of 34,000 and had an ambient temperature of approximately 20°C.

**(a) Uniform Wall Temperature.** The measurements of the local heat transfer coefficients for a uniform wall temperature were taken from Kraabel et al. (1982) in the same wind tunnel as the uniform heat flux measurements described below. They used a local heat flux sensor, which is illustrated in Fig. 2(a). The sensor was mounted in a thick wall copper cylinder, which was heated by an internal element and had guard heaters at both ends. The thick wall copper provided a uniform wall temperature by conduction (i.e., the Biot modulus was very low). The local heat flux sensor had its own small heater and

Table 1 Uncertainty analysis

| $X_i$      | Value            | $\delta X_i$ | $\frac{\delta X_i}{(Nu/\sqrt{Re})} \frac{\partial(Nu/\sqrt{Re})}{\partial X_i} \times 100$ |                     |
|------------|------------------|--------------|--|---------------------|
|            |                  |              | $\theta = 22.5^\circ$  | $\theta = 88^\circ$ |
| C          | 1.0              | 0.01         | 0.5  | 0.5                 |
| D          | 0.06 (m)         | 0.0003       | 0.3  | 0.3                 |
| f          | 1.0              | 0.02         | 2.1  | 2.2                 |
| L          | 0.12 (m)         | 0.0003       | 0.3  | 0.3                 |
| $P_a$      | 32.25 ("Hg)      | 0.1          | 0.1  | 0.1                 |
| $\Delta P$ | 0.216 ("oil)     | 0.001        | 0.1  | 0.1                 |
| R          | 8.7 ( $\Omega$ ) | 0.01         | 0.1  | 0.1                 |
| $T_a$      | 26.1 (°C)        | 0.1          | 0.4  | 0.4                 |
| $T_{ic}$   | 41.3 (°C)        | 0.15         | 1.1  | 1.1                 |
| V          | 11.0 (Volt)      | 0.01         | 0.1  | 0.2                 |
| $\epsilon$ | 0.5              | 0.1          | 0.9  | 2.1                 |

Uncertainty of  $Nu/\sqrt{Re}$  (%) = 2.7 3.3

used a null method to establish the heat flux as described by Kraabel et al. (1980). The heat flux sensor was nulled at the same temperature as the wall, producing the desired uniform wall temperature even for the surface of the sensor. The angle subtended by the sensor was approximately 7 deg. The wall temperature was typically 7–10°C above the ambient temperature. The uncertainty of the heat flux measurement was estimated to be 1.1 percent at the stagnation point and 1.8 percent at the minimum heat transfer point using standard estimation methods. This results in an uncertainty in  $Nu/\sqrt{Re}$  of 1.4 percent at the stagnation point and 2.2 percent at the minimum heat transfer point.

**(b) Uniform Surface Heat Flux.** The uniform surface heat flux measurements were achieved using the heated-coating method described by Baughn et al. (1985, 1986a, 1989). In the heated-coating method a very thin conductive coating (vacuum-deposited gold in this case) on the surface of a plastic substrate (a thin polyester sheet mounted to a plastic tube in this case) is electrically heated as illustrated in Fig. 2(b). Conduction in the plastic substrate is very low relative to the surface heating (less than 1 percent as determined by a two-dimensional heat conduction analysis) so that the surface thermal boundary condition is that of a uniform heat flux. Axial conduction is also negligible in this case so guard heaters are not necessary. Several methods for measuring the surface temperature have been used including thermocouples (Baughn et al., 1985) and liquid crystals (Hippensteele et al., 1983; Simonich and Moffat, 1982; Baughn et al., 1986a). Since the heat flux can be adjusted by changing the electrical voltage on the electrodes, the surface temperatures can be increased or decreased. When this is done an isotherm on the surface corresponds to a line of constant heat transfer coefficient. The local heat transfer coefficient at the position of the color play is then given by

$$h = \frac{q_c}{(T_{ic} - T_a)} \quad (1)$$

where  $q_c$  is given by

$$q_c = \frac{IV}{A} - \epsilon\sigma(T_{ic}^4 - T_a^4) - q_l \quad (2)$$

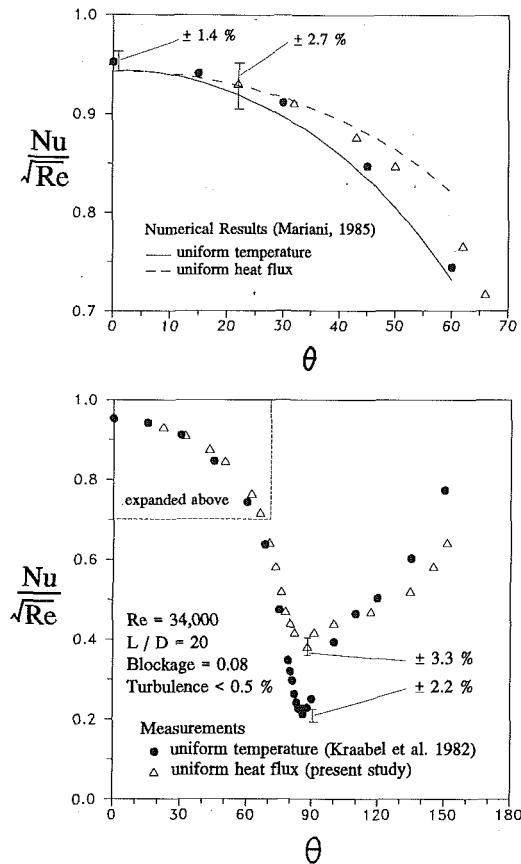


Fig. 3 Effect of the thermal boundary condition on the heat transfer distribution from a long cylinder in crossflow

This equation assumes that the electrical heating of the gold coating is uniform. The nonuniformity in the coating was approximately 2 percent and is included in the uncertainty analysis. This relatively low nonuniformity was obtained by careful selection of the small section of the sheet used in these measurements. Larger sections have been found by the authors and others to have a nonuniformity up to 8 percent. The radiation correction is very small (1–3 percent).

In the present study, a narrow band liquid crystal with a color play of 0.7°C at approximately 42.3°C is used. The ambient temperature was approximately 25°C.

The uncertainty in  $Nu/\sqrt{Re}$  for the present measurements has also been estimated using a standard uncertainty analysis with odds of 20:1. The contributions of the measurands and the total estimated uncertainty for the stagnation region and the point of minimum heat transfer are shown in Table 1.

## Results and Discussion

The results of the uniform heat flux measurements are compared to those of the uniform wall temperature in Fig. 3. The stagnation line values are nearly identical for both thermal boundary conditions as they should be (the stagnation value is independent of the thermal boundary condition). In fact, near the stagnation region, the two methods agree much better than would be expected by the estimated uncertainties. This suggests that either the measured values are more accurate than suggested by the estimated uncertainties or that both methods err in the same direction. In either case, the high resolution of both sets of measurements makes it possible to observe the effect of the thermal boundary conditions for variations less than the estimated uncertainties.

As the laminar boundary layer builds on the front of the cylinder, the heat transfer measurements with the uniform heat

flux diverge and are higher than those of the uniform temperature. This behavior is similar to that observed by both Papell (1981) and O'Brien et al. (1986). The heat transfer on the front (including the stagnation values) measured here is 5–7 percent lower than that of Papell (1981) and O'Brien et al. (1986). This is probably due to the lower turbulence, longer cylinders, and lower blockage in the present measurements. Because of this difference in conditions we have not shown their data on the graph of Fig. 3.

The numerical predictions for the leading edge laminar boundary layer by Mariani (1985) are also shown in Fig. 3. They are only shown for the first 60 deg of the leading edge since they are based on pressure distributions whose uncertainty increases rapidly at and beyond 60 deg. The numerical predictions agree quite well with the measurements for the first 30 deg beyond which they show a somewhat greater divergence than measured (probably due to the uncertainty in the pressure distribution used in the analysis). At the rear of the cylinder the heat transfer coefficient for the uniform temperature boundary condition increases rapidly and becomes greater than that for the uniform heat flux boundary condition on the far back side. This behavior is a consequence of the difference in the growth of the thermal boundary layer (on the front) and the difference in the temperature of the separated recirculating flow (on the back).

It is apparent from these results that extreme caution must be taken when making measurements of the local heat transfer on a surface with a thermal boundary layer buildup. Measurements with either of the thermal boundary condition cases considered here cannot be compared directly and measurements with mixed boundary conditions or thermal boundary conditions that are unknown or unreported may be of little value.

## References

- Baughn, J. W., Takahashi, R. K., Hoffman, M. A., and McKillop, A. A., 1985, "Local Heat Transfer Coefficient Measurements Using an Electrically Heated Thin Gold-Coated Sheet," *ASME JOURNAL OF HEAT TRANSFER*, Vol. 107, pp. 953–959.
- Baughn, J. W., Hoffman, M. A., and Makel, D. B., 1986a, "Improvements in a New Technique for Measuring Local Heat Transfer Coefficients," *Review of Scientific Instruments*, Vol. 57, pp. 650–654.
- Baughn, J. W., Elderkin, A. A., and McKillop, A. A., 1986b, "Heat Transfer From a Single Cylinder, Cylinders in Tandem, and Cylinders in the Entrance Region of a Tube Bank With a Uniform Heat Flux," *ASME JOURNAL OF HEAT TRANSFER*, Vol. 108, pp. 386–391.
- Baughn, J. W., Ireland, P. T., Jones, T. V., and Sanici, N., 1989, "A Comparison of the Transient and Heated-Coating Methods for the Measurement of Local Heat Transfer Coefficients on a Pin Fin," *ASME JOURNAL OF HEAT TRANSFER*, Vol. 111, pp. 877–881.
- Hippensteele, S. A., Russell, L. M., and Stepka, F. S., 1983, "Evaluation of a Method for Heat Transfer Measurements and Thermal Visualization Using a Composite of a Heater Element and Liquid Crystals," *ASME JOURNAL OF HEAT TRANSFER*, Vol. 105, pp. 184–189.
- Kraabel, J. S., McKillop, A. A., and Baughn, J. W., 1980, "An Instrument for the Measurement of Heat Flux From a Surface With Uniform Temperature," *ASME JOURNAL OF HEAT TRANSFER*, Vol. 102, pp. 576–578.
- Kraabel, J. S., McKillop, A. A., and Baughn, J. W., 1982, "Heat Transfer to Air From a Yawed Cylinder," *International Journal of Heat and Mass Transfer*, Vol. 25, pp. 409–418.
- Mariani, P., 1985, "Numerical Evaluation of Heat for Flow Over Circular Cylinder at Different Blockages," Master's Thesis, University of California, Davis.
- O'Brien, J. E., Simoneau, R. J., LaGraff, J. E., and Morehouse, K. A., 1986, "Unsteady Heat Transfer and Direct Comparison for Steady-State Measurements in a Rotor-Wake Experiment," *Proceedings, 8th International Heat Transfer Conference*, pp. 1243–1248.
- Papell, S. S., 1981, "Influence of Thermal Boundary Conditions on Heat Transfer From a Cylinder in Crossflow," NASA Technical Paper 1894.
- Siegel, R., and Sparrow, E. M., 1960, "Comparison of Turbulent Heat Transfer for Uniform Wall Heat Flux and Uniform Wall Temperature," *ASME JOURNAL OF HEAT TRANSFER*, Vol. 82, pp. 152–153.
- Simonich, J. C., and Moffat, R. J., 1982, "A New Technique for the Measurement of Heat Transfer Coefficient," *Review of Scientific Instruments*, Vol. 53, pp. 678–683.
- Taylor, R. P., Coleman, H. W., Hosni, M. H., and Love, P. H., 1989, "Thermal Boundary Condition Effects on Heat Transfer in the Turbulent In-

## An Experimental Study of Entrainment Effects on the Heat Transfer From a Flat Surface to a Heated Circular Impinging Jet

J. W. Baughn,<sup>1,3</sup> A. E. Hechanova,<sup>2,3</sup> and Xiaojun Yan<sup>2,3</sup>

### Nomenclature

|            |  |
|------------|--|
| $A_p$      | = area of gold film  |
| $D$        | = diameter of nozzle   |
| $h$        | = local heat transfer coefficient  |
| $k$        | = air thermal conductivity (evaluated at the adiabatic wall temperature) |
| $L$        | = jet exit to surface distance   |
| $M$        | = jet exit Mach number   |
| $Nu$       | = local Nusselt number = $hD/k$  |
| $q_c$      | = local convective surface heat flux                                     |
| $q_l$      | = conduction loss  |
| $q_r$      | = radiation surface heat flux  |
| $q_t$      | = total surface heat flux  |
| $r_R$      | = local surface recovery factor  |
| $r_{tc}$   | = thermocouple recovery factor   |
| $R$        | = radial coordinate of surface   |
| $Re$       | = jet Reynolds number  |
| $R_s$      | = resistance of shunt resistor   |
| $T_{aw}$   | = local adiabatic wall temperature                                       |
| $T_{awo}$  | = adiabatic wall temperature at stagnation point                         |
| $T_\infty$ | = ambient air temperature  |
| $T_j^m$    | = measured jet temperature   |
| $T_j^o$    | = jet total temperature  |
| $T_j^*$    | = nondimensional jet temperature   |
| $T_{lc}$   | = liquid crystal color temperature                                       |
| $T_r$      | = local recovery temperature   |
| $T_w$      | = local wall temperature   |
| $T_{wo}$   | = wall temperature at stagnation point                                   |
| $V_r$      | = voltage across the gold film   |
| $V_s$      | = voltage across the shunt resistance                                    |
| $\gamma$   | = ratio of specific heats for air  |
| $\epsilon$ | = surface emissivity   |
| $\eta$     | = effectiveness  |
| $\sigma$   | = Stefan-Boltzmann constant  |

### Introduction

There have been numerous analytical and experimental investigations of heat transfer to impinging jets. The heat transfer

<sup>1</sup>Professor; Fellow ASME.

<sup>2</sup>Research Assistant.

<sup>3</sup>Department of Mechanical, Aeronautical and Materials Engineering, University of California, Davis, CA 95616.

Contributed by the Heat Transfer Division and presented at the 3rd ASME/JSME Thermal Engineering Joint Conference, Reno, Nevada, March 1991. Manuscript received by the Heat Transfer Division December 17, 1990; revision received April 16, 1991. Keywords: Augmentation and Enhancement, Forced Convection, Measurement Techniques.

is influenced by many factors including the jet velocity, temperature, and turbulence distribution. These factors are often quite different (and sometimes unknown) for different experimental studies of impingement heat transfer making it difficult to compare or generalize experimental results. Most experimental studies on impinging jet heat transfer are for the case where the jet temperature is the same as the temperature of the ambient air, even though in many applications the jet may be at a higher or lower temperature than the ambient.

The present study investigates the effect of ambient air entrainment into a heated impinging jet on the heat transfer from a flat surface. It provides a well-characterized jet by using a long circular pipe to obtain fully developed pipe flow for the jet and a uniform heat flux surface thermal boundary condition by electrically heating a vacuum-deposited gold coating. The surface temperature distribution is measured using a liquid crystal.

Prior experimental work on heated single jets to study entrainment effects include studies by Bouchez and Goldstein (1975), Striegl and Diller (1984), Hollworth and Wilson (1984), Hollworth and Gero (1985), and more recently by Goldstein et al. (1990). Goldstein et al. (1990) use a heated jet from an ASME nozzle impinging on an electrically heated flat stainless steel plate instrumented with thermocouples. They measure the local effectiveness of the jet, which they define in terms of the local adiabatic wall temperature, and show that the local heat transfer coefficients for an unheated jet can be used for the heated jet if the local adiabatic wall temperature is used for the fluid temperature in the definition of the heat transfer coefficient. The present study is similar to that of Goldstein et al. (1990) but uses a different jet source (fully developed pipe flow versus an ASME nozzle), a different Reynolds number range (23,300 to 55,000 versus 61,000 to 124,000) and a different experimental technique employing liquid crystals. It also introduces a nondimensional jet temperature  $T_j^*$  similar to that of Striegl and Diller (1984).

### Experimental Apparatus and Technique

Figure 1 is a diagram of the experimental apparatus. It is basically the same as that used by Baughn and Shimizu (1989) for an unheated jet with the addition of a heater. The pipe is a thin-walled PVC pipe with an i.d. of 2.6 cm, a wall thickness of 0.36 cm, and a length of 72 diameters. The velocity and temperature distributions just inside the exit were measured. The velocity distribution is that for fully developed pipe flow and the temperature was nearly uniform across the pipe. The turbulence level at the center of the jet at the exit was approximately 4.1 percent as measured with a hot-wire anemometer.

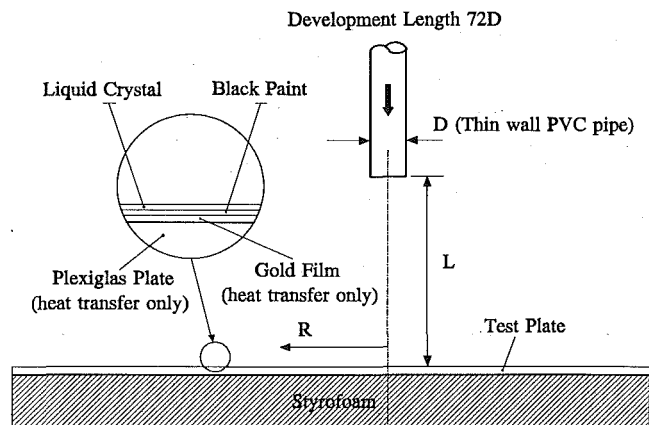


Fig. 1 Diagram of jet and test plate

## An Experimental Study of Entrainment Effects on the Heat Transfer From a Flat Surface to a Heated Circular Impinging Jet

J. W. Baughn,<sup>1,3</sup> A. E. Hechanova,<sup>2,3</sup> and Xiaojun Yan<sup>2,3</sup>

### Nomenclature

|            |  |
|------------|--|
| $A_p$      | = area of gold film  |
| $D$        | = diameter of nozzle   |
| $h$        | = local heat transfer coefficient  |
| $k$        | = air thermal conductivity (evaluated at the adiabatic wall temperature) |
| $L$        | = jet exit to surface distance   |
| $M$        | = jet exit Mach number   |
| $Nu$       | = local Nusselt number = $hD/k$  |
| $q_c$      | = local convective surface heat flux                                     |
| $q_l$      | = conduction loss  |
| $q_r$      | = radiation surface heat flux  |
| $q_t$      | = total surface heat flux  |
| $r_R$      | = local surface recovery factor  |
| $r_{tc}$   | = thermocouple recovery factor   |
| $R$        | = radial coordinate of surface   |
| $Re$       | = jet Reynolds number  |
| $R_s$      | = resistance of shunt resistor   |
| $T_{aw}$   | = local adiabatic wall temperature                                       |
| $T_{awo}$  | = adiabatic wall temperature at stagnation point                         |
| $T_\infty$ | = ambient air temperature  |
| $T_j^m$    | = measured jet temperature   |
| $T_j^o$    | = jet total temperature  |
| $T_j^*$    | = nondimensional jet temperature   |
| $T_{lc}$   | = liquid crystal color temperature                                       |
| $T_r$      | = local recovery temperature   |
| $T_w$      | = local wall temperature   |
| $T_{wo}$   | = wall temperature at stagnation point                                   |
| $V_r$      | = voltage across the gold film   |
| $V_s$      | = voltage across the shunt resistance                                    |
| $\gamma$   | = ratio of specific heats for air  |
| $\epsilon$ | = surface emissivity   |
| $\eta$     | = effectiveness  |
| $\sigma$   | = Stefan-Boltzmann constant  |

### Introduction

There have been numerous analytical and experimental investigations of heat transfer to impinging jets. The heat transfer

<sup>1</sup>Professor; Fellow ASME.

<sup>2</sup>Research Assistant.

<sup>3</sup>Department of Mechanical, Aeronautical and Materials Engineering, University of California, Davis, CA 95616.

Contributed by the Heat Transfer Division and presented at the 3rd ASME/JSME Thermal Engineering Joint Conference, Reno, Nevada, March 1991. Manuscript received by the Heat Transfer Division December 17, 1990; revision received April 16, 1991. Keywords: Augmentation and Enhancement, Forced Convection, Measurement Techniques.

is influenced by many factors including the jet velocity, temperature, and turbulence distribution. These factors are often quite different (and sometimes unknown) for different experimental studies of impingement heat transfer making it difficult to compare or generalize experimental results. Most experimental studies on impinging jet heat transfer are for the case where the jet temperature is the same as the temperature of the ambient air, even though in many applications the jet may be at a higher or lower temperature than the ambient.

The present study investigates the effect of ambient air entrainment into a heated impinging jet on the heat transfer from a flat surface. It provides a well-characterized jet by using a long circular pipe to obtain fully developed pipe flow for the jet and a uniform heat flux surface thermal boundary condition by electrically heating a vacuum-deposited gold coating. The surface temperature distribution is measured using a liquid crystal.

Prior experimental work on heated single jets to study entrainment effects include studies by Bouchez and Goldstein (1975), Striegl and Diller (1984), Hollworth and Wilson (1984), Hollworth and Gero (1985), and more recently by Goldstein et al. (1990). Goldstein et al. (1990) use a heated jet from an ASME nozzle impinging on an electrically heated flat stainless steel plate instrumented with thermocouples. They measure the local effectiveness of the jet, which they define in terms of the local adiabatic wall temperature, and show that the local heat transfer coefficients for an unheated jet can be used for the heated jet if the local adiabatic wall temperature is used for the fluid temperature in the definition of the heat transfer coefficient. The present study is similar to that of Goldstein et al. (1990) but uses a different jet source (fully developed pipe flow versus an ASME nozzle), a different Reynolds number range (23,300 to 55,000 versus 61,000 to 124,000) and a different experimental technique employing liquid crystals. It also introduces a nondimensional jet temperature  $T_j^*$  similar to that of Striegl and Diller (1984).

### Experimental Apparatus and Technique

Figure 1 is a diagram of the experimental apparatus. It is basically the same as that used by Baughn and Shimizu (1989) for an unheated jet with the addition of a heater. The pipe is a thin-walled PVC pipe with an i.d. of 2.6 cm, a wall thickness of 0.36 cm, and a length of 72 diameters. The velocity and temperature distributions just inside the exit were measured. The velocity distribution is that for fully developed pipe flow and the temperature was nearly uniform across the pipe. The turbulence level at the center of the jet at the exit was approximately 4.1 percent as measured with a hot-wire anemometer.

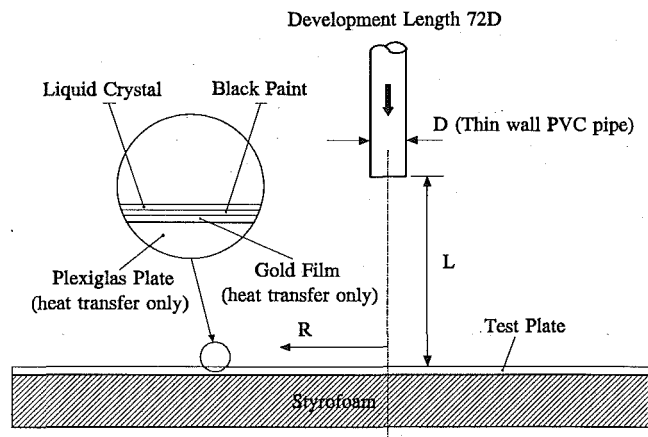


Fig. 1 Diagram of jet and test plate



Two types of test plates were used, one for the effectiveness measurements and one for the heat transfer measurements. The test plate for the effectiveness measurements was a smooth foam plate, which was painted black and air brushed with a thin layer of liquid crystals. As the jet was heated, circular rings of color (isotherms) formed on the surface. At equilibrium these rings measured the local adiabatic wall temperature and the corresponding local effectiveness of the heated jet. The test plate for the heat transfer measurements was a Plexiglas plate (0.64 cm thick) on which a thin polyester sheet (0.013 cm thick) containing a vacuum-deposited gold coating was mounted. The black paint and liquid crystal were also air brushed on the surface of the gold coating, which was electrically heated. This heat transfer measurement technique is described by Baughn et al. (1986). The electrically heated gold coating produces a uniform heat flux since conduction to the plastic substrate is negligible. Again, color rings form when the surface comes to equilibrium.

Two different types of microencapsulated liquid crystals were used in these experiments. For the effectiveness measurements a narrow band (1°C wide) liquid crystal calibrated with a yellow red transition at  $34.95^\circ\text{C} \pm 0.13^\circ\text{C}$  was used. For the heat transfer measurements a broader band (4°C wide) liquid crystal calibrated at a red of  $29.6^\circ\text{C} \pm 0.1^\circ\text{C}$  and at a yellow of  $30.1^\circ\text{C} \pm 0.1^\circ\text{C}$  was used.

### Data Reduction and Results

The effectiveness,  $\eta$ , and the heat transfer coefficient,  $h$ , are defined here the same as in Goldstein et al. (1990).

$$\eta = \frac{T_{aw} - T_r}{T_j^o - T_\infty} \quad (1)$$

$$h = \frac{q_c}{T_w - T_{aw}} \quad (2)$$

For the ring isotherm at the liquid crystal temperature,  $T_{lc}$ , the local adiabatic wall temperature can be determined by an energy balance at the surface ( $q_c + q_r + q_l = 0$ ), which is given by

$$T_{aw} = T_{lc} + \frac{\epsilon\sigma}{h} (T_{lc}^4 - T_\infty^4) + \frac{q_l}{h} \quad (3)$$

where the second term on the right represents a radiation correction and the  $q_l$  is the conduction loss through the styrofoam. The radiation correction raises the measured effectiveness by 2–6 percent and the conduction loss is negligible.

The jet total temperature,  $T_j^o$ , is

$$T_j^o = T_j^m \left( 1 + r_{tc} \frac{\gamma - 1}{2} M^2 \right) \quad (4)$$

where  $T_j^m$  is the measured thermocouple temperature and  $r_{tc}$  is the recovery factor for the thermocouple, which was mounted perpendicular to the flow (a value of  $0.68 \pm 0.1$  was used). This correction is insignificant since the Mach numbers for the jet were 0.047 ( $\text{Re} = 23,300$ ) and 0.11 ( $\text{Re} = 55,000$ ).

The local recovery temperature at the wall is the same as the adiabatic wall temperature for an unheated jet and is given by

$$T_r = T_\infty \left( 1 + r_R \frac{\gamma - 1}{2} M^2 \right) \quad (5)$$

In the present study a local recovery factor,  $r_R$ , of 1.0 was used.

The measured results of effectiveness for jet to plate spacings,  $L/D$ , of 2, 6, and 10 are shown in Fig. 2. The correlations from Goldstein et al. (1990) are also shown in Fig. 2.

The convective heat flux is given by

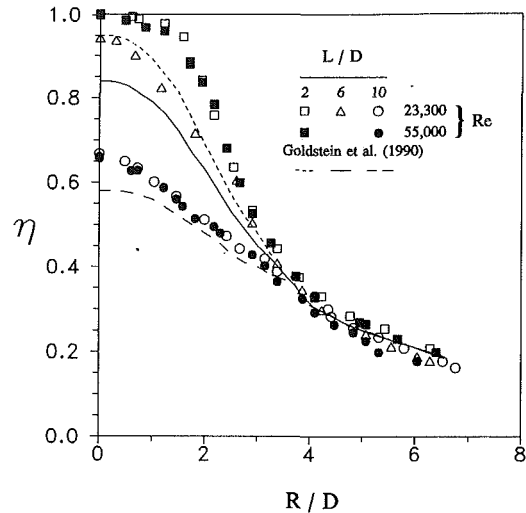


Fig. 2 Effectiveness distributions for  $L/D = 2, 6,$  and  $10$  for Reynolds numbers  $23, 300,$  and  $55,000$

$$q_c = q_t - q_r - q_l \quad (6)$$

where the total heat flux  $q_t$  is given by

$$q_t = \frac{V_r V_s}{R_s A_p} \quad (7)$$

and the radiation correction is given by

$$q_r = \epsilon\sigma (T_w^4 - T_\infty^4) \quad (8)$$

The radiation correction represents approximately 5 percent of the total heat flux and the conduction correction is negligible.

In order to examine the effect of the jet heating it is useful to define a nondimensional jet temperature in terms of the temperature increase of the jet above the ambient temperature relative to the wall temperature increase.

$$T_j^* = \frac{T_j^o - T_\infty}{T_{w_o} - T_{aw_o}} \quad (9)$$

When the jet is unheated  $T_j^*$  is 0.0. As the jet is heated the value of  $T_j^*$  increases for a given surface heat flux (which determines the difference between the stagnation point wall temperature and the adiabatic wall temperature). If the heat flux is increased then  $T_j^*$  will decrease. Entrainment effects should be small for low  $T_j^*$  since this corresponds to either small amounts of jet heating or to very high wall temperatures (relative to the difference between the jet and ambient temperatures). When  $T_j^*$  is on the order of 1.0, the entrainment effects should be large since the difference between the jet and ambient temperatures is on the order of the wall-to-fluid temperature difference. In the present study, the ambient temperatures were typically  $14\text{--}17^\circ\text{C}$  and the jet temperatures ranged from 0 to  $8.4^\circ\text{C}$  above the ambient temperature. The heat fluxes were adjusted to give values for  $T_j^*$  of 0.0, 0.33, and 1.0. The results for the Nusselt number distributions for  $L/D$  of 2, 6, and 10 are shown in Fig. 3.

A standard uncertainty analysis (using 20:1 odds) was performed on the measured parameters (Hechanova, 1988). The uncertainty in the effectiveness was found to range from 1.5 percent at the stagnation point of 3.5 percent at maximum  $R/D$ . The uncertainty in the Nusselt number ranged from 2.3 percent at the stagnation point to 3.0 percent at the maximum  $R/D$ . The uncertainty in the Reynolds number was typically 2 percent and the uncertainty in  $T_j^*$  was typically 4 percent.

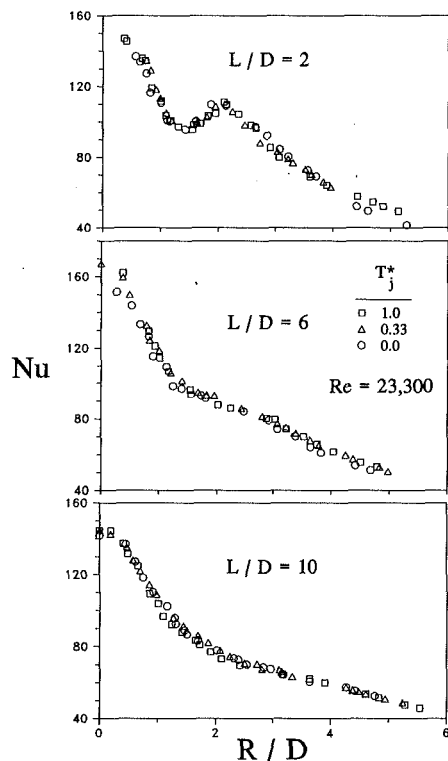


Fig. 3 Nusselt number distributions for  $L/D = 2, 6,$  and  $10$  for  $Re = 23,300$

### Discussion and Conclusions

The effectiveness measurements are compared in Fig. 2 to those of Goldstein et al. (1990). The effectiveness measurements in the present study are higher than those of Goldstein et al. (1990) in the stagnation region but agree well for larger  $R/D$  (greater than 3.5). There are several possible explanations for this. The jet in the present study is from the exit of a fully developed pipe flow whereas Goldstein et al. (1990) used an ASME nozzle. Conduction and radiation effects could also cause some small differences near the stagnation region. The effectiveness measurements in the present study have essentially no wall conduction. Goldstein et al. (1990) use a stainless steel plate and estimate that their conduction error is less than 0.5 percent. In the present study a radiation correction is used that raises the effectiveness by 2–6 percent with the smaller correction near the stagnation region and the larger correction at larger  $R/D$ .

The present results confirm those of Goldstein et al. (1990), which showed that the effectiveness is independent of the Reynolds number. The effectiveness is also shown to be independent of the jet temperature mismatch by both Hollworth and Wilson (1984) and by Goldstein et al. (1990). This is expected if the fluid (air) properties are not temperature dependent. The heat transfer results shown in Fig. 3 for the unheated jet ( $T_j^* = 0.0$ ) agree with those of Baughn and Shimizu (1989). The collapse of the Nusselt number distributions for  $T_j^* = 0.33$  and  $T_j^* = 1.0$  on the same curves confirms the results of Goldstein et al. (1990) (while extending the Reynolds number range and jet characteristics), which show that it is possible to use heat transfer data from unheated jets for the heated jet if the effectiveness is known and the local heat transfer coefficient is defined in terms of the adiabatic wall temperature. This does not mean that the entrainment effects are negligible nor that the data for unheated jets can be used directly for heated jets. It simply shows that the entrainment effects, in this case, can be described by an effectiveness. The technique employed in the present study to measure the effectiveness is considerably simpler than that required to measure the heat transfer.

### Acknowledgments

The authors wish to thank Professor Brian E. Launder, who originally encouraged our investigations of impinging jets and who has made valuable suggestions.

### References

- Baughn, J. W., Hoffman, M. A., and Makel, D. B., 1986, "Improvements in a New Technique for Measuring and Mapping Heat Transfer Coefficients," *Review of Scientific Instruments*, Vol. 57, pp. 650–654.
- Baughn, J. W., and Shimizu, S. S., 1989, "Heat Transfer Measurements From a Surface With Uniform Heat Flux and a Fully Developed Impinging Jet," *ASME JOURNAL OF HEAT TRANSFER*, Vol. 111, pp. 1096–1098.
- Bouchez, J. P., and Goldstein, R. J., 1975, "Impinging Cooling From a Circular Jet in a Cross Flow," *International Journal of Heat and Mass Transfer*, Vol. 18, pp. 719–730.
- Goldstein, R. J., Sobolik, K. A., and Seol, W. S., 1990, "Effect of Entrainment on the Heat Transfer to a Heated Circular Air Jet Impinging on a Flat Surface," *ASME JOURNAL OF HEAT TRANSFER*, Vol. 112, pp. 608–611.
- Hechanova, T. E., 1988, "An Experimental Study of Entrainment Effects on Heat Transfer With a Fully-Developed Impinging Jet," Masters Thesis, University of California, Davis.
- Hollworth, B. R., and Wilson, S. I., 1984, "Entrainment Effects on Impingement Heat Transfer: Part I—Measurements of Heated Jet Velocity and Temperature Distributions and Recovery Temperatures on Target Surface," *ASME JOURNAL OF HEAT TRANSFER*, Vol. 106, pp. 797–803.
- Hollworth, B. R., and Gero, L. R., 1985, "Entrainment Effects on Impingement Heat Transfer: Part II—Local Heat Transfer Measurements," *ASME JOURNAL OF HEAT TRANSFER*, Vol. 107, pp. 910–915.
- Striegl, S. A., and Diller, T. E., 1984, "The Effect of Entrainment Temperature on Jet Impingement Heat Transfer," *ASME JOURNAL OF HEAT TRANSFER*, Vol. 106, pp. 27–33.

## An Investigation of Ejection, Mixing, and Suction Mechanisms in an Open-Ended Horizontal Annulus

J. Eftefagh<sup>1</sup> and K. Vafai<sup>1,2</sup>

### Nomenclature

- $g$  = gravitational acceleration,  $m/s^2$
- $R^*$  = radial coordinate,  $m$
- $Ra$  = Rayleigh number =  $g\beta R_2^2 \Delta T / \alpha \nu$
- $t^*$  = time,  $s$
- $t$  = dimensionless time =  $t^* \alpha / R_2^2$
- $T$  = temperature,  $K$
- $\Delta T$  = temperature difference =  $T_1 - T_2$ ,  $K$
- $\alpha$  = thermal diffusivity,  $m^2/s$
- $\beta$  = thermal expansion coefficient of fluid,  $K^{-1}$
- $\theta$  = dimensionless temperature =  $(T - T_\infty) / (T_1 - T_\infty)$
- $\nu$  = kinematic viscosity,  $m^2/s$

### Subscripts

- 1 = inner cylinder
- 2 = outer cylinder

### 1 Introduction

The basic features of unsteady three-dimensional buoyancy-driven convection in an open-ended cavity are numerically investigated in this work and the effects of far field boundary conditions on the convective flow and heat transfer are ana-

<sup>1</sup>Department of Mechanical Engineering, The Ohio State University, Columbus, OH 43210.

<sup>2</sup>Professor; Mem. ASME.

Contributed by the Heat Transfer Division of the AMERICAN SOCIETY OF MECHANICAL ENGINEERS. Manuscript received by the Heat Transfer Division August 22, 1990; revision received February 7, 1991. Keywords: Natural Convection, Numerical Methods, Transient and Unsteady Heat Transfer.

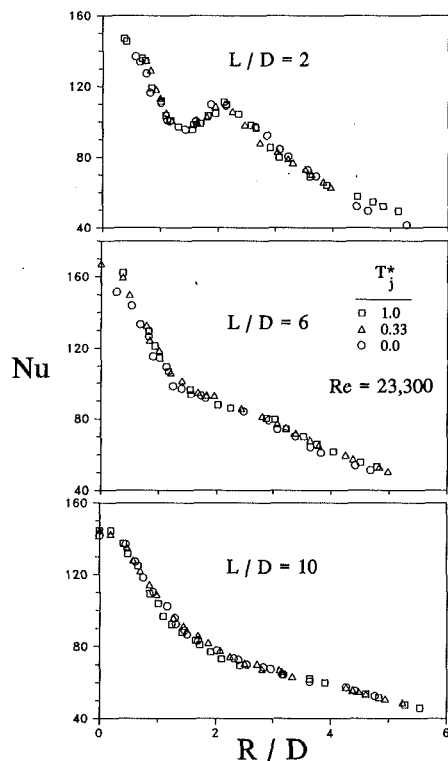


Fig. 3 Nusselt number distributions for  $L/D = 2, 6,$  and  $10$  for  $Re = 23,300$

### Discussion and Conclusions

The effectiveness measurements are compared in Fig. 2 to those of Goldstein et al. (1990). The effectiveness measurements in the present study are higher than those of Goldstein et al. (1990) in the stagnation region but agree well for larger  $R/D$  (greater than 3.5). There are several possible explanations for this. The jet in the present study is from the exit of a fully developed pipe flow whereas Goldstein et al. (1990) used an ASME nozzle. Conduction and radiation effects could also cause some small differences near the stagnation region. The effectiveness measurements in the present study have essentially no wall conduction. Goldstein et al. (1990) use a stainless steel plate and estimate that their conduction error is less than 0.5 percent. In the present study a radiation correction is used that raises the effectiveness by 2–6 percent with the smaller correction near the stagnation region and the larger correction at larger  $R/D$ .

The present results confirm those of Goldstein et al. (1990), which showed that the effectiveness is independent of the Reynolds number. The effectiveness is also shown to be independent of the jet temperature mismatch by both Hollworth and Wilson (1984) and by Goldstein et al. (1990). This is expected if the fluid (air) properties are not temperature dependent. The heat transfer results shown in Fig. 3 for the unheated jet ( $T_j^* = 0.0$ ) agree with those of Baughn and Shimizu (1989). The collapse of the Nusselt number distributions for  $T_j^* = 0.33$  and  $T_j^* = 1.0$  on the same curves confirms the results of Goldstein et al. (1990) (while extending the Reynolds number range and jet characteristics), which show that it is possible to use heat transfer data from unheated jets for the heated jet if the effectiveness is known and the local heat transfer coefficient is defined in terms of the adiabatic wall temperature. This does not mean that the entrainment effects are negligible nor that the data for unheated jets can be used directly for heated jets. It simply shows that the entrainment effects, in this case, can be described by an effectiveness. The technique employed in the present study to measure the effectiveness is considerably simpler than that required to measure the heat transfer.

### Acknowledgments

The authors wish to thank Professor Brian E. Launder, who originally encouraged our investigations of impinging jets and who has made valuable suggestions.

### References

- Baughn, J. W., Hoffman, M. A., and Makel, D. B., 1986, "Improvements in a New Technique for Measuring and Mapping Heat Transfer Coefficients," *Review of Scientific Instruments*, Vol. 57, pp. 650–654.
- Baughn, J. W., and Shimizu, S. S., 1989, "Heat Transfer Measurements From a Surface With Uniform Heat Flux and a Fully Developed Impinging Jet," *ASME JOURNAL OF HEAT TRANSFER*, Vol. 111, pp. 1096–1098.
- Bouchez, J. P., and Goldstein, R. J., 1975, "Impinging Cooling From a Circular Jet in a Cross Flow," *International Journal of Heat and Mass Transfer*, Vol. 18, pp. 719–730.
- Goldstein, R. J., Sobolik, K. A., and Seol, W. S., 1990, "Effect of Entrainment on the Heat Transfer to a Heated Circular Air Jet Impinging on a Flat Surface," *ASME JOURNAL OF HEAT TRANSFER*, Vol. 112, pp. 608–611.
- Hechanova, T. E., 1988, "An Experimental Study of Entrainment Effects on Heat Transfer With a Fully-Developed Impinging Jet," Masters Thesis, University of California, Davis.
- Hollworth, B. R., and Wilson, S. I., 1984, "Entrainment Effects on Impingement Heat Transfer: Part I—Measurements of Heated Jet Velocity and Temperature Distributions and Recovery Temperatures on Target Surface," *ASME JOURNAL OF HEAT TRANSFER*, Vol. 106, pp. 797–803.
- Hollworth, B. R., and Gero, L. R., 1985, "Entrainment Effects on Impingement Heat Transfer: Part II—Local Heat Transfer Measurements," *ASME JOURNAL OF HEAT TRANSFER*, Vol. 107, pp. 910–915.
- Striegl, S. A., and Diller, T. E., 1984, "The Effect of Entrainment Temperature on Jet Impingement Heat Transfer," *ASME JOURNAL OF HEAT TRANSFER*, Vol. 106, pp. 27–33.

### An Investigation of Ejection, Mixing, and Suction Mechanisms in an Open-Ended Horizontal Annulus

J. Eftefagh<sup>1</sup> and K. Vafai<sup>1,2</sup>

#### Nomenclature

- $g$  = gravitational acceleration,  $m/s^2$
- $R^*$  = radial coordinate,  $m$
- $Ra$  = Rayleigh number =  $g\beta R_2^2 \Delta T / \alpha \nu$
- $t^*$  = time,  $s$
- $t$  = dimensionless time =  $t^* \alpha / R_2^2$
- $T$  = temperature,  $K$
- $\Delta T$  = temperature difference =  $T_1 - T_2$ ,  $K$
- $\alpha$  = thermal diffusivity,  $m^2/s$
- $\beta$  = thermal expansion coefficient of fluid,  $K^{-1}$
- $\theta$  = dimensionless temperature =  $(T - T_\infty) / (T_1 - T_\infty)$
- $\nu$  = kinematic viscosity,  $m^2/s$

#### Subscripts

- 1 = inner cylinder
- 2 = outer cylinder

### 1 Introduction

The basic features of unsteady three-dimensional buoyancy-driven convection in an open-ended cavity are numerically investigated in this work and the effects of far field boundary conditions on the convective flow and heat transfer are ana-

<sup>1</sup>Department of Mechanical Engineering, The Ohio State University, Columbus, OH 43210.

<sup>2</sup>Professor; Mem. ASME.

Contributed by the Heat Transfer Division of the AMERICAN SOCIETY OF MECHANICAL ENGINEERS. Manuscript received by the Heat Transfer Division August 22, 1990; revision received February 7, 1991. Keywords: Natural Convection, Numerical Methods, Transient and Unsteady Heat Transfer.

lyzed. The strong coupling effects between the flow inside the annulus and that of the surroundings are shown to include three physical and fundamental transport mechanisms. These are identified as the "ejection," "mixing," and "suction" mechanisms. The crucial importance of the interaction among these different mechanisms in directly influencing the fluid mechanics and heat transfer inside open-ended geometries will be examined. The numerical results indicate that the amount of energy lost through the aperture plane increases considerably with an increase in the Rayleigh number. It is important to note that while a number of geometries can be effectively represented as their two-dimensional counterparts, such as the work of Caltagirone (1976), the open-ended annulus geometry cannot be approximated by any type of two-dimensional structure.

Three-dimensional buoyancy-driven flow in a cavity with the vertical walls heated to different temperatures has been analyzed by a number of investigators. With some modification of the boundary conditions, Mallinson and de Vahl Davis (1976) employed an approach similar to Aziz and Hellums (1967) to obtain steady-state solutions in a cavity heated from the side. Chan and Banerjee (1979) used the MAC technique for the numerical analysis of the same problem. More recently, Viskanta et al. (1986) employed Patankar's (1980) SIMPLER numerical scheme to make a detailed analysis of the three-dimensional natural convection of a liquid metal in a cavity. Their results revealed several interesting features such as the fact that for low Prandtl number fluids three-dimensional effects are important not only near the wall but also at the center of the cavity. Kuhn and Oosthuizen (1986) employed the vorticity-vector potential approach to study transient three-dimensional transient buoyancy-driven flow in a cavity with localized heating. They found that the three-dimensional flow tends to increase the local heat transfer rate close to the edge of the heating element, causing the mean heat transfer rate to be higher than the corresponding two-dimensional case.

While three-dimensional natural convection in rectangular enclosures has been investigated by few researchers, analysis of three-dimensional flow in horizontal annuli with finite length and impermeable axial end walls is significantly more limited in the literature. Furthermore, the analysis of buoyancy-driven flows in an open-ended annulus has not been done (Vafai and Etefagh, 1991). Although the geometry of an open-ended horizontal annulus has some superficial similarities to that of an annulus with impermeable axial boundaries, the physics of the transport process are very different.

## 2 Problem Formulation and Analysis

The geometric model, the coordinate systems, the governing equations, the proper set of boundary conditions and stability, verification and benchmarking of our numerical algorithm have been discussed in previous investigations (Vafai and Etefagh, 1991; Etefagh and Vafai, 1988; Etefagh et al., 1991) and will not be presented here. The local Nusselt number for this problem is defined as

$$Nu = \frac{q_{\text{actual}}}{q_{\text{cond}}} \quad (1)$$

where

$$q_{\text{cond}} = \frac{2\pi kL(T_1 - T_2)}{\ln(R)} \quad \text{and} \quad R = \frac{R_2^*}{R_1^*} \quad (2)$$

The mean Nusselt number is defined as the angular average of its local values at the midaxial plane. Therefore, the local Nusselt numbers at the inner and outer cylinders,  $Nu_1$  and  $Nu_2$ , are represented as

$$Nu_1 = -R \ln(R) \left. \frac{\partial \theta}{\partial r} \right|_{r=R} \quad (3)$$

$$Nu_2 = -\ln(R) \left. \frac{\partial \theta}{\partial r} \right|_{r=1} \quad (4)$$

## 3 Numerical Results and Discussion

Numerical simulations of buoyancy-induced flow and heat transfer in an open-ended horizontal concentric annulus were performed over a range of Rayleigh numbers. The effects of open boundary on the axial convection and its crucial influence on heat transfer characteristics within the annulus were explored. The numerical results were obtained for cases with inner cylinder surface temperature of  $\theta_1 = 1$  and using air as the working fluid. The outer cylinder surface temperature was taken to be that of the ambient temperature, i.e.,  $\theta_2 = 0$ . An annular radius ratio of  $R_2/R_1 = 2.5$  and length-to-radius ratio of  $L/R_2 = 4$  was considered. An annulus with length-to-outer-radius ratio of at least 4 was used accurately to detect the two-dimensional nature of the flow field in the core region. The radius ratio was chosen such that it would be in the same range as those used in the most pertinent available results. Due to the symmetric nature of the velocity and temperature fields, the results are presented in the  $0 \leq \phi \leq \pi$  domain. In all cases, the full transient behavior for the heat transfer characteristics inside the annulus were studied. The fluid was considered to be initially stagnant and at a uniform temperature everywhere. An extended computational domain was utilized in order to account properly for the open boundary effects. Proper extensions of the open-ended boundaries and mesh sizes as established by Vafai and Etefagh (1991) will be used in the present work.

The flow pattern at the aperture plane is illustrated in Fig. 1. The maximum value of velocity vectors on this plane is 12.7 and the vectors are normalized by a factor of 3 for graphic clarity. In this figure the maximum value of axial velocity is 18; its minimum is  $-12$ . Like the other figures in this paper, vectors with values less than 0.01 are not shown. As can be seen in Fig. 1, at the aperture plane due to the open boundary effects, the recirculating flow pattern completely breaks down and the hot fluid around the outer cylinder rises radially in the  $R-\phi$  plane. The presence of a strong axial component of the velocity field forces the hot fluid to be ejected out of the annulus, around the upper outer and lower inner cylinders.

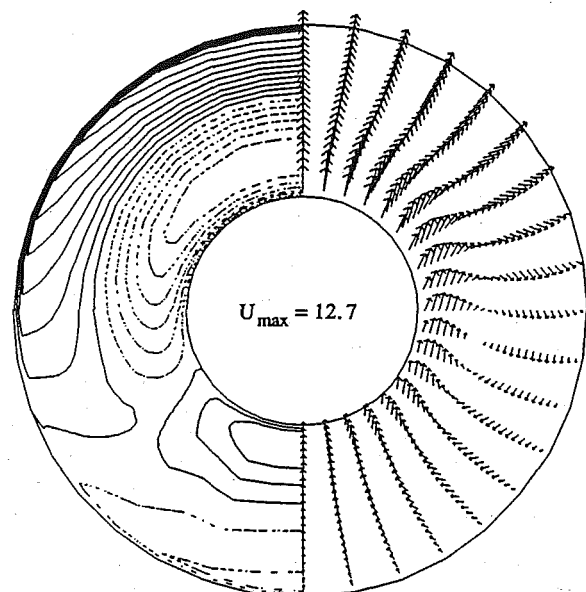


Fig. 1 Flow pattern for  $Ra = 4.3 \times 10^3$  at aperture plane

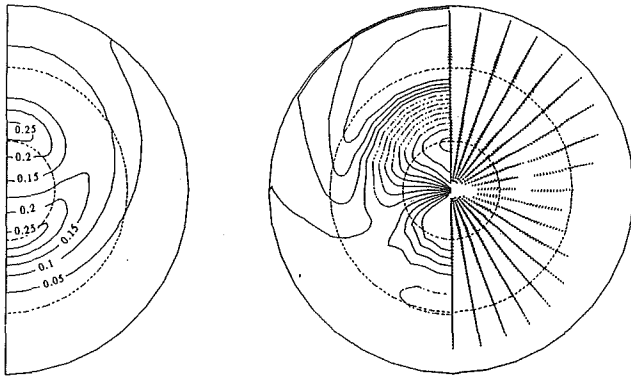


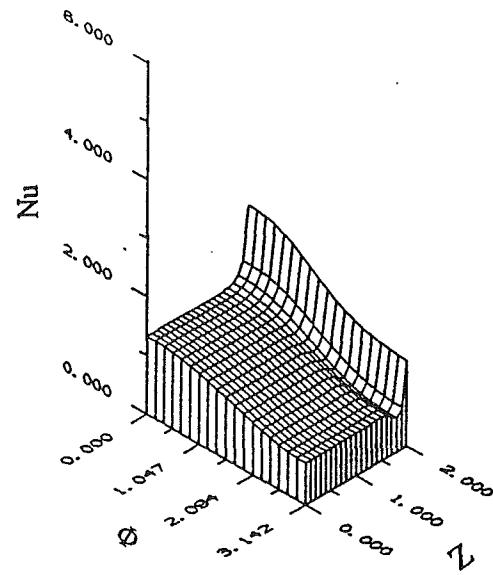
Fig. 2 Isotherms and flow pattern for  $Ra = 4.3 \times 10^3$  just outside of the aperture plane: (a) isotherms,  $\Delta\theta = 0.05$ ; (b) flow pattern,  $U_{\max} = 9.5$ , vectors normalized by 3, contours incremented by 2

The cold fluid from the outer region enters the annulus around the upper inner and lower outer cylinders to compensate for the loss of mass that is experienced as a result of this ejection mechanism. The maximum axial velocity of fluid exiting the annulus around the upper cylinder is substantially higher than that of the fluid entering around the lower cylinder. However, the cold fluid entering the annulus along the lower section of the outer cylinder has the same average axial speed as the hot fluid exiting the lower portion of the inner cylinder. Hence, the cold fluid entering in the lower angular section of the annulus occupies almost the same portion of the aperture plane as the hot exiting flow.

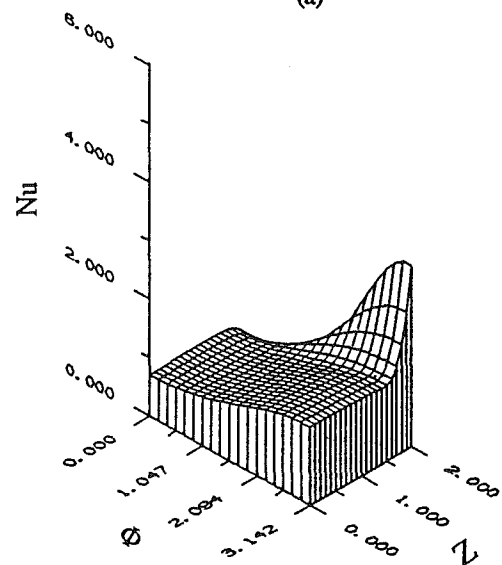
The interactions between the hot exiting fluid along the lower part of the inner cylinder and the cold fluid entering through the upper part of this cylinder are illustrated in Figs. 2(a) and 2(b) for  $Ra = 4.3 \times 10^3$  at an axial plane just outside of the aperture plane. The maximum value of velocity vectors in this figure is 9.5 and the vectors are normalized by a factor of 3 for graphic clarity. The maximum and minimum values of the axial velocity are 7.6 and  $-19$ , respectively. The dotted semicircles in the above figures are the projected view of the annulus boundaries. As a result of this interaction a radial temperature inversion is created in the vicinity of the inner cylinder. This is primarily due to the "mixing" mechanism of the hot exiting fluid from the lower part of the inner cylinder with the cold fluid, which has entered the annulus through the upper part of the inner cylinder. This "mixing" mechanism has a direct influence in rising the temperature of the surrounding fluid. This influence is clearly indicated by the values of the isotherms in Fig. 2.

The distribution of local Nusselt numbers for inner and outer cylinders for Rayleigh of  $4.3 \times 10^3$  are presented in Fig. 3. As can be seen, both Nusselt numbers remain unchanged along most of the axial length. However, about 1/8 of the annulus length from the opening, the Nusselt number starts to deviate from its value at the core region. Figure 3(a) illustrates that the values of the inner cylinder Nusselt number at the opening increase from its value at the core region by a factor of 2 at  $\phi = \pi$  and by a factor of 3 at  $\phi = 0$ . The inner cylinder Nusselt number experiences a minimum over a region ( $\pi/3 \leq \phi \leq \pi$ ) within which the open boundary effects have penetrated. On the other hand Fig. 3(b) shows that the outer cylinder Nusselt number at the aperture plane increases by factor of 2.4 at  $\phi = \pi$  and decreases by a factor of 1/3 at  $\phi = 0$  from its value at the midaxial plane. As seen in Fig. 3(b), the magnitude of local Nusselt number increases significantly around the aperture plane ( $\pi/3 \leq \phi \leq \pi$ ).

The distribution of local Nusselt numbers for inner and outer cylinders with  $Ra = 1 \times 10^4$  are presented in Figs. 4(a) and 4(b), respectively. As seen in Fig. 4(a), the value of midaxial plane



(a)



(b)

Fig. 3 The distribution of local Nusselt number for  $Ra = 4.3 \times 10^3$ : (a) inner cylinder; (b) outer cylinder

inner cylinder Nusselt number remains unchanged for about 1/4 of the annulus length. Beyond this length, the inner cylinder Nusselt number increases with an increase in the axial direction. Figure 4(a) illustrates that the inner cylinder Nusselt number at the opening increases from its value at the core region by factors of 1.2 and 3 at the  $\phi = \pi$  and  $\phi = 0$  planes, respectively. Also as seen in Fig. 4(a), due to the penetration depth of the open boundary effects inside the annulus, the distribution of inner cylinder Nusselt number experiences several maxima within the  $\pi/3 \leq \phi \leq \pi$  region. Figure 4(b) shows that the outer cylinder Nusselt number at the aperture planes increases by a factor of 5 at the  $\phi = \pi$  plane and decreases by 1/2 at the  $\phi = 0$  plane. The distribution of outer cylinder Nusselt number also experiences several maxima within the  $\pi/4 \leq \phi \leq \pi$  region within which the open boundary effects penetrate.

Often, following the onset of the fluid motion, the flow field and heat transfer characteristics are quite different from those at steady state. This is an important and often crucial consideration in these circumstances where rapid cooling or heat

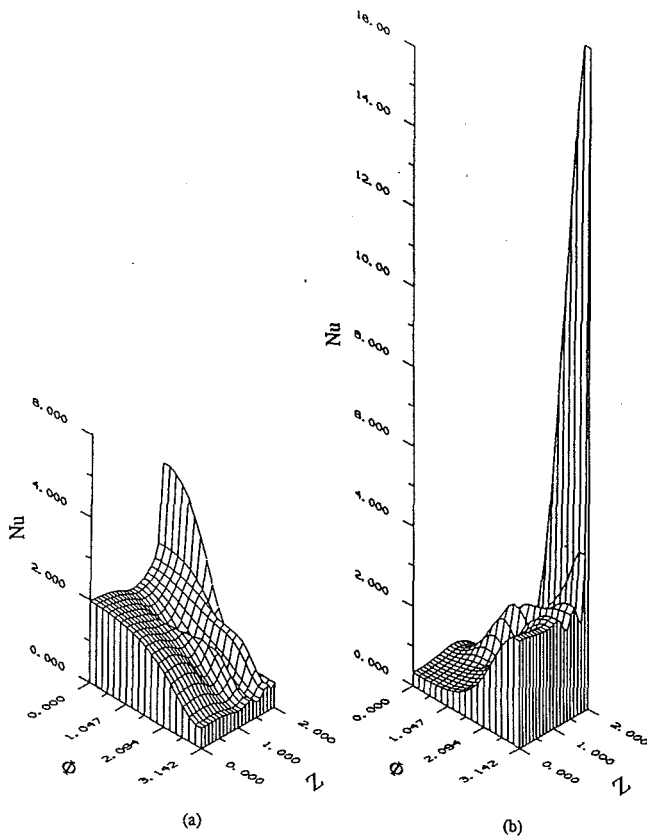


Fig. 4 The distribution of local Nusselt number for  $Ra = 1 \times 10^4$ : (a) inner cylinder; (b) outer cylinder

removal is of major concern. In the early stages of flow development ( $0 \leq t \leq 20\Delta t$ ), our analysis has shown that the dominant heat transfer mechanism throughout the open-ended annulus is by conduction. During this period, the isotherms are spaced closer together at the aperture plane than the corresponding ones at the midaxial plane. This is primarily due to the cold fluid entering from the surroundings (around the aperture plane), which increases the heat transfer from the inner cylinder. For  $30\Delta t \leq t \leq 40\Delta t$ , the magnitude of velocity vectors on the  $R-\phi$  plane increases due to larger energy transfer from the inner cylinder. The same trend continues in time up to a point when the convection through the aperture plane becomes dominant, after which the convective heat transfer from the upper part of the outer cylinder increases considerably. For later times, the convection through the aperture plane results in an enhanced convective heat transfer from the upper part of the outer cylinder as well as the lower part of the inner cylinder. This leads to the formation of a buoyant plume at the aperture plane.

Figures 5(a) and 5(b) illustrate the temperature distribution and flow pattern at steady state for  $Ra = 1 \times 10^4$  just outside the aperture plane. The maximum value of velocity vectors on this plane is 30.23 and the maximum and minimum values of the axial velocity are 36 and  $-23$ , respectively. The isotherms in Fig. 5(a) are incremented by 0.05 for more accurate presentation of temperature distribution on this plane and the axial velocity contours are incremented by 5 to eliminate the clustering effects. The maximum dimensionless temperature in Fig. 5(a) is 0.3, which indicates a greater energy loss to the environment than the lower Rayleigh number case (there the maximum dimensionless temperature was 0.25). Figure 5(a) also shows radial temperature inversion in the upper angular section of the outside domain. This phenomenon along with the shape of isotherms in the above figure is indicative of some convective recirculating zone in that region. Comparison of Fig. 5(b) with Fig. 2(b) shows that, as  $Ra$  increases, the speed of the outgoing

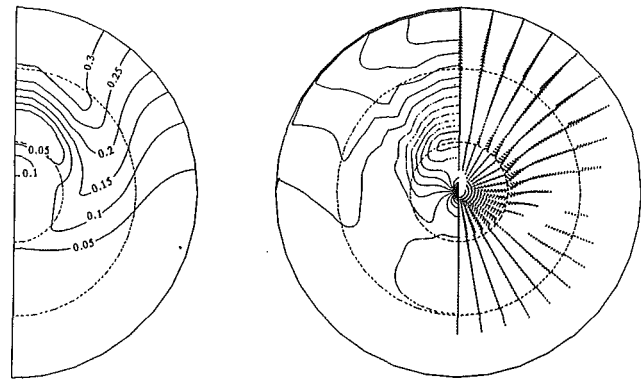


Fig. 5 Isotherms and flow pattern  $Ra = 1 \times 10^4$  at axial position one node away from the aperture plane: (a) isotherms,  $\Delta\theta = 0.05$ ; (b) flow pattern,  $U_{\max} = 30.2$ , vectors normalized by 9, contours incremented by 5

fluid increases, resulting in a thinner buoyant plume within the outside domain. It should be noted that for this type of geometry a multicellular flow pattern such as the kind described by Caltagirone et al. (1980) does not occur.

#### 4 Conclusions

A study of the resulting flow and temperature fields inside an open-ended annulus and the corresponding interactions with the open boundary was carried out. The results illustrate the existence of a complex three-dimensional flow field at the aperture plane. The strong coupling effects between the flow fields inside and outside of the annulus are shown to include three physical and fundamental transport mechanisms. These are identified as the "ejection," "mixing," and "suction" mechanisms. An increase in the Rayleigh number is shown to cause a sharp augmentation of heat transfer in the vicinity of the aperture plane due to significantly larger energy losses through the aperture plane.

#### Acknowledgments

A grant from Ohio Supercomputer Center is acknowledged and appreciated.

#### References

- Aziz, A., and Hellums, J. D., 1967, "Numerical Solution of the Three-Dimensional Equations of Motion for Laminar Natural Convection," *Physics of Fluids*, Vol. 10, pp. 314-324.
- Caltagirone, J. P., 1976, "Thermoconvective Instabilities in a Porous Medium Bounded by Two Concentric Horizontal Cylinders," *Journal of Fluid Mechanics*, Vol. 76, pp. 337-362.
- Caltagirone, J. P., Combarous, M., and Mojtabi, A., 1980, "Natural Convection Between Two Concentric Spheres: Transition Toward a Multicellular Flow," *Numerical Heat Transfer*, Vol. 3, pp. 107-114.
- Chan, A. M. C., and Banerjee, M., 1979, "Three-Dimensional Numerical Analysis of Transient Natural Convection in Rectangular Enclosures," *ASME JOURNAL OF HEAT TRANSFER*, Vol. 101, pp. 114-119.
- Ettefagh, J., and Vafai, K., 1988, "Natural Convection in Open-Ended Cavities With a Porous Obstructing Medium," *International Journal of Heat and Mass Transfer*, Vol. 31, pp. 673-693.
- Ettefagh, J., Vafai, K., and Kim, S. J., 1991, "Non-Darcian Effects in Open-Ended Cavities Filled With a Porous Medium," *ASME JOURNAL OF HEAT TRANSFER*, Vol. 113, pp. 747-756.
- Kuhn, D., and Oosthuizen, P. H., 1986, "Three-Dimensional Transient Natural Convective Flow in a Rectangular Enclosure With Localized Heating," *Natural Convection in Enclosures*, ASME HTD-Vol. 63, pp. 55-62.
- Mallinson, G. D., and DeVahl Davis, G., 1976, "Three-Dimensional Natural Convection in a Box: A Numerical Study," *Journal of Fluid Mechanics*, Vol. 83, pp. 1-31.
- Patankar, S. V., 1980, *Numerical Heat Transfer and Fluid Flow*, Hemisphere, New York.
- Vafai, K., and Ettefagh, J., 1991, "Axial Transport Effects on Natural Convection Inside of an Open-Ended Annulus," *ASME JOURNAL OF HEAT TRANSFER*, Vol. 113, pp. 627-634.
- Viskanta, R., Kim, D. M., and Gan, C., 1986, "Three-Dimensional Natural Convection Heat Transfer of a Liquid Metal in a Cavity," *International Journal of Heat and Mass Transfer*, Vol. 29, pp. 475-485.

J. G. Georgiadis

## Nomenclature

- $a$  = thermal diffusivity,  $m^2s^{-1}$   
 BO = article by Bertin and Ozoe (1986)  
 CCO = article by Chao, Churchill, and Ozoe (1982)  
 $g$  = gravitational acceleration  
 $L$  = thickness of horizontal fluid layer, m  
 Nu = Nusselt number, net heat transfer rate through layer  
 Pr = Prandtl number =  $\nu/a$   
 $Ra$  = Rayleigh number =  $g\beta\Delta TL^3/(\nu a)$   
 $Ra_l$  = Rayleigh number on the marginal curve  
 $Ra_c$  = critical Rayleigh number according to Rayleigh's model, Eq. (1)  
 $Ra'_c$  = critical Rayleigh number according to Bertin and Ozoe (1986)  
 $Ra_l$  = second critical Rayleigh number for onset of oscillatory convection, Eq. (2)  
 $\alpha$  = wavenumber =  $2\pi/\lambda$   
 $\alpha_c$  = critical wavenumber for the onset of convection, Eq. (1)  
 $\beta$  = volumetric thermal expansion coefficient,  $K^{-1}$   
 $\Delta T$  = temperature difference across fluid layer, K  
 $\lambda$  = wavelength of basic horizontal convection rolls  
 $\nu$  = kinematic viscosity,  $m^2s^{-1}$

## 1 Introduction

The phrase that provides the title for the present article refers to the criterion of spontaneous initiation of motion in an infinite horizontal layer of fluid subject to a destabilizing temperature gradient. Using linear stability theory, Lord Rayleigh (1916) demonstrated that the only parameter that determines the stability of the conductive state is the nondimensional Rayleigh number,  $Ra$ . It would be safe to assume that the question posed in the title can be answered with a definite "yes" almost a century after the phenomenon was reported. However, Chao et al. (1982) challenged the result of linear stability analysis, arguing that the nonlinear inertial terms cannot be neglected from the momentum equations for small values of the Prandtl number,  $Pr < 0.1$ . They developed a correlation for the critical Rayleigh number as a function of  $Pr$ . Seeking to reinforce the previous result, Bertin and Ozoe (1986) determined numerically a "critical"  $Ra$  number by extrapolating from finite-amplitude steady supercritical solutions. This "critical"  $Ra$  was shown to increase significantly above the theoretical (given by linear stability analysis) as  $Pr$  decreases for  $Pr < 0.1$ . It is the primary mission of the present article to show that the premises and method in the articles of Chao et al. (1982) and Bertin and Ozoe (1986) [in the following, referred to as CCO and BO, respectively] are flawed because indiscriminate extrapolation is not permissible for low Prandtl numbers and that there is no corroborative experimental evidence for  $Pr$  number influence on the onset of convection. The question is posed in order to accentuate the lack of response in the literature following the publication of CCO and BO.

## 2 The Rayleigh-Bénard Problem

At the turn of this century, Bénard (1900) published his

<sup>1</sup>Department of Mechanical Engineering and Materials Science, Duke University, Durham, NC 27706.

Contributed by the Heat Transfer Division of THE AMERICAN SOCIETY OF MECHANICAL ENGINEERS. Manuscript received by the Heat Transfer Division September 17, 1990; revision received March 23, 1991. Keywords: Flow Instability, Natural Convection, Numerical Methods.

careful observations on the onset of convection in a horizontal layer of fluid heated from below. Seeking to derive a mathematical model of the Bénard problem, Lord Rayleigh (1916) linearized the governing (Navier-Stokes) equations for small perturbations around the stagnant conductive state. Despite the fact that he ignored some important physics (i.e., the effect of surface tension), his analysis helped establish a bifurcation problem that is currently being used in the study of dynamics of driven dissipative systems. The reader is referred to the excellent monograph by Joseph (1976) for a comprehensive treatment of bifurcation theory of the Rayleigh-Bénard problem and its variations.

The first bifurcation (onset of convection) occurs at the linear stability limit  $Ra_c = \min\{Ra_l(\alpha)\}$  and is supercritical; the inequality  $Ra(\alpha) < Ra_l(\alpha)$  is the necessary and sufficient condition for stability of the conductive state. The critical values are *independent* of Prandtl number and are given approximately by

$$Ra_c = 1707.762, \quad \alpha_c = 3.116 \quad (1)$$

Being unstable to infinitesimal disturbances, the conductive state is unstable to *any* finite-amplitude disturbance for  $Ra(\alpha) > Ra_l(\alpha)$ .

Beyond the first bifurcation (1), the role of linear theory is to assess the stability characteristics of the (finite-amplitude) bifurcating solutions of the governing equations. The stability domain of two-dimensional rolls has been delineated in the pioneering work of Busse and co-workers and was reviewed by Busse (1978). Figure 13 of the above paper gives the stability "balloon." The so-called "Busse balloon" delineates the region in the  $Ra$ - $Pr$ - $\alpha$  space in which two-dimensional rolls are stable to infinitesimal disturbances. This balloon shrinks dramatically as  $Pr$  decreases but the critical  $Ra_c$  remains constant. In the absence of lateral boundaries, the two-dimensional convection problem is degenerate since rolls within a continuous wavenumber interval (defined by the "Busse balloon") are stable.

We will concentrate on the theoretical results for the low  $Pr$  domain involved in the controversy. Practically, this involves the range between  $Pr = 0.71$  (air) and  $Pr = 0.025$  (mercury), which was analyzed by Clever and Busse (1974). For  $Pr = 0.71$ , the stability domain is bounded from above by the oscillatory and the skewed varicose instability boundaries. The lower boundary is given by the Eckhaus curve, which corresponds to a two-dimensional side-band instability analogous to the Benjamin-Feir instability of a Stokes water wave: The rolls become unstable to disturbances of the form of rolls parallel to themselves. This curve converges with the marginal stability curve at  $Ra = Ra_c$  and  $\alpha = \alpha_c$ . For  $Pr = 0.025$ , the stability domain for two-dimensional rolls is bounded from above by only the oscillatory instability curve  $Ra_l(\alpha)$ , as shown in Fig. 1. This oscillatory instability curve corresponds to a Hopf bifurcation, which amplifies the bending of the rolls and leads to a time-dependent three-dimensional wavepattern.  $Ra_l(\alpha)$  depends strongly on  $\alpha$  and decreases quadratically with  $Pr$ . From the plot of the stability diagrams of Clever and Busse we can estimate the second bifurcation point for  $\alpha = \alpha_c$ ,

$$Ra_l \approx 13,000 \quad (Pr = 0.71); \quad Ra_l \approx 1940 \quad (Pr = 0.025) \quad (2)$$

We turn our attention to the estimation of the net heat transfer flux through the layer (as characterized by the Nusselt number,  $Nu$ ). In addition to a weakly nonlinear analysis, Malkus and Veronis (1958) introduced the "power integral" method (which provides an *estimate* of the  $Nu$  over a wide range of  $Ra$ ) and selected the wavenumber  $\alpha$  in accordance to certain ad-hoc criteria. Schlüter et al. (1965) performed the analysis for arbitrary  $\alpha$  and predicted that  $Nu$  is proportional to  $Ra$  near the onset of convection  $Ra \approx Ra_c$ . The asymptotic formula for  $\alpha = \alpha_c$  is

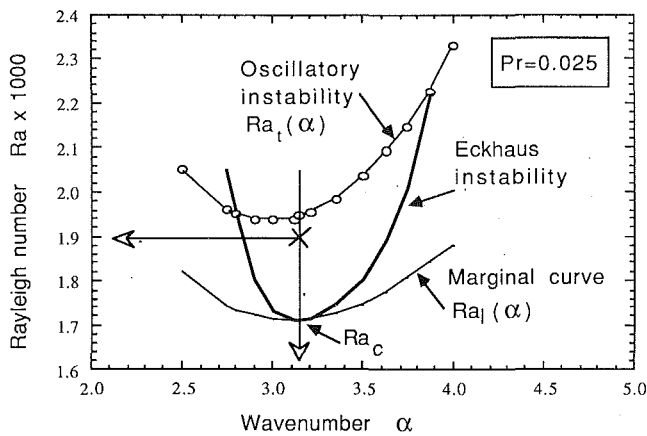


Fig. 1 Cross section of the "Busse balloon" for  $Pr=0.025$ , adapted from the article of Clever and Busse (1974). Within the closed region, two-dimensional rolls are stable to infinitesimal disturbances. The vertical arrow represents the extrapolation procedure in BO and its intersection with the horizontal arrow marks the predicted "critical"  $Ra'_c$ .

$Nu \rightarrow 1$

$$+ \frac{Ra - Ra_c}{Ra_c} (0.69942 - 0.00472 Pr^{-1} + 0.00832 Pr^{-2})^{-1} \quad (3)$$

For  $Pr \ll 1$ , the above formula implies that  $Nu$  decreases proportionally to  $Pr^2$  at a given  $Ra$ . The asymptotic analysis is based on the assumption that  $Pr$  is of order 1. As Malkus and Veronis (1958) hypothesized (footnote on page 244) and Clever and Busse demonstrated [comparison of Eq. (3) with finite-amplitude results in Fig. 3 of Clever and Busse (1974)], the radius of convergence of the asymptotic expansion decreases rapidly with decreasing  $Pr$ , i.e., the validity of Eq. (3) deteriorates for small  $Pr$ . For example, the finite amplitude results for  $Pr < 0.025$  agree with the asymptotic formula (3) only for  $Ra < Ra_c + 30$ . Furthermore, the numerical results of Clever and Busse (1981) show that the  $Nu$ - $Ra$  curve becomes less sensitive to  $Pr$  as  $Ra$  approaches 5000.

### 3 The Bertin-Ozoe (1986) Solution

We intend to show that both the theoretical basis and methodology employed in BO to study the critical  $Ra$  for the onset of convection are flawed. The theme of this section is simple: After outlining the main points, we examine their validity one by one. The text in italics implies direct quotation from the designated references.

- (i) From the Introduction of BO: "...no definite agreement on the stable width of a roll cell. Linear stability analysis at  $Pr \rightarrow \infty$  suggests the critical wavenumber  $\alpha = 3.117...$ " Also, "In accordance with experimental observations the motion of fluid, just above the critical state, is postulated to be a series of identical square roll cells with parallel axes." Finally, Bertin and Ozoe (1986) support their predictions by claiming that "Verhoeven (1969) determined a value of  $1808 \pm 16$  for the critical Rayleigh number of mercury ( $Pr = 0.025$ ) in a cylinder."

The above statements are contradicted by all the available theoretical and experimental evidence as reviewed in the preceding and current sections. In fact, the conclusion of Verhoeven's (1969) experimental study was that "The first oscillatory mode appeared at a Rayleigh number 10% higher than the critical ( $Ra_c$ )". This statement agrees with modern experimental findings (Croquette, 1989) but was misinterpreted in BO as referring to the onset of convection (first critical  $Ra$ ). Furthermore, Verhoeven (1969) admits that his "...study has not confirmed or denied the linear stability analysis..." and adds that "...steady velocities of reasonably small size could well have been present in the cell prior to the appearance of

oscillations, and still not have been detected by measurements...limited to accuracies of  $0.05^\circ C$ ."

- (ii) The steady-state form of the governing equations is solved for fixed wavenumber  $\alpha = \pi$  and two-dimensional roll solutions are sought.

Since this is the method employed in BO to determine the critical  $Ra$ , the authors have tacitly assumed that the first bifurcation point can be approached by fixing the wavenumber and solving the governing equations for stationary solutions. If we take into account the dynamics of the phenomenon (by considering the *unsteady* governing equations), every wavenumber  $\alpha \neq \alpha_c$  is not stable at  $Ra > Ra_c$  for convection in infinite layers. For  $Pr = 0.025$  and  $\alpha = \pi$ , the two-dimensional rolls are destabilized by the Eckhaus instability at slightly supercritical  $Ra$ , as shown in Fig. 1. By seeking steady-state solutions, BO naturally ignore the oscillatory instability that prevails at low  $Pr$ . Furthermore, experiments (Koschmieder and Pallas, 1974; Croquette et al., 1986) and theory (Buell and Catton, 1986) have shown that the *selected* wavenumber varies significantly with  $Ra$  above the onset. In short, steady-state calculations in a fixed roll configuration fail to represent the physics of the bifurcation phenomena involved in the Rayleigh-Bénard problem. Given the strong dependence of  $Nu$  on  $\alpha$  [see Fig. 10 of Clever and Busse (1981)], this disqualifies an extrapolation procedure in BO (which is solely based on the  $Nu$  versus  $Ra$  curve) for determining the onset of convection.

- (iii) A second-order finite-element method is employed and the accuracy of the solution is improved by extrapolating in  $Nu$  to "zero grid size."

The steady-state two-dimensional computation has been performed earlier by Clever and Busse (1974, 1981). They used a standard Galerkin scheme and showed that the  $Nu$  converged in an asymptotic fashion as the order of the spectral expansion was increased [Fig. 1 of Clever and Busse (1981)]. The results of grid refinement of BO, as depicted in their Fig. 6 for  $Pr = 0.01$ , do not exhibit the correct asymptotic convergence that the formal order of their method implies. Extrapolation to "zero grid size" is not permissible unless the asymptotic regime is reached. The computations in BO (their Table 3) consistently underpredict the  $Nu$  compared to the calculations of Clever and Busse (1981) (their Table 1 and Fig. 2). To emphasize the consequences of this discrepancy, we remark that for  $\alpha = \alpha_c$ ,  $Pr = 0.01$ , and  $Ra = 2095$ , Clever and Busse (1981) predict  $Nu \approx 1.035$  with less than 1 percent error (as estimated from their Table 1) while the extrapolation scheme of BO gives  $Nu = 1$  (since  $Ra'_c = 2095$ ).

- (iv) The "critical"  $Ra'_c$  is determined by extrapolating the  $Nu$  versus  $Ra$  curve according to the following "correlating equation":

$$Nu = 1 + \text{funct}(Pr) \times \left(1 - \frac{Ra_c'}{Ra}\right) \quad (4)$$

The power integral of Malkus and Veronis (1958) was derived in accordance with the linear stability analysis and consequently complements Eq. (1). The power integral method has served its purpose well; it has been shown to predict heat transport within 10 percent error, cf. Catton (1966). Expression (4), although similar to the power integral result, is not consistent with the asymptotic relation (3) in terms of its dependence on the critical  $Ra$  and it does not account for the complicated dependence of the  $Nu$  versus  $Ra$  curve on the  $Pr$ , as predicted by Clever and Busse (1981). Lage et al. (1991) extended the numerical study of the convection onset to Prandtl numbers as low as  $10^{-4}$ , i.e., to  $Pr$  numbers an order of magnitude lower than those considered in BO. Their results agree with the linear stability limits (1) and the asymptotic formula (3), and essentially support the arguments presented in this article.



(v) The “critical”  $Ra_c'$  is found to increase with decreasing Pr. Some representative values obtained from steady-state solutions are given below:

$$Ra_c' = 1894 \quad Pr = 0.025, \text{ extrapolation } 2100 \leq Ra \leq 2300 \quad (5)$$

$$Ra_c' = 2095 \quad Pr = 0.01, \text{ extrapolation } 2300 \leq Ra \leq 4000$$

The most serious criticism of the methods and results in BO lies with the fact that the Nu extrapolation involves areas of the Busse balloon where two-dimensional rolls are unstable. As Fig. 1 shows for the case of  $Pr = 0.025$ , the range  $2100 < Ra < 2300$  belongs to the oscillatory regime. BO predict  $Ra_c' = 2095$  for  $Pr = 0.01$ , which is clearly inside the oscillatory regime [cf. Clever and Busse (1974)] since the balloon shrinks further. Clever and Busse (1990) demonstrated numerically that  $Ra_c' = 1854$  in the limit  $Pr \rightarrow 0$ . Concerning the significance of these steady-state computations for low Pr fluids, it is important to quote Clever and Busse (1974): “...calculations of the heat transport for two-dimensional convection do not correspond to physically realizable solutions beyond the second critical Rayleigh number  $Ra_c'$  of instability, which also decreases significantly as Pr decreases...”. In addition to being unsteady, physically realizable (stable) solutions for  $Ra > Ra_c'$  are three dimensional.

(vi) No converged solution was obtained in BO for  $Pr \leq 0.001$ .

For  $Pr = 0.001$  and  $Ra = 2800$ , the solution oscillated with apparently fixed amplitude.

This oscillatory behavior, which was not reported in Clever and Busse’s (1981) computation, is indicative of the changing spectral properties of the evolution equations for the Rayleigh–Bénard problem at  $Ra > Ra_c'$ . The solution of the steady-state equations via an iterative process mimics—in a certain sense—the solution of a linearized version of the unsteady governing equations with random initial conditions. Following Goldhirsch et al. (1987), we can show that the dominant part of the solution of this initial value problem is a linear combination of the eigenfunctions of that linearized version of the evolution equations. The spectrum of the corresponding eigenvalue problem contains all the information necessary to determine the stability of a base state to infinitesimal disturbances. Given that two-dimensional rolls lose stability to oscillatory disturbances (Hopf bifurcation) at  $Ra = Ra_c'$ , the oscillatory behavior of the BO solution signals that the steady low-Pr solutions are unstable.

#### 4 Conclusion

During the ninety-odd years since Bénard (1900) reported the instability phenomenon in a horizontal liquid layer heated from below, an immense literature and exegesis has spread out round the so-called canonical Rayleigh–Bénard problem. The theoretical model put forward by Lord Rayleigh (1916) to explain the onset of convection is consistent with both theory and experiment. In contrast, there is no theoretical basis or experimental evidence supporting the contention of the authors of CCO and BO that the critical Rayleigh number for the onset of convection depends on Prandtl number. The reported increase of the critical value, as Pr decreases below 0.1, is caused by the adoption of an inaccurate extrapolation scheme and the suppression of the dynamics (i.e., time-dependence) of the governing equations. A simple juxtaposition of the experimental evidence by Verhoeven (1969) (misinterpreted in BO) with modern findings confirms our point. For  $Pr < 0.01$ , the “critical” (according to BO) Rayleigh numbers for the onset of convection correspond to domains where the oscillatory mode of convection dominates and they are, consequently, meaningless. The present paper serves primarily as an organized rebuttal to the conjectures expressed in BO. Furthermore, this work serves to demonstrate that, although the route from physics to heat transfer applications is smooth, the reverse, i.e., relying exclusively on heat transfer coefficients (as ex-

pressed by the Nu number) to deduce the physics of natural convection, can be treacherous.

#### Acknowledgments

The author wishes to thank Professors Ivan Catton (University of California at Los Angeles) and Fritz Busse (Bayreuth University) for their input. This work is performed under the aegis of the National Science Foundation (grants CTS-8909119 and CTS-9006189) and the U.S. Department of Energy (grant DE-FG05-90ER14141).

#### References

- Bénard, H., 1900, “Les tourbillons cellulaires dans une nappe liquide,” *Revue Gén. Sci. Pur. Appl.*, Vol. 11, pp. 1261–1271, 1309–1328.
- Bertin, H., and Ozoe, H., 1986, “Numerical Study of Two-Dimensional Natural Convection in a Horizontal Fluid Layer Heated From Below, by Finite-Element Method: Influence of Prandtl Number,” *Int. J. Heat Mass Transfer*, Vol. 29, pp. 439–449.
- Buell, J. C., and Catton, I., 1986, “Wavenumber Selection in Large-Amplitude Axisymmetric Convection,” *Phys. Fluids*, Vol. 29, pp. 23–30.
- Busse, F. H., 1978, “Non-linear Properties of Thermal Convection,” *Rep. Prog. Phys.*, Vol. 41, pp. 1929–1967.
- Catton, I., 1966, “Natural Convection in Horizontal Liquid Layers,” *Phys. Fluids*, Vol. 9, pp. 2521–2522.
- Chao, P., Churchill, S. W., and Ozoe, H., 1982, “The Dependence of the Critical Rayleigh Number on the Prandtl Number,” in: *Convection Transport and Instability Phenomena*, J. Zierep and H. Oertel, Jr., eds., G. Braun, Karlsruhe, Germany, pp. 55–70.
- Clever, R. M., and Busse, F. H., 1974, “Transition to Time-Dependent Convection,” *J. Fluid Mech.*, Vol. 65, pp. 625–645.
- Clever, R. M., and Busse, F. H., 1981, “Low-Prandtl-Number Convection in a Layer Heated From Below,” *J. Fluid Mech.*, Vol. 102, pp. 61–74.
- Clever, R. M., and Busse, F. H., 1990, “Convection at Very Low Prandtl Numbers,” *Phys. Fluids A*, Vol. 2, pp. 334–339.
- Croquette, V., Le Gal, P., Pocheau, A., and Guglielmetti, R., 1986, “Large-Scale Flow Characterization in a Rayleigh–Bénard Convective Pattern,” *Europhysics Letters*, Vol. 1, pp. 393–399.
- Croquette, V., 1989, “Convective Pattern Dynamics at Low Prandtl Number: Part II,” *Contemporary Physics*, Vol. 30, pp. 153–171.
- Goldhirsch, I., Orszag, S. A., and Maulik, B. K., 1987, “An Efficient Method for Computing Leading Eigenvalues and Eigenvectors of Large Asymmetric Matrices,” *J. Sci. Components*, Vol. 2, pp. 33–58.
- Joseph, D. D., 1976, *Stability of Fluid Motions II*, Springer, Berlin, § 61.
- Koschmieder, E. L., and Pallas, S. G., 1974, “Heat Transfer Through a Shallow, Horizontal Convecting Fluid Layer,” *Int. J. Heat Mass Transfer*, Vol. 17, pp. 991–1002.
- Lage, J. L., Bejan, A., and Georgiadis, J. G., 1991, “On the Effect of the Prandtl Number on the Onset of Bénard Convection,” *Int. J. Heat Fluid Flow*, Vol. 12, pp. 184–188.
- Malkus, W. V. R., and Veronis, G., 1958, “Finite Amplitude Cellular Convection,” *J. Fluid Mech.*, Vol. 4, pp. 225–260.
- Rayleigh, Lord, 1916, “On Convection Currents in a Horizontal Layer of Fluid, When the Higher Temperature Is on the Under Side,” *Phil. Mag.*, Vol. 32, pp. 529–546.
- Schlüter, A., Lortz, D., and Busse, F. H., 1965, “On the Stability of Steady Finite Amplitude Convection,” *J. Fluid Mech.*, Vol. 23, pp. 129–144.
- Verhoeven, J. D., 1969, “Experimental Study of Thermal Convection in a Vertical Cylinder of Mercury Heated From Below,” *Phys. Fluids*, Vol. 12, pp. 1733–1740.

#### Natural Convection From a Horizontal Heated Copper-Graphite Composite Surface

Wen-Jei Yang,<sup>1</sup> H. Takizawa,<sup>1</sup> and D. L. Vrbale<sup>2</sup>

#### 1 Introduction

One important objective of heat transfer research is to de-

<sup>1</sup>Department of Mechanical Engineering and Applied Mechanics, The University of Michigan, Ann Arbor, MI 48109.

<sup>2</sup>Division of Thermal & E. M. Components Technology, Sparta, Inc., San Diego, CA 92121.

Contributed by the Heat Transfer Division of THE AMERICAN SOCIETY OF MECHANICAL ENGINEERS. Manuscript received by the Heat Transfer Division July 16, 1990; revision received April 16, 1991. Keywords: Augmentation and Enhancement, Natural Convection.

(v) The “critical”  $Ra_c'$  is found to increase with decreasing Pr. Some representative values obtained from steady-state solutions are given below:

$$Ra_c' = 1894 \quad Pr = 0.025, \text{ extrapolation } 2100 \leq Ra \leq 2300 \quad (5)$$

$$Ra_c' = 2095 \quad Pr = 0.01, \text{ extrapolation } 2300 \leq Ra \leq 4000$$

The most serious criticism of the methods and results in BO lies with the fact that the Nu extrapolation involves areas of the Busse balloon where two-dimensional rolls are unstable. As Fig. 1 shows for the case of  $Pr = 0.025$ , the range  $2100 < Ra < 2300$  belongs to the oscillatory regime. BO predict  $Ra_c' = 2095$  for  $Pr = 0.01$ , which is clearly inside the oscillatory regime [cf. Clever and Busse (1974)] since the balloon shrinks further. Clever and Busse (1990) demonstrated numerically that  $Ra_c' = 1854$  in the limit  $Pr \rightarrow 0$ . Concerning the significance of these steady-state computations for low Pr fluids, it is important to quote Clever and Busse (1974): “...calculations of the heat transport for two-dimensional convection do not correspond to physically realizable solutions beyond the second critical Rayleigh number  $Ra_c'$  of instability, which also decreases significantly as Pr decreases...”. In addition to being unsteady, physically realizable (stable) solutions for  $Ra > Ra_c'$  are three dimensional.

(vi) No converged solution was obtained in BO for  $Pr \leq 0.001$ .

For  $Pr = 0.001$  and  $Ra = 2800$ , the solution oscillated with apparently fixed amplitude.

This oscillatory behavior, which was not reported in Clever and Busse’s (1981) computation, is indicative of the changing spectral properties of the evolution equations for the Rayleigh–Bénard problem at  $Ra > Ra_c'$ . The solution of the steady-state equations via an iterative process mimics—in a certain sense—the solution of a linearized version of the unsteady governing equations with random initial conditions. Following Goldhirsch et al. (1987), we can show that the dominant part of the solution of this initial value problem is a linear combination of the eigenfunctions of that linearized version of the evolution equations. The spectrum of the corresponding eigenvalue problem contains all the information necessary to determine the stability of a base state to infinitesimal disturbances. Given that two-dimensional rolls lose stability to oscillatory disturbances (Hopf bifurcation) at  $Ra = Ra_c'$ , the oscillatory behavior of the BO solution signals that the steady low-Pr solutions are unstable.

#### 4 Conclusion

During the ninety-odd years since Bénard (1900) reported the instability phenomenon in a horizontal liquid layer heated from below, an immense literature and exegesis has spread out round the so-called canonical Rayleigh–Bénard problem. The theoretical model put forward by Lord Rayleigh (1916) to explain the onset of convection is consistent with both theory and experiment. In contrast, there is no theoretical basis or experimental evidence supporting the contention of the authors of CCO and BO that the critical Rayleigh number for the onset of convection depends on Prandtl number. The reported increase of the critical value, as Pr decreases below 0.1, is caused by the adoption of an inaccurate extrapolation scheme and the suppression of the dynamics (i.e., time-dependence) of the governing equations. A simple juxtaposition of the experimental evidence by Verhoeven (1969) (misinterpreted in BO) with modern findings confirms our point. For  $Pr < 0.01$ , the “critical” (according to BO) Rayleigh numbers for the onset of convection correspond to domains where the oscillatory mode of convection dominates and they are, consequently, meaningless. The present paper serves primarily as an organized rebuttal to the conjectures expressed in BO. Furthermore, this work serves to demonstrate that, although the route from physics to heat transfer applications is smooth, the reverse, i.e., relying exclusively on heat transfer coefficients (as ex-

pressed by the Nu number) to deduce the physics of natural convection, can be treacherous.

#### Acknowledgments

The author wishes to thank Professors Ivan Catton (University of California at Los Angeles) and Fritz Busse (Bayreuth University) for their input. This work is performed under the aegis of the National Science Foundation (grants CTS-8909119 and CTS-9006189) and the U.S. Department of Energy (grant DE-FG05-90ER14141).

#### References

- Bénard, H., 1900, “Les tourbillons cellulaires dans une nappe liquide,” *Revue Gén. Sci. Pur. Appl.*, Vol. 11, pp. 1261–1271, 1309–1328.
- Bertin, H., and Ozoe, H., 1986, “Numerical Study of Two-Dimensional Natural Convection in a Horizontal Fluid Layer Heated From Below, by Finite-Element Method: Influence of Prandtl Number,” *Int. J. Heat Mass Transfer*, Vol. 29, pp. 439–449.
- Buell, J. C., and Catton, I., 1986, “Wavenumber Selection in Large-Amplitude Axisymmetric Convection,” *Phys. Fluids*, Vol. 29, pp. 23–30.
- Busse, F. H., 1978, “Non-linear Properties of Thermal Convection,” *Rep. Prog. Phys.*, Vol. 41, pp. 1929–1967.
- Catton, I., 1966, “Natural Convection in Horizontal Liquid Layers,” *Phys. Fluids*, Vol. 9, pp. 2521–2522.
- Chao, P., Churchill, S. W., and Ozoe, H., 1982, “The Dependence of the Critical Rayleigh Number on the Prandtl Number,” in: *Convection Transport and Instability Phenomena*, J. Zierep and H. Oertel, Jr., eds., G. Braun, Karlsruhe, Germany, pp. 55–70.
- Clever, R. M., and Busse, F. H., 1974, “Transition to Time-Dependent Convection,” *J. Fluid Mech.*, Vol. 65, pp. 625–645.
- Clever, R. M., and Busse, F. H., 1981, “Low-Prandtl-Number Convection in a Layer Heated From Below,” *J. Fluid Mech.*, Vol. 102, pp. 61–74.
- Clever, R. M., and Busse, F. H., 1990, “Convection at Very Low Prandtl Numbers,” *Phys. Fluids A*, Vol. 2, pp. 334–339.
- Croquette, V., Le Gal, P., Pocheau, A., and Guglielmetti, R., 1986, “Large-Scale Flow Characterization in a Rayleigh–Bénard Convective Pattern,” *Europhysics Letters*, Vol. 1, pp. 393–399.
- Croquette, V., 1989, “Convective Pattern Dynamics at Low Prandtl Number: Part II,” *Contemporary Physics*, Vol. 30, pp. 153–171.
- Goldhirsch, I., Orszag, S. A., and Maulik, B. K., 1987, “An Efficient Method for Computing Leading Eigenvalues and Eigenvectors of Large Asymmetric Matrices,” *J. Sci. Components*, Vol. 2, pp. 33–58.
- Joseph, D. D., 1976, *Stability of Fluid Motions II*, Springer, Berlin, § 61.
- Koschmieder, E. L., and Pallas, S. G., 1974, “Heat Transfer Through a Shallow, Horizontal Convecting Fluid Layer,” *Int. J. Heat Mass Transfer*, Vol. 17, pp. 991–1002.
- Lage, J. L., Bejan, A., and Georgiadis, J. G., 1991, “On the Effect of the Prandtl Number on the Onset of Bénard Convection,” *Int. J. Heat Fluid Flow*, Vol. 12, pp. 184–188.
- Malkus, W. V. R., and Veronis, G., 1958, “Finite Amplitude Cellular Convection,” *J. Fluid Mech.*, Vol. 4, pp. 225–260.
- Rayleigh, Lord, 1916, “On Convection Currents in a Horizontal Layer of Fluid, When the Higher Temperature Is on the Under Side,” *Phil. Mag.*, Vol. 32, pp. 529–546.
- Schlüter, A., Lortz, D., and Busse, F. H., 1965, “On the Stability of Steady Finite Amplitude Convection,” *J. Fluid Mech.*, Vol. 23, pp. 129–144.
- Verhoeven, J. D., 1969, “Experimental Study of Thermal Convection in a Vertical Cylinder of Mercury Heated From Below,” *Phys. Fluids*, Vol. 12, pp. 1733–1740.

#### Natural Convection From a Horizontal Heated Copper-Graphite Composite Surface

Wen-Jei Yang,<sup>1</sup> H. Takizawa,<sup>1</sup> and D. L. Vrbale<sup>2</sup>

#### 1 Introduction

One important objective of heat transfer research is to de-

<sup>1</sup>Department of Mechanical Engineering and Applied Mechanics, The University of Michigan, Ann Arbor, MI 48109.

<sup>2</sup>Division of Thermal & E. M. Components Technology, Sparta, Inc., San Diego, CA 92121.

Contributed by the Heat Transfer Division of THE AMERICAN SOCIETY OF MECHANICAL ENGINEERS. Manuscript received by the Heat Transfer Division July 16, 1990; revision received April 16, 1991. Keywords: Augmentation and Enhancement, Natural Convection.

velop high-performance heat transfer surfaces. There are numerous advantages to high-performance surfaces. They allow for more energy extraction or utilization from an energy source (especially low energy-density sources), more energy recovery from waste heat, and efficient cooling of electric components. They are also compact and lightweight, which is important in vehicular applications. It is well known that the size of heat exchangers dictates the practical use of a Stirling engine and that the size of its boiler and condenser impede the feasibility of an OTEC (ocean thermal energy conversion) system. Highly effective high heat flux surfaces for electronic chip (very large scale integration, VLSI) cooling are required to keep pace with the evolving chip technology. Higher computer speeds require more circuit power packaged into smaller volumes. This will require enhanced heat transfer surfaces to deal with the higher heat flux requirements. Chu and Simmons (1988) revealed the trend of the heat flux at the module level in several computer systems.

Recently, an experimental study was performed on nucleate boiling heat transfer of Freon 113 (i.e., R-113) on a copper-graphite composite surface (Yang et al., 1991). The direction of the ultrahigh thermal conductivity graphite fibers is normal to the boiling surface. It was revealed that the heat transfer performance on the composite surface is from three to six times higher than on a copper surface.

The graphite fiber reinforced copper (Gr-Cu) produced by Sparta, Inc., consists of graphite fibers 0.008 to 0.010 mm in diameter imbedded uniaxially in a copper matrix (50 percent area fraction). The thermal conductivity of the graphite fiber is three times greater than that of the adjacent matrix. The fibers act like highly efficient pin fins extruding into the copper surface. The effect of the high heat conducting fibers is to transfer heat to or from the contacting fluid or to increase nucleation sites on the surface. It is thermal enhancement that is provided by tailored thermal properties internal to the heat transfer surface. The key properties of the Gr-Cu composite include: (i) high thermal conductivity in the fiber direction of up to 1000 W/m-K for the advanced pitch-based graphite fiber, as compared with 401 W/m-K for pure copper at 300 K, and (ii) low density at 6.14 g/cc, lighter than pure copper with 8.93 g/cc. Other unique aspects of this material are a modulus near 140 Msi and a negative coefficient of thermal expansion. By controlling both the directional layup and the volume fraction of the fiber, the directional conductivity, coefficient of the thermal expansion, strength and stiffness can be tailored to optimize the thermal/structural performance of the cooling concept.

This paper investigates natural convective heat transfer from a copper-graphite composite with the heated surface facing upward in liquid Freon 113 and air. The heat transfer coefficients are determined and compared with those of isotropic pure copper. A comprehensive coverage of heat transfer and fluid motion induced by buoyancy forces is available from Gebhart et al. (1988).

## 2 Test Apparatus and Procedure

Figure 1 depicts a schematic of the experimental apparatus for natural convection from a horizontal surface facing upward. The heating surface consisted of a Gr-Cu composite plate, 25 mm in diameter and 10 mm thick. It was in contact with a heating copper block 25 mm in diameter and 41 mm thick. The lower end of the copper block was in contact with an electrically heated hot plate. Three 30-gage copper-constantan thermocouples (Nos. 1, 2, and 3) were installed in the copper block 3.2 mm apart on the center line, with one at the composite-copper interface. Two similar thermocouples (Nos. 4 and 5) were placed in the composite plate also 3.2 mm apart from its interface with the copper block. Temperature measurements were extrapolated to determine the fluid surface in-

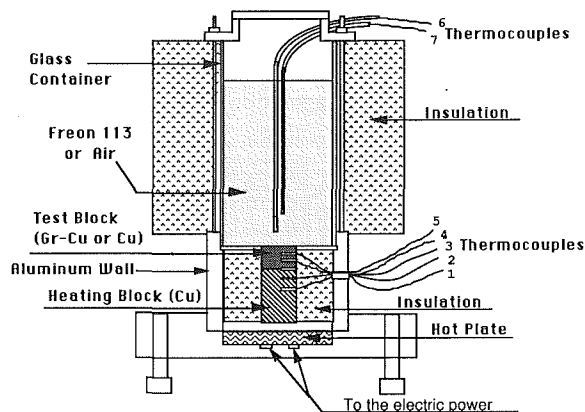


Fig. 1 Schematic of experimental apparatus

terfacial temperature  $T_s$ . Two 30-gage copper-constantan thermocouples (Nos. 6 and 7) measured the bulk fluid temperature  $T_f$ . A recorder/datalogger manufactured by Wahl Instruments, Inc. was employed in temperature recordings.

The vertical surfaces of the Gr-Cu composite and Cu blocks were insulated with mica flakes. The blocks and insulation were placed in an aluminum container. The upper edge of the composite block was undercut with a bevel, and an undersized thin stainless-steel mating piece was attached by a shrink fit to provide a continuous surface to keep heat loss by conduction at a minimum. Power input (heat flux) was varied within the natural convection region. Freon 113 and air were selected as free convection fluids. The test vessel was also insulated on the sides in order to minimize heat loss to the ambient.

Another experiment was conducted with the Gr-Cu composite surface replaced by a pure copper surface (isotropic properties) to provide a baseline for comparison. The only difference between the two surfaces was their thermal conductivities. Both heating surfaces were polished with a 1- $\mu$ m diamond abrasive. With the same surface finishes, the principal difference between the two tested surfaces is internal thermal property characteristics.

## 3 Experimental Results

Two Gr-Cu surfaces and one pure copper surface was used as the heating surfaces, while Freon 113 and air were employed as the testing fluids. Freon 113 was heated at various heat fluxes by varying the electric power, which was increased incrementally until the boiling point was reached. The liquid level in each test was maintained at 11 cm. In the case of air, the heat flux was varied by incrementing the power input until the heating surface temperature reached about 110°C, when surface oxidization was detected. The steady-state temperature distribution was achieved in 5 to 7 hours in the case of Freon 113, and 3 to 4 hours in the case of air. In each test, temperature readings were made after steady state was achieved in the system.

In the case of air, heat loss by radiation must be taken into account in order to correlate the natural convection performance of the pure copper surface with the empirical formulas recommended by McAdams (1955):

$$\left. \begin{aligned} Nu &= 0.54 Ra^{1/4} \text{ for } 10^4 \leq Ra \leq 10^7 \\ Nu &= 0.14 Ra^{1/3} \text{ for } 10^7 \leq Ra \leq 10^{11} \end{aligned} \right\} \quad (1)$$

Here, Nu and Ra are the Nusselt and Rayleigh numbers, respectively. The same procedure was followed in correlating the natural convection performance of the Gr-Cu composite surfaces. The surface heat flux are determined from the temperature gradient between thermocouples No. 4 and No. 5. The result was checked against the power calculated from the measurement of the electrical voltage input.

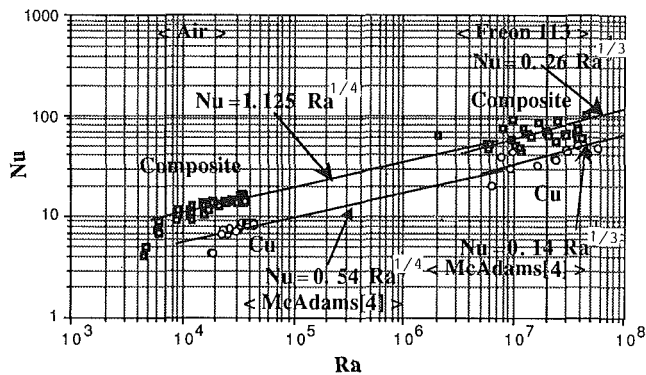


Fig. 2 Correlation of natural convection data

Test data are correlated in Fig. 2 in the form of a Nu versus Ra graph with the diameter of the heating surface as the characteristic length. Included for comparison are the empirical formulas recommended by McAdams (1955) for a heated horizontal plate facing upward. Fixing the exponents based on the McAdams recommendations, one finds the coefficients that best fit the data of the composite surface. This yields:

$$\left. \begin{aligned} Nu &= 1.125 Ra^{1/4} \text{ for } 10^4 \leq Ra \leq 5 \times 10^5 \text{ (laminar flow)} \\ Nu &= 0.26 Ra^{1/3} \text{ for } 5 \times 10^6 \leq Ra \leq 10^{11} \text{ (turbulent flow)} \end{aligned} \right\} \quad (2)$$

The higher heat transfer performance of the composite surface can be explained as follows: For the same temperature drop over the same thickness, the heat flux through the composite material (in the fiber direction) will be 3 to 4 times higher than through pure copper because the thermal conductivity of the composite is 3 to 4 times higher than that of pure copper. Therefore, a higher heat flux is transferred to the ambient from the composite surface than from a pure copper surface.

It is important to note that the evaporation of Freon 113 during experiments caused data scattering, especially at higher heating surface temperatures (at higher Ra). In contrast, data scattering in the case of air is minimal in the absence of phase change. The uncertainty estimations are evaluated by the method of Kline and McClintock (1953). The uncertainty intervals are  $\pm 10$  percent for air and  $\pm 15$  percent for Freon 113, since at high heat fluxes, the temperature differences in the Gr-Cu composite become very small. The sharp drop in Nu at Ra of approximately  $10^4$  in Fig. 2 suggests the lower limit of validity of the correlation formulas.

#### 4 Conclusion

The reproducibility of test data for natural convection on the copper-graphite composite with a 25-mm dia heated surface facing upward is good. This is especially true in the case of air, where data scattering is much less than in Freon 113. It is revealed from this study that natural convection heat transfer on the composite surface is about two times higher than that of a pure copper surface, in both the laminar and turbulent regions. A substantial enhancement was also observed in the case of pool boiling in a previous study (Yang et al., 1991).

This work was supported by the Natural Science Foundation under Grant No. CBT-8811065.

#### References

- Chu, R. C., and Simmons, R. E., 1988, "Heat Transfer in Large Scale Composites," *Heat Transfer: Korea—U.S. Seminar on Thermal Engineering and High Technology*, J. H. Kim, Sung Task Ro, and Taik Sik Lee, eds., Hemisphere, Washington, DC, pp. 55-88.
- Gebhart, B., Jaluria, Y., Mahajan, R. L., and Sammakia, B., 1988, *Buoyancy Induced Flows and Transport*, Hemisphere, Washington, DC.

Kline, S. J., and McClintock, F. A., 1953, "Describing Uncertainties in Single-Sample Experiments," *Mechanical Engineering*, Vol. 75, pp. 3-8.

McAdams, W. H., 1955, *Heat Transmission*, 3rd ed., McGraw-Hill, New York.

Yang, Wen-Jei, Takizawa, H., and Vrable, D. L., 1991, "Augmented Boiling on Copper-Graphite Composite Surface," *International Journal of Heat and Mass Transfer*, in press.

## Natural Convection in a Vertical Enclosure Filled With Anisotropic Porous Media

J. Ni<sup>1</sup> and C. Beckermann<sup>2</sup>

### Introduction

Anisotropic porous media are encountered in numerous systems in industry and nature. Examples include fibrous materials (e.g., insulation, filters), sedimentary soils, rock formations, certain biological materials, columnar dendritic structures formed during solidification of multicomponent mixtures, and preforms of aligned ceramic or graphite fibers used in casting of metal matrix composites. Stacks of perforated plates and tube bundles (e.g., in nuclear reactor cores) may also be modeled as anisotropic porous media. Natural convection in such anisotropic porous media has received relatively little research attention. Several studies have been reported on natural convection in horizontal anisotropic porous layers heated from below (Epherre, 1977; Castinel and Combarous, 1977; Kvernfold and Tyvand, 1979; McKibbin and Tyvand, 1982; Gjerde and Tyvand, 1984; Nilsen and Storesletten, 1990), where the permeability and/or effective thermal conductivity were taken to be different in the horizontal and vertical directions. These investigations deal mainly with the onset of convection and the flow and heat transfer phenomena at moderately supercritical Rayleigh numbers.

Castinel and Combarous (1977) also analyzed the case of inclined layers, while Burns et al. (1977) examined natural convection in a vertical slot filled with an anisotropic porous medium. In these two studies, the porous medium was taken to be thermally isotropic. As shown by Neale (1977), this represents a good approximation for clusters of parallel fibers; however, no general conclusions can be drawn for a conducting matrix (e.g., with thin parallel copper threads introduced into the matrix) (Kvernfold and Tyvand, 1979). Furthermore, Burns et al. (1977) only studied natural convection in a relatively large aspect ratio slot and for relatively small differences in the permeabilities in the horizontal and vertical directions, which is relevant to fibrous insulation between walls in building structures. Detailed information on the flow and heat transfer phenomena in anisotropic porous media heated/cooled from the sides is presently not available.

Of related interest are the numerous studies of natural convection in porous media with layers of different permeabilities and/or effective thermal conductivities (e.g., McKibbin and O'Sullivan, 1981; Poulidakos and Bejan, 1983; McKibbin and Tyvand, 1983; Lai and Kulacki, 1988) as well as with a non-

<sup>1</sup>Research Assistant, Department of Mechanical Engineering, The University of Iowa, Iowa City, IA 52242.

<sup>2</sup>Assistant Professor, Department of Mechanical Engineering, The University of Iowa, Iowa City, IA 52242; Assoc. Mem. ASME.

Contributed by the Heat Transfer Division of THE AMERICAN SOCIETY OF MECHANICAL ENGINEERS. Manuscript received by the Heat Transfer Division February 14, 1991; revision received May 8, 1991. Keywords: Flow Nonuniformity, Natural Convection, Porous Media.

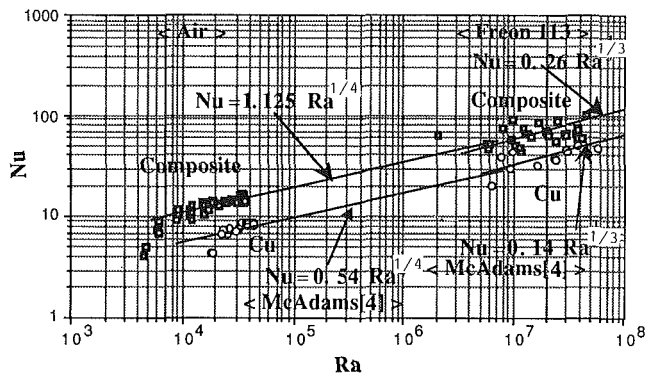


Fig. 2 Correlation of natural convection data

Test data are correlated in Fig. 2 in the form of a Nu versus Ra graph with the diameter of the heating surface as the characteristic length. Included for comparison are the empirical formulas recommended by McAdams (1955) for a heated horizontal plate facing upward. Fixing the exponents based on the McAdams recommendations, one finds the coefficients that best fit the data of the composite surface. This yields:

$$\left. \begin{aligned} Nu &= 1.125 Ra^{1/4} \text{ for } 10^4 \leq Ra \leq 5 \times 10^5 \text{ (laminar flow)} \\ Nu &= 0.26 Ra^{1/3} \text{ for } 5 \times 10^6 \leq Ra \leq 10^{11} \text{ (turbulent flow)} \end{aligned} \right\} \quad (2)$$

The higher heat transfer performance of the composite surface can be explained as follows: For the same temperature drop over the same thickness, the heat flux through the composite material (in the fiber direction) will be 3 to 4 times higher than through pure copper because the thermal conductivity of the composite is 3 to 4 times higher than that of pure copper. Therefore, a higher heat flux is transferred to the ambient from the composite surface than from a pure copper surface.

It is important to note that the evaporation of Freon 113 during experiments caused data scattering, especially at higher heating surface temperatures (at higher Ra). In contrast, data scattering in the case of air is minimal in the absence of phase change. The uncertainty estimations are evaluated by the method of Kline and McClintock (1953). The uncertainty intervals are  $\pm 10$  percent for air and  $\pm 15$  percent for Freon 113, since at high heat fluxes, the temperature differences in the Gr-Cu composite become very small. The sharp drop in Nu at Ra of approximately  $10^4$  in Fig. 2 suggests the lower limit of validity of the correlation formulas.

#### 4 Conclusion

The reproducibility of test data for natural convection on the copper-graphite composite with a 25-mm dia heated surface facing upward is good. This is especially true in the case of air, where data scattering is much less than in Freon 113. It is revealed from this study that natural convection heat transfer on the composite surface is about two times higher than that of a pure copper surface, in both the laminar and turbulent regions. A substantial enhancement was also observed in the case of pool boiling in a previous study (Yang et al., 1991).

This work was supported by the Natural Science Foundation under Grant No. CBT-8811065.

#### References

- Chu, R. C., and Simmons, R. E., 1988, "Heat Transfer in Large Scale Composites," *Heat Transfer: Korea—U.S. Seminar on Thermal Engineering and High Technology*, J. H. Kim, Sung Task Ro, and Taik Sik Lee, eds., Hemisphere, Washington, DC, pp. 55-88.
- Gebhart, B., Jaluria, Y., Mahajan, R. L., and Sammakia, B., 1988, *Buoyancy Induced Flows and Transport*, Hemisphere, Washington, DC.

Kline, S. J., and McClintock, F. A., 1953, "Describing Uncertainties in Single-Sample Experiments," *Mechanical Engineering*, Vol. 75, pp. 3-8.

McAdams, W. H., 1955, *Heat Transmission*, 3rd ed., McGraw-Hill, New York.

Yang, Wen-Jei, Takizawa, H., and Vrable, D. L., 1991, "Augmented Boiling on Copper-Graphite Composite Surface," *International Journal of Heat and Mass Transfer*, in press.

## Natural Convection in a Vertical Enclosure Filled With Anisotropic Porous Media

J. Ni<sup>1</sup> and C. Beckermann<sup>2</sup>

### Introduction

Anisotropic porous media are encountered in numerous systems in industry and nature. Examples include fibrous materials (e.g., insulation, filters), sedimentary soils, rock formations, certain biological materials, columnar dendritic structures formed during solidification of multicomponent mixtures, and preforms of aligned ceramic or graphite fibers used in casting of metal matrix composites. Stacks of perforated plates and tube bundles (e.g., in nuclear reactor cores) may also be modeled as anisotropic porous media. Natural convection in such anisotropic porous media has received relatively little research attention. Several studies have been reported on natural convection in horizontal anisotropic porous layers heated from below (Epherre, 1977; Castinel and Combarous, 1977; Kvernfold and Tyvand, 1979; McKibbin and Tyvand, 1982; Gjerde and Tyvand, 1984; Nilsen and Storesletten, 1990), where the permeability and/or effective thermal conductivity were taken to be different in the horizontal and vertical directions. These investigations deal mainly with the onset of convection and the flow and heat transfer phenomena at moderately supercritical Rayleigh numbers.

Castinel and Combarous (1977) also analyzed the case of inclined layers, while Burns et al. (1977) examined natural convection in a vertical slot filled with an anisotropic porous medium. In these two studies, the porous medium was taken to be thermally isotropic. As shown by Neale (1977), this represents a good approximation for clusters of parallel fibers; however, no general conclusions can be drawn for a conducting matrix (e.g., with thin parallel copper threads introduced into the matrix) (Kvernfold and Tyvand, 1979). Furthermore, Burns et al. (1977) only studied natural convection in a relatively large aspect ratio slot and for relatively small differences in the permeabilities in the horizontal and vertical directions, which is relevant to fibrous insulation between walls in building structures. Detailed information on the flow and heat transfer phenomena in anisotropic porous media heated/cooled from the sides is presently not available.

Of related interest are the numerous studies of natural convection in porous media with layers of different permeabilities and/or effective thermal conductivities (e.g., McKibbin and O'Sullivan, 1981; Poulidakos and Bejan, 1983; McKibbin and Tyvand, 1983; Lai and Kulacki, 1988) as well as with a non-

<sup>1</sup>Research Assistant, Department of Mechanical Engineering, The University of Iowa, Iowa City, IA 52242.

<sup>2</sup>Assistant Professor, Department of Mechanical Engineering, The University of Iowa, Iowa City, IA 52242; Assoc. Mem. ASME.

Contributed by the Heat Transfer Division of THE AMERICAN SOCIETY OF MECHANICAL ENGINEERS. Manuscript received by the Heat Transfer Division February 14, 1991; revision received May 8, 1991. Keywords: Flow Nonuniformity, Natural Convection, Porous Media.

uniform porosity, for example, near the walls in packed beds of spheres (e.g., Hong et al., 1987; David et al., 1988). In general, studies of natural convection in such *heterogeneous* porous media have revealed that the flow is channeled in regions (or layers) of higher permeability, while discontinuities between layers cause sharp bends in both streamline and isotherm patterns. McKibbin and Tyvand (1982) and Gjerde and Tyvand (1984) have shown that a periodically layered porous medium can be modeled as a *homogeneous* anisotropic medium, provided the length scale of the flow is larger than the layering period. Therefore, convection phenomena such as flow channeling may be expected to be present also in the homogeneous anisotropic porous media studied here. Whereas detailed comparisons between periodically layered and homogeneous anisotropic porous media have been made for the case of heating from below (McKibbin and Tyvand, 1982; Gjerde and Tyvand, 1984), no results have been reported for the corresponding cases with heating/cooling from the sides. More recently, Angot and Caltagirone (1990) have developed a numerical method for calculating natural convection flows inside periodic heterogeneous porous structures.

The objective of the present study is to obtain an improved understanding of natural convection flow and heat transfer in a vertical enclosure filled with homogeneous porous media that are both hydrodynamically and thermally anisotropic. This fundamental study considers a two-dimensional, square enclosure with sides of length  $L$ . The left and right vertical walls are held isothermally at  $T_H$  and  $T_C$ , respectively, while the horizontal top and bottom walls are adiabatic. Relatively large ranges of the Rayleigh number (based on the permeability) and the ratios of the permeabilities and effective thermal conductivities in the horizontal and vertical directions are examined, in order to obtain a complete understanding of their influence on the flow and heat transfer processes. Results are reported in terms of streamlines, isotherms, and the overall heat transfer rates across the enclosure.

### Model Equations

The flow in the square enclosure is steady, laminar, two-dimensional, and incompressible, and the thermophysical properties are assumed to be constant except for the density in the buoyancy term. The principal directions of the permeabilities ( $K$ ) and (effective) thermal conductivities ( $k$ ) coincide with the horizontal ( $x$ ) and vertical ( $y$ ) coordinate axes. Assuming the validity of Darcy's law and thermal equilibrium between the solid matrix and the fluid, the governing equations can be written in dimensionless form as

$$\frac{\partial u}{\partial \xi} + \frac{\partial v}{\partial \eta} = 0 \quad (1)$$

$$0 = -\frac{\partial p}{\partial \xi} - u \quad (2)$$

$$0 = -\frac{\partial p}{\partial \eta} - \frac{v}{K^*} + \text{Ra}\Theta \quad (3)$$

$$u \frac{\partial \Theta}{\partial \xi} + v \frac{\partial \Theta}{\partial \eta} = \frac{\partial^2 \Theta}{\partial \xi^2} + k^* \frac{\partial^2 \Theta}{\partial \eta^2} \quad (4)$$

The boundary conditions are

$$\Theta = 1 \quad \text{at } \xi = 0, 0 \leq \eta \leq 1$$

$$\Theta = 0 \quad \text{at } \xi = 1, 0 \leq \eta \leq 1$$

$$\frac{\partial \Theta}{\partial \eta} = 0 \quad \text{at } \eta = 0, 1, 0 \leq \xi \leq 1 \quad (5)$$

$$u, v = 0 \quad \text{on all enclosure walls.}$$

In the above equations, the coordinates ( $\xi, \eta$ ), velocities ( $u, v$ ), and pressure ( $p$ ) are made dimensionless using  $L, \alpha/L$ , and  $\mu\alpha/K_x$  as the reference length, velocity, and pressure, respectively, where  $\alpha$  is the thermal diffusivity based on  $k_x$  and  $\mu$  is the dynamic viscosity. The dimensionless temperature  $\Theta$  is defined as  $(T - T_C)/(T_H - T_C)$ . Equations (1)–(5) show that the present problem is governed by three dimensionless parameters, namely

$$\text{Ra} = \frac{g\beta(T_H - T_C)K_x L}{\nu\alpha} \quad \text{Rayleigh number,}$$

$$K^* = \frac{K_y}{K_x} \quad \text{permeability ratio,} \quad (6)$$

$$k^* = \frac{k_y}{k_x} \quad \text{thermal conductivity ratio}$$

where  $g, \beta$ , and  $\nu$  are the gravitational acceleration, coefficient of thermal expansion, and kinematic viscosity, respectively.

The overall heat transfer rate across the enclosure is expressed by the average Nusselt number at the left and right vertical walls defined as

$$\text{Nu}|_{\xi=0,1} = \frac{\bar{h}L}{k_x} = - \int_0^1 \frac{\partial \Theta}{\partial \xi} \Big|_{\xi=0,1} d\eta \quad (7)$$

where  $\bar{h}$  is the average convective heat transfer coefficient. Note that the Nusselt number is equal to unity in the absence of convection.

### Numerical Procedures

Numerical solutions of the governing equations were obtained using the control-volume formulation described in detail by Patankar (1980). The algorithm was somewhat modified to accommodate the special form of the momentum equations and the different thermal conductivities in the  $\xi$ - and  $\eta$ -directions in the energy equation.

Numerical experiments were performed to establish the number and distribution of control volumes required to produce accurate results. The numerical solutions presented in this paper were acquired using  $50 \times 50$  control volumes. Doubling of the number of control volumes produced essentially the same results. The distribution of the control volumes was strongly skewed toward all solid surfaces in order to resolve velocity and temperature gradients accurately. For this purpose, the grid spacing was adjusted in a trial and error fashion according to the thickness of the boundary layers. Convergence of the numerical solution was checked by performing overall mass and energy balances. The calculations were performed on an Encore minicomputer and typically required 200 CPU minutes. For the limiting case of an isotropic porous medium, a comparison of the average Nusselt numbers with those obtained in other studies is presented in Table 1. It can be seen that the present Nusselt numbers fall within 1 percent of the high-resolution finite difference calculations of Shiralkar et al. (1983). It was already noted by Walker and Homsy (1978) that their semi-analytical technique gave Nusselt numbers that are somewhat lower than previous numerical results. Good agreement was also obtained with analytical solutions for the limiting case of two-dimensional anisotropic heat conduction in a square region (Ozisik, 1980).

**Table 1 Comparison of Nusselt numbers between present and previously published results ( $K^* = 1, k^* = 1$ , square enclosure)**

| Ra   | Present<br>(50 × 50 grid) | Walker and<br>Homsy (1978) | Shiralkar<br>et al. (1983) |
|------|---------------------------|----------------------------|----------------------------|
| 100  | 3.103                     | 3.097                      | 3.115                      |
| 500  | 8.892                     | 8.66                       | 8.944                      |
| 1000 | 13.42                     | 12.96                      | 13.534                     |

## Results and Discussion

It is first instructive to examine the ranges of the governing dimensionless parameters  $Ra$ ,  $K^*$ , and  $k^*$  considered in the present study. Results are presented for Rayleigh numbers of 100, 500, and 1000. Preliminary computational runs indicated that the trends for the Nusselt numbers are similar for somewhat lower and higher Rayleigh numbers. The permeability and conductivity ratios were varied (independently) from 0.001 to 1000. Whereas permeability ratios of more than 100 have been observed, for example, in sedimentary rocks (Davis, 1969), very large (or small) thermal conductivity ratios are unlikely to exist in practical systems (Neale, 1977). Also, in reality the permeability and thermal conductivity ratios are often related to each other. However, the present ranges were chosen to illustrate the trends and limiting behaviors present in natural convection in anisotropic media. Consideration of such extreme values of these ratios also aids in understanding the heat and fluid flow phenomena in the present system.

**Isotherms and Streamlines.** Representative streamlines and isotherms are shown in Fig. 1 for  $Ra=1000$ . Figure 1(a) illustrates the streamlines and isotherms for the isotropic case (i.e.,  $K^*=k^*=1$ ). A clockwise rotating convection cell exists in the enclosure with thermal and velocity boundary layers at the isothermal left and right walls. The isotherms outside the thermal boundary layers are almost horizontal and equally spaced, indicating that the heat transfer is by conduction between the horizontally flowing fluid streams through the relatively stagnant core.

Figure 1(b) shows the streamlines and isotherms for  $K^*=1000$  and  $k^*=1$ . For  $K^*=1000$ , the permeability in the  $\eta$  direction is much greater than the permeability in the  $\xi$  direction. Consequently, the buoyancy-induced flow along the vertical isothermal wall is much stronger than for  $K^*=1$ . Interestingly, the flow is channeled along the vertical walls, such that the velocity boundary layer is very thin. This occurs even though the porous medium is homogeneous. The channeling effect can be attributed to the fact that the relatively low permeability in the  $\xi$  direction prevents the vertical boundary layer from thickening. The fluid attains the hot (cold) wall temperature within a short distance from the bottom (top) of the left (right) wall, and uniformly spreads over the remaining length of the wall into the horizontal direction. The isotherms form a diagonal band extending from the lower left to the upper right corner, while the upper left and lower right triangles on either side of the diagonal are virtually isothermal and at the hot and cold wall temperatures, respectively. The diagonal band of isotherms can be directly attributed to the flow patterns described above and indicates strong heat exchange between the hot and cold fluid flowing on either side.

The opposite extreme is shown in Fig. 1(c). For  $K^*=0.001$  (and  $k^*=1$ ), no velocity (or thermal) boundary layers exist along the vertical walls, while the horizontally flowing fluid is strongly channeled along the upper and lower adiabatic walls. Due to the relatively low permeability in the  $\eta$  direction, the natural convection flow is very weak when compared to  $K^*=1$ . Consequently, the isotherms are almost vertical and equally spaced, indicating that the heat transfer across the enclosure is mostly by conduction. The low permeability in the  $\eta$  direction also causes the flow outside the "horizontal channels" to be completely parallel to the vertical walls and evenly spread over the left and right halves of the enclosure. In other words, the relatively high permeability in the  $\xi$  direction effectively prevents any nonuniformities from forming in the velocity profile of the vertically flowing fluid. Once the fluid reaches the upper or lower walls, it bends sharply and merges into the fast flowing fluid in the horizontal channels. Again, this channeling occurs, even though the porous medium is homogeneous.

Figures 1(d) and 1(e) show the streamlines and isotherms for different thermal conductivity ratios and  $K^*=1$ . For

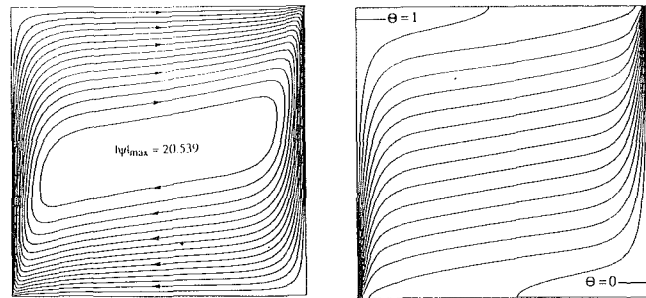


Fig. 1(a)  $K^*=1, k^*=1$

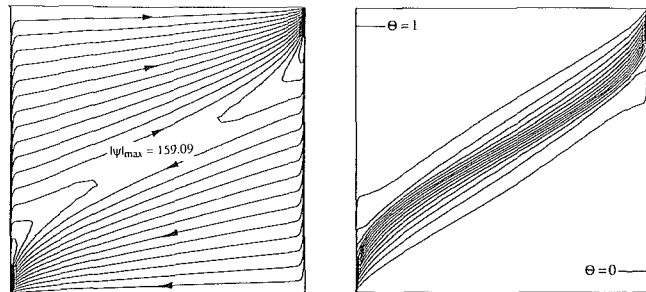


Fig. 1(b)  $K^*=1000, k^*=1$

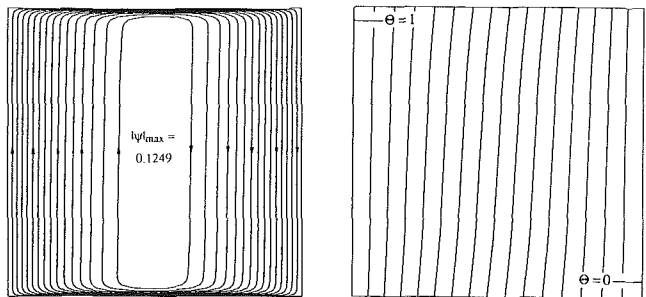


Fig. 1(c)  $K^*=0.001, k^*=1$

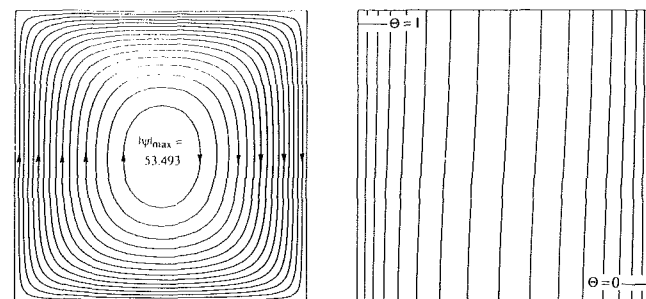


Fig. 1(d)  $K^*=1, k^*=1000$

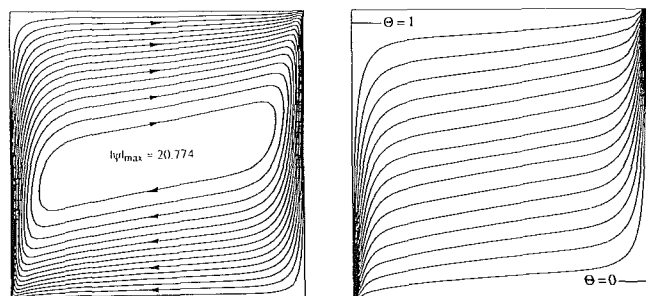


Fig. 1(e)  $K^*=1, k^*=0.001$

Fig. 1 Streamlines (left) and isotherms (right) for  $Ra=1000$  (equal increments)

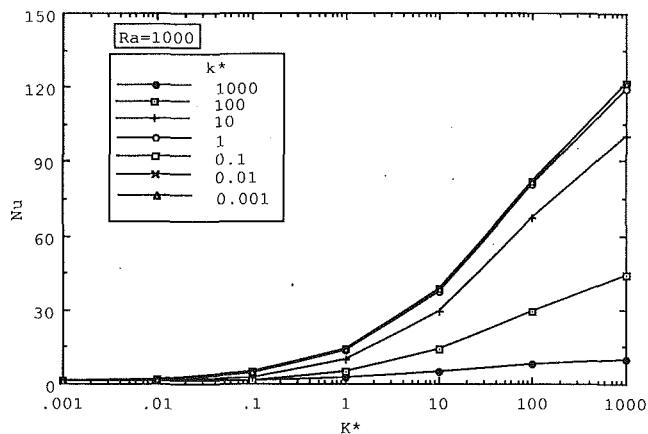


Fig. 2 Effect of permeability and thermal conductivity ratios on Nusselt number for  $Ra = 1000$

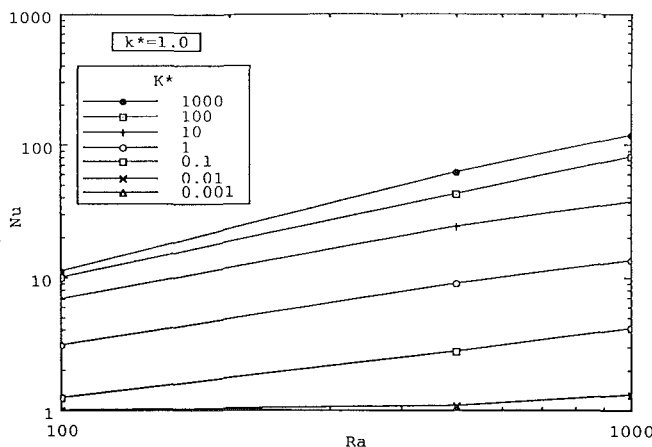


Fig. 3(a)  $k^* = 1$  and various permeability ratios

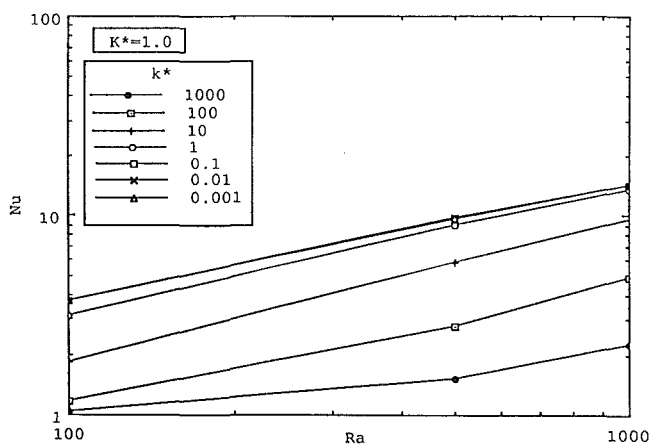


Fig. 3(b)  $K^* = 1$  and various thermal conductivity ratios

Fig. 3 Nusselt number as a function of Rayleigh number

$k^* = 1000$  (Fig. 1d), the thermal conductivity is much higher in the  $\eta$  direction than in the  $\xi$  direction. Due to the relatively high thermal conductivity in the  $\eta$  direction, there exist virtually no temperature gradients in the  $\eta$  direction and the isotherms are almost vertical. The isotherms are only slightly more concentrated near the left and right isothermal walls, indicating that the heat transfer is mostly by conduction. Consequently, the flow exhibits almost no boundary layers and is typical of natural convection at a much lower Rayleigh number. However, the flow intensity is more than 2.5 times higher than for  $k^* = 1$  (Fig. 1a).

Interestingly, a low thermal conductivity ratio has very little influence on the flow and heat transfer patterns. The streamlines and isotherms shown in Fig. 1(e) for  $k^* = 0.001$  are very similar to the ones for  $k^* = 1$  (Fig. 1a). For  $k^* = 0.001$ , the thermal conductivity is much lower in the  $\eta$  direction than in the  $\xi$  direction. It can be seen that the isotherms outside the thermal boundary layers are slightly more horizontal than for  $k^* = 1$ , indicating the influence of the low thermal conductivity in the  $\eta$  direction. Because the isotherm patterns are almost identical for  $k^* \approx 0.001$  and 1, the natural convection flow for  $k^* = 0.001$  is also very similar to the one for  $k^* = 1$ .

**Nusselt Numbers.** Figure 2 shows the effect of the permeability and thermal conductivity ratios on the Nusselt number for  $Ra = 1000$ . It can be seen that for all thermal conductivity ratios, the Nusselt numbers approach unity as  $K^* \rightarrow 0$ . As expected Nu increases with increasing  $K^*$ . For all permeability ratios, the Nusselt numbers approach unity for  $k^* \rightarrow \infty$  and increase with decreasing  $k^*$ . At a given permeability ratio, the Nusselt numbers are about the same for  $k^* < 1$ . All of the above results are in agreement with the observations made in the previous section. One important conclusion is that  $K^*$  and  $k^*$  have generally opposing effects on Nu.

Figure 3 summarizes all numerical data for the Nusselt number obtained in the present study. In this figure, Nu is plotted as a function of Ra for various permeability (Fig. 3a) and thermal conductivity (Fig. 3b) ratios. For isotropic porous media, it has been found that the Nusselt number can be well correlated by an equation of the form  $Nu = cRa^n$ , with the exponent  $n$  being a weak function of Ra (Shiralkar et al., 1983). Figure 3 shows that the slopes of the Nu versus Ra curves are quite similar for relatively large ranges of the permeability and thermal conductivity ratios. However, the curves are shifted considerably upward or downward (relative to  $K^* = k^* = 1$ ) for the various permeability and thermal conductivity ratios (except for  $k^* < 1$ ). This indicates that in the Nusselt number correlation, the exponent  $n$  of the Rayleigh number is only a weak function of  $K^*$  and  $k^*$ , while the "constant"  $c$  depends strongly on both  $K^*$  and  $k^*$  (except for  $k^* < 1$ ). In fact, for relatively small deviations of  $K^*$  and  $k^*$  from unity (i.e.,  $0.1 < K^* < 10$  and  $0 < k^* < 10$ ), correlations for Nu such as those proposed by Shiralkar et al. (1983) for an isotropic porous medium may be utilized, if the "constant"  $c$  is appropriately modified to reflect its dependence on  $K^*$  and  $k^*$ .

## Conclusions

A numerical study has been performed of natural convection in a vertical enclosure containing hydrodynamically and thermally anisotropic porous media. When compared to isotropic porous media, natural convection in the anisotropic case has the following physical characteristics:

(i) A large permeability ratio ( $K^* > 1$ ) caused channeling of the flow along the vertical isothermal walls, a higher flow intensity in the enclosure, and, consequently, a higher Nusselt number.

(ii) A low permeability ratio ( $K^* < 1$ ) causes channeling of the flow along the horizontal boundaries, thicker velocity boundary layers along the vertical walls, a lower flow intensity in the enclosure, and, hence, a smaller Nusselt number. All Nusselt numbers approach unity in the limit of  $K^* \rightarrow 0$ .

(iii) A large thermal conductivity ratio ( $k^* > 1$ ) causes a higher flow intensity in the enclosure, the isotherms to be more vertical, the heat transfer to be more dominated by conduction, and, hence, a lower Nusselt number. All Nusselt numbers approach unity in the limit of  $k^* \rightarrow \infty$ .

(iv) A low thermal conductivity ratio ( $k^* < 1$ ) has very little influence on the flow and heat transfer patterns, and the Nusselt numbers for a given Ra and  $K^*$  are approximately the same as for  $k^* = 1$ .



(v) The permeability and thermal conductivity ratios generally have opposing effects on the Nusselt number.

(vi) The dependence of the flow and heat transfer on the Rayleigh number is quite similar to the isotropic case, while the absolute values of the Nusselt number change drastically for  $K^* \neq 1$  and  $k^* > 1$ .

In conclusion, the present results revealed a number of interesting convection phenomena that need more research attention. It is hoped that this exploratory numerical study will stimulate further research into the important, but hitherto rather neglected, area of natural convection in both hydrodynamically and thermally anisotropic porous media. Additional work should also include investigations of inertia effects for relatively small Prandtl numbers and boundary effects for large Darcy numbers (i.e., permeabilities). The latter effect could be particularly important in the present system, due to the strong flow channeling observed along the solid boundaries.

### Acknowledgments

The work reported in this paper was supported, in part, by the National Science Foundation under Grant No. CBT-8808888. Computer facilities were made available by The University of Iowa WEEG Computing Center.

### References

- Angot, Ph., and Caltagirone, J. P., 1990, "Natural Convection Through Periodic Porous Media," in: *Heat Transfer 1990*, G. Hetsroni, ed., Hemisphere, New York, Vol. 5, pp. 219-224.
- Burns, P. J., Chow, L. C., and Tien, C. L., 1977, "Convection in a Vertical Slot Filled With Porous Insulation," *Int. J. Heat Mass Transfer*, Vol. 20, pp. 919-926.
- Castinel, G., and Combarous, M., 1977, "Natural Convection in an Anisotropic Porous Layer," *Int. Chemical Eng.*, Vol. 17, pp. 605-614.
- David, E., Lauriat, G., and Cheng, P., 1988, "Natural Convection in Rectangular Cavities Filled With Variable Porosity Media," in: *ASME Proceedings of the 1988 National Heat Transfer Conference*, H. R. Jacobs, ed., ASME, New York, Vol. 1, pp. 605-612.
- Davis, S. N., 1969, "Porosity and Permeability of Natural Materials," in: *Flow Through Porous Media*, J. M. De Wiest, ed., Academic Press, New York, pp. 53-89.
- Epherre, J. F., 1977, "Criterion for the Appearance of Natural Convection in an Anisotropic Layer," *Int. Chemical Eng.*, Vol. 17, pp. 615-616.
- Gjerde, K. M., and Tyvand, P. A., 1984, "Thermal Convection in a Porous Medium With Continuous Periodic Stratification," *Int. J. Heat Mass Transfer*, Vol. 27, pp. 2289-2295.
- Hong, J. T., Yamada, Y., and Tien, C. L., 1987, "Effects of Non-Darcian and Nonuniform Porosity on Vertical Plate Natural Convection in Porous Media," *ASME JOURNAL OF HEAT TRANSFER*, Vol. 109, pp. 356-362.
- Kvernlyod, O., and Tyvand, P. A., 1979, "Nonlinear Thermal Convection in Anisotropic Porous Media," *J. Fluid Mechanics*, Vol. 90, pp. 609-624.
- Lai, F. C., and Kulacki, F. A., 1988, "Natural Convection Across a Vertical Layered Porous Cavity," *Int. J. Heat Mass Transfer*, Vol. 31, pp. 1247-1260.
- McKibbin, R., and O'Sullivan, M. J., 1981, "Heat Transfer in a Layered Porous Medium Heated From Below," *J. Fluid Mechanics*, Vol. 111, pp. 141-173.
- McKibbin, R., and Tyvand, P. A., 1982, "Anisotropic Modelling of Thermal Convection in Multilayered Porous Media," *J. Fluid Mechanics*, Vol. 118, pp. 315-339.
- McKibbin, R., and Tyvand, P. A., 1983, "Thermal Convection in a Porous Medium Composed of Alternating Thick and Thin Layers," *Int. J. Heat Mass Transfer*, Vol. 26, pp. 761-780.
- Neale, G., 1977, "Degrees of Anisotropy for Fluid Flow and Diffusion Through Anisotropic Porous Media," *AIChE Journal*, Vol. 23, pp. 56-62.
- Nilsen, T., and Storesletten, L., 1990, "An Analytical Study on Natural Convection in Isotropic and Anisotropic Porous Channels," *ASME JOURNAL OF HEAT TRANSFER*, Vol. 112, pp. 396-401.
- Ozisik, M. N., 1980, *Heat Conduction*, Wiley, New York.
- Patankar, S. V., 1980, *Numerical Heat Transfer and Fluid Flow*, McGraw-Hill, New York.
- Poulikakos, D., and Bejan, A., 1983, "Natural Convection in Vertically and Horizontally Layered Porous Media Heated From the Side," *Int. J. Heat Mass Transfer*, Vol. 26, pp. 1805-1814.
- Shiralkar, G. S., Haajizadeh, M., and Tien, C. L., 1983, "Numerical Study of High Rayleigh Number Convection in a Vertical Porous Enclosure," *Numerical Heat Transfer*, Vol. 6, pp. 223-234.
- Walker, K. L., and Homsy, G. M., 1978, "Convection in a Porous Cavity," *J. Fluid Mechanics*, Vol. 87, pp. 449-474.

## Analysis of Heat Flux Measurement by Circular Foil Gages in a Mixed Convection/Radiation Environment

C. H. Kuo<sup>1,3</sup> and A. K. Kulkarni<sup>2,3</sup>

### Nomenclature

- $h$  = convective heat transfer coefficient
- $I_0(r), I_1(r)$  = Bessel's functions of the first kind
- $k$  = thermal conductivity of the circular foil
- $m = \sqrt{h/k\delta}$
- $q_c$  = convective heat flux per unit area to the surface (or wall)
- $q_g$  = gage-sensed heat flux per unit area
- $q_m$  = mixed (radiative and convective) heat flux per unit area to the surface (or wall) when  $T_w = T_B$
- $q_r$  = total heat flux per unit area to the surface (or wall) obtained from the gage output using radiation-based calibration
- $q'_r$  = radiative heat flux per unit area absorbed by the gage
- $q_w$  = total (mixed) heat flux per unit area to the surface when  $T_w \neq T_B$
- $r$  = radial coordinate of circular foil
- $R$  = radius of the circular foil
- $T(r)$  = temperature distribution in circular foil
- $T_o$  = temperature at the foil center
- $T_B$  = temperature of heat sink (base), which is maintained constant
- $T_w$  = surface (wall) temperature
- $T_\infty$  = temperature of gas flowing over the surface
- $\delta$  = thickness of foil
- $\Delta T_r, \Delta T_c, \Delta T_m$  = temperature difference between the foil center and edge with pure radiation heat flux, pure convection heat flux, and mixed convection/radiation heat flux, respectively

### Introduction

Principles of heat flux measurement by circular foil heat flux sensors, also known as Gardon gages, are analyzed when the gages are subjected to a mixed convective/radiative heat flux. A schematic of the Gardon gage is shown in Fig. 1. The gage is constructed using a copper cylinder (usually water-cooled) with a thin constantan foil mounted on the top. A copper wire is welded at the foil center and the copper cylinder is used as the other conductor, creating a differential thermocouple between the center and the edge of the foil. The gage is mounted flush on a surface at a location where a measurement of total heat flux to the surface is desired. The heat flux incident on the constantan foil of the gage causes a temperature difference,  $\Delta T$ , between the foil center and the edge, which generates a corresponding voltage signal. Measurement of  $\Delta T$  is then converted into the total incident heat flux using a calibration curve or chart. Calibration is usually

<sup>1</sup>Graduate Student.

<sup>2</sup>Associate Professor.

<sup>3</sup>Department of Mechanical Engineering, The Pennsylvania State University, University Park, PA 16802.

Contributed by the Heat Transfer Division and presented at the ASME/JSME Joint Heat Transfer Conference, Reno, Nevada, March 1991. Manuscript received by the Heat Transfer Division June 23, 1990; revision received February 15, 1991. Keywords: Conjugate Heat Transfer, Instrumentation, Measurement Techniques.

(v) The permeability and thermal conductivity ratios generally have opposing effects on the Nusselt number.

(vi) The dependence of the flow and heat transfer on the Rayleigh number is quite similar to the isotropic case, while the absolute values of the Nusselt number change drastically for  $K^* \neq 1$  and  $k^* > 1$ .

In conclusion, the present results revealed a number of interesting convection phenomena that need more research attention. It is hoped that this exploratory numerical study will stimulate further research into the important, but hitherto rather neglected, area of natural convection in both hydrodynamically and thermally anisotropic porous media. Additional work should also include investigations of inertia effects for relatively small Prandtl numbers and boundary effects for large Darcy numbers (i.e., permeabilities). The latter effect could be particularly important in the present system, due to the strong flow channeling observed along the solid boundaries.

### Acknowledgments

The work reported in this paper was supported, in part, by the National Science Foundation under Grant No. CBT-8808888. Computer facilities were made available by The University of Iowa WEEG Computing Center.

### References

- Angot, Ph., and Caltagirone, J. P., 1990, "Natural Convection Through Periodic Porous Media," in: *Heat Transfer 1990*, G. Hetsroni, ed., Hemisphere, New York, Vol. 5, pp. 219-224.
- Burns, P. J., Chow, L. C., and Tien, C. L., 1977, "Convection in a Vertical Slot Filled With Porous Insulation," *Int. J. Heat Mass Transfer*, Vol. 20, pp. 919-926.
- Castinel, G., and Combarous, M., 1977, "Natural Convection in an Anisotropic Porous Layer," *Int. Chemical Eng.*, Vol. 17, pp. 605-614.
- David, E., Lauriat, G., and Cheng, P., 1988, "Natural Convection in Rectangular Cavities Filled With Variable Porosity Media," in: *ASME Proceedings of the 1988 National Heat Transfer Conference*, H. R. Jacobs, ed., ASME, New York, Vol. 1, pp. 605-612.
- Davis, S. N., 1969, "Porosity and Permeability of Natural Materials," in: *Flow Through Porous Media*, J. M. De Wiest, ed., Academic Press, New York, pp. 53-89.
- Epherre, J. F., 1977, "Criterion for the Appearance of Natural Convection in an Anisotropic Layer," *Int. Chemical Eng.*, Vol. 17, pp. 615-616.
- Gjerde, K. M., and Tyvand, P. A., 1984, "Thermal Convection in a Porous Medium With Continuous Periodic Stratification," *Int. J. Heat Mass Transfer*, Vol. 27, pp. 2289-2295.
- Hong, J. T., Yamada, Y., and Tien, C. L., 1987, "Effects of Non-Darcian and Nonuniform Porosity on Vertical Plate Natural Convection in Porous Media," *ASME JOURNAL OF HEAT TRANSFER*, Vol. 109, pp. 356-362.
- Kvernoyld, O., and Tyvand, P. A., 1979, "Nonlinear Thermal Convection in Anisotropic Porous Media," *J. Fluid Mechanics*, Vol. 90, pp. 609-624.
- Lai, F. C., and Kulacki, F. A., 1988, "Natural Convection Across a Vertical Layered Porous Cavity," *Int. J. Heat Mass Transfer*, Vol. 31, pp. 1247-1260.
- McKibbin, R., and O'Sullivan, M. J., 1981, "Heat Transfer in a Layered Porous Medium Heated From Below," *J. Fluid Mechanics*, Vol. 111, pp. 141-173.
- McKibbin, R., and Tyvand, P. A., 1982, "Anisotropic Modelling of Thermal Convection in Multilayered Porous Media," *J. Fluid Mechanics*, Vol. 118, pp. 315-339.
- McKibbin, R., and Tyvand, P. A., 1983, "Thermal Convection in a Porous Medium Composed of Alternating Thick and Thin Layers," *Int. J. Heat Mass Transfer*, Vol. 26, pp. 761-780.
- Neale, G., 1977, "Degrees of Anisotropy for Fluid Flow and Diffusion Through Anisotropic Porous Media," *AIChE Journal*, Vol. 23, pp. 56-62.
- Nilsen, T., and Storesletten, L., 1990, "An Analytical Study on Natural Convection in Isotropic and Anisotropic Porous Channels," *ASME JOURNAL OF HEAT TRANSFER*, Vol. 112, pp. 396-401.
- Ozisik, M. N., 1980, *Heat Conduction*, Wiley, New York.
- Patankar, S. V., 1980, *Numerical Heat Transfer and Fluid Flow*, McGraw-Hill, New York.
- Poulikakos, D., and Bejan, A., 1983, "Natural Convection in Vertically and Horizontally Layered Porous Media Heated From the Side," *Int. J. Heat Mass Transfer*, Vol. 26, pp. 1805-1814.
- Shiralkar, G. S., Haajizadeh, M., and Tien, C. L., 1983, "Numerical Study of High Rayleigh Number Convection in a Vertical Porous Enclosure," *Numerical Heat Transfer*, Vol. 6, pp. 223-234.
- Walker, K. L., and Homsy, G. M., 1978, "Convection in a Porous Cavity," *J. Fluid Mechanics*, Vol. 87, pp. 449-474.

## Analysis of Heat Flux Measurement by Circular Foil Gages in a Mixed Convection/Radiation Environment

C. H. Kuo<sup>1,3</sup> and A. K. Kulkarni<sup>2,3</sup>

### Nomenclature

- $h$  = convective heat transfer coefficient
- $I_0(r), I_1(r)$  = Bessel's functions of the first kind
- $k$  = thermal conductivity of the circular foil
- $m = \sqrt{h/k\delta}$
- $q_c$  = convective heat flux per unit area to the surface (or wall)
- $q_g$  = gage-sensed heat flux per unit area
- $q_m$  = mixed (radiative and convective) heat flux per unit area to the surface (or wall) when  $T_w = T_B$
- $q_r$  = total heat flux per unit area to the surface (or wall) obtained from the gage output using radiation-based calibration
- $q'_r$  = radiative heat flux per unit area absorbed by the gage
- $q_w$  = total (mixed) heat flux per unit area to the surface when  $T_w \neq T_B$
- $r$  = radial coordinate of circular foil
- $R$  = radius of the circular foil
- $T(r)$  = temperature distribution in circular foil
- $T_o$  = temperature at the foil center
- $T_B$  = temperature of heat sink (base), which is maintained constant
- $T_w$  = surface (wall) temperature
- $T_\infty$  = temperature of gas flowing over the surface
- $\delta$  = thickness of foil
- $\Delta T_r, \Delta T_c, \Delta T_m$  = temperature difference between the foil center and edge with pure radiation heat flux, pure convection heat flux, and mixed convection/radiation heat flux, respectively

### Introduction

Principles of heat flux measurement by circular foil heat flux sensors, also known as Gardon gages, are analyzed when the gages are subjected to a mixed convective/radiative heat flux. A schematic of the Gardon gage is shown in Fig. 1. The gage is constructed using a copper cylinder (usually water-cooled) with a thin constantan foil mounted on the top. A copper wire is welded at the foil center and the copper cylinder is used as the other conductor, creating a differential thermocouple between the center and the edge of the foil. The gage is mounted flush on a surface at a location where a measurement of total heat flux to the surface is desired. The heat flux incident on the constantan foil of the gage causes a temperature difference,  $\Delta T$ , between the foil center and the edge, which generates a corresponding voltage signal. Measurement of  $\Delta T$  is then converted into the total incident heat flux using a calibration curve or chart. Calibration is usually

<sup>1</sup>Graduate Student.

<sup>2</sup>Associate Professor.

<sup>3</sup>Department of Mechanical Engineering, The Pennsylvania State University, University Park, PA 16802.

Contributed by the Heat Transfer Division and presented at the ASME/JSME Joint Heat Transfer Conference, Reno, Nevada, March 1991. Manuscript received by the Heat Transfer Division June 23, 1990; revision received February 15, 1991. Keywords: Conjugate Heat Transfer, Instrumentation, Measurement Techniques.

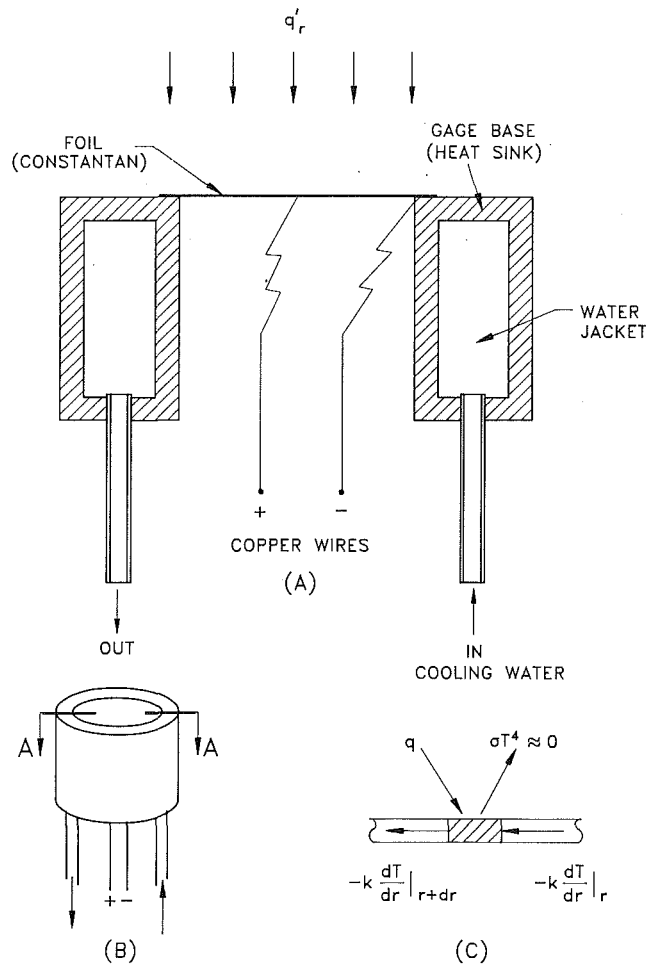


Fig. 1 (A) Cross-sectional view of a water-cooled Gardon gage, (B) an overall schematic, and (C) physical model for heat transfer in the foil

based on radiative heat flux, including the manufacturer-supplied calibration charts. The voltage output of the Gardon gage is almost linearly proportional to the incident heat flux when used to measure thermal radiation.

Several attempts have been made to analyze the operating principles and the error-including mechanisms for the circular foil heat flux sensor. Among the various effects studied are those of the transient characteristics of heat flux (Keltner and Wildin, 1975), the center wire heat loss and the heat sink temperature variation (Ash, 1969), the correction for measuring pure convection heat transfer (Borell and Diller, 1987), and the free-stream velocity and its angle of attack (Young et al., 1983). The performance of Gardon gages in mixed convective-radiative environments has, however, not been investigated in depth, which is the thrust of this work.

Gardon gages are often used in the measurement of heat feedback from flames to the burning surface in a wall fire, which are exposed to a mixed heat flux consisting of comparable fractions of convection and radiation (see, for example, Saito et al., 1989). In this situation, the use of a standard calibration chart based on a purely radiative flux is questionable. Also, the gage has to be cooled by maintaining a constant heat sink temperature in order to avoid melting of the junction of the foil and center wire and to provide a reference for calibration. This can cause a substantial temperature difference between the gage and the surrounding wall on which it is mounted, and introduces an error in the sensing of the convective heat flux at the location where the gage is mounted.

The specific objective of this work is to present the analysis

and a methodology for estimating the error in the measurement of mixed convective-radiative heat flux, which is the difference between the true surface-sensed heat flux and the flux determined from the gage output using a calibration based on purely radiative heat flux.

## Analysis

Figure 1 helps illustrate the mathematical model used for the Gardon gage. To derive the governing equation for the temperature distribution in foil, the following assumptions were employed: (i) Temperature gradient across the foil thickness is negligible; (ii) heat loss from rear surface and center wire is negligible; and (iii) the convective heat transfer coefficient,  $h$ , is nearly constant on the foil. Justification of these assumptions is given by Borell and Diller (1987) and Kuo and Kulkarni (1991); the latter paper also contains more details on the present work.

The thermal diffusion equation for the foil, when exposed to a mixed convection/radiation heat flux, can be expressed as

$$\frac{d^2T}{dr^2} + \frac{1}{r} \frac{dT}{dr} + \frac{q'_r}{\delta k} + \frac{h}{\delta k} (T_\infty - T) = 0 \quad (1)$$

with two boundary conditions:

at  $r = R$ ,  $T(R) = T_B$ , where  $T_B$  is the cooling water temperature; at  $r = 0$ ,  $dT/dr = 0$ .

### 1 Pure Radiative Heat Flux

The solution of Eq. (1) with  $h = 0$  is a second-order polynomial in  $r$ , and the temperature difference between the foil center and edge is given by

$$\Delta T_r = T_o - T_B = \frac{q_r R^2}{4\delta k} \quad (2)$$

Here,  $q_r = q'_r$ , and  $\Delta T_r$  is directly related to the sensor output of the measurement. This solution has been discussed previously by Gardon (1953) and Borell and Diller (1987).

The radiation loss from the gage to the surrounding atmosphere due to its temperature rise from the base temperature resulting from the external heat flux is neglected here, which represents a very small fraction of  $q_r$ . If the surrounding surface has a different emissivity (and absorptivity) compared to that of the gage foil,  $q_r$  must be corrected by subtracting the term  $\sigma(\epsilon_g - \epsilon_w) T_w^4$ , where  $\sigma$  is the Stefan-Boltzmann constant,  $\epsilon_g$  and  $\epsilon_w$  are emissivities of the gage and the surrounding surface, respectively, and  $T_w$  is expressed in an absolute temperature scale. However, this correction also will be small in most situations. It is assumed that the above two corrections are applied to  $q_r$  when necessary and, therefore, they are not discussed separately in the following discussion.

### 2 Pure Convective Heat Flux

With  $q'_r = 0$ , Eq. (1) can be rewritten as a modified Bessels's equation and its solution can be expressed in terms of the modified Bessels's function of the first kind. This case for Gardon gages was analyzed in detail by Borell and Diller (1987); therefore, only the important results are mentioned here, which are needed later. For the center-to-edge temperature difference,

$$\Delta T_c = T_o - T_B = \frac{q_g R}{2m\delta k} \cdot \frac{I_0(mR) - 1}{I_1(mR)} \approx \frac{q_g R^2}{4\delta k} \frac{1 + (mR)^2/16}{1 + (mR)^2/8} \quad (3)$$

for small values of the parameter  $mR$ , where  $m = \sqrt{h/\delta k}$ . Here,  $q_g$  is the average heat flux per unit area sensed by the gage foil, computed as  $-k(dT/dr) \cdot 2\delta/R$  at  $r = R$ . [There is a typographical error in the corresponding expression of Borell and Diller (1987).] Note that  $\Delta T_c$  is less than  $\Delta T_r$  when  $q_r = q_g$ . Alternatively, if  $\Delta T_c = \Delta T_r$ , i.e., when the gage

output is the same in the pure convective and pure radiative environments,  $q_g$  is greater than  $q_r$ .

The heat transfer measurements that are usually of interest are those sensed by the *surface* or *wall*, not by the water-cooled gage. In this respect, two important points should be noted. First, the foil temperature is maximum at the center, which continuously decreases with radius to its base temperature at  $r = R$ . Therefore, the local heat transfer rate on the foil varies with radius, and it has an average value of  $q_g$  over the entire foil. This needs to be corrected to the heat flux sensed by the wall in the absence of the gage, denoted by  $q_c$ . Second, the gage base temperature ( $T_B$ ) is usually a fixed value because of water-cooling. If the surrounding surface temperature ( $T_w$ ) is different, one more correction must be made. The case of  $T_w \neq T_B$  is discussed in a later section.

The gage output gives a value of  $q_r$  when using a purely radiation-based calibration chart. When  $T_w = T_B$ , the analysis shows that

$$\frac{q_c}{q_r} = \frac{(mR/2)^2 I_o(mR)}{I_o(mR) - 1} \cong \frac{1 + (mR/2)^2}{1 + (mR/4)^2} \quad (4)$$

### 3 Mixed Heat Transfer With $T_w = T_B$

In many situations, the total heat flux to a surface has both convective and radiative components. In this case, the temperature difference between the foil center and the edge is given by

$$\Delta T_m = \left( \frac{T_B - T_\infty - q'_r/h}{I_o(mR)} + T_\infty + q'_r/h \right) - T_B = \frac{q_g R}{2m\delta k} \cdot \frac{I_o(mR) - 1}{I_1(mR)} \quad (5)$$

and the average heat transfer per unit area sensed by the gage is expressed as

$$q_g = -k \cdot \frac{T_B - T_\infty - q'_r/h}{I_o(mR)} \cdot m I_1(mR) \cdot \frac{2\delta}{R} \quad (6)$$

Note that Eq. (5) is similar to Eq. (3) with a different definition of  $q_g$ . If a calibration based on radiation is used to deduce the heat flux from the measurement of  $\Delta T_m$ , then  $\Delta T_m$  is equated to  $\Delta T_r$ , and the result is given by

$$\frac{q_g}{q_r} = \frac{mR}{2} \frac{I_1(mR)}{I_o(mR) - 1} \quad (7)$$

Finally, the *wall-sensed*, mixed heat transfer per unit area for  $T_w = T_B$  can be expressed as

$$q_m = q'_r + h(T_\infty - T_B) = q_r \frac{(mR/2)^2 I_o(mR)}{I_o(mR) - 1} \cong q_r \frac{1 + (mR/2)^2}{1 + (mR/4)^2} \quad (8)$$

which has a similar form to Eq. (4).

The ratio  $q_m/q_r$  is the correction that needs to be applied when a calibration chart based on only radiative heat flux is available. Figure 2 shows  $q_m/q_g$ ,  $q_g/q_r$ , and  $q_m/q_r$  ratios as a function of the parameter  $mR$ . Figure 3 shows the heat flux ratios as a function of  $h$  to further illustrate the dependence of the correction on  $h$ .

### 4 Mixed Heat Transfer With $T_w \neq T_B$

When  $T_w$  is not equal to  $T_B$ , an additional correction is needed to deduce wall-sensed heat transfer from the gage-sensed heat transfer. The relations for wall-sensed heat transfer ( $q_m$ ) remain the same as in the case for mixed heat transfer with  $T_w = T_B$ , given by Eq. (8). The wall-sensed heat transfer with  $T_w \neq T_B$  is expressed as

$$q_w = q_m + h(T_\infty - T_w) \quad (9)$$

In order to evaluate the measurement error caused by using

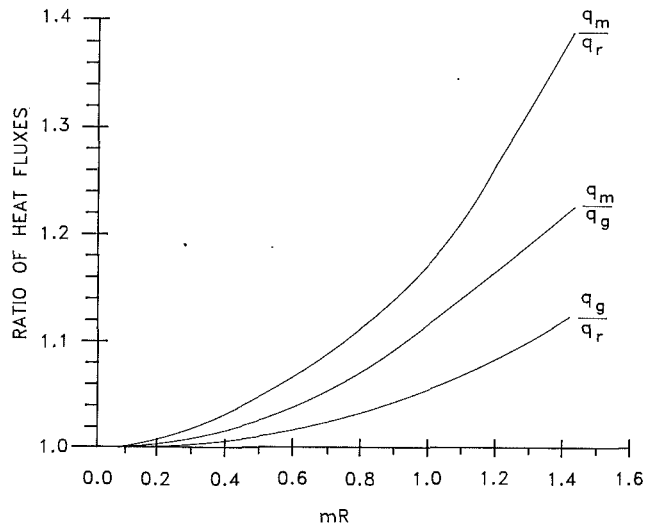


Fig. 2 Ratios of heat fluxes in the mixed convection-radiation environment as a function of the dimensionless parameter  $mR$ . The ratio  $q_m/q_r$  indicates the difference (error) between the actual heat flux sensed by the surface and the heat flux indicated by the gage using radiation-based calibration, with  $T_w = T_B$ .

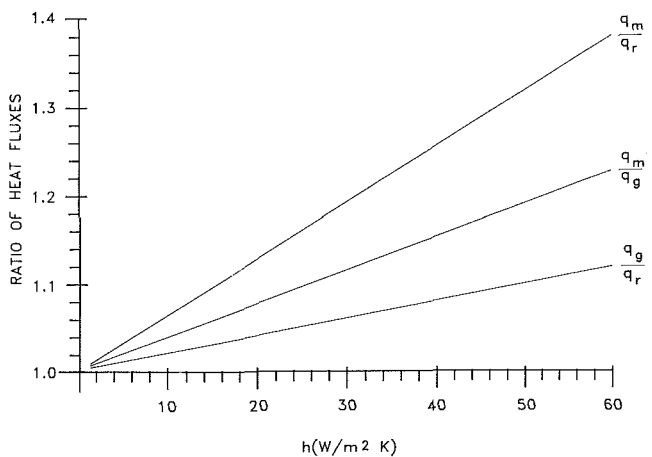


Fig. 3 Ratios of the fluxes in the mixed convection-radiation environment as a function of the heat transfer coefficient for a gage having  $\delta = 12.7 \mu\text{m}$ ,  $R = 3.11 \text{ mm}$ ,  $k = 23 \text{ W/mk}$ , with  $T_w = T_B$

the radiation-based calibration,  $q_r$  is compared with  $q_w$  and the following relation is obtained:

$$\frac{q_r - q_w}{q_r} = \frac{q_r - q_m}{q_r} + \frac{q_m - q_w}{q_r} = 1 - \frac{(mR)^2}{4} \frac{I_o(mR)}{I_o(mR) - 1} + \frac{h(T_w - T_B)}{q_r} \quad (10)$$

The value of  $T_w$  can be measured directly in experiments, and  $h$  has to be either known or estimated to obtain the correction to derive  $q_w$  from  $q_r$ . A series of curves is plotted for  $(q_r - q_w)/q_r$  versus  $h$  with parametric curves for several values of wall temperature  $T_w$  and two values of  $q_r$  in Fig. 4 using  $T_B = 300 \text{ K}$ .

### Discussion

The standard calibration charts for a Gardon gage are usually prepared using a radiative heat source. When the gage is used to measure heat flux to a surface in a mixed convective-radiative heat transfer environment, the calibration is not appropriate. This happens because the gage foil temperature is not uniform. Also, during a measurement of total heat flux to a heated surface, the gage base is normally kept at a constant

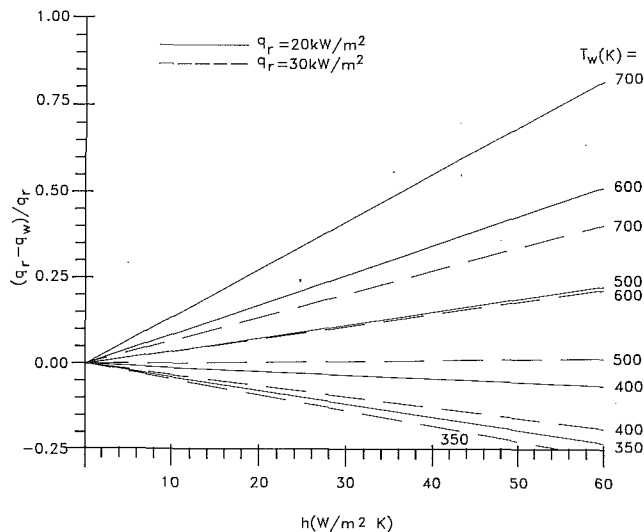


**Fig. 4** Relative difference (error) caused by using radiation-based calibration for a gage subjected to a mixed convection-radiation environment as a function of the heat transfer coefficient for two different values of  $q_r$  and several values of surface temperature ( $T_w$ ). Here,  $T_B = 300$  K,  $\delta = 12.7 \mu\text{m}$ ,  $R = 3.11$  mm, and  $k = 23$  W/mK.

temperature using cooling water, and therefore, it becomes isolated from the surrounding surface. In order to estimate the true heat flux to the surface, corrections must be applied to the heat flux that is obtained from the radiation-based calibration.

When the local wall temperature is equal to the heat sink, the error involved in the measurement of the mixed or convective heat flux is only a function of the dimensionless parameter,  $mR$  ( $=\sqrt{h/k\delta} \cdot R$ ). From Figs. 2 and 3, it is clear that a smaller  $mR$  value introduces a smaller error, and that the circular foil radius has a greater effect on the magnitude of error than the heat transfer coefficient according to the definition of  $mR$  itself. Therefore, a smaller diameter foil for the gage is preferable to reduce the measurement errors. The gage sensitivity, however, will be inevitably reduced due to the smaller foil diameter and the experimentalist must weight the relative advantages of sensitivity and calibration errors, which have opposite trends of dependence on the foil diameter.

Another important result revealed by the results of analysis for mixed heat transfer with  $T_w = T_B$  as shown in Figs. 3 and 4 is that the correction in the measurement of mixed heat transfer using a radiation-based calibration (expressed as the ratio of  $q_m$  and  $q_r$ ) is *independent of the fraction of convective heat flux in the total heat flux and it only depends on the magnitude of  $h$* . That is, if  $h$  is fixed, the correction to be applied does not depend on whether the heat flux is predominantly convective or predominantly radiative. It may also be noted that Figs. 3 and 4 are applicable in absence of radiation, i.e., for purely convective heat flux environment.

Figure 4 shows the importance of correcting the heat flux measurement when  $T_w \neq T_B$  for  $T_B = 300$  K. The convective heat feedback to a surface can be substantially different at higher  $h$  if the difference between  $T_w$  and  $T_B$  is large. As discussed earlier, there can be flow "tripping" if there is a large difference between  $T_w$  and  $T_B$  resulting in a different local value of  $h$  (Young et al., 1983). The experimentalist should be aware of either avoiding such a situation (for example, by keeping  $T_w$  as close to  $T_B$  as possible) or by properly accounting for the difference in local  $h$ .

Another concern here is how to estimate  $h$  for making the correction. In this situation, one may resort to a trial-and-error estimate of  $h$  in which a value of  $h$  is first assumed, the total heat flux is then derived, the convective part of it is then computed if radiative heat flux is known (or if it is zero),  $h$  is

calculated based on the equation  $q_c = h(T_w - T_\infty)$ , which is then compared with the first assumption, until converged. A second possibility is to estimate  $h$  independently and check for the sensitivity of the heat flux value to the variation in  $h$  and then decide whether to resort to a completely new method of heat flux measurement.

## Summary and Conclusions

When a Gardon gage is used to measure convective or mixed heat flux, there is an error encountered in the measurement if the gage output is converted into heat flux using a calibration based on radiative heat flux. A theoretical analysis is presented to determine the error caused by the use of radiation-based calibration in the measurement of total heat flux that includes convective and radiative components, and in a situation where the wall temperature does not match the gage heat sink temperature. In case of mixed heat transfer, the error depends on the heat transfer coefficient *irrespective* of the magnitude of the fraction of convective heat flux in the total flux. An additional correction is necessary if the wall temperature is not the same as the base temperature. A sensor having smaller foil radius is preferable to reduce the error involved in the measurement of convective heat transfer and mixed heat transfer.

## References

- Ash, R. L., 1969, "Response Characteristics of Thin Foil Heat Flux Sensors," *AIAA J.*, Vol. 7, No. 12, pp. 2332-2335.
- Borell, G. J., and Diller, T. E., 1987, "A Convection Calibration Method for Local Heat Flux Gages," *ASME JOURNAL OF HEAT TRANSFER*, Vol. 109, pp. 83-89.
- Gardon, R., 1953, "An Instrument for Direct Measurement of Intense Thermal Radiation," *Rev. Sci. Instruments*, Vol. 24, No. 5, pp. 366-370.
- Keltner, N. R., and Wildin, M. W., 1975, "Transient Response of Circular Foil Heat Flux Gages to Radiative Fluxes," *Rev. Sci. Instruments*, Vol. 46, pp. 1161-1166.
- Kuo, C. H., and Kulkarni, A. K., 1991, "Analysis of Heat Flux Measurement by Circular Foil Gages in a Mixed Convection/Radiation Environment," *ASME/JSME Joint Thermal Engineering Conference*, Reno, NV, Mar. 17-22.
- Saito, K., Williams, F. A., Wichman, I. S., and Quintiere, J. G., 1989 "Upward Turbulent Flames Spread on Wood Under External Radiation," *ASME JOURNAL OF HEAT TRANSFER*, Vol. 111, pp. 438-445.
- Young, M. F., LaRue, J. C., and Koency, J. E., 1983, "Effect of Free Velocity Vector on the Output of a Circle Disk Heat Flux Gage," *ASME Paper No. 83-HT-58*.

## Evaluation of Direct-Exchange Areas for a Cylindrical Enclosure

J. Sika<sup>1</sup>

### Introduction

Direct-exchange areas are needed for zonal analysis. In a system with absorptive medium the direct-exchange areas for pairs of surface and volume zones are difficult to calculate, which particularly curbs the use of the zone method. The definition relationships for direct-exchange areas are generally given by four- and sixfold integrals, which in concrete geometric applications can mostly be expressed only numerically. This multiplicity of integrals results in considerable duration of the computation and moreover, in many instances, in an uncontrollable loss of precision of the results obtained. If the

<sup>1</sup>National Research Institute for Machine Design, Prague, Czechoslovakia.

Contributed by the Heat Transfer Division of THE AMERICAN SOCIETY OF MECHANICAL ENGINEERS. Manuscript received by the Heat Transfer Division September 12, 1990; revision received March 1, 1991. Keywords: Radiation, Radiation Interactions.

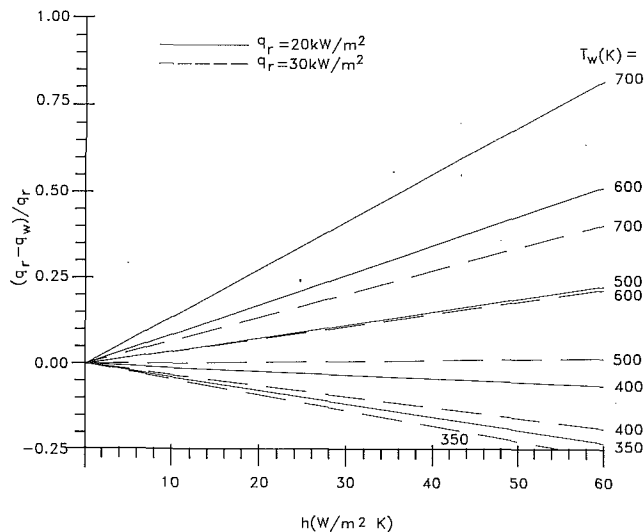


**Fig. 4** Relative difference (error) caused by using radiation-based calibration for a gage subjected to a mixed convection-radiation environment as a function of the heat transfer coefficient for two different values of  $q_r$  and several values of surface temperature ( $T_w$ ). Here,  $T_B = 300$  K,  $\delta = 12.7 \mu\text{m}$ ,  $R = 3.11$  mm, and  $k = 23$  W/mK.

temperature using cooling water, and therefore, it becomes isolated from the surrounding surface. In order to estimate the true heat flux to the surface, corrections must be applied to the heat flux that is obtained from the radiation-based calibration.

When the local wall temperature is equal to the heat sink, the error involved in the measurement of the mixed or convective heat flux is only a function of the dimensionless parameter,  $mR$  ( $=\sqrt{h/k\delta} \cdot R$ ). From Figs. 2 and 3, it is clear that a smaller  $mR$  value introduces a smaller error, and that the circular foil radius has a greater effect on the magnitude of error than the heat transfer coefficient according to the definition of  $mR$  itself. Therefore, a smaller diameter foil for the gage is preferable to reduce the measurement errors. The gage sensitivity, however, will be inevitably reduced due to the smaller foil diameter and the experimentalist must weight the relative advantages of sensitivity and calibration errors, which have opposite trends of dependence on the foil diameter.

Another important result revealed by the results of analysis for mixed heat transfer with  $T_w = T_B$  as shown in Figs. 3 and 4 is that the correction in the measurement of mixed heat transfer using a radiation-based calibration (expressed as the ratio of  $q_m$  and  $q_r$ ) is *independent of the fraction of convective heat flux in the total heat flux and it only depends on the magnitude of  $h$* . That is, if  $h$  is fixed, the correction to be applied does not depend on whether the heat flux is predominantly convective or predominantly radiative. It may also be noted that Figs. 3 and 4 are applicable in absence of radiation, i.e., for purely convective heat flux environment.

Figure 4 shows the importance of correcting the heat flux measurement when  $T_w \neq T_B$  for  $T_B = 300$  K. The convective heat feedback to a surface can be substantially different at higher  $h$  if the difference between  $T_w$  and  $T_B$  is large. As discussed earlier, there can be flow "tripping" if there is a large difference between  $T_w$  and  $T_B$  resulting in a different local value of  $h$  (Young et al., 1983). The experimentalist should be aware of either avoiding such a situation (for example, by keeping  $T_w$  as close to  $T_B$  as possible) or by properly accounting for the difference in local  $h$ .

Another concern here is how to estimate  $h$  for making the correction. In this situation, one may resort to a trial-and-error estimate of  $h$  in which a value of  $h$  is first assumed, the total heat flux is then derived, the convective part of it is then computed if radiative heat flux is known (or if it is zero),  $h$  is

calculated based on the equation  $q_c = h(T_w - T_\infty)$ , which is then compared with the first assumption, until converged. A second possibility is to estimate  $h$  independently and check for the sensitivity of the heat flux value to the variation in  $h$  and then decide whether to resort to a completely new method of heat flux measurement.

## Summary and Conclusions

When a Gardon gage is used to measure convective or mixed heat flux, there is an error encountered in the measurement if the gage output is converted into heat flux using a calibration based on radiative heat flux. A theoretical analysis is presented to determine the error caused by the use of radiation-based calibration in the measurement of total heat flux that includes convective and radiative components, and in a situation where the wall temperature does not match the gage heat sink temperature. In case of mixed heat transfer, the error depends on the heat transfer coefficient *irrespective* of the magnitude of the fraction of convective heat flux in the total flux. An additional correction is necessary if the wall temperature is not the same as the base temperature. A sensor having smaller foil radius is preferable to reduce the error involved in the measurement of convective heat transfer and mixed heat transfer.

## References

- Ash, R. L., 1969, "Response Characteristics of Thin Foil Heat Flux Sensors," *AIAA J.*, Vol. 7, No. 12, pp. 2332-2335.
- Borell, G. J., and Diller, T. E., 1987, "A Convection Calibration Method for Local Heat Flux Gages," *ASME JOURNAL OF HEAT TRANSFER*, Vol. 109, pp. 83-89.
- Gardon, R., 1953, "An Instrument for Direct Measurement of Intense Thermal Radiation," *Rev. Sci. Instruments*, Vol. 24, No. 5, pp. 366-370.
- Keltner, N. R., and Wildin, M. W., 1975, "Transient Response of Circular Foil Heat Flux Gages to Radiative Fluxes," *Rev. Sci. Instruments*, Vol. 46, pp. 1161-1166.
- Kuo, C. H., and Kulkarni, A. K., 1991, "Analysis of Heat Flux Measurement by Circular Foil Gages in a Mixed Convection/Radiation Environment," *ASME/JSME Joint Thermal Engineering Conference*, Reno, NV, Mar. 17-22.
- Saito, K., Williams, F. A., Wichman, I. S., and Quintiere, J. G., 1989 "Upward Turbulent Flames Spread on Wood Under External Radiation," *ASME JOURNAL OF HEAT TRANSFER*, Vol. 111, pp. 438-445.
- Young, M. F., LaRue, J. C., and Koency, J. E., 1983, "Effect of Free Velocity Vector on the Output of a Circle Disk Heat Flux Gage," *ASME Paper No. 83-HT-58*.

## Evaluation of Direct-Exchange Areas for a Cylindrical Enclosure

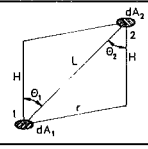
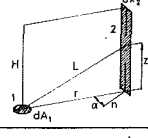
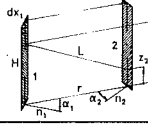
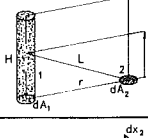
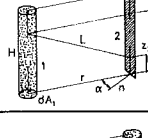
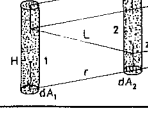
J. Sika<sup>1</sup>

### Introduction

Direct-exchange areas are needed for zonal analysis. In a system with absorptive medium the direct-exchange areas for pairs of surface and volume zones are difficult to calculate, which particularly curbs the use of the zone method. The definition relationships for direct-exchange areas are generally given by four- and sixfold integrals, which in concrete geometric applications can mostly be expressed only numerically. This multiplicity of integrals results in considerable duration of the computation and moreover, in many instances, in an uncontrollable loss of precision of the results obtained. If the

<sup>1</sup>National Research Institute for Machine Design, Prague, Czechoslovakia. Contributed by the Heat Transfer Division of THE AMERICAN SOCIETY OF MECHANICAL ENGINEERS. Manuscript received by the Heat Transfer Division September 12, 1990; revision received March 1, 1991. Keywords: Radiation, Radiation Interactions.

Table 1 Direct-exchange areas for zone elements

| Configuration  | Direct-exchange area   |
|--|--|
|   | $d\bar{s}_{12} = \frac{1}{\pi} \frac{H^2}{(r^2 + H^2)^2} e^{-K\sqrt{r^2 + H^2}} dA_1 dA_2$   |
|   | $d\bar{s}_{12} = \frac{1}{\pi} r \cos\alpha \int_{L=r}^{\sqrt{r^2 + H^2}} \frac{e^{-KL}}{L^3} dL dA_1 dx_2$  |
|   | $d\bar{s}_{12} = \frac{2}{\pi} r^2 \cos\alpha_1 \cos\alpha_2 \int_{L=r}^{\sqrt{r^2 + H^2}} \left( \frac{H}{\sqrt{L^2 - r^2}} - 1 \right) \frac{e^{-KL}}{L^3} dL dx_1 dx_2$ |
|   | $\frac{d\bar{g}_{12}}{K} = \frac{1}{\pi} \int_{L=r}^{\sqrt{r^2 + H^2}} \frac{e^{-KL}}{L^2} dL dA_1 dA_2$   |
|   | $\frac{d\bar{g}_{12}}{K} = \frac{2}{\pi} r \cos\alpha \int_{L=r}^{\sqrt{r^2 + H^2}} \left( \frac{H}{\sqrt{L^2 - r^2}} - 1 \right) \frac{e^{-KL}}{L^2} dL dA_1 dx_2$        |
|  | $\frac{d\bar{g}_{12}}{K^2} = \frac{2}{\pi} \int_{L=r}^{\sqrt{r^2 + H^2}} \left( \frac{H}{\sqrt{L^2 - r^2}} - 1 \right) \frac{e^{-KL}}{L} dL dA_1 dA_2$                     |

integrals can be reduced analytically, there is a significant increase in the computing effectiveness. Methods to reduce the integrals to evaluate direct-exchange areas for rectangular zones are tackled by, e.g., Oppenheim and Bevans (1960), Becker (1977), and Siddal (1986).

For a cylindrical space only numerical results are available (Erkku, 1959) and tabulated by Hottel and Sarofim (1967). However, these results are derived only for a constant modulus of zone dimension and distance in both the radial and axial directions and for the discrete values of absorption coefficient. Therefore, the uses of Erkku's results are very limited.

A method for calculating the radiative heat transfer direct-exchange areas for surface-to-surface, volume-to-surface, and volume-to-volume pairs of zones in axisymmetric cylindrical geometries was developed. With this method the calculation of the direct-exchange areas can be transformed from the original four-, five-, and sixfold integrals in the defining relations to just single and/or double integrals. Gray gas with absorption coefficient  $K$  is assumed.

**Analysis**

The relationships for the direct-exchange areas in cylindrical enclosure are derived by integration in two directions: axial and radial.

*Elements of Zones.* The resulting differential direct-exchange areas after axial integration are shown in Table 1. For strip-to-strip, gas tube-to-strip, and tube-to-tube, double integrals to single integrals were reduced, changing the order of integration. The variable  $L$  (the separating distance of surface and volume elements) is used for the substitution of distances  $z_1$  and  $z_2$ .

*Basic Zone Configurations.* Exchange areas between two finite zones can be obtained by integrating the exchange areas shown in Table 1 along the radial direction. The resulting direct-exchange areas are shown in Table 2. These basic zone configurations consist of two axial disks, disk and cylinder wall, cylinder wall to itself, cylindrical gas volume and disk, cylindrical gas volume-to-cylinder wall, and two cylindrical volumes immersed in each other.

As an example, the evaluation of the direct-exchange area  $\bar{s}_{12}$  for two axial disks can be described (Fig. 1). Assuming that  $R_1 \leq R_2$ , the element  $dA_1 = \rho d\rho d\omega$  moves inside the area  $A_1$  along the circle with radius  $\rho$ . The element area  $dA_2 = r dr d\alpha$  draws circles (at  $0 < r \leq R_2 - \rho$ ) or circular arches (at  $R_2 - \rho < r \leq R_2 + \rho$ ) with center  $dA_1$  and radius  $r$ . Using  $d\bar{s}_{12}$  from Table 1, the direct-exchange area  $\bar{s}_{12}$  can be described as a sum of two fourfold integrals:

$$\bar{s}_{12} = \frac{1}{\pi} \int_{\omega=0}^{2\pi} \int_{\rho=0}^{R_1} \int_{r=0}^{R_2-\rho} \int_{\alpha=0}^{2\pi} \rho r F d\alpha dr d\rho d\omega + \frac{2}{\pi} \int_{\omega=0}^{2\pi} \int_{\rho=0}^{R_1} \int_{r=R_2-\rho}^{R_2+\rho} \int_{\alpha=0}^{\alpha_{\max}} \rho r F d\alpha dr d\rho d\omega \quad (1)$$

where

$$F = \frac{H^2}{(r^2 + H^2)^2} e^{-K\sqrt{r^2 + H^2}} \quad (2)$$

In both integrals integration can be performed using the independent variables  $\omega$  and  $\alpha$ . After integration we get two twofold integrals

$$\frac{\bar{s}_{12}}{4} = \pi \int_{\rho=0}^{R_1} \int_{r=0}^{R_2-\rho} \rho r F dr d\rho + \int_{\rho=0}^{R_1} \int_{r=R_2-\rho}^{R_2+\rho} \rho r F \alpha_{\max} dr d\rho \quad (3)$$

Reversing the order of integration we obtain a sum of four twofold integrals. In all four integrals integration can be made using the independent variable  $\rho$ . After integration and modification there will be a sum of two single integrals

$$\bar{s}_{12} = \int_{r=R_2-R_1}^{R_2+R_1} r M F dr + 2\pi R_1^2 \int_{r=0}^{R_2-R_1} r F dr \quad (4)$$

where

$$M = 2R_1^2 \cos^{-1} \frac{R_1^2 - R_2^2 + r^2}{2R_1 r} + 2R_2^2 \cos^{-1} \frac{R_2^2 - R_1^2 + r^2}{2R_2 r} - \sqrt{[(R_2 + R_1)^2 - r^2][r^2 - (R_2 - R_1)^2]} \quad (5)$$

Equation (4) will reach the final shape in Table 2 through substituting

$$r^2 = R_1^2 + R_2^2 - 2R_1 R_2 \cos \beta \quad (6)$$

for the first integral and

$$r = H \tan \beta \quad (7)$$

for the second. After introducing  $R_{\min}$ , the resultant relationship will be valid for an arbitrary mutual size relation of the radii  $R_1$  and  $R_2$  where  $R_{\min}$  is the smaller of the two. For the case of  $R_1 = R_2$ , i.e., for two identical disks, the second integral in  $\bar{s}_{12}$  is zero and the direct-exchange area is given only by a single very simple onefold integral.

The radial integrations for cylindrical gas volume-to-disk and for two cylindrical gas volumes in Table 2 are analogous as for the two-disk description, arising from the pattern on Fig. 1 and using relationships from Table 1. Performing a radial integration for the disk-to-cylinder wall and for the cylindrical gas volume-to-wall, the element  $dA_1$  from Table 1 moves inside the disk with radius  $R_1$  and element  $dx_2$  along the perimeter of cylinder wall. The direct-exchange area for the cylinder wall to itself will be obtained through integration of the relationship for strip-to-strip from Table 1 with elements

Table 2 Direct-exchange areas for zones in basic configurations

| Configuration | Direct-exchange area   |
|---------------|--|
|               | $\overline{s_1 s_2} = 2R_1 R_2 H^2 \int_0^\pi \int_0^\psi \frac{e^{-K\sqrt{r^2+H^2}}}{(r^2+H^2)^2} d\beta + 2\pi R_{\min}^2 \int_0^\pi \sin\beta \cos\beta e^{-KH/\cos\beta} d\beta$   |
|               | $\overline{s_1 s_2} = R_1^2 R_2^2 \int_0^\pi \int_0^\psi \left[ \frac{e^{-Kr}}{r^4} - \frac{e^{-K\sqrt{r^2+H^2}}}{(r^2+H^2)^2} \right] d\beta + 2\pi \frac{R_1^2 R_2^2}{(R_1+R_2)^2} \int_0^\pi \sin\beta \cos\beta e^{-K(R_1+R_2)/\cos\beta} d\beta$  |
|               | $\overline{s_1 s_1} = 2 \int_0^\pi \int_0^\psi r^2 (\tan\psi - \tan\phi) \cos^2\phi e^{-Kr/\cos\phi} d\phi d\beta$   |
|               | $\frac{\overline{s_1 s_2}}{K} = \frac{R_1 R_2}{2} \int_0^\pi \left[ (2Pr^2 + UR_1^2 R_2^2) \left[ \frac{e^{-Kr}}{r^3} - \frac{e^{-K\sqrt{r^2+H^2}}}{\sqrt{(r^2+H^2)^3}} \right] d\beta + \pi \frac{R_1^2 R_2^2}{R_1+R_2} \int_0^\pi \sin\beta e^{-K(R_1+R_2)/\cos\beta} d\beta + \pi R_{\min}^2 \left[ e^{-KL} dL - \left( 1 - \frac{H^2}{L^2} \right) e^{-KL} dL \right] \right]$ |

|  |  |
|--|--|
|  | $\frac{\overline{s_1 s_2}}{K} = 8R_1^2 R_2^2 \int_0^\pi \int_0^\psi \frac{\sin\beta}{r} (\tan\psi - \tan\phi) \cos\phi e^{-Kr/\cos\phi} d\phi d\beta$  |
|  | $\frac{\overline{s_1 s_2}}{K^2} = 4R_1 R_2 \int_0^\pi \int_0^\psi (\tan\psi - \tan\phi) e^{-Kr/\cos\phi} d\phi d\beta + 2\pi R_{\min}^2 \left\{ \frac{\sqrt{(R_2-R_1)^2+H^2}}{ R_2-R_1 } \left[ L^2 - (R_2-R_1)^2 - 2H\sqrt{L^2 - (R_2-R_1)^2} \right] \frac{e^{-KL}}{L} dL + (2H-L) e^{-KL} dL + \frac{\sqrt{(R_2-R_1)^2+H^2}}{H} \left[ (H-L)^2 \frac{e^{-KL}}{L} dL \right] \right\}$ |
| <p>Parameters:</p> $P = \left( R_1^2 \cos^2 \frac{R_1 - R_2 \cos\beta}{r} + R_2^2 \cos^2 \frac{R_1 - R_2 \cos\beta}{r} - R_1 R_2 \sin\beta \right) \sin\beta$ <p>- for <math>R_1 = R_2 = R</math> is <math>P = R^2 (\pi - \beta - \sin\beta) \sin\beta</math></p> $U = (2\beta - \sin 2\beta) \sin\beta$ $r = \sqrt{R_1^2 + R_2^2 - 2R_1 R_2 \cos\beta}$ <p>- for <math>R_1 = R_2 = R</math> is <math>r = 2R \sin(\beta/2)</math></p> $\psi = \tan^{-1} \frac{H}{r}$ $R_{\min} = \min\{R_1, R_2\}$ |  |

$dx_1$  and  $dx_2$  moving along the perimeter of cylinder wall. Using appropriate algebraic substitutions, in all the cases of radial integration, the order of integration can be changed, and then integration can be performed.

Setting the absorption coefficient  $K$  to zero, the first three direct-exchange areas  $\overline{s_1 s_2}$  in Table 2 can be integrated and these results can be modified to existing analytical view factor expressions (e.g., Hottel and Sarofim, 1967).

**General Zone Configuration.** The standard rules of the exchange area algebra (e.g., Hottel and Sarofim, 1967) in connection with Eq. (A5) in the appendix make it very simple to evaluate the direct-exchange areas in arbitrary mutual location of the zones with the use of the direct-exchange areas for the basic zone configurations in Table 2.

The resulting computing relationships are shown in Table 3. These are simple summation equations from which it becomes evident that the values of the direct-exchange areas of the universally located pairs of zones are given by the sum of direct-exchange areas obtained for the corresponding basic zone configurations from Table 2 with changing parameters  $X_i$ ,  $Y_j$ , and  $Z_k$ . The values  $X_i$ ,  $Y_j$ ,  $Z_k$  and  $\xi_i$ ,  $\xi_j$ ,  $\xi_k$  are substituted according to the list in Table 4.

The equations in Table 3 are valid for the exchange areas for configurations such as in Fig. 2 with cases of partial or complete overlapping of surfaces and volumes in the axial direction too. Arising from the rule (A5), the zone distance can be in these cases denoted alternatively by the dimension  $H$  or the dimension “(H),” as shown on Fig. 2.

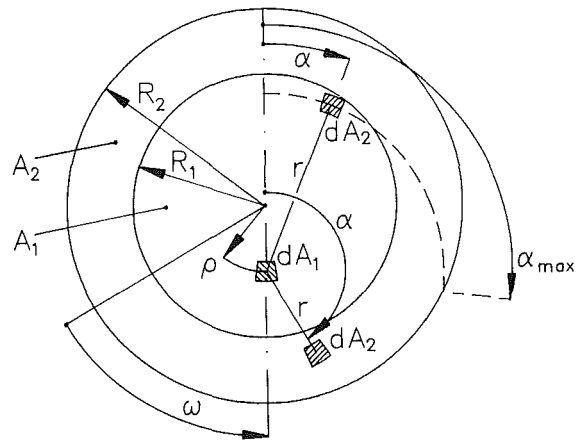


Fig. 1 Radial integration pattern for two disks, for gas-to-disk, and for two cylindrical gas volumes in Table 2

**Verifying the Relationships**

The derived relationships determine reliably the direct-exchange areas for practically any size and mutual zone configuration with arbitrarily selected values of the gas absorption coefficient. To give some source of comparison, numerical results of direct-exchange areas computation between pairs of surface and volume zones designed for parameters identical with tabulated values according to Erkkü (1959) were evaluated. The 20-point Gauss integration formula was chosen. It was observed that the agreement with all of Erkkü's results is



Table 3 Direct-exchange areas for zones in universal configurations. The index  $l_o$  marks the corresponding direct-exchange areas from Table 2.

| Configuration | Direct-exchange area  |
|---------------|---|
|               | $\overline{s_1 s_2}(R_1, B_1, R_2, B_2, H) =$ $= \sum_{i=1}^2 \sum_{j=1}^2 \xi_i \xi_j \overline{s_1 s_2} _o(X_i, Y_j, H)$  |
|               | $\overline{s_1 s_2}(R_1, H_1, R_2, B_2, H) =$ $= \sum_{j=1}^2 \sum_{k=1}^2 \xi_j \xi_k \overline{s_1 s_2} _o(R_1, Y_j, Z_k)$  |
|               | $\overline{s_1 s_2}(R, H_1, H_2, H) =$ $= \frac{1}{2} \sum_{k=1}^4 \xi_k \overline{s_1 s_2} _o(R, Z_k)$   |
|               | $\overline{g_1 g_2}(R_1, B_1, H_1, R_2, B_2, H) =$ $= \sum_{i=1}^2 \sum_{j=1}^2 \sum_{k=1}^2 \xi_i \xi_j \xi_k \overline{g_1 g_2} _o(X_i, Y_j, Z_k)$                  |
|               | $\overline{g_1 g_2}(R_1, B_1, H_1, R_2, H_2, H) =$ $= \frac{1}{2} \sum_{i=1}^2 \sum_{k=1}^4 \xi_i \xi_k \overline{g_1 g_2} _o(X_i, R_2, Z_k)$                         |
|               | $\overline{g_1 g_2}(R_1, B_1, H_1, R_2, B_2, H_2, H) =$ $= \frac{1}{2} \sum_{i=1}^2 \sum_{j=1}^2 \sum_{k=1}^4 \xi_i \xi_j \xi_k \overline{g_1 g_2} _o(X_i, Y_j, Z_k)$ |

Table 4 Coefficients of equations in Table 3

|                       | i, j, k |             |             |                   |
|-----------------------|---------|-------------|-------------|-------------------|
|                       | 1       | 2           | 3           | 4                 |
| $X_i$                 | $R_1$   | $R_1 - B_1$ |             |                   |
| $Y_j$                 | $R_2$   | $R_2 - B_2$ |             |                   |
| $Z_k$                 | $H$     | $ H - H_1 $ | $ H - H_2 $ | $ H - H_1 - H_2 $ |
| $\xi_i, \xi_j, \xi_k$ | +1      | -1          | -1          | +1                |

perfect. Only one figure, the direct-exchange area  $\overline{gg}$  for self-irradiated gas cylinder with  $R = H = B$ , differed for  $KB = 0$  from Erkku's result by about 5 percent. This discrepancy might have arisen only from a better computer and a better numerical scheme utilized by the present evaluations.

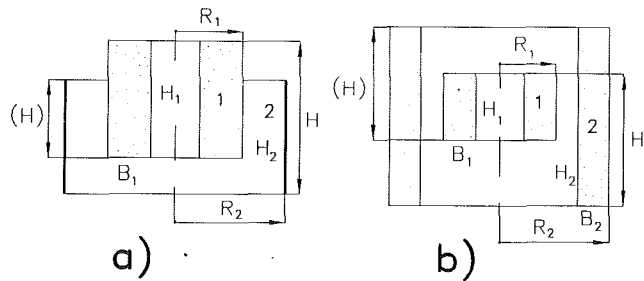


Fig. 2 Zone configuration marking in the case of (a) partial and (b) complete zone overlapping in axial direction

## Conclusions

Simple formulae for calculating direct-exchange areas in axisymmetric cylindrical enclosures are developed. The new formulations reduce computational efforts substantially for the zonal analysis, allowing for an arbitrary zoning of cylindrical volumes. These exchange areas may be evaluated with a high degree of accuracy. The zone method can be now applied with the confidence that the overall radiative energy balance will be satisfied.

## References

- Becker, H. B., 1977, "A Mathematical Solution for Gas-to-Surface Radiative Exchange Area for a Rectangular Parellelepiped Enclosure Containing a Gray Medium," ASME JOURNAL OF HEAT TRANSFER, Vol. 99, pp. 203-207.
- Erkku, H., 1959, Sc.D. Thesis in Chemical Engineering, M.I.T., Cambridge, MA.
- Hottel, H. C., and Sarofim, A. F., 1967, *Radiative Transfer*, McGraw-Hill, New York.
- Oppenheim, A. K., and Bevans, J. T., 1960, "Geometric Factors for Radiative Heat Transfer Through an Absorbing Medium in Cartesian Co-ordinates," ASME JOURNAL OF HEAT TRANSFER, Vol. 86, pp. 360-368.
- Siddal, R. G., 1986, "Accurate Evaluation of Radiative Direct-Exchange Areas for Rectangular Geometries," *Proceedings of the Eight International Heat Transfer Conference*, San Francisco, CA, pp. 751-756.

## APPENDIX

### A Generalized Rule of Exchange Area Algebra

Figure 3(a) shows an example of the surface zones 1 and 2 having parallel sides of identical length  $X$  in the  $x$  directions. The functional dependence of  $\overline{s_1 s_2}$  on length  $X$  will be

$$\overline{s_1 s_2} = \overline{s s_o}(X) \quad (A1)$$

For the generally positioned zones 1 and 2 plotted in Fig. 3(b), the direct-exchange area can be expressed (with the use of imaginary zones 3, 4, 5, and 6) as

$$\overline{s_1 s_2} = \frac{1}{2} [\overline{s_{1+3} s_{2+4+6}} - \overline{s_{3+5} s_{2+4}} - \overline{s_{1+3} s_{4+6}} + \overline{s_3 s_4}] \quad (A2)$$

i.e., by direct-exchange area values of basic zone configuration (A1) at varying length  $X$ . If zones 1 and 2 overlap in the  $x$  direction, as indicated in Fig. 3(c) and/or 3(d), the direct-exchange area can be expressed again in the same way by the basic zone configuration values,

$$\overline{s_1 s_2} = \frac{1}{2} [\overline{s_{1+3} s_{2+4}} - \overline{s_{1a} s_4} - \overline{s_3 s_{2a}} + \overline{s_{1b} s_{2b}}] \quad (A3)$$

for the configuration shown in Fig. 3(c), and/or

$$\overline{s_1 s_2} = \frac{1}{2} [\overline{s_{1a+1b} s_{2+4}} - \overline{s_{1a} s_4} - \overline{s_{1c} s_6} + \overline{s_{1b+1c} s_{2+6}}] \quad (A4)$$

for zones 1 and 2 in Fig. 3(d). Using the description of dimensions and zone positions from Figs. 3(b), 3(c), and 3(d) and the functional dependence (A1), we can write the expressions (A2) to (A4) as a universal relationship

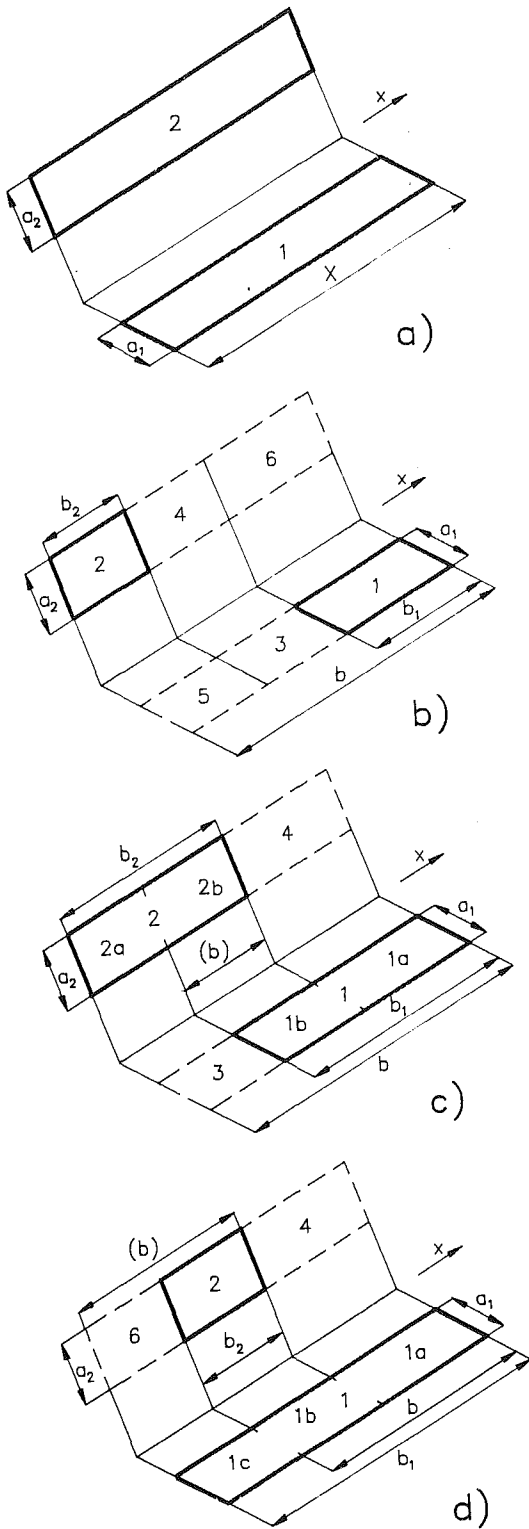


Fig. 3 Scheme for derivation of generalizing rule (A5)

$$\overline{s_1 s_2} = \frac{1}{2} [\overline{s s_0}(b) - \overline{s s_0}(|b - b_1|) - \overline{s s_0}(|b - b_2|) + \overline{s s_0}(|b - b_1 - b_2|)] \quad (\text{A5})$$

With overlapping zones, we can, according to Fig. 3(c) and Fig. 3(d), alternatively substitute into (A5) for distance  $b$  the

dimension marked “(b)”. Using it, the same result will be reached.

The derived simple generalized rule (A5) is independent of the absorptivity function of the medium between the zones and is valid also, e.g., for two parallel cylinders, band-to-rectangular rod, etc. This rule can be applied not only to pairs of surface zones, but similarly to direct-exchange areas of volume-to-surface zones  $gs$  and volume-to-volume zones  $gg$ .

## Accelerating the Hemi-Cube Algorithm for Calculating Radiation Form Factors

H. E. Rushmeier,<sup>1</sup> D. R. Baum,<sup>2</sup> and D. E. Hall<sup>3</sup>

### Introduction

The calculation of form factors for the analysis of radiation heat transfer is computationally expensive when surfaces are not in full view of one another. For an enclosure of  $N$  surfaces,  $N^2$  factors are needed. Brute force methods require  $O(N^3)$  time to compute the required factors (Walton, 1987). A few methods have been introduced that reduce the time to  $O(N^{2+x})$  where  $x$  is on the order of 0.3 (Emery et al., 1988). The hemi-cube algorithm (Cohen and Greenberg, 1985) calculates the  $N^2$  factors in  $O(N^2)$  time. Because of its lower time complexity, the hemi-cube method is efficient for problems with large numbers of surfaces. In this note, methods to improve the hemi-cube algorithm by taking advantage of graphics hardware and two types of geometric coherence are presented. The implementation of the methods on a computer workstation is described, and timings demonstrating speedups by factors of up to 6.7 are given.

The acceleration of the calculation of form factors is not an isolated computational problem. The ability to calculate form factors very quickly can alter the overall computational methodology used to analyze radiant heat transfer, and can greatly extend the complexity of geometries that can be studied.

### Review of the Hemi-Cube Algorithm

The hemi-cube algorithm approximates the form factor  $F_{ij}$  from an area  $A_i$  to area  $A_j$  by the factor from a differential area  $dA_i$  at the center of area  $A_i$ :

$$F_{ij} \cong \int_{A_j} \cos \theta_i \cos \theta_j dA_j / \pi r_{ij}^2$$

where the angles  $\theta_i$  and  $\theta_j$  are measured respectively from the surface normals at  $dA_i$  and  $dA_j$  to a line joining the two differential areas, and  $r_{ij}$  is the distance between  $dA_i$  and  $dA_j$ . Surfaces in the enclosure are subdivided to make this approximation valid.

The hemi-cube method is based on Nusselt's unit sphere method. The hemisphere in Nusselt's method is replaced by a hemi-cube, as shown in Fig. 1. The sides of the hemi-cube are

<sup>1</sup>George W. Woodruff School of Mechanical Engineering, Georgia Institute of Technology, Atlanta, GA 30332-0405; Assoc. Mem. ASME.

<sup>2</sup>Silicon Graphics Computer Systems, Mountain View, CA 94039-7311.

<sup>3</sup>George W. Woodruff School of Mechanical Engineering, Georgia Institute of Technology, Atlanta, GA 30332-0405.

Contributed by the Heat Transfer Division of THE AMERICAN SOCIETY OF MECHANICAL ENGINEERS. Manuscript received by the Heat Transfer Division September 12, 1990; revision received April 2, 1991. Keywords: Numerical Methods, Radiation.

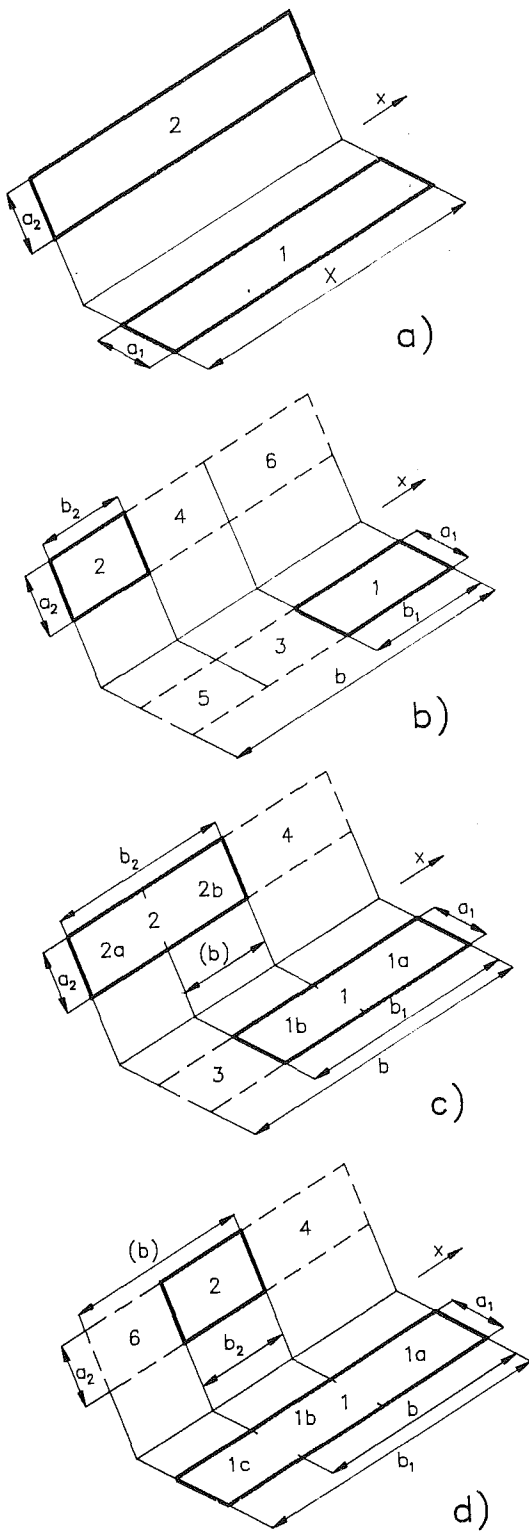


Fig. 3 Scheme for derivation of generalizing rule (A5)

$$\overline{s_1 s_2} = \frac{1}{2} [\overline{s s_0}(b) - \overline{s s_0}(|b - b_1|) - \overline{s s_0}(|b - b_2|) + \overline{s s_0}(|b - b_1 - b_2|)] \quad (\text{A5})$$

With overlapping zones, we can, according to Fig. 3(c) and Fig. 3(d), alternatively substitute into (A5) for distance  $b$  the

dimension marked “(b)”. Using it, the same result will be reached.

The derived simple generalized rule (A5) is independent of the absorptivity function of the medium between the zones and is valid also, e.g., for two parallel cylinders, band-to-rectangular rod, etc. This rule can be applied not only to pairs of surface zones, but similarly to direct-exchange areas of volume-to-surface zones  $gs$  and volume-to-volume zones  $gg$ .

## Accelerating the Hemi-Cube Algorithm for Calculating Radiation Form Factors

H. E. Rushmeier,<sup>1</sup> D. R. Baum,<sup>2</sup> and D. E. Hall<sup>3</sup>

### Introduction

The calculation of form factors for the analysis of radiation heat transfer is computationally expensive when surfaces are not in full view of one another. For an enclosure of  $N$  surfaces,  $N^2$  factors are needed. Brute force methods require  $O(N^3)$  time to compute the required factors (Walton, 1987). A few methods have been introduced that reduce the time to  $O(N^{2+x})$  where  $x$  is on the order of 0.3 (Emery et al., 1988). The hemi-cube algorithm (Cohen and Greenberg, 1985) calculates the  $N^2$  factors in  $O(N^2)$  time. Because of its lower time complexity, the hemi-cube method is efficient for problems with large numbers of surfaces. In this note, methods to improve the hemi-cube algorithm by taking advantage of graphics hardware and two types of geometric coherence are presented. The implementation of the methods on a computer workstation is described, and timings demonstrating speedups by factors of up to 6.7 are given.

The acceleration of the calculation of form factors is not an isolated computational problem. The ability to calculate form factors very quickly can alter the overall computational methodology used to analyze radiant heat transfer, and can greatly extend the complexity of geometries that can be studied.

### Review of the Hemi-Cube Algorithm

The hemi-cube algorithm approximates the form factor  $F_{ij}$  from an area  $A_i$  to area  $A_j$  by the factor from a differential area  $dA_i$  at the center of area  $A_i$ :

$$F_{ij} \cong \int_{A_j} \cos \theta_i \cos \theta_j dA_j / \pi r_{ij}^2$$

where the angles  $\theta_i$  and  $\theta_j$  are measured respectively from the surface normals at  $dA_i$  and  $dA_j$  to a line joining the two differential areas, and  $r_{ij}$  is the distance between  $dA_i$  and  $dA_j$ . Surfaces in the enclosure are subdivided to make this approximation valid.

The hemi-cube method is based on Nusselt's unit sphere method. The hemisphere in Nusselt's method is replaced by a hemi-cube, as shown in Fig. 1. The sides of the hemi-cube are

<sup>1</sup>George W. Woodruff School of Mechanical Engineering, Georgia Institute of Technology, Atlanta, GA 30332-0405; Assoc. Mem. ASME.

<sup>2</sup>Silicon Graphics Computer Systems, Mountain View, CA 94039-7311.

<sup>3</sup>George W. Woodruff School of Mechanical Engineering, Georgia Institute of Technology, Atlanta, GA 30332-0405.

Contributed by the Heat Transfer Division of THE AMERICAN SOCIETY OF MECHANICAL ENGINEERS. Manuscript received by the Heat Transfer Division September 12, 1990; revision received April 2, 1991. Keywords: Numerical Methods, Radiation.

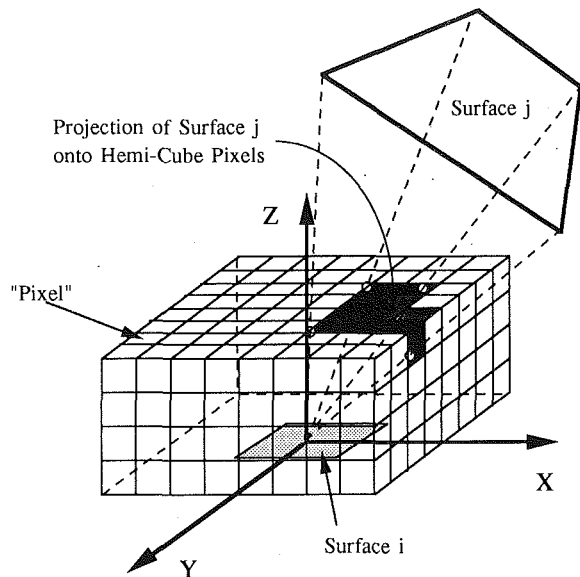


Fig. 1 Calculation of  $F_{ij}$  using a low-resolution hemi-cube

discretized into small surfaces, referred to as pixels. The form factor to each pixel, referred to as a delta-form factor, is calculated and stored in a buffer. Since the same hemi-cube is used for all surfaces, the values in the delta-form factor buffer are calculated only once.

The surface visible through each hemi-cube pixel for each differential area  $dA_i$  is found efficiently using backface elimination, the Sutherland-Hodgeman clipping algorithm, and the depth buffer algorithm. (The details of these techniques can be found in standard computer graphics texts such as Foley et al., 1990.) The result is an item buffer, in which the identifier of the surface visible through each pixel is recorded.

After the hidden surface problem has been solved, the form factors are calculated by scanning the item buffer and summing the delta form factors associated with the pixels through which a surface  $j$  is visible.

The hemi-cube algorithm is summarized in the following pseudocode:

```

FOR each hemi-cube pixel  $q$  calculate  $\Delta\text{Factor}(q)$ ;
FOR each surface  $i$ 
  FOR each hemi-cube face  $s$ 
    FOR each surface  $j$ 
       $\text{FormFactor}(ij) = 0$ ;
      Transform coordinates to system centered on  $i$  and
      oriented toward  $s$ ;
      IF (not back facing)
        Clip to viewing frustum;
        IF (portion of  $j$  inside the frustum)
          Find pixels  $p$  onto which  $j$  is projected;
          FOR each pixel  $p$ 
            IF (depth of  $j < \text{depth}(p)$ )
               $\text{item}(p) = j$ ;
               $\text{depth}(p) = \text{depth of } j$ ;
            END IF
          END FOR each pixel
        END IF portion left
      END IF not back facing
    END FOR each surface  $j$ 
  END FOR each hemi-cube face
  FOR each pixel  $q$  on the hemi-cube  $\text{FormFactor}(i, \text{item}(q)) + = \Delta\text{Factor}(q)$ ;
END FOR each surface  $i$ .

```

The  $O(N^2)$  time complexity of the algorithm is achieved by determining the effect of each surface  $j$  as an obstructor of

other surfaces as the factor  $F_{ij}$  is being computed. Inherently, any algorithm that simultaneously computes visibility and form factors cannot take advantage of the reciprocity relation used in  $O(N^3)$  and  $O(N^{2+x})$  algorithms. However, for large values of  $N$  the factor of 2 speedup from reciprocity is much smaller than the factor of  $N$  or  $N^x$  time difference between the hemi-cube algorithm and alternative methods.

The accuracy of the hemi-cube algorithm is discussed in more detail elsewhere (Baum et al., 1989). Overall, the method converges to an exact solution with the discretization of the enclosure into smaller surfaces, and the discretization of the hemi-cube into a larger number of pixels.

#### Acceleration of the Hemi-Cube Method Using Hardware

Recently computer graphics workstations have been introduced by several vendors with specialized graphics processors, which perform many of the operations required by the hemi-cube algorithm in hardware rather than software. A library of subroutine calls to the graphics hardware is provided with the workstation.

The use of the graphics hardware in the hemi-cube algorithm begins by allocating a window on the graphics screen to represent a face on the hemi-cube. The surfaces are then displayed in this window by sending the coordinates of the vertices of each surface to the graphics processor. The integer identifier of each surface is sent to the graphics processor as the color to be displayed. After all the surfaces have been displayed, the item buffer is filled by reading the color being displayed in the graphics window at each pixel.

Using graphics hardware, the pseudo-code for the loop over each surface  $i$  becomes:

```

Allocate a window on the workstation to be used as a face
of the hemi-cube;
FOR each surface  $i$ 
  FOR each hemi-cube face  $s$ 
    FOR each surface  $j$ 
       $\text{FormFactor}(ij) = 0$ ;
       $\text{Color} = j$ ;
      Send a list of vertices for surface  $j$  to the graphics
      processor;
    END for each surface  $j$ 
  END FOR each hemi-cube face
  Read the workstation window color buffer into the item
  buffer;
  FOR each pixel  $q$  on the hemi-cube  $\text{FormFactor}(i, \text{item}(q)) + = \Delta\text{Factor}(q)$ ;
END FOR each surface  $i$ .

```

Typical timing results for the software and hardware implementations of the hemi-cube algorithm are shown in Table 1. All timings are for a Silicon Graphics Personal Iris W-4D20G workstation. The timings include only the time to compute the  $N^2$  form factors, not the time to write the factors to a file, or to perform radiant transfer calculations.

Results are shown for two geometries. Geometry 1 consists of a cubical enclosure 1 unit on each side, which contains a uniformly distributed three-dimensional array of 64 cubes, each 0.1 unit on a side. Geometry 2 is the same enclosure containing two cylinders. One cylinder is centered at (0.7, 0.5, 0.5), has radius 0.1, height 0.3, and is tilted 20 deg. The other cylinder is centered at (0.3, 0.4, 0.6), has radius 0.2, height 0.4, and is tilted 30 deg. Each cylinder is discretized into 140 planar polygons. Results are given for two different levels of hemi-cube discretization. In Table 1 the speedup obtained using the hardware ranges from 1.6 for Geometry 1 using a low resolution hemi-cube to 3.5 for Geometry 2 using a higher resolution hemi-cube.

Once the vertices of a surface have been sent to the graphics processor, the operations of back face elimination, clipping and updating the depth buffer are spedup by a factor of 100

or more. However, since parts of the algorithm are still performed in software, the overall speed up obtained by using hardware is much lower. In the hardware implementation of the hemi-cube algorithm, the operations of sending the vertices to the graphics processor and adding up the delta form-factors account for essentially all of the time to compute factors.

### Accelerating the Hemi-Cube Using Spatial Coherence

The time spent sending vertices to the graphics processor can be reduced by taking advantage of spatial coherence. Groups of polygons that lie behind the current polygon can be identified, so that individual polygons in these groups do not have to be processed. Polygons can be divided into groups by sorting them into a fixed spatial grid. Polygon vertices are sent to the graphics processor only if they lie in grid elements that lie in front of the current polygon. The sorting of polygons into a spatial grid is similar to the spatial subdivision techniques used to accelerate ray tracing in computer graphics (Glassner, 1984; Fujimoto et al., 1986). Also, Emery et al. (1987), using an idea presented by Hedgeley (1982), developed a method in which surfaces were sorted into a spatial grid to identify potential obstructions between a pair of surfaces rapidly.

The pseudocode for this variation of the algorithm is:

```

FOR each surface i
  Determine which volumes in the spatial grid contain
  surface i;
  FOR each volume v which contains i add i to list of
  surfaces associated with v;
END FOR surface i
Allocate a workstation window to be used as the hemi-cube
face;
FOR each surface i
  FOR each surface j Front(j) = 0
  FOR each volume v
    IF (v or part of v is in front of i)
      FOR each surface k on the list associated with v
        Front(k) = 1;
      END FOR each volume;
    FOR each hemi-cube face s
      FOR each surface j
        FormFactor(i, j) = 0;
        Color = j;
        IF (Front(j) = 1) send a list of vertices for surface
        j to the graphics processor;
      END FOR each surface j
    END FOR each hemi-cube face
  (continue as before)
END FOR each surface i.
  
```

Typical timing results for the spatial coherence variation of the hemi-cube algorithm are given in Table 1. The overall speedup over the original software implementation of the hardware version with spatial coherence ranges from a factor of 1.9 to a factor of 3.6 for the results in Table 1. The incremental speedup over of the hardware version without coherence ranges from little more than 1.0 to 1.2. Although the factors are small, Table 1 shows that using spatial coherence always reduced the total computational time.

The spatial coherence method could also be applied to a purely software implementation of the hemi-cube. In the software implementation both the absolute time and the fraction of time spent projecting each surface onto the hemi-cube are different from the hardware version. As a result, both the absolute time saved and the factor of speedup for using spatial coherence would be different when applied to the software implementation.

Greater speedups could be obtained by determining which grid volumes will be visible through each of the five hemi-cube faces and further limiting the number of vertices that have to be sent to the graphics processor. The average number of

**Table 1 Timings for form factor calculations on a SGI Personal Iris workstation (in CPU seconds)**

| Geometry | Hemi-cube res., R* | Method** | Time | Overall speedup*** | Coherence speedup**** |
|----------|--------------------|----------|------|--------------------|-----------------------|
| 1        | 50                 | SW       | 118  | —                  | —                     |
|          |                    | HW       | 72   | 1.6                | —                     |
|          |                    | HWSC     | 60   | 2.0                | 1.2                   |
|          |                    | HWSCPC   | 54   | 2.2                | 1.3                   |
| 1        | 300                | SW       | 1353 | —                  | —                     |
|          |                    | HW       | 387  | 3.5                | —                     |
|          |                    | HWSC     | 380  | 3.6                | 1.0                   |
|          |                    | HWSCPC   | 201  | 6.7                | 1.9                   |
| 2        | 50                 | SW       | 66   | —                  | —                     |
|          |                    | HW       | 42   | 1.6                | —                     |
|          |                    | HWSC     | 35   | 1.9                | 1.2                   |
|          |                    | HWSCPC   | 32   | 2.1                | 1.3                   |
| 2        | 300                | SW       | 855  | —                  | —                     |
|          |                    | HW       | 282  | 3.0                | —                     |
|          |                    | HWSC     | 276  | 3.1                | 1.0                   |
|          |                    | HWSCPC   | 141  | 6.1                | 2.0                   |

\* Number of hemi-cube pixels =  $R^2 + 4(0.5)(0.6R \times 0.6R)$

\*\* SW = Software implementation

HW = Hardware implementation

HWSC = Hardware implementation with spatial coherence

HWSCPC = Hardware implementation with spatial coherence and pixel coherence

\*\*\* Overall speedup = (Time for software implementation)/(Time)

\*\*\*\* Coherence speedup = (Time for HW)/(Time)

vertices sent to the graphics processor for each screen could be reduced by as much as a factor of 5. The overall speedup of the form factor calculation produced by this improvement would still depend on the fraction of the overall computation time spent sending vertices to the processor.

### Accelerating the Hemi-Cube Using Pixel Coherence

Surfaces projected onto a hemi-cube tend to cover contiguous sets of pixels. Adding the delta-form factors can be sped up using this coherence by updating the value of the form factor for continuous runs of hemi-cube pixels, rather than for every pixel. Instead of storing a delta-form factor for each pixel, the cumulative form factor is stored, i.e., CumulativeFactor( $q$ ) is equal to the sum of all DeltaFactor( $q'$ ) factors for pixels 1 to  $q$ . In the loop to add delta-form factors, an addition is performed only when the value in the item buffer is different for two neighboring pixels, i.e;

Start = item(1);

OldValue = 0.

FOR each pixel  $q$  on the hemi-cube

IF (item( $q$ ) not equal to Start):

TempValue = CumulativeFactor( $q - 1$ );

FormFactor( $i$ , Start) = TempValue - OldValue;

Start = item( $q$ );

OldValue = TempValue;

END IF item( $q$ )

END FOR each pixel.

Results for the pixel coherence variation are shown in Table 1. The overall speedup over the original software implementation of the hardware version with spatial and pixel coherence ranges from 2.1 to 6.7. The incremental speedup over the basic hardware implementation ranges from 1.3 to 2.0. The speedup depends on the average number of pixels through which each polygon is viewed. Accuracy requires that each surface be visible through more than one pixel, and so this variation will always result in some speedup.

The pixel coherence variation can also be applied to the purely software implementation. In the software implementation the same absolute time is spent summing delta-form factors as in the hardware version, but this time is a smaller percentage of the overall computation time. As a result, the absolute time saved using pixel coherence would be the same

for both the software and hardware implementations but the factor of speedup would be different.

### Summary

Three methods to accelerate the hemi-cube method for finding form factors have been presented: use of graphics hardware, use of spatial coherence and use of pixel coherence. The overall speedup resulting from these methods depends on the particular enclosure studied, and the required accuracy. Results have been presented illustrating speedups of factors up to 6.7.

### Acknowledgments

This work was funded, in part, by NSF grant ECS-8909251, "Progressive Refinement Algorithms for Radiant Transfer."

### References

Baum, D. R., Rushmeier, H. E., and Winget, J. M., 1989, "Improving Radiosity Solutions Through the Use of Analytically Determined Form-Factors," *ACM Computer Graphics (Proceedings of SIGGRAPH 89)*, Vol. 23, No. 3, pp. 325-334.

Cohen, M. F., and Greenberg, D. P., 1985, "The Hemi-Cube: A Radiosity Solution for Complex Environments," *ACM Computer Graphics (Proceedings of SIGGRAPH 1985)*, Vol. 19, No. 3, pp. 31-40.

Emery, A. F., Johansson, O., and Abrous, A., 1987, "Radiation Heat Transfer Shapefactors for Combustion Systems," *Fundamentals and Applications of Radiation Heat Transfer, 24th National Heat Transfer Conference and Exhibition*, T. F. Smith and A. M. Smith, eds., ASME HTD-Vol. 72, pp. 119-126.

Emery, A. F., Johansson, O., Lobo, M., and Abrous, A., 1988, "A Comparative Study of Methods for Computing the Diffuse Radiation Viewfactors for Complex Structures," presented at the AIAA/ASME/ASCE/ASH 29th SDM Conference, Apr. 18-20, Williamsburg, VA, Paper No. AIAA-88-2223.

Foley, J. D., Van Dam, A., Feiner, S. K., and Hughes, J. F., 1990, *Computer Graphics Principles and Practices*, Addison Wesley, Reading, MA.

Fujimoto, A., Tanaka, T., and Iwata, K., 1986, "ARTS: Accelerated Ray-Tracing System," *IEEE Computer Graphics and Applications*, Vol. 6, No. 4, pp. 16-26.

Glassner, A. S., 1984, "Space Subdivision for Fast Ray Tracing," *IEEE Computer Graphics and Applications*, Vol. 4, No. 10, pp. 15-22.

Hedgeley, D. R., Jr., 1982, "A General Solution to the Hidden Line Problem," NASA Reference Pub. 1085.

Walton, G. N., 1987, "Algorithms for Calculating Radiation View Factors Between Plane Convex Polygons With Obstructions," *Fundamentals and Applications of Radiation Heat Transfer, Proceedings of the 24th National Heat Transfer Conference and Exhibition*, T. F. Smith and A. M. Smith, eds., ASME HTD-Vol. 72, pp. 45-52.